**NATIONAL CENTER FOR EARTHQUAKE
ENGINEERING RESEARCH**

State University of New York at Buffalo

Proceedings from the
Third Japan-U.S. Workshop on Earthquake
Resistant Design of Lifeline Facilities and
Countermeasures for Soil Liquefaction

Edited by

T. D. O'Rourke and M. Hamada

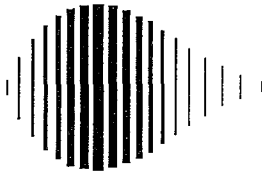Technical Report NCEER-91-0001

February 1, 1991

NOTICE

This report was prepared by the National Center for Earthquake Engineering Research (NCEER). Neither NCEER, associates of NCEER, its sponsors, nor any person acting on their behalf:

a. makes any warranty, express or implied, with respect to the use of any information, apparatus, method, or process disclosed in this report or that such use may not infringe upon privately owned rights; or

b. assumes any liabilities of whatsoever kind with respect to the use of, or the damage resulting from the use of, any information, apparatus, method or process disclosed in this report.

50272-101

REPORT DOCUMENTATION PAGE	1. REPORT NO. NCEER-91-0001	2.	3. PB91-179259

4. Title and Subtitle Proceedings from the Third Japan-U.S. Workshop on Earthquake Resistant Design of Lifeline Facilities and Countermeasures for Soil Liquefaction		5. Report Date February 1, 1991
		6.

7. Author(s) T. D. O'Rourke and M. Hamada	8. Performing Organization Rept. No.

9. Performing Organization Name and Address	10. Project/Task/Work Unit No.
	11. Contract(C) or Grant(G) No. (C) 89-3008 (G) ECE 86-07591

12. Sponsoring Organization Name and Address National Center for Earthquake Engineering Research State University of New York at Buffalo Red Jacket Quadrangle Buffalo, New York 14261	13. Type of Report & Period Covered Technical report
	14.

16. Abstract (Limit: 200 words)

As part of a joint United States-Japan research program, this conference proceedings represents the third time researchers from the United States and Japan have convened to collaborate and exchange information concerning ground deformations and ground movement effects on the performance of lifeline facilities during earthquakes. The 40 papers presented in this volume are grouped in the following major areas: ground deformation and lifeline performance during past earthquakes; analytical and experimental modeling of soil liquefaction; seismic analysis of lifelines and earthquake resistant design; earthquake countermeasures and emergency response. Also presented in this volume and based on these major areas, are the results of four working groups convened during this conference.

17. Document Analysis   a. Descriptors

b. Identifiers/Open-Ended Terms

EARTHQUAKE ENGINEERING   LIQUEFACTION   GROUND DEFORMATION
FOUNDATION PILES   LIFELINES   BURIED PIPELINES
GROUND FAILURE   DISPLACEMENT   OIL PIPELINES
BASE ISOLATION   BUCKLING
TELECOMMUNICATION NETWORKS   EARTHQUAKE RESISTANT DESIGN

c. COSATI Field/Group

18. Availability Statement Release Unlimited	19. Security Class (This Report) Unclassified	21. No. of Pages
	20. Security Class (This Page) Unclassified	22. Price

(See ANSI-Z39.18)   See Instructions on Reverse   OPTIONAL FORM 272 (4-77)
(Formerly NTS-35)

Proceedings
from the
Third Japan-U.S. Workshop on Earthquake Resistant Design of Lifeline Facilities and Countermeasures for Soil Liquefaction

held at the
Cathedral Hill Hotel
San Francisco, California
December 17-19, 1990

Technical Report NCEER-91-0001

Edited by: T.D. O'Rourke[1] and M. Hamada[2]
February 1, 1991

NCEER Project Number 89-3008

NSF Master Contract Number ECE 86-07591

1   Professor, School of Civil and Environmental Engineering, Cornell University
2   Professor, Faculty of Marine Science and Technology, Tokai University

PREFACE

It is fitting that the Third Japan-U.S. Workshop on Earthquake Resistant Design of Lifeline Facilities and Countermeasures for Soil Liquefaction was held in San Francisco. During this century, San Francisco has been subjected to the effects of three severe earthquakes in 1906, 1957, and 1989. The recent Loma Prieta earthquake caused widespread liquefaction. In addition, there was abundant evidence of site amplification as ground waves traversed from rock through overlying sediments and Recent Bay Mud to have an especially strong effect on loose fills in waterfront properties throughout the San Francisco Bay region. The Loma Prieta earthquake demonstrated how closely the performance of lifeline systems are related to site response and liquefaction-induced ground failures.

There were strong similarities between the effects of the 1906 and 1989 earthquakes. Within the City of San Francisco, the locations of most severe seismic shaking and soil liquefaction were the same. Lateral and vertical ground deformations ruptured critical water supply pipelines in both earthquakes. The lack of water and ensuing fires in 1906 resulted in the destruction of nearly 500 city blocks, which still represents the worst single fire loss in U.S. history. In 1989 liquefaction-induced ground movements again ruptured pipelines, resulting in loss of water in the Marina district, where a severe fire erupted after the earthquake.

The importance of lifelines and their vulnerability to soil liquefaction is well recognized by Japanese engineers and planners. After the 1923 Kanto earthquake, a substantial part of Tokyo burned at the same time that vital water supplies were cut by damaging ground movements from soil liquefaction.

The Third Japan-U.S. Workshop was not only an international event, but a forum for Bay Area engineers and utility personnel to learn about state-of-the-art developments and to participate in the presentations and discussions as experienced members of a community which must implement seismic resistant design of lifeline facilities and countermeasures for soil liquefaction. Accordingly, there is real and urgent business to be done. It is our hope that research results presented in these proceedings will be applied in engineering decisions and planning, and that the workshop has acted as a catalyst in promoting the transfer of technology from theory to practice.

T. D. O'Rourke
January 26, 1991

TABLE OF CONTENTS

U.S.-JAPAN COOPERATIVE RESEARCH PROGRAM AND WORKSHOPS

The U.S.-Japan Research Program on Earthquake Resistant Design of Life-line Facilities and Countermeasures for Soil Liquefaction focuses on the earthquake performance of vital systems, such as water supply, transportation, gas and liquid fuel, telecommunications, electric power, and wastewater convey-ance and treatment. Emphasis is placed on liquefaction-induced soil movements and their effects on lifelines. Currently, there is a growing recognition in the civil and earthquake engineering communities of the importance of large ground deformations, yet our understanding of the mechanisms of movement and our ability to predict magnitude and distribution of displacements are limited and in need of substantial improvement. Permanent ground movements are known to have been the most troublesome source of subsurface structural damage during previous earthquakes. Both U.S. and Japanese researchers have worked in this subject area, and it is recognized that considerable benefits will result from a cooperative effort to collect case history data and recommend analytical and design methods on the basis of a careful data review.

The program was initiated formally in November, 1988 with the signing of a Memorandum of Understanding between the Japanese and U.S. sides. The document was signed at a ceremony during a workshop in Tokyo, Japan by K. Kubo, Professor Emeritus of Tokyo University, and M. Shinozuka, Sollenberger Professor of Civil Engineering of Princeton University. Professor Kubo signed on behalf of the Association for the Development of Earthquake Prediction (ADEP), the Japanese sponsoring agency. Professor Shinozuka signed on behalf of Robert L. Ketter, then Director of the National Center for Earthquake Engineering Research (NCEER), the U.S. sponsoring agency. A second Memorandum of Understanding was signed in December, 1990 to continue the cooperative program of research. The signatures were K. Kubo, representing ADEP, and M. Shinozuka, the Director of NCEER.

The research program concentrates on case histories of both ground deformations and ground movement effects on lifeline facilities. The case histories are being collected in two volumes and will be published as a joint U.S.-Japan effort. The earthquakes included in the U.S. case history summary are: 1906 San Francisco, 1964 Alaska, 1971 San Fernando, 1979 Imperial Valley, and 1989 Loma Prieta earthquakes. The earthquakes included in the Japanese case history summary are: 1923 Kanto, 1948 Fukui, 1964 Niigata, 1983 Nihonkai-Chubu, and 1990 Philippine earthquakes. The U.S. and Japanese case history studies are being coordinated by Professor M. Hamada of Tokai University and T.D. O'Rourke of Cornell University.

The products of the research will include: 1) case history volumes with assessments of the most important geologic features, siting criteria, and struc-tural features which have influenced previous lifeline performance in response to soil displacements, 2) U.S.-Japan workshops and associated publications covering case history data, analytical modeling, and recommendations for improved practices, and 3) a technical summary and recommendations for improved modeling, siting, design, and construction of buried structures.

Major instruments for collaboration and cooperative exchange are program workshops. To date, there have been three workshops. The first was held in Tokyo and Niigata, Japan on November 16-19, 1988. The proceedings of this workshop were published by ADEP, and are available from NCEER. The second workshop was held in Buffalo and Ithaca, NY on September 26-29, 1989. The third

workshop was held in San Francisco, CA on December 17-19, 1990. This volume contains the proceedings of the third workshop.

Cooperative research between U.S. and Japanese earthquake engineers has resulted in significant new findings about the ways in which large ground deformations are caused by soil liquefaction, their influence on lifelines, and the most effective means of modeling and protecting both soils and structures in the event of a future earthquake. New developments presented and discussed at the workshops include the use of aerial photographs before and after major earthquakes to map ground displacements by photogrammetric techniques, the effects of large ground movements on water supply pipelines and fire following earthquakes, lateral movement effects and damage to pile foundations, and the most suitable modeling methods for large ground deformation and buried lifeline response.

It is hoped that the spirit of cooperation fostered by these workshops and research program will contribute to a strong and enduring relationship among Japanese and U.S. engineers. It is believed that the research accomplishments of this collaborative activity will encourage additional joint projects and lead to improved understanding and mastery in the field of earthquake engineering.

M. Hamada
Professor, Tokai University

T.D. O'Rourke
Professor, Cornell University

ACKNOWLEDGMENTS

M. Hamada
Professor, Tokai University

T.D. O'Rourke
Professor, Cornell University

Conference Organizers

I. RESEARCH ORGANIZATION

The Current Status of Studies on Ground Behavior During
Earthquakes and Earthquake-Resistant Design of Lifeline
Facilities in Japan
K. Kubo

THE CURRENT STATUS OF STUDIES ON GROUND BEHAVIOR DURING EARTHQUAKES AND EARTHQUAKE-RESISTANT DESIGN OF LIFELINE FACILITIES IN JAPAN

by Keizaburo Kubo

INTRODUCTION

The U.S.-Japan joint studies on liquefaction, the induced large ground deformations, and its effects on lifeline facilities began in December 1987 and continued until March 1990.   Over this period, workshops were held twice, once in Tokyo and once in Buffalo and Ithaca, while this workshop has been planned in San Francisco by courtesy of the U.S. side.   This is considered very significant, for reasons mentioned later.

San Francisco was struck by the 1989 Loma Prieta earthquake, resulting in damage to bridges and elevated highways. Water supply facilities and water supplies of fire service were destroyed in areas of reclaimed land. Moreover, sand volcano and subsidence of the ground also occurred. Abnormal amplification of the earthquake motion by the soft surface layer, and the resulting damage, brought earthquake engineers' attention once again to the importance of studying seismic motion amplification by the surface layer and in the irregular shape ground.

A new study project, beginning in July 1990 and expected to end in June 1993, has been undertaken. The formal title of the study is "The analysis of ground behavior during an earthquake and earthquake-proof lifeline facilities." The study is now sponsored by 27 organizations, and the special researchers who will give special support to this project are organized by members of eight universities and four public research institutes. The project is being carried out by three working groups. Group one is assigned to the study of ground behavior during an earthquake, Group two studies the dynamic behavior of pile foundations and underground structures in soft ground and their earthquake-resistant design, and Group three looks into the behavior of lifeline facilities during an earthquake and their aseismicity. A few months have passed since the study actually began and the research items to be carried out by each group were discussed, selected, and approved at the first plenary session held early in November. An outline of the work of each working group is given below.

Study of Ground Behavior During Earthquake

Past surveys of damages caused by earthquakes and records of severe earthquakes indicate that the most serious damage occurs in thick layers of soft ground, and also that in such areas, earthquake motion is amplified

1

compared with that in hard ground. Recently, array observations of earthquakes motions have been made at many sites, confirming that earthquake motion in the irregular shape ground shows a peculiar distribution. On the basis of this knowledge, the work of Group one was selected as follows.

1)   To develop a characteristic analysis model for earthquake motion in soft ground, to numerically simulate the earthquake motion experienced in the Cypress area during the 1989 Loma Prieta earthquake, and to compare the simulation results with the observed behavior.

2)   To analyze the seismic response of the irregular shape ground and to investigate examples of damage to structures on the same type of ground.

3)   To continue studies on the mechanism of large deformations, as liquefaction of the ground and induced large ground deformations occurred in an earthquake in Luzon, the Philippines, in 1990.

Study into the Dynamic Behavior of Pile Substructures and Underground Structures in Soft Ground, and Their Earthquake-Resistant Designs

The dynamic resistance of piles and the dynamic interaction between soil and substructures are the important areas of study in the field of earthquake engineering. An understanding of these effects, especially in soft ground, is essential if the damage caused by an earthquake is to be reduced. In this project, and beginning with a survey of the reports on this theme, numerical analysis on non-linear seismic response of piles, and other substructures and liquefaction effect on them will be studied, and examples of damage will be used to rationalize earthquake-resistant design of inground structures.

Study Into the Behavior of Lifeline Facilities During an Earthquake and Their Earthquake-Resistant Designs

Since a modern citizen's life depends so critically on lifeline facilities such as electricity, water, and gas, damage to such facilities would plunge society in a disaster-stricken area into confusion. To improve the earthquake-resistance of lifeline facilities, the forces and the ultimate bearing load acting on facilities in ground subject to a large deformation will be studied. A numerical analysis of lifeline facilities in soft ground and irregular shape ground will be prepared. It is planned to summarize the results of the study, and to propose guidelines for earthquake-resistant design. Further, in order to develop a method of analyzing the loss of function of the system and its recovery process, an algorithm will be created and a general purpose library set up.

SUMMARY AND CONCLUSIONS

The U.S.-Japan joint studies on liquefaction, large ground deformation, and its effects on lifeline facilities began in December 1987 and ended this March. Excellent results were obtained through the presentation of study papers, discussions, and actual measurements of ground displacement (using aerial photogrammetry technique) in the 1964 Alaska earthquake and the 1971 San Fernando earthquake. Preparations for the study committee within the Association for Development of Earthquake Prediction (ADEP) on the analysis of ground behavior during an earthquake and the earthquake-resistance of lifeline facilities are now taking place as a part of joint study with the National Center for Earthquake Engineering Research (NCEER). Most members of the ADEP study committee participated in the survey mission of the Luzon earthquake in the Philippines in 1990 and were able to obtain new data on ground liquefaction. We are planning to increase the depth of the U.S.-Japan joint study on liquefaction in sandy ground and the analysis of the resulting damage. We believe that the results of this study will not only benefit the U.S.-Japan study but will also contribute to the development of earthquake engineering in the world.

Finally, I would like to express my thanks for the efforts of all members of the ADEP study committee and also say how indebted I am to the chairmen of the three working groups, Dr. T. Iwatate, Prof. H. Watanabe, and Prof. M. Hamada. Moreover, I extend my gratitude to those who worked to prepare this U.S.-Japan workshop, especially Prof. M. Shinozuka, Director of the NCEER and Prof. T.D. O'Rourke, of Cornell University.

II. EXPERIENCE DURING PAST EARTHQUAKES

ESTIMATION OF EARTHQUAKE DAMAGE TO LIFELINE SYSTEMS IN JAPAN

by

MASANORI HAMADA
Professor
Department of Civil Engineering
School of Marine Science and Technology
Tokai University, Shimizu, Japan

ABSTRACT

Large-scale development projects are now proceeding on the waterfront in many major Japanese cities, including Tokyo and Osaka. These waterfront projects are often conducted on soft ground reclaimed from the sea or a river. In the 1989 Loma Prieta earthquake, lifeline facilities were seriously damaged as a result of liquefaction of reclaimed land in the San Francisco Bay area. The Loma Prieta earthquake taught us the importance of earthquake-resistant design of structures on and in reclaimed ground. Accordingly, local governments such as Tokyo Metropolitan Government and the companies providing lifelines services, such as electricity and gas companies, are now energetically studying ways of estimating damage to such structures and facilities resulting from a strong future earthquake. Pre-earthquake measures to reinforce facilities and post-earthquake recovery strategies are also being investigated based on the results of the damage estimations. In these studies, the effects on lifeline facilities of liquefaction-induced ground displacement are also being examined. This paper describes the current status of damage estimation of lifeline facilities, including estimations of the loss of function and the research subjects still to be solved in making these estimations in Japan.

ESTIMATION OF EARTHQUAKE DAMAGE
TO
LIFELINE SYSTEMS IN JAPAN

by Masanori Hamada

Professor
Dept. of Civil Engineering
School of Marine Science and Technology
Tokai University, Shimizu, Japan

INTRODUCTION

Large-scale development projects are now proceeding on the waterfront in many major Japanese cities, including Tokyo and Osaka. These waterfront projects are often conducted on soft ground reclaimed from the sea or a river. In the 1989 Loma Prieta earthquake, lifeline facilities were seriously damaged as a result of liquefaction of reclaimed land in the San Francisco Bay area. The Loma Prieta earthquake taught us the importance of earthquake-resistant design of structures on and in reclaimed ground. Accordingly, local governments such as Tokyo Metropolitan Government and the companies providing lifeline services, such as electricity and gas companies, are now energetically studying ways of estimating damage to such structures and facilities resulting from a strong future earthquake. Pre-earthquake measures to reinforce facilities and post-earthquake recovery strategies are also being investigated based on the results of the damage estimations. In these studies, the effects on lifeline facilities of liquefaction-induced ground displacement are also being examined. This paper describes the current status of damage estimation of lifeline facilities, including estimations of the loss of function and the research subjects still to be solved in making these estimations in Japan.

DAMAGE ESTIMATION OF LIFELINE FACILITIES AND SYSTEM FUNCTION

The damage estimation of lifeline facilities, the loss of the function, and the recovery process follows the work flow shown in Figure 1. Lifeline facilities are generally distributed over a wide area, so seismic activity is surveyed for the whole area and an anticipated earthquake, the subject of the study, is determined based on the survey. For cities on the Pacific coast, such as Tokyo and Osaka, an undersea earthquake of the magnitude 8 class and an inland one of magnitude 7 class with the hypocenter right under a city, are sometimes assumed. If the earthquake under the ocean is assumed, the effects of tsunami must be taken into consideration because some lifeline facilities such as thermal power stations are located on the coast.

The earthquake motion on the bedrock throughout the area on which lifeline facilities are distributed is estimated by using attenuation formulae. In this case, correct estimation of the earthquake motion in the neighborhood of faults will be one of the important subjects, for the reason described later.

The next step is to estimate the earthquake motion on the ground surface as well as in the ground by dynamic response analysis, the input for which is the earthquake motion on the bedrock. Besides acceleration, velocity, and displacement, it is required to determine the relative displacement and strain in order to estimate the damage to buried lifeline facilities.
Since lifeline facilities are distributed over a wide area, the area of interest is generally divided into meshes with a size of 1 kilometer to 500 meters, and the earthquake motion for each mesh, where the ground conditions is assumed to be uniform, is calculated. For example, the ground in Tokyo area is divided into about 10,000 meshes as shown in Figure 2 with 150 kinds of ground conditions.

Based on the calculated earthquake motion on the surface and in the ground, the probability of liquefaction and slope sliding is examined. Since many areas of Japan's large coastal cities are constructed on reclaimed land, the exact estimation of liquefaction potential is one of the key subjects for damage estimation of lifeline facilities. The damage to lifeline facilities is estimated based on the calculated earthquake motion, by taking into the consideration the effects of ground failure such as liquefaction.

The damage degree to facilities is generally represented as a probabilistic value. For example, the damage degree of buried pipes is given as the average number of failures per unit length of pipe or as the damage probability of connection point with the manhole pipe.

As for the effects of liquefaction, we must consider the permanent ground displacements, subsidence, heaving, and floating up of manholes. In places where lifeline pipes cross a river, the effects of the subsidence of the embankment behind bridge abutments must also be taken into consideration.

The following two methods can be used to obtain a damage probability.
The first method is by empirical formulae obtained by statistically analyzing the damage caused to lifeline facilities in past earthquakes. For example, the following empirical formula is proposed for the buried pipes.

$$R_f = C_G \cdot C_L \cdot C_P \cdot C_E \cdot R_s \tag{1}$$

R_f: Damage probability of buried pipes
R_s: Standard damage probability
C_G: Correction factor by ground condition
C_L: Correction factor by liquefaction
C_P: Correction factor by pipe's material and diameter
C_E: Correction factor by strength of earthquake motion

Figure 3 shows damage rate of buried pipes (mean number of the failure points per 1 km) obtained from 1971 San Fernando and 1978 Miyagiken-Oki earthquakes. From these data the standard damage probability can be determined. However,

most of the damage resulting from these earthquakes were caused to pipes with a relatively small diameter and low strength, so it is necessary to make a correction to the standard damage probability according to strength and ductility when it is applied to strong, large-diameter pipes.

Recently, large-diameter steel pipes or ductile iron pipes with flexible joints have come into wide use for lifeline system mains. It is one of the most difficult subjects to determine a correction factor suitable for these pipes, since almost no actual damage data are available.

The second method of the evaluation of the damage probability of facilities is to compare the stress, the strain and the deformation which are calculated based on predicted earthquakes with the ultimate strength of the facilities. Figure 4 shows the process of calculating the damage probability for buried pipes. Besides the relative ground displacement and the ground strain resulting from earthquake motion, the permanent ground displacement due to liquefaction is taken into consideration in the calculation of the stress, the strain and the deformation of buried pipes.

The functionality of lifeline system after an earthquake is evaluated based on the damage estimation of the facilities. A lot of numerical methods of network analysis have been proposed. However, practical networks of lifeline facilities consists of an enormous number of elements and such an analysis covering all elements is actually impossible. Thus, to achieve the objectives, some simplifications are conducted by taking into account the characteristics of the network. An electricity supply substation, for example, consists of many transformers, circuit breakers, and other components, but is substituted by a simple system with fewer elements upon the judgement of experts.

The post-earthquake recovery strategy right after an earthquake is studied on the basis of estimated damage to facilities and the function. The recovery process is simulated in accordance with several probable recovery strategies and based on the simulation the best strategy is chosen by referring to expert's opinions. The pre-earthquake policy for the reinforcing facilities is also determined by the damage estimation and by the simulation of recovery process.

FURTHER SUBJECTS ON EARTHQUAKE RESISTANCE OF LIFELINE SYSTEMS

The areas needing future study to enable accurate damage estimation of lifeline facilities and their functions are described below.

Earthquake Motion in the Neighborhood of Fault

Many attenuation formulae, which take earthquake magnitude and epicentral or hypocentral distance as functions for estimating earthquake motion, have been proposed. Some examples are shown in Figure 5. Most of the earthquake

records which were used to develop these attenuation formulae were collected relatively far from the earthquake fault during large or medium-magnitude earthquakes, or were measured during small-magnitude earthquakes. Earthquake motions which are recorded near faults are insufficient to establish a reliable attenuation formula. Thus, ground motions within an epicentral distance of 0-20 km due to earthquakes with a magnitude of 7-8 are estimated by extrapolation.

When an inland earthquake occurs, some facilities are inevitably located in the fault zone because lifeline facilities are distributed over a wide area. The damage probability for facilities in the fault zone is high, and the degree of damage to those facilities has a great influence on the overall functioning of the system. Therefore, one of the most important tasks is to estimate correctly the earthquake motion in a fault zone for the damage estimation of lifeline facilities.

Dynamic Response of Soft Ground

Figure 6 shows an example of a maximum acceleration map for the ground surface. This map was used by the Tokyo Metropolitan Government to estimate the damage resulting from a future earthquake in the metropolitan area. The maximum acceleration was calculated by non-linear dynamic analysis. According to this map, the maximum acceleration in Shinjuku Ward, on the diluvial plateau, is greater than that in Koto Ward along the Sumida River on alluvial low land. This map shows that the acceleration on soft ground is less than that on firm ground.

In the Loma Prieta earthquake, the acceleration on reclaimed land around San Francisco Bay was two to three times greater than that on firm ground. And in the 1985 Mexico City earthquake, too, acceleration was amplified significantly on land reclaimed from the lake in the city and many tall buildings were seriously damaged.

Figure 7 shows maximum accelerations on the ground surface and on the bedrock as measured on reclaimed land around Tokyo Bay. The maximum acceleration on reclaimed land is two to three times greater than that on the bedrock. It seems that the maximum acceleration given in Figure 6 somewhat contradicts the actually measured accelerations in Figure 7.

The results of a dynamic analysis of reclaimed land in Tokyo, shown in Figures 8 and 9, illustrate this contradiction. Figure 8 shows the ground conditions and the numerical model. Figure 9 shows the acceleration on the surface calculated by non-linear response analysis using the R.O. model. The calculated maximum acceleration on the surface is 121 Gal, assuming the maximum acceleration on the bedrock to be 100 Gal. Some amplification of earthquake motion from the bedrock to the ground surface can be seen. However, the surface acceleration becomes 156 Gal, if the maximum acceleration on the bedrock is 200 Gal, so the amplification factor is less than 1.0. The reason for this is that, for a larger acceleration on the bedrock, the natural period of the ground increases and the damping effect is enhanced by the more significant influence of non-linear soil

9

characteristics. Consequently, the accelerations on soft ground are estimated to be less than those on firm ground, as shown in Figure 6.

The probable reasons for the underestimated acceleration on the soft ground are as follows.

1) Evaluation of soil properties for the analysis is not adequate. In particular, there may be problems in evaluating the damping coefficient.

2) The numerical model is not adequate. One-dimensional models such as SHAKE are generally used for the calculation of the ground acceleration. In these numerical models, the effect of seismic waves propagating in a horizontal direction, which are caused by variations in ground conditions are not taken into consideration.

In order to carry out accurate damage estimation of lifeline facilities, it is critical that earthquake motion of soft ground such as reclaimed land be evaluated. Research activity on this subject must take the form of analysis of observed earthquake motions on soft ground, such as those recorded during the Loma Prieta earthquake.

Liquefaction-Induced Permanent Ground Displacement

The author and his research team reported that liquefied ground was displaced as much as several meters in the horizontal direction, depending on topographical conditions, at the time of the 1983 Nihonkai-Chubu earthquake.[1] Since that research, case studies of liquefaction-induced ground displacements caused by eight earthquakes in Japan and the U.S. have been conducted by the Japan U.S. joint research team.[2],[3],[4] Moreover, the ground displacements resulting from liquefaction during the 1990 Philippines earthquake have also been surveyed. On the basis of these case studies, the topographical and soil conditions under which liquefied soil is moved can be summarized as shown in Figure 10.

The mechanism of liquefaction-induced ground displacement has been studied by analyzing the collected data as well as by numerical and experimental studies. However, no mechanism which gains a consensus of researchers has been found so far.

Only the following empirical formula has been proposed;

$$D = 0.75 \sqrt{H} \sqrt[3]{\theta}$$

        D: Liquefaction-induced ground displacement (m)
        H: Thickness of liquefied soil layer
        θ: Gradient of ground surface or of liquefied soil layer

Estimating the effects of liquefaction-induced displacements on lifeline facilities, especially on buried pipes, requires accurate estimates of the displacement magnitude, its direction and the distribution pattern. To make this information available, the mechanism of ground displacement needs to be

fully clarified. Model tests using shaking tables are now being undertaken at the Public Works Research Institute of the Ministry of Construction, at the Central Research Institute of the Electric Power Industry, Tokai University, and in other places, while work on numerical models to calculate the permanent ground displacement is proceeding.

Effects of Permanent Ground Displacement on Lifeline Facilities

Many buried pipes and foundation piles were damaged by liquefaction-induced ground displacement during the 1964 Niigata and 1983 Nihonkai-Chubu earthquakes. The effects of liquefaction on lifeline facilities are as follows.

1)   Settlement and inclination of structures due to reduction of the ground's bearing capacity.

2)   Floating of underground structures such as manholes due to buoyancy in the liquefied soil.

3)   Liquefaction-induced permanent ground displacement.

Effects 1) and 2) are already taken into consideration in the earthquake-resistant design of facilities, but the effects of permanent ground displacement 3) are at present not considered.

When large permanent ground displacements, with a magnitude of several meters, are considered in the earthquake-resistant design of buried pipes, two matters become a problem. One is whether the response displacement method, which has conventionally been used for the design of underground structures, is applicable or not. And if it is applicable, there is also the problem of how to evaluate the spring coefficient of partially liquefied ground.

The other is the evaluation of the ultimate strength of facilities. It is impossible to design the facilities using the conventional allowable-stress method when the permanent displacement is several meters, and information on the ultimate strength of lifeline facilities such as buried pipes is insufficient at present.

The former problem has been studied in an experiment on a pile foundation model in liquefied soil, and it was reported that the force acting on the pile during lateral movement of liquefied soil is similar to the drag force in a liquid. The second problem is now being studied in bearing tests on piles and pipes.

CONCLUSIONS

In this paper, the current status of damage estimation of lifeline facilities in Japan and problems needing solution in future are described. As stated in

the introduction, large-scale waterfront projects have already progressed greatly in major cities. To create an earthquake-proof urban society, the study of damage to lifeline facilities must proceed much more quickly.

References

1) M. Hamada et al., Study on Liquefaction-Induced Permanent Ground Displacements, Association for the Development of Earthquake Prediction, November 1986, Tokyo, Japan.

2) T.L. Youd and S.F. Bartlet, U.S. Case Histories of Liquefaction-Induced Ground Displacement, Proceedings of 1st Japan-U.S. Workshop on Liquefaction, Large Ground Deformation and Their Effect on Lifeline Facilities, November 1988, Tokyo, Japan.

3) M. Hamada, K. Wakamatsu and S. Yasuda, Liquefaction-Induced Ground Displacement during the 1948 Fukui Earthquake, Proceedings of 2nd U.S.-Japan Workshop on Liquefaction, Large Ground Deformation and Their Effects on Lifelines.

4) T.D. O'Rourke, B.L. Roth and M. Hamada, A Case Study of Large Ground Deformation during the 1971 San Fernando Earthquake, Proceedings of 2nd U.S.-Japan Workshop on Liquefaction, Large Ground Deformation and Their Effects on Lifelines.

```
                        ┌─────────────────────┐
                        │ Survey on Earthquake│
          ┌─────────────┤ Activity and Determi-│
          │             │ nation of Earthquake │
          │             │ for Study            │
          │             └─────────────────────┘
          │                        │
          │                        ▼────── (Attenuation Formula)
          │                        │
   ┌──────▼──────┐       ┌─────────────────────┐
   │ Effects     │       │ Estimation of Earth-│
   │ of          │       │ quake Motion on     │
   │ Tsunami     │       │ Bedrock             │
   └─────────────┘       └─────────────────────┘
                                    │
                                    ▼────── (Zoning and Classification
                                    │          of Ground Condition)
                         ┌─────────────────────┐
                         │ Estimation of Earth-│
                         │ quake Motion on     │
                         │ Ground Surface and  │
                         │ in Ground           │
                         └─────────────────────┘
                                    │  1
   ┌─────────────────────┐  2  ┌─────────────────┐
   │ Estimation of Ground│────▶│ Estimation of   │
   │ Failure; Liquefaction│    │ Damage to       │
   │ and Slope Sliding   │    │ Lifeline        │
   └─────────────────────┘    │ Facilities      │
                              └─────────────────┘
┌─────────────────────┐  ┌─────────────────┐  ┌─────────────────────┐
│ Policy for Reinforce-│  │ Estimation of Loss│  │ Establishment of   │
│ ment of Facilities   │◀─│ of System's      │  │ Strategy for        │
│ Before the Next      │  │ Function         │──│ Recovery After      │
│ Earthquake           │  │                  │  │ an Earthquake       │
└─────────────────────┘  └─────────────────┘  └─────────────────────┘
                              │
                         ┌─────────────────┐
                         │ Simulation of   │◀──
                         │ Recovery Process│
                         └─────────────────┘
```

Figure 1   General Flow of Damage Estimation of Lifeline Systems
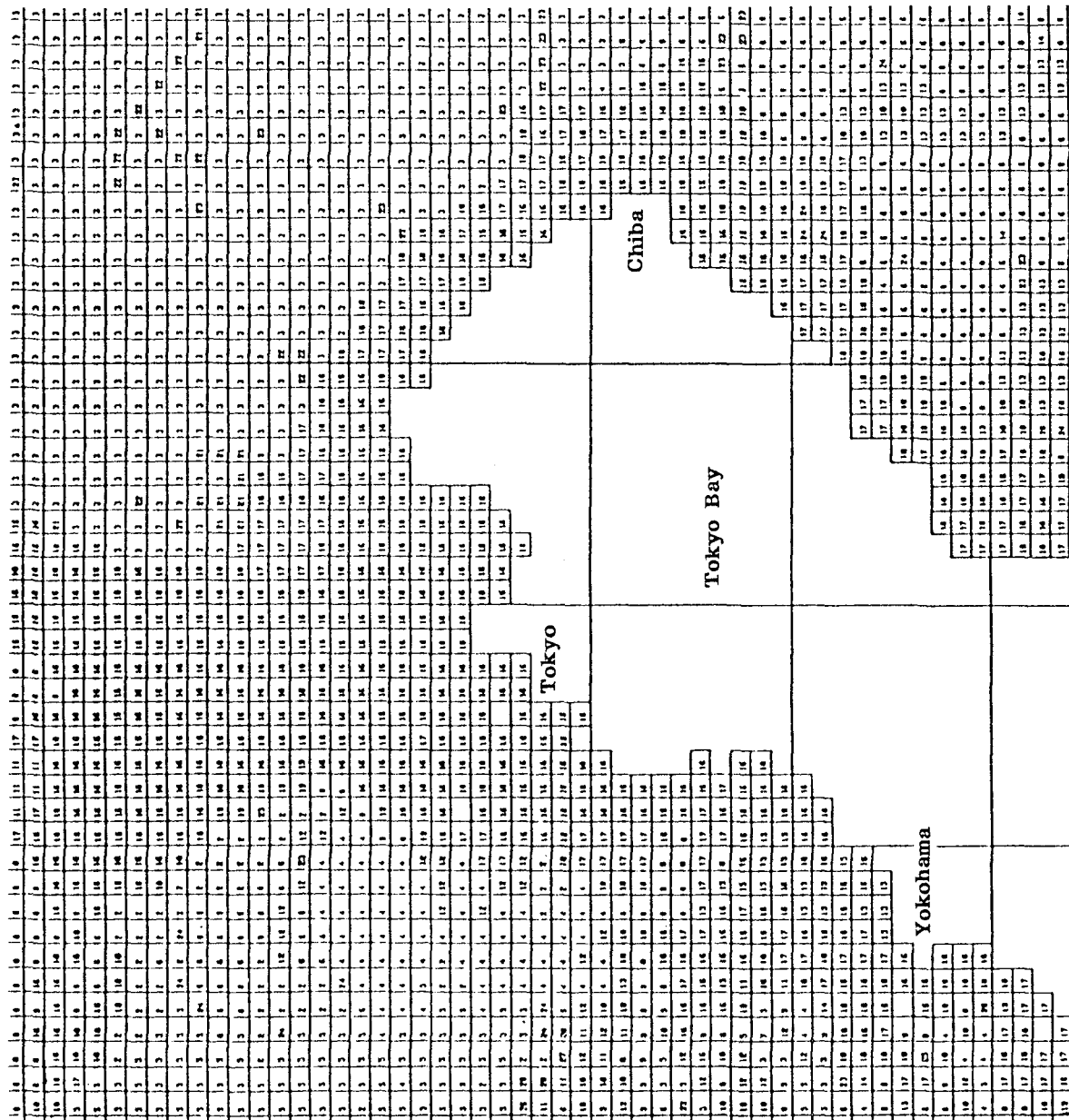
Figure 2 Example of Meshes for Calculation of Ground Response in Tokyo Metropolitan Area (1 km Mesh)

14
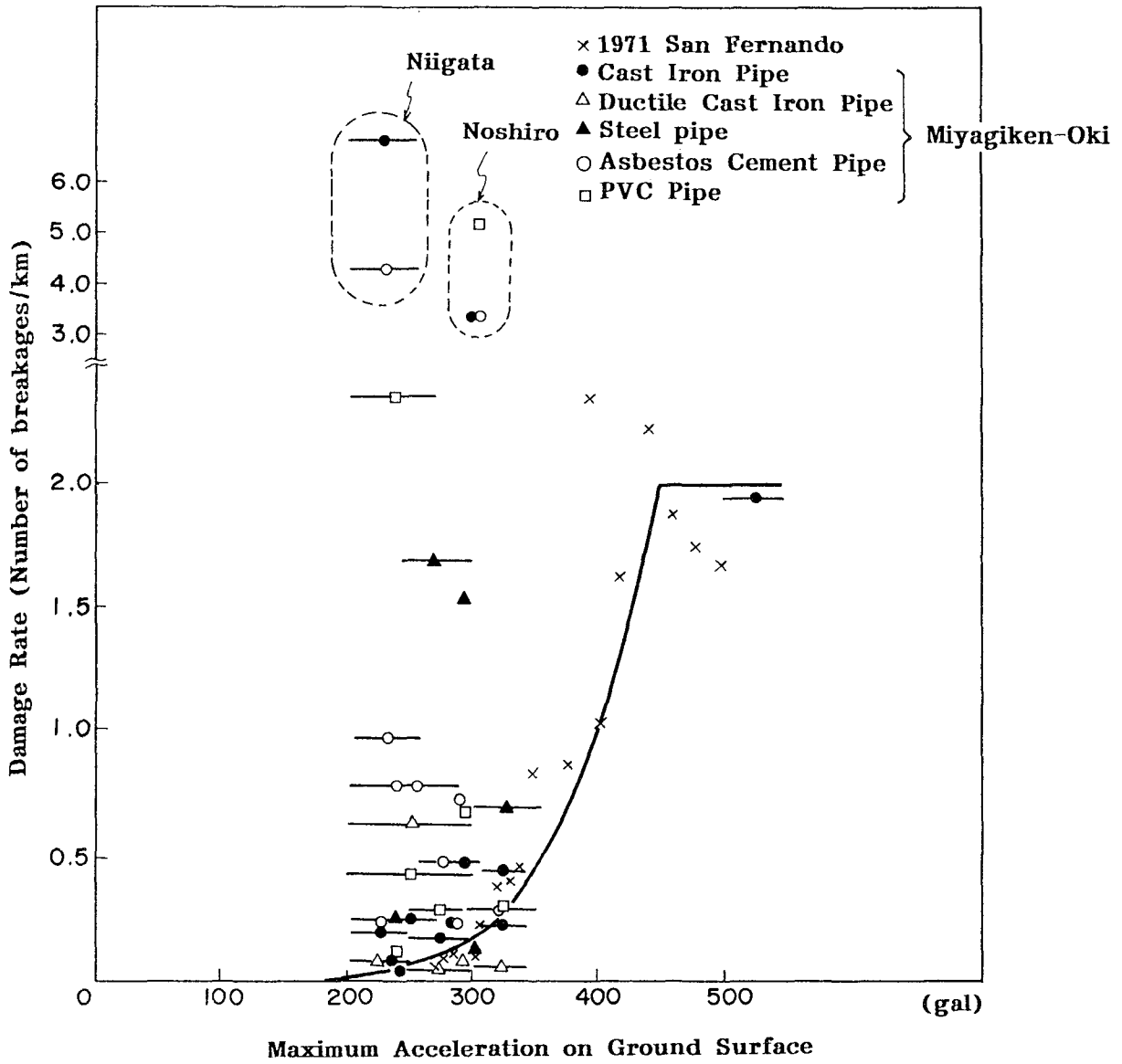
Figure 3　Water Pipe Damage Rate in 1971 San Fernando
and 1978 Miyagiken-Oki Earthquake
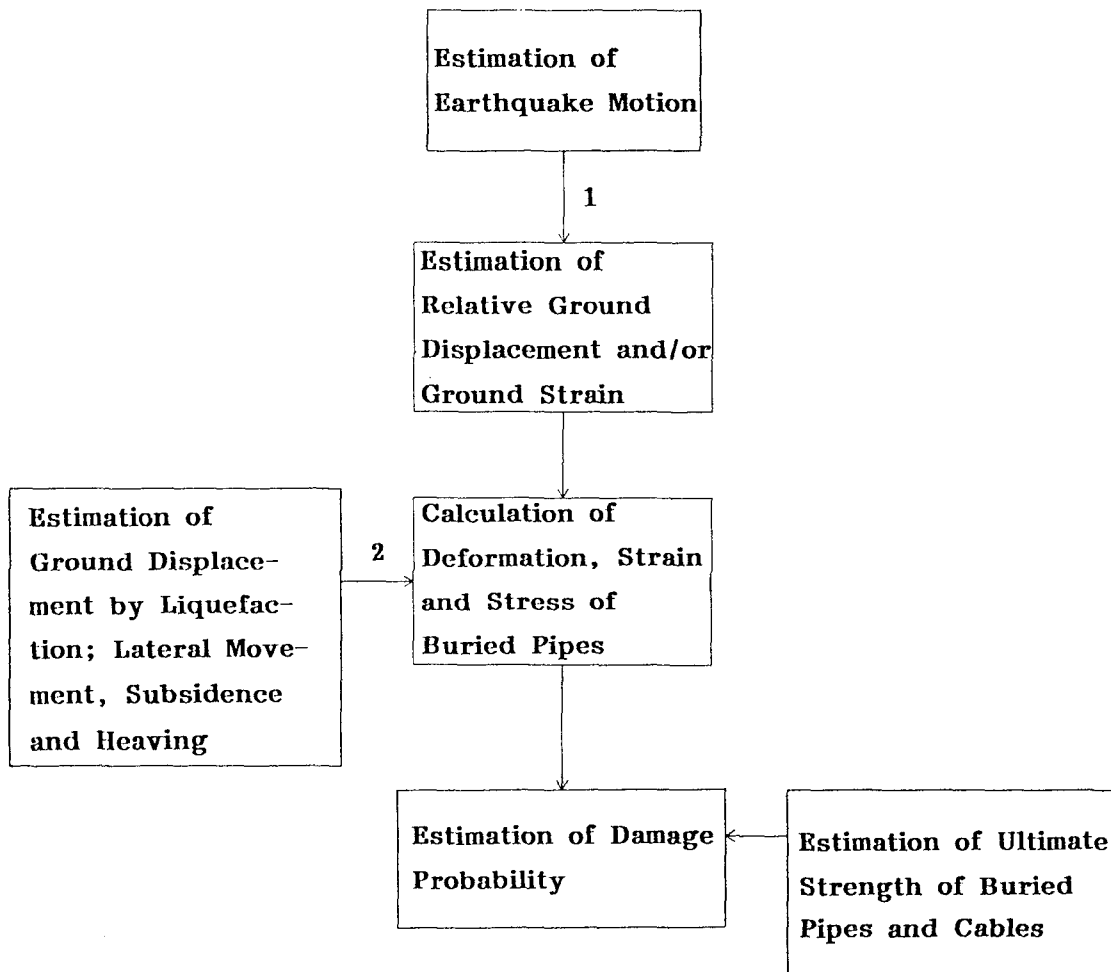
Figure 4   General Flow for Estimating Damage Probability
          for Buried Pipes
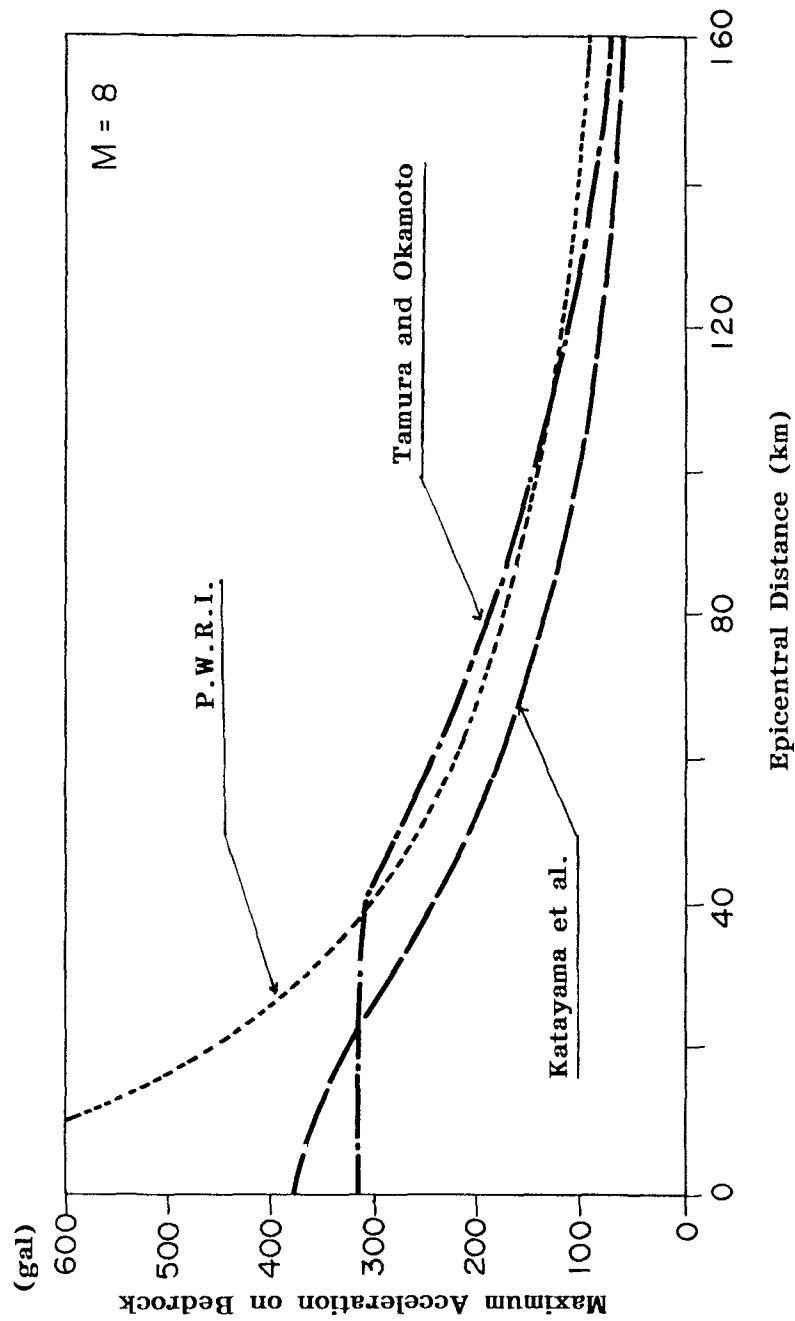
Figure 5   Attenuation Formula for Estimation of Ground Motion
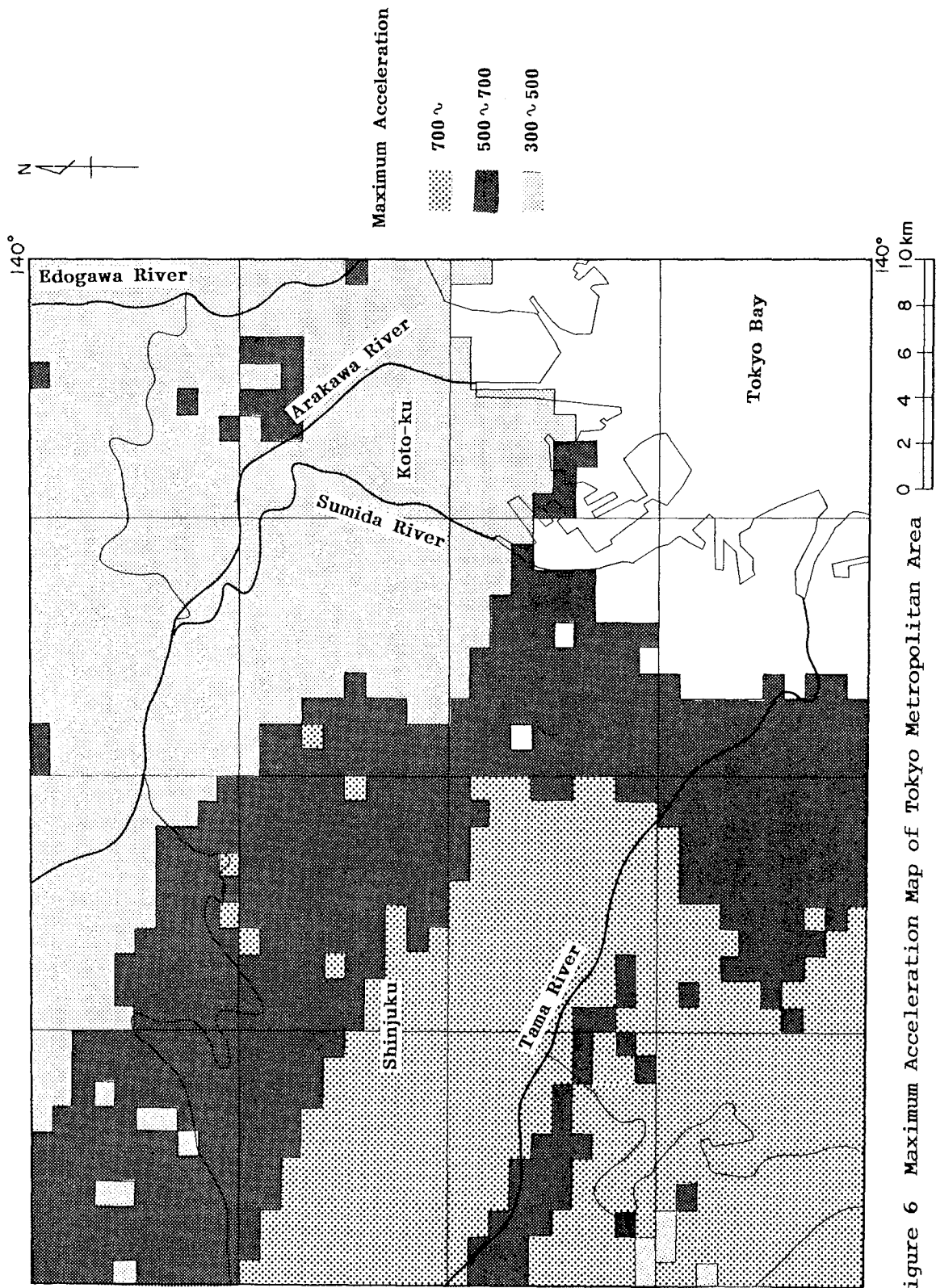
Figure 6 Maximum Acceleration Map of Tokyo Metropolitan Area
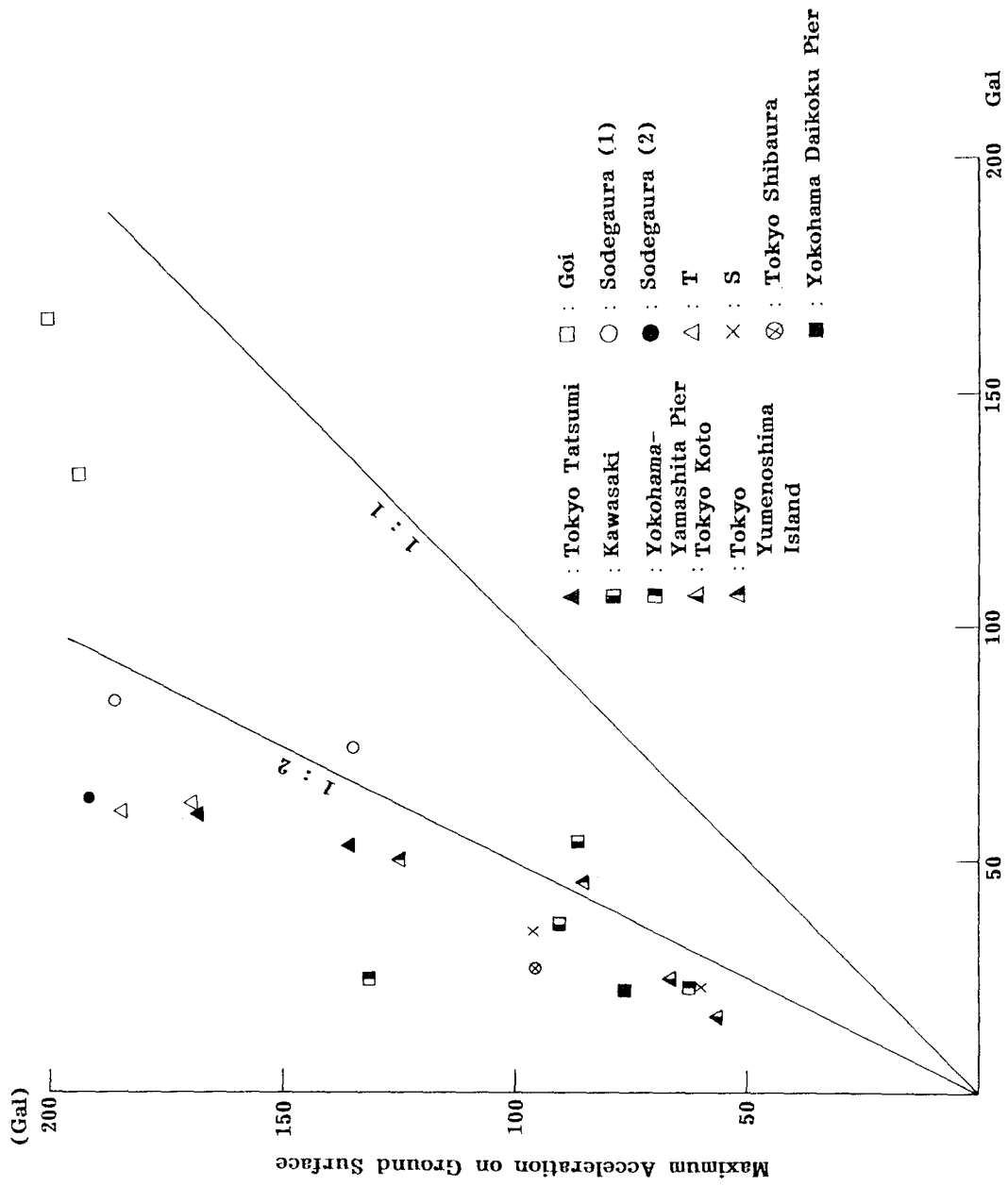
Figure 7　Maximum Acceleration on the Ground Surface and Bedrock Recorded on Reclaimed Land in Tokyo Bay Area

Depth (m)	Soil	Thickness (m)	Shear Wave Velocity (m/s)	Density	Numerical Model
	Fine Sand	3.8	170	1.65	
	Silt	2.0	170	1.50	
	Sandy Silt	4.5	130	1.50	
−10	Sandy Clay	2.0	200	1.50	
	Sand	6.3	330	1.80	
−20	Fine Sand	1.5	330	1.90	
	Hard Clay	11.1	380	2.00	
−30					
	Tertiary Layer	10.8	440	2.00	
−40					
−50	Tertiary Layer	——	530	2.00	
−60					

Figure 8   Ground Conditions and Numerical Model for Dynamic
Response Analysis (Alluvial Soil in Tokyo)

20

Max. Acceleration on Ground Surface (121 Gal)

Max. Acceleration on Bedrock (100 Gal)

(a) CASE I

Max. Acceleration on Ground Surface (156 Gal)

Max. Acceleration on Bedrock (200 Gal)

TIME [SEC]
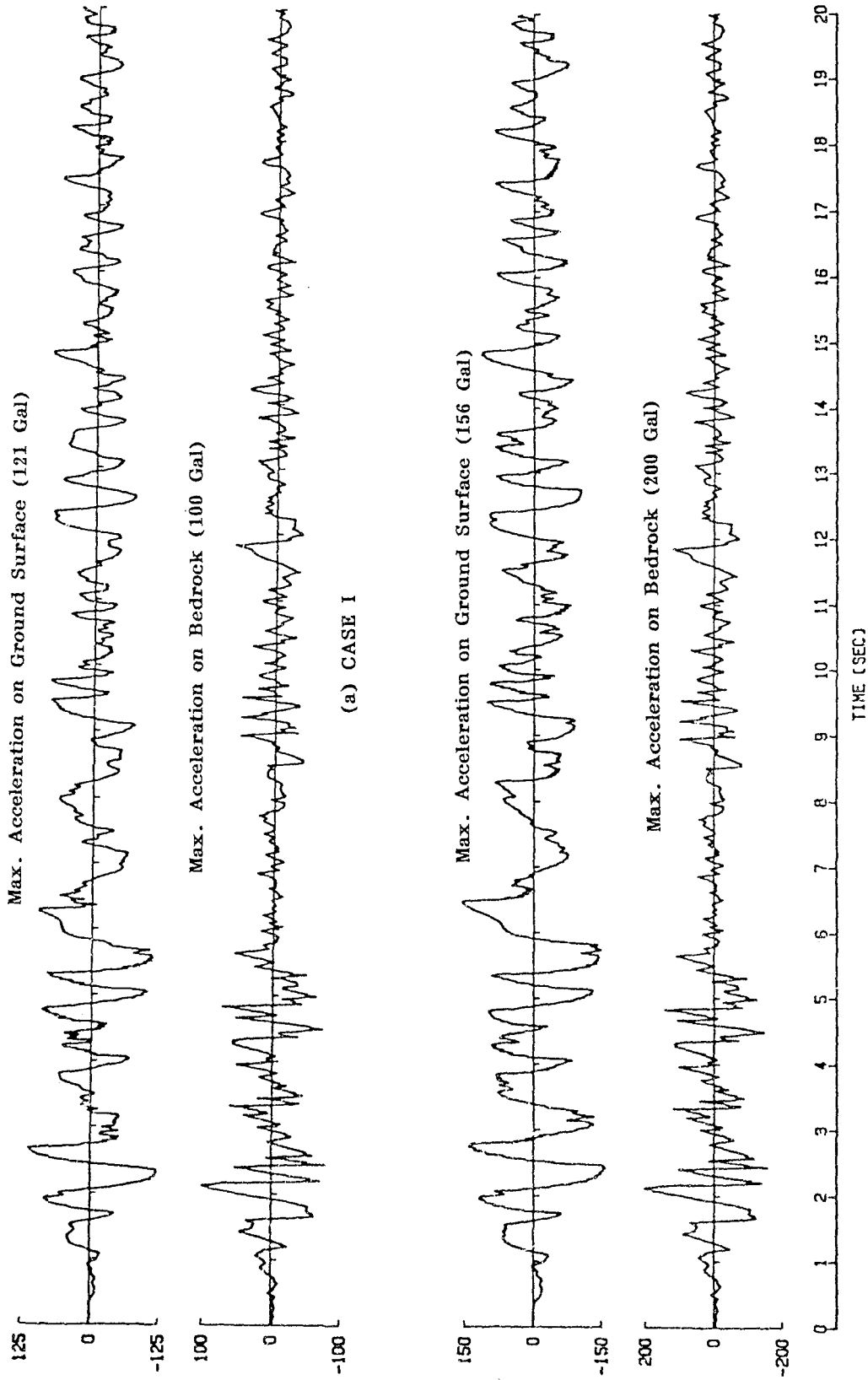
(b) CASE II

Figure 9 Response Acceleration on Ground Surface

21
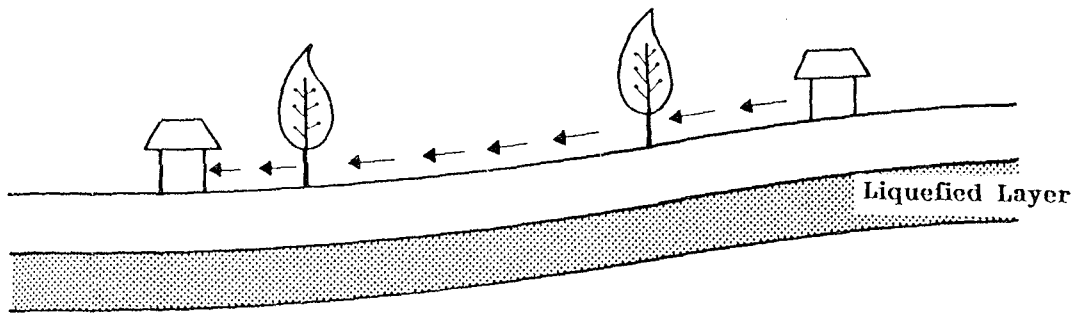
(a) CASE I: Ground Surface is Sloped
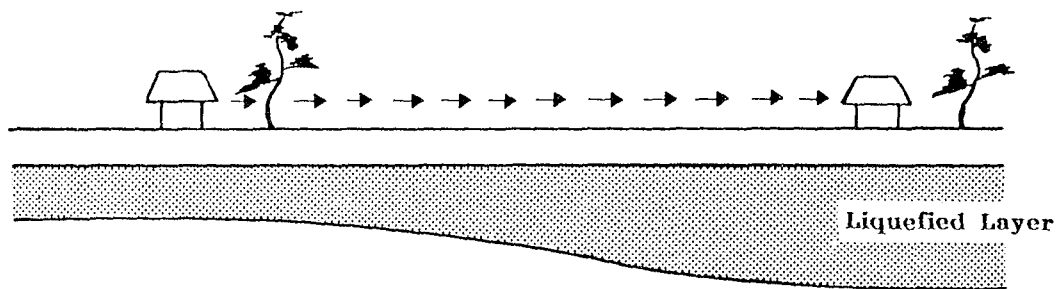
(b) CASE II: The Neighborhood of River Bank
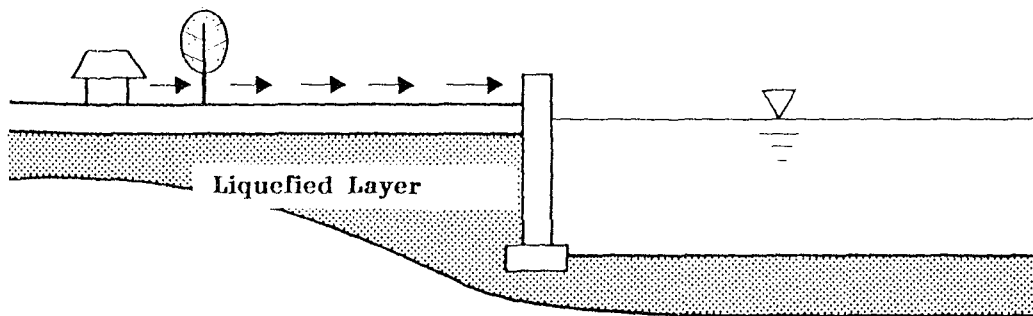
(c) CASE III: Lower Boundary of Liquefied Layer is Inclined

Figure 10 Topographical and Soil Conditions for Liquefaction-Induced
Permanent Ground Displacement

22

LIQUEFACTION-INDUCED GROUND FAILURE DURING THE 1990 PHILIPPINES EARTHQUAKE

Kazue Wakamatsu
Research Associate, Science and Engineering Research Laboratory
Waseda University

Masanori Hamada
Professor of the Faculty of Marine Science and Technology
Tokai University

Takashi Tazoh
Senior Research Engineer, Institute of Technology
Shimizu Corporation

Nozomu Yoshida
Research Head, Engineering Research Institute
Sato Kogyo Co., Ltd.

Tomoaki Ando
Senior Research Engineer
Fuji Research Institute Corporation

ABSTRACT

Extensive liquefaction occurred during the July 16,1990 Philippines earthquake
in the northern part of the Central Plain, Luzon Island, Philippines. The
authors conducted reconnaissance and subsurface investigations between August
5 and 9, and September 23 and 28, 1990. This paper describes liquefaction-
induced ground failures and their structural effects during the earthquake
mainly in the Dagupan City and coastal region of the Lingayen Gulf.
Furthermore, sites where ground displacement occurred as a result of
liquefaction identified, and magnitude and direction of the displacements are
estimated according to the field survey and interview to the residents.
Geotechnical and geomorphological conditions of the displacement sites are
also studied, and liquefied layers are evaluated.

INTRODUCTION

An earthquake of Magnitude 7.7 struck the Luzon Island, Philippines, on July 17, 1990. Soil liquefaction occurred in a widespread area during the earthquake, which caused lots of damage to the structures. The authors conducted reconnaissance and subsurface investigations in the affected region twice, from August 5 to 9 and from September 23 to 29. In this paper, liquefaction-induced ground failure and their effect on the structures during the earthquake in the Dagupan City and coastal region of the Lingayen Gulf are mainly described.

BRIEF FEATURE OF AFFECTED AREA AND LOCATIONS OF LIQUEFIED SITES

Figure 1 shows the affected region by the July 16, 1990 earthquake and the locations of liquefaction identified by several reconnaissance teams as well as by the authors. the Central Plain extends for about 200 km in the center part of Luzon Island, Philippines, bounded by the Lingayen Gulf in the north and Manila Bay in the south. Many rivers, the Pampanga River, the Agno River et al., are meandering through the plain and big damp areas are formed along the southern coast of the Lingayen Gulf and northern coast of the Manila Bay.

Liquefaction occurred at many sites in the northern half of the Central Plane. Liquefaction effects were particularly pronounced at the Dagupan City which faces to southern coast of the Lingayen Gulf. Liquefaction is supposed to occur more sites than shown in Fig.1, but found liquefied sites are limited to the regions along the principal road because of the security and traffic reasons.

Liquefied site located the most far from the epicenter is the Pasay city in Manila metropolitan area, the epicentral distance of which is about 120 km. Figure 2 shows the relationships between the Magnitude of the earthquake and the maximum epicentral distance of the liquefied site during the past 69 Japanese earthquakes from 1885 to 1989[1]. The data during this earthquake is also plotted as hollow circles in the figure, which indicates that maximum epicentral distance of the liquefied site during this earthquake is within the boundary of the Japanese earthquakes.

GROUND FAILURE AND DAMAGE TO STRUCTURE DUE TO LIQUEFACTION

Several case studies of the ground failure and the damage to the structure due to liquefaction are described hereafter.

Dagupan City

One of the most significant liquefaction occurred in the Dagupan city. The city with population of about 130,000 is located about 200 km north-northwest of Manila, capital of Philippines, and faces to the Lingayen Gulf in the north. Many sandbars and dunes are formed along the coastline of the Lingayen Gulf and lots of fishponds are made at the swampy lowland between the bars and/or dunes. Central Dagupan, shown in Fig. 3, is located at the back of this swampy ground, where the Pantal River, a branch of the Agno River, flows through in the east and in the north. According to the interviews to the residents, the city area had been lagoon in the 18th century, which was developed into rice fields and/or fishponds. Central Dagupan have been developed gradually since 1880.

Various types of damage, settlement and/or tilting of the structure, falling down of the bridge, breakage of the underground pipeline, settlement and tilting of the electric pole, and lateral spreading along the river, et al. occurred at Dagupan City, as a consequence of soil liquefaction. The damage to the structures according to the Dagupan City Civilian Reconstruction Fund Foundation were as follows:

66 buildings condemned
over 500 buildings damaged
over 2000 houses affected and destroyed
80% of city roads dilapidated
2 bridges collapsed
supermarket condemned

Figure 4 shows in detail the feature of liquefaction effects occurred in central Dagupan. Here, lateral displacements in the figure are not measured value based on the aerial photographs but the estimated values based on the field survey and interviews to the residents. Damage due to liquefaction was significant especially along Angel Fernandez Ave. and Perez Blvd. in the central Dagupan City. Most of the R/C buildings in the central Dugupan are 3 or 4 story buildings. These buildings settled down and/or tilted as a result of liquefaction as shown in Photo.1. The average and maximum settlement of the building were estimated about 50cm and 2m, respectively, among the 120 buildings along these two streets and about a half of the buildings tilted more than 1 degree.

According to the City Planning Director, most buildings do not have basement floor and is constructed by the use of spread foundations. Actually, there are buildings without earth floor beam among the investigated buildings by the authors very frequently. Furthermore, according to the Vice Mayor, there are only two buildings which uses pile foundation; a building is located in the non-liquefied region(No.1 site in Fig.4), hence not damaged, and the location of the other building is not known at present.

Photograph 2 shows a 4 story R/C building located at the No.2 site in Fig.4, which building tilted about 18 degree, the maximum tilting among the buildings in the central Dagupan. Settlement of the buildings is severe around this building, magnitude of which is 1 to 2 meters, and nearly a half height of the first floor are buried in the ground as shown in Photo.3. Furthermore, at the No.3 site in Fig.4, large crack with maximum 3 meters separation appears and there are evidences that the ground moved toward north. According to the residents, hot water was boiled up near the building, and the building at the No.3 site in Fig.4 moved 3m to the north. The creek which flows through at the back of the Perez Blvd. (see Fig.4) was originally 5 meters wide, which becomes 2.5 - 3 meters after the earthquake. The land nearby had been fishpond and reclaimed with coconut leaves, and after that reclaimed with beach sand around 1960.

Large amount of lateral spreading occurred toward the Pantal River near the Magsaysay Bridge as shown in Fig.4 and Photo.4, which caused severe damage. The Magsaysay Bridge is a 7 span concrete bridge across the Pantal River. The four span concrete plate-girder was collapsed and two piers fell down. A warehouse in No.4 site moved for 1 to 2 meters and fell forward the river as shown in Photo.5. Cracks of 2.5m wide appears at No.5 site in Fig.4 due to lateral

spreading of ground. The 3 story R/C hospital nearby was dragged and tilted toward the river due to the lateral spreading of the foundation ground. The gymnasium of the school built beside the river which is located south to the hospital, settled severely and the whole building wad dragged toward the river.

As described, razed buildings concentrate around here, which seems to be caused due to soil liquefaction of foundation ground and subsequent lateral spreading. Considering from the geomorphological condition, both river sides of the Pantal River around here are supposed to be an old riverbed.

Figure 5 shows a geotechnical section along A-A', Perez Blvd. in Figure 4. The ground surface is approximately 0 to 1m above sea level. Water level after the earthquake ranged in depth from 0 to 1.5m based on our field survey. About a 5 to 10m thick layer of fine sand lies beneath the fill or clayey soil layer. The liquefied layer was estimated using the procedure outlined in the Japanese High way Bridge Code. 200gal of a peak horizontal acceleration was applied based on the estimated value by Sato[2]. In the computing the FL value, N-value obtained from SPT Test are multiplied by a half, because the energy absorbing capacity of the ground by the weight in the penetration test in the Philippines method is smaller than that in the Japanese method.

The results of the analysis show that the fine sand layer would be completely liquefied as indicated by the shaded portion in the Figure 5. The upper surface of estimated liquefied layer lies at shallow depth from the ground surface in the section where heaviest damage to the buildings occurred. Both upper and lower surface of the liquefied layer are inclined toward the Pantal River in the section where lateral spreading of the ground was observed.

Lateral spreading of the ground was also seen at both river sides of the Pantal River in the north of the central Dagupan City as shown in Fig.4. At the No.6 site in Fig.4, the river side moved 3 meters at maximum toward the center of the river and settled about 1 meter for about 50 meters long. The failure of the river side affected to the Angel Fernandez Ave.; there were a separation between the pavement and the roadway and settlement of 0.5 meter in the north of the avenue. It is noted that there was no revetment near here. On the other hand, there was simple R/C revetment in the north river side, which may be the reason why ground problems in this side, about 1m lateral spreading and settlement, are smaller than the ones in the southern riverside. At the residential area along the north side of the river, however, boiled sand accumulated about 30cm thick and differential settlement of more than 50cm occurred at the wooden houses.

North of the residential district there are uncultivated land and fish pond. Sand boils could be observed on the way to the uncultivated land 2 months after the earthquake. According to the residents, sand boiled from the bottom of the fishpond with 1.3 meters deep for more than 1 minutes and formed a deposit over the pond as thick as 40cm.

Sand boils and lateral spreading were observed at the sparsely developed residential area which lies on the left bank of the Pantal River in the south of the central Dagupan. Photograph 6 shows cracks of the concrete slab occurred in the yard of sales office of beer company at No.7 site in Fig.4. Maximum separation of the cracks of concrete slab is 290cm, whereas that of the ground under the slab is 350cm. About 10 cracks appear parallel to the

26

river at this site, the sum of which reaches about 8 meters. The revetment moved about 5 meters toward the center of the river and two buildings located beside the river were completely destroyed. According to the employees, sand/water mixture with black color boiled to maximum 1.8 meters high for about 30 minutes.

Sto. Thomas and Ago

A sand bar develops like a peninsula in the south of Sto. Thomas as shown in Fig.1. Here is a rice field area and is dotted fishponds and villages. Ground failure such as cracks and sand boils are observed everywhere along the road from the west of Ago to the tip of the peninsula, which is shown in the topographical map in Fig.6. Most drastic event is the sink of the Narvacan village into the sea, which is located at the tip of the peninsula. According to the village headman and residents, the situations in the earthquake was as follows:

Narvacan is a fishing village with population of about 1000, 360 families and about 150 houses, and people lived beside the inlet facing to the main island. There was a small church and school, too. The ground motion during the earthquake was very severe; vertical motion was followed by the horizontal motion. The earthquake struck at the low tide. Hot water expelled everywhere in the village, and water spouting was also seen in the sea. The ground was flooded with the expelled ground water water after five minutes, hence duration of sand boil is not known. At the same time, settlement of the ground could be felt. Settlement continued for about 30 minutes and finally water came up to the height of breast. Settlement was 3 meters at maximum. People had to spend on the boat for several days following the earthquake, and after that they moved to temporary houses at the opposite bank in main island or an upland. The ground had been nearly level ground before the earthquake, which expanded in a direction toward the main island about 10 meters after the earthquake. Soils in the Pacific Ocean side is relatively dense sand deposit, but those in the main island side contain clay and is soft.

Photograph 8 shows the village at high tide in the neap tide. The land can be seen in some places. Most houses are wooden houses with high floor level, and a few houses are made with concrete block. At the high tide in the spring tide the water reaches under the eaves, hence the village completely sank under the sea. The authors conducted Swedish Sounding Test at two sites in the village, which shows that the ground to G.L.-2.3 to 3.5 meters is loose deposit whose estimated N-value is less than 10.

Same kind of submerged villages are also seen at Alaska village which is located at the mouth of the Aringay River in the west of Aringay. Furthermore, it is reported that the Lauris (the Spelling is not sure since it is based on the pronunciation) village with several tens houses sank due to which the ground was covered by the water of the fish pond to a depth of 60 cm at high tide.

Photograph 9 shows a crater at San Julian in the west of Agoo, which was caused by violent expulsion of water. The diameter is about 4 meters and boiled sand spreads about 15 meters in diameter. According to the residents, spewed water was so hot that fish seemed to be boiled, and it covered the ground up to the height of the knee. As seen in the photograph, just over the village is sea shore. They grow rice using irrigation water brought from the

mountain area in the east, which suggests that clayey soil are borrowed over the beach sand. Hence, water might came out from relatively a deep aquifer.

Inland Area

Liquefaction occurred in the inland area is roughly divided into two classes: river side region along the Agno River from Tarlac to Dagupan and the eastern region along the fault line.

Two bridges, Sison Bridge (or Carmen Bridge) and Calvo Bridge, fell down. Both bridges are steel bridge; the former one is a 13 span bridge with 600 meters long and the latter one is a 4 span bridge with 140 meters long. Sand boils were seen in the flood plain just under the fallen girder and evidences of lateral spreading were found.

In the fault area, sand boils and mud boils were observed at the rice field along the fault near the epicenter as shown in Fig.1. Although structural damage was not much, Maniela Bridge, one span concrete bridge at No.20 site in Fig.1, fell down in the northern movable girder because southern abutment moved largely to the backward. Since sand boils, cracks and settlement of the ground are found nearby, damage is supposed to be caused due to soil liquefaction.

CONCLUSION

Soil liquefaction occurred in a widespread area during the 1990 Philippines earthquake, which is nearly the same order with the 1983 Nihonkai-chubu earthquake, Japan. Liquefaction feature observed by our reconnaissance team conducted during the limited duration is as follows:

1) Ground failure due to liquefaction including sand boils, cracks, settlement, lateral spreading and failure of the embankment occurred at many sites in the coastal region of the Lingayen Gulf, river side region of the Agno River, and lowland along the fault line.

2) Variety of structures such as buildings, roads, bridges, underground pipelines and embankments et al., were damaged due to the ground failure.

3) In addition to the large scale of liquefaction, lack of the protection works against liquefaction along the seaside and riverside caused large lateral spreading, which enlarged the damage due to liquefaction. Furthermore, shortage of bearing capacity and the lack of the rigidity of foundations, which were observed very frequently, also enlarged the damage of the buildings and bridges.

REFERENCES

1)Kazue Wakamatsu:Distribution maps of liquefied sites in Japan, Proceeding of the 8th Japan Earthquake Engineering Symposium, pp.915-920, 1990 (in Japanese with English abstract)

2)Tadanobu Sato:Damage of Cabanatuan-estimation of maximum acceleration-, preliminary report of the 1990 Philippines earthquake, Japan Society of Civil Engineers, pp.6-7, 1990 (in Japanese)
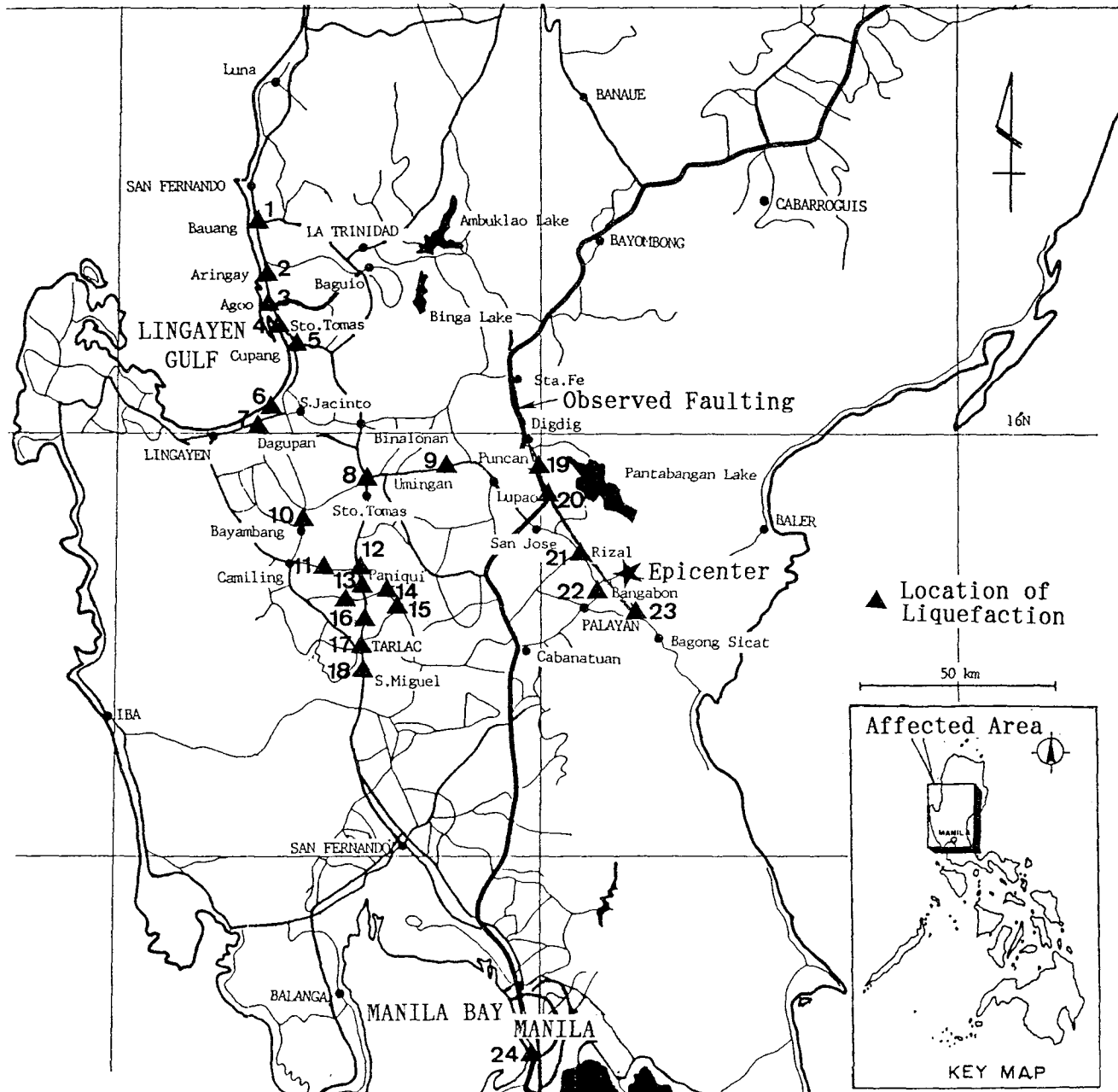
Fig.1   Map of Central Part of Luzon showing the region affected by the July 16, 1990 Earthquake and Locations of Liquefaction

29
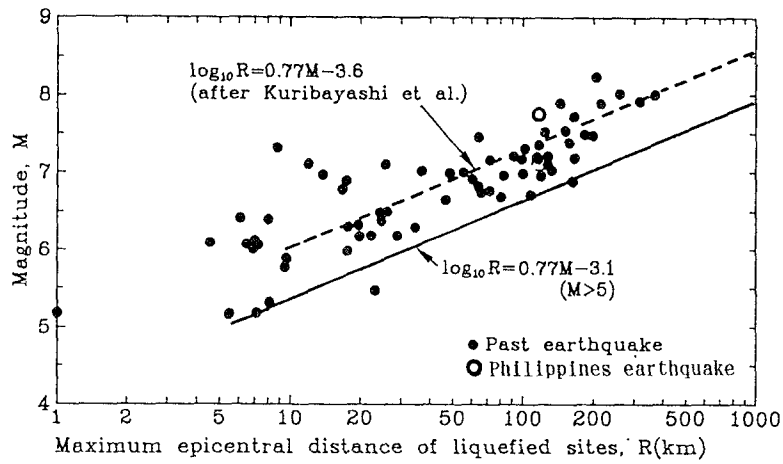
Fig.2 Relationship of the Magnitude of the earthquake and Maximum Epicentral Distance of Liquefied Site[1]
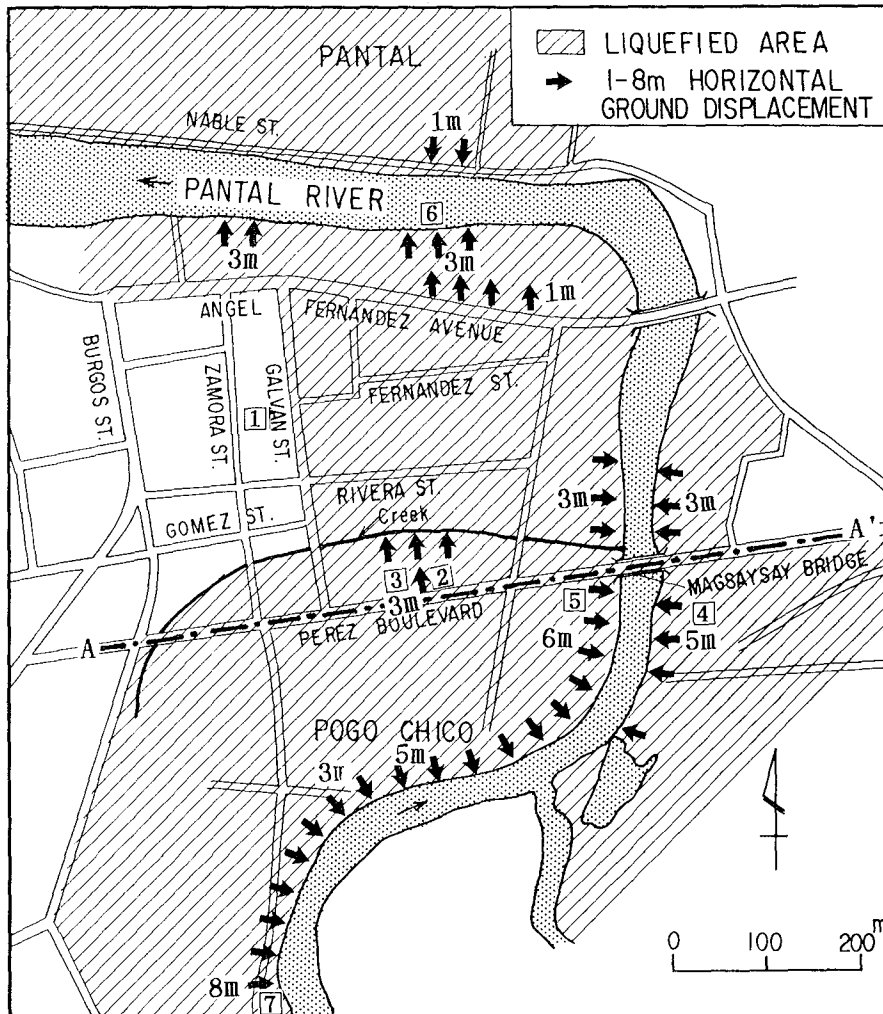
Fig.4 The Extent of Liquefaction-induced Ground Failure in Central Dagupan
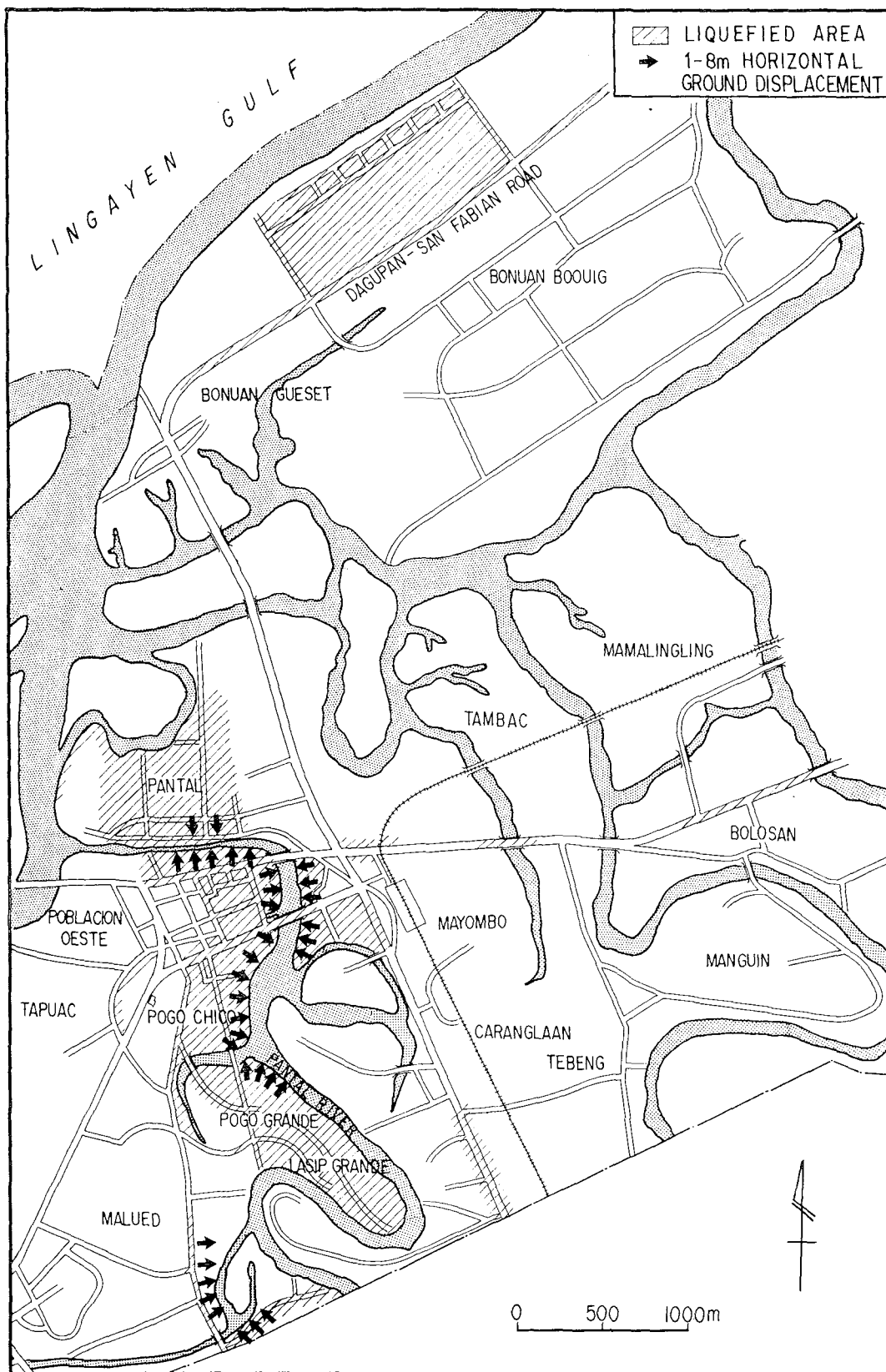
Fig.3 The Approximate Extent of Liquefaction in Dagupan City
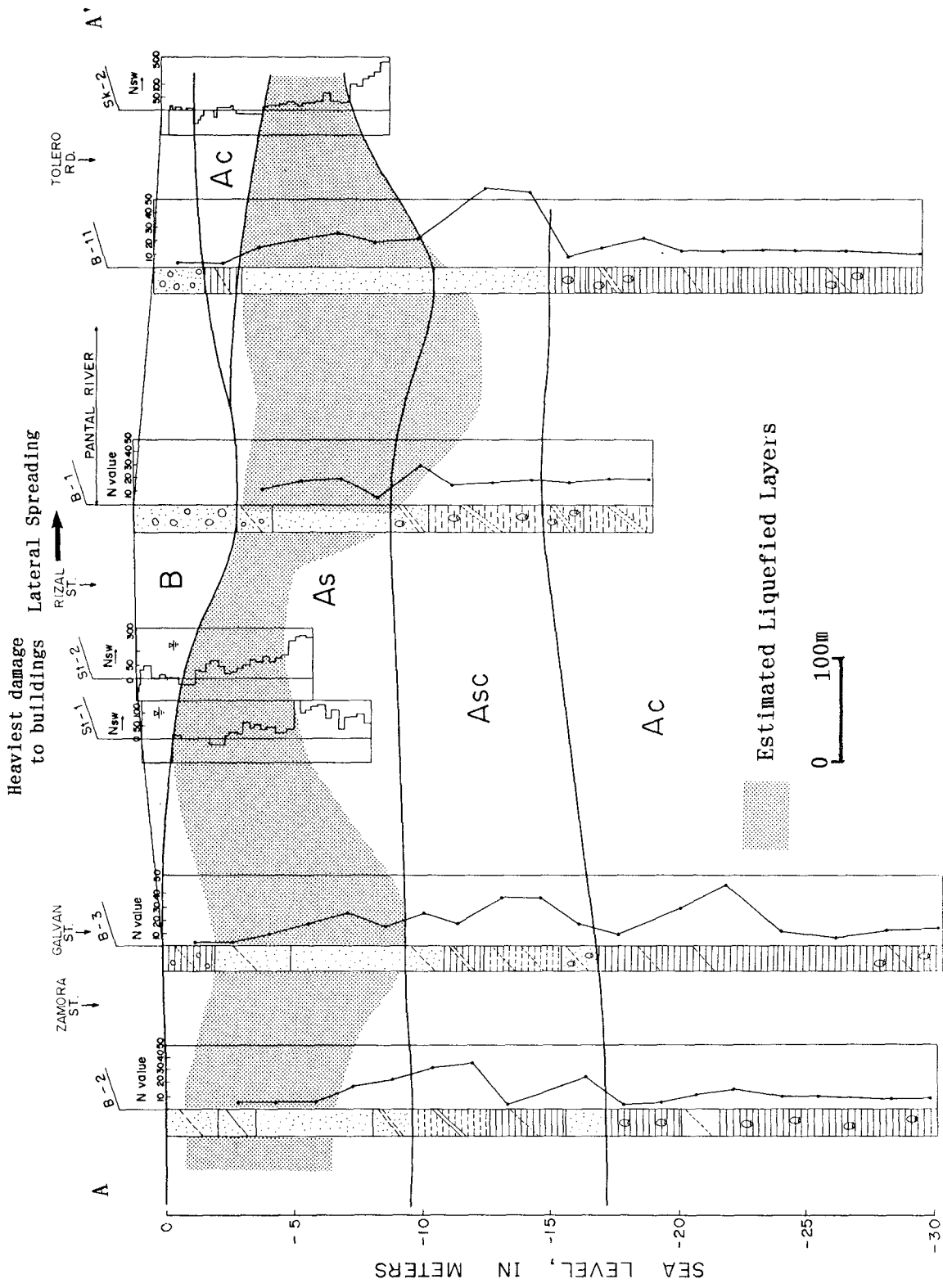
Fig.5 Cross-section of Sediments at Central Dagupan showing Geotechnical Features and Estimated Liquefied Layers
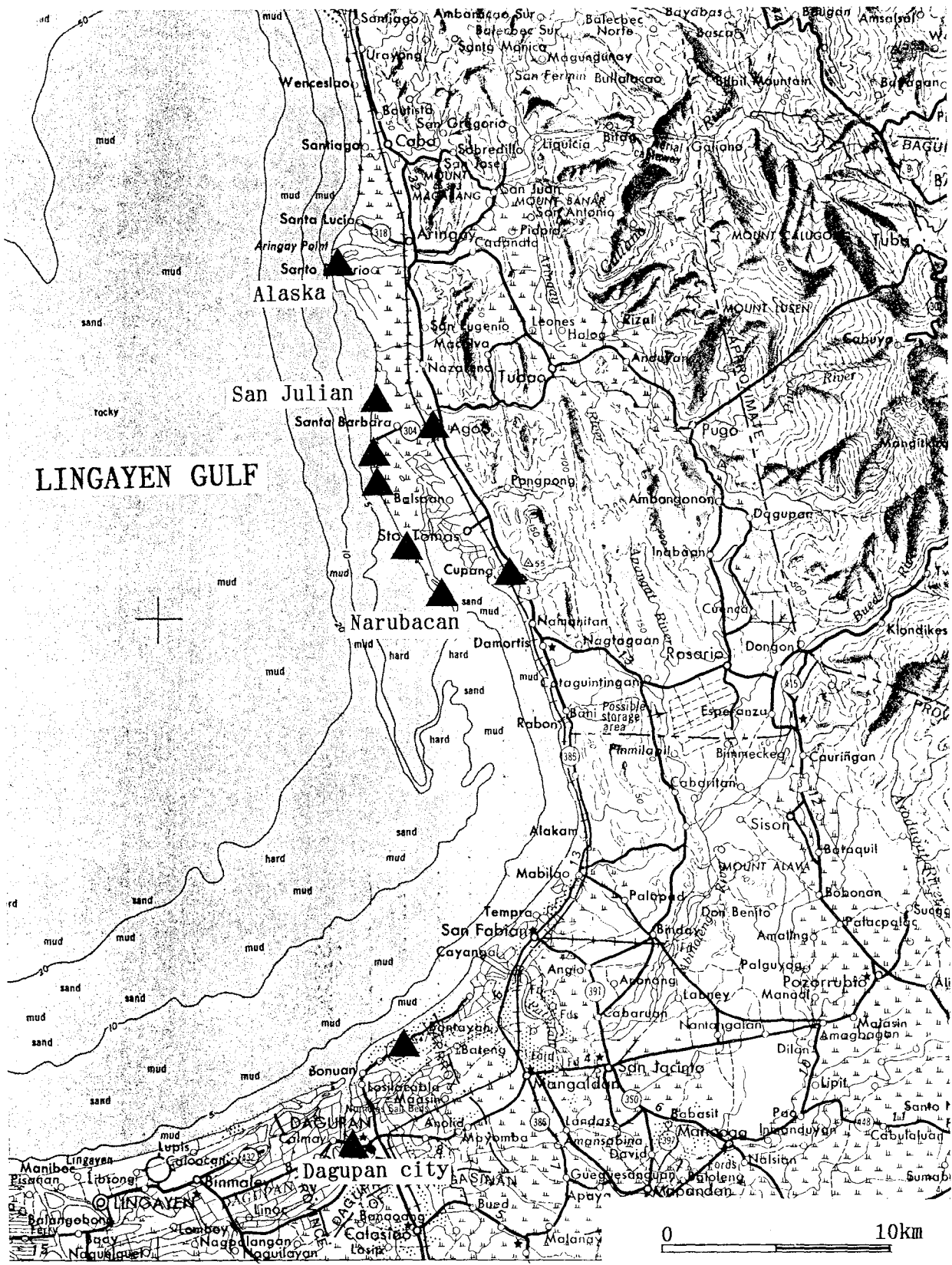
Fig.6　Sites of Liquefaction in the Eastern Coast of the Lingayen Gulf

33
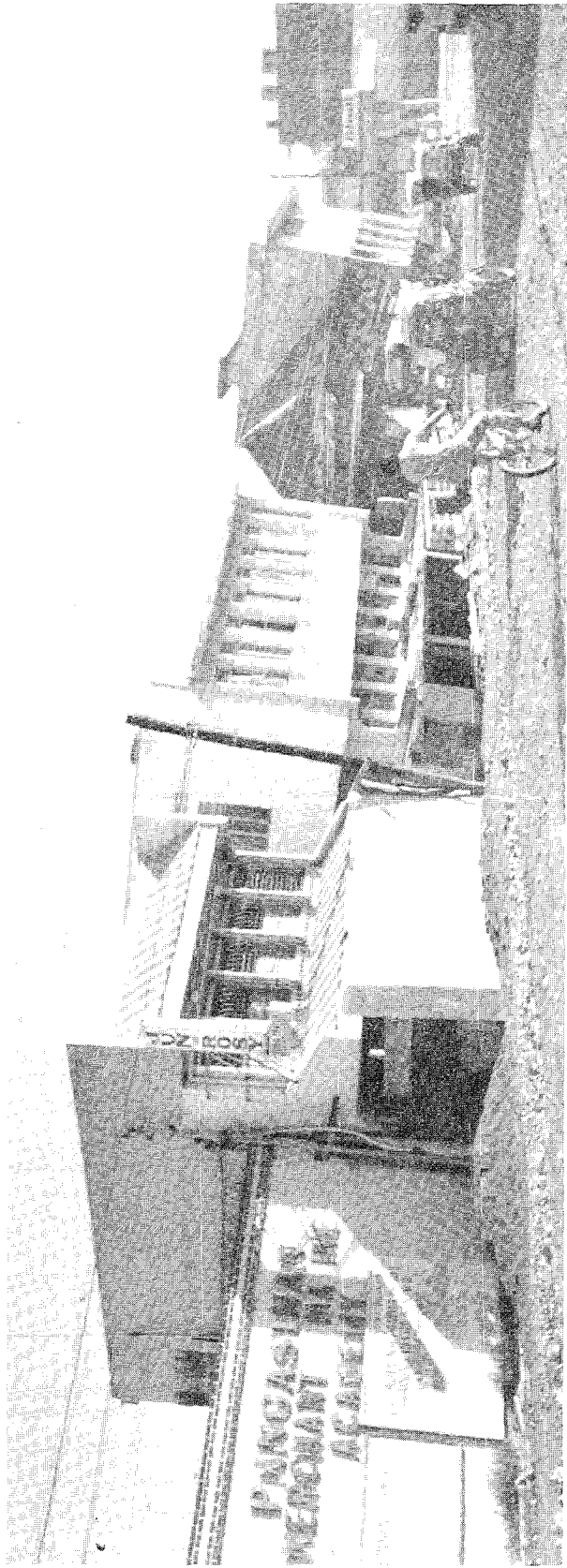
Photo.1 The buildings in Central Dagupan along Perez Blvd. were severely damaged due to liquefaction
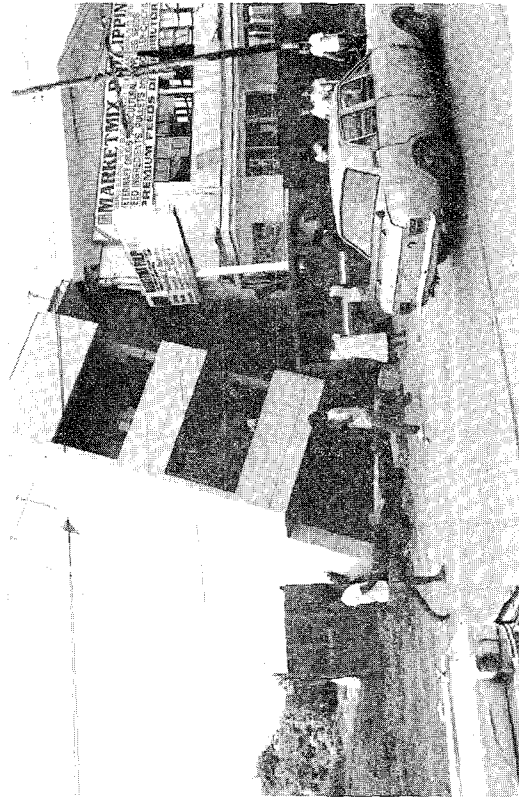
Photo.2 The four-story building in Perez Blvd. tilted as much as 18 degree from the vertical
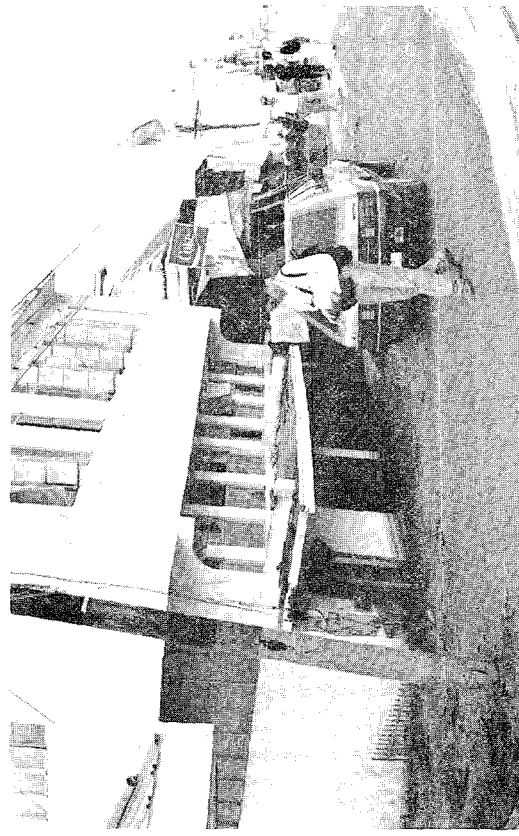
Photo.3 The three-story building that settled about 1.5 meter in the central district of Dagupan

34

Photo.4 Lateral spreading of the right bank which
pushed the wooden house into the river

Photo.5 The four-span concrete place-girder Magsaysay
Bridge in Dagupan City collapsed due to lateral
spreading of the riverbanks toward the stream
channel and/or loss bearing capacity of the
piers due to liquefaction
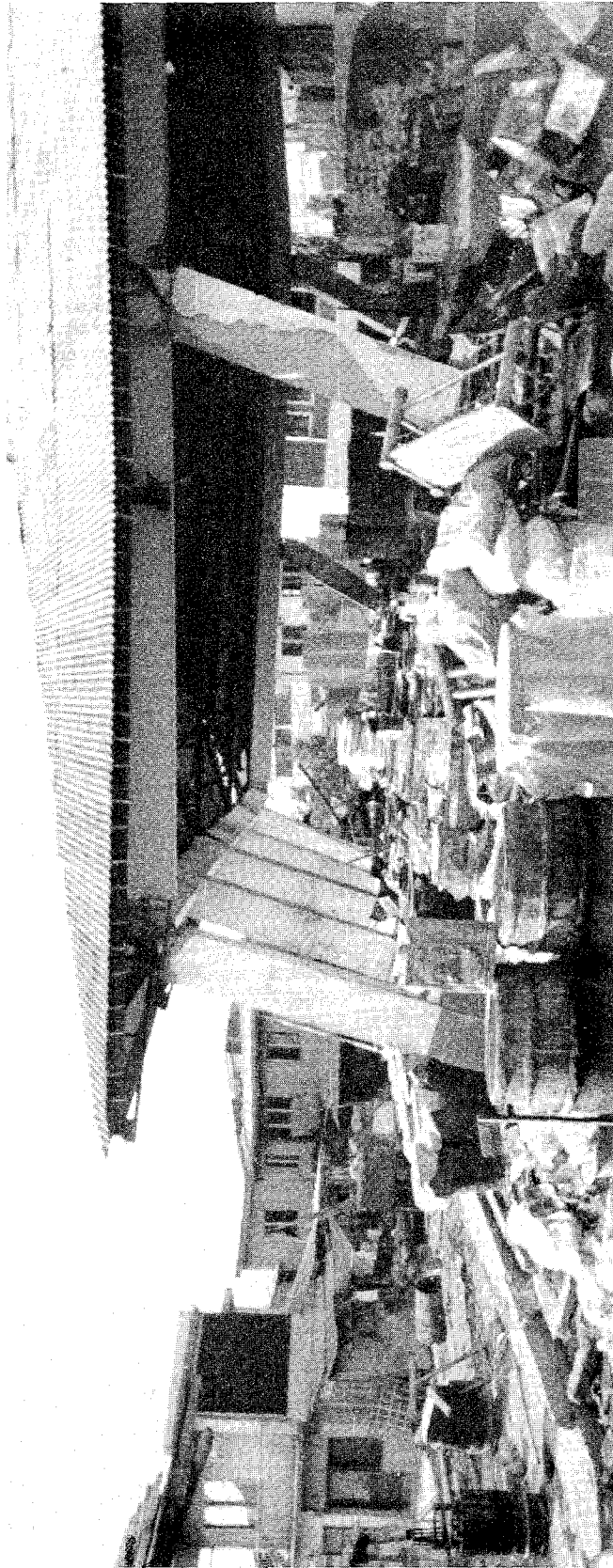
Photo.6 The warehouse learned due to lateral
spreading of the riverbank toward
the river channel
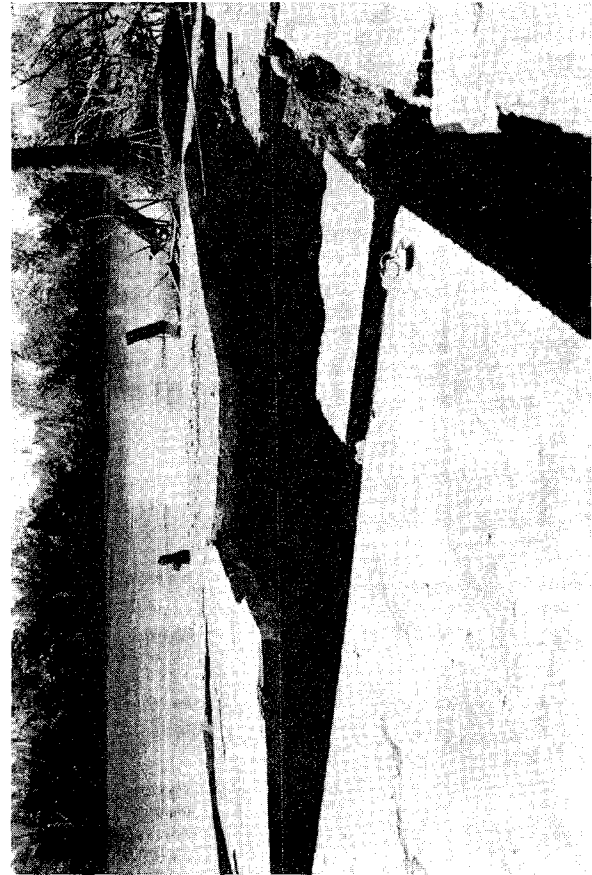
Photo.7 The concrete slab cracked due to
the lateral spreading toward
the stream channel

36
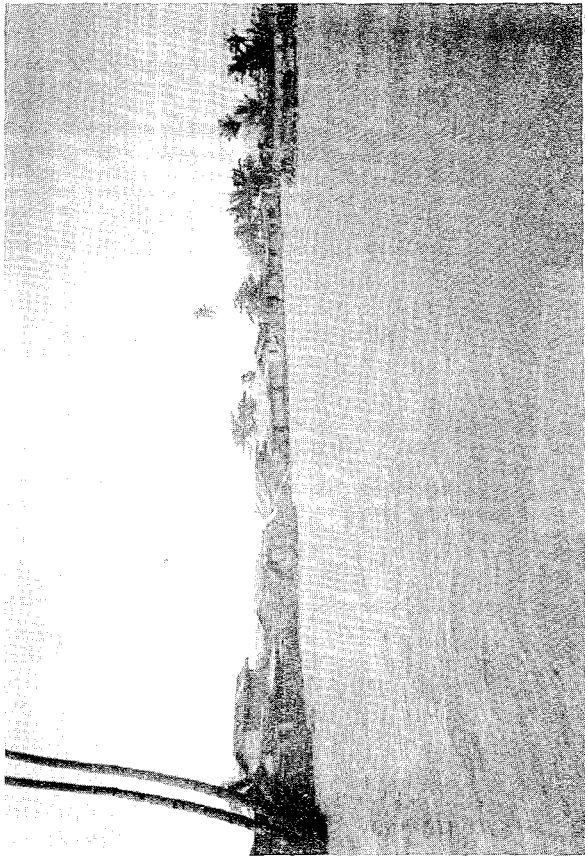
Photo.8 The village in Sto.Tomas sank a maximum 3 meter due to lateral spreading and settlement of the ground due to liquefaction
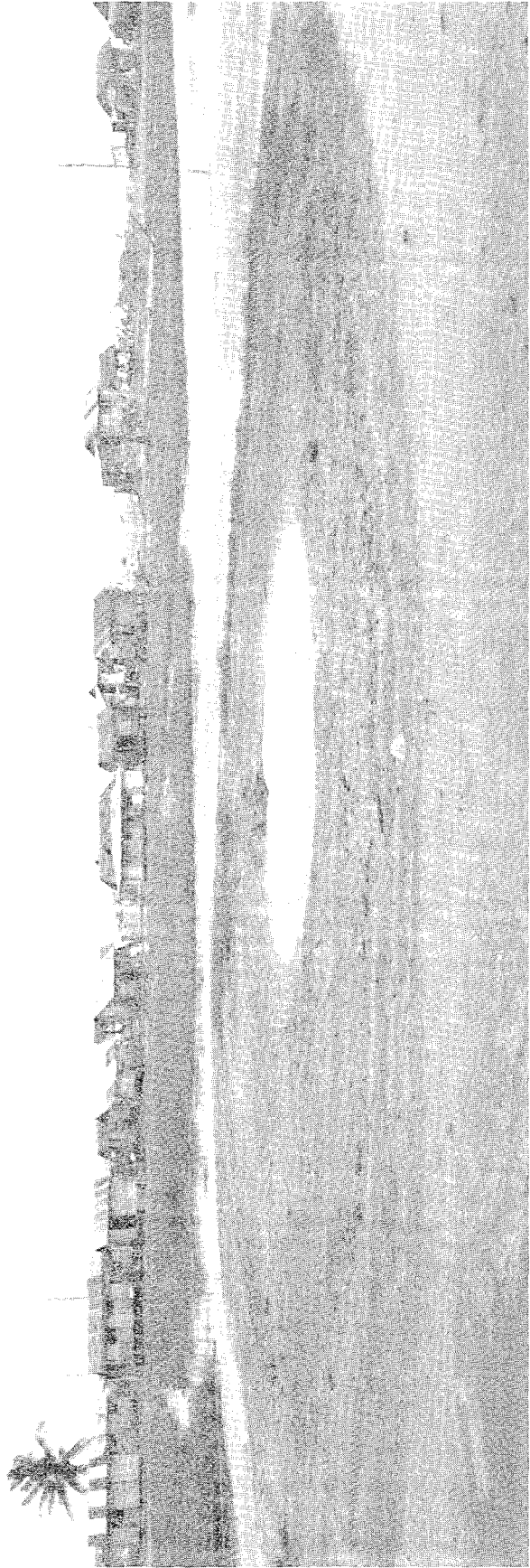
Photo.9 The crater created in rice field in San Julian, Agoo, which erupted a quantity of hot water

37

LIQUEFACTION AND LANDSLIDING FROM THE JULY 16, 1990, LUZON, PHILIPPINES EARTHQUAKE

by

Gerald F. Wieczorek
U.S. Geological Survey
Reston, VA

Ronaldo Arboleda
Philippine Institute of Volcanology and Seismology

Bella Tubianosa
Philippine Institute of Volcanology and Seismology

ABSTRACT

A magnitude 7.8 earthquake occurred in north-central Luzon at 4:26 P.M. local time (PDT) on July 16, 1990 (fig. 1). At least 1600 people died, mostly in the collapse of multi-story buildings at considerable distance away from the epicenter. Numerous roadways and bridges were damaged by ground shaking or earthquake-induced ground failure (landslides and liquefaction). Major economic costs are anticipated for reconstruction of buildings and infrastructure and from the disruption of commerce. This is a preliminary descriptive report of the ground failures in the earthquake, adapted from an administrative report by the U.S. Geological Survey and Philippine Institute of Volcanology and Seismology (1990) on the July 16, 1990 Luzon earthquake.

LIQUEFACTION AND LANDSLIDING FROM THE JULY 16, 1990, LUZON, PHILIPPINES EARTHQUAKE

GERALD F. WIECZOREK (1), RONALDO ARBOLEDA (2),BELLA TUBIANOSA (2)

(1) U.S. GEOLOGICAL SURVEY, (2) PHILIPPINE INSTITUTE OF VOLCANOLOGY AND SEISMOLOGY

Introduction

A magnitude 7.8 earthquake occurred in north-central Luzon at 4:26 p.m. local time (PDT) on July 16, 1990 (fig. 1). At least 1,600 people died, mostly in the collapse of multi-story buildings at considerable distance from the epicenter. Numerous roadways and bridges were damaged by ground shaking or earthquake-induced ground failure (landslides and liquefaction). Major economic costs are anticipated for reconstruction of buildings and infrastructure and from the disruption of commerce.

Earthquake-induced landslides and liquefaction caused a significant portion of the damage and continuing problems from the earthquake. Roads, bridges, buildings, and irrigation systems were affected directly by ground failures; in addition, search-and-rescue efforts were delayed, as was the recovery, because the rainy season had just begun. The long-term consequences of the widespread and abundant ground failures from this earthquake could persist for months throughout much of central and northern Luzon and perhaps for years in some locations.

This is a preliminary descriptive report of the ground failures in the earthquake adapted from an administrative report by the U.S. Geological Survey and Philippine Institute of Volcanology and Seismology (1990) on the July 16, 1990, Luzon earthquake. Further analyses of data and observations are forthcoming in future reports. The terminology used to describe ground failures is from Varnes (1978).

Liquefaction and Secondary Effects

Liquefaction, the vibration-induced transformation of water-saturated sediment into a fluid slurry, caused ground failure as manifested by bearing capacity failure, subsidence, and lateral spreading. These effects occurred locally in Nueva Ecija and Tarlac Provinces, and extensively in coastal and river delta areas of Pangasinan and La Union Provinces. Liquefaction was also reported in artificial fill near the Philippine Plaza Hotel along Manila Bay (Prof. Jose Ma. de Castro, University of the Philippines, oral communication, 7/28/90). Loose deposits of fluvial, deltaic, and beach sands at various depths liquefied in this earthquake, and under high artesian water pressure vented to the surface and covered the ground with deposits of ejected sand. The vent and conical sandy deposits are referred to as sand boils.

The most dramatic liquefaction effects occurred within a 0.5 to 0.6 km^2 area of central Dagupan, which was built on as much as 5 m of loose saturated sand. During the earthquake these sands

liquefied, and as a consequence of loss of bearing capacity the buildings severely tilted (fig. 2). The Perez Blvd. bridge collapsed as the ground shifted laterally beneath it toward the center of the river, and entire blocks of the central part of the city subsided as much as 1 to 2 m (fig. 3). Underground gasoline storage tanks at service stations behaved buoyantly in the liquefied sands and floated to the surface. Wooden structures collapsed along the banks of the San Pablo River. Fissures in the ground parallel to the river indicated lateral spreading of the ground toward the channel. Deposits of fine gray sand, sand boils, and open fissures filled with vented sands were abundant throughout the damaged portion of Dagupan. Sedimentologic controls, such as the presence of especially loose sands deposited in an abandoned river meander, may have controlled the areal distribution of liquefaction in Dagupan. No structural damage was observed elsewhere in the city where liquefaction was not observed. At the time of our visits, pumps were being used to remove water from sunken first stories of buildings. Coastal areas that have subsided during the earthquake, such as Dagupan, could be subject to future flooding during high tides and typhoons. These dramatic effects due to liquefaction in Dagupan were similar to those observed in the 1964 Niigata, Japan earthquake (Seed and Idriss, 1982).

Other buildings, bridges and roads experienced liquefaction-induced damage in Rosales, Gerona, Paniqui, Aringay, and Agoo. Near Rosales three sections of the 13-section Carmen bridge over the Agno River collapsed from liquefaction-induced loss of bearing capacity. Sections of decking and superstructure fell from bridge supports, which had tilted up to 30 degrees from vertical. Large sand boils covered parts of the floodplain on both sides of the Agno River and were both brown and gray, which indicates that two different subsurface strata of sand had liquefied. Sand also came up along fissures, some of which extended for hundreds of meters across the floodplain on both sides of the river. These fissures were open as much as 1 to 2 m and were very numerous across the broad floodplain. They were primarily oriented parallel to the river and indicated extensional movement related to lateral spreading of perhaps 10 m of cumulative displacement toward the center of the channel. The disruption of transportation across the Carmen bridge necessitated rerouting of earthquake relief traffic to Baguio from Manila through the lengthier route through Camiling and Dagupan. These types of liquefaction effects were noted along many of the river banks throughout the western part of the area affected by the earthquake. During the 1964 Alaska earthquake, comparable bridge damage was caused by liquefaction and similar lateral ground displacements (McCulloch and Bonilla, 1970).

In Gerona, the town hall was severely damaged by collapse of the heavy structure due to settlement of the load bearing columns and walls into a zone of liquefied sand. The heavy walls and columns supporting the two-story concrete structure settled as much as 1.3 m into the ground. Steps that originally led up to the first floor level were now left suspended in mid air at the edge of the building. Sand boils occurred within and adjacent to the town

hall; they were reported to be shooting sand and water about 4 m into the air in the nearby city park during the earthquake. The water table in this vicinity was reported to be only about 2 meters deep.

About 1 km north of Paniqui, subsidence and lateral spreading from liquefaction affected a 0.1-km section along the banks of the Santa Lucia River. To the west of Highway 3 at this locale, a newly constructed meat processing plant subsided about 2 m and tilted because of loss of bearing capacity. The entire area flooded as a result of the diversion of flow from the river into this new topographic depression. Fissures and sand boils were abundant to the east of the highway; sand and water reportedly came out of the ground as fountains that vented up to 4 m in height for 10 s after the earthquake.

Abundant sand boils and ground fissures in the coastal areas between Dagupan and Aringay could be observed from a light airplane; however, inaccessability on the ground limited detailed examination of these areas. Near Aringay, several of the piles of the abandoned Manila Railroad bridge over the Aringay River tilted in a direction that indicated lateral spreading toward the channel. Open fissures extended for hundreds of meters along the banks of the Aringay river and also indicated lateral movement of the ground. A small village on the outskirts of Santa Rita on the south side of the Aringay River to the west of the main highway was extensively damaged by liquefaction-induced lateral spreading. A series of multiple fissures, spaced at roughly 1-m intervals, paralleled the river and extended at least 250 m from its edge. Some individual fissures opened as much as 0.5 to 1.0 m and were filled with sand and water (fig. 4). Cumulative horizontal displacement across these extensional features amounted to at least several meters toward the river. Several one- and two-story wooden structures collapsed, but the presence of open ground fissures beneath these buildings and nearby sand boils indicated that liquefaction-induced ground failure was the primary cause of the damage. About a kilometer to the west, still along the south side of the Aringay River, large sand boils up to 4 m in diameter filled entire sections of rice paddies.

In the small villages among the fish ponds to the southwest of Agoo, subsidence and lateral displacements accompanied liquefaction. Large isolated sand boils were noted both on the ground and from the air; the largest individual sandboil was approximately 10 m in diameter. The four-room San Nicholas Elementary School subsided 0.5 m and had cracks in the walls associated with lateral ground movements. This low-lying area has a high ground-water table and, as a consequence of subsidence and collapse of small dikes, much of the area flooded and remained isolated because of submergence of the few roads.
Landsliding and Secondary Effects
Landslides triggered by the earthquake occurred throughout central and northern Luzon. Landslides were most abundant in the mountainous areas west and northwest of fault rupture along the

Philippine and Digdig faults. We observed landslides from Dingalan Bay on the east to Lingayen Gulf on the west, and as far north as Sante Fe and Baguio, although others reported landslides almost as far north as Vigan. Some landslides probably were triggered throughout the mountainous terrain of northern Luzon given the large magnitude of the earthquake and historic worldwide documentation of landslides generated by similar earthquakes elsewhere (Keefer, 1984). Landslides were abundant as far north as we could travel in the Digdig valley and near Baguio. To the south, within the broad flat alluvial valley of the Central Luzon plain, only a few small landslides occurred, principly slumps or earth block slides of road embankments, which may have been caused by liquefaction of underlying saturated materials.

In mountainous areas, landslides were predominantly shallow (less than 1 m deep) soil and rock slides of tropical residual soils incorporating minor weathered bedrock. Only a few block slides and slumps of soil and rock were observed. Few dormant landslides were reactivated by the earthquake. In the most affected areas, landslides denuded entire hillsides, including vegetation, and carried this debris into first order and higher tributaries (fig. 5).

These soil and rock slides occurred preferentially on steep slopes of ridge crests and noses where focusing of incoming seismic waves may have caused high tensile stresses in weak surficial materials. This pattern of slope response to earthquakes is in marked contrast to that which results during storms, where landslides are initiated by high pore-water pressures due to concentration of subsurface runoff in topographic depressions. The topographic setting, distribution, and major types of landslides in this earthquake were similar to those in the 1976 Guatemala (Harp et al, 1981) and 1987 Ecuador earthquakes (Nieto and Schuster, 1988).

Landslides in this earthquake hampered search and rescue as well as emergency response efforts to bring food and medical supplies to remote areas. In addition, heavy monsoon rains caused continued movement of landslides initiated by the earthquake. Debris flows mobilized from the loose soil and rock debris that had accumulated at the base of slopes and in the primary and higher order channels. These debris flows caused additional casualties, destroyed buildings, covered roads, and kept many areas isolated. The accumulated landslide debris also accentuated the flooding problems by increasing the sediment content of streams and rivers. Some rivers overflowed their banks in storms early in the monsoon season, and some bridges were blocked by logs and sediment (fig. 6). Some landslide dams blocked channels that later breached and released unsuspected floods. "At least 13 people are feared dead after being buried beneath a torrent of water, rocks, and mud in a remote town...Landslides after a devastating earthquake on July 16 blocked the path of the river and created a natural dam which gave way on Sunday [7/29/90] evening on the outskirts of Carranglan, Nueva Ecija Province" (Philippine Star, 7/31/90). The headwaters of the Abra River near Vigan were likewise filled with

43

debris following the earthquake, and the river was reported to have fluctuated suddenly with high sediment content, suggesting repeated breaching of landslide dams on upstream tributaries (Jesse Umbal, Philippine Institute of Volcanology and Seismology, personal communication, 7/26/90).

Perhaps the area of most abundant landsliding was the Caraballo Mountains, where the Dalton Pass Highway from San Jose to Sante Fe links Manila with northern Luzon. Continuous shallow soil and rock slides denuded entire hillsides from crown to base of slope. Over a distance of 27 km the highway was blocked by 14 major landslides and at least 82 minor slides having a total estimated cumulative volume of 1.45 million cubic meters (Philippine Department of Public Works and Highways, 8/2/90). In addition to removing landslide debris, other areas of the highway had problems caused by ground cracking that formed by incipient landsliding. Presence of the cracks suggested that additional movement could be triggered by either storms or earthquakes. This road was cleared and opened by 7/31/90, but in the afternoon an aftershock triggered a landslide that reportedly struck a bus along the highway and killed 17 people.

The monsoon season reactivated some landslides initiated by the earthquake and triggered additional new landslides as well. Such effects were observed along the Dalton Pass Highway and the Naguilian Road to Baguio, which was covered with new debris after every heavy rainfall. Rain water infiltrated and accumulated in places where the earthquake fractured a mass of soil or rock, building up excessively high pore water pressures, which triggered new landslides. In other cases, debris was shaken loose by the earthquake, transported and deposited in steep primary drainages, and then mobilized into debris flows and avalanches by concentrations of runoff from high on the hillsides.

Evidence of debris flows since the earthquake was observed at the mouths of the canyons where the Dipalo and Banila Rivers emerge from the mountains northwest of San Jose. On the Dipalo River many episodes of debris flows were noted beginning three days after the earthquake and as recently as 7/31/90, a day before our visit. This most recent debris flow started two hours after the rain began and lasted for 3 to 4 hours. The debris-flow front consisted of boulders, logs, and sediment, was about 4 m high, and extended 30 m in width across the channel.

At the Cuardaneta crossing of the Banila River, pulses of debris flows or hyperconcentrated flows were observed on 7/29 and 7/30. These flows sounded like a train as they came down the channel. Flow deposits were fine-grained and included logs, but they built no levees or had no other distinctive debris-flow morphology. However, about 3 km upstream, where the Banila River emerges from the canyon, a distinct 2- to 3-m-high levee attested to a debris flow from this canyon. The flow was about 100 m wide across the channel and widened significantly downstream, where it probably changed into a hyperconcentrated flow.

On August 27-30, 1990, Typhoon Abe triggered floods and landslides that killed 85 people in central and northern Luzon, swept away 250 houses, and left 1500 people homeless in villages along Dalton Pass. Hundreds of people bound for the rice-producing Cagayan valley were marooned by new landslides blocking the Dalton Pass Highway. On 8/27/90, a landslide buried 12 students of the Kalahan Academy, Sante Fe. In areas where the extent of denudation of hillsides by landsliding was estimated to be as high as 60 percent after the earthquake, the area was 100 percent bare after passage of the typhoon (Kelvin Rodolfo, University of Illinois, Chicago, oral communication, 9/27/90).

Rock falls, rock block slides, and rock and soil slides in the earthquake posed a serious problem to all roads leading to Baguio. These landslide problems along the Kennon Road in the valley of the Bued River stranded hundreds of travelers immediately after the earthquake and, together with the blockage of the Naguilian and Cagayan Roads, prevented ground traffic access to Baguio for two weeks. This prevented heavy construction equipment, such as cranes, from reaching the sites of collapsed hotels and other structures in Baguio to assist in the rescue operations.

Landslides also damaged structures within Baguio, including the airport runway and terminal buildings. On a moderately flat slope a 100-m-wide earth block slide slightly displaced the runway, taxiways, and terminal buildings. Although both horizontal and vertical movements across the main scarp and individual internal cracks were small, typically less than 0.4 m, the walls and floors of the buildings had cracked and rotated. The runway had been repaved to fill the cracks, but a noticeable bump remained as a result of vertical offset across the crack on the runway.

Ground failure appeared to be only a very minor factor at most of the sites in Baguio where several large structures collapsed. At the Hyatt Terraces Hotel (fig. 7), only a small rotational earth slump occurred in the driveway on the north side of the Hotel. The arcuate cracks of the main scarp of this small slump, perhaps 5 m wide, showed less than 0.3 m total movement across the scarp and contributed to the collapse of a small masonry wall on the outside edge of the driveway. Near the building these cracks did not pass beneath the structure. Other discontinuous cracks in the road on the northeast side of the hotel along the driveway were probably a result of compaction and settlement of the fill used as a subbase for the road.

At the Export Processing Zone, where a three-story factory building collapsed (fig. 8), cracking in a road was noted along the southern side of the building. About six discontinuous cracks, each several meters long, opened less than 5 cm. No lateral or vertical shear movement was discernable. These cracks were parallel to the southern edge of the building and were aligned with the direction of the road; they did not trend under any part of the structure. The cracks did not indicate landsliding and probably represented

45

compaction and settlement of the fill beneath the road and building.

The collapse of the Nevada Hotel in Baguio was accompanied by a slump beneath the northwestern corner of the building. The back of this building is founded upon a steep slope where a slump initiated. The main scarp of this slump cut through the hotel parking lot and passed beneath the foundation of the northeastern corner of the hotel. Total maximum displacement across the scarp of about 0.4 m gradually decreased where the scarp passed beneath a nearby business and residence, which were both damaged by the slump. The scarp became a single crack to the northwest, where the scarp ended in the driveway about 10 m beyond the residence.

In and around Baguio landsliding damaged other houses that had been built on steep slopes, backed up to steep slopes, or were located along the edges of a ridge where there was an abrupt change of slope. In these cases, shallow slides undermined the foundation of the structure or the rapidly moving landslide destroyed the house upon impact from above. In nearby Trinidad Valley landslides reportedly swept some homes downslope and broke waterlines at various points, leaving 20 areas without water.

An unusual landslide was triggered by the earthquake at Bateria, near Ligaya, in Nueva Ecija province. A large soil lateral spread travelled more than 500 m across a wide flat broad field. The overall slope between the crown of the main scarp and the toe where the slide came to rest was only 2.5 to 3.5 degrees. Near the crown the slide was 266 m wide; previously a road had crossed the gently sloping area. A 5-m-high main scarp exposed a gravelly gray sand with some angular to semi-rounded boulders (up to 0.3 m) having little or no stratification, possibly deposited as an alluvial fan. Eyewitness reports said that the landslide started moving during the earthquake and that black water and sand gushed out of the ground on the north flank of the landslide. There was a wavy motion of the ground as the slide advanced; slide movement was sufficiently slow that a farmer was able to outrun the advancing toe. Vegetation, including two trees, remained intact as it was rafted on the advancing toe of the slide. The toe of the slide was about 0.8 m thick. The slide stopped in a corn field, which subsequently flooded because the slide mass blocked drainage.

The Bateria slide was unusual because of the gentle slope on which it initiated and the great distance it moved. However, liquefaction and the consequent loss of strength along a basal sliding surface could account for this behavior. Depending upon age of deposition, saturated alluvial fan deposits can have varying degrees of susceptibility to liquefaction; younger deposits generally have higher susceptibility than older deposits (Youd and Perkins, 1978). The description of sand and water gushing from the ground strongly suggests that liquefaction was involved, although shallow water was not observed in the crown of the slide or elsewhere. However, the crown is only about 200 m from the mouth of a small canyon where surface and subsurface flow could

46

concentrate. Rain had not occurred in the week before the earthquake, which might account for the brittle behavior of the ground surface. A liquefied layer at shallow depth might account for the initiation of movement and a relatively high mobility of a thin brittle landslide mass moving over it. The waviness of the movement possibly could be attributed to the reflections on the surface of the original topography over which the brittle slide mass moved. Soil lateral spreads that move in a translational manner on zones of liquefied sand are not unusual; however, in previous documented earthquakes most have occurred in flood-plain alluvium, only a relative few have been noted in alluvial fan deposits (Keefer, 1984).

References

Harp, E.L., Wilson, R.C., and Wieczorek, G.F., 1981, Landslides from the February 4, 1976, Guatemala earthquake: U.S. Geological Survey Professional Paper 1204-A, 35p.

Keefer, D.K., 1984, Landslides caused by earthquakes, Geological Society of America Bulletin, v. 95, p. 406-421.

McCulloch, D.S., and Bonilla, M.G., 1970, Effects of the earthquake of March 27, 1964, on the Alaska railroad: U.S. Geological Survey Professional Paper 545-D, p.D1-D161.

Nieto, A.S., and Schuster, R.L., 1988, Mass wasting and flooding induced by the 5 March 1987 Ecuador earthquakes: Landslide News, newsletter of the Japan Landslide Society, 2:1-3.

Seed, H.B. and Idriss, I.M., 1982, Ground Motions and Soil Liquefaction During Earthquakes: Earthquake Engineering Research Institute, Berkeley, California, 134p.

U.S. Geological Survey and Philippine Institute of Volcanology and Seismology, 1990, The July 16, 1990, Luzon Earthquake: Final Administrative Report, October 29, 1990, 59p.

Varnes, D.J., 1978, Slope movement types and processes, in Schuster, R.L., and Krizek, R.J., eds., Landslides Analysis and Control: Transportation Research Board Special Publication 176, National Academy of Sciences, p. 11-33, 1 pl.

Youd, T.L., and Perkins, J.B., 1978, Mapping liquefaction-induced ground failure potential: American Society of Civil Engineers, Journal of the Geotechnical Engineering Division, GT4, p. 433-446.
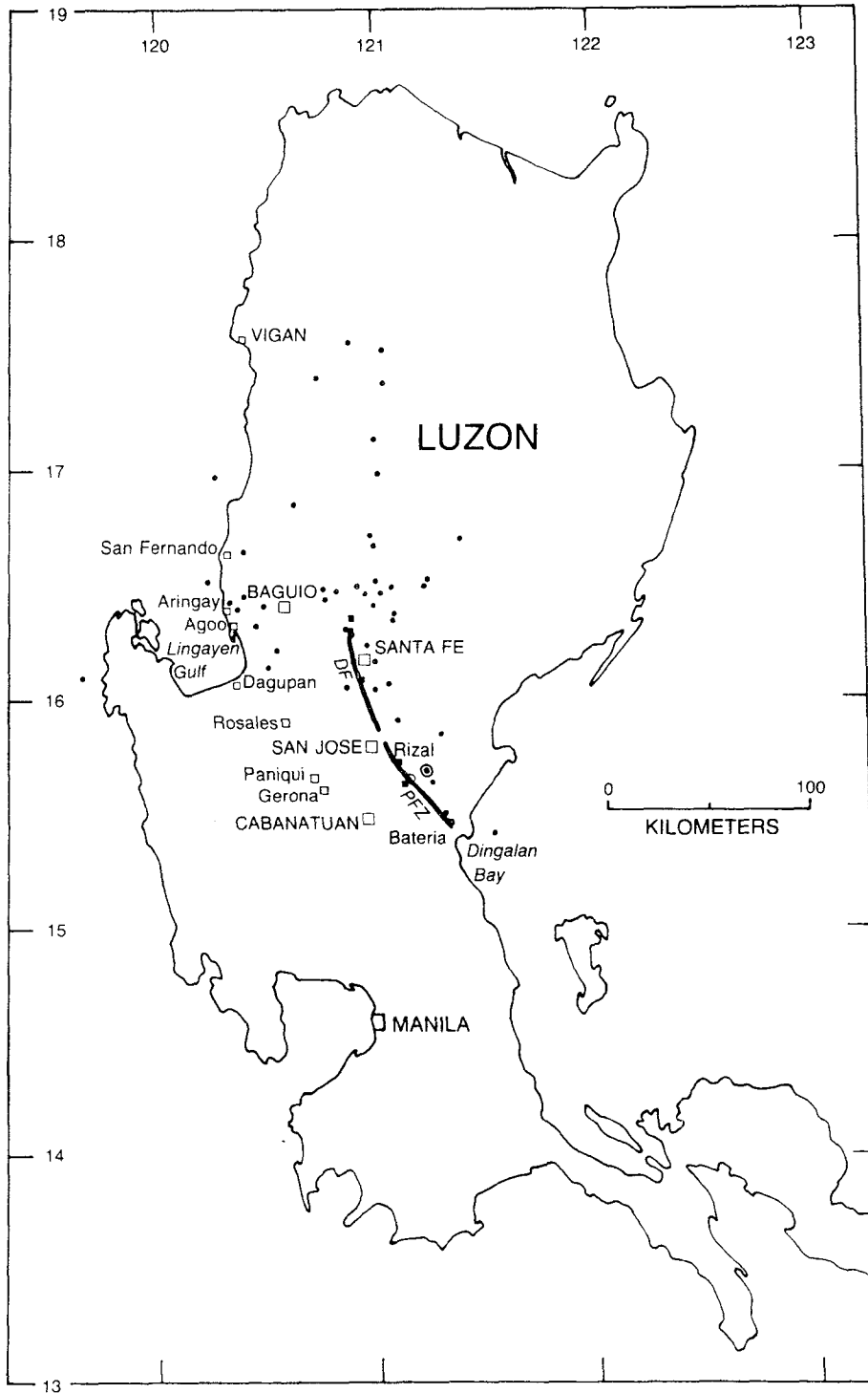
Figure 1 - Area affected by the July 16, 1990, Luzon, Philippines earthquake. Heavy lines labeled PFZ and DF indicate the Philippine fault zone and Digdig fault which experienced left-lateral rupture in the earthquake. The circled dot represents the epicenter of the mainshock and the other dots represent epicenters of aftershocks within 27 days of mainshock, located by the U.S. Geological Survey National Earthquake Information Center.

Figure 2 - Building that tilted as a result of bearing capacity foundation failure due to liquefaction on Perez Blvd., Dagupan City. Ground shaking turned sandy, water-saturated soils beneath Dagupan into liquid that could no longer support buildings. Sand that had spouted to the ground surface is visible on the road surface in the foreground.

Figure 3 – Building that tilted and settled at least 1 meter due
to liquefaction at the corner of Perez Blvd. and Galvan St.,
Dagupan City. The ground floor that was previously at or above
street level is now below street level.

Figure 4 - Ground fissures of a liquefaction-induced lateral
spread, parallel to the Aringay River near Aringay. Ground surface
fractured and moved towards river upon liquefied zone of
cohesionless soil at shallow depth.

Figure 5 - Abundant, shallow-seated landslides near the trace of the Digdig fault. Note that most soil slides originated at ridge-crests or the tops of steep slopes-- a pattern typical of earthquake-induced landslides.
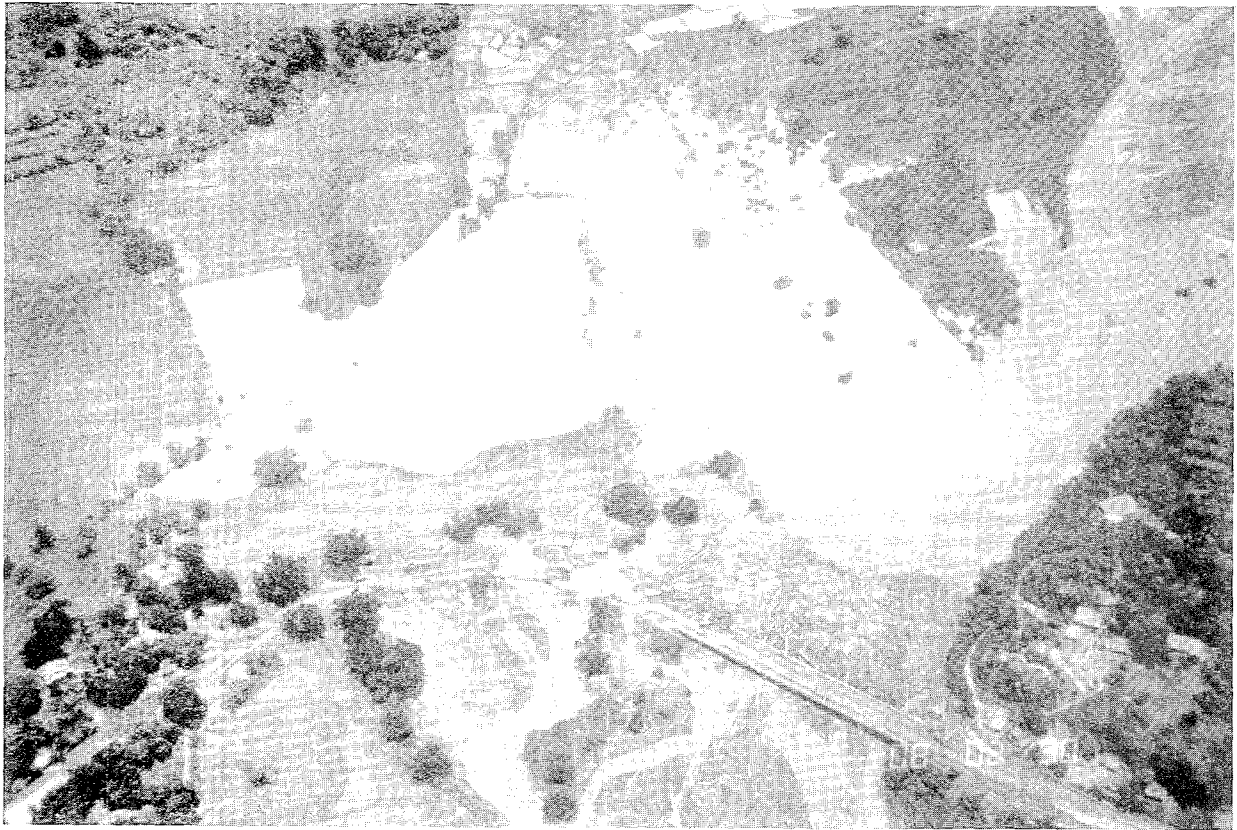
Figure 6 - Flooding over the Puncan Bridge, between San Jose and Sante Fe. Landslides brought abundant soil and trees into streams; erosion (including breakouts of small landslide dams) carried the debris downstream, where at the bridge, it jammed the channel. (photograph by Chris Newhall)

53
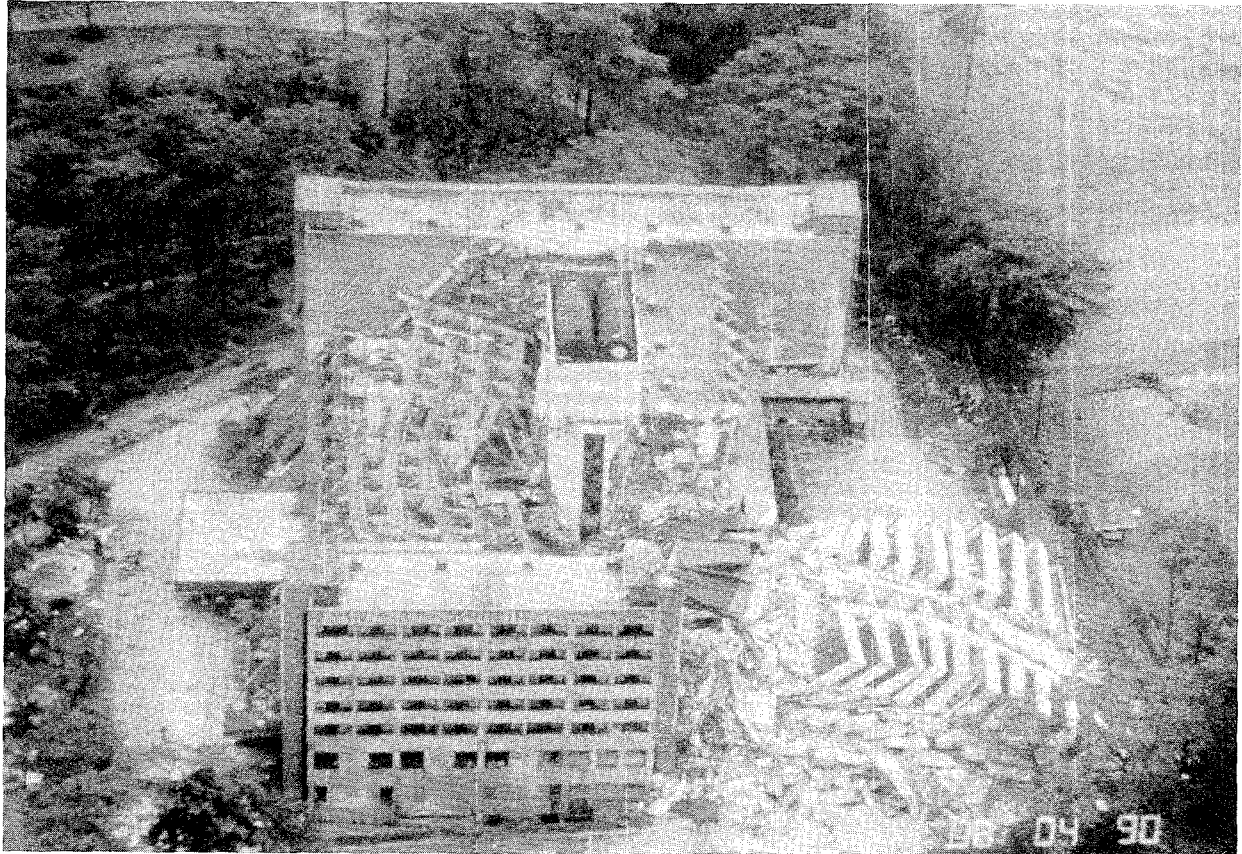
Figure 7 - Hyatt Terraces Hotel, Baguio City. Condominium section
(lower right) collapsed during the main shock; central atrium
section collapsed during an aftershock two hours after the main
shock. Small slump occurred in the driveway on the north side of
the hotel (upper left). (photograph by Chris Newhall)

54
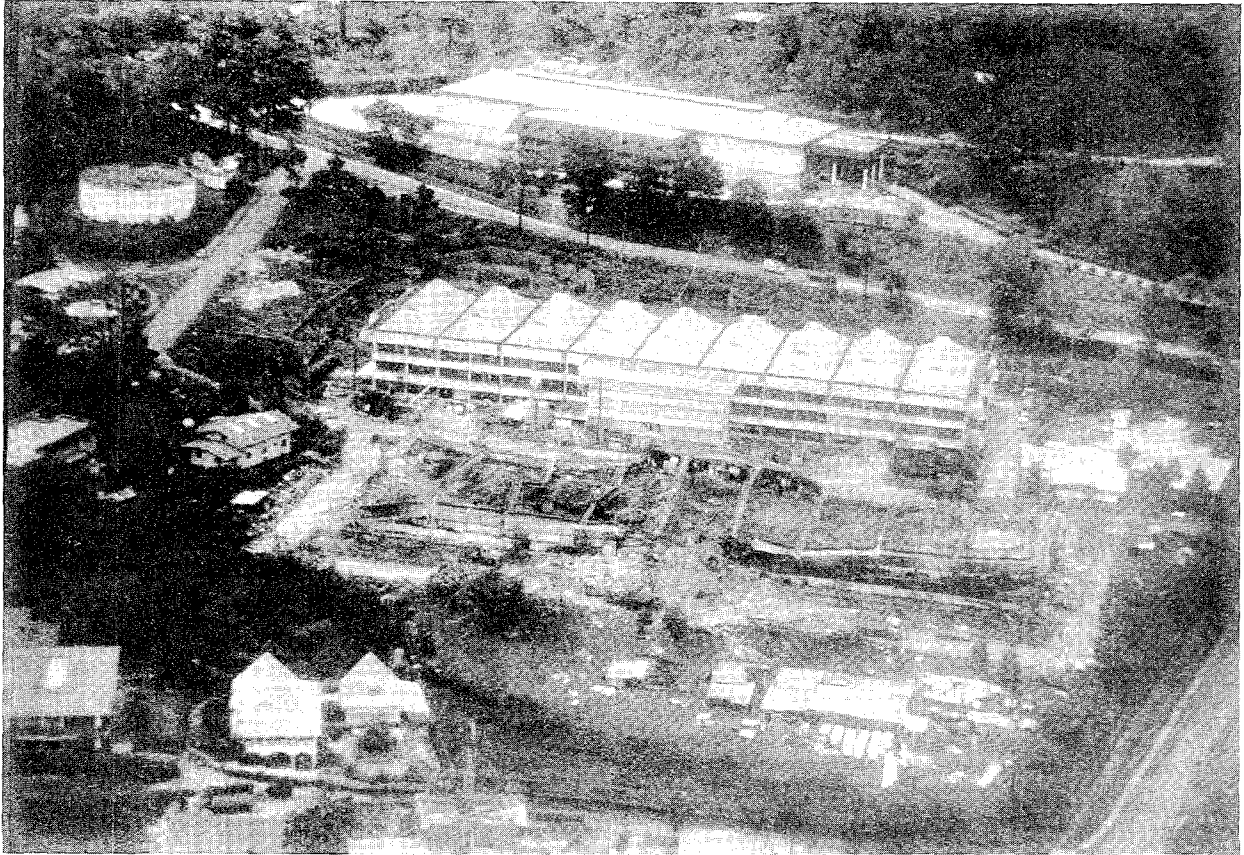
Figure 8 – Standard Factory Building 1 (standing, center) and
Building 2 (collapsed, foreground), Baguio Export Processing Zone.
The foundation of Building 1 was cut into a gentle hillslope; the
foundation of Building 2 was on fill. Minor cracking was detected
in road (center) parallel to long direction of collapsed building.

LIQUEFACTION-RELATED GROUND DEFORMATION AND EFFECTS ON FACILITIES AT TREASURE ISLAND, SAN FRANCISCO, DURING THE 17 OCTOBER 1989 LOMA PRIETA EARTHQUAKE

John A. Egan[1] and Zhi-Liang Wang[2]

[1]Senior Engineer, [2]Senior Staff Engineer
Geomatrix Consultants, Inc.
One Market Plaza, Spear Street Tower, Suite 717
San Francisco, California   94105

ABSTRACT

Treasure Island is a man-made island situated in San Francisco Bay approximately midway between the cities of San Francisco and Oakland, California. The island was constructed during the 1930's by hydraulically placing sand fill behind a series of perimeter rock dikes founded on the bay bottom. Following the 17 October 1989, $M_w7.0$ Loma Prieta earthquake, liquefaction-related phenomena, including sand boils, ground surface settlement, and bayward lateral spreading movements, were evident at many locations across the island. Buildings and underground utilities were affected by lateral spreading and ground settlement deformations, with more than half-a-dozen buildings suffering significant damage and more than forty underground utility pipeline breaks occurring among water, sewage, and gas lines. This paper presents the liquefaction-related ground deformation phenomena observed at Treasure Island during the Loma Prieta earthquake and examines the relationships among lateral spreading movements and ground settlement deformation patterns, subsurface ground conditions, and performance of structures and underground utility lines.

INTRODUCTION

Treasure Island is situated in San Francisco Bay, approximately midway between the cities of San Francisco and Oakland, California. The island is man-made and was constructed in the late 1930's using mostly fine-to-medium-grained sands dredged from borrow areas within the Bay and placed hydraulically on the Bay bottom sediments. The 17 October 1989 Loma Prieta earthquake ruptured along a portion of the San Andreas fault in the southern Santa Cruz Mountains, approximately 50 miles (80 km) south of the San Francisco-Oakland metropolitan area. Ground motions recorded at Treasure Island during the Loma Prieta earthquake are characterized by a horizontal peak ground acceleration of 0.16 g and were approximately triple the level of motion recorded on rock at the adjacent Yerba Buena Island. Following the earthquake, effects of strong ground shaking were evident across Treasure Island. The recorded ground motion levels were determined to be sufficient to induce liquefaction in many portions of the island fill. Sand boils, noted at numerous locations, substantiated the occurrence of liquefaction of subsurface materials. Liquefaction within the island fill is attributable for bayward lateral spreading movements in the vicinity of the island perimeter and ground settlement across the island. Ground cracking associated with the bayward lateral spreading was readily visible and exhibited translational and slumping components of displacement. Individual cracks as wide as 6 inches (150 mm) were observed and the overall cracking distribution indicated lateral displacements as large a foot (0.3 m) at the island perimeter. Observations of ground settlement, both areal and localized, were made in many portions of the island. Available ground survey measurements indicate that the surface of the island subsided by approximately 2 to 6 inches (50 to 150 mm), variably across the island; but there are indications of areas within which the estimated settlement may have been as large as 8 to 10 inches (200 to 250 mm). Liquefaction-related ground deformations resulted in distortion and significant damage to several structures, numerous broken underground utility lines, and other forms of distress to Treasure Island facilities.

TREASURE ISLAND CONSTRUCTION HISTORY

Treasure Island was originally conceived of as a mid-Bay airport facility; but the concept quickly evolved into a site for a celebration of the completion of the Golden Gate and San Francisco-Oakland Bay bridges, which took the form of the 1939 Golden Gate International Exposition. The shape and dimensions of the island [approximately 5,500 ft (1,680 m) long by 3,400 ft (1,040 m) wide] were dictated by requirements for the airport concept. Over 29 million cubic yards (22 mil. m^3) of mostly fine-to-medium-grained sand material was dredged from various borrow sources located within San Francisco Bay during filling operations that began in February 1936 and were completed in August 1937 (Lee, 1969). Approximately 21 million cubic yards (16 mil. m^3) remained in-place to create the 397-acre island over the shallow Yerba Buena Shoals north of Yerba Buena Island; the remainder being lost to wind and wave erosion, fill and soft clay settlement, and washing away of fines during deposition. The bay bottom in the Shoals area varied in elevation between -2 ft (-0.6 m) and -26 ft (-8 m) Mean

Lower Low Water (MLLW) across the island footprint. Approximately 65 percent of the bay bottom sediments in this area were composed of sand, with soft clay exposed over the remainder of the site.

The island was constructed under the direction of the U.S. Army Corps of Engineers by hydraulically placing the fill materials using pipeline, hopper, and clam shell dredge equipment. In areas where the Shoals were deeper than El. -6 ft (-1.8 m) MLLW, a bed of hydraulic sand fill was placed. Next, along the island perimeter, a low mound of rock was placed on either the native soil or fill materials and acted as a retaining dike for subsequently placed sand fill. Fill material was pumped or deposited in place until it approximately reached the top of the low rock mound. Another low rock mound was then placed on the previously constructed rock dike and fill and the process continued. This process was repeated until the surface of the fill reached approximately El. 13 ft (4 m) MLLW. The 1937 photograph of construction progress presented in Figure 1 (as viewed from the north) shows that the rock dikes were not constructed to surround the entire island concurrently, but rather they progressed outward as fill was deposited, starting at the southwest corner of the island and worked their way around the west, south and east towards the north. A low weir was installed near the center of the north seawall to allow water from the hydraulic dredges and soft mud displaced by the fill to escape as the operation proceeded from south to north. On occasion, however, the mud became trapped within the island perimeter and a small dredge was set up inside the dike to excavate the trapped mud as it was pushed up by the filling operations.

A failure of the perimeter dike occurred during construction near the north end of the east dike. A 500-foot-long (150-m) section of dike settled 10 to 14 ft (3 to 4 m). This area was stabilized by flattening the slope and placing a bed of "heavy" sand beyond the toe of the dike to act as a counter weight. As a result of the failure, the north seawall was modified by excavating a trench approximately 400 ft (120 m) wide and 20 to 30 ft (6 to 9 m) deep along the seawall, backfilling the trench with coarse sand, and then constructing the initial rock dike on that bed of sand (Lee, 1969).

GEOTECHNICAL SUBSURFACE CONDITIONS

Treasure Island is a relatively flat island. The crest of the perimeter dike varies in elevation between 10.5 and 16 ft (3.2 and 4.9 m) MLLW. The island's interior ground surface varies betweem approximately El. 6.5 and 14.5 ft (2 and 4.4 m) MLLW. Ground water levels at Treasure Island are affected by the fluctuation of tide level, which reaches an average elevation of 6 ft (1.8 m) MLLW during flooding tides and an elevation of 0 MLLW during ebbing tides. Water levels in the island perimeter area are affected by the rate of seepage into and out of the sand fill materials and may not reach the same levels as in the bay. During the Loma Prieta earthquake, the tide was ebbing; consequently, we believe that the water was at approximately El. 3 ft (1 m) MLLW. In the Treasure Island interior, ground water levels are less affected by tides and are typically at depths of 5 to 8 ft (1.5 to 2.4 m) below the ground surface.

Since 1953, more than 300 locations at the island have been explored by either drilling and sampling borings or in situ cone penetration testing, as illustrated by Figure 2. Subsurface materials encountered by the borings and cone penetration tests can generally be divided into four strata: loose to medium dense hydraulically-placed sand fill materials; loose to medium dense native, Yerba Buena Shoals sands and medium stiff native clays; recent Bay sediments consisting primarily of medium stiff to stiff olive gray silty clay (referred to locally as Bay Mud), but containing some soft clay zones as well; and older Bay sediments consisting of brownish and greenish gray very stiff sandy, silty, and/or peaty clays and dense sands. The generalized stratigraphic conditions across the island are illustrated in north-south and east-west cross sections presented in Figure 3. These cross sections are located as shown on Figure 2.

The fill material encountered in the borings matches quite well with the material described by Lee (1969). The fill is a fine-to-medium-grained sand that has gradations ranging from well to poorly graded, and contains different amounts of gravel, silt and clay depending on its location. The material can, in some areas, be differentiated from the native Yerba Buena Shoals sands and clays by its density, with the fill material being somewhat looser and having lower penetration resistances and lower shell contents. However, on the average, the fill and shoals materials appear to be very similar in engineering characteristics and their behavior during earthquakes is expected to be similar; therefore, they are treated herein as a combined stratigraphic unit. Thickness contours for the fill and native, Yerba Buena Shoals materials are illustrated in Figure 4. Except for a deeper section along a reach of the perimeter dike on the northern side of the island and a small thinner pocket on the island's south side, the combined thickness of the hydraulic fill and Yerba Buena Shoals materials varies between approximately 30 and 50 ft (9 and 15 m), being thinnest at the southwest corner of the island and thickening toward the North. Along the dike on the northern side of the island, reports on the island's construction history indicate that a key was dredged out within the native shoals and recent bay sediments and backfilled with a bed of "heavy sand" (Lee, 1969). This foundation of heavy sand material makes the total thickness of fill approximately 70 ft (21 m) in this area.

Figure 5 presents cross sections of Standard Penetration Test (SPT) blowcount, $(N_1)_{60}$, contours in the fill and native Shoals materials. These cross sections correspond to the stratigraphic cross sections illustrated in Figure 3. The SPT blowcounts were derived from the data available from both the borings in which the penetration tests were conducted using appropriate procedures (i.e., rotary wash drilling techniques, appropriate hammer size and drop, sampler, etc...), and Cone Penetrometer Test (CPT) probes, for which the data were converted to blowcount data utilizing a site-specific SPT-CPT correlation developed from the SPT blowcount data, soil classification, and the CPT tip resistance at locations where SPT borings and CPT probes were immediately adjacent to one another. All blowcounts were corrected to "Standard" blowcounts, $(N_1)_{60}$, as detailed by Seed and others (1985). The blowcount contours indicate the fill and native Shoals materials to be, in general, loose to medium dense and susceptible to liquefaction under earthquake ground shaking. Near surface materials are generally denser than the deeper materials. This layer of denser surficial material appears to vary in thickness across the island in no consistent pattern.

Below the hydraulic fill and native Shoal materials is a stratum of recent Bay sediments composed primarily of a medium plastic, olive gray silty clay (known locally as Bay Mud); although in some areas, this stratum also includes interlayered beds of sand and silt. The recent Bay sediments vary in thickness between 10 and 120 ft (3 and 36 m), being thinnest on the eastern perimeter of the island and thickest at the northwestern side of the island. The bottom of the recent Bay sediments is distinguished as the interface between the upper materials that were likely deposited in a marine environment and are normally-consolidated, and older Bay sediments that are lightly-to moderately overconsolidated, yellowish-brown, and may have been exposed to a non-marine environment.

The older Bay sediments are generally stiff to very stiff sandy, silty and/or peaty clays that extend to Franciscan bedrock. The variation of thickness for these older Bay sediments is not known as only one exploratory boring on the island penetrated to bedrock. This boring, drilled in 1966, indicates that bedrock is about 280 ft (85 m) below ground surface at the boring location (Boring Index #69 shown in Figure 2). Based on this information and information contained in Goldman (1969), we believe that the bedrock varies between El. -150 and -320 ft (45 m and -100 m) MLLW, being most shallow at the south side of Treasure Island (nearest Yerba Buena Island) and deepest to the north. This indicates thicknesses of the older Bay sediments between approximately 20 and 170 ft (6 and 50 m).

LOMA PRIETA EARTHQUAKE GROUND SHAKING

Treasure Island lies within the San Francisco Bay Area, considered to be one of the more seismically active regions of the world. The location of Treasure Island relative to active faults in the Bay Area is shown in Figure 6. The San Andreas fault, which extends over 750 miles (1200 km) from the Gulf of California to Cape Mendocino, is the predominant fault within the region and was the source for the 17 October 1989 Loma Prieta earthquake. The Loma Prieta earthquake (moment magnitude, M_w 7.0; surface wave magnitude, M_s 7.1) occurred on the portion of the San Andreas fault in the Southern Santa Cruz Mountains; the closest point of the Loma Prieta earthquake rupture zone along the fault was approximately 50 miles (80 km) from Treasure Island (see Figure 6).

The Loma Prieta earthquake triggered more than 130 strong-motion instruments of the California Division of Mines and Geology, the U.S. Geological Survey, and the University of California at Santa Cruz throughout the Central Coast area of California, to distances of about 100 miles (160 km) from the fault rupture. The largest horizontal peak ground acceleration recorded during the event was 0.64 g, obtained at the town of Corralitos on an instrument founded on shallow stiff soil and located about 3 miles (5 km) from the fault rupture. A significant observation resulting from the Loma Prieta earthquake was the apparent amplification of ground motion levels at sites underlain by thick deposits of Bay sediments (e.g., Bay Mud) relative to nearby rock sites. The strong-motion recordings obtained on Treasure Island and Yerba Buena Island, illustrated in Figure 7, provide an example of such amplification. The peak ground accelerations of 0.16 and 0.10 g recorded on the horizontal components of the

Treasure Island instrument, located at the island fire station, were approximately three times larger than those recorded by the Yerba Buena Island instrument which is founded on rock. Other deep, soft sediment sites within the San Francisco-Oakland-Emeryville area exhibited similar amplification. Strong-motion recordings of the mainshock at such stations had horizontal peak ground accelerations in the range of 0.22 to 0.29g, whereas for nearby rock-site stations, horizontal peak ground accelerations were typically in the range of 0.05 to 0.10g, indicating amplifications on the order of 2 to 4 times. Site amplification effects of this order were also exhibited by recordings obtained at temporary stations in Oakland and in the San Francisco Marina District during aftershocks.

Examination of the Treasure Island record presented in Figure 7 indicates that a period of intense ground shaking was experienced, followed by a period in which the ground shaking intensity was substantially subdued. This intensity change is speculated to correspond to the onset of liquefaction in the sand fill. The time at which liquefaction is likely to have occurred is at approximately the 15 second mark of the Treasure Island record in Figure 7 and is about five seconds after the beginning of strong shaking.

LOMA PRIETA EARTHQUAKE EFFECTS

Following the Loma Prieta earthquake on October 17, 1989, effects of strong ground shaking were evident across Treasure Island. Liquefaction-related phenomena, including sand boils, ground cracking associated with bayward lateral spreading, and ground settlement, were readily visible. Observable effects to Treasure Island facilities included distortion and cracking of buildings and other structures, broken utility lines, and buckled pavements and curbs. A map of significant distress features and effects of the Loma Prieta earthquakes on Treasure Island is illustrated in Figure 8. The information illustrated on the map was compiled from several sources including: field mapping conducted by Geomatrix geologists and USGS geologist, Michael J. Bennett, aerial photographs taken by Pacific Aerial Surveys on 18 October 1989 and 1 November 1989, a post-earthquake Facility Inspection Report prepared for the Navy by Applied Management Engineering, information provided by Naval Station personnel on damage and repairs to housing units, and information provided by the Public Works section of the Naval Supply Center on utilities damage and repair.

Liquefaction

Sand boils were observed at many locations across the island, substantiating that liquefaction of subsurface materials had occurred. Utilizing the ground motions recorded on Treasure Island during the Loma Prieta earthquake in the empirically-based procedures presented in Seed and others (1985) and National Research Council (1985), critical $(N_1)_{60}$ blowcounts were estimated to be between 10 and 15, such that materials having a blowcount value greater than the critical $(N_1)_{60}$ would not be likely to liquefy and those having a value less than the critical $(N_1)_{60}$ would be likely to liquefy. Examination of Figure 5 indicates that substantial portions of the island's

subsurface materials have blowcounts less than 10 and could reasonably be expected to have liquefied during the Loma Prieta earthquake ground shaking. For zones of material in Figure 5 with $(N_1)_{60}$ blowcount values between 10 and 15, the occurrence of liquefaction was marginal, and materials with $(N_1)_{60}$ blowcount values greater than 15, liquefaction is not expected to have occurred. Materials in this latter category are located primarily near the ground surface, in many cases above ground water and not expected to liquefy anyway. Sand boil evidence was especially prevalent in the northwest quadrant of the island. Examination of subsurface conditions for that area indicated that liquefied zones may have been within about 5 ft (1.5 m) of the ground surface in some locations of that area. In fact, comparison of reported sand boil locations from across the island with the $(N_1)_{60}$ blowcount contours indicated that boils were observed in areas where the liquefied fill was within about 10 ft (3 m) of the ground surface.

Lateral Spreading

Lateral spreading movement was most prevalent along the eastern side of the island, especially between 3rd and 5th Streets and near 11th Street. At both of these locations, cracks of 0.5 inches (15 mm) or more were observable along Avenue M, approximately 550 ft (170 m) inland from the perimeter dike. Summation of horizontal crack widths toward the perimeter indicates that bayward movements of 6 to 12 inches (150 to 300 mm) may have occurred at the dike in these areas. Pre- and post-earthquake horizontal coordinates data for a benchmark situated near the perimeter dike, near the intersection of Avenue N and 3rd Avenue, indicated approximately 10 inches (250 mm) of lateral movement in a primarily eastward direction. In most other areas of the island, lateral spreading cracking was limited to much lesser inland extent; the northeastern corner showed movements as far as about 200 ft (60 m) from the dike, the western side was generally limited to inland distances of 150 ft (45 m) or less, and on the northern side, cracking was observed as far as 100 ft (30 m) from the dike and here the zone of spreading was localized within the area of deep fill. No significant lateral movement was observed along the remainder of the northern side, nor in the northwestern portion of the island involving the residential housing area. This lack of observed ground movement for the Loma Prieta earthquake may be a result of improved stability due to the wider perimeter rock dike in this area.

Observations made on Treasure Island immediately following the earthquake, and during subsequent days and weeks, indicate that the lateral spreading movement occurred during the ground shaking and did not continue to move after the earthquake. Based upon slope stability and deformation analyses conducted for several cross sections through lateral spreading zones using simplified procedures modified from Newmark (1965) and Makdisi and Seed (1978), the recorded ground shaking at Treasure Island, and the observed lateral deformations, undrained residual strengths exhibited by the liquefied sand fill and Shoals materials were on the order of 400 psf (19 kPa). This is consistent with the range of empirical data presented by Seed and Harder (1990).

Ground settlement

Ground surface settlement was quite obvious across the island, especially differential settlement adjacent to or inside of buildings, localized sinkholes, or vertical slumping associated with lateral spreading. Observations of ground surface settlement adjacent to piled structures (e.g., Buildings 2 and 3) and/or old pilings indicated that the magnitude of settlement associated with shaking-induced compaction of the subsurface materials was approximately 4 to 6 inches (100 to 150 mm). Areal subsidence of the island was not as evident by visual observation. The available pre- and post-earthquake ground survey data were compared and indicate that the surface of the island subsided by approximately 2 to 6 inches (50 to 150 mm), variably across the island. The benchmarks for the ground survey were established at various times during the past 50 years and the most recent pre-earthquake elevation data for each of these benchmarks was measured on different dates within the period June 1986 to April 1989. The post-earthquake ground survey was conducted primarily in December 1989, with some benchmarks surveyed in February 1990.

To obtain a more complete picture of the settlement variation across the island than provided by the limited survey data, estimated ground surface settlements associated with shaking-induced compaction were analyzed using $(N_1)_{60}$ blowcount data from the project geotechnical database, the observed Loma Prieta earthquake ground motions, and an approach for estimating the magnitude of earthquake-induced settlement of sandy materials modified from Tokimatsu and Seed (1987). [Note: The Tokimatsu and Seed (1987) procedures were found to overestimate the shaking-induced compaction settlement for the Loma Prieta earthquake by about a factor of two. A modified approach was developed that utilized the simplified framework of Tokimatsu and Seed (1987) as a basis, and incorporated the liquefaction assessment models of Liao and others (1988) and the influence of grain-size on post-cyclic volumetric strain described by Lee and Albaisa (1974).] The results of these analyses are illustrated in Figure 9, showing contours of estimated ground surface settlement associated with the Loma Prieta earthquake. Elevation changes at survey monument or reference point locations determined from the available ground survey measurements are also shown in Figure 9. There is reasonably good agreement between surveyed elevation changes and the settlement estimated from nearby SPT/CPT data. Figure 9 indicates that there are zones for which settlement may have been as large as 8 to 10 inches (200 to 250 mm). These areas typically correspond to areas where the thickest zones of liquefied fill/soil were expected to have occurred based upon examination of cross sections in Figure 5. Localized settlement, or more accurately slumping, accompanied lateral spreading near the perimeter dike. One particular area of interest is the northern dike area (in the vicinity of Section M-M', see Figure 2). Comparison of the pre- and post-earthquake aerial topographic survey photos indicate that the ground surface is about 1.5 to 2 ft (0.45 to 0.6 m) lower after the earthquake. Our estimate of Loma Prieta earthquake shaking-induced compaction settlement for this area is about 8 inches (200 mm), which would indicate that approximately a foot (0.3 m) of the elevation change may be associated with bayward lateral spreading.

Building Performance

The effects of the Loma Prieta earthquake on Naval Station Treasure Island facilities varied across the island and appears to correlate reasonably well to areas of more significant ground distress. Most of the buildings on the Naval Station reportedly suffered no or insignificant damage or distress that was limited to minor cracking or differential settlement. Several buildings did, however, experience greater damage. The buildings that suffered greater damage were generally situated near the perimeter dike and in areas of mapped significant ground distress, primarily lateral spreading, but also in areas that experienced estimated settlements of 6 to 10 inches (150 to 250 mm). It is also interesting to note that buildings located in areas that experienced settlements estimated to be on the order of less than 6 inches (150 mm) performed with generally only minor damage.

Buildings founded on improved ground or piles generally performed reasonably well during the Loma Prieta earthquake. No major structural damage was detected for three multi-story buildings founded in ground improved by densification using sand compaction piles and non-structural timber piles. Areas improved using stone columns also performed well. The densified areas exhibited no signs of ground deformation, while sink-holes and sand boils developed in adjacent areas. The ground around the pile-supported buildings settled noticeably, but the pile foundations for such buildings, as well as the structures themselves, performed reasonably well. The slab-on-grade interior floor systems of these buildings however, suffered from settlement of the underlying fill. Differential settlement between a pile-supported building and an attached section supported on shallow footings caused substantial distress at the interface between them. One building (No. 461) that was founded in ground improved to shallow depths [about 7 ft (2 m)] by soilcrete did suffer significant damage, but was in an area of bayward lateral spreading and the structure suffered from differential slumping movements.

Underground Utilities Performance

Underground utilities were significantly affected by lateral spreading movements and ground settlement associated with liquefaction. Forty-four breaks of utility pipelines were reported on maps provided by the Public Works section of the Naval Supply Center, and were distributed across the island at locations shown on Figure 5. The utility line breaks included 28 fire and freshwater lines of steel or asbestos cement construction, 10 sewage lines of vitrified clay construction, and 6 welded-steel gas lines. Broken lines had pipe diameters ranging up to 16 inches (400 mm). Many of the breaks occurred in the area adjacent to the perimeter dike and are probably primarily due to lateral spreading movements, however, it is not clear from the available data what amount of lateral spreading movement was required to cause a break. For the steel and asbestos cement pipelines, spreading cracks on the order of an inch or more are mapped near the breaks of smaller diameter lines, up to 4 inches (100 mm); whereas for the larger diameter lines, 12 to 16 inches (300 to 400 mm), lateral movements appear to have been in the range of 6 to 12 inches (150 to 300 mm). Breaks of vitrified clay pipelines were reported for some locations where lateral spreading cracks as small as a quarter-of-an-inch (6 mm) were mapped. Some of the breaks also appeared to occur as a result of differential

vertical (slumping) movement on lateral spreading cracks. In the interior area of the island, breaks cannot be associated with lateral spreading, but rather appear to be generally associated with ground settlement and/or areas where liquefied fill materials are at shallow depths below the ground surface. Comparison of the break locations shown in Figure 8 with the settlement contours shown in Figure 9 indicates that, typically, breaks occurred in areas with estimated ground settlements of at least 6 to 8 inches (150 to 200 mm).

ACKNOWLEDGEMENTS

REFERENCES

Engineering News-Record, 1937, Large Dredging Fleet Assembled for Filling Golden Gate Fair Site: March 18, pp.412-414.

Engineering News-Record, 1938, An Island Built to Order: October 13, pp.459-461.

Goldman, H.B., 1969, Geology of San Francisco Bay: found in Geologic and Engineering Aspects of San Francisco Bay Fill, California Division of Mines and Geology, Special Report 97, pp.11-29.

Lee, C. H., 1969, Bay Mud Developments, Case History 2, Treasure Island Fill: found in Geologic and Engineering Aspects of San Francisco Bay Fill, California Division of Mines and Geology, Special Report 97, pp.69-72.

Lee, K.L., and A. Albaisa, 1974, Earthquake Induced Settlements in Saturated Sands: ASCE, J. Geotechnical Engineering Division, v.100, n.GT4, pp.387-406.

Liao, S.S.C., D. Veneziano, and R.V. Whitman, 1988, Regression Models for Evaluating Liquefaction Probability: ASCE, J. Geotechnical Engineering, v.114, n.4, pp.389-411.

Makdisi, F.I., and H.B. Seed, 1978, Simplified Procedure for Estimating Dam and Embankment Induced Deformation: ASCE, J. Geotechnical Engineering Division, v.104, n.GT7, pp.849-867.

National Research Council, 1985, Liquefaction of Soils During Earthquakes: National Academy Press, Washington, D.C., 240p.

Newmark, N.M., 1965, Effects of Earthquakes on Dams and Embankments: Geotechnique, v.15, n.2, pp.139-160.

Seed, H. B., K. Tokimatsu, L. F. Harder, R. M. Chung, 1985, Influence of SPT Procedures in Soil Liquefaction Resistance Evaluations: ASCE, J. Geotechnical Engineering, v.111, n.12, pp.1425-1445.

Seed, R. and L.F. Harder, 1990, SPT-based Analysis of Cyclic Pore Pressure Generation and Undrained Residual Strength: Proceedings, H.B. Seed Memorial Symposium, v.2, pp.351-376, May.

Tokimatsu, K., and H.B. Seed, 1987, Evaluation of Settlements in Sands due to Earthquake Shaking: ASCE, J. Geotechnical Engineering, v.113, n.8, pp.861-878.

Figure 1. Aerial view of Treasure Island construction progress (5 February 1937)
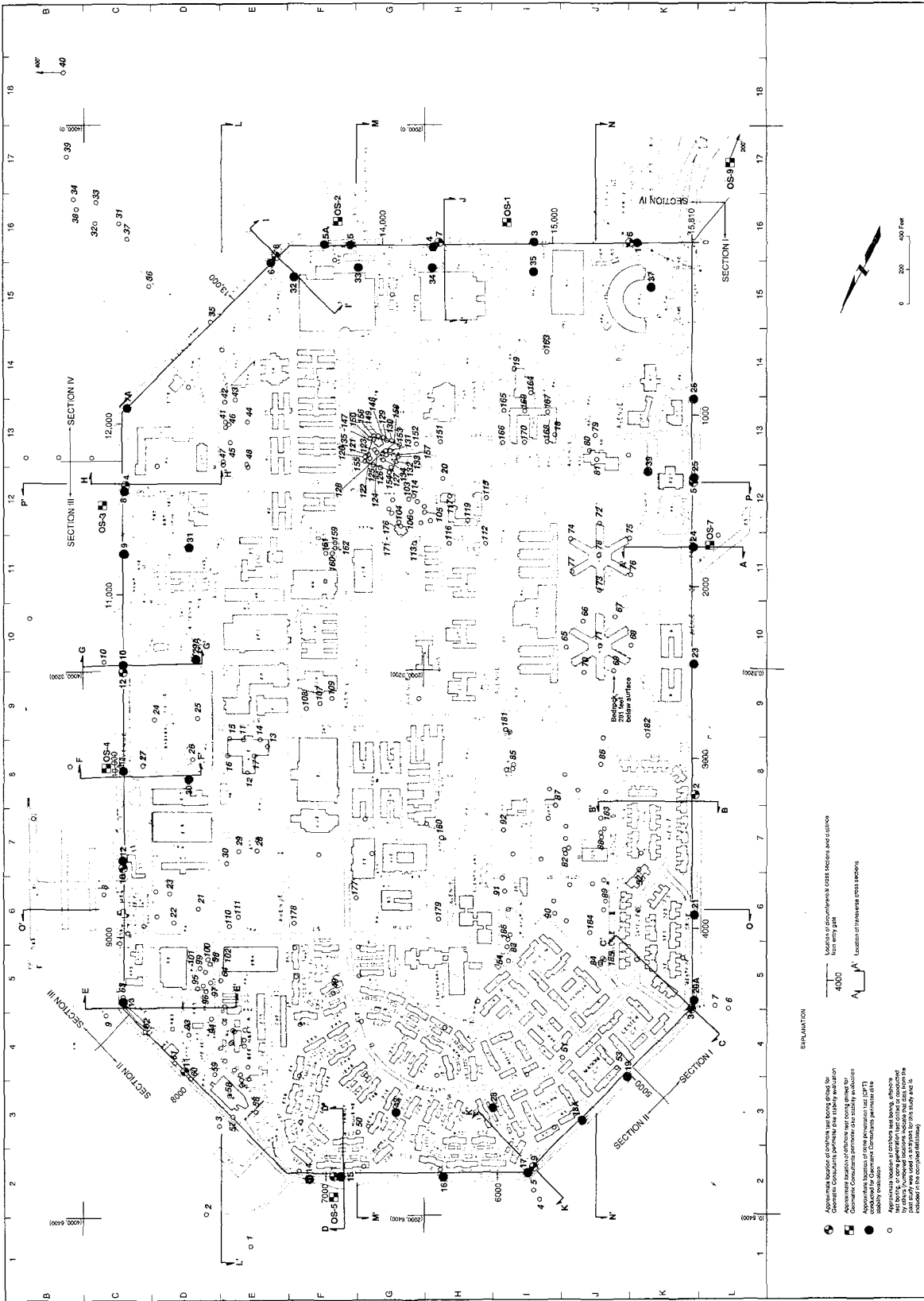
Figure 2. Treasure Island site plan

Figure 3. Stratigraphic cross sections
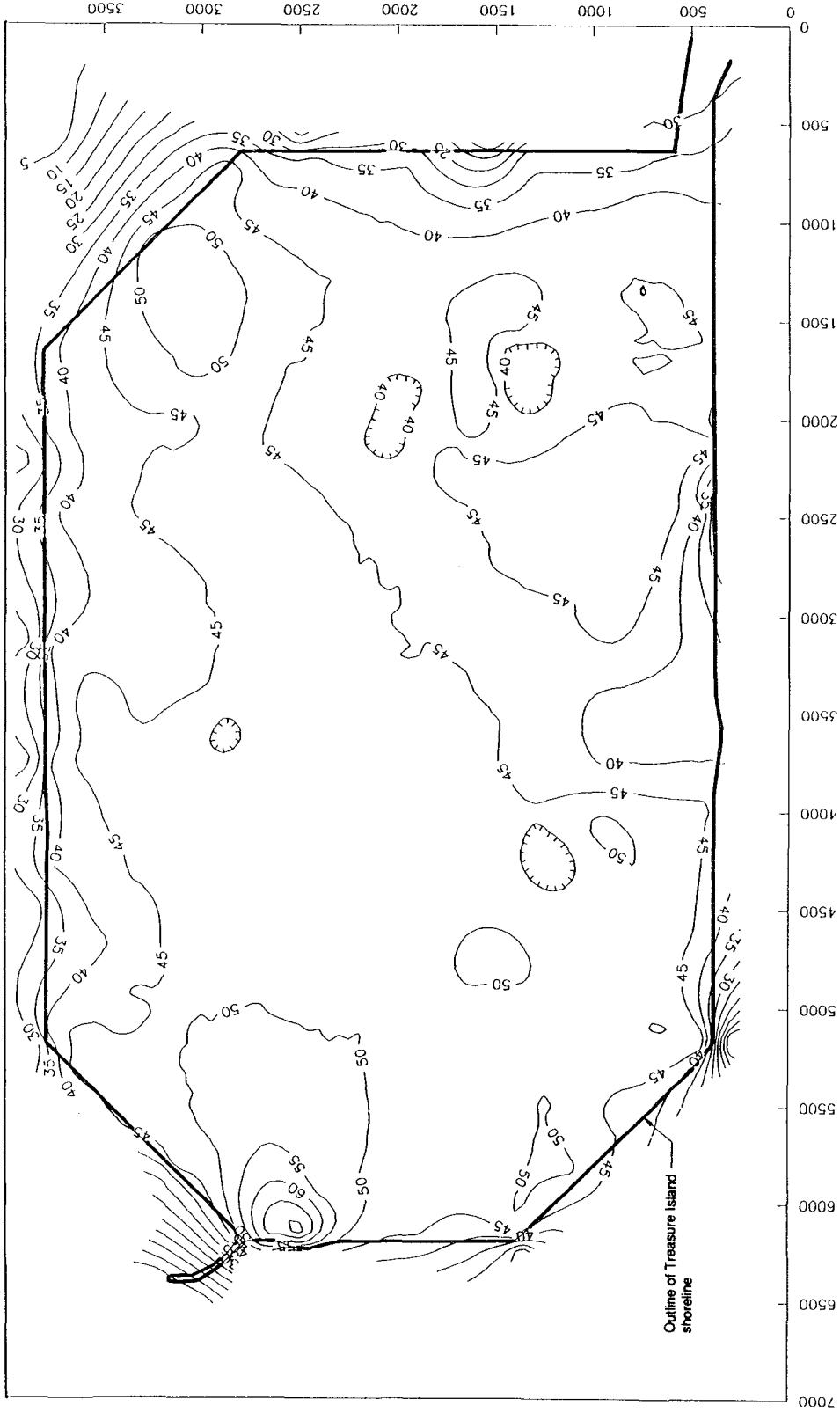
Figure 4. Thickness of fill and native shoals materials

Notes
1. Contour interval = 5 feet
2. See Section 2.5.1 for description
   of Fill and Native Shoal Materials.

Outline of Treasure Island
shoreline

500 Feet
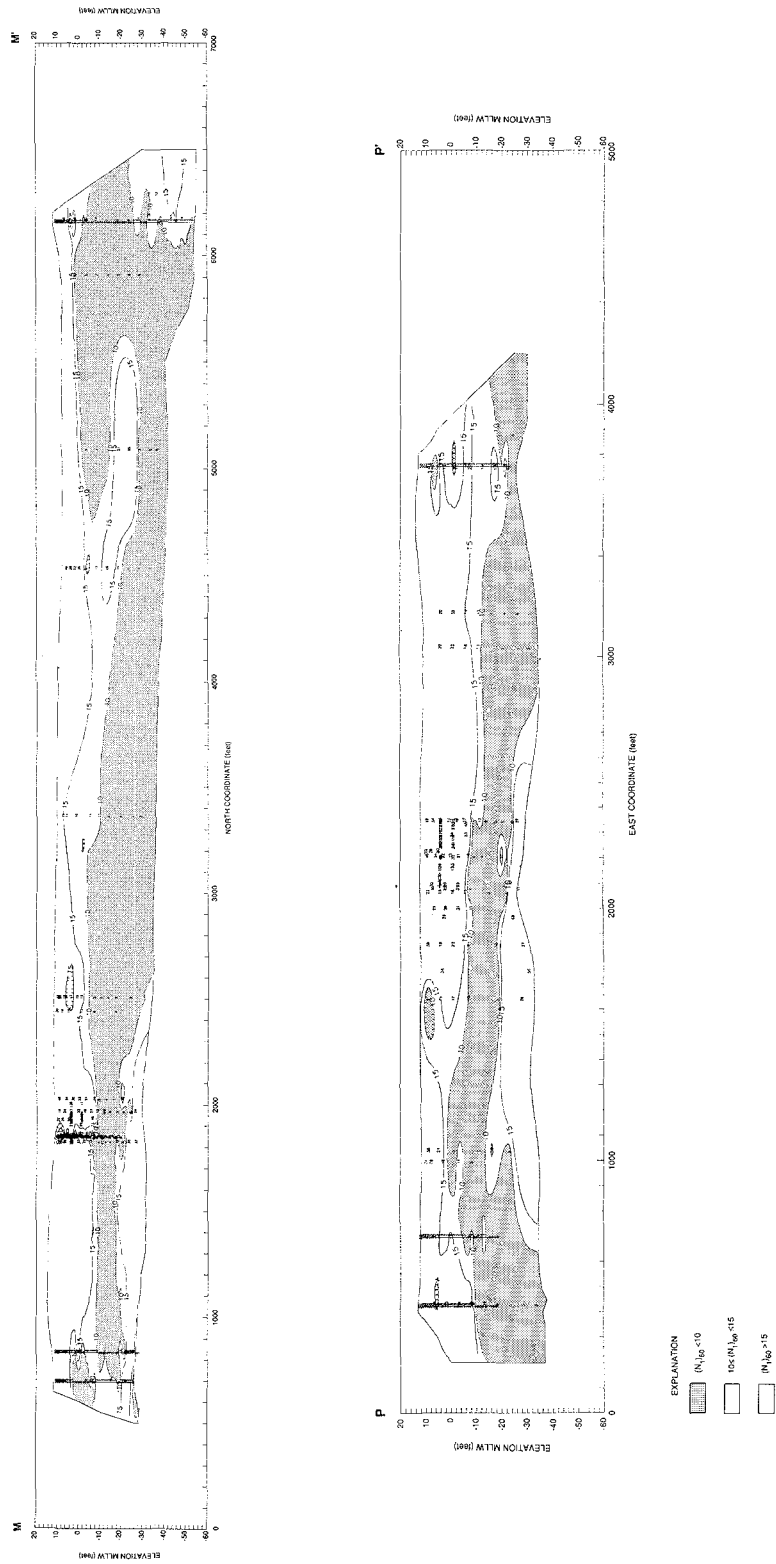
Figure 5. $(N_1)_{60}$ distribution in sand fill and native shoals materials

72
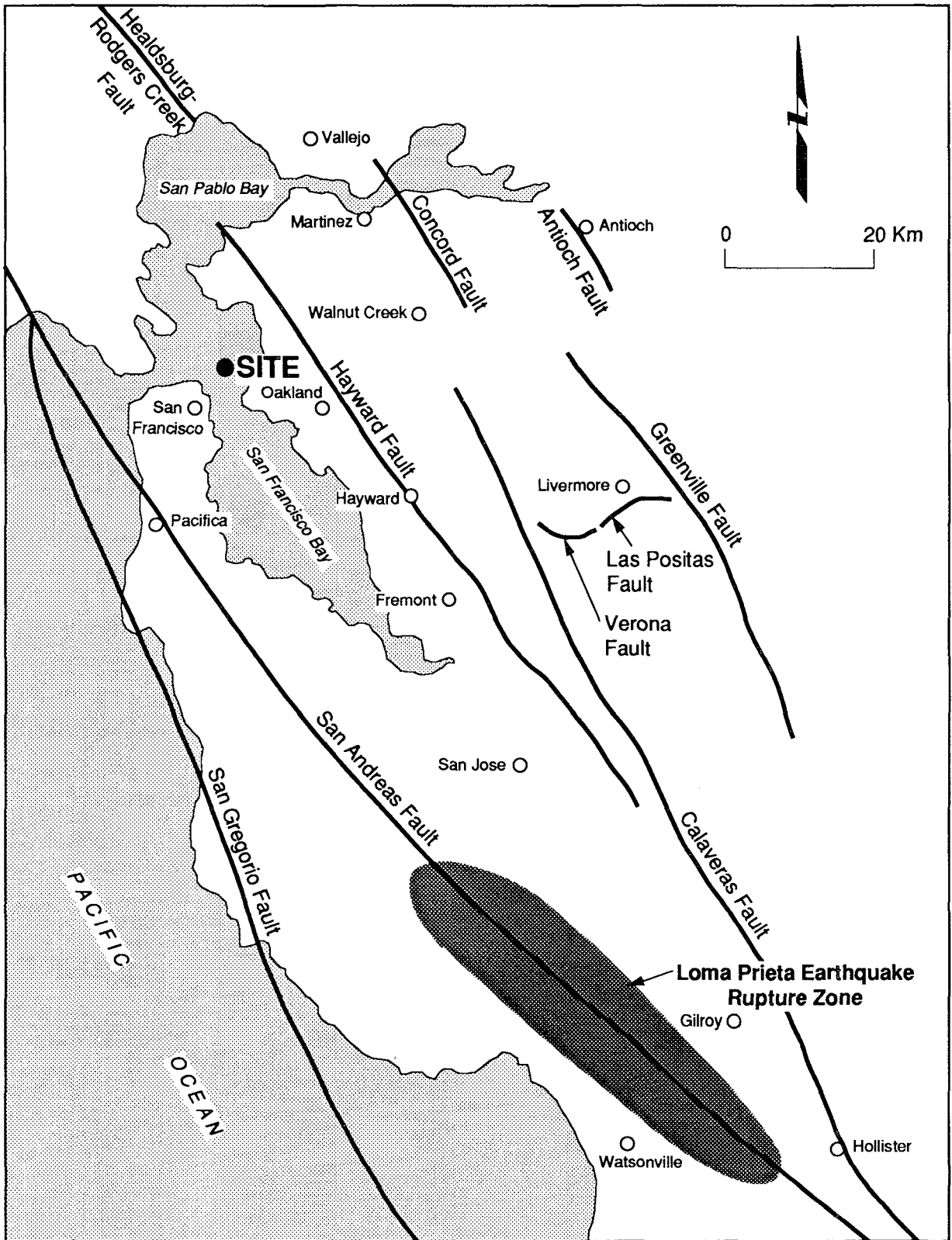
Figure 6. Map of active faults in San Francisco Bay area

TREASURE ISLAND
UNCORRECTED ACCELEROGRAM 58117-S2598-89296.01 111789.2035-QL89A117

CHN 1: 90 DEG   MAX = -0.161 G

CHN 2: UP   MAX = 0.018 G

CHN 3: 0 DEG   MAX = 0.101 G

TIME (SEC)

YERBA BUENA ISLAND
UNCORRECTED ACCELEROGRAM 58163-S1720-89296.01 112189.1619-QL89A163

CHN 1: 90 DEG   MAX = -0.068 G

CHN 2: UP   MAX = 0.028 G

CHN 3: 0 DEG   MAX = 0.031 G

TIME (SEC)
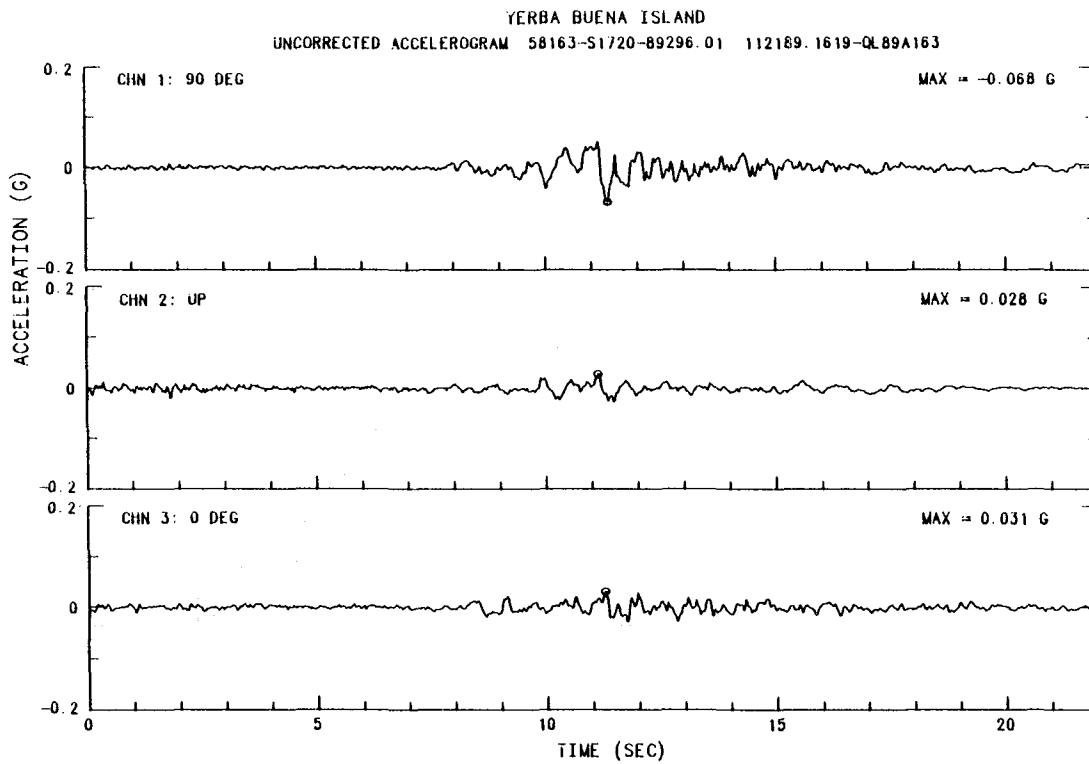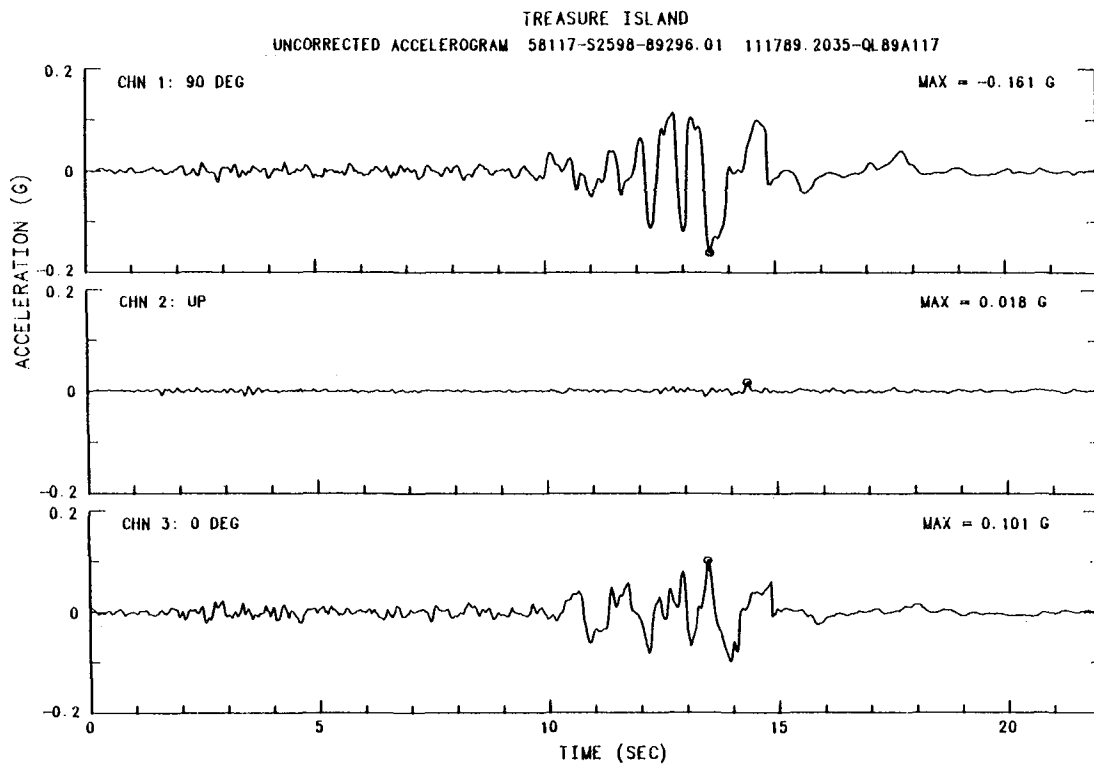
Figure 7. Loma Prieta earthquake strong-motion recordings

74

Figure 8. Map of ground deformation features and facilities' distress during Loma Prieta earthquake
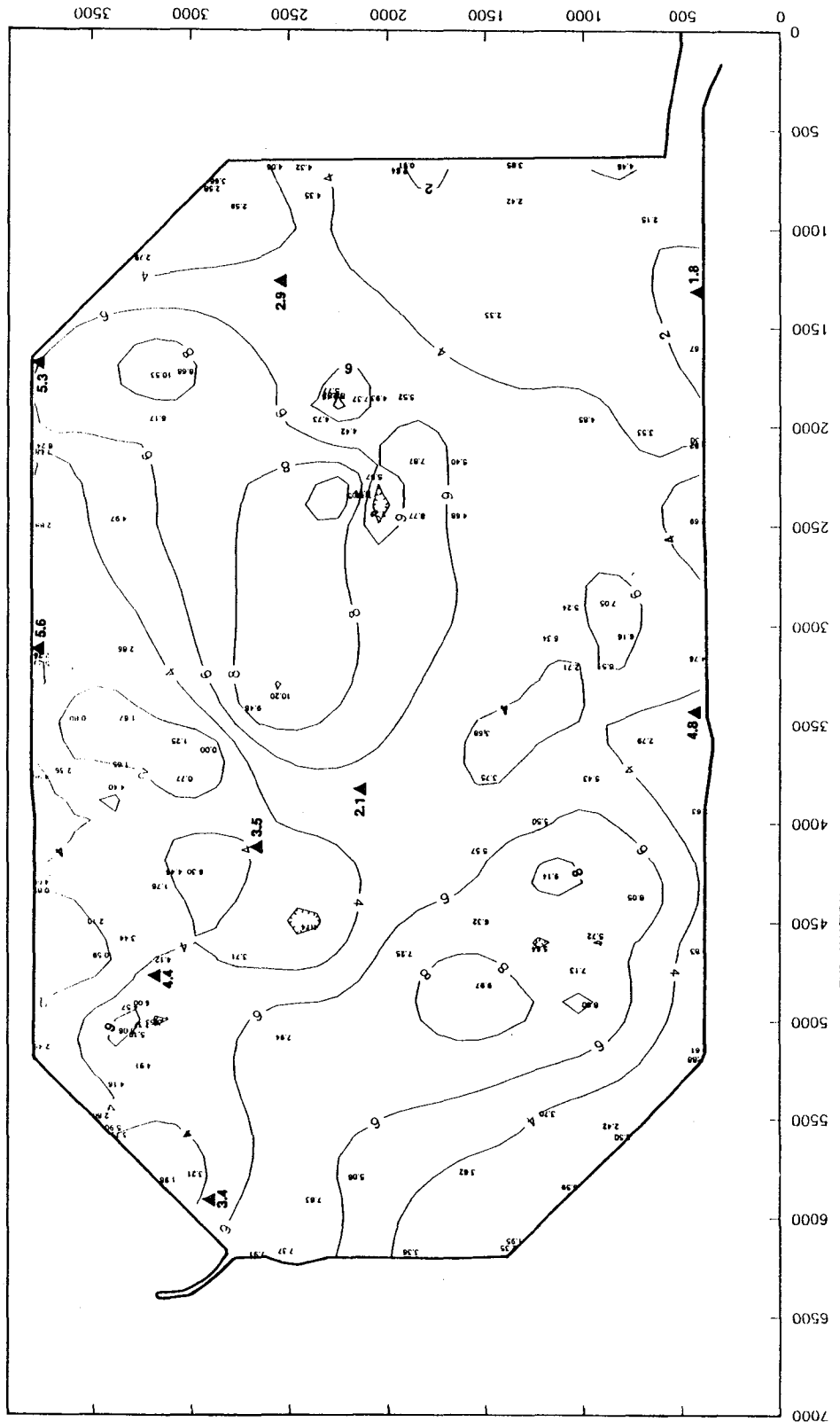
Figure 9. Shaking-induced compaction settlement associated with Loma Prieta earthquake

Analysis of Liquefaction Damages and Aseismic Countermeasures for Conduits

Syunji Nagamachi
Senior Engineer
Nippon Telegraph and Telephone Corporation (NTT)
Tsukuba Field Engineering Development Center

ABSTRACT

This study examines the great damage to underground facilities due to liquefaction during the Niigata Earthquake (1964) and the Nihonkai-chubu Earthquake (1983).
This damage is especially concentrated at the junctions between conduits and a manhole, and at joints between conduits.
Focusing on these sites, this study reports the following studies.

  (a) Statistical analysis of the damaged conduits and ground displacements
       in the Niigata Earthquake.
  (b) Structural analysis of the damaged conduits in the Nihonkai-chubu Earthquake.
  (c) Analysis and verification for the effect of our countermeasures for the
       liquefied ground to the observed ground displacements in the Nihonkai-chubu
       Earthquake.

The results of these studies are as follows.

  (a) With axial compressive stress, the rate of damages tends to be high.
  (b) In the response analysis of conduits to ground displacements, the damaged points
       nearly agree with the simulated damage points.
  (c) The design of conduits resistant to liquefied ground in which we use steel pipe
       with expansion joints, is effective with the actual ground displacements.

This design is now applied for the "New-haneda Airport" route presently under construction in the Tokyo Bay area with the possibility of liquefaction.

INTRODUCTION

Society is highly information-oriented society, and the dependence of social and economic activities on telecommunications continues to increase. Interruption of communication therefore has a very large social effect. For this reason, high reliability is demanded of the underground communication facilities supporting telecommunication service.

Japan has experienced many earthquakes causing liquefaction phenomena that has heavily damaged underground communication facilities. In examining this earthquake disasters, the authors have elucidated the mechanism of damage and have developed designs for liquefaction countermeasures. In this paper, the Niigata Earthquake (1964) and the Nihonkai-chubu Earthquake (1983) are examined, damages are statistically and structurally analyzed, and the design of conduits resistant to liquefied ground is described.

I. Examples of disasters due to liquefaction

(1) Niigata Earthquake

At the time of the Niigata Earthquake, the liquefaction of ground heavily damaged underground communication facilities. Conduits in the old city consisted of cast iron pipes constructed before the war, steel pipes constructed after the war, and asbestos cement pipes.

For both cast iron and steel pipes, the damage rate reached 50 %. Regarding the state of damage, conduit bodies broke down, junctions between conduits and a manhole came out, or damage was concentrated at joints of conduits. The joints at that time were the spigot-form inserting type for cast iron pipes, and threaded joints on which asphalt was wound were used for preventing corrosion of steel pipes. Expansion parts installed to compensate for expansion and contraction of conduits due to temperature change also separated. Few facilities had asbestos cement pipes, but almost all of them were damaged.

(2) Nihonkai-chubu Earthquake

In the Nihonkai-chubu earthquake, underground communication facilities were damaged due to liquefaction. At that time, the threaded steel pipes of nominal diameter (75 mm) and hard vinyl pipes were used. The damage to conduits was similar to that in the Niigata Earthquake, breakdown of threaded joints, damage to the joints of hard vinyl pipes, and collapse of stacks in the conduits when many lines were laid together.

In this earthquake, the duct sleeves for the junctions between conduits and manholes into expansible structures were partially used. There was no damage to these manholes confirming the effectiveness of this countermeasure.

(3) Summary of damages

The damage to the underground communication facilities due to liquefaction is summarized as follows.
(Conduits)
  • Breakdown and separation of the weaker joint parts.
  • Deviation of the axis lines of conduits.
  • Breakdown at the immediate side of fixed points, such as the immediate side of

78

manholes.
- Breakdown of the conduits with inferior materials.

II.   Statistical analysis of conduits damaged in the Niigata Earthquake

(1) Method of analysis
      Using the aerial-survey-based prediction of ground deformation by Hamada et al., the
relationship of the relative displacement between manholes and the proportion of conduit
or manhole damages was investigated. The object of this analysis is 6.0 km of conduit
facilities on five routes in the Nishi-niigata district on the left bank of the Shinano
River (see Fig. 1). This is the area in which liquefaction has been observed. The length
of the area suffering damage was 2.8 km. The unit of damage, however, is the section
between manholes, and even if only one span in a section between manholes cannot be used,
the whole section is regarded as damaged.
      The outline of the method of statistical analysis follows.
① From the aerial survey data, the displacement in the vicinity of a manhole along the
    object route is determined at 3 ~4 points.
② The displacement vector quantity of the position of a manhole is determined as the
    average value, and by dividing it into the direction of a conduit and the normal
    direction, (u_i, v_i) are calculated for every manhole.
③ For every section between manholes, the axial strain ε_i and the strain γ_i in the
    direction normal to the axis are determined by the following equations.
$$\varepsilon_i = (u_{i+1} - u_i)/\ell_i$$
$$\gamma_i = (v_{i+1} - v_i)/\ell_i$$
    where, ℓ_i is the distance between manholes, and the axial strain is tensile in the
    case of (+) and compressive for (-).
④ With ε_i and γ_i, stratification is carried out at 0.2 % pitch, and the proportion of
    damaged facilities is determined. In this way, the tendencies of damage is investigated

(2) Results of analysis
      The relation of the axial strain to the proportion of the quantity of damaged
facilities is plotted in Fig. 2. The proportion of damage in the facilities with
compressive strain is relatively high, 78 %. In facilities with tensile strain, 40 % were
damaged. The relative displacement of manholes was within 1 % of the length of sections,
at most 1 m in 100 m.
      The results of similarly analyzing the strain in the direction normal to the axis are
plotted in Fig. 3. Independent of the increase of the strain in this direction the
proportion of damaged conduits was constant at about 50 %.

(3) Summary of results of analysis
      The results of the statistical analysis of damaged conduits in the Niigata Earthquake
are summarized below.
① In the liquefied ground, damage was considerably large in the buried small-bore pipes
    (nominal diameter. about 75 mm), and this is considered to occur because those conduits
    are apt to undergo deformation due to the flow of ground.

79

② The proportion of damage tends to be especially high when ground is deformed so that two manholes approach each other.

③ The relative displacement in 100~150 m sections was at most about 1 %.

III. Structural analysis of damaged conduits in the Nihonkai-chubu Earthquake

(1) Method of analysis

The ground deformation along the Torigoya route in Aoba-cho, Noshiro City was predicted from aerial survey data, and the structural analysis was carried out by modeling it with a beam on an elastic floor. The comparative investigation was carried out with the state of damage shown in Fig. 5 and Fig. 6. One threaded steel pipe (PS pipe) and two hard vinyl pipes (V pipe) were laid, and two places in the PS pipe and one place in the V pipes were damaged.

The following assumptions were made for this analysis. (see Fig.4)

 i) The buried conduit is regarded as the beam on an inelastic floor supported with non-linear springs.

 ii) The movement of ground acts only as forced deformation, and it is applied to the buried conduit through a ground spring at that point.

iii) The springs between the buried conduit and ground have nonlinear characteristics. That is, in the conduit-axis direction, due to the frictional force acting between the conduit and the earth, the conduit is assumed to follow the movement of ground. When the maximum frictional force is exceeded, however, sliding occurs between the conduit and the earth, and in the direction normal to the conduit axis, the earth changes from the elastic condition to the plastic condition.

iv) Regarding the joints in the structural model for the buried conduit, conduit bodies are considered to be connected with longitudinal springs or with rotational springs. The position of a joint is such that an axial force is transmitted in the conduit-axis direction, and a shearing force and a bending moment are transmitted in the direction normal to the conduit axis. Furthermore, it is assumed that the springs at a joint have the nonlinearity corresponding to their characteristics.

 v) The conduit bodies are in the elastic range also after the deformation.

 vi) The softening of ground due to liquefaction is taken into account by reducing the spring constant of ground. However, it is assumed that the effect of softening is not exerted when sliding in the conduit-axis direction, nor in the plastic condition, when sliding in the direction normal to the conduit axis.

vii) It is assumed that manholes are sufficiently rigid compared with the buried conduit. And since the constraint by surrounding ground also is large, they are assumed to be rigid bodies moving with the ground.

(2) Prediction of ground deformation

From the aerial survey of the vicinity of the Torigoya route, vectors on both sides of the road are obtained at intervals of about 20 m along the straight road. Assuming here that the conduit is located at the center of the road, the average of vectors on both sides is determinedand separated into the conduit-axis direction (x-direction), the horizontal direction normal to the conduit axis (y-direction), and the vertical direction

(z-direction). The results of predicting the distribution of deformation at the position of the conduit are shown in the Fig. 7.

In the x-direction, deformation was shown when manholes of about 250 m apart approached each other by about 1 m. In the y-direction, the deformation was such that the axis line deviated about 30 cm at most, in the z-direction, the subsidence of about 30~50 cm occurred.

The relation difference between adjoining deformations was calculated and divided by the distance, and Fig. 8 shows the distribution of ground strain determined in this way. In the x-direction, compressive strain as a whole was dominant, but there was also some tensile strain. In the y-direction and z-direction, it can further be said that there was no particular directionality. When the ground strain was observed in terms of strain value, it resulted in less than 2 % in all three directions, and this strain value can be said to be nearly equal to the level of the ground strain.

(3) Results of response calculation

An analysis is done by modeling the threaded steel pipes damaged in the Nihonkai-chubu Earthquake. At the time of modeling, the nonlinear characteristics for the threaded joints were experimentally measured.

Nonlinear characteristics determined on the basis of the experimental data on the sliding of threaded steel pipes (internal data of NTT) are used for reducing the spring constant of ground to 1/10. In addition, response calculation is attempted without taking into account the softening due to liquefaction and reducing the spring constant of ground to 1/100.

Fig. 9 shows the results of response calculation. The distribution of axial force in the x-direction and the distribution of bending moment in the y-direction and z-direction are shown. As a result of the compressive strain of ground, the axial force became remarkably large. The axial force attained the maximum value about 100 m from No. 2 manhole, which was nearly one of the damaged points of the threaded steel pipes.

As for the deformation in the y-direction and z-direction, the arising section force was not very large, and its stress decreased to 1/10 as that of the axial force.

The results of calculation in the x-direction and the y-direction when changing the condition of the spring constant of ground are shown in Fig. 10 and Fig. 11. With the spring constant of ground equal to 1/100, the distribution of section force became smooth and the section force decreased. Furthermore, without reducing the spring constant of ground, the section force increased and the peak in the distribution became clear. As for the bending direction, the discontinuity of displacement input at intervals of about 20 m is conspicuous.

(4) Summary of response calculation

The results of the response calculation from modeling the buried conduit of the damaged Torigoya route are summarized below.
① From the analysis in the axial direction rather than the direction normal to the axis, for a beam on an inelastic floor having nonlinearity, the section force was large and damaged occured near the place where the maximum axial force occurred.
② From the analysis in the direction normal to the axis, notwithstanding the level of ground strain nearly equal to that in the axial direction, the section force was

considerably small and the effect of deviation of the axis line by several tens of cm was also small.

③ When the spring constant of ground was changed, the response resulted in a large difference. According to the results of comparing the sites of damage with the distribution of axial force, the first gradient of ordinary ground springs is about 1/10.

④ Assuming that the conduits are elastic, the estimated strain of the conduit bodies was about 0.3 %, and this value slightly exceeded the yield point.

⑤ Compared with the strain of ground estimated from the relative displacement of manholes , a somewhat larger strain of ground sometimes arose, but the effect exerted on the whole was small.

IV. Analysis and verification of design of conduits resistant to liquefied ground

(1) Outline of design
    As mentioned in the paragraph of "Examples of disasters due to liquefaction", for the damage to conduits in the Niigata Earthquake and Nihonkai-chubu Earthquake, the breakdown and separation of weaker joints and the breakdown of conduits made of insufficient materials strength were most commonly.

    A design for conduits was therefore developed, in which the joints are resistant to separation, and the stopper joints have improved expansion and contraction functions. Since the validity of the analysis method using the response analysis of conduits to ground displacements was established in Chapter II, this design of conduits for liquefied ground was applied to the analysis model, and verification of its effect was attempted. Moreover, the result of the analysis confirmed that the aseismatic effect occurred in metallic pipes rather than in V pipes. This Chapter therefore reports the results of the analysis for metallic pipes.

    The outline of the design of conduits resistant to liquefied ground is as follows.
① In consideration of material strength, metallic pipes are used for the conduits.
② The analysis is carried out for two cases, that is, the PL-PS pipes, to which the stopper joint was applied only at the immediate side of MH [new specification pipes (1)] and the PL-PS pipes, to which the stopper joints were applied in all sections (every two joints at intervals of 11m) [new specification pipes (2)]. (See Fig. 14.)

(2) Results of response calculation
    Response analysis was carried out for the new specification pipes by using the analysis model in Chapter II. This analysis was compared with that of the old specification pipes analyzed in Chapter II (see Fig. 12 and Fig. 13). However, for the stresses in the direction normal to the conduit axis and in the vertical direction (subsidence), a remarkable difference was not observed between the old specification pipes and the new specification pipes. The results reported below are therefore results of calculation in the conduit-axis direction.
① The maximum stress occurring in the new specification pipes (1) was a compressive stress, and it was reduced to 29 % of the stress occurring in the old specification pipes.

② The stress in the new specification pipes (2) was reduced further than that in the new specification pipes (1), and the maximum stress was reduced to 6 % of that in the old specification pipes.

③ The stress occurring in the old specification pipes largely exceeded the breaking stress of conduit bodies, and compressive breakdown occurred. However, in both new specification pipes (1) and (2), the stress never exceeded the breaking stress, the ratios to the breaking stress being 46 % for pipes (1) and 9 % pipes (2) .

④ In the old specification pipes, the limit value for joints was exceeded at almost all joints and the breakdown occurred. However, in both new specificationion pipes (1) and (2), all joints showed displacement within the limit value.

(3) Summary

For both the PL-PS pipes to which stopper joints were applied only at the immediate side of MH [new specification pipes (1)], and PL-PS pipes to which stopper joints were applied in all sections (every two joints, at intervals of 11 m) [new specification pipes (2)], the response analysis was carried out.

① In the new specification pipes (1), the stress that occurred was within the breaking stress, and the limit value for joints was within. Therefore, the safety of the conduit structure and its aseismatic effect were confirmed.

② In the new specification pipes (2), those values were within the breaking stress of conduit bodies and within the limit value for joints. Therefore, the safety of the conduit structure and its aseismatic effect were confirmed.

CONCLUSION

We analyzed statistically and structurally damages of conduit facilities due to liquefaction, we found the following, from the results of this study.

 • With axial compressive stress, the rate of damages tends to be high.
 • The damaged points nearly agree with the simulated damage points by using analysis model.

Besides, the design of conduits resistant to liquefied ground was analyzed by using the analysis model, we found the following.

 • This design is effective with the actual ground displacements.

Therefore, this design was applied to the New Haneda Airport Route in the Tokyo Bay area from February, 1990, and this route (shown in Fig. 15) is under construction at present.

REFERENCES

1. "Investigation on Ground Deformation and Earthquake Damage of Underground Structures," ADEP (JAPAN), Mar. 1990

2. "Analysis of Aseismatic Countermeasures for Conduits in the Liquefied Ground," Tsukuba Field Engineering Development Center, Nippon Telegraph and Telephone Corporation (NTT), Apr. 1990

83
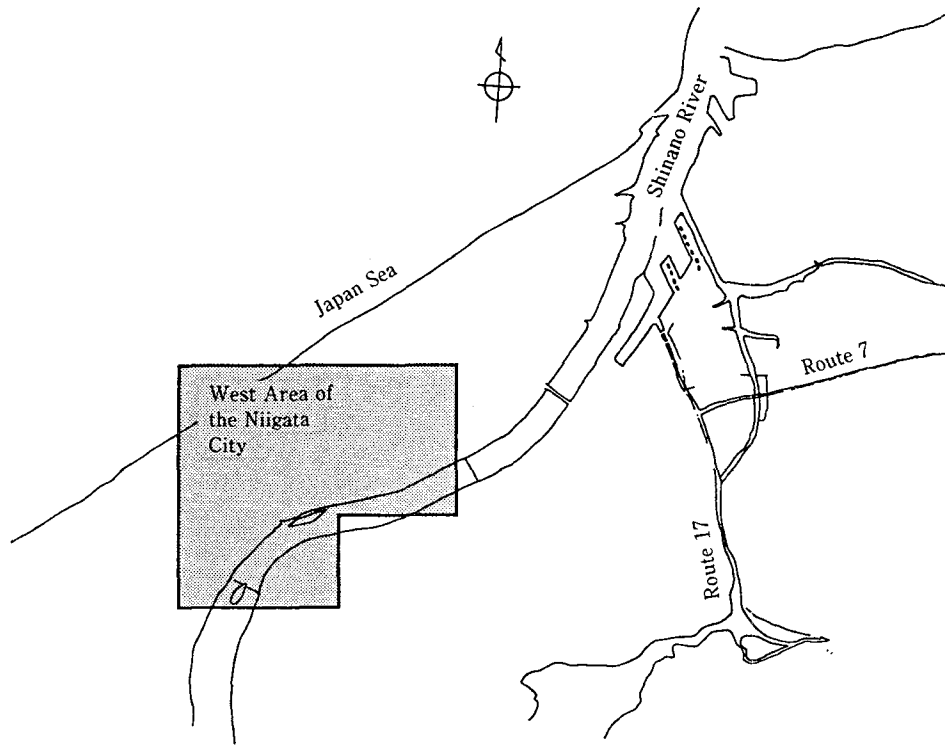
Fig. 1
Area of Ground Movement Researched
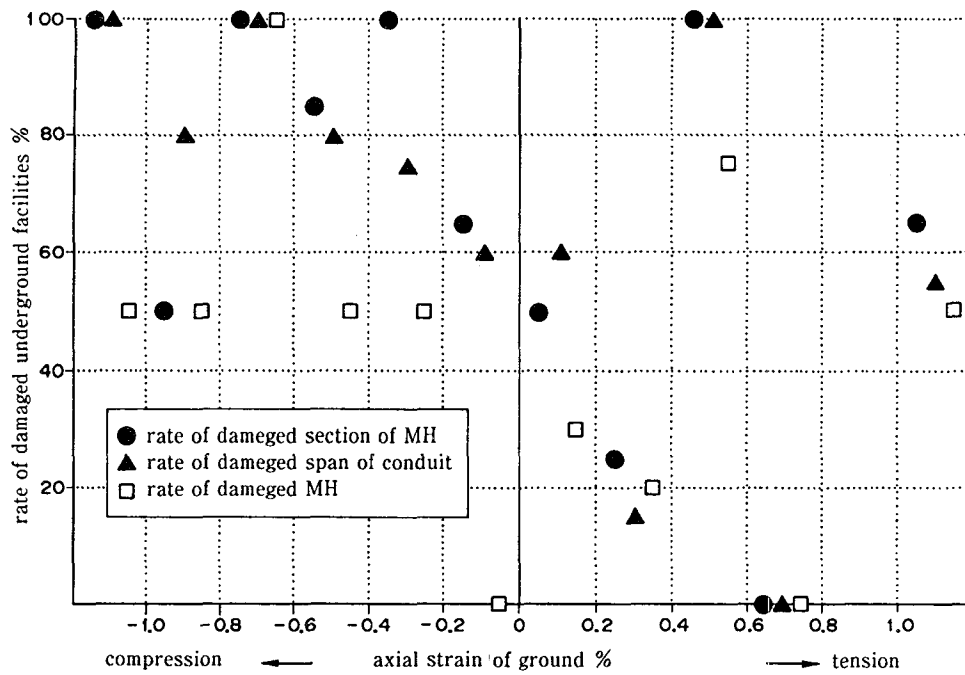
Fig. 2   Relation between rate of damaged conduit and ground strain

84
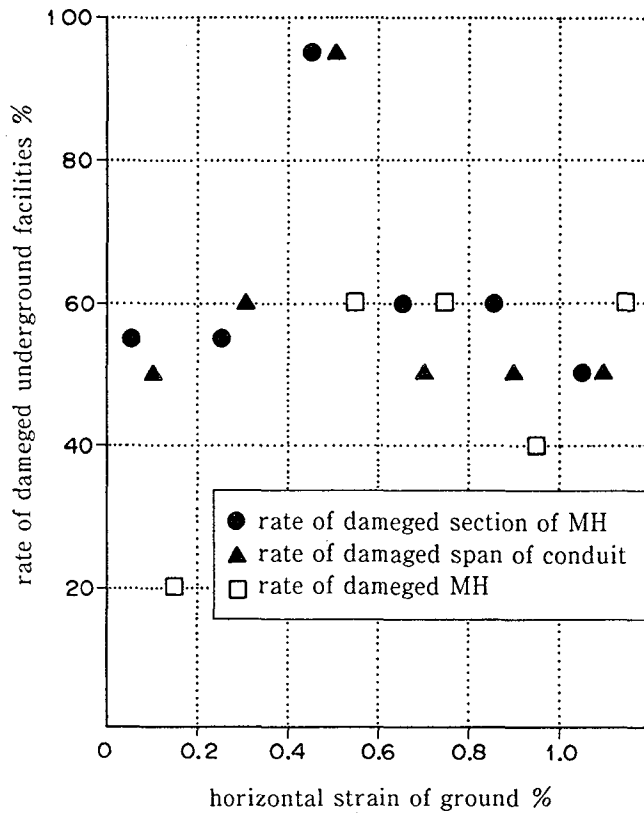
Fig. 3　Relation between rate of damaged conduit and ground strain
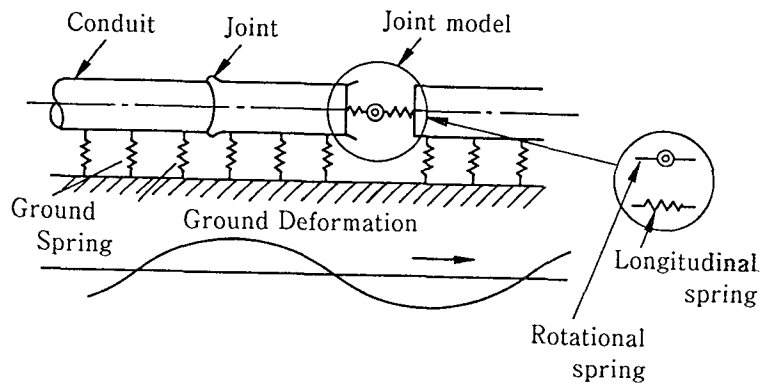
Fig. 4　Analytical Model

85
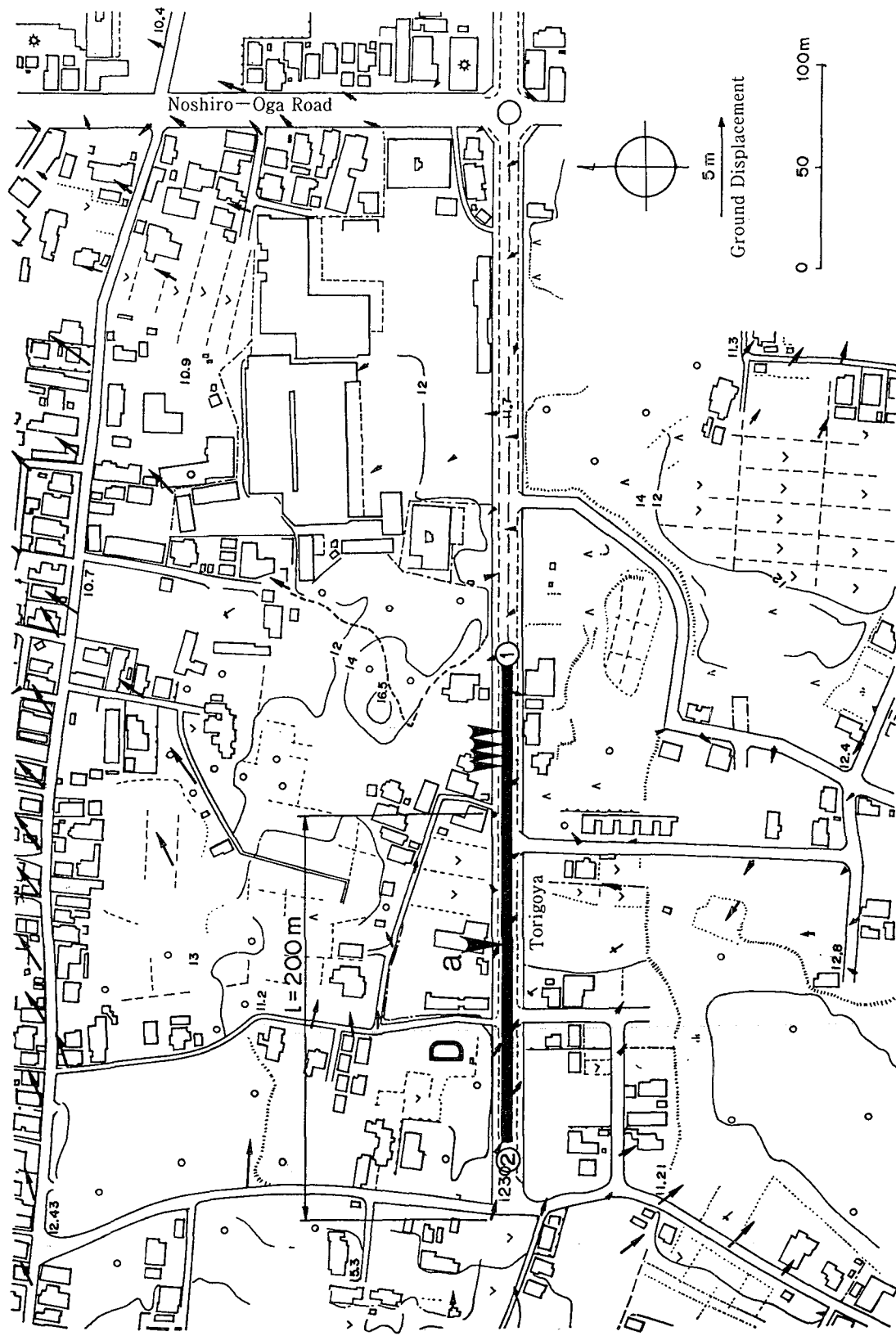
Fig. 5 Damage and Ground Displacement of Torigoya Route

Manhole duct (from manhole interior)

Conduit joint causing cable damage

Conduit joint causing cable damage (buckling)

Manhole duct (from manhole interior)

V—Pipe
PS PS

V—Pipe
PS

Torigoya Route No. 1 MH
×: dameged point

Torigoya Route No. 2 MH

249.5 m
banking
non banking
143.0 m
55.0 m
25 cm
49.8 m
44.0 m
38.0 m
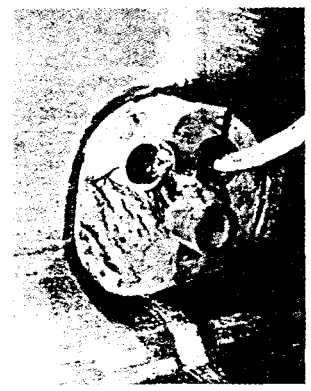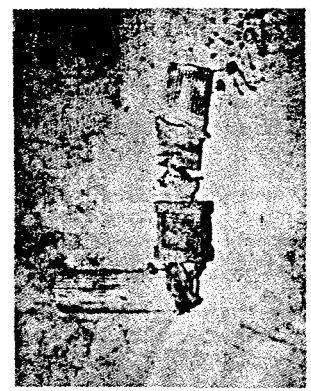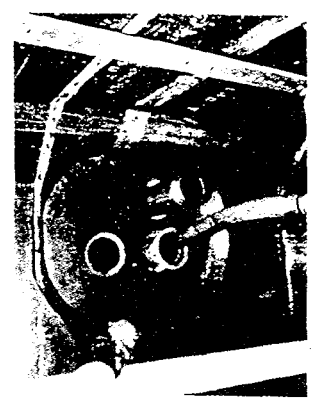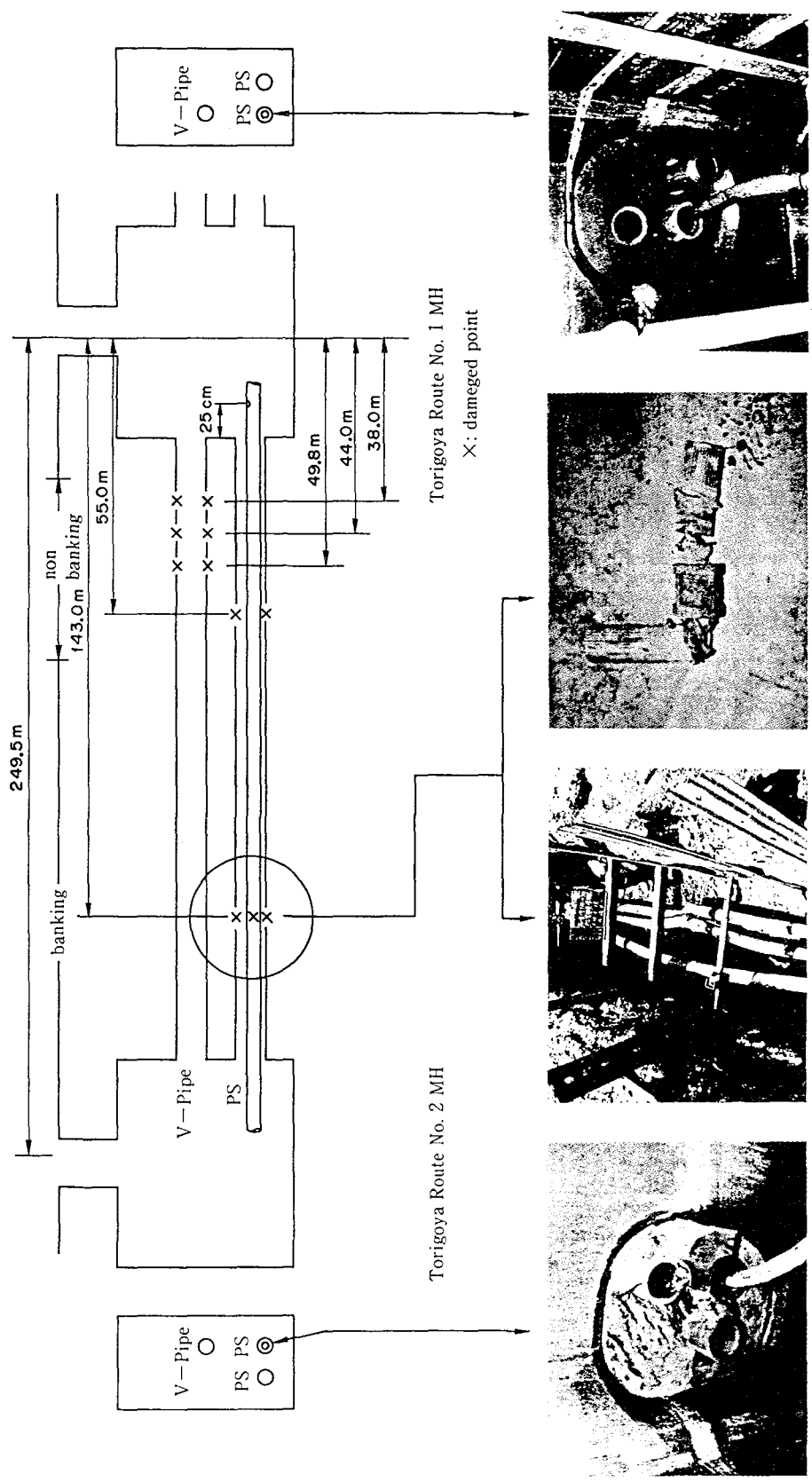
Fig. 6 Damage of Torigoya Route
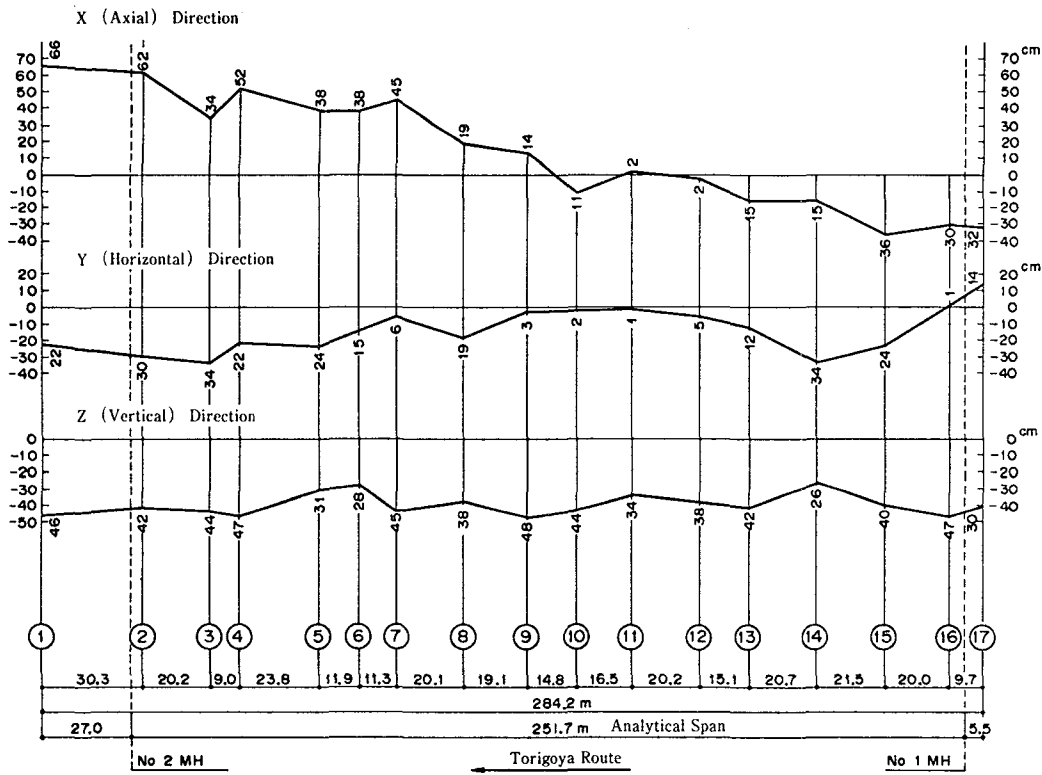
Fig. 7 Distribution of Ground Displacement
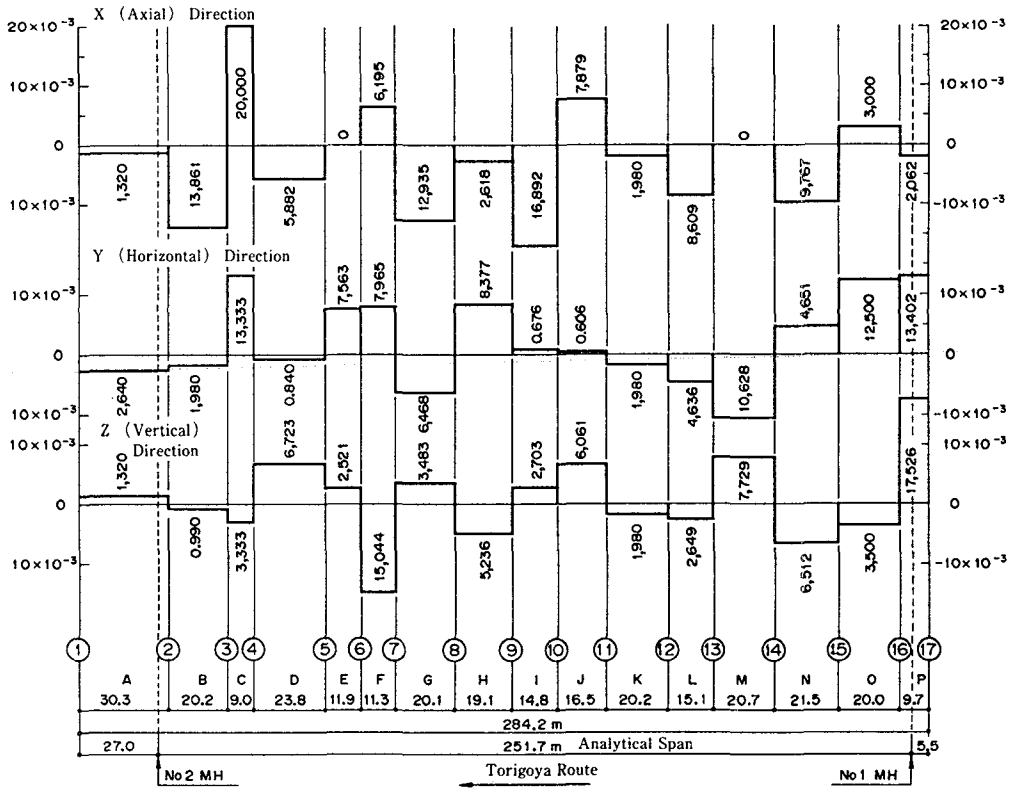
Fig. 8 Distribution of Ground Strain
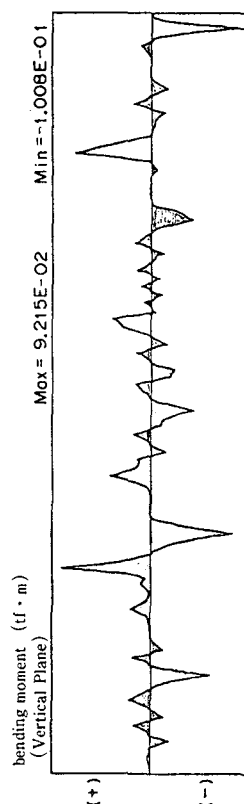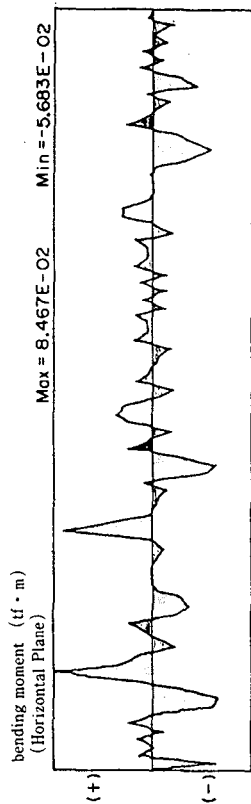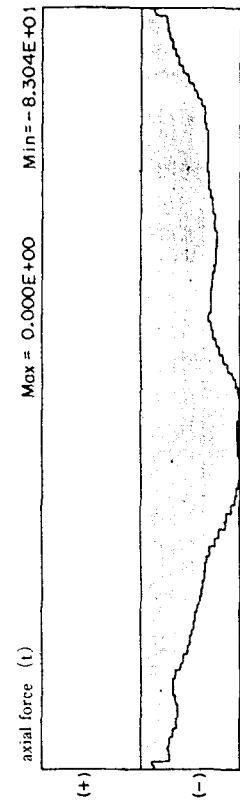
88

axial force (t) Max = 3,407E+00 Min =-8,541E+01

bending moment (tf·m) Max = 1,528E-01 Min =-1,210E-01

Fig. 10 Result of Response Calculation
(Reduction Rate of Ground Spring: 1/1)

axial force (t) Max = 0.000E+00 Min =-3,909E+01

bending moment (tf·m) Max = 3,899E-02 Min=-3,606E-02
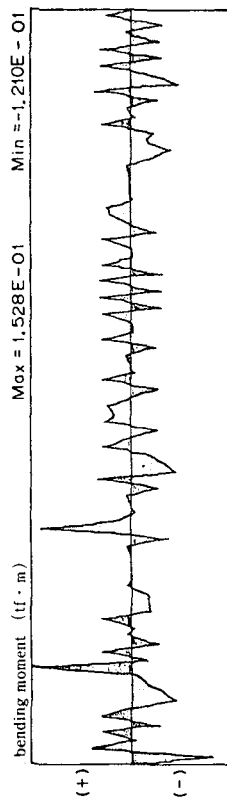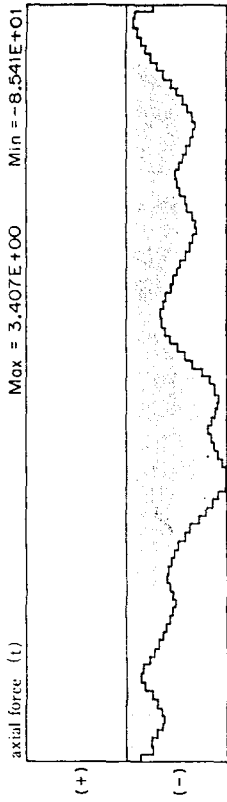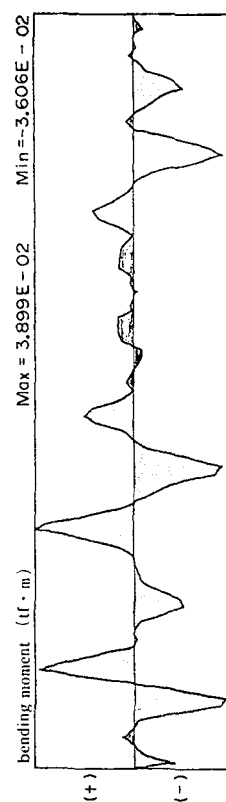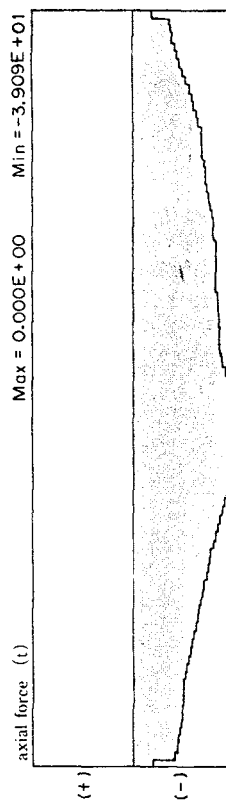
Fig. 11 Result of Response Calculation
(Reduction Rate of Ground Spring: 1/100)

axial force (t) Max = 0.000E+00 Min=-8,304E+01

bending moment (tf·m)
(Horizontal Plane) Max = 8,467E-02 Min=-5,683E-02

bending moment (tf·m)
(Vertical Plane) Max = 9,215E-02 Min=-1,008E-01

Fig. 9 Result of Response Calculation
(Reduction Rate of Ground Spring: 1/10)

89

① axial stress (kg/cm²) Max = 0.000E+00 Min = -5.628E+03

② axial stress (kg/cm²) Max = 1.317E+02 Min = -1.614E+03
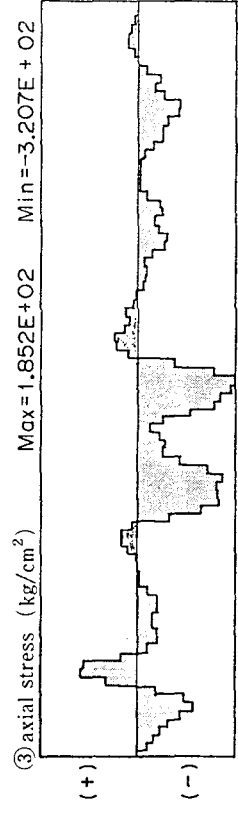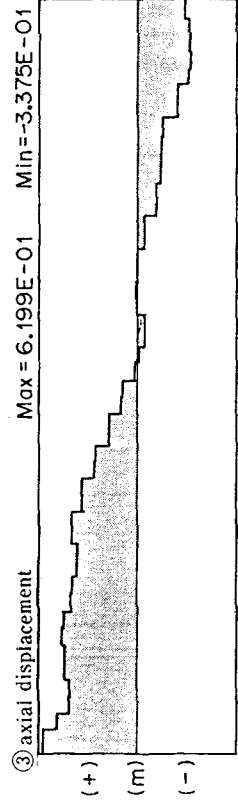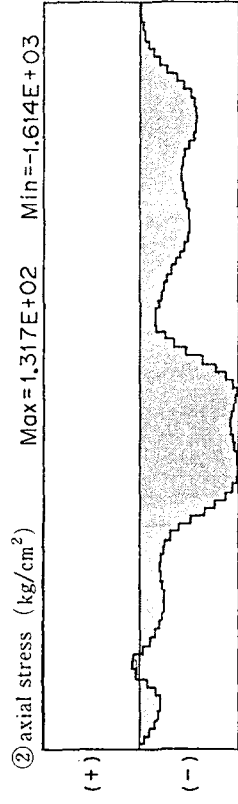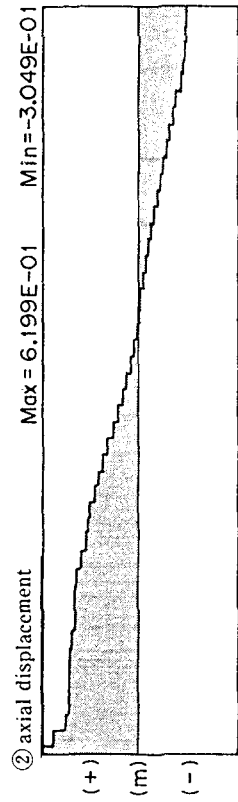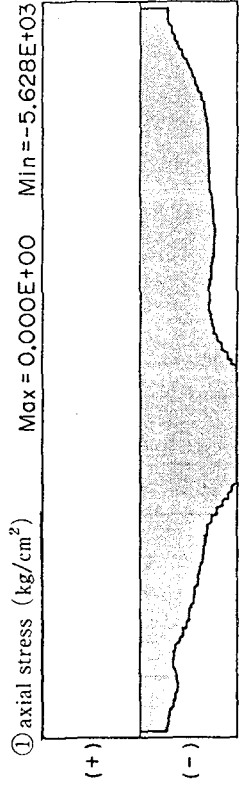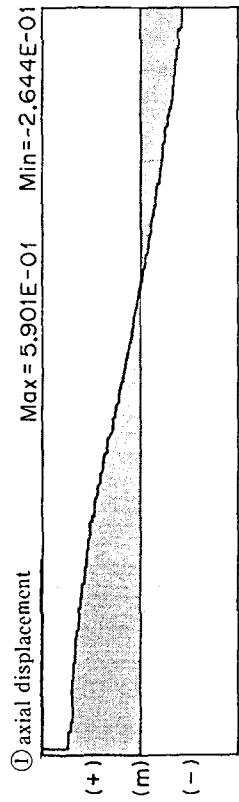
③ axial stress (kg/cm²) Max = 1.852E+02 Min = -3.207E+02

Fig. 13 result of response calculation
(① old-type ② new-type(1) ③ new-type(2))

① axial displacement Max = 5.901E-01 Min = -2.644E-01

② axial displacement Max = 6.199E-01 Min = -3.049E-01

③ axial displacement Max = 6.199E-01 Min = -3.375E-01

Fig. 12 result of response calculation
(① old-type ② new-type(1) ③ new-type(2))

90

D : duct   ◇ : expansion   ◈ : screw   • : joint
  socket   joint   joint

△ : duct   □ : stopper   ○ : push lock joint   • : joint
  sleeve   joint

△ : duck   □ : stopper   ○ : push lock joint   • : joint
  sleeve   joint
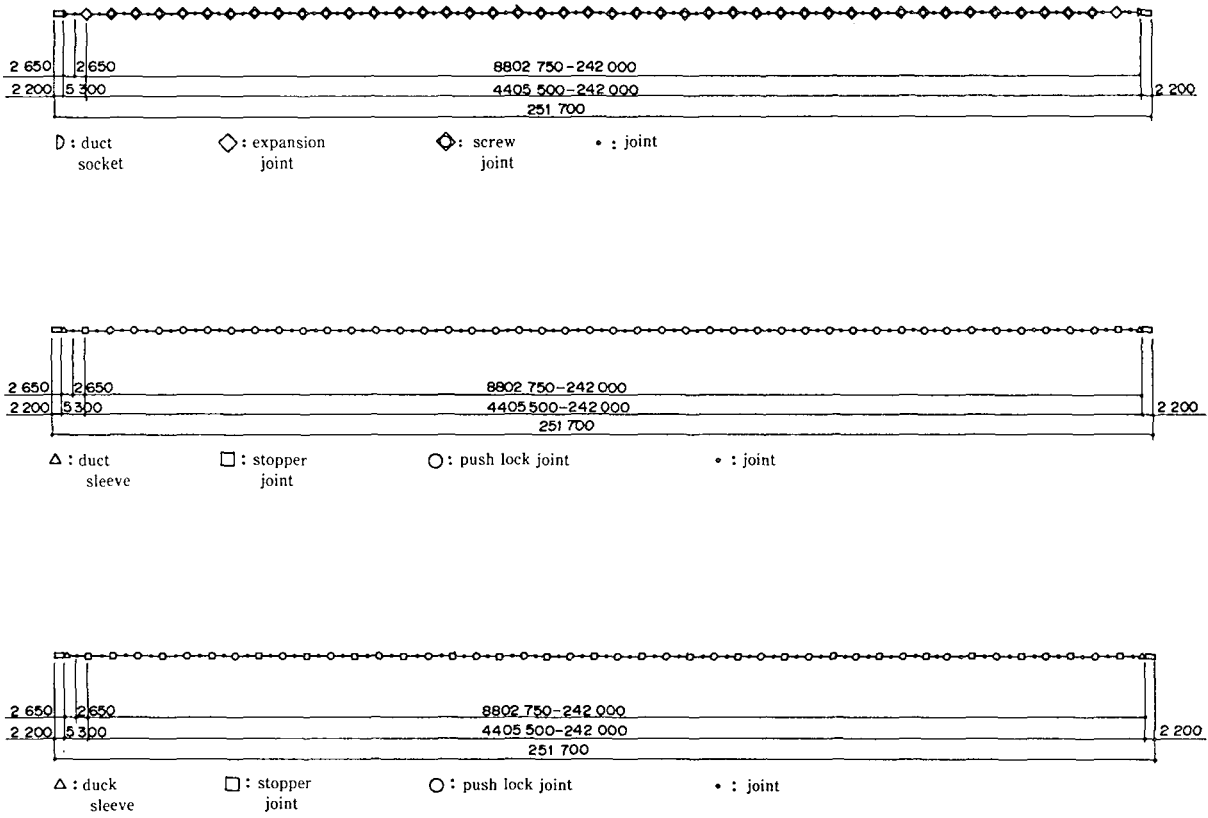
Fig. 14   Conduit constitution
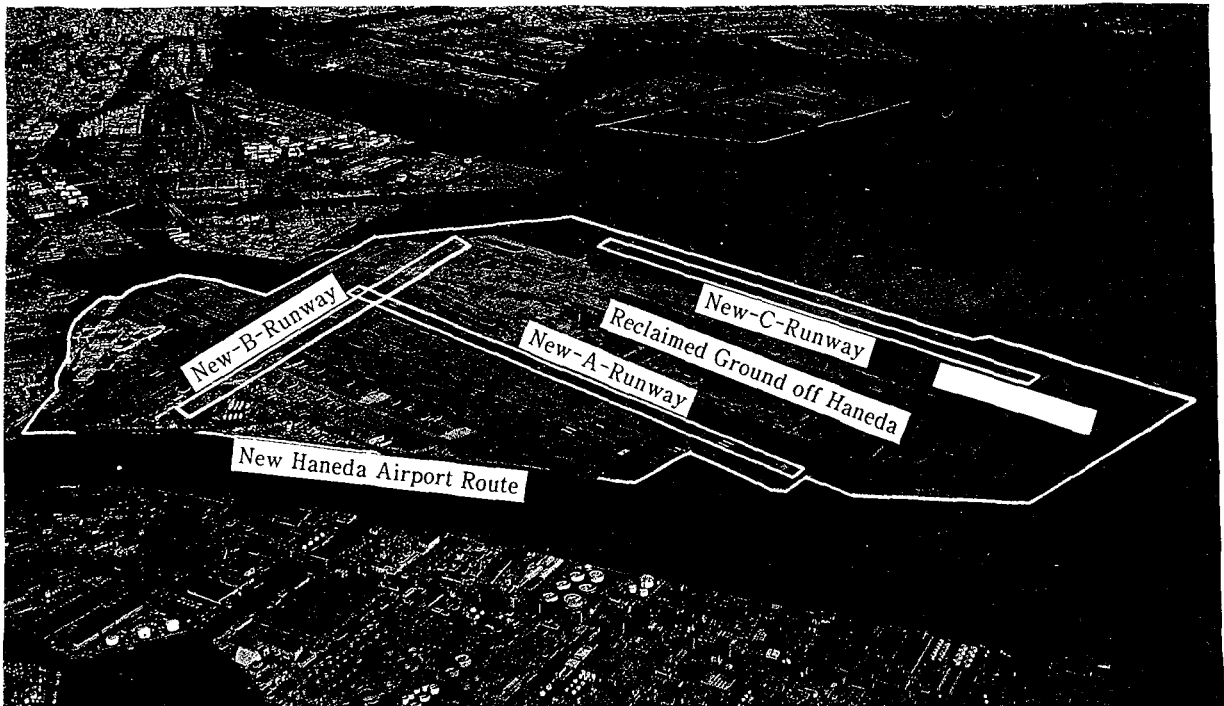
Fig. 15   New Haneda Airport Route

91

GROUND DEFORMATION IN ANCHORAGE DURING THE 1964 ALASKA EARTHQUAKE

T. Leslie Youd[1] and Scott R. McMullin[2]

[1]Professor of Civil Engineering, Brigham Young University
[2]Engineer, Westinghouse Savannah River Co.

ABSTRACT

During the 1964 Alaska earthquake (M_w = 9.2), large landslides generated massive ground displacements and inflicted near total destruction to many parts of Anchorage. Behind the major landslides, even larger ground deformation zones developed in sympathy with the landslide movements. Based on pre- and post-earthquake surveys, displacement vectors were calculated and plotted on maps to define the magnitude and distribution of ground displacements in deformation zones behind the Turnagain Heights, L-street and 4th-Avenue slides. The Turnagain Heights zone encompasses at least 350 acres, an area nearly 3 times larger than the major slide, and consists of two lobes corresponding to the two lobes of the landslide. The eastern lobe contains three identifiable subzones that are roughly concentric to the head scarp and appear to mark blocks of terrain that had separated, begun to slip, and were at a threshold for incorporation into the massive landslide. The L-Street-4th-Avenue zone extended over a 4,300-ft long east-west segment of downtown Anchorage and encompassed about 260 acres. Displacements were generally westward toward and in sympathy with movement of the L-Street Landslide. The 4th-Avenue landslide had little influence on displacements within the L-Street-4th-Avenue zone. That landslide slumped northward into the Ship Creek lowland with very little diversion to the generally westward movement in the adjacent deformation pattern.

INTRODUCTION

On March 27, 1964, southern Alaska was shaken by one of the largest earthquakes in recorded history. That event measured 8.5 on the M_s scale and 9.2 on the M_w scale (Kanamori, 1978). The earthquake produced about $300 million (1964 value) in direct damage with more than half that total inflicted by the many landslides, lateral spreads, flow failures and other forms of ground failure generated by the strong ground shaking (Youd, 1978). More than half the total damage was sustained by Anchorage, the most populous city, where several large and destructive landslides developed. The earthquake was centered in Prince William Sound, about 80 mi east-southeast of Anchorage. The earthquake was felt throughout nearly all of Alaska and generated crustal warping and strong ground shaking throughout much of southern Alaska.

Of the several major landslides that devastated parts of Anchorage, the largest and most destructive were the Turnagain Heights, L-Street, 4th Avenue, and Government Hill failures (Fig .1). These landslides were extensively studied following the earthquake and have been the
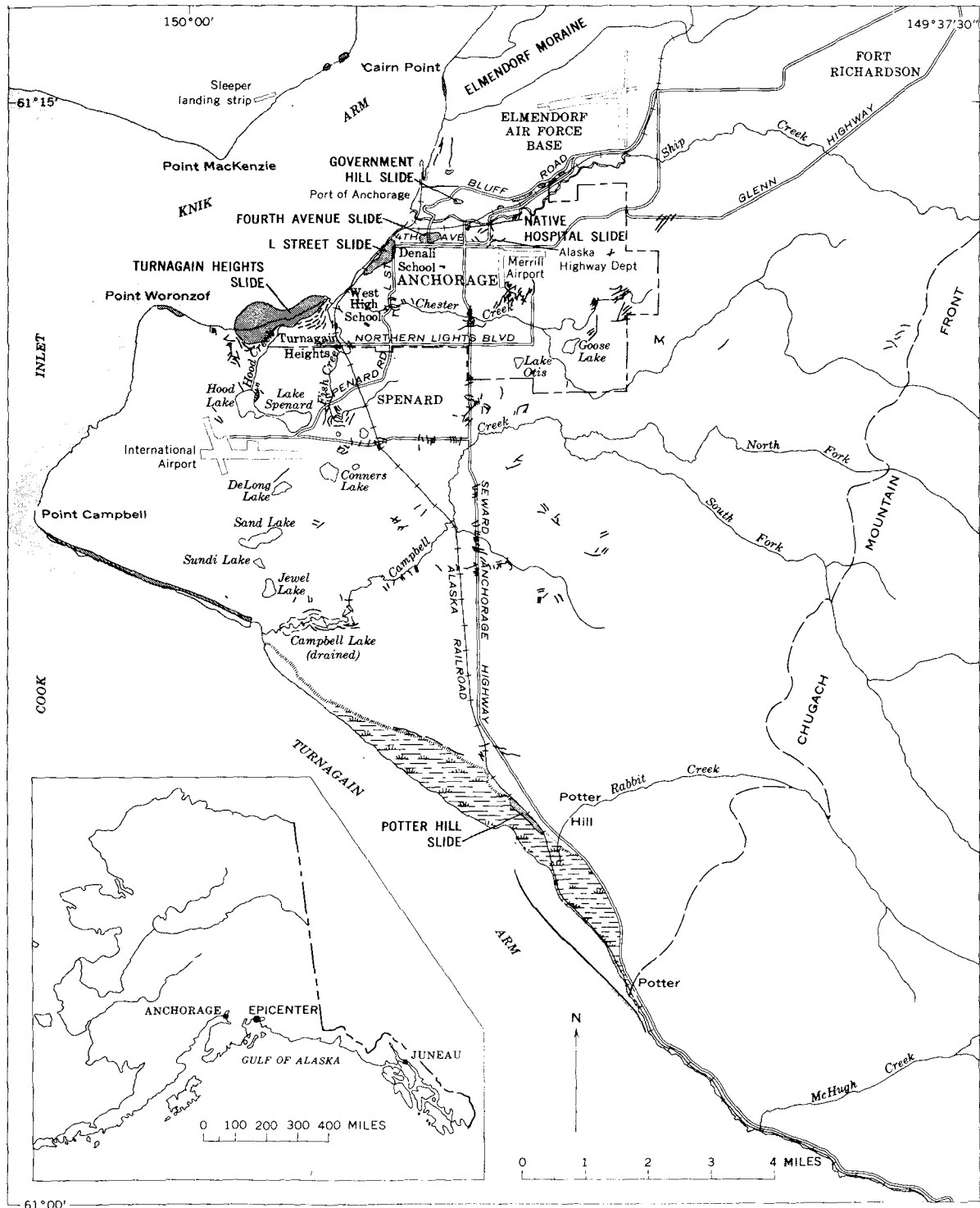
Figure 1. Map of Anchorage, Alaska, and vicinity showing locations of major landslides and ground cracks, much generalized (After Hansen, 1985).

focus of several investigations since that time (Hansen, 1965; Idriss, 1985; Long, 1973; Moriwaki and others, 1985; Olsen, 1989; Seed and Wilson, 1964, Shannon and Wilson, Inc., 1964; 1989;Updike and others, 1987). With respect to ground movement, past studies have concentrated on large displacements within the landslide masses where movements ranged tens of feet to hundreds of feet.

Some ground effects were noted by past investigators indicating that smaller ground displacements occurred in large areas behind the major slides. Such effects included an extensive pattern of ground fissures behind the Turnagain Heights slide and a few fissures and noted ground displacements behind the L-Street and 4th-Avenue slides (Hansen, 1965). The objective of this study is to evaluate the magnitudes and distributions of these smaller displacements by collecting and analyzing pre- and post-earthquake survey data. Vectors of ground displacement are calculated and plotted on maps to define displacements in deformation zones behind the Turnagain Heights, L-Street, and 4th-Avenue slides.

GEOLOGIC SETTING

Anchorage occupies a triangular shaped lowland area that lies between the Chugach Mountains to the east and the Cook Inlet to the west. The Knik Arm of the Cook Inlet lies to the northwest of the triangular area and the Turnagain Arm of Cook Inlet lies to the southwest (Fig. 1). The lowlands consist of glacial and alluvial outwash deposits overlying the finer-grained Bootlegger Cove clay. The topography is characterized as hummocky to hilly with intervening channels and depressions. Incised streams and wave action have created 20- to 80-ft high bluffs bordering coastal areas and some stream valleys. These bluffs, combined with sensitive clays within the Bootlegger Cove clay Formation, create areas of potential ground instability. Geologic and geomorphic evidence indicate that those bluffs may have failed prehistorically with landslides of similar type and size as those that developed in 1964 (Miller and Dobrovolny, 1959; Shannon and Wilson, Inc., 1964). The triggering agent for those ancient landslides is unknown, but could have been undercutting by wave action or stream erosion, or strong ground shaking produced by earthquakes.

The Cook Inlet is a deep structural trough filled with moderately consolidated Tertiary rocks. Near Anchorage, the Tertiary rocks are overlain by up to 600 feet of Pleistocene glacial sediment that was intermittently deposited during piedmont glacial advances into Cook Inlet. The glacial deposits consist chiefly of three categories of material: glacial till deposited as ground moraine; proglacial silty clays (including the Bootlegger Cove clay) deposited in estuarine-marine or lacustrine-estuarine environments; and fluvioglacial deposits of several types, but chiefly outwash sand and gravel. Most of Anchorage lies on coarse outwash sediment laid down during retreat of the most recent Pleistocene glacier that entered the area. That glacier constructed a large end moraine, called the Elmendorf Moraine, that lies immediately north of Anchorage (Fig. 1). Outwash sand and gravel from that glacier spread southward across the Anchorage lowland, burying underlying ground moraine and Bootlegger Cove clay alike to depths as great as 60 feet. In general, the outwash deposit thins with distance to the west and south away from the source and wedges out completely near the International Airport, south of the Turnagain Heights area (Hansen, 1965).

The Bootlegger Cove clay formation lies buried beneath glacial outwash deposits under most of Anchorage. The Bootlegger Cove clay is the infamous sediment unit that weakened during the 1964 earthquake and allowed the major landslides to develop. The Bootlegger Cove clay consists of about 100 feet of fine-grained materials (clays and silts) with some layers of sand. Updike (1982) identified several layers and facies within the formation; near the major landslides, the formation consists of three main layers, termed the upper, central and lower zones.

The upper zone consists of 25 to 35 feet of interbedded layers of overconsolidated clays, sandy silts, and silty sands. Those sediments were deposited near the source during a period of glacial advance.

The central zone is 40- to 50-ft thick and consists of soft, sensitive silty clays and clayey silts intercalated with sand lenses. These fine-grained clays and silts are substantially weaker than the coarse-grained and clayey materials that lie above and below the central zone. This weaker sediment was deposited in a marine-estuarine environment during a time of glacial recession. These materials have flocculated structure typical of marine clays. Sand lenses contained within the finer sediment were deposited by meandering streams emanating from upland glaciers.

The lower zone is 35- to 50-feet thick and consists of stiff overconsolidated clayey silt and silty clay with random stones. This facies was deposited during a time of glacial retreat.

CALCULATION OF GROUND DISPLACEMENTS

To calculate displacements in ground deformation zones adjacent to the major landslides, we collected and analyzed pre- and post-earthquake survey data obtained from the Department of Engineering, Municipality of Anchorage, and from private engineering firms. Most of the pre-earthquake surveys were performed by Hewitt V. Lounsbury, under a contract to the city of Anchorage. Post-earthquake survey data were taken from field work performed by several firms who were contracted to provide survey support for reconstruction activities after the earthquake.

Unfortunately, the different surveys were done independently and not intended to relate one to another. During the survey process each surveyor assumed an initial reference point or point of beginning and a basis of bearing that was generally unique to that particular project. To form one compatible set of data, we chose a stable point of reference and developed a local coordinate system referenced to that point. We then rotated bases of bearings and translated coordinates until best-fit matches were achieved between the different surveys. We did not tie our local coordinate system to a regional coordinated system.

Along with differences in bearings and points of reference, the older surveys also used a method of latitudes and departures to compute each traverse leg. That method of survey, although a standard procedure and basic to survey computations, does not easily allow one set of data to be related to another. To connect the different data sets, a coordinate data base was generated by summing latitudes and departures relative to the point of beginning. That coordinate system was then rotated and translated to match adjoining surveys.

The accuracy with which the different surveys were performed is also of concern. Survey data is subject to many possible sources of error, some of which can be controlled while others can

only be minimized. We assume that the pre- and post-earthquake surveys were executed using reasonable care to preclude human error. In all instances, instruments and survey methods used by the surveyors were properly recorded in the field notes. The pre-earthquake surveys were performed using a transit and chain. The angles and distances were measured twice, providing 3rd-order accuracy. The error ratio for 3rd-order accuracy ranges from 1/5000 to 1/3000. For that accuracy, the expected measurement error for the length of an average 360-foot long city block in Anchorage would be 0.07 to 0.12 ft.

Post-earthquake surveys were conducted using methods providing a higher order of accuracy than the pre-earthquake surveys. Although still using transits and tapes, angular measurements were repeated six times and distance measurements were corrected for temperature and tension. This procedure gave an error ratio of 1/20,000 (Shannon and Wilson, Inc., 1964), meaning that for a 360-ft long block, the expected error would be 0.02 ft. From our analysis of the survey data, we estimate that differences between pre- and post-earthquake block lengths could be as great as 0.20 ft per block due to survey error.

Finally, geodetic studies show that regional tectonic displacements associated with the earthquake affected Anchorage. Those displacements ranged from 2 to 4 ft of crustal subsidence and about 3 ft of southward crustal shift (Parkin, 1966; Plafker, 1968). Those regional displacements were rather uniform across the city and should not significantly influence the local relative displacements developed in this study.

TURNAGAIN HEIGHTS LANDSLIDE AND DEFORMATION ZONE

Landslide

The Turnagain Heights landslide, located approximately 3 miles southwest of downtown Anchorage, began as two separate failures which eventually coalesced into one large landslide complex. This slide was the largest in Anchorage, covering an area of about 130 acres. The final failed area measured 8,500 ft east to west along the head scarp; the western lobe retrogressed 1,200 ft inland from the shoreline while the eastern lobe retrogressed inland about 600 ft (Fig. 2). The slide movement disrupted the ground surface into a complex pattern of scarps, fissures, horsts and grabens. Seventy-five homes were destroyed in a part of the Turnagain Heights subdivision undercut by the eastern lobe of the landslide. The slide developed inland from a line of bluffs, some as high as 65 feet, that parallel the shoreline of the Knik Arm. The face of the bluffs sloped northward toward the sea at an angel of about 30 degrees (Hansen, 1965).

The Turnagain Heights slide developed as a progressive translatory slide. Seed and Wilson (1973) suggest that this progressive action was induced by seismic waves which successively separated new blocks of terrain as previous blocks slid seaward. The progressive nature of the slide was observed by Mr. Brooke Marston. He described his actions and the events he observed, as reported by Hansen (1965), as follows:

N 22° W
360 FT.

N 2° E
365 FT.

N 18° E
80 FT.

N 35° W
315 FT.

Approximate Mean
High Water Line

N 18° W
330 FT.

N 8° W
300 FT.

Slide Area
Eastern Lobe

N

feet
0   5   10
vector scale

A

Pre-Quake
Bluff Line

B

C

Slide Area
Western Lobe

Clay Products Road

McKenzie Drive

Turnagain Parkway

Northern Lights Blvd.

0   1/4   1/2
         miles

0   500 1000 1500 2000 2500
              feet
HORIZONTAL SCALE
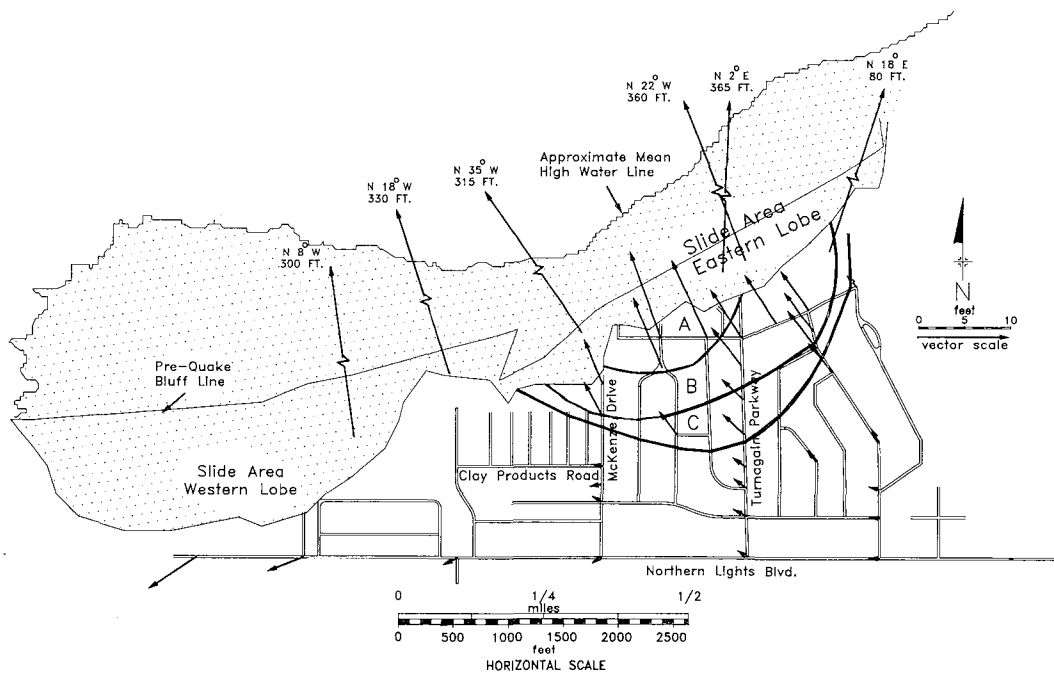
Figure 2. Map of Turnagain Heights landslide and deformation zone showing vectors of ground displacement and subzones A, B, and C that apparently displaced as intact subunits. (Vectors within the landslide area are reproduced from Hansen, 1965).

As soon as the quake subsided I proceeded to drive westward to the corner of McCollie Avenue and Turnagain Parkway. After turning right on Turnagain Parkway and driving approximately 180 feet north, I realized the bluff was gone north of my driveway, which paralleled the bluff in an east-west direction. I got out of the car, ran northward toward my driveway, and then saw that the bluff had broken back approximately 300 feet southward from its original edge. Additional slumping of the bluff caused me to return to my car and back southward approximately 180 feet to the corner of McCollie and Turnagain Parkway. After I stopped at this point, the bluff continued to slowly slide northward as I continued to back my auto southward on Turnagain Parkway. The bluff slowly broke away until the corner of Turnagain Parkway and McCollie had slumped northward.

Mr. Marston's report indicates that the Turnagain Heights slide slumped northward in segments and that much of the sliding occurred after the cessation of strong earthquake shaking.

Deformation Zone

The extent of the Turnagain Heights deformation zone was partially defined by Hansen (1965) who mapped ground fissures in a zone extending inland as far as 2,000 ft from the final head scarp. Those fissures generally paralleled the bluff line and were more numerous near the head scarp where they disrupted houses, underground utilities, streets, curbs, etc.

98

To more fully define this deformation zone and the displacements that occurred therein, we calculated and plotted vectors of ground displacement using the following procedure. A stable reference, consisting of a point of beginning and basis of bearing, was located by analyzing pre- and post-earthquake survey data from Northern Lights Blvd. We compared angular measurements at street intersections, working eastward from the affected area, until we found an intersection with very small differences between pre- and post-earthquake surveys. The locality we selected is at the intersection of Northern Lights Blvd. and Forest Park Drive, approximately one mile east and 1/4 mile south of the nearest point on the head scarp. A basis of bearing of N. 89° 56' W. was assumed along Northern Lights Blvd., in agreement with the bearing recorded in the original survey notes. Measured angles varied by only a few seconds between the pre- and post-earthquake surveys, indicating that very little local ground deformation had occurred at that locality.

Using this point of beginning and basis of bearing and data recorded by various surveyors, we calculated pre- and post-earthquake coordinates for major survey points in the Turnagain Heights area north or Northern Lights Blvd. By comparing pre- and post-earthquake coordinates, we calculated and plotted vectors of displacement shown on Fig. 2. These vectors show the magnitude and extent of ground displacement in the Turnagain Heights deformation zone. (The number of vectors on the map could be increased with additional investigation; data could be obtained from a wider area and surveys incorporating more points, such as property corners, might be found.) The extent of the deformation zone was much greater than we anticipated. We assumed, based on the map of ground fissures by Hansen (1965) and speculative comments by Shannon and Wilson, Inc. (1964), that deformation had not occurred south of Northern Lights Blvd., and we did not collect survey data for areas beyond that street. The calculated vectors, however, show that the western end of Northern Lights Blvd. was affected by ground deformation which continued an unknown distance further south.

Displacement vectors within the landslide mass show ground movements ranging from 12 ft near the head scarp to as much as 365 ft for features near the former bluffs (Fig. 2). (Those vectors were reproduced from Hansen (1965).) Within the deformation zone (our vectors), displacements ranged from 0.2 ft to 10 ft and generally decreased in magnitude with distance from the head scarp. The vectors show displacement patterns leading to the following general observations:

(1) Ground deformation extended at least as far south as Northern Lights Blvd., which lies as far as 2200 ft inland from the head scarp. The area encompassed in the deformation zone is at least 350 acres, an area almost 3 times greater than the 130 acres encompassed in main slide mass.

(2) Displacements in the deformation zones behind each of the two landslide lobes are distinctively different, indicating persistent differences in their modes of deformation. Displacement vectors behind the western lobe are consistently oriented in a southwesterly or westerly direction and increased in magnitude with distance westward along Northern Lights Blvd. In that instance, the vectors generally paralleled the head scarp rather than being directed toward the head scarp. The latter direction would be expected for movements in sympathy with the landslide in which deformation is caused by yielding toward the area from which lateral restraint has been removed. The reason for the anomalous southwestward displacement is unknown. It is possible that lateral restraint was removed from a zone further to the south by landslide or some other ground displacement and that the vectors are pointing toward that zone. Hansen

mapped a zone of large fissures about 0.25 mile southwest of the landslide (Fig. 1) and roughly on line with the direction of the vectors. It is also possible that survey error could have contributed to the unexpected direction of movement; we found no irregularities in survey procedures or data, however, that would suggest such an error.

Vectors behind the eastern lobe point toward the head scarp and decrease in magnitude with distance from that scarp. Those displacements are consistent with deformation induced directly by landslide movement. The vectors indicate soil yielding toward the area of reduced lateral restraint. A transition zone lies between the two lobes of the deformation zone. That transition is in the vicinity of Clay Products Road where ground displacements were very small (Fig. 2).

(3) The eastern deformation zone consists of at least three subzones, A, B, and C, as marked on Fig. 2. Each of these subzones contain vectors with similar magnitude (roughly 9 ft, 5 ft, and 3 ft, respectively) and direction. The subzones are roughly concentric to the head scarp and indicate incipient blocks of terrain that apparently had separated and were at a condition of incipient instability. Had the strong earthquake shaking continued for an even longer period of time in 1964, those subzones would likely have continued to move and eventually would have been incorporated into the landslide mass.

(4) Most of the displacement vectors are oriented roughly perpendicular to the many ground fissures that developed in the deformation zone (as mapped by Hansen (1965, Plate 1)). That relationship is consistent with extensional strain across the deformation zone as indicated by the decrease of vector length with distance. Such extensional strain produces tension in the ground parallel to the vectors which would fracture a brittle surface. The soil within a few feet of ground surface was frozen and thus brittle at the time of the earthquake which enhanced the development of the fissures.

(5) Shannon and Wilson, Inc., (1964) estimated horizontal extension across the deformation zone by summing the widths of open fissures that intersected Turnagain Parkway between Northern Lights Blvd and the landslide head scarp. The sum of the fissure widths was 3 ft. The difference in vectorial displacements across this same segment was 5.6 ft. These measurements indicate that only about half of the total ground displacement was accounted for by brittle ground fracture and open fissures. The remaining displacement must have been accommodated by ductile stretching of the ground surface.

L-STREET AND FOURTH AVENUE LANDSLIDES AND DEFORMATION ZONE

L-Street Landslide

The L-Street landslide disrupted a residential and commercial neighborhood of northwest Anchorage. The slide extended approximately 4,800 ft along and 500 ft inland from the bluff line above Knik Arm (Fig. 3). The slide surface encompassed nearly 30 city blocks or about 90 acres with measured horizontal displacements as great as 14 ft (Hansen, 1965). The slide, which moved horizontally with translatory type of displacement, was characterized by a well-defined scarp and associated graben at its head and a pressure ridge at its toe near the base of the bluffs. Buildings astride the head-scarp and graben were torn apart to varying degrees. Most

EXPLANATION

Fracture

Pressure ridge

Graben

Bluff line

14◄
Lateral displacement (feet)

A'——————— A
Line of geologic section

N

KNIK ARM

Approximate mean high tide

Approximate high tide

ALASKA RAILROAD

Bootlegger Cove

STOLT LANE

DAVID LANE

BEECH LANE

SCENIC WAY

LAURENCE CT

Four Seasons
apartment building

Inlet View
School

INLET PLACE

W 2ND AVE
W 3RD AVE
W 4TH AVE
W 5TH AVE
W 6TH AVE
W 7TH AVE
W 8TH AVE
W 9TH AVE
W IOTH AVE
W IITH AVE
W 12TH AVE
W 13TH AVE
W 14TH AVE
W 15TH AVE

0   400   800   1200 FEET

Figure 3. L-Street landslide area showing major fissures, grabens and pressure ridges (after Hansen, 1965).
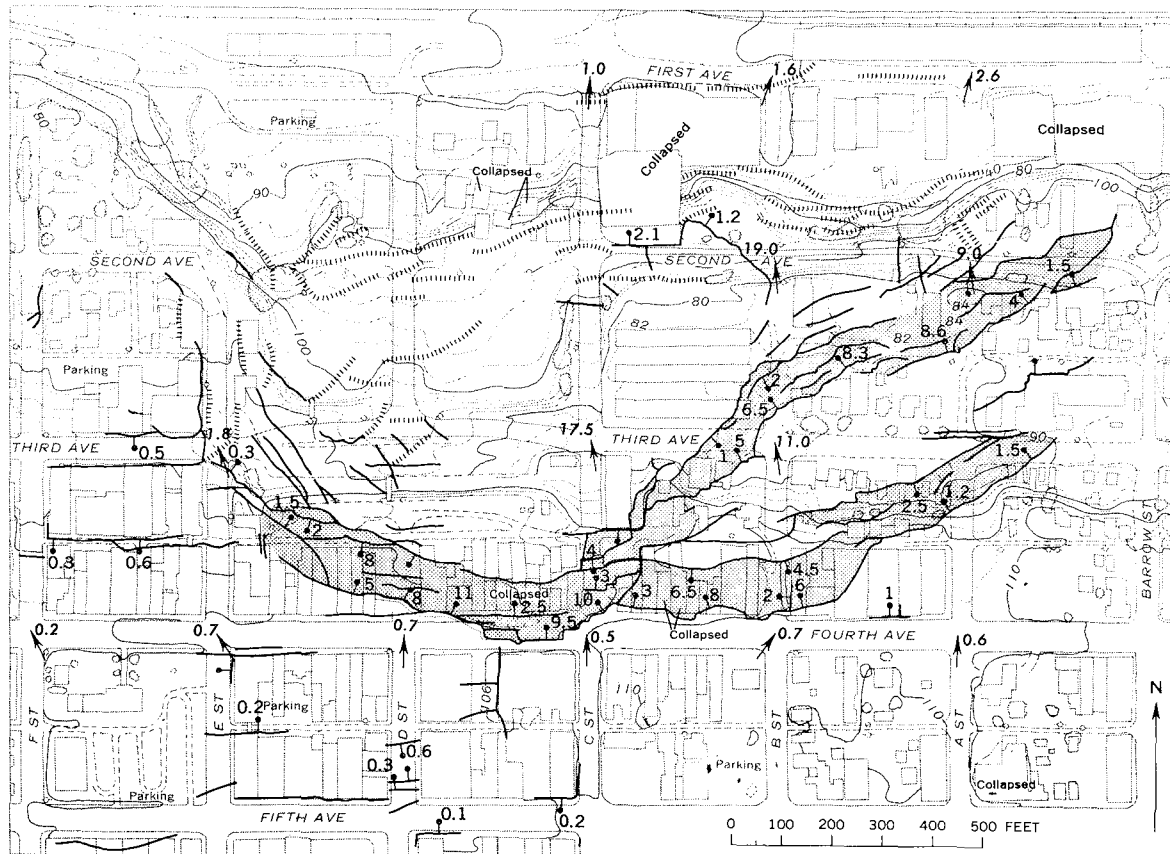
EXPLANATION

1.5
────────────
Fracture, showing downthrown
side and displacement in feet

⁜⁜⁜⁜⁜⁜⁜⁜⁜⁜⁜⁜⁜⁜⁜⁜⁜
Pressure ridge

Graben

9.0
Lateral displacement of
bench mark, in feet.
New position at point
of arrow. No appre-
ciable movement since
earthquake
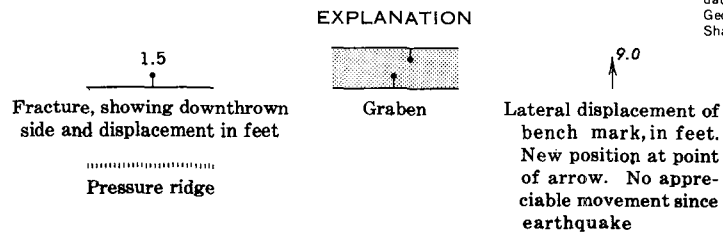
Figure 4. 4th-Avenue landslide area showing major fissures, grabens and pressure ridges (after Hansen, 1965).

of those buildings were dismantled, but several were repaired. Homes straddling the pressure ridge at the toe were lifted, compressed or tilted. The interior of the slide generally moved horizontally as a block with little internal disruption. Many buildings were transported westward with the displaced ground without suffering significant structural damage.

Other than a few fissures mapped by Hansen, there was little evidence of a ground deformation zone inland from the L-Street slide.

4th Avenue Landslide

The Fourth Avenue landslide, located about 2,000 ft east of the L-Street failure, developed in 30- to 40-ft high, north-facing bluffs above the Ship Creek lowlands (Fig. 4). The area affected was a commercial zone in the northern part of downtown Anchorage. The slide was about 1,000 feet in length, north to south, and 2,000 ft in width, east to west and encompassed about 45 acres. A deep graben formed along the head scarp. The graben bifurcated into two strands in the eastern part of the slide zone. Scattered pressure ridges formed at the toe of the slide, near the base of the bluffs. Horizontal displacements within the slide mass were as large as 20 ft but varied greatly from place to place. Vertical scarps were as highs as 10 ft along the head scarp and graben walls (Hansen, 1965). All of the structures located within or astride the margins of this landslide were raised, either because of extensive structural damage or to clear the area for a buttress that was constructed to stabilize the slide.

Hansen (1965) noted several evidences of ground deformation near the 4th street slide. Those evidences included small fissures with up to 0.6 ft of vertical separation that developed as far as 500 feet south of the head scarp. Hansen also plotted preliminary displacement vectors that had been calculated for street intersections along 4th Avenue (Fig. 4). Those vectors show ground displacements ranging up to 0.7 ft directed toward the head scarp.

L-Street-4th-Avenue Deformation Zone

Because of the close proximity of the L-Street and 4th-Avenue slides, survey data were collected for the combined area surrounding those failures. The point of beginning and basis of bearing for the L-Street-4th-Avenue area were determined using the same general method of angular comparison as was used for the Turnagain Heights zone. From measurements recorded in the survey notes, we developed three independent angular relationships and compared them at several localities to check for consistency. The angular similarities in the L-Street-4th-Avenue area were not as well constrained as those from the Turnagain Heights area. The most consistent angular relationship from the collected data was at the intersection of Gambel Street and 9th Avenue; we chose that locality as the point of beginning with an assumed basis of bearing northward along Gambel Street in agreement with the bearing recorded in the original survey notes.

Although we selected this locality as the best possible point of reference, variations between the different computations provided a locus of 0.11 ft of possible location error and angular deviations that range up to one minute of angle. This accuracy is generally acceptable, but a better point might have been found if we had collected survey data for areas even more remote from the landslide zones.

Figure 5 shows displacement vectors for the L-Street-4th Avenue deformation zone. Note that the scale of these vectors is larger than that used for the Turnagain Heights zone which magnifies the effects of survey error and gives more randomness to the lengths and orientations of the vectors, particularly for small displacements. Nevertheless, the data is sufficient to show the general distribution, patterns and magnitudes of deformation.
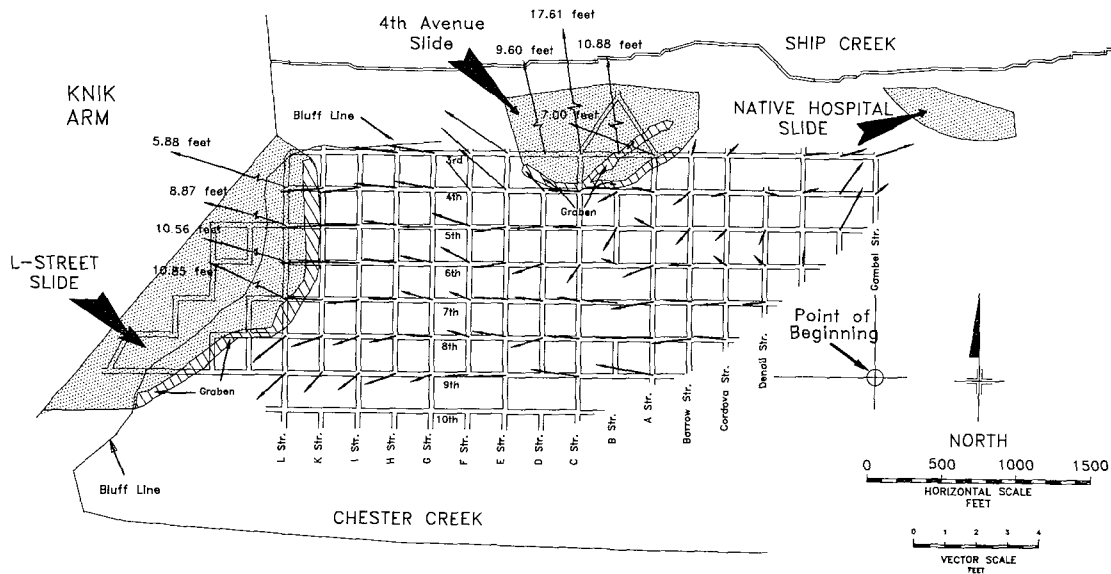
Figure 5. Map of L-Street-4th-Avenue landslide areas and deformation zones showing vectors of ground displacement and other pertinent features. (Vectors within the landslide area are reproduced from Hansen, 1965).

The deformation zone covers most of the area between 3rd and 9th Streets and between L and Denali Streets, an area of about 260 acres excluding the major landslides. Deformations Apparently occurred in adjacent areas both to the east and to the south of the area we mapped. Not realizing the extent of the zone during our data collection work, we did not collect sufficient information during this study to define ground displacements in these adjacent areas. The plotted vectors show displacement patterns, however, leading to the following general observations:

(1) The L-Street-4th Avenue deformation zone lies on a generally flat upland area that is bounded by lowlands on three sides: Ship Creek to the north, Knik Arm of Cook Inlet to the west, and Chester Creek to the south. West of Denali Street, there was general westward displacement of the ground throughout the upland area. The vectors generally decrease in length with distance eastward from about 1.5 ft near the head to about 0.5 ft near Denali Street. This decrease in length indicates that the upland peninsula stretched westward toward Knik Arm in sympathy with movement of the L-Street slide.

Compared to the Turnagain Heights zone, the stretching of the ground surface west of Denali Street produced very few fissures or other surface evidences of ground deformation. The probable reasons for this general absence of fissures is smaller overall displacements and more uniform distribution of displacement. Also, the ground surface was probably less frozen and brittle due to the many buildings and streets in the area. Those structures likely reduced the general continuity and thickness of the frozen layer creating a more ductile surface.

(2) In addition to the general westward trend, some areas tended to move toward adjacent lowlands. An example of this trend lies along 9th Street between G and L Streets where the vectors have a southward component indicating movement toward Chester Creek.

104

(3) The vectors show surprisingly little displacement northward toward Ship Creek. For example, the 4th Avenue landslide slumped northward into the Ship Creek lowland with little apparent influence on the westward deformation pattern. Only a few vectors to the east and west of the main slide mass exhibit a northward component. The vectors south of the slide, even as close as along 4th Avenue, indicate generally westward movement toward the L-Street failure.

The above finding is in apparent disagreement with the preliminary vectors plotted on Fig. 5 for the segment of 4th Avenue between A and F Streets. To resolve this apparent discrepancy we carefully analyzed the survey data from the 4th Avenue vicinity. We obtained a composite worksheet from the City of Anchorage showing survey measurements made prior to stabilization of the Fourth Avenue landslide. (This work sheet has no identifying title block, but is labeled as 1-18 and 1-19.) The data on the worksheet indicate a northward displacement of 0.7 ft at the intersection of 4th Avenue and D street, matching the displacement reported on the map published by Hansen. However, those data also indicate a westerly movement of 1.18 ft along 4th Avenue. To correctly compute the displacement at the intersection of D Street and 4th Avenue, the northward component along D Street and the westward component along 4th Avenue should be added vectorially to determine the actual displacement. Using only the worksheet data, we calculated a vector displacement of 1.37 ft oriented N. 59.3° W. From the pre- and post-earthquake survey notes, we computed a displacement of 1.31 ft oriented N. 64° W. Given possible survey error, those two vectors are in good agreement.

The discrepancies in vectors showing little northward movement are not as easily explained but could have been due to errors in interpretation of survey data. For example, planned block lengths between intersections were 360 ft. The pre-earthquake survey notes, however, show that measured field distances between intersections deviate by as much as 1 ft from these planned distances. Without taking into account the difference between planned and actual distances, one would calculate vectors similar to those plotted on Fig. 4.

(4) The displacement pattern east of Denali Street is greatly different than that to the west (the northeastern part of Fig. 5). In that area, the vectors point northeastward in a direction obliquely toward the Ship Creek lowland and almost directly toward the Native Hospital landslide. The latter slide was a relatively small slump in the bluff line about 2,500 ft east of the 4th Avenue slide. These vectors could indicate significant ground deformation toward that slide. Analysis of survey data from the Native Hospital area would be required to more fully define those suspected ground deformations.

DAMAGE RELATED TO GROUND DEFORMATION

One of the objectives of this study is to evaluate amounts of damage in the deformation and landslide zones as a function of total and differential ground displacement. Although, some observations of damage were made during the course of the study, the data and analyses are incomplete. We plan to continue study of this topic in future investigations.

CONCLUSIONS

During the 1964 Alaska earthquake, the Turnagain Heights, L-Street and 4th-Avenue landslides disrupted urban areas within the city of Anchorage, inflicting considerable damage. Associated with those landslides were even larger areas of ground deformation characterized by ground displacements up to several feet in magnitude, with movement generally toward one of the major landslide masses. We analyzed pre- and post-earthquake survey data to calculate and plot ground displacements in these deformation zones and drew the following conclusions.

1. The Turnagain Heights deformation zone encompasses at least 350 acres, an area nearly 3 times larger than that of the landslide. The deformation zone consists of two lobes corresponding to the two lobes of the landslide. The eastern lobe contains three identifiable subzones characterized by displacements of roughly 9 ft, 5 ft and 3 ft, respectively. The subzones are roughly concentric to the head scarp and appear to mark blocks of terrain that had separated, begun to slip, and were at a threshold for incorporation into the massive landslide. Had the duration of ground shaking continued for an even longer period of time, the landslide would likely have retrograded further into the Turnagain Heights subdivision by incorporating these subzones.

2. The L-Street-4th-Avenue zone extended over a 4,300-ft long east-west segment of downtown Anchorage and encompassed about 260 acres. Displacements were generally westward toward and in sympathy with movement of the L-Street Landslide. The magnitude of displacement generally decreased from about 1.5 ft near the head scarp of the L-Street slide to about 0.5 ft near the eastern margin of the zone.

3. The 4th-Avenue landslide had little influence on displacements within the L-Street-4th-Avenue zone. That landslide slumped northward into the Ship Creek lowland with very little diversion to the generally westward movement in the adjacent deformation zone.

4. In the northeastern part of the mapped L-Street-4th-Avenue zone, displacements were northeastward and directed roughly toward the Native Hospital landslide. Those displacements indicate that a significant deformation zone may be associated with The Native Hospital slump. Further analysis of survey data would be required to fully define the latter deformation zone.

ACKNOWLEDGEMENTS

REFERENCES

Hansen, W.R., 1965, Effects of the earthquake of March 27, 1964, at Anchorage, Alaska: U.S. Geological Survey Prof. Paper, 542-A, 68p.

Idriss, I.M., 1985, Evaluating seismic risk in engineering practice: Proceedings, 11th International Conference on Soil Mechanics and Foundation Engineering, San Francisco, v. 1, p. 255-320.

Kanamori, H., 1978, Quantification of earthquakes:, Nature, v. 271, p. 411-414.

Long, E. W., 1973, Earth slides and related phenomena: The Great Alaska Earthquake of 1964, National Academy of Sciences, v. 6 (Engineering), p. 644-773.

Miller, R.D., and Dobrovolny, E., 1959, Surficial geology of Anchorage and vicinity, Alaska: U.S. Geol. Survey Bull. 1093, 128 p.

Moriwaki, Y., Vicente, E.E., and Lai, Shyn-Shiun, 1985, A re-evaluation of the 1964 L-Street slide: unpublished final report, Woodward-Clyde Consultants, Santa Ana, Calif., to State of Alaska, Dept. of Transportation and Public Facilities, Fairbanks, Alaska.

Parkin, E.J., 1966, Horizontal displacements, pt. 2 of Alaskan surveys to determine crustal movement: U.S. Coast and Geodetic Survey, 11 p.

Plafker, G., 1968, Tectonics of the 1964 Alaska earthquake: U.S. Geol. Survey Prof. Paper 543-I,   p.

Olsen, H.W., 1989, Sensitive strata in Bootlegger Cove Formation: Journal of Geotechnical Engineering, ASCE, v. 115, no. 9, p. 1239-1251.

Seed, H.B., and Wilson, S.D., 1973, The Turnagain Heights landslide: The Great Alaska Earthquake of 1964, National Academy of Sciences, v. 6 (Engineering), p. 120-143.

Shannon and Wilson, Inc., 1964: Anchorage area soil studies, Alaska: unpublished report to U.S. Army Engineer District, Anchorage, Alaska.

Shannon and Wilson, Inc., 1989, Geotechnical report Turnagain landslide re-evaluation, Anchorage, Alaska: unpublished report to Municipality of Anchorage.

Updike, R.G., 1982, Engineering geologic facies of the Bootlegger Cove Formation, Anchorage, Alaska: Geol. Soc. of America Abstracts with Programs, v. 14, no. 7, p. 636.

Updike, R.G., Olsen, H.W., Schmoll, H.R., Kharaka, Y.K., and Stokoe, K.H., 1987, Geologic and geotechnical conditions adjacent to the Turnagain Heights landslide, Anchorage Alaska", U.S. Geological Survey Bulletin, 1817.

Youd, T.L., 1978, Major cause of earthquake damage is ground failure: Civil Engineering, v. 48, no. 4, p. 47-51.

PRELIMINARY RESULTS ON THE THE DYNAMIC RESPONSE OF THE MARINA DISTRICT OF SAN FRANCISCO DURING THE LOMA PRIETA EARTHQUAKE

JP. Bardet, M.Kapuskar, G.R. Martin and J. Proubet
Civil Engineering Department,
University of Southern California, Los Angeles.

ABSTRACT

This report presents the preliminary results of the ongoing research at the University of Southern California on the dynamic response of the Marina District of San Francisco during the Loma Prieta earthquake. The objective of our research is to assess the validity of liquefaction analyses based on the data set about the Marina District. One of our specific goals is to assess the importance of three-dimensional effects on the dynamic response of the Marina District. We plan to develop a 3D finite element model of the Marina District and to establish the 3D effects by comparing the results of 3D analyses with 1D and 2D results. At the present, we will report only the construction of the 3D model and a preliminary 1D analysis of site response.

BACKGROUND

The Loma Prieta earthquake occured at 5:04pm, October 17, along the San Andreas Fault in the Santa Cruz Mountains approximately 50 miles Southeast of San Francisco. This is the largest earthquake to occur in the San Francisco Bay since the catastrophic San Francisco earthquake of 1906. About forty houses were destroyed or condemned in the Marina district, 67 miles away from the epicenter. The displacement of the ground underlying the Marina District caused vertical settlement and lateral displacement of most buildings as well as the buckling of the sidewalks, the cracking of the asphalt pavements, and the rupture of underground pipes.

A reconnaissance team of the University of Southern California visited the Marina District of San Francisco on October 1989 and collected data on the sand boils and the ground displacement in the Marina District (Bardet and Kapuskar, 1990, and Bardet, 1990). As shown in Fig.1, the area investigated stretches between Baker St., Fillmore St., Marina Blvd. and Lombard St. Sand boils were easily observed in this area. They were highly visible on the concrete floors of buildings and sidewalks. The area under investigation was of limited access, which was unintentionally beneficial to our research. The police protection preserved the perishable sand boils which, otherwise, would have been cleaned up by the Marina residents.

Fig.1 summarizes our observations on sand boils, ground displacement and structural collapses. 74 sand boils were recorded. The largest sand boils are represented by an hollow circle while the smaller ones are indicated by using a full circle. 42% of the sand boils were smaller than 0.2 m^3. The cumulative volume of sand ejected during the earthquake exceeds 37 m^3. The largest sand boil (3.5 m^3) completely flooded the backyard of an apartment building. The ejected sand was fine, dark gray, odorless, and accompanied with San Francisco Bay muds. In some cases, the sand seeped through the lawn and littered the grass and flower beds. Contrarily to common beliefs, the sand boils were not caused by the breaking of water or sewage pipe, but by liquefaction.

As shown in Fig.1, all the sand boils, without an exception, were located on a 1906 lagoon which was filled in 1915 to host the Panama-Pacific International Exposition. Lawson, 1908, reported a severe ground shaking around this lagoon during the 1906 San Francisco earthquake, even in the absence of the Marina District. The Marina District was therefore constructed in 1915 on a landfill which was predisposed to ground amplification. The liquefaction of the sands filling the 1906 lagoon was consequently triggered by the amplification of the motion of the landfill laid before 1906.

OBJECTIVES

Bardet (1990) and Bardet and Kapuskar (1990) made only qualitative observations on the dynamic response of the Marina District but did not present any quantitative results. They did not explain the reason of the amplification noticed during the 1906 and 1989 earthquakes and did not estimate the level of acceleration that liquefied the artificial fill 65 miles away from the earthquake epicenter in 1989.

This report summarizes the preliminary results of the ongoing research at the University of Southern California on the dynamic response of the Marina District of San Francisco during the Loma Prieta earthquake. The objective of our research is to assess the validity of liquefaction analyses based on the data set about the Marina District. One of our specific goal is to estimate the importance of three-dimensional effects on the dynamic response of the Marina District. We plan to develop a 3D finite element model of the Marina District and to establish the 3D effects by comparing the results of 3D analyses with 1D and 2D results. At the present, we will report only the construction of the 3D model and a preliminary 1D analysis of site response. The 2D and 3D analyses are not yet completed.

Following the introduction, section 1 describes the geological evolution of the Marina site. Section 2 describes the construction of a 3D finite element model which integrates the data of previous site investigations. It depicts the geological units and synthesizes the stratigraphy. Section 3 presents a one-dimensional dynamic analysis at a particular location of the Marina.

THE GEOLOGY OF THE MARINA SITE

The Marina District is located on the northern waterfront of San Francisco a mile east of the Golden Gate Bridge between the Presidio and Fort Mason (see Fig.1).

Natural deposits

During the last one millions years of the Pleistocene glaciation period (Pleistocene is between 15,000 to 3.5 million years ago), at least three glacial stages occured under and near the San Francisco Bay, each marked by a period of material deposition during high sea levels followed by a period of desiccation and erosion due to lower sea levels (Hensolt, 1988).

Between 0.7 to 1.8 million years ago, when the sea level was more than 300 ft higher than it is today, the Golden Gate channel was formed and the San Francisco Bay came into existence. As suggested by Schlocker, 1974, the bedrock underlying the Marina site is made of Franciscan rocks eroded by the waters the ancient Sacramento and San Joaquin Rivers flowing through the Golden Gate channel about 1.5 million years ago.

The earliest stage of development of the Golden Gate channel and San Francisco Bay occured in the Pliocene Glacial period (0.5 to 1.0 million years ago) when unconsolidated estuarine sandy materials were deposited during high sea levels. These old materials, referred to as the Colma Formation, are firm sands of orange to light-brown color underlying the estuarine deposits of the Alameda Formation.

During the most recent stage of the Pleistocene period, called the Sangamon Interglaciation (75,000 to 125,000 years), thick estuarine clay deposits of gray color containing interbeds of sand and shells were formed (Schlocker, 1974, USGS 1990). These materials (also referred to as "older bay mud") belong to the San Antonio Formation and cover virtually all of the deep soils and bedrock under the Marina site.

Boring logs as early as 1912 (Schlocker 1961, USGS 1927) and more recent investigations (e.g., USGS 1989/1990) have indicated that beds of dense sands cover the older clay deposits under the Marina site. It is assumed that that these firm materials, called "Yellow Hardpan," are Eolian deposits from the early stages of the Altonian glacial period (30,000 to 40,000 years ago) that were subjected to surface erosion during the low sea level of the Wisconsinan glaciation. These hard strata are expected to be about least 10,000 yrs old.

Some 15,000 years ago during the Wisconsinan glaciation of the Holocene period, estuarine materials were deposited on the Marina site due to high sea levels flooding the Golden Gate channel. These materials (now often referred to as the "younger bay mud") consist of semi-consolidated fine sands and clay of olive gray color and cover most the Marina site.

Artificial fill

The history of the shoreline of the Marina District is shown in Fig.1. By 1906, the Marina cove was closed by an artificial sea wall. The Panama Pacific International Exposition of 1915 had the largest impact on the Marina environment. A.H. Markwart, assistant director of works for the exposition wrote in 1915 that the fill started on April 13, 1912 along the shoreline in order to create solid land for the exhibition. The fillings of the tidelands continued for five months, and by September 1915, 1.3 millions cubic yards of sand and muds had been pumped into the area. The artificial material used for land fill was mainly made up of sand with silt, gravel, debris and organic waste. It is occasionally hard to identify in the descriptions given in boring logs. According to Markwart, the fill was roughly 70 percent sand and 30 percent sea mud. He also filled 114 acres of marshlands on the grounds of the Presidio for the exposition. The fills proved satisfactory he wrote as the installation of roads and gardens and the work of pile driving and construction of the Exhibition Palaces took place immediately upon completion of the fill, a procedure which is unusual in the case of many new fills. There has been no damage from settlement. After the Panama Pacific international exposition closed, the area remain unused. Then in the 1920s real estate developers began to develop the Marina District.

THREE-DIMENSIONAL MODEL OF THE MARINA SUBSOILS

The area of the Marina District under investigation covers about 1.2 km^2 between Lyon St., Lombard St., Laguna St. and the northern waterfront, including the Yacht Harbor with the San Francis Club. As shown in Fig.2, a cartesian grid is defined with its origin on the northeast corner of Greenwich and Lyon Streets. The horizontal axis runs along Greenwich St. and the vertical axis passes through the Palace of Fine Arts. All the available data on stratigraphy and soil properties were compiled to construct a solid model of the subsoils of the Marina District. Based on the compilation of 86 boring logs, ten geological units were distinguished: Franciscan formation, Franciscan Serpentine, Colma Formation, Late Pleistocene Bay Clay, Holocene Bay Clay, Shells, Beach Sands, Dune Sands, Tidal Marsch and artificial fills. Theses geological units were grouped in five layers. The Franciscan Formation and Serpentine defines the bedrock surface that supports the model. The bottom layer above the bedrock is made of Pleistocene Bay Clay. The yellow Hardpan/Green Sand forms the second layer. Holocene Bay Clay with traces of

111

Holocene-Pleistocene Green Sand forms the third layer. The upper layer is made of artificial silt-sand-gravel mixture, Beach Sands and Dune Sands.

Site investigation in September, 1990

Deep boring logs were too scarce to provide sufficient information on the depth, thickness and soil properties of the hardpan and old bay mud. The purpose of the site investigation was to collect additional soil profiles and to obtain soil samples for laboratory testing. The site investigation includes nine electric cone penetration tests (CPT) and three downhole seismic CPTs; the locations are shown in Fig.3.

In order to delineate the subsurface strata at the north of the site, two cone penetration tests were positioned on the Marina waterfront (C-1 and C-5). Two seismic downhole CPTs were performed at C-1. In order to calibrate the interpretation of the CPT results, an electric CPT was positioned in the center of the Marina cove next to the USGS M4 boring (C-2). The third seismic test was placed on the 1857 shoreline (C-17) where surficial dune sand is located.

The CPT tests were performed in September 1990 by the Earth Technology Corporation using a 20 CPT ton system. The principal soil columns interpreted from these CPT tests are shown in Fig.4. They were obtained after calibrating the CPT results obtained at location C-2 against the USGS soil column M4 (USGS, 1990). Our interpreted soil columns at other locations were found to match the boring logs obtained by Dames & Moore and Harding Lawson Associates.

The hardpan was pierced at locations C-1 and C-5. Its thickness was found to be less than 1.2 m. At location C-1, the hardpan was pierced at a depth of 31 m. At location C-3, the hardpan was reached at 27.7 m, which is 5 m below the depth predicted by Dames & Moore, 1977.

During our CPT investigation of the Marina District, problems were experienced with the sticky Pleistocene mud. At location C-1, the CPT was terminated at 12 m below the hardpan due to excessive sleeve-friction build-up. At location C-2, C-8 and C-12, penetration failed due to rod buckling and high tip bearing resistance. In all other locations, the dense sand layer was not reached due to sleeve-friction build-up in the hydraulic fill and/or excessive probe inclination.

Principle of construction for 3D model of subsoils

Based on a compilation of all the available soil borings, a four-layer model was estimated to represent the subsoils of the Marina District with an accuracy sufficient for a dynamic analysis of site response.

The three-dimensional model was constructed from discrete boring logs. It covers a horizontal area of 1500 m by 1100 m and is made of 1152 nodes. Its construction consisted of identifying the top and bottom surfaces and three interfaces, i.e. 6 surfaces in all the available boring logs. Each surface was generated by the elevation of nodes on a uniform grid of 16 by 12 nodes. A Delaunay triangulation was used to interpolate the elevations of these evenly spaced nodes from the scattered data of boring logs. In the process, erroneous identifications of soils were filtered and the interface positions were smoothed. The layers were stacked in a sandwich fashion without intersecting one another. The elevation of grid points were slightly adjusted by trial and error until interfaces stopped intersecting. We will now describe each surface and layer of the 3D model.

Ground surface

The ground surface generates the upper surface of the three-dimensional model. It was defined by 650 scattered elevation points digitized from the 1973 USGS topographic maps inside a rectangular 4000 m by 3000 m frame. Fig.5 shows an isometric bay view of the Marina and its surroundings.

Bedrock surface

The bedrock surface generates the lower surface of the three-dimensional model. In geotechnical engineering, the definition of a bedrock is generally a subjective task closely dependent on the particular problems to be solved. In the case of the Marina District, the bedrock was rather easily identified since it was possible to locate a significant discontinuity between superficial and deep sediments. The bedrock underlying the Marina site is made up of serpentine and of sandstone and weathered shale from the Franciscan Series. A bedrock depression was inferred from (1) the distribution, size and shape of nearby outcrops, (2) a few reliable deep borings and (3) geological considerations.

The reconstitution of the three-dimensional surface of the bedrock was rendered difficult by the lack of deep boreholes data. At this date, only three boreholes reached the bedrock. A high resolution profiling based geophysical seismic reflection would have been an appropriate technique to define the exact position of the bedrock. However, the high cost of this investigation and its limitations in presence of deep sediments in a heavily urbanized area ruled out their uses.

The determination of the bedrock was also complicated by the presence of a Hardpan layer 60 m above the real bedrock. This hard layer has been misinterpreted as a bedrock by several investigators (e.g. Schlocker, 1961) who based their definition of bedrock on available geotechnical soundings. The hardpan layer may have been correctly identified as bedrock for geotechnical investigations aiming at designing building foundations; but this confusion was unacceptable in our present investigation. We discovered this error in the 1974 USGS map after noting the anomaly in the bedrock contours at the east of Webster St.

The rock outcrops in the geological map of Schlocker (1961) were useful to reconstruct the bedrock of the Marina site. The following bedrock outcrops surrounding the Marina site were included: Fort Mason, Russian Hill and Nob Hill, around Lafayette square (Fillmore Hill), intersection of Scott St. and Greenwich St., Alta Plaza east of the Presidio, central Presidio and Crissy Field (Fig.6). The bedrock depths determined in the USGS bore hole WSS and in the UCD borehole BH-3A (at the USGS boring M4) were extremely useful to calibrate the bedrock depth. Old drill holes at the center of Funston Playground (USGS, 1990) and south of the Palace of Fine Arts (Dames and Moore, 1961) were also included.

The bedrock elevation contours were obtained by interpolating (with a Delaunay triangulation) the scattered data of 130 known elevations and about 20 virtual elevations. The virtual elevations were obtained based on geological considerations, such as the gradients of the bedrock drainage paths towards the Golden Gate Channel as shown in Fig.6 (Schlocker 1974, Hensolt 1990). The bedrock surface is assumed to be a half-basin surrounded by rock outcrops. It opens towards the bay in a northwest trend. Under the Marina waterfront the depression is bounded by the outcrops at Fort Mason and Fort Scott. The depression is assumed to reach -87 m under Marina Blvd. Offshore, the basin bounded by the outcrop of Alcatraz Island in the far northeast (Schlocker, 1961), which is less than two miles from the Marina, and by an underwater pile of rock called Anita Rock (Carlson, McCulloch, 1970).

Layer of Pleistocene Bay Clay

The Pleistocene Bay Clay covers the bedrock under the site. Its thickness reaches about 60 m under Marina Blvd between Scott and Fillmore Streets. Only few deep borings were available to yield reliable information on this layer. It is assumed that this clay layer is continuous and is overlain by the hardpan layer throughout the Marina.

Layer of Yellow Hardpan

The top surface of the hardpan was modelled based on 74 borings. The bottom interface was modelled from 35 borings; 39 borings did not go through the hardpan layer. The hardpan top surface is shown in Fig.7. It deepens towards the waterfront and

dramatically dips down to below 28 m at location C-3 and 31 m at location C-1. Compared to others layers, the hardpan is generally very thin (0.3 to 1.2 m thick). It thickens considerably (11 m) under the Palace of Fine Arts (Dames and Moore, 1961).

Layer of Holocene Bay Clay

The layer of Holocene Bay Clay was constructed from 87 boring logs. This layer extends landward past the 1869 shoreline from Fort Mason across Funston Playground and under Lombard St. towards the Presidio. This layer has a fairly smooth top interface, which could be explained by the lack of erosion since its deposition. A layer of hard green sand underlies the Holocene Bay Clay under most of the Marina District.

Top layers

The top layer is made of Marsh Deposits, Beach Sands, Dune Sands and artificial fills. A band of tidal marsh deposits is found under the Presidio (Crissy Field) and the adjoining southwest of the Marina District between Scott St. and Fillmore St. as far south as Lombard St. They contain organic clays and silts and some Holocene materials such as bay clays and beach sand. The natural deposits of Beach Sand along the present shore west of the Golden Gate between Fort Point and Telegraph Hill are now overlain by artificial materials that were used for landfill in the past decade. These deposits underlays the west of the site as part of the former Strawberry Island. Also, according to the older maps, a small band of beach sand is located to the south of Alhambra St. Dune Sand that probably covered the western beach deposits is found mainly between Webster St. and Fort Mason.

The final three-dimensional model

Fig.8 shows the ground and bedrock surfaces as seen from the waterfront. The ground surface elevates from 0 m to about 15 m in the southwestern part of the Marina. At the southeast of the Presidio, the bedrock surface meets the ground surface.

Figs.9 show the soil profiles along four cross-sections through the three-dimensional model. The locations of the cross-sections are shown in Fig.2. Similar cross sections will be used in the 2D analysis of the site response.

ONE-DIMENSIONAL DYNAMIC ANALYSIS

One-dimensional analyses of site amplification are commonly performed in earthquake engineering. They estimate the vertical and horizontal accelerations of the ground surface after prescribing the earthquake acceleration at the bottom of soil columns. They assume that the 2D and 3D effects are negligible. The one-dimensional effective-stress analyses were performed by using the finite element code LINOS. LINOS is a finite element program (Bardet, 1989) capable of 3D dynamic analyses with material nonlinearity and coupling between soil and water.

Soil geometry and input motion

The soil column used for this analysis was synthesized to represent the conditions in the center of the liquefaction zone shown in Fig.1. As shown in Fig.10, it is made up of 6 materials layers with a thin dense sand layer, 12 m deep, at the transition between the younger and older bay mud.

The east-west component of the acceleration recorded at the CSMIP station on Yerba Buena Island (CSMIP, 1989) was prescribed at the bottom of the soil column of Fig.10. Yerba Island is built on San Franciscan sandstone and is located 6 km east of the Marina District. The acceleration record has a peak acceleration of 6.7% of g and a duration of 40 seconds.

Shear strength and other soil properties

The unit weights, water contents and shear strengths are reported in Fig.10. The soil properties were taken from the tests results of the USC site investigation and also compiled from Kayen et al., 1990, Dames and Moore, 1975, Denby, 1978, Bonaparte and Mitchell, 1979, Schlocker, 1974, and Seed and Sun, 1989. Based on the shear strength correlations from CPT and on a selection of vane shear tests (Ertec, 1981, Denby, 1961, Seed and Sun, 1989), the undrained shear strengths were chosen to increase linearly with depth (see Fig.12). Based on the equivalent blow count determined from CPT results, the effective friction angle varies between 30° and 40°i n the artificial fill. An friction angle of 35° and 37° is selected for the artificial fill and the hardpan, respectively.

Wave velocity

Shear and compressional wave velocities were determined from three seismic CPTs performed at locations C-1, C-5 and C-17. As shown in Fig.11, four zones can be distinguished for the interpreted shear wave velocities.

(1) In the loose unsaturated and unconsolidated sandy and gravelly fill, the velocities of shear and compression waves are v_s=290-415 m/sec and v_p=580-870 m/sec. The large variation in the velocities is attributed to the non-homogeneity of the fill, which widely ranges in composition from silty sand and debris (C-17) to clayey sand and scattered rock fragments near the Fair sea seawall (C-1 and C-5) and wood pieces from pilings left over from the exposition.

(2) In the saturated sandy fill, the natural sand deposits and the Holocene bay mud, v_s=120-225 m/sec and v_p=1520- 1650 m/sec. The lower range is confirmed by measurements in the USGS hole WSS (Kayen et al., 1990), where v_s was measured to range from 128 to 160 m/sec. The higher value of v_s applies for more consolidated Holocene bay mud.

(3) v_s=290-460 m/sec in the hardpan layer. These velocities were measured at the USGS hole WSS in a layer of Hardpan 11m thick. An average value of 366 m/sec was adopted in our dynamic analyses similarly to Seed and Sun, 1989 who selected v_s=335 and 365 m/sec.

(4) Below the hardpan, v_s>225 m/sec and v_p=1740 m/sec. At location C-1, seismic measurements were made down to a depth of 43 m, which is about 10 m into the Pleistocene bay mud. The velocities v_s were found to be identical to the ones in the lowest portions of the Holocene Bay Mud. In the absence of other deep measurement of v_s in the Marina District, the shear wave velocities were supplemented by measurements at three other locations: the WSS deep bore hole, the Southern Pacific Building (about 1.5 km southeast of the Marina site) and the Embarcadero Center (Seed and Sun, 1981). At the WSS hole, a shear wave velocity of 265 m/sec was measured. The Southern Pacific Building has soil conditions similar to the the Marina site; v_s was estimated to 335 m/sec for a stiff, consolidated (Pleistocene) clay layer 30 m thick. Fig.11 shows the shear wave velocities measured at these other locations and the velocity profile selected in our analysis.

Results

Material nonlinearity and coupling between soil and water are two main factors to account for in the study of dynamic site responses. Several preliminary analyses were performed in order to assess these effects in the 1D analysis of the dynamic response of the Marina District. For the sake of conciseness, we will only summarize the results of three analyses and omit all the theoretical derivations. Detail on the material modelling and the finite element formulation may be found in Bardet (1989, 1990) and Bardet and Proubet (1990).

The first analysis was elastic and undrained. The elastic properties of the soil layers are listed in Fig.10. The soil column is made of 14 plane elements. All the elastic elements were damped by using a Rayleigh damping with 2% of critical damping ratio on the stiffness term. As shown in Fig.13, the peak acceleration is 1.7 m/s² at the top of the column whereas the peak input acceleration is 0.7 m/s². The natural period of the soil column is 1.08 second as identified by the peak in the Fourier spectrum. The maximum relative displacement is 3 cm. The clay layers experience cyclic shear strain amplitudes smaller than 10^{-4} and the cyclic shear stresses do not exceed the undrained shear strength shown in Fig.12. This low strain level implies that the clays behave elastically and that all the permanent deformations are expected to concentrate in the upper sand layers (when liquefied).

In the second and third analyses, the clay layers were assumed to behave elastically whereas the upper layers of sand were modelled with a nonlinear hypoplastic model that derives from the elastoplastic Drucker-Prager model (Bardet and Proubet, 1990). The model has only seven material constants that are easily calibrated from conventional material properties. The BDP model is a simple constitutive model that does not describe all the nonlinear features of sand behavior, but only the ones relevant to dynamic analysis. The sand was modelled as three layers of BDP model to demonstrate liquefaction effects.

The elastic properties of the BDP model were calibrated from the elastic shear wave measurement. The Young's modulus E is a power function of the mean pressure p:

$$E = E_o \, p_a \left(\frac{p}{p_a}\right)^n \tag{1}$$

where E_o and n are material constants, and p_a is the atmospheric pressure (p_a=100 kPa). E was selected equal to 200 and n to 0.5. The elastic Poisson ratio was selected equal to 0.3. The bounding surface of the BDP model is the Drucker-Prager failure surface:

$$J = \alpha \, p \tag{2}$$

where J is the second invariant of deviatoric stress. The slope α of the failure surface was calculated to match the shear strength of Mohr-Coulomb materials in simple shear test (α = 0.7833, ϕ=35°).The parameter β that controls the non-associative flow rule was arbitrarily selected as -0.05 to account for irreversible compaction during cyclic loadings. The plastic modulus H is a function of the distance between the stress point and the failure surface.

$$H = H_o \, G \, \frac{(J/p_a - \alpha \, p/p_a)^m}{J} \tag{3}$$

where G is the elastic shear modulus and H_o and m are two material constants that were selected equal to 0.5 and 1, respectively.

In the second analysis, the upper layers of sands were assumed to be undrained. As shown in Fig.14, the top layer liquefies after 12 seconds. The acceleration at the top reaches a peak value of 2 m/s² then drops down to zero when liquefaction takes place (undrained shear strength is assumed zero after liquefaction). Fig.14 shows that the mean effective pressure and the second invariant of deviatoric stress also drops down to zero. The pore pressure builds up mainly during the main shock. After liquefaction, the pore pressure becomes equal to the hydrostatic pressure generated by a fluid of density γ_{sat}.

Fig.14 also shows the stress-strain response of the top layer. The response ε_{12}-σ_{12} gets softer as the pore pressure build up then softens rapidly at liquefaction.

In the third analysis, the pore pressure is allowed to diffuse. The value of the permeability coefficient is listed in Fig.10. There are three degrees of freedom per node: two for the solid displacement and one for the vertical fluid velocity. The interstitial fluid is assumed to be incompressible. In contrast to Fig.14, Fig.15 shows that liquefaction does not take place. The pore-pressure builds up rapidly during the main pulse but is not large enough to liquefy the upper sand layer. The response ε_{12}-σ_{12} gets softer as the pore pressure build up but does not reach failure as in Fig.15. In spite of the nonlinear effect, the Fourier spectrum of acceleration in Fig.15 is similar to the elastic spectrum shown in Fig.13.

CONCLUSIONS

Preliminary results on the dynamic response of the Marina District have been presented. A 3D model has been constructed for the subsoils of the Marina District. This 3D model was based on bore holes data and considerations of structural geology.

Preliminary results of 1D analyses illustrate the influence of material nonlinearity and soil-water coupling on the dynamic response of soil columns. Liquefaction was obtained in the undrained condition for a low level of shaking. It was not obtained when pore pressure was allowed to diffuse. The soft clay layer amplified the acceleration in the upper sand layers as it was noticed in the 1906 and 1989 earthquakes. The clay layers were mainly subjected to elastic deformation.

At this stage of our research work, it is premature to draw definitive conclusion on the dynamic response of the Marina District. More quantitative 1D analysis are required, and comparison between LINOS and DESRA analyses are planned. However, it is anticipated that the three-dimensional effect will be important in influencing the dynamic response of the Marina District due to the three-dimensional shape of the bedrock.

ACKNOWLEDGEMENTS

REFERENCES

Arulanandan, K. and G. Yogachandran, 1990, "A Preliminary Analysis of Ground Response and Soil Liquefaction of Sites in the Marina District of San Francisco Subjected to the Loma Prieta Earthquake of October 17, 1989." UCD Report 1990-1, Department of Civil Engineering, University of California, Davis.

Bardet, J.P., 1989, "LINOS: a nonlinear finite element program for Geomechanics and Geotechnical Engineering," *University of Southern California, Los Angeles.*

Bardet, J.P., 1990, "Damage at a distance," *Nature,* Vol.346, August, p.799

Bardet, J.P., and M. Kapuskar, 1990, "An Analysis of the Sand Boils Due to Liquefaction in the San Francisco Marina District During the 1989 Loma Prieta

Earthquake." accepted for publication in *Journal of Geotechnical Engineering Division, ASCE*.

Bardet, J.P., 1990, "Hypoplastic model for sands,"*Journal of Engineering Mechanics, ASCE*, Vol.116, No.9, pp 1973-1994.

Bardet, J.P., and J.Proubet, 1990, "The BDP model for sands: Theory and FE implementation," in preparation.

Bonaparte, R. and J.K. Mitchell, 1979, "The Properties of San Francisco Bay Mud at Hamilton Air Force Base," California, Civil Engineering Department, University of California, Berkeley.

CSMIP,1989, "Strong-Motions Records from the Santa Cruz Mountains (Loma Prieta), California Earthquake of 17. October 1989," *California Department of Conservation, Division of Mines and Geology, Reports OSMS 89-06 and OSMS 89-08*.

Dames & Moore, 1962 (1961), "Main Building Rehabilitation, Palace of Fine Arts Project," *Report Job No. 185-033-03*.

Dames & Moore, 1977 (1961), "North Shore Outfalls Consolidation Project. Supplementary" *Soils Report Job No. 185-118-03*.

Denby, G.M., 1978, "Self-Boring Pressuremeter Study of San Francisco Bay Mud," Technical Report No. CE-232, Dept. of Civil Engineering, Stanford University.

Ertec Western, Inc., G.R. Martin, Tsai, 1981, "Nonlinear Response of Soft Clay Sediments to High-Strain Earthquake Ground Motions." *Contract No. USGS-14-08-0001-19106,* Long Beach, California, p.29-46.

Hensolt, W.H., 1988 (revision), "Pleistocene Glaciation, Chronology of Sediments under San Francisco Bay and Sea Level Changes." Chin and Hensolt Engineers, Inc. (private communication).

Hensolt, W.H., and R.D. Darragh, 1990, "The Marina District and the loma Prieta Earthquake, Deep Bedrock and Soft Soil Conditions, San Francisco." Chin and Hensolt Engineers, Inc.; Dames and Moore (private communication).

Holzer, T. and Prof.T.D. O'Rourke, 1990, "Effects of the Loma Prieta Earthquake on the Marina District, San Francisco, California." *in Dept.Interior U.S. Geological Survey Report*.

Kayen, Liu et al., 1990, "Engineering and Seismic Properties of the Soil Column At Winfield Scott School, San Francisco." *in Dept.Interior U.S. Geological Survey Report*.

Lawson, A.C., 1914, "Description of the San Francisco District, California." *U.S. Survey Geology. Atlas, Folio 193*.

Lee, M.K.W. and W.D.L. Finn, 1976, "DESRA-2, Program for the Dynamic Effective Stress Response Analysis of Soil Deposits with Energy Transmitting Boundary Including Assessment of Liquefaction Potential." *Soil Mechanics Series No. 38,* Department of Civil Engineering, University of British Columbia, Vancouver, Canada.

Martin, G.R., W.D.L. Finn and P.M. Byrne, 1975, "Seismic Response and Liquefaction of Sands." *Soil Mechanics Series No. 24*, University of British Columbia, Vancouver, Canada.

Schlocker, J., 1961, "Geological Topographic Bedrock-Map of the San Francisco North Quadrangle, California." *U.S. Geological Survey open-file map, scale 1:31,680*.

Schlocker, J., 1974, "Geology of the San Francisco North Quadrangle, California." *U.S. Geological Survey Professional Paper 782, U.S. Government Printing Office, Washington, D.C.*

Seed, H.B. and J.I. Sun, 1989 (UBC/EERC Report), "Implications of Site Effects in the Mexico City Earthquake of Sept. 19, 1985 for Earthquake-Resistant Design Criteria in the San Francisco Bay Area of California." *Contract No. UCB/EERC-89-03,* University of California at Berkeley, College of Engineering, pp.27-40.

Treasher, R.C., 1963, "Geology of the Sedimentary Deposits in San Francisco Bay, California." *California Dept. of Conservation, Division of Mines and Geology, Special Report 82, pp.11-19.*
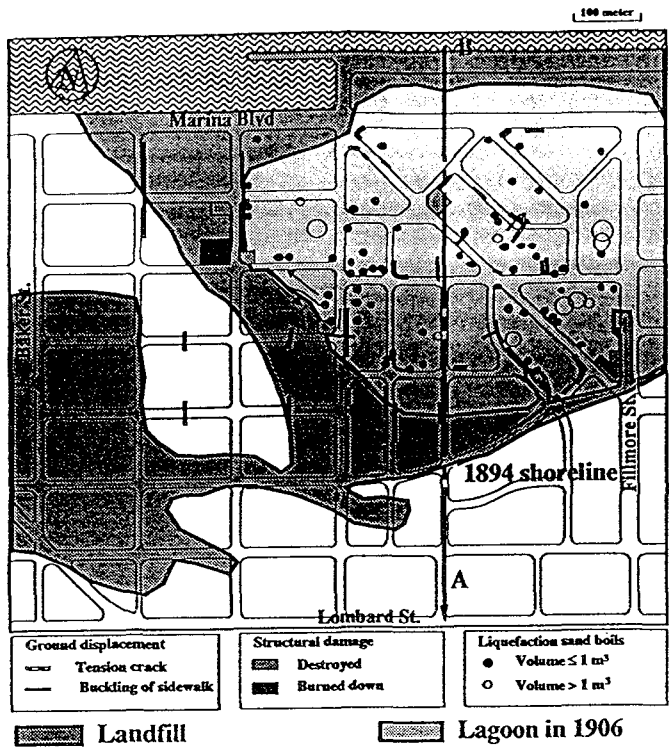
Figure 1. Map of the Marina site of San Francisco summarizing the results of the USC investigation of October 1989.
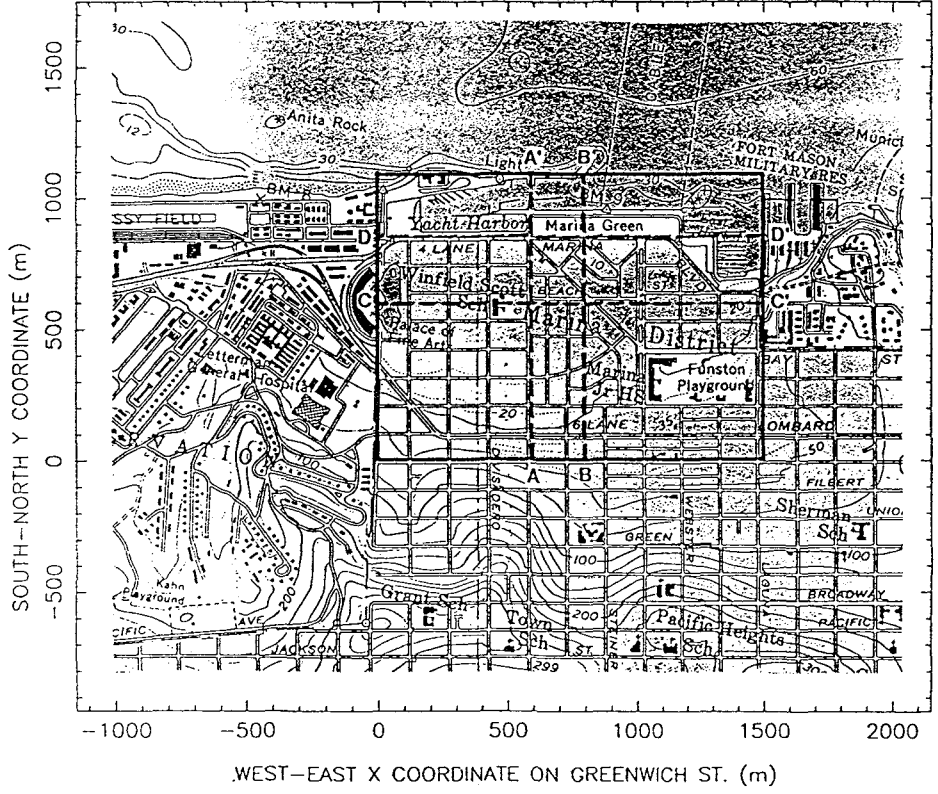

Figure 2. Map of the area under investigation and orientation of cross sections through 3D model.
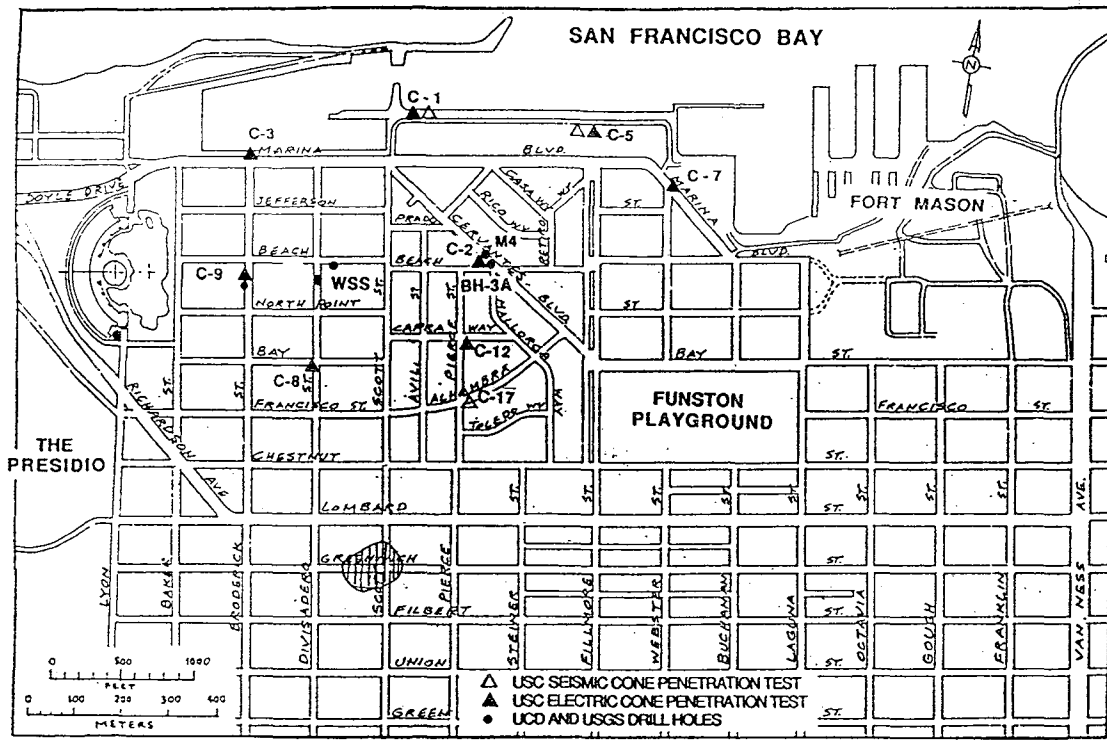
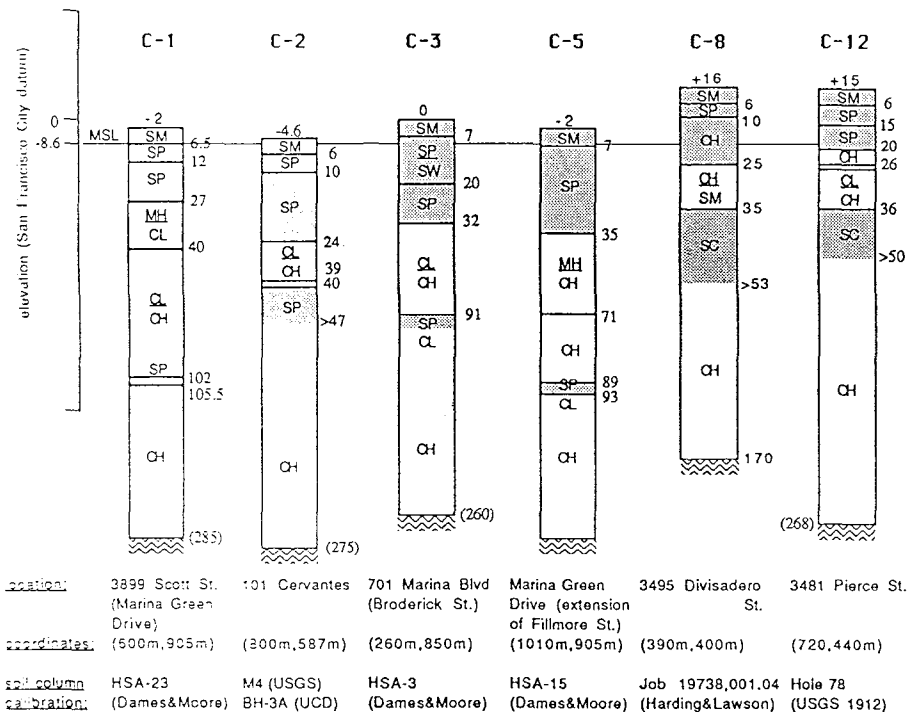Figure 3. Location of CPT during the USC site investigation.

Figure 4. Composite idealized soil columns interpreted from CPT and boreholes results.
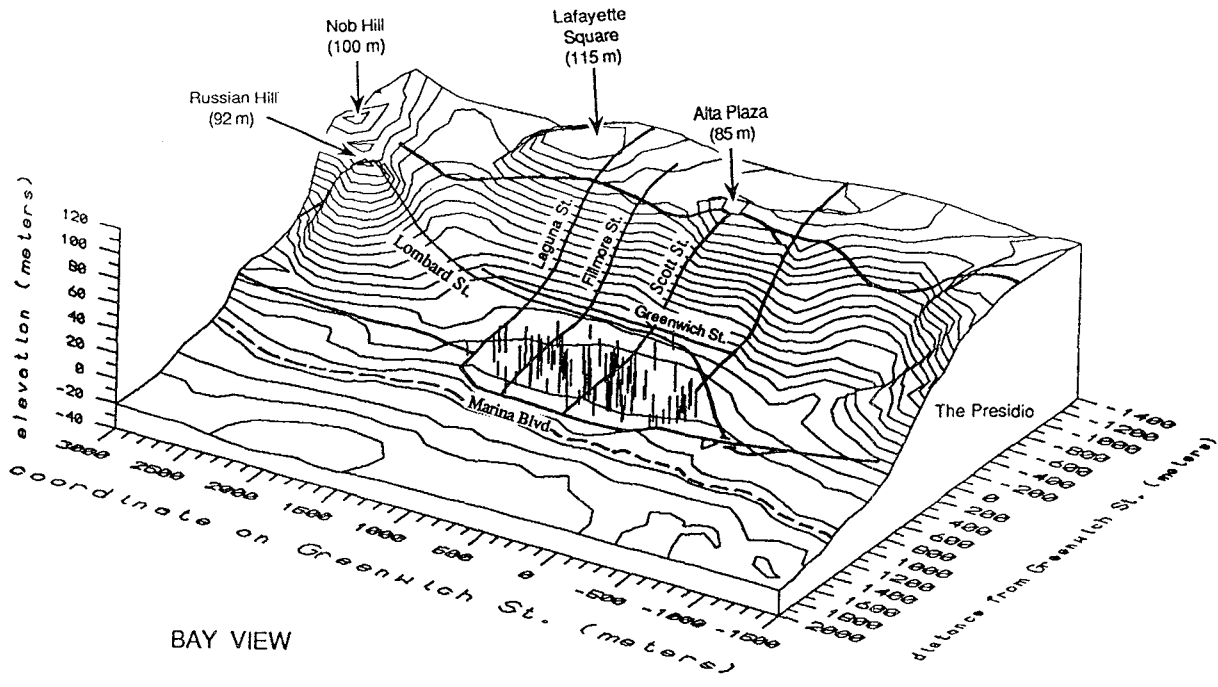
Figure 5. Isometric view of the ground surface of the Marina site.
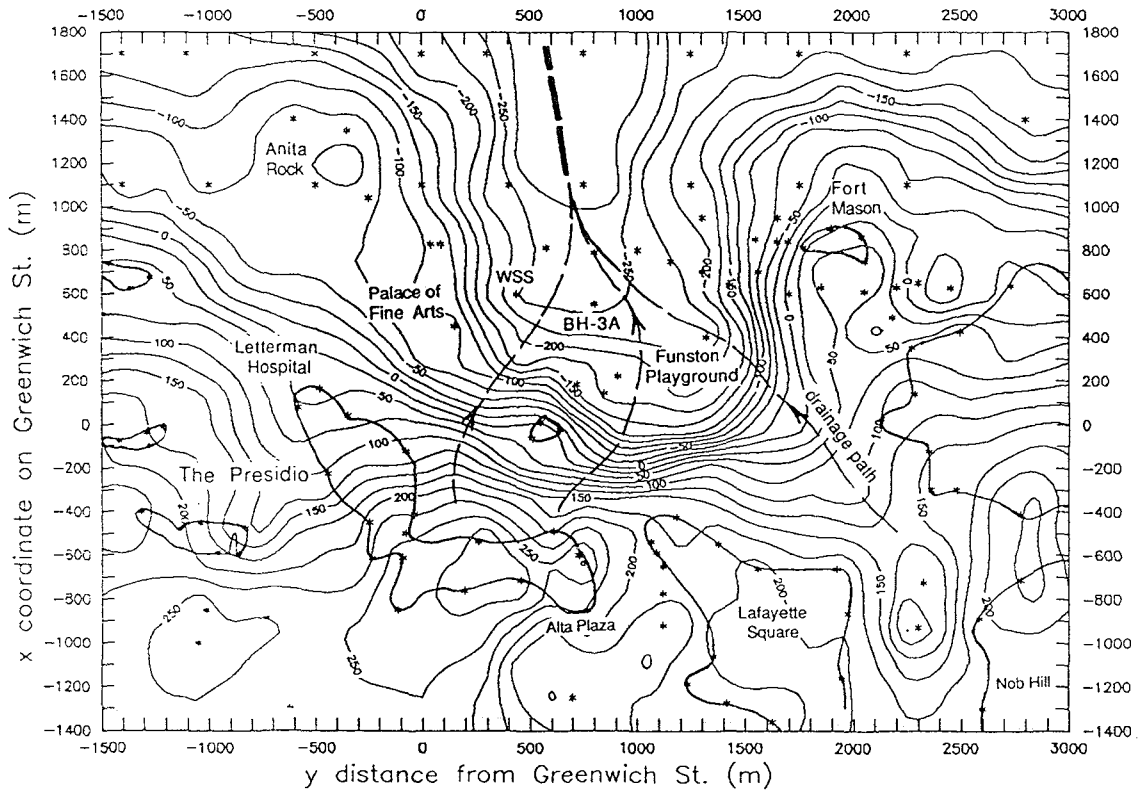
Figure 6. Estimated bedrock contours.

122

TOP SURFACE CONFIGURATION OF HARDPAN
IN THE MARINA DISTRICT

BEDROCK
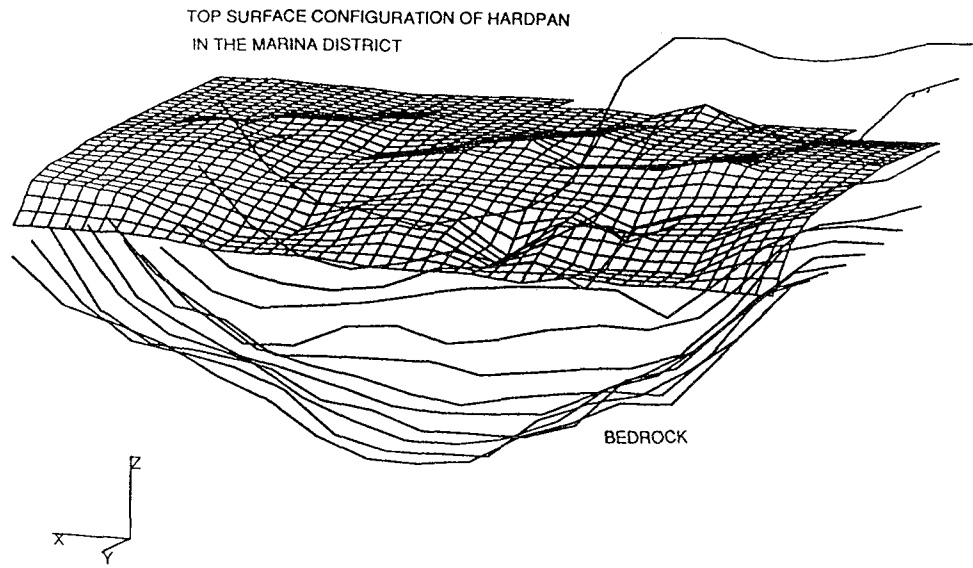
Figure 7. The hardpan surface.

GEOMETRIC SUBSOIL MODEL OF THE MARINA DISTRICT

LAGUNA ST.   GREENWICH ST.   THE PRESIDIO →

PALACE OF
FINE ARTS

BEDROCK   BAY VIEW

NORTH
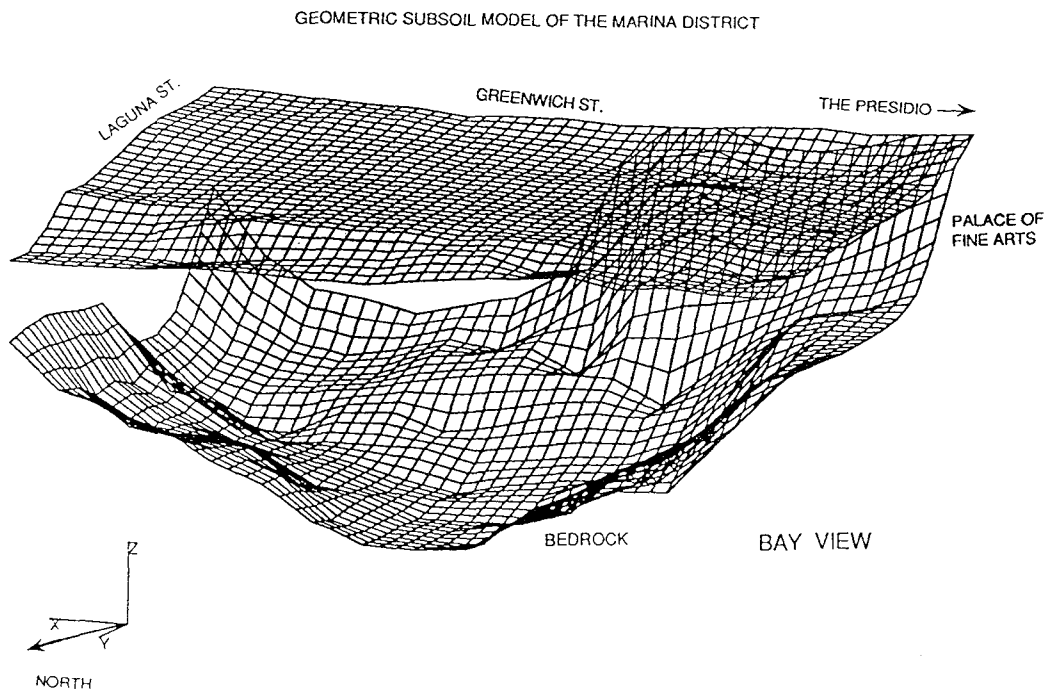
Figure 8. Isometric wire frame view of the 3D model.

Figure 9. Cross sections through the 3D model.

Figure 10. Discretized soil column near location M4.

Figure 11. Shear waves profile at the Marina site.
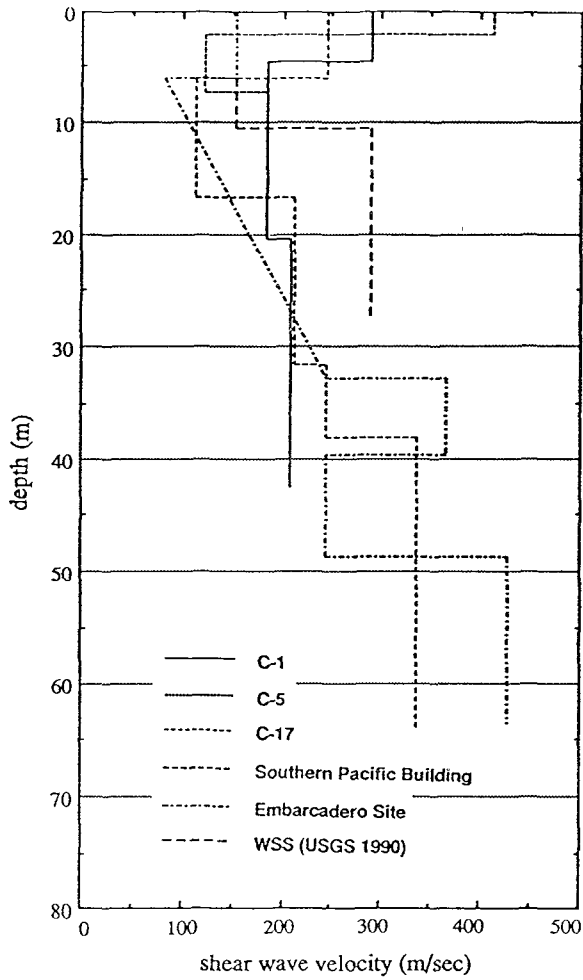
Figure 12. Variation of undrained shear strength versus depth.

$$S_u = 0.122z^2 - 3.49z + 46.5$$

125
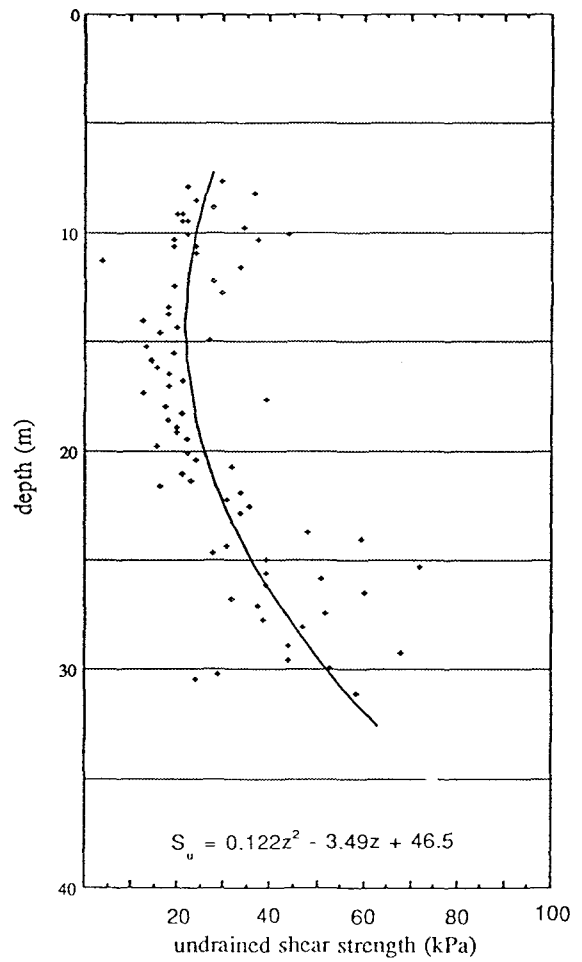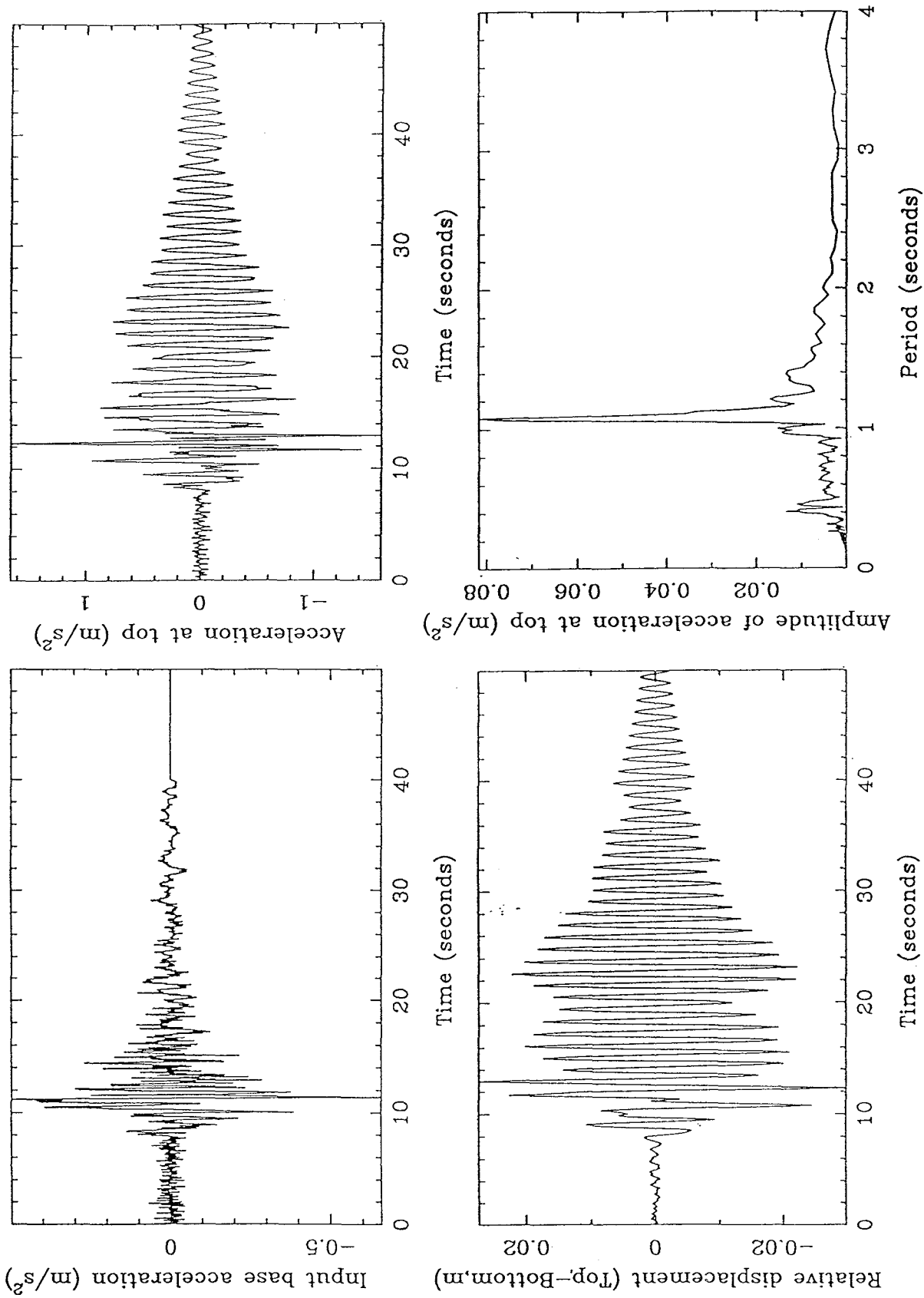
Figure 13. Input and output accelerations, relative displacement and Fourier spectrum of response for an elastic undrained soil column.

126
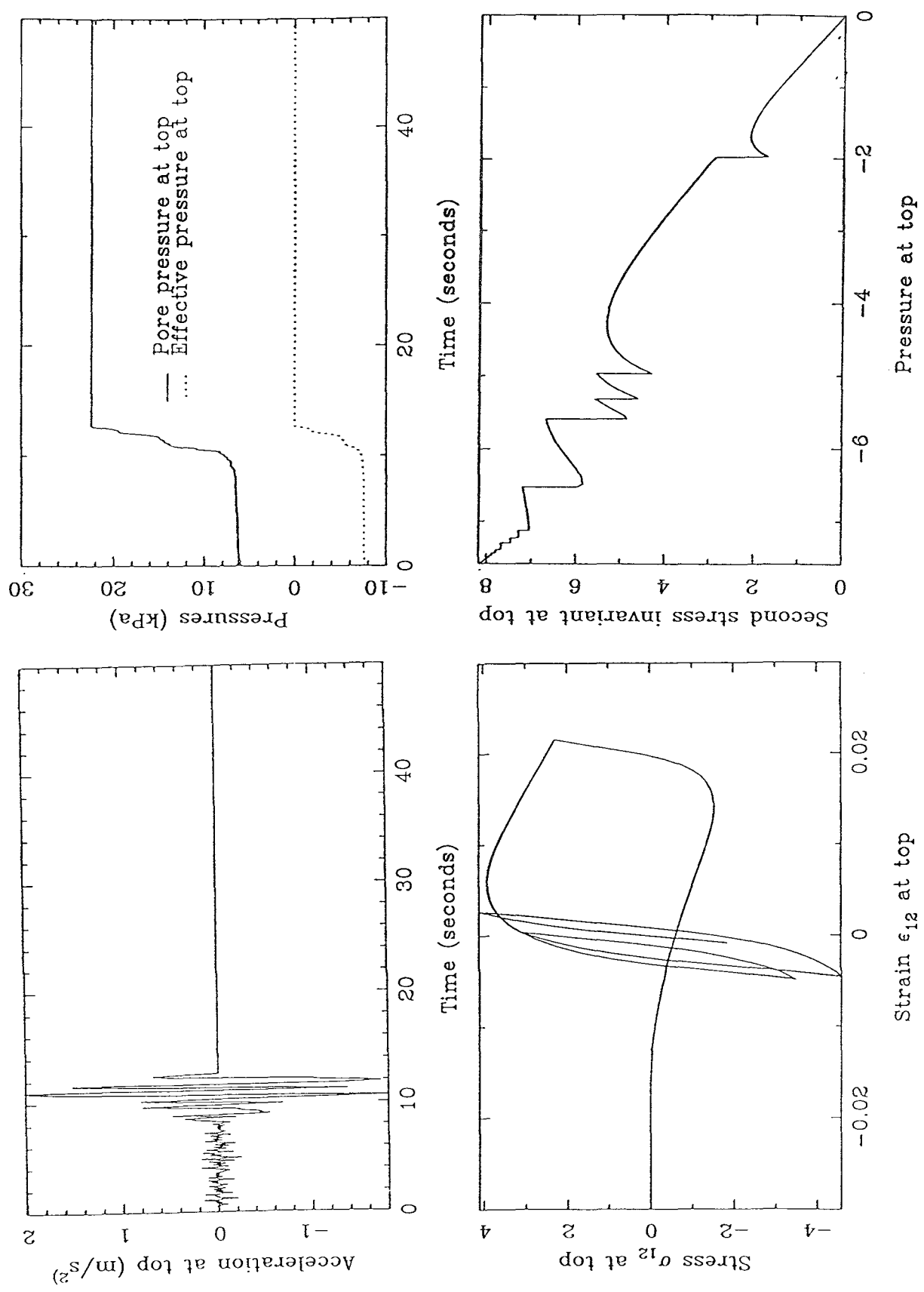
Figure 14. Acceleration, pore pressure, effective stress path and stress-strain response at the top of the BDP column (undrained).

127
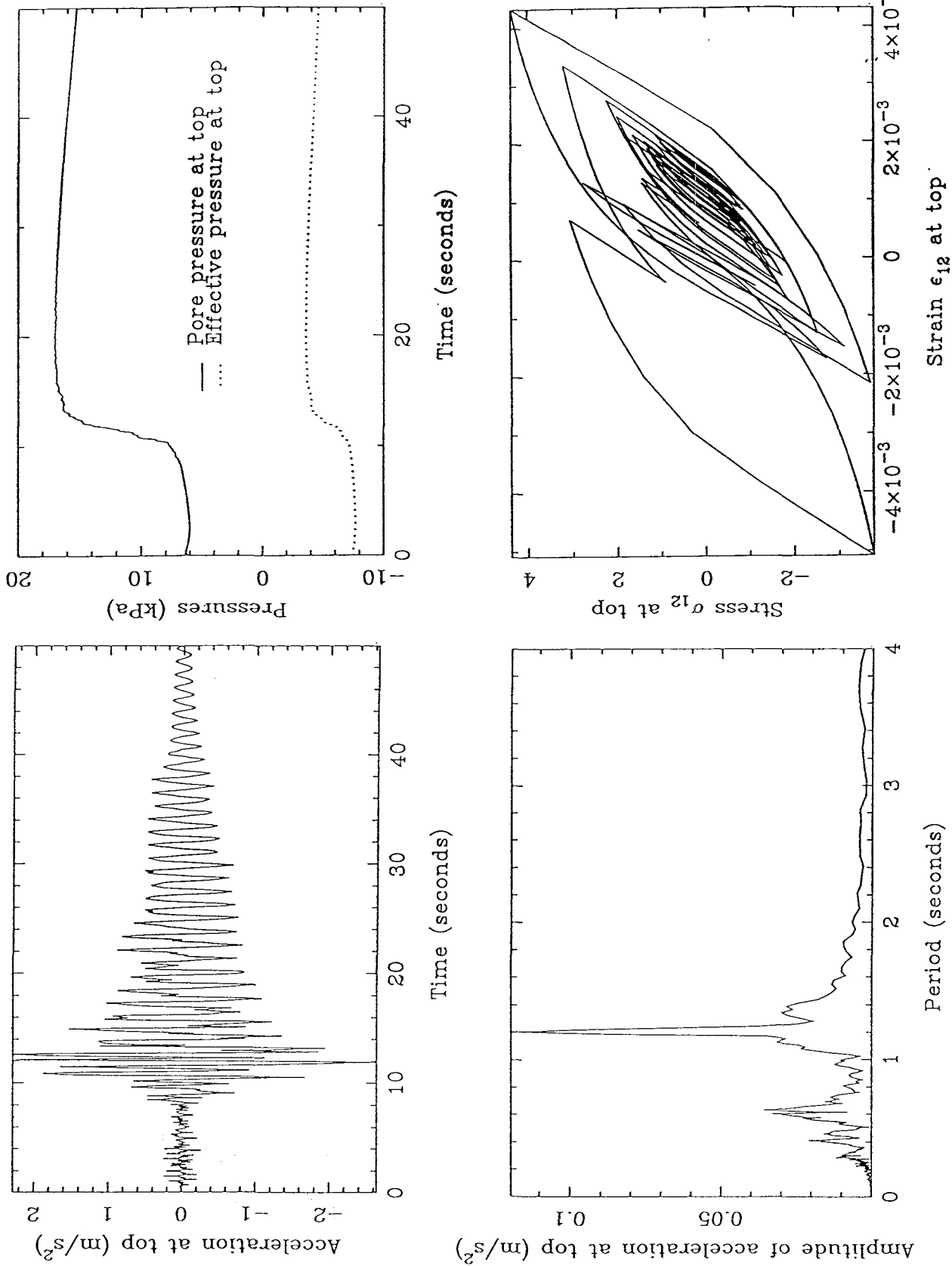
Figure 15. Acceleration, pore pressure, Fourier spectrum and stress-strain response at the top of the BDP column (with water diffusion).

128

LIFELINE PERFORMANCE AND GROUND DEFORMATION IN THE MARINA DURING 1989 LOMA PRIETA EARTHQUAKE

T. D. O'Rourke[1], T. E. Gowdy[2], H. E. Stewart[3], and J. W. Pease[4]

1, 2, 3, 4 - Professor, Undergraduate, Associate Professor, and Graduate Teaching Assistant, respectively; Cornell University, Ithaca, NY

ABSTRACT

A description is presented of subsurface conditions and settlements associated with soil liquefaction in the Marina district of San Francisco during the 1989 Loma Prieta earthquake. An evaluation is given of lifeline performance of the water supply, gas distribution, and wastewater conveyance systems in the Marina. The response of the Municipal Water Supply System (MWSS) is shown to be strongly related to the pattern of surface settlements caused by consolidation of sand and associated liquefaction. Measured settlements are compared with those estimated on the basis of simplified procedures, and good agreement is shown for portions of the Marina underlain by natural soils and land-tipped fills. The measured settlements of the hydraulic fill are nearly twice the amounts predicted. This discrepancy may be the result of the fines content and small grain size of the hydraulic fill. An adjustment of corrected SPT values is suggested to account for the influence of fines in the simplified procedure for estimating settlement. The very low in-situ density of the hydraulic fill makes it susceptible to liquefaction and flow failure. The possibility of flow failure underscores the importance of the seawall in providing lateral support and encourages measures to promote its seismic stability.

INTRODUCTION

The Marina is a microcosm of the types of site response and damage patterns which can be sustained in the most vulnerable settings of the San Francisco Bay Area. During the 1989 Loma Prieta earthquake, the deep alluvial basin and thick deposit of Recent Bay Mud underlying the Marina amplified accelerations and altered the natural period of seismic waves transmitted from bedrock to surface structures. Liquefaction of loose sandy fill led to settlement and lateral movement of the ground. Of special importance was the influence of ground deformations on buried utilities. Damage of the water distribution system in the Marina cut off critical water resources, which were needed during the outbreak of fire that followed the earthquake.

Several reports already have been written about the Marina, most notably studies by USGS (1990), Mitchell, et al. (1990), and O'Rourke, et al. (1990). Additional investigations are underway, including work reported in this conference (Bardet, et al., 1991). This paper is intended to supplement and extend current efforts into what is likely to emerge as one of the most comprehensively studied sites in any earthquake and a premier case history of the 1989 Loma Prieta earthquake.

The paper begins with a historical review of land filling and construction in the Marina. The damage to buried lifeline systems is evaluated, including water supply, natural gas, and wastewater conveyance networks. The relationship between utility damage and ground deformation associated with liquefaction is examined. Finally, the settlements observed in the Marina in locations underlain by natural soils and land-tipped and hydraulic fills are analyzed and compared with the settlements predicted for these deposits by existing simplified procedures.

HISTORIC DEVELOPMENT OF THE MARINA

Like several other sites in the Bay Area, the Marina has been developed by placing sandy fills on soft clays and silts. Figure 1 shows a plan view of the Marina on which is superimposed the 1857 shoreline, as mapped by the U.S. Coast Survey (1857). Along its western boundary, there was a prominent sand bar known as Strawberry Island, with adjacent salt water marshes. Sand dunes, 6 to 12 m high, were located south of the shoreline and marshy ground.

To aid in the construction of industrial facilities, a seawall was built in the 1890s (Olmsted, et al., 1977). The seawall was constructed by dumping rock, which had been hauled to the site on barges, and backfilling behind the rock embankment with sand taken primarily from the dunes. Similar construction was performed by the San Francisco Gas and Light Company to establish an earthen mole. Figure 2 shows the seawall and earthen mole (Sanborn and Ferris, 1905) which represents the waterfront and extent of filling at the time of the 1906 earthquake. This configuration of seawall, embankment, and artificial fill remained essentially unchanged until 1912, when construction on site was started for the 1915 Panama Pacific International Exposition.

Although the Marina was not extensively developed in 1906, there are nevertheless several historic accounts of damage in this area (Jones, 1906; Gilbert, et al., 1907; Lawson, et al., 1908), some of which are summarized in Figure 2. Lawson, et al. (1908), for example, drew attention to evidence of severe ground shaking in the hatchured zone of Figure 2, extending from North Point St. between Lyons and Broderick to the shore. In this area, timber structures were thrown out of vertical, reminiscent of the shear deformation sustained by four-story timber buildings during the 1989 earthquake. Moreover, the Baker St. sewer was damaged, which implies that permanent ground deformation occurred in this area.

The most extensive observations of damage are associated with the coal gasification plants, which were located in the southwestern part of the Marina in 1906. Gilbert, et al. (1907) reported that not a building at the San Francisco Gas and Electric (renamed from the original San Francisco Gas and Light Co.) plant escaped damage, and that the ground settled very considerably at this location. Jones (1906) reported from 600 to 900 mm of settlement adjacent to the principal gas holder at the North Beach Station. The settlement ruptured the 600-mm diameter outlet connections of the holder, causing all the stored gas to escape.

In 1912, the lagoon enclosed by the seawall was filled with dredged soil pumped from depths of 10 to 15 m at distances of 180 to 600 m offshore. Relatively strict control of the fill material was exercised. The opening along the northern line of the seawall was used to sluice out fine grained and organic materials during hydraulic filling. It was estimated that 70% of the fill placed in this way was sand (Olmsted, et al, 1977).

In summary, the placement of fill and development in the Marina may be simplified as having occurred in two prominent stages. The first stage was associated with the placement of land-tipped and barge-tipped fills adjacent to the original shoreline and the old Strawberry Island until about 1900. The second major stage of filling occurred in 1912, when sandy sediments were dredged and pumped into the lagoon bounded by the old seawall. On the basis of historic development, it is possible to discriminate three general types of soils in the Marina: 1) natural soils associated with the original beach and sand bar deposits, 2) land and barge-tipped fills, and 3) hydraulic fill. Areas underlain by each of these soil types behaved differently during the 1989 earthquake, and are analyzed in a later part of the paper.

WATER SUPPLY LIFELINE DAMAGE

Water to the Marina is supplied by two systems of pipelines: The Municipal Water Supply System (MWSS) and the Auxiliary Water Supply System (AWSS). The MWSS supplies potable water for domestic and commercial uses, as well as for fire fighting via hydrant and sprinkler systems. The AWSS supplies water exclusively for fire fighting purposes.

Within the Marina, in an area bounded by the 1857 shoreline on the south (U.S. Coast Survey, 1857) and the current shoreline on the north, there are approximately 11,300 m of pipelines belonging to the MWSS and 2290 m of pipelines belonging to the AWSS. The MWSS water mains are 100, 150, 200, and 300 mm in
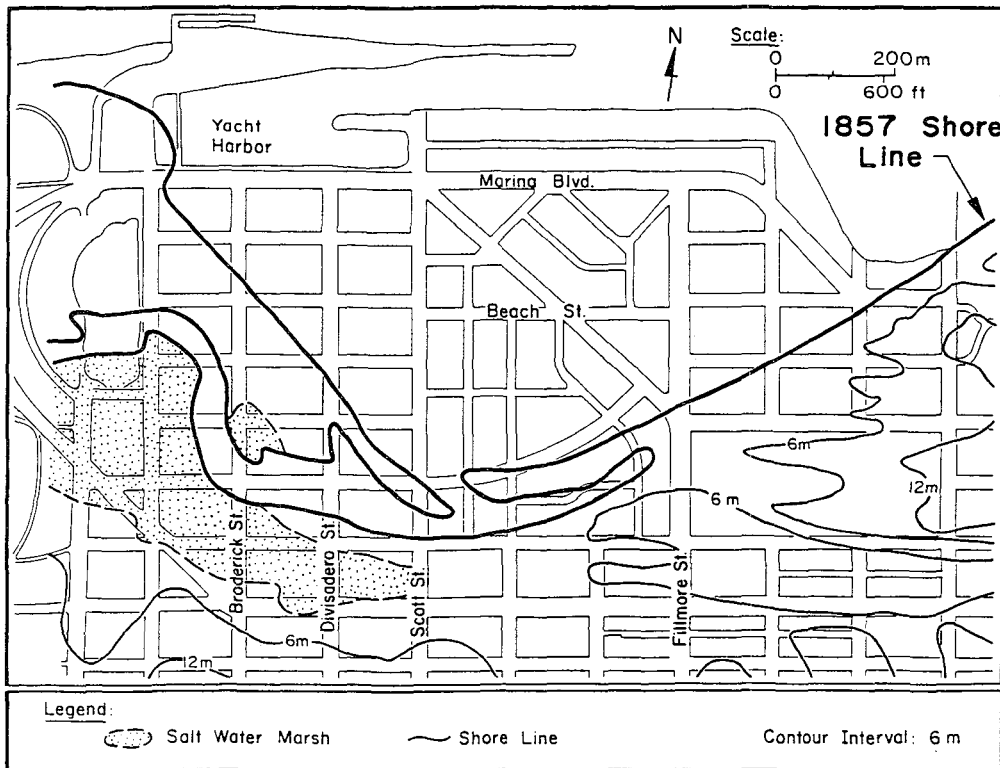
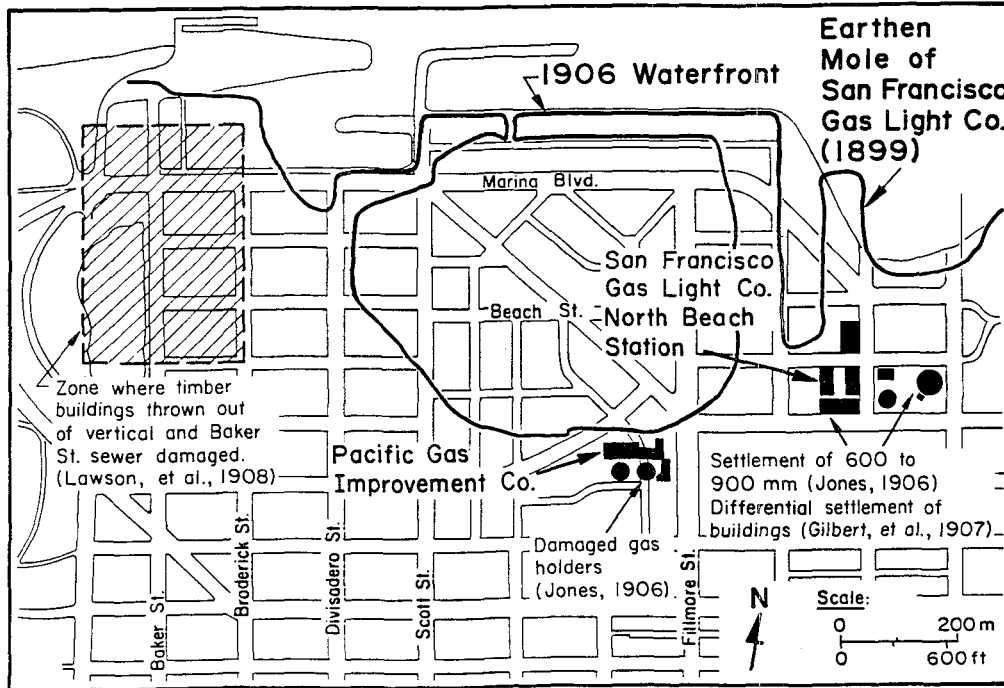FIGURE 1. 1957 Shoreline Relative to Current Marina Development

FIGURE 2. 1906 Waterfront and Earthquake Damage Relative to Current Marina Development

diameter, whereas the AWSS water mains are predominantly 250 and 300 mm in diameter. The pipelines in both systems are composed of pit cast iron and most were installed in the Marina between late 1924 and 1925. The MWSS pipelines were built with cement caulked, bell-and-spigot couplings, whereas the AWSS pipelines were built with special couplings, as described in the discussion of pipeline damage which follows. All pipelines were buried at nominal depths to top of pipe between 0.9 and 1.2 m.

Figure 3 shows a plan view of the MWSS pipelines and repairs relative to the current street system, 1906 waterfront, and 1857 shoreline. There were about 123 repairs in the Marina, more than three times the number of repairs in the entire MWSS outside the Marina. Repairs were made at locations of sheared or disengaged service connections with mains, flexural round cracks in mains, and longitudinally split sections of main. In some cases, damage was concentrated at or near gate valves. These devices tend to anchor the pipelines and therefore may contribute to locally pronounced deformation and stresses. The figure shows the locations of repairs to: a) services, b) mains, and c) sections of line at or near gate valves.

As reported elsewhere (O'Rourke and Roth, 1990), the rate of main repair, expressed as repairs per km of pipeline, was inversely proportional to diameter. This observation, in combination with the fact that over 80% of main repairs were for round cracks, implies that pipeline bending in response to permanent ground deformation was the principal cause of rupture.

Figure 4 shows a plan view of the MWSS water mains which eventually were replaced. These mains were the most heavily damaged in areas of largest surface settlement, and therefore most likely to be subject to continuing rupture and maintenance difficulties in the future. Approximately 2.7 km of main were replaced, primarily in or immediately adjacent to areas underlain by hydraulic fill.

Figure 5 shows the locations of pipeline repairs to the AWSS and high pressure gas distribution network in the Marina. It should be noted that the term "high pressure" is intended to distinguish pipelines conveying gas at approximately 200 kPa from low pressure distribution lines at approximately 2 kPa.

Even though substantial damage was sustained by the MWSS in the Marina, there was only one instance of AWSS repair in this area. This occurred at a leaking joint at Scott and Beach Sts. Pipelines of the AWSS are equipped with sleeved joints, which are restrained against pullout by longitudinal bolts. Cast iron pipelines of 250 and 300-mm diameters are used in the Marina with joint-to-joint lengths of 3.7 m. The relatively large diameter-to-length ratio, in conjunction with joints which are able to rotate and are axially restrained, allows the pipelines to accommodate differential ground movement.

GAS DISTRIBUTION LIFELINE DAMAGE

Only one location of damage was reported for the high pressure gas distribution lines at a miter joint near the boundary of hydraulic fill and 1857 shoreline.
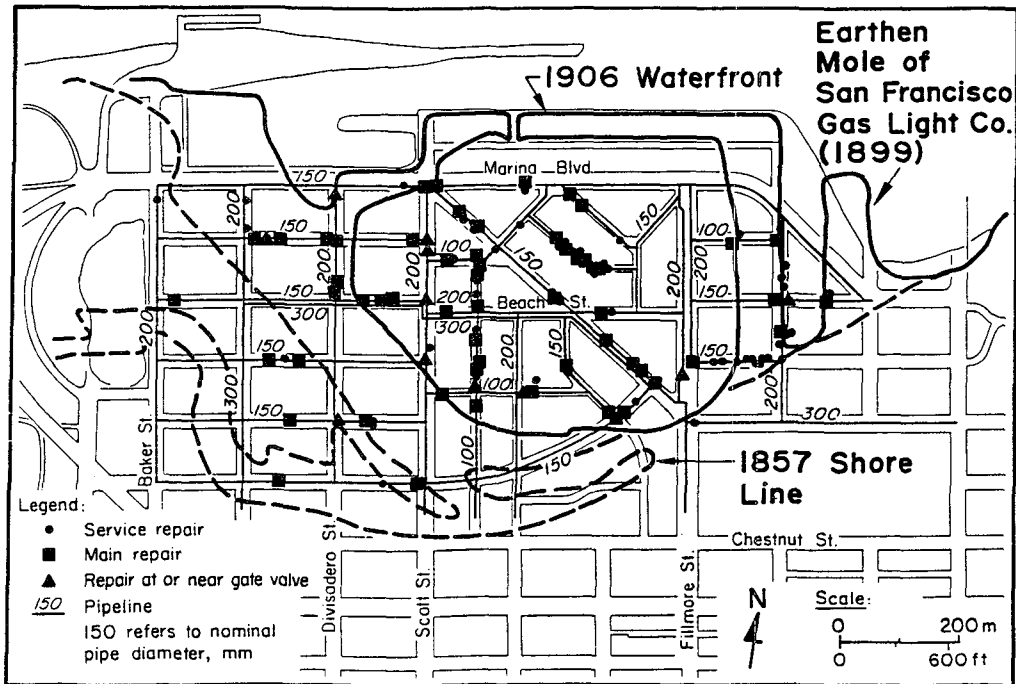
133

FIGURE 3. Plan View of Repairs to the MWSS in the Marina
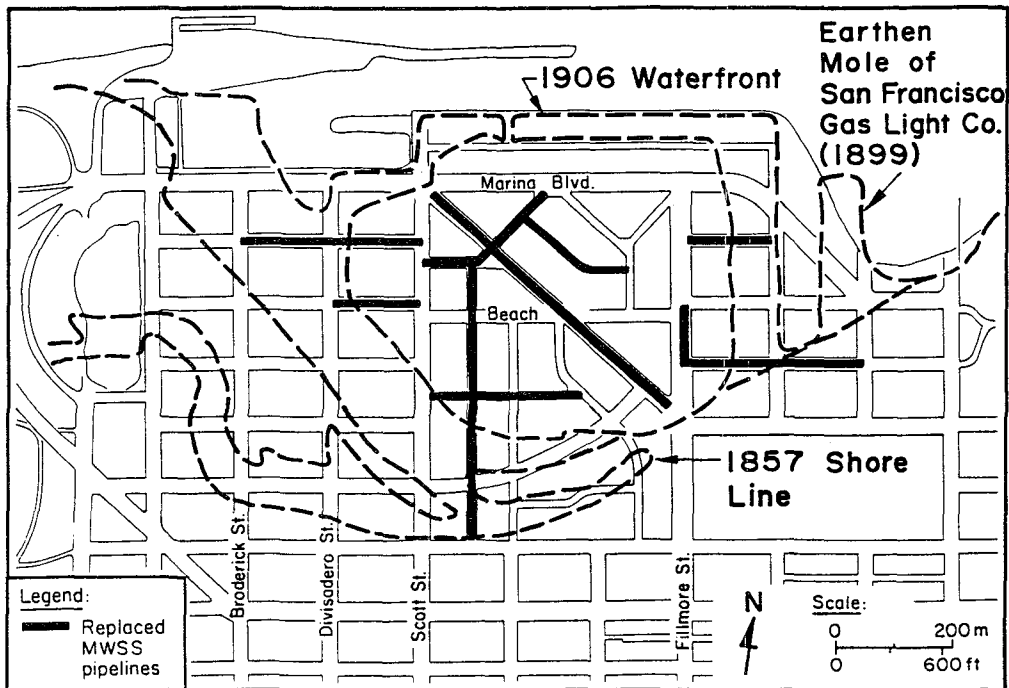

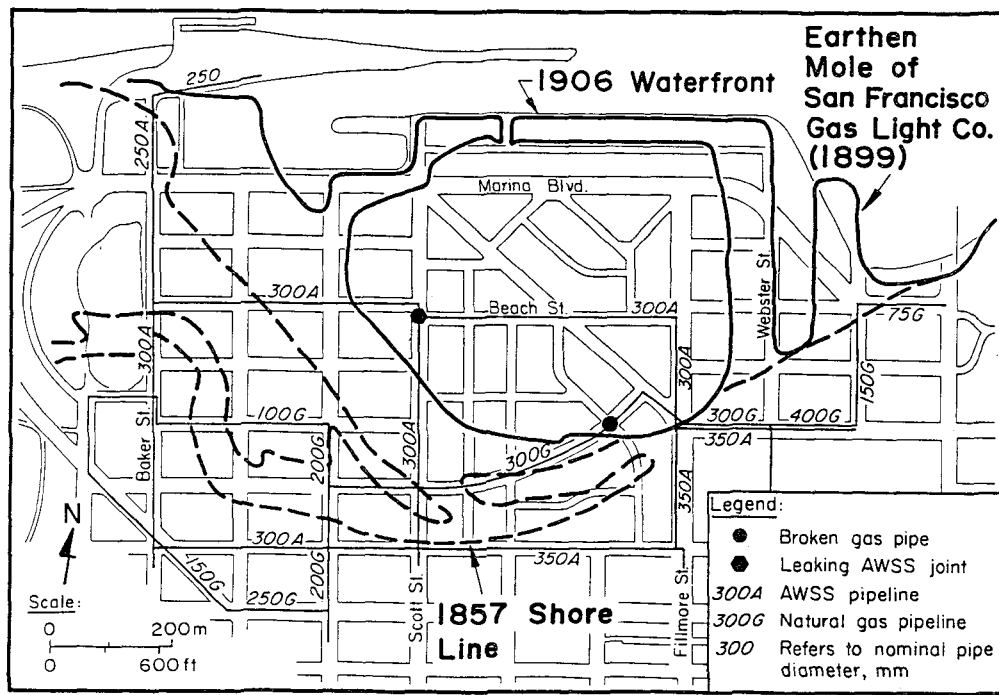**FIGURE 4.** Plan View of Replaced MWSS Mains in the Marina

FIGURE 5. Plan View of Repairs to AWSS and High Pressure Gas Distribution Pipelines in Marina
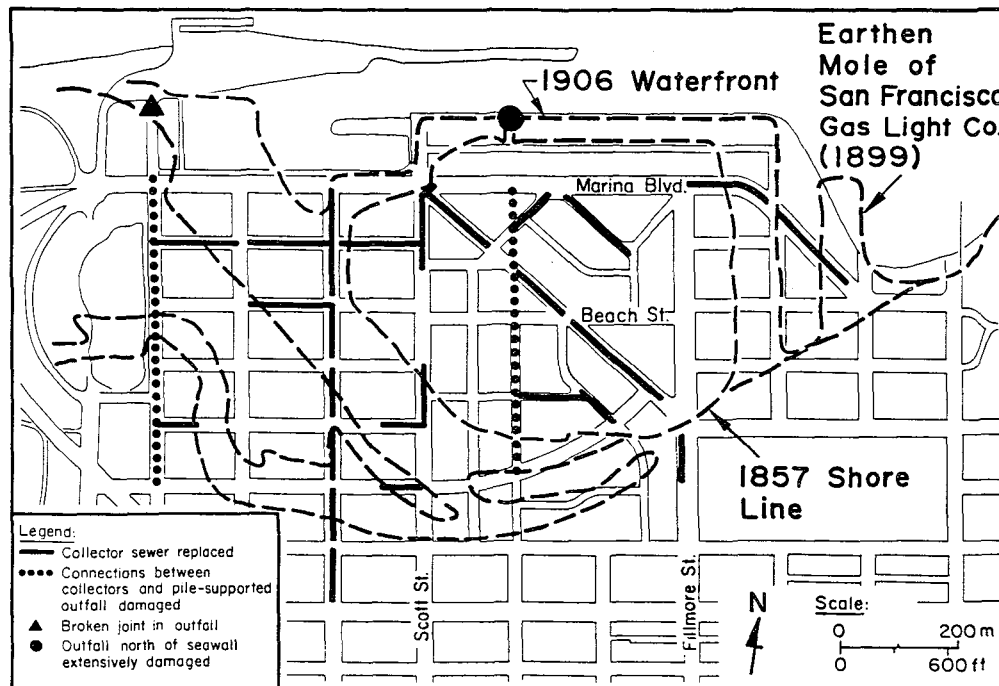

FIGURE 6. Plan View of Damaged and Replaced Wastewater Conveyance System in Marina

135

The high pressure mains were constructed mostly of Grade B steel with electric arc girth welds.

In contrast to the high pressure system, there was substantial damage of the low pressure gas distribution mains. Because of the extensive damage, the low pressure system was isolated in the Marina by closing shutdown valves. Approximately 13.6 km of steel and cast iron mains, ranging from 100 to 300 mm in diameter, were replaced within the area bounded by Laguna, Lombard, Lyon St., and the Bay (Phillips and Virostek, 1990). A little over half this number were replaced with medium density polyethylene (MDPE) piping inserted within existing steel and cast iron pipes. The remainder was replaced by direct burial of MDPE piping. The nominal diameters of replacement pipes were 50 to 150 mm, with about 90% of the piping having a 50 mm diameter.

WASTEWATER CONVEYANCE LIFELINE DAMAGE

In San Francisco, wastewater is collected, transported, and treated under the Clean Water Program. The wastewater system consists of 1159 km of collector sewers, ranging in diameter from 200 mm to 600 mm, 241 km of transport sewers, ranging in diameter from 900 mm to 2.3 m; and a series of storage culverts to hold water during heavy runoff for later transport and treatment. Approximately 77% of the collection and transport sewers are over 50 years old.

One of the most serious instances of earthquake-related damage occurred in a 1.7-m diameter force main near the corner of 7th and Channel St. The force main was a concrete-coated steel cylinder pipe, which ruptured at a point of local constraint where it crossed a pile-supported concrete box sewer. Because the main carries one-third of the city sanitary load, a temporary repair was effected. Full repair was implemented over half a year after the earthquake, when the total sanitary load was low enough to divert flows elsewhere. The ruptured section of pipe was replaced with a 1.5-m diameter, mortar-coated pipe with bell-and-spigot joints.

The heaviest concentration of damage to the wastewater conveyance system occurred in the Marina, as is illustrated in Figure 6. Three types of sewage conduit are located in the Marina: 1) collector sewers, ranging in diameter from 200 to 600 mm, 2) outfall sewers, ranging in diameter from 1.5 to 2.3 m, and 3) a 3 to 5-m-wide reinforced concrete box culvert along Marina Blvd.

As shown in Figure 6, damage at the outfall sewers occurred primarily because of broken connections between the pile-supported outfalls and collector sewers, which settled differentially relative to the outfalls. The outfall sewer along Pierce St. at the center of the figure was a circular reinforced concrete structure, ranging in diameter from 1.8 to 2.3 m, supported on timber piles, with an invert depth about 3 m below ground surface. It was heavily damaged north of the seawall on Marina Green. The 1.5-m diameter Baker St. outfall, which was of similar construction, was cracked and fractured at a turning point (location of triangle in Figure 6), where a joint connects it to an overflow weir. Minor cracking was observed along the invert of the Marina Blvd. box culvert.

Within the area bounded by Baker St., Marina Blvd., Chestnut St., and Buchanan St., there are approximately 9.4 km of collector sewers, of which 3.8 km were replaced as a result of the earthquake. Locations of replaced collectors are shown in the figure. The damaged collectors were composed of vitrified clay pipe (VCP) nominally 1.5 to 1.8 m long, with mortared bell-and-spigot joints. Damage was primarily in the form of cracked and crushed joints.

The relatively small nominal length of the collector pipes, in combination with the brittle nature of vitrified clay, makes them especially vulnerable to damage at joints. Crushing and cracking of the joints implies that damage was caused in part by longitudinal deformation, and therefore related partially to shaking and traveling ground wave effects. In contrast to the MWSS damage in Figures 3 and 4, which was related primarily to permanent differential ground movement, the collector damage in Figure 6 seems to correlate both with locations of strong shaking and differential settlement from soil liquefaction. Approximately 50% of the replaced collectors were outside the zone of hydraulic fill. Damage was concentrated on Divisadero, Jefferson, and Beach Sts., all west of Scott St., where the heaviest concentration of shaking damage to surface structures was observed.

GROUND DEFORMATION AND PIPELINE REPAIR

Settlements of sand caused by the Loma Prieta earthquake were evaluated on the basis of survey data collected in 1961, 1974, and 1989 and published by Bennett (1990), as well as a detailed evaluation of subsurface conditions in the Marina by O'Rourke, et al. (1991). It was assumed that the settlement from 1961 to 1974 was caused principally by secondary compression of Recent Bay Mud. From the survey data base, the incremental secondary compression, ΔS, was regressed relative to the thickness of Recent Bay Mud, H, to obtain the best linear fit of the data with slope $\Delta S/H = 0.0011$. This slope is related to soil properties in the form:

$$\frac{\Delta S}{H} = C_{\alpha\epsilon} \, \log(t_2/t_1) \tag{1}$$

in which $C_{\alpha\epsilon}$ is the coefficient of secondary compression defined as the ratio of the change in one-dimensional vertical strain to the change in log time after the end of primary consolidation, and t_2 and t_1 are times since the placement of hydraulic fill in 1912 to 1961 and 1974, respectively.

A value of $C_{\alpha\epsilon} = 0.011$ was calculated with Eqn. 1, which compares very favorably with $C_{\alpha\epsilon}$ determined for Recent Bay Mud on the basis of one-dimensional consolidation tests (Dames and Moore, 1989). On the basis of 42 test results with stress increments to levels of 1.2 to 2.5 times the preconsolidation pressure, the mean value for $C_{\alpha\epsilon}$ was 0.011, with a standard deviation of 0.004.

The value of $C_{\alpha\epsilon} = 0.011$ was used to calculate the incremental secondary compression for each survey point between 1974 and 1989. These values were subtracted from the difference in actual survey measurements to yield "corrected" settlements that would represent best the amount of vertical movement caused by

liquefaction-associated consolidation of the fills underlying the Marina. Settlement contours were developed from these corrected measurements with the computer program "Surfer" (Golden Software, 1985), using a procedure referred to as kriging, in which contours are developed with minimal estimation variance from a statistical evaluation of the input data (Ripley, 1981).

The resulting settlement contours are shown in Figure 7. The maximum settlements occurred in the hydraulic fill, with decreasing amounts of vertical deformation in the land-tipped fills and areas underlain by natural beach and sand bar deposits.

To represent the distribution of MWSS damage, the Marina was divided into a grid of approximately 40 cells, and the number of repairs per length of pipeline in each cell was counted. Each repair rate then was normalized with respect to a reference length of 300 m to provide a consistent basis for evaluation. Contours of equal repairs per 300 m of pipeline were drawn and superimposed on the street system and previous shorelines, as illustrated in Figure 8. The contours of pipeline repair rates are related closely to the settlement contours, hydraulic fill, and 1857 shoreline. High concentrations of pipeline repair fall within the area of hydraulic fill, and the heaviest repair concentration occurs at the junction of the hydraulic fill, seawall, and 1857 shoreline.

SETTLEMENT EVALUATION

Knowledge of the historic development of the Marina permits one to map areas underlain by natural soils, including beach and sand bar deposits; land and barge-tipped fills; and hydraulic fill. Accordingly, the Marina provides a good opportunity to evaluate methods for estimating earthquake-induced settlements of saturated sands by a comparison of settlements estimated through current simplified methods with those measured in the field. As described by O'Rourke, et al. (1991), a substantial number of soil borings have been performed in the Marina for engineering projects that preceded the Loma Prieta earthquake, in addition to borings performed to clarify foundation conditions beneath individual buildings during reconstruction and repair after the earthquake.

On the basis of Standard Penetration Test (SPT) data acquired from approximately 120 borings distributed throughout the Marina, Figure 9 has been developed to show the range of cyclic stress ratios and corrected SPT values for the various Marina soil types relative to the plot for simplified estimation of earthquake-induced settlement in saturated sand proposed by Tokimatsu and Seed (1987). The SPT values have been corrected for effective confining stress and energy adjustments in accordance with the recommendations of Seed, et al. (1983). The cyclic stress ratios have been developed assuming a peak ground acceleration of 0.2 g, and correcting for a M = 7.1 earthquake, according to the recommendations of Tokimatsu and Seed (1987). Also summarized in the figure are the mean corrected SPT values and coefficients of variation for the different Marina soils. The sample sizes associated with natural, land-tipped, and hydraulic fill soils are 73, 16, and 64, respectively.

138

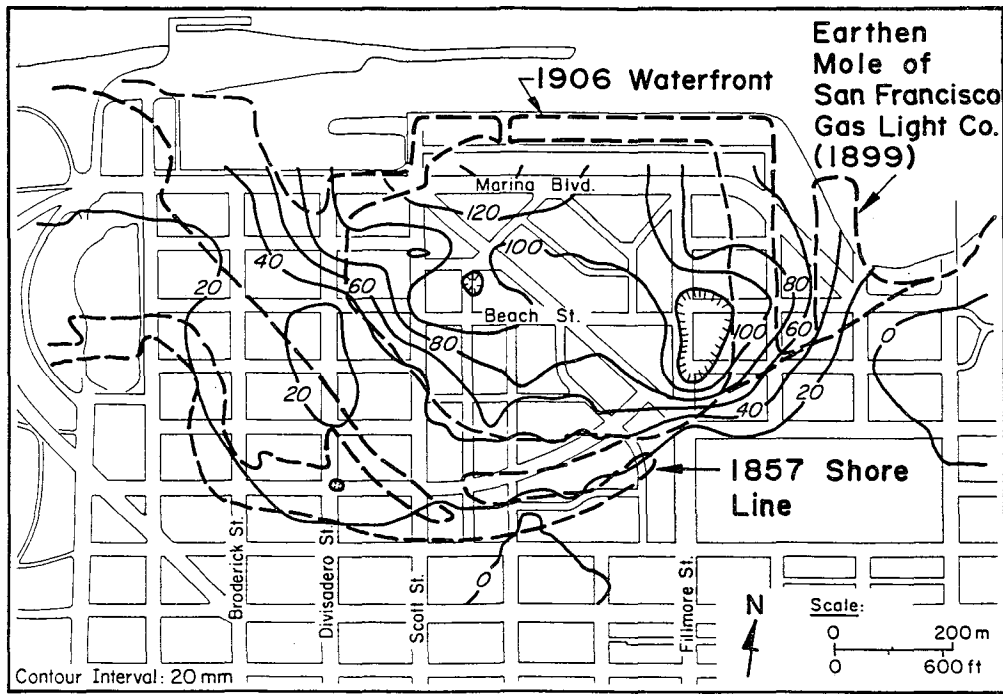FIGURE 7. Settlement Contours Associated with Consolidation of Fills Caused by the 1989 Loma Prieta Earthquake
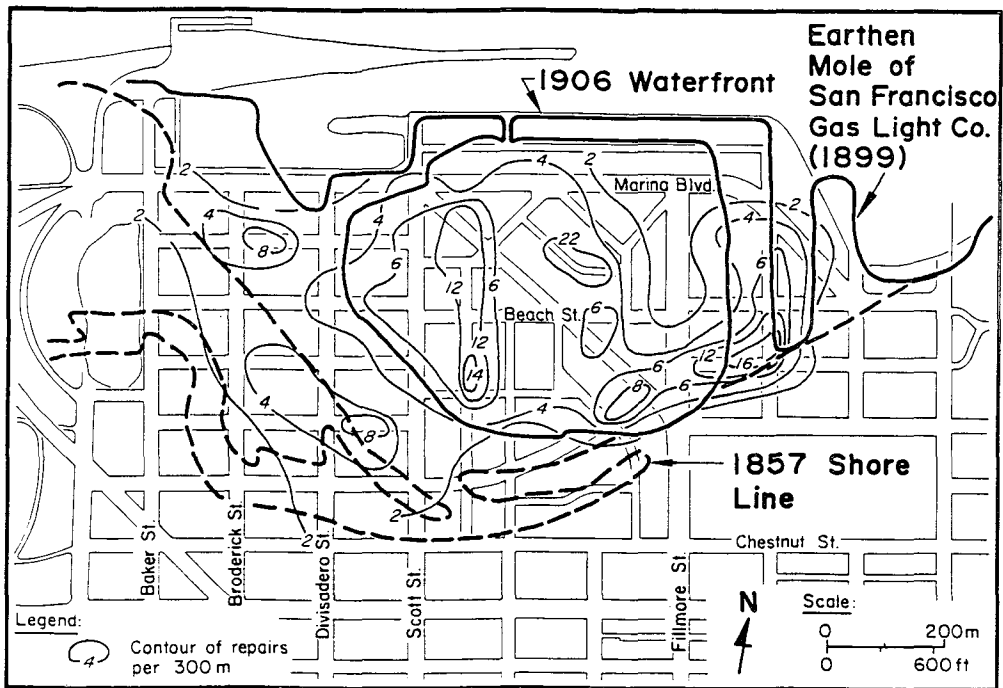

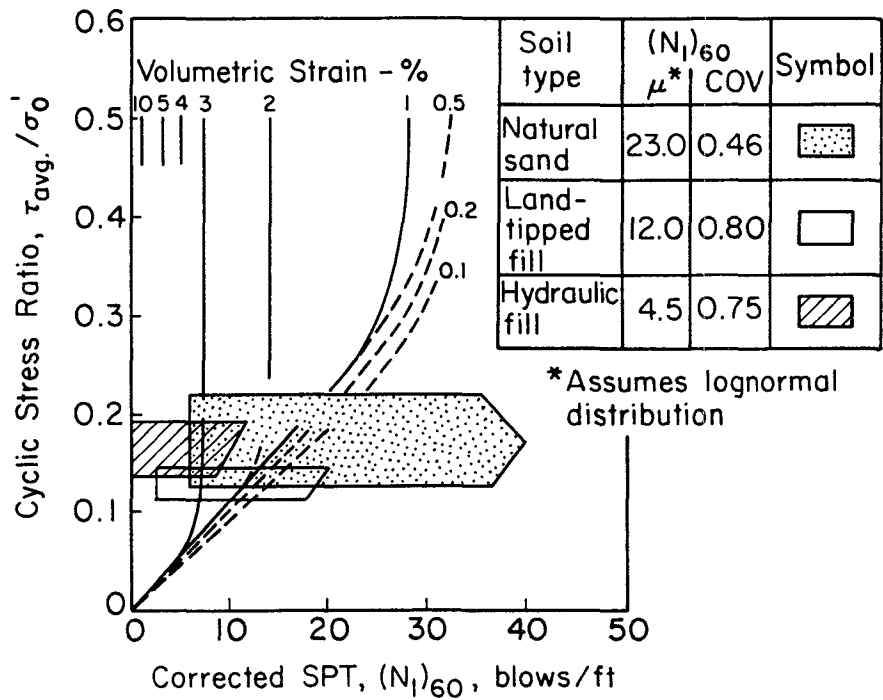FIGURE 8. Contours of MWSS Repairs/300 m as a Result of the 1989 Loma Prieta Earthquake

FIGURE 9.   Marina Soils and Simplified Procedure for Estimating Volumetric
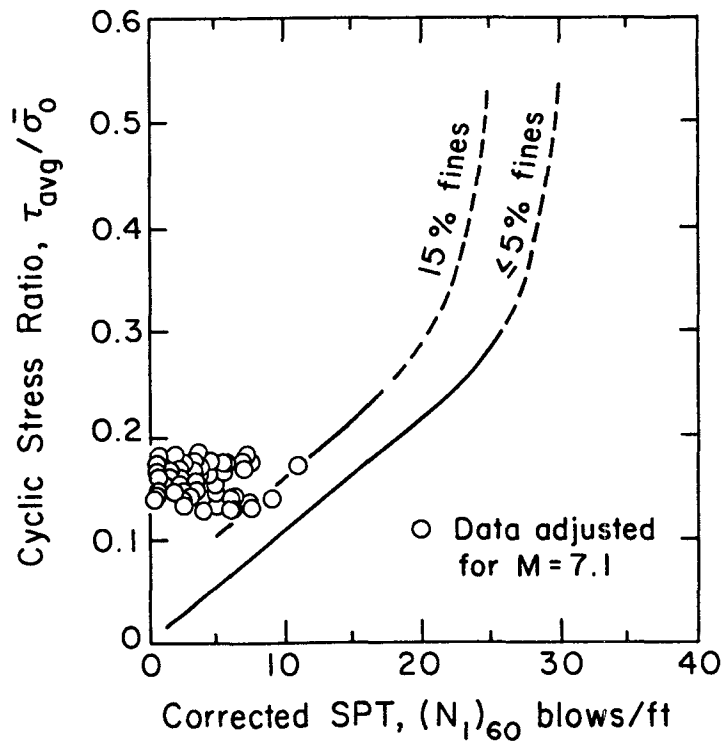Strains After Liquefaction (after Tokimatsu and Seed, 1987)

FIGURE 10.   Hydraulic Fill Data on Cyclic Stress Ratio Plot

TABLE 1. Comparison of Estimated and Measured Settlements in Marina

Soil Type	Estimated[1] Settlement, mm	Measured Settlement, mm
Natural Soils	30 - 40	20 - 30
Land-Tipped Fill	50 - 60	40 - 60
Hydraulic Fill	170 - 240	80 - 120

1 - On basis of simplified procedures after Tokimatsu
    and Seed (1987)

Table 1 summarizes the settlements measured in the field and those estimated by the simplified procedures of Tokimatsu and Seed (1987). On average, the depth to water table in the Marina is approximately 2.4 m. Very little settlement, typically less than 1 to 2 mm, was estimated for the dry granular soils above the water table, so that the majority of estimated settlement is derived from loose saturated sands below the water table. The land overlying natural soils of the old Strawberry Island apparently had been filled and regraded, because relatively loose clean sands were found to depths of approximately 4.5 m at several locations.

In general, there is good agreement between the estimated and measured settlements for the natural soils and land-tipped fill. Estimated settlements of the hydraulic fill are almost twice as much as those observed in the field. A procedure for estimating settlement recently proposed by Ishihara (1990) also was used to predict settlement of the hydraulic fill. It too resulted in estimated movements exceeding twice those measured.

To investigate further the characteristics of the hydraulic fill, data were analyzed and summarized in Figures 10 through 12. Figure 10 shows the plot of cyclic stress ratio adjusted for M = 7.1. Figure 11 presents a histogram showing the frequency of corrected SPT values. The skewed shape of the histogram indicates that a normal distribution would not be appropriate, and the mean, μ, and coefficient of variation, COV, were calculated assuming a lognormal distribution.

The corrected SPT values for the majority of measurements in the sample are less than 5. This implies that the hydraulic fill would have a very low undrained residual shear strength, perhaps lower than 5 kPa, based on the empirical relationship suggested by Seed (1987). Such low strength makes the hydraulic fill vulnerable to flow failure. Accordingly, the stability of the seawall in the Marina is especially critical because it provides lateral confinement of soil, which might otherwise be subject to retrogressive sliding in the event of a major earthquake.
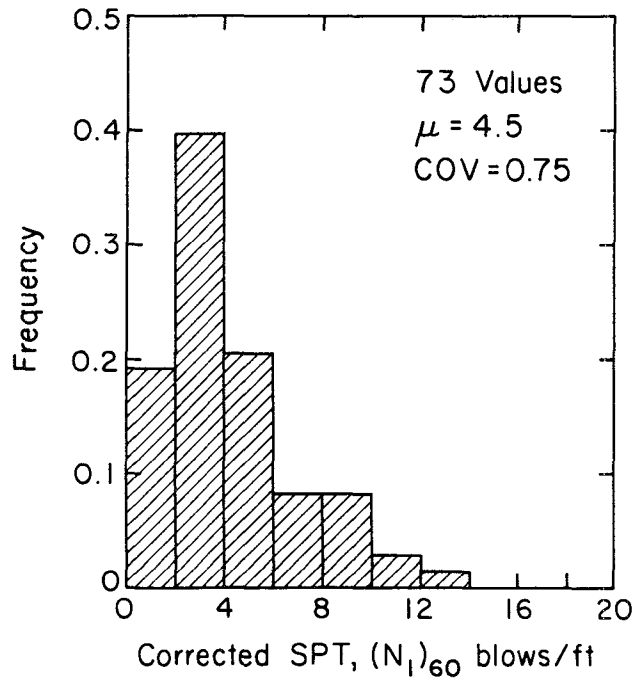
FIGURE 11. Histogram of Corrected SPT Values for Hydraulic Fill
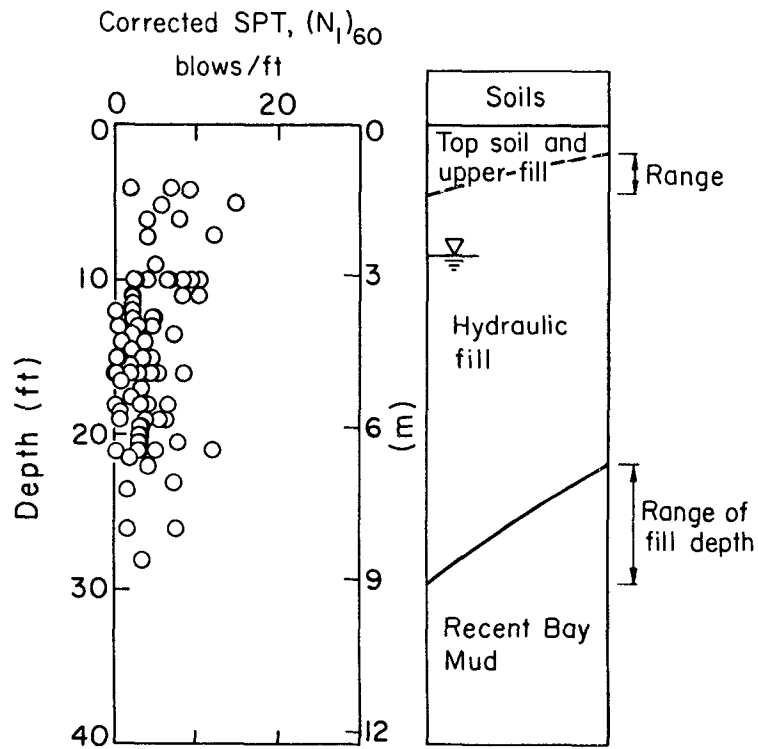

FIGURE 12. Corrected SPT Values of Hydraulic Fill Plotted with Respect to Depth and Soil Profile

Figure 12 shows a typical profile view of the hydraulic fill with corrected SPT values plotted as a function of depth. The plot indicates a relatively uniform distribution of in-situ density with depth below water table.

The lack of agreement between estimated and measured settlement of the hydraulic fill may be related to the relatively small median grain size and percentage of fines in this material. The percentage of fines and median grain size typically are less than 5% and between 0.2 and 0.4 mm, respectively, for the natural soils and land-tipped fills. These relatively clean, medium sands are consistent with the type of soils used to establish the predictive relationships in Figure 9. In contrast, the hydraulic fill has a median grain size between 0.1 and 0.2 mm and an average percentage of fines of 15%.

The percentage of fines can have an important influence on the combination of density, cyclic stress ratio, and number of cycles required for initial liquefaction. As illustrated in Figure 10, the corrected SPT values at initial liquefaction are diminished by approximately 5 for sands with 15% fines. Data reported by Lee and Albaisa (1974) show that reconsolidation volumetric strains are influenced by grain size, with more than a two-fold decrease in strain after initial liquefaction as the median grain size decreases from 0.6 to 0.1 mm. If an adjustment in corrected SPT values similar to that for 15% fines in Figure 10 is made in the simplified settlement plot in Figure 9, then the data for the hydraulic fill would be shifted by $(N_1)_{60} = 5$ to the right. This shift results in a volumetric strain prediction of 2.7% and 110 to 160 mm of settlement, which is in good agreement with field measurements.

It is recognized that the duration of shaking will influence liquefaction, and adjustments were made in the cyclic stress ratio as recommended by Tokimatsu and Seed (1987) to account for the approximate six cycles of strong ground shaking recorded by accelerographs relatively close to the Marina. This adjustment did not significantly reduce the estimated volumetric strains.

Consideration also was given to the 150 linear km of timber piles which were driven in the Marina as deep foundations for buildings of the 1915 Panama Pacific Exhibition (Mitchell, et al., 1990). The settlement pattern in Figure 7 was evaluated relative to the site plan of the 1915 Exhibition. If remnant piles were effective in reducing settlement after the Loma Prieta earthquake, then areas of locally reduced settlement should correlate with the footprints of previous pile-supported buildings. No such correlation could be found. Moreover, settlements in the areas underlain by natural soils and land-tipped fills showed good agreement with estimated settlements, irrespective of the location of previous pile-supported Exhibition buildings.

SUMMARY

This paper summarizes historic information pertaining to the development of the Marina, including a review of damage and observed ground deformation after the 1906 earthquake. Damage of the water supply, gas distribution, and wastewater conveyance networks in the Marina after the 1989 Loma Prieta earthquake are described. The performance of the Municipal Water Supply System (MWSS) is shown

to be strongly related to the pattern of surface settlements caused by consolidation of sand and associated liquefaction. Measured settlements are compared with those estimated on the basis of simplified procedures, and good agreement is shown for portions of the Marina underlain by natural soils and land-tipped fills. The predicted settlements of the hydraulic fill are nearly twice the amounts measured. This discrepancy may be the result of the fines content and small grain size of the hydraulic fill. An adjustment of corrected SPT values is suggested to account for the influence of fines in the simplified procedure for estimating settlement. The very low in-situ density of the hydraulic fill makes it susceptible to liquefaction and flow failure. The possibility of flow failure underscores the importance of the seawall in providing lateral support and encourages measures to promote its seismic stability.

ACKNOWLEDGMENTS

REFERENCES

1.	Bardet, J.P., M. Kapuskar, and G.R. Martin, "Dynamic Response of the Marina District of San Francisco During the 1989 Loma Prieta Earthquake," Proceedings, 3rd Japan-U.S. Workshop on Earthquake Resistant Design of Lifeline Facilities and Countermeasures for Soil Liquefaction, (this volume).

2.	Benett, M.J., "Ground Deformation and Liquefaction of Soil in the Marina District," Open File Report 90-253, USGS, Menlo Park, CA, Effects of the Loma Prieta Earthquake on the Marina District, San Francisco, CA, Apr. 1990, pp. D-1 - D-36.

3.	Dames and Moore, "Factual Report, Site Investigation for Completion of Preliminary Design - Phase I Muni Metro Turnaround Facility," Vol. II, Report for Bechtel National, Inc., Dames & Moore, San Francisco, CA, Job No. 185-215-03, Nov. 1989, Vols. I, II, and III.

4.	Gilbert, G.K., R.L. Humphrey, J.S. Sewell, and F. Soule, "The San Francisco Earthquake and Fire of April 18, 1906 and Their Effects on Structures and Structural Materials," Bulletin 324, U.S. Geological Survey, U.S. Government Printing Office, Washington, D.C., 1907.

5. Golden Software, Inc., "Surfer," Golden, CO, 1985.

6. Ishihara, K., "Evaluation of Liquefaction Potential and Consequent Deformation of Sand Fills," presented at POLA Seismic Workshop, Los Angeles, CA, Mar. 1990, 34 p.

7. Jones, E.C., "The Story of the Restoration of the Gas Supply in San Francisco After the Fire," Proceedings, 14th Annual Meeting of the Pacific Gas Association, Sept. 1906, pp. 350-364.

8. Lawson, A.C., et al., The California Earthquake of April 18, 1906: Report of the California State Earthquake Investigation Commission, Pub. No. 87, Carnegie Institute, Washington, D.C., 1908, Two Volumes and Atlas.

9. Lee, K.L. and A. Albaisa, "Earthquake-Induced Settlements in Saturated Sands," Journal of the Soil Mechanics and Foundations Division, ASCE, Vol. 100, No. 4, Apr. 1974, pp. 387-400.

10. Mitchell, J.K., M. Tahir, R.E. Kayen, and R.B. Seed, "Soil Conditions and Earthquake Hazard Mitigation in the Marina District of San Francisco," a report to the Mayor of San Francisco, May 1990.

11. Olmsted, R., N. Olmsted, and A. Pastron, "San Francisco Waterfront: Report on Historical Cultural Resources for the North Shore and Channel Outfalls Consolidation Projects," San Francisco Wastewater Management Program, City of San Francisco, CA, Dec. 1977.

12. O'Rourke, T.D. and B.L. Roth, "Performance of Pipeline Systems in the Marina," Open File Report 90-253, USGS, Menlo Park, CA, Effects of the Loma Prieta Earthquake on the Marina District, San Francisco, CA, Apr. 1990, pp. E1-E8.

13. O'Rourke, T.D., T.E. Gowdy, H.E. Stewart, and J.W. Pease, "Lifeline and Geotechnical Aspects of the 1989 Loma Prieta Earthquake," Proceedings, 2nd International Conference on Recent Advances in Geotechnical Earthquake Engineering and Soil Dynamics, St. Louis, MO, Mar. 1991.

14. O'Rourke, T.D., H.E. Stewart, F.T. Blackburn, and T.S. Dickerman, "Geotechnical and Lifeline Aspects of the October 17, 1989 Loma Prieta Earthquake in San Francisco," Technical Report NCEER-90-001, National Center for Earthquake Engineering Research, Buffalo, NY, Jan. 1990.

15. Phillips, S.H. and J.K. Virostek, "Natural Gas Disaster Planning and Recovery: the Loma Prieta Earthquake," Pacific Gas and Electric Company, San Francisco, CA, Apr. 1990.

16. Plafker, G. and J.P. Galloway, Eds., "Lessons Learned from the Loma Prieta, California Earthquake of October 17, 1989," U.S. Geological Survey Circular 1045, U.S. Geological Survey, Denver, CO, 1989.

17. Ripley, B.D., Spatial Statistics, John Wiley and Sons, New York, NY, 1981, 252 p.

18. Sanborn Ferris Map Company, "Insurance Maps, San Francisco, California," Vol. 4, New York, NY, 1899 updated to 1905.

19. Seed, H.B., "Design Problems in Soil Liquefaction," _Journal of the Geotechnical Engineering Division_, ASCE, Vol. 113, No. 8, Aug. 1987, pp. 827-845.

20. Seed, H.B., I.M. Idriss, and I. Arango, "Evaluation of Liquefaction Potential Using Field Performance Data," _Journal of Geotechnical Engineering_, ASCE, Vol. 109, No. 3, Mar. 1983, pp. 458-482.

21. Tokimatsu, K. and H.B. Seed, "Evaluation of Settlements in Sands Due to Earthquake Shaking," _Journal of Geotechnical Engineering_, ASCE, Vol. 113, No. 8, Aug. 1987, pp. 861-878.

22. U.S. Coast Survey, Topographic Map of "City of San Francisco and Its Vicinity, California," surveyed by A.F. Rodgers, 1857.

23. U.S. Geological Survey, "Effects of the Loma Prieta Earthquake on the Marina District, San Francisco, California," _Open File Report 90-253_, Menlo Park, CA, Apr. 1990.

DAMAGE TO FOUNDATION PILES AND DEFORMATION PATTERN OF GROUND DUE TO LIQUEFACTION-INDUCED PERMANENT GROUND DEFORMATIONS

Nozomu Yoshida

Research Head, Engineering Research Institute
Sato Kogyo Co., Ltd.

Masanori Hamada

Professor of Faculty of Marine Science and Technology
Tokai University

ABSTRACT

Detailed investigations to the damage of the piles of two buildings which were damaged in the 1964 Niigata Earthquake were performed. All piles were completely destroyed, which were supposed to be damaged due to liquefaction-induced ground deformations.

Numerical analyses were performed based on the seismic deformation method to make clear the mechanism of the damage to the pile and to know the ground deformation patterns in the vertical direction. Deformed shapes of the piles and crack patterns are shown to be able to explain by the analysis, which suggests that damage to the piles was caused due to lateral movement of the liquefied ground. It is also suggested that displacements near the upper boundary of the liquefied layer may be larger than that of the nonliquefied layer above it, and partial liquefaction should be considered near the lower boundary of the liquefied layer to obtain more accurate prediction.

INTRODUCTION

Large ground deformations (lateral spreading) were found to occur at the past earthquakes both in Japan[1] and in U.S.A.[2]. It can be easily recognized that underground structures may be damaged when this kind of ground deformations occur. Actually, investigations on the underground lineal structures such as gas or water pipelines were sometimes performed and correspondences between the damage to them and soil liquefaction were shown to be good[3]. On the other hand, investigations on the foundation piles were hardly performed since it is necessary to demolish the superstructure.

Damages to piles due to soil liquefaction were reported for three buildings[3], but detailed investigations were not performed since they were found accidentally during the construction of the structures. The authors and their co-researchers performed detailed investigations on the piles of two buildings which were damaged in the 1964 Niigata earthquake, which is firstly described in this paper.

Seismic design codes for underground structures have been revised to consider soil liquefaction after the 1964 Niigata earthquake in which soil liquefaction was firstly recognized to cause severe structural damage, but lateral spreading of the ground is still not considered. To establish the design method against lateral spreading of the ground, it is necessary to know the deformation patterns under the ground as well as the displacement of the ground surface. Although several techniques are available to measure the surface displacement, there is no direct method to measure deformation patterns under the ground. Case studies of the damage to the foundation piles are good tool to know them. A trial is performed in this paper to make clear the mechanism of the damage to the pile and to know the deformation patterns of the lique-fied ground.

INVESTIGATIONS ON THE PILE DAMAGE

Investigations on the damage to the piles of two buildings which were damaged in the 1964 Niigata earthquake were performed in 1989. The locations of the buildings are shown in Fig. 1; a building north to the Shinano River is called A-building and that south to the Shinano River is called S-building hereafter. The buildings had been repaired after the earthquake and had been used until they were demolished for constructing new buildings.

Damage to Piles of A-building

A-building is a 3-storied R/C building. Foundation plan is shown in Fig. 2, in which there are 3 types of foundations: F5, F4 and F1 which are composed of 5, 4, and single piles, respectively. Two circled F1 type foundations were chosen to be investigated considering the easiness of excavation. The piles, designed as bearing piles, are R/C piles with 14 meters long in the design, whose cross section is shown in Fig. 3.

Figure 4 shows topographical map at the beginning of the Meiji Era (1868-1912), which shows that the site was an old river bed. Soil profiles and N-value distributions obtained by the boring investigation in 1987 at the locations shown in Fig. 5 are shown in Fig. 6. Figure 5 also shows permanent dis-

placements measured by comparing the aerial photographs taken before (1962) and after (several hours) the earthquake. Since A-building do not appear in the photograph before the earthquake as it was constructed in 1964, permanent displacement of A-building was measured by the use of as-built drawing instead of the aerial photograph. In general, the ground moved toward east to north-east for about 1 meter. A-building moved, however, toward north, which is supposed to be the error caused by the use of as-built drawing.

Sheet piles were firstly driven surrounding the pile and the soils inside the sheet piles were taken off by the reverse circulation boring method. After that, concrete mat was made at about 10 meters from the ground surface to prevent boiling when water would be pumped out. Therefore, deformation patterns under the ground could be measured directly from the pile top to about 10 meters from the ground surface, which seems to be enough for measuring the liquefaction-induced damage because liquefaction is estimated to occur to about 10 meters from the ground surface.

Since the piles seems to deform within an plane in general when looking at the measured deflection, the projection of the displacement on this plane is shown in Fig. 7, where displacement δ_2 is relative displacement from the lowest portion where displacement are measured. Photographs 1 and 2 show damage to the piles and Fig. 8 shows crack patterns schematically. Many cracks are observed in No. 1 pile at around 2m from the pile top which locates 2m below the ground surface. Tensile cracks appear in one side and compression failure appears in the other side, which indicates that the pile was damaged due to monotonically increasing load. Damage of No. 2 pile is observed around 2m and 7m from the pile top which locates 1.9m below the ground surface. Concrete was crashed and lost for about 60cm length and reinforcing bar deformed very much at the upper portion as shown in Photo. 2. The damage at the lower portion is similar to that to No. 1 pile. The building was reported to incline about 7/500 toward west in the Niigata earthquake[4]. Considering the damage of building and failure of the pile, soils around the pile tip of the No. 1 pile is supposed to liquefy although that of No. 2 pile did not liquefy.

Damage to Piles of S-building

S-building is also 3-storied R/C building. Figures 9 and 10 show foundation plan and detail of foundation, respectively. The piles, designed as friction pile, are R/C piles with 25cm outer diameter, 13cm inner diameter and about 5.5m length.

Figure 11 shows ground failure[5] and permanent ground displacement in the Niigata earthquake near the site. The site was also an old river bed of the Shinano River and reclaimed around 1930. There was a creek with about 8 meters width next to the site in 1964, which is now reclaimed. Figure 12 shows soil profile and N-value distributions obtained by the boring investigation at 1988. Upper sand layer is composed of loose sand which is supposed to be river bed deposit. The building was reported to tilt 15.2/500 toward southwest and 9.8/500 toward northwest.

Steel pipe with 60cm outer diameter and with spirals outside the pipe, which is called jet auger, was used in the investigation. It was driven into the ground surrounding the pile by throwing jet water into the soil for mixing the

sand. After cutting the friction between the soil and piles off, jet auger was firstly pulled up and after that the pile was pulled up. Since jet auger was hanged by a pin at the top, it can move along the pile even if the pile bends. Therefore it is possible to pull up the piles without changing the original shape when lateral deflection is smaller than about 30cm.

When head of the pile was looked for to be pulled up by taking off the footing, lots of piles could not be found; the piles were supposed to settle down by its self weight during the earthquake because liquefied ground could not sustain the weight. Therefore, found three piles, locations of which are shown in Fig. 10, were pulled up. Photograph 3 shows pulled up piles and Fig. 13 shows crack patterns schematically. No. 1 pile were severely damaged at two portions, one of which is shown in Photo. 4. On the other hand, cracks with 5 - 20mm wide appears with nearly equal distances to each other for the Nos. 2 and 3 piles.

Figure 14 shows lateral deflection of the Nos. 2 and 3 piles δ_1; that of No. 1 pile was not measured because the deflection seemed to be too large to be pulled up without changing the original shape by jet auger. Deflection occurred within an plane which is parallel to the permanent ground displacement vector around the site in Fig. 11. Considering the damage to the building and investigation on the piles, the mechanism of the damage of the building during the earthquake seems to be as follows: liquefaction occurred around the site and the building settled down because soil liquefaction had occurred around the pile tip. However, since liquefaction did not occur near the southeast corner or porewater pressure dissipation characteristics were somewhat different there compared to the other portion, No. 1 pile sustained the weight of the building when the building began to settle down, hence was damaged seriously. Moreover, although pile top existed above the water table in Fig. 12, liquefaction is supposed to occur around the pile top at that time considering that many piles settled down.

NUMERICAL ANALYSIS

As described in the preceding section, all the investigated piles were completely destroyed. Moreover, although the piles of A-building were designed as a friction pile and those of S-building were designed as bearing pile, actual situation may be different with the design as described in the previous section. Figure 15 shows relative positions between the liquefied layer and the piles schematically based on the investigation; all types of the relative positions are seen. The analysis should explain all these damages.

Method of the Analysis

Seismic deformation method is used to analyze pile-foundation system. The moment M versus curvature ϕ relationship of the pile is firstly computed using the stress-strain relationships shown in Fig. 16(a) and (b), where f_t denotes tensile crack stress, f_c denotes compression failure stress and σ_c denotes yield stress, and, to make the analysis sample, it is replaced into piesewise linear model shown in Fig. 16(c), whose kink points, the coordinate of which is shown in Table 1, correspond to the tensile crack of the extreme fiber concrete, yield of extreme reinforcing bar and compression failure of the extreme fiber concrete.

Coefficient of subgrade reaction k is expressed based on the Japanese Highway Bridge Code as

$$k = 0.2 * 28N * D^{-0.35} \qquad (kgf/cm^3)$$

where D denote diameter of the pile in cm and N denotes N-value. Spring constant of the spring connecting the pile and ground is computed by multiplying the diameter of the pile to the coefficient of subgrade reaction. That for liquefied layer is set one-tenth of that for nonliquefied layer. N-values used in the analysis are shown as dashed lines in Figs. 6 and 12.

Since the surface displacements of the ground are fairly large although the ground is near the level ground, displacements in the liquefied layer seems to be predominant. In the analysis, therefore, ground displacement at the lower boundary of the liquefied layer is assumed to be 0, and that above the liquefied layer is assumed to be constant.

Figure 17 shows typical ground displacement patterns. It is obvious that linear ground displacement, (a) and (b), cannot explain the damage of Nos. 2 and 3 piles of S-building, because no stress occurs under these displacement. Type (d) displacement seems not to be able to explain the damage because the curvature of the displacement is opposite sign to the pile deformation. Therefore, type (c) displacement seems to have the most possibility. Considering this, sinusoidal displacement,

$$y = \delta \cos(\pi/2 * x/l)$$

is chosen as the ground displacement, where notations are shown in Fig. 18. The thickness of the liquefied layer for the analysis of the pile of S-building is assumed to be 10.8 meters. That of the No. 2 piles of S-building is assumed to be 7 meters. The lower boundary of the liquefied layer is assumed to be the same depth with the pile tip of the No. 1 pile of A-building considering the damage. The length of the piles of S-building is set as 5.5 meters. That of A-building is set as 9 meters although actual pile length are not known. Moment is assumed to be zero both at the pile tip and pile top.

Result and Discussions

The results of the analysis are shown and compared to the observed displacements in Figs. 19, 20 and 21. Here it is noted that the definition of the displacement in the analysis, shown in Fig. 18, is a little different to the definition of the measurement.

Figure 19 shows the result of the No. 1 pile of A-building at which computation is performed until δ=1.5m. Deflected shape when δ=0.75m agrees well with the measured one except slight differences. Peak moment occurs at 3.5m from the pile top whereas damage is observed at about 2m from the pile top in the actual pile. Moreover, although compression failure seems to occur slightly in the actual pile, but maximum moment is a little smaller than the compression failure moment in the analysis. These differences suggest that the curvature near the upper portion of the liquefied layer is larger than the assumed one. In other words, the displacement near the upper boundary of the liquefied layer is larger than the one at the ground surface. This is not curious phe-

nomena when considering that the rigidity of the upper nonliquefied soil is so large that they may resist against the movement of the liquefied ground. Moreover, damage to the underground lineal structure which seemed to be caused due to the ground movement of this kind was reported[3].

Figure 20 shows the result of the No. 2 pile of A-building. Compression failures at the compression side concrete occur at the lower portion when $\delta=0.53m$ and at the upper portion when $\delta=0.88m$. After that, deflection increases with two kinks at the failed portions. Therefore, the damage of the upper portion of the actual pile do not seem extraordinary. However, the portion where failure occurs in the actual pile is higher than the one obtained by the analysis, which again suggest that the displacement at the upper portion of the liquefied layer is larger than the one at the ground surface. On the other hand, compression failure at the compression side concrete occurs earlier, hence damage is more serious at the lower boundary of the liquefied layer than at the upper portion in the analysis, which seems to be different to the observed one. This comes from the discontinuous change of spring constant. Only two states, liquefied and nonliquefied, are considered in the analysis, but material properties seem to change continuously in the actual ground. Therefore, if partial liquefaction is considered to make the change smooth, the result of the analysis will move to the actual situation.

The analysis for No. 1 pile of S-building is not performed because displacement was not measured. Figure 21 shows the result of the Nos. 2 and 3 piles of S-building. Tensile crack occurs when $\delta=0.12m$, and reinforcing bar yields when $\delta=0.28m$. The moment distribution tend to become flat at the center portion and the portion of peak moment moves upward after that. Compression failure occurs when $\delta=4.88m$ and δ_2 exceeds 30cm at that time, which deflection is much larger than observed, hence deflection until $\delta_2=1$ meter are compared in Fig. 19 (d). The damaged portion of the actual pile is higher than the analysis, which also suggest that displacement at the upper portion of the liquefied layer is larger than the one at the ground surface.

CONCLUDING REMARKS

Investigations of the foundation piles of the buildings damaged in the Niigata earthquake are described. All the piles were completely destroyed, which were supposed to be damaged due to monotonically increasing liquefaction-induced ground deformations.

The analysis based on the seismic deformation method is performed to make clear the mechanism of the damage to the pile and to guess the deformation patterns of the ground in the vertical direction. The analysis is shown to be able to explain the damage of the pile. Through the comparison between the measurement and analysis, following conclusions are obtained.

1) Linear and concave ground displacement in the vertical direction cannot explain the damage to the pile; convex displacement pattern seems to explain it.
2) Lateral displacement at the ground surface may be smaller than the one near the upper boundary of the liquefied layer.
3) Partial liquefaction should be considered to obtain more accurate prediction.

152

REFERENCES

1) Hamada, M. et al, Case Study on Liquefaction-induced Ground Failure during Earthquakes in Japan, Proc. First Japan-U.S. Workshop on Liquefaction, Large Ground Deformation and Their Effects on Lifeline Facilities, Nov. 1988, Japan, pp. 3-21

2) Youd, T.L. and Bartlett, S.F., US Case Histories of Liquefaction-induced Ground Displacement, Proc. First Japan-U.S. Workshop on Liquefaction, Large Ground Deformation and Their Effects on Lifeline Facilities, Nov. 1988, Japan, pp. 22-31

3) Report on the Study on the Ground Failure and Damage of Underground Structures, ADEP, 1988 (in Japanese)

4) Niigata Earthquake and Damage to Reinforced Concrete Buildings in Niigata City, Report of the Building Research Institute, Ministry of Construction, March 1965 (in Japanese)

5) Map of the Ground Failure during the Niigata Earthquake, Niigata University, 1964 (in Japanese)

Table 1   Parameters

Bldg.	Pile	Axial Load (t)	M_c	M_y	M_u	ϕ_c	ϕ_y	ϕ_u	l
			(t m)			$(\times 10^{-4} /m)$			(m)
A	1	0	1.3	3.9	7.7	0.069	1.15	6.1	9.0
A	2	30	3.1	6.7	11.3	0.167	0.66	4.0	7.0
S	2	0	0.4	0.5	0.92	6.9	65	1000	10.8
S	3	0	0.4	0.5	0.92	6.9	65	1000	10.8
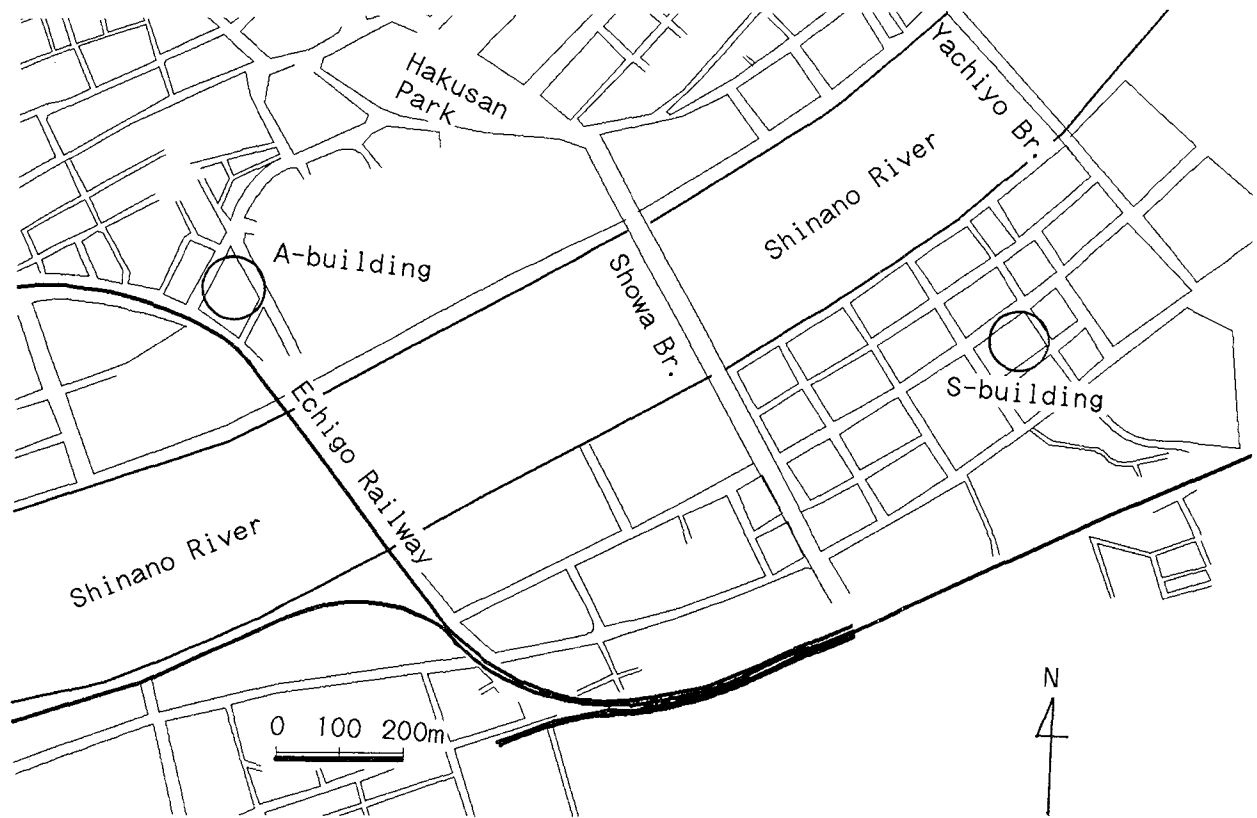
Fig. 1 Locations of the investigated buildings
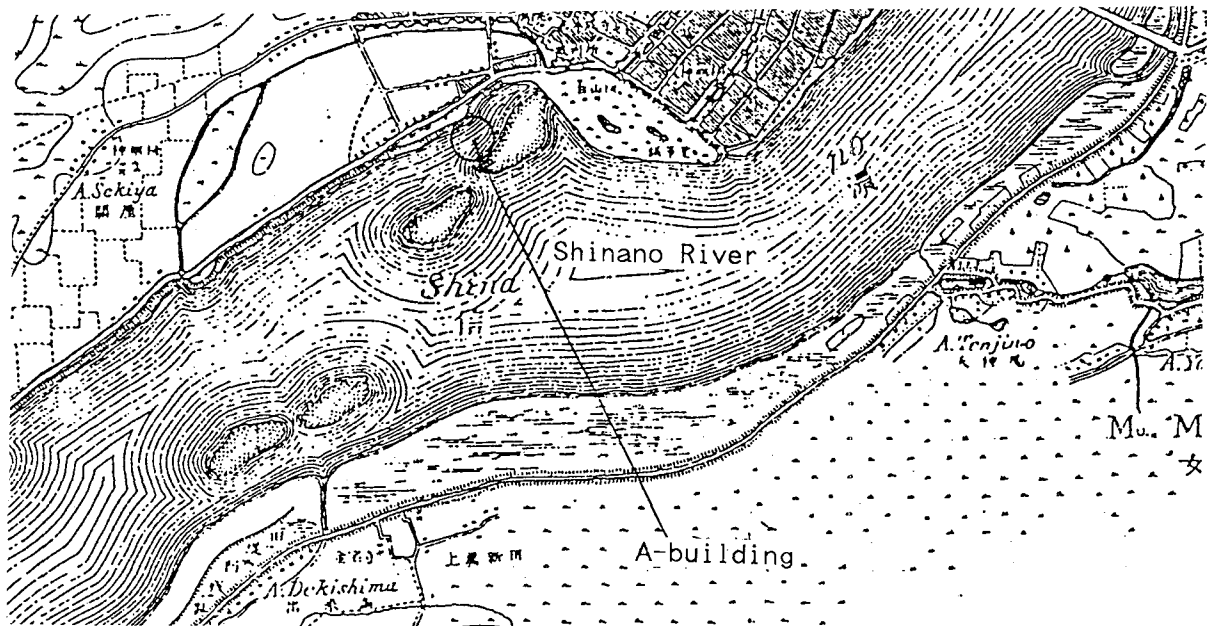
Fig. 4 Topographical Map near A-building at Meiji Era

Fig. 3 Cross-section of Pile of A-building

Fig. 2 Foundation Plan of A-building

155

Fig. 6 Soil Profiles and
N-value Distribution

Fig. 5 Permanent Ground Displacement
near A-building

156
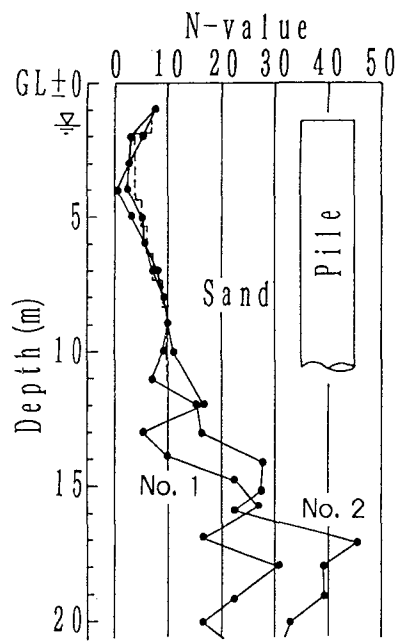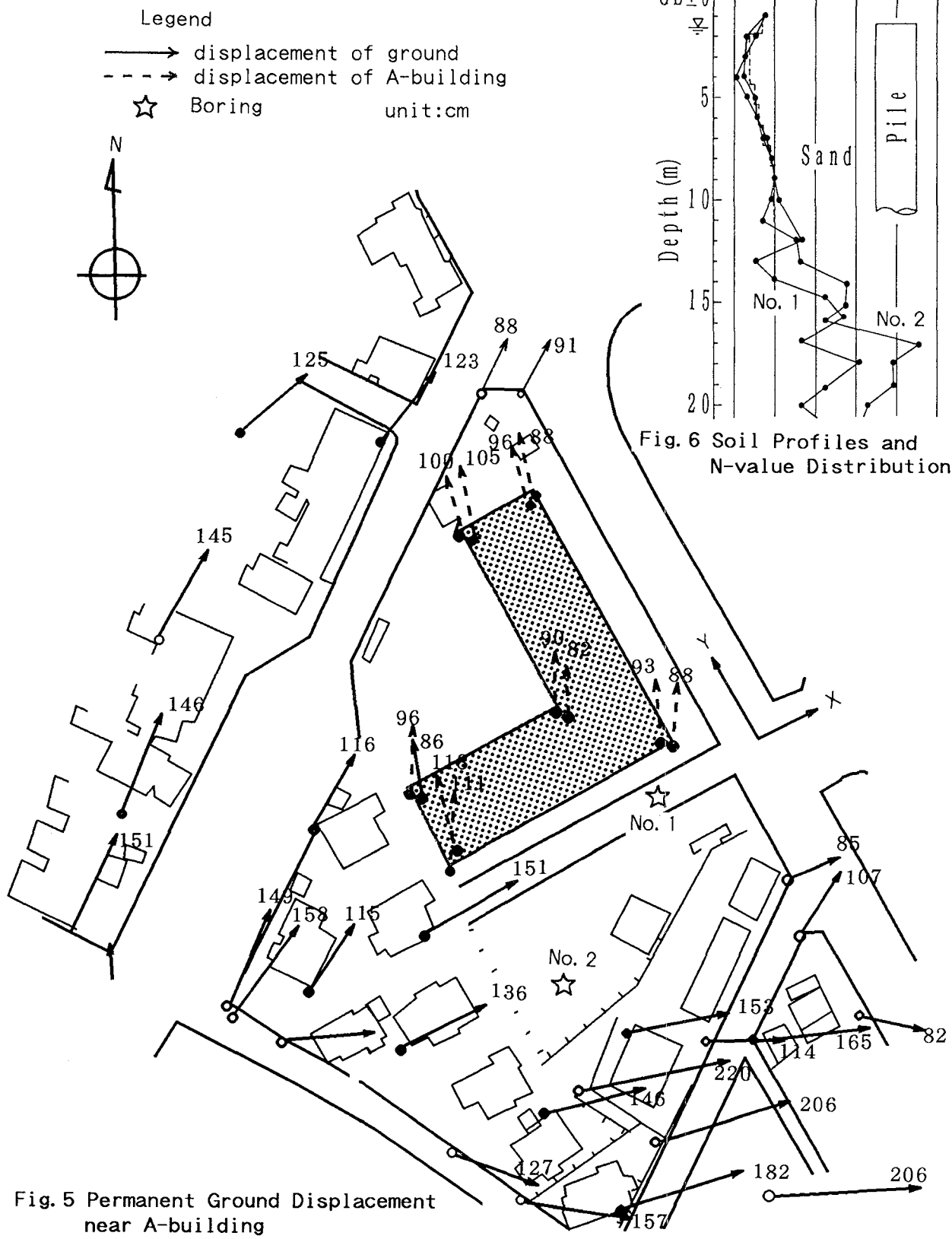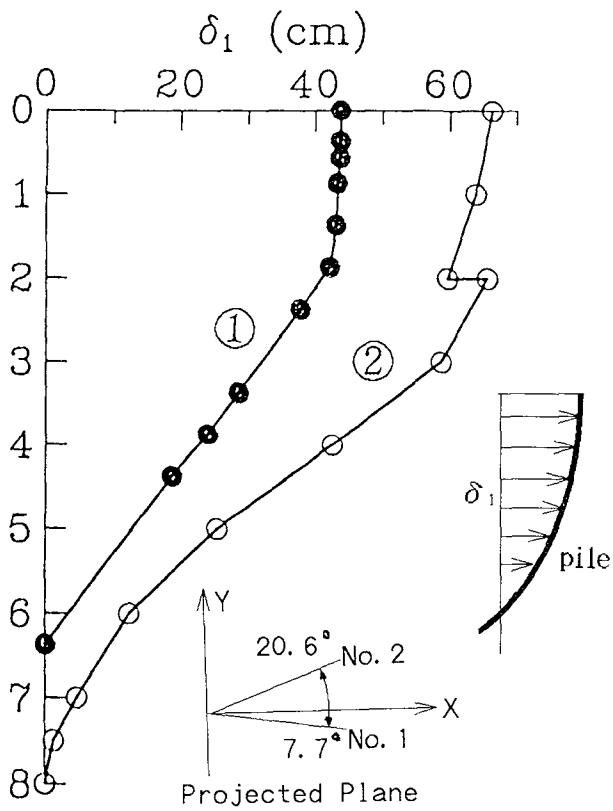
Fig. 7 Deflection Pattern of Piles
of A-building
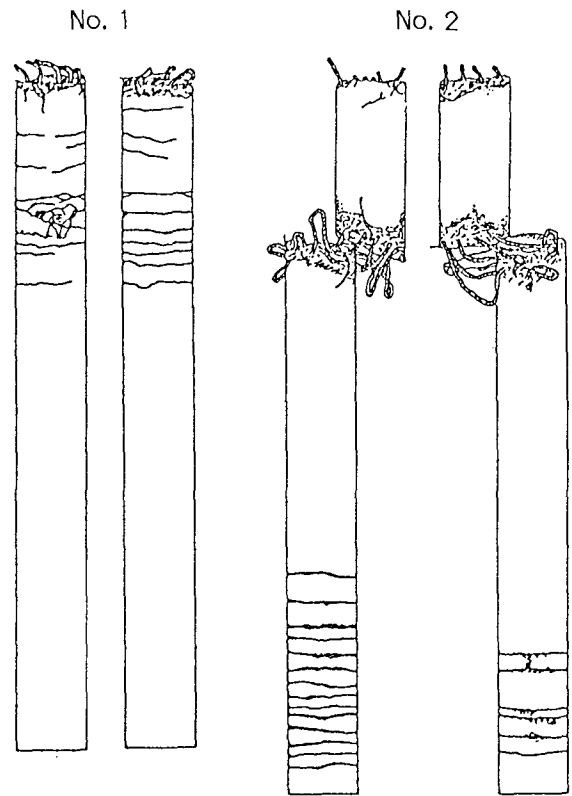
Fig. 8 Crack Pattern of Piles
of A-building
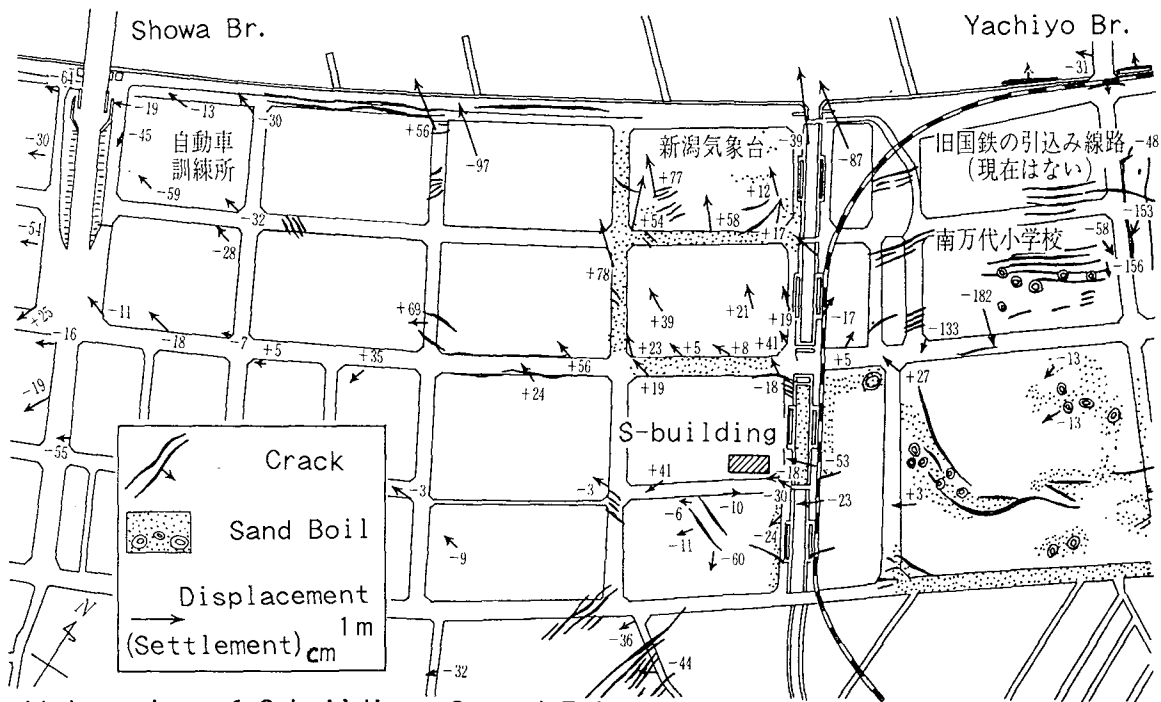
Fig. 11 Location of S-building, Ground Failure and Permanent Ground Displacements
in the Niigata earthquake.

157
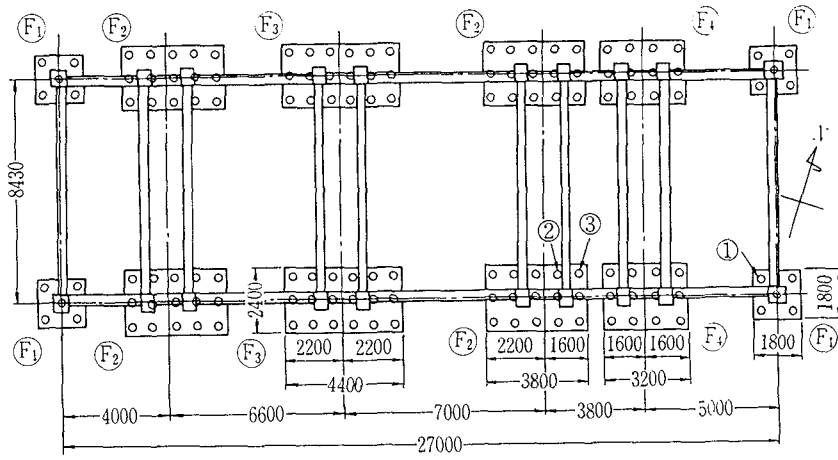
Fig. 9 Foundation Plan of S-building
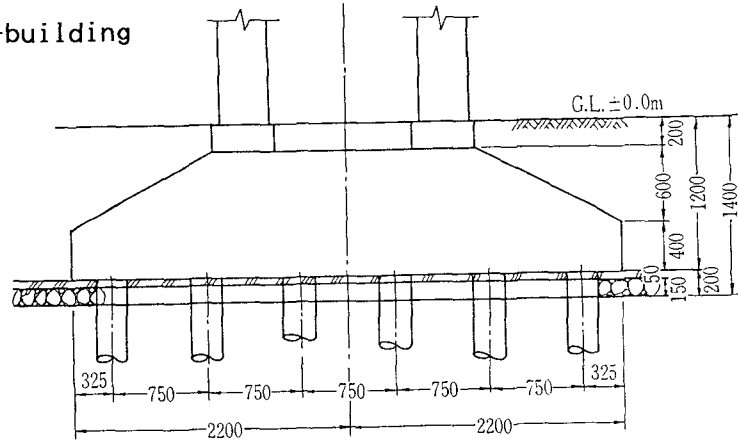
Fig. 10 Detail of Foundation
of S-building
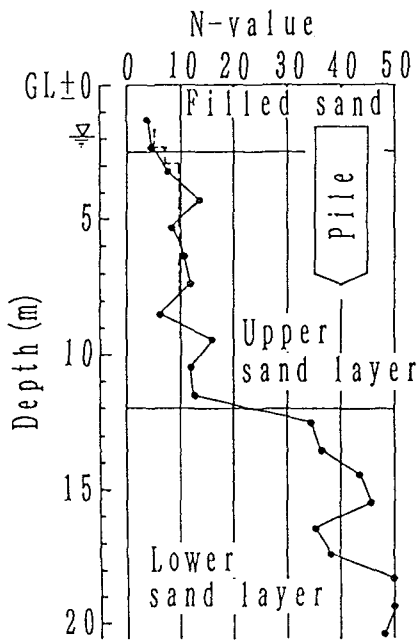
Fig. 12 Soil Profile and
N-value Distribution
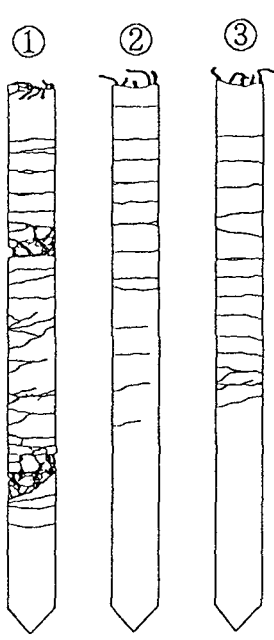
Fig. 13 Crack Pattern of
Piles of S-building
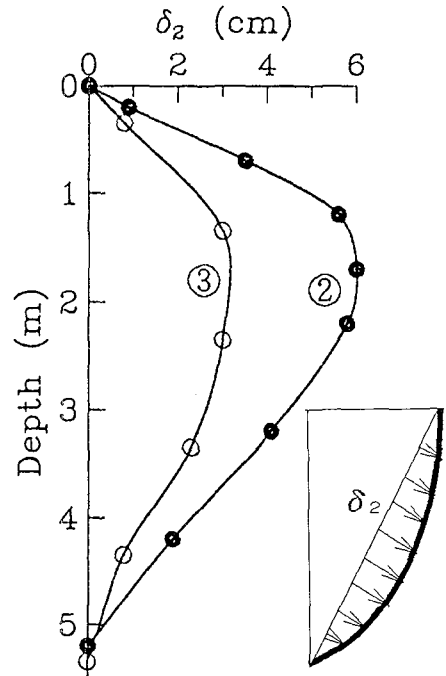
Fig. 14 Deflection of
the Piles
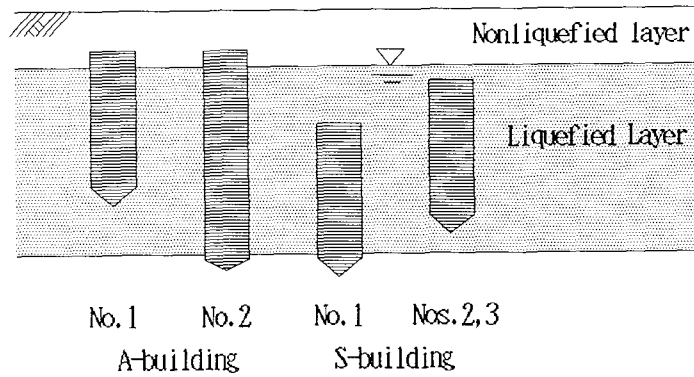
Fig. 15 Relative Positions between the Pile and Liquefied Layer

(a) Concrete   (b) Reinforcing Bar   (c) M- φ
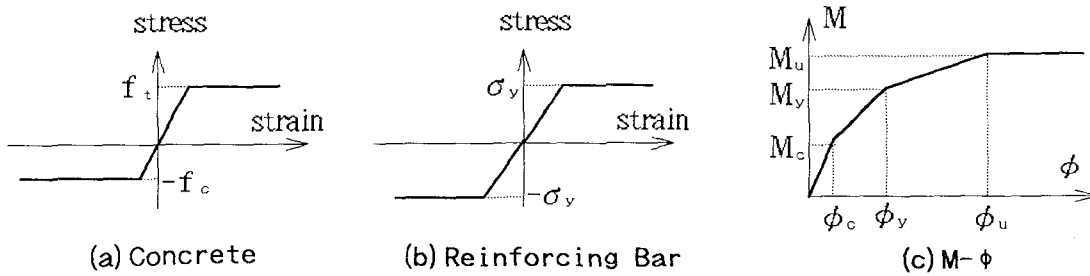
Fig. 16 Stress-strain and Moment-curvature Relationship

(a)   (b)   (c)   (d)
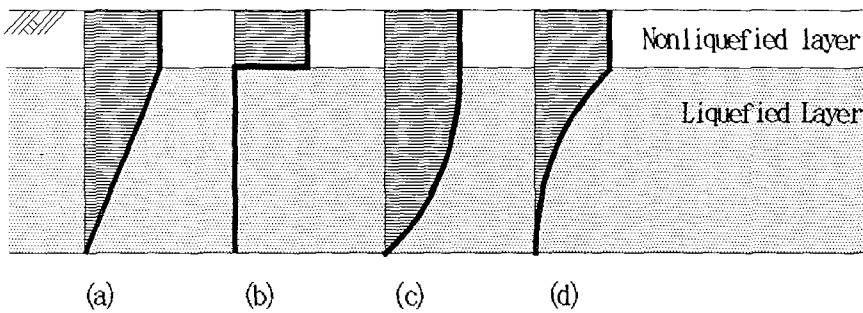
Fig. 17 Typical Ground Displacement Patterns
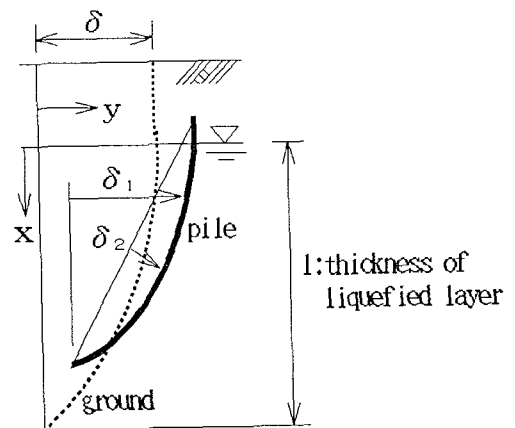
Fig. 18 Notations Used in the Analysis

159
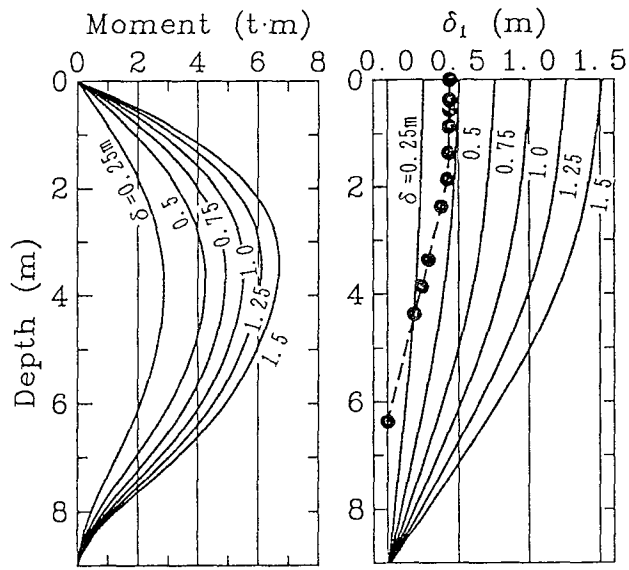
Fig. 19 Result of the Analysis of No. 1 Pile of A-building
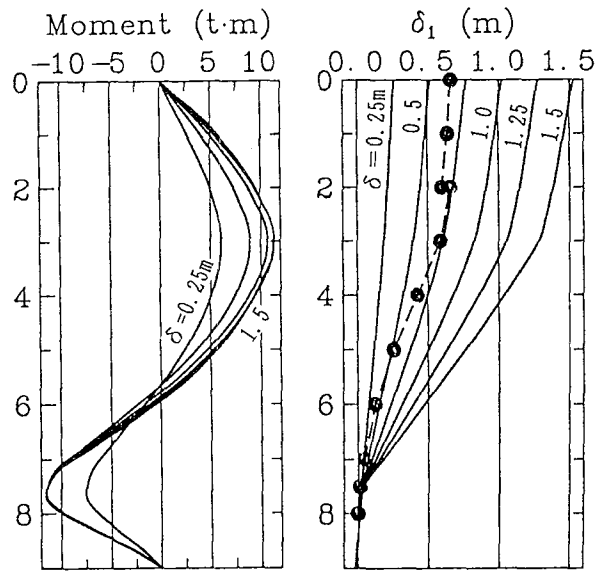
Fig. 20 Result of the Analysis of No. 2 Pile of A-building
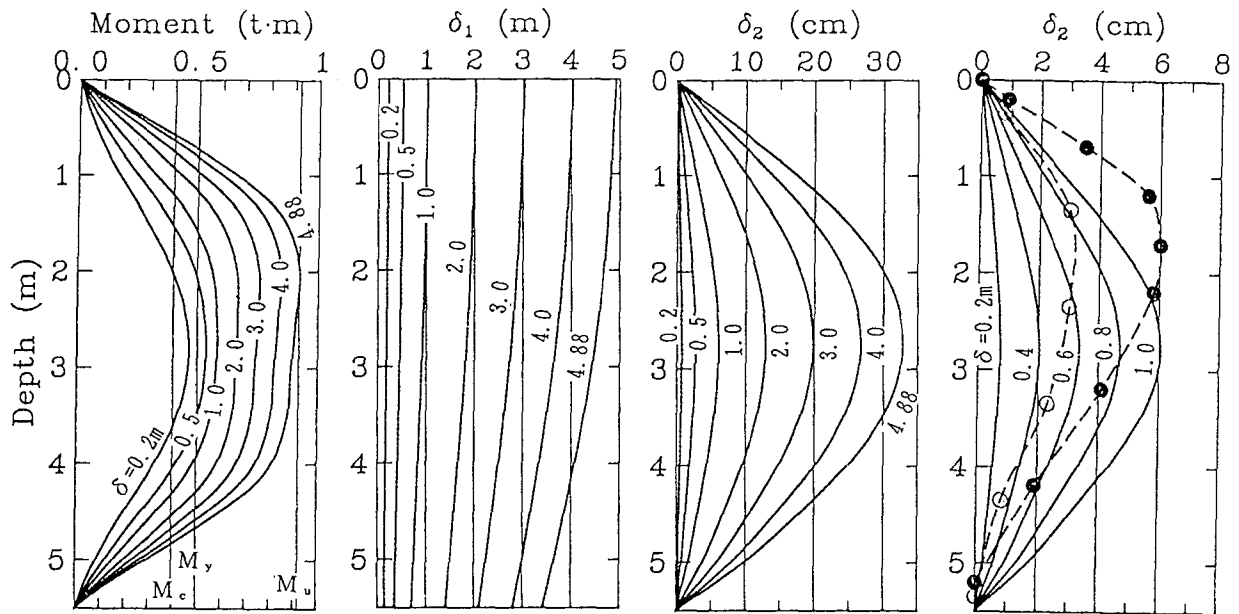
Fig. 21 Result of the Analysis of Nos. 2 and 3 Piles of A-building

Tensile Crack
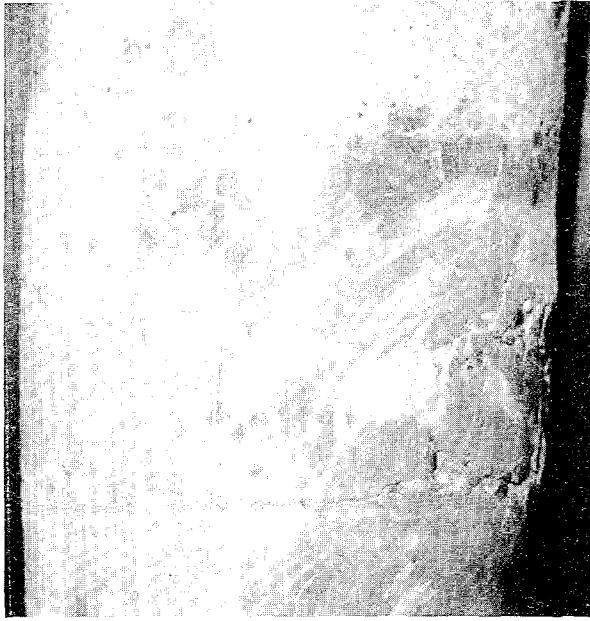
Compression Failure

Photo. 1 Damage of No. 1 Pile of A-building
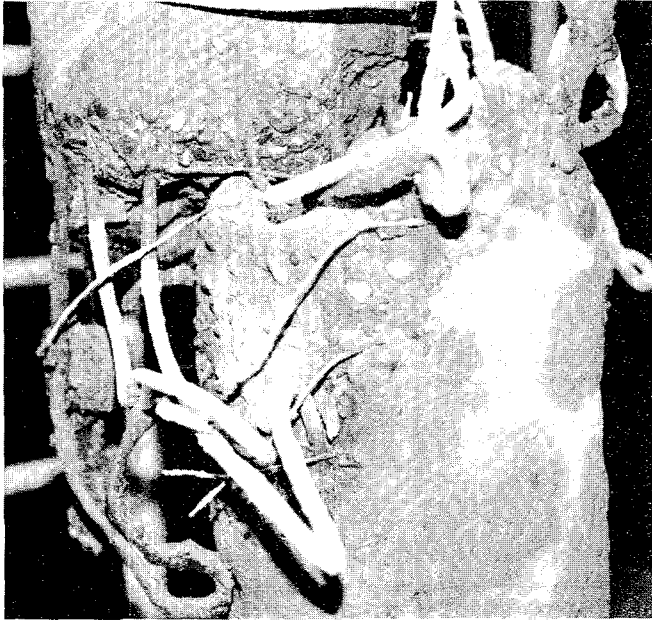
Photo. 2 Damage of the upper portion of No. 2 Piles of A-building

Photo. 3 Deformed Shapes of the Piles of S-building

Photo. 4 Damage of the Pile of S-building

161

RESPONSE OF PIPELINE AT PARKFIELD, CA TO GROUND MOTION FROM LOMA PRIETA EARTHQUAKE

By Jeremy Isenberg[1], Edward Richardson[2]
and Hiroyki Kameda[3]

ABSTRACT

Pipeline segments were constructed and instrumented near Parkfield, CA to develop field-scale data on the response of buried pipelines to lateral offsets and ground strains from traveling wave effects. Although intended to capitalize on the predicted recurrence of a moderate earthquake on the Parkfield-Cholame segment of the San Andreas Fault, the first data was obtained during the surface wave phase from the Loma Prieta earthquake whose epicenter was about 175 km to the north. Close correlation was obtained between ground strains derived from local accelerograph data and the transient pipeline strains; permanent offset also correlated well with residual pipeline strains.

---

[1]Prin., Weidlinger Assoc., 4410 El Camino Real, Ste. 110, Los Altos, CA 94022

[2]Assoc., Weidlinger Assoc., 4410 El Camino Real, Ste. 110, Los Altos, CA 94022

[3]Prof. & Dir. Eng., Disas. Prev. Res. Inst., Kyoto Univ, Japan

INTRODUCTION

A field experiment designed to investigate the performance of buried pipelines subjected to lateral offsets and to ground strains from seismic wave propagation has been constructed at Owens' Pasture near Parkfield, CA., (Isenberg et al, 1988). The site was chosen to capitalize on the predicted recurrence of the 1966 Parkfield-Cholame earthquake sequence on the San Andreas Fault. Although this earthquake has not yet occurred, the October 17, 1989, Loma Prieta earthquake caused low levels of transient ground strain and right lateral strike-slip at Owens' Pasture that resulted in transient and residual strains in the instrumented pipe segments. The distribution of strains in the pipes and their correlation with ground movement yields important insight into the behavior of girth-welded steel pipelines of the type used for oil, gas and water transmission. Many analytical models of traveling wave effects postulate that soil strain is transferred to the pipeline without appreciable slip at the pipe-soil interface. In contrast, analytical models of pipes that intersect offset zones assume that the pipe is in equilibrium with pipe-soil interface friction stresses whose limit state is reached only after significant slip has occurred. The data from the Loma Prieta earthquake that are presented below and from the main Parkfield event yet to come make it possible to evaluate these assumptions and, if necessary, to revise them.

RESPONSE TO LATERAL OFFSET

Fig. 1 illustrates the deformation mode assumed in analytical models of pipeline response to lateral offset at a fault crossing proposed by Newmark and Hall (1975) and by Kennedy et al (1977). Important parameters of the model are the anchor length over which pipe-soil interface friction is assumed to be mobilized; the magnitude of interface friction stress, which is assumed to depend on interface soil pressure; and the angle between the strike of the surface rupture and the axis of the pipe. The welded steel segments being studied in the present experiment are 200 ft. long, or approximately 200 pipe diameters. The ends of each segment are encased in large concrete anchors in order to define the end conditions of the pipe precisely. Ductile iron segments are 36 ft. or 54 ft. long.

To investigate the behavior of pipelines intersected by surface ruptures and to provide data for evaluating design and analysis methods for the deformation mode shown in Fig. 1, continuously welded steel pipe and jointed ductile iron pipe segments were instrumented with strain gages and displacement transducers, respectively, and buried at the Owens' Pasture site. A line of monuments was placed across the predicted location of the surface rupture in order to measure lateral offset during both pre-earthquake creep and earthquake-induced surface rupture phases.

Based on data obtained by O'Rourke (1988) and also reported in Isenberg et al (1989) pertaining to the steel and shear characteristics of the sand-steel interface, it is possible to evaluate the maximum strain in the test pipeline for a right lateral strike-slip movement of 4 inches along the San Andreas Fault, which is the maximum expected lateral offset at Owens' pasture that would accompany a moderate earthquake of Magnitude 6.0. The Newmark-Hall model leads to a maximum tensile strain in the tension pipeline segment of 0.18% at the fault crossing for steel yield stress derived from a sample adjacent to the longitudinal seam. Higher strain is predicted if the yield stress is based on samples taken elsewhere in the pipe section. Application of the Kennedy, et al. model gives a maximum axial strain at the fault crossing of 0.16% and a maximum combined strain from summing the axial and bending components of 0.86%.

RESPONSE TO SEISMIC WAVE EFFECTS

The second aim of the experiment is to evaluate the response of pipelines to transient ground strains from traveling wave effects. Analytical models have also been proposed to support design of pipelines exposed to such effects by Keusel (1969), Shinozuka and Koike (1979), Shinozuka et

al. (1981), Datta et al (1982), and O'Rourke et al (1984). Fig. 2 illustrates the interaction of a pipe segment with an obliquely incident train of waves. Such models usually assume that the ground deformation is due to a wave train propagating with a predominant wave length and group velocity and is imposed on the pipeline with deformation and, in some cases, damping of the soil considered, but with negligible slip at the pipe-soil interface. The Parkfield experiment measures ground strain and corresponding pipe response within the expected zone of surface rupture. Ground strains are derived from records of three seismographs which were contributed to the project under a U.S.-Japan cooperative agreement between the National Center for Earthquake Engineering Research and the Urban Hazards Research Institute at Kyoto University.

INSTRUMENTATION

Each welded steel pipe segment is instrumented with 18 strain gages; two gages are placed on opposite sides of a springline at nine stations. For the ductile iron pipes, each of six push-on joints is instrumented with one transducer to measure relative extension (or compression) and another to measure relative rotation. To measure permanent offset across the pipeline segments, survey monuments were placed approximately on a straight line about perpendicular to the assumed fault strike. There are twelve such monuments with 5 m spacing near the fault and 10 m spacing at greater distances. Survey measurements are supplemented by USGS creepmeter XPK1 (see Fig. 3) which has a 10 m span and records a measurement every 10 seconds. Observations suggest a zone of creeping offset which wanders but is generally consistent with an average value of about 13 mm/year right lateral creep observed over about eight years by USGS Creepmeter XPK1.

To measure ground motion due to transient wave propagation, three 3-axis SAMTAC 17E seismographs are installed at the corners of a roughly equilateral triangle 50 m on a side as is indicated in Fig. 3. These were loaned to the project by the Urban Hazards Research Institute of the University of Kyoto, Japan. Strain-time histories are derived by applying the two horizontal components of measured ground displacement at each of three locations as boundary conditions to a triangular finite element representing the ground between the seismographs.

OBSERVED RESPONSE IN LOMA PRIETA EARTHQUAKE

The Loma Prieta Earthquake of October 17, 1989, was a magnitude 7.1 earthquake whose epicenter was located on the San Andreas Fault approximately 175 km north of the Owens' Pasture site. Ground records from Loma Prieta indicate a peak acceleration of about 0.02g in both surface (0-40 sec) and body wave (about 40-80 sec) phases.

Another procedure for computing ground strains is to consider the triangular region of ground defined by the three seismographs (triangle ABC in Fig. 3) to deform with constaWhen horizontal components of ground displacements are imposed on vertices of a triangular, constant strain finite element having vertices at the locations of the instruments values of strain components can be computed. Typical pipeline strains are shown in Fig. 4, 5. The pipeline strain records do not start at the same time as the ground motion and ground strain records because the permanent memories of their respective recording devices are triggered by different quantities.

In Fig. 4a, strain-time history records from both sides of station -15 on the compression segment are shown. Also shown to the same time and strain amplitude scale is the time history of the ground strain component parallel to the compression segment axis. In Fig. 4b, similar data from station +30 of the compression segment are shown together with the same ground strain component as in Fig. 4a. A similar ensemble of records is shown in Fig. 5a for pipe strains at station -15 of the tension segment, and in Fig. 5b for pipe strains at station +30 of the tension

segment. Also shown in Fig. 5a,b is the component of ground strain parallel to the tension segment axis. These figures illustrate the following points:

1. The pipeline strains are not recorded during the interval dominated by body waves (0-34 sec, approximately). They are recorded during the surface wave phase (34-120 sec).

2. The pipeline strains on opposite sides of a diameter are approximately equal. This shows that, at least in the horizontal plane, direct extension or compression dominates and bending is less significant.

3. The frequency content of the direct ground strain and of the pipe strain-time histories agree closely. In the interval between 34 and 50 seconds, the ground and pipe strains are nearly the same at a number of stations with peaks and valleys of the same amplitude occurring almost simultaneously.

4. There is a shift in the amplitude of the pipe strain-time history records that appears to occur between 40 and 50 seconds. The shift corresponds to the development of a permanent strain in the pipe segments. The shift is tensile in the tension segment and compressive in the compression segment. There is no corresponding shift in the ground strain-time histories derived from accelerograph records.

5. If the permanent component of ground strain were to be removed from the time histories of pipeline strains shown in Figs. 4,5, the ground and pipe strain components would be nearly equal. This is a point in favor of pipe-soil interaction models that assume transient ground strain is transmitted to pipelines without significant reduction due to slip or pipe-soil interaction.

CONCLUSIONS

At the Owens' Pasture site near Parkfield, CA, about 175 km from the Loma Prieta epicenter, the surface wave phase caused peak accelerations of about 20 gal. and maximum transient ground strains of about 50-100 microstrain in directions parallel and perpendicular to the axes of buried, welded steel pipe segments. Longitudinal strains of about the same magnitude, sense and frequency were observed in the pipes. These data suggest that, for low amplitude shaking, negligible slip occurs between the soil and pipeline. It follows that, in analytical models, the ground strain and pipeline strain can be assumed to be equal under the conditions prevailing here. This conclusion may need to be significantly modified when data from the predicted Parkfield-Cholame earthquake becomes available. Residual strains in the pipeline segments correlate closely with coseismic creep. However, the strains are not concentrated at any point on the pipeline segments but are distributed roughly uniformly along the segments. This suggests that the soil-pipe interface shear stress is approximately constant along the length of each segment and that the strains are dominated by the relative displacements of the end anchors.

ACKNOWLEDGEMENT

APPENDIX I. REFERENCES

1. Burford, Sandra (1989). Geologist, USGS. Personal communication addressed to E. Richardson.

2. Datta, S. K., Shah A. H., and El-Akily, N. (1982). "Dynamic Behavior of a Buried Pipe in a Seismic Environment." J. of Applied Mechanics, Trans. ASME, 49, 141-148.

3. Isenberg, J., Richardson, E. and O'Rourke, T. D. (1989). "Experiment on Performance of Buried Pipelines Across San Andreas Fault." Technical Report NCEER-89-0005, Weidlinger Associates.

4. Isenberg, J., Richardson, E. and O'Rourke, T. D. (1988). "Buried Pipelines Across San Andreas Fault." 9th World Conf. on Earthquake Engineering, Tokyo-Kyoto.

5. Kawashima, K. (1987). Public Works Research Institute, Ministry of Construction, Government of Japan. Private communication.

6. Kennedy, R. P., Chow, A. W. and Williamson, R. A. (1977). "Fault Movement Effects on Buried Oil Pipelines. "J. of the Transportation Engineering Div. Proc. ASCE, 103.

7. Kuesel, T. R. (1969) "Earthquake Design Criteria for Subways." J. of the Structural Div. Proc. ASCE, 95(ST6), 1212-1231.

8. Newmark, N. M. and Hall, W. J. (1975). "Pipeline Design to Resist Large Fault Displacement." Proc. U.S. National Conf. on Earthquake Engineering, Ann Arbor, Michigan.

9. O'Rourke, M. J., Castro, G. and Hossain, I. (1984). "Horizontal Soil Strain Due to Seismic Waves," J. of Geotechnical Eng., 110(9), 1173-1187.

10. O'Rourke, T. D. (1988). "Evaluation of Pipeline and Soil-Pipe Interface Shear Characteristics for the Owens' Pasture Test Site." Report No. 88-WEID-April 1988.

11. Shinozuka, M. and Koike, T. (1979) "Estimation of Structural Strains in Underground Lifeline Pipes." Technical Report No. NSF-PFR-78-15049-CU-4, Dept. of Civil Engineering and Engineering Mechanics, Columbia University.

12. Shinozuka, M., Tan, R. Y. and Koike, T. (1981). "Serviceability of Water Transmission Systems Under Seismic Risk." Proc. of the 2nd Specialty Conf. of the Tech. Council on Lifeline Earthquake Eng. ASCE.

13. Takada, S. (1983). "Experimental Study on Mechanical Behavior of PVC Pipelines Subjected to Ground Subsidence." Proc. of the 4th National Congress on Pressure Vessel and Piping Technology, Earthquake Behavior and Safety of Oil and Gas Storage Facilities, Buried Pipelines and Equipment, ASME PVP 77, Portland, Oregon.

14. Trautmann, C. H. and O'Rourke, T. D. (1983). "Load-Displacement Characteristics of A Buried Pipe Affected by Permanent Earthquake Ground Movements." Proc. of the 4th National Congress on Pressure Vessel and Piping Technology, Earthquake Behavior and Safety of Oil and Gas Storage Facilities, Buried Pipelines and Equipment, ASME PVP 77, Portland, Oregon.

15. Wang, L. R-L, (1983). "Role and Development of Soil Parameters for Seismic Response of Buried Lifelines." Proc. of the 4th National Congress on Pressure Vessel and Piping Technology, <u>Earthquake Behavior and Safety of Oil and Gas Storage Facilities, Buried Pipelines and Equipment</u>, ASME PVP 77, Portland, Oregon.

16. Wilmesher, J. F. (1988). Geologist, USGS. Personal communication addressed to E. Richardson.

Appendix II. Notation

The following symbols are used in this paper:

A = displacement due to wave propagation

c = phase velocity

d_f = relative displacement across a fault offset

e = ground strain component in direction of particle velocity

ℓ = projection of wave length along axis of a pipe segment

L = wave length

R_c = radius of curvature

t = time

U = $A \sin\left[\dfrac{2\pi x'}{L}\right]$

v = particle velocity

ε_{yy} = extensional strain in soil normal to a pipe segment

ε_{xx} = extensional strain in soil parallel to a pipe segment

γ_{xy} = shear strain (engineering) in soil
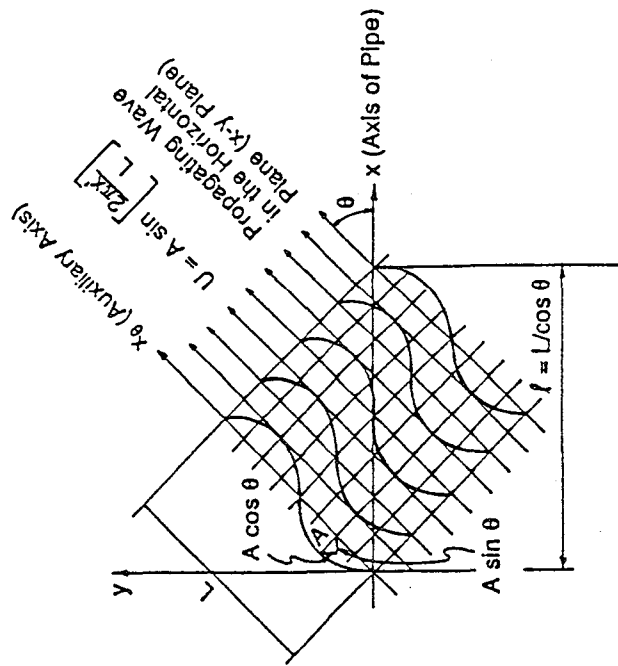
Axial Displacement (In x - Direction)

Displacement: $U_A = A \sin \theta \cdot \sin \left[\dfrac{2\pi \cos \theta \cdot x}{L} \right]$

Strain: $\dfrac{dU_A}{dx} = \dfrac{2\pi A}{L} \sin \theta \cdot \cos \theta \cos \left[\dfrac{2\pi \cos \theta \, x}{L} \right]$

Transverse Displacement (In y - Direction)

Displacement: $U_r = A \cos \theta \cdot \sin \left[\dfrac{2\pi \cos \theta}{L} \, x \right]$

Curvature: $\varnothing = \dfrac{d^2 U_r}{dx^2} = \dfrac{-4\pi^2}{L^2} A \cos^3 \theta \cdot \sin \left[\dfrac{2\pi \cos \theta \, x}{L} \right]$

Figure 2. Pipeline response to traveling waves.
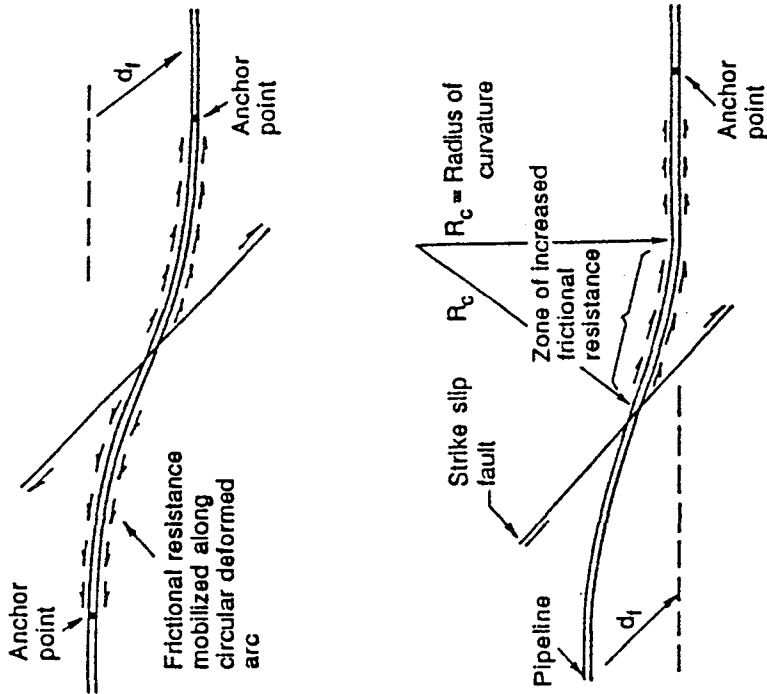
Figure 1. Pipeline response to lateral offset (d$_f$)

170
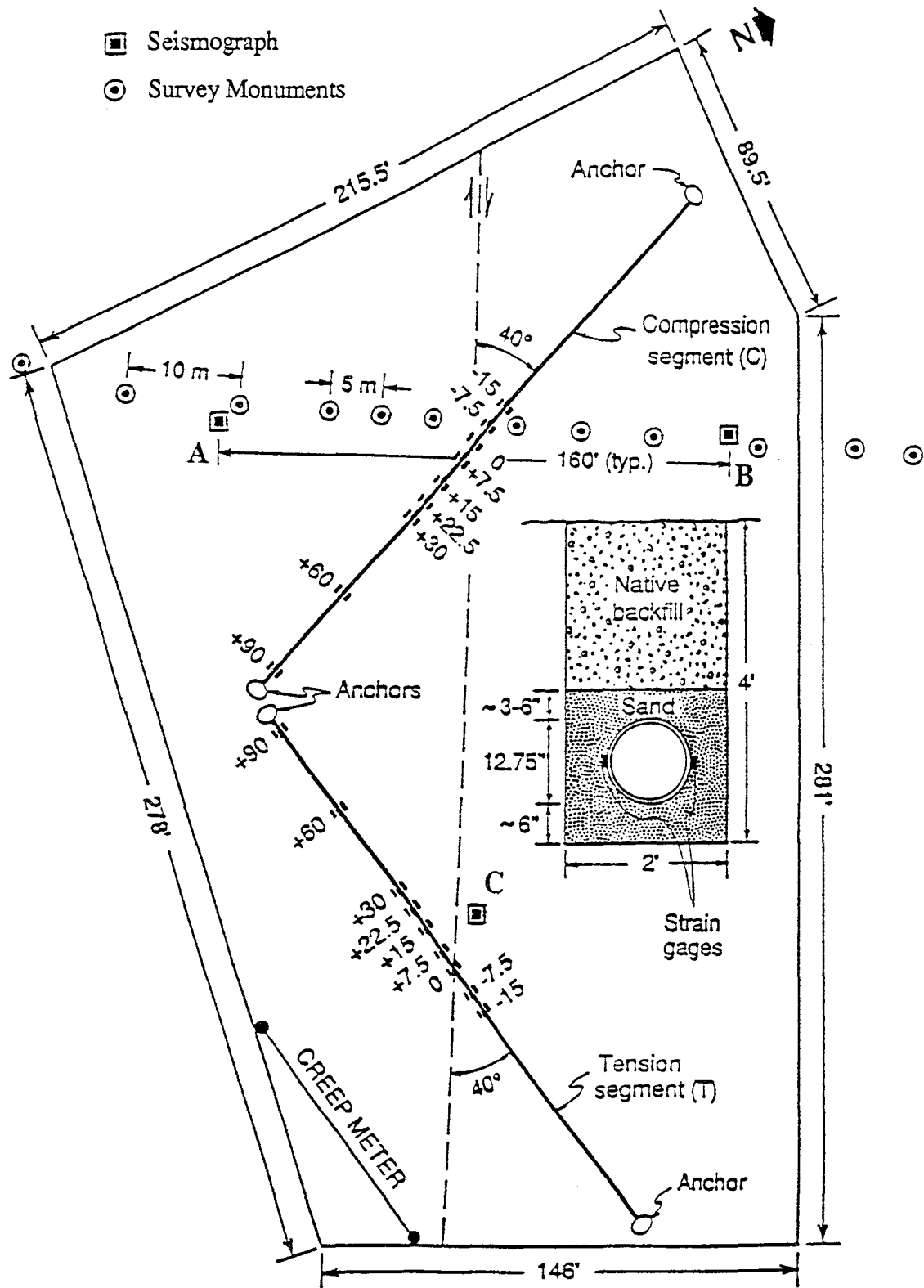
Figure 3. Orientation and strain gage locations, welded steel pipe segments.
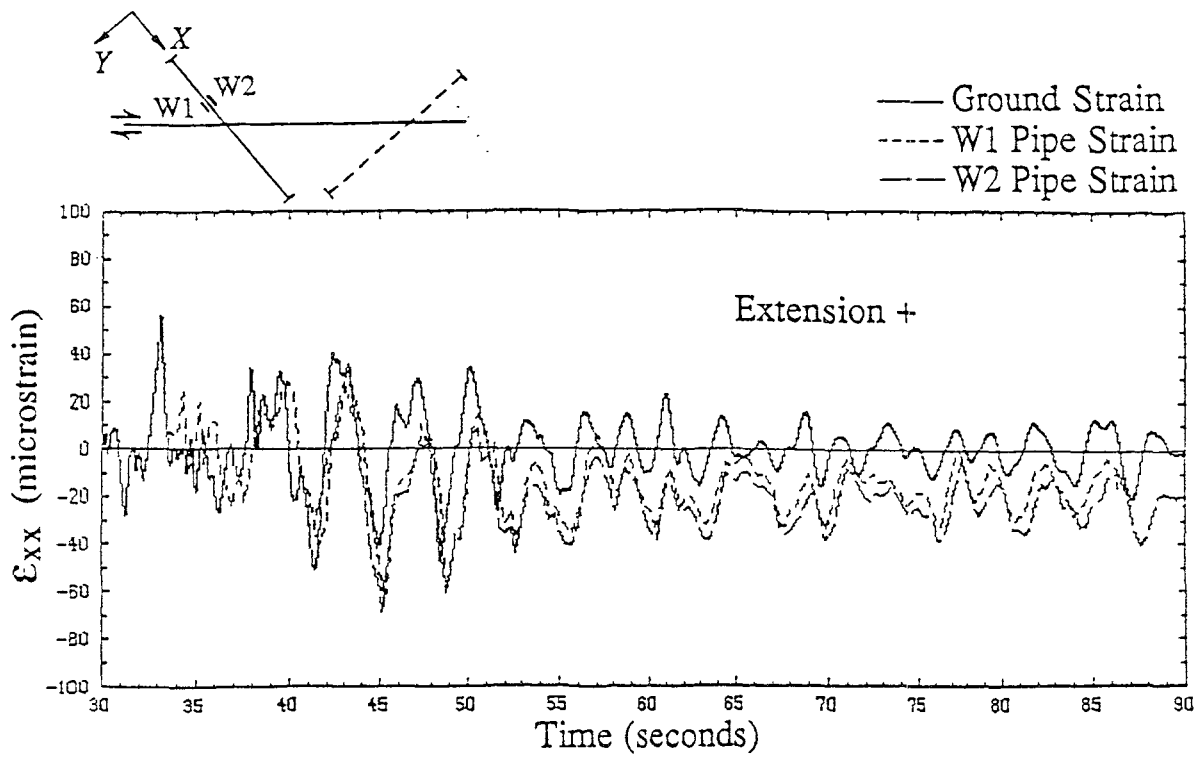
a. Station -15, compression line.
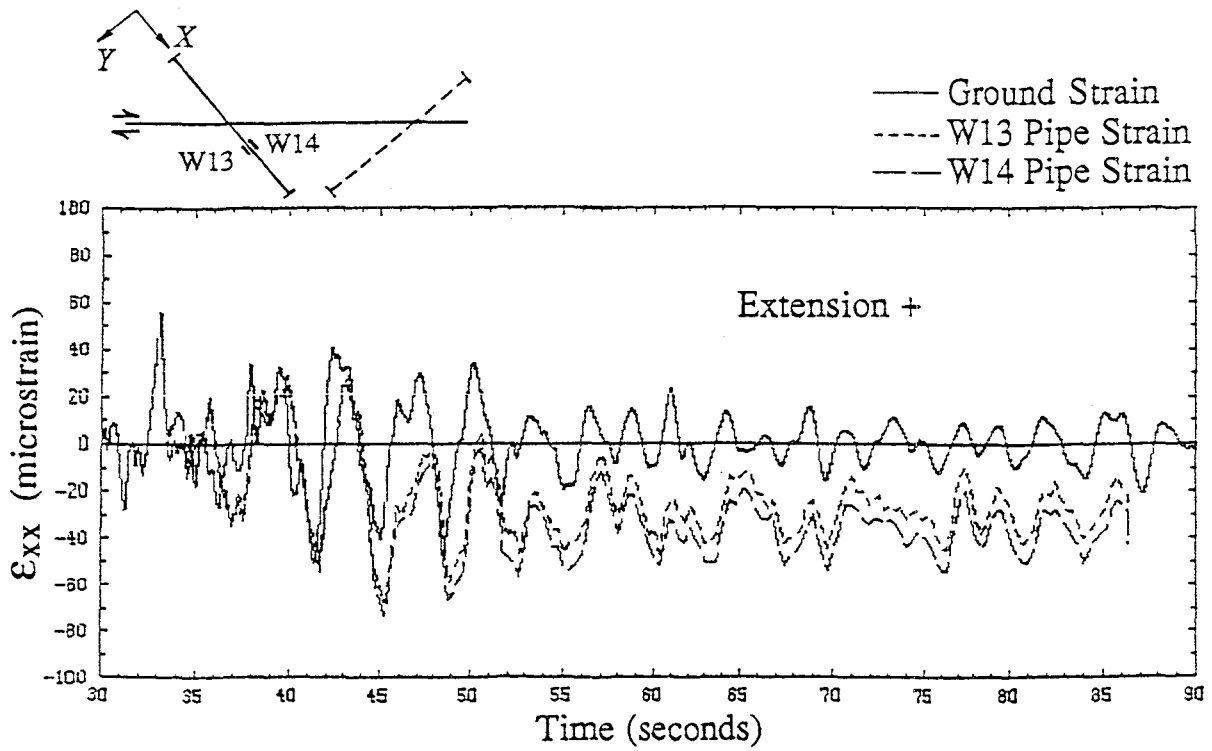
b. Station +30, Compression line.

Figure 4. Ground and pipe strain-time histories, compression segment.

172
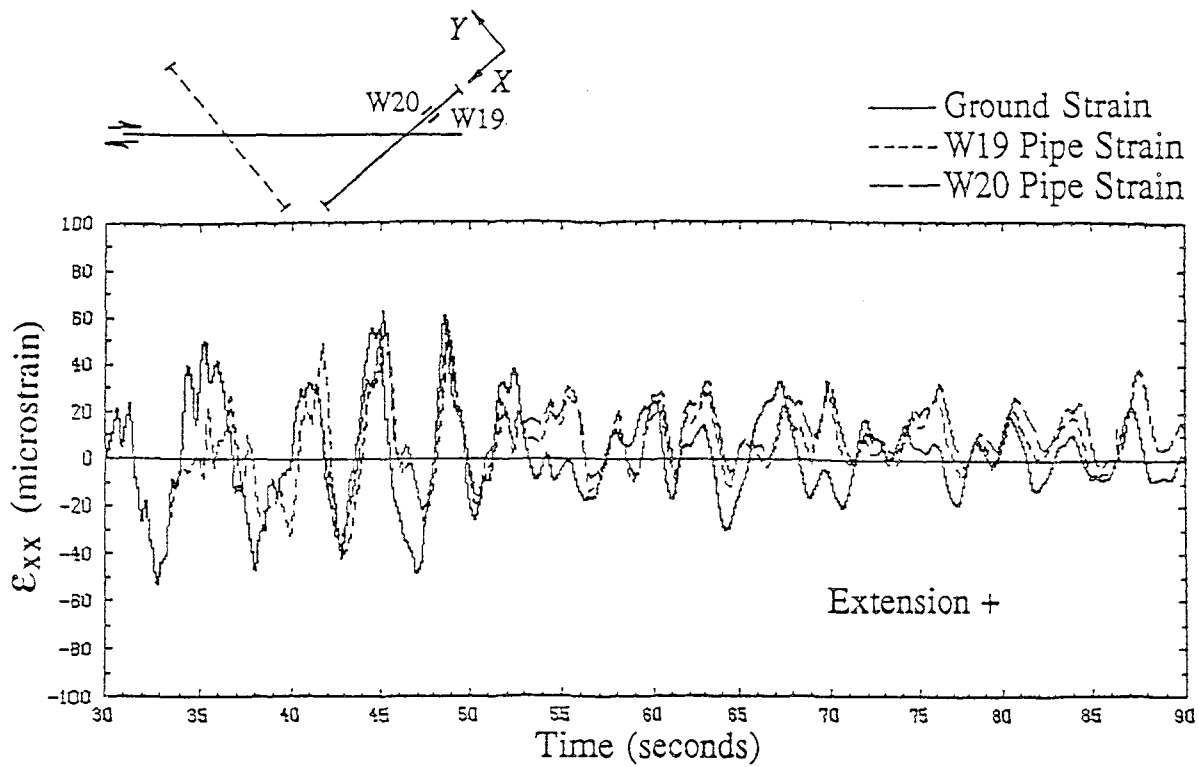
a. Station -15, tension line.
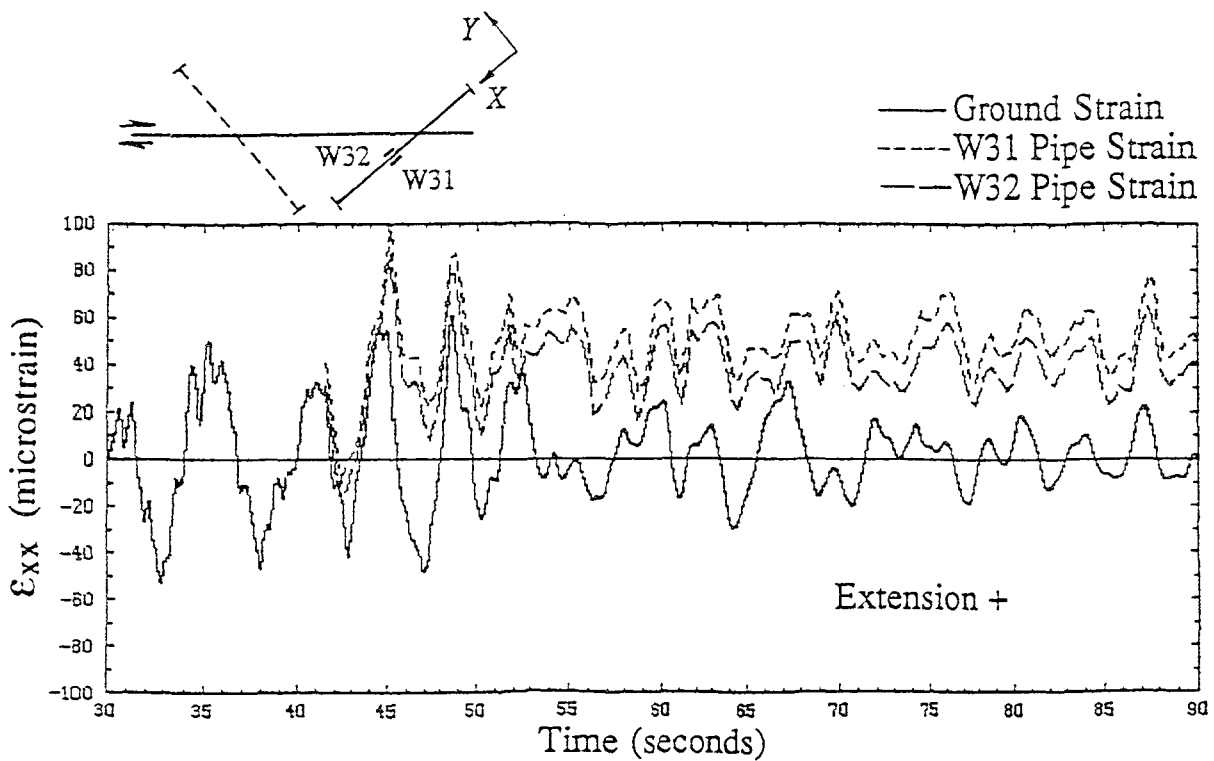
b. Station +30, tension line.

Figure 5. Ground and pipe strain-time histories, tension segment.

CASE HISTORIES OF LATERAL SPREADS FROM THE 1964 ALASKA EARTHQUAKE

T. Leslie Youd[1] and Steven F. Bartlett[2]

[1]Professor of Civil Engineering
[2]Research Assistant
Brigham Young University

ABSTRACT

The 1964 Alaska earthquake (M_w = 9.2) caused severe damage to railway and highway bridges as a consequence of liquefaction-induced lateral spread. We compiled geotechnical, topographic, damage and displacement information for bridge sites in the Matanuska Valley, near Portage, across Snow River, and across the Resurrection River. Analyses and comparisons of this information yields the following general findings. Sediment and slope conditions are generally similar in the Matanuska Valley and near Portage; ground displacements, however, were much greater near Portage (3 m to 4 m versus 0.3 m to 0.6 m). The greater peak acceleration near Portage (0.3 g versus 0.2 g) apparently lead to the greater displacement. About 2.4 m of lateral displacement occurred at the Snow River crossing on a slope of only 0.1 percent. A very deep section (about 30 m) apparently contributed tho this large displacement. Down-river displacements of unattached bridge piers were as great as 0.6 m in the Matanuska Valley on a slope of about 0.5 percent, and 2.4 m or more down a slope of 0.1 percent at the Snow River. These slopes are much smaller than the 0.3 percent minimum noted from prior investigations. Thus, during large magnitude earthquakes, lateral spreads on highly susceptible materials may undergo considerable displacement on slopes as gentle as 0.05 percent. Displacements were only up to 0.7 m at the Resurrection River which was very near the seismic energy source. The apparent reason for these smaller displacements were the thinner liquefied layer (3 to 5 m) and the gravelly texture of the liquefied sediment.

INTRODUCTION

The March 27, 1964 Alaska earthquake was one of the most powerful earthquakes to strike the world this century. The main shock was assigned a magnitude of 8.3 to 8.4 on the M_L scale and 9.2 on the M_w scale (Hansen and others, 1966; Kanamori, 1978). Fault rupture began beneath the Chugach Mountains with an epicenter near the northern end of Prince William Sound about 130 km east-southeast of Anchorage (McCulloch and Bonilla, 1970). The rupture propagated primarily southwestward creating a zone of tectonic deformation 550 km long and 400 km wide that encompassed all of Prince William Sound and Kodiak Island. Seismologists suggest that the primary source of seismic energy was roughly coincident with the zone of crustal uplift which occupied the southern part of the zone of tectonic deformation (George Plafker, US Geological Survey, oral communication, 1977).

Seismic energy released from this large rupture zone propagated a train of earthquake waves that caused long and intense ground shaking over a large part of south-central Alaska. Three to four minutes of moderate to severe ground shaking affected 50,000 to 75,000 square miles surrounding the deformation zone (Hansen and others 1966, Housner and Jennings, 1973). Fortunately, most of the stricken region was sparsely populated, lessening loss of life and property. Nonetheless, the earthquake had enormous social and economic impact to the residents of Alaska including 114 casualties. Public and private property losses were estimated at $311 million (1964 value). Lifelines including the transportation system were disrupted for months following the event (Hansen and others, 1966).
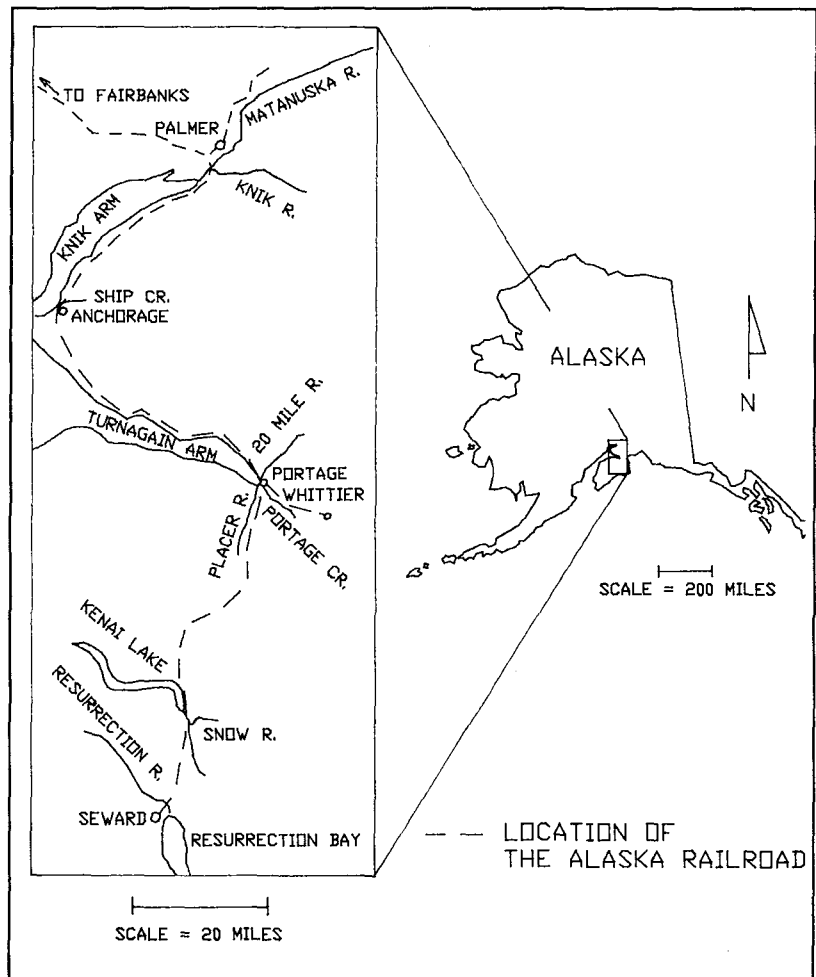
Figure 1 Map of south-central Alaska showing route of Alaska Railroad and localities investigated.

The intense shaking triggered numerous destructive ground failures including flow failures, lateral spreads and landslides. Several large landslides devastated parts of Anchorage destroying lifelines and buildings in that community. Communities such as Cordova, Homer, Kodiak, Seward, Valdez and Whittier suffered severe damage to port and coastline facilities from liquefaction-induced flow failures, tsunamis and costal subsidence.

Lateral spreads were particularly destructive to highway and railroad bridges within a 130 km radius of the zone of energy release. Ninety-two highway bridges were severely damaged or destroyed. Another 49 highway bridges received moderate to light damage. Total damage to the highway system was $46 million (1964 value), $25 million was incurred by highway bridges and $21 million by roadways (Kachadoorian, 1968). Approximately 75 railroad bridges were moderately to severely damaged. Estimated cost to repair damaged railroad facilities approached $35 million (1964 value); 25 percent of that total for reconstruction of embankment and tracks and 7 percent to repair railroad bridges and culverts (McCulloch and Bonilla, 1970).

176

This report summarizes findings of a case-history study (Bartlett and Youd, in press) of lateral spread damage to railroad and highway bridges on the Knik, Matanuska, Twentymile, Placer, Snow and Resurrection Rivers and Portage Creek (figure 1). To understand and analyze seismic, geological, topographical and soil conditions contributing to ground displacement and damage, we 1) estimate the duration and amplitude of strong motion at the damaged bridges, 2) describe the type of damage and estimate the amount of horizontal ground displacement occurring at each bridge, 3) summarize available borehole data and discuss local geologic conditions, 3) present topographical maps and channel cross-sections from surveys completed at the damaged bridges and 4) evaluate liquefaction susceptibility of the foundation soil by analyzing standard penetration and grain-size distribution data.

LATERAL SPREADS

Liquefaction-induced lateral spreads during the 1964 Alaska earthquake shifted floodplain deposits toward stream channels at many localities reducing channel widths by as much as 2 m. Ground fissures generally developed parallel to the river banks at lateral spread localities. At some sites, fissures formed as far as 300 m from river banks (McCulloch and Bonilla, 1970). In most instances, the major component of lateral-spread displacement was into the river; at some bridge crossings, however, down stream movement also occurred. At several bridges, piles in the middle of the channel rose relative to those near the bank, indicating that channelward movement was accompanied by upwelling of material within the channel (McCulloch and Bonilla, 1970).

Compressive forces from channel narrowing arched, buckled or jack-knifed many railroad bridge decks, leaving the rail bent and unusable. In several instances, simply-supported concrete highway bridge decks collapsed onto the river bottom due to differential movement between support piers. Many bridge abutments were tilted as the base moved channelward while the top remained fixed to the bridge deck and stayed nearly in place. Streamward displacement of railroad bridge abutments and bulkheads commonly fractured wooden deck stringers leaving those members splintered and broken. In some instances, the stringers were driven up and over the bulkheads in order to accommodate channel compression (McCulloch and Bonilla, 1970).

INVESTIGATION

To estimate ground displacements at lateral spread sites, we reviewed reports of bridge damage, taking special note of reported relative displacements in damage bridge sections. The reports on the Alaska Railroad by McCulloch and Bonilla (1970) and by Ross and others (1970) on highway bridges were particularly useful in providing measurements from which ground displacements could be derived.

To investigate subsurface soil conditions, we acquired soil logs from the Alaska Department of Transportation. These reports contained bore-hole logs displaying standard penetration resistance, grain-size data and soil classifications. The Alaska Division of Geology and Geophysics also provided logs showing standard penetration and cone penetration resistance from sites near Portage.
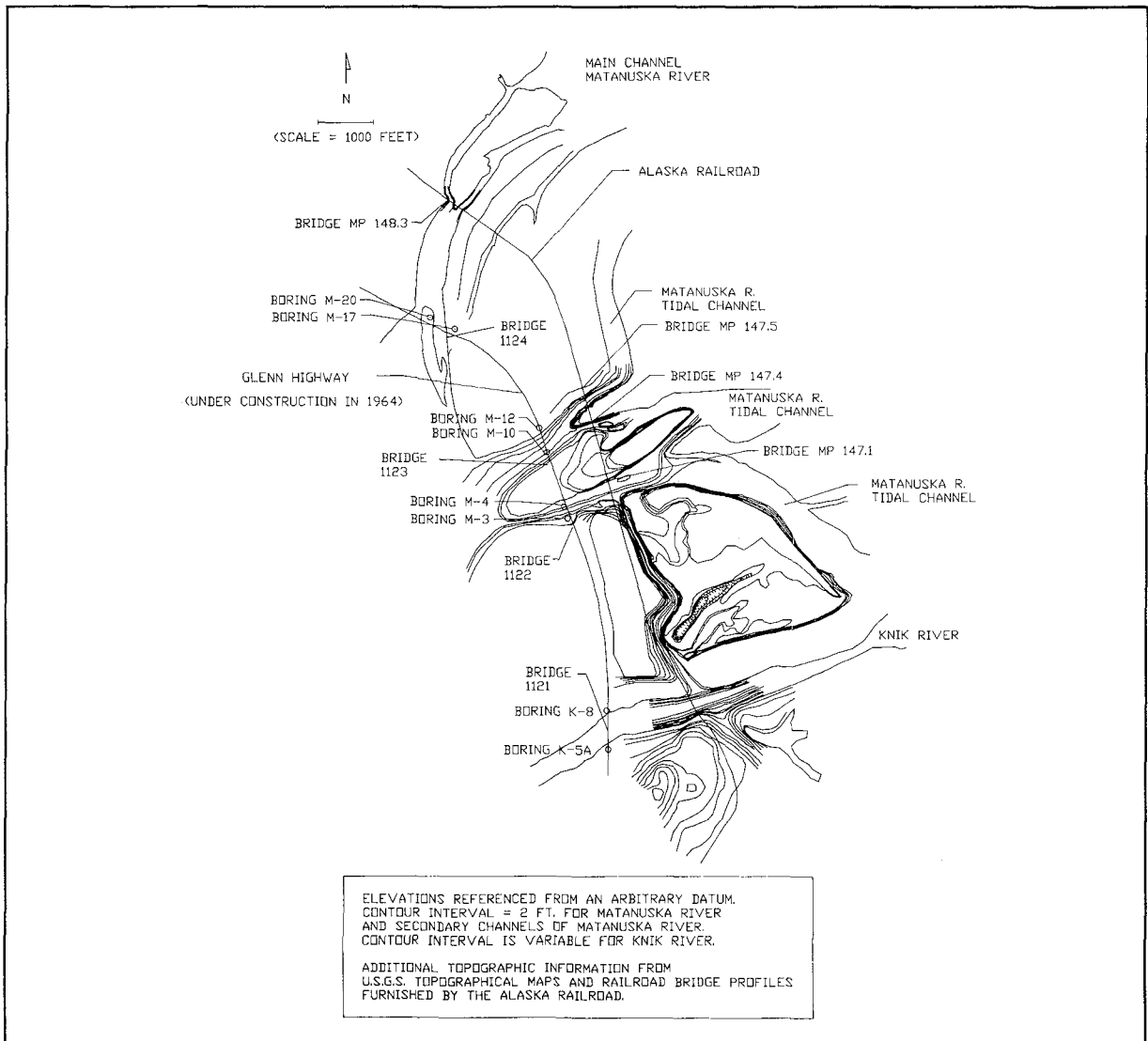
Figure 2 Map of lower Matanuska Valley area showing bridge and borehole locations.

Existing topographical surveys and maps were not generally at a sufficient scale to allow adequate definition of ground slope, channel depth and downstream gradient for scientific evaluation of ground displacement. To improve the topographic data base, we surveyed nearly all of the bridge sites to compile more detailed cross-sectional profiles and localized topographic maps with sufficient detail for our investigation. We also collected design cross sections and maps from the Alaska Railroad and the Alaska Department of Transportation to supplement our survey data.

Pertinent displacement, geotechnical, topographic data are presented in a report by Bartlett and Youd (in press) that is to be published in the Case History volume for the US-Japan cooperative research program on liquefaction, large ground deformation and their effects on lifelines.

178

BRIDGES IN THE MATANUSKA VALLEY

Approximately 50 km northeast of Anchorage and a few kilometers east of the northern end of the Knik Arm of Cook Inlet, the Alaska Railroad and Glenn Highway turn northward and cross the Knik and Matanuska Rivers which jointly occupy the lower Matanuska Valley at this location (Fig. 1). The area lies approximately 100 km northwest of the zone of seismic energy release and marks the farthest and northernmost locality of significant damage due to liquefaction. Five railroad and 4 highway bridges cross various channels of these rivers; the bridges suffered varying amounts of displacement and damage during the 1964 earthquake.

At this locality, the westward flowing Knik River leaves the Chugach Mountains and joins the southwesterly flowing Matanuska River to form a broad floodplain at the head of the Knik Arm. At the railroad and highway crossing, the two rivers are separated by about a 1-km width of lowland (Fig. 2). Utermohle (1963) reports that the Matanuska Valley has been heavily glaciated and in its lower reaches, the valley is primarily underlain by glacial outwash and glacial drift. In addition, fluvial and tidal processes have reworked the glacial sediment forming a thick sequence of fluvial, deltaic and estuarine sediments. The present river systems meander back and forth across the lowland dissecting the surface into braided stream beds separated by 2.5-m to 3.5-m high flat-topped islands of glacial outwash (McCulloch and Bonilla, 1970).

Foundation investigations for bridges on the Glenn Highway show an upper stratum of Holocene glacial outwash sediment 15 m to 24 m thick underlain older and finer-grained lacustrine or estuarine sediment. (Foundation reports are not available for railroad bridges at this locality or at the other railroad bridge sites that we studied.) The upper stratum consists of interbedded layers of riverine and glacial-outwash sands and gravels with sporadic thin layers of sand and silt (McCulloch and Bonilla, 1970; Utermohle, 1963). The lower stratum consist of 0.3-m to 1-m thick beds of fine sand and silt.

We estimated the thickness of liquefied layers generated by the 1964 earthquake by applying the simplified procedure as updated by Seed and others (1985). For this site, we estimated a peak acceleration of 0.21 g at ground surface (and a duration of strong shaking of about 75 sec). We used N-values, measured by the standard penetration test, as an indicator of liquefaction resistance of the subsurface sediment. We analyzed standard penetration results from eight boreholes that were drilled during foundation investigations for the four highway bridges crossing the Knik and Matanuska Rivers. Fig. 3 is a composite plot of N-values from these eight borings versus depth along with a curve providing an N-value bound beyond which liquefaction would not have been expected to occur during the 1964 earthquake. This plot shows that the sediment was generally liquefiable to a depth of about 5 m, partially liquefiable to a depth of about 20 m, and nonliquefiable below that level. More detail on the liquefaction analysis is given by Bartlett and Youd (in press).

Lateral displacement of railroad bridge peers int the Matanuska Valley were typically about 0.3 m toward the channel and 0.3 m downstream. These displacements caused slight to moderate damage to the 5 railroad bridges. Lateral spreads also shifted highway bridge piers that were under construction at the time of the earthquake as much as 0.6 m downstream. In the latter instance, the down slope gradient was only about 0.05 percent. One isolated and particularly susceptible point-bar deposit shifted about 1.3 m toward a nearby river channel.

The following information for the railroad bridge at milepost 147.5 illustrates the types of data we collected and the analyses we performed in the compilation of lateral spread case histories for the 1964 Alaska earthquake. That bridge crosses a secondary channel of the Matanuska River and is one of nine bridges in the area for which we compiled case-history information.

Railroad Bridge at Milepost 147.5

The 200-m long bridge at milepost 147.5 is composed 10 simply supported steel-girders resting on concrete piers (McCulloch and Bonilla, 1970). McCulloch and Bonilla report the following damage and displacements at the bridge:

Figure 3 Composite plot of standard penetration N-values from eight borings near highway bridges in the lower Matanuska Valley.

[The] piers and abutments were jammed streamward against the central spans. Piers and abutments were also displaced horizontally; the
north abutment and pier shifted about 1 foot [0.3 m] west [downstream] and the third pier [from the north] moved about 1 foot [0.3 m] south, toward the channel.

These investigators did not report displacement of the south abutment or piers. During our field inspection of the bridge, we found that the two steel base plates, through which girders bear on the pier caps, had been shifted several centimeters and reset during post-earthquake repairs. Apparently the piers moved with the ground during the earthquake and the resetting was required to realign the bridge to its pre-earthquake position. Similar resetting of base plates had occurred on piers of other bridges. By comparing the pre- and post-earthquake base plate sets (Fig. 4), we estimate that the southernmost pier of the bridge shifted approximately 0.10 m northward toward the channel and about 0.16 m westward in a downstream direction.

Our survey of the area showed that slopes in the vicinity of Bridge 147.5 are very gentle. The river beneath the bridge flows westward down a gradient of 0.04 to 0.06 percent. Slopes of floodplains at the highway bridge, 300 m west of Bridge 147.5, are 0.3 percent to the south on the north side of the river and, due to a natural levee in the area, about 0.1 percent to the south on the south side of the river. An approximate 1 m to 2 m incision of the river into the flood plain provided additional gradient for ground displacement. Slopes and topography at the railroad bridge are approximately the same as at the highway crossing. Liquefaction susceptibility of

subsurface materials was determined from borehole data reported in foundation investigations for the highway bridges. Bore hole M-12 is located near the Glen Highway bridge approximately 300 m west of Railroad Bridge 147.5. The upper 19 m of sediment is composed of layered sand and gravel. Below 20 m, the sediment is chiefly alternating layers of silty sand and silt (see profile and grain-size data shown in Fig. 5).

Application of the simplified procedure reveals that most materials in the upper 10 m of are susceptible to liquefaction (Fig. 5). N-values in the liquefiable zone range from 2 to 18 with and average of 11. Below 10 m, N increased sufficiently to render that part of the profile immune to liquefaction.
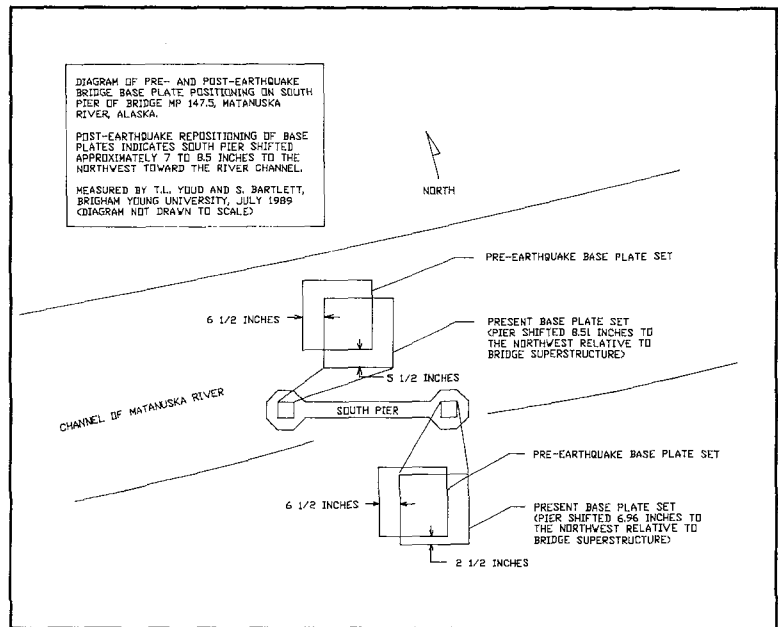
Figure 4 Pre- and post-earthquake positions of base plates revealing displacement of southern pier of railroad bridge 147.5.

BRIDGES NEAR PORTAGE

At the southern end of the Turnagain Arm of Cook Inlet, both the Alaska Railroad and the Seward highway cross the floodplains of the Placer and Twentymile Rivers and Portage Creek (Fig. 1). Like the Matanuska Valley, the Turnagain Arm is a glacially carved trough where glacially fed braided rivers and streams meet the ocean. Heavy sediment loads carried by the rivers and the tidal action of the sea have formed a broad alluvial and tidal flat at the head of the Arm. The annual tidal range in the arm is about 40 feet.

The floodplains of the Twentymile River, Portage Creek and the Placer River coalesce at the southeastern edge of Turnagain Arm to form a broad flat tidal and flood plain dissected by sloughs and secondary channels. The floodplain is relatively flat with low topographical relief; the highest parts of the plain lie only 6 m above high tide (McCulloch and Bonilla, 1970). At high tide, sea water fills the sloughs and river beds near and beneath the bridges.

The steepness of the valley walls bordering the arm suggests that bedrock lies at considerable depth beneath the valley floor. This great depth is confirmed by two water wells drilled at Portage that penetrated unconsolidated sediment to depths as great as 200 m without reaching bedrock. The general sediment profile for areas near the highway and railroad bridges is as follows: The upper 3 m generally consists of estuarine silty sands and sandy silts that have generally been deposited since the 1964 earthquake. (Subsidence in the Portage area was about 3 m due to both tectonic warping and sediment compaction. Sedimentation since 1964
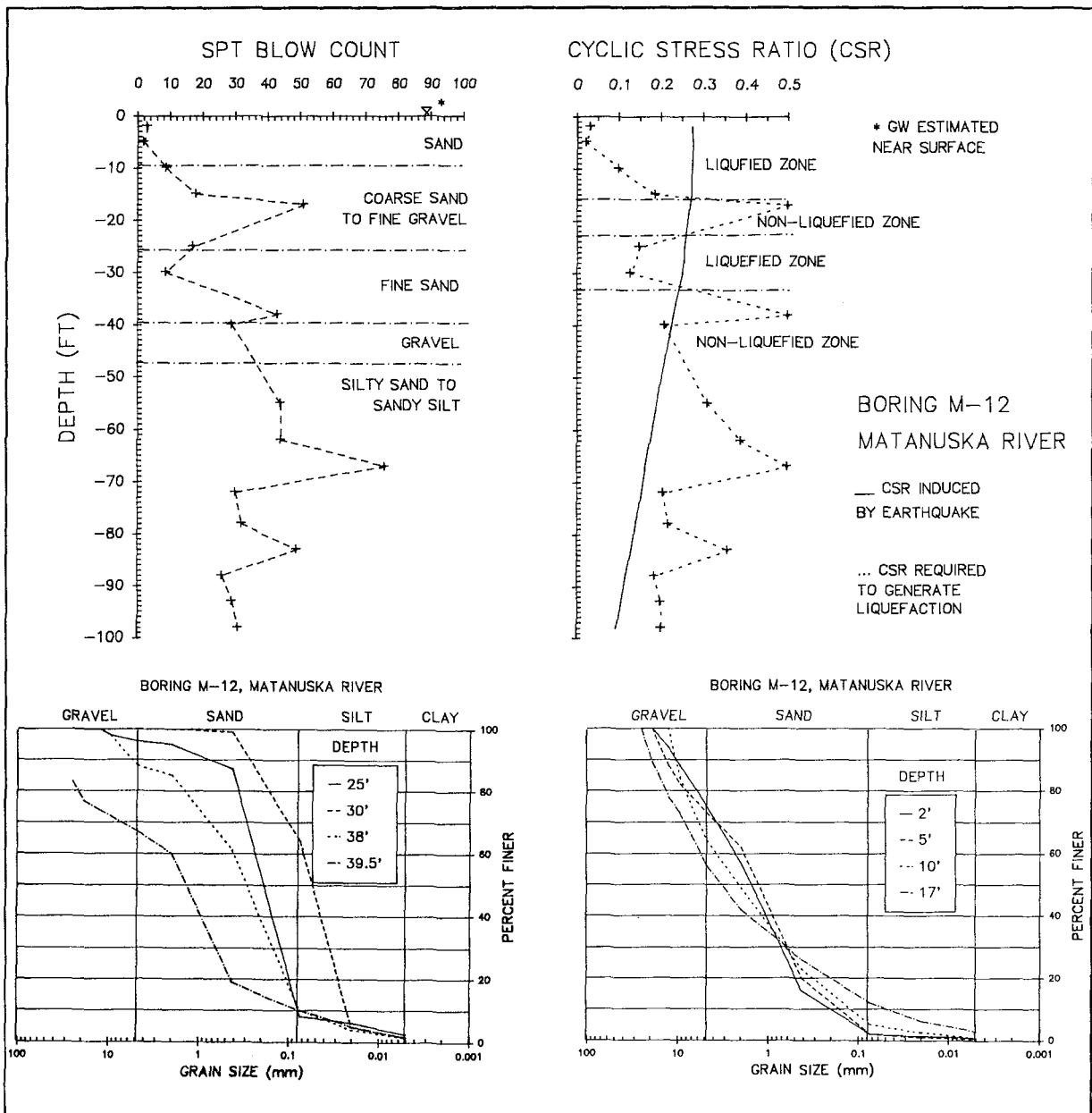
Figure 5 Log and liquefaction analysis for Borehole M-12 drilled near Highway Bridge 1122 and about 300 m downstream from the railroad bridge 147.5, Matanuska Valley.

has returned the ground surface approximately to its pre-earthquake level.) From 3 m to 10 m, the sediment generally consists of sandy gravels or gravely sands with varying amounts of silt. From about 10 m to the deepest penetration during foundation investigations, the sediment consists of layered strata of silty sands and sandy silts, apparently of estuarine origin. The water-table is close to the surface throughout most of the area. Kachadoorian reported that groundwater was within generally 0.6 m of ground surface at the time of the 1964 earthquake (Kachadoorian, 1968).

At bridge sites, liquefaction-induced lateral spread displacement toward river channels ranged up to 3 m, and up to 2 m of channel closure was common. In addition, downstream displacements of abutments and piers ranged up to 0.3 m.

Damage to railroad and highway bridges along the southern end of Turnagain Arm was extensive. McCulloch and Bonilla (1970) reported that 15 of the 17 railroad bridges in the area were open wood trestles on wooden piles. Most of these bridges were severely damaged and four were damaged beyond repair. Highway bridges were even more severely damaged. All of the 15 highway bridges in the area were severely damaged and several of the structures collapsed (Kachadoorian, 1968).

An analyses of reported standard penetration data, plotted as a composite on Fig. 7, shows that the sediment is generally liquefiable to a depth of 5 m. Below 5 m, only part of the sediment is liquefiable and that part decreases with depth so that below about 17 m the sediment was probably nonliquefiable. Seismic parameters estimated for the 1964 earthquake in the Portage area include a peak acceleration of 0.31 g with an estimated duration of about 75 sec. Liquefaction analyses for each bridge site are given by Bartlett and Youd (in press).

Lateral displacements near Portage (2 m to 3 m) were much larger than in the Matanuska Valley (0.2 m versus 0.6 m). Comparison of the data from the two localities indicates that sediment conditions, ground slopes, and duration of ground shaking were roughly similar. The one factor that is significantly different is peak acceleration. The estimated acceleration near Portage is 0.31 g, whereas that in the Matanuska Valley is 0.21 g. This comparison indicates that peak acceleration is a primary parameter controlling lateral-spread displacement.

HIGHWAY BRIDGES AT SNOW RIVER

Approximately 20 km north of Seward, the Seward-Anchorage Highway crosses the Snow River and Snow River Valley about 400 m north of the southern shore of Kenai Lake (Fig. 1). The north-south trending valley is

Base from U.S. Geological Survey
1:63,360 Seward D-6, 1965
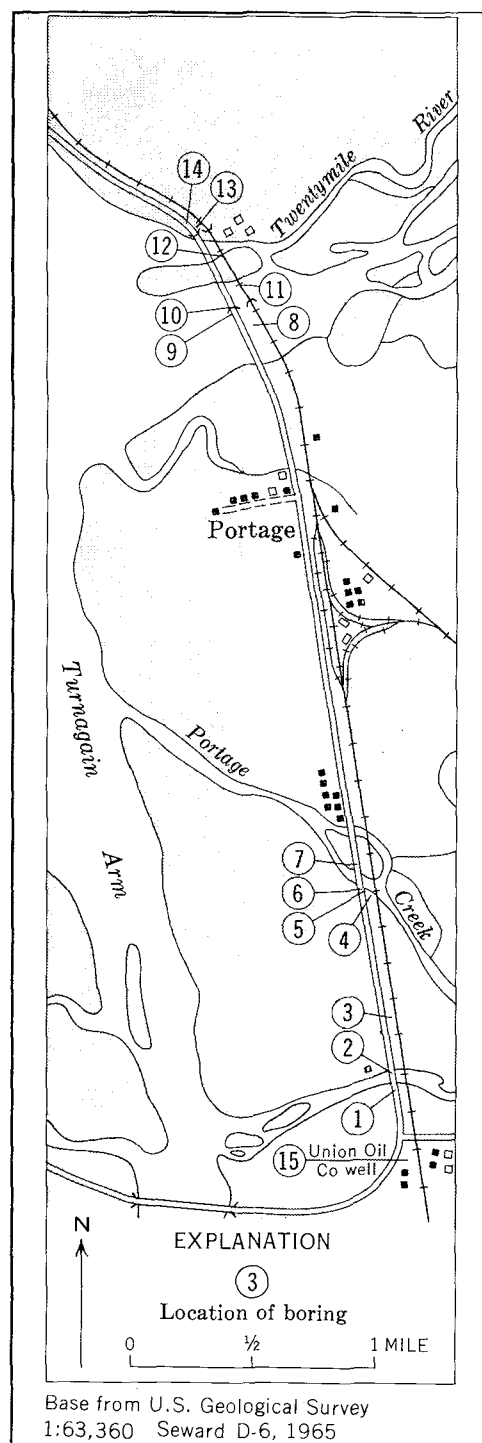
Figure 6 Map showing railroads, highways, rivers, and boreholes at the southern end of Turnagain Arm (after McCulloch and Bonilla, 1970).

183

glacially carved and filled with unconsolidated fluvial and deltaic deposits. McCulloch and Bonilla (1970) suggest that Kenai Lake once extended farther south into the valley, but rapid deposition at the mouth of the sediment laden river caused the shoreline to regress northward to its presents position. The sediments beneath the Snow River Bridge consists of up to 8 m of fluvial gravely sands underlain by lacustrine and deltaic silty sand. The deepest bore hole penetrated fine sand and silt to a depth of 52 m (Utermohle, 1962).
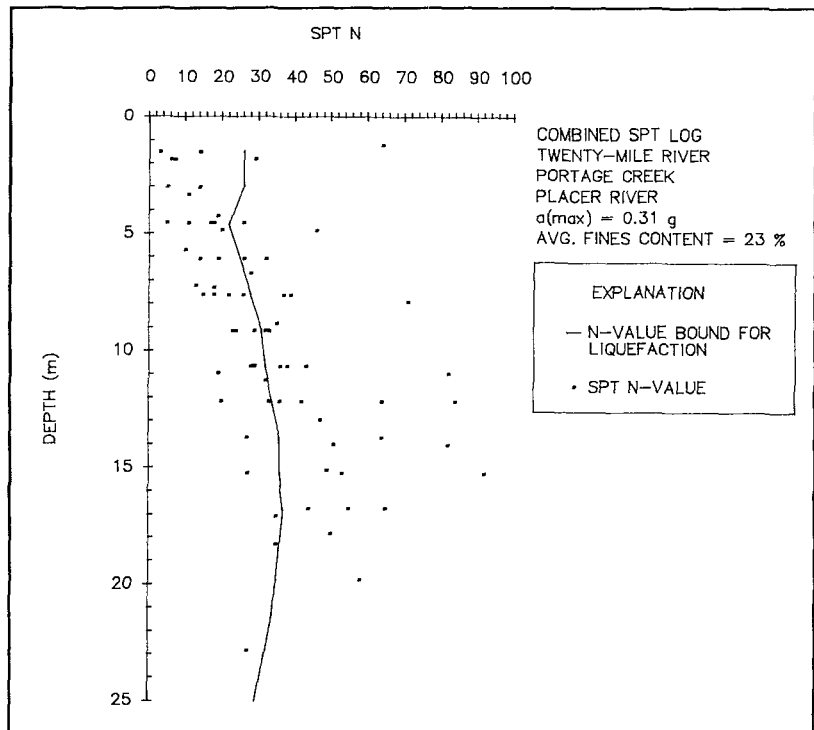
Figure 7. Composite plot of N-values versus depth for all borings near Portage.

In 1964, a construction project was in progress to replace four old low-level timber bridges with one new high-level steel and reinforced-concrete structure. The old highway bridges suffered severe damage from horizontal ground displacement and differential settlement. Kachadoorian (1968) reported damage as "severe" to Bridge 603, at the southwest edge of the valley. The bridge deck was compressed and buckled with the deck separated from the pile caps. The approach fills on both sides of the bridge subsided from 1 m to 2 m. Kachadoorian reported that the next bridge east, No. 604, was compressed by inward movement of floodplain sediment which bowed the deck upward at the middle and pulled the deck off the pile caps. The approaches settled about 1.8 m. Nearby settlements were as great as much as 3.6 m.

Highway bridge 605, at the main channel crossing, was damaged beyond repair. The third bent from north end did not settle; however, all others settled as much as 3.6 m. The 3 spans nearest the south end slightly twisted and rolled. The approach subsided about 1.8 m.

Highway bridge 606, an overpass structure which spanned the Alaska Railroad on the southeastern edge of Kenai Lake, collapsed onto the railroad tracks.

At the new highway bridge, four of six concrete piers founded on 20-m deep piles were in place at the time of the 1964 earthquake. (The new alignment was several meters downstream and paralleled to the old highway.) Liquefaction-induced ground failure displaced one of the four free standing piers at least 2.4 m downstream toward Kenai Lake (Fig. 8). The other 3 piers also displaced an unspecified amount downstream. Ross and others (1973) describe the liquefaction and ground displacement observed in the vicinity of the piers as follows:

184
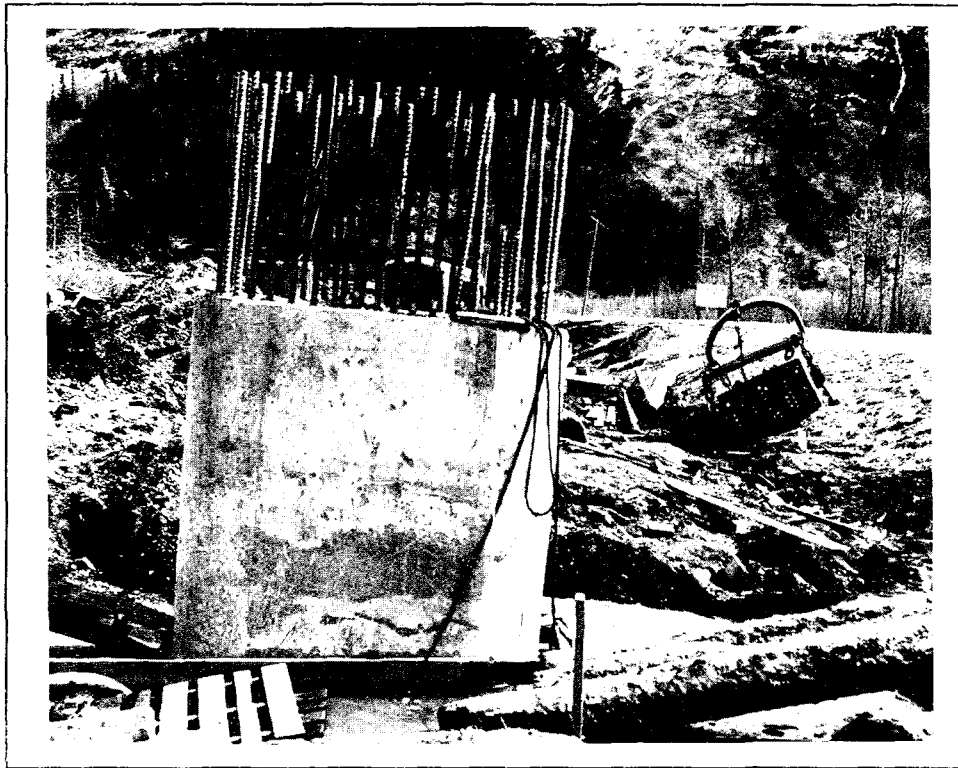
Figure 8. Displaced Highway Pier for new Snow River bridge (looking east, after McCulloch and Bonilla, 1970).

Four of the heavy concrete piers had been completed to top of shaft. These piers (each supported on 21 concrete-filled steel-tube piles, extending an average of about 30 m below adjacent streambed level) underwent tilting and lateral displacement during the earthquake. Damage surveys revealed a maximum of 2.4 m lateral displacement of the shaft tops downstream and up to 15 degrees tilt upstream. . . Longitudinal movements were less.

From comments of first hand observers and from the behavior of bridge foundations, it is clear that liquefaction of cohesionless soils did occur in this region. Reports mention that "mud" oozed up in cracks and that the 3-m high road embankment was reduced to the level of the flood plain. The preferred downstream movement of the footings and upstream tilt of the pier shafts indicates liquefaction at depth below footing level, possibly accompanied by a lakeward flow along a zone that was well below the ground surface.

These pier displacements were primarily downstream along the regional gradient of about 0.1 percent toward Kenai Lake.

A liquefaction analyses of the combined penetration data from 4 bore holes at Snow River (Fig. 8) indicates that the sediment is generally liquefiable to a depth of about 30 m. That depth is the deepest for any of the sites we studied and among the deepest of any previously documented liquefaction sites. For this analysis, we used an estimated peak acceleration of 0.4 g and

185

estimate the duration of strong ground shaking as about 90 sec. Bartlett and Youd (in press) give further detail on this analysis.

The apparent reasons for large displacements down the gentle gradient of the Snow River (about 0.1 percent) is the great depth of the liquefied layer (about 30 m), the relatively large peak acceleration (estimated at 0.4 g), and the relatively long duration of strong shaking (about 90 sec).

RAILROAD BRIDGES CROSSING THE RESURRECTION RIVER

A few kilometers north of Seward, the Alaska Railroad and Seward-Anchorage Highway cross the floodplains

Figure 9 Composite plot of N-values versus depth for all borings for bridge crossing of Snow River.

of Resurrection River and Mineral Creek (Fig. 1). Ground fissures and displacements were abundant on the Resurrection River floodplain after the earthquake. McCulloch and Bonilla (1970) describe the nature of liquefaction ground failure and consequent damage as follows:

Where the parallel highway and railroad fills passed from Jap Creek fan onto the Resurrection River floodplain, cracking between the fills was more pronounced and water was discharged along the fractures. These fractures did not seriously affect the fills. However, were the fills lay on the extensively and severely fractured active and inactive floodplain sediments along the rivers, damage increased. Minor failures occurred within the fills, but most of the damage resulted from lateral displacement and cracking of the underlying sediments. As indicated by damage to the bridges, all of which were so severely damaged that they had to be replaced with entirely new structures, the flood-plain sediments were mobilized to depths in excess of 30 feet [9 m]. The movement of the underlying sediments carried the railroad fill as much as 30 inches [0.7 m] to the southeast, and the grade was broken by tension fractures.

The several river channels are incised 1 m to 2 m into flatlying floodplains that slope between 0.05 and 0.1 percent toward the channels. The rivers flow down a gradient of about 0.1 percent to the southeast toward Resurrection Bay.

McCulloch and Bonilla (1970) describe the subsurface conditions from bore holes taken at the adjacent highway bridges:

All the sediments are noncohesive; field identifications range from sandy and silty gravel to fine gravel to gravel. With the exception of hole 2, at bridge 3.0, in which cobbles were found below 20 feet[6 m], the gravel averaged less than three-fourths of an inch [18 mm] in diameter, with a maximum of about 3 inches [75 mm]. All the sediments were saturated, the ground-water table lying at, or within 2 feet [0.6 m] of, the surface. Penetration resistance generally increased downward, although there were some inversions. Within the depth of the

Figure 10 Composite plot of N-values for four borings in Resurrection River flood plain.

sediments penetrated by the piling, the materials were compact to dense. Penetration resistance on a standard penetrometer (140-lb [63.5 kg], 30-in drop [760 mm], 2-in [51 mm] sample spoon) was 30 to 40 blows per foot, a second penetrometer (342-lb [155 kg] hammer, 30-in [760 mm] drop 2 1/2 in [63.5 mm] penetrometer) encountered resistance of 20 to 25 blows per foot.

A liquefaction analysis of the composite standard penetration data is shown in Fig. 9. Penetration values from the nonstandard 342-lb (155 kg) hammer and 2.5 in (63.5 mm) sampler were converted to equivalent standard penetration or N-values using standard procedures based on energy delivered per unit cross-sectional area of sampler. No corrections were made to N-values to account for gravel content. The data from the upper 4 m indicate generally liquefiable material, but below that depth, the penetration values indicate that the sediment is generally resistant to liquefaction. Thus, it appears that most of the liquefaction and ground deformation occurred in the upper 5 m even though McCulloch and Bonilla speculated that displacements may have occurred to depths of 9 m based on observations of verticality of displaced piles. However, if the piles fractured or sheared at depth, then verticality could have been preserved with displacement restricted to the upper 5 m.

Although estimated peak acceleration and duration of ground motions are greater for the Resurrection River area (0.4 g and 90 sec., respectively) compared to the other areas, ground displacements were much smaller (about 0.45 m) than those at the Snow River (2.4 m) or near Portage (2 m to 3 m), and about the same as those in the Matanuska valley (0.3 m to 0.6 m). The

187

apparent reasons for the smaller displacement at the Resurrection River is the thinner layer of liquefied sediment and the courser composition (gravels) of that sediment.

CONCLUSIONS

Comparison of ground displacements, seismic and geotechnical factors at the several bridge sites investigated lead to the following conclusions concerning factors affecting ground displacement at lateral spread sites.

1. Lateral displacements were much larger near Portage (2 m to 3 m) than in the Matanuska Valley (0.2 m to 0.6 m). Comparison of the data from the two localities indicates that sediment conditions, ground slopes, and duration of ground shaking were roughly similar. The peak acceleration near Portage (0.31 g) was much greater than in the Matanuska Valley (0.21 g), indicating that peak acceleration is a primary parameter controlling lateral-spread displacement.

2. About 2.4 m of lateral ground displacement occurred at the Snow River crossing. In this instance the displacement was down a very gentle slope of about 0.1 percent. A major factor leading to such large displacement on such gentle a slope was the approximate 30-m depth of the liquefied layer. This is one of the thickest liquefied layers determined at liquefaction sites.

3. Down-river displacements of unattached bridge piers were as great as 0.6 m in the Matanuska Valley on a slope of about 0.5 percent, and 2.4 m or more down a slope of 0.1 percent at the Snow River. These slopes are much smaller than the 0.3 percent minimum noted from prior investigations (National Research Council, 1985). Thus, during large magnitude earthquakes, lateral spreads on highly susceptible materials may undergo considerable displacement on slopes as gentle as 0.05 percent.

4. Displacement ranging up to 0.7 m at the Resurrection River are smaller than might be expected for a locality so near the zone of seismic energy release where peak accelerations and duration of strong ground motion were estimated to be about 0.4 g and 90 sec. respectively. The apparent reasons for these smaller displacements compared to other sites were the thinner liquefied layer (3 to 5 m) and the gravelly texture of the liquefied material.

REFERENCES

Bartlett, S.F., and Youd, T.L., in press, "Case Histories of Lateral Spreads From the 1964 Alaska Earthquake," Case History Volume, US-Japan Workshop on Liquefaction, Large Ground Deformation, and Their Effects on Lifelines.

Hansen, W.R., Eckel, E.B., Schaem, R.E., Lyle, W.G., Chance, G., 1966, "The Alaska Earthquake, March 27, 1964: Field Investigations and Reconstruction Effort," US Geological Survey Professional Paper 541, 111 p.

Housner, G.W., and Jennings, P.C., 1973, "Reconstituted Earthquake Ground Motion at Anchorage," The Great Alaska Earthquake, Engr. Volume, Nat. Acad. of Sciences, p 43-72.

Kachadoorian, R., 1968, "Effects of the Earthquake of March 27, 1964 on the Alaska Highway System," US Geological Survey Professional Paper 545-C, 66 p.

Kanamori, H., 1978, "Quantification of Earthquakes," Nature, V. 271, p. 411-414.

McCulloch, D.S. and Bonilla, M.G., 1970, "Effects of the Earthquake of March 27, 1964, on the Alaska Railroad," US Geological Survey Professional Paper 545-D, 161 p.

National Research Council, 1985, Liquefaction of Soils During Earthquakes, Washington, D.C., Nat. Acad. Press, 240 p.

Ross, G.A., Seed, H.B., and Migliaccio, R.R., 1973, "Performance of Highway Bridge Foundations," The Great Alaska Earthquake, Engr. Volume, Nat. Acad. of Sciences, p 190-242.

Seed, H.B., Tokimatsu, K., Harder, L.F., and Chung, R.M., 1985, "Influence of SPT Procedures in Soil Liquefaction Resistance Evaluations," Journal of Geotechnical Engineering, ASCE, Vol. 111, No. 12, p. 1425-1445.

Utermohle, G.E., 1962. "Amended Copy, Foundation Study Report, Snow River Bridge #605, Project Number F 031-1(6), Anchorage District, Alaska Department of Transportation.

Utermohle, G.E., 1963, "Foundation Study Report, Knik and Matanuska River Bridges Bridge Numbers 1121, 1122, 1123, 1124, Project Number F 042-1(7), Anchorage District," Alaska Department of Transportation.

Utermohle, G.E., 1965, "Foundation Investigation, Twenty Mile River, Bridge No. 634, Project No. ERFO-36(1), Anchorage District, "Alaska Department of Transportation.

Utermohle, G.E., 1965, "Foundation Investigation, Portage River No. 1 (#630) and Portage River No. 2 (#631), Project No. ERFO-20(1), Anchorage District," Alaska Department of Transportation.

Utermohle, G.E., 1965, "Foundation Investigation, Placer River #1 and Placer River Main Crossing, Bridges #627 and 629, Project No. ERFO-20(1), Anchorage District,"   Alaska Department of Transportation.

LIFELINE PERFORMANCE DURING THE 1979 IMPERIAL VALLEY EARTHQUAKE

B. L. Roth
Engineer, GAI Consultants, Inc., Pittsburgh, PA

T. D. O'Rourke
Professor, Cornell University, Ithaca, NY

R. Dobry
Professor, Renssalaer Polytechnic Institute, Troy, NY

C. E. Pierce
Undergraduate, University of New Hampshire, Durham, NH

ABSTRACT

This paper presents a review of the performance of natural gas, irrigation, and drainage facilities during the 1979 Imperial Valley earthquake. Of special interest is the damage sustained by the irrigation and drainage network. Repairs to these systems are evaluated as a function of the shortest distance to either the Imperial or Brawley faults. A clear trend of increasing damage in relation to the distance from the fault can be seen. Approximately 50 percent of the repairs occurred within 3 km of one of the faults, and about 95% of the repairs occurred within 10 km of the faults. Canal repairs show a well defined relationship with the level of peak vertical and horizontal acceleration. However, the frequency of pipeline repairs is shown to depend upon the level of peak horizontal acceleration, but not upon the level of peak vertical acceleration.

LIFELINE FACILITY PERFORMANCE: 1979 IMPERIAL VALLEY

INTRODUCTION

The Imperial Valley is an agricultural region which adjoins the U.S.-Mexican border in south-central California. It is one of the most seismically active areas in the world. Since 1900, about 23 earthquakes with felt effects of MMI V or greater have occurred there[1]. Moderate to large-size earthquakes (MMI VIII or more) occurred in 1906, 1915, 1927, 1930, 1940, 1950, and 1979. During the 1979 earthquake, all accelerograph stations within a 100-km radius of the epicenter were triggered. The records of this event provide the most complete source of near field data ever obtained[2]. Surface fault movements for this event were more thoroughly monitored than any previous earthquake. Creepmeters produced valuable information on pre-seismic creep, co-seismic slip, and afterslip[3].

This paper focuses on damage sustained by natural gas pipelines and the canal system. Difficulties with gas pipelines were caused primarily by surface faulting along the Imperial fault. Damage to the irrigation and drainage network was related to distance from causative fault and peak value of earthquake acceleration.

LOCATION, INTENSITY, AND FELT EFFECTS

The earthquake occurred on Monday, October 15, 1979 at 4:16 p.m. Pacific Standard Time. Its epicenter was located about 5 km south of the U.S.-Mexican border at geographical coordinates 32° 38.61' N, 115° 18.53' W, focal depth 10 km[4]. It registered magnitude 6.5 on the Richter scale, and generally was felt over a 128,000 km^2 area[5]. Surface faulting occurred along 30.5 km of the Imperial fault, which included the north half of the 1940 fault trace. Surface faulting also was triggered along the Brawley, Superstition Hills[6], and San Andreas faults[7]. Maximum co-seismic right lateral slip along the Imperial fault was 550 to 600 mm at Heber Dunes. Up to 290 mm of afterslip was measured at McCale Road 160 days after the earthquake[8].

The felt effects of the 1979 earthquake were evaluated by the U.S. Geological Survey[5,9]. A MMI of VII was experienced by most of the inhabitants of the Imperial Valley. The damage to buildings generally consisted of cracked veneers, collapse of roofs and unreinforced brick walls, and overturned shelves in stores. The Imperial County Services Building was assigned an MMI of IX. This earthquake-resistant designed structure experienced severe distortion but did not collapse. Injuries resulting from the earthquake and its aftershocks were sustained by 91 persons.

192

LARGE GROUND DEFORMATION

Surface faulting occurred along both the Imperial and the Brawley faults. Because the Imperial Valley is an agricultural region, the faults damaged canals, tile drains, and roads. The lineament of the faults could plainly be seen in some locations because the rows of crops and pavement centerlines were offset laterally. A detailed description of the surface trace of the Imperial and Brawley faults is given by Sharp, et al.[8].

Youd and Wieczorek[10] observed permanent ground deformations at 38 sites throughout the Imperial Valley. Permanent ground deformation resulting from liquefaction and landslides was observed on flatlands, embankments, and canals. Sand boils and ground cracks were common at many ground deformation sites. Youd and Wieczorek reported that liquefaction occurred in two broad settings: 1) channel, flood-plain, and artificial fill deposits along the New and Alamo Rivers, and 2) cultivated areas of sandy subsoil. Much of the liquefaction was concentrated in an area south of Holtville.

NATURAL GAS PIPELINES

Three natural gas pipelines operated by the Southern California Gas Company (SCG) were affected by ground deformation along the Imperial fault. The location of the pipelines relative to the Imperial fault are shown in Figure 1. Information about the pipelines has been presented by McNorgan[14]. In this paper, the installation date, composition, coating, joint type, depth of soil cover, and operating pressure are summarized for each pipeline in Table 1.

Along Highway S-80, about 60 m north of the westbound lane, a 114-mm-diameter natural gas pipeline was intersected by the Imperial fault. To evaluate the magnitude of fault displacement imposed on the pipeline since its 1948 installation, it is important to recognize that fault deformation at this site actually was the sum of three components: preseismic creep, coseismic slip, and afterslip. Preseismic creep along the Imperial fault was monitored at several locations[11,12]. The measurements from a special alignment array at County Highway S-80 are presented graphically in Figure 2. The figure shows four well-defined pulses of motion at time intervals of about every two years. The sum of these four pulses divided by the 12-year monitoring period yields an average creep rate of 6.2 mm/yr. By extrapolating this average rate back to 1948, one would infer that 192 mm of right-lateral creep occurred at the pipeline location before the 1979 earthquake.

Offsets of the Highway S-80 pavement caused by coseismic slip were measured by Sharp, et al.[8]. The magnitude of slip measured by Sharp[8], four days after the earthquake, was 275 mm.
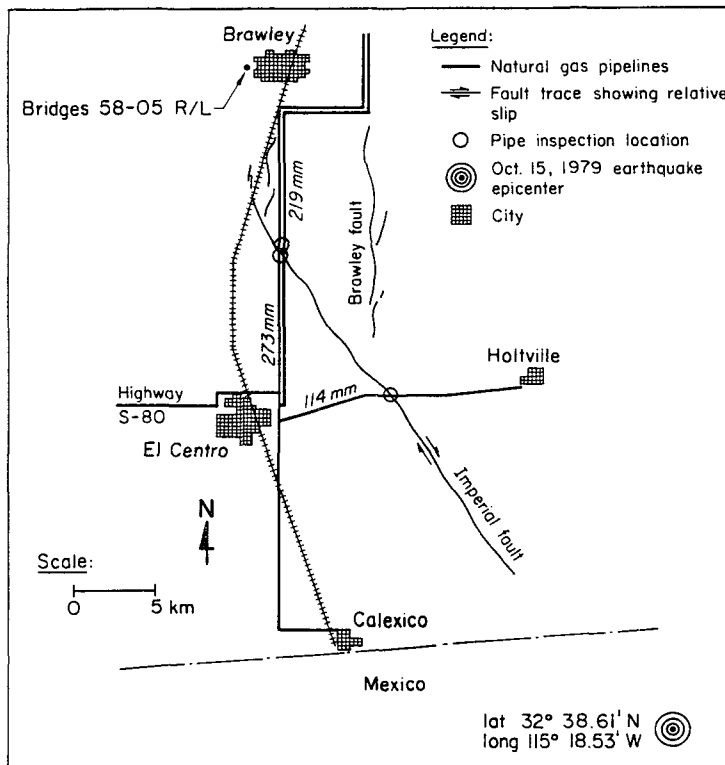
FIGURE 1.   Natural Gas Pipelines Intersected by the 1979 Imperial Fault Pipeline Along Highway S-80

Afterslip at a rate greater than the background creep rate continued for several years after the main shock. Sharp, et al.[8] and Cohn, et al.[12] determined that the afterslip rate decreased logarithmically with increasing time after the earthquake. The equation proposed by Sharp[8] for determining the total fault displacement resulting from coseismic slip and afterslip is:

$$D = a + b \log(t)$$ (1)

in which D is the fault displacement calculated in cm, t is the time in days, and a and b are constants characterizing the best fit linear regression of measured slip versus the logarithm of time. For the Highway S-80 site, the values for a and b were found to be 20.7 and 12.9, respectively.

Using Equation 1, 408 mm of slip were calculated between the time of the earthquake and November 20, 1979, the time of pipeline inspection. Therefore, between the time of installation and inspection, it is possible that 600 mm of cumulative fault displacement occurred at the pipeline from a combination of preseismic creep, coseismic slip, and afterslip. Another estimate of the cumulative fault displacements is given by Hart[13], who observed 1000 mm of offset in the old pavement of Highway S-80 since the 1940

194

TABLE 1. Characteristics of the Pipelines Influenced by Fault Movements During the 1979 Imperial Valley Earthquake

| Characteristic | Pipeline Location | | |
	North Side State Rt. S-80	East Side Dogwood Rd. Line No. 6000	West Side Dogwood Rd. Line No. 6001
Installation Date	1948	1948	1966
Dimensions	114 mm O.D. 5 mm wall	219 mm O.D. 7 mm wall	273 mm O.D. 5 mm wall
Composition	A-25 Steel	API Grade B Steel	Grade X-42 Steel
Weld Type	Acetylene	Electric Arc	Electric Arc
Coating	No. 56[a]	Somastic[b]	No. 56[a]
Depth of Cover	900 mm sandy backfill dumped and rolled	900 mm sandy backfill dumped and rolled	900 mm sandy backfill dumped and rolled
Operating Pressure	2.8 Mpa	2.8 Mpa	5.0 Mpa
Yield Stress	170 Mpa	240 Mpa	290 Mpa

a - No. 56 coating consists of successive layers of: 1) red oxide primer, 2) filled asphalt, 3) two spiral wraps of cellulose acetate, 4) filled asphalt, and 5) paper wrapper
b - Somastic coating composed of asphalt, aggregate, and fiber mixture

earthquake.

A detailed description of the pipeline inspection along Highway S-80 is provided by McNorgan[14]. The inspection of the pipeline by SCG began with a 9.8-m-long excavation centered at the fault. Upon removal of the backfill, it was noted that the pipeline was deformed in an S shape. The displacements perpendicular to the pipeline, relative to its position at the western edge of the trench, were measured by SCG personnel[14]. A sketch of the pipeline-fault intersection, the deformed shape of the pipeline, and the results of these initial measurements are presented in Figure 3. Measurements by SCG disclosed a maximum offset of approximately 146 mm
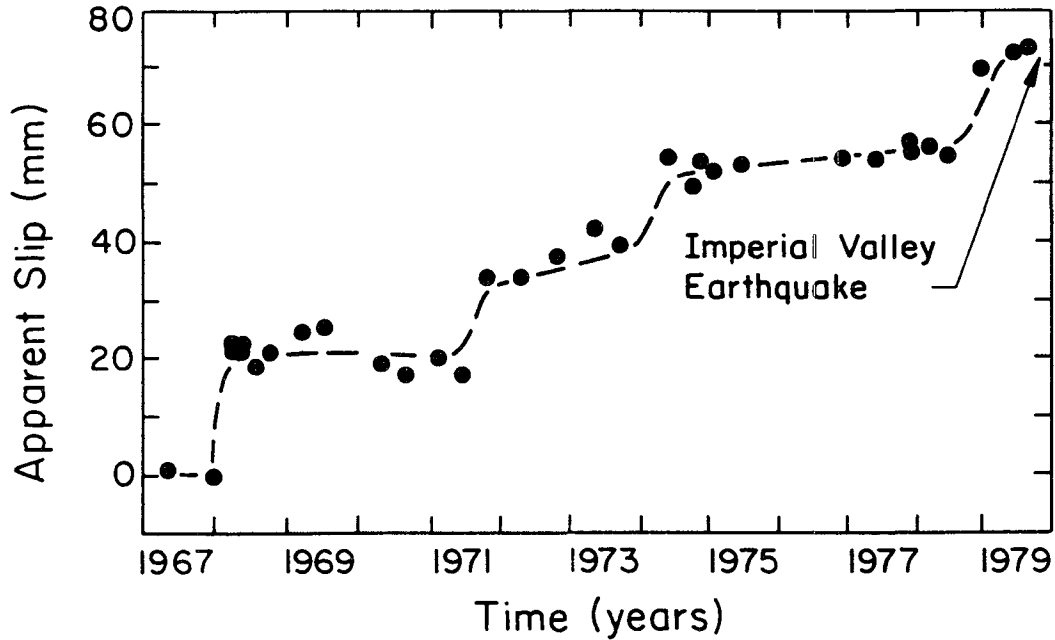
FIGURE 2. Preseismic Creep Along the Imperial Fault at Highway S-80 (after Cohn, et al.[12])

Distance from Fault (m)	Offset from Linear Length (mm)
6.1	6
5.5	6
4.9	3
4.3	0
3.7	0
3.0	13
2.4	19
1.8	32
1.2	57
0.6	89
0	117
0.6	133
1.2	140
1.8	146
2.4	146
3.0	143
3.7	140

FIGURE 3. Deformed Shape of 114-mm Natural Gas Pipeline Along Highway S-80 After Excavating 9.8-m-Long Trench (after McNorgan[14])

within a 9.6-m-wide zone astride the fault centerline. Because the fault-pipeline intersection was less than 90 degrees, elongation, and therefore net tensile stresses, were induced by the right-lateral fault displacement. Pipeline stresses associated with the constraining influence of the adjacent soil were relieved by excavating the backfill. Since no pipeline damage was observed, the excavation was backfilled without further remediation.

Pipelines Along Dogwood Road

Two high pressure pipelines, 219 mm and 273 mm in diameter, were crossed by the Imperial fault along Dogwood Road, approximately 9.5 km north of the City of El Centro. The location of the fault-pipeline intersections are shown by circles in Figure 1. The main fault intersected the pipelines at about 120 degrees, and a splay of the fault intersected the pipelines about 170 m north of the main fault at an angle of 163 degrees.

The pipelines along Dogwood Road were subjected to three components of fault movement: preseismic creep, coseismic slip and afterslip. The closest preseismic creep observation station was at the intersection of the Imperial fault with Worthington Road, 4 km southeast of the Dogwood Road site. A nail file had been installed here in 1977, about two years before the October 15, 1979 earthquake. The creep rate determined by this nail file during the two-year monitoring period was about 8 mm/yr. Thus, the magnitude of preseismic creep imposed on Pipeline Nos. 6000 and 6001 may have been as high as 248 mm and 104 mm, respectively. These preseismic creep magnitudes are believed to represent upper bound values because the preseismic creep rates measured at Worthington Road were influenced by an abnormally high displacement of 15 mm in 1978.

Displacements caused by coseismic slip and afterslip on the main fault were calculated using Equation 1. The values of the constants a and b were 9.4 and 5.9, respectively[8]. Thus, 186 mm of combined coseismic slip and afterslip were calculated for the day that the pipeline was inspected on November 21, 1979, and about 250 mm of combined slip w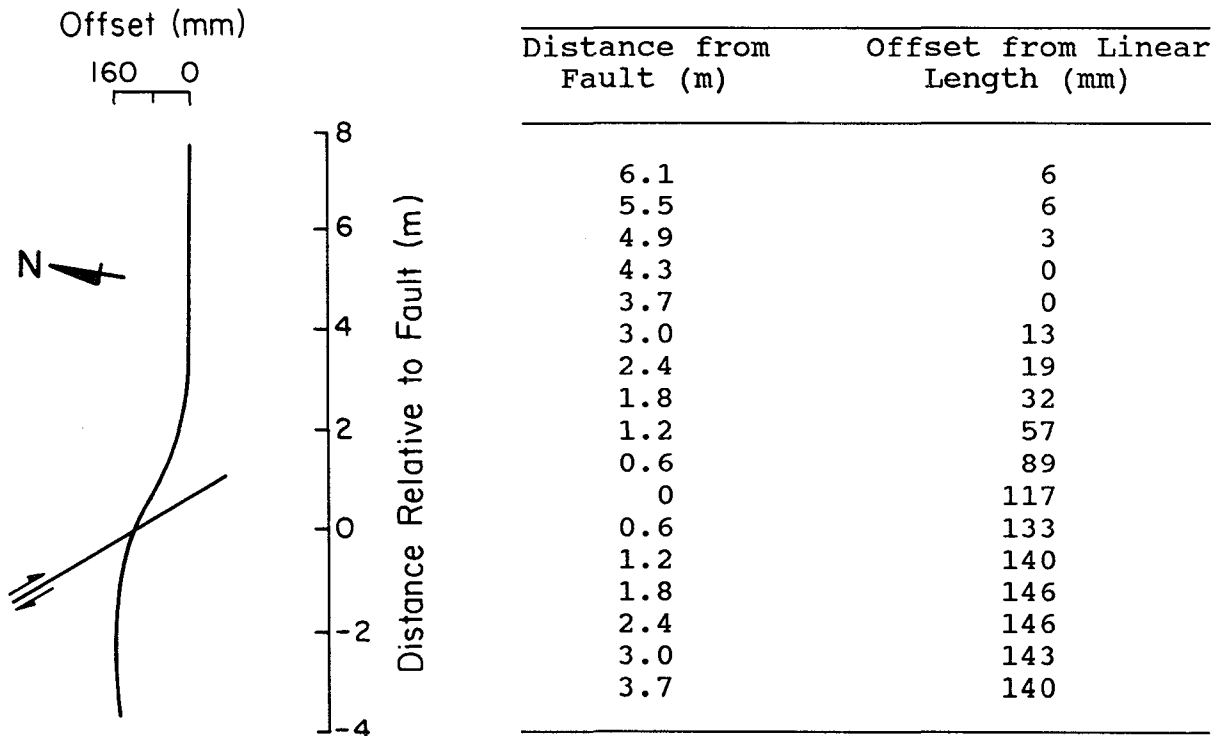ere calculated for the day that the pipeline was cut in February, 1981. Between the time of installation and cutting, it is possible that 500 mm and 355 mm of cumulative fault displacement had been imposed on the 219-mm and 273-mm-diameter pipelines, respectively. Vertical displacements also were imposed on the pipeline. Twelve days after the earthquake, 50 mm of vertical displacement, southwest side up, were measured by Hart[13].

A detailed description of the inspection of Pipeline No. 6001 is given by McNorgan[14]. Because the fault intersects the pipeline at an angle greater than 90 degrees, compressive stresses were known to exist in the pipelines. Because of this potentially hazardous condition, SCG elected to relieve the stresses in the pipeline

using a carefully planned procedure. Details of the stress removal operation carried out in February, 1981 are presented by McNorgan[14]. To relieve the compressive stresses, a 3-m-long section of pipe was removed. After removing the pipe section and excavating 61 m of the line, approximately 120 mm of expansion were observed.
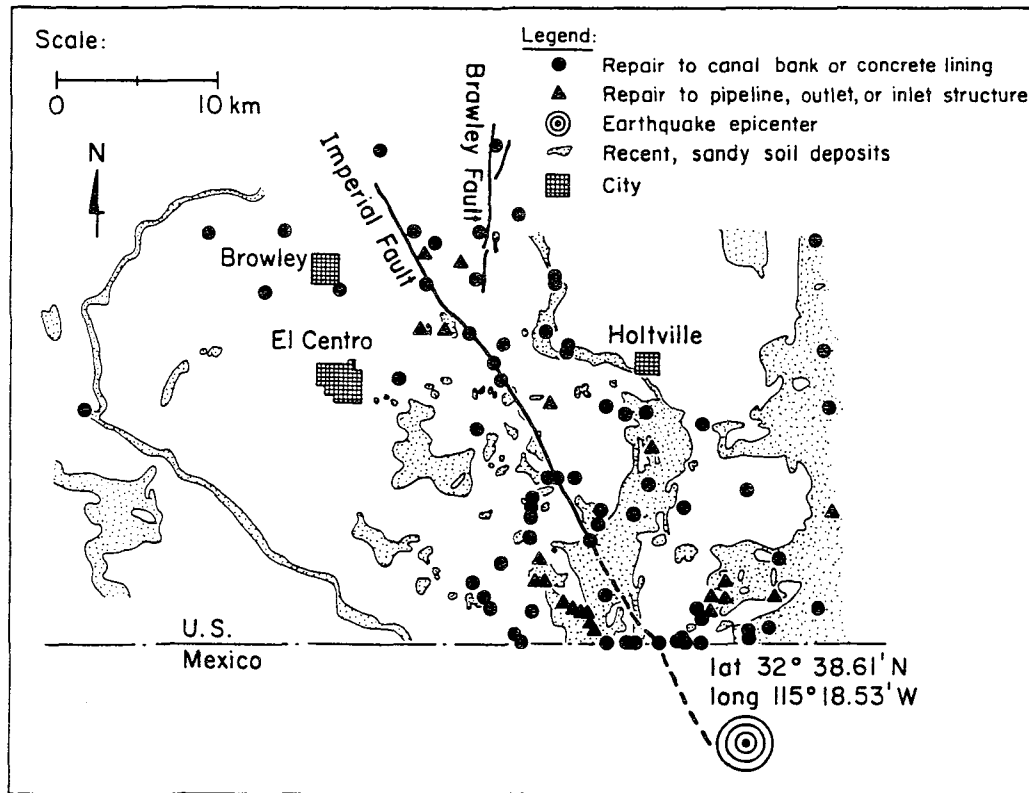
DAMAGE TO IRRIGATION AND DRAINAGE SYSTEMS

Figure 4 shows a plan view of the southern half of the Imperial Valley on which are superimposed circles and triangles representing repairs to the drainage and irrigation network. The triangles represent repairs to pipelines and locations where pipelines slipped off of inlet and outlet structures. The circles represent repairs to cracked canal linings or areas where slumps occurred. Also shown in the figure are the outlines of sandy soils as reported on the USDA soil survey map of 1924[15]. These sandy soils are described as gravelly, fine, loamy, or coarse sands, riverwash, and dune sand. The areas not identified as sandy soils are clay and silty clay deposits.

It is of interest to comment on the spatial distribution of repairs and soil types. Excluding repairs to canals which crossed the fault, about half the repairs were in or on the margins of sandy soils, even though they comprise only about 20% of the total land area. The response of buried facilities seems to have been affected by soil type. Of a total 21 sites of pipeline repairs, all but three were situated in areas of sandy soils.

Figure 5 presents a histogram of the frequency of repairs as a function of the shortest distance to the Imperial or Brawley faults. At each repair location, the shortest distance to either the Imperial or Brawley fault was measured. Each bar on the histogram represents the fraction of total repairs within a 1-km-wide band parallel to, and on both sides of, the fault. The total number of repairs was 89. A clear trend of increasing damage in relation to distance from the fault can be seen in this plot. Approximately 50% of the repairs occurred within 3 km of one of the faults, and about 95% of the repairs occurred within 10 km of the faults. The frequency of repairs was evenly distributed east and west of the faults.

The rate of repair, expressed as repairs/km, is shown in Figure 6 as a function of distance from a fault as defined above. The length of canal and pipeline within 1-km-wide bands either side of the causative faults was estimated by measuring the length of canals in each square mile section of the U.S.G.S. Quadrangle maps. The mean length of the canals in any section was found to be 4.8 km/square mile, which equals 1.74 km/km^2. The similarity in shape of histograms in Figures 5 and 6 arises from the fact that the density of irrigation conduit is relatively constant within the

FIGURE 4. Relationship Between Repairs to Irrigation and Drainage Systems and Recent Soils (after Strahorn[15])
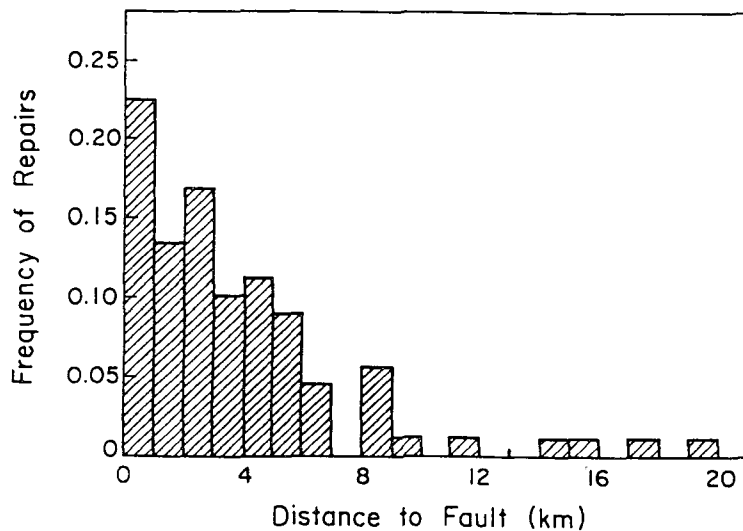
FIGURE 5. Frequency of Repairs to Irrigation and Drainage Facilities versus Distance to Imperial and Brawley Faults
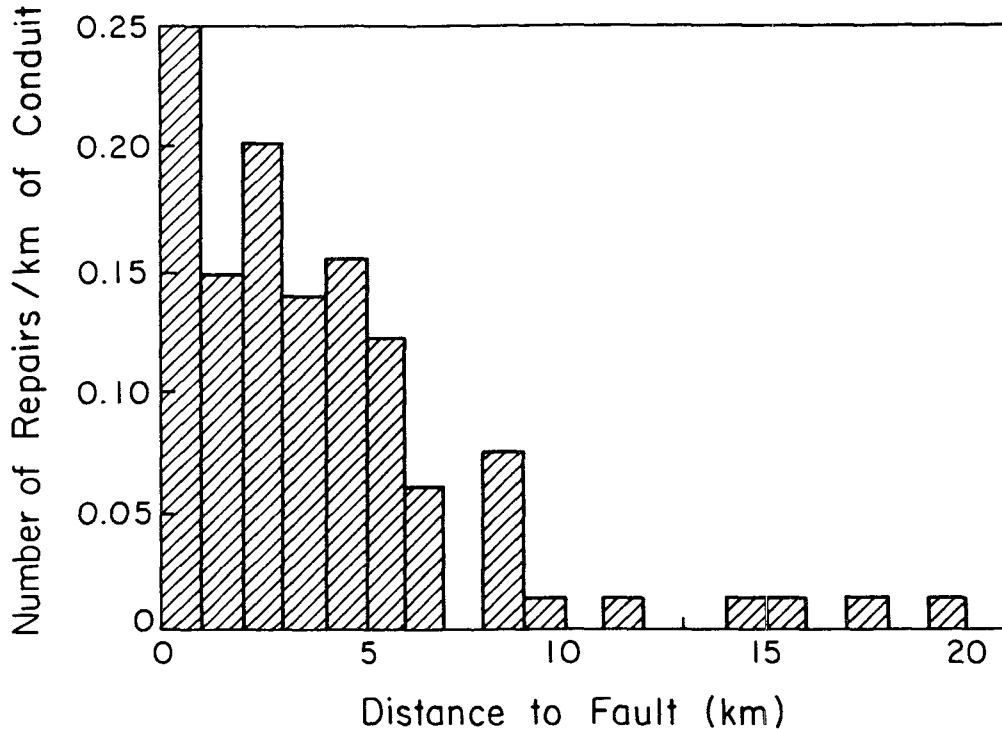
FIGURE 6. Number of Repairs/km versus Distance to Imperial and Brawley Faults

area of study.

Figure 7 shows the peak horizontal and vertical accelerations recorded by the El Centro strong motion accelerometer array plotted on the histogram presented in Figure 5. The accelerometer station numbers are indicated in parentheses adjacent to the data points in the figure. The El Centro array stations are shown in Figure 8. The distance from each array station to the nearest fault trace was measured. The six stations east of the Imperial fault were closer to the Brawley fault, and the seven stations west of the Imperial fault were closer to the Imperial fault. The range and average peak acceleration are shown when two array stations are the same distance from a fault. For example, at Array Station 6, which is 1 km from the Brawley fault, the peak horizontal acceleration was 0.72 g and at Array Station 7, which is 1 km from the Imperial fault, the peak horizontal acceleration was 0.52 g. The average peak horizontal acceleration, 0.62 g, is plotted as a square, and the peak horizontal acceleration range, 0.52 to 0.72 g, is represented by a vertical bar in the figure. The peak vertical accelerations at Array Stations 6 and 7 are presented in a similar manner.

Peak accelerations generally decrease as distance to a fault increases. The curve which connects the peak vertical accelerations closely follows the trend between frequency of repairs as a
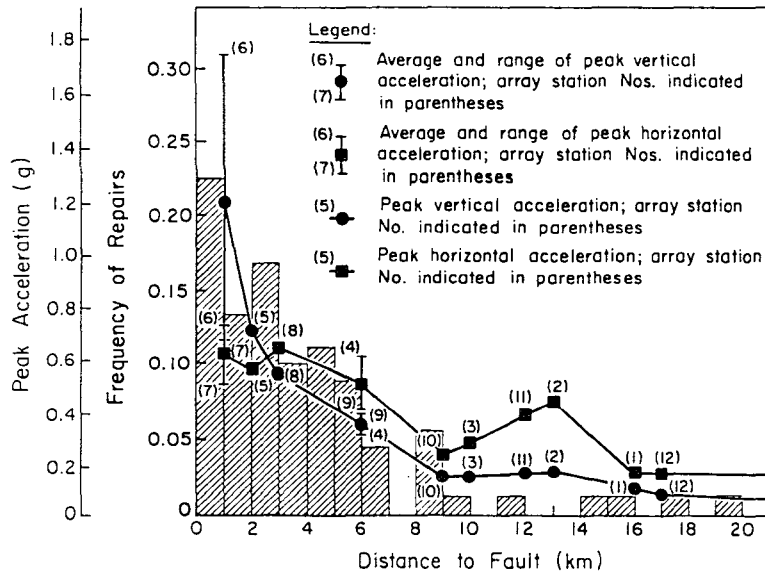
FIGURE 7. Frequency of Repairs to Irrigation and Drainage
Facilities and Peak Vertical and Horizontal
Acceleration versus Distance to Imperial and Brawley
Faults
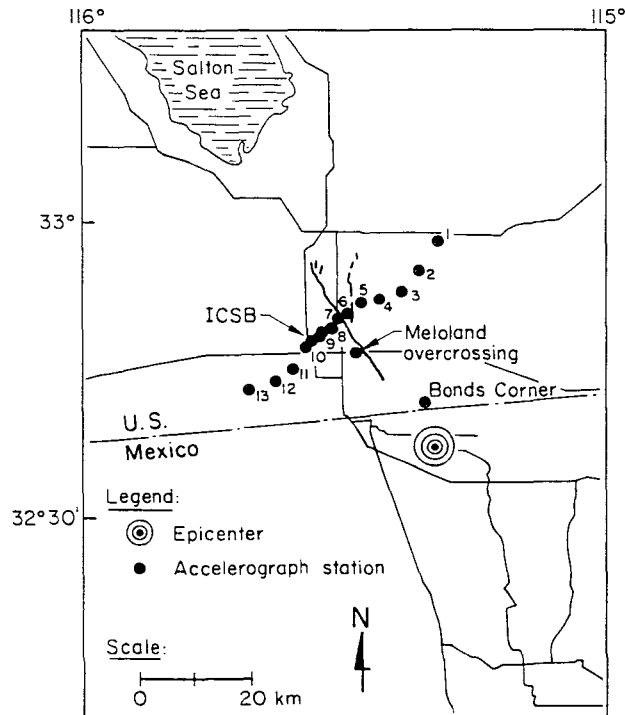
FIGURE 8. Close-In Strong-Motion Stations Operating During 1979
Earthquake (after Porcella, et al.[2]).

function of distance to a fault. The peak horizontal acceleration also shows a trend consistent with repair frequency, although the trend is not as well matched with repairs as that of the vertical accelerations. The peak horizontal and vertical acceleration curves have an increasing slope between 9 and 13 km from a fault. This trend is not reflected in the frequency of repairs histogram, which shows an approximately constant level between 9 and 20 km from the fault traces.

Repairs increase as accelerations become more severe. Considering that surface structures, such as canal linings and canal banks, can be especially sensitive to acceleration, it is reasonable to expect that damage would increase at a nonlinear rate with increasing acceleration. Such a trend can be represented by an exponential function which is relatively simple in form and easy to evaluate.

To establish an upper bound relationship between number of repairs and peak acceleration, exponential regressions were developed as shown in Figures 9a to 9d. These regressions represent conservative estimates of damage because their exponential form, by definition, requires that points of zero repair are discounted from the relationships. The number of repairs is related to the number of repairs per kilometer by dividing number of repairs by the approximate length of canals within a 1-km wide band.

There appears to be a well defined trend between the number of canal repairs and both peak horizontal and vertical acceleration. As shown in Figures 9a and 9b, the coefficients of determination, r^2, are 0.72 and 0.68 for exponential regressions between non-zero repairs and peak vertical and horizontal acceleration, respectively.

A multiple regression was performed to develop a nonlinear fit between number of repairs and combined horizontal and vertical acceleration. The best fit equation is in the form of a polynomial:

$$y = 15.6 \ (\mathring{X}_H^{0.14}) \ (\mathring{X}_V^{0.98}) \tag{2}$$

in which y is the number of repairs, $\mathring{X}_H$ is the peak horizontal acceleration, and $\mathring{X}_V$ is the peak vertical acceleration. The r^2 associated with Equation 2, is 0.79, which likewise is based on a correlation for non-zero repair frequencies.

Figures 9c and 9d show the number of pipeline repairs as a function of peak horizontal and peak vertical acceleration. Figure 9c shows that the non-zero number of repairs correlates reasonably well with peak horizontal acceleration. In contrast, Figure 9d does not show a clear relationship between number of pipeline repairs and peak vertical acceleration. The lack of correlation between pipeline damage and vertical acceleration is consistent with theoretical models. Vertically oriented ground motion causes bending
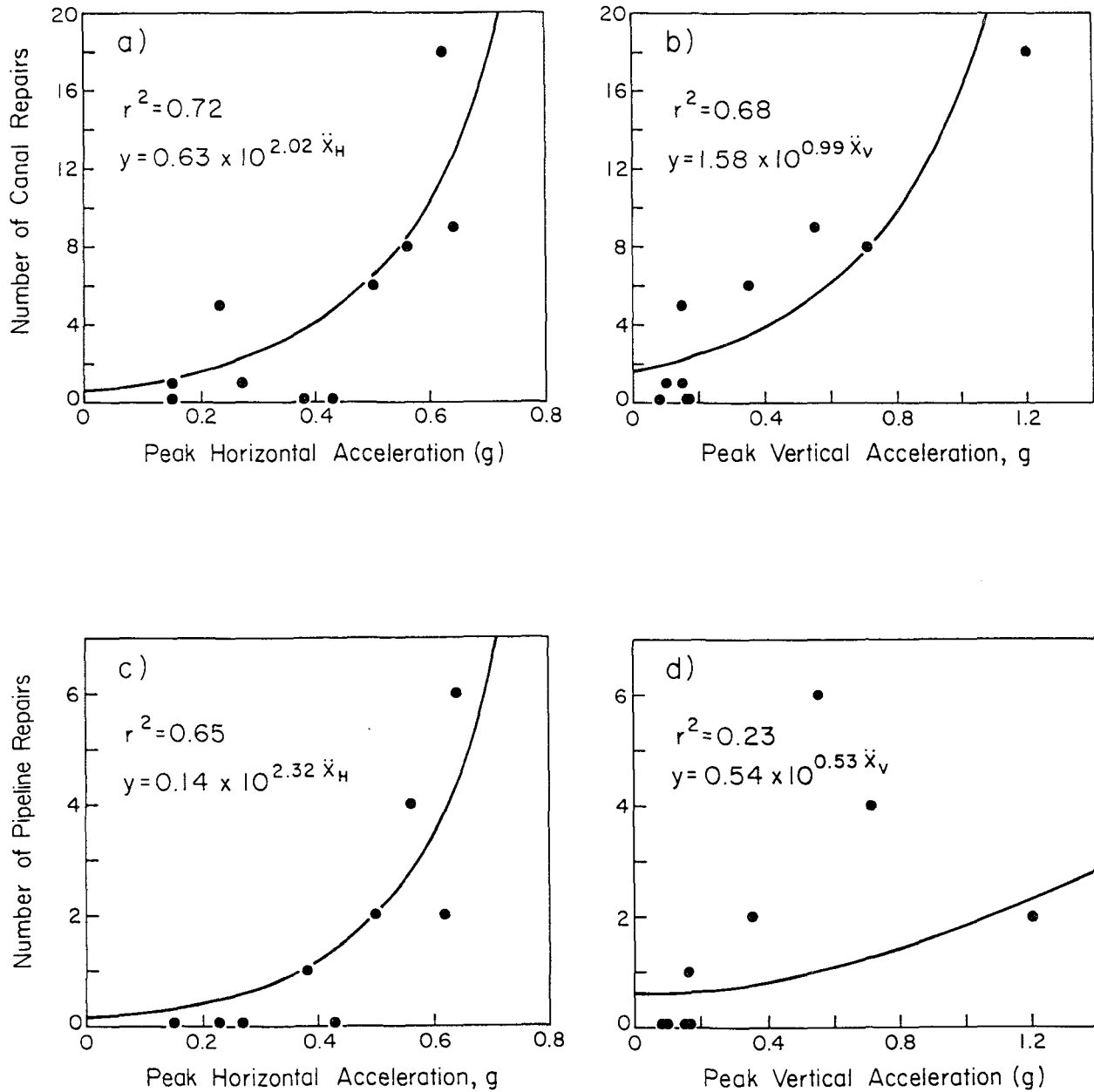
FIGURE 9. Relationships Between Number of Repairs to: a) Canals versus Peak Horizontal Acceleration, b) Canals versus Peak Vertical Acceleration, c) Pipelines versus Peak Horizontal Acceleration, and d) Pipelines versus Peak Vertical Acceleration

deformation and associated pipeline strains which are from 1 to 2 orders of magnitude less than the longitudinal strains caused by horizontally oriented components of ground motion[16].

The frequency of repairs also was investigated with respect to distance from the earthquake epicenter. Circular arcs centered at the epicenter were drawn at radial increments of 5 km. The number of repairs within each band then was counted. The results of the analysis are presented as a histogram in Figure 10. The number of repairs decreases as the distance from the epicenter increases. Moreover, 60% of the repairs are within 5 to 20 km of the epicenter. Data were not available for the closest 5 km, which were located in Mexico. An anomalously large group of 7 repairs was observed at a distance of 45 to 50 km from the epicenter. These data can be attributed to the aftershocks which occurred near Brawley around midnight on the 15th of October. This aftershock was reported by the residents of Brawley to have had a larger felt effect than the felt effect of the main shock: MMI VIII versus MMI VII, respectively[9].

SUMMARY

During the 1979 Imperial Valley earthquake, damage was sustained by lifeline systems. Of particular interest in this paper is the damage sustained by natural gas pipelines and by the irrigation and drainage networks.

Three natural gas pipelines operated by the Southern California Gas Company were intersected by the Imperial fault. The magnitude of fault displacement imposed on the pipelines since their installation was the sum of three components: preseismic creep, coseismic slip, and afterslip. The cumulative fault displacement imposed on the 114-mm pipeline along S-80 was estimated to be 600 mm. Because the fault-pipeline intersection was less than 90 degrees, elongation, and therefore net tensile stresses, were induced by the right-lateral fault displacement. On the other hand, the two high pressure pipelines along Dogwood Road were intersected by the fault at an angle greater than 90 degrees. Compressive stresses, therefore, were known to exist in the pipelines. The compressive stresses caused a potentially hazardous condition which was remediated with carefully planned excavation, cutting, and rewelding of the lines.

The distribution of damage to the irrigation and drainage system was analyzed for this case study. A histogram was developed which shows the frequency of repairs as a function of the shortest distance to either the Imperial or Brawley faults. Approximately 50% of the repairs occurred within 3 km of one of the faults. The shape of the frequency of repairs as a function of distance to either fault is similar to the shape of the repairs/km histogram
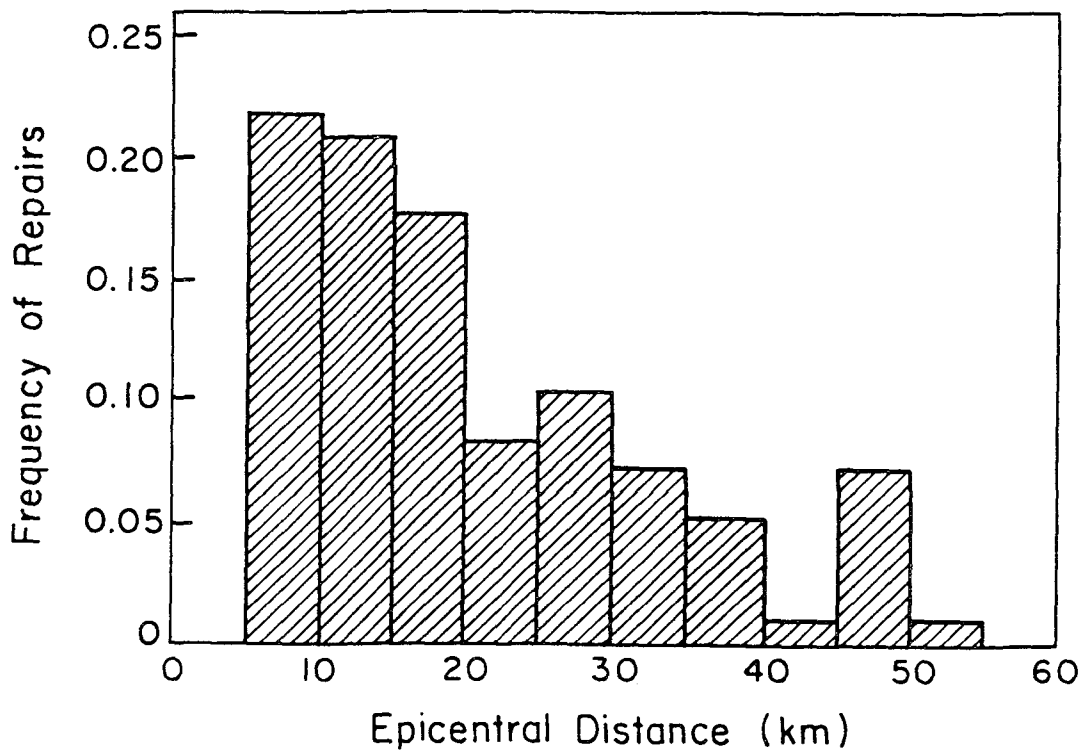
FIGURE 10. **Frequency of Repairs to Irrigation and Drainage Facilities versus Distance to Epicenter**

as a function of distance to a fault because the density of the conduits is relatively uniform throughout the Imperial Valley.

The frequency of repairs is seen to increase as peak horizontal acceleration and vertical acceleration increases. The number of canal repairs shows a well defined trend with the level of peak vertical and horizontal acceleration. However, the number of pipe repairs is shown to depend upon the level of peak horizontal acceleration, but not upon the level of peak vertical acceleration. The lack of a correlation between pipeline damage and vertical acceleration is consistent with theoretical models, which show that vertically oriented ground motions produce smaller strain than the horizontal components of ground motion[16].

ACKNOWLEDGMENTS

by A. Avcisoy and K. Stewart, respectively.

REFERENCES

1. Coffman, K.L., C.A. Von Hake, and C.W. Stover, <u>Earthquake History of the United States, Publication 541-1</u>, U.S. National Oceanic and Atmospheric Administration, U.S. Geological Survey, Boulder, CO, 1982.

2. Porcella, R.L., R.B. Matthiesen, and R.P. Maley, "Strong-Motion Data Recorded in the United States," <u>The Imperial Valley, California Earthquake of October 15, 1979</u>, Geological Survey Professional Paper 1254, Washington, D.C., 1982, pp. 289-318.

3. Johnson, C.E., C. Rojahn, and R.V. Sharp, Introduction to <u>The Imperial Valley, California Earthquake of October 15, 1979</u>, Geological Survey Professional Paper 1254, Washington, D.C., 1982, pp. 1-14.

4. Chavez, D., J. Gonzales, A. Reyes, M. Medina, and C. Duarte, "Main-Shock Location and Magnitude Determination Using Combined U.S. and Mexican Data," <u>The Imperial Valley, California Earthquake of October 15, 1979</u>, Geological Survey Professional Paper 1254, Washington, D.C., 1982, pp. 51-54.

5. Reagor, B.G., C.W. Stover, S.T. Algermissen, K.V. Steinbrugge, P. Hubiak, M.G. Hopper, and L.M. Barnhard, "Preliminary Evaluation of the Distribution of Seismic Intensities," <u>The Imperial Valley California Earthquake, October 15, 1979</u>, U.S. Geological Survey Professional Paper 1254, 1982, pp. 251-258.

6. Fuis, G.S., "Displacement of the Superstition Hills Fault Triggered by the Earthquake," <u>The Imperial Valley, California Earthquake of October 15, 1979</u>, U.S. Geological Survey Professional Paper 1254, Washington, D.C., 1982, pp. 145-154.

7. Sieh, K.E., "Slip Along the San Andreas Fault Associated with the Earthquake," <u>The Imperial Valley, California Earthquake of October 15, 1979</u>, U.S. Geological Survey Professional Paper 1254, Washington, D.C., 1982, pp. 155-160.

8. Sharp, R.V., J.L. Lienkaemper, M.G. Bonilla, D.B. Burke, B.F. Fox, D.G. Herd, D.M. Miller, D.M. Morton, D.J. Ponti, M.J. Rymer, J.C. Tinsley, and J.C. Yount, "Surface Faulting in the Central Imperial Valley," <u>The Imperial Valley, California Earthquake of October 15, 1979</u>, U.S. Geological Survey Professional Paper 1254, Washington, D.C., 1982, pp. 119-144.

9. Nason, R.D., "Seismic Intensity Studies in the Imperial Valley," _The Imperial Valley, California Earthquake of October 15, 1979_, U.S. Geological Survey Professional Paper 1254, Washington, D.C., 1982, pp. 259-264.

10. Youd, T.L. and G.F. Wieczorek, "Liquefaction and Secondary Ground Failure," _The Imperial Valley, California Earthquake of October 15, 1979_, U.S. Geologic Survey Professional Paper 1254, Washington, D.C., 1982, pp. 223-246.

11. Goulty, N.R., R.O. Burford, C.R. Allen, R. Gillman, C.E. Johnson, and R.P. Keller, "Large Creep Events on the Imperial Fault, California," _Seismological Society of America Bulletin_, Vol. 68, No. 2, 1978, pp. 517-521.

12. Cohn, S.N., C.R. Allen, R. Gillman, and N.R. Goulty, "Pre-Earthquake and Post-Earthquake Creep on the Imperial Fault and the Brawley Fault Zone," _The Imperial Valley, California Earthquake of October 15, 1979_, U.S. Geological Survey Professional Paper 1254, Washington, D.C., 1982, pp. 161-167.

13. Hart, E.W., "Preliminary Map of October 1979 Fault Rupture, Imperial and Brawley Faults, Imperial Valley, California," California Division of Mines and Geology, 7.5 Minute Quadrangle, Scale 1:24,000, 1981.

14. McNorgan, J. D., "Relieving Seismic Stresses Locked in Gas Pipelines," _Proceedings_, 2nd U.S.-Japan Workshop on Liquefaction, Large Ground Deformation, and Their Effects on Lifelines, National Center for Earthquake Engineering Research, _NCEER-89-0032_, Buffalo, NY, 1989, pp. 363-369.

15. Strahorn, A.T., E.B. Watson, A.E. Kocher, and E.C. Eckmann, "Soil Survey of the El Centro Area, California," _Field Operations of the Bureau of Soils, 1981_, Washington, D.C., 1924, pp. 1633-1688.

16. O'Rourke, T.D., M.D. Grigoriu, and M.M. Khater, "Seismic Response of Buried Pipelines," _Pressure Vessel and Piping Technology - A Decade of Progress_, C. Sundararjan, Ed., ASME, New York, NY, 1985, pp. 281-3.

III. ANALYTICAL AND EXPERIMENTAL MODELING OF SOIL LIQUEFACTION

EVALUATION OF GROUND DEFORMATION
CAUSED BY LATERAL SPREADING

R. Dobry and M. H. Baziar

Professor and Graduate Research Assistant
Rensselaer Polytechnic Institute

ABSTRACT

The Newmark sliding block approach is applied to evaluate the permanent ground deformation caused by lateral spreading during an earthquake. A laboratory based technique is used to obtain the post–liquefaction steady–state strength S_{us} of very loose, recently deposited, layered fluvial silty sand deposits susceptible to lateral spreading. In these tests the soil is pluvially deposited in layers and then consolidated in an attempt to simulate the in situ fabric. Results of undrained monotonic triaxial tests ($\overline{CIU}$) previously reported by the authors, and covering a range of consolidated pressures $\overline{\sigma}_{1c} = 0.21$ to 0.91 kg/cm^2, provide a value $S_{us} = 0.12\, \overline{\sigma}_{1c}$. It is proposed to use this soil strength in conjunction with the sliding block analysis to predict permanent displacement due to a lateral spread.

The approach is successfully used to evaluate the Wildlife Site case history in Southern California during the 1987 earthquake. It is further applied to estimate lateral spreading of a typical mildly sloping site with shallow water level subjected to earthquakes in the Western United States. Twenty recorded accelerograms corresponding to magnitudes $M_w = 5.3$ to 7.4 and distances $R = 7$ to 107 km, are used for this purpose. The computed displacements are compared with those observed in the field and compiled in their Liquefaction Severity Index chart by Youd and Perkins, with excellent agreement.

INTRODUCTION

Ground deformation due to liquefaction–induced lateral spreading of loose, saturated sand deposits constitutes one of the most common and destructive phenomena caused by earthquakes. For example, during the 1964 Alaska earthquake more than 92 bridges suffered extensive damage due to ground lateral spreading. The total damage to bridges and highway embankments in this earthquake was estimated at $46 million (Bartlett and Youd, 1991). For most of the bridges for which soil conditions were reported, silty sand soil deposits were responsible for the liquefaction and associated lateral spreading. A lateral spread typically involves predominantly horizontal displacements of a large, superficial soil block, with the displacements due to the combined effect of static and seismic forces. Lateral spreads generally develop downhill on very mildly sloping terrain containing late Holocene, loose, fluvially sedimented sand or silty sand. Permanent displacements ranging between a few centimeters and several meters have been observed in the U.S., Japan, and other countries, causing damage to roads, canals, embankments, buried pipes and foundations of buildings (National Research Council, 1985; Youd and Perkins, 1987).

Clearly, the evaluation of engineering effects of liquefaction at a site for a given earthquake implies the ability of predicting the magnitude and spatial distribution of the permanent ground displacements. However, although we can currently predict if a site will liquefy or not with a reasonable degree of confidence using penetration charts, no such general method exists for the evaluation of the displacement. Intensive research efforts on the subject are currently underway, especially in the United States and Japan (Hamada, et al., 1986; US–Japan, 1988, 1989). The magnitude of the displacements depends on the intensity and the duration of the ground shaking, and Youd and Perkins (1987) have developed an empirical chart for the Western United States, valid for the worst site conditions, which gives the maximum displacement as a function of earthquake magnitude and distance. No such charts are available for other site conditions. Under the assumption that displacements accumulate only during shaking, the use of Newmark's method (Newmark, 1965; Lambe and Whitman 1969), in conjunction with the post–liquefaction steady–state or residual soil shear strength has been proposed. Castro (1987) backfigured a value of 100 psf for this strength at the Heber Road site in the Imperial Valley, CA, from the displacement observed after the 1979 earthquake.

A main problem in the application of the Newmark method is the selection of the soil strength for the analysis. The use of laboratory techniques to evaluate this value is complicated by the shallow depths and low confining pressures involved in lateral spreading and the well–known problems associated with undisturbed sampling of granular soil under the water table. The authors (Baziar and Dobry, 1991) have proposed a laboratory approach for evaluating the in situ steady–state shear strength of very loose, water–sedimented silty sand for the range of consolidation pressures of interest in lateral spreads. This laboratory technique is used here to calculate the horizontal displacements of mildly sloping deposits subjected to twenty earthquake accelerograms recorded on soil in the Western United States. The records cover a range of magnitudes and distances to the source. Newmark's sliding block method is used in the calculations, and these computed displacements are compared with those measured in the field by Youd and Perkins (1987) with good agreement.

NEWMARK SLIDING BLOCK MODEL

Figure 1 shows a slope of angle α subjected to an acceleration time history $a(t)$ acting parallel to the slope. The rigid block on top (representing the sliding part of the soil in the lateral spread) tends to accelerate together with the slope. However, the acceleration of the block is limited by the strength of the block-slope interface. If the interface contact area is A and the interface strength is S, the maximum force that the interface can transmit is S A.
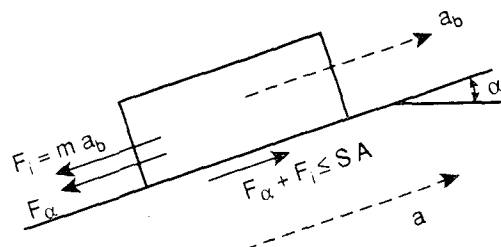
Fig. 1. Accelerations and forces used in the sliding block analysis.

In the figure it is assumed that the slope is accelerating up with acceleration a and the block is also accelerating up with acceleration a_b. It is:

$$a_b \leq a$$

where $a_b = a = a_y$ when $F_\alpha + F_i = S A$, and the yield acceleration a_y is given by:

$$a_y = \frac{S A - F_\alpha}{m} \tag{1}$$

In this expression, F_α is the component of the weight of the block parallel to the slope and m is the mass of the block. When $a < a_y$, $a_b = a$ and no relative displacement takes place between block and slope. When $a > a_y$, $a_b = a_y$ and the block slides <u>downslope</u> relative to the base.

The situation when the slope is accelerating down is the same, except that now the yield acceleration is:

$$a_y = - \frac{S A + F_\alpha}{m} \tag{2}$$

(The convention in both Eqs. 1 and 2 is that upslope accelerations are positive.) Again, when $|a| < a_y$, $a_b = a$ and there is no relative displacement. However, when $|a| > a_y$, $a_b = a_y$ and the block slides <u>upslope</u>.

It can be seen that the value $|a_y|$ needed to start downslope displacements (Eq. 1) is larger than that needed to start upslope movements (Eq. 2), with the difference increasing as α and F_α increase. Therefore, a slope subjected to a typical earthquake accelerogram having more or less the same acceleration in both directions, will tend to have a net downslope movement at the end of the record, thus simulating the observed effect of topography in controlling the direction of lateral spreads.

The previous analysis assumes that the interface strength S is constant and is not affected by the magnitude of the displacement. This presumes a perfectly plastic mode of failure, and in fact both Newmark (1965) and others have typically assumed rigid-plastic material behavior. The relative displacement of the block with respect to the slope is calculated by double integration of the input acceleration during the times when $|a| > a_y$.

Figure 2 illustrates the process of accumulation of displacement for a sinusoidal input base excitation parallel to the slope, $a = a_0 \sin(2\pi t/T)$, under the assumption that only downward sliding can occur and that the interface strength S corresponds to rigid-plastic behavior. When the upslope acceleration $a > a_y$, the interface yields, $a_b = a_y$, and displacement accumulates. Therefore, due to the difference in the acceleration of the block and that of the slope, a relative velocity develops and the block continues to accumulate displacement as long as it has such a relative velocity, even for a while after the base acceleration has dropped below the yield acceleration. It can be demonstrated (Baziar, 1991) that the total displacement at the end of this sinusoidal loading is proportional to: the maximum amplitude of the loading, a_0, the square of the loading period, T^2, the number of loading cycles, N, and a function of the ratio a_y/a_0:

$$d = (1 / 2\pi)^2 \, a_0 \, T^2 \, N \, f(a_y / a_0) \qquad\qquad (3)$$

Fig. 2. Downslope velocity and displacement of sliding block for sinusoidal acceleration.

Equation 3 provides insight into some of the factors controlling the value of the lateral spreading caused by earthquakes represented here by d. (Although Eq. 3 was developed

212

assuming only downslope movements, an identical expression is valid if upslope movements also occur, with only the function of (a_y/a_0) being defined differently).

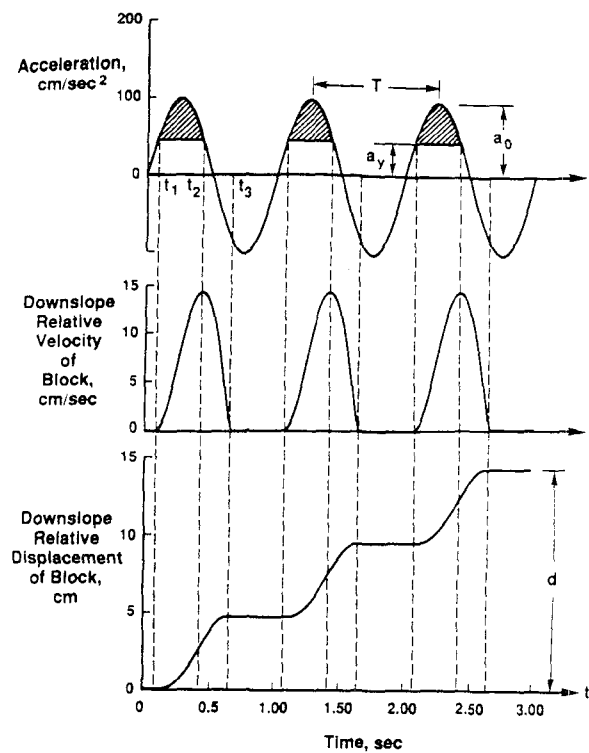Equation 3 indicates that d must be affected by both the slope α and the liquefied shear strength of the soil S, as α and S determine a_y; with d increasing as α increases and S decreases. The influence of the rest of the parameters in Eq. 3 is also consistent with the known fact that for given soil and topographic conditions, d increases with earthquake magnitude and attenuates with distance to the source (Youd and Perkins, 1987). The effect of magnitude is explained by greater earthquake sizes inducing larger a_0, T and N. This accumulated impact of greater a_0, T and N as shown by Eq. 3 suggests that d should be very sensitive to earthquake size, other things being equal; this has been confirmed by observations (Youd and Perkins, 1987). The effect of distance in Eq. 3 is mostly associated with the attenuation of a_0, which should predict d = 0 for those magnitudes and distances for which $a_0 < a_y$.

THE RDWPSS SAMPLE PREPARATION METHOD

Baziar and Dobry (1991) have proposed a method to determine the shear strength of a liquefied silty sand at large strains, $S = S_{us}$, needed for the sliding block analysis, from undrained monotonic and cyclic torsional tests. The definition of S_{us} in this method is the same used by Castro (1987). In an attempt to simulate the geologic history and layered in situ structure of a loose, recent fluvial deposit, the specimens are formed by discontinuous sedimentation in water followed by consolidation and undrained testing. This Remolded Discontinuously Wet Pluvial Soil Sample (RDWPSS) preparation method is the same previously used by Vasquez–Herrera & Dobry (1989), and Vasquez–Herrera, et al. (1990) to successfully reanalyze the 1971 hydraulic fill flow failure in the upstream slope of the Lower San Fernando Dam. The same Batch SF7 sand sampled from the Lower San Fernando Dam, containing about 50% non–plastic silt under the #200 sieve, previously tested by Vasquez–Herrera and by GEI (1989), was used herein to determine S_{us} for the range of confining pressures relevant to lateral spread evaluations.

The RDWPSS preparation technique used at RPI is illustrated in Figure 3 for a 4–layer specimen. Boiled deaired water is poured into a 2" diameter, 4" high mold covered inside with a stretched triaxial membrane, and fitted with an extension in the upper part of the mold (extension not shown in Fig. 3). Before dumping the first 1" soil layer, the water layer is 1.5" above the bottom of the mold, and more water is poured later to have always the water level about 0.5" over the surface of the soil layer about to be dumped. Each 1" layer is formed by dumping an equal weight of soil (60 grams) and waiting enough time (30 minutes) for all soil particles to settle before pouring more water and dumping the next layer. The 30–minutes time interval was based on calculations, and the authors later verified experimentally that more than 99% of the weight of the soil had sedimented at the end of the interval. A number of layers are deposited this way in the mold and extension, followed by removal of the extension and excess soil and water and the final, 4–layer configuration of the sample shown in Fig. 3.

One of the tests was performed with a specimen having only one 4" thick layer so as to verify the influence of the number of layers on the results. In this case, the mold plus extension were filled with water to a height of 6", and the 240 grams of soil were dumped in the water at once. In both 4–layer and 1–layer specimens, the specimen was very loose after sedimentation, with an average void ratio, $e \simeq 1.4$. After sedimentation,

the triaxial cap and assembly was locked and an effective cell pressure of 3 psi (0.21 kg/cm²) was applied by vacuum to the specimen which was then allowed to consolidate. Under this very low confining pressure, the soil consolidated significantly to an average void ratio, e ≃ 0.9.

The RDWPSS method produces silty sand specimens that are non—uniform and have a naturally induced internal stratification, with an overall void ratio substantially larger than anything attainable by other preparation techniques aimed at creating more uniform specimens. It is reasonable to assume that the fabric, void ratio and engineering behavior of these RDWPSS specimens are similar to those of in situ, very loose, recently deposited, fluvial or other natural or man—made hydraulic fills. This was confirmed by Vasquez—Herrera, et al. (1990), who found that SF7 RDWPSS specimens consolidated to the field stresses had similar void ratios to those measured in situ in the Lower San Fernando Dam.
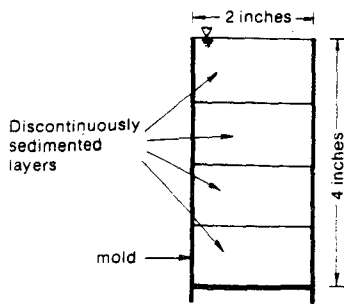
Fig. 3. Silty sand Remolded Discontinuously Wet Pluvial Soil Sample (RDWPSS) prepared using four layers.
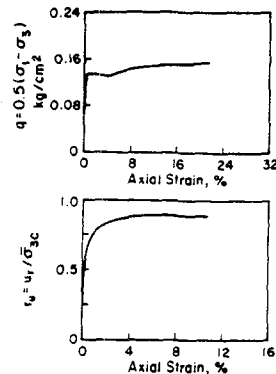
Fig. 4. Monotonic undrained triaxial compression test ($\overline{CIU}$).

TEST RESULTS

The authors (Baziar & Dobry, 1991) performed several CyT—$\overline{CAU}$ and $\overline{CIU}$ tests on RDWPSS SF7 silty sand specimens to evaluate steady—state strength and triggering characteristics of layered silty sand. Figure 4 shows the results of one of the $\overline{CIU}$ tests. The same as in the rest of the $\overline{CIU}$ experiments, the stress—strain behavior is essentially elastic—perfectly plastic, with yield occurring at a strain of about 1%, and with a steady—state value of $q = q_{us} = 0.15$ kg/cm² up to 22% strain. A value of the steady-state friction angle $\phi_{us} = 33.6°$ was obtained from this and the other tests. Thus, $S_{us} = q_{us} \cos \phi_{us} = 0.125$ kg/cm² for the specimen. In Fig. 4, both the stress—strain and pore pressure ratio $r_u = u_r/\bar{\sigma}_{3c}$ curves show that the soil was contractive during the experiment. In fact, all $\overline{CIU}$ and CyT—$\overline{CAU}$ tests reported by Baziar and Dobry exhibited contractive behavior, including those consolidated to the lowest confining pressure, $\bar{\sigma}_{3c} = 0.21$ kg/cm².

For the four $\overline{CIU}$ tests, including three 4—layer specimens and one 1—layer specimen, the consolidation pressures ranged between 0.21 and 0.91 kg/cm². The shear strength of these soil specimens, S_{us}, is plotted against vertical consolidation pressure, $\bar{\sigma}_{1c}$ in Fig. 5a. This figure indicates that the ratio $S_{us}/\bar{\sigma}_{1c}$ is constant and equal to about 0.12. This is a very important conclusion which allows estimating S_{us} in the field for this type of very loose, water-deposited silty sand soil without the need for in situ density

214

measurements. Figure 5b shows the variation of the void ratio for the same four tests. All four specimens were initially consolidated to 0.21 kg/cm^2, and then the pressure was increased to the value of the test. This figure illustrates the decrease of void ratio with increasing vertical pressure.
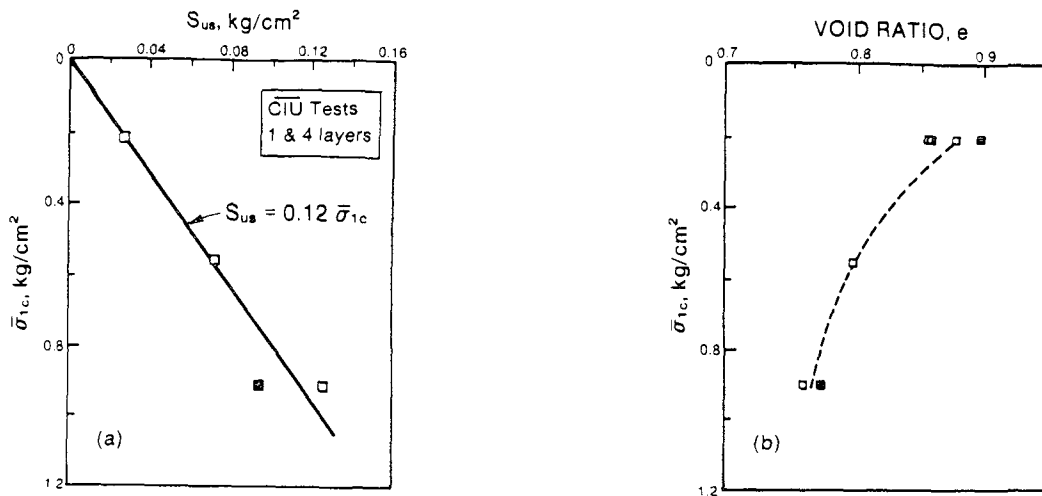
Fig. 5.   Variation with $\bar{\sigma}_{1c}$ of a) steady-state strength S_{us}, and
b) void ratio after consolidation, obtained from $\overline{CIU}$ tests.

A similar "c/p ratio" approach to that illustrated by the constant $S_{us}/\bar{\sigma}_{1c}$ in Fig. 5a, has been used for many years to estimate the undrained peak shear strength of cohesive soil deposits from laboratory tests, and was further developed in the last 15 years in their SHANSEP method by Ladd and Foott (1974). They relate this ratio to the overconsolidation ratio of the clay, OCR, with the smallest value corresponding to normally consolidated soil, and with the "c/p ratio" increasing as OCR increases. In the case of interest here of layered silty sandy soil susceptible to liquefaction, the "$S_{us}/\bar{\sigma}_{1c}$ ratio" where $\bar{\sigma}_{1c} = \bar{\sigma}_v$ can be taken as the in situ vertical effective pressure, should be related to the density of the soil at deposition time (which in turn is controlled by factors such as the velocity of the water) and to subsequent changes throughout the life of the deposit (e.g., due to overconsolidation, densification caused by vibrations, etc.). Here the assumption is made that the value $S_{us}/\bar{\sigma}_{1c} = S_{us}/\bar{\sigma}_v = 0.12$ from Fig. 5a is directly applicable to very loose, normally consolidated, recently deposited soil.

APPLICATION TO WILDLIFE SITE

The authors (Baziar and Dobry, 1991) conducted a preliminary study to evaluate the lateral displacement developed at the Wildlife site in Imperial Valley, California, by the November 27, 1987 Superstition Hill Earthquake, using the ratio $S_{us}/\bar{\sigma}_v = 0.12$.

This site liquefied and developed sand boils and cracks and moved 18cm horizontally in the N15E direction, toward the Alamo River (Dobry, et al., 1991). Figure 6 shows the cross–section and soil profile used in the analyses. The groundwater level was at 1.5 m depth; based on SPT blow counts and analyses performed by Dobry, et al. (1989) it was concluded that the very loose, soft interbedded silt and sand silt layer between the depths
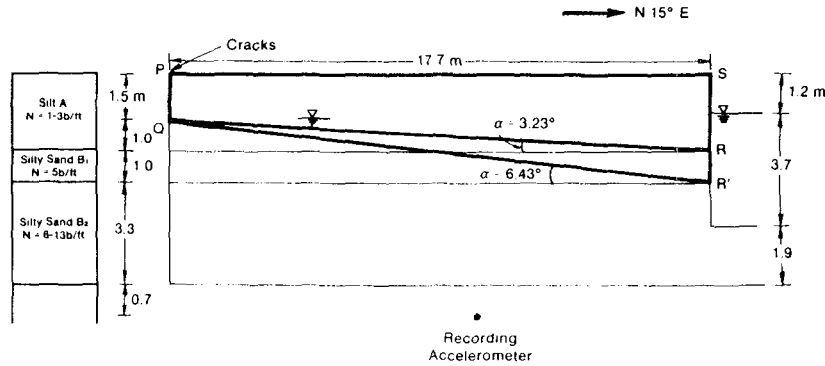
Fig. 6. Soil profile and assumed failure planes for sliding
block analyses, Wildlife site, November 24, 1987 Earthquake.

of 1.5 and 3.5 m were responsible for the observed lateral movement. This also was confirmed by Holzer, et al. (1989) who reached the same conclusion based on the post—earthquake monitoring of an inclinometer located near the cracks shown in Fig. 6. Based on this, two failure mechanisms were postulated as sketched in Fig. 6. These two failure planes are bounded by the cracks observed at the ground surface, by the groundwater level and by the free face at the river side.

These failure planes define angles $\alpha = 3.23°$ and $\alpha = 6.43°$, used in the Newmark sliding block analyses by Baziar and Dobry (1991) to evaluate the lateral movement toward the river of rigid blocks PQRS or PQR'S.

For a very mildly sloping failure surface as is the case here, and assuming that the earthquake excitation is parallel to the failure plane, the yield acceleration, a_y, needed to start the block sliding toward the river is given by:

$$a_y/g = (\overline{\sigma}_v/\sigma_v)(\cos \alpha \tan \phi - \sin \alpha) \tag{4}$$

where g = acceleration of gravity, and ϕ is an "equivalent angle of internal friction" related to the ratio $S_{us}/\overline{\sigma}_v$ by the expression:

$$(S_{us}/\overline{\sigma}_v) = (1 - \sin \phi) \tan \phi \tag{5}$$

Note that this ϕ is related to the ratio between S_{us} and the consolidation stress $\overline{\sigma}_v = \overline{\sigma}_{1c}$, and therefore has no relation to ϕ_{us}. For $S_{us}/\overline{\sigma}_v = 0.12$, $\phi = 8°$. It can also be demonstrated that for a case such as shown in Fig. 6, $\overline{\sigma}_v$ and σ_v can be taken at the midpoint of failure plane QR or QR'. Finally, $a_y = 0.074$ g and $a_y = 0.022$ g were found for QR and QR', respectively.

Figure 7a includes the NS component of the accelerogram recorded at 7.5 m depth, below the liquefied soil. Based on the recorded ground surface accelerogram and the site response analyses reported by Dobry, et al. (1989), the ordinates of this record were multiplied by a factor 1.05 prior to using it in the analyses, to account for the amplification of the motions between 7.5 m depth and the base of the sliding block, at 2 or 3 m depth.

216
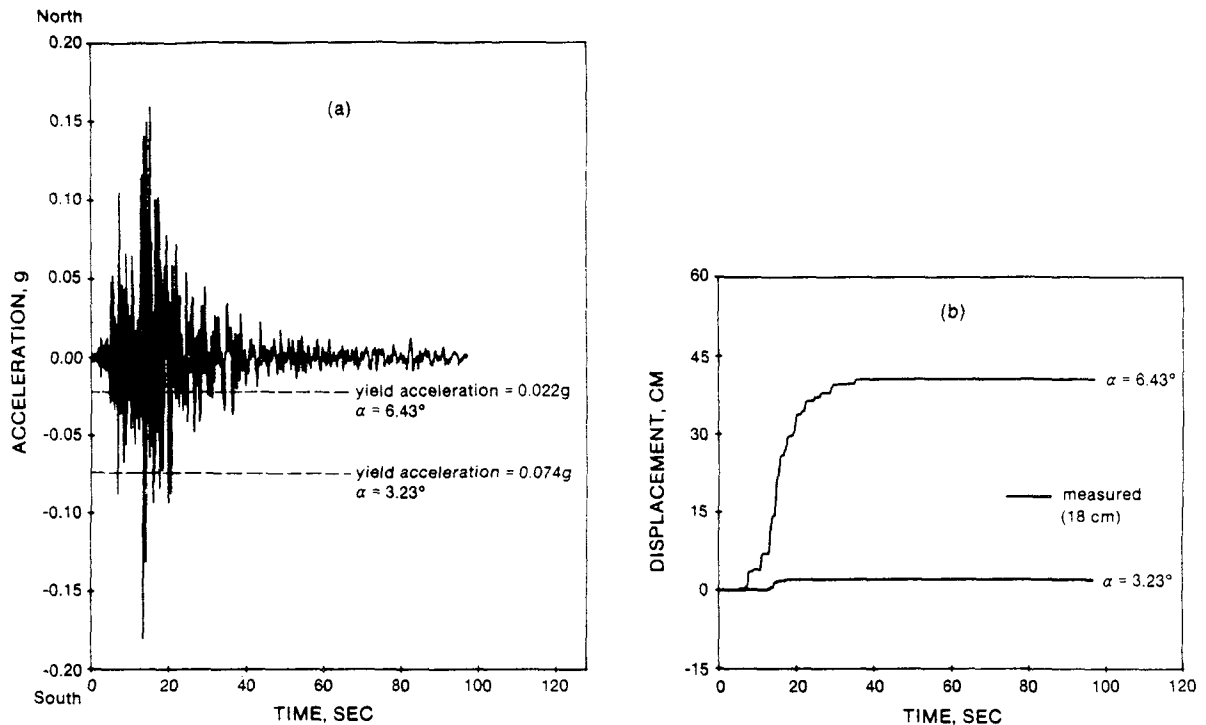
Fig. 7. a) Input acceleration, and b) measured and recorded displacement, using sliding block analyses, Wildlife site, November 24, 1987 Earthquake.

Figure 7b presents the displacement time histories calculated with the sliding block analyses for the two values of α. In the calculations, the block was only allowed to slide toward the river, on the assumption that the material filling up the cracks did not permit a sliding back up of the block away from the free face. This assumption that only downslope permanent movements are possible is the same made previously in Fig. 2. For $\alpha = 3.23°$ (block PQRS), a total displacement of 0.21 cm is calculated at the end of the earthquake, while for $\alpha = 6.43°$ (block PQR'S), the calculated displacement is 40.5 cm. These two values bound the measured displacement of 18 cm, as illustrated by the figure, thus showing the reasonableness of the assumed failure mechanism and of the $S_{us}/\bar{\sigma}_v$ used in the calculations. The wide variation between these two calculated values of displacement illustrates the sensitivity of the prediction to the selected angle α.

PREDICTION OF LIQUEFACTION SEVERITY INDEX (LSI)

Based on measurements of lateral displacement observed in a number of Western United States locations after earthquakes, Youd and Perkins (1987) developed the liquefaction susceptibility (LSI) chart of Fig. 8. LSI is defined as "... the general maximum d-value (in inches) for lateral spreads generated on wide active flood plains, deltas, or other areas of gently-sloping late Holocene fluvial deposits." Values of d larger than 100 inches are assigned a limiting LSI of 100. That is, LSI is the maximum d associated essentially with the worst site conditions. As further explained by Youd and Perkins (1987), at the sites associated with d ≃ LSI "... the liquefiable soil layers are usually

217
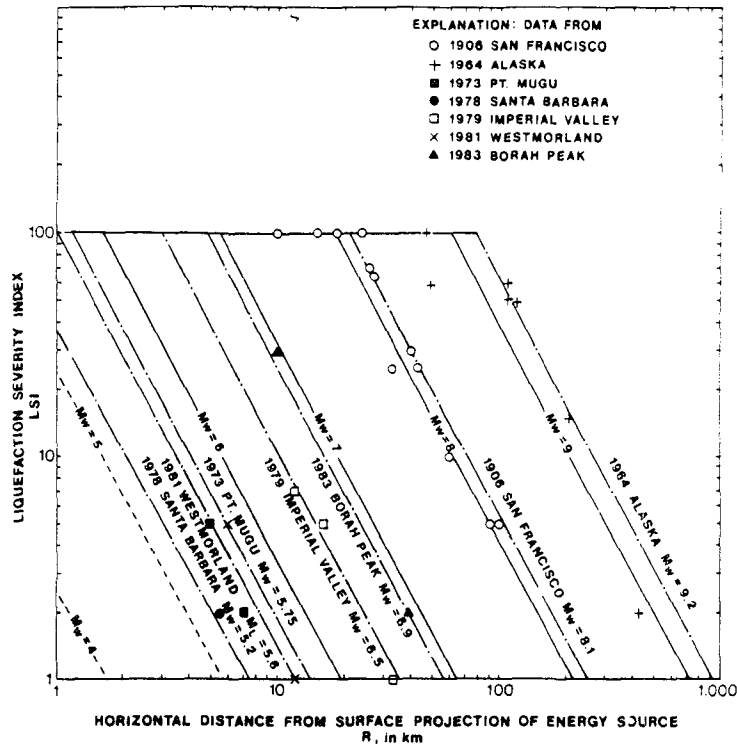
Fig. 8. LSI from several Western US Earthquakes with lines calculated from Equation 6.

thicker than 0.3m (1 ft) and are continuous over a large area; slopes generally range between 0.5% and 5%; groundwater depths are generally shallow unless the river is deeply incised; and standard penetration resistances of granular materials generally range between 2 and 10 blows per foot." (Youd and Perkins, 1987). Many of these sites correspond to liquefiable silty sand rather than clean sand layers (Youd, 1990).

In Fig. 8, the data points correspond to earthquakes ranging from moment magnitude $M_w = 9.2$ (Alaska 1964) to $M_w = 8.1$ (San Francisco 1906) to $M_w = 5.2$ (Santa Barbara, CA 1978). The minimum horizontal distance to the surface projection of the seismic energy source ranges from $R = 0$ to $R = 420$ km. Figure 8 shows that LSI increases with M_w and decreases with R, with LSI being extremely sensitive to M_w for a given R; this is consistent with the previous discussion of Eq. 3. Youd and Perkins fitted the following expression to their data points for the Western United States:

$$\log(\text{LSI}) = -3.49 - 1.86 \log R + 0.98 M_w \tag{6}$$

The lines in Fig. 8 correspond to Eq. 6 and to the condition LSI $\leq$ 100.

Figure 9 includes a comparison of LSI predicted by Eq. 6 versus actual LSI for all Youd and Perkins' data points corresponding to $M_w \leq 7.4$. This range of magnitudes ($M_w = 5.2$ to 7.4) coincides with the range used by the authors in their study, as discussed later in this section. Approximate upper and lower bounds (dashed lines) have been traced in Fig. 9, which indicate that Youd and Perkins' equation predicts LSI within a factor of 2 or 3 (correct order of magnitude).

218
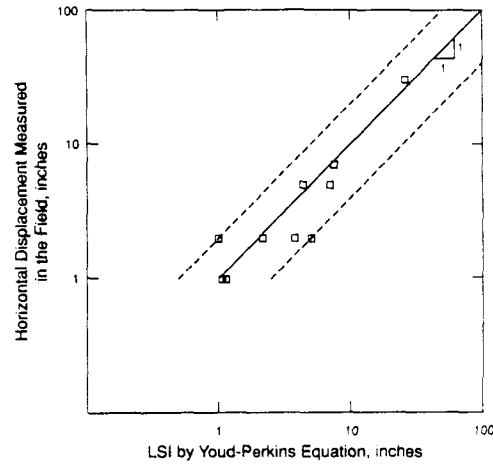
Fig. 9.   Comparison of displacements measured in the field and predicted by LSI Equation 6.

The authors used the sliding block method in conjunction with their laboratory results to evaluate LSI, and compared the predictions with those measured in the Western United States by Youd and Perkins and summarized by Figs. 8 and 9 and Eq. 6. The idealized typical site profile of Fig. 10 was selected for the analyses as representative of the conditions described by Youd and Perkins. The profile corresponds to an infinite slope of
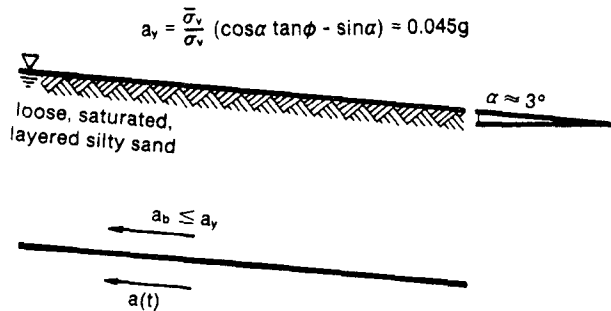
Fig. 10.   Typical site condition used in sliding block analyses of lateral spreads.

angle $\alpha \simeq 3°$ (5% slope) with the groundwater level at the ground surface. The seepage forces associated with this very gently sloping groundwater level are neglected in the analyses. The soil is assumed to have the strength $S_{us}/\bar{\sigma}_v = 0.12$ determined for very loose layered silty sand in the laboratory. For this combination of α and $S_{us}/\bar{\sigma}_v$, Eq. 4 gives a yield acceleration $a_y = 0.045$ g, independent of depth, for a failure surface parallel to the slope. The same as in the Wildlife site, only down slope movements were allowed when computing d = LSI.

Twenty earthquake records obtained on soil in the Western United States and having a maximum acceleration $a_p > a_y = 0.045$ g were used in the analyses. These records cover ranges of magnitudes $(M_w = 5.3$ to $7.4)$ and distances (R = 7 to 107 km) comparable to those used by Youd and Perkins. Seven earthquake events were included:

219

Lytle Creek 1970 $(M_w = 5.3)$,
Parkfield 1966 $(M_w = 6.1)$,
Imperial Valley 1979 $(M_w = 6.5)$,
San Fernando 1971 $(M_w = 6.6)$
Borrego Mountain 1968 $(M_w = 6.6)$,
Imperial Valley 1940 $(M_w = 7.0)$, and
Kern County 1952 $(M_w = 7.4)$.

APPLICATION TO LATERAL SPREADING

The earthquake records were provided by the U.S. Geological Survey and California Institute of Technology, and the site distances R and earthquake magnitudes M_w were selected based on the information furnished by Joyner and Boore (1981).

In Fig. 11, the twenty values of d = LSI calculated by the authors are plotted versus M_w and R using the same format of the original LSI chart. Superimposed in Fig. 11 are the lines predicted by Youd and Perkins' Eq. 6 for the corresponding earthquake
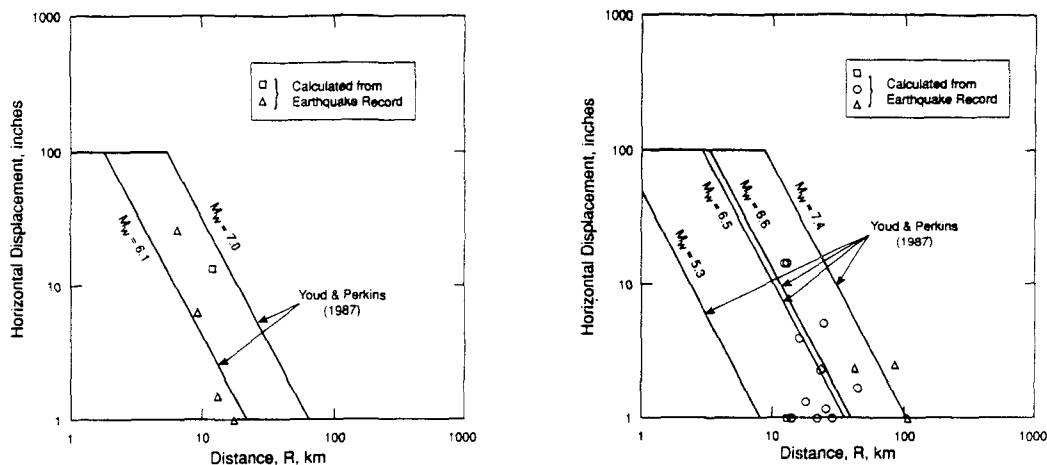
Fig. 11. Comparison of displacements calculated from earthquake records using sliding block analyses and displacements predicted by LSI Equation 6 for various earthquake magnitudes.

magnitudes. Both Youd and Perkins' lines and the data points calculated by the authors show the same trend of LSI increasing with M_w and decreasing with R. Furthermore, the calculated data points group nicely around the lines, indicating that the analysis done by the authors predicts not only the trend but also the correct order of magnitude of LSI. This is very encouraging and is confirmed by Fig. 12, which includes a comparison of LSI predicted by Eq. 6 for all twenty records, versus d = LSI computed in the analysis. The upper and lower bounds from Fig. 9 have also been superimposed on Fig. 12.

Figure 12 indicates that, indeed, the sliding block analysis using actual earthquake records and $S_{us}/\bar{\sigma}_v = 0.12$ can predict the correct order of magnitude of LSI within a factor of 2 or 3, doing almost as good a job as Eq. 6, which had been fitted empirically to the observed data.
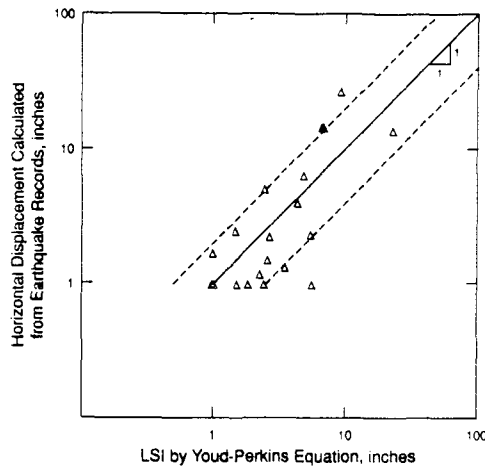
Fig. 12. Comparison of displacement calculated from earthquake records using sliding block analyses and displacements predicted by LSI Equation 6.

CONCLUSIONS

Based on the results of this study -- including the laboratory test results as well as the case history calculations at the Wildlife site and at other Western United States locations -- it is possible to arrive to the following conclusions:

1. Lateral spreads can be evaluated using the sliding block model, which predicts well the observed influence of earthquake magnitude and distance on displacement in the Western United States.

2. The lateral displacement d predicted using the model is quite sensitive to the specific assumptions and values of parameters selected for the analysis. As a result, only the order of magnitude of d can be predicted. This is consistent with the large scater of values of d observed in the field.

3. Undrained laboratory tests on remolded layered pluvially deposited silty sand simulates the in situ fabric of the late Holocene loose fluvial deposits typically affected by lateral spreads. Tests on contractive specimens conducted by the authors suggest a value of shear strength $S_{us} = 0.12\ \bar{\sigma}_v$ to calculate the yield acceleration needed for the sliding block analyses.

4. Sliding block analyses using recorded accelerograms and this shear strength predict very well the Liquefaction Susceptibility Index chart developed by Youd and Perkins for the Western United States based on field observations of the lateral displacement.

ACKNOWLEDGMENTS

REFERENCES

Bartlett, S. F., and Youd, T. L., (1991) "Case History of Lateral Spreads from the 1964 Alaska Earthquake,"Case Studies of Earthquakes for Large Ground Deformation, O'Rourke, T. and Hamada, M.(eds.), in press.

Baziar, M.H., and Dobry, R., (1991) "Liquefaction Ground Deformation Predicted from Laboratory Tests," Second International Conference on Recent Advances in Geotechnical Earthquake Engineering and Soil Dynamics, St. Louis, MO, March.

Baziar, M.H., (1991) "Engineering Evaluation of Ground Deformation Due to Seismically-Induced Liquefaction," Ph.D Thesis, Department of Civil Enginering, RPI, Troy, NY 12180, in progress.

Castro, G., (1987) "On the Behavior of Soils during Earthquake–Liquefaction," Developments in Geotechnical Engineering 42, Soil Dynamics and Liquefaction, Ed. by A. S. Cakmak, Dept. of Civil Eng., Princeton University, Princeton, NJ 08544.

Dobry, R., Baziar, M. H., O'Rourke, T., Roth, B., and Youd, T. L., (1991) "Liquefaction and Ground Failure in the Imperial Valley, Southern California, During 1979, 1981, and 1987 Earthquakes,", Case Studies of Earthquakes or Large Ground Deformation, O'Rourke, T. and Hamada, M.(eds.), in press.

Dobry, R., Elgamal, A.–W., Baziar, M. H., and Vucetic, M., (1989) "Pore Pressure Build Up and Acceleration Induced in Wildlife Site Due to 1987 Earthquake," 2nd U.S.–Japan Workshop on Liquefaction, Large Ground Deformation and their Effects on Lifeline Facilities, Niagara Falls, NY, September.

GEI, (1989) "An Investigation of the February 9, 1971 Slide," Report to the U.S. Army Engineer Waterways Experiment Station, 2 Vols, GEI Consultants, Inc., Winchester, MA.

Hamada, M., Yasuda, S., Isoyama, R., and Emoto, K. (1986) "Study on Liquefaction Induced Permanent Ground Displacements," Research Report, Assn. for the Development of Earthquake Prediction, November.

Holzer, T., Youd, T. L., and Bennett, M. J., (1989) "*In Situ* Measurement of Pore Pressure Build Up During Liquefaction," Proc. 20th Joint Meeting of U.S.–Japan Cooperative Program in the Natural Resources, Panel on Wind and Seismic Effects, U.S. Dept. of Commerce.

Joyner, W. B., and Boore, D.M., (1981) "Peak Horizontal Acceleration and Velocity from Strong–Motion Records Including Records from the 1979 Imperial Valley, California, Earthquake," Bulletin of Seismological Society of America, Vol. 71, No. 6, pp 2011–2038, December.

Ladd, C. C., and Foott, R. (1974) "New Design Procedure for Stability of Soft Clays," J. of Geotechnical Eng., ASCE, Vol. 100, No. GT7, July.

Lambe, T. William and Whitman, Robert V. (1969) Soil Mechanics, John Wiley & Sons, Inc., New York.

National Research Council, (1985) <u>Liquefaction of Soils During Earthquakes</u>, National Academy Press, Washington, DC.

Newmark, N. M. (1965) "Effect of Earthquakes on Dams and Embankments," Geotechnique, Vol. 5, No. 2.

U.S.–Japan, (1988) Proceedings of First Workshop on Liquefaction, Large Ground Deformation and Their Effects on Lifeline Facilities, Hamada, M., and O'Rourke, T. D., editors, Tokyo, Japan, November 16–19.

U.S.–Japan, (1989) Proceedings of Second Workshop on Liquefaction, Large Ground Deformation and Their Effects on Lifeline Facilities, O'Rourke, T. D., and Hamada, M., editors, Grand Island, NY, September 26–29.

Vasquez–Herrera, A., and Dobry, R., (1989) "The Behavior of Undrained Contractive Sand and its Effect on Seismic Liquefaction Flow Failure of Earth Structures," Research Report, Dept. of Civil Eng., Rensselaer Polytechnic Institute, Troy, NY.

Vasquez–Herrera, A., Dobry, R., and Baziar, M. H., (1990) "Re–Evaluation of Liquefaction Triggering and Flow Sliding in the Lower San Fernando Dam during the 1971 Earthquake," 4th U.S. National Conf. on Earthquake Eng., Palm Springs, CA, May.

Youd, T. L., and Bartlett, S. F., (1988) "U.S. Case Histories of Liquefaction–Induced Ground Displacement," 1st U.S.–Japan Conference on Liquefaction, Large Ground Deformation and their Effects on Lifeline Facilities, Tokyo, Japan, November.

Youd, T. L., and Perkins, D. M., (1987) "Mapping of Liquefaction Severity Index," J. of Geotechnical Eng., ASCE, Vol. 113, No. 11, November.

Youd, T. L., (1990) Personal communication.

A SIMPLIFIED PROCEDURE FOR THE ANALYSIS OF THE PERMANENT GROUND DISPLACEMENT

Susumu Yasuda
Associate Professor of Civil Engineering
Kyushu Institute of Technology

Hideo Nagase
Lecturer of Civil Engineering
Kyushu Institute of Technology

Hiroyoshi Kiku
Graduate Student of Civil Engineering
Kyushu Institute of Technology

Yutaka Uchida
Graduate Student of Civil Engineering
Kyushu Institute of Technology

ABSTRACT

To study the mechanism of permanent ground displacement due to liquefaction, shaking table tests were conducted. Moreover, vane tests and cyclic torsional shear tests were carried out to measure the rate of decrease of the elastic modulus and the shear strength due to liquefaction. Based on these tests results, the authors proposed a simplified procedure for the prediction of permanent ground displacement. Measures to counter permanent ground displacement were also discussed based on the analysis and shaking table tests.

INTRODUCTION

Recently, Hamada et al.(1986) clarified that extremely large ground displacements, up to several meters, occurred in ground liquefied during the 1964 Niigata Earthquake and the 1983 Nihonkai-chubu Earthquake, though the ground surface was almost flat. The authors conducted shaking table tests, vane tests and cyclic shear tests to study the mechanism of ground displacement and to ascertain the rate of decrease of the elastic modulus and the shear strength. Based on these tests, a simplified procedure for forecasting permanent ground displacement was proposed. To confirm the accuracy of this method, it was applied to models of the shaking table tests and to two typical cross sections in Niigata City, and the analytical results were compared with the actually observed measurements. Finally, countermeasures against permanent ground displacement were discussed.

SHAKING TABLE TESTS

Shaking table tests were conducted on 24 soil models,shown in Table 1, to study the mechanism of permanent ground displacement due to soil liquefaction. In these tests, series A, B, C, D, E and F were conducted at first. Then, other series were continued to confirm the mechanism of permanent ground displacement. The shaking table used was 1 m in length and 1 m in width in plane. The soil container used for series A, B, C, D, E and F was 80 cm in length , 65 cm in depth and 60 cm in width. For series G, H and I, slightly bigger container of 100 cm in length and 65 cm in depth and 60 cm in width was used.

A soil model consisted of two sand layers : an upper layer of loose sand which would liquefy during shaking, and a lower layer of dense sand which would not liquefy during shaking. The same kind of sand was used for both sand layers ; however, the method of compaction used for each layer was different . First, the lower sand layer was compacted by shaking at 300 gals of acceleration for two minutes. Then, the upper sand layer , which will be called the "liquefied layer" hereafter, was passed through a sieve in air or in water.

Three types of sand were used for the tests: (1) very clean sand taken from a beach in Yamaguchi Prefecture and passed through a sieve with a mesh of 0.42 mm, (2) sand with fines taken from a hill in Chiba Prefecture and (3) Toyoura sand. The fine contents of the two sands were 0 %, 6 % and 0 %, respectively.

Models tested were classified into nine series, as shown in Fig.1. and Table 1:
A. the ground surface is flat , but the bottom surface of the liquefied layer is sloped,
B and C. both the ground surface and the bottom surface of the liquefied layer are sloped in the same direction,
D. the ground surface and the bottom surface of the liquefied layer are sloped in opposite directions,
E. the ground surface is flat and the bottom surface of the liquefied layer

Table 1 Test conditions

Model No.	Soil	H (cm)	θ s (%)	θ b (%)	D r (%)	Density	D (cm)
A-2	CS	17.5	0	5	47	MD	0.28
A-3	CS	17.5	0	10	52	MD	0.35
A-4	CS	7.5	0	5	50	MD	-0.05
A-5	CS	27.5	0	5	56	MD	0.45
B-2	CS	17.5	5	5	66	MD	1.64
B-3	CS	17.5	10	10	56	MD	3.04
B-4	CS	7.5	5	5	66	MD	0.59
B-5	CS	27.5	5	5	50	MD	1.75
B-2-L	CS	17.5	5	5	-37	VL	2.3
C-2	FS	17.5	5	5	62	MD	0.85
C-2-L	FS	17.5	5	5	0	VL	1.2
C-2-M	FS	17.5	5	5	46	L	0.97
D-1	CS	17.5	0	-10	52	MD	0.35
D-2	CS	17.5	2	-10	89	MD	2.20
D-3	CS	17.5	10	-10	67	MD	6.64
E-1	CS	17.5	0	±5	-34	VL	0.47
E-2	CS	17.5	0	+10	-43	VL	0.08
F-1	CS	27.5	5	5	8	L	1.26
G-1	TS	18	0	5	37	MD	1.99
G-2	TS	18	0	10	30	MD	2.39
G-3	TS	18	5	5	37	MD	3.29
G-4	TS	18	10	10	35	MD	5.99
H-1	TS	18	0	5	20	MD	1.88
I-1	TS	7.5	5	5	0	VL	5.19
	TS	12.5	5	5	30	MD	

· CS : clean sand, FS: sand with fines, TS: Toyoura sand
· H : thickness of the liquefied layer at the center
· θ s: slope of the ground surface
· θ b: bottom surface of the liquefied layer
· D r: relative density of the liquefied layer
· MD : medium dense, L: loose, VL: very loose
· D : displacement on the ground surface
· soil container used for series G, H and I is slightly
  bigger than that for other series
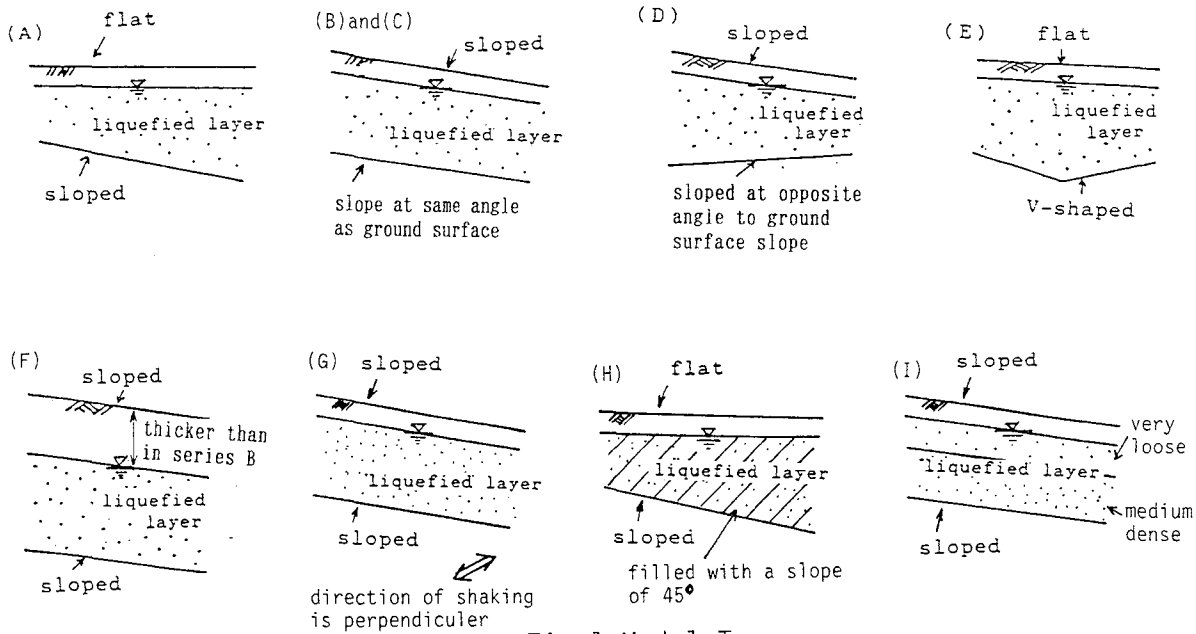
Fig.1 Model Types

is sloped toward the center,
F. the ground surface and the bottom surface of the liquefied layer are sloped in the same direction, but the top surface of the liquefied layer is deep,
G. ground condition is almost same as Model A-2, A-3, B-2 and B-3, but the shaking motion was applied in the opposite direction, perpendicular to the horizontal axis,
H. ground condition is almost same as Model A-2, but the "liquefied layer" was filled with a slope of 45° as shown in Fig.1(H), and
G. both the ground surface and the bottom surface of the liquefied layer are sloped as same as Model B-2, but the "liquefied layer" is separated to two sublayers; very loose layer and medium dense layer.

Several slopes of the surface or the bottom surface of the liquefied layer and two densities were adopted for series A and B. Test conditions for all models are shown in Table 1.

Shaking motion was applied in one direction parallel to the horizontal axis except series G, at a frequency of 3 Hz and with appropriate accelerations to induce liquefaction after several cycles of shaking. The shaking was finished 10 seconds after liquefaction. Acceleration and excess pore water pressure during the shaking were measured at two points. Displacement at several points in the liquefied layer was measured by two methods : (1) deformations of nine noodles, placed vertically in the soil at the front of the model, just behind the glass, were measured by photo at intervals of 2.5 seconds during shaking, and (2) displacement of 30 pins on the ground surface was measured by a scale after stopping the shaking.

Test results of series A, B, C, D, E and F have already shown during the First Japan-US Workshop in 1988 (Towhata, Yasuda, Ohtomo and Yamada). Therefore, only main observations are shown in this paper:

228

(1) The displacement increased linearly in a vertical direction from zero at the bottom surface of the liquefied layer to a maximum value at the ground surface. This means that displacement did not occur at the boundary between the liquefied layer and the non-liquefied layer, but occurred with a constant shear strain in the liquefied layer.

(2) In series A, displacements were not so large. However , it seems that displacement was induced from the bottom to the middle part of the
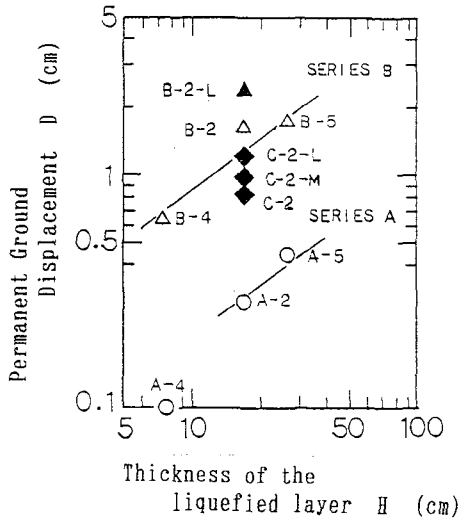
Fig.2 Relationships between D and H
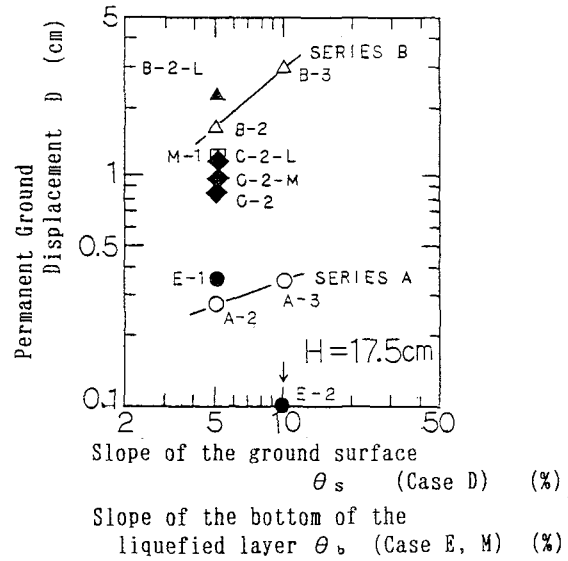
Fig.3 Relationships between D and θ

liquefied layer, toward the direction of slope of the bottom surface of the liquefied layer. Displacements near the ground surface were small.

(3) In series B, the settlement at the lower part of the surface was less than that at the upper part. This means that settlement, due to compaction, and uplift of the ground surface was induced in the lower part, due to movement of soil from the upper part.

(4) According to Fig.2 and Fig.3, the displacement of loose sand was greater than that of medium dense sand , and the displacement of sand with fines was less than that

——————— Before liquefaction
---------- 2 sec. after liquefaction
········· 4 sec. after liquefaction
——————— 6 sec. after liquefaction
·· — · — 8 sec. after liquefaction
——————— 10 sec. after liquefaction

(a)Model G-3

(b)Model H-1   (c)Model I-1
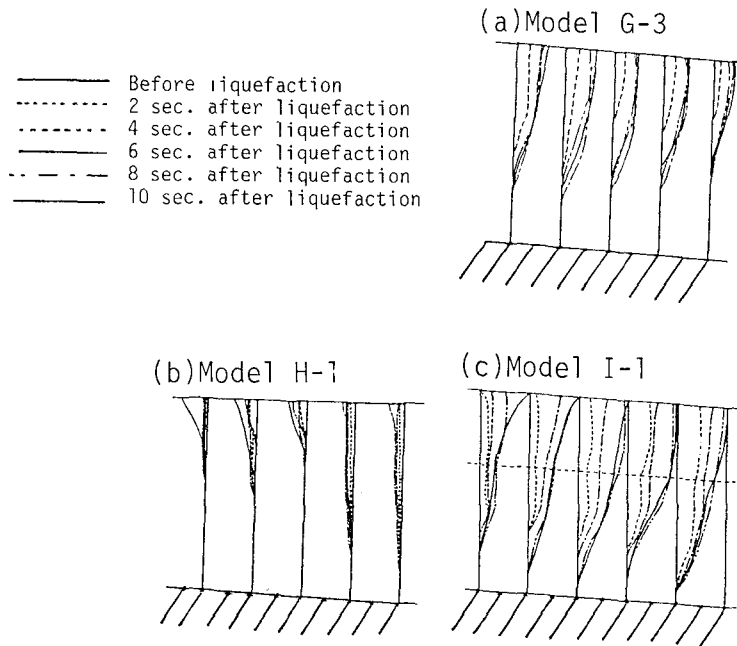
Fig.4 Deformation of the noodles

229

of clean sand.

(5) According to these results, it is summerized that permanent displacement of the ground would not occur at the surface of a rupture due to a slide, but would occur through out a liquefied layer because of a fall of shear strength due to liquefaction.

In Model G-3, displacement was slightly smaller than Model B-2. However, displacement developed gradually after the occurrence of liquefaction as shown in Fig.4(a) as almost same as Model B-2. In Model H-1, displacement occurred not toward the slope of the bottom surface of the liquefied layer, but toward the slope of the filled layers as shown in Fig.4(b). The displacement of Model I-1 was larger than Model B-2.

VANE SHEAR TESTS

Vane shear tests and cyclic torsional shear tests were conducted to evaluate the rate of reduction of the shear strength and the elastic modulus in the process of liquefaction.

The vane shear test apparatus was set on the top of the same soil container as used in the shaking table tests, as shown in Fig.5, and the soil container was vibrated by the shaking table to liquefy the sample. The vane used was 5 cm in height and 2.5 cm in width, and the sand used was Toyoura sand. Samples were prepared by dropping the sand from different heights into the container to obtain several relative densities. The vane shear tests were carried out at a rotational speed of 6 degrees per second in the strain control method. On each sample, tests were conducted before shaking and during liquefaction and the test results were compared. Fig.6 shows the relationship between the rate of reduction of shear strength due to liquefaction and relative density. According to the test results, the shear strength decreased to about 1/100 to 1/500 of the original strength due to liquefaction.
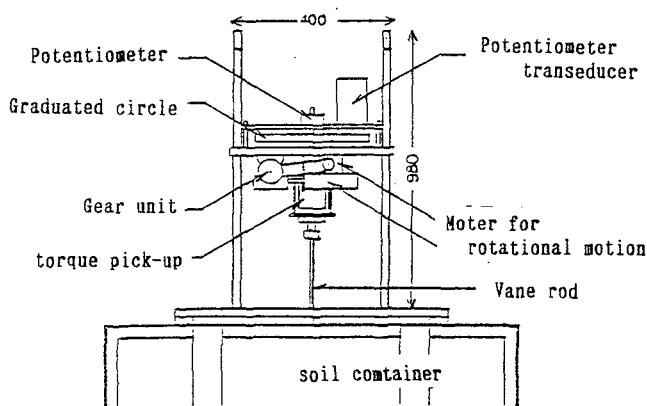
Fig.5 Vane shear test apparatus
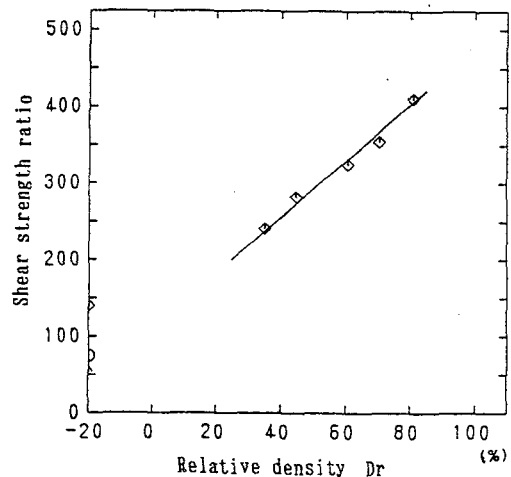
Fig.6 Rate of reduction of shear strength

230

CYCLIC TORSIONAL SHEAR TESTS

Cyclic torsional shear tests were conducted to clarify the rate of decrease of the elastic modulus due to liquefaction. The sand used for these tests was also Toyoura Sand. All tests were carried out at relative densities of 30 % to 40 % and at an effective isotropical confining pressure, σ_0', of 0.5 kgf/cm² . Hollow cylindrical specimens of 10 cm in height, 10 cm in outer diameter and 6 cm in inner diameter were used.

After fully saturated specimens were consolidated, as shown in Fig.7, a cyclic shear stress of 0.1 Hz was applied until the excess pore pressure ratio, $\Delta u / \sigma_v'$, reached a prescribed amount. Finally, static shear stress was applied under a constant strain rate of 0.1 % per minute. The prescribed amount of the excess pore pressure ratio, $\Delta u / \sigma_v'$, was changed for each specimen from 0 to 1.0. A specimen of $\Delta u / \sigma_v' = 1.0$ is a fully liquefied specimen.

Fig.8 shows the test results during the application of static shear stress. It is clear that if the excess pore pressure ratio increases, the shear strain under the same shear stress increases extremely. This means that the inclination of the stress-strain curve, which can be viewed as an elastic modulus, G, decreases with the excess pore pressure. The relationship between the excess pore pressure ratio and decreasing ratio of the elastic modulus in small strain, G/G_0, in which G_0 is the elastic modulus of $\Delta u / \sigma_v' = 0$, is plotted in Fig.9. The elastic modulus in small strain, G/G_0, decreases rapidly with an increase in excess pore pressure ratio, $\Delta u / \sigma_v'$, and reaches a very small value, almost 0.001, if a specimen is liquefied fully. However, though the specimen is fully liquefied, the elastic modulus increases under very large strain, such as almost 10% of shear strain,
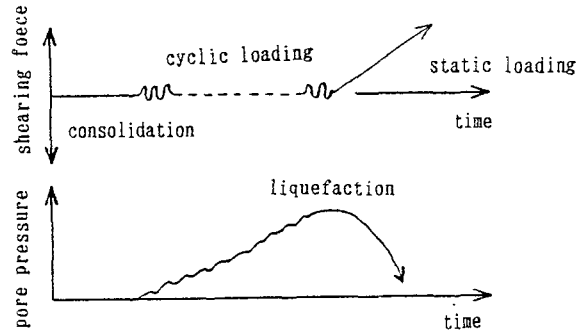
Fig.7 Typical pattern of Test
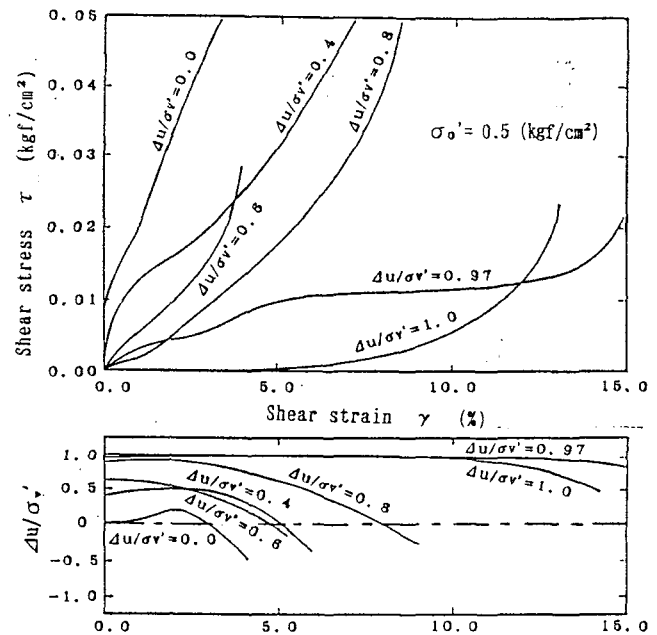
Fig.8 Stress-strain relationships during static tests after cyclic loading
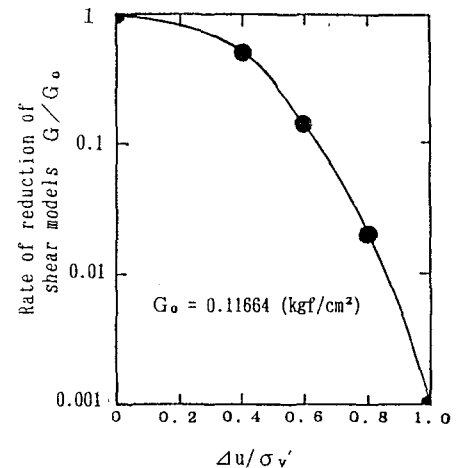
Fig.9 Rate of reduction of shear models

231

due to dilatancy, as shown in Fig.8.

A SIMPLIFIED PROCEDURE FOR THE ANALYSIS OF THE PERMANENT GROUND DISPLACEMENT

Based on the test results mentioned above and case studies conducted by Hamada et al. (1986) , the authors proposed a simplified procedure for the analysis of permanent ground displacement. In this procedure, the authors assumed that permanent ground displacement would occur in liquefied softened ground due to shear stress present before liquefaction. The finite element method was applied twice as follows :
(1) In the first stage, the distribution of stresses in the ground is calculated by the finite element method using the elastic modulus before the earthquake. In the calculation, model layers must be made in several steps, because the soil layers in a natural ground have filled gradually.
(2) Then, holding the stress constant, the finite element method is conducted again using the the decreased modulus due to liquefaction by the earthquake.
(3) The difference in deformation measured by the two analyses is supposed to equal the permanent ground displacement.

To confirm the accuracy of this procedure, several analyses of the soil models used for the shaking table tests were conducted. In these analyses, the shear modulus was determined by a triaxial test. Poisson's ratio during filling, Poisson's ratio during an earthquake and the rate of decrease in the elastic modulus, G/G_0 , due to liquefaction, were assumed as 0.35, 0.499 and 1/1000, respectively. Fig.10 shows the result of analysis of Model B-3. Deformation towards the right side occurred in the liquefied layer and displacement increased in a vertical direction from zero at the bottom surface of the liquefied layer to a maximum value at the ground surface. These tendencies coincide fairly well with the test results.

In the next step, permanent ground displacements at the site of Showa Bridge and around Niigata Railway Station in Niigata City during the 1964 Niigata Earthquake were analyzed. These
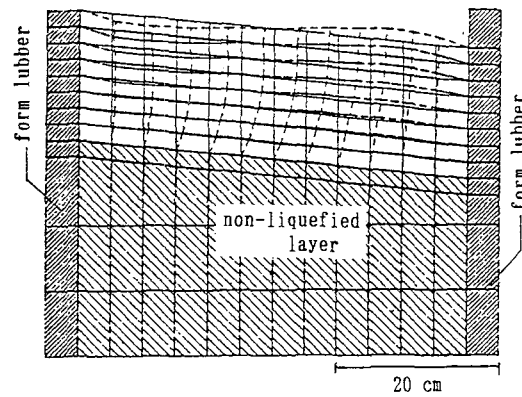
Fig.10 Analyzed deformation of model grounds (B-3)
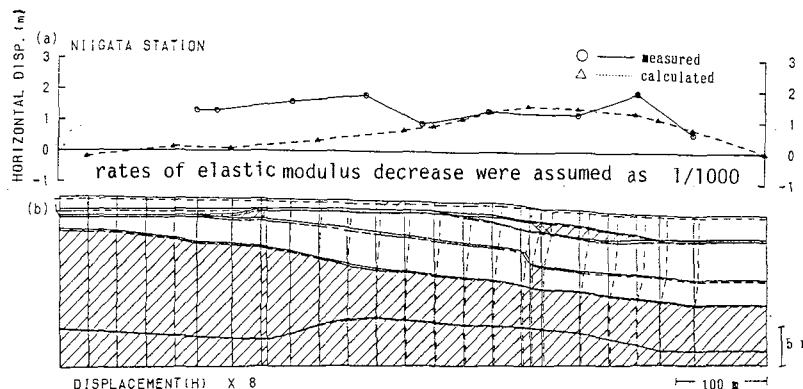
Fig.11 Comparison between calculated displacements and measured displacements (Niigata Railway Station)

results were compared with the results measured by Hamada et al(1986). In these analyses, Young's modulus ,E, was estimated from SPT N-value by using the formula , E=28N. Poisson's ratios during filling and during an earthquake were assumed as 0.35 and 0.499, respectively, as in the analyses of soil models used for shaking table tests. Three rates of elastic modulus decrease were assumed: 1/1000, 1/500, and 1/2000. Fig.11 compares the results of analysis of ground around Niigata Railway Station with the displacements measured in that area. In Fig.11(a), analyzed displacements and measured displacements have the same tendency: displacement increases with the thickness of the liquefied layer. By comparing the amount of deformation analyzed with that measured, it can be said that the analysis assuming an elastic modulus of decrease rate of almost 1/1000 is appropriate. This decreasing ratio coincides well with the result of the cyclic torsional shear test in Fig.8.
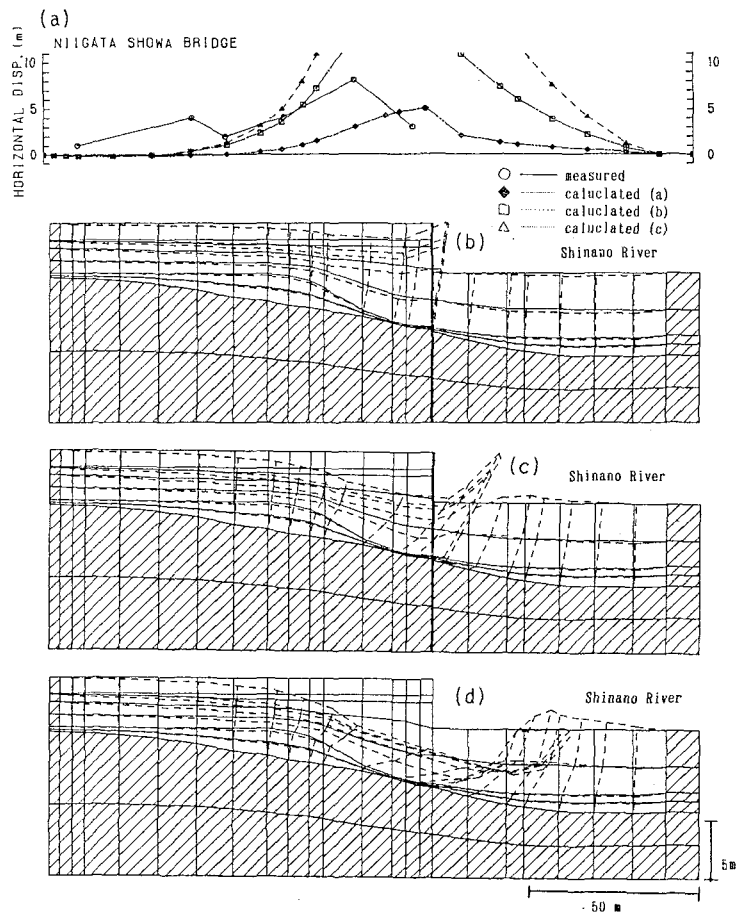
Fig.12 Comparison between calculated displacements and measured displacements (Niigata Showa Bridge)

According to a civil engineer in Niigata City, retaining walls made by steel sheet along the banks of Shinano River near Showa Bridge were bent and fell into the river due to the Niigata Earthquake, and he could not find the retaining walls after the earthquake. Therefore,in the analysis of ground at Showa Bridge, the following three models of the retaining wall were supposed, as shown in Fig.12 :
(1) the retaining wall had been installed below the bottom of the liquefied layer, and was not bent during the earthquake (Fig.12(b)) ,
(2) the retaining wall had been installed up to the bottom of the liquefied layer, and was bent during the earthquake (Fig.12(c)) , and
(3) the retaining wall had been installed only up to the middle of the liquefied layer, and fell entirely into the river (Fig.12(d)).

According to the results of analysis, shown in Fig.12(b) , the deformation is not so large if the retaining wall is not bent. However, if the

233

retaining wall is bent, extremely large deformation occurs near the river edge, as shown in Fig.12(c) and (d). This suggests that vertical walls are effective in decreasing permanent ground displacement. By comparing the displacements predicted by analysis with the measured displacements on Fig.12(a), it can be seen that the measured values fall between the values of analysis based on the assumptions (1) and (2). As the depth of the retaining wall at this site is not clear, more detailed discussion on the accuracy of the analysis can not be continued.

PROPOSAL OF COUNTERMEASURES AND DISCUSSION OF THEIR EFFECTIVENESS

It is not clear what kind of countermeasures are effective against permanent ground displacement due to liquefaction, because no countermeasures have been applied. However,based on the tests, analyses and case studies, the following three categories of countermeasures seem to be effective : (1) improving the ground in all area by densification to prevent liquefaction, (2) strengthening structures to prevent their collapse, and (3) strengthening

(a)

DISPLACEMENT(H)   X 2
DISPLACEMENT(V)   X 1

(d)

sheet pile

DISPLACEMENT(H)   X 2
DISPLACEMENT(V)   X 1

(b)

compaction

DISPLACEMENT(H)   X 2
DISPLACEMENT(V)   X 1

(e)

sheet pile

DISPLACEMENT(H)   X 2
DISPLACEMENT(V)   X 1

(c)

compaction

DISPLACEMENT(H)   X 2
DISPLACEMENT(V)   X 1

$E / E_o = 1/1000$
$\nu = 0.499$

(f)

sheet pile

Horizontal scale   10 m ⊢——⊣
Vertical   scale   5 m ⊢——⊣
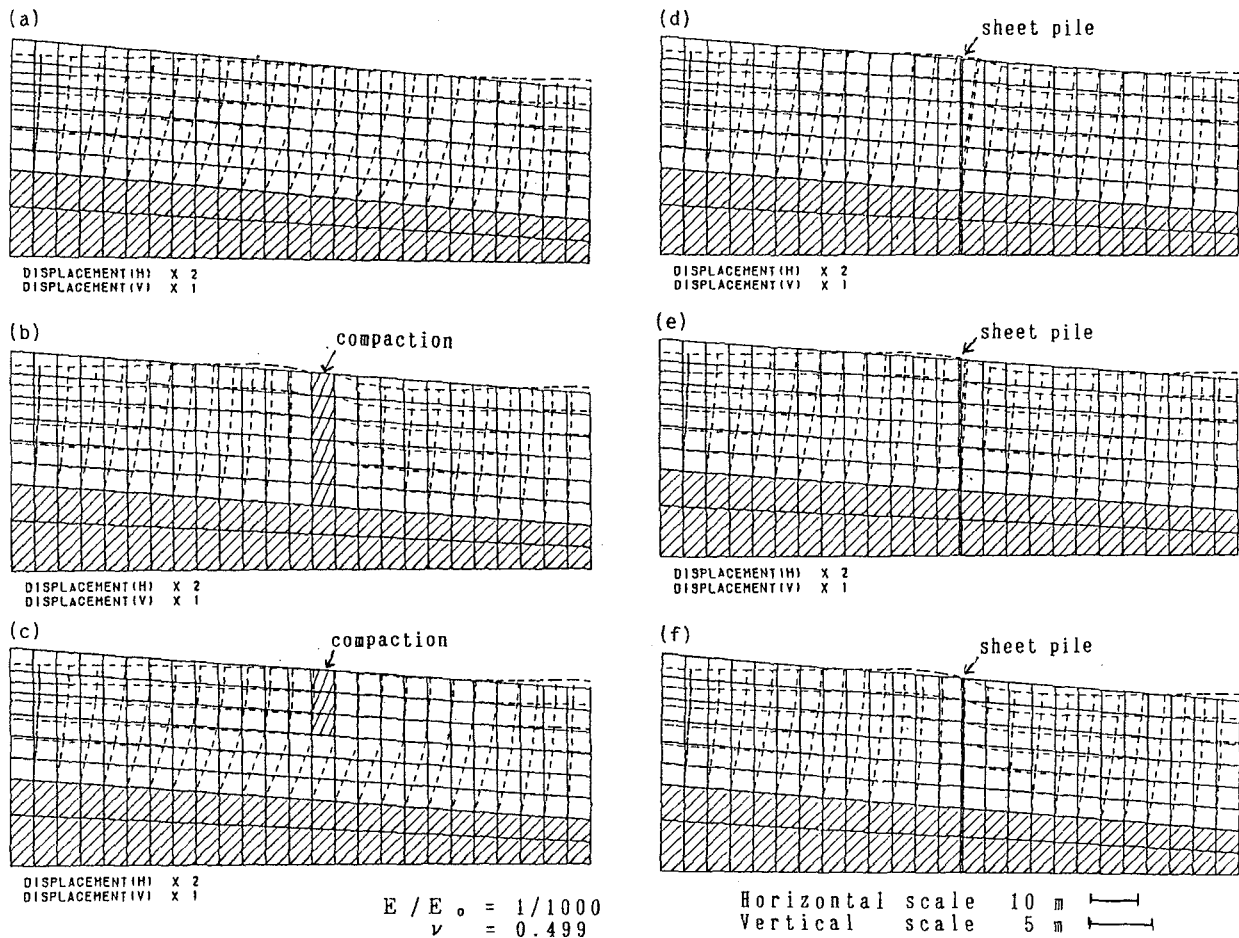
Fig.13 Analyzed deformation of model grounds with Countermeasure

234
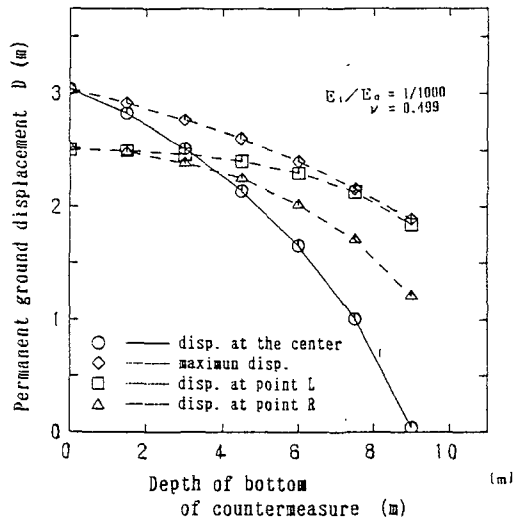
Fig.14 Relationships between D and depth
of the bottom of countermeasure
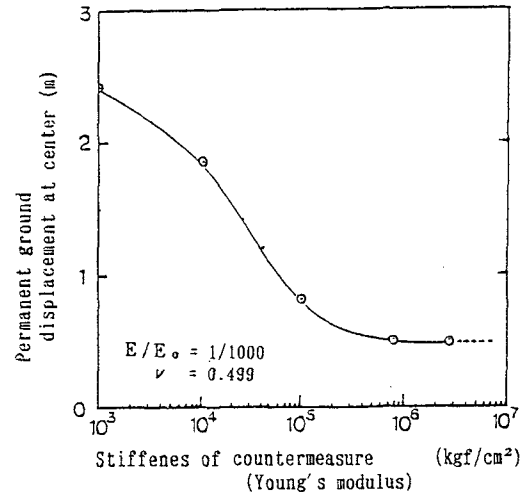
Fig.15 Relationship between D and the
stiffness of countermeasure

the ground with walls, steel piles or
sand piles to prevent large ground
displacement if liquefaction occurs.
Ground densification is generally
considered uneconomical, because it must
be applied to a wide area. Different
methods must be used to strengthen
different structures making this approach
somewhat impractical. Therefore,
strengthening the ground with walls is
discussed in this paper.

According to the analyses of ground at
Showa Bridge ,the effectiveness of the
retaining wall has been suggested, as
shown in Fig.12. Therefore, the
installation of sheet piles or continuous

o model steel pile
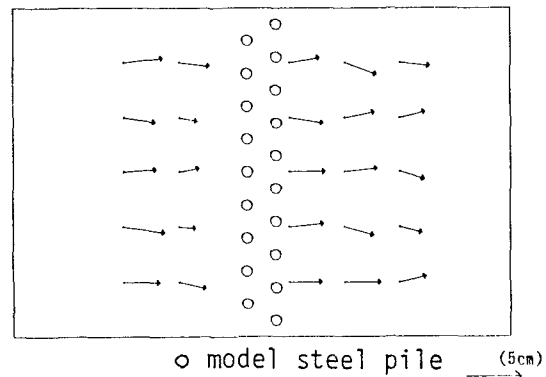
Fig.16 Displacement of pins on the
ground surface

walls into the ground and the ground compaction were studied. Several
analyses were performed, assuming different countermeasure parameters, on a
ground model of 100m in length, with a liquefied layer 10m in thickness and a
3 % slope of the ground surface. The SPT-N values of liquefied layer and the
non-liquefied layer were assumed as 3 and 20, respectively. The rate of
decrease of the elastic modulus due to liquefaction was supposed as 1/1000.

Six of the results of analysis are shown in Fig.13. Analysis showed that the
amount of ground displacement was decreased by installing sheet pile or
continuous wall, or by compacting the ground in some zone. Moreover, the
effectiveness of the countermeasures decreases if the compacted zone does not
reach the bottom of the liquefied layer, or if the sheet pile is weak.
These relationships are summarized in Fig.14 and Fig.15.

235

Now, shaking table tests on countermeasures are conducting. Ground conditions of these tests are same as Model B-2 in Table 1. Model steel piles are installed in the ground. One test result for steel piles is shown in Fig. 16. Twenty arrows show displacements of pins on the ground surface. It can be seen that displacements in front of the piles are decreased.

CONCLUSIONS

To study the mechanism of two permanent ground displacements due to liquefaction, shaking table tests, vane shear tests and cyclic torsional shear tests were conducted. In the shaking table tests, displacement did not occur at the boundary between the liquefied layer and the non-liquefied layer, but occurred with a constant shear strain in the liquefied layer. By the cyclic torsional shear tests, it was clarified that the elastic modulus decreased to a very small value, almost 1/1000, due to liquefaction. Based on these results, a simplified procedure for the analysis of permanent ground displacement was proposed. In applying this method to the models of the shaking table tests and to two typical cross sections in Niigata City, the accuracy of the method was confirmed. This method seems to be effective not only to predict permanent ground displacement during a future earthquake, but also to evaluate the effectiveness of countermeasures.

ACKNOWLEDGEMENT

REFERENCES

Hamada,M., Yasuda,S., Isoyama,R. and Emoto,K. (1986), "Study on Liquefaction Induced Permanent Ground Displacement", Association for the Development of Earthquake Prediction.

Towhata,I., Yasuda,S., Ohtomo,K. and Yamada,K. (1988), "Experimental Studies on Liquefaction Induced Permanent Ground Displacement", Proc. of the 1st Japan-US Workshop on Liquefaction, Large Ground Deformation and Their Effects on Lifeline Facilities, pp.81-92, 1988.

236

Prediction of Permanent Lateral Displacement of Liquefied
Ground by Means of Variational Principle

Towhata,I.[1] , Tokida,K.[2] , Tamari,Y.[3] , Matsumoto,H.[2]
and Yamada,K.[4]

ABSTRACT

The lateral displacement of a seismically liquefied ground
was studied by shaking table tests. It was found, firstly,
that the liquefied sandy soil behaves as a liquid material
which flows under gravity force. Secondly, the surface
unsaturated layer, if any, moves together with the under-
lying liquefied sand. This surface layer does not liquefy
and behaves like an elastic bar resisting against the flow
of subsoil. Finally, the distribution of the lateral
ground displacement in any vertical cross section was
found to be approximated by a sinusoidal curve, maximum at
the surface and null at the bottom. Based on these, an
analytical method to predict the permanent ground dis-
placement was developed in which the principle of minimum
potential energy was employed to derive a closed-form
solution. The solution was applied to several case histo-
ries to show good agreement with observations.

INTRODUCTION

The permanent displacement of seismically-liquefied ground
was studied through air-photo surveys by Hamada et al.
(1986). Being as large as several meters at the maximum,
the ground displacement induces breakage of buried pipe-
lines as well as failure of piled foundations. Fig.1
illustrates the ground displacement in Noshiro City,
Japan, caused by an intense shaking in 1983. The observed
ground displacement near a small Maeyama Hill is oriented
in the radial downslope direction. In the Tagomukai Area,
similarly, the ground displacement occurred from higher
elevation towards the lower places. Cracks and sand boils
in Fig.2 indicate that liquefaction occurred intensely in

---

(1) Associate Professor of Civil Engineering, University
    of Tokyo, Tokyo, Japan.
(2) Public Works Research Institute.
(3) Tokyo Electric Power Services.
(4) Fudo Construction.
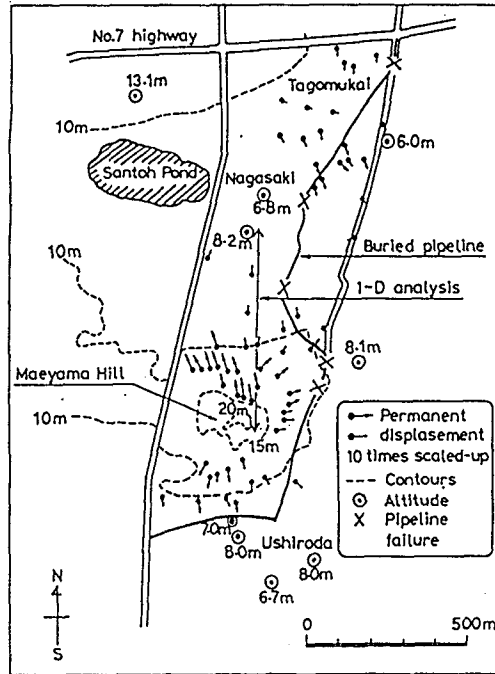
Figure 1. Ground displacement detected by Hamada et al. (1986) in Noshiro City, Japan.
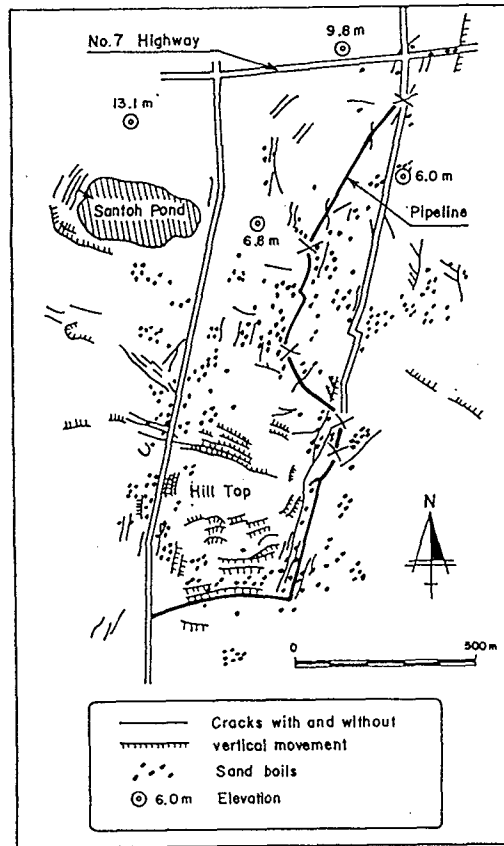
Figure 2. Cracks and sand boils in liquefied area on Noshiro City.
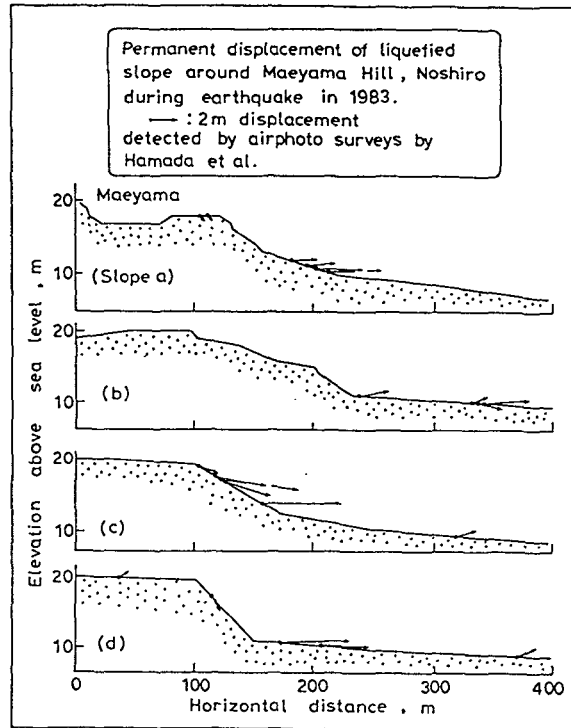
Figure 3. Subsidence and heaving of liquefied slope in Noshiro City as detected by Hamada et al. (1986).

the particular area. These observations lead to;

(Obs.1) Cracks occur near the top of a slope. They are oriented perpendicular to the direction of ground movement.

(Obs.2) The magnitude of the displacement is larger near the top of a slope.

(Obs.3) The displacement is smaller, conversely, in the lower portion of a slope.

Fig.3 is indicative of a vertical movement of the ground surface at the Maeyama gentle slope. It reveals;

(Obs.4) As for vertical displacements, subsidence is predominant in the upper portion of a slope, while heaving occurs in the lower portion.

SMALL-SCALE SHAKING TABLE TESTS.

Small-scale shaking table tests were conducted at the University of Tokyo in 1988 and 1989. Table I indicates the main features of the tests. The ground displacement was clearly observed by using a grid of dyed sand in a vertical cross section. This grid could move together with the ground without posing resistance. The model ground was

prepared by water pluviation and then was shaken in the longitudinal direction in harmonic manners. Shaking was continued until all the possible displacement was attained. Thus, the present study is interested in the ultimate ground deformation.

Fig.4 shows a deformation of a level liquefied layer overlain by a dry embankment below which a thin layer of coarse sand was placed. Similar to Obs.4, the embankment

Table I.   Main features of shaking table tests.

	Small scale tests 1988	1989	Large scale tests
Tested sand:			
Specific gravity	2.612	2.639	2.655
D_{50}, mm	0.27	0.19	0.27
e_{max}	1.041	0.947	0.976
e_{min}	0.653	0.616	0.596
Model ground:			
Length, m	1.0	1.0	6.0
Width, m	0.4	0.2	0.8
Relative density	about 50%	30-40%	30-50%
Acceleration, gal	250	100-150	variable
Frequency, Hz.	3	2	2
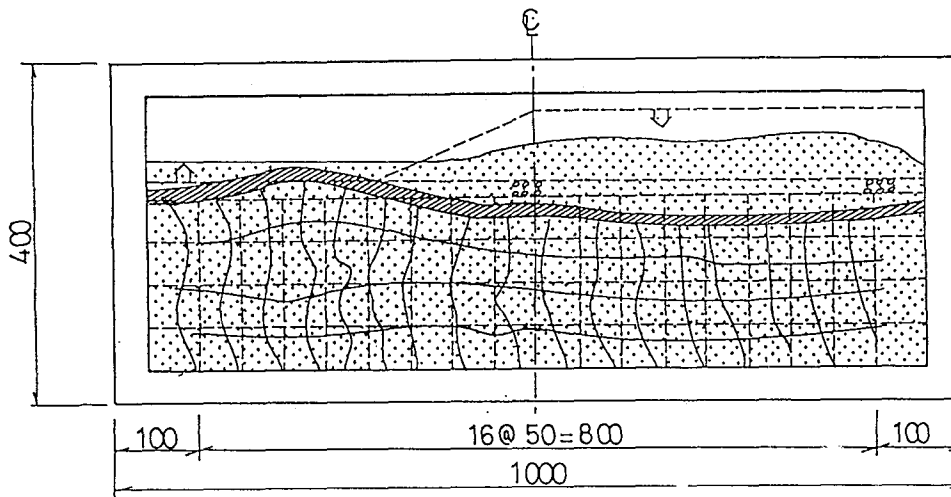
Figure 4. Deformation of liquefied ground overlain by dry embankment.

subsided while the surface of the liquefied layer heaved at the toe. The different overburden induced this soil movement. The lateral displacement was negligible at the base while maximum near the surface.
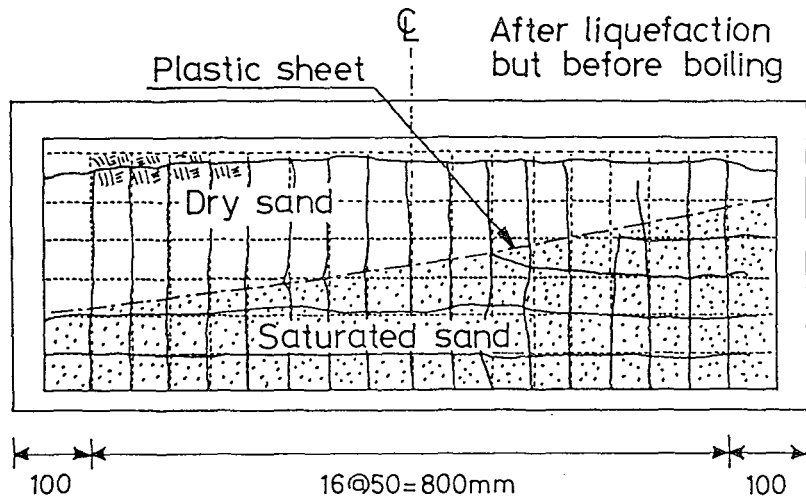
Figure 5. Lateral displacement under null hydraulic gradient.
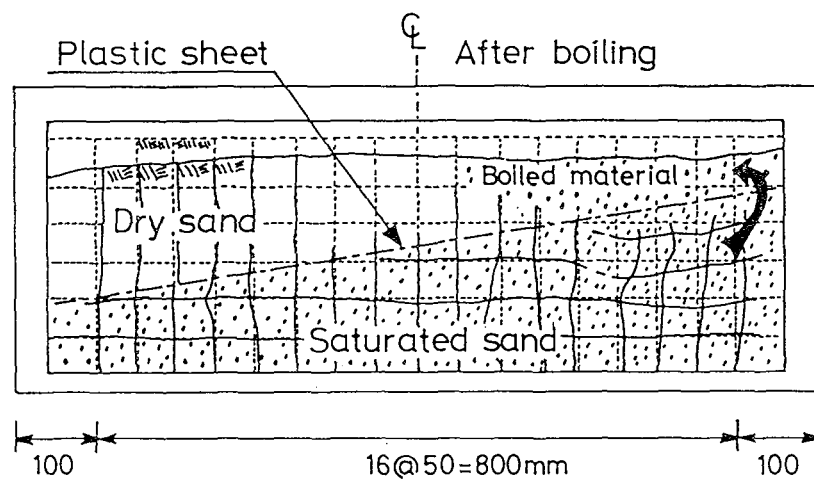
Figure 6. Effects of boiling on deformation of liquefied ground.

The effect of boiling was studied in 1988. A liquefiable water-saturated layer was prepared with an inclined surface and was made undrained by a plastic sheet. A dry sandy layer was placed above it so that its level surface made the overburden pressure more or less uniform in the lateral direction. Thus, it was expected to obtain a uniform total head, as defined in hydraulics, of the liquefied layer. Hence, the displacement of sand at the onset of liquefaction was negligible (Fig.5). Fig.6 illustrates the boiling phenomenon which took place when the plastic sheet was broken at one end. This accident reduced the pressure head nearby and a significant hydraulic gradient induced a soil flow towards the breakage point.

241
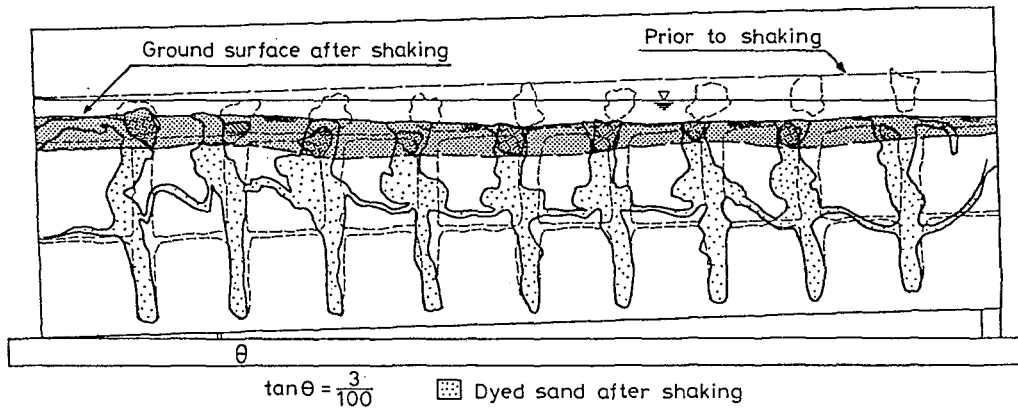
Figure 7. Model slope with ground water flow.
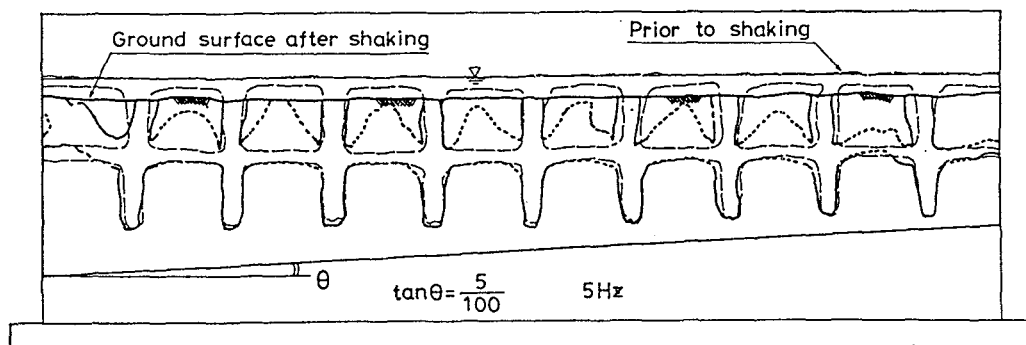
Figure 8. Null lateral displacement of level ground after liquefaction.

In 1989, a study was made of a slope associated with an inclined water table and a resultant seepage flow (Fig.7). Both liquefiable and surface unsaturated layers were dyed in a grid configuration. After liquefaction, the surface became level (Obs.4). Noteworthy is that the dyed portion of the liquefied and unsaturated layers moved together without slip at the interface. Fig.8 indicates a level ground with an inclined bottom. After shaking at 5 Hz., there is no lateral movement, although a boiling and associated soil movement were observed in the vertical direction. The level surface created null hydraulic gradient in sand, inducing no lateral soil flow.

The findings mentioned above are summarized as;

(Obs.5) Liquefied sand behaves as liquid whose flow is governed by the hydraulic gradient.

(Obs.6) The lateral displacement is maximum at the top of a liquefied layer, while negligible at the base.

(Obs.7) A surface unsaturated layer, if any, does not liquefy. There is no slip at its interface with a liquefied subsoil.

242

LARGE-SCALE SHAKING TABLE TESTS.

Eight large-scale tests were conducted at the Public Works Research Institute, and two of them are described herein. For main features, Table I is referred to. The loose sandy layer was placed in water on a compacted dense sandy layer. The ground was excited longitudinally at 2 Hz. with a constant amplitude for 20 seconds. Although each ground was shaken in 3 or 4 stages with different intensities at one-hour interval, the present study pays attention only to the displacement observed at the end of the last stage.

Fig.9 shows a result of a test with a model dry embankment. The acceleration amplitude was 61, 107, 160, and 160 gals in respective stages. The cross section indicates a distribution of the lateral displacement which supports the aforementioned Obs.6. No slip was observed between the liquefied layer and the dry embankment (Obs.7). The embankment sank substantially, while the toe did not, or even rose slightly (Obs.4), because the liquefied sand lost its stiffness and got squeezed out laterally by the sinking embankment.
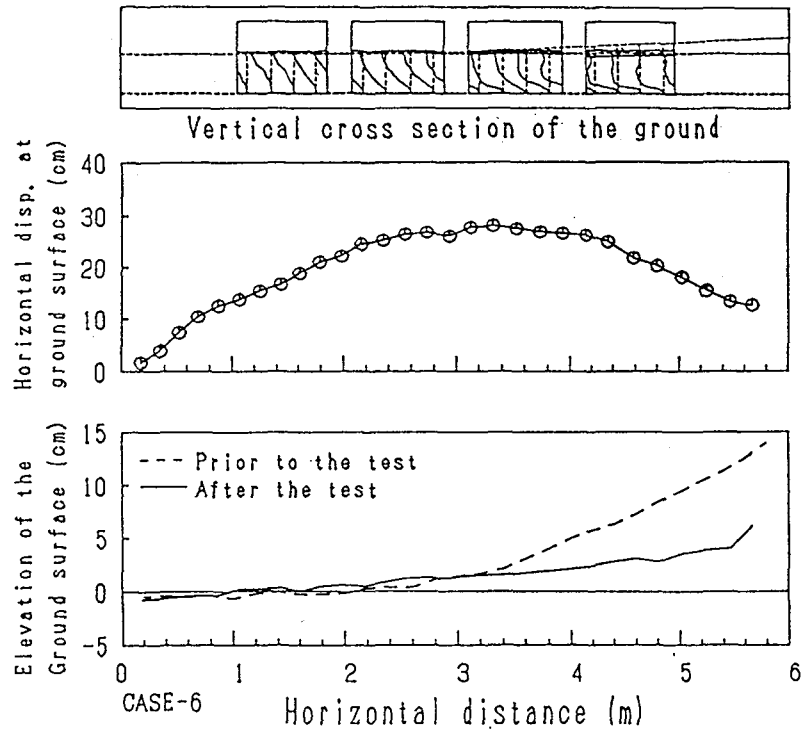
Figure 9. Deformation of large-scale model embankment.

Fig.10 demonstrates a test result in which a liquefiable deposit of 2 m in radius and 0.25 m in height was overlain by a cone-shaped embankment. This half of an axisymmetric model was shaken in the longitudinal direction in three

243
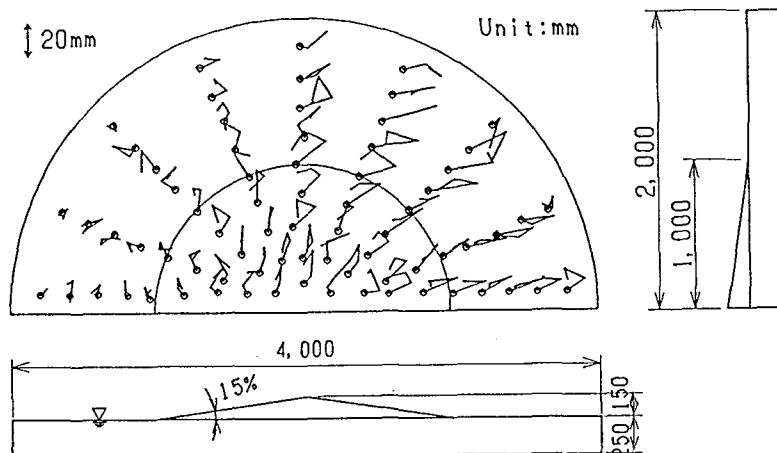
Figure 10. Displacement of axisymmetric model ground with cone-shaped embankment at center.

stages and the displacement trajectories were studied. It seems reasonable that the permanent displacement occurred in radial directions, approximately, without much influence from the dynamic acceleration. Hence,

(Obs.8) The cyclic acceleration influences the permanent displacement only indirectly by affecting the extent and duration of liquefaction.

This observation justifies the calculation of the permanent displacement in a static manner which will be presented in what follows.

VARIATIONAL THEORY OF PERMANENT DISPLACEMENT

Fig.11 is an illustration of a model ground which consists of an unliquefiable base (B), a liquefiable layer (H), and a surface unsaturated layer (T). The surcharge (P) includes the weight of the surface layer which moves together with the liquefied layer (Obs.7). The horizontal and vertical displacements are denoted by u and w, respectively. The ground configuration varies linearly with the horizontal coordinate, x;

$$B = B_0 + ax, \quad H = H_0 + bx, \quad T = T_0 + cx, \quad P = P_0 + ex, \quad (1)$$

Furthermore, four assumptions were made to enable the analysis;

(Asm.1) The lateral displacement is approximated by a sinusoidal distribution function in z direction (Eq.2), wherein F is an unknown function of x and stands for the displacement at the surface (z=B+H).

244
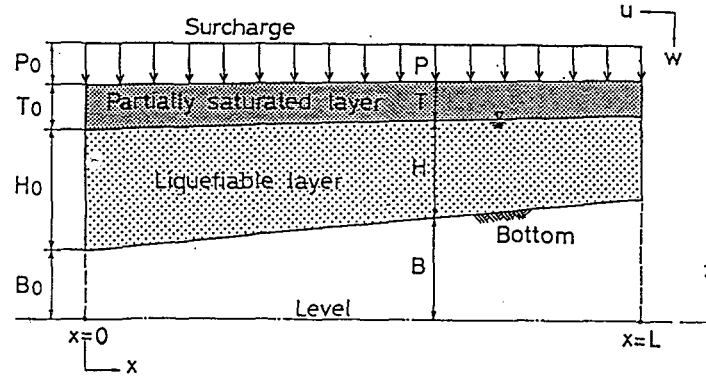
Figure 11. Model ground for development of predictive measure.

(Asm.2) Soil flows with a constant volume (Eq.3). The consolidation settlement is thus separately considered.

(Asm.3) Stress-strain relationship of the liquefied sand is simply modeled by Eq.4. (Obs.5) requires, however, G = 0 and τ_r = 0.

(Asm.4) The surface unsaturated layer behaves as a solid bar of Young modulus E.

$$u = F(x) \sin \frac{\pi(z-B)}{2H} \qquad (2)$$

$$\frac{\partial u}{\partial x} + \frac{\partial w}{\partial z} = 0 \qquad (3)$$

$$\tau = G \frac{\partial u}{\partial z} + \tau_r \qquad (4)$$

Substituting Eq.2 in Eq.3 and considering zero displacement at the base (z=B), the function w is expressed in terms of F(x). The increment of the surface elevation, δH, due to lateral soil flow is derived from the flux of ground movement (Fig.12).

$$\delta H = \frac{2}{\pi} \left(H \frac{dF}{dx} + b F \right) \qquad (5)$$

The present analysis is based on the principle of minimum potential energy which consists of the strain and gravity components of the liquefied and the surface unsaturated layers. At an arbitrary value of x coordinate,

the increment of the gravity energy in the surface layer or surcharge

$$= - P w(\text{at } z=B+H) \qquad (6)$$
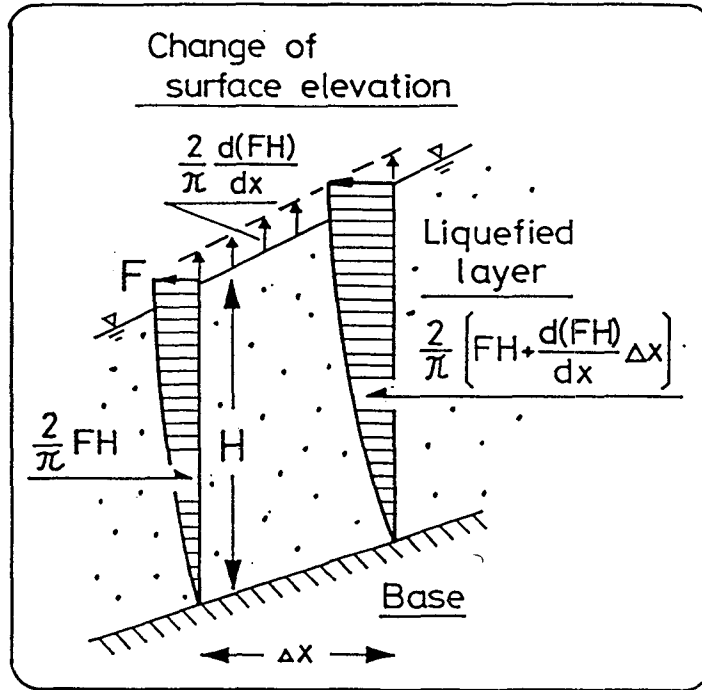
Figure 12. Calculation of change in surface elevation.

the increment of the gravity energy in the liquefied
layer

$$= (\gamma/2)\{(B{+}H{+}\delta H)^2 - (B{+}H)^2\} \qquad (7)$$

where γ is the unit weight of soil. Note that Eq.7 is
similar to expressions for liquid (Obs.5).

The calculation of strain energy normally employs all the
strain tensor components. To avoid complexity, however,
the present analysis makes use of only predominant compo-
nents. For the liquefied layer, the lateral surface
displacement of 5 m is possible when the layer thickness
is, for instance, 10 m. Thus, the shear strain of $\partial u/\partial z$ is
about 0.5. In contrast, the length of a slope is typically
500 m and hence the normal strain, $\partial u/\partial x$, is only 0.01.
Another normal strain, $\partial w/\partial z$, is small as well (Fig.3).
Since the strain energy is proportional to squared strain,
the shear strain $\partial u/\partial z$ is the predominant component from
anenergy view point. The surface unsaturated layer behaves
as a bar and its axial strain $\partial u/\partial x$ at z=B+H is important.
Accordingly,

the strain energy of the surface unsaturated layer

$$= \frac{ET}{2} \left(\frac{\partial u}{\partial x} \right)^2 \qquad (8)$$

the strain energy of the liquefied layer

$$= \int_B^{B+H} \left\{ \frac{G}{2} \left(\frac{\partial u}{\partial z} \right)^2 + \tau_r \frac{\partial u}{\partial z} \right\} dz \tag{9}$$

Eq.2 and w are substituted in these equations and the total potential energy, Q, is derived and minimized;

$$Q = \int_0^L q\left(F, \frac{dF}{dx}, x\right) dx \longrightarrow min. \tag{10}$$

in which

$$q = Eq.6 + Eq.7 + Eq.8 + Eq.9$$

This is a typical problem of variational principle to detect F function which makes Q minimum.

CLOSED-FORM SOLUTION OF PERMANENT DISPLACEMENT

Eq.10 is equivalent to an Euler's differential equation which is simplified by substituting $G = 0$. Null shear modulus of the liquefied layer is reasonable since this layer behaves as liquid (Obs.5). Consequently,

$$\frac{dF}{dx} = \frac{C_4 x^2 + C_5 x + A_1}{C_1 x^2 + C_2 x + C_3} \tag{11}$$

where

$$C_1 = \frac{4\gamma b^2}{\pi^2}, \quad C_2 = \frac{8\gamma bH_0}{\pi^2} + Ec, \quad C_3 = \frac{4\gamma H_0^2}{\pi^2} + ET_0,$$

$$C_4 = -\frac{1}{2} \left[(a+b)\left(e + \frac{2\gamma b}{\pi}\right) + \frac{2eb}{\pi} \right]$$

$$C_5 = \tau_r - (a+b)\left(P_0 + \frac{2\gamma H_0}{\pi}\right) - \frac{2eH_0}{\pi}$$

A_1 is a parameter which takes into account the boundary condition. The solution of Eq.11 is described below;

when b=0 and Ec=0,

$$F(x) = F_0 + \frac{F_L - F_0}{L}x + \frac{x(L-x)}{6(4\gamma H_0^2/\pi^2 + ET_0)}$$

$$\cdot \left[ae(L+x) - 3\{\tau_r - a(P_0 + \frac{2\gamma}{\pi}H_0) - \frac{2e}{\pi}H_0\} \right]$$

when $b=0$ and $Ec \neq 0$

$$F(x) = F_o + \frac{C_4}{2Ec}x^2 + \frac{1}{Ec}(\frac{C_3 C_4}{Ec} - C_5)$$

$$\cdot \left[L\frac{\ln|Ecx/C_3 + 1|}{\ln|EcL/C_3 + 1|} - x \right]$$

$$+ (F_L - F_o - \frac{C_4}{2Ec}L^2)\frac{\ln|Ecx/C_3 + 1|}{\ln|EcL/C_3 + 1|}$$

when $b \neq 0$ and $D = C_2{}^2 - 4C_1 C_3 > 0$,

$$F(x) = F_o + \frac{1}{2C_1}\left[2C_4 x + (C_5 - \frac{C_2 C_4}{C_1})\ln|\frac{C_1 x^2 + C_2 x + C_3}{C_3}|\right.$$

$$- \{2C_4 L + (C_5 - \frac{C_2 C_4}{C_1})\ln|\frac{C_1 L^2 + C_2 L + C_3}{C_3}| - 2C_1(F_L - F_o)\}$$

$$\left. \cdot \frac{\ln|\frac{(C_1 x^2 + C_2 x + C_3)(C_2 + \sqrt{D})^2}{C_3(2C_1 x + C_2 + \sqrt{D})^2}|}{\ln|\frac{(C_1 L^2 + C_2 L + C_3)(C_2 + \sqrt{D})^2}{C_3(2C_1 L + C_2 + \sqrt{D})^2}|} \right]$$

when $b \neq 0$ and $D = C_2{}^2 - 4C_1 C_3 = 0$,

$$F(x) = F_o + \frac{C_4}{C_1}x + \frac{C_1 C_5 - C_2 C_4}{2C_1{}^2}\ln|\frac{C_1 x^2 + C_2 x + C_3}{C_3}|$$

$$+ \frac{x(2C_1 L + C_2)}{L(2C_1 x + C_2)}\left[F_L - Fo - \frac{C_4}{C_1}L\right.$$

$$\left. - \frac{C_1 C_5 - C_2 C_4}{2C_1{}^2}\ln|\frac{C_1 L^2 + C_2 L + C_3}{C_3}|\right]$$

when $b \neq 0$ and $D = C_2{}^2 - 4C_1 C_3 < 0$,

$$F(x) = F_o + \left[\frac{C_4}{C_1}x + \frac{1}{2C_1}(C_5 - \frac{C_2 C_4}{C_1})\ln|\frac{C_1 x^2 + C_2 x + C_3}{C_3}|\right]$$

$$- \left[\frac{C_4}{C_1}L + \frac{1}{2C_1}(C_5 - \frac{C_2 C_4}{C_1})\ln|\frac{C_1 L^2 + C_2 L + C_3}{C_3}|\right.$$

$$\left. - (F_L - F_o)\right] \cdot \frac{\tan^{-1}(\frac{\sqrt{-D}}{C_2 x + 2C_3}x)}{\tan^{-1}(\frac{\sqrt{-D}}{C_2 L + 2C_3}L)} \tag{12}$$

248

where F_0 and F_L are values of $F(x)$ at $x=0$ and $x=L$, respectively.
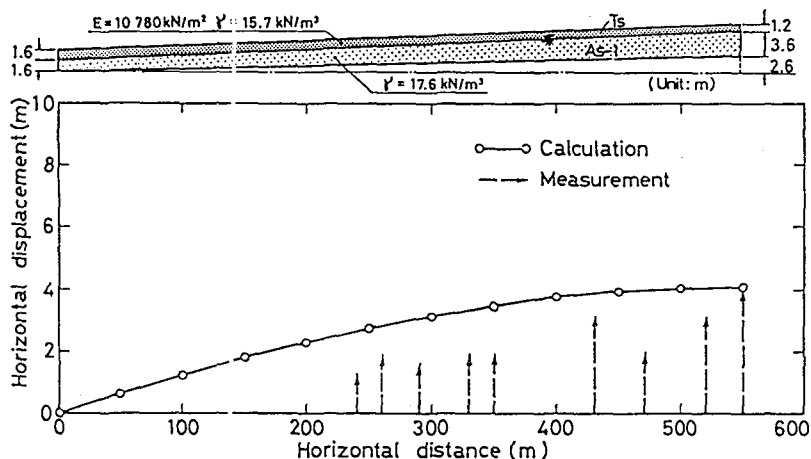
Figure 13. Analysis on Noshiro case.

ANALYSES ON CASE HISTORIES

It is difficult in case history analyses to evaluate soil parameters even approximately. In the present study, therefore, $E = 10780$ kPa is employed in all the cases without consideration to individual situations. Similarly, the unit weight of soil is always equal to 17.6 kN/m³ in the liquefied layer and 15.7 kN/m³ in the surface unsaturated layer.

The first analysis in Fig.13 is made of the Noshiro slope (Fig.1). A fixed boundary $F=0$ at the bottom ($x=0$) and a free boundary $dF/dx=0$, standing for an open crack, at the top of a slope ($x=L$) (Obs.1) are employed. Note that the calculated displacement is greater towards the top of the slope (Obs. 2 and 3). Although slightly overestimating, the analysis shows a good agreement with the observation.

The second and the third analyses were made of Kasukabe (Fig.14) and Oogata (Fig.15) sites which liquefied during the 1923 Kanto and the 1964 Niigata Earthquakes, respectively (Wakamatsu et al., 1989; Yasuda et al., 1989). The irregular topography was considered by dividing the ground into piecewise linear segments whose closed-form solutions were connected with continuous F and dF/dx at the interface. Note that the lateral displacement is predicted reasonably. Furthermore, the vertical rise of the river bed in both cases were calculated to be 0.23m and 1.65m, respectively (Obs.4). An eyewitness reported that the riverbed in Oogata site rose a few meters (Yasuda et al., 1989), which seems to support the validity of the proposed method of analysis.

249
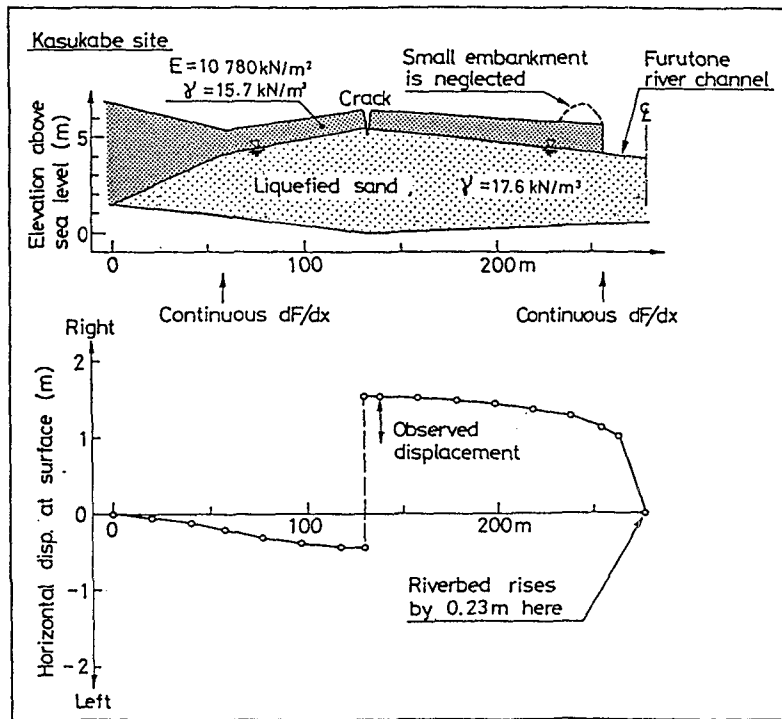
Figure 14. Analysis on Kasukabe case.
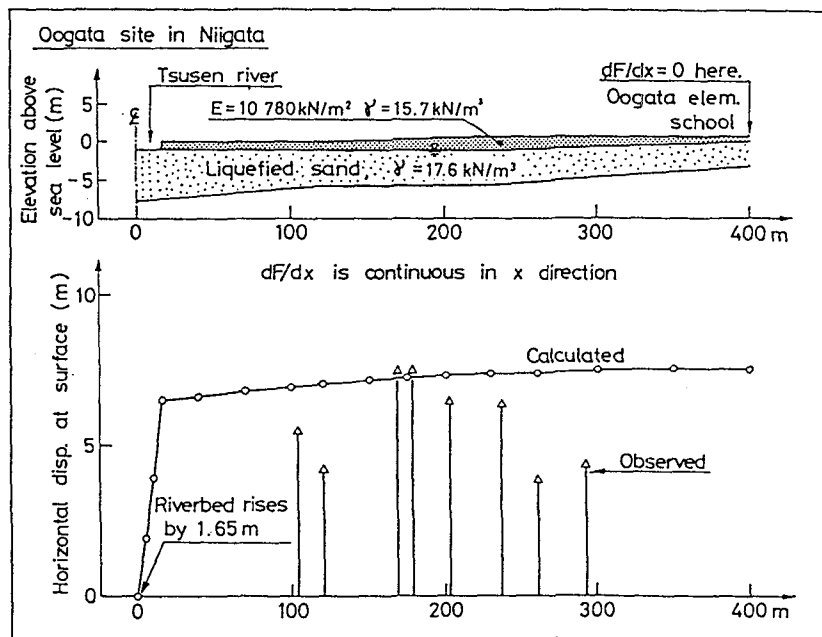
Figure 15. Analysis on Oogata case in Niigata.

250

CONCLUSIONS

A series of shaking table tests were performed to understand the nature of the flow of the liquefied ground. The experimental findings led to a development of a closed-form solution of the ground displacement. The solution thus derived was applied to several cases and a good agreement with observation was derived. Hence, the solution is going to be used to detect potential seismic hazards of lifeline networks and urban facilities induced by lateral flow of liquefied sand.

ACKMOWLEDGMENT

LIST OF REFERENCES

Hamada,M., Yasuda,S., Isoyama,R., and Emoto,K. (1986). Study on Liquefaction Induced Permanent Ground Displacements, ADEP, Tokyo.

Wakamatsu,K., Hamada,M., Yasuda,S., and Morimoto,I. (1989). Liquefaction Induced Ground Displacement during the 1923 Kanto Earthquake, Proc. 2nd U.S.-Japan Workshop on Liquefaction, Large Ground Deformation and Their Effects on Lifelines, 36-49.

Yasuda,S., Hamada,M., Wakamatsu,K., and Morimoto,I. (1989). Liquefaction Induced Ground Displacement in Niigata City, Proc. 2nd U.S.-Japan Workshop on Liquefaction, Large Ground Deformation and Their Effects on Lifelines, 67-81.

PRELIMINARY RESULTS OF A NUMERICAL TECHNIQUE TO MODEL FLOW FAILURE INDUCED BY SOIL LIQUEFACTION

Catherine M. Keane[1] and Jean H. Prevost[2]

Department of Civil Engineering and Operations Research
Princeton University
Princeton, NJ 08544

ABSTRACT

Although much has been learned through field studies and experimentation about soil liquefaction, flow failure associated with soil liquefaction remains a very difficult phenomenon to predict and simulate. To this end, formulation and implementation of a finite element analysis procedure to predict and simulate flow failure associated with soil liquefaction are being performed. An arbitrary Lagrangian-Eulerian (ALE) kinematic description is proposed to handle the large deformations which result from soil liquefaction. The model is also able to track the motions of the free surface. The methodology is able to treat incompressible/compressible and inviscid/viscous fluids. An upwinding technique has been implemented to control the problems associated with the integration of convection terms. Several sample problems are presented to demonstrate the capabilities of the methodology thus far. Results are discussed in detail as well as further research goals.

[1] Graduate Student

[2] Professor of Civil Engineering and Operations Research

INTRODUCTION

Flow failure induced by soil liquefaction is a phenomenon which often has disastrous effects on a variety of structures. During ground shaking, saturated soils may experience a loss of strength significant enough to result in liquefaction. Large ground deformations as well as settlement and/or tipping of structures occur until the strength of the soil is restored. Soil liquefaction and the resulting flow failure are costly and life-threatening events associated with earthquake occurrence. Even though much is known about soil liquefaction, it remains a very difficult hazard to predict and simulate.

The goal of the present work is to advance the state of numerical procedures to model flow failure induced by soil liquefaction. In the following, capabilities of the proposed ALE technique are demonstrated in the solution of several problems. The necessity for incorporating an upwinding technique is shown in the solution of flow over a step. A free surface wave propagation problem is solved to demonstrate the ability of the free surface to track fluid motion. The ability to treat compressible fluids is demonstrated in the solution of flow over a still fluid; whereas a generalization of the free surface tracking is illustrated in the solution of flow over a dry bed. Finally, further research goals are discussed.

PRELIMINARIES

The Eulerian kinematic description is a popular choice in fluid mechanics for flows which pass through a fixed region in space. It consists of a moving material and a stationary mesh. Although large distortions can be easily handled since there is no mesh deformation, troublesome convective effects may arise. In the Lagrangian description, the mesh and the material move together so there are no convective effects. However, for problems involving large deformations, the finite element mesh may become excessively entangled.

The (arbitrary) Lagrangian-Eulerian (ALE) kinematic description attempts to unite the advantages of each description while minimizing the disadvantages. First developed in finite differences by Noh (1964) and Hirt et al. (1974), and then extended to finite elements by Donea et al. (1977), Belytschko and Kennedy (1978), Hughes et al. (1981), and Donea (1983), the ALE description consists of a moving material and an arbitrarily moving mesh. Although convective terms arise if the mesh does not move with the fluid, the ability to prescribe an arbitrary mesh velocity may allow the convective effects to be reduced. Further, large distortions without element entanglement are more easily handled in the ALE description than in the Lagrangian description.

The ALE description includes a material, spatial, and referential domain, where z_i are the material coordinates, y_i the spatial coordinates, and x_i the referential coordinates. Since the referential domain remains fixed, it is convenient to express quantities in terms of referential coordinates. For example, if an arbitrary function is expressed as $f = f(x_i, t)$, then the material time derivative expressed in referential coordinates is:

$$\frac{\mathrm{d}f(x_i,t)}{\mathrm{d}t} = \left.\frac{\partial f(x_i,t)}{\partial t}\right|_{x_i} + \frac{\partial f}{\partial x_i}c_i \tag{1}$$

where c_i is the convective velocity to be discussed subsequently. The conservation of momentum and conservation of mass equations are then defined in the ALE description using Eq. (1).

The proposed numerical procedure is able to handle incompressible and compressible fluids. The penalty function formulation, proposed in the Eulerian description by Hughes et al. (1979)

and extended to the ALE description by Hughes et al. (1981), is adopted here for incompressible fluids. Treatment of compressible fluids is discussed in the Section IV.

An implicit predictor-(multi)corrector solution algorithm, similar to that presented by Hughes et al. (1981), is used. A pressure update for comprssible fluids has been added. In the following, γ is the algorithmic parameter applied to the fluid equations, whereas $\hat{\gamma}$ is applied to the mesh equations.

PROBLEMS

Flow over a step

It is well known that the convection term which arises in the Eulerian and ALE formulations causes numerical oscillations. The following problem is presented to demonstrate the necessity of employing an upwinding technique to overcome this difficulty for problems with convection.

Convection can be quantified through the convective velocity, c_i, as:

$$c_i = v_i - \hat{v}_i \tag{2}$$

where v_i is the material velocity and $\hat{v}_i$ is the mesh velocity. For problems in the Eulerian description, the mesh remains stationary, so $\hat{v}_i = 0$, and the convective velocity is the material velocity, $c_i = v_i$. In the Lagrangian description, the mesh moves with the material, $v_i = \hat{v}_i$, and there is no convection, $c_i = 0$.

Spurious node-to-node oscillations develop when convection dominates on an element level and a Galerkin treatment of the governing equatins has been employed (see Brooks and Hughes (1982)). These oscillations are well illustrated in the following problem. Figure 1 contains a schematic diagram of the flow domain. The finite element mesh consists of 4 node bilinear quadrilateral elements of dimension 0.1 by 0.2. Material parameters for a RE = 200 are listed in Table 1.

An implicit calculation was performed, and results are reported as nodal velocity vectors at steps 10, 20, 30, 40, and 50 in Figure 2a. The spurious oscillations which develop due to the convective term are clearly illustrated on the upstream side of the step.

To control these oscillations, the concept of upwinding was first introduced into the finite difference literature by Richtmyer and Morton in 1967. It was extended to the finite element method in 1976 by Christie et al. Further work includes that by Hughes (1978), Heinrich et al. (1977), Hughes and Brooks (1979) and (1982), and Brooks and Hughes (1982).

The (consistent) Streamline Upwind/Petrov Galerkin (SU/PG) formulation proposed by Brooks and Hughes (1982) is adopted here. This technique works well in multi-dimensional cases and situations where source and transient terms are present. The SU/PG method amounts to modifying the usual weighting function, w_i, with the addition of an upwind weighting function, $\tilde{p}_i$, such that:

$$\tilde{w}_i = w_i + \tilde{p}_i \tag{3}$$

and applying $\tilde{w}_i$ to all terms in the governing equaion. The upwind weighting function, $\tilde{p}_i$, is constructed to act only in the direction of flow. (See Brooks and Hughes (1982) for a complete discussion.)

Results using the SU/PG method are shown in Figure 2b. It is clear that the upstream "wiggles" have been removed due to the upwinding technique.

Free surface wave propagation problem

The ability to track the motion of a free surface is critical in generalizing the ALE formulation to problems of flow failure induced by soil liquefaction and failure of earth structures.

The governing equations (conservation of momentum, conservation of mass, and constitutive equation) are expressed in terms of the material velocity. Therefore, treatment of the free surface involves a general method to solve for the mesh velocity from the fluid velocity. This can be accomplished by employing a split description at each node as presented in Hughes et al. (1981) and further discussed in Huerta and Liu (1988). Let α_i^a be the Euler-Lagrange parameter in direction i for node a. Node a can then be defined as Eulerian, $\alpha_i^a = 0$, or Lagrangian, $\alpha_i^a = 1$, for degree of freedom (DOF) direction i. If Eulerian, the mesh velocity of the node must be zero, whereas the mesh velocity equals the fluid velocity if Lagrangian. In two-dimensions, this can be expressed as:

$$\hat{v}_1 = \alpha_1 v_1 - \alpha_1 c_2 \frac{\partial y_1}{\partial x_2} \tag{4a}$$

$$\hat{v}_2 = \alpha_2 v_2 - \alpha_2 c_1 \frac{\partial y_2}{\partial x_1} \tag{4b}$$

where:

$$\alpha_i = \sum_{a=1}^{\text{NFSN}} N^a \alpha_i^a \quad \text{and} \quad \frac{\partial y_i}{\partial x_j} = \sum_{a=1}^{\text{NFSN}} \bar{N}^a_{,j} y_i^a \tag{5}$$

and all other quantities have been previously defined. In Eq. (4), NFSN is the number of free surface nodes and $\bar{N}^a$ are the shape functions corresponding to the dimension of the free surface. For example, in a two-dimensional domain, $\bar{N}^a$ are the one-dimensional shape functions. Nodal quadrature is used to solve Eq. (4).

The technique to track free surface motions can be illustrated through the solution of a free surface wave propagation problem. The problem statement and dimensions are shown in Figure 3a; the wave is generated so as to propagate without distortion and dissipation. The finite element mesh, as well as Eulerian-Lagrangian DOF's, are presented in Figure 3b. Table 2 contains a listing of material parameters.

Results are illustrated in Figure 4 as plots of the displacement of the free surface at steps 60, 80, 100, 120, 140, and 160. The wave travels across the free surface with very little dissipation, as it should. This problem illustrates the ability of the proposed methodology to track free surface motion.

Flow over a still fluid

For some situations, it may be desirable to use a compressible fluid. To demonstrate the ability of this procedure with a compressible fluid, a problem which can be visualized as the breaking of a dam and is referred to as flow over a still fluid (FSF) in the literature (see Huerta and Liu (1988)) is solved. This problem demonstrates the ability of the procedure to handle compressible fluids.

In referential coordinates, the conservation of mass equation is expressed as:

$$\left.\frac{\partial \rho}{\partial t}\right|_{x_i} + c_i \frac{\partial \rho}{\partial y_i} + \rho \frac{\partial v_i}{\partial y_i} = 0 \tag{6}$$

256

where ρ is the mass density of the fluid and all other quantities have been defined previously. By employing $\partial P/\partial \rho = B/\rho$, where P is the hydrostatic pressure and B is the fluid Bulk Modulus, Eq. (6) can be reexpressed (after rearrangement) in terms of P as:

$$\dot{P} = -B \text{ tr } \dot{\epsilon}_{ij} - c_i P_{,i} \tag{7}$$

where the term $c_i P_{,i}$ is the convection of the pressure. To solve Eq. (7), a fully backward technique is employed:

$$P_{n+1} = \Delta t \dot{P}_{n+1} + P_n \tag{8}$$

Then substituting Eq. (8) into Eq. (7) yields:

$$P_{n+1} = P_n - B\Delta t \text{ tr } (\dot{\epsilon}_{ij})_{n+1} - \Delta t (c_k)_{n+1}(P_{,k})_{n+1} \tag{9}$$

which is solved iteratively. Since the pressure within each element is constant, the pressure at the nodes of each element must be obtained in order to compute the gradient of the pressure, $P_{,i}$. Nodal pressure values are obtained by employing a nodal projection procedure proposed by Lee (1978).

A schematic representation of the FSF problem statement is illustrated in Figure 5, and material parameters are listed in Table 3. The mesh used to model the physical domain has 41 elements of unit width. One element spans the length ΔL. Nodes along the free surface are Eulerian in direction 1 and Lagrangian in direction 2 (i.e., nodes along the free surface cannot move horizontally but are allowed to move vertically). All other nodes are fully Eulerian.

An implicit calculation using a time step of 0.25 was performed, and results are reported as displacement of the free surface at steps 10, 20, 30, and 40. They are shown in Figure 6 along with the analytical solution by Ritter (1892) based upon shallow water theory (i.e., the St. Venant equations). There is very good agreement between the numerical and the analytical results in the height of the water as it falls and in the velocity of the flooding wave for both fluids. From these results, the procedure is seen to work well with a compressible fluid.

Flow over a dry bed

For certain liquefaction flow problems, the mesh may be required to follow the free surface in one direction and to translate in another. The requirement of translating elements in one direction while tracking the free surface in another results in an additional complexity. The ability to pre-scribe a portion of the mesh velocity is an essential ingredient in the solution of such problems. To this end, the procedure for tracking the motion of the free surface has been expanded. That is, an implementation has been performed which allows the mesh velocity of a certain degree-of-freedom direction at a node to be:

- Eulerian (the mesh does not move)
- Lagrangian (the mesh moves with the fluid)
- Lagrangian Free Surface (the mesh tracks the free surface motion, as previously discussed)
- Prescribed (the mesh velocity of a node is prescribed to equal the mesh velocity of a different node in a particular direction)
- Interpolated (the mesh velocity is obtained by linearly interpolating the velocities of 2 other nodes)

To illustrate the necessity of a general procedure for the mesh motion, another problem is solved. The problem can be visualized as the breaking of a dam and is referred to as flow over a dry bed (FDB) (see Huerta and Liu (1988)). This problem differs from the FSF problem in that

nodes are required to translate horizontally as well as follow the vertical motion of the free surface. This requires a prescribed mesh velocity at certain nodes and an interpolated mesh velocity at other nodes.

Table 4 contains a list of the material parameters for the viscous and relatively inviscid compressible flow problems. A schematic representation of the 2-dimensional FDB problem statement is shown in Figure 7. Along the bottom row of the finite element mesh, nodes are on frictionless rollers. The top left-most node is on a frictionless vertical roller. However, the bottom left-most node is fixed. The mesh, which has one element through its depth, consists of 35 bilinear quadrilateral elements and 72 nodes, and it has been graded to account for the increase in mesh velocity from left to right. The nodes are translated by prescribing a horizontal mesh velocity that varies linearly betwen zero at the wall and the tip velocity at the downstream boundary. Mesh velocities of nodes along the top surface in direction 1 are prescribed to equal the velocities of the nodes below to avoid elements toppling over. In order to define the problem accurately (see the discussion by Huerta and Liu (1988)), an initial tip velocity of 2.0 must be applied.

For the inviscid case, shallow water theory predicts a tip velocity of 2.0 and a parabolic shape for the free surface (see Ritter (1892)). The displacement of the free surface shown in Figure 8 for the nearly inviscid case are consistent with the predictions. Results for the viscous case are illustrated in Figure 8 also. From Figure 8, it is clear that the present formulation is able to follow the vertical motion of the free surface as well as translate elements horizontally.

FURTHER WORK

The complete soil liquefaction problem begins with a soil deposit subjected to ground motion. Upon liquefaction, the soil behaves like a fluid and flow occurs until the strength of the soil is restored. Therfore, the work presented here must be coupled with a nonlinear soil model in order to predict and simulate the full soil liquefaction problem.

CONCLUSIONS

The results of the four problems presented demonstrate some of the abilities of the proposed numerical procedure to model flow failure induced by soil liquefaction. The large deformations which may result from liquefaction are handled using the ALE kinematic description as well as appropriately tracking the free surface and translating elements. The numerical procedure is capable of handling both incompressible and compressible fluids. Problems associated with the convective term have been eliminated using the upwinding technique.

The methodology has purposely been formulated in a general environment to allow solution of actual flow problems. The results shown here are encouraging and indicate that this procedure is able to predict and simulate the flow portion of soil liquefaction problems.

ACKNOWLEDGEMENTS

258

REFERENCES

1. T. BELYTSCHKO AND T. M. KENNEDY, (1978) "Computer models for subassembly simulation", *Nucl. Engrg. Design*, Vol. 49, 17-38.

2. A. N. BROOKS AND T. J. R. HUGHES, (1982) "Streamline upwind/Petrov-Galerkin formulations for convection dominated flows with particular emphasis on the incompressible Navier-Stokes equations", *Comput. Meths. Appl. Mech. Engrg.*, Vol. 32, 199-259.

3. I. CHRISTIE, D. F. GRIFFITHS, A. R. MITCHELL AND O. C. ZIENKIEWICZ, (1976) "Finite element methods for second order differential equations with significant first derivatives", *Internat. J. Numer. Methods Engrg*, Vol. 10, 1389-1396.

4. J. DONEA, (1983) "Arbitrary Lagrangian-Eulerian finite element methods", in T. Belytschko and T. J. R. Hughes, eds., Computational Methods for Transient Analysis (North - Holland, Amsterdam) 473-516.

5. J. DONEA, P. FASOLI-STELLA, AND S. GIULIANI, (1977) "Lagrangian and Eulerian finite element techniques for transient fluid structure interaction problems", in Transactions of the 4th International Conference on Structural Mechanics in Reactor Technology, Paper B1/2.

6. J. C. HEINRICH, P. S. HUYAKORN, O. C. ZIENKIEWICZ, AND A. R. MITCHELL, (1977) "An 'upwind' finite element scheme for two-dimensional convective transport equation", *Internat. J. Numer. Methods Engrg.*, Vol. 11, 134-143.

7. C. W. HIRT, A. A. AMSDEN, AND J. L. COOK, (1974) "An arbitrary Lagrangian-Eulerian computing method for all flow speeds", *J. Comput. Physics*, Vol. 14, 227-253.

8. A. HUERTA AND W. K. LIU, (1988) "Viscous flow with large free surface motion", *Comput. Meths. Appl. Mech. Engrg.*, Vol. 69, 277-324.

9. T. J. R. HUGHES, (1978) "A simple scheme for developing 'upwind' finite elements", *Internat. J. Numer. Methods Engrg.*, Vol. 12, 1359-1365.

10. T. J. R. HUGHES AND A. BROOKS, (1979) "A multi-dimensional upwind scheme with no crosswind diffusion", in T. J. R. Hughes, ed., Finite Element Methods for Convection Dominated Flows, AMD Vol. 34 (ASME, New York).

11. T. J. R. HUGHES AND A. BROOKS, (1982) "A theoretical framework for Petrov-Galerkin methods with discontinuous weighting functions: Application to the streamline-upwind procedure", in R. H. Gallagher, D. H. Norrie, J. T. Oden, and O. C. Zienkiewicz, eds., Finite Elements in Fluids, Vol. 4 (John Wiley, New York).

12. T. J. R. HUGHES, W. K. LIU, AND A. BROOKS, (1979) "Finite element analysis of incompressible viscous flows by the penalty function formulation", *J. Comput. Physics*, Vol. 30, 1-60.

13. T. J. R. HUGHES, W. K. LIU, AND T. K. ZIMMERMANN, (1981) "Lagrangian-Eulerian finite element formulation for incompressible viscous flows", *Comput. Meths. Appl. Mech. Engrg.*, Vol. 29, 329-349.

14. R. L. LEE, P. M. GRESHO, AND R. L. SANI, (1978) "Numerical smoothing techniques applied to some finite element solutions of the Navier-Stokes equations", Second International Conference on Finite Elements in Water Resources, London, England, July 10-14, 1978.

15. W. F. Noh, (1964) "CEL: A time-dependent two-space-dimensional coupled Eulerian-Lagrangian code", in B. Alder, S. Fernbach, and M. Rotenberg, eds., Methods in Computational Physics 3 (Academic Press, New York).

16. R. D. Ritchmyer and K. W. Morton, Difference Methods for Initial-Value Problems (Interscience, New York, Second Edition, 1967).

17. A. Ritter, (1892) "Die Fortpflanzung der Wasserwellew", Z. Vereines Deutscher Ingenieure, Vol. 36 (33), 947-954.
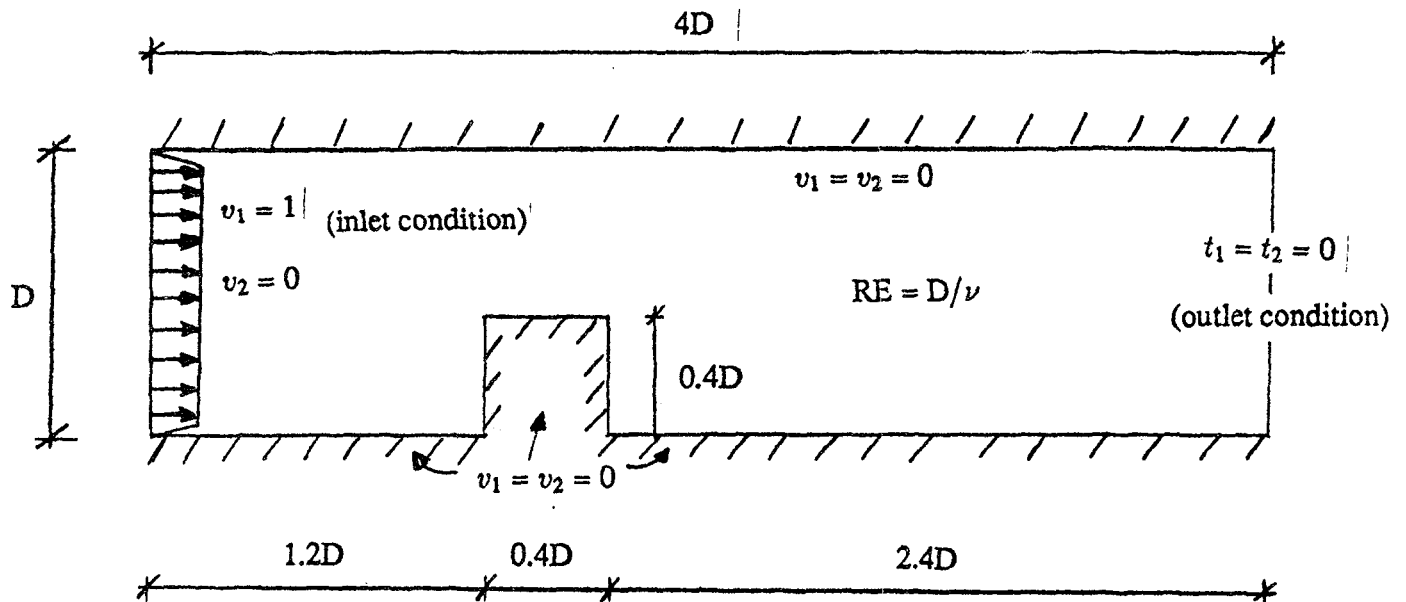
Figure 1 : Problem statement and schematic description - flow over a step

Table 3 : Dam Break Problem (FSF) - Material Parameters

	Inviscid Flow	Viscous Flow
H	1.0	1.0
ΔH	1.0	1.0
L	41.0	41.0
ΔL	1.0	1.0
g	1.0	1.0
ρ = density	1.0	1.0
μ = dynamic viscosity	0.01	0.50
B = fluid bulk modulus	2.2×10^{10}	2.2×10^{10}
$\gamma = \hat{\gamma}$ = algorithmic parameter	0.5	0.5
Δt = time step	0.25	0.25

Table 4 : Dam Break Problem (FDB) - Material Parameters

	Inviscid Flow	Viscous Flow
H	1.0	1.0
g	1.0	1.0
ρ = density	1.0	1.0
μ = dynamic viscosity	0.01	0.50
B = fluid bulk modulus	2.2×10^{10}	2.2×10^{10}
γ = algorithmic parameter (fluid)	1.0	1.0
$\hat{\gamma}$ = algorithmic parameter (mesh)	0.65	0.65
Δt = time step	0.06	0.25

Table 1 : Flow over a Step Problem - Material Parameters for RE = 200

RE = Reynolds Number	200.0
ρ = density	200.0
μ = dynamic viscosity	1.0
λ = incompressible flow parameter (penalty parameter)	1.0×10^{8}
$\gamma = \hat{\gamma}$ = algorithmic parameter	1.0
Δt = time step	0.07

Table 2 : Free Surface Wave Propogation Problem Material Parameters for an Incompressible Fluid

	Incompressible Fluid
D = domain height	10.0
L = domain length	949.095
H = input displacement parameter	0.86
g = input displacement parameter	1.0
h = element width	5.895
ρ = density	1.0
μ = dynamic viscosity	0.0
λ = penalty parameter	2.6089×10^{7}
$\gamma = \hat{\gamma}$ = algorithmic parameter	0.5
Δt = time step	1.7888

261

n=10

n=20

n=30

n=40

n=50

Figure 2b : Flow over a step(RE = 200)
Finite element results with upwinding

Figure 2a : Flow over a step (RE = 200)
Finite element results

$$\hat{u}_1(0, x_2, t) = \frac{H}{\kappa}[1 + \tanh\left(\frac{c\kappa t}{D} - 4\right)]$$

$$c = \sqrt{gD(1 + \frac{H}{D})}$$

$$\kappa = \sqrt{\frac{3H}{4D}}$$

$$\Delta t = h/c$$

——— Reference Domain Ω_x

– – – Deformed Domain Ω_y
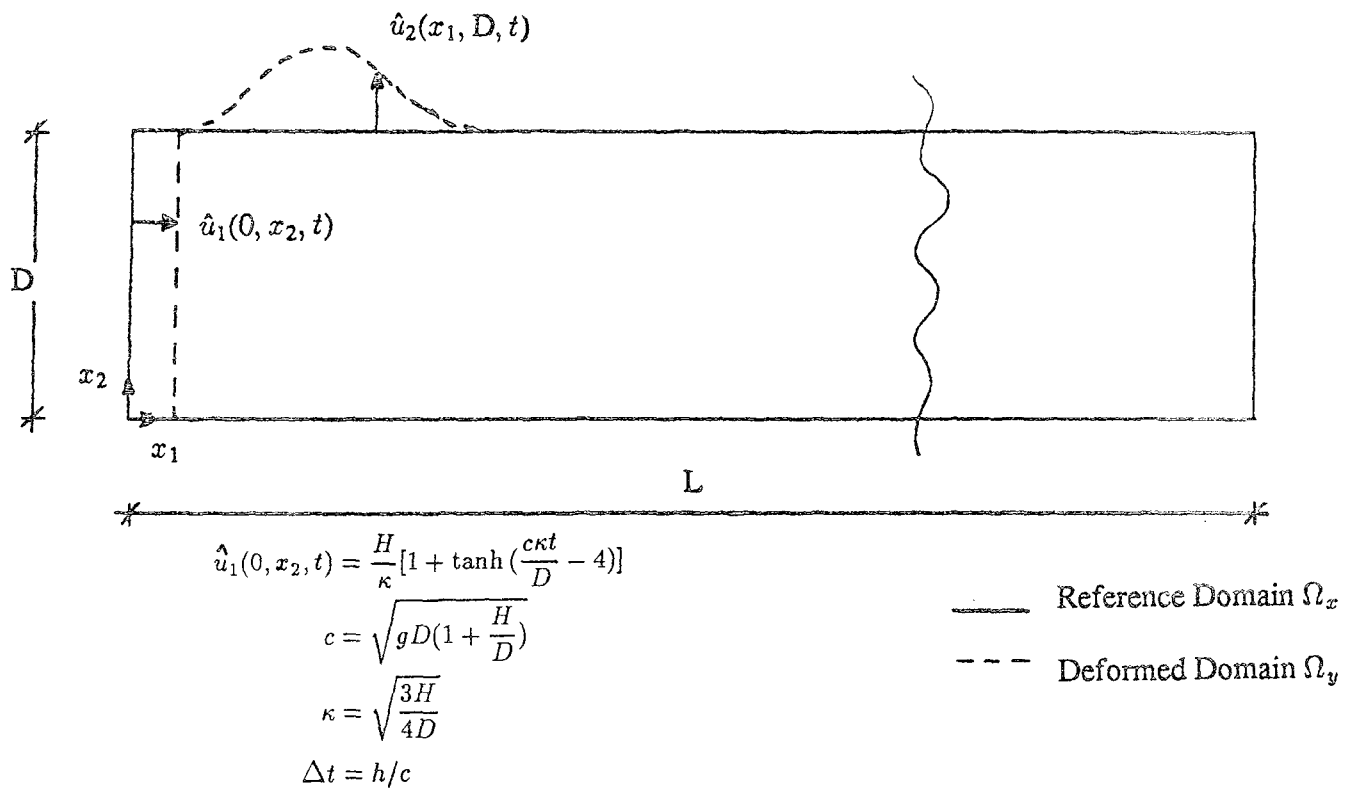
Figure 3a : Problem statement - free surface wave propagation problem

L = Lagrangian degree-of-freedom

E = Eulerian degree-of-freedom
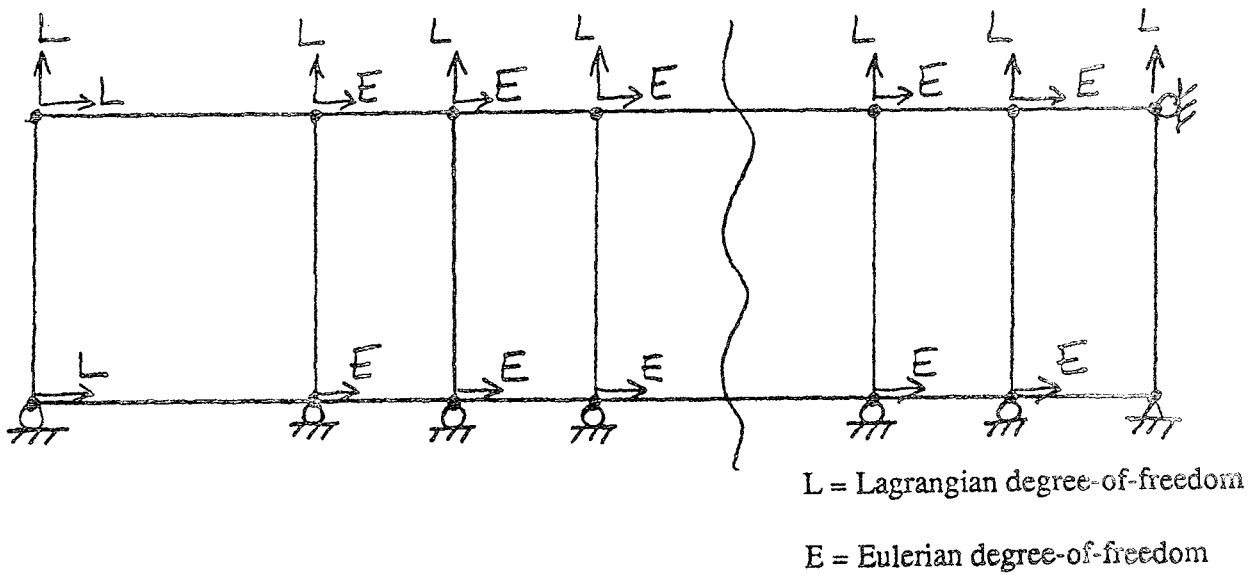
Figure 3b : Finite element mesh - free surface wave propagation problem

263
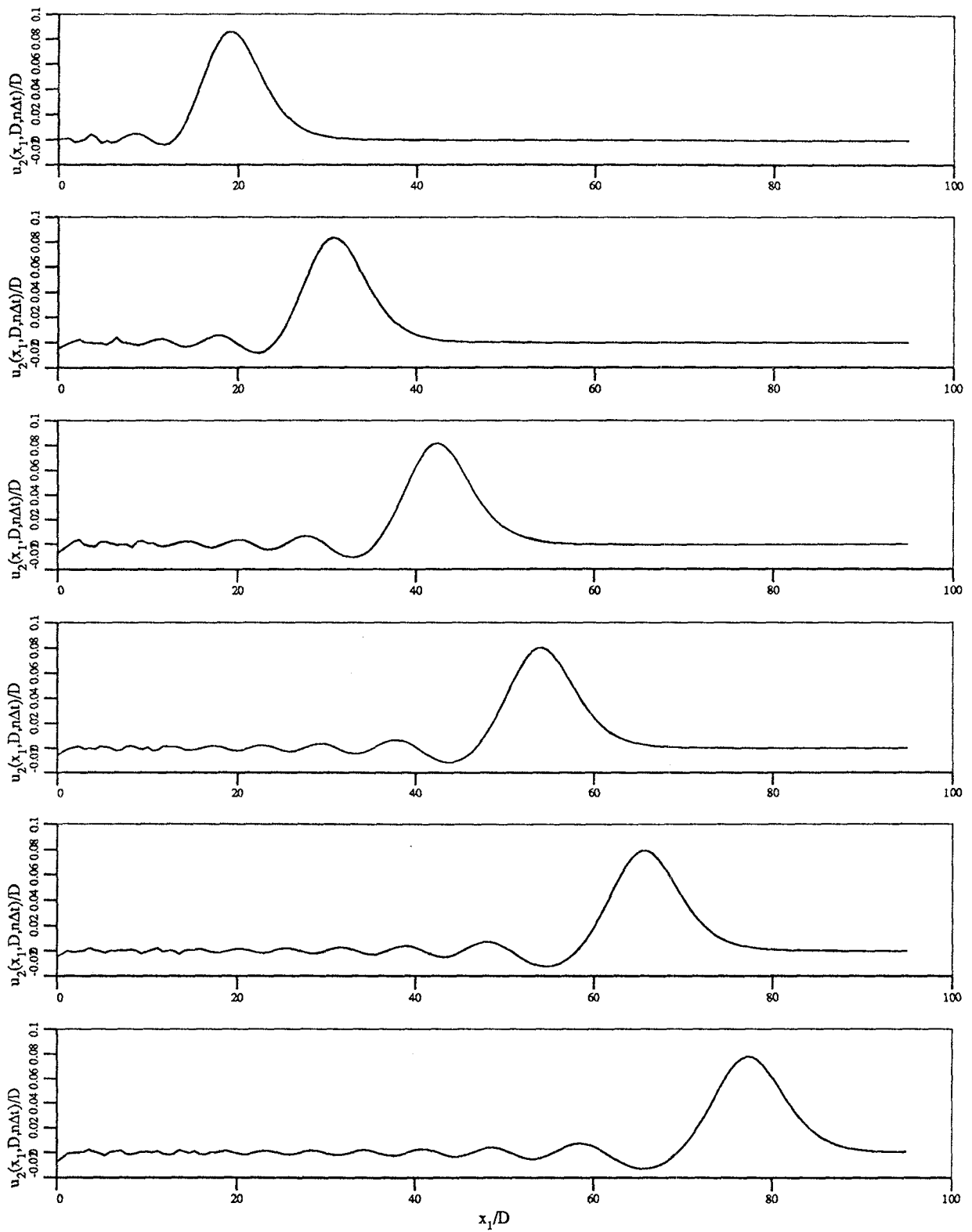
Figure 4 : Results - free surface wave propagation problem

264
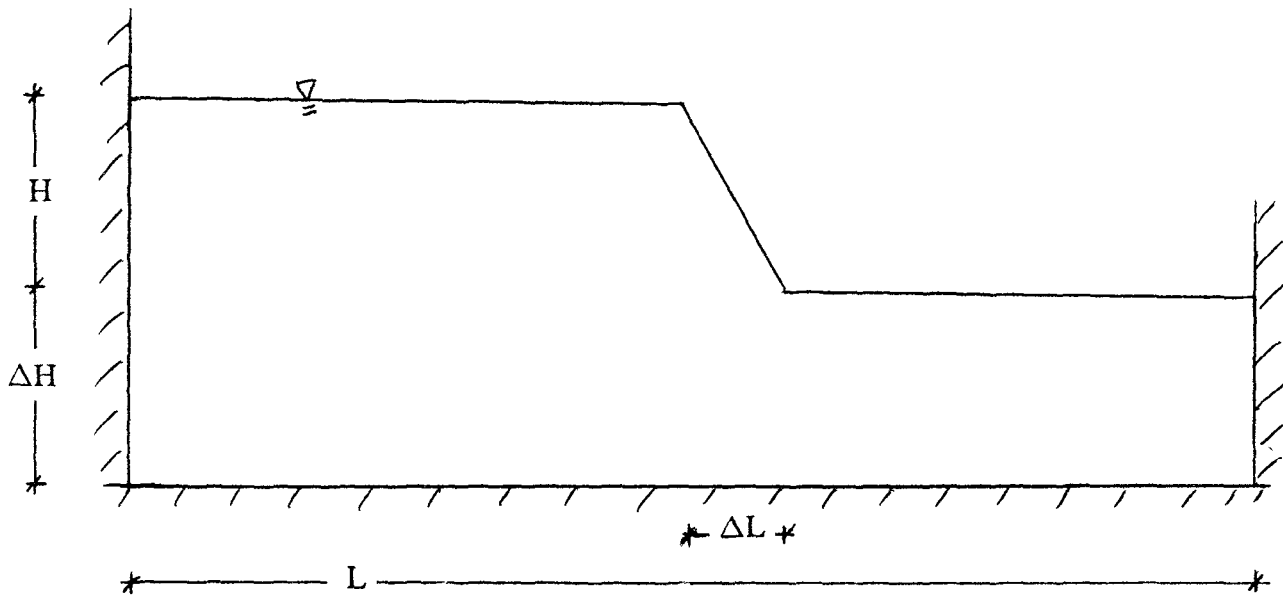
Figure 5: Problem statement of flow over a still fluid
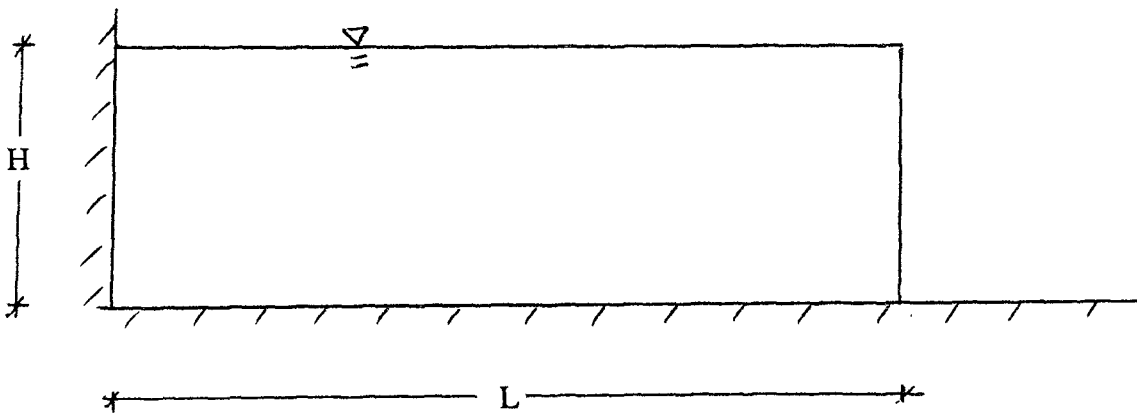
Figure 7: Problem statement of flow over a dry bed
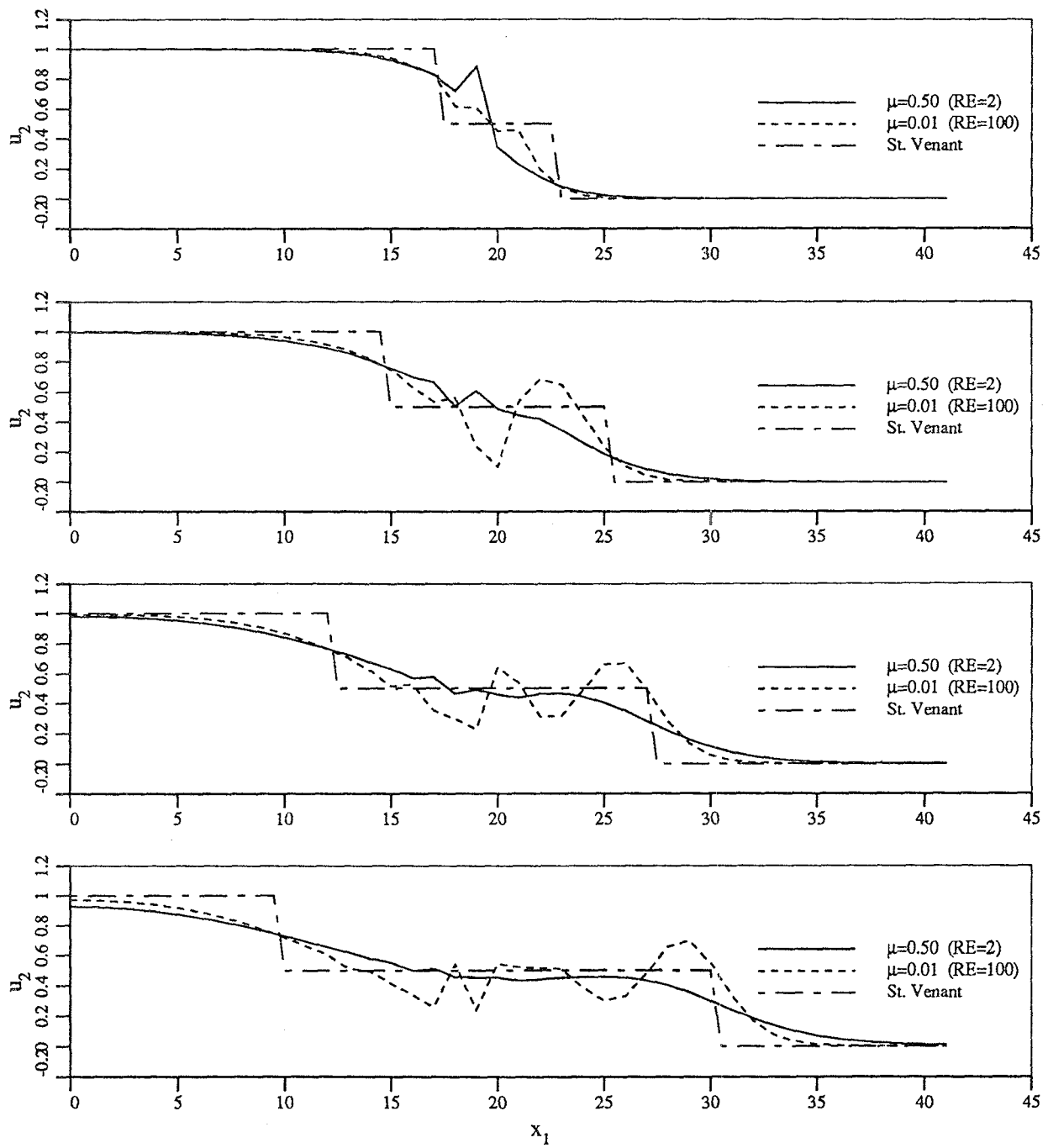
Figure 6 : Results - flow over a still fluid

266
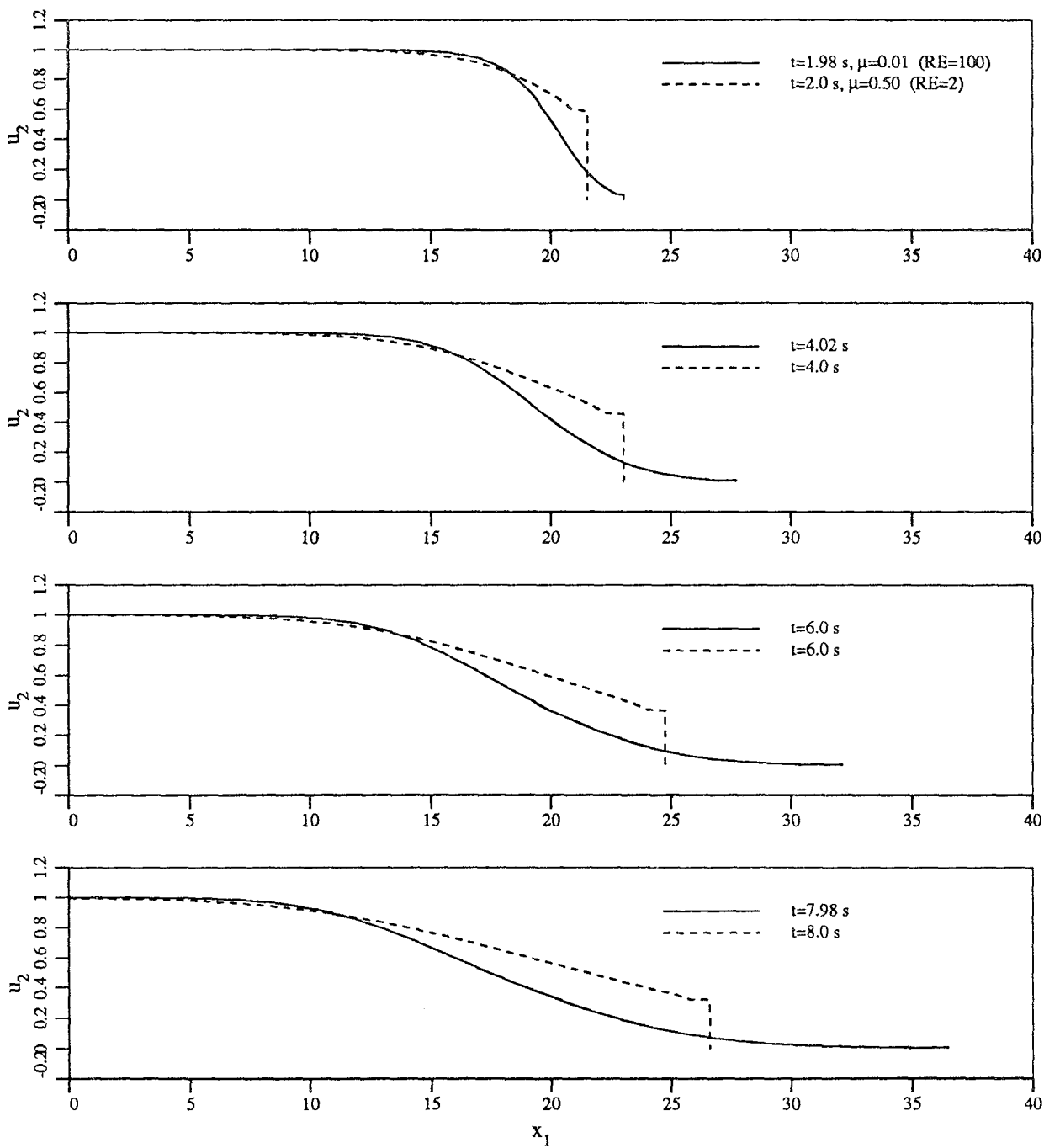
Figure 8 : Results - flow over a dry bed

267

EXPERIMENTS ON LIQUEFACTION-INDUCED
LARGE GROUND DEFORMATION

Masakatsu MIYAJIMA [1], Masaru KITAURA [2] and Kohji ANDO [3]

1) Assistant Professor, Department of Civil Engineering, Kanazawa University
2) Professor, Department of Civil Engineering, Kanazawa University
3) Graduate Student, Department of Civil Engineering, Kanazawa University

ABSTRACT

This paper presents a prediction method of permanent ground deformation. The permanent ground displacement can be obtained from the product of the duration time of ground deformation and its velocity. The authors investigated the relationship between these and other factors. Small scale vibration tests were conducted using sloping loose sand layers. Based on the test results, the duration time of ground deformation and thickness of the loose sand layer showed a good correlation. The velocity of ground deformation and slope of loose sand layer also correlate with each other.

INTRODUCTION

Research on the large ground deformation induced by soil liquefaction has been conducted extensively [1]. Some research work on the causes of large ground deformation and its effects on civil engineering structures has been undertaken. As one of the results of these studies, Hamada et al. presented the regression formula for evaluating the permanent ground displacement in the horizontal direction by using the data obtained from the 1983 Nihonkai-Chubu, the 1964 Niigata and the 1971 San Fernando Earthquakes [2]. However, the mechanism of the liquefaction-induced permanent ground deformation has not been clarified sufficiently. The goal of this study is to establish the prediction method of permanent ground displacement. The permanent ground displacement can be obtained from the product of the duration of ground deformation and its velocity. The relationship between these two, the duration and velocity of ground deformation, and other factors was investigated through small scale vibration tests in the present paper.

BRIEF REVIEW OF EXPERIMENTAL STUDIES ON LARGE GROUND DEFORMATION

Permanent ground displacement depends on many factors such as the thickness, width and slope of liquefied layer, magnitude and duration time of earthquake and so on. Vibration tests were conducted in order to evaluate the principal factors affecting the large ground deformation and to establish a prediction method of permanent ground displacement. Table 1 lists the conditions of experiments conducted by some researchers in Japan. Yasuda et al. conducted a series of vibration tests in order to clarify the effects of the thickness and slope of liquefied layer, and relative density on the permanent ground deformation [3],[4]. Miyajima et al. investigated the effects of depth, width and slope of liquefied area on permanent ground deformation. The study suggested that the width of the liquefied area was one of the most influential factors to the maximum permanent ground displacement [5]. Sasaki et al. focused on the thickness of liquefied layer, duration time of liquefaction and response acceleration at the surface ground, and presented an empirical equation for evaluating permanent ground displacement [6]. Yamada et al. conducted small scale vibration tests in order to understand the performance of model sloping ground during liquefaction and then performed large scale vibration tests to compare the results of theoretical analysis [8]. Hamada et al. conducted liquefaction tests using sand boxes to test the assumption that sand boils was one of the most important factors affecting liquefaction-induced large ground displacement [9],[10],[11].

As mentioned above, some experimental results were revealed. However, accumulation of experimental data is necessary before appropriate prediction method of the permanent ground displacement can be established.

VIBRATION TESTS

Test Procedure

The diagram of test apparatus is shown in Fig. 1. The sand box was 500 mm in width, 1500 mm in length and 350 mm in height. The model sand deposit had a slope of 2 % to 6 %. The sand deposit was made from loose saturated sand, whose physical properties are listed in Table 2. Sixteen pins were installed at the surface of the sand stratum to measure the horizontal deformation of the ground surface. The deformation of the ground surface during excitation was recorded by a video camera. The model sand stratum was covered by an acryl board in order to prevent the dissipation of excess pore water pressure from the ground surface and to lengthen the duration time of soil liquefaction. The model sand stratum was vibrated by a harmonic wave with a frequency of 5 Hz. Target acceleration of the table was 120 cm/s^2 and it took about 5 seconds for the table to reach the given acceleration. The duration of the test was 30 seconds.

Test Results

Fig. 2 shows the relationship between the duration of liquefaction and that of ground deformation. The duration of liquefaction is defined as the time when lower response ground acceleration than the input acceleration appears in the accelerograph in this study. This coincides with the time from the accumulation of excess pore water pressure to its dissipation at the site where the accelerometer was installed. It can be seen in Fig. 2 that the duration of liquefaction and that of ground deformation correlate to each other and the latter is larger than the former. Since the measurement of duration of liquefaction is more precise and easier to do than the measurement of that of ground deformation, the duration of liquefaction was used instead of the duration of ground deformation. Fig. 3 shows the relationship between the maximum and average displacements of the sixteen pins. This figure shows good correlation between the maximum and average displacements. Fig. 4 presents the relationship between the thickness of loose sand layer and average displacement. The average displacement increases with an increase of the thickness of loose sand layer. Fig. 5 shows the average displacement in relation to the slope of loose sand layer. The good correlation is shown in each other. These results are in accordance with those of the previous research works mentioned above.

The permanent ground displacement is expressed as the product of the duration time of ground deformation and its velocity. First, the duration time of ground deformation was investigated in relation to the other experimental parameters. Fig. 6 illustrates the relationship between the thickness of loose sand layer and duration time of soil liquefaction. This figure indicates that the

duration time of soil liquefaction seems to be directly proportional to the thickness of loose sand layer. The whole sand layer liquefied at almost the same time because of relatively small thickness of loose sand layer in these tests. Therefore, the greater the thickness of the liquefied layer, the longer the time of dissipation of the excess pore water pressure. Fig. 7 reflects the duration time of soil liquefaction in relation to the slope of loose sand layer. This figure shows no correlation between the two factors.

Next, the effects of the velocity of ground deformation on the other test parameters were investigated. Fig. 8 shows that there is no relationship between the thickness of loose sand layer and velocity of ground deformation. Fig. 9 shows the relationship between the velocity of ground deformation and the slope of the loose sand layer. Since the whole sand layer was liquefied completely in these tests, the effect of gravity on the deformed ground increases with an increase of the slope, therefore, the velocity of ground deformation increases.

DISCUSSION

Based on the test results obtained in the present study, the duration of ground deformation and thickness of loose sand layer showed a good correlation. The velocity of ground deformation and slope of loose sand layer also correlate well. Since the permanent ground displacement is expressed as the product of the duration time of ground deformation and its velocity, the average displacement of ground deformation is shown in relation to the product of the thickness and slope of loose sand layer in Fig. 10. This figure reveals that the average displacement is directly proportional to the product of the thickness and slope of loose sand layer.

The tests results suggest that it is reasonable to divide the ground displacement into the duration time and velocity of the ground deformation in the establishment of a prediction model. The duration of ground deformation depends mainly on the duration of liquefaction. The liquefaction potential, strength and duration of earthquake, etc. seem to be influential factors of the duration time of ground deformation. The velocity of ground deformation depends on the slope of liquefied layer, degree of liquefaction, that is, softness of the ground, area of the liquefied layer, etc. Further studies on quantitative evaluation of these relation are needed.

CONCLUDING REMARKS

This paper experimentally investigated permanent ground deformation induced by soil liquefaction. The small scale vibration tests were conducted in order to establish the prediction method of permanent ground displacement. As the permanent ground displacement can be expressed as the

product of the duration of ground deformation and its velocity, the relationship between these two and other factors. The duration of ground deformation and thickness of loose sand layer have a good correlation. The velocity of ground deformation and slope of loose sand layer also correlate to each other. Further studies on quantitative evaluation of these two major factors in relation to the other factors are needed.

ACKNOWLEDGEMENTS

REFERENCES

1) Proceedings of the 1st and 2nd US-Japan Workshop on Liquefaction, Large Ground Deformation and Their Effects on Lifeline Facilities, NCEER, ADEP, 1988, 1989.

2) Hamada, M., Yasuda, S., Isoyama, R. and Emoto, K.: Study on Liquefaction-Induced Permanent Ground Displacements and Earthquake Damage, Proceedings of Japan Soc. Civil Eng., No. 376, pp. 221-229, 1986 (in Japanese).

3) Yasuda, S., Tada, H., Fukusaki, S., Nakashima, R. and Yamamoto, Y.: Shaking Table Test of Liquefaction Induced Permanent Ground Displacement, Proceedings of the 22nd Japan National Conference on Soil Mech. and Found. Eng., pp. 731-734, 1987 (in Japanese).

4) Yasuda, Y., Nagase, H., Tauchi Y. and Furuta, Y.: Shaking Table Tests on Permanent Grund Displacement of Sand Deposits with Different Condition due to Liquefaction, Proceedings of the 25th Japan National Conference on Soil Mech. and Found. Eng., pp.1041-1042, 1990 (in Japanese).

5) Miyajima, M., Kitaura, M. and Nomura, Y.: Characteristics of Permanent Ground Displacement Induced by Soil Liquefaction, Memoirs of the Faculty of Technology, Kanazawa University, Vol.21, No. 1, pp. 1-10, 1988.

6) Sasaki, Y., Matsumoto, H. and Saya, S.: Shaking Table Tests on Lateral Spread of Ground Due to Soil Liquefaction, Proceedings of the 24th Japan National Conference on Soil Mech. and Found. Eng., pp.1025-1028, 1989 (in Japanese).

7) Matsumoto, H., Tokida, K. and Saya, S.: Experimental Study on Lateral Flow of Ground Due to Soil Liquefaction, Proceedings of the 25th Japan National Conference on Soil Mech. and Found. Eng., pp. 1045-1046, 1990 (in Japanese).

8) Yamada, K., Ishihara, K., Towhata, I., Kubo, H. and Kikuchi, M.: Study on Permanent Displacement of Liquefied Ground by Shaking Table Tests, Proceedings of the 24th Japan National Conference on Soil Mech. and Found. Eng., pp.1029-1032, 1989 (in Japanese).

9) Tachibana, N., Kojima, Y. and Hamada, M.: Investigation on Mechanism of Liquefaction-Induced Permanent Ground Displacement, Proceedings of the 1989 Chubu Branch of JSCE Annual Meetings, pp.134-135, 1989 (in Japanese).

10) Tachibana, N. and Hamada, M.: Experimental Investigation on Mechanism of Permanent Ground Displacement Induced by Soil Liquefaction, Proceedings of the 44th JSCE National Conference, Vol.1, pp. 886-887, 1989 (in Japanese).

11) Wakabayashi, T., Okamoto, H., Hamada, M. and Tachibana, N.: Study on Mechanism of Liquefaction-Induced Permanent Ground Displacement by Shaking Table Tests, Proceedings of the 45th JSCE National Conference, Vol.1, pp. 1064-1065, 1990 (in Japanese).

Table 1 Review of experiments on permanent ground deformation.

References	Scale of sand box (cm) Length x Height x Width	Test conditions Gradient(%)	Surface	Bottom
Yasuda et al. (1987) [3] (1990) [4]	80 x (7.5-27.5) x 50	0, 5, 10%	Slope Flat	Slope Slope
Miyajima et al. (1988) [5]	150 x (10-20) x 50	2, 4, 6%	Slope	Slope
Sasaki et al. (1989) [6]	600 x about 105 x 80	1.8-7.7%	Slope	Flat
Matsumoto et al. (1990) [7]	400 x (5-70) x 200	2.5-15%	Slope Slope Flat	Flat Slope Slope
Yamada et al. (1989) [8]	100 x about 34 x 40 301.2 x 55 x ?	16% 1%	Flat Flat	Slope Slope
Hamada et al. (1989) [9] (1990) [10],[11]	85 x 27 x 24 199 x 41.6 x 99 300 x 75 x 100	5% 5% 0% 3, 5%	Slope Slope Flat Flat	Slope Slope Flat Slope

Table 2 Physical properties of sand.

Specific Gravity	2.67	
Uniformity Coefficient	2.96	
Maximum Void Ratio	1.030	
Minimum Void Ratio	0.721	
50 Percent Diameter	0.2	(mm)
Coefficient of Permeability	1.92×10^{-2}	(cm/s)
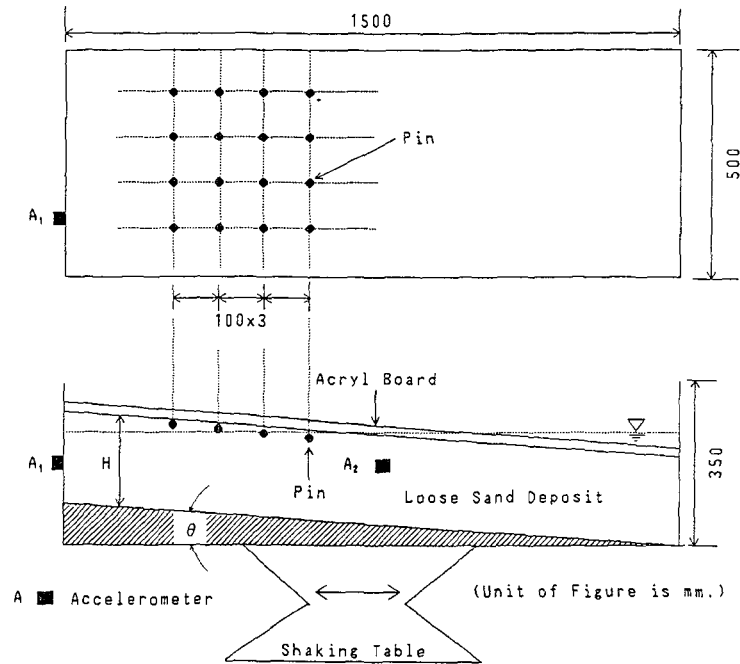
Fig. 1 General view of experimental apparatus.
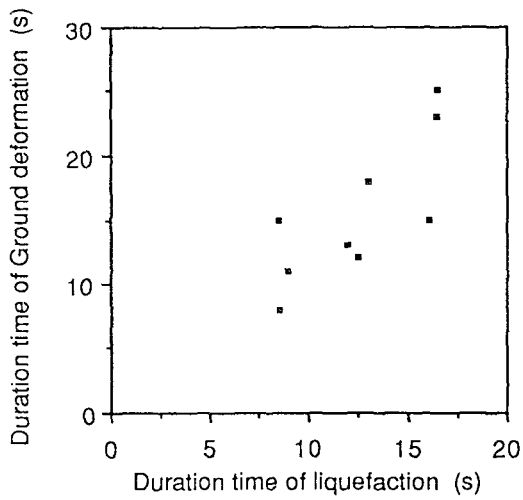
Fig. 2 Relationship between duration time of liquefaction and ground deformation.
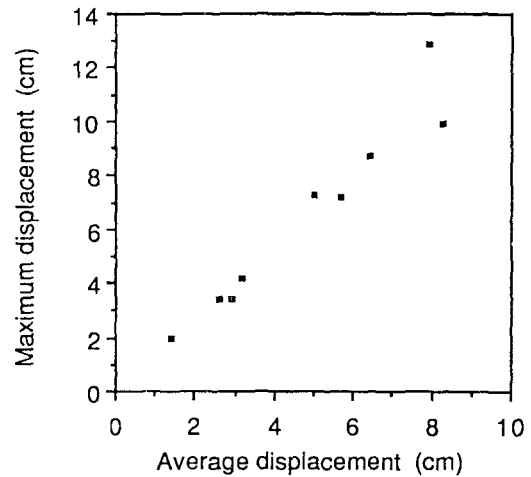
Fig. 3 Relationship between average displacement and maximum displacement.
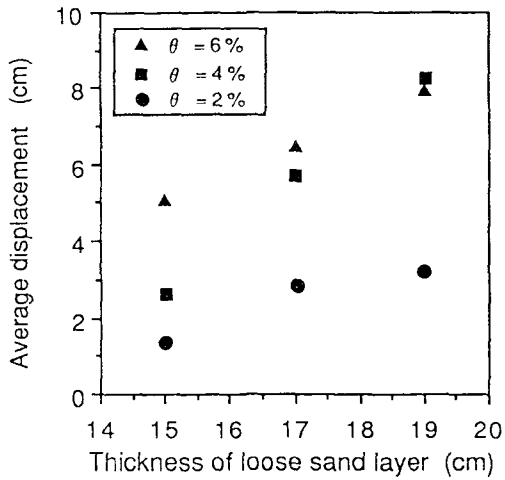
Fig. 4 Relationship between thickness
of loose sand layer and average
displacement.
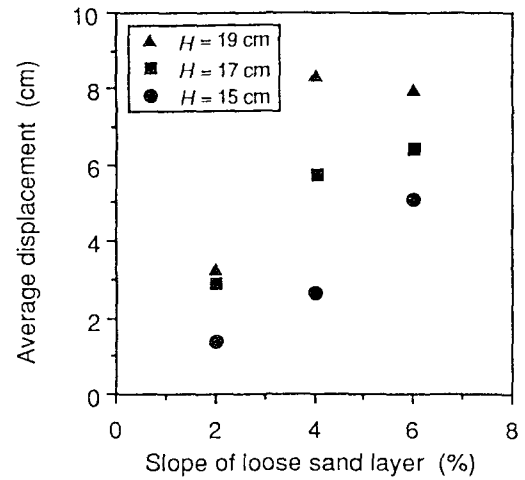
Fig. 5 Relationship between slope of
loose sand layer and average
displacement.
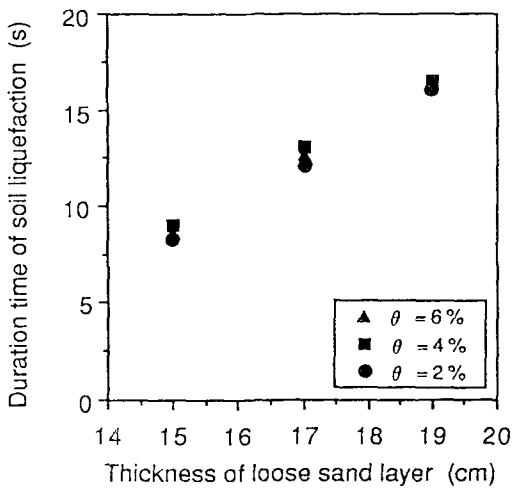
Fig. 6 Relationship between thickness
of loose sand layer and duration
time of soil liquefaction.
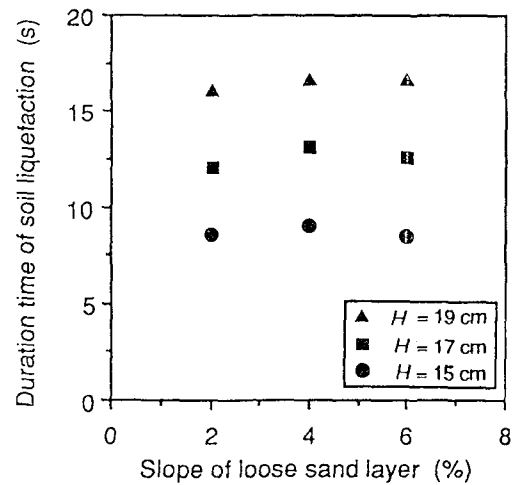
Fig. 7 Relationship between slope of
loose sand layer and duration
time of soil liquefaction.
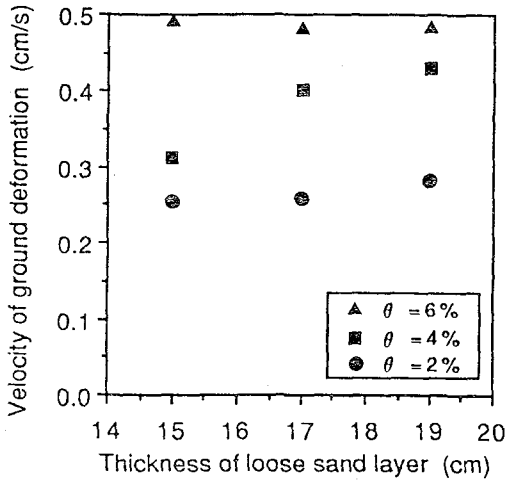
Fig. 8 Relationship between thickness
of loose sand layer and velocity
of ground deformation.
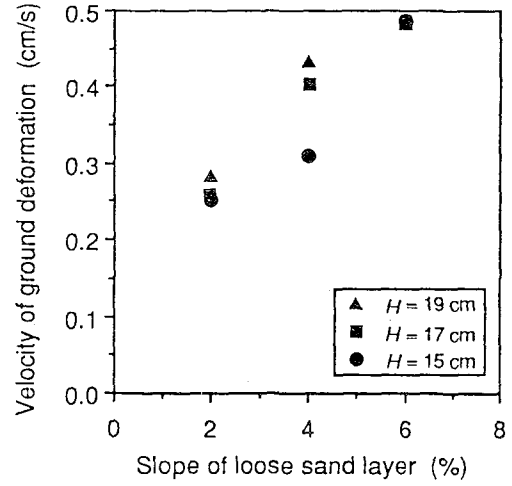
Fig. 9 Relationship between slope of
loose sand layer and velocity of
ground deformation.
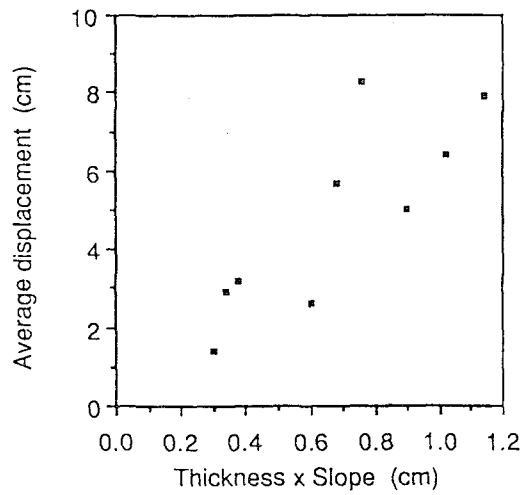
Fig. 10 Relationship between
thickness x slope and average
displacement.

278

MECHANISM OF SAND BOIL FORMATION IN LAYERED SOILS AS OBSERVED IN CENTRIFUGE TESTS

B. L. Kutter[1] and G. L. Fiegel[2]

[1,2] - Associate Professor and Graduate Research Assistant, respectively; University of California, Davis

ABSTRACT

Preliminary results from centrifuge tests simulating the effect of base shaking on the response of a layered soil deposit are presented. The models consisted of a layer of saturated liquefiable fine sand covered by a layer of relatively impermeable silica flour (silt). Pore pressures, settlements, and accelerations were measured during shaking and the subsequent densification of the sand. Boils were observed on the surface of the centrifuge models. It is believed that this is the first reported instance of liquefaction-induced "boils" in a centrifuge model. The location of the boils appears to be concentrated near zones of weakness in the silt layer. There is some evidence that a water gap or a very loose zone of soil develops at the interface between the sand and silt layers due to the discontinuous permeability. The formation of boils is attributed to the sudden venting of the water from this gap through cracks which develop at weak zones in the silt layer.

INTRODUCTION

While in a condition of zero effective stress, the particles of soil are not supported by neighboring particles and will settle due to the fact that they are heavier than water. The rate of settlement is restricted by the fact that water must flow upward around the particles. The rate of flow of the water is governed by Darcy's Law, $v = ki$. If a layer of soil is subject to shaking of sufficient severity to cause the effective stresses to drop to zero, the principle of effective stress indicates that there will be an upward hydraulic gradient (the critical hydraulic gradient) of excess pore pressure equal to $i_{crit} = \gamma'/\gamma_w$. This gradient results in upward flow of pore water at an apparent velocity of $v = k\, i_{crit}$. If there is no downward drainage, the relative velocity of flow at the surface of the soil, by continuity, must be equal to the velocity of settlement of the soil surface (Scott, 1986, Heidari and James, 1982, Whitman, et. al., 1982, and Florin and Ivanov, 1961). Schofield (1981) has suggested that while in a condition of very small effective stresses, microcracks or fissures may form within the soil which may cause a dramatic increase in the apparent permeability of the soil.

In natural soil deposits, it is unusual to find a uniform deposit of liquefiable soil that extends from the surface to a significant depth. In most cases, some stratification is present, and often, liquefiable deposits are covered by topsoils and other less permeable soils. Overlying deposits of less permeable materials can prevent the escape of pore water that is expelled from the liquefiable soil.

If a layer of liquefiable soil is overlain by a less permeable deposit of soil, a scenario depicted in figure 1 is possible. The velocity of upward flow of water through the liquefiable sand is larger than that possible through the overlying soil. This means that there will be some accumulation of pore water in the form of a gap or a very loose zone of soil at the interface. This possibility was clearly pointed out by Whitman (1985), National Research Council (1985) and Seed (1987). The overlying soil could, temporarily, be floating on the water gap as shown in figure 1b. The pore pressure in the water gap would, by equilibrium, be equal to the total overburden pressure. Thus, the overlying soil, even if it is not a loose sand, would be subject to the critical hydraulic gradient. The upper layer will therefore be subject to a condition of zero effective stresses, and since any soil has very low strength at very low effective stresses, it is likely to break apart.

The failure of the upper layer is most likely to occur at some weak point such as a thin zone as depicted in figure 1c. Heavier, thicker zones are likely to fall through the gap, pushing water toward a weak or thin portion of the deposit. The water will seep upward through the overlying deposit, but flow velocities will be greater along the path of least resistance at the weak zone. Once water velocities at this zone become sufficiently high to cause erosion, particles of soil will be dragged along, creating an enlarging orifice and a concomitant increase in flow velocities. The process is analogous to a chain reaction; it is not a continuum phenomenon. A bifurcation occurs, and the problem transforms from one of relatively uniform upward flow of water through the overlying soil to a situation where flow occurs at concentrated locations around blocks of fractured soil. This scenario has been envisioned by Schofield (1981).

If the ground surface is not level, the presence of a water gap beneath a soil overlying liquefiable sand results in a dramatic reduction in sliding resistance, and lateral spreading or debris flows may result. National Research Council (1985) and Youd (1984) have described such a mechanism, where an overlying soil cracks, breaks up, and flows laterally, even for cases where the slope is very gentle.

CENTRIFUGE MODEL TESTS

Four centrifuge model tests were conducted for this paper, and results from two of these tests are described here. All of the tests were carried out at a centrifugal acceleration of 50 g on the Schaevitz centrifuge at the University of California, Davis. This centrifuge is equipped with a servo-hydraulic actuator that is capable of reproducing realistic scaled earthquake time histories and spectra (Chang, 1990). The models described in this paper were subject to ten approximately uniform cycles of predominantly 1 Hz base acceleration. Both of the models were constructed using three types of soil (figure 2). The fine sand is Nevada Sand with a mean grain size of 0.13 mm , a relative density of 60% and a permeability of about $3 * 10^{-3}$ cm/s. The silt is a white silica flour with a void ratio of 0.78 and a permeability of about $3 * 10^{-6}$ cm/s. The coarser sand had a mean grain size of 0.4 mm and was compacted to a relative density of about 100%.

The scaling laws for dynamic centrifuge modeling are described in some detail by Schofield (1981). The basic reason for testing the models on a centrifuge is to obtain prototype stress levels and pore pressures in a small scale model. All accelerations in the model are increased by an arbitrary factor, N, and all length dimensions are reduced by the same factor N, as compared to the full scale prototype. This is accomplished by increasing the frequency of base shaking by the same factor N. There is a well known conflict between time scale factors for dynamic shaking and pore pressure dissipation. In order to resolve this conflict, the model soil can be assumed to represent a prototype soil with a permeability N times greater than that for the model. Thus the model sand and silt materials having permeabilities listed above correspond to prototype soils with permeabilities of $1.5 * 10^{-1}$ and $1.5 * 10^{-4}$ cm/s respectively. From the standpoint of permeability, the fine sand and silt in the model thus more closely represent a coarse sand and a silty sand in the prototype.

Test GF3

This test was designed to simulate a level, stratified deposit of soil. The model consisted of 2" of silt, 1.75" of fine sand (Dr = 60%), and a layer of coarser, dense sand below, as shown in figure 2. This arrangement corresponded to a prototype consisting of 100" of silt and 87.5" of fine sand. The model was actually constructed with the surfaces curved at a radius corresponding to the radius of the centrifuge. Since the centrifuge actually produces a radial acceleration field, it was necessary to construct curved layers to simulate level ground. The purpose of placing the dense, coarser sand beneath the fine sand was to provide a curved base for the fine sand. Since the coarser sand was very dense it did not settle significantly during shaking, and since it is confined by the box and fine sand, it was not expected to provide a drainage path for excess pore pressures.

The fine sand was prepared by pouring it dry through a funnel and a screen and allowing it to free fall for a distance of about 18 inches. The deposition was interrupted at appropriate times to allow placement of pore pressure transducers and accelerometers at various depths in the dry sand. The top surface of the sand was smoothed to provide an accurately curved surface. The sample box was then sealed and subject to a vacuum of 29 inches of Mercury. After applying the vacuum, the box was flooded with CO_2 gas and allowed to sit for about 5 minutes to permit the gas to permeate into the soil and the pore pressure transducers. Next, the CO_2 gas was evacuated, again to 29" of Mercury. While maintaining the vacuum, de-aired water was allowed to drip into the box from the top until the sand was completely covered. It is felt that this procedure produced a sample close to 100% saturation.

281

After saturating the sand, silica flour (silt) was stirred with de-aired water to form a slurry and poured into the box, providing a flat surface of silt in the model. In order to form a curved surface, additional slurry was prepared and poured into the box, and the centrifuge was quickly brought up to speed. The slurry settled and consolidated while the centrifuge spun thereby naturally forming an appropriately curved surface. The centrifuge was then stopped to permit a thin layer of colored sand to be placed on the surface, photographs to be taken, and additional instrumentation to be placed.

Prior to shaking the model, it was brought up to a centrifuge acceleration of 50 g and allowed to consolidate at this speed for 20 minutes. The model was then shaken with 10 approximately uniform cycles of base motion with an amplitude of about 0.3 g (prototype acceleration). Figure 3 shows the accelerations recorded at the base and at the interface of the model. During the first cycle, the interface acceleration follows the base motion fairly accurately. During the second cycle, the interface acceleration shows flat portions with large spikes of acceleration. The reason for the large spikes is not clear. These spikes may be associated with a locking up of the soil that occurs at large strains as is often observed in laboratory tests on sand in a state of initial liquefaction. During the last eight cycles of shaking, the interface acceleration is very low, indicating that the accelerometer is embedded in completely liquefied soil, effectively isolated from the base.

In this test sand boils were observed to form, mostly along the side of the sample against the window. Sand was clearly carried upward along the window, and eruptions were apparent at the surface. Most of the material carried to the surface was, however, the silt. Mounds of ejected silt on the order of 2 inches in diameter and 0.25 inches thick were observed.

The pore water pressures recorded in this test are shown in figure 4. It appears that the soil does become liquefied at all locations. It is interesting that the pore pressures within the sand (figures 4c and 4d) build up very rapidly while those at the interface (figure 4b) and within the silt (figure 4a) reach their maximum at the end of shaking. This indicates that the pore pressures are generated within the sand and that the upward flow of water causes large pore pressures at the interface and within the silt. Immediately after shaking subsides, the pore pressures at the bottom of the sand begin to dissipate indicating that the sand is solidifying. The solidification front proceeds upward, and about 5 seconds later, the pore pressure at the top of the sand begins to dissipate. The leveling off of the pore pressures in the sand at about 23 seconds corresponds to the pore pressure due to the liquefied silt (which can be viewed as a heavy fluid) above the sand. On a longer time scale plot (not shown) it is clear that all of the pore pressures eventually drop to zero. The solidification of the silt is much slower than that for the sand.

The settlements recorded by the four LVDT's are shown in figure 5. All of these plots are presented in terms of the prototype; actual model settlements can be found by dividing displacement values by 50. The displacement just below the interface in the sand shows a monotonic increase at a high rate during shaking (from about 2 to 13 seconds along the time scale) followed by a small settlement after shaking (figure 5d). The 1 Hz components of the recordings may be due to some flexibility in the LVDT supports. This 1 Hz component is most dramatic in the transducer at the top of the silt on the side (figure 5a). The effect of the flexibility cannot explain the longer duration oscillations observed after shaking stops. In the time period from 13 to 18 seconds, all of the displacement transducers show some irregularity. The transducer at the interface (silt) actually indicates a small incremental swell followed by settlement at the same time that the top of the silt shows a settlement followed by a swell. The top of silt (center) shows a static period between 13 to 17 seconds followed by a sudden increment of settlement. The erratic nature

of the recorded settlements is consistent with the mechanism suggested in figure 1. Blocks of silt may be shifting, buoying up, and dropping independently as the interface opens and boils intermittently vent the water which collects at the interface.

It is also interesting to compare the rate of settlement to the values expected based on Darcy's Law. The settlements during shaking occur at a rate of about 6 inches over a period of 10 seconds (prototype dimensions). In metric units the velocity is about 1.5 cm per second. If the soil is liquefied, we would expect the settlement velocity to be approximately equal the permeability of the soil. The permeability of the sand and silt converted to prototype scale are $1.5 * 10^{-1}$ and $1.5 * 10^{-4}$ cm/s respectively. The settlement rates during shaking appear to be about an order of magnitude larger than the permeability of the sand and about four orders of magnitude larger than that for the silt. This suggests that the liquefied soil is not behaving as a continuum; the water must be draining out of pipes or fissures that produce a larger apparent permeability. It should be noted that the relatively rapid settlement of the ground is noticeable in other centrifuge test data (e.g. Whitman et.at., 1982), however, the result was not emphasized since it was not clear that the LVDT supports did not sink into the liquefied soil causing erroneously large recorded settlements. In this study, an effort was made to make the LVDT supports neutrally buoyant so that they would not have a tendency to sink in liquefied soil.

Test GF4

This test was planned in an attempt to observe sand boil formation away from the windows of the model container. It was felt that edge effects may have contributed to the results. So, model GF4 was constructed, again with an approximately level silt surface, but with the sand thickness reduced near all four sides of the box as shown in figure 6. This figure shows an approximately flat surface, but the surface was actually curved corresponding to the radius of the centrifuge in order to simulate a level prototype. The model was prepared following a procedure similar to Test GF3.

It should be noted that while the sand surface could be accurately contoured, there is some inevitable error in the formation of the silt surface. As can be seen in figure 6, which is drawn to scale, the model actually represented a gentle mound, with a high point near the center of the model and low points at both ends. This gentle slope turned out to be a significant factor influencing the behavior of the model. Boils were observed to develop near the ends of the model at the locations where the silt was the thinnest. This is consistent with the idea that boils occur at points where the soil is the weakest.

After test GF4, the sample was dissected and cross sections were photographed. One such cross section, cut through the centerline of an apparent soil volcano (boil), is shown in figure 7. It is clear that the silt layer settled more directly adjacent to the boil. This increased settlement appears to be due to the erosion of underlying soil in the form of piping. A small mouth is clear at the ground surface. In addition, the layer of white soil above the dark line is material that has been ejected from the mouth of the volcano. The location of this particular boil was about halfway between the side walls of the box and near the right end of the box. The approximate location is labelled as point A in figure 6.

Figure 8 shows the ground surface and water table locations with and exaggerated vertical scale before and after the earthquake. The dimensions have been converted to prototype units in this figure. As expected, the ground surface settlement was largest at the center of the sample on the top of the small mound. On the right side of the model, the ground surface actually swelled. This swelling is probably due to a combination of lateral flow down the slope and the fact that soil was ejected through boils at the low point on the right

283

side of the model. It is also interesting to note that the ground water table rose about 1 ft so that the final ground surface was almost completely submerged. The final ground surface was considerably flatter than the initial ground surface.

Also shown in figure 8 are the locations of a pore pressure transducer that was buried in the silt. By observing the original and final locations of the ground water table, the depth of the transducer could be calculated based on the recorded static pore pressures. The location of the transducer was also accurately measured after the test when the sample was dissected. From this data it appears that the transducer settled approximately the same amount as the ground surface. Furthermore, these measurements agreed well with ground surface displacements measured by LVDT's. This is important since it lends credence to the LVDT measurements.

CONCLUSIONS

1) The centrifuge is shown to be a valuable tool for studying the basic processes that occur during liquefaction of layered soils. Lateral flow, ground settlement and the formation of soil volcanos were observed.

2) Stratification of soils has a significant impact on the mechanisms of pore pressure dissipation. An overlying, relatively impermeable soil tends to retard the escape of pore water produced by the settlement of an underlying liquefiable sand layer. This can result in the formation of a water gap or a very loose zone at the interface.

3) If supported on a layer of water, the overlying soil will inevitably crack at weak points thereby allowing blocks of the relatively impermeable soil to shift. Tinner zones are buoyed up, and thick zones settle through the water gap. This action may result in temporary bulging of the ground surface at some locations while rapid settlements occur at other locations.

4) Water which collects at the interface escapes rapidly through the cracks in the liquefied soil. The relatively high velocities of water through the cracks causes erosion and piping along with the development of volcanos of soil in the form of slurry.

5) The development of cracks also results in a much higher apparent permeability of the soil. Observed settlement velocities are orders of magnitude larger than that calculated based on the permeability of the intact material. This increase in permeability is a significant factor affecting the duration of time that a soil deposit can be in a liquefied state.

6) Cross-sections cut through observed boils indicate that the settlement of the overlying silt layer was much larger directly adjacent to the boil. Material removed from the base of the silt permits these large settlements to occur.

REFERENCES

Chang, G.S., "Centrifugal and Numerical Modeling of Soil-Pile-Building Interaction During Earthquakes," PhD Thesis, University of California, Davis, 1990.

Florin, V.A., and Ivanov, P.L. "Liquefaction of Saturated Sandy Soil," Proceedings 5th Int. Conf. on Soil Mech. and Found. Eng., Paris, p.106, 1961.

Heidari, M., and James, R.G. " Centrifuge Modelling of Earthquake Induced Liquefaction in Saturated Sand," Proceedings of the Conference on Soil Dynamics and Earthquake Engineering, Vol. 1, A.A. Balkema, Rotterdam, Netherlands, 1982, pp. 271-281.

National Research Council "Liquefaction of Soils During Earthquakes." Report No. CETS-EE-001, Committee on Earthquake Engineering. National Academy Press., Washington, D.C., 1985.

Scott R.F. "Solidification and Consolidation of a Liquefied Sand Column," Soils and Foundations, JSSMFE, Vol. 26, No.4, pp.23-31, Dec. 1986.

Seed, H.B. "Design Problems in Soil Liquefaction," Journal of Geotechnical Engineering, ASCE, Vol. 113, No. 8, August, 1987, pp.827-845.

Schofield, A.N. "Dynamic and Earthquake Geotechnical Centrifuge Modeling," Proc. Int Conf. on Recent Advances in Geotechnical Earthquake Engineering and Soil Dynamics, University of Missouri, Rolla, Missouri,Vol. 3, pp. 1081-1100, 1981.

Whitman, R.V. "On Liquefaction," Proc. 11th Int. Conf. on Soil Mech. and Found. Engr., Vol. 4, San Francisco, August, 1985, pp.1923-1926.

Whitman, R. V., Lambe, P.C., and Akiyama, J., " Consolidation during Dynamic Tests on a Centrifuge," Preprint 82-063, ASCE National Convention, Las Vegas, Nevada, April, 1982.

Youd, T.L. "Geologic Effects--Liquefaction and Associated Ground Failure," Proc. Geologic and Hydrologic Hazards Training Program, Open File Report 84-760, U.S. Geological Survey, Menlo Park, California., 1984.

a)

Low k

liquefiable sand

u

$v = k\,i \sim k_m$ $(10^{-4}$ cm/s$)$

$v = k\,i \sim k_s$ $(0.1$ cm/s$)$

$u = \sigma_v$

z

$, i = \gamma_b / \gamma_w \sim 1$

b)

WATER ACCUMULATES AT INTERFACE

c)

WATER AND ERODED SOIL ERUPT AT WEAK POINT

d)

LOCAL SETTLEMENT MAY BE LARGER THAN AVERAGE SETTLEMENT
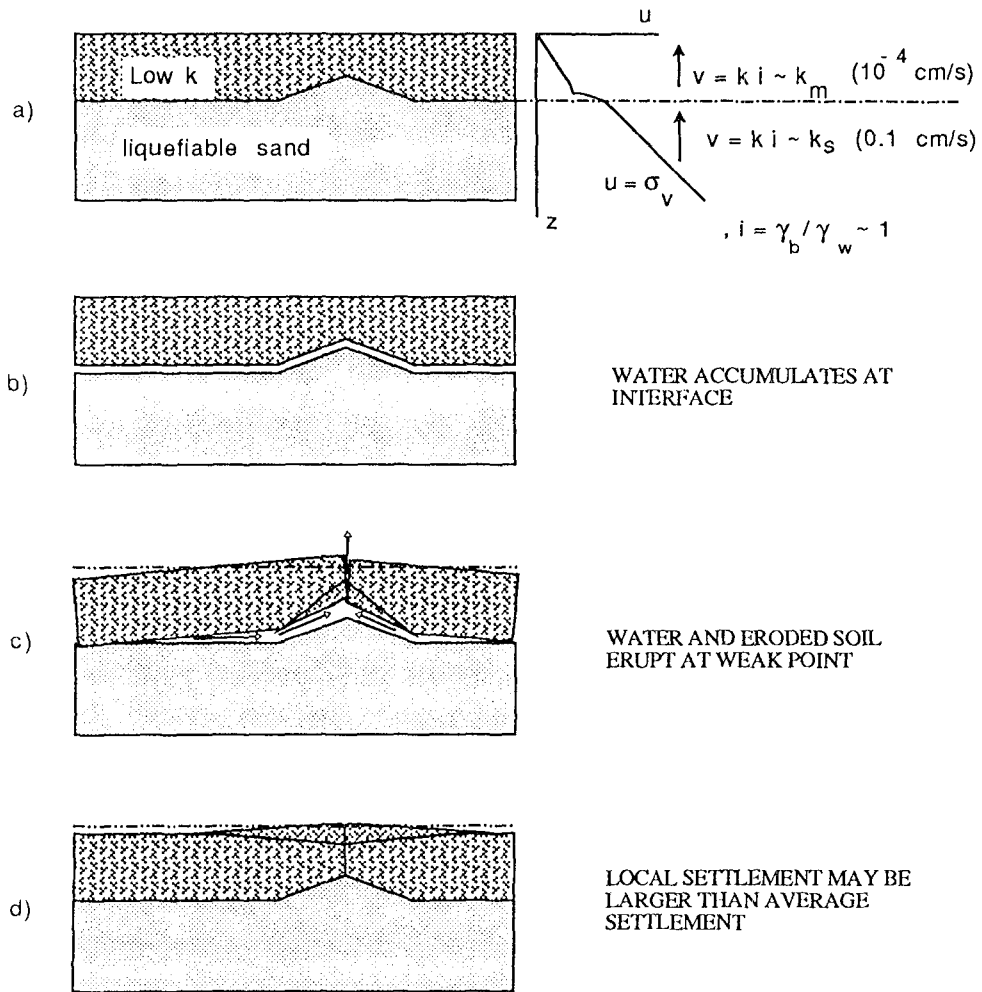
Figure 1. One mechanism for development of sand boils
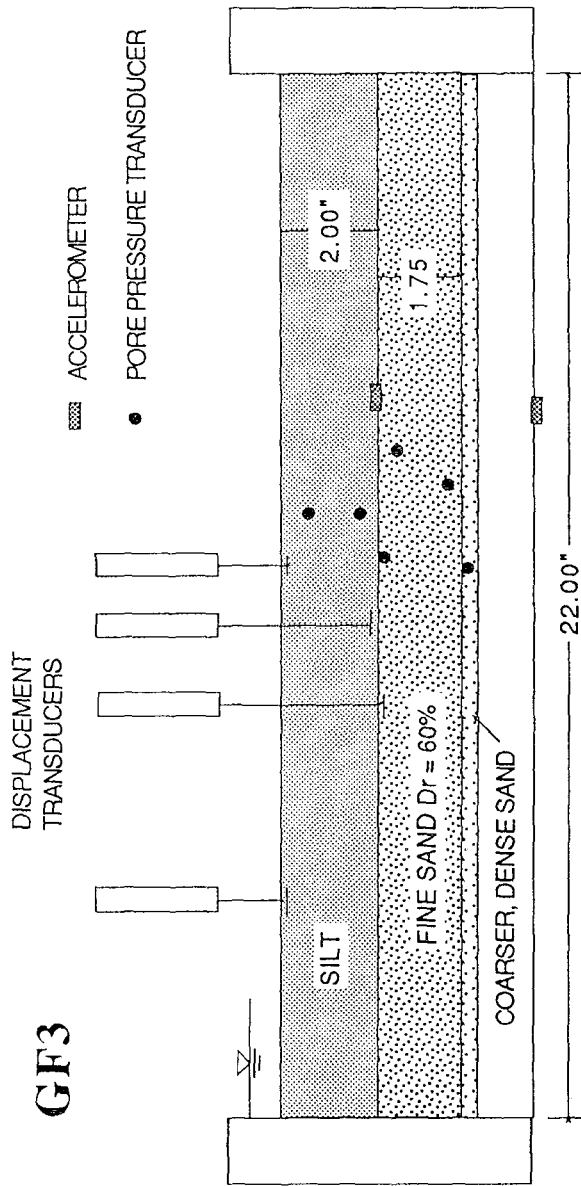
Figure 2. Test arrangement for test GF3

BASE ACCELERATION: HORIZONTAL
TEST GF3 - DYNAMIC PLOT

(a)

ACCELERATION: INTERFACE
TEST GF3 - DYNAMIC PLOT

(b)
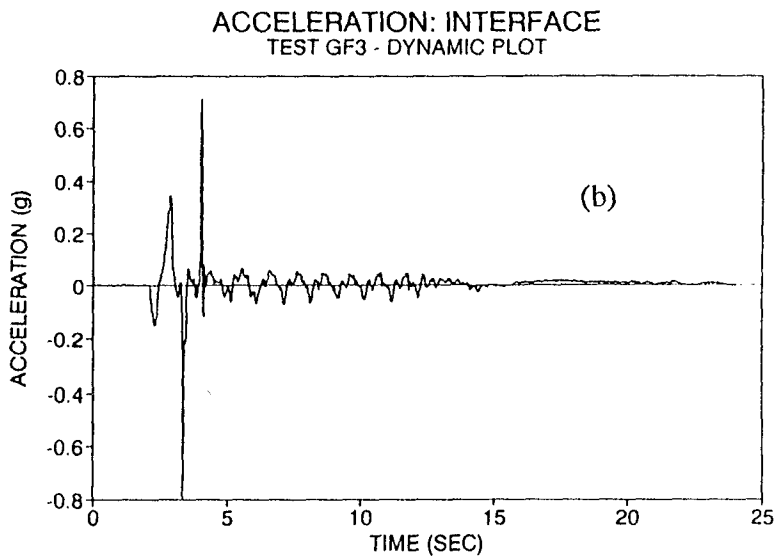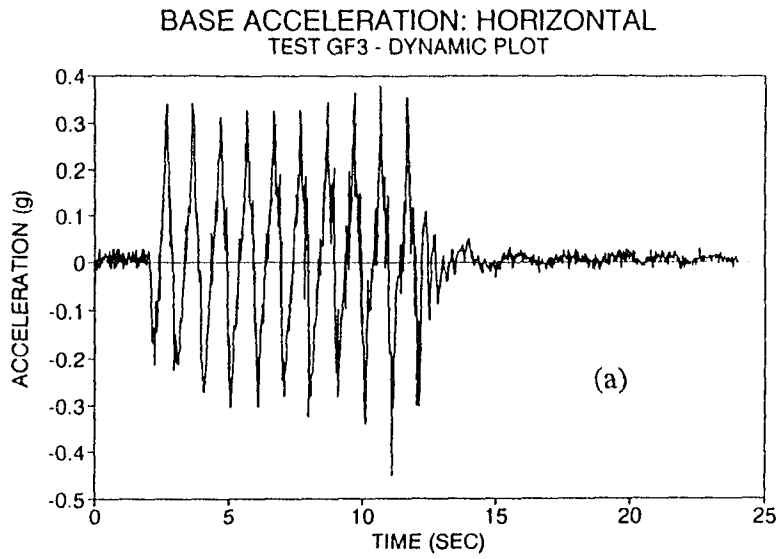
Figure 3. Acceleration plots for test GF3

288
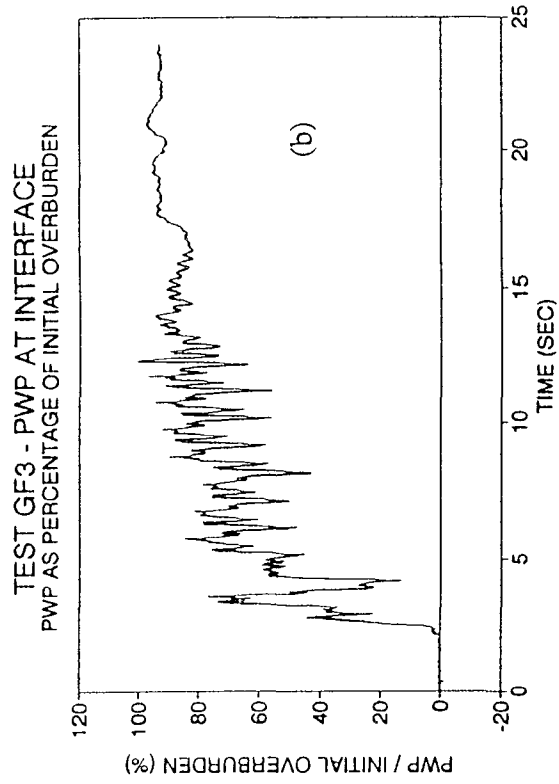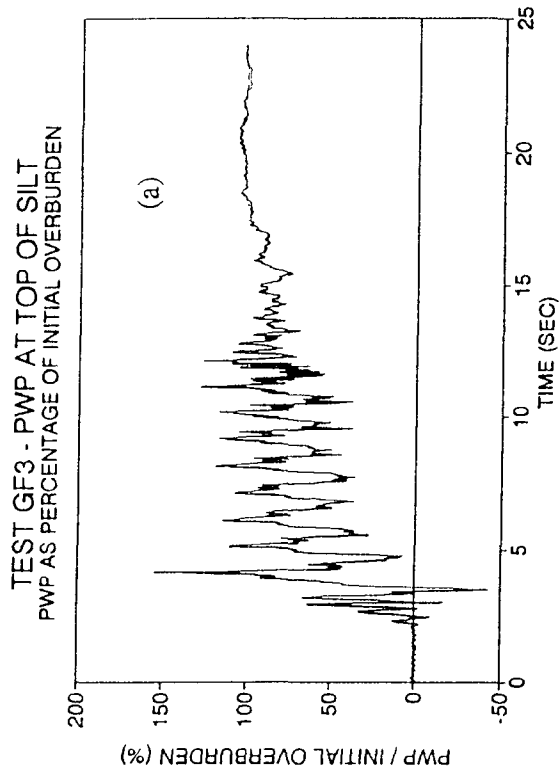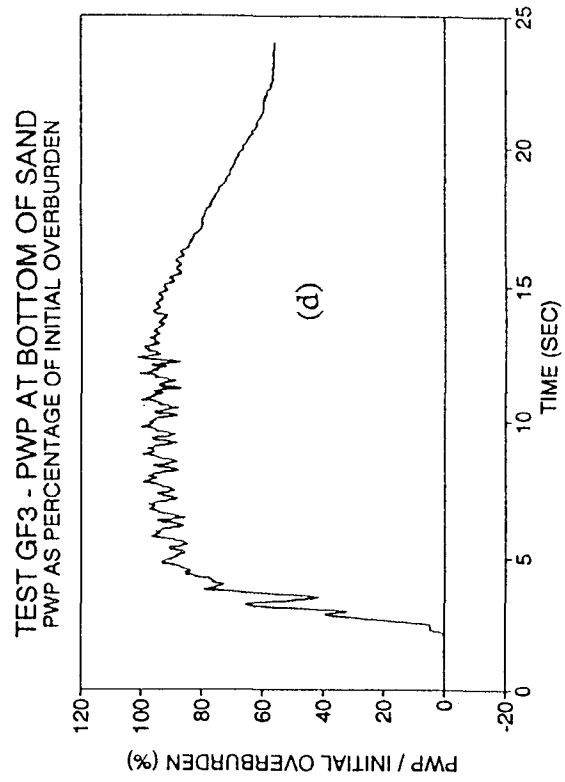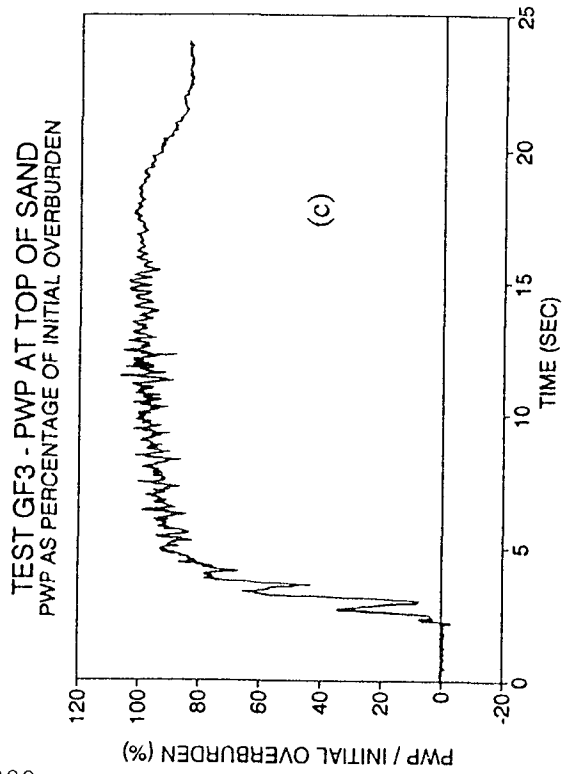
Figure 4. Plots of pore water pressure for test GF3
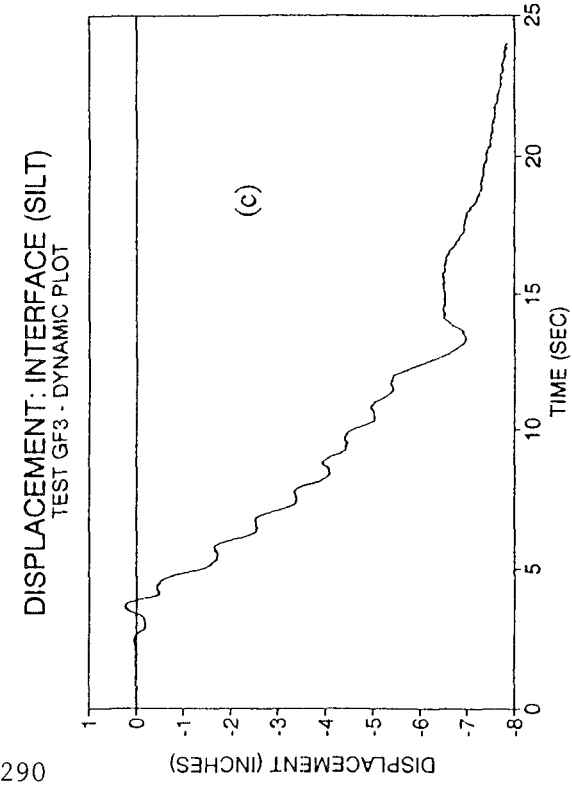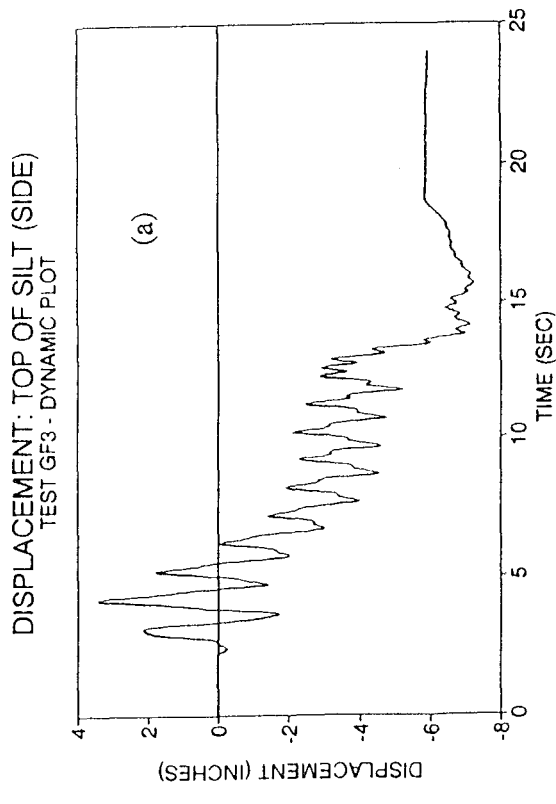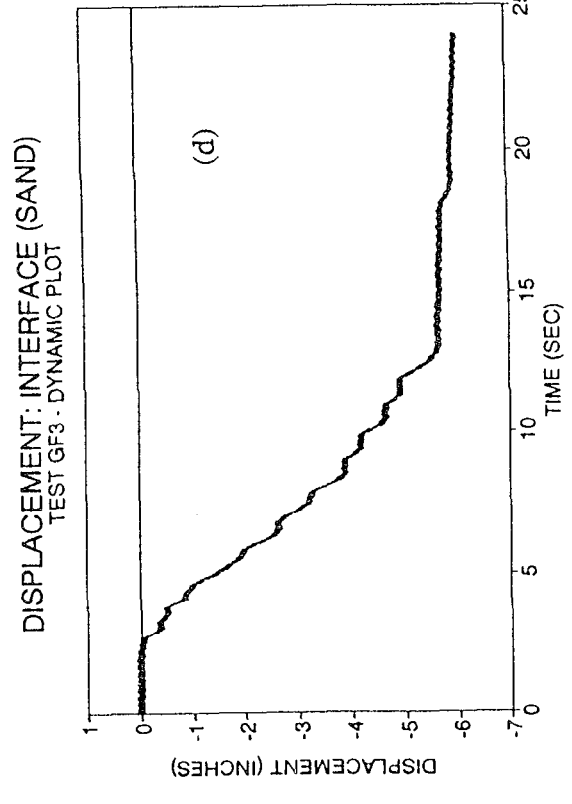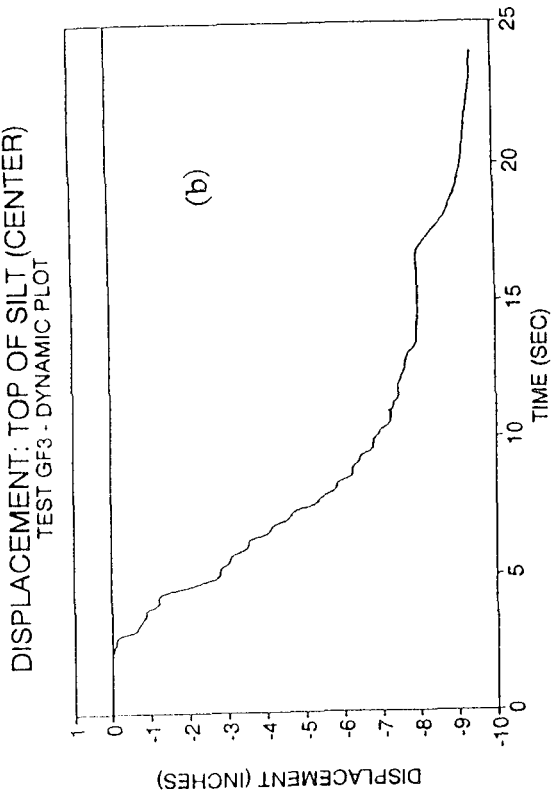
Figure 5. Plots of settlement for test GF3

290
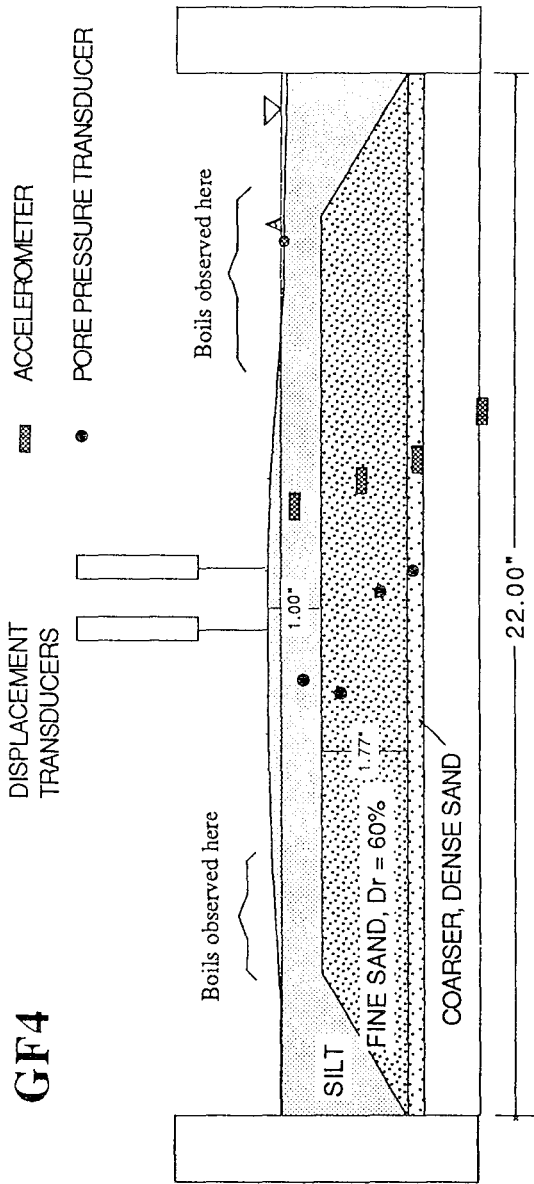
Figure 6. Test arrangement and locations of observed boils due to liquefaction for test GF4

Figure 8. Ground surface and water table profiles for test GF4. Note that the vertical scale is exaggerated.
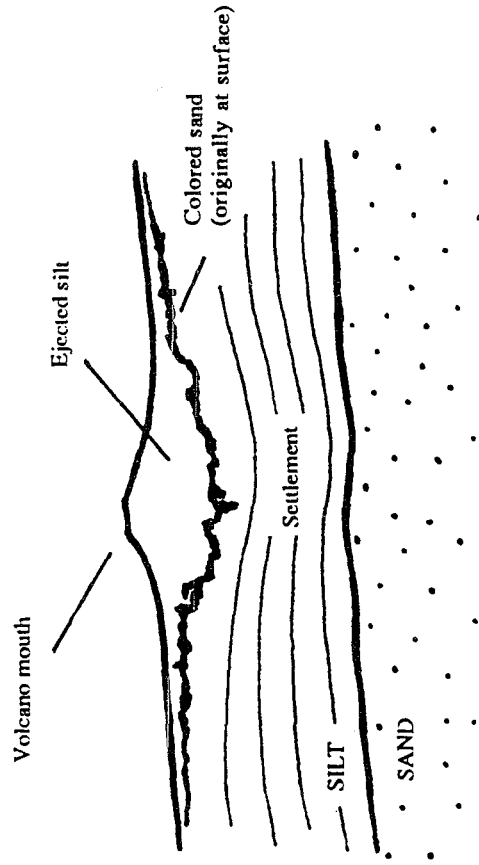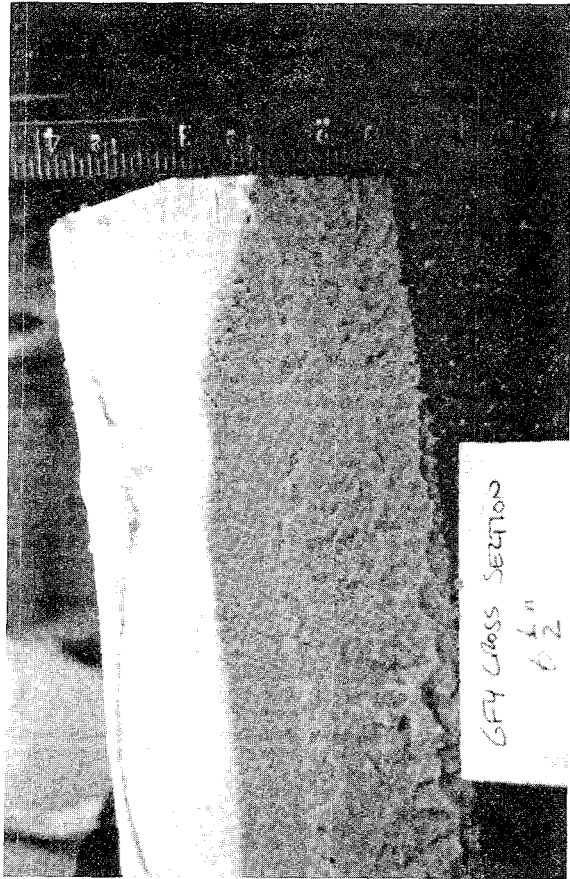
Figure 7. Cross section of a soil volcano (boil) for test GF4 (photograph and line drawing)

COMMENTS ON THE DETERMINATION OF IN SITU
UNDRAINED STEADY STATE STRENGTH OF SAND SOILS

by

Gonzalo Castro
GEI Consultants, Inc.
Winchester, MA

ABSTRACT

Seismically induced failures of earth structures generally involve relatively loose sandy soils. The failures can be divided into: a) those caused by a loss of stability and b) those where sufficiently large deformations accumulate during the earthquake to constitute cause of "failure" for structures or lifelines. In this case the earth structure has not actually failed in the sense of a loss of stability.

Case histories of the Lower San Fernando Dam and for the Heber Road site are used to show how estimates of undrained steady state strength have been obtained. The foundation evaluation of an existing earth dam is used in this paper to illustrate the limitations of the use of index penetration tests. In this illustration SPT data do not reflect the presence of sand layers disclosed by CPT logs. The cone data can be interpreted to indicate a "true" tip penetration resistance of the sand layers of at least 60 tsf, indicating a medium dense sand.

COMMENTS ON THE DETERMINATION OF *IN SITU*
UNDRAINED STEADY STATE STRENGTH OF SANDY SOILS

by

Gonzalo Castro, Ph.D., P.E.
GEI Consultants, Inc.

Seismically induced failures of earth structures generally involve relatively loose sandy soils. The failures can be divided into: a) those caused by a loss of stability and b) those where sufficiently large deformations accumulate during the earthquake to constitute cause of "failure" for structures or lifelines. In this case the earth structure has not actually failed in the sense of a loss of stability.

A typical case of a loss of stability is the slide of the Lower San Fernando Dam caused by the 1971 San Fernando earthquake. Cross sections of the dam prior to and after the slide are shown in Fig. 1. Detailed descriptions of the slide are presented in Seed et al (1975) and Castro et al (1989). The slide was caused by the loss in strength of the soil in the lower part of the hydraulic fill shell which is shown darkened in Fig. 1. This zone of the hydraulic fill consists of silty sands and sandy silts with SPT blowcounts mostly in the range of 15 to 20 blows/foot and cone tip resistance typically in the range of 50 to 100 tsf.

A review of the stability of the dam prior to the earthquake indicates that the shear stresses within the failure zone in the hydraulic fill average about 900 psf. Computations of the dynamics of the movement of the center of gravity of the sliding mass indicated that the average shear resistance in the same zone during the slide was about 500 psf, Davis et al (1988). The peak seismic shear stresses in the same zone were estimated by Seed et al (1975) to be about 2,000 to 3,000 psf. Based on

294

this information one can infer that the stress strain behavior of the soil in the lower part of the hydraulic fill was as shown in Fig. 2 and that it represents undrained behavior. Thus, even though the dam was stable since its construction in 1915 until the 1971 earthquake, there was a potential for instability because the undrained strength available at large strains was lower than the statically applied shear stresses. However, actual instability occurred only when there was an earthquake large enough to overcome the peak strength and to strain the soil sufficiently so that the mobilized shear resistance became lower than the statically applied shear stresses. At that point the slide movements were driven by the static and not the seismic shear stresses. Note that during the slide the available strength in the hydraulic fill of about 500 psf was a small fraction of the drained strength of about 3,500 psf, i.e., the soil was strongly contractive.

A typical case of large deformations without a loss of stability is the lateral spreading that occurred at a site adjacent to Heber Road in the Imperial Valley in Southern California, during an earthquake in 1979, Bennett, et al (1981). A cross section along the area of movements is shown in Fig. 3. The movements are believed to have occurred mostly along a zone of loose silty sands at a depth of about 10 to 12 feet. The standard penetration resistance was only about one blow/foot, and the cone tip resistance was about 10 tsf. Because of the flatness of the terrain, the static shear stresses in this zone are very low, about 40 psf. The earthquake shear stresses at this level had peak values of about 450 psf, Castro (1987), based on a peak ground surface acceleration recorded at a nearby site of 0.8 g. Based on the observed lateral movements and a Newmark type of analysis, it was estimated that the shear resistance of the soil during the movement was of about 100 psf. The inferred stress strain behavior of the soil along the failure zone is shown in Fig. 4. The soil mass is inherently stable both prior to and during the earth-

quake; however, the high seismic stresses caused a successive accumulation of strains, initiated each time the sum of static plus seismic shear stresses exceeded the available resistance. Note also that the available strength of about 100 psf was much smaller than the drained strength of about 500 psf, indicating that again the soil was strongly contractive. Thus large pore pressures were present in the soil during the movements, which is consistent with the observation of sand boils in the area.

In both cases discussed above the key soil parameter is the soil shear strength at large strains. The value of this strength determines whether instability could be triggered by the earthquake, and if instability is not possible, it determines the amount of soil displacement that will be accumulated. In both cases the soil behavior can be assumed to have been undrained given the relatively short duration of the movements and the relatively low permeability of the soil. In both cases the undrained strength at large strains is a small fraction of the drained strength; however, the available strength was not zero.

Poulos (1971) defined the steady state strength as "the state in which the soil mass is continuously deforming at constant volume, constant normal effective stress, constant shear stress, and constant velocity." Even though in the two cases of seismically induced failures discussed above, the velocity of deformation was not constant, the effect of rate deformation on the value of undrained steady state strength has been shown to be negligible, Castro, et al (1982). Thus the strength that governs the two types of seismically induced failures discussed above is the undrained steady state strength (referred to as S_{us}). Laboratory determinations of S_{us} indicate that S_{us} is only a function of void ratio for a given soil and also that it is a sensitive function of void ratio. For sandy soils, changes in values of S_{us} by a factor of 10 correspond to changes in void ratio typically of 0.08 to 0.15.

296

Laboratory test methods used to determine steady state strength in the laboratory are shown in Table 1. The most widely used method for sands is the triaxial compression test, generally undrained, Castro (1969). Results obtained by four laboratories on a sand from the Lower San Fernando Dam are shown in Figs. 5 and 6. The results obtained by the four laboratories are generally in good agreement. The correlation between void ratio and S_{us} in Fig. 5 is independent of stress path and method of loading. Results as shown in Figs. 5 and 6 require the preparation of uniform specimens and the use of methods to prevent the development of nonuniformities during shear, i.e., lubricated end platens. Tests involving axial extension reported by Vaid et al (1990) result in considerable scatter indicating probably that substantial nonuniformities developed in axial extension.

The results discussed above relate to the determination of S_{us} on laboratory prepared specimens of an homogeneous batch of soil at known void ratios. The determination of *in situ* values of S_{us} must consider the heterogeneity of natural soil deposits and the changes in void ratio than even the most careful sampling procedure will cause in "undisturbed" soil samples. A procedure proposed by Poulos et al (1985) is presented schematically in Fig. 7.

The results of the application of the Poulos et al procedure to the hydraulic fill from the Lower San Fernando Dam are presented in Fig. 8. The results presented were obtained from tests performed by two laboratories, indicating no significant difference among the two laboratories. More importantly the results are in good agreement with the strengths estimated from the mechanics of the actual slide thus providing verification of the soundness of the method used to determine *in situ* values of S_{us}.

For soils other than sandy soils, the strains required to reach steady state are generally larger than those that can be achieved in the triaxial test. The vane test can be used to obtain S_{us} values for clays, Poulos et al (1985b), as noted in Table 1. For nonplastic silts the vane test can be used if it is performed fast enough so that the test is undrained. Castro and Troncoso (1989) present results of tests on silts from copper tailings performed at high rates of rotation to ensure that the silt along the failure zone remained undrained during the test. Drained rotation shear tests on thin samples have also been used to determine the steady state strengths of clays and silts, LaGatta (1970).

A successful test for the determination of S_{us} must comply with two key characteristics, namely, a) sufficient strains must be possible in the test so that S_{us} can be reached and b) the sample must maintain its initial uniformity of void ratio so that the void ratio in the zone of failure is known.

Analysis of past failures can be performed to obtain estimates of in situ values of S_{us}, as presented above for the Lower San Fernando Dam and for the Heber Road site, see for example, Seed (1987) and Ishihara (1989). These authors compared the backfigured S_{us} values with blowcounts and cone tip resistance, respectively. Both SPT and cone tip resistance in sandy soils correspond to at least partially drained conditions in the soils being penetrated. In the cases of interest the soils are contractive, and thus the undrained strength is generally substantially lower than the drained strength. Thus the penetration resistance is strongly influenced by the degree of drainage during the penetration test, which is generally unknown and depends on minor stratification details, soil permeability and velocity of penetration. Therefore, one cannot expect a unique correlation of S_{us} with SPT or cone penetration resistance applicable to all sandy soils. Nevertheless, a collection of well-documented cases is

298

valuable. Preliminary evaluations can be performed by comparing the case being evaluated with actual failures.

The evaluation of the foundation of an existing earth dam is presented below and serves to illustrate the limitations of the use of index penetration tests. A typical soil profile is shown in Fig. 9. The soils of concern for seismic stability are the silty sand layers in the stratum of stratified layers of clay and silty sands. The reason for the concern were the low blowcounts, often lower than 10, and the potential for the sand layers to be continuous, raising the possibility of a failure along sand layers with low S_{us} values.

A program of sampling and testing of the sands following the procedures in Poulos et al (1985) resulted in a recommended S_{us} value of 1200 psf. This value was selected conservatively to be equal to the average minus one standard deviation of all tests results. There was a concern that this relatively high value of S_{us} may be inconsistent with the low SPT and cone penetration resistances.

An expanded plot of the cone tip resistance is shown in Fig. 10. The tip resistance has a "base value" of about 5 tsf (about 10 tsf in the example shown in Fig. 9). Sharp peaks are superimposed on the base value and are interpreted to correspond to sand layers based on the associated decreases in the values of friction ratio, Fig. 9. Electric resistivity plots confirmed this interpretation. Practically all the peaks of the cone resistance in the sand layers are essentially triangular. The resistance increases rapidly and approximately linearly as the cone enters the sand layer and then abruptly drops, again about linearly. The shape of the peak suggests that the sand layers are not sufficiently thick for the cone resistance to be representative only of the properties of the sand. Rather the measured maximum cone resistance in the relatively thin sand

299

layers is strongly influenced by the properties of the clay above and below the sand layer. This observation is in agreement with a Federal Highway Administration report (1978) which states that the minimum layer thickness needed to develop the full value of q_c in a layer is equal to 15 times the cone tip diameter about equal to 2 feet which corresponds to the maximum sand layer thickness encountered in the stratified stratum.

The peaks can be analyzed by defining a width of the peak as shown in Fig. 10 as the distance between the beginning and the end of the increased cone resistance. This distance is probably equal to or slightly larger than the thickness of the layer. Cone penetration data are presented in Fig. 11 as a plot of the peak values of cone penetration versus the width of the peaks. The plot shows that larger peaks correspond to thicker layers with a relatively narrow range for peak resistance for layers thinner than about one foot. This result indicates that the peak cone value for layers thinner than about one foot is primarily a function of the thickness of the layer and to a lesser degree on the denseness of the sand. At thicknesses over about one foot, the scatter increases indicating a larger effect of the density of the sand on the peak cone resistance.

A comparison of the SPT and CPT data from borings is shown in Fig. 9. The SPT and CPT correlate well in the stiff clay layer and it indicate a gradual decrease of the strength of the clay with depth. However, the SPT does not reflect the presence of the sand layers disclosed by the CPT logs. The sand layers are too thin for the SPT to reflect the sand properties. Schmertmann (1979) has indicated that for cone friction ratios of 2 to 4, more than 50 percent of the SPT blowcount resistance is derived from the frictional resistance along the outside of the spoon. Thus, if the tip of the spoon is in a sand layer but a significant length of the spoon length is in clay, the blowcount is mostly due to the clay.

300

Furthermore, similar to the cone penetration resistance, even the tip resistance of the SPT spoon would be influenced strongly by the strength of the clay above and below the sand layers.

The results of the analysis of the penetration test data indicate that the SPT does not reflect the presence of the sand layers, and thus it is not an index of the denseness of the sand. The cone data can be interpreted to indicate a "true" tip penetration resistance of the sand layers of at least 60 tsf, indicating a medium dense sand.

The case discussed above illustrates the need for a careful examination of soil conditions and of the significance of the results of laboratory and field tests, whether one is examining a past failure or evaluating the behavior of an earth structure under a potential earthquake.

REFERENCES

Bennett, M. J.; Youd, T. L.; Harp, E. L., and Wieczorek, G. F. (1981) "Subsurface Investigation of Liquefaction, Imperial Valley Earthquake, California, October 15, 1979," U.S. Geological Survey Open File Report 81-502.

Castro, G. and Troncoso, J. (1989) "Effects of 1985 Chilean Earthquake on Three Tailings Dams" Fifth Chilean Congress of Seismicity and Earthquake Engineering, August, 1989.

Castro, G.; Keller, T. O.; and Boynton, S. S. (1989). "Re-evaluation of the Lower San Fernando Dam, Report 1, An Investigation of the Feb. 9, 1971 Slide," 2 Vols., GEI Consultants, Inc., U.S. Army Corps of Engineers Contract Report GL-89-2, Sept.

Castro, G. (1987) "On the Behavior of Soils During Earthquakes - Liquefaction," *Soil Dynamics and Liquefaction*, A. S. Cakmak, Editor, Elsevier.

Castro, G.; Poulos, S. J.; France, J. W. and Enos, J. L. (1982) "Liquefaction Induced by Cyclic Loading," report by Geotechnical Engineers Inc. to the National Science Foundation, Washington, D.C. March, pp. 1-80.

Castro, G. (1969) "Liquefaction of Sands," thesis presented to Harvard University, Cambridge, Massachusetts, in fulfillment of the requirements for the degree of Doctor of Philosophy.

Davis, A. P.; Castro, G.; and Poulos, S. J. (1988) "Strengths Backfigured from Liquefaction Case Histories," the Second International Conference on Case Histories in Geotechnical Engineering, Rolla, Missouri.

Federal Highway Administration (1978), Office of Research and Development, "Guidelines for Cone Penetration Test - Performance and Design," Report FHWA TS-78-209, July.

Ishihara, K.; Yasuda, S.; and Yoshida, Y. (1989) "Liquefaction-Induced Flow Failure of Embankments and Residual Strength of Silty Sand," International Seminar on Dynamic Behavior of Clays, Sands and Gravels, Kitakyusku, Japan, Nov. 1989.

LaGatta, D. P. (1970) "Residual Strength of Clays and Clay-Shales by Rotation Shear Tests, thesis presented to Harvard University, Cambridge, Massachusetts, in fulfillment of the requirements for the degree of Doctor of Philosophy.

Poulos, S. J.; Castro, G.; and France, J. W. (1985) "Liquefaction Evaluation Procedure," *Journal of Geotechnical Engineering*, ASCE, Vol. III, GT6, pp. 772-791.

Poulos, S. J.; Robinsky, E. I. and Keller, T. O. (1985b) "Liquefaction Resistance of Thickened Tailings," *Journal of Geotechnical Engineering*, ASCE, Vol. III, GT12, December, pp. 1380-1394.

Poulos, S. J. (1971) "The Stress-Strain Curves of Soils," Geotechnical Engineers, Inc. Winchester, Massachusetts, pp. 1-80.

302

Schmertmann, J. H. (1979) "Statics of SPT," *Journal of the Geotechnical Engineering Division*, ASCE, Vol. 105, GT5, Proc. Paper 14573, May, pp. 655-670.

Seed, H. B. (1987) "Design Problems in Soil Liquefaction," *Journal of Geotechnical Engineering Division*, ASCE, Vol. 113, GT8, pp. 827-845.

Seed, H. B.; Lee, K. L.; Idriss, I. M.; and Makdisi, F. I. (1975) "The Slides in the San Fernando Dams During the Earthquake of February 9, 1971," *Journal of the Geotechnical Engineering Division*, ASCE, Vol. 101, GT7, pp. 651-688.

Vaid, Y. P.; Chung, E. K. F.; and Kuerbis, R. H. (1990) "Stress Path and Steady State," *Canadian Geotechnical Journal*, Vol. 27, No. 1, February, pp. 1-7.

TABLE 1 - LABORATORY DETERMINATION OF S_{us}

TEST TYPE ------------ Test Condition	TRIAXIAL COMPRESSION ------------------ Drained or Undrained	VANE ------------ Undrained	ROTATION SHEAR -------- Drained
Sand	√		
Silt		√	√
Clay		√	√

CROSS-SECTION THROUGH EMBANKMENT AFTER EARTHQUAKE
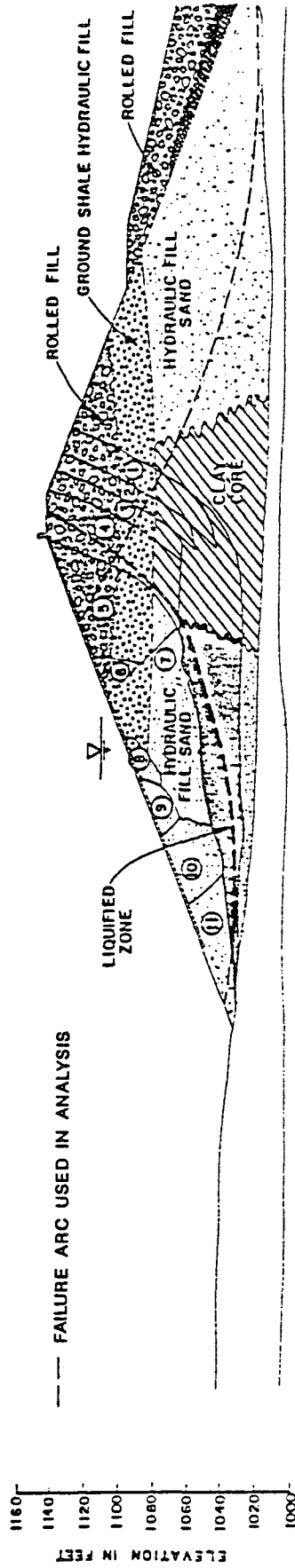
RECONSTRUCTED CROSS-SECTION

Fig. 1. CROSS SECTIONS-LOWER SAN FERNANDO DAM

(AFTER SEED et al, 1975)
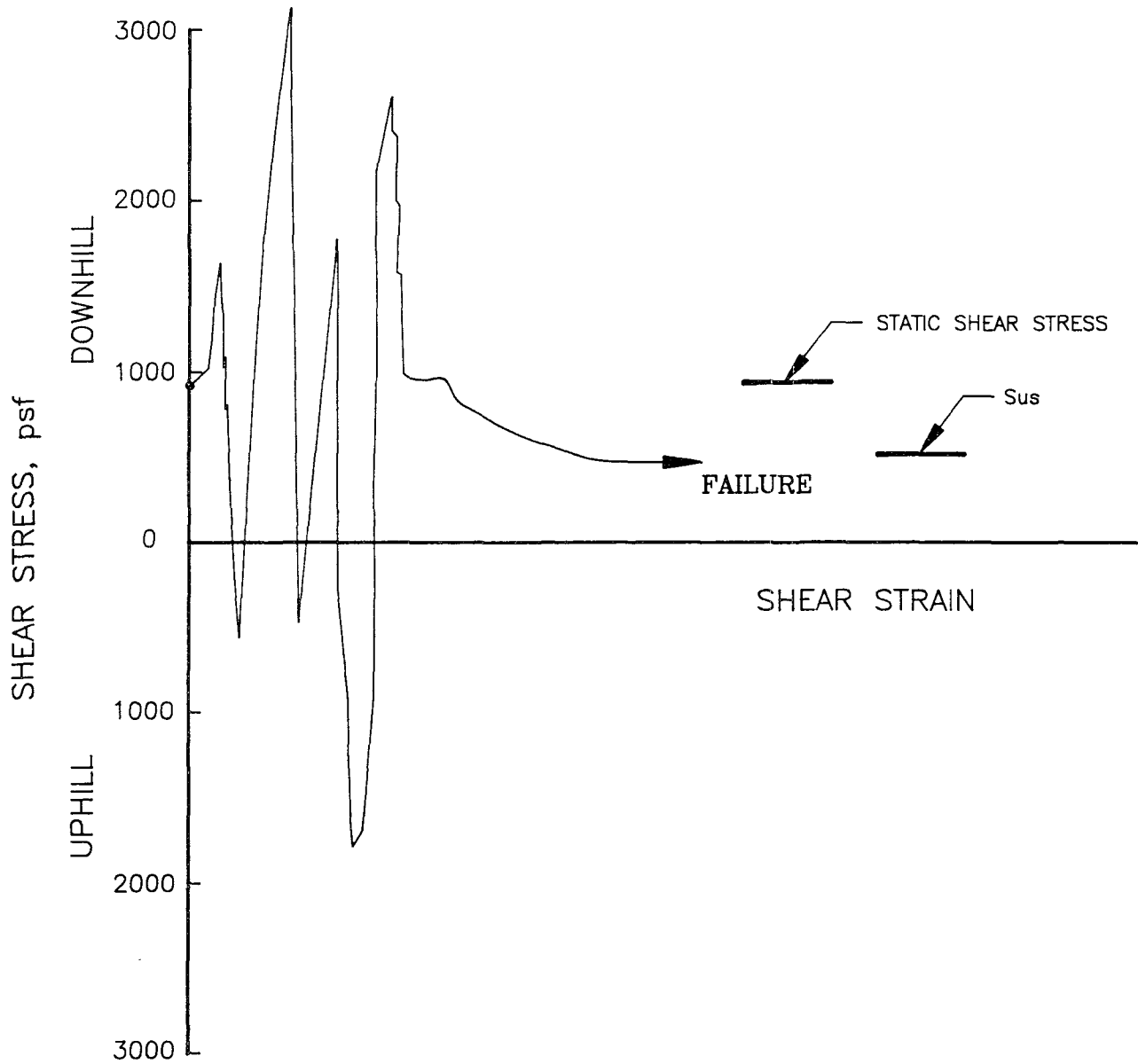
Fig. 2.   STRESS STRAIN BEHAVIOR
STABILITY FAILURE, LOWER SAN FERNANDO DAM
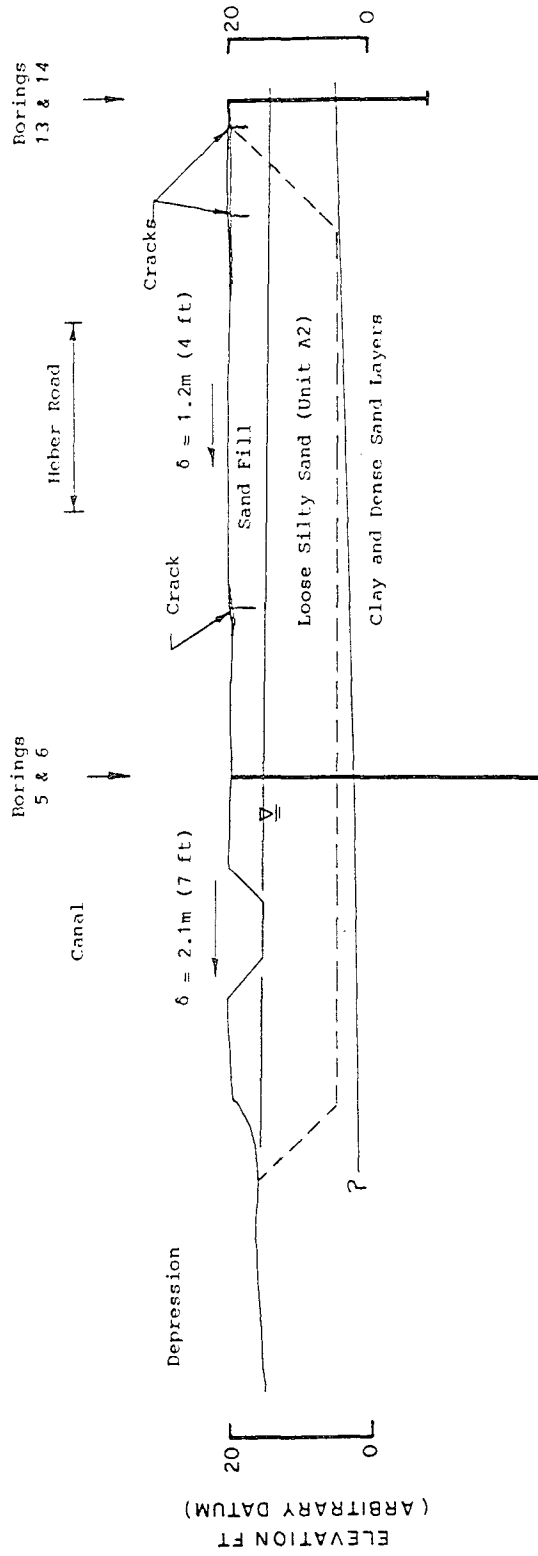
Fig. 3. HEBER ROAD SITE – CROSS SECTION

307
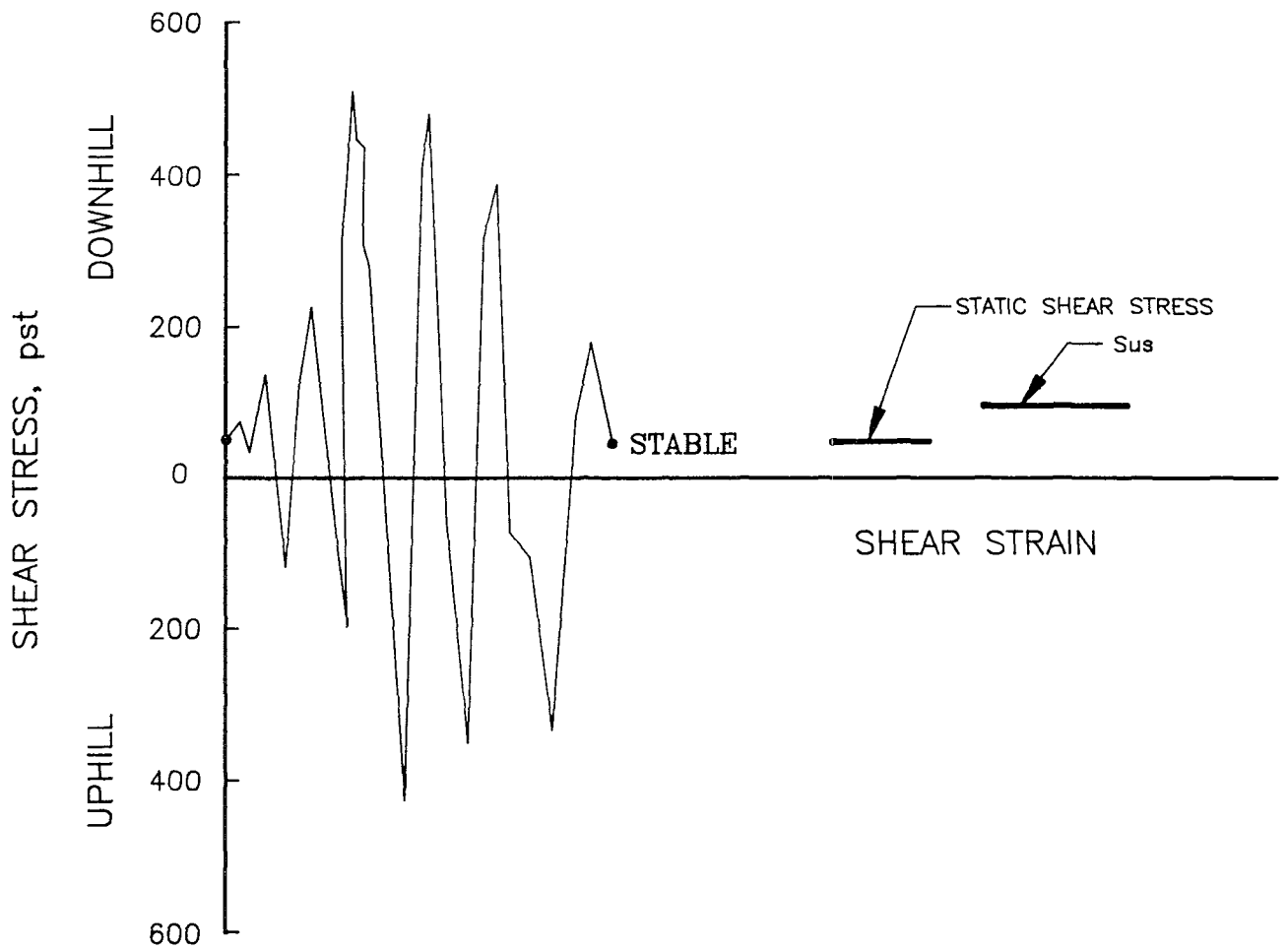
Fig. 4. STRESS STRAIN BEHAVIOR
LATERAL SPREADING — HEBER ROAD

308
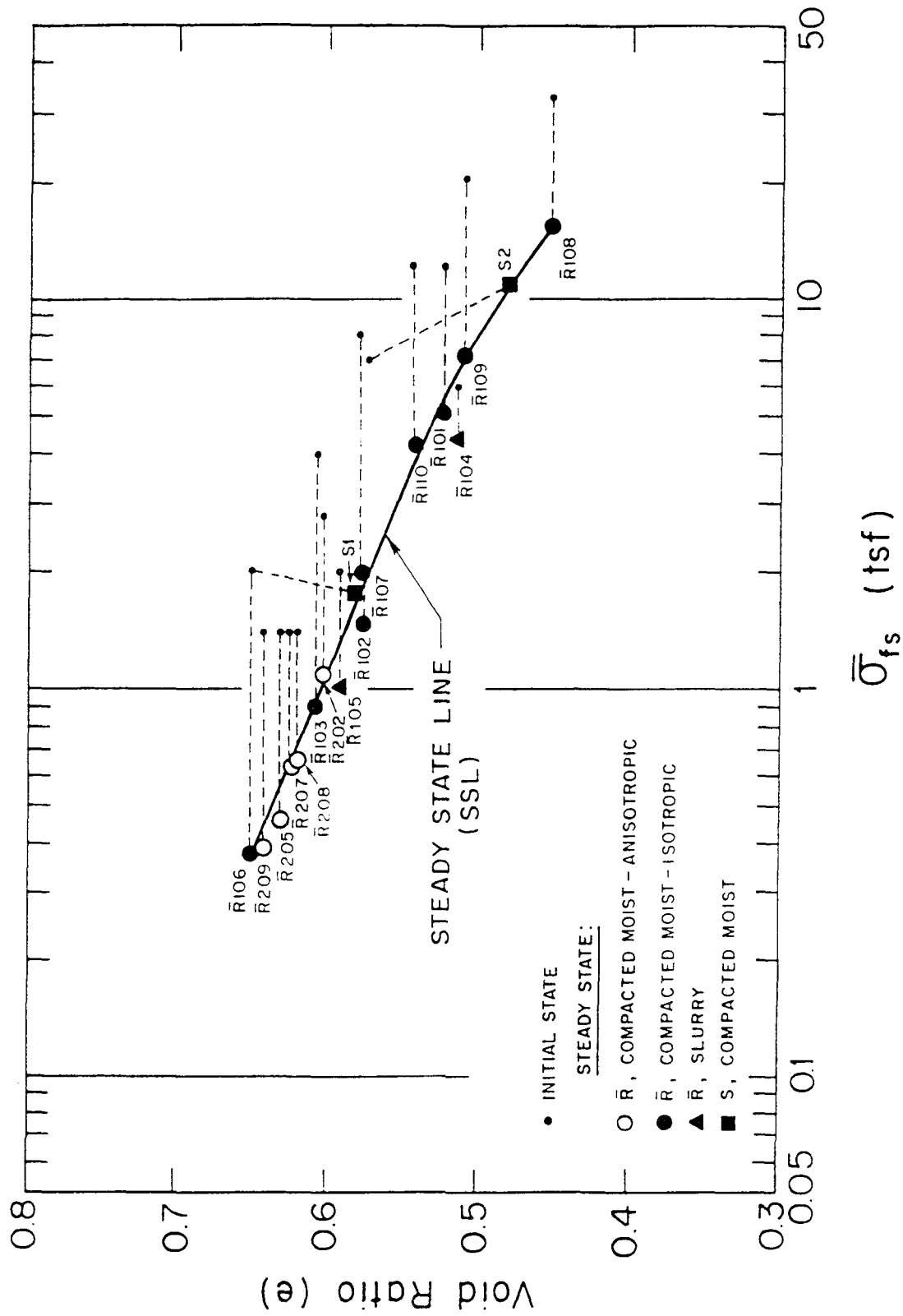
Fig. 5. STEADY STATE LINE OBTAINED WITH VARIOUS STRESS PATHS
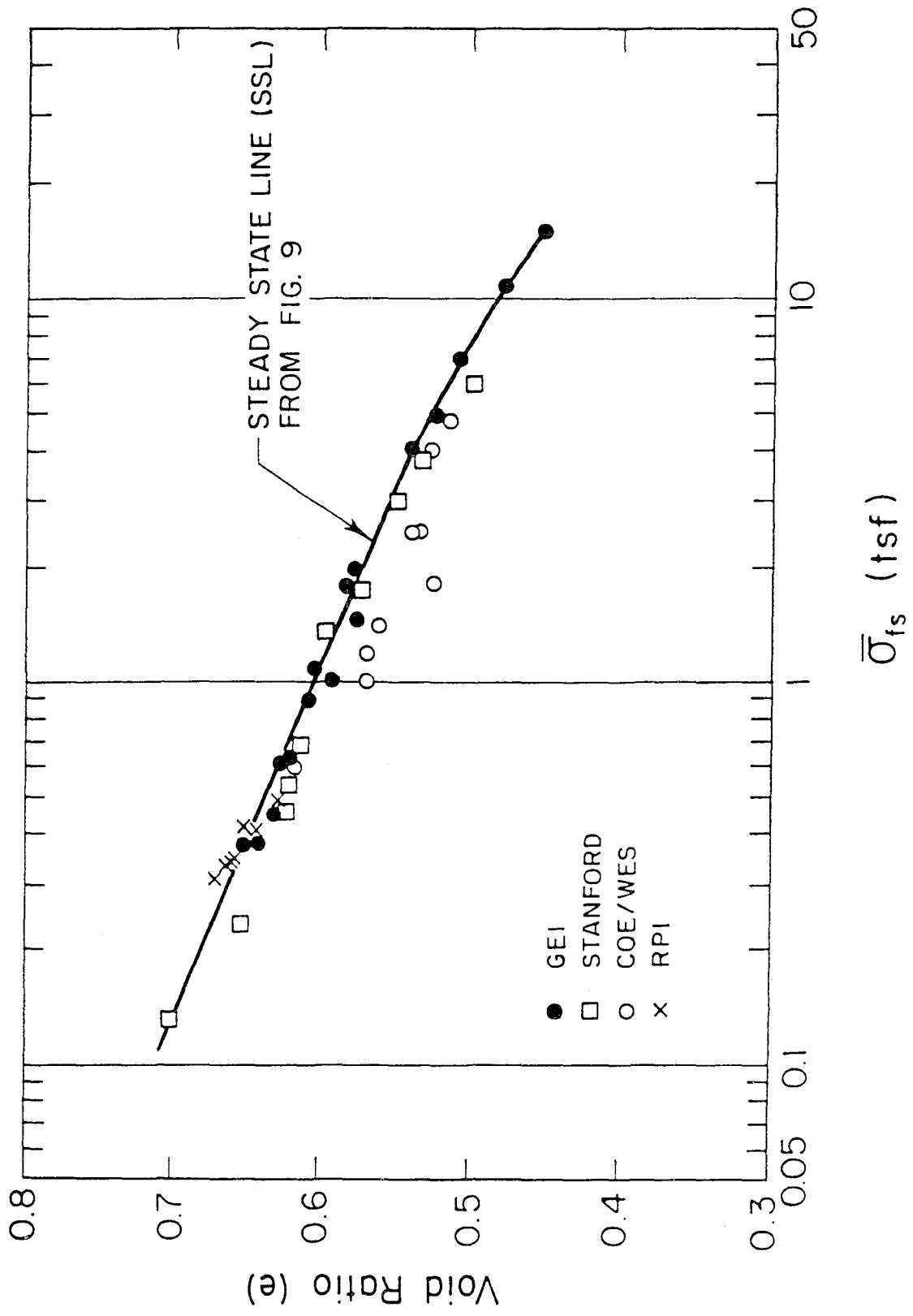
Fig. 6. STEADY STATE LINE WITH DATA FROM FOUR LABORATORIES

e_L = Void ratio of undisturbed sample after consolidation in laboratory

e_f = Void ratio of sample in-situ

$(S_{us})_L$ = Steady state strength of soil as determined in laboratory at void ratio e_L

$(S_{us})_f$ = Steady state strength at void ratio e_f

Steady state Line for Re-constituted Samples

Void Ratio, e

e_f

e_L

$(S_{us})_f$

$(S_{us})_L$

Steady-state Strength, S_{us} (Log scale)
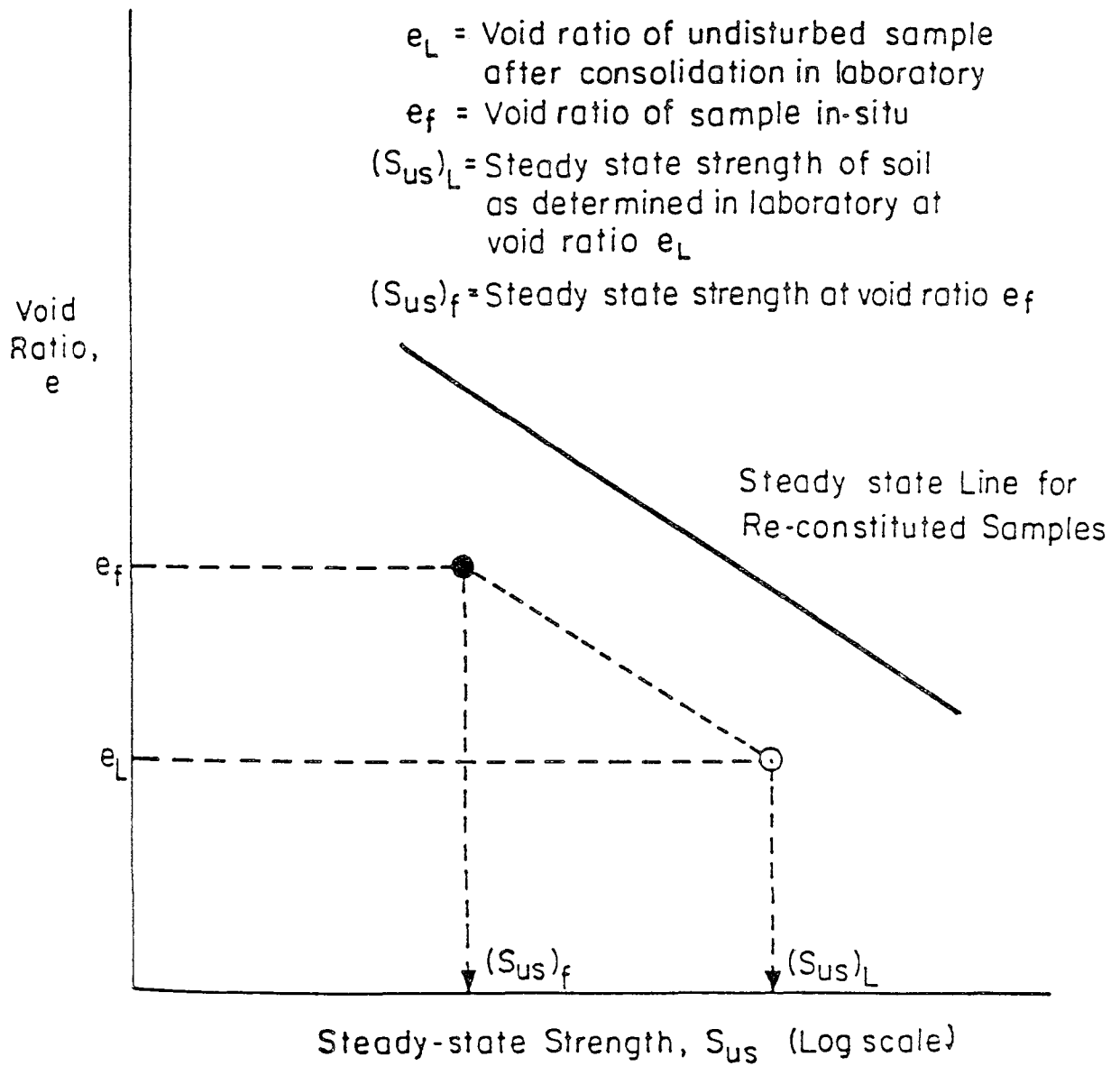
Fig. 7.   PROCEDURE FOR DETERMINING IN SITU
STEADY STATE STRENGTH OF SOIL
(AFTER POULOS et al.. 1985)
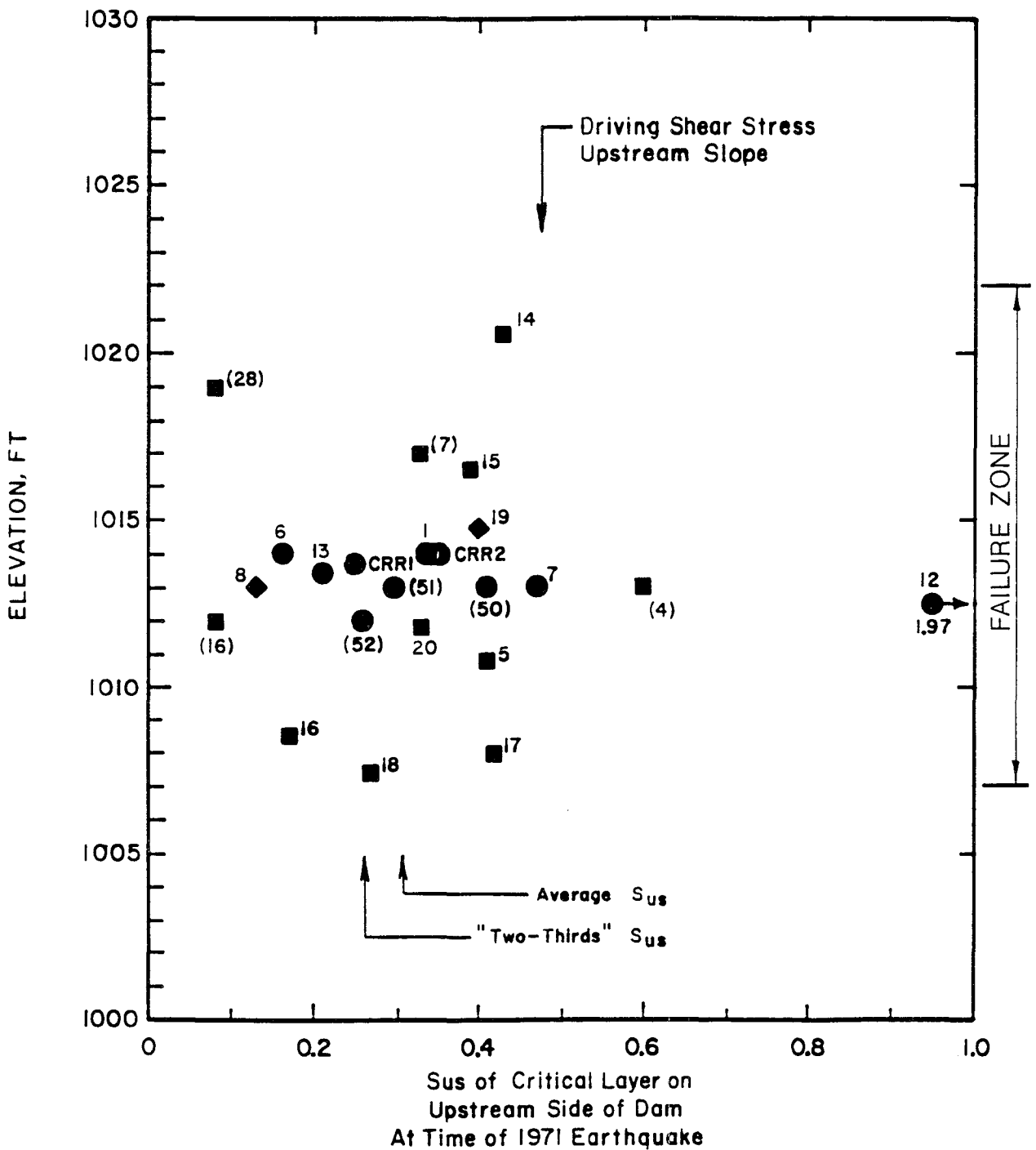
311

Fig. 8. IN SITU Sus VALUES FOR LOWER SAN FERNANDO DAM

CONE TIP RESISTANCE, tsf

FRICTION RATIO, %

DEPTH, ft

SPT, BLOWS/ft

STIFF CLAY

STRATIFIED CLAY & SILTY SAND

DENSE SAND

LEGEND

● SPT
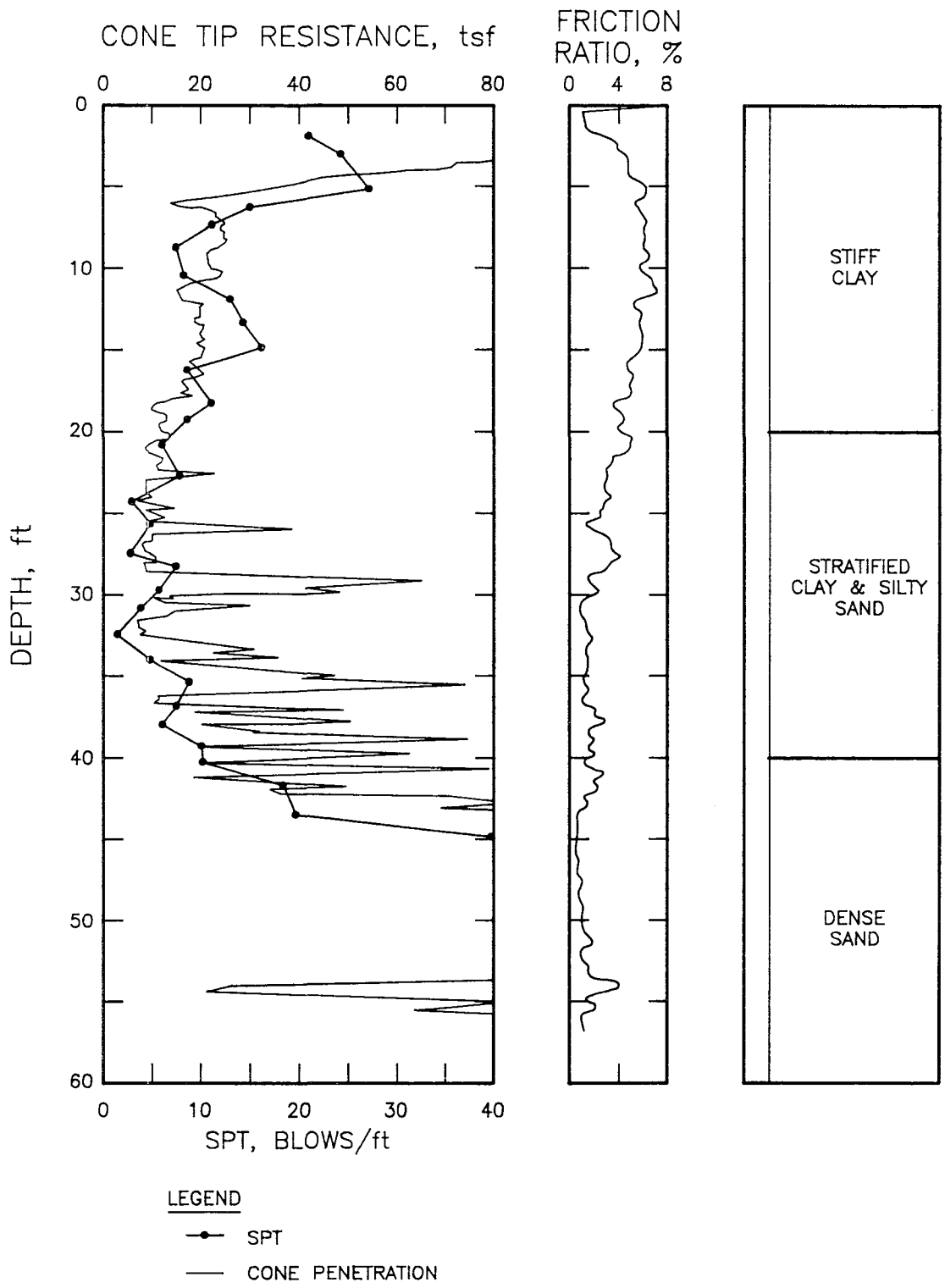
— CONE PENETRATION

Fig. 9. TYPICAL SOIL PROFILE
EARTH DAM FOUNDATION

CONE PENETRATION RESISTANCE , q_c , tsf

Fig. 10. EXPANDED CONE LOG

d = width of peak

Depth in feet

314
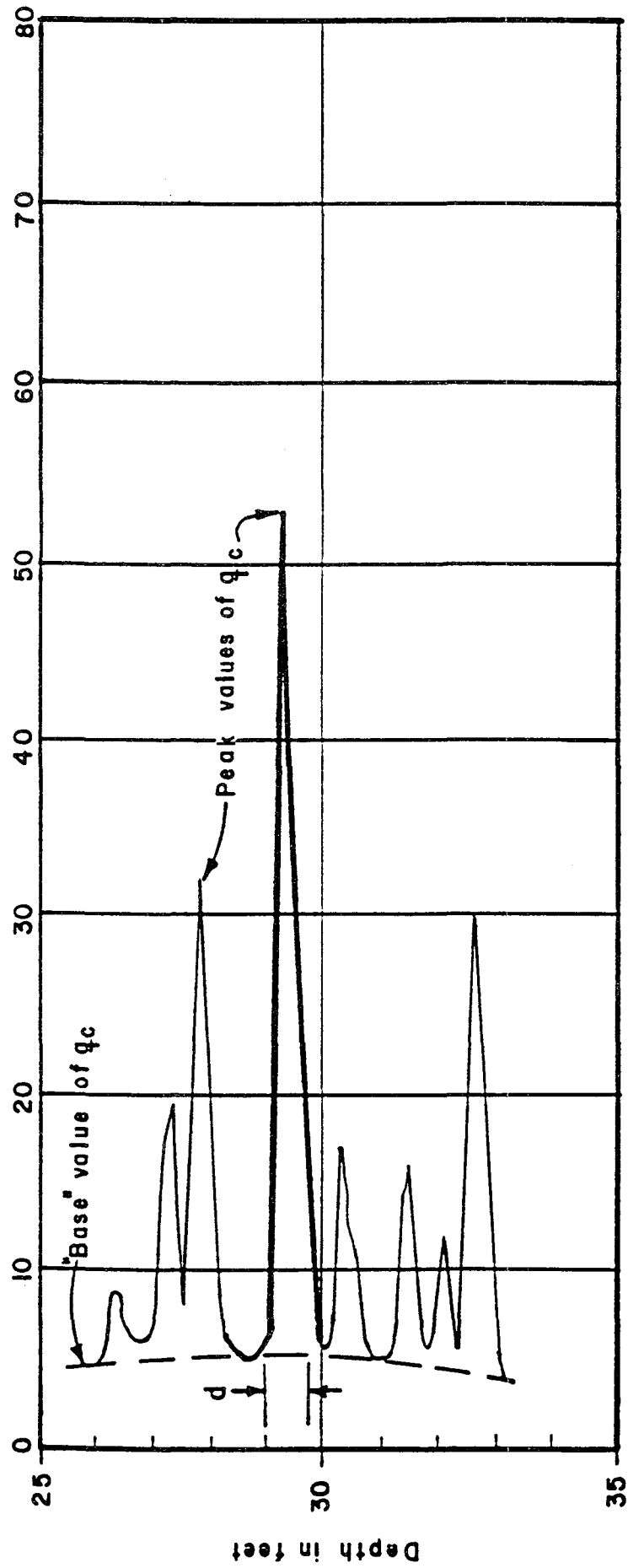
Fig. 10
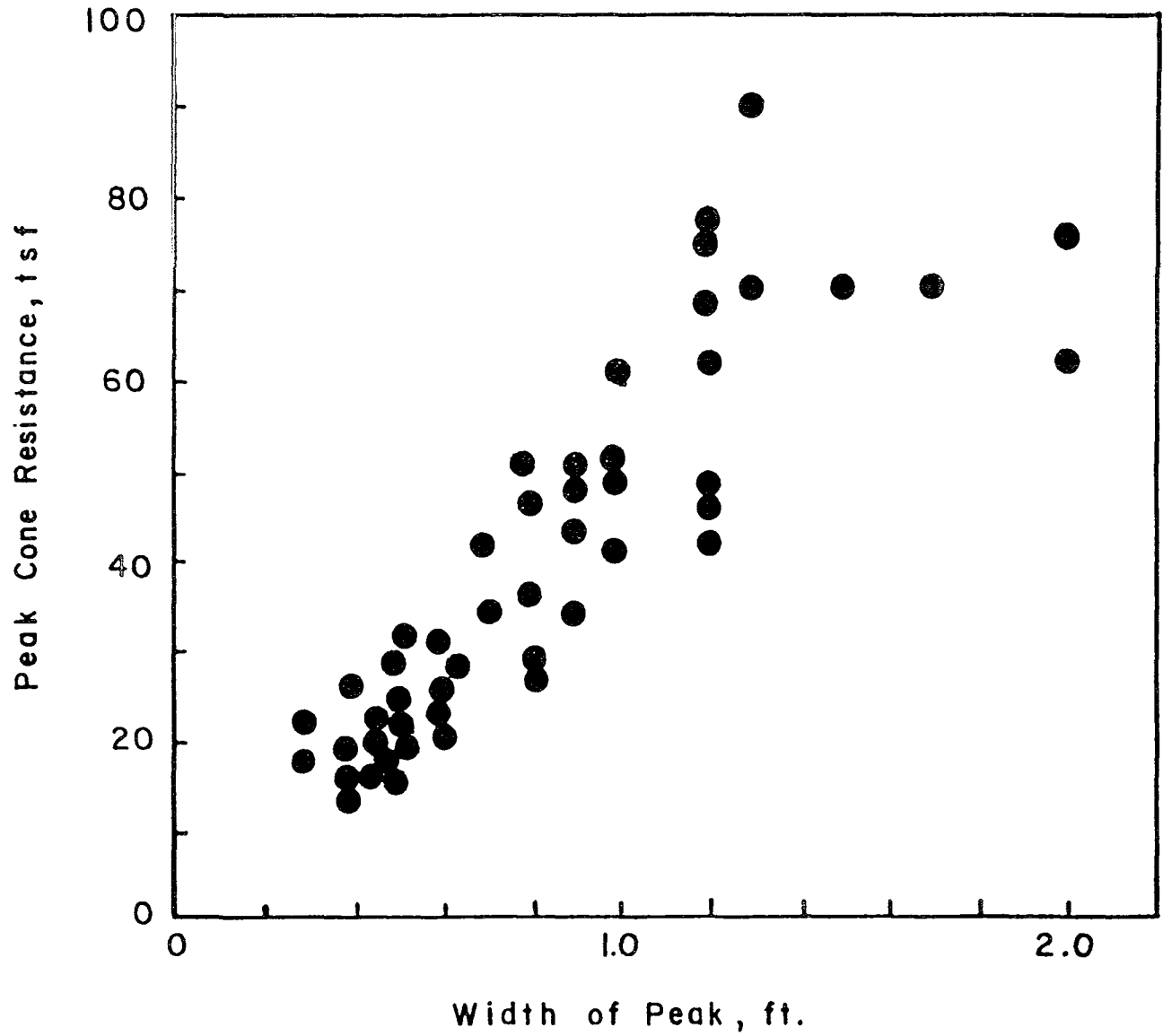
Fig. 11. PEAK CONE RESISTANCE AS A FUNCTION OF WIDTH OF PEAK

Fig. 11

SEISMICALLY INDUCED STICK–SLIP LARGE DISPLACEMENTS IN EARTH STRUCTURES

by

Mohamed F. Succarieh
Asst. Professor of Civil Engineering
University of Alaska
Fairbanks, Alaska 99775

and

Ahmed W.–M. Elgamal
Asst. Professor of Civil Engineering
Rensselaer Polytechnic Institute
Troy, New York 12180

ABSTRACT

The recorded behavior of La Villita Dam, an earth and rockfill dam located in Mexico, during five earthquake events is discussed. Seismically induced permanent displacements during these events have occurred on the upstream and downstream slopes. Bias in the recorded crest acceleration time histories, which is similar to that observed in an experimentally measured sliding block acceleration response, is thought to indicate the occurrence of stick–slip deformations. A simplified decoupled approach and a proposed contact finite element (FE) formulation (both of which model stick–slip type deformations) are used to model the observed displacements. The decoupled approach is a two step procedure: a) dynamic response of the intact dam is calculated using a 1–dimensional nonlinear shear wedge model; b) crest acceleration time histories from the first step are used in a Newmark–type sliding block analysis and permanent displacements are estimated. This approach decouples the dynamic response phase (step a) from the sliding block phase (step b) and assumes that the sliding zone behaves as a rigid body. The main advantage of the decoupled approach is its simplicity. The contact formulation involves a dynamic finite element analysis of distinct domains in contact. This formulation allows for the development of large magnitude permanent displacements between pre–defined zones of the structure. Stick–slip displacements may accumulate along the contact interface(s) during dynamic response computation. Elasto–plastic material behavior within the different interacting zones is also accounted for. Implementation of the contact FE procedure is relatively complex and expensive.

317

INTRODUCTION

La Villita is a sixty meters high earth and rock fill dam located 350 km south west of Mexico City, Mexico. In the period 1975 — 1985, the dam was subjected to five major earthquakes (the most recent being that of September 19, 1985 which also caused extensive damage in Mexico city) which contributed to significant measured vertical and horizontal permanent displacements in the dam. Acceleration records for some of these earthquakes are available at four locations including nearby bedrock (right bank) and dam crest (center section). The crest acceleration records associated with the five earthquake events consistently exhibit a peculiar asymmetric response pattern. This pattern is found to be similar to that observed in the experimentally measured and numerically computed sliding block acceleration response. Stick—slip type deformations may therefore have occurred in the dam during these events. In this study, the resulting permanent displacements are estimated, for the November 15, 1975 earthquake, using a simplified decoupled approach and a developed contact finite element procedure (both approaches account for stick—slip type deformations). The simplified approach follows a two phase analysis: a) the dynamic response of the intact dam is calculated using a one dimensional nonlinear shear wedge model; b) permanent displacements are estimated using a Newmark sliding block model with the computed crest accelerations from the first step as input. The contact finite element procedure is a finite element analysis of distinct domains in contact. This procedure allows for the development of large magnitude permanent displacements between pre—defined zones of the structure. Stick—slip displacements may accumulate along the contact interface(s) during dynamic response computation. Elasto—plastic material behavior within the different interacting zones is also accounted for. The contact FE procedure essentially extends the Newmark—type sliding block analysis (step b of the decoupled approach) in the following fashion: a) allows for the modeling of contact surfaces of arbitrary geometric shape; b) accounts for flexibility of the interacting domains; and c) allows for stick—slip displacements to take place simultaneously along several predefined contact surfaces.

In the following, the observed behavior of La Villita dam is described and compared to the experimentally recorded response of a block sliding on an inclined plane. The proposed contact finite element procedure together with the simplified decoupled approach are presented. The response of the sliding block is computed using both techniques. Finally, the observed deformations at La Villita are numerically estimated (using both procedures) and some of the advantages and limitations of both procedures are indicated.

OBSERVED BEHAVIOR OF LA VILLITA DAM

La Villita is a 60 meters high earth and rock—fill dam located in Mexico 13 Kilometers upstream from the mouth of the Balsas River which empties into the Pacific Ocean [1–5]. An alluvial layer of varying thickness (maximum thickness of 70 meters) lies between the embankment and bedrock. Maximum cross section of the dam is shown in Figure 1. During its construction, the dam was instrumented with inclinometers, surface reference points and accelerographs. In the period

1975–1985, five earthquake events subjected the dam to measurable horizontal and vertical displacements (see Figure 2; measured horizontal and vertical displacements during the October 11, 1975 and November 15, 1975 earthquakes are about 1.6 cm and 1.0 cm respectively). In addition, acceleration time histories at the dam crest (e.g. Figure 3) and nearby bedrock (Figure 4) were recorded during these events [1–5]. All of the observed transverse crest records (Figure 3) display an unusual bias in terms of positive versus negative peaks. This bias is similar to that observed in an experimentally measured block acceleration response (Figure 5) where the block is placed on an inclined shake table and subjected to a harmonic motion such that sliding takes place in the downslope direction only [2,5]. The maximum inertial force that can be transmitted to the block is limited by the friction force at the sliding interface (or the maximum accelerations that can be transmitted to the block are limited by a yield acceleration at the interface). This limitation leads to the observed bias in the block acceleration response [2,5]. Relative sliding between the block and the shake table takes place whenever this friction force (yield acceleration) is exceeded. The bias in the crest acceleration response at La Villita is therefore attributed to the location of the recording instrument on a section of the dam where localized type stick–slip deformations have taken place during the five earthquake events (October 11, 1975; November 15, 1975; March 14, 1979; October 25, 1981; and September 19, 1985) [2,5]. An average yield acceleration may be inferred [2,5] from the recorded crest accelerations as shown in Figure 3 (average yield acceleration = 100 cm/s^2 for November 15, 1975 earthquake for example).

SIMPLIFIED DECOUPLED PROCEDURE

The decoupled procedure utilizes a nonlinear shear wedge model and a Newmark–type sliding block model in a two step approach:

Step No. 1: dynamic response of the structure under investigation is computed using a 1D hysteretic inhomogeneous shear–wedge which permits horizontal shear deformation only [6]. This step is necessary if the effect of flexibility of the structure is to be accounted for.

Step No. 2: accelerations from step 1 are used in a Newmark [7] sliding block model and the block response is computed. An estimate of the permanent displacement in the structure under investigation is obtained by superimposing the permanent displacements from steps 1 and 2.

CONTACT FINITE ELEMENT PROCEDURE

The developed contact finite element procedure is a finite element analysis of distinct domains in contact. The structure under investigation is divided into different zones separated by slide interfaces. Each zone is modeled using an Updated Lagrangian Jaumann finite element formulation [8,9]. Interaction between these zones is monitored using a contact interaction algorithm. The steps followed in this procedure are:

– Gravity is applied pseudo–statically, in the form of a ramp load. The own weight static stresses define the stress state in the structure prior to dynamic loading.

– Dynamic analysis is performed.

Linear elastic or nonlinear elasto–plastic material properties may be used. In the nonlinear analyses, a simple elastic–perfectly plastic constitutive law is used herein to describe the soil behavior [2]. Components of the proposed procedure including the utilized constitutive law and the method used to model interaction are described briefly below.

Equation of motion

The matrix form of the equation of motion (obtained from finite element discretization of the weak form of the equation of motion) is as follows:

$$M\ddot{U} = f^{ext} - f^{int} \qquad (1)$$

where M = lumped mass matrix obtained from the element mass matrix by assembling the mass contribution of each element; $\ddot{U}$ = vector of nodal accelerations; f^{int} = vector of internal nodal forces obtained by assembling element internal force contributions; and f^{ext} = vector of nodal external forces obtained by assembling element external force contributions.

This matrix form (Equation 1) is integrated in time using an Explicit step–by–step integration scheme. A small time step is necessary in order to satisfy the conditions of stability and convergence.

Constitutive law

The employed constitutive law relates the rate of deformation tensor to the Jaumann stress rate tensor as follows:

$$\overset{o}{\tau} = CD \qquad (2)$$

where $\overset{o}{\tau}$ = Jaumann stress rate tensor = $\dot{\tau} - \omega\tau + \tau\omega$; D_{ij} = rate of deformation tensor = $(v_{i,j} + v_{j,i})/2$; ω_{ij} = spin tensor = $(v_{i,j} - v_{j,i})/2$; τ = Cauchy stress tensor; and $\dot{\tau}$ = Cauchy stress rate tensor.

Material behavior is modeled using an elastic–perfectly plastic law with a conical failure surface [2].

320

Contact interaction algorithm

Interaction between different zones constituting the structure under investigation is monitored using a contact interaction algorithm which enforces geometric compatibility at slide interfaces. This is accomplished by prohibiting the penetration of nodes of one zone (slave nodes) into elements (master elements) of the other so that a penetrating slave node is returned to the surface of the penetrated master element as follows (Figure 6):

If there is no friction at the interface between the different zones, The slave node is returned to the surface of the penetrated element along the normal to the interacting side of that element, side 1–2. If friction is present at the interface the slave node is returned to the surface of side 1–2 according to [10]:

$$\bar{x}_f = a\bar{s} + \bar{x}_n \qquad (3)$$

where

$$\bar{s} = (\bar{x}_p - \bar{x}_m)/|\bar{x}_p - \bar{x}_m|$$

$$a = \beta|\bar{x}_m - \bar{x}_n| \quad \text{if } \beta|\bar{x}_m - \bar{x}_n| < |\bar{x}_p - \bar{x}_m|$$

otherwise,

$$a = |\bar{x}_p - \bar{x}_m|$$

and β = coefficient of friction; $\bar{x}_0$ = position of slave node at time $t - \Delta t$; $\bar{x}_n$ = position of slave node at time t as calculated from the finite element analysis before correction due to penetration; $\bar{x}_m$ = position of the point of intersection of normal to sliding surface drawn through $\bar{x}_n$; $\bar{x}_f$ = corrected position of slave node.

The change in velocity due to correction is given by:

$$\Delta\bar{v}_S = \Delta\bar{r}/\Delta t \quad , (\Delta\bar{r} = \bar{x}_f - \bar{x}_n)$$

The velocity of the slave node is then modified by:

$$\bar{v}_S \leftarrow \bar{v}_S + \Delta\bar{v}_S$$

The loss of momentum associated with this adjustment is $M_S\Delta\bar{v}_S$ where M_S is the mass of the slave node. This momentum is transferred to the nodes of the

321

penetrated master element according to how far the particular node is from the final position of the slave node and such that the total linear momentum is conserved.

DYNAMIC RESPONSE OF A BLOCK ON AN INCLINED PLANE

The dynamic response of a block on an inclined plane subjected to a harmonic excitation is calculated using the simplified decoupled procedure (step 2 of this procedure). The resulting displacement, velocity and acceleration responses of the block are shown in Figure 7 [2,5]. It can be seen from this figure that permanent block displacements accumulate during the period over which the yield acceleration of the block is exceeded and that the block acceleration record is asymmetric with a transient response (spike) occurring at the end of each sliding phase after which the block and the slope move together [2,5]. This block acceleration response (Figure 7) is similar in pattern to that obtained from the laboratory experiment (Figure 5).

The response of a block on an inclined plane is also computed in a simulation performed using the proposed contact finite element model [2]. The block–plane system is discretized using finite elements (Figure 8). A harmonic inertial motion with a normalized amplitude of 1.5 in the horizontal direction and − 0.5 in the vertical direction (resultant motion in the slope direction) is used as input. Figure 9 shows the computed block relative displacement, relative velocity and absolute acceleration time histories (at node 12 of Figure 8). The deformed shape of the finite element mesh is shown in Figure 10. The response computed using the finite element model is similar to the measured and calculated rigid block on an inclined plane response (Figures 5 and 7). The calculated permanent block displacements using the finite element model compare well to the permanent displacements obtained from the analytical solution of the equation of motion of a rigid block on an inclined plane subjected to the same sinusoidal base excitation [2].

The versatility of the proposed contact FE procedure is demonstrated by the simulations shown in Figures 11 and 12. In Figure 11 the response of a sliding block system with two contact interfaces is shown. A larger coefficient of friction is specified at the lower interface. In Figure 12, it may be seen that the computational analysis continues even after the block slides off the slope and undergoes a free–fall phase under the action of gravity.

EARTHQUAKE RESPONSE OF LA VILLITA DAM

The decoupled procedure and the proposed finite element model are used in this section to numerically estimate the measured La Villita crest displacement due to the November 15, 1975 earthquake (Figure 4). Results from the simplified approach are described first followed by those from the contact finite element procedure.

Dam Response: Simplified Procedure

– Response of intact dam (step No. 1)

The dam is modeled as a 1D hysteretic inhomogeneous shear–wedge as indicated earlier [6]. It is idealized to have the following characteristics: height = 80 m, which accounts for the presence of the underlying alluvial deposit, density = 204 $(Kg–mass)/m^3$ and shear modulus =16012 $Tons/m^2$. These properties are chosen so as to match the first natural frequency of the dam (1.26 Hz) as observed from the Fourier Amplitude Spectrum of the recorded crest accelerations (November 15, 1975). Using the bedrock upstream–downstream record of the November 15, 1975 earthquake (Figure 4a) as input, the intact dam crest displacement and acceleration responses are computed.

– Sliding block analysis (step No. 2)

The crest acceleration time history obtained from step No. 1 together with the observed yield acceleration are now used as input to the sliding block model. The calculated permanent displacement time history is superimposed on the crest displacement time history obtained from the 1D dynamic analysis of the dam and the resulting plot is shown in Figure 13a. The sliding block acceleration response of the (corresponds to the recorded dam crest acceleration) is shown in Figure 13b. Directional bias or asymmetry appears since the acceleration peaks on one side of the record are totally truncated beyond the selected yield acceleration magnitude (100 cm/sec^2). The calculated permanent displacement at the end of this earthquake (Figure 13a) is found to be in the neighborhood of the corresponding observed horizontal displacement (about 2 cm).

Dam Response: Contact Finite Element Procedure

The proposed contact finite element procedure is used to compute the response of La Villita Dam during the strong shaking phase (7 seconds) of the November 15, 1975 earthquake (Figure 4; the horizontal and vertical components of the bedrock record are used as input). Two finite element meshes (Figure 14), each with one specified slide interface and a prescribed friction coefficient of 1.0 along this interface, are developed to model the maximum cross section of the dam (Figure 1). An average thickness of 30 meters is used to represent the underlying alluvial deposit. Three materials represent the dam body, and one material represent its alluvial foundation (Figure 15). These material properties allow the numerical model to match the observed fundamental natural frequency (1.26 Hz) of the dam [2]. During the dynamic analysis, a viscous stiffness–proportional damping ratio of 5% (at the fundamental frequency of the intact structure) is applied and a simple elastic–perfectly plastic constitutive law [2] is used to describe the material behavior. The computed response using the mesh shown in Figure 14a is described first followed by that using the mesh shown in Figure 14b.

The computed displacement response of the dam to the November 15, 1975

earthquake at nodes 84 (intact zone) and 69 (sliding zone) of Figure 14a is shown in Figure 16. Figure 16a shows that undetectable permanent displacement results from material plasticity in the intact part of the dam. Consequently, the computed permanent displacement (2.3 cm) of the sliding zone (Figure 16b) is mainly due to relative sliding. Note that the permanent displacement magnitudes mentioned above (and the ones to follow) correspond to the square root of the sum of squares of the horizontal and vertical components of permanent displacement (vertical component not shown).

The displacement response of the dam (using the mesh of Figure 14b) at nodes 84 (intact zone) and 69 (sliding zone) is shown in Figure 17. It can be seen from Figure 17a that no detectable permanent displacement results from the soil plasticity. Noticeable permanent displacements however result from relative sliding (Figure 17b). The computed permanent displacement is similar in magnitude to that calculated using the mesh of Figure 14a (2 cm in this case as opposed to 2.3 cm in the other).

The computed permanent displacement (using both procedures) due to the November 15, 1975 earthquake (about 2 cm) is in the neighborhood of that actually observed at La Villita dam. This is not meant to imply however that the proposed procedure (at its current state of development) is capable of predicting displacements in large earth structures (e.g. earth dams) to such a level of accuracy (of the order of a centimeter). The above numerical examples are only for illustrative purposes as no distinct slide interfaces have been detected within the body of La Villita Dam.

SUMMARY AND CONCLUSIONS

Evidence of the occurrence of stick–slip deformations is shown from the recorded data at La Villita Dam in Mexico. Two numerical procedures are presented for the estimation of such deformations: a) a decoupled simplified procedure based on the Newmark sliding block approach, and b) a nonlinear Finite Element Formulation which allows for large magnitude slippage along predefined contact interfaces. Both numerical procedures are employed in estimating the deformation magnitudes observed at La Villita Dam due to the earthquake of November 15, 1975. The simplified procedure appears to be a viable option for preliminary investigations. The developed contact FE formulation on the other hand offers the potential for more accurate and detailed analyses albeit at a great effort and expense.

ACKNOWLEDGEMENTS

REFERENCES

1— Comision Federal De Electricidad (Mexico), 1980, "Performance of El Infiernillo and La Villita Dams Including the Earthquake of March 14, 1979," February.

2— Succarieh, Mohamed F., 1990, "Analysis of Earthquake Induced Large Displacements In Earth Structures," PhD Thesis, Rensselaer Polytechnic Institute, Troy, New York.

3— Comision Federal De Electricidad (Mexico), 1985, "Behavior of Dams Built in Mexico (1974–1984)," XV Intl. Congress on Large Dams, Vol. 11, Lausanne, Switzerland.

4— Comision Federal De Electricidad (Mexico), 1987, "Effects of the September 1985 Earthquakes on Dams Built on the Balsas River," Sym. on Dams and Earthquakes, China.

5— Elgamal, A W.–E., Scott, R. F., Succarieh, M.F. and Yan, L. P., 1990, "La Villita Dam Response During Five Earthquakes Including Permanent Deformation," Jour. of Geo. Engrg. Division, Vol. 116, No. 10, October.

6— Elgamal, A.–W.M., "Shear Hysteretic Elasto–Plastic Earthquake Response of Soil Systems," Earthquake Engrg and Struct. Dyn., to appear.

7— Newmark, N.M., 1965, "Effects of Earthquakes on Dams and Embankments," Geotechnique 145(2), pp 139–160.

8— Belytschko, T. and Hughes, T., Eds., 1983, Chapter 1, _Computational Methods for Transient Analysis_, Vol. 1, North — Holland Publishing Company.

9— Bathe, K.J., 1982, _Finite Element Procedures in Engineering Analysis_, Prentice Hall, Englewood Cliffs, New Jersey.

10— Belytschko, T. and Lin, J., 1987, "A Three Dimensional Impact–Penetration Algorithm with Erosion," Computers and Structures, Vol. 25, pp.95–104.

Figure 1   La Villita dam: maximum cross section [1–5].
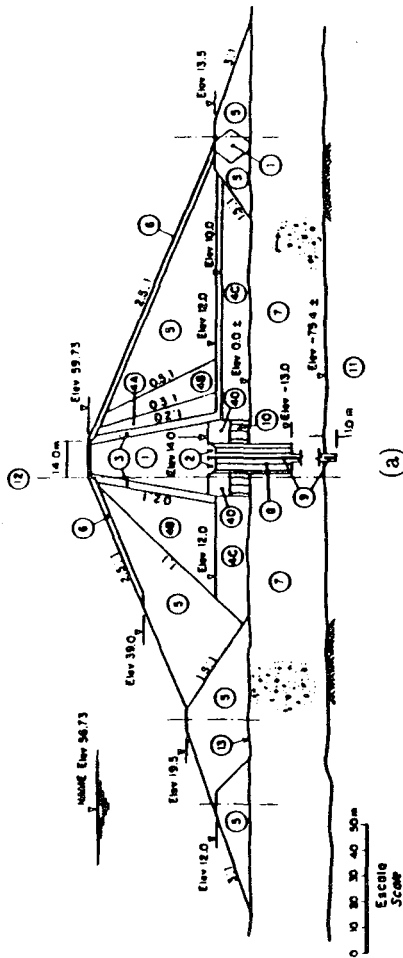
1. Compacted impervious material
2. Highly plastic clay
3. Sand filters
4A. Well graded gravel and sand
4B. Gravel and sand
4C. Dumped gravel and sand
4D. Compacted gravel, sand and muck
5. Rockfill
6. Selected rockfill
7. Alluvium (gravel and sand)

8. Grout curtain
9. ICOS-type concrete cut-off wall
10. Consolidation grouting
11. Andesitic breccia
12. Dam axis
13. Original ground surface

Elev Elevation, in m

NAME Maximum water level

1 Horizontal displacements, in cm
2 Surface reference points and stations in m
3 Datum date: 10–3–68
4 Effects of 10–11–75 and 11–15–75 earthquakes
5 Effects of 03–14–79 earthquake
4 Effects of 10–25–81 earthquake
5 Effects of 09–19–85 and 09–21–85 earthquakes
RB Right bank
LB Left bank

Figure 2   La Villita Dam: recorded downstream slope horizontal displacements close to the crest [1–5].

326
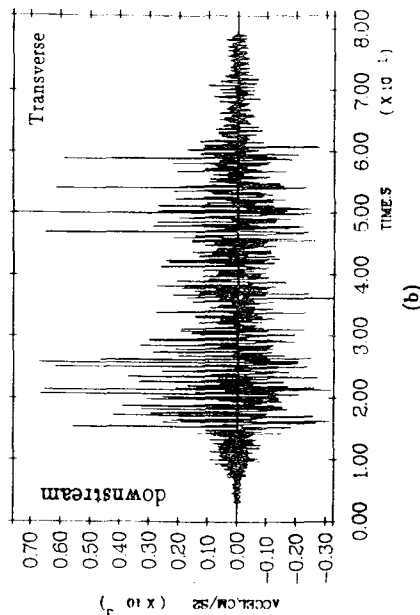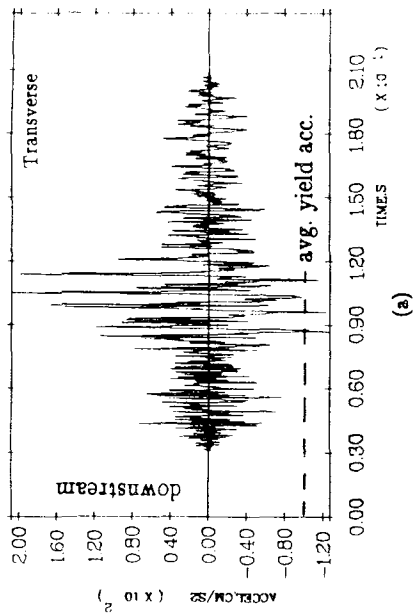
Figure 3 La Villita Dam: time history of acceleration recorded at dam crest; a) November 15, 1975, b) September 19, 1985.
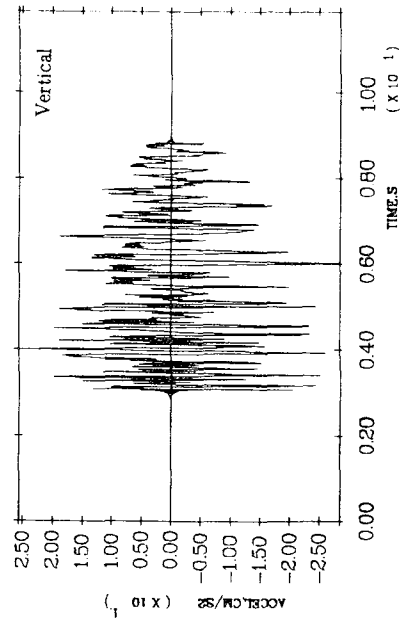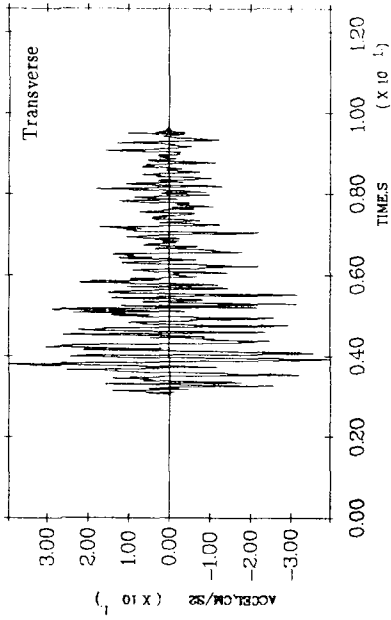
Figure 4 La Villita dam: time history of acceleration recorded at right bank (bedrock) due to November 15, 1975 earthquake.

327
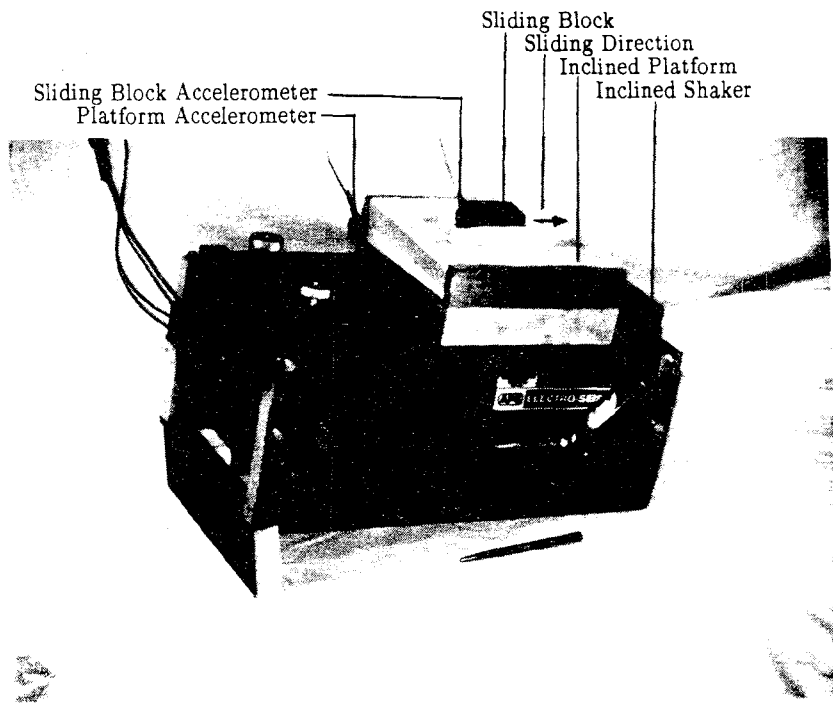
(a)
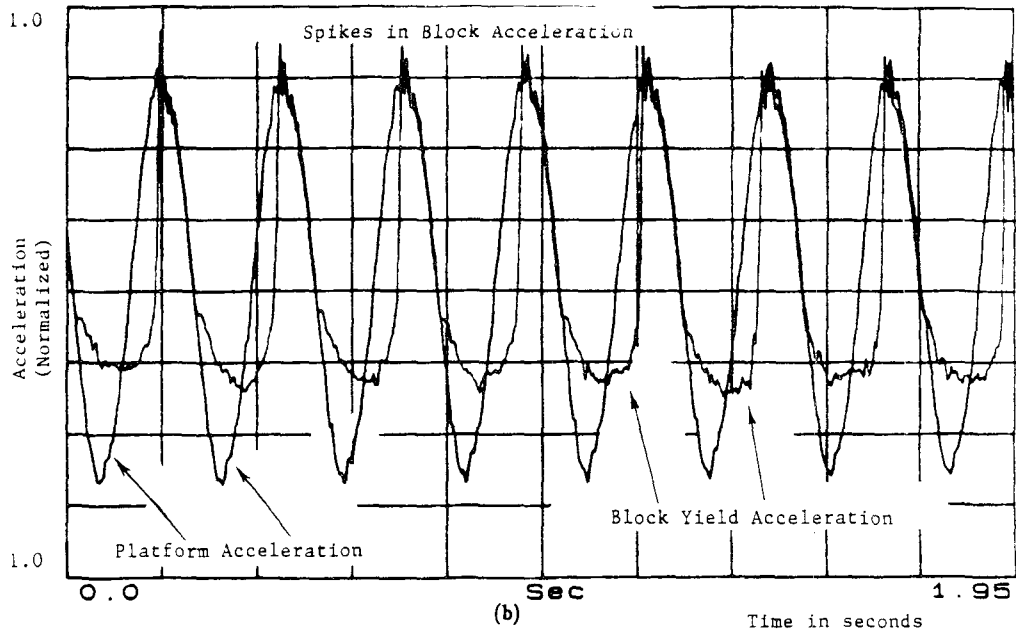
(b)

Figure 5   Block on an inclined shake table experiment: a) experimental setup;
             b) block absolute acceleration response.
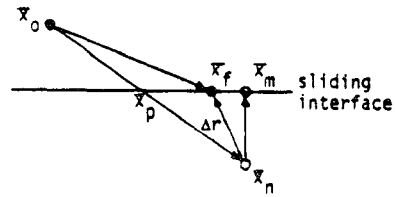
Figure 6   Slave node position adjustment.

328

Figure 7 (a)

Relative Block Displacement
Relative Block Velocity

$\times 10^{-2}$

spike   spike   spike

Time (seconds)

Figure 7 (b)

Input Acceleration
Block Acceleration

spike   spike

Yield Accel.

Acceleration

Time (seconds)
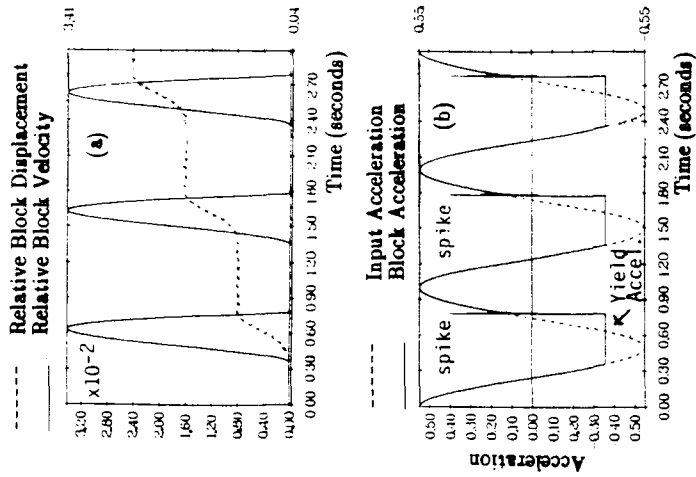
Figure 7   Block-slope response (step 2 of decoupled approach):a) relative block velocity and displacement; b) input and block absolute acceleration.
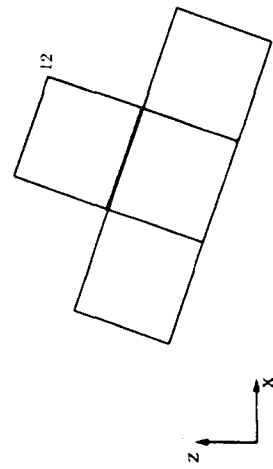
Figure 8   Block-slope finite element discretization.

Figure 9

(a)   (b)   (c)

HORIZ DIS (x 10 ^{6})

VERTICAL DIS (x 10 $^{-1}$)

HORIZ VEL (x 10 $^{-1}$)

HORIZ ACC (x 10 ^{0})

TIMES (x 10 ^{0})
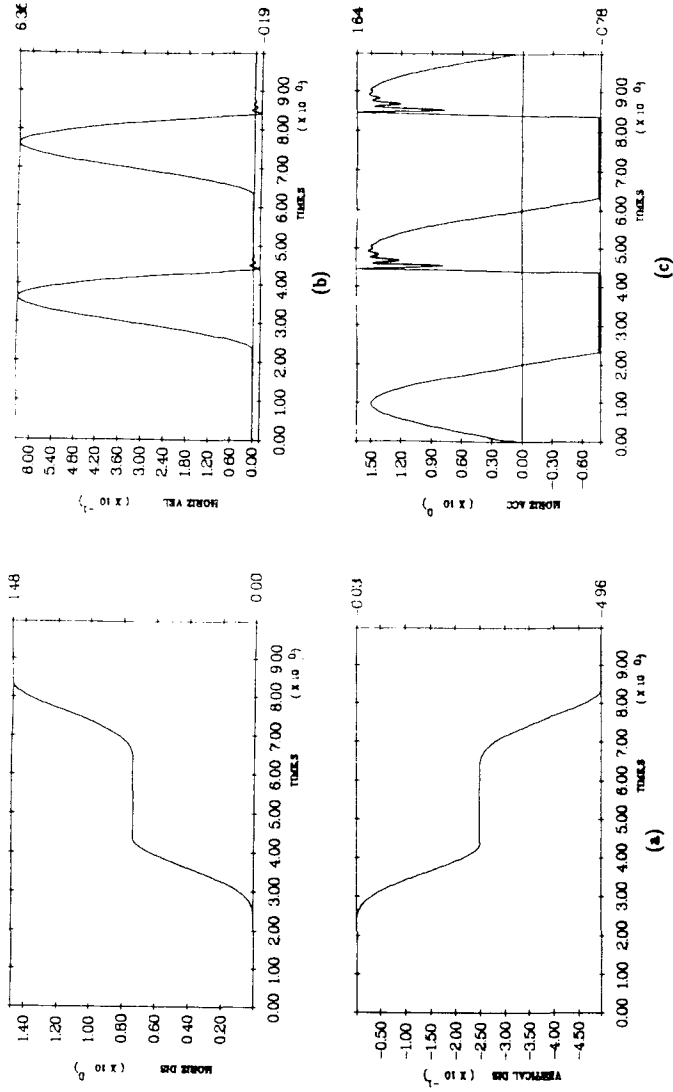
Figure 9   Block response to a harmonic input motion (node 12 of Figure 14); a) displacement, b) velocity, c) acceleration.
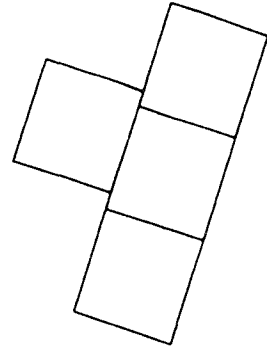
Figure 10   Deformed shape of finite element mesh.

329
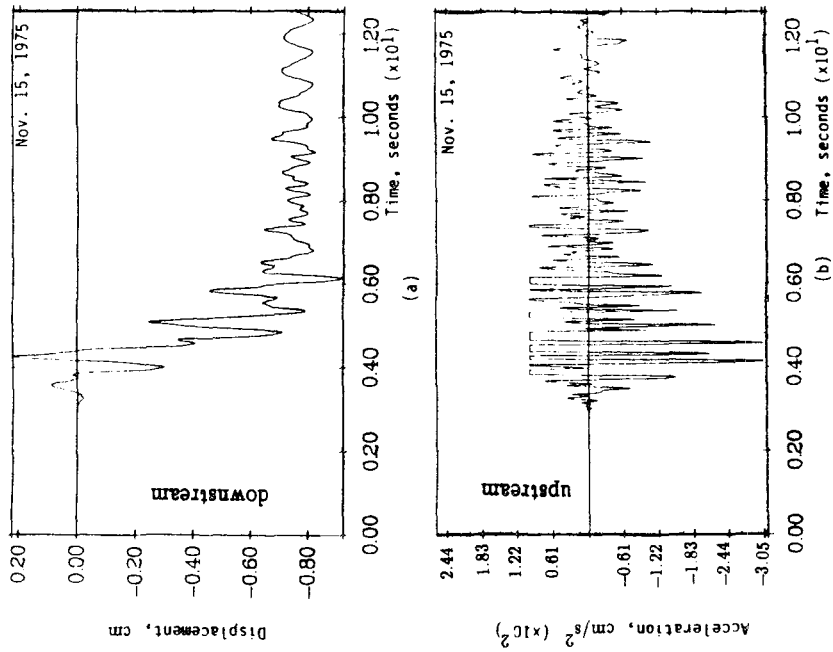
Figure 13   Response (decoupled approach) due to November 15, 1975 earthquake with $a_y = 100 \text{ cm/s}^2$; a) displacement from Newmark analysis superimposed on calculated crest displacement, b) absolute acceleration of the Newmark sliding block.
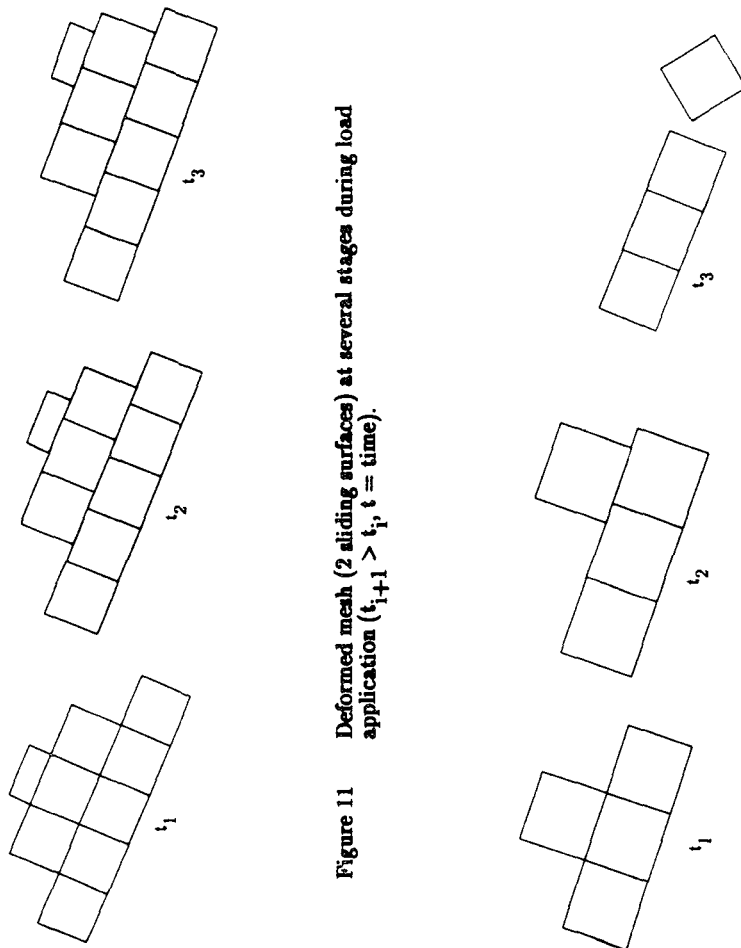
Figure 11   Deformed mesh (2 sliding surfaces) at several stages during load application ($t_{i+1} > t_i$, t = time).

Figure 12   Deformed mesh at several stages during load application (plot scale varies, $t_{i+1} > t_i$, t = time).

Figure 15   Material properties of different dam zones.

Material	E, T/m²	ν	γ, T/m³
1	6.2X10⁴	0.48	2.04
2	6.4X10⁴	0.15	2.22
3	6.2X10⁴	0.15	2.08
4	6.4X10⁴	0.15	2.08
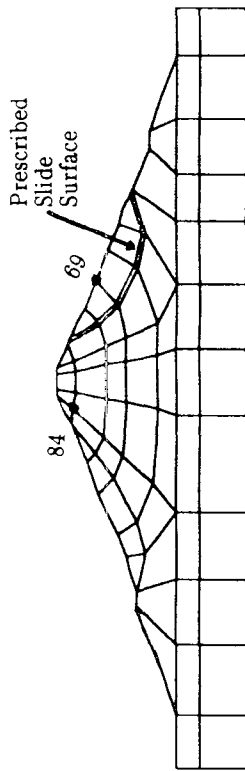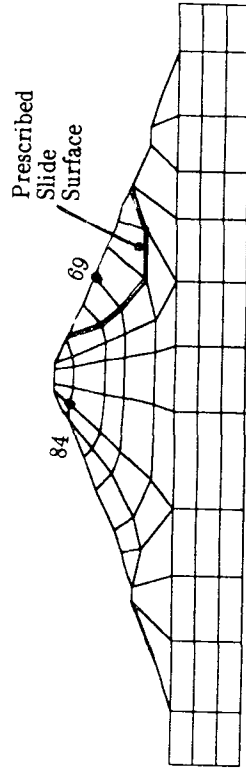
Figure 14   Finite element discretization of La Villita Dam with one sliding interface.

Figure 17 Displacement response due to November 15, 1975 earthquake: a) within intact zone (node 84 of Figure 14b); b) within sliding zone (node 69 of Figure 14b).

Figure 16 Displacement response due to November 15, 1975 earthquake: a) within intact zone (node 84 of Figure 14a); b) within sliding zone (node 69 of Figure 14a).

SEISMIC DESIGN CHART FOR ANCHORED BULKHEADS

George Gazetas
Professor of Civil Engineering, State Univiversity of
New York, Buffalo

and

Panos Dakoulas
Asstistant Professor of Civil Engineering, Rice University,
Houston, Texas

INTRODUCTION: Evaluation of numerous case histories reveals that the seismic performance of anchored sheetpile quaywalls depends primarily on the anchoring system. Current pseudo-static procedures often lead to deficient anchoring, whose excessive displacements or failure trigger excessive permanent seaward displacement at the top of the bulkhead, accompanied by cracking and settlement behind the anchor. The results of the case histories lead to a Seismic Design Chart to be used in conjunction with the pseudostatic procedure. The Chart delineates between acceptable nd and unacceptable degrees of damage, depending on the values of two dimensionless parameters that are functions of the material and geometric characteristics of the bulkhead, and the intensity of seismic shaking. Soil softening/degradation due to development of porewater-pressures is indirectly accounted for in the proposed method; however, the engineer must ensure that no liquefaction-flow failure of cohesionless soils will occur in the backfill or the foundation.

Anchored bulkheads, also called anchored (steel) sheetpile walls, are quite vulnerable to strong earthquake shaking. Failures of such facilities have often resulted in major disruptions of post-earthquake emergency operations and have had serious economic consequences for the stricken regions.

Earthquake performance accounts of over a hundred anchored quaywalls in about 30 harbors in Japan (mainly), in Alaska, in West Indies, and in Chile have been published by Duke et al 1963; Hayashi et al 1970, Hung et al 1982, and Kitajima et al 1978. Detailed listings of these reported case histories may be found in the theses of Abraham (1985) and Dennehy (1985), and in a report by Agbabian Associates (1980). A study of the performance of anchored bulkheads in these harbors leads to the following main conclusions:

o   Most of the observed major earthquake failures have resulted from large-scale liquefaction of loose, saturated, cohesionless soils in the backfill and/or in the supporting base (foundation). Such soils are not rare at port and harbor facility sites. Perhaps the most dramatic such failures have occurred in the Niigata, Japan, harbor during the 1964 earthquake.

o   Another frequent, although not as dramatic, type of anchored bulkhead damage takes the form of excessive permanent seaward tilting of the sheet-pile wall, accompanied by excessive seaward movement of the anchor block or plate relative to the surrounding soil; such an anchor movement manifests itself in the form of settlement of the soil and cracking of the concrete apron directly behind the anchor, as sketched in Fig. 1. Apparently, and in accord with the conclusions of pertinent detailed studies, such failures are the outcome of inadequate passive soil resistance against the anchor. Development of detrimental residual excess pore-water pressures in the backfill, leading to some soil strength degradation, cannot be excluded as having contributed to this type of failures in some of the reported cases.

To the authors' knowledge, no comprehensive method of realistic dynamic analysis of anchored bulkhead systems subjected to strong shaking is well enough developed and validated to be used in practice. It is fair, however, to state that dynamic codes developed for site response or soil-structure interaction analyses **have** been utilized, albeit to study specific aspects (only) of the response of the system (Hung & Werner, 1982). Simplified dynamic models specific for anchored bulkheads have also been developed, including those by Karkanins (1983), Abraham (1985), and Dennehy (1985). The "beam-on-Winkler-Foundation" model developed in these studies is illustrated in Fig. 2.

The difficulty of providing a comprehensive rigorous method arises from several factors, which include: the complicated wave diffraction pattern due to "ground-step" geometry; the presence of two different but interconnected structural elements in contact with the soil; the inevitably nonlinear hysteretic behavior of soil in strong shaking, including pore-pressure buildup and degradation, both in front and behind the sheetpile; the no-tension behavior of the soil-sheetpile interface; the presence of radiation damping effects due to stress waves propagating away from the wall in the backfill and in the foundation; and the hydrodynamic effects on both sides of the sheetpile wall. Until codes which can properly handle all these phenomena are developed, improving the pseudo-static procedures currently used in practice so that they can lead to safe and economic design merits our effort.

Pseudo-static procedures are of an empirical nature and determine dynamic lateral earth pressures with the well-known Mononobe-Okabe seismic coefficient analysis. Differences arise primarily with respect to the assumed point of application of the resultant active and passive forces P_{AE} and P_{PE} (on the two sides of the sheetpile wall), and the partial factors of safety introduced in the design.

The procedure developed and extensively used in Japan (JSCE, 1980) is perhaps the most elaborate and complete pseudo-static design procedure. As illustrated in the sketch of Fig. 3, it combines the use of the Mononobe-Okabe

method with conventional static design procedures of ~ ___ ~ d
bulkheads. The vertical component of the ground acceleration is
ignored, while the horizontal seismic coefficent, k, is chosen
for a particular site as a product of three factors (according to
the Japanese Code): a regional seismicity factor (0.10 ± 0.05) ,
a factor reflecting the subsoil conditions (1 ± 0.2), and a
factor reflecting the importance of the structure. (1 ± 0.5). To
account for the presence of water in the design procedure, and
"apparent" seismic coefficient k' is used for soils below the
water table:

$$\mathbf{k'} = [\gamma_s/(\gamma_s - \gamma_w)] \; k \;\; \dots\dots\dots\dots\dots\dots\dots\dots (1)$$

in which γ_s = the saturated unit weight of the soil, and γ_w = the
unit weight of water.

Subsequently, the design proceeds as follows:

1. Estimation of the necessary length of the sheetpile
embedment(D): This is computed by the free-earth support method.
The safety factors usually required against the failure of
embedment are 1.5 and 1.2 for static and seismic conditions
respectively in sandy stratum. In cohesive soil strata, the
usually required safety factor is 1.2 for both the static and
seismic conditions.

2. Design of the tie rod: In the case of a sheet pile bulkhead
constructed in sandy ground, tie rod tension is computed on the
assumption that the bulkhead is a simple beam supported at the
dredge line and the point of tie rod connection, and which
carries the lateral earth pressure and the residual water
pressure. In case of cohesive soil, tie rod tension is computed
by the fixed-earth support method. Allowable stress of tie rods:
40% and 60% of the yield strength of steel for static and seismic
conditions, respectively. These relatively low values of
allowable stress are intended to account for bending moment in
the tie rod due to surcharge, and for concentration of lateral
earth pressure at the point of tie- rod connection.

3. Design of the sheetpile cross-section: In sandy ground, the
maximum bending moment is computed for the aforementioned simple

336

beam. This maximum moment, which is about 40-50% of that computed by the free-earth support method, corresponds to the value computed by fully taking into account the moment reduction due to the flexibility of the sheetpile (Rowe, 1952). The allowable stresses of the sheetpile for static and seismic conditions are 60% and 90% of the yield strength of steel, respectively.

4. Design of the anchor plate or block: Lateral resistance of an anchor plate should be 2.5 times the tie rod tension for both static and seismic conditions. Anchor plates should be placed behind the active failure wedge starting from the dredge line (Fig. 3). When the passive wedge of the anchor plate crosses the active wedge behind the sheet pile, the passive resistance of the soil above the point of intersection should be neglected in the computation of the lateral resistance of the anchor plate.

WEAKNESS OF PSEUDO-STATIC DESIGN PROCEDURES

Kitajima & Uwabe (1978) have compiled information on the seismic performance of 110 quaywalls (mostly anchored bulkheads) in Japan. Table 1 summarizes the conclusions of their study. The conveyed message for the adequacy of the pseudo-static design methods is negative: the percentage of bulkheads that suffered some degree of seismic damage did not decline following the adoption of the previously-described design procedure... (Year of construction seems also to have had little effect on damage statistics.)

Many of the "failures" included in the statistics of the foregoing Table were clearly due to extensive liquefaction of the backfill and/or the supporting base stratum; these cases will not be further addressed in this paper. Carefull study (Dennehy, 1985) of the remaining "failures" leads to the following conclusions regarding the major weaknesses of the psuedo-static procedure:

First, the values of the Code-specified seismic coefficient are not representative of the actual levels of acceleration that may develop in the backfill during moderate and strong earthquake shaking. Indeed there is little justification for the selected values. As noted by Seed (1975): "it is entirely possible that

337

such empirical values of the seismic coefficient may lead to safe designs in many cases but until some means of judging their validity is developed, their use must be considered of questionable value". Futhermore, Wood (1973) has observed that: "In general, seismic coefficients are chosen that are significantly less than the peak accelerations to be expected in a suitable design earthquake, apparently on the assumption that some permanent outward movement of the wall can be tolerated. There appears to be no rational basis for the magnitude of the reduction made."

Indeed, despite the increase of the design coefficient form k to k' ≈ 2k for soils under the water table, some of the failed bulkheads may have experienced greater "effective" peak accelerations than they were designed for. Strong ground shaking can induce accelerations in excess of 0.50g. On the other hand, moderately-strong ground shaking might be amplified by the (non-liquefiable) backfill and foundation stratum. Such an amplification could be substantial if a thick backfill-foundation profile underlain by very stiff soil or rock is excited by an earthquake motion rich in frequencies near its own natural frequency(ies). To demonstrate the possiblitiy for such an amplification, theoretical, experimental and field evidence is available.

Some examples: Nadim & Whitman (1978) have shown for rigid retaining walls that the permanent displacement computed with a finite element model incorporating a Coulomb-type sliding surface in the backfill is substantially greater than the value obtained form rigid-plastic analysis, in which soil layer response (and amplification) is ignored. Small-scale shaking-table experiments conducted by the Japanese Port and Harbor Research Institute tend to confirm this behavior for anchored bulkheads. Although both the Nadim-Whitman and the shaking table models may exaggerate such an amplification due to spurious wave reflections at the lateral boundaries, some field evidence to this effect is also available.

Furthermore, the vertical component of the ground acceleration, which is ignored by the method, increases the "effective" acceleration that controls the seismic active and passive pressures (Davies et al, 1986, Richards & Elms 1979) by a

338

factor of $(1-k_v)^{-1}$ [see Fig.40]. On the other hand, the increase of k by a factor of about 2 for soils below the water table may only partially accomodate the detrimental effects of strength degradation due to pore-water pressure buildup. Also note that in the majority of the studied Japanese case histories the aforementioned increase in the seismic coefficient had little effect in the design of the anchor, as a significant part of the latter is located above the water table. And, finally, this increase of k was undermined by the unfortunate 20%-33% reduction in the required factors of safety, as outlined in the previous section.

In conclusion, it appears that many of the "failed" bulkheads experienced "effective" peak accelerations which were essentially 30% to 50% higher than what these walls had been designed for.

Second, the available passive soil resistance against the anchor is often seriously overestimated by the Code procedure. While there is ample indirect empirical evidence supporting the above statement (recall the most frequent modes of failure), it is important to develop an understanding of the causes of this inadequecy of the Codes.

To begin with, recall that the Japanese Code requires that the active sliding surface should start at the elevation of the dredge line. By contrast, even the static design of anchored bulkheads most often assumes that this surface originates at the point of contraflexure, or the point of zero moment in the sheetpile. Tschebotarioff's (1978) "hinge at the dredge line" concept, useful as it may be for determining maximum bending moments in the sheetpile, is un-conservative for choosing the location and size of the anchor block/plate (Tsinker 1983). In fact, it is more likely that the active failure surface originates at or near the "point of rotation" rather than at the points of contraflexure or zero-moment. The location of this point depends on the relative stiffness of the sheetpile wall and the overall rigidity of the anchoring system -- but, no doubt, is generally deeper than the points of contraflexure and zero moment.

Moreover, under seismic loading the "point of rotation" tends to move farther down, as repeatedly demonstrated in small-scale

shaking-table tests (Kitajima et al 1978, Murphy 1960) and in the theoretical studies using the model of Fig. 2. The explanation is clear: when acceleration increases, the active soil pressures against the wall increase while the passive ones supporting the wall decrease (see Fig. 4). Hence, the effective "span" of the sheetpile beam (in the terminology of the free-earth support method) tends to increase, and the origin of the active sliding surface ($\approx$ "point of rotation") tends to be pushed downward. It appears that in several of the studied Japanese cases this "point" might have been located at a depth $f \gtrsim D/2$, where the depth of embedment, D, usually takes values in the range of 50% to 80% of H. It is thus evident that the Code recommendation of placing the origin at the dredge line (Fig.3) would in most cases underestimate the required tie-rod length, L.

An additional factor in the Code procedure contributing to an overestimation of the available passive anchor resistance stems from the use of the seismic coefficient k rather than the "effective" peak acceleration in the backfill, or at least of the increased coefficient k'. As illustrated in Fig. 4, increased acceleration levels imply not only reduced passive forces, but also flatter failure surfaces. And it is obvious that a smaller in reality angle α_{PE} than that assumed in the Code design would (further) reduce the capacity of the anchor.

EMPIRICAL SEISMIC DESIGN CHART

To arrive at a practical design chart (using the results of those case histories that did not involve liquefaction flow failures), two simple dimensionless indices have been selected. Their definition, significance, and methods of computation are explained below.

(a) The "Effective Anchor Index" (EAI), representing the relative magnitude of the available passive anchor force: EAI is defined in Fig. 5, in terms of the horizontal distance d from the active failure surface to the tie-rod-anchor connecting point:

$$EAI = \frac{d}{H} \quad \dots\dots\dots\dots\dots\dots\dots\dots\dots\dots\dots\dots\dots\dots\dots\dots\dots\dots\dots \quad (2)$$

Note that the width of the anchor, 2B, does not appear directly in this index, despite its importance for the anchor resistance. This was a reluctant choice, out of necessity: in only a few of the analyzed case histories was this width reliably known! But, at least, 2B is indirectly reflected in Eqn 2 through the height H; indeed, according to the Code procedure, 2B depends chiefly on H and the backfill angle of shearing resistance ϕ.

The active failure surface is assumed to originate at the effective "point" of rotation, at depth f from the dredge line. In actual design f could be estimated from a numerical analysis, for example using the "Beam-on-Winlker-Foundation" model of Fig. 2. Taking f = D would lead to a slightly conservative length L.

The angle, α_{AE}, of inclination of the active sliding wedge is a decreasing function of the effective acceleration coefficient, k_e, as plotted in Fig. 4 for ϕ = 30° and dry soil, where

$$k_e = \frac{k_h}{1 - k_v} \quad \ldots\ldots\ldots\ldots\ldots\ldots\ldots\ldots\ldots\ldots\ldots\ldots\ldots\ldots (3)$$

The horizontal and vertical seismic coefficients, k_h and k_v, should be taken as fractions of the anticipated peak ground acceleration components during the design earthquake shaking; e.g., as suggested by Seed,

$$k_h \approx \frac{2}{3} \frac{\max a_h}{g} \quad \ldots\ldots\ldots\ldots\ldots\ldots\ldots\ldots\ldots\ldots\ldots\ldots (4)$$

For cohesionless soils under the water table, to indirectly take into account both the potential strength degradation due to pore-water pressure buildup and the hydrodynamic effects, we suggest that k_e should increase to

$$k_e' \approx 1.50 \, k_e \approx \frac{\max a_h}{1 - \frac{2}{3} \max} \quad \ldots\ldots\ldots\ldots\ldots\ldots\ldots\ldots\ldots (5)$$

Finally, having established k'_e, the angle α_{AE} can computed from the Coulomb-Mononobe-Okabe sliding-wedge analysis (Prakash 1981, Richards & Elms 1979).

(b) The "Embedment Participation Index" (EPI), provides a measure of the likely contribution of the embedment depth. If the wall were acting as a free cantilever (with no anchor), it would undergo horizontal displacement and rotation the magnitude of which would depend on the potential active and passive forces, F_{AE} and F_{PE}, and the respective moments of these forces about the 'point' of rotation. In the interest of simplicity, and being restricted by the available data of the analyzed case histories, EPI is defined as:

$$\text{EPI} = \frac{F_{PE}}{F_{AE}} \left(1 + \frac{f}{f + H}\right) \quad \dots\dots\dots\dots\dots\dots\dots\dots\dots\dots\dots\dots \quad (6)$$

which for uniform backfill and foundation can be approximated as:

$$\text{EPI} \approx \frac{K_{PE}}{K_{AE}} r^2 (1 + r) \quad \dots\dots\dots\dots\dots\dots\dots\dots\dots\dots\dots\dots \quad (7a)$$

where

$$r = \frac{f}{f + H} \quad \dots\dots\dots\dots\dots\dots\dots\dots\dots\dots\dots\dots\dots\dots\dots\dots \quad (7b)$$

The ratio K_{PE}/K_{AE} of the passive to the active earth pressure coefficient is, in general, obtained from a Coulomb-Mononobe-Okabe analysis. K_{PE}/K_{AE} is a monotonically decaying function of the seismic coefficient and the angle of shearing resistance. Note that, for a wall-soil friction angle $\delta = 0$ and cohesionless soil,

$$1 \leq \frac{K_{PE}}{K_{AE}} \leq \tan^4(45^\circ + \phi/2) \quad \dots\dots\dots\dots\dots\dots\dots\dots\dots\dots\dots \quad (8)$$

where the upper bound is the familiar ratio of the static ($k = 0$) Rankine earth pressure coefficients, whereas the lower bound is reached at a critical effective acceleration (Richards & Elms, 1979).

$$\frac{k_h}{1 - k_v} = \tan \phi \quad \cdots\cdots\cdots\cdots\cdots\cdots\cdots\cdots\cdots\cdots\cdots\cdots \quad (9)$$

It is noted that the flexural rigidity $E_p I_p$, of the sheetpile does not appear explicitly in the above definition of EPI, despite its obvious importance on the magnitude and shape of the wall deformation. Again, this was done reluctantly since the sectional moment of inertia, I_p, was only rarely reported in the studied cases. Nonetheless $E_p I_p$ relates to the wall height H and the depth f, and hence it does affect (indirectly) EPI.

The two indices, EAI and EPI, computed for each one of the studied 75 anchored bulkheads, produce a point on the diagram of Fig. 6. The degree of damage of the particular bulkhead is reflected on the size and shading of the circle. Thus five different degrees of damage (0 - 4) are distinguished, as explained in the Table of Fig. 1, according to Kitajima & Uwake (1978). With justified reservation, in view of the rather crude way of characterizing the adequacy of the anchoring system and the effectiveness of embedment, and of the uncertainties regarding soil strength parameters and estimated ground acceleration, a clear picture emerges in Fig. 6. Two fairly distinct zones can be identified: Zone A, comprising mostly anchored bulkheads that suffered acceptable damage (degrees of damage 0, 1, or 2); and Zone B, within which bulkheads suffered unacceptable deformation or even failure (degrees of damage 3 and 4).

The shape of the line delineating the two zones does indeed suggest that the degree of damage suffered by an anchored bulkhead is dependent on both the adequacy of the anchoring system and the relative depth of embedment. Notice, however, that the flat shape of these lines implies that the importance of the Effective Anchor Index (EAI) is far greater than that of the Embedment Participation Index (EPI), as one might have anticipated from the earlier discussion on the types of observed failures.

Fig. 6 can serve as a Seismic Design Chart to be used in conjunction with (and to rectify the inadequacies of) the aforementioned pseudo-static design procedures. For instance,

one can first follow the design steps 1,2,and 3 that were outlined in the second section of this article, but then determine the required length of the tie-rod form the following geometric expression:

$$L \geq (h + f) \cdot \cot\alpha_{AE} + (EAI)_C \cdot H \quad \dots\dots\dots\dots\dots\dots\dots (10)$$

where the critical value of the Effective Anchor Index, $(EAI)_C$, is read from the delineating line of the Chart for the specific value of the Embedment Participation Index (EPI), as illustrated in Fig. 6.

CONCLUSION

An empirical chart has been developed (Fig. 6) for guiding the design of anchored steel sheetpile bulkheads against strong earthquake shaking. Use of this Chart, along with the Mononobe-Okabe-based pseudostatic design procedure would lead to safer anchored bulkheads.

ACKNOWLEDGEMENT

REFERENCES

Abraham, R, (1985). "Dynamic Analysis of Anchored Bulkheads," Master's Thesis, Rensselaer Polytech. Institute, Troy, N.Y.

Agbabian Associates, (1980). "Seismic Response of Port and Harbor Facilities," Report P80-109-499., E. Segundo, Calif.

Christiano, P.P. and Bielak J., (1985). "Nonlinear Earthquake Reponse of Tiedback Retaining Walls," Research Rep., Carnegie-Mellon Univ. 1985.

T.G. Davies, R.R. Richards Jr., & K. H. Chen, (1986). "Passive Pressure During Seismic Loading" Jnl. Geotech. Engrg. ASCE, Vol. 112, No. 4, 1986.

K.T. Dennehy, "Seismic Vulnerability, Analysis and Design of Anchored Bulkheads," Ph.D. Thesis, Rensselaer Polytech Institute, Troy, N.Y. 1985.

Duke, C.M. and Leeds, D.J., (1963). "Response of Soils, Foundations, and Earth Structures," Bull. Seism. Soc. Am., 53, 309-357.

Hayashi, S. and Katayama T., (1970). "Damage to Harbor Structures by the Tokachioki Earthquake, "Soils and Foundations, Vol. X, 83-102,.

S.J. Hung & S.D. Werner, (1982) "An Assessment of Earthquake Response Characteristics and Design Procedures for Port and Harbor Facilities," Proc. 3rd Int. Earthq. Microzonation Conf., Seattle.

Japan Society of Civil Engineers, JSCE (1980). "Earthquake Resistant Design of Quaywalls and Piers in Japan," Earthquake Resistant Design for Civil Engineering Structures, Earth Structures and Foundations in, pp. 31-85.

Karkanias, S., (1983). "Seismic Behavior and Simplified Analysis of Anchored Sheetpile Bulkheads," Master's Thesis, Rensselaer Polytech. Institute, Troy, N.Y.

Kawakami, F. and Asada, A. (1966). "Damage to the Ground and Earth Structures by the Niigata Earthquake of June 16, 1964," Soils and Foundations, Vol. VI, 14-60.

Kitajima, S., and Uwabe, T., (1978). "Analysis on Seismic Damage in Anchored Sheet-piling Bulkheads, "Rep. of the Japanese Port and harbor Res. Inst., Vol. 18, pp. 67-130. (in Japanese).

Murphy, V.A., (1960). "The Effect of Ground Characteristics on the Aseismic Design of Structures," Proc. 2nd World Conf. on Earthq. Engrg., Tokyo, 1960, pp. 231-247.

Nadim, F. and Whitman, R.V., (1983) "Seismically Induced Movement of Retaining Walls, " Jnl. Geotech. Engrg. Div. ASCE, Vol. 109, No. 7, pp. 915-931.

Prakash, S., (1981) Analysis of Rigid Retaining Walls during Earthquakes," Int. Conf. on Recent Advances in Geotech. Earthq. Engrg. and Soil Dyn., Vol. 3, St. Louis, Mo., pp. 1-28.

Rowe, P.W. (1952), "Anchored Sheetpile Walls,"Proc. Inst. Civ. Engrs., 1, 27-70.

Richards, R. and Elms, D. (1979), "Seismic Behavior of Gravity Retaining Walls," J. Geotech. Engr. Div., ASCE, 105.

Seed, H.B., (1973). "Stability of Earth and Rockfill Dams during Earthquakes," Embankment-Dam Engineering, Casagrande Vol., John Wiley and Sons, pp. 239-269.

Seed, H.B. and Whitman, R.V., (1970) "Design of Earth Retaining Structures for of Dynamic Loads," ASCE Spec. Conf. Lateral Stresses in the Ground and Design of Earth Retaining Structures, Ithaca, N.Y., pp. 103-147.

Tschebotarioff, G.P. (1978), "Foundations, Retaining and Earth Structures," McGraw-Hill.

Tsinker, G.P., (1983). "Anchored Sheet Pile Bulkheads: Design Practice," Jrl. Geotech. Engrg. ASCE, Vol. 109, No. 8, 1983, pp 1021-1038.

Wood, J.H., (1973). "Earthquake-Induced Soil Pressures on Structures," Ph.D. Thesis, Calif. Inst. of Tech.

TABLE 1. STATISTICS OF SEISMIC DAMAGE TO ANCHORED BULKHEADS IN JAPAN

	Total Numbers	Number of Damaged Bulkheads	Percent of Damaged Bulkheads %
Total Numbers	110	70	64
Number of bulkheads designed according to the Japanese procedure	45	29	64
Year Constructed Before 1950	37	22	59
1951 - 1960	11	6	55
1961 - 1966	40	30	75
After 1966	22	11	55
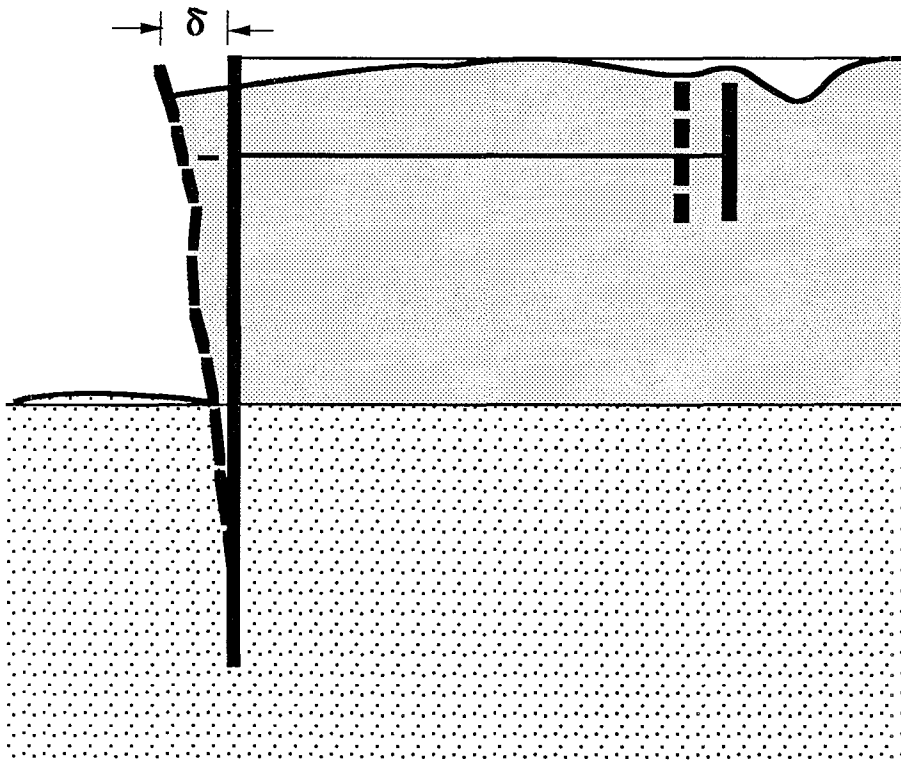
δ (cm)	ASSIGNED DEGREE OF DAMAGE
≤ 2	0
2 - 10	1
10 - 30	2
30 - 60	3
> 60	4

Figure 1. Sketch of usual seismic deformation of anchored bulkheads: permanent tilting of wall due to excessive relative motion of anchor. (Degrees of damage assigned by Kitajima and Uwabe, 1978.)
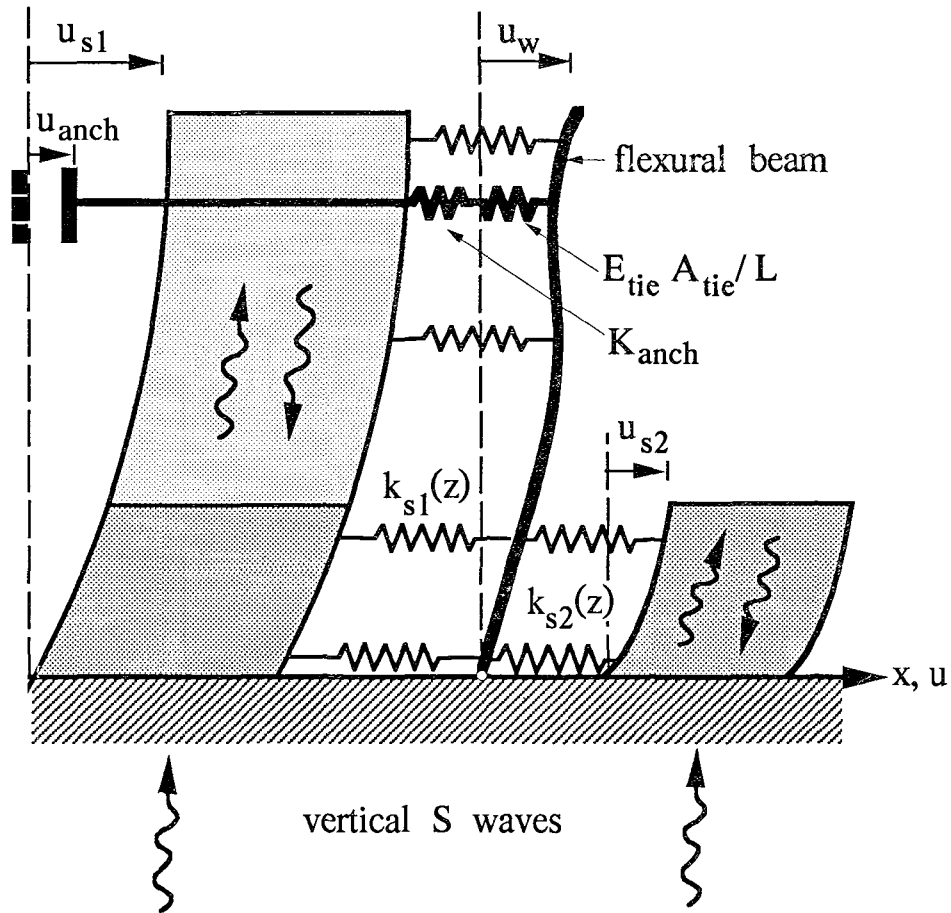
Figure 2. "Beam-on-Winkler-Foundation" model with complex "springs" (distributed and concentrated) used for obtaining a qualitative picture of the seismic response of the anchored bulkhead and for estimating the effective "point" of rotation, shown in Fig. 5.

$$k = 0.12 \pm 0.7$$

$$k' \approx 2k$$

$$\gamma' K_{AE}(k')$$

$$\gamma' K_A$$

Static   M-O
with k'

Static   Mononobe - Okabe
with k or k'
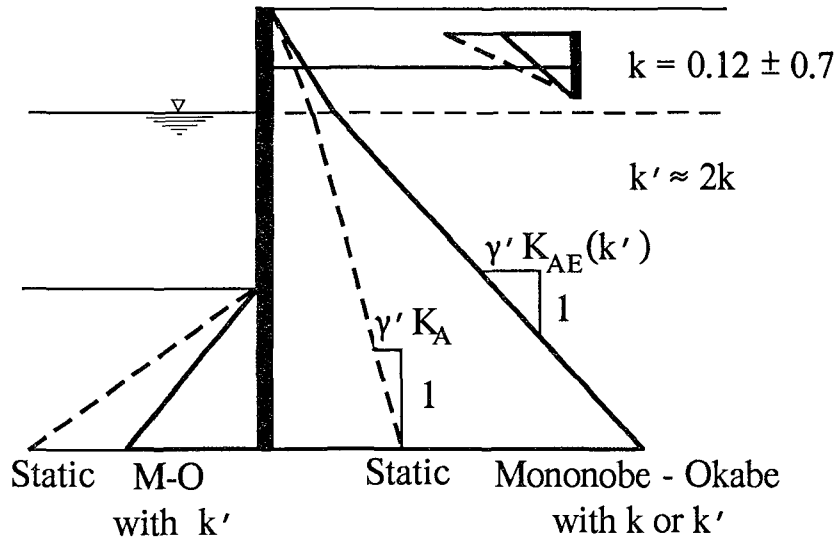
resistance provided by the anchor above
the point of intersection of the active
failure surface of the wall and the
passive failure of the anchor is neglected
in the design

passive failure surface
α_{AE} \ due to anchor movement

assumed active failure surface

α_{AE} and α_{PE} are computed for
the nominal seismic coefficient k
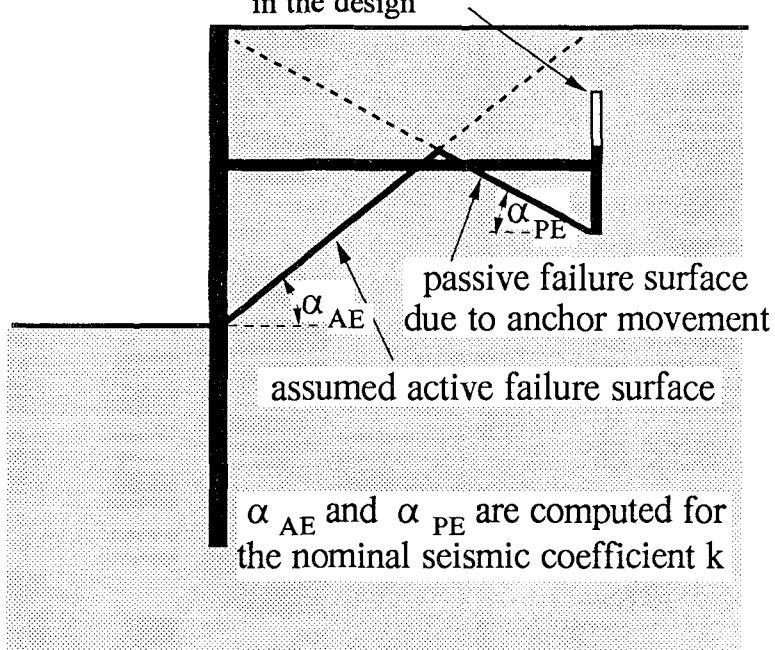
Code procedure for designing the anchor

Figure 3.   Illustration of the pseudo-static design procedure
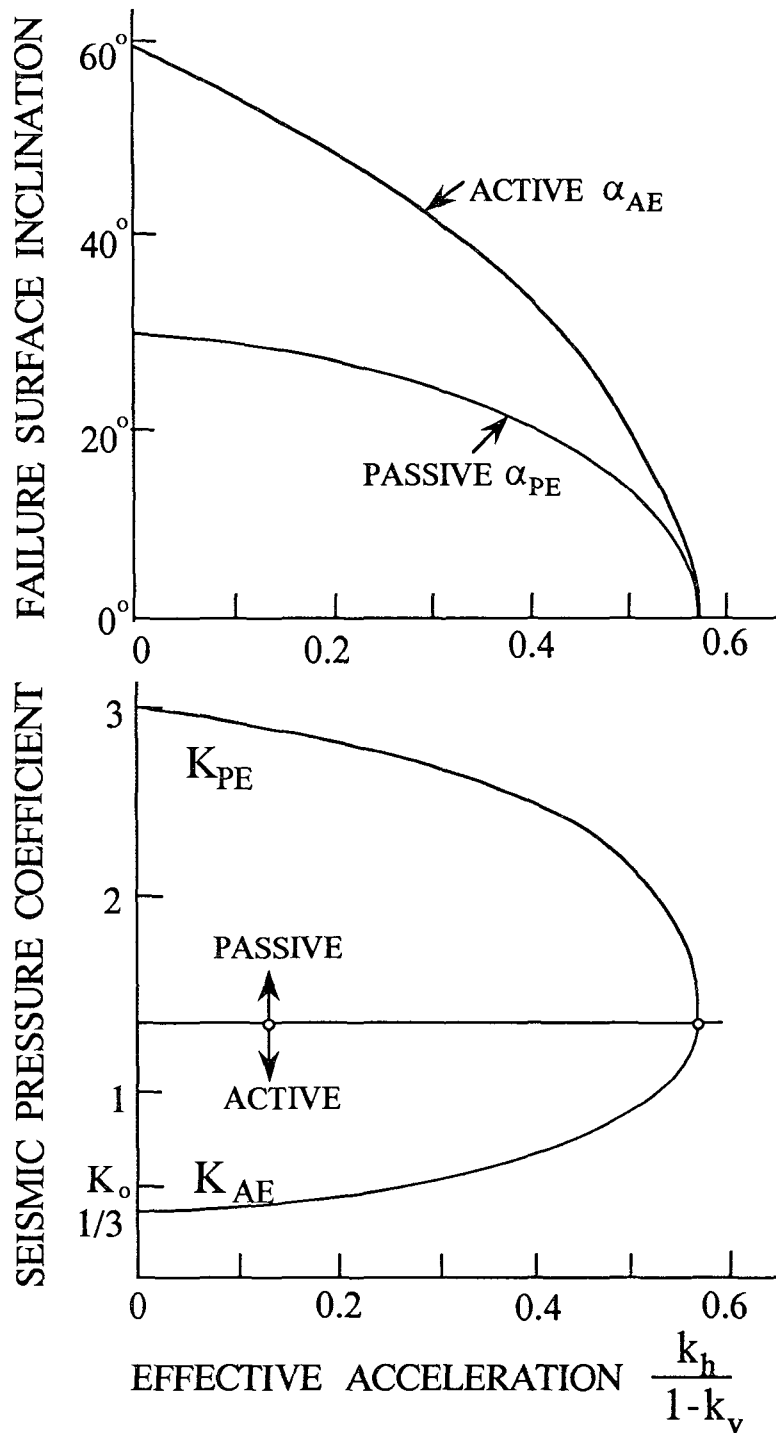
Figure 4. Effect of horizontal and vertical seismic coefficients on :
(a) the angles of active and passive sliding wedges, and (b) the active
and passsive earth pressure coefficients (Davies et al, 1986; Richards
and Elms, 1979.)
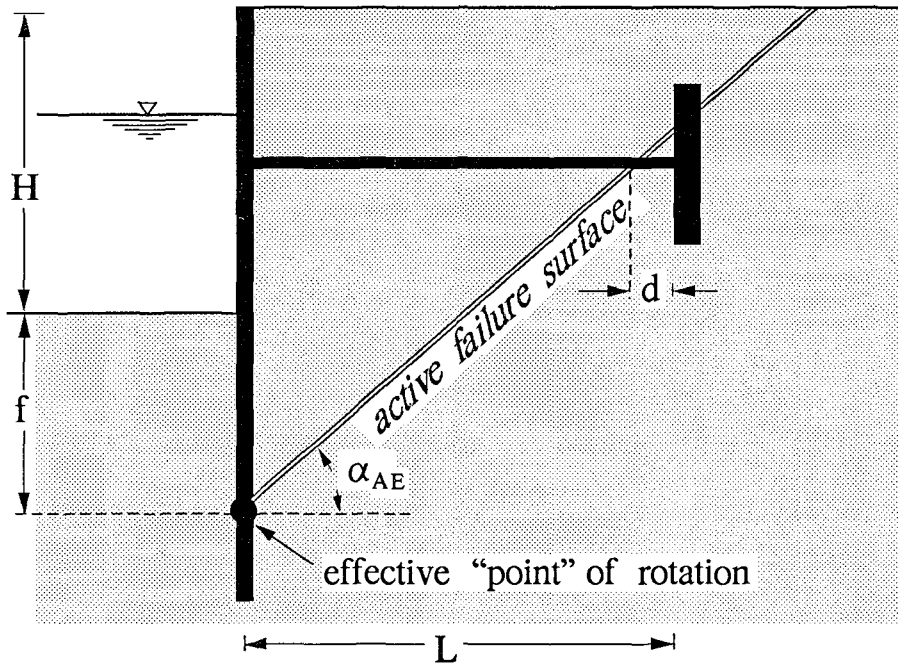
Figure 5. Definition of the Effective Anchor Index: EAI = d / H
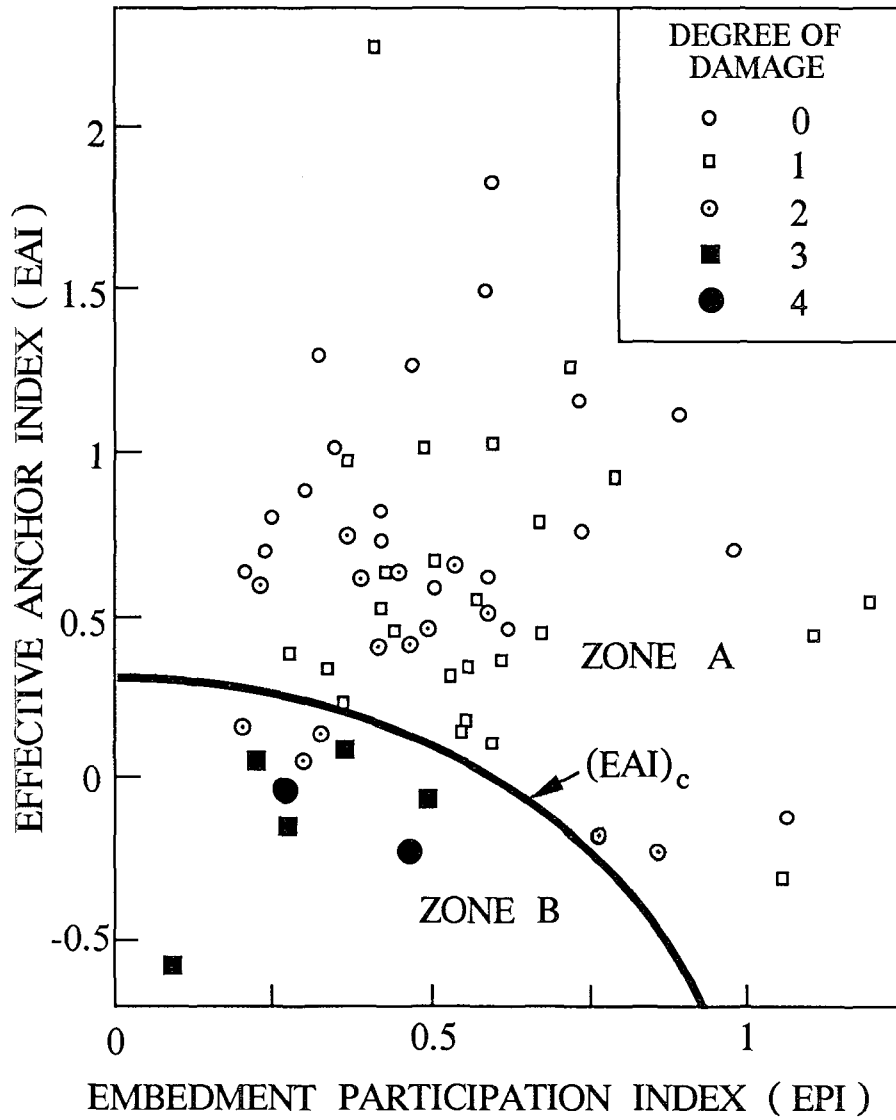
Figure 6. The developed Seismic Design Chart

SEISMICALLY INDUCED PERMANENT DISPLACEMENTS
OF RETAINING WALLS DUE TO LIQUEFACTION

by

Sreenivas Alampalli
Engineering Research Specialist I
Engineering R & D Bureau, NYSDOT
1220 Washington Avenue
Albany, NY 12232, USA

and

Ahmed–Waeil Elgamal
Assistant Professor
Department Of Civil Engineering
Rensselaer Polytechnic Institute
Troy, NY 12180, USA

ABSTRACT

A two dimensional (2D) dynamic wall–soil nonlinear computational model is proposed. The model accounts for wall and soil resonance, nonlinear wall–backfill soil interaction, simultaneous wall base sliding and rotation, nonlinear soil properties and possible pore pressure buildup effects. A bending beam with a base yielding rotational spring and a base translational slide element represents the wall. A 2D shear beam represents the soil system. The wall and supporting soil interact through a Winkler type nonlinear no–tension spring system. An elasto–plastic path–dependent hysteretic model accounts for nonlinear soil behavior and possible pore pressure buildup. Seismic response of a cantilever wall and a gravity wall supporting a saturated loose sand backfill is studied in detail. The computed results indicate the importance of including seismically induced moments in a dynamic wall stability evaluation. It is also found that retaining walls with loose saturated backfill soils may accumulate excessive permanent displacements well beyond the strong shaking phase of an earthquake.

INTRODUCTION

A number of analytical models which investigate the dynamic behavior of retaining wall systems have been developed. Tajimi (1973) used an elastic two dimensional (2D) wave propagation theory to investigate earth pressures on a basement wall assumed to undergo periodic vibrations of horizontal translation and rotation. Scott (1973) proposed a one dimensional elastic shear beam to model backfill soil connected to a supporting wall by a system of Winkler springs. Wood (1973) studied the dynamic earth pressure on retaining walls using a 2D plane—strain analysis. Arias et al. (1981) developed a 2D shear model to analyze fixed rigid wall response.

In addition to modeling the vibration of the wall—soil system, some nonlinear soil—structure interaction aspects may have a major influence on potential plastic deformations. Wall—backfill soil as well as wall—base interaction control the magnitude of dynamic earth pressure and resulting wall deformation. Prakash (1981) outlines a method for calculating permanent sliding displacement of retaining walls. In this method, the wall and soil are modeled as a single degree of freedom mass supported by a nonlinear yielding base spring. Prakash et al. (1981), Nadim and Whitman (1984), and Siddarthan et al. (1990) show that the rotational deformation of the wall structure may be quite significant in some cases and should be accounted for in analysis procedures. Nadim and Whitman (1983), and Siddarthan et al. (1989) investigated retaining wall response using a nonlinear plane strain finite element (FE) analysis incorporating slip elements along the active failure wedge boundaries and the wall base—soil interface. Importance of nonlinear soil properties and amplification of backfill motion in the dynamic analysis of wall soil systems is emphasized in the above mentioned FE studies.

In this paper a nonlinear model which accounts for wall and soil resonant dynamic response is proposed. The retaining wall is represented by a bending beam with a yielding base rotational spring and a translational slide element. Backfill soil is represented by a 2D shear beam. The wall and supported soil interact through a Winkler type nonlinear no—tension spring system. A formulation is developed in which the free vibration mode shapes of the wall and the soil are employed. An elasto—plastic constitutive relation is incorporated to model the nonlinear soil properties. Soil strength and stiffness degradation with pore pressure increase is also allowed. A small matrix equation (about 15 x 15) will incorporate the above response features and provide solution of sufficient accuracy. The seismic response of a cantilever wall and a gravity retaining wall are studied in detail using this model.

FORMULATION OF GENERAL MODEL

A wall model is assumed to interact under dynamic loading with a soil model through a system of Winkler—type springs. Two dimensional in—plane vibration conditions are assumed. The response features incorporated in this model are discussed below followed by the formulation details.

Features Of Proposed Dynamic Model

In this section, the features incorporated in the proposed dynamic wall—soil model (see Fig. 1) are presented. Some of these features are included in currently available models and some are unique to this model. These features are:

a) <u>Simultaneous wall translation and rotation</u>: A translational slide element is available at the retaining wall base. Under dynamic loading conditions, the sliding yield force of this element is:

$$F_y = \text{Active Earth Pressure Force} \times (\text{ F.S. against sliding } - 1.0) \qquad (1)$$

where F.S. is the static factor of safety. F_y may be further adjusted to include the effects of vertical earthquake shaking, and of increased static earth pressure and reduced base friction coefficient due to pore pressure buildup.

An elastic perfectly plastic rotational spring is also available at the base. The yield moment is chosen to account for wall rotational failures under dynamic loading:

$$M_y = \text{Overturning Moment} \times (\text{F.S. against overturning} - 1.0) \qquad (2)$$

Alternate expressions for M_y may be defined if wall rotation occurs about points other than the wall toe. Modifications to account for effects of pore–pressure buildup are also possible. M_y may be also chosen to represent the resistance to bending of a plastic hinge which may develop at the wall stem–base juncture.

b) <u>No–tension wall–soil interface</u>: A nonlinear Winkler type spring system is chosen as a wall–soil interface. No tension properties are intended to represent the dynamic component of wall–soil interaction. These nonlinear Winkler springs may be adapted to fill any gaps (partially or fully) created during transient seismic interaction. Such gaps may occur due to wall sliding, wall rotation or due to difference in inertia and stiffness of wall and soil. The nonlinear Winkler springs may also be used to exert additional stresses on the wall which may arise from backfill densification.

c) <u>Flexible wall model</u>: An Euler bending beam represents the wall. In many practical cases one or two mode shapes of this beam (1 or 2 degrees of freedom) will provide sufficient accuracy in defining the dynamic wall response. This wall model provides a realistic boundary for wall–backfill dynamic interaction. Gravity as well as flexible walls may be modeled. In addition, a base mass may be included to simulate the wall foundation.

d) <u>Soil model with ground motion amplification</u>: A simple soil model is proposed. Only lateral shear vibration is included (2D shear beam). In most cases, few degrees of freedom (10 or less) will represent the soil response with sufficient accuracy. As mentioned earlier, no–tension Winkler springs allow wall–backfill soil interaction. Other backfill boundaries (base and far end) are modeled by appropriate spring–dashpot mechanisms. Note that the soil base boundary may be aligned with the available geological profile (Fig. 1). Boundary springs and dashpots can be chosen so as to account for far–field compliance and radiation damping effects. Elasto–plastic nonlinear hysteretic soil properties may be included in this model.

In summary, the following aspects of wall–soil response are accounted for: wall flexibility, simultaneous wall translation and rotation, no–tension wall–soil interface, 2D soil geometry, amplification of dynamic/earthquake input motions, radiation damping effects, and soil elasto–plastic nonlinear response. A small matrix equation

357

(15x15 or less) will in general incorporate the above features and provide solutions of sufficient accuracy.

Wall—Soil Model (Alampalli, 1990, Elgamal and Alampalli, 1990)

In the present analysis a simplified version (Fig. 2) of the above described general wall—soil model is employed (see Alampalli, 1990 for general model formulation). In this simplified model, the following assumptions are made: 1) Soil is fixed at the far end, 2) Soil base is fixed, 3) Wall height is equal to soil domain height.

Free Vibration Response Of Wall Model

The retaining wall is represented by a one dimensional Euler bending beam with a fixed base. Dynamic soil pressure on the wall is represented by continuous Winkler type springs alongside the wall as shown in Fig. 2.
The equation of motion for the wall system (Fig. 2) can be written as

$$m \, u_{b,tt} + E'I \, u_{b,zzzz} + k \, u_b = 0 \qquad (3)$$

along with the boundary conditions

$$u_b = 0, \qquad u_{b,z} = 0 \qquad \text{at } z = 0$$

$$u_{b,zz} = 0 \,, \qquad u_{b,zzz} = 0 \qquad \text{at } z = H$$

where u_b is wall displacement relative to its base, E' is modulus of elasticity of wall material, I is moment of inertia, t is time , m is wall mass per unit length, H is wall height and k is wall—backfill interaction spring constant. Using the method of separation of variables [$u_b = T(t) \, W(z)$], the following equations can be written for the time and space variables respectively:

$$T_{,tt} + p^2 \, T = 0 \qquad (4)$$

$$W_{,zzzz} - \lambda^4 \, W = 0 \qquad (5)$$

in which,

$$\lambda^4 = (m \, p^2 - k)/(E'I) \qquad (6)$$

and p_i, i = 1,2,....∞ are the natural frequencies of the beam.
The solution of the Eq. 5 can be written as

$$W(z) = C_1 \sin (\lambda z) + C_2 \cos (\lambda z) + C_3 \sinh (\lambda z) + C_4 \cosh (\lambda z) \qquad (7)$$

and using the boundary conditions of Eq. 3, the following frequency equation can be derived:

$$\cos(\lambda H) \cosh(\lambda H) + 1.0 = 0$$

The roots λ_i, $i = 1,2,...\infty$ of this frequency equation are evaluated using a numerical scheme. For each λ_i, $i = 1,2, ...\infty$, the constants C_1–C_4 can be evaluated and Eq. 7 can be used to obtain the corresponding mode shapes, ψ_i, $i = 1,2,...\infty$. Associated natural frequencies, p_i, $i = 1,2,...\infty$ may be calculated using Eq. 6.

The bending beam described above will be supported on a stick–slip translational element and a torsional spring. This base support system (degrees of freedom u_{bs} in translation and θ in rotation) will be used later to allow for wall sliding and overturning.

Free Vibration Response Of Soil Model

Lateral vibration of the backfill soil is represented by a two dimensional domain. The soil model along with different boundary conditions is shown in Fig. 2. The soil model interacts on one side with the wall through Winkler type springs. In this section, soil properties will be assumed constant with depth for simplicity.

The equation of motion representing the soil domain (Fig. 2) can be written as:

$$G\, u_{,zz} + E\, u_{,xx} = \rho\, u_{,tt} \tag{8}$$

along with the boundary conditions,

$$u = 0 \quad \text{at } z = 0, \qquad G\, u_{,z} = 0 \quad \text{at } z = H$$

$$u = 0 \quad \text{at } x = L, \qquad E\, u_{,x} = k\, u \quad \text{at } x = 0$$

where G is soil shear modulus, E is soil Youngs modulus, u is soil displacement relative to the ground, ρ is soil mass density, and L and H are length and height of the soil domain respectively. Using the method of separation of variables [u = T(t) X(x) Z(z)], the following equations are obtained by substitution in Eq. 8:

$$T_{,tt} + \omega^2\, T = 0 \tag{9}$$

$$Z_{,zz} + \beta^2\, Z = 0 \tag{10}$$

$$X_{,xx} + \alpha^2\, X = 0 \tag{11}$$

where ω is the natural frequency, and α as well as β are constants to be determined by imposing the boundary conditions. The relation between ω, α and β is governed by:

$$\beta^2 = [\omega^2 - (E/\rho)\, \alpha^2]\, (\rho/G) \tag{12}$$

The solution of Eqs. 8 along with the boundary conditions yields:

$$U(x, z) = X(x) \, Z(z) = \sum_{n=1}^{\infty} \sum_{r=1}^{\infty} A_{nr} \, \text{Sin}(\alpha_n x + \eta_n) \, \text{Sin}(\beta_r z) \qquad (13)$$

in which A_{nr} are arbitrary constants, and,

$$\beta_r = (\pi/H) \, (r-0.5), \qquad\qquad r=1,2,3,\ldots\infty$$

$$\alpha_n L + \tan^{-1}(\alpha_n E/k) = n \, \pi, \qquad\qquad n=1,2,3,\ldots\infty$$

$$\eta_n = \tan^{-1}(\alpha_n E/k) \qquad\qquad n=1,2,3,\ldots\infty$$

The natural frequencies ω_{nr} , $n=1,2,3,\ldots\infty$, $r=1,2,3,\ldots\infty$ can be evaluated from Eq. 12. For each α_n and β_r, a mode shape ϕ_{nr} can be obtained from Eq. 13.

Forced Response Of Combined Wall–Soil Model

The above discussed wall and soil models are used to represent the vibrational response of combined wall–soil systems. The wall base, as mentioned earlier, will be allowed one translational and one rotational degree of freedom. In translation, the wall will be allowed to slide away from the backfill once the dynamic lateral forces exceed the base frictional force as dictated by the static factor of safety against sliding. An additional elastic–perfectly–plastic base rotational spring will also allow rotation (away from the backfill) if base moment exceeds the available resistance as dictated by the static factor of safety against overturning.

a) Wall Base Translation: The equation describing the retaining wall base translational element in a sliding mode is expressed as (see Fig. 2):

$$\int_0^H [m \, (u_{g,tt} + u_{bs,tt} + u_{b,tt} + z \, \theta_{,tt}) + F_{ws}] \, dz - F_y = 0 \qquad (14)$$

where u_g is ground input displacement, u_{bs} is wall base displacement, θ is wall base rotation (radians), F_{ws} is wall–backfill interaction pressure (see Fig. 3a) and F_y is a user specified base yield force. Eq. 14 describes the behavior of the system in the sliding phase. Whenever the base sticks to the foundation i.e. no relative motion between base and foundation soil, the non–sliding condition will be:

$$u_{bs,t} = 0 \qquad (15)$$

which holds as long as (see Figs. 2 and 3a):

Wall inertial forces + Wall and backfill interaction spring forces $- F_y \leq 0$ (16)

As soon as the stick condition given by Eq. 16 fails, slip occurs and Eq. 14 is employed.

b) Wall Base Rotation: The equation of motion for retaining wall base rotation can be written as (Fig. 2):

$$M + \int_0^H [m \{u_{g'tt} + u_{b'tt} + u_{bs'tt} + z\, \theta_{,tt}\} + F_{ws}]\, z\, dz = 0 \tag{17}$$

where $M = K_t\, \theta$, and K_t = rotational spring constant. Dynamic base moment is not allowed to exceed a user prescribed value of M_y ($M \geq - M_y$), after which, permanent base rotation occurs (see Fig. 3b).

c) Wall–Soil Model: The wall will interact with soil through a no–tension Winkler type springs (k) as shown in Fig. 2. Under dynamic excitation, these springs will sustain compressive forces only. It may be noted from Fig. 4 that the force–displacement relation of the springs (k) will always fill any tensile gaps and maintain continued interaction between wall and backfill.

Considering interaction forces and ground motion excitation, the equations of motion of the wall–soil system can be written as:

$$\rho\, u_{,tt} - G\, u_{,zz} - E\, u_{,xx} = - \rho\, u_{g'tt} \qquad \text{(Soil System)} \tag{18}$$

$$m\, u_{b'tt} + E'I\, u_{b'zzzz} + F_{ws} = - m\, (u_{g'tt} + u_{bs'tt} + z\, \theta_{,tt})$$

$$\text{(Retaining Wall)} \tag{19}$$

Employing the mode shapes obtained for the wall system and for the soil system to represent the solution in the respective domains, we can write:

$$u(x,z,t) = \sum_{i=1}^{N} \phi_i(x,z)\, q_{si}(t) \text{ ,and} \qquad u_b(z,t) = \sum_{j=1}^{R} \psi_j(z)\, q_{bj}(t) \tag{20}$$

in which q are generalized time coordinates (q_s represent soil domain and q_b represent wall), and, N and R are the number of modes chosen to represent the soil and the wall systems respectively. Employing a Galerkin implementation of the method of weighted residuals (Finalyson, 1972) a matrix equation of order I (N+R+2 = I) is obtained. Proportional viscous damping may be introduced as a weighted combination of the inertial and stiffness terms derived from the spatial domain (beam and soil).

Time Integration

Newmark's predictor–multi–corrector implicit integration scheme with or without user specified numerical damping is employed to obtain a step–by–step solution of the matrix equation obtained in the previous sections (Belytschko and Hughes, 1983). Note that due to the nonlinear force–displacement relations, iterations will in general be performed at each time step so as to achieve a specified convergence tolerance.

361

Elasto–Plastic Constitutive Model

A soil elasto–plastic path–dependent hysteretic model is incorporated in the 2D computational model described above. The flow or incremental theory of plasticity is used. This model is capable of generating the Massing–type behavior exhibited by soil under cyclic loading. A hardening rule proposed by Mroz and Zienkiewicz (1984) is adopted herein. This hardening rule leads to an infinite yield surface formulation in which evolution of stress state is piecewise linear between computational steps (see Fig. 5). A simple pore pressure generation logic is also included in order to account for degradation of stiffness and strength in loose saturated sandy soils (see Fig. 6).

SEISMIC RETAINING WALL RESPONSE

In this section, the proposed simplified model is used to investigate the seismic response and the associated base translation of a gravity wall (Fig. 7) and a cantilever wall (Fig. 8). Retaining walls in general are designed for a factor of safety (F.S.) of at least 1.5 against possible base sliding or overturning. Only the resistance in excess of the design static loads will be available to resist additional forces on the wall when subjected to dynamic/seismic excitation. In the following sections, only translational yielding is allowed and the initial yield value is chosen based on a static factor of safety of 1.5 against possible translation. Static earth pressure is evaluated using the Rankine theory. A scaled El Centro 1940 S00E earthquake acceleration record is used to represent ground excitation ($\ddot{u}_g$) in the present analysis. For simplicity a ground water table is assumed to coincide with ground surface on the backfill side only. The initial wall–foundation soil friction angle $\delta_b(0)$ is assumed to be equal to the angle of internal friction (φ).

The base translational yield force $F_y(t)$ changes at every time step with the increase in pore water pressure. This pore pressure will increase the static active earth pressure and decrease the wall base–foundation soil friction angle (δ_b). $F_y(t)$ will be chosen to change in the following manner:

$$F_y(t) = (F_y(0) - F_i(t)) \, (\tan \delta_b(t) \, / \tan \delta_b(0))$$

in which, $F_i(t)$ = increase in static earth pressure force on the wall at time t,

$$\tan(\delta_b(t)) = (1 - K(t)) \, / \, (2 \sqrt{K(t)}), \quad \text{(note that } K(0)=(1-\sin \varphi)/(1+\sin \varphi))$$

and, $K(t)$ = Coefficient of active earth pressure at time t.

In the above, K is assumed to vary with the change in excess pore pressure ratio $(r_u, \; 0 \leq r_u \leq 1)$ in the following simple fashion:

$$K(t) = (1 - r_u(t)) \, K(0) + r_u(t).$$

In computing $F_y(t)$, the excess pore pressure ratio (r_u) developed in the soil near the

wall base is employed. In computing $F_i(t)$, excess pore pressures along the wall–soil interface are employed. It is noted that the above relations for $F_y(t)$ and $K(t)$ are not intended to represent any particular field situation and other such relations may be used.

a) Gravity Retaining Wall: The seismic response of a gravity wall of 5 m height and 2.0 m thickness supporting a 100 m long soil backfill is investigated (Fig. 7). Various model properties of the system are (see also Alampalli, 1990): $E' = 2.2 \times 10^9$ Kg/m^2, mass density of wall $= 240$ Kg sec^2/m^4, $k = 5 \times 10^5$ kg/m, $E = 3.12 \times 10^7$ Kg/m^2, $G = 1.2 \times 10^7$ Kg/m^2, $\rho = 180$ Kg sec^2/m^4, proportional viscous damping $= 3\%$, soil internal friction angle $= 30$ degrees, and nonlinear wall base rotational spring constant $K_T = 4.5 \times 10^9$ Kg m/radian. Six beam mode shapes and ten soil mode shapes are employed. The El centro acceleration record scaled to a maximum of 0.6 g is used as input excitation (Fig. 9a).

The computed time histories of excess pore pressure ratio near the wall base (at the wall–soil interface), wall base acceleration, wall base displacement, base force, and base moment are presented in Fig. 9. Pore pressure in the sampled location reaches a peak of 0.556 (Fig. 9b). The base force history (Fig. 9e) depicts a trend of diminishing resistance (decreasing base translational yield value) with the pore–pressure increase. The positive peaks in Fig. 9e are truncated at the yield value which is gradually decreasing as the pore–pressure increases. The same trend may be observed from the wall base moment (Fig. 9f) and acceleration (Fig. 9c) histories. During this earthquake, the wall is displaced (Fig. 9d) by a distance of 18.6 cms.

b) Cantilever Retaining Wall: A reinforced concrete wall of 15 m height and 1.2 m thickness supporting a 150 m long dense sand backfill is studied (Fig. 8). The various modal properties are identical to those of the gravity wall above with the exception of: $\rho = 216$ Kg sec^2/m^4 and soil internal friction angle $= 36^\circ$. Input motion in this case (Fig. 9a) is scaled to a maximum of 0.34 g.

Computed time histories of wall top acceleration, wall top displacement, wall base force, stress at the wall center, and stress–strain as well as excess pore–pressure ratio near the wall base are shown in Fig. 10. In this case, the excess pore–pressure at the base increases to a maximum of 0.74 (Fig. 10d). This increase in pore–pressure reduces the soil strength as may be observed from the stress–strain history of Fig. 10f. A significant decrease in wall base translational resistance is also observed (Fig. 10c). The decrease is very sharp in the period 1–3 seconds of shaking (during the strong shaking phase of the earthquake). A wall translation of about 4.0 cms occurs during that period (Fig. 10b). In view of the significant reduction of base translational resistance during the first 3 seconds, an additional wall translation of about 20 cms occurs in the period 4–15 seconds despite the decrease in input acceleration magnitudes (see Figs 9a and 10b). In the last 12 seconds of the earthquake, the wall continues to translate (4 more cms) despite the dramatic decrease in input acceleration.

SUMMARY AND CONCLUSIONS

A two dimensional (2D) dynamic wall—soil computational model is proposed. The model accounts for wall and soil resonance, nonlinear wall—backfill soil interaction, simultaneous wall base sliding and rotation, nonlinear soil properties, and possible pore pressure buildup. An elasto—plastic path—dependent hysteretic model accounts for nonlinear soil behavior and excess pore pressure buildup. The seismic response of a 5 m high gravity wall and a 15 m cantilever wall supporting a saturated loose sand backfill is studied in order to investigate seismically induced wall translational yield mechanisms. It is shown that excess pore—pressure during the earthquake may substantially reduce the wall base translational resistance. As the base resistance decreases, wall displacement accumulates and may even continue after the strong shaking phase of the earthquake.

ACKNOWLEDGEMENTS

REFERENCES

Alampalli, S. "Earthquake Response Of Retaining Walls; Full Scale Testing And Computational Modeling", Ph. D. Thesis, Department Of Civil Engineering, Rensselaer Polytechnic Institute, Troy, NY, 1990.

Arias, A., Sanchez—Sesma, F.J., and Ovando—Shelley, E. "A Simplified Elastic Model For Seismic Analysis Of Earth—Retaining Structures With Limited Displacements", Proc., International Conference On Recent Advances In Geotechnical Earthquake Engineering & Soil Dynamics, Rolla, Missouri, 1981.

Belytschko, T., and and Hughes, J.R.T. eds., "Computational Methods For Transient Analysis", Vol. 1, Chapter 2, Section B.IV, North—Holland, 1983.

Elgamal, A—W., and, Alampalli, S. "Dynamic Response Of Retaining Walls Including Supported Soil Backfill", submitted for journal publication, 1990.

Finalyson, B.A. "The Method Of Weighted Residuals And Variational Principles", Academic Press, New York, 1972.

Mroz, Z., and Zienkiewicz, O.C., "Uniform Formulation Of Constitutive Equations For Clays And Sands", Mechanics Of Engineering Materials, Desai, C.S., and Gallaghar, R.H., eds., John Wiley & Sons Ltd., 1984.

Nadim, F., and Whitman,R.V. "Seismically Induced Movement Of Retaining Walls", Journal Of Geotechnical Engineering, ASCE, Vol. 109, No. 7, 1983.

Nadim, F., and Whitman, R.V. "Coupled Sliding And Tilting Of Gravity Retaining Walls During Earthquakes", Proc., Eighth World Conference On Earthquake Engineering, San Francisco, California, 1984.

Prakash, S. "Soil Dynamics", McGraw—Hill Book Company, New York, 1981.

Prakash, S., Puri, V.K., and Khandoker, J.U. "Displacement Analysis Of Rigid Retaining Walls In Rocking", Proc., International Conference On Recent Advances In Geotechnical Earthquake Engineering & Soil Dynamics, Rolla, Missouri, 1981.

Scott, R.F. " Earthquake–Induced Earth Pressures On Retaining Walls", Proc., Fifth World Conference On Earthquake Engineering, Rome, 1973.

Siddarthan, R., Norris, G.M., and Maragakis, E. "Deformation Response Of Rigid Retaining Walls To Seismic Excitation", Proc., Fourth International Conference On Soil Dynamics And Earthquake Engineering, Mexico, 1989.

Siddarthan, R., Ara, S. and Anderson, J.G. "Seismic displacements Of Rigid Retaining Walls", Proc., Fourth U.S. National Conference On Earthquake Engineering, Palm Springs, California, Vol. 3, pp. 673–682, 1990.

Tajimi, H. "Dynamic Earth Pressures On Basement Wall", Proc., Fifth World Conference On Earthquake Engineering, Rome, 1973.
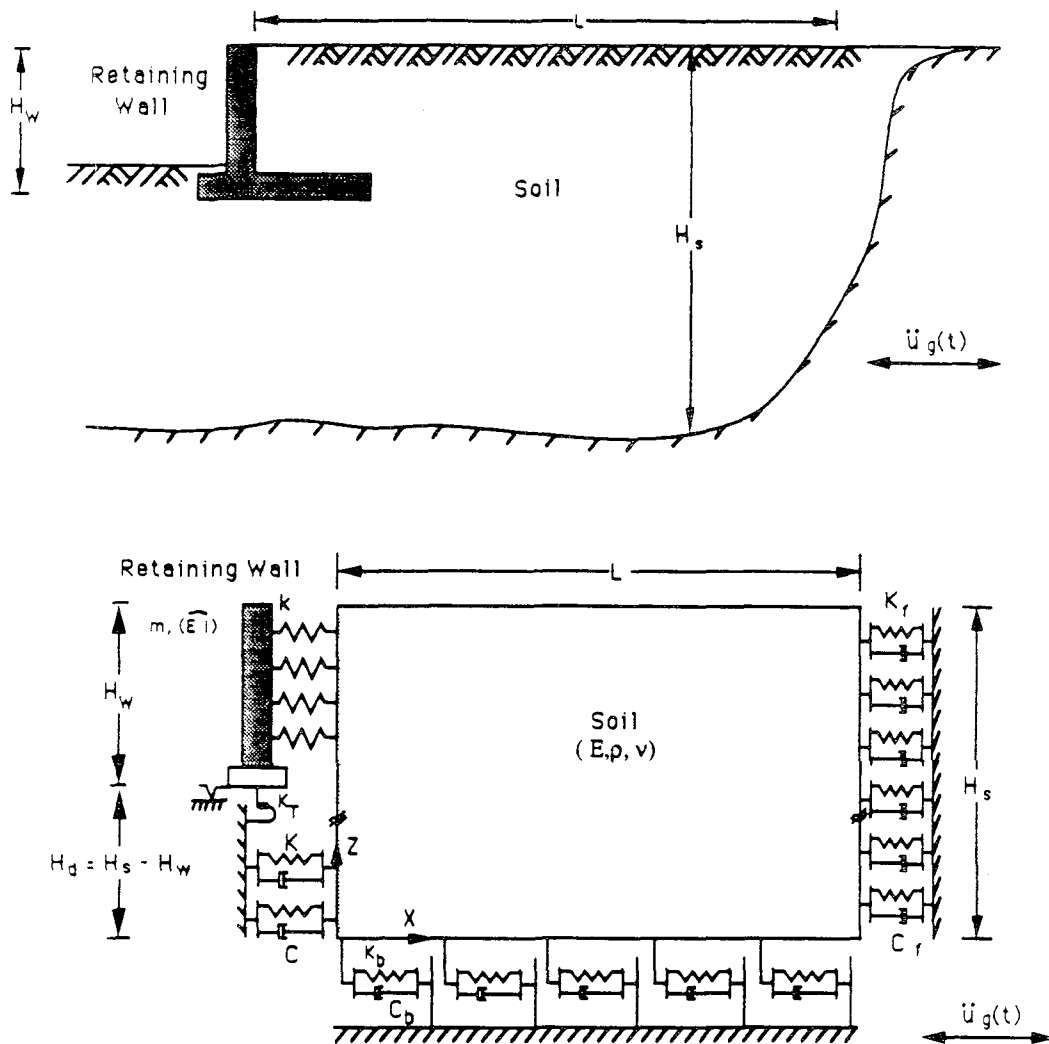
Figure   1.   Wall-Soil Configuration And Corresponding Computational Model.
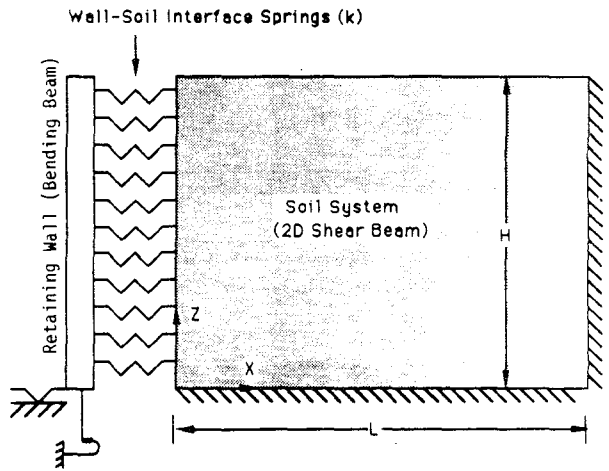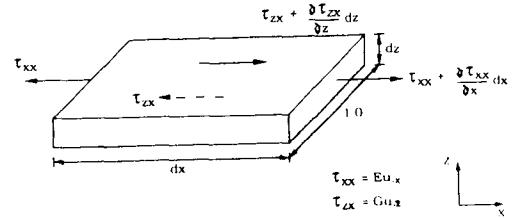
Figure 2. Simplified Wall-Soil Computational Model.
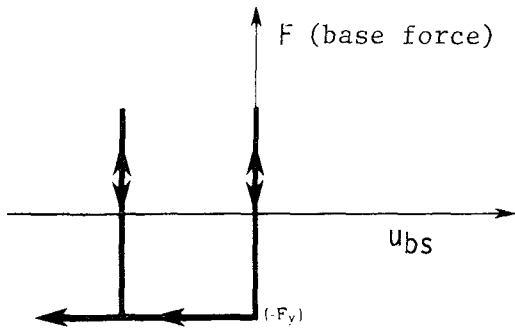
(a) Wall Base Translational Sliding Element.
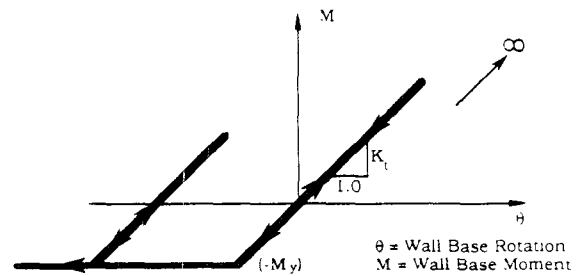
(b) Wall Base Rotational Spring.

Figure 3. Nonlinear Wall Base Translational And Rotational Formulation.
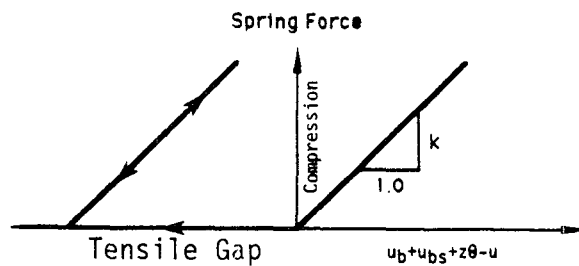
Figure 4. Wall-Backfill Soil Interaction Nonlinear
Spring Formulation.
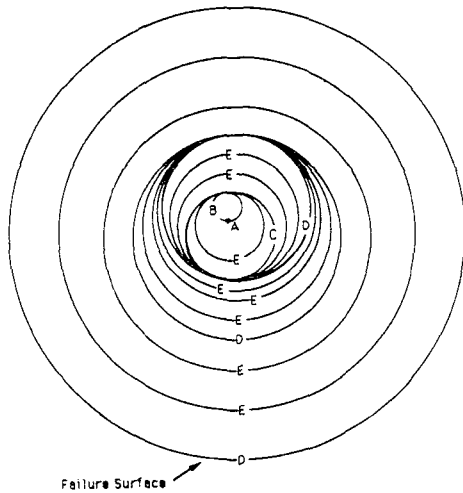
A. Current Stress State
B. Current Yield Surface (f_y)
C. Current Outer Surface (f_o)
D. Stored Memory Surfaces
E. Conceptual Representation of interpolation surfaces

Figure 5. Conceptual Configuration
           Of Hardening Process In
           General Stress Space.
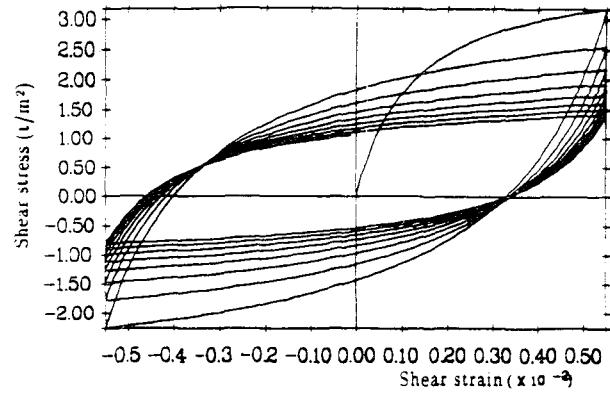
Figure 6. Material Stress-Strain
           Behavior Under Cyclic
           Loading.
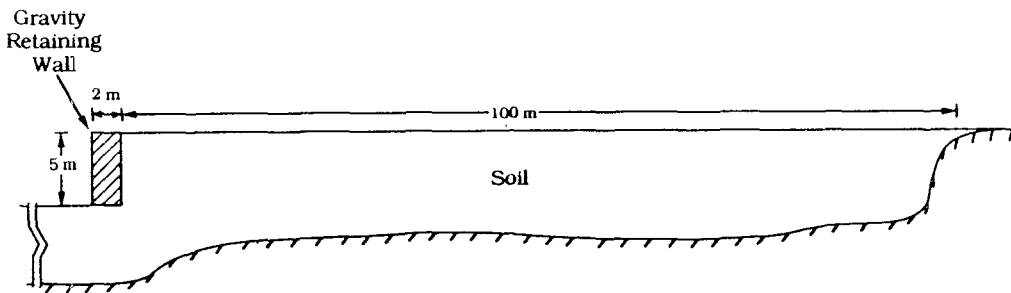
Figure 7. Gravity Retaining Wall-Soil System Used In
           Numerical Simulation.
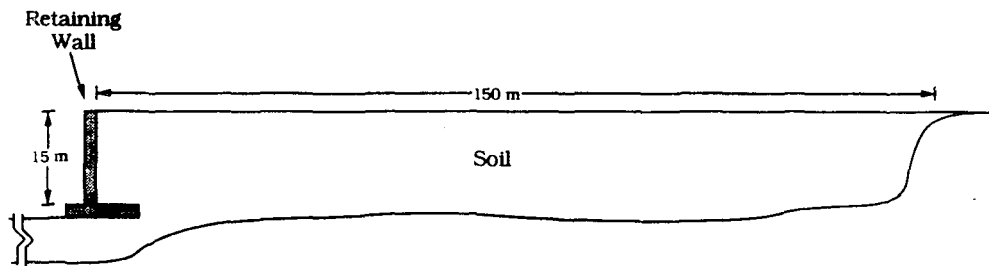
Figure 8. Cantilever Retaining Wall-Soil System Employed In
            Numerical Simulation.
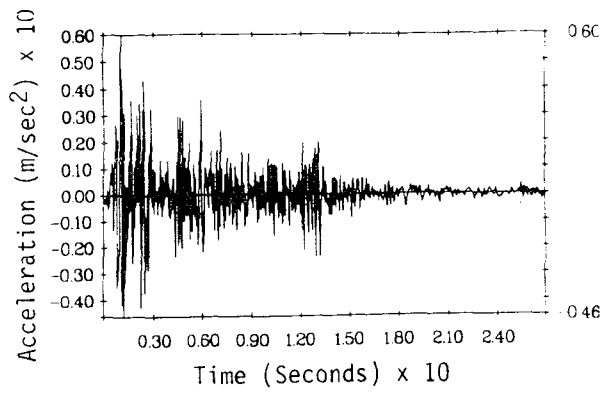
(a) Input Base Excitation.
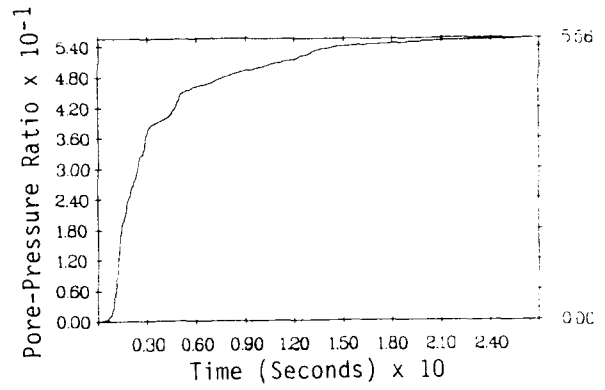
(b) Excess Pore-Pressure Ratio At Wall Base.
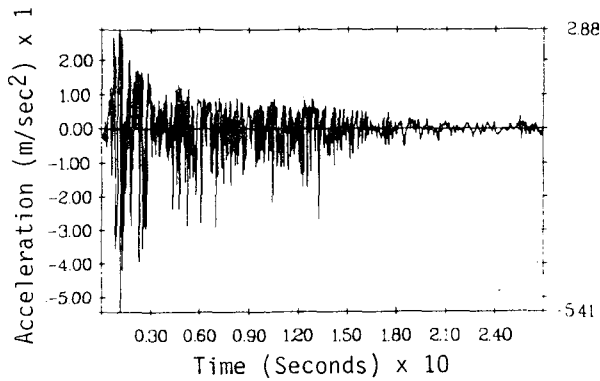
(c) Wall Base Acceleration.
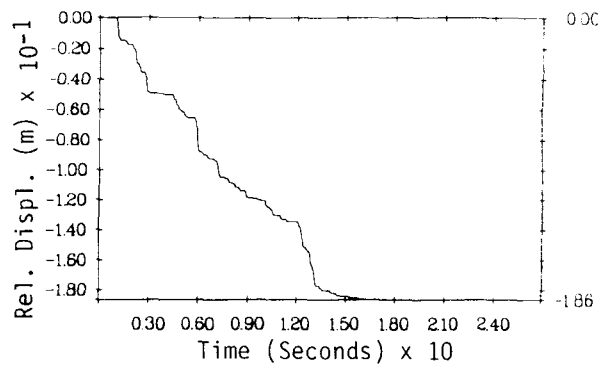
(d) Wall Top Relative Displacement.
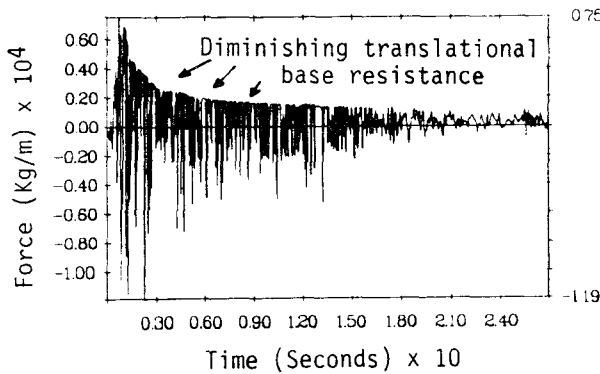
(e) Wall Base Force.
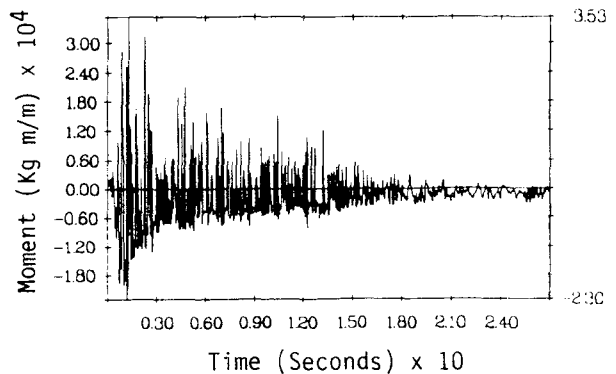
(f) Wall Base Moment

Figure 9. Computed Seismic Response Of 5 m High Gravity Retaining Wall With Saturated Backfill (Only Base Translational Yielding Allowed).

368
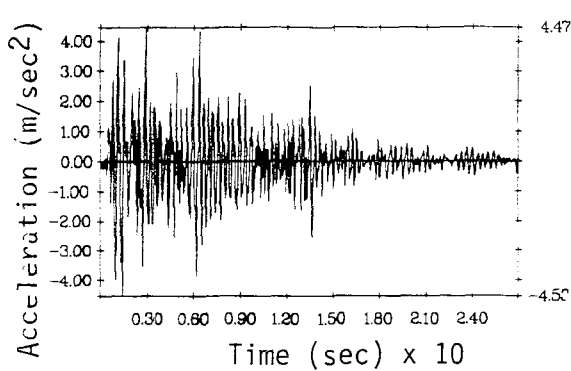
(a) Acceleration At Soil Surface.
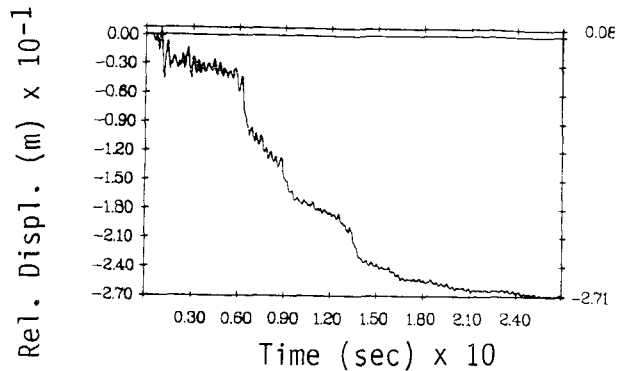
(b) Rel. Displacement at Wall Top.
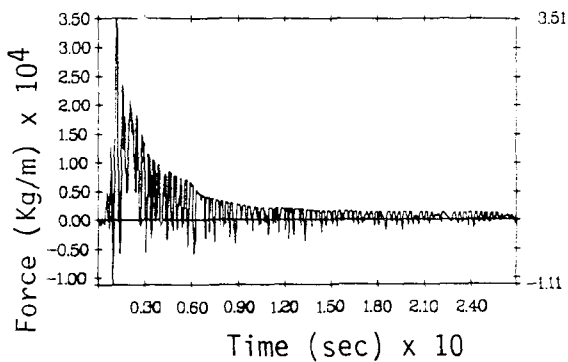
(c) Wall Base Force.
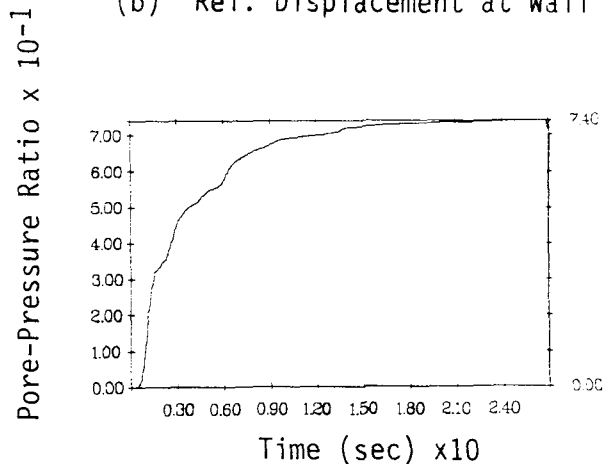
(d) Excess Pore-Pressure Ratio at Wall Base.
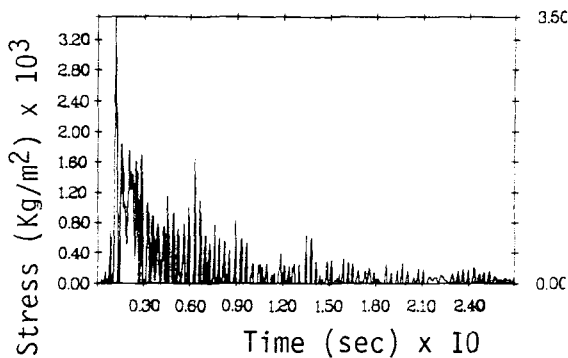
(e) Wall Pressure Near Mid Height
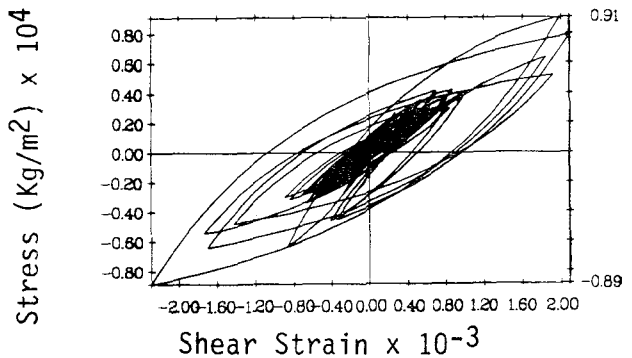
(f) Shear Stress vs Shear Strain Near Wall Base.

Figure 10. Computed Seismic Response Of A 15 m High Cantilever Retaining Wall With Saturated Backfill (Only Base Translational Yielding Allowed).

369

SHAKE TABLE TESTS ON LATERAL GROUND FLOW
INDUCED BY SOIL LIQUEFACTION[1]

Yasushi Sasaki[1], Ken-ichi Tokida[2]
Hideo Matsumoto[3] and Syoichi Saya[4]

Earthquake Disaster Prevention Department,
Public Works Research Institute,
Ministry of Construction,
Tsukuba, JAPAN

ABSTRACT

A series of shake table tests is carried out on the lateral flow of the ground due to soil liquefaction during earthquakes. The model grounds are 6.0 m long, 0.8 m wide and their average height is 1.2 m. The slope of the ground surface and the lower boundary condition of liquefiable layer are varied, and the sinusoidal accelerations with a frequency of 2 Hz are inputted for 20 seconds. The deformation of model grounds, the excess pore water pressure of the liquefied layer, and the acceleration of the grounds are monitored. Based on the test results, the influence of the slope, the input motion and the thickness of liquefied layer to the ground flow is examined, and the fundamental characteristics of lateral ground flow induced by soil liquefaction are clarified experimentally.

INTRODUCTION

The liquefaction has caused severe damages for structures during the past earthquakes in Japan. Hamada et. al. (1986,1988) pointed out that the fairly big amount of lateral flow of ground could be seen broadly at the areas in and/or around Tokyo, Fukui, Niigata and Noshiro where the liquefaction of the ground apparently took place during the Kanto Earthquake (1923, M=7.9), the Fukui Earthquake (1948,M=7.3), the Niigata Earthquake (1964, M=7.5) and the Nihonkai-chubu Earthquake (1983, M=7.7), respectively.

Therefore it becomes necessary to consider two types of effect induced by soil liquefaction for the earthquake resistant design of structures; the loss of bearing capacity of liquefied ground and the lateral flow of the inclined ground induced by liquefaction. The loss of bearing capacity of liquefied layers has been considered in the "Specifications for Highway Bridges" (1980, 1990) in Japan.

However, the mechanism of ground flow induced by soil liquefaction, the predicting method of ground flow and the applying method of its effect to the earthquake resistant design of structures are not yet clarified at present.

Under these circumstances, as the first stage of investigations, the authors conduct a series of shake table tests to study the mechanism of ground flow induced by soil liquefaction and to establish the procedure for estimating ground flow. This paper describes the essential factors relating to the lateral ground flow due to soil liquefaction explained from the experiments.

METHOD OF EXPERIMENTS

Shake table tests on eight model grounds (Model-1~8) are carried out. The conditions of ground models are shown in Fig. 1 and Table 1. The two types of containers placed on a shake table are prepared to set up model grounds: a square container for Model-1~7 is 6.0 m long, 0.8 m wide and 2.0 m high, and another semicircular one for Model-8 is 4.0 m long with a diameter and 0.4 m high. Four transparent glass windows (each is 0.8 m wide and 1.8 m high) are installed at the one side of the square container. Models-1~7 are prepared as a two-dimensional ground model to investigate the influence of the ground conditions on the lateral ground flow, and on the other hand, Model-8 is prepared as a three-dimensional ground model to know the influence of the direction of excitation on the lateral ground flow. The model grounds fundamentally consist of three layers: a lowermost nonliquefiable layer, a middle liquefiable layer and a uppermost unsaturated layer. However, Models-7 and 8 do not have the uppermost unsaturated layer and the lowermost nonliquefiable layer, respectively. The materials used for model grounds are shown in Table 2, i.e., mountain sand taken from Mt. Sengen-yama for three

layers and shot of lead or gravel for the uppermost layer.

As for preparation of the model grounds, the lowermost sand layer is firstly compacted enough in the container not to liquefy during excitation, a certain amount of water is poured, and then the middle liquefiable sand layer is prepared by means of the underwater drop method. Upon completion of the lowermost and middle layers, the uppermost unsaturated layer is prepared forming the surface ground with a slope. In the Models-5, 6 and 8, shot of lead or gravel is used as the material of the unsaturated layer to give the larger overburden pressure and lesser cohesion than Mt. Sengen-yama Sand. Based on Table 2 as for the unit weight of unsaturated surface layer, the unit weight of gravel is not so different from that of Mt. Sengen-yama Sand, but the unit weight of shot of lead is about four times than that of Sand. The thickness of liquefiable layer (H_1), the slopes of surface (θ_s) and lower boundary of liquefiable layer (θ_b) are varied to have different conditions in order to examine the influence of these factors on the ground flow. The water level is set equal to the upper boundary of liquefiable layer, i.e., horizontal regardless of the slope of ground surface in this series of tests.

The typical conditions of each model ground are indicated as follows:

Model-1: θ_s= 5 %, θ_b= 0 % and H_1= 700 mm. H_1 is larger than Model-4 (H_1= 350mm).

Model-2: θ_s=7.5 %, θ_b= 0 % and H_1= 350 mm. θ_s is larger than Model-4 (θ_s=5.0%).

Model-3: θ_s= 5 %, θ_b= 5 % and H_1= 350~50mm. The lower boundary of liquefiable layer inclines comparing with Model-4 (θ_b= 0 %).

Model-4: θ_s= 5 %, θ_b= 0 % and H_1= 350 mm.

Model-5: θ_s=2.5 %, θ_b= 0 % and H_1= 350 mm. The slope of shot of lead (converted into about θ_s= 10 % as sand) is larger than Model-4 (θ_s= 5 %) and Model-2 (θ_s = 7.5 %).

Model-6: θ_s= 0, 5 %, θ_b= 0 % and H_1= 350 mm. The ground surface is inclined and horizontal.

Model-7: θ_s= 0 %, θ_b= 5 % and H_1= 650~350mm. Only lower boundary of liquefiable layer is inclined.

Model-8: θ_s= 15 %, θ_b= 0 % and H_1= 250 mm. The surface ground shapes a semi-corn with gravel.

In each test, constant sinusoidal acceleration with a frequency of 2 Hz is employed for 20 seconds (40 cycles), and several levels of maximum acceleration (60~190 gals) are applied stepwise to the shake table as input motion. The measured maximum accelerations of the shake table and the results of typical lateral displacement on the ground surface at Section-B are summarized in Table 3 for all tests.

As shown in Fig. 1, accelerometers, pore water pressure meters, strain gage meters and displacement meters are installed in or on the ground models to measure the time history of acceleration, pore water pressure and

displacement of layers during excitation. These meters are installed at four sections, i.e., Sections-A , B , C and D for Models-1~7, and at two sections, i.e., Section-OA (direction of excitation) and Section-OE (right-angle direction of excitation) for Model-8. Vertical marked lines with a white-colored sand are also installed behind the transparent glass windows at intervals of 20 cm for Models-1~7 to trace or photograph the deformation of the layers in the direction of depth. Bench mark points are also set on the ground surface to measure manually or photograph the change of lateral displacement of ground surface.

RESULTS OF EXPERIMENTS

From the above shake table tests, principal characteristics of lateral ground flow due to liquefaction and factors concerning to the ground flow are drawn as follows.

Distribution of Ground Flow

Figs. 2(a) and 2(b) show the successive change of vertical marked lines during excitation at the Step-2 in the cases of Models-4 and 6, respectively. These figures are drawn from photographs taken through the four transparent glass windows which is 4.0 m long on the side of the container. Based on these figures, it can be noted that the lateral displacement of the model ground increase gradually in the direction of slope according to the lapse of exciting time, and the unsaturated surface layer seems to deform uniformly in the direction of depth, i.e., the deformations of surface layers are not induced by the deformation of itself but by the deformation of the liquefied layer. Because the lowermost nonliquefied layer is not deformed, the displacement at the lower boundary of the middle liquefied layer is almost zero, and the lateral displacement increases upwards in the liquefied layer. The shape of deformation of liquefied layers seems to be different according to the position of the section and the lapse of exciting time. In the case of Model-6, the horizontal ground neighboring with the inclined surface ground is deformed laterally by the flow of slope, but the deformation decreases far away from the boundary of the slope.

Fig. 3 shows the typical distribution of lateral displacement and strain at the surface in the case of Models-4 and 6. The lateral displacements are estimated by measuring the positions of bench marked points set on the ground surface after each step of excitation, and indicate the magnitude of lateral movement in the direction of slope. The lateral strains are calculated based on the relative displacement and the distance of two bench marked points neighboring each other, and the tensile and compressive strains indicate the spread and shrink of the surface ground, respectively. In the case of Model-4, the middle sand layer doesn't liquefy and the ground flow doesn't occur at the Step-1,

374

but the ground displacements increase according to the increase of input accelerations. Because the displacements are largest in the middle of slope, the tensile strains occur at the upper-side of slope, and on the other hand, the compressive strains occur at the lower-side of one. In the case of Model-6, the displacements are largest at the middle of slope, the tensile strains occur at the slope and the compressive strains occur at the horizontal ground.

Relation between Acceleration, Excess Pore Water Pressure and Ground Flow During Excitation

Fig. 4 shows the typical relation of time histories between input motion, ground acceleration, excess pore water pressure in the liquefied layer and lateral displacement on the surface for Section-A at the Step-2 in the case of Model-6. From this result, it can be seen that the acceleration in the liquefiable layer seems to increase according to increase of excess pore water pressure and becomes maximum just before the excessive pore water pressure approaches to the effective overburden pressure, and decreases to zero gradually after the sand layer liquefies almost perfectly. On the other hand, the lateral displacement of the surface seems to begin to increase just before the excess pore water pressure increase to maximum, and continue to increase according to the lapse of exciting time.

Fig. 5 shows the relation of time history between the lateral displacement at four points on the surface and the excess pore water pressure in liquefied layer at Section A, B, C and D. From these figures, the displacement on the ground surface also can be seen to begin to increase suddenly just after the excess pore water pressure ratio ($\Delta u / \sigma'v$) approaches to the range of 0.8 to 1.0, and also continue to increase gradually during excitation after the complete liquefaction.

Behavior of Ground after Excitation

Fig. 4 also shows the behavior after stopping excitation. After excitation, the excess pore water pressure seems to keep the high pressure constantly by seepage pressure for about 2 minutes, and it takes more than 10 minutes for high excess pore water pressure to decrease to almost zero. On the other hand, the displacement on the ground surface increases a little after excitation, but it seems very small comparing with that during excitation. From the site observation on the liquefaction and lateral ground flow in the past earthquakes, sand boils, water springs and ground movements are reported to continue for a while after the earthquake. However the water spring can be observed at the ground surface for a while after excitation in this experiments, the progress of lateral deformation of ground can't be observed. The cause of the difference on ground flow induced by liquefaction between the actual phenomena at sites during earthquakes and the experiments

375

can not be cleared at present.

Relation between Input Motion and Direction of Ground Flow

Fig. 6(a) shows the direction and quantity of displacement of the bench mark points which are set on the radial lines (Section-0A ~ Section-0I) at the ground surface at the Step-2 in the case of Model-8, comparing the direction of ground flow with that of excitation. From this figure, the surface of the semi-corn shaped slope and the neighboring horizontal ground seem to move almost radially, that is, in the direction of slope. Fig. 6(b) shows the distribution of displacement in the direction of slope for each Section, i.e., the vertical and lateral axes indicate the distance from the center of semi-circle in Fig. 6(a) and the position of Sections in the direction of circumference, respectively, and the shadowed area means the quantity of displacement in the direction of slope. As shown in Fig. 6(b), the displacement of surface ground in the direction of slope seems almost uniformly, except for the Sections neighboring the container which may be affected by the friction of the side wall.

Figs. 7(a) and 7(b) show the relation of time histories between excess pore water pressure (Δu) in the liquefied layer and the lateral displacement (D) at the middle of surface of semi-corn, comparing the meters set at the Section-0A in the direction of excitation with the one set at the Section-0E in the direction
of right-angle of excitation, respectively. Based on Figs. 7(a) and 7(b), the dynamic behavior of the pore water pressure seems similar in each layer, and the displacement at the surface seems to begin to increase at almost the same time just before the perfect liquefaction (see Fig. 4). Because the displacement meter in Fig. 7(a) is set in the direction of excitation and the one in Fig. 7(b) is set in the direction of right-angle of excitation, the displacement at the Section-0A increases vibrationally in the direction of excitation and the one at the Section-0E increases gradually in the direction of right-angle of excitation. This means that the surface ground at the Section-0E is vibrated in the direction of excitation, but the ground flow occurs in the direction of slope. It can be noted that the excitation is not the cause for ground flow but that for soil liquefaction.

Judging from these characteristics concerning the ground flow, it seems that whichever the direction of excitation is, the ground flow due to soil liquefaction is induced towards the direction of slope. Because the direction of slope means that of the initial shear stress enforced by sloped overburden load, the ground seems to flow in the direction of the initial shear stress in the liquefiable layer before excitation.

Effects by Thickness of Liquefiable Layer, Surface Slope and Lower Boundary Slope

Fig. 8 compares the distribution of the lateral displacement and the lateral strains (see Fig.3) for Models-1, 3, 4 and 7, because their test conditions are similar and suitable for investigating the influence by the thickness of liquefiable layer, slopes of surface and/or lower boundary of liquefiable layer on ground flow at the surface. Comparing the results for Model-1 (θ_s= 5 %, θ_b= 0 %, H_l= 700 mm) with that for Model-4 (θ_s= 5 %, θ_b= 0 %, H_l= 350 mm), the lateral displacement and strains for Model-1 are larger than that for Model-4, and so it can be seen that the thickness of the liquefiable layer relates to the ground flow, and the displacement of ground seems to increase according to the increase of the thickness of liquefiable layer. Comparing the results for Model-3 (θ_s= 5 %, θ_b= 5 %, H_l= 350 mm) with that for Model-4, the lateral displacement and strains for Model-3 are larger than that for Model-4, and so it can be noted that the ground with both surface slope and lower boundary slope seems to be induced more than that with only surface slope. Comparing the results for Model-7 (θ_s= 0 %, θ_b= 5 %, H_l= 650~350 mm) with that for Model-1 and Model-4, the lateral displacement and strains for Model-7 are very small, and so it can be indicated that the effect of lower boundary slope by itself seems very small for the ground flow. However, comparing the results for Model-7 with that for Model-3 and Model-4, the lower boundary slope seems to become effective for the ground flow when the surface inclines.

As mentioned above, the influence of the slope of the lower boundary of liquefiable layer to the ground flow seems very small. However, when both ground surface and lower boundary of liquefiable layer incline as the case of Model-3, the slope of the lower boundary of liquefiable layer is likely to increase the ground flow.

Effects by Slope of Ground Surface

Table 3 shows the typical lateral displacement measured on the ground surface at Section-B for all Models and Steps of excitation. In this Table, the ground conditions for Model-2 (θ_s= 7.5 %, θ_b= 0 %, H_l= 350 mm), Model-4 (θ_s= 5 %, θ_b= 0 %, H_l= 350 mm) and Model-5 (θ_s= 2.5 %, θ_b= 0 %, H_l= 350 mm) are similar except for the slope of ground surface. However, the shot of lead is used as the materials for Model-5, and so the slope of surface ground is converted about 10 % as sand.

Comparing the results for Models-2 and 4, it can be seen that the displacement of the ground surface seems to increase according to the increase of the surface slope, but the results for Model-5 doesn't indicate the similar tendency with Models-2 and 4. As for the cause of the difference, it can be estimated that the geotextile sheet which is set only for Model-5 between the shot of lead and the liquefiable sand layer not to mix shot of lead with sand layer, and the cables connecting the meters laid in the ground may affect the ground

flow.

Estimation of Ground Flow

From the above mentioned test results, it is deduced that the slope of surface (θ_s:%) relates to the ground flow, and the ground flow seems to increase according to the increase of the surface slope (see Table 3). And the thickness of liquefied layer (H:cm) where the excess pore water pressure ratio ($\Delta u/\sigma'_v$) is almost equal to 1.0 relates to the ground flow (see Table 3, Fig. 8 and Fig. 5). Further, the duration time of excitation (T:sec) while the ratio ($\Delta u/\sigma'_v$) is almost 1.0 also relates to the ground flow (see fig. 4).

Therefore, these three parameters, i.e., θ_s, H and T can be considered as the main factors relating to the quantity of ground flow (D:cm) measured at the surface. Fig. 9 shows the relation between the parameter $D/(T \cdot H)$ [$*10^{-4}/\text{sec}$] and the slope of surface (θ_s : %) at the Sections A, B, C and D at the Steps-1 and 2 for all Models excepting Model-8. The slope of surface is calculated as the average slope around the measured point on the surface at each Section. Based on this figure, it can be indicated that the parameter $D/(T \cdot H)$ has a tendency to increase according to the increase of the slope θ_s.

CONCLUSION AND FUTURE RESEARCH

Based on the experimental study on the lateral ground flow due to soil liquefaction using shake table, the following can be concluded;

(1) The pore water pressure in the liquefiable layer increases firstly during excitation, preceding the lateral ground deformation, and the lateral displacement of the inclined surface begins to increase remarkably when the excess pore water pressure ratio ($\Delta u/\sigma'_v$) in the underlying layer exceeds about the range of 0.8~1.0, and continues to increase according to the lapse of exciting time.

(2) The lateral deformation occurs only in the liquefied layers, and the unsaturated surface layer is displaced by the deformation of underlying liquefied layers.

(3) The ground seems to be deformed by shear force during excitation and the deformation mode of ground in the direction of depth differs according to the position and the lapse of exciting time.

(4) Just after stopping the excitation, the excess pore water pressure in the liquefied layer keeps the high pressure by seepage for a while and begins to decrease gradually. On the other hand, the lateral ground flow almost stops.

378

(5)The lateral ground flow is affected severely by the slope of ground surface, and the slope of the lower boundary of the liquefiable layer doesn't affect so much by itself, but affects when the ground surface also inclines.

(6)The direction of excitation has no significant influence to the direction of the lateral flow of ground, and the lateral ground deformation is related to the direction of the slope of surface, i.e., the direction of initial shear stress in the liquefiable layer before excitation. The excitation doesn't relate with the direct cause for ground flow but that for soil liquefaction.

(7)The lateral ground flow at the ground surface (D) in this series of experiments can be expressed by the slope of surface (θ_s), the thickness of almost perfectly liquefied layer (H) and the duration time of excitation after almost complete liquefaction (T). The relation between the parameter $D/(T \cdot H)$ and θ_s can be indicated as Fig. 9.

As mentioned above, the fundamental characteristics on ground flow due to soil liquefaction are investigated experimentally and the principal factors which cause the ground flow are clarified qualitatively. However, it should be noted that the results are derived from the limited conditions for shake table tests and further investigation should be executed from now on.

The subjects in the future can be considered as follows:

(1)Establishment of the test conditions considering the actual site conditions during earthquakes, for example, the scale of a container, the relative density of liquefiable layer and the ground water level.

(2)Investigation of the cause of the difference between the experimental characteristics and the actual phenomena observed during earthquakes, for example, the progress of the ground flow after excitation.

(3)Investigation of the influence of ground flow on the structures, for example, pile foundations of bridges.

(4)Application of the effect of ground flow to the specifications for earthquake resistant design of structures.

ACKNOWLEDGEMENTS

REFERENCES

Hamada, M., Yasuda, S. and Wakamatsu, K. (1988), "Case Study on Liquefaction-Induced Ground Failures During Earthquakes in Japan", Proc. of First Japan-United States Workshop on Liquefaction, Large Ground Deformation and Their Effects on Lifeline Facilities, Tokyo.

Hamada, M., Yasuda, S., Isoyama, R. and K. Emoto (1986), "Observation of Permanent Ground Displacements Induced by Soil Liquefaction", Proc. of JSCE, No.376／Ⅲ-6, pp.211-220, (in Japanese).

Japan Road Association (1980,1990), "Part V Earthquake Resistant Design of Specifications for Highway Bridges" (in Japanese).

Sasaki,Y., Tokida, K., Matsumoto, H. and S. Saya (1990), "Experimental Study on Lateral Flow of Ground Induced by Soil Liquefaction", The Eighth Japan Earthquake Engineering Symposium 1990, Tokyo.

Table 1 Characteristics of Ground Models

Model No.	Slope of Surface θ_s (%)	Slope of Lower Boundary of Liquefiable Layer θ_b (%)	Thickness of Liquefiable Layer H_L (cm)	Liquefiable Layer Unit Weight γ_{t1} (tf/m³)	Unsaturated Surface Layer Unit Weight γ_{t2} (tf/m³)	Materials
1	5	0	70	1.93	1.49	sand
2	7.5	0	35	1.88	1.37	sand
3	5	5	5~35	1.93	1.57	sand
4	5	0	35	1.90	1.49	sand
5	2.5	0	35	2.06	5.71	shot of lead
6	0~5	0	35	2.00	1.48	gravel
7	0	5	35~65	1.93	———	———
8	15	0	25	1.84	1.36	gravel

Model-1~5

Model-6

Model-7

Model-8

Fig. 1 Ground Models and Measurements

Table 2 Characteristics of Materials used for the Experiments

1) Sand (Mt. Sengen-yama Sand)

Specific Gravity of Soil Particle G_s	2.655
Maximum Void Ratio e_{max}	0.976
Minimum Void Ratio e_{min}	0.596
Maximum Grain Size (mm)	4.76
Mean Grain Size D_{50} (mm)	0.27
Coefficient of Uniformity U_c	1.37

2) Shot of Lead

Specific Gravity of Soil Particle G_s	11.34
Mean Grain Size D_{50} (mm)	2.00

3) Gravel

Maximum Grain Size (mm)	9.52

Table 3 Input Motion and Lateral Displacement

Model No.	Shaking Step No.	Maximum Acceleration at Table α_{max} (gal)	Lateral Displacement at Surface (Section B) (mm)
1	1	80	61
	2	110	169
	3	160	118
	4	220	56
2	1	65	28
	2	110	144
	3	155	165
	4	105	62
3	1	65	68
	2	110	156
	3	90	87
	4	85	35
4	1	65	6
	2	95	72
	3	140	142
	4	190	44
5	1	60	1
	2	101	4
	3	152	210
	4	154	69
6	1	60	1
	2	104	101
	3	153	106
	4	154	54
7	1	64	-2
	2	103	17
	3	154	11
	4	151	6
8	1	51	14
	2	94	11
	3	95	5
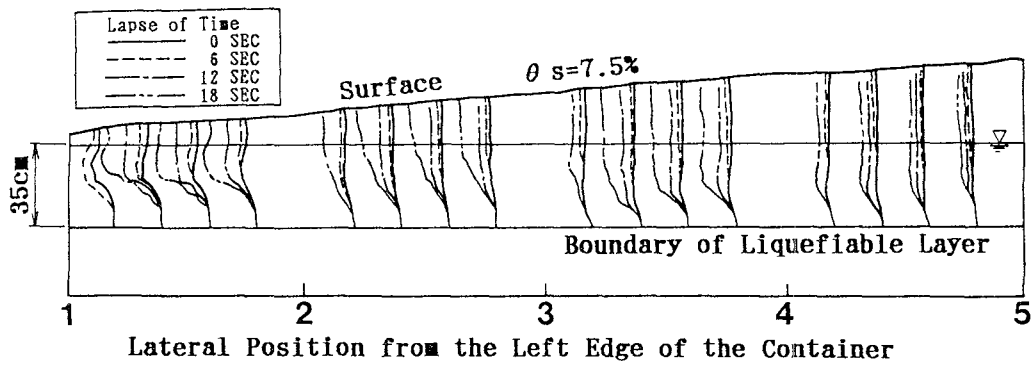
(a) Model-2 (Step-2: α_{max}=110gal)
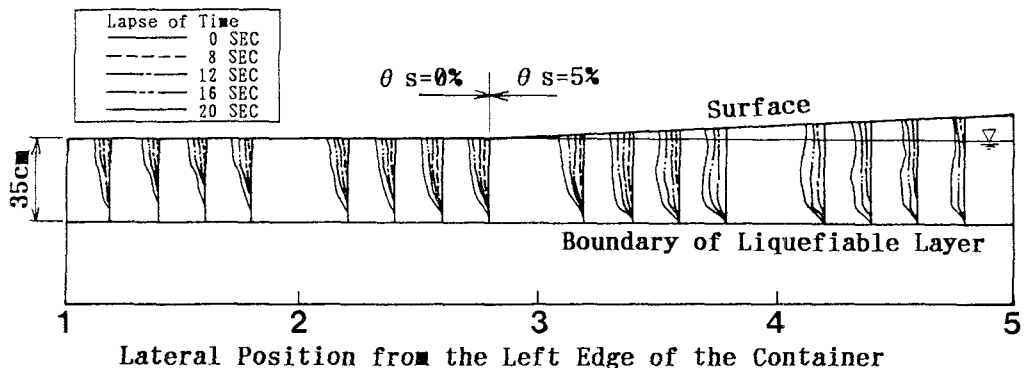
(b) Model-6 (Step-2: α_{max}=104gal)

Fig. 2 Time History of Lateral Deformation
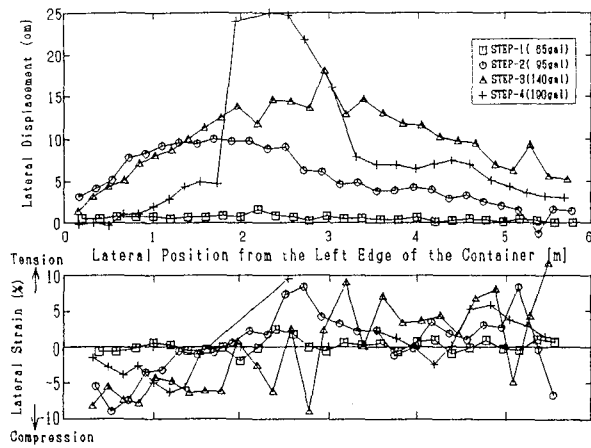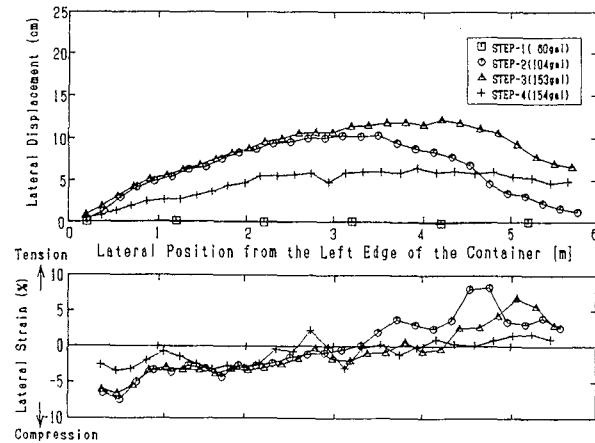
(a) Model-4 (θ_s=5%, θ_b=0%, H_1=350mm)   (b) Model-6 (θ_s=0,5%, θ_b=0%, H_1=350mm)

Fig. 3 Lateral Deformation of Ground Surface Measured by Bench Mark Points

(a) Lateral Displacement of Surface

(b) Pore Water Pressure of in the middle
Liquefiable Layer

(c) Response Acceleration of Liquefiable Layer

(d) Acceleration of Input Excitation
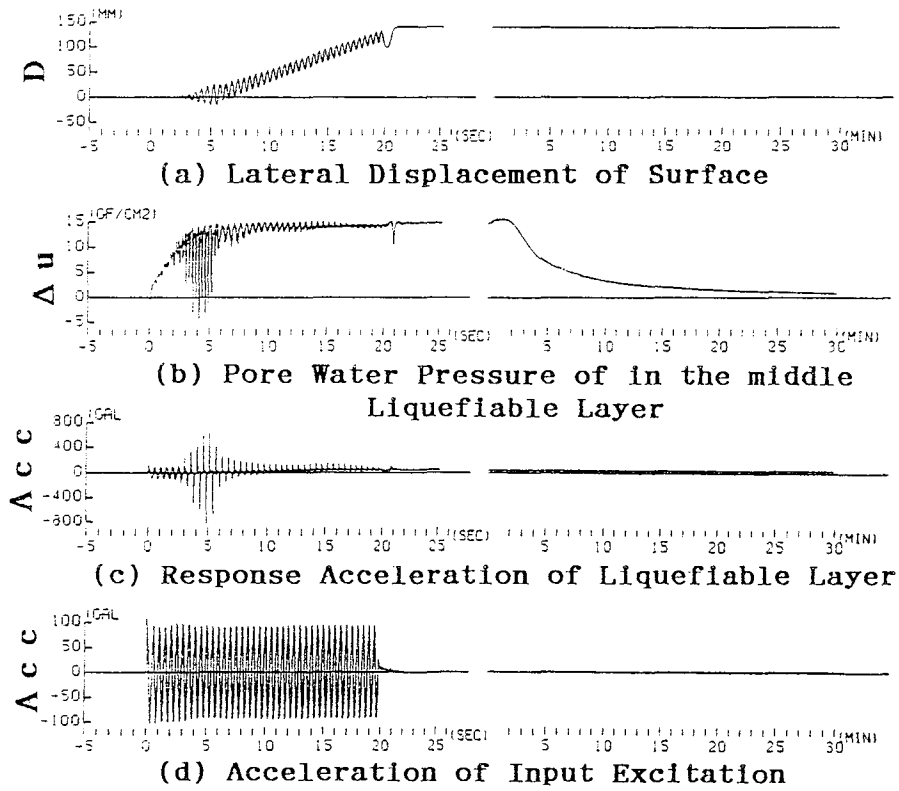
Fig. 4 Relation Between Lateral Displacement of Surface, Pore
Water Pressure and Acceleration of Liquefiable Layer
(Model-6, Step-2, Section-A)

(a)Section-A   (b)Section-B   (c)Section-C   (d)Section-D
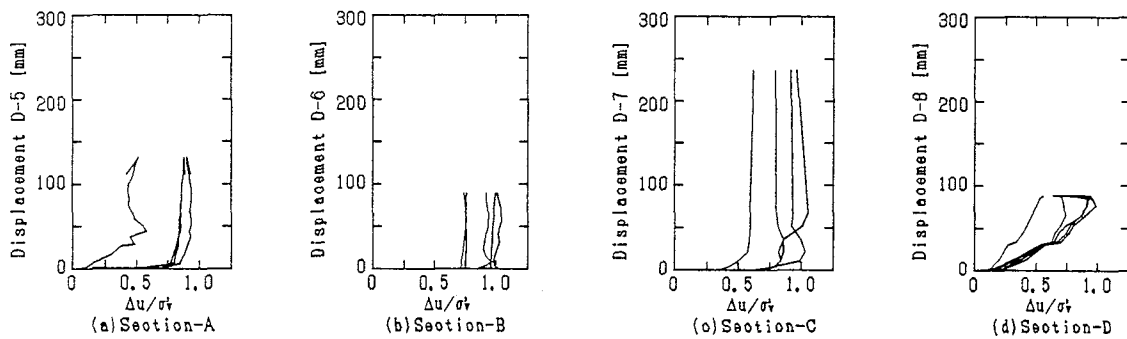
Fig. 5 Pore Water Pressure Ratio and Displacement of Surface
(Model-6, Step-2)

383
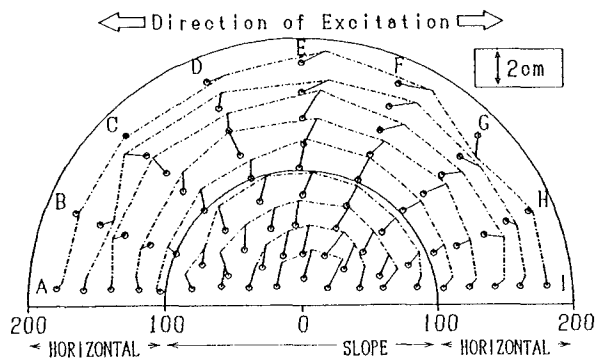
(a) Direction of Ground Flow
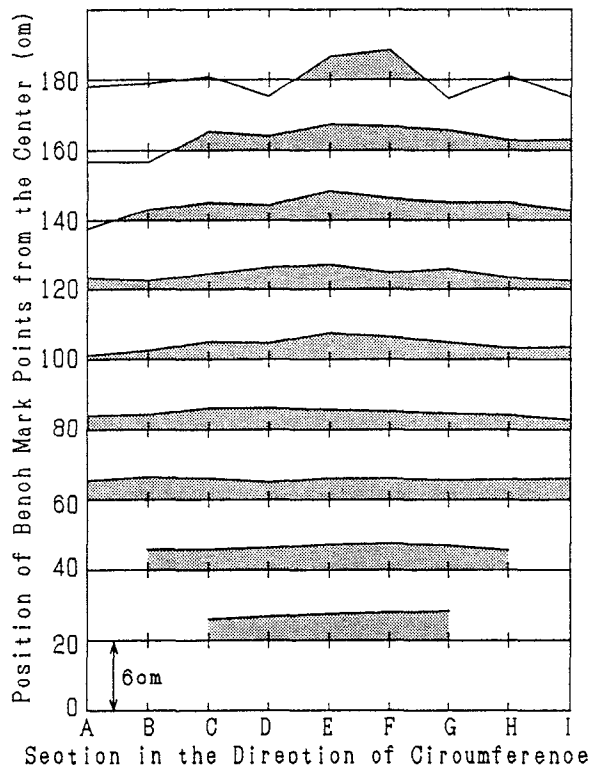
(b) Distribution of Ground Flow

Fig. 6 Directions of Ground Flow and
Input Motion (Model-8, Step-2)

Lateral Displacement of Surface

Pore Water Pressure in the
Liquefied Layer
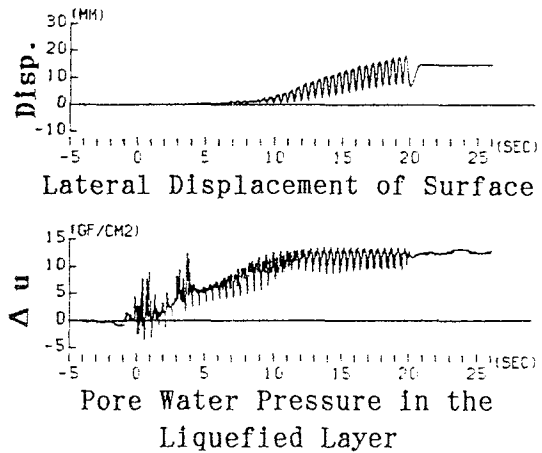
(a) At the Section-OA in the direction
of excitation

Lateral Displacement of Surface

Pore Water Pressure in the
Liquefied Layer
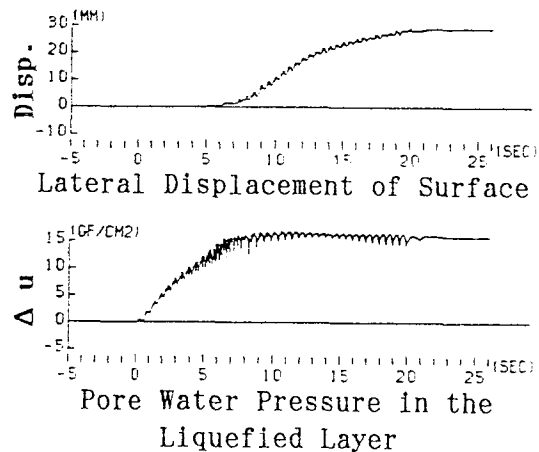
(b) At the Section-OE in the direction
of right-angle of excitation

Fig. 7 Time History of Pore Water
Pressure and Displacement
(Model-8, Step-1)

384
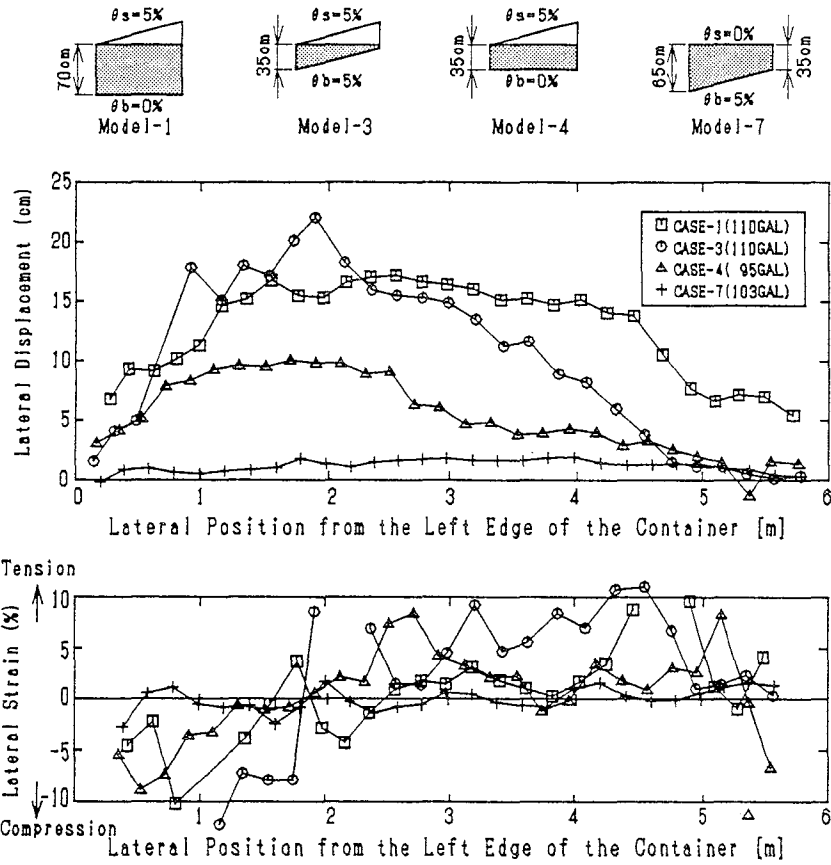
Fig. 8 Influence by Thickness and Slopes
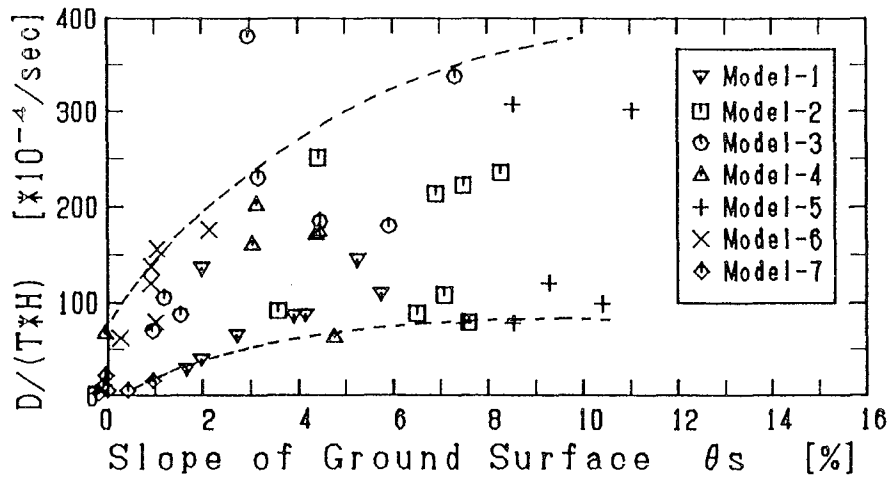
Fig. 9 Lateral Ground Flow and Slope of Surface

LIQUEFACTION OF SANDY SOIL DEPOSITS
- ANALYSIS AND EXPERIMENTS -

by

NAOTO OHBO[2], YOICHI NOJIRI[1], KAZUO HAYASHI[3]
and KENJI UENO[3]

1) Assistant Director
2) Senior Research Engineer
3) Research Engineer
Kajima Institute of Construction Technology

and

JEAN H. PREVOST

Professor of Civil Engineering and Operation Research
Princeton University

ABSTRACT

Numerous constitutive laws have been proposed by researchers for expressing the behavior of sand as an elastoplastic material in analyses of liquefaction which occurs in sandy soil deposits during earthquakes. Sophisticated engineering judgment is often required in defining the required material constitutive parameters for such analyses. The one-dimensional liquefaction analysis program "DYNA1D" is based on the three-dimensional multi-surface plasticity theory and all the required material parameters can be obtained from triaxial compression and extension tests.

In this paper, the basic components of the analysis procedure namely, the multi-surface theory and the methods of establishing the material parameters are presented, together with the results of liquefaction experiments using a shaking table and computed results obtained in the simulation of the liquefaction tests by DYNA1D. Comparison of the computed results and test results indicates that the trends in the excess pore water pressure ratio distribution and shear strain distribution are represented satisfactorily by the simulation analysis.

INTRODUCTION

Considerable attention has been given in the past decade to the develop-

ment of elastoplastic constitutive equations for soil media. The most popular and most widely used models are Cap models [1,3,20,22], based on classical isotropic plasticity theory with associated flow, and are variations and refinements of the basic Cap model pioneered by Drucker, Gibson and Henkel[4]. The most obvious limitations of these Cap models are: (1) They do not adequately model soil stress-induced anisotropy; (2) They are not applicable to cyclic loading conditions, and therefore they are not applicable for liquefaction analyses of sandy soil deposits. In order to account for hysteretic effects, more elaborate plastic models based on a combination of isotropic and kinematic plastic hardening rules have recently been proposed (see e.g., [5,13,16]). However, although many different models have been proposed, many are not practical because of unrealistic requirements for their use [9] such as: (1) sophistication in required soil tests to determine parameters, and (2) user familiarity with the constitutive model.

DYNA1D [15] is a finite element computer program for nonlinear seismic site response analysis. Dry, saturated and partially saturated deposits can be analyzed. DYNA1D has been developed to allow site response analyses to be performed taking into account: (1) the nonlinear, anisotropic and hysteretic stress strain behavior of the soil materials: and (2) the effects of the transient flow of the pore water through the soil strata. The procedures used (field [2] and constitutive equations [16-18]) are general and applicable to multidimensional situations. The goal was to provide a realistic and reliable analysis procedure for use in engineering design practice. Therefore, although no sacrifices have been made as to the rigor and generality of the field and constitutive equations used, attempt have been made to simplify as much as possible, the use of the code. For that purpose, features such as automatic (i.e., user transparent) initialization procedures have been implemented. Also, required material constitutive parameters are identified in terms of "classical" soil mechanics parameters (e.g., elastic moduli, friction angles, permeabilities, etc.), and do not require user's familiarity with the constitutive model nor sophisticated soil test data.

In this paper the multi-yield plasticity model implemented in DYNA1D is first described. The model is applicable to both cohesive and cohesionless soils, and has been tailored to reflect the strong dependency of the shear dilatancy on the effective stress ratio in both cohesionless [11,21] and cohesive [6] soils. The procedure used to generate the required material parameters from the results of conventional triaxial soil tests, is presented. Validation of the analysis procedure is then provided. Validation was first performed by analyzing data obtained at the Wildlife Liquefaction site [10]. Here further validation is provided by analyzing shaking table data. Measured and computed test results are presented and compared.

As for notation, boldface letters denote vectors, second and fourth-order tensors in three dimensions. A superposed dot denotes the (solid) material derivative, the symbol $|\,.\,|$ the norm of a vector or tensor, and the prefix tr

the trace. The summation over repeated indices is implied, and the following notation is used: $a:b = tr \ a \cdot b = a_{ij} \ b_{ji}$. All stresses are effective stresses.

BASIC THEORY

Constitutive Equations:

The constitutive equations are written in the following form:

$$\dot{\sigma} = E : (\dot{\varepsilon} - \dot{\varepsilon}^P) \tag{1}$$

where $\dot{\sigma}$ =effective (Cauchy) stress tensor, $\dot{\varepsilon}$ =rate of deformation tensor (= symmetric part of the spatial solid velocity gradient); $\dot{\varepsilon}^P$ =plastic rate of deformation tensor; and a dot denotes the (solid) material derivative. In Eq. 1, E is the fourth-order isotropic elastic coefficient tensor, viz.,

$$E_{ijkl} = (B - \frac{2G}{3}) \delta_{ij} \delta_{kl} + G (\delta_{ik} \delta_{jl} + \delta_{il} \delta_{jk}) \tag{2}$$

where B=elastic bulk modulus; G=elastic shear modulus; and δ_{ij} =kronecker delta.

Yield Function:

The yield function is selected of the following form:

$$f(\sigma, \alpha, M) = |s - \overline{p} \ \alpha| + \sqrt{\frac{2}{3}} M \overline{p} = 0 \tag{3}$$

where

$$|s - \overline{p} \ \alpha| = [tr (s - \overline{p} \ \alpha)^2]^{1/2} \tag{4a}$$

$$s = \sigma - p \ \delta \qquad \textit{deviatoric stress tensor} \tag{4b}$$

$$p = \frac{1}{3} tr \ \sigma \qquad \textit{effective mean normal stress} \tag{4c}$$

$$\overline{p} = (p - a) \tag{4d}$$

with a =attraction (=$c / \tan \phi$; c =cohesion; ϕ =friction angle); α =kinematic deviatoric tensor defining the coordinates of the yield surface center in deviatoric stress subspace; M=material parameter. The yield function plots as a conical yield surface in stress space with its apex located along the hydrostatic axis at the attraction. For cohesionless soils a =0 and the apex of the cone is at the origin. Unless α =0, the axis of the cone does not coincide with the space diagonal. The cross section of the yield surface by any deviatoric plane (=constant) is circular with radius $R = -\sqrt{\frac{2}{3}} M \overline{p}$. Its

389

center does not generally coincide with the origin but is shifted by the amount $\overline{p}\,\alpha$. This is illustrated by Figure 1 in the principal stress space. The outer normal Q to the yield surface:

$$Q = Q' + Q'' \,\delta \qquad (5)$$

is computed as follows (from Eq. 3):

$$Q = \partial_\sigma f = \frac{(s - \overline{p}\,\alpha)}{|s - \overline{p}\,\alpha|} + \frac{1}{3}\left[\sqrt{\frac{2}{3}}\,M - \frac{(s - \overline{p}\,\alpha):\alpha}{|s - \overline{p}\,\alpha|}\right]\delta \qquad (6)$$

Flow Rule:
The plastic strain rate is defined as follows:

$$\dot{\varepsilon}^P = <\dot{\lambda}> P \qquad where \qquad P = P' + P''\,\delta \qquad (7)$$

and $\dot{\lambda}$ =plastic loading function. The plastic potential is selected such that the deviatoric plastic flow be associative. However, a non associative flow rule is used for its dilatational component, and in the following:

$$P' = Q' \qquad 3P'' = \frac{(\eta/\overline{\eta})^2 - 1}{(\eta/\overline{\eta})^2 + 1} \qquad (8)$$

where $\eta = (\frac{3}{2}s : s)^{1/2}/\overline{p}$ =mobilized stress ratio; and $\overline{\eta}$ =material parameter. When $\eta < \overline{\eta}$, 3P">0 and plastic compaction takes place, whereas when $\eta > \overline{\eta}$, 3P">0 and plastic dilation takes place. The case $\eta = \overline{\eta}$ corresponds to no plastic volumetric strains. This is illustrated in Figure 2. In the following, $\overline{\eta} = \overline{\eta}_C$ when $tr\ s^3 < 0$, and $\overline{\eta} = \overline{\eta}_E$ when $tr\ s^3 > 0$.

Hardening Rule:
A purely deviatoric kinematic hardening rule is adopted and in the following,

$$\overline{p}\,\dot{\alpha} = <\dot{\lambda}> \frac{H'}{Q':\mu}\,\mu \qquad (9)$$

where H' =plastic modulus; and μ =(deviatoric) tensor defining the direction of translation. Note that the direction of translation remains arbitrary at this stage, and thus may be selected independently of any formal plasticity constrains.

Consistency Condition:
The plastic loading function $\dot{\lambda}$ (Eqs 7 and 9) is determined by the consistency condition which emanates from time differentiation of Eq. 3, viz.,

$$\dot{f} = Q:\dot{\sigma} - \overline{p}\,Q':\dot{\alpha} = 0 \qquad (10)$$

combining Eqs 1, 7 and 9, one finally gets:

$$\dot{\lambda} = \frac{1}{H'} \, Q : \dot{\sigma} = \frac{1}{H' + H_0} \, Q : E : \dot{\varepsilon} \tag{11}$$

with

$$H_0 = Q : E : P = 2G + B \, (3P'') \, (3Q'') \tag{12}$$

Multi-Yield Model:

In order to allow for the adjustment of the plastic hardening rule to any kind of experimental data, for example, data obtained from axial or simple shear soil tests, a collection of nested yield surfaces (Mroz, 1967) is used. The yield surfaces are all similar conical surfaces (Eq. 3). Upon contact, the yield surfaces are to be translated by the stress point. In order to avoid overlappings of the surfaces (which would lead to a nonunique definition of the constitutive theory), the direction of translation μ (Eq. 9) of the active yield surface is selected such that

$$\mu = \frac{M'}{M} \, (s - \bar{p} \, \alpha) - (s - \bar{p} \, \alpha') \tag{13}$$

where M' and α' are the plastic parameters associated with the next outer surface (M'>M). This is illustrated in Figure 3.

Remarks:

The dependence of the moduli upon the effective mean normal stress is assumed of the following form

$$G = G_1 \, (\frac{p}{p_1})^n \qquad B = B_1 \, (\frac{p}{p_1})^n \qquad H' = H'_1 \, (\frac{p}{p_1})^n \tag{14}$$

respectively, where n = experimental parameter (n = 0.5 for most cohesionless soils, and n = 1 for cohesive soils (Richard et al., 1970)); p_1 = reference effective mean normal stress. The assumed dependence of the elastic moduli on the material state renders the material's elasticity (Eq. 1) hypoelastic.

MODEL PARAMETERS IDENTIFICATION

In addition to the usual state parameters (i.e., mass density, porosity, permeability), the constitutive parameters required to model the behavior of the solid porous soil skeleton are as summarized hereafter:
  (i) Elastic Parameters:
      · Shear Modulus: G
      · Bulk Modulus: B
      · Power Exponent: n

(ii) Plastic Parameters:
- Dilation Parameters: $\overline{\eta}_C, \overline{\eta}_E$
- Yield Surfaces Parameters:
  - Position: α
  - Size: M
  - Plastic Modulus: H'

The constitutive parameters required to characterize the behavior of any given soil are to be determined by fitting the model to available experimental soil test data.

The (hypo-)elastic shear G and bulk B moduli (low strain moduli) are best determined through seismic (wave velocity)-type measurements. Their dependence on the mean stress with the power of n (Eq. 14) is empirical in nature, and is suggested by Richard et al.(1970). Correlation formula (relating moduli to initial void ratio, confining stress, overconsolidation ratio, etc...) based on the results of resonant column tests are also available (see, e.g., Hardin and Drenevitch (1972)). Typically, $B = 2G/3$.

All required plastic model parameters can be derived entirely from the results of conventional soil tests (e.g., "triaxial" or simple shear soil tests). In the following, a systematic calibration procedure of the required plastic parameters from triaxial soil test data is presented.

"Triaxial" Soil Test:

In this section, attention is restricted to the "triaxial" soil test for which the two effective (lateral) principal stresses are equal, $\sigma_2 = \sigma_3$. In order for the soil specimen to deform in an axisymmetric fashion ($\varepsilon_2 = \varepsilon_3$), the axes of loading must coincide with the principal axes of the anisotropic tensor α, and $\alpha_2 = \alpha_3$. In the following, in order to follow common usage in soil mechanics, compressive stresses and strains are counted as positive and the discussion is presented in terms of the following stress and strain variables:

$$q = (\sigma_1 - \sigma_3) \qquad p = (\sigma_1 + 2\sigma_3)/3 \qquad (15)$$

$$\overline{\varepsilon} = (\varepsilon_1 - \varepsilon_3) \qquad \varepsilon_v = \varepsilon_1 + 2\varepsilon_3 \qquad (16)$$

where the reference axes 1 and 3 are assumed to be in the vertical and horizontal directions, respectively Eq. 3 then simplifies to:

$$f(\sigma, \alpha, M) = f(\eta, \alpha, M) = \eta - (\alpha \pm M) = 0 \qquad (17)$$

where $\alpha = (\alpha_1 - \alpha_3) = 3\alpha_1/2,$ and

$$\eta = q/\overline{p} = \textit{Mobilized Stress Ratio} \qquad (18)$$

The trace of the yield surface onto the triaxial (q, p) stress plane con-

sists of two straight lines of slopes $(\alpha + M)$ and $(\alpha - M)$, respectively. The two lines are anchored along the hydrostatic p - axis at location $p = -\alpha$. This is illustrated in Figure 4. Yielding, accordingly with the proposed model, is therefore directly related to the mobilized stress ratio, η which is related to the mobilized friction angle ϕ commonly used in soil mechanics, viz.,

$$\sin\phi = \frac{|(\sigma_1 - \sigma_3)|/2}{a + (\sigma_1 + \sigma_3)/2} \tag{19}$$

by the following relation (combining Eqs 15, 18 and 19):

$$\sin\phi = \frac{3|\eta|}{6 + \eta} \tag{20}$$

inversely, one can also write:

$$\eta_C = \left(\frac{q}{p}\right)_C = +\frac{6\sin\phi_C}{3 - \sin\phi_C} = \alpha + M \qquad \text{in compression tests} \tag{21a}$$

$$\eta_E = \left(\frac{q}{p}\right)_E = -\frac{6\sin\phi_E}{3 + \sin\phi_E} = \alpha - M \qquad \text{in extension tests} \tag{21b}$$

where ϕ_C and ϕ_E=mobilized friction angles in compression and extension loading conditions, respectively.

Model calibration is to be achieved by matching directly the model equations (Eqs 1-12) with the experimental test data. For the triaxial soil test the stress-strain relations (Eq. 1) simplify to:

$$\frac{\dot{\bar{\varepsilon}}}{\dot{q}} = \frac{1}{2G} + \frac{1}{H'}(1 - \eta\dot{p}/\dot{q}) \tag{22}$$

$$\frac{\dot{\varepsilon}_v}{\dot{p}} = \frac{1}{B} \pm \frac{1}{H'}\sqrt{\frac{2}{3}}\frac{1 - (\eta/\bar{\eta})^2}{1 + (\eta/\eta)^2}(\dot{q}/\dot{p} - \eta) \tag{23}$$

for the shear and dilatational components, respectively. In Eq. 23, the plus (+) sign is for compression, and the minus (-) sign for extension loading conditions; $\bar{\eta} = \bar{\eta}_C$ in compression; and $\bar{\eta} = \bar{\eta}_E$ in extension. Yielding, i.e., plastic flow, occurs on the yield surface f (Eq. 17) with associated plastic parameters (α, M, H') when the mobilized stress ratios $\eta = (\alpha \pm M)$, is positive in compression ($\eta = \eta_C = \alpha + M$), and negative in extension ($\eta = \eta_E = \alpha - M$), respectively. The plastic modulus H' associated with the yield level defined by the parameters α and M is obtained as follows. Given the experimental shear stress strain curve(q vs $\bar{\varepsilon}$), for the particular stress path (q vs p) followed in the test, the functional dependence of the plastic modulus H' on the mobilized stress ratio η, i.e., $H' = H'(\eta)$ in both com-

pression and extension loading conditions is obtained by inverting Eq. 22 as:

$$H' = \frac{2\,G\,H}{2\,G\,-\,H}\,(\,1\,-\,\eta\,/\,s\,)\tag{24}$$

where $s = \dot{q}\,/\,\overset{\circ}{p}$ =slope of the effective stress path followed in the (q,p) plane; and $H = \dot{q}\,/\,\dot{\overline{\varepsilon}}$ =slope of the shear stress-train curve. Clearly, for monotonic stress paths:

$$H\,=\,H(\,q,p\,)\,=\,H(\,\eta\,)\qquad and\qquad s\,=\,s(\,q,p\,)\,=\,s(\,\eta\,)\tag{25}$$

and therefore, the variation of the plastic modulus H' with the mobilized stress ratio η can be computed from the test results. This is illustrated in Figure 4.

The proposed constitutive model approximates the (measured) smooth functional dependence of the plastic modulus H' on the stress ratio η, by requiring that H' be constant between each selected yield levels. Evidently, the degree of accuracy achieved by such a representation of the experimental curve H'=H'(η) is directly dependent upon the number of selected yield levels. For a given H', the associated yield parameters (α, M), are computed from the corresponding mobilized stress ratios $\eta = \eta_C$ in compression ($\dot{\eta}$ >0), and $\eta = \eta_E$ in extension ($\dot{\eta}$ <0), respectively, as (from Eq. 21):

$$\alpha = (\eta_C + \eta_E)\,/\,2\qquad\qquad M = (\eta_C - \eta_E)\,/\,2\tag{26}$$

therefore, once the number of yield levels has been selected, the identification of the plastic parameters (α, M, H') associated with each yield level is straightforward and can easily be automated [15].

The dilation parameters $\overline{\eta}_C$ and $\overline{\eta}_E$, are obtained from Eq.23, viz.,

$$\dot{p}\,=\,B\,\dot{\varepsilon}_v\qquad when\quad \eta\,=\,\overline{\eta}\tag{27}$$

In undrained tests (constant volume tests), they correspond to the effective stress ratios at which the effective stress path changes concavity (i.e., $s = \dot{q}\,/\,\dot{p} = \infty$). In drained tests, they are close to the effective stress ratios at which the material experiences maximum compaction. The dilation parameters are related to the dilatancy angles $\overline{\phi}_C$ and $\overline{\phi}_E$ commonly used in soil mechanics as (from Eq. 21)

$$\overline{\eta}_C\,=\,+\,\frac{6\,sin\,\overline{\phi}_C}{3\,-\,sin\,\phi_C}\qquad\qquad \overline{\eta}_E\,=\,-\,\frac{6\,sin\,\overline{\phi}_E}{3\,+\,sin\,\phi_E}\tag{28}$$

Typically, (see e.g., [21]) $\overline{\phi}_C = \overline{\phi}_E = 30$ degrees (which in cohesionless soils corresponds to $\dfrac{\sigma_j}{\sigma_{jjj}} = 3$), and (from Eq. 28) $\overline{\eta}_C = 1.2$; $\overline{\eta}_E = -0.86$.

LIQUEFACTION TESTS USING SHAKING TABLE

The liquefaction tests were performed using the shaking table, in order to investigate the adaptability of DYNA1D and the conditions of the liquefaction observed in the tests. A shear box was used for obtaining simple shear deformation in the model ground. The shear box is composed of nine shear frames, each joined with bearings to prevent the friction in the shaking direction and reduce the movements in the other two directions perpendicular to the shaking direction.

Outline of Experiment:

The model ground was made by Fujigawa sand. The grain size distribution of Fujigawa sand is shown in Figure 5. Fujigawa sand was placed in a shear box with a base 2.5 m by 1.0 m and a height of 1.0 m and compacted with a vibroplate to obtain a relative density of 60%. The vibroplate compaction stress was 0.6 kgf/cm^2. The model ground was then saturated with water.

Accelerometers A1~A13, pore water pressure meters W1~W13 and non-contact deformation meter DV were installed at the positions indicated in Figure 5(a).

Vibration excited tests were implemented using a sinusoidal waves (4 Hz) and two seismic waves (Hachinohe Wave and TAFT Wave), their maximum amplitudes to be adjusted as shown in Table 2. The maximum excess pore water pressure ratios (excess pore water pressure/initial effective stress) observed at point W4 are given in Table 2. It can be seen from this table that the maximum excess pore water pressure ratio increases with the input acceleration within the same input wave. The test case, in which the excess pore water pressure ratio reached 1, was selected for the purpose of simulating the liquefaction phenomena by use of the liquefaction analysis program DYNA1D. The dynamic behavior characteristics of the model ground observed in this test case are to be discussed in the following.

Dynamic Behaviors of Model Ground:

Figure 7 shows the vertical distributions of the maximum excess pore water pressure ratios on the cross-section a-a at the center of the model ground and on the cross-section b-b 60 cm away from it subjected to a sinusoidal wave (4 Hz, 200 gal). The distributions of the maximum excess pore water pressure ratios on the two cross-sections were in good agreement and, therefore, it was confirmed that the excess pore water pressures had risen uniformly throughout the model ground.

The time histories of the settlements of the ground, measured with the non-contact deformation meter (measurement point: DV) and the time histories of the pore water pressure meter (measurement point: W3), are shown in Figure 8. It can be observed from this figure that negative excess pore water pressure occurred during the first 4 seconds of excitation and the ground surface rose at the same time. This phenomena is due to the model ground being dense.

The vertical distributions of the excess pore water pressure ratios at one second intervals in the cross-section a-a of the model are shown in Figure 9. The excess pore water pressure ratio is negative in the whole of the model ground for the first 3 seconds of excitation and is still negative at 5 seconds at around 20 cm in depth. At 10 seconds of excitation, the excess pore water pressure ratio has risen to around 1.0 (liquefaction occurring) at depths of between 40 and 60 cm.

Figure 10 shows the vertical distributions of the shear strain[14] at 1 second intervals obtained from the deformation time histories which in turn are determined by double-integrating the acceleration response time histories in the cross-section a-a of the model ground. The shear strain was the largest at around 70 cm in depth during the excitation.

SIMULATION OF LIQUEFACTION TESTS BY DYNA1D

Assuming the behavior of the model ground to be one-dimensional in the test case subjected to the sinusoidal wave (4 Hz, 200 gal). This test case was simulated by use of the one-dimensional liquefaction analysis program DYNA1D. The following shows the comparison of the test results and the computed results obtained using DYNA1D.

Analysis Model and Required Material Constitutive Parameters:
The one-dimensional model of the ground used in the liquefaction tests is shown in Figure 6(b). The model consists of 22 nodes and 21 elements, and the boundary conditions were fixed at the bottom, free at the top and semi-infinite at the sides. The acceleration response wave observed at point A1 was used as the input wave.

The required material constitutive parameters are determined based on the methods as given in Table 1. The total number of yield surfaces, n, was set at 20, assuming there to be yield surfaces at intervals of 0.25% of the shear strain.

Time history response analysis using input waves was computed after the stress condition in model ground was determined by taking account of the stress history due to compaction.

Comparison between Experimental and Computed Results:
Figure 11 shows the computed vertical distributions of the excess pore water pressure ratios at 1 second intervals. In this figure, the excess pore water pressure ratios are negative for the first 4 seconds of excitation, with its peak around 20 cm in depth. On the other hand excess pore water pressure ratios are observed to be around 0.9 at depth of between 40 and 60 cm at 10 seconds of the excitation, indicating that liquefaction condition have been nearly reached. The excess pore water pressure distributions obtained through the liquefaction analysis (Figure 11) have the same tendency as the observed

results (Figure 9) in the occurrence of the negative excess pore water pressure ratios, the rise of the excess pore water pressure ratios and the vertical distribution of the maximum excess pore water pressure ratios.

The vertical distributions of the shear strain τ_{13} at 1 second intervals, as obtained by DYNA1D, are shown in Figure 12, where the subscripts 1 and 3 mean the vertical and horizontal directions, respectively, in the coordinate system in Figure 6. It can be seen from this figure that the peak shear strains are observed at a depth of around 70 cm during excitation. By comparing the above results with the results through the actual tests shown in Figure 10, it can be seen that both results have a close correspondence to each other in the shear strain distributions.

Figure 13 compares the time history response wave forms of the excess pore water pressures at observation points W2 and W3 obtained in the experiment and the corresponding ones through the analysis. The computed results compares well with the tested ones.

CONCLUSION

The liquefaction test on the shaking table has been carried out for the purpose of checking the adaptability of the liquefaction analysis program "DYNA1D" using the constitutive law of soil proposed by J. H. Prevost.

As a result, it was confirmed that the liquefaction analysis using DYNA1D is capable of closely simulating the occurrence of negative excess pore water pressure ratios, the vertical distribution of the maximum excess pore water pressure ratios, the trends in the vertical distribution of the maximum shear strains and the time history response of the excess pore water pressure obtained in the liquefaction tests.

The study reported here was conducted as a part of the joint research between Kajima Corporation and Princeton University.

REFERENCES

1. Baladi, G. Y. and Rohani, B., "Elastic-Plastic Model for Saturated Sand", J. Geotech. Eng. Div. ASCE, Vol.105, No.GT4, April 1979, pp.465-480.
2. Biot, M. A., "Mechanics of Deformation and Acoustic Propagation in Porous Media", J. App. Phys., Vol.33, No.4, 1962, pp.1482-1498.
3. DiMaggio, F. L. and Sandler, I.S., "Material Models for Granular Soils", J. Eng. Mech. Div., ASCE, Vol.97, NO.EM3, 1962, pp.935-950.
4. Drucker, D.C., Gibson, R.E. and Henkel, D.J., "Soil Mechanics and Work-Hardening Theories of Plasticity", Proceedings, ASCE, Vol.81, 1955, pp.1-14, also Transactions, ASCE, Vol.122, 1957, pp.338-346.
5. Ghaboussi, J., and Momen, H., "Modeling and Analysis of Cyclic Behavior of Sands", Soil Mechanics - Transient and Cyclic Loads, Eds. G.N. Pande and O.C. Zienkiewicz, Wiley, 1982, pp.313-346.

6. Hicher, P.Y., "Comportement Mechanique des argiles saturees sur divers chemines de sollicitations monotones et cycliques. Application a une modelisation elastoplastique et viscoplastiquees", These de Doctoral d'Etat, Universite Paris 6, Paris, France, December 1985.

7. Hardin, B.O. and Drnevich, V.P., "Shear Modulus and Damping in Soils: DEsign Equations and Curves", J. Soil Mech. Found. Div., ASCE, Vol.98, No.SM7, 1972, pp.667-692.

8. Ishihara K., Tatsuoka F. and Yasuda S., "Undrained Deformation of Sand under Cyclic Stresses Reversing Direction, Soils and Foundation, Vol.15, No.1, pp.29-44,1975.

9. Japanese Society of Soil Mechanics and Foundation Engineering; Committee Report "2. Effective Stress analysis f Ground and Soil Structures", Symposium on Behaviour of Ground and Soil Structures during Earthquakes, 1989. (in japanese).

10. Kean, C. M., and Prevost, J. H., "An Analysis of Earthquake Data Observed at the Wildlife Liquefaction Array Site, Imperial County, California", Proc., 2nd Us-Japan Workshop on Liquefaction, Large Ground Deformation and their Effects on Lifelines, Report NCEER-89-0032, Dec., 1989, pp.39-53.

11. Luoung, M.P., "Phenomenes Cycliques dans les Sols Pulverulents", Revue Francaise de Geotechnique, Vol.10, 1980, pp.39-53.

12. Mroz Z., "On the Description of Anisotropic Work-Hardening", J. Mech. Phys. Solids, Vol.15 1967, pp.163-175.

13. Mroz, Z. and Pietruszak, S.T., "A Constitutive Model for Sand with Anisotropic Hardening Rule", Int. J. Num. Meth. Geom., Vol.7, 1983, pp.305-320.

14. Nagai F., Hayashi H. and Ohbo N., "Dependence of shear Rigidity on Constraint in Saturated Sand on Shaking Table tests Proc. 25th Soil Engineering Research Conference, 1990 (in japanese).

15. Prevost J. H., "DYNA1D: A Computer Program for Nonlinear Seismic Site Response Analysis, Report No. NCEER-89-0025, Dept. of Civil Eng. and Oper. Re., Princeton Univ., 1988.

16. Prevost J.H., "A Simple Plasticity Theory for Frictional Cohesionless Soils", Soil Dynamics and Earth. Eng., 1985, Vol.4, No.1, pp.9-17.

17. Prevost, J.H., "Two-Surface vs. Multi-Surface Plasticity Theories", Int. J. Num. Meth. Geom., Vol.6, 1982, pp.323-338.

18. Prevost J.H. "Mathematical Modeling of Monotoric and Cyclic Undrained Clay Behavior, Int. J. Num. Meth. Geom., Vol.1, No.2, 1977, pp.195-216.

19. Richard, R. E., Woods, R.D. and Hall, J.R., Vibrations of Soils and Foundations, Prentice-hall, N.J., 1970.

20. Roscoe, K. H., and Burland, J.B., "On the Generalized Stress-Strain Behavior of Wet Clay", Engineering Plasticity, J. Heyman and F. Leckie, eds., Cambridge University Press, Cambridge, England, 1968, pp.535-609.

21. Rowe, P.W., "The Stress-Dilatancy Relation for Static Equilibrium of an Assembly of Particles in Contact, Proc. Roy. Soc., Vol.A269, 1962, pp.500-527.

22. Schofield, A.N., and Wroth, C.P., Critical State Soil Mechanics, Mcgraw Hill, Inc., London, England, 1968.

stress path of triaxial
compression and
extension tests.
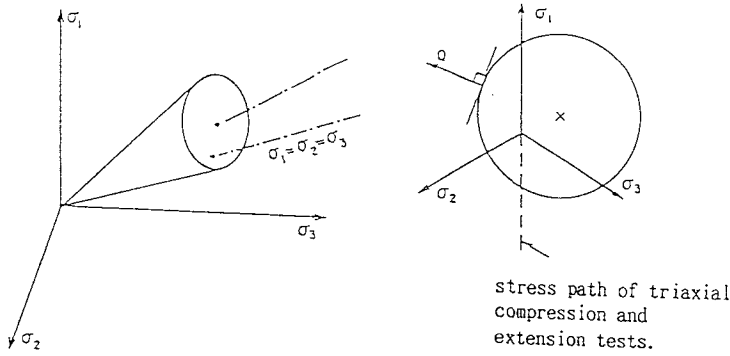
Fig. 1 Yield Surface in Principal Space

(a) η/η^* vs. $3p''$

(b) P vs. q

Fig. 2 Dilatational Plastic Flow

Fig. 3 Yield Surface
Translation by the Stress
Ponit in Deviatoric
Stress Space

(a) P vs. q

(b) $|\gamma|$ vs. q

(c) ε_v vs. P
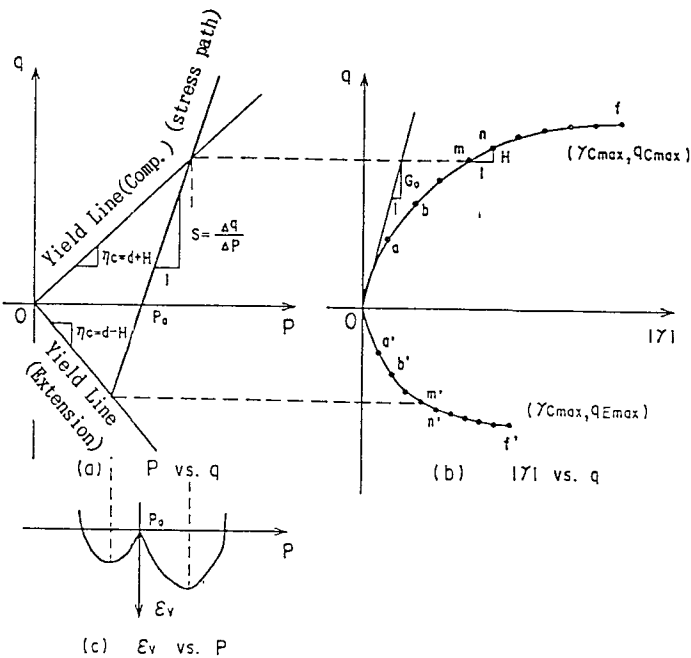
Fig. 4 Example of Triaxial Compression and
Extension Tests

D_{max}	$= 6mm$
D_{00}	$= 0.75mm$
U_c	$= 4.2$
e_{max}	$= 0.806$
e_{min}	$= 0.513$

silt	sand	gravel
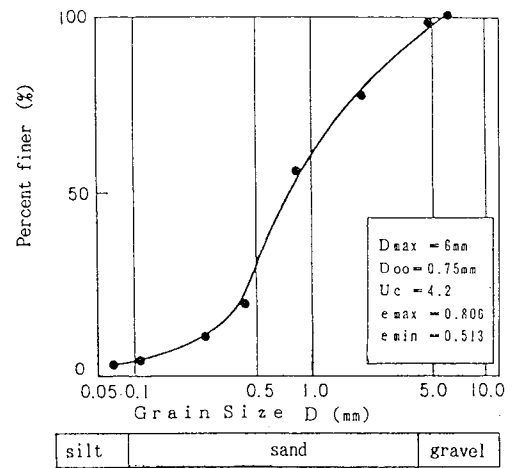
Fig. 5 Grain Size Accumulation
Curve of Fujigawa Sand

399

Table 1 Input data

Equations in DYNA1D	Input Data	Value	Test Method
2-Phase Effective Stress Analysis	·Specific Gravity of Soil ρs	2.7	Specific Gravity test
	·Specific Gravity of Water ρw	1.0	Known Quantity
	·Bulk Modulus of Water Bw	2×10^6 kgf/cm^2	Known Quantity
	·Porosity nw	38 %	Moisture Content Test
	·Coefficient of Permeability k	0.01cm/sec	Permiablity Test
Multi- Surface Theory	·Shear Modulus of Soil Gs	153kgf/cm^2	PS-Logging
	·Bulk Modulus of Soil Bs	270kgf/cm^2	Triaxial Test(Drained)
	·Initial Effective Stress p_0'	0.1kgf/cm^2	Known Quantity
	·Number of Yield Surface	20	Assumption
	·Cohesion Force C	0kgf/cm^2	Triaxial Test(Drained)
	·Friction Angle φ	38 °	〃
	·Max. Com. Shear Strain	5 %	〃
	·Max. Ext. Shear Strain	3 %	〃

(a) Model Ground   (b) Analyzed Model

Fig. 6   Model

Table 2 Maximum Excess Pore Water Pressure Ratio

Input Wave	Amax	Maxmum Excess Pore Water Pressure Ratio
Sine Wave 4Hz	100gal	0.15
Sine Wave 4Hz	200gal	1.0(liquefaction)
Taft Wave	100gal	0.03
Taft Wave	300gal	0.25
Hachinohe Wave	100gal	0.02
Hachihohe Wave	300gal	0.3
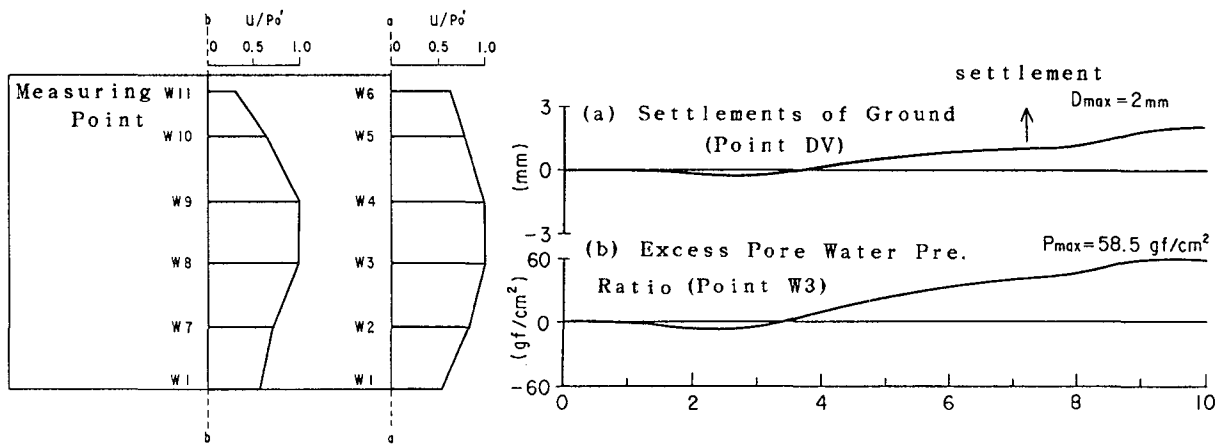
Fig. 7 Maximum Excess Pore Water Pressure Ratio Distribution

Fig. 8 Response Wave of Liquefaction Test
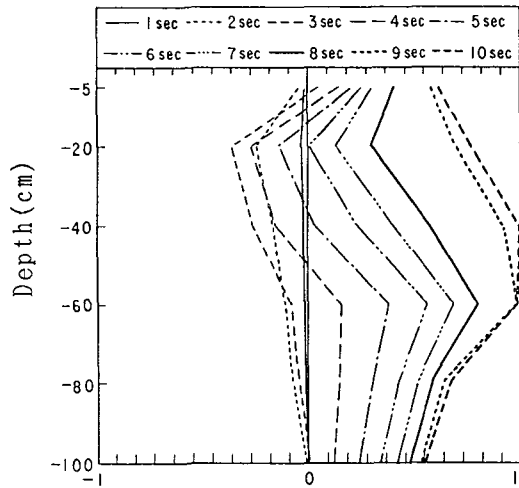
Fig. 9 Excess Pore Water Pressure
Ratio Distribution(Tests)
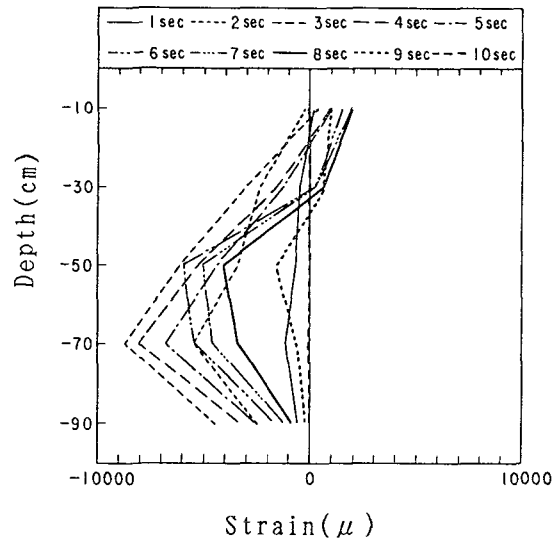
Fig. 10 Shear Strain Distribution(tests)
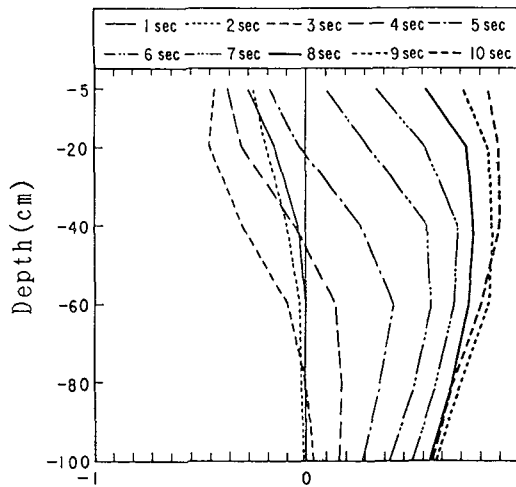
Fig. 11 Excess Pore Water Pressure
Ratio Distribution(Computed)
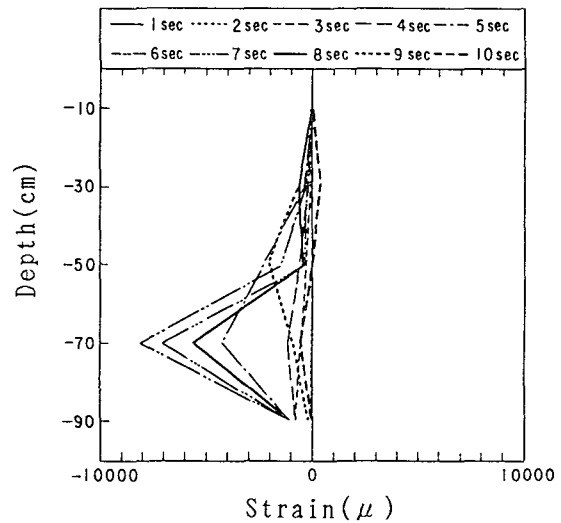
Fig. 12 Shear Strain Distribution
(Computed)
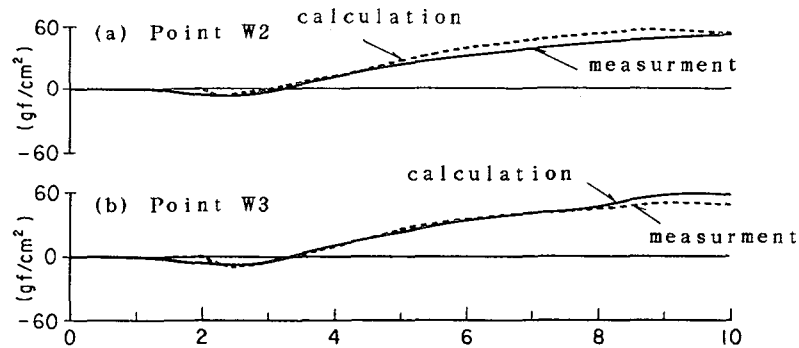
Fig. 13 Comparison between the Test and Computed Results

401

THE EFFECTS OF LIQUEFACTION PROCESS ON
THE SPECTRAL CONTENT OF STRONG GROUND MOTION

M. Vucetic

Assistant Professor of Civil Engineering
University of California, Los Angeles

G.T. Zorapapel

Project Engineer
Englkirk & Hart Consulting Engineers, Inc., Los Angeles

ABSTRACT

The effects of a gradual buildup of seismic pore pressures and associated degradation of stiffness of shallow saturated liquefiable deposits on the spectral content of the ground surface motion are investigated. The Fourier Transforms of the acceleration-time histories and layer gain factors are employed. The investigation consists of the analyses of ground surface and subsurface accelerations and pore pressures recorded at a site which liquefied during a strong earthquake. The results of the analyses are compared to (i) the spectral contents of the motions generated by a smaller earthquake which shook the same site and did not cause a pore pressure buildup, and (ii) the results of an analysis of the same liquefaction seismic response obtained by a nonlinear computer model. The analysis of stronger shaking shows that even a relatively small seismic excess pore pressures can cause a significant lengthening of the predominant period of the ground surface motion and strong amplification of the incoming motion in the range of these increased periods. For the smaller earthquake, this phenomena were not obtained.

INTRODUCTION AND OBJECTIVES

During large earthquakes, in shallow, fully saturated and relatively loose silty and sandy deposits pore pressures are continuously building up and consequently the soil stiffness and strength continuously degrade. If the shaking is strong and long enough, the excess pore pressures, u, may eventually reach the level of the initial effective vertical consolidation stresses, $\bar{\sigma}_{vc}$, and the deposit fully liquefies. At that moment, the effective vertical stresses $\bar{\sigma}_v = \bar{\sigma}_{vc} - u = 0$, and the normalized excess pore pressures $u^* = u/\bar{\sigma}_{vc} = 1.0$. While the phenomenon of the full liquefaction and its consequences have been extensively studied (Ref. 9), the effects of a gradual buildup of seismic pore pressures on the ground surface motions and the supported structures has not received enough attention. The objective of this paper is to provide more information on that subject, in particular on the characteristics of the ground surface motion and the ability of the liquefiable deposit to transmit the seismic shear waves.

It can be expected that the degradation of soil stiffness caused by seismic pore pressure buildup, which is characterized by a decrease of shear modulus, will produce certain lengthening of the predominant period of the motion at the ground surface due to the inability of the soft deposit to transmit a high frequency incoming shear waves. If a large softening occurs as a result of very high excess pore pressures corresponding closely to the state of full liquefaction, a rather dramatic increase of the predominant period of the motion should be expected. This is illustrated in Fig. 1, which shows a record of a horizontal acceleration component obtained on a liquefied site; after approximately 7 seconds, the accelerogram exhibits a clear 5 seconds period component. A preliminary study by the writers (Ref. 15) provided some insight into that phenomenon of increased periods and their possible effects, while in some other related analyses (Refs. 10, 11, 12 and 14) a mechanism behind such seismic response has been proposed.

To separate the effects of the earthquake source and wave propagation path on the ground surface motion, it is desirable to analyze the response of a site where the accelerations on the ground surface and at the bottom of the deposit are recorded simultaneously during an earthquake. In such a case the acceleration-time histories recorded at the bottom already contain the effects of the source and path. Consequently, the difference between the ground surface and subsurface accelerograms reflects the influence of the properties of the deposit on the response. The opportunity for such unique analysis was provided by the seismic records obtained in 1987 at the Wildlife Liquefaction Array. At the Wildlife site the accelerations at the ground surface and at 7.5m depth, as well as the pore pressures between approximately 2 and 7m and at 12m depth, were recorded simultaneously during two successive earthquakes in 1987 (Ref. 2). Given such unique set of seismic data, the effect of a gradual pore pressure buildup in a liquefiable deposit on the characteristics of the ground surface motion could be isolated. Such analysis is described in this paper, focussing in particular on the effect of pore pressure buildup on the variation of the frequency content of the ground surface motion (variation of the predominant period) and the amplification of the motion through the liquefiable deposit.

THE LIQUEFACTION SITE, EARTHQUAKES AND SEISMIC RECORDS

The soil profile of the Wildlife Liquefaction Site is sketched in Fig. 2. It consists of a top unit of loose silt between 0 and 2.5m with the water table at approximately 1.5m, the liquefiable deposit of silty sand between 2.5 and 6.8m, a stiff silty clay deposit between 6.8 and approximately 11.5m, and a silt deposit below. Other details about the Wildlife Site can be found elsewhere (Refs. 1 and 4). As shown in Fig. 2, the site has been instrumented with accelerometers at

404
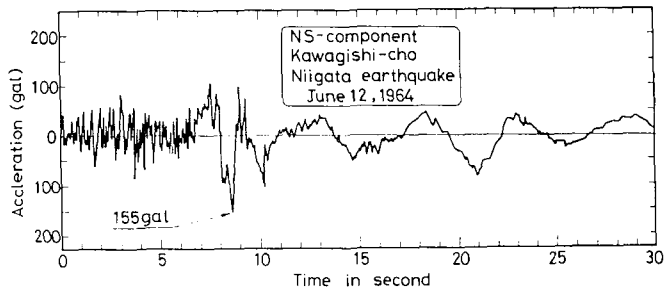
Fig. 1 Accelerations on top of liquefiable site (Ishihara, 1985)
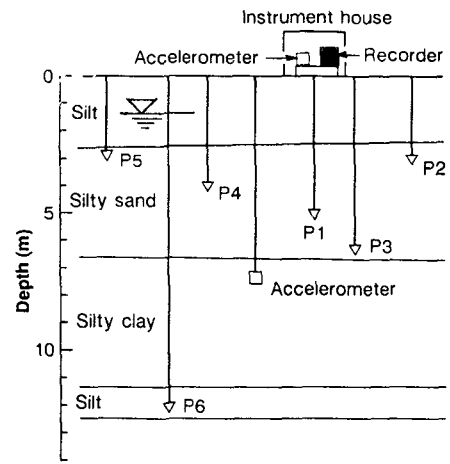
Fig.2 Wildlife liquefaction site (Bennett et al., 1984; Holzer et al., 1989)
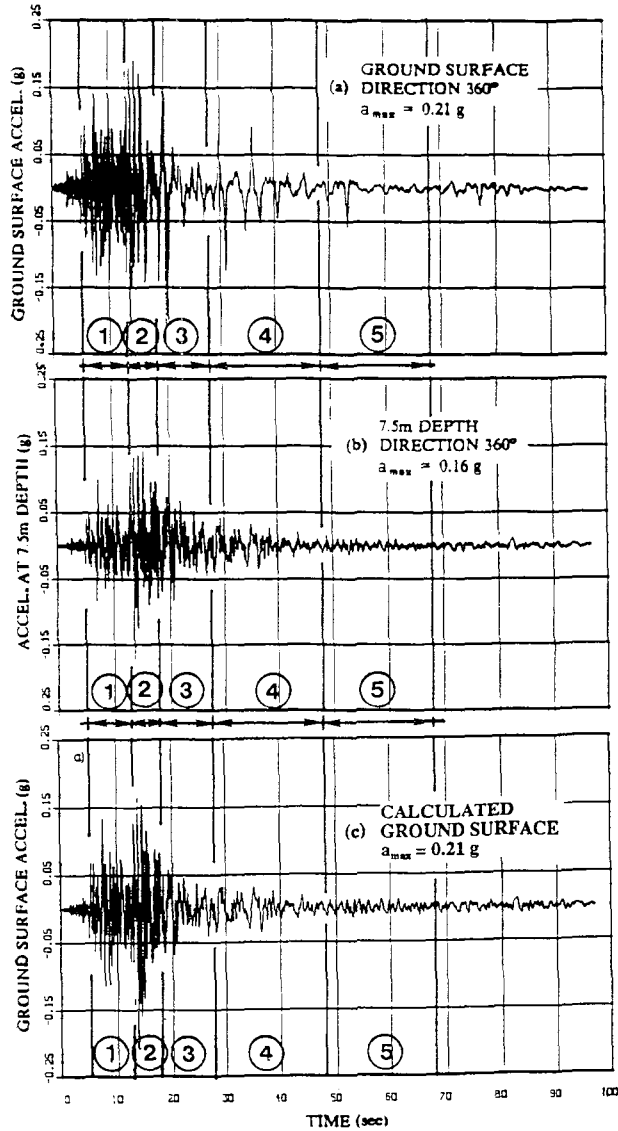
Fig. 3 Recorded and calculated acceleration-time histories of the second Superstition Hills Earthquake (Brady et al., 1989; Vucetic and Thilakaratne, 1989)

TABLE 1 Summary of earthquake data

	① Elmore Ranch Earthquake	② Superstition Hills Earthquake
Date & Time	November 24, 1987 0154 GMT	November 24, 1987 1315 GMT
M_L Magnitude	5.8	6.1
M_S Magnitude	6.2	6.6
Epicentral distance from Wildlife Site	23 km	32 km
Max. ground surface acceleration	recorded: 0.13g calculated: 0.11g	recorded and calculated: 0.21g
Max. acceleration at 7.5 m depth	recorded: 0.078g	recorded: 0.16g

405
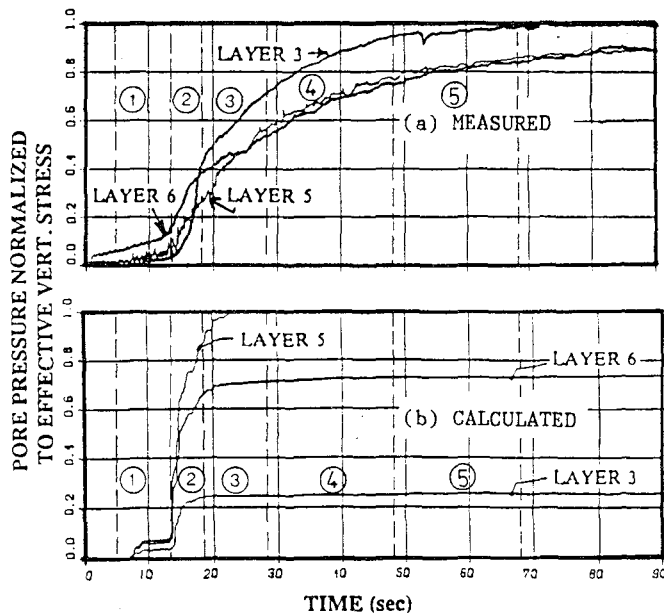
Fig. 4 Pore pressure-time histories (Brady
et al., 1989; Vucetic and Thilakaratne, 1989)
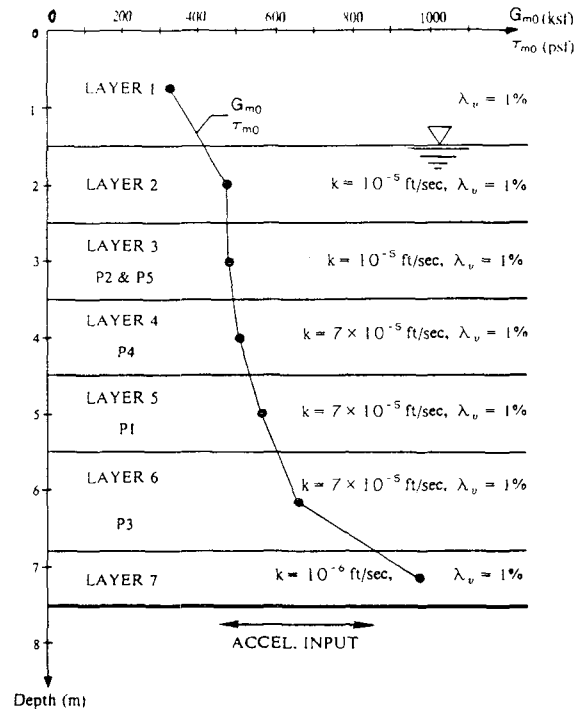
Fig. 5 Wildlife site analytical
soil profile (Vucetic, 1986; Vucetic
and Thilakaratne, 1989)

the ground surface and downhole at 7.5m, immediately below the liquefiable silty sand deposit. Five piezometers P1 to P5 for recording of seismic pore pressures have been installed in the liquefiable deposit and one piezometer P6 has been installed in the silty sand at approximately 12m depth. The instruments were installed by U.S. Geological Survey (USGS) in 1982 (Ref. 2).

On November 24, 1987, two earthquakes shook the Wildlife Site, first a smaller earthquake which did not generate measurable excess pore pressures, and than a larger earthquake which caused a full liquefaction of the silty sand deposit. More information on these two successive earthquake are given in Table 1.

Complete acceleration and seismic pore pressure records are given in the corresponding USGS report (Ref. 2; see also Ref.10). In Figs. 3 and 4 some of these records are replotted in a more convenient form, along with the corresponding time histories which were analytically obtained by a nonlinear computer model. These analytical results will be explained in more detail in the next chapter. In Figs. 3a and 3b the 360 degrees horizontal acceleration components recorded at the ground surface and at 7.5m depth respectively are presented. In Fig. 3c the corresponding calculated ground surface accelerogram is shown. It should be noted that, just like in the case of the Niigata record shown in Fig. 1, after the high-frequency oscillations at the beginning, the period of oscillation at some point remarkably increases while the acceleration magnitude simultaneously decreases. As shown in Fig. 3c, a similar acceleration-time history has also been obtained analytically. In Figs. 4a and 4b measured and calculated seismic pore pressures are presented in the normalized form $u^* = u/\overline{\sigma}_{vc}$. Only three measured pore pressure records are plotted in Fig. 4a, because piezometer P4 was not operational during the earthquake and

406

records P2 and P5 are practically identical. The layer numbers in Fig. 4 correspond to the layers of the analytical Wildlife Site soil profile shown in Fig. 5. The centers of the layers 3 to 6 in Fig. 5 correspond to the levels of the piezometers in Fig. 2.

Comparison between Figs. 3 and 4 shows that the first occurrence of low frequency oscillations in Figs. 3a an 3b at around 18 seconds corresponds to the level of the normalized field seismic pore pressures u^* between 0.3 and 0.5. It should be also noted that beyond approximately 48 seconds the reduction of the accelerations to the values close to zero corresponds to u^* between approximately 0.8 and 1.0, i.e. to the level of u^* corresponding to the liquefaction of the deposit.

SUMMARY OF ANALYTICAL STUDY

The liquefaction of Wildlife Site during the 1987 earthquakes and some previous earthquakes has been analyzed by several research teams (Refs. 1, 3, 4, 6, 10, 11, 12 and 14). Some of these analyses (Refs. 3, 10, 11, 12 and 14) were performed using a computer program called DESRAMOD (Ref. 12), which is a modification of program called DESRA-2 (Ref. 8). The acceleration-time and pore-pressure time histories in Figs. 3c and 4b were obtained by the DESRAMOD computer code. Both programs, i.e., DESRASMOD and DESRA-2, employ a multi-degree-of-freedom, one-dimensional lumped parameter model of the soil to simulate the nonlinear seismic response of a horizontally layered profile to one-directional input base acceleration excitation. The analytical soil profile of the Wildlife Site employed has been already shown in Fig. 5. The seismic response analysis of this profile was performed by exciting it at its base at 7.5m by the downhole accelerogram shown in Fig. 3b.

The major modification of DESRA-2 included in the DESRAMOD is the replacement of the original pore pressure buildup subroutine with a subroutine which incorporates the cyclic pore pressure model developed by Dobry (see Ref. 12). Dobry's pore pressure model can be obtained from the results of a series of undrained cyclic strain-controlled (constant cyclic strain amplitude) laboratory tests. The model directly incorporates threshold shear strain, γ_t, below which no permanent (residual) pore pressures develop. For Wildlife sands $\gamma_t=0.02\%$ (Ref. 13). The model can also be easily modified to approximately describe the pore pressure buildup that would have developed during two-directional cyclic loading. The pore pressure model for Wildlife sands used in the DESRAMOD analysis is (Refs. 12 and 13):

$$u^* = \frac{1.04 \times 2.6 \times 2.0 \times n_c \times (\gamma_{cy} - \gamma_t)^{1.7}}{1 + 2.6 \times 2.0 \times n_c \times (\gamma_{cy} - \gamma_t)^{1.7}} \tag{1}$$

In Eq. (1) $u^* = u/\overline{\sigma}_{vc}$, where u is the residual cyclic pore pressure which corresponds to the seismic excess pore pressure u defined before, while γ_{cy} and n_c are the uniform cyclic shear strain amplitude and the number of cycles respectively applied in the cyclic strain-controlled testing. The degradation of soil stiffness caused by the pore pressure buildup u, which is one of the main factors influencing the seismic response of the liquefiable deposits is described in DESRAMOD as the reduction with time, t, of the initial shear hear modulus G_{mo} at very small strains and the soil shear strength τ_{mo} at very large strains:

$$G_{mt} = G_{mo} \times \sqrt{1 - u^*} \quad \text{and} \quad \tau_{mt} = \tau_{mo} \times (1 - u^*) \tag{2}$$
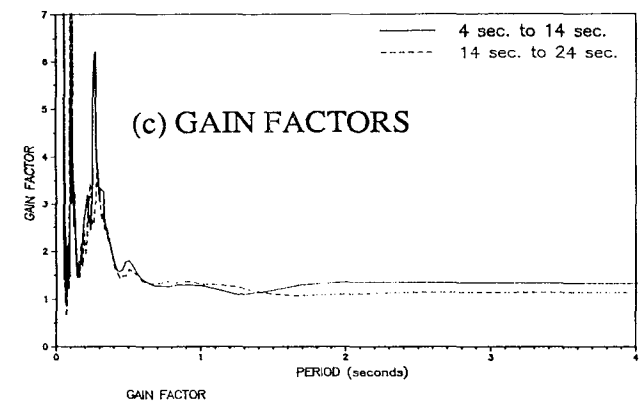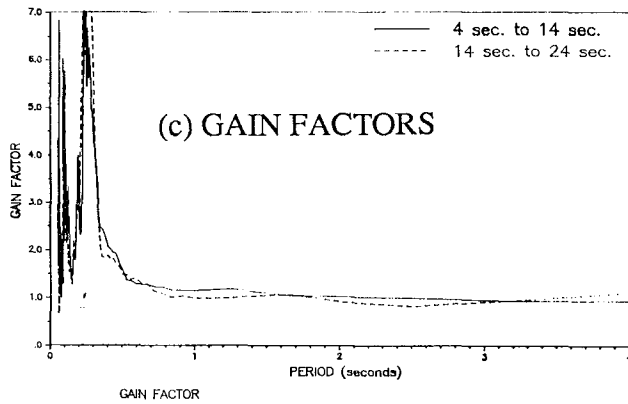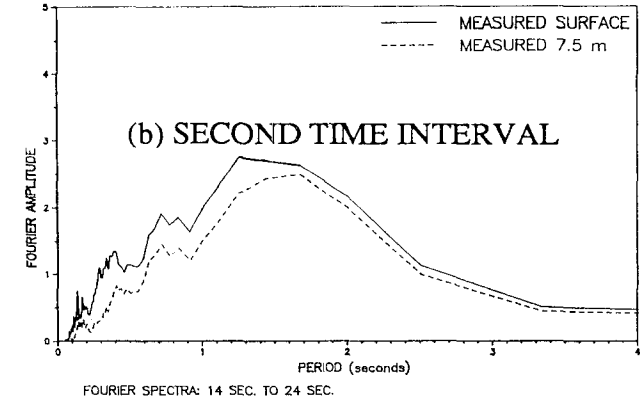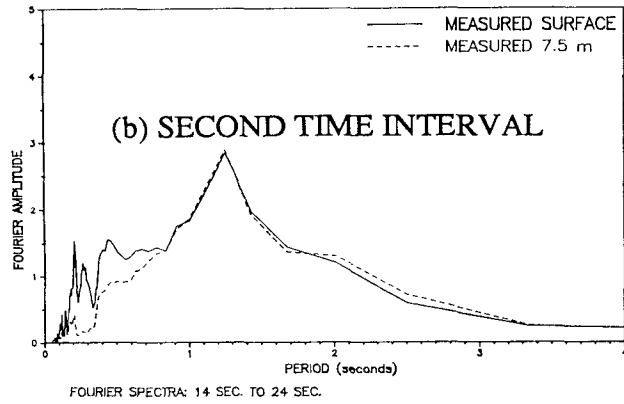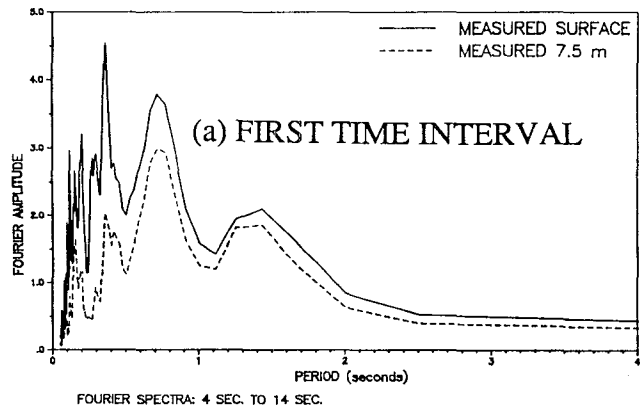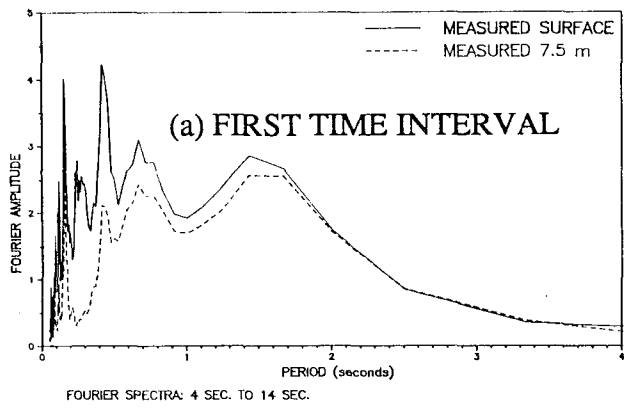
Fig. 6 First earthquake - Fourier spectra and gain factors of the motions measured in 360 degrees direction

Fig. 7 First earthquake - Fourier spectra and gain factors of the motions measured in 90 degrees direction

The shear modulus and shear strength at time t, G_{mt} and τ_{mt} respectively, are the parameters used in DESRAMOD to describe the hyperbolic cyclic stress-strain relationship of the soil (Ref. 7). The distribution of the initial G_{mo} and τ_{mo} is given in Fig. 5, together with two other important liquefaction response parameters, damping at small strains λ_v and the soil permeability k.
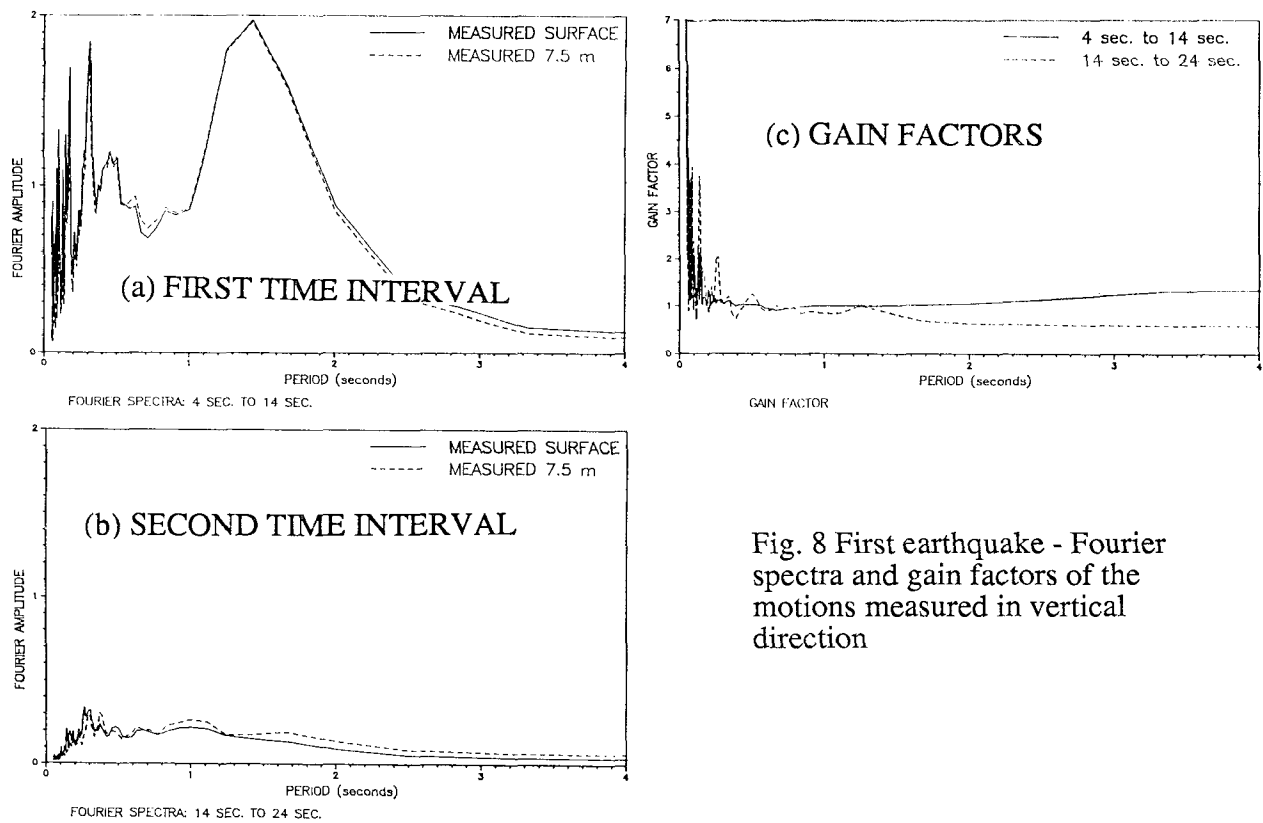
Fig. 8 First earthquake - Fourier
spectra and gain factors of the
motions measured in vertical
direction

Figure 4 shows that the calculated excess pore pressures differ from the recorded ones. Only one layer liquefied in approximately 20 seconds and pore pressures in all layers build up much faster in the beginning. Reasons for such difference between the field and calculated pore pressures are discussed elsewhere (Refs. 3, 10, 11 and 14). However, full liquefaction has been obtained analytically for the second (stronger) earthquake, while practically no pore pressure increase has been calculated for the first (weaker) earthquake, as described elsewhere (Refs. 10 and 11). Also, a comparison between the calculated acceleration-time and pore pressure-time histories shown in Figs. 3c and 4b respectively, shows that a qualitative relation between the pore pressure buildup and the ground surface acceleration similar to that recorded in the field can be obtained analytically. Following a considerable pore pressure buildup the high frequency accelerogram transformed into a low frequency accelerogram, and the magnitude of the acceleration dropped close to zero when very large pore pressures developed.

FOURIER SPECTRA AND GAIN FACTORS

The effect of the gradual pore pressure buildup in the Wildlife liquefiable deposit on the characteristics of the ground surface motion is assessed here in terms of (i) the variation of the frequency content of the ground surface motion (variation of the predominant period) and (ii) the amplification of the motion through the liquefiable deposit. This is done by analyzing the Fourier spectra of the acceleration-time histories. Two representations of the spectral content are used: the Fourier Transform of the acceleration-time history and the layer gain factor, which is the ratio between the Fourier Transforms of the ground surface motion (output) and the motion at 7.5m depth (input). The gain factor directly characterizes the amplification produced by the soil deposit.

(a) FIRST TIME INTERVAL

FOURIER SPECTRA: 4.7 SEC. TO 12.9 SEC.

(b) SECOND TIME INTERVAL

FOURIER SPECTRA: 12.9 SEC. TO 18 SEC.

(c) THIRD TIME INTERVAL

FOURIER SPECTRA: 18 SEC. TO 28 SEC.

(d) FOURTH TIME INTERVAL

FOURIER SPECTRA: 28 SEC. TO 48 SEC.

(e) FIFTH TIME INTERVAL

FOURIER SPECTRA: 48 SEC. TO 68 SEC.
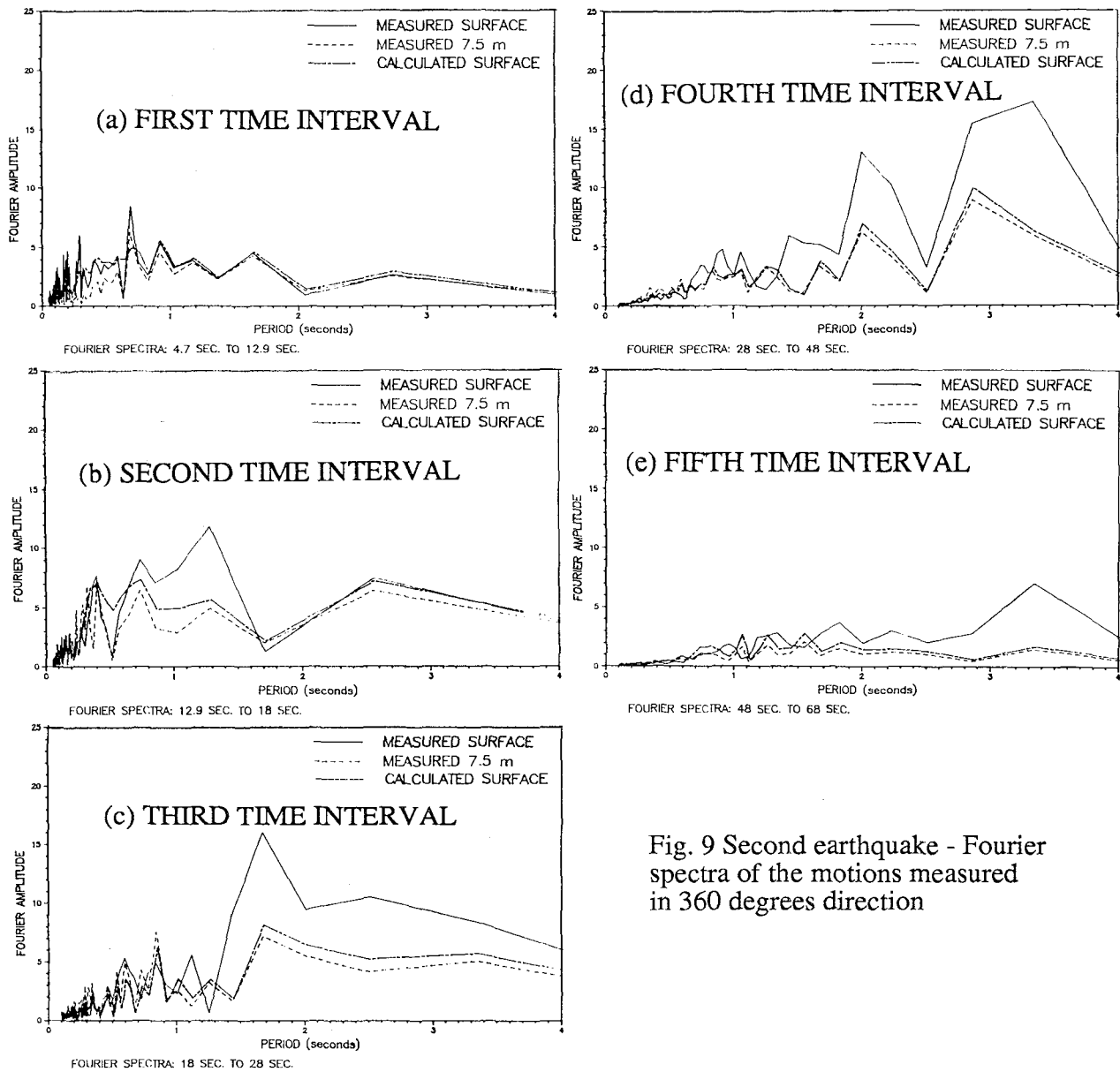
Fig. 9 Second earthquake - Fourier spectra of the motions measured in 360 degrees direction

Because of the long duration of the acceleration records analyzed and an uncustomary variation of their frequency contents, it would be difficult to reach a reliable conclusion from the spectral representations of the complete records. Therefore, the acceleration-time histories are partitioned into several time intervals which are then studied separately. The three components of both the surface and downhole records of the first smaller seismic event were split in two time intervals: (i) from 4 to 14 seconds, which is approximately from the arrival of seismic shear waves until the appearance of the accelerations of somewhat smaller frequency, and (ii) from 14 to 24 seconds. For the second stronger earthquake which produced more complex accelerograms, the records were partitioned in five time intervals, with a special care given to the timing of the first two intervals. These five intervals are: (i) from 4.7 seconds, corresponding approximately to the arrival of the S waves, to 12.9 seconds, corresponding to the sudden increase of the calculated and noticeable increase of the field pore pressures, (ii) from 12.9 to 18.0 seconds, when in the field u has build up significantly (u^*=0.2 to 0.4), while in layer 5 the calculated u^*=0.9,

410
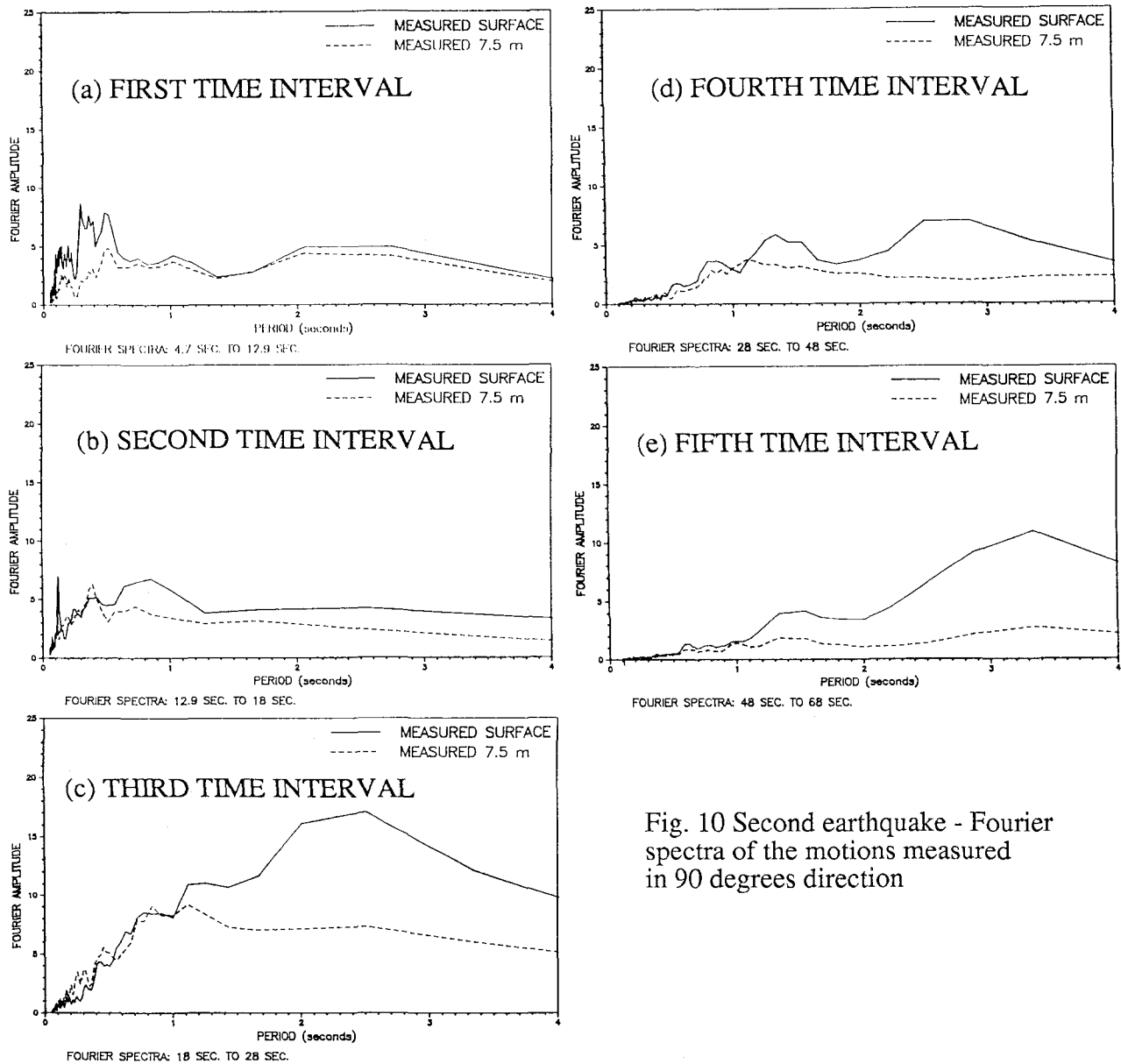
Fig. 10 Second earthquake - Fourier spectra of the motions measured in 90 degrees direction

corresponding practically to the state of full liquefaction, (iii) from 18 to 28 seconds, when in the field pore pressures increase from u^*=0.4 to approximately 0.7, while in the calculated response layer 5 is in the state of full liquefaction, (iv) from 28 to 48 seconds, when in the field the deposit has fully liquefied, and (v) from 48 seconds to 68 seconds when the accelerations became extremely small.

Figures 6 through 8 present the Fourier spectra and gain factors for all time intervals and direction components of the first event. Figures 9 to 14 present the same information for the second stronger seismic event, including the associated analysis of the calculated surface motion.

Figures 6 through 8 show that for the first smaller event the shapes of the Fourier spectra of the downhole and ground surface accelerograms are rather similar. During the first time interval (Figs. 6a and 7a) the spectral peaks of the horizontal motion are observed for the periods of

MEASURED GAIN FACTOR

CALCULATED GAIN FACTOR
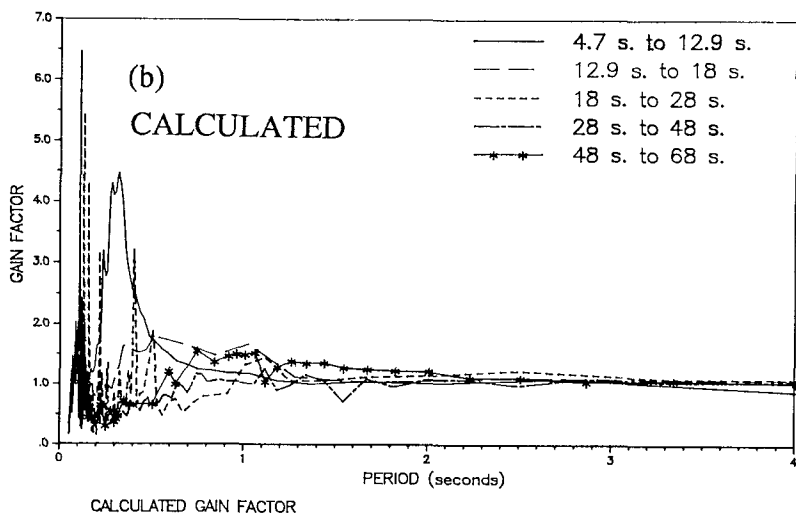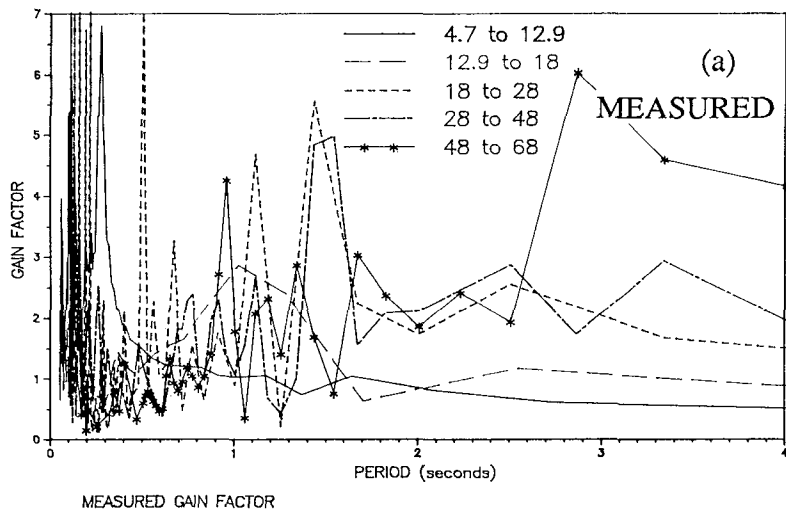
Fig. 11 Second earthquake - Gain factors of the measured and calculated motions in 360 degrees direction
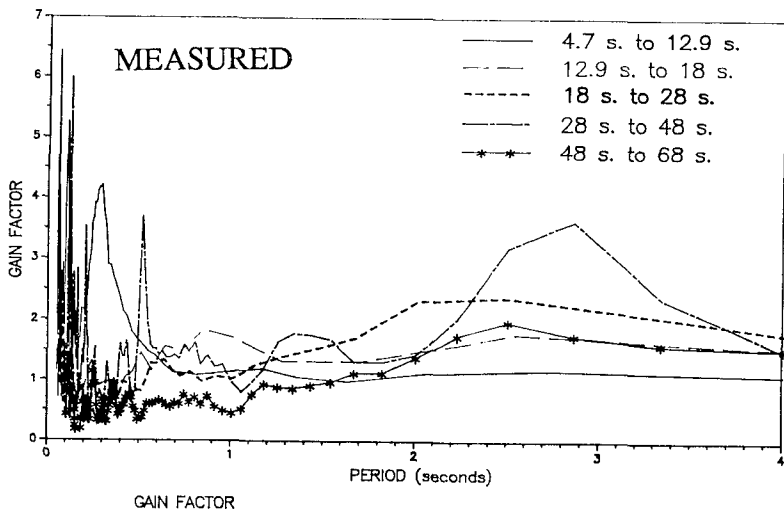
GAIN FACTOR

Fig. 12 Second earthquake - Gain factors of the motions measured in 90 degrees direction

412

1.4 sec., 0.7 sec., 0.4 to o.5 sec. and approximately 0.15 sec. During the second time interval between 14 and 24 seconds (Figs. 6b and 7b), in both horizontal directions long periods become predominant. Although the spectral content of the horizontal motion changes from the first to the second time interval, Figs. 6c and 7c show that the gain factors for the two intervals are very similar, exhibiting peaks in both directions at periods of 0.10 and 0.27 sec. In this paper such predominant periods of the gain factor function will be called *the characteristic periods*. The characteristics of the spectral content and gain factors of the vertical motion, which are shown in Fig. 8, are rather similar to the characteristics of the horizontal motion just described. The gain factor functions in Figs. 6c, 7c and 8c clearly show that amplifications occurs in the domain of small periods, because practically no softening (degradation) of the soil stiffness has occurred.

As opposed to the first event, during the second, stronger event large seismic pore pressures gradually built up and significant softening of the soil deposits has occurred. Consequently, the filtering properties of the soils have drastically changed. The Fourier spectra of the measured and calculated 360 degrees horizontal components of the motion of the second earthquake are shown in Fig. 9. During the first time interval between 4.7 and 12.9 seconds (Fig. 9a), a predominant period of 0.7 seconds and practically identical amplitudes of Fourier Spectra for both the measured and calculated response can be observed. During the second time interval between 12.9 and 18.0 seconds (Fig. 9b), the above two amplitudes of 0.7 seconds component remain almost unchanged. However, during this interval, when seismic pore pressures started to build up, a new component of measured response corresponding to much larger period of 1.25 seconds emerges and tends to govern the motions at the ground surface. In addition to that, it can be noticed that a new component corresponding to smaller period of 0.39 seconds emerges for both the measured and calculated response. It should be noted that periods similar to all these three periods corresponding to the spectral peaks have been calculated for the first event. During the third time interval between 18 and 28 seconds (Fig. 9c), when a considerable pore pressure is generated, the long period of measured surface motion which dominates the response has shifted towards 1.7 seconds. A similar shift towards a larger period of 1.7 seconds can be observed for the measured downhole and the calculated surface motion. During the fourth and fifth time intervals between 28 and 68 seconds (Figs. 9d and 9e), when large pore pressures continue to build up, the predominant period is shifting even further towards the values of around 3 seconds. The Fourier spectra corresponding to the 90 degree direction of motion which is shown in Fig. 10, exhibit the same shift of the predominant period towards larger values as the pore pressure builds up and the soil deposit becomes softer.

The gain factors of the measured and calculated 360 degrees horizontal motions are shown in Figs. 11a and 11b respectively, while the gain factors of measured motions in 90 degrees direction are shown in Fig. 12. These results show that during the first time interval the gain factors of both horizontal directions are very similar to that generated by the first smaller earthquake shown in Fig. 6c. The components of the motion corresponding to periods around 0.27 seconds and below are largely amplified by the sand layer, while longer periods motions pass through the layer practically unmodified. The measured and calculated gain factors for the 360 degree direction are in good agreement during this first time interval. During the second time interval, the measured gain factors of horizontal motions shift their peaks to larger values of the characteristic (predominant) period, i.e., from 0.27 seconds to 1.0 second in the case of the 360 degrees direction, and from 0.27 to 0.85 seconds in the case of the 90 degrees direction. The smooth character of the gain curve around this longer characteristic period indicates a continuous shifting of the predominant period of the layer during this 5 seconds interval. The calculated gain during the second time interval has a peak at 0.5 seconds and it is not any longer in agreement with the gain of the measured motion. During the third time interval, the measured gains in both horizontal directions show large amplification for periods higher than 1.0 second. For the 360 degrees component the gains reach 4 to 5 at periods between 1.0 and 1.5 seconds, while for the 90 degrees component the gain reaches around 2 to 2.5 at periods between 2 and 2.5 seconds. Such response

strongly suggests further lengthening of the predominant period due to the continuous pore pressure increase. Also, very pronounced gains in 360 degrees direction and smaller gains in the 90 degrees direction suggests the polarization of the horizontal motion in the 360 degrees direction during this time interval.

As shown in Fig. 11b, large gains at such long periods are not obtained for the calculated motion. The field oscillations beyond 12.9 seconds exhibit longer periods than calculated (see Fig. 3), indicating that DESRAMOD cannot simulate so accurately the response when large pore pressures and associated large deformations occur in the deposit.

During the fourth time interval between 28 and 48 seconds, the peak gains occur in both direction at the characteristic periods of 1.5 and around 3.0 seconds. For the 360 degrees direction the maximum gain reaches 5 at the period of 1.5 seconds, while for the 90 degrees direction the peak gain reaches 3.5 at the period of 3.0 seconds. During the fifth time interval, the gain factor for 360 degrees reaches a value of 6 for a period of 2.8 seconds, while the gain factor function for the 90 degrees direction reaches the peak of 2.0 at the period of 2.5 seconds.

The Fourier spectra of the vertical acceleration component are shown in Fig. 13. The spectra show the shifting of the predominant period with time similar to that obtained for the horizontal components. Also, for third, fourth and fifth time interval, Fig. 14 shows peaks of the gain factors in the domain of large periods beyond approximately 0.8 seconds. However, the gain factors at these large periods do not exceed 2.2, which is relatively small compared to the gain factors obtained for the horizontal motions corresponding to the same time intervals and periods.

CORRELATION BETWEEN PREDOMINANT PERIOD
AND SEISMIC PORE PRESSURE

The periods corresponding to peaks in gain factor functions have already been defined as the characteristic periods of gain functions. The longest characteristic period of a gain function is defined here as "the first characteristic period". As shown in the previous chapter, longer first characteristic periods correspond to larger seismic pore pressures. Such relation suggests that the predominant periods increase as the soil deposit which transmits the motion to the ground surface becomes softer, and that a correlation between the first characteristic period and the level of the excess pore pressure may be established. Such correlation is presented in Fig. 15. Data points in the figure represent the first characteristic period for a certain time interval and a certain direction of the motion plotted versus the average measured pore pressure during the same time interval. For the vertical motion there is a clear trend of the increase of the first characteristic period with the increase of the pore pressure. For the horizontal directions the same trends are obvious. However, during the fourth and fifth time interval, when large pore pressures developed, the trends are not so perfect. The suggested reason for such behavior at these late time intervals is the polarization of different spectral components of motion with time. Therefore, to get a more convenient correlation, the average of the first characteristic periods obtained for the two horizontal corresponding to for the same time intervals are plotted versus the average pore pressure. In this way a general correlation between the first characteristic period of the horizontal motions and the average pore pressures could be obtained. This average correlation follows a clear trend of the period increase with the seismic pore pressure buildup.
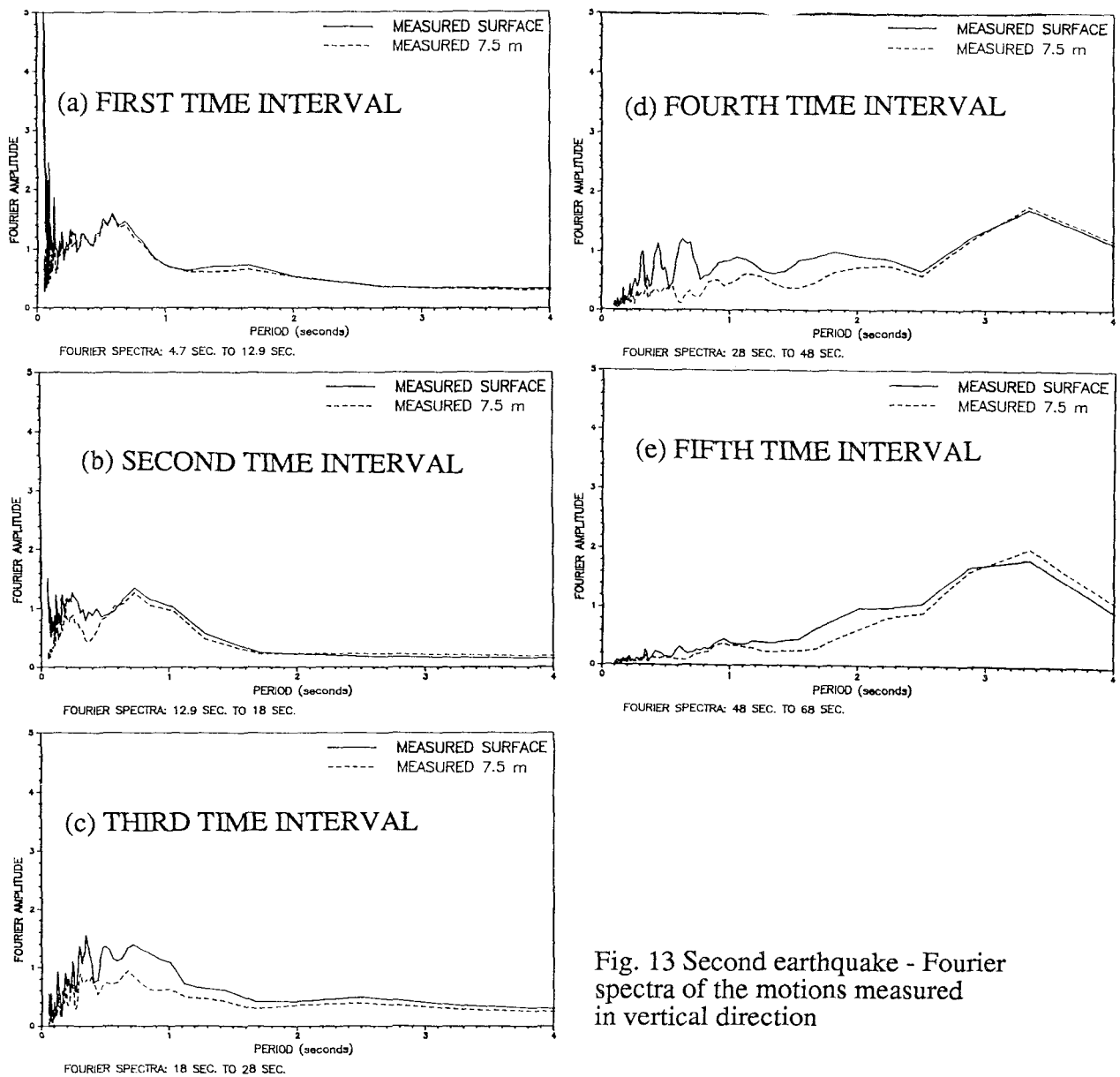
Fig. 13 Second earthquake - Fourier
spectra of the motions measured
in vertical direction

DISCUSSION AND CONCLUSIONS

Several important conclusions can be derived from the results presented, regarding the response and amplification of the motion in the field, and the capability of the computer model to simulate the field response. Also, it is appropriate at this point to discuss the practical implications of the results obtained.

The analysis of the field records clearly shows that the period of the sandy saturated site significantly increases due to the buildup of pore water pressures. Such lengthening of the site period is evidently caused by the associated degradation of soil stiffness. The important result of the present analysis is the amplification of the horizontal field motions in the long period ranges by factors between 3 and 6 (Figs. 11a and 12), and the amplification of the vertical motion in the long period range by a factor of up to 2.2 (Fig. 14). It must be emphasized that such amplifica-
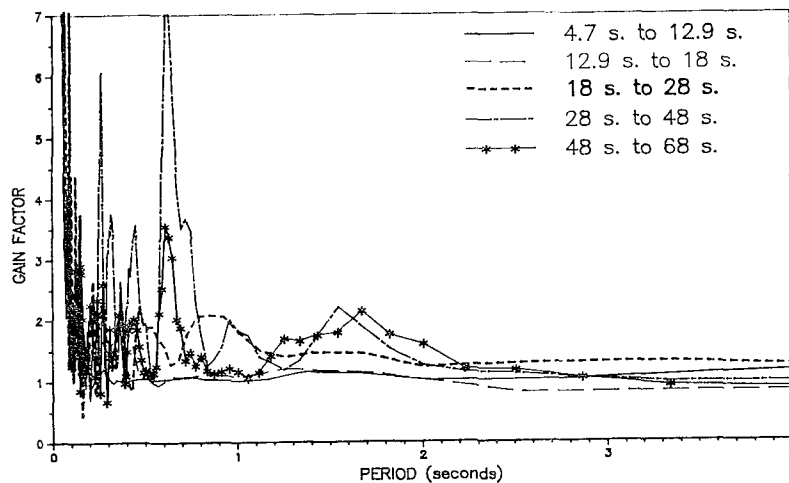
Fig. 14 Second earthquake - Gain factors of the motions measured in vertical direction

tion started at relatively small excess pore pressures corresponding to u^* approximately between 0.2 and 0.4 (during the second time interval). This means that a relatively small pore pressure increase at some depth of a sandy deposit can remarkably change the characteristics of incoming ground motion. With respect to that, it should be also noted that a long period component of the input motion recorded at 7.5m depth (Figs. 9 and 10) may indicate a certain pore pressure increase at larger depths. The 10% pore pressure increase recorded in 1987 at 12m depth in the Wildlife deposit (Ref. 2) may partially explain that.

The most interesting result of the present analysis is, however, a consistent correlation between the excess seismic pore pressures and the largest periods corresponding to the peaks of the gain factor functions, called here the first characteristic periods. Such consistent correlation indicates that, in general, other liquefiable sites may be susceptible to the amplification of incoming motion at large periods when the seismic pore pressures start to build up. An important consequence is the need for incorporating the likelihood of such amplification at long periods in the forecast of the design spectra for the sites with moderate and high potential of liquefaction. As shown in this paper, the lengthening of the predominant period starts at pore pressures well below the pore pressures corresponding to the full liquefaction of the deposit. Hence, dramatic modifications of the response characteristics of the deposit may occur even if the deposit will not eventually liquefy. Such amplification can have serious consequences and designers of flexible structures and base isolated buildings should take into account this phenomenon.

The comparison between the measured and calculated responses shows that in the range of small pore pressures and the associated small degrees of stiffness degradation, the computer model DESRAMOD simulates the field response very well. Also, DESRAMOD can predict the overall occurrence of liquefaction and some aspects of the lengthening of the site period due to pore pressure increase. However, because the model did not predict accurately the pore pressure-time histories and, as shown in this study, the ground surface response is sensitive to the pore pressure buildup, the model could not predict accurately the amplification of the motion by the deposit. The process of the pore pressure buildup and softening of natural deposits seem to be too complex to be accurately described by such relatively simple model like DESRAMOD. It should be mentioned that field pore pressures are greatly affected by a number of processes which are not incorporated into DESRAMOD model, such as the dissipation and redistribution of pore pressures in horizontal directions, upward migration of pore water which results in a continuous variation of soil density, surface cracking, lateral spreading and sand boiling. Some studies suggested, however, that the DESRAMOD model can be improved to account approximately for some of these factors (Refs. 3 and 10). If such improved model is developed, the amplification of the incoming seismic motion caused by the pore pressure buildup could be assessed for design purposes.
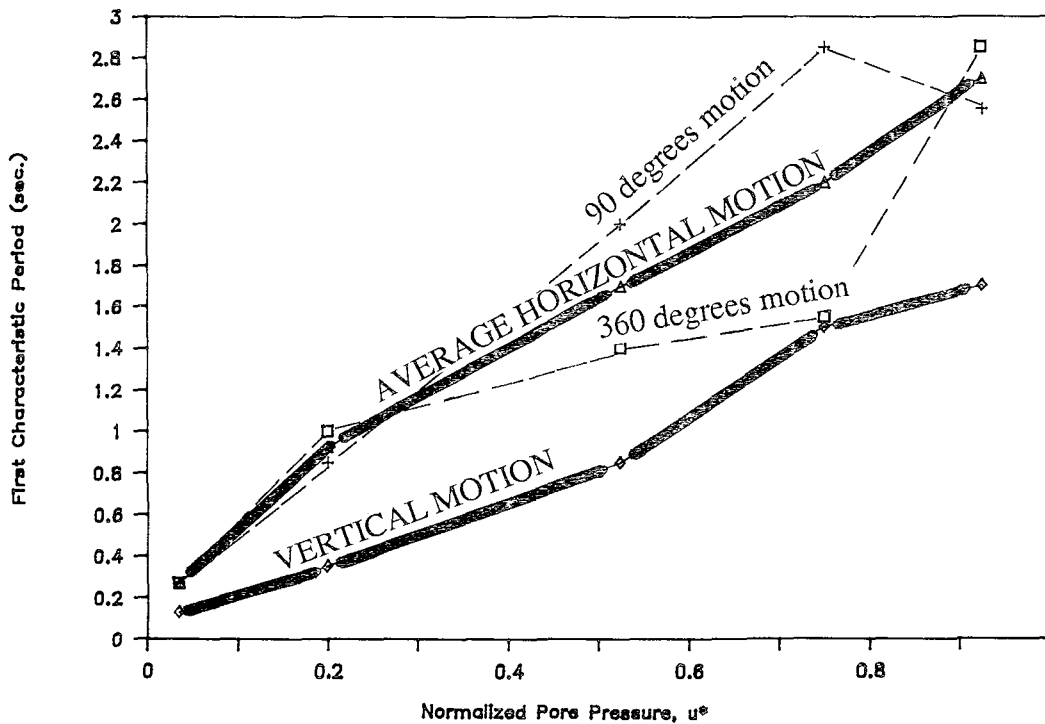
Fig. 15 Correlations between the average seismic pore pressures and the first characteristic periods of the gain factor functions

ACKNOWLEDGEMENTS

REFERENCES

1. Bennett, M.J., McLaughlin, P.V., Sarmiento, J.S. and Youd, T.L. "Geotechnical Investigation of Liquefaction Sites - Imperial Valley California", USGS Open File Report 84-252, 1984.

2. Brady, A.G., Mork, P.N., Seekins, L.C. and Switzer, J.C. "Processed Strong-motion Records from the Imperial Wildlife Liquefaction Array - Superstition Hills Earthquakes of Nov. 24, 1987", USGS Open File Report 89-87, 115 , 1989.

3. Dobry, R., Elgamal, A.W., Baziar, M. and Vucetic, M. " Pore Pressure and Acceleration Response of Wildlife Site during the 1987 Earthquake", Second U.S.-Japan Workshop on Liquefaction, Niagara Falls, N.Y., Sessions 1-4, Sept. 26-29, 1989.

4. Holzer, T.L., Youd, T.L. and Hanks, T.C. "Dynamics of Liquefaction During the 1987 Superstition Hills California Earthquake", Science, Vol. 244, pp. 56-59, 1989.

5. Ishihara, K. "Stability of Natural Deposits during Earthquakes", Proc. 11th Intl. Conf. on Soil Mech. and Found. Eng., San Francisco, Vol.1, pp. 321-376, 1985.

6. Keane, C.M. and Prevost, J.H. "An Analysis of Earthquake Data Observed at the Wildlife Liquefaction Array Site, Imperial County, California", Second U.S.-Japan Workshop on Liquefaction, Niagara Falls, N.Y., Sessions 1-4, Sept. 26-29, 1989.

7. Kondner, R.L. and Zalasko, J.S. "A hyperbolic stress-strain formulation for sands", Proceedings, 2nd Pan American Conference on Soil Mechanics and Foundations Engineering, 289-324, 1963.

8. Lee, K.W. and Finn, W.D.L. "DESRA-2 Dynamic Effective Stress Response Analysis of Soil Deposits with Energy Transmitting Boundary Including Assessment of Liquefaction Potential", Report, Univ. Of British Columbia, 60 p, 1978.

9. Natl. Res. Council "Liquefaction of soils during earthquakes", NRC report No. CETS-EE-001, 240 p, 1985.

10. Thilakaratne, V. and Vucetic, M. "Analysis of Liquefaction Occurrence at Wildlife Site During 1987 Superstition Hills Earthquake", Research Report, Civ. Eng. Dept., Univ. of California, Los Angeles, 1989.

11. Thilakaratne, V. and Vucetic, M. "Analysis of the Seismic Response at the Imperial Wildlife Liquefaction Array in 1987", Proc. 4th. U.S. Natl. Conf. Earthq. Eng., Palm Springs, CA, pp. 773-782, 1990.

12. Vucetic, M. "Pore Pressure Buildup and Liquefaction at Level Sandy Sites During Earthquakes", Ph.D. Thesis, Rensselaer Polytech. Inst., Troy, N.Y. (Available from Univ. Microfilms Int., Ann Arbor, MI 48106) 611 p, 1986.

13. Vucetic, M. and Dobry, R. "Cyclic Triaxial Strain-Controlled Testing of Liquefiable Sands, ASTM Spec. Tech. Publ. 977, pp.475-485, 1988.

14. Vucetic, M. and Thilakaratne, V. "Liquefaction at the Wildlife Site- Effect of Soil Stiffness on Seismic Response", Proc. 4th Int. Conf. on Soil Dyn. And Earthquake Eng., Mexico City, pp. 37-52, October 1989.

15. Zorapapel, G.T. and Vucetic, M. "The Effect of Pore Pressure Increase in a Sandy Liquefiable Deposit on the Spectral Content of Strong Motion", Proc. 4th. U.S. Natl. Conf. Earthq. Eng., Palm Springs, CA, pp. 793-802, 1990.

IV. SEISMIC ANALYSIS OF LIFELINES AND EARTHQUAKE RESISTANT DESIGN

Simplified Dynamic Analysis Method for Buried Structures (Grambs)
  I. Katayama, M. Adachi, and K. Ozeki
Analysis Procedures for Buried Pipelines Subject to Longitudinal and Transverse Permanent Ground Deformation
  M. O'Rourke and C. Nordberg
Idealization of Permanent Ground Movement and Strain Estimation of Buried Pipes
  N. Suzuki and N. Masuda
Pipeline Buckling Caused by Compressive Ground Failure During Earthquakes
  W.D. Meyersohn and T.D. O'Rourke
Tension/Bending Behavior of Buried Pipelines Under Large Ground Deformations in Active Faults
  T. Ariman and B.-J. Lee
Nonlinear Analyses of Piles Subjected to Liquefaction Induced Large Ground Deformation
  F. Miura and T.D. O'Rourke
Seismic Response of Shaft for Underground Transmission Line
  N. Kaizu

SIMPLIFIED DYNAMIC ANALYSIS METHOD FOR BURIED STRUCTURES (GRAMBS)

by

Ikuo Katayama[*], Masanobu Adachi[**], and Katsumi Ozeki[**]

 [*] Dr. Eng., Director, Advanced Engineering
   Operation Center,
 [**] Deputy Manager and Engineer
   Seismic Design Department
   Tokyo Electric Power Services Company Limited.
   3-1, Uchisaiwai-cho 1-chome, Chiyoda-ku,
   Tokyo 100, Japan

ABSTRACT

A simplified analysis method GRAMBS(Ground Response Acceleration Method for Buried Structures) for the cross-sectional design of structures such as buried ducts, tunnels and shafts in layered soil was proposed. The proposed method approximately predicts the maximum response of buried structures surrounded by layered soil which otherwise would require a more time consuming and expensive two-dimensional dynamic finite element analysis.

By introducing the acceleration distribution at the time when the portion of the soil in contact with a buried structure reaches the maximum strain energy state as the conserved body force acting on the system and using the converged strain-dependent soil properties, both given by the one-dimensional response analysis of the free-field soil surrounding the structure, the method replaces two-dimensional dynamic analysis by two-dimensional quasi-static analysis.

It is reported that the maximum dynamic response of a single-story duct obtained by an experiment was well reproduced by the analysis using FLUSH. The good coincidence of the recorded dynamic maximum response of an existing shaft during an earthquake with the predicted response by FLUSH is also reported.

The proposed method clearly reproduced the maximum response of both buried ducts with various installation conditions and an existing shaft in layered soil that were obtained by the more rigorous two-dimensional dynamic analysis code FLUSH-VB.

These results lead to conclude that the proposed method can be applied reliably and economically to the cross-sectional design analyses of buried structures surrounded by layered soil.

INTRODUCTION

There are increasing demands for more rational and reliable methods for the seismic design analysis of buried structures of lifeline systems such as buried ducts, shield tunnels and shafts, whereas the stress states of these structures are strongly affected by the dynamic behavior of the surrounding soil which usually shows very wide fluctuation with varying nature of soil properties inherent to the soil. Therefore, there arises the need for some analysis tool which may give reliable response results of these structures with a small computer time even if the variability of soil properties is introduced as parameters.

In some conventional design codes, we can find simplified analytical methods of buried ducts; e.g. so-called "Response Displacement Method" that has been recommended in currently available design codes. However, the method has yet too many options in its application assumptions and often significantly over-estimates or under-estimates the response of buried ducts if compared with the results obtained by rigorous analyses (I. Katayama et al, 1984). Such irregular or unreliable results are caused by the poor mechanism for converting the shear deformation of the surrounding soil into the response of the ducts(I. Katayama et al, 1985).

With the above situation and to provide a practical and reliable tool for practicing design engineers in refinement of the cross-sectional design of buried structures which is frequently controlled by highly varying properties of soil materials, a simplified analysis method GRAMBS (Ground Response Acceleration Method for Buried Structures) for the cross-sectional design of structures such as buried ducts, tunnels and shafts in layered soil is developed.

First the theoretical background of the proposed quasi-static method, GRAMBS, is described and the procedure to be followed in the calculation follows.

Next, the applicability of the proposed method to one-story duct surrounded by a uniform soil is shown and the results are compared with those obtained by the two-dimensional dynamic finite element code, FLUSH-VB(I. Katayama et al, 1984 and 1985). The study which compared the moment distribution of one-story duct surrounded by a uniform soil obtained by an experiment and the analysis by FLUSH are referred and used for validation of the GRAMBS.

Finally, the validation of GRAMBS for a multi-story shaft in a layered soil is shown by comparing the results obtained by GRAMBS and FLUSH-VB with the recorded response of an existing underground power transmission shaft.

THEORETICAL BACKGROUND OF THE PROPOSED METHOD

When a structure is buried in a soil, the structure in most cases can not behave independently from the surrounding soil. Here, the major external force to the structure is provided by the effective dynamic response of the

surrounding soil. The dynamic problem of such buried structures certainly becomes the quasi-static interaction problem of the system consisting of a structure and its surrounding soil.

Consider a system in a plane strain state which consists of a concrete duct with unit length and the surrounding uniform soil layer with unit width as illustrated in Fig. 1, and assume that the shear vibration will dominate this whole system.

When this two-dimensional system is excited by the horizontal input ground motion, $\ddot{Z}(t)$, the equation of motion is written by

$$[M]\ddot{X}(t) + [C]\dot{X}(t) + [K]X(t) = -[M]\ddot{Z}(t) \tag{1}$$

where $[M]$, $[C]$ and $[K]$ are the mass matrix, the damping matrix, and the stiffness matrix, respectively. The $X(t)$ means the relative displacement vector.

It is usual in a system like this one that the reduced specific weight and rigidity of the structure, which are calculated by redistributing the weight and rigidity uniformly over the entire area covered by the structure in the soil, are almost the same as those of the surrounding soil. Therefore, first we neglect the actual duct and assume the above system to consist only of the layered soil.

The problem therefore turns out to be that of the free-field response of a uniform soil. Define $[D]$ and $[B]$ as the stress matrix and the strain matrix, respectively. Take the time t_m when S^j = the stress of a small portion of the soil from the depth j to j+1; e.g.

$$S^j = [D][B]u^j \tag{2}$$

reaches maximum, then u^j = the relative displacement between the depth j and j+1 must be maximum and also satisfies Eq.(1) as

$$X^j(t_m) = X^{j+1}(t_m) + u^j \tag{3}$$

Eq.(1) can be rewritten as

$$[K]X(t_m) = -[M](\ddot{X}(t_m)) + \ddot{Z}(t_m)) - [C]\dot{X}(t_m) \tag{4}$$

where the right hand side is the dynamic force applied working on the whole system at time t_m. Because the time is fixed, the solution of Eq.(4) becomes a solution of the static problem.

If the damping of the soil is small, Eq.(4) may be approximated as

$$[K]X_a(t_m) = -[M](\ddot{X}(t_m) + \ddot{Z}(t_m)) \tag{5}$$

and the new approximate relative displacement vector $X_a(t_m)$ and corresponding stress vector S_a at time t_m will be obtained by solving the Eq.(5). In the above, if the soil reached its non-linear strain level at time t_m, the strain-dependent soil property at the time is preserved in the subsequent

procedure.

If in Eq.(5) the portion of the soil, that originally consisted of the duct and its cavity but was once assumed as the surrounding soil, is then replaced by the original duct and its cavity with their original material properties and the rest of the matrices [M], [K], [D] and [B] are assigned with the material properties corresponding to those determined by the free-field response analysis which are compatible with the stress state the vector u^j gives the maximum relative displacement between the top and bottom levels of the duct. If this new system is solved, the stress state of the system at the time when the portion replaced by the duct reaches the maximum stress state must be obtained; e.g., the maximum stress state of the duct surrounded by the soil is approximately predicted.

For more general case of multi-story ducts and multi-layered soil, at the time when the shear strain energy of the portion of the soil in contact with the structure becomes maximum, the maximum stress state will be generated in the structure:

Let $G^i(t)$, $e^i(t)$ and h^i be the shear modulus, the shear strain and the thickness of the i-th soil layer, and $U^j(t)$, the shear strain energy of the portion of the soil between the depth j and j+1, is obtained as

$$U^j(t) = \text{Sum } [(1/2)G_i(t)e_i^2(t)h_i] \quad (i=j \text{ to } j+1) \quad\quad (6)$$

Here we assume that the duct is surrounded by a uniform soil, then because $G_i(t)=G(t)$, $e_i(t)=e(t)$ and $h_i=h$, $U^j(t)$ becomes maximum when $u^j=e(t)h$ the relative displacement between the depth j and j+1 becomes maximum. Therefore, the above condition to define t_m, the time when the portion of the soil to be replaced by a buried structure shows the maximum relative displacement between the top and bottom levels of the duct, is derived as a special case of a single-story duct and uniform soil of a more general multi-story duct and multi-layered soil system.

Thus the case of combined duct and soil system, in which the duct is either single-storied or multi-storied and the soil is either uniform or layered, can be solved by maximizing the above shear strain energy in Eq.(6) and following the process described for the single-story duct in uniform soil.

Summarizing the above, the analysis procedure needed for the proposed GRAMBS is stated as follows:

(1) The duct as shown in Fig. 1(a) is idealized in a two-dimensional model following standard finite element technique. The maximum height of the horizontally layered mesh is determined similar to an analysis using codes like FLUSH, and the lateral and vertical size of the soil region must be determined considering the propagation of the affected force disturbance by the redistribution of stresses surrounding the duct. The side boundary condition of the soil region should be that of horizontal rollers.

(2) Neglecting the duct, the free-filed soil response analysis by the equivalent linear method as is used in SHAKE is performed for the

surrounding soil with the soil column having the same layering pattern as that of the two-dimensional model shown in Fig. 1(b). The time dependent displacement and acceleration response of each layer are stored with the converged soil properties.

(3) The time-dependent shear strain energy $U^j(t)$ in Eq.(6) is calculated using the time-dependent displacement, the converged shear modulus and the thickness of each layer within the depth interval of the top and bottom levels of the duct, and the time t_m when the energy becomes maximum is sought. The response acceleration profile at t_m is taken over the full depth of the soil column and converted into the seismic coefficient of each layer to be used for the input data for the body force in the static analysis.

(4) In the two-dimensional static finite element model prepared in (1) above, the converged soil moduli obtained in (2) above, the mass and the seismic coefficient derived in (3) above are used to solve the stress analysis problem under the body force by static finite element analysis. The resultant stress state of the duct at the time t_m is deemed as the approximate maximum stress state.

APPLICATION TO A SIMPLE DUCT AND ITS VALIDATION

Model duct and input ground motions used

A one-story multi-cell concrete duct shown in Fig. 2 is analyzed by GRAMBS under various installation conditions considering possible situation in practical design as is shown in Table 1 for different cases analyzed(I.Katayama et al, 1984). The burial depth of the duct is varied from the ground surface to the top of the soft rock. The depths of both the soil and rock are varied. The case number of the analyses is denoted by the model numbers. The dynamic material properties of the duct, the surrounding soil and the underlying soft rock are indicated in Table 2. To evaluate the nonlinear soil behavior during strong ground motion excitation, the strain dependent properties of the soil and the rock in Fig. 3 are used.

To examine the possible change of dynamic response of the duct with different input ground motions, two strong motion time histories with peak accelerations of 300 gals shown in Fig. 4 were prepared as the input ground motions of both numerical models described below; a strong motion from the Taft records obtained at the 1957 Kern County earthquake (deconvolved to the free-field motion at the outcrop of the underlying soft rock of the site) and a strong motion record obtained at the Lake Hughes array station No. 9(rock site) recorded in event of the 1971 San Fernando earthquake.

Numerical models and analyses

Two numerical models were prepared for each model as shown in Fig. 5 in which

the lower boundaries were set at the depth of 80 m below the ground surface and the figure shows the first 40 m portion of these models. One is semi-infinite horizontally layered model for use in the one-dimensional wave propagation analysis neglecting the presence of ducts. The other is a two-dimensional finite element model with plane strain assumption used in the dynamic analyses by FLUSH-VB and GRAMBS. As for the model used for FLUSH-VB, the viscous dampers are attached to the lower boundary in both the horizontal and vertical directions and the transmitting boundaries were adopted for the side boundaries; whereas the model used for GRAMBS was fixed at the lower boundary and the horizontal rollers were attached to its side boundaries.

First the free-field soil response analysis was performed to obtain each response acceleration distribution over all models of different depths at the time when the relative displacement of the soil between the top and bottom level of the submerged duct of each model in the previous Table 1 becomes maximum. The resultant response acceleration distributions are converted into the seismic intensity distributions, shown in Fig. 5 for Model-9 as an example, to the elements in the two-dimensional quasi-static finite element models containing the ducts.

Next, the analyses using GRAMBS and FLUSH-VB were performed as for all the models shown in Table 1. The results of the analyses were expressed in terms of the cross-sectional moment(M), axial force(N) and shear force(Q).

Results

The representative results of both analyses by FLUSH-VB and GRAMBS are summarized for the maximum cross-sectional forces in Table 3 and the details of the bending moment distribution of Model-2 are shown in Fig. 6 as an example. It is evident that the results obtained by GRAMBS are amazingly close to those obtained by FLUSH-VB.

The end-moments obtained by Model-2 and Model-9 are shown in Figs. 7 and 8, respectively, in comparative manner with the additional results by other simplified analysis methods(I.Katayama et al, 1985); these include the so-called Response Displacement Method (hereafter called as RDM) and the similar method proposed by CRIEPI(hereafter called RDM-C) in its report to the JSCE (JSCE, 1984). From these figures, it is evident that the results obtained by FLUSH-VB and GRAMBS are very close regardless of the condition of the duct relative to the surrounding soil, whereas the results obtained by RDM and RDM-C give either under-estimated or over-estimated results depending on the conditions.

The above simplified methods, RDM and RDM-C simply prescribe the maximum lateral relative displacement of the free-field soil between the top and bottom of the duct with the soil springs connected to the duct in the way they are assumed as independent normal springs and shear springs by ignoring the constitutive law governing the above two springs in a continuum element of the soil. If these methods should have used the compatible springs consistent with the resultant stress distribution around the duct obtained by FLUSH and GRAMBS as is shown in Fig. 9, almost same results may have been

obtained; however, such stress distribution as shown in this figure may not be foreseeable before doing a rigorous analysis, say by FLUSH-VB. Further, the RDM-C method applies additionally the time independent maximum response acceleration distribution of the soil to the duct, resulting in an inconsistent simplification caused by neglecting the basic equation of motion of the dynamic system.

Table 4 compares all the results obtained through the models in Table 1 but only for the maximum end-moments obtained by FLUSH-VB and GRAMBS. From this table and Table 5 showing similar results when the input ground motion was changed, the results obtained by GRAMBS always give very close results with those obtained by FLUSH-VB and stable for the possible change of the embedment depth of the duct, the shear wave velocity of the surface soil and the input ground motion. As for the time required for GRAMBS, it took only one tenth of the computer time required for the analysis by FLUSH-VB.

From all the above analytical results, it can be said with confidence that the GRAMBS proposed by the authors will be a good approximate method for predicting the maximum stress state of the type of buried ducts analyzed here or for similar single-story structures in uniform soil that would otherwise require a more rigorous two-dimensional finite element analysis like FLUSH-VB.

Validation of GRAMBS by the result of an experimental and numerical study

The dynamic response of a simple duct embedded in loose sand layer during strong ground motion has been studied using a shear soil column on a shaking table by Tohma and others of CRIEPI(Tohma and others, 1985).

The simple duct made of plastics of the size 45 cm by 60 cm was embedded in a naturally dried state fine sand packed in a cylindrical tank of internal diameter 300 cm and height 150 cm. This model was designed to correspond to the prototype duct of concrete embedded in soil with a shear wave velocity of around 250 m/s which is very close to the numerical models shown in Table 1.

The model was forced to vibrate by the transient motion equivalent to the 1940 El Centro record. The results of the shaking test for the case when the duct is embedded in the sand as the bottom of the duct reaches the depth equal to its height are given in terms of the maximum bending moment of the duct walls as shown plotted by open circles in Fig. 10(b).

The response of this duct during the shaking test was analyzed using the strain-dependent properties of the sand which was obtained by performing the resonance column test using the same shear column without the model duct as one case of the series of experiments. The calculated motion by FLUSH and the observed motion at the surface of the sand column are shown in forms of response spectra in Fig. 10(a). The numerical results are similarly given by the maximum bending moment distribution of the duct walls which is also plotted in the previous Fig. 10(b) by solid lines. The maximum bending moment distributions of the duct obtained by the experiment and the numerical analysis using FLUSH coincide well with each other.

425

The above comparative study of the experimental and numerical response behavior of the model duct clearly shows that the two-dimensional dynamic analysis code which considers the non-linear effect of the soil surrounding the duct can reproduce the dynamic behavior of the buried duct adequately.

The fundamental situation of the models in our numerical study and the above experimental study is almost common. Therefore, it can be finally concluded that the proposed GRAMBS can predict the maximum stress state of the type of prototype buried ducts having the conditions assumed here or for similar single-story structures in uniform soil.

APPLICATION TO AN UNDERGROUND POWER TRANSMISSION SHAFT IN LAYERED SOIL

Observed response and analytical results

Kaizu et al(1989(a)) and Kaizu et al(1989(b)) have reported the characteristics of the dynamic behavior of a shaft for underground power transmission system during earthquake and they simulated the maximum response accelerations, re-bar stresses and soil pressures by the two-dimensional finite element analysis using FLUSH.

The vertical section with the installed measuring sensors, the soil profile and soil properties explored in-situ are shown in Fig. 11, in which the values of the shear wave velocity and damping ratio of each soil layer were determined as those giving a best fit to the observed free-field response of the records of the vertical array installed about 31 m away from the shaft to observe the free-field soil response. The examples of the soil response motions recorded by the vertical array and the response of the shaft in the event of the Southern Ibaragi Prefecture Earthquake on October 4, 1985 are shown in Fig. 12.

To simulate the response of the shaft during the earthquake, the ground response at the vertical array was first simulated and the deconvolved outcrop motion at the depth of -82.55 m was used as the input ground motion for the numerical model shown in Fig. 13(a) by the code FLUSH and they obtained the results of the simulation as shown in Fig. 13(b), in which the absolute maxima obtained in the re-bar extensometers and soil pressure meters by the simulation analysis and observation are clearly shown with good agreement.

Simulation by GRAMBS

To simulate by GRAMBS the same maximum observations shown above, first the free-field response analysis was performed using basically the same soil profile and properties used in Kaizu et al(1989(b)) and the resultant acceleration profile of the soil at the time t_m=5.75 sec when the shear strain energy between the portion of the soil from the ground surface to the bottom of the shaft became maximum was obtained and converted into the

seismic intensity profile as shown in Fig. 14(b) for use in subsequent analysis. The determination of the time t_m was easy and unique as shown in Fig. 15.

The seismic intensity and the converged values of soil properties were used in the quasi-static finite element model of the system shown in Fig. 14(a) consisting of the shaft and the surrounding soil for the analysis by GRAMBS. The model used this time has more wide soil regions than the model used for the aforementioned simulation by FLUSH, because the analysis by GRAMBS is basically a static analysis and the applied body force does not alternate its direction as in an actual seismic load. The boundary conditions of the model are basically the same as were already described in the foregoing section.

The results of the simulation by GRAMBS, additional simulation by us using FLUSH-VB, and the record responses indicated for time t_m already mentioned are shown in Fig. 16. This figure indicates the alternate nature of the response of the duct which is different from the maximum absolute values given in the previous Fig. 13(b); however, the results obtained by GRAMBS coincide well with the maximum indications of the records and also those calculated by FLUSH-VB.

With the above results, it is already evident that the GRAMBS first developed for single-story duct within uniform soil can be applied also to structures like this shaft which consists of multi-story structures surrounded by multi-layered soil through the assumption of determining the time t_m that maximize the contribution of the shear strain energy of the soil to the embedded structure.

CONCLUSIONS

For providing a practical yet reliable tool for practicing design engineers and for refinement of the cross-sectional design of buried structures, a simplified analysis method GRAMBS for the cross-sectional design of structures such as buried ducts, tunnels and shafts in layered soil was proposed.

When a structure is buried under a soil, the major external force to the structure is provided by the effective dynamic response of the surrounding soil. Assuming a plane strain dynamic system consisting of buried structures surrounded by layered soil, it was shown theoretically that the proposed GRAMBS is a quasi-static method which approximately predicts the maximum response of the buried structures surrounded by soil which can be obtained by a more rigorous two-dimensional dynamic finite element analysis.

By introducing the acceleration distribution at the time when the portion of the soil in contact with the structure reaches the maximum strain energy state as the conserved body force acting on the system and by using the converged strain-dependent soil properties, both given by the response analysis of the free-field soil surrounding the structure, the GRAMBS solves the system idealized by a two-dimensional finite element model as a static problem.

The procedure of the calculation and the application results were shown as for a single-story duct surrounded by a uniform soil with varying embedment depth, soil properties, thickness of the soil layer and input ground motion. The results shown by the maximum cross-sectional forces of the ducts have well reproduced the corresponding forces obtained by a representative dynamic analysis code FLUSH-VB.

With the above results and based on the fact that the FLUSH could successfully reproduce the cross-sectional bending moment of a single-story duct model embedded in a dry sand layer obtained by an experiment performed, the validity of GRAMBS was confirmed for application to the single-story duct surrounded by uniform soil.

Further, the observed response of re-bar stress and contact soil pressure of an existing multi-story shaft in a multi-layered soil during an earthquake could be well reproduced by the the analysis using FLUSH. Utilizing the data used of the above simulation study, the numerical analyses were performed by GRAMBS and FLUSH-VB. The above observational results were again well reproduced by the both method.

With the results obtained in the above, it is concluded that the proposed GRAMBS will provide a practical yet reliable tool for refinement of the cross-sectional design of buried structures.

REFERENCES

(1) Katayama, I., M. Adachi, M. Shimada and T. Tsuzuki, On the practical analysis method for design analysis of buried structures, 19th Annual Meeting of Japan Society of Soil and Foundation, Abstracts, pp. 1445-1446, June, 1984(in Japanese).
(2) Katayama, I., M. Adachi, M. Shimada, T. Tsuzuki and Y. Seshimo, A quasi-static analysis method for for buried structures - A proposal of "Response Acceleration Method", Abstracts, 40th Annual Meeting of Japan Society of Civil Engineers, Part 1, pp. 737-738, Sept., 1985 (in Japanese).
(3) JSCE, Study on the evaluation of foundation - The study on the standardization of evaluation methodology of foundation, 1984.
(4) Tohma, J. et al, Model experiment of sea water intake duct of nuclear power plant, Denryoku doboku, No. 197, pp. 36-44, July, 1985(in Japanese).
(5) Kaizu, N., T. Annaka, and H. Ohki, Analysis of behavior of underground power transmission shaft during earthquake, 20th Oral Meeting of Earthquake Engineering Research, Japan Society of Civil Engineers, July, 1989(a)(in Japanese).
(6) Kaizu, N., M. Harada, T. Annaka and H. Ohki, Observation and numerical analyses of shaft for underground transmission lines, The American Society of Mechanical Engineers, PVP - Vol. 162, pp. 183-190, 1989(b).

Table 2 Dynamic material properties used for the model

	Specific weight t/qub.m	Poisson's ratio	Shear wave velocity m/s	Shear modulus t/sq.m
R.F.Concrete	2.4	0.1667	----	1.16 million
Surface soil	1.8	0.4	200	7,350
Soft rock	1.9	0.35	500	48,470
Base rock	2.3	0.3	1,000	234,690

Table 3 The results obtained by FLUSH-VB and GRAMBS(Vs=200 m/s;Taft record).

	FLUSH – VB			GRAMBS		
	2.8 1.8 2.6			2.8 1.8 2.6		
MODEL – 1						
	M	N	Q	M	N	Q
MODEL – 2	27	11	18	27	11	19
	M	N	Q	M	N	Q
MODEL – 9	68	33	51	61	34	45
	M	N	Q	M	N	Q

Notes: M; Maximum end moment (ton·m)
N; Maximum axial force (ton)
Q; Maximum shear force (ton)

Table 1 Installation conditions of model and case numbers

(Unit:m)

Ls	Ls/L	Ld= 2.75 Ld/L= .069	Ld= 15.0 Ld/L= .375	Ld= 27.75 Ld/L=.694	Ld= 40.0 Ld/L=1.00
40.0	1.00	MODEL - 1	MODEL - 2	MODEL - 3	MODEL - 4
27.8	.694	MODEL - 5	MODEL - 6	MODEL - 7	Legend
15.0		MODEL - 8	MODEL -9		

Notes: L ; Total depth of model
Ld; Embedment depth of duct
Ls; Depth of surface soil
denotes soft rock layer

Table 5 The maximum end-moments of Model-3 under different Vs and input ground motion.

| | Shear velocity of surface soil (Vs) | | | |
| | 200 m/s | | 300 m/s | |
	FLUSH-VB	GRAMBS	FLUSH-VB	GRAMBS
TAFT RECORD	47 M	47 M	61 M	56 M
LAKE HUGHES RECORD	21 M	22 M	29 M	29 M

UNIT: M (ton·m)

Table 4 The maximum end-moments by FLUSH-VB and GRAMBS (Vs=200 m/s and Taft record).

	FLUSH-VB	GRAMBS
MODEL-1	2.8 M	2.8 M
MODEL-2	27 M	27 M
MODEL-3	47 M	47 M
MODEL-5	3.7 M	3.7 M
MODEL-6	35 M	37 M
MODEL-7	80 M	80 M
MODEL-8	6.6 M	6.5 M
MODEL-9	68 M	61 M

UNIT: M (ton·m)
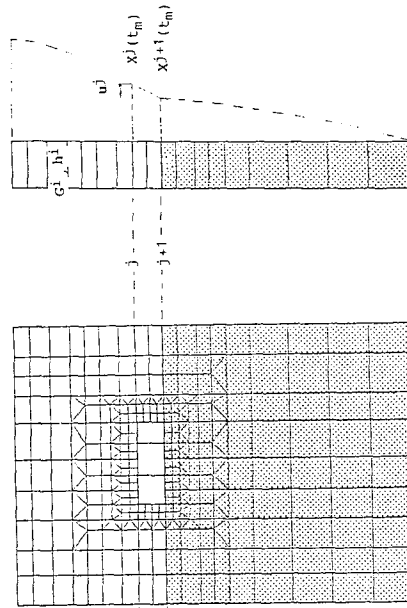
(a) 2-D FEM model (b) Free-field model

Fig. 1 Numerical model scheme of GRAMBS

430

Fig. 2 One-story concrete duct
used for the study
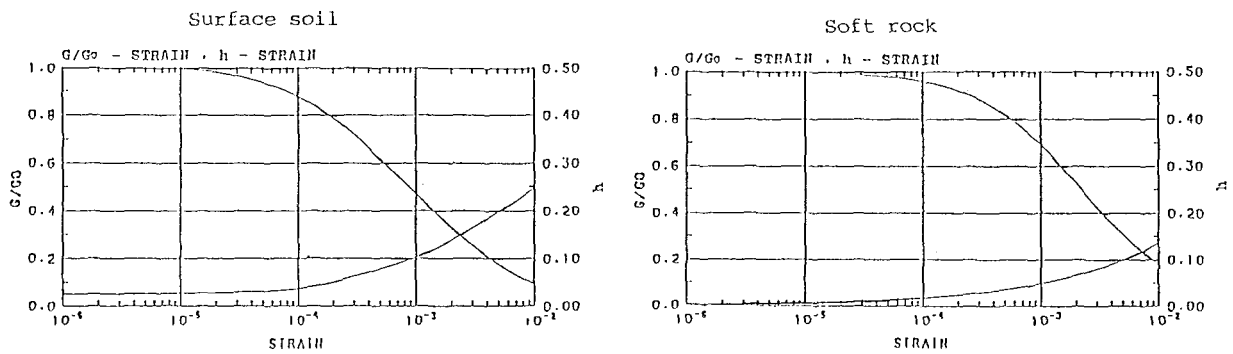
Fig. 3 Dynamic properties of the
soil and the soft rock
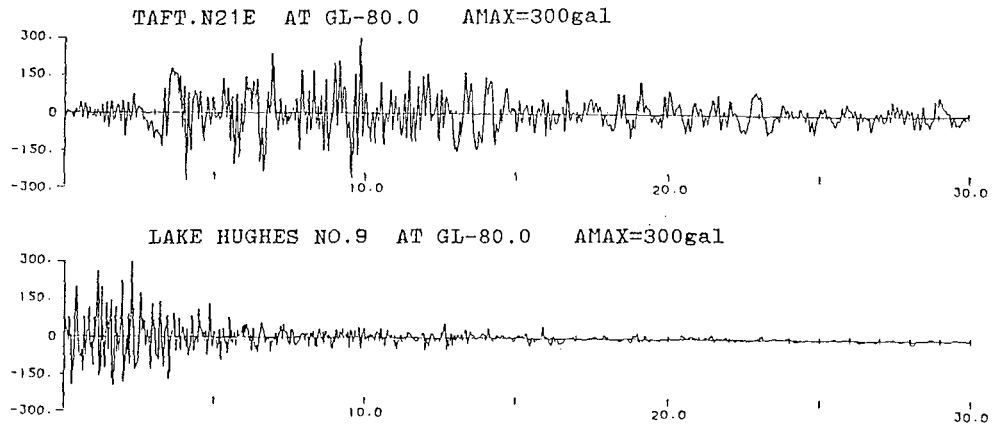
Fig. 4 Input ground motions used for analyses; the
upper figure shows the strong motion originated
from Taft records (1957) and the lower from
Lake Hughes array No. 9 (1971).

431
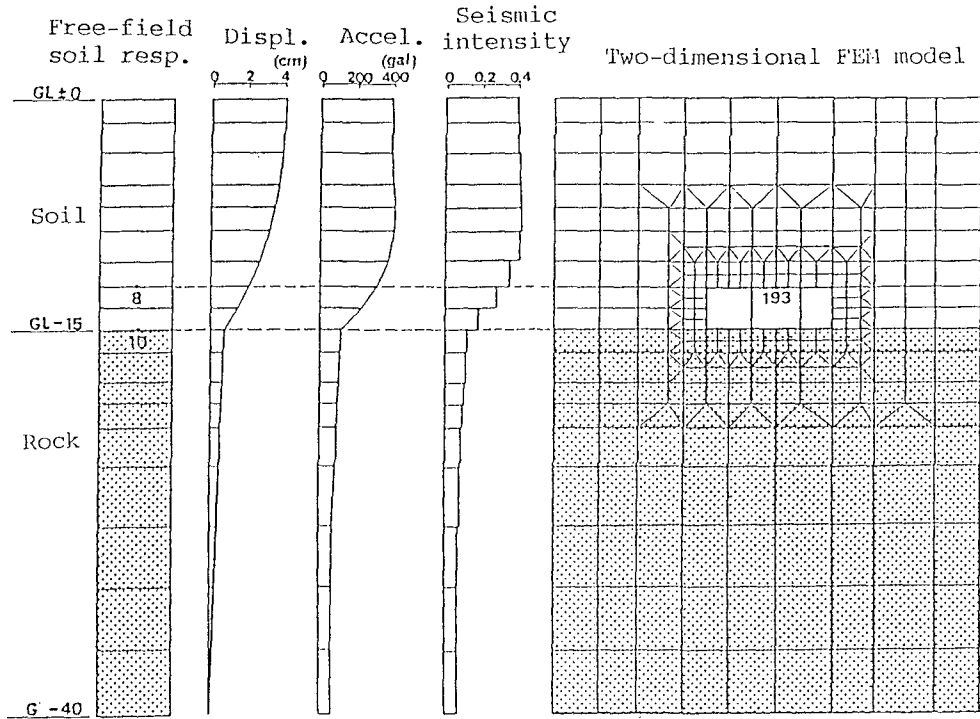
Fig. 5 Analysis procedure of the quasi-static analysis
by GRAMBS; dynamic response of free-field soil
is introduced into static FEM model.

(a) The results by FLUSH-VB

(b) The results by GRAMBS
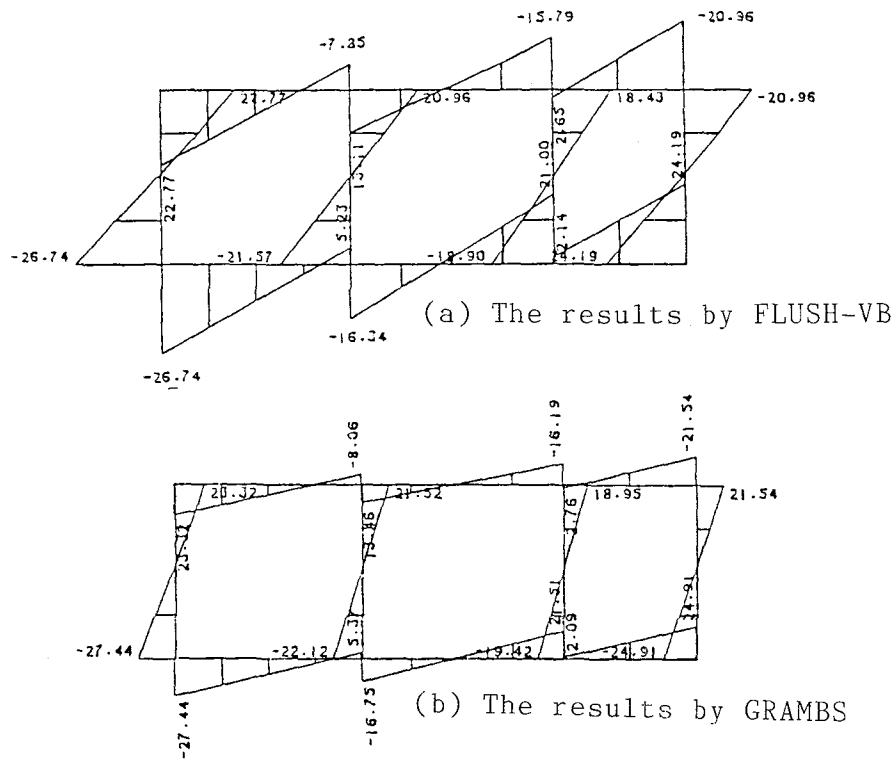
Fig. 6 The cross-sectional force distribution
of Model-2 indicated for T_M=4.02 sec.

432

(a) Normal stress

(b) Shear stress

Fig. 9 Comparison of the stress distribution at the outer surface of Model-9 by FLUSH-VB and GRAMBS.
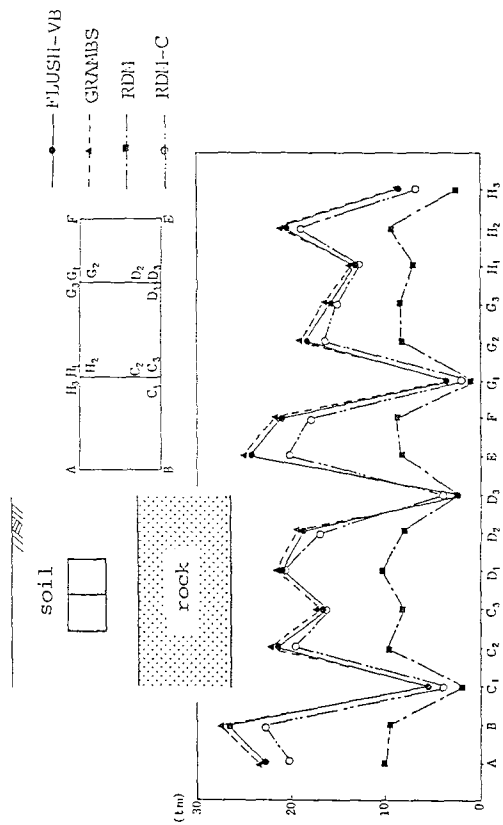
Fig. 7 The end-moment distributions of Model-2 (for GRAMBS at T_M=4.06 sec).
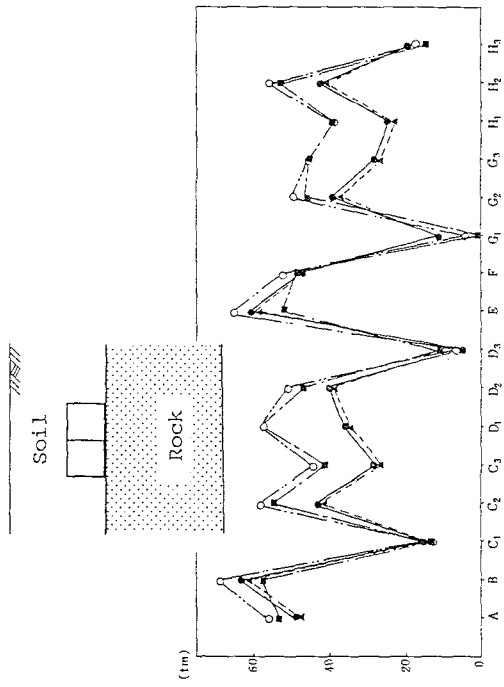
Fig. 8 The end-moment distributions of Model-9 (for GRAMBS AT T_M=6.82 sec.)

(5% damping)

Experim.
Analysis

Obs.
Calc.
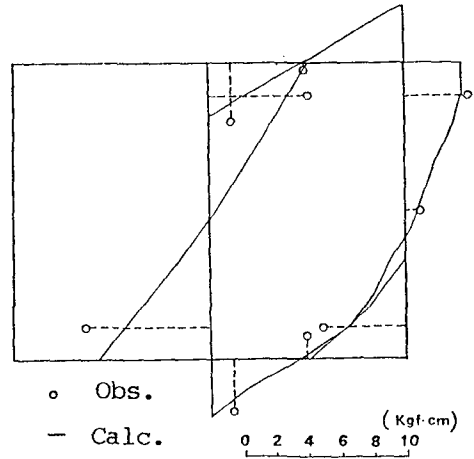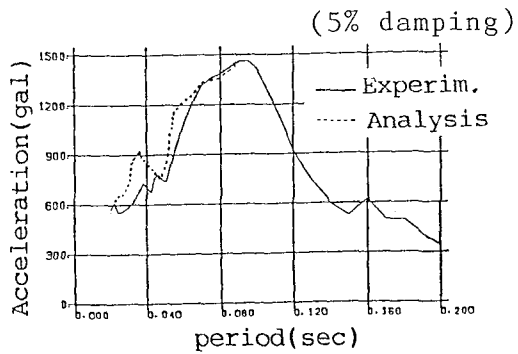
(a) Acceleration response spectra
    of free-field soil column

(b) Maximum bending moment
    distribution of the model.

Fig. 10 Experimental and computed results of
        the model by Tohma et al(1985).

GL m	SOIL PROFILE	N-VALUE 0 20 40	H m	ρ t/m³	Vp m/s	Vs m/s	G kg/cm²	h %
	SILT							
-5	FINE SAND		4.70	1.82	1500	110	225	4.0
-10	SILT		12.30	1.71	1500	110	211	3.5
-15								
-20	SILT							
	CLAY		3.75	1.69	1660	250	1078	2.9
	FINE SAND							
-25	SILT							
	CLAY		6.25	1.69	1660	250	1078	2.5
	MEDIUM SAND	58						
	GRAVEL	125						
-30		115						
	MEDIUM SAND	88	11.00	1.96	1770	480	4608	2.0
-35								
-40	FINE SAND	85	7.00	1.82	1770	360	2407	2.0
-45		75						

● : SEISMOMETERS
▮ : SOIL PRESSURE METERS
‖ : RE-BAR EXTENSO-METERS

Fig. 11 Vertical section of shaft, location of
        instruments, soil profile and properties
        of the surrounding soil.
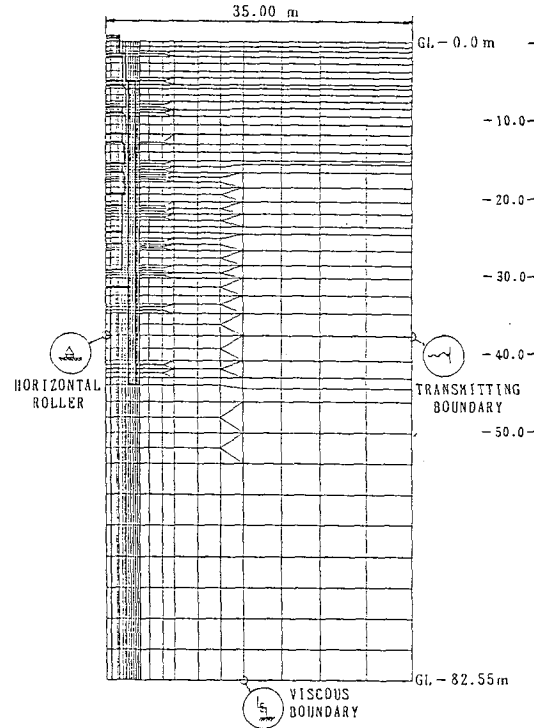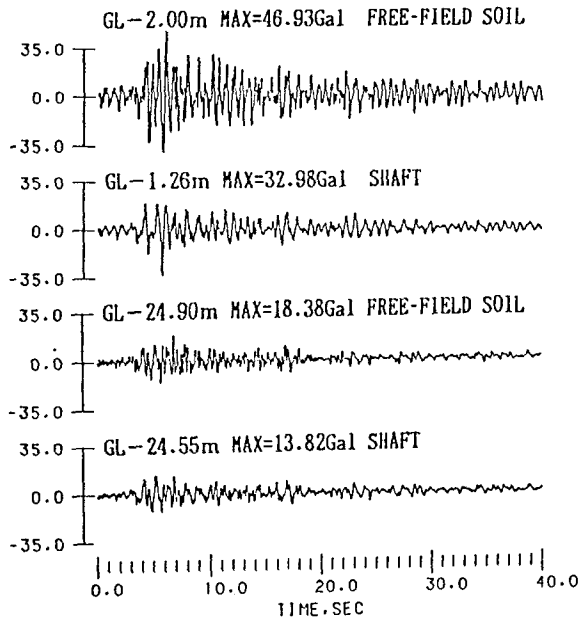
Fig. 12 Acceleration response of shaft and free-field soil in the shorter axis of the shaft.

(a)

(b)
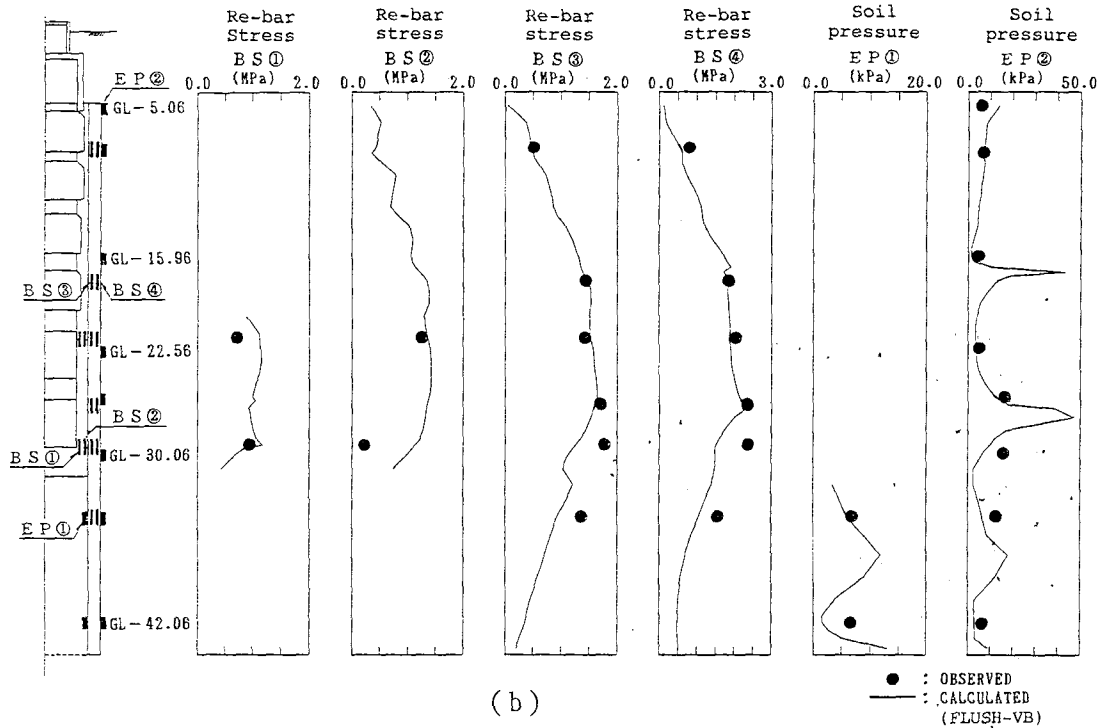
● : OBSERVED
──── : CALCULATED
       (FLUSH-VB)

Fig. 13 Numerical model and the comparison of the predicted results by FLUSH with the observed absolute maximum indications of re-bar extensometers and soil pressure meters of the shaft(Kaizu et al, 1989).

435

(UNIT: m)   INPUT INTENSITY(G)

(a) Numerical model   (b) Seismic
     for GRAMS   intensity
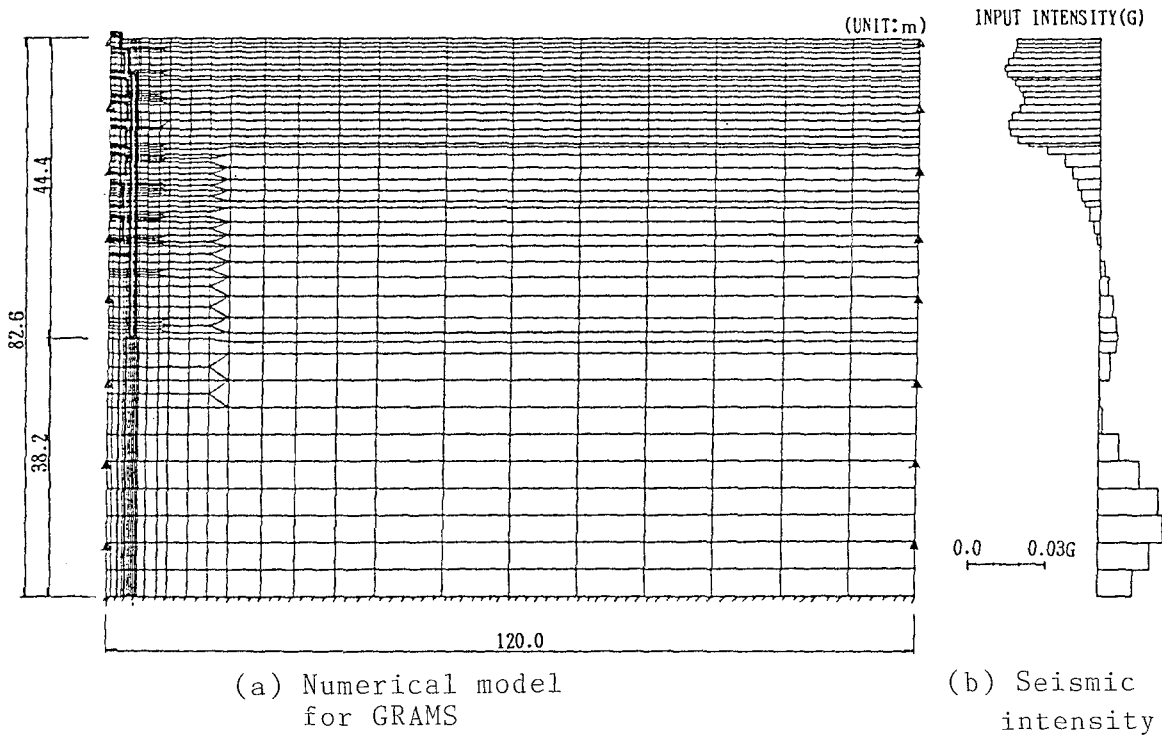
Fig. 14 Numerical model and seismic intensity distribution
        used in the quasi-static analysis by GRAMBS(direction
        of the shorter axis of the shaft).
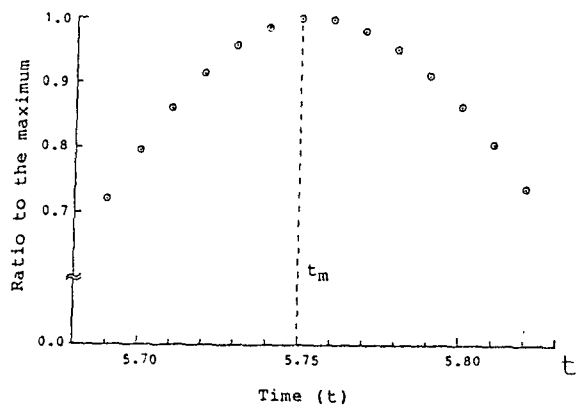
Fig. 15 Sensitivity of determination
        of the time t_m.
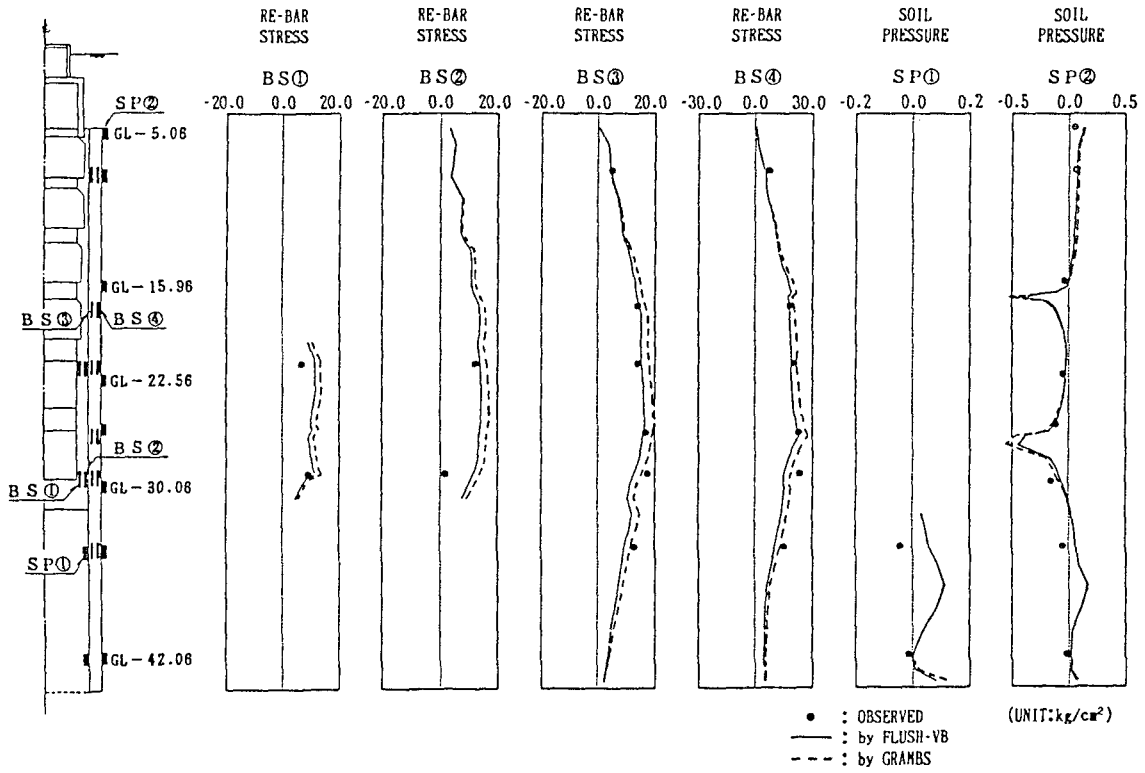
Fig. 16 Comparison of the results obtained by GRAMBS with the observed and calculated by FLUSH-VB at the time t_m=5.75 sec in terms of re-bar extensometers and soil pressure meters of the shaft.

ANALYSIS PROCEDURES FOR BURIED PIPELINES SUBJECT TO LONGITUDINAL AND TRANSVERSE PERMANENT GROUND DEFORMATION

Michael O'Rourke & Carl Nordberg

Professor and Graduate Student in Civil Engineering
Rensselaer Polytechnic Institute

ABSTRACT

Approximate analysis procedures for both segmented and continuous buried pipelines subject to Permanent Ground Deformation (PGD) are presented. Transverse PGD, where the ground movement is perpendicular to the pipeline axis, is considered as well as longitudinal PGD, where the ground movement is parallel to the pipeline axis. For segmented pipelines, the amount of relative displacement at the pipeline joints is determined and compared to leakage thresholds. For continuous pipelines, the assumed failure mode is local bucking of the pipeline wall. The analysis is based upon recent information on the geometry of lateral spreads in Japan. For continuous pipelines subject to transverse PGD, previously developed analytical results are compared to finite element (FE) results by others. For realistic values of the spatial extent of the lateral spread zone, it is shown that the approximate analytical results compare favourably with the FE results. Finally, the approximate analysis procedures developed herein suggest that longitudinal PGD is more likely to cause damage to both segmented and continuous pipe than transverse PGD.

INTRODUCTION

In the past, earthquakes have caused significant damage to buried pipelines. The damage mechanism have been permanent ground deformation (PGD) due to faulting, landslides, liquefaction or seismic settlements, and seismic wave propagation.

In this paper approximate analysis procedures are presented for both segmented and continuous pipe subject to transverse or longitudinal PGD where the abrupt relative displacements at the margins of the lateral spread zone are small. A key element in such an analysis is proper quantification of the geometry of the lateral spread zone. For example, previous analytical results by O'Rourke (1989) and finite element results by Kobayashi et al. (1989), O'Rourke (1988) and Suzuki et al (1988) clearly show the importance of the width of the lateral spread zone to the response of continuous pipe to transverse PGD.

LATERAL SPREAD GEOMETRY

Modeling PGD due to liquefaction is an area of ongoing research. In his state of the art report, Finn (1988) summarizes some of the more important contributions. He cites work by Hamada, et al. (1986) which suggests PGD induced by liquefaction of sandy soil is

closely related to the geometrical configuration of estimated liquefiable layers. They have proposed a regression formula to predict the magnitude of horizontal PGD in meters as a function of the thickness of the liquefied layer H, in meters and the slope θ_g in percent, of the lower boundary of the liquefied layer or the ground surface, which is larger.

$$\delta = 0.75 \sqrt[2]{H} \cdot \sqrt[3]{\theta_g} \tag{1}$$

Youd and Perkins (1987) introduce the concept of a Liquefaction Severity Index (LSI) which is defined as the amount of PGD (in inches) associated with lateral spreads on gently sloping ground and poor soil conditions. LSI is arbitrarily truncated at 100. They present an empirical relationship for LSI as a function of the earthquake magnitude M_w and distance R to the site, in kilometers, for Western U.S. Earthquakes.

$$\log LSI = -3.49 - 1.86 \log R + 0.98 \, M_w \tag{2}$$

For situations considered herein where the abrupt relative displacement at the margins of the lateral spread zone is small, the length (plan dimension parallel to the direction of PGD) and width (plan dimension perpendicular to the direction of PGD) of the lateral spread zone are key design parameters. Using data from the 1964 Niigata Earthquake, and the 1983 Nihonkai Chubu Earthquake, Suzuki and Hagio (1990) developed graphs of the amount of PGD, δ, versus the length, L, and width, W, of the lateral spread zone as shown in Figure 1. For longitudinal PGD (pipelines parallel to section BB in Figure 1) α and L are the key parameters. Data developed by Suzuki and Hagio (1990) suggest that L and α generally fall in the range $25 \text{ m} \leq L \leq 200 \text{ m}$ and $1/400 \leq \alpha \leq 1/50$ with an average value of $\alpha \simeq 1/130$

Suzuki and Hagio (1990) observed two types of transverse PGD behavior (pipelines parallel to section AA in Figure 1.), a "sinusoidal" variation shown in Fig. 1b and a "shear mode" variation shown in 1c. For the sinusoidal type, the Japanese data suggests that the minimum observed width was roughly 80 m, and the ratio of the maximum ground movement δ to the width W of the lateral spread zone generally fall in the range $1/1000 \leq \delta/W \leq 1/100$ with an average value of $\delta/W \simeq 1/350$. It can be shown that the "shear mode" of transverse PGD is equivalent to the sinusoidal since, for a given δ, typical values for the shear mode W are half those for the sinusoidal.

SEGMENTED PIPELINES – TRANSVERSE PGD

For segmented pipelines, transverse PGD induces bending in the pipe segments, and relative rotation at the pipeline joints due to the induced ground curvature. In addition, the change in the length induces axial tension in the pipe segments and relative axial displacement at the pipeline joints.

As a first approximation, one can look at a segmented pipeline as a series of relatively short rigid links connected by relatively flexible joints. Assuming that the pipeline segments are rigid, the transverse PGD is accomodated by relative axial displacement and rotations at the joints. Failure is assumed to occur when the total joint opening due to displacement plus rotation exceeds a leakage threshold.

440

Relative Axial Displacement at Joints

To evaluate the relative joint displacement due to arc length effects, we assume that the lateral displacement at the midpoint of the rigid pipe segment exactly matches the lateral ground movement at that point. Referring to Figure 2, relative axial displacement

$$\Delta x_t = l_{arc} - l \tag{3}$$

where l_{arc} is distance between the midpoints of adjacent pipe segments and l is the pipe segment length. If $y(x)$ is the lateral ground displacement.

$$\Delta x_t = l \left[\sqrt{1 + \left[\frac{dy}{dx}\right]^2} - 1 \right] \tag{4}$$

Assuming a sinusoidal variation of lateral soil displacement

$$y(x) = \frac{\delta}{2} \left[1 - \text{Cos } 2\pi x/W\right] \tag{5}$$

the relative axial displacement at a joint becomes

$$\Delta x_t = l \left[\sqrt{1 + \left[\frac{\delta\pi}{W}\sin\frac{2\pi x}{W}\right]^2} - 1 \right] \simeq \frac{l}{2}(\frac{\pi\delta}{W}\sin\frac{2\pi x}{W})^2 \tag{6}$$

This function is a maximum at $x = W/4$ and $3W/4$.

Relative Rotation at Joints

To evaluate the relative joint rotation due to ground curvature effects, we assume that the slope of the pipe segment in the horizontal plane exactly matches the ground slope at the pipe segments midpoint. Referring to Fig. 3, the relative rotation $\Delta\theta$ at the joint is

$$\Delta\theta = \frac{dy}{dx}(A) - \frac{dy}{dx}(B) \tag{7}$$

where $\frac{dy}{dx}(A)$ and $\frac{dy}{dx}(B)$ are the ground slopes at the midpoint of adjacent pipe segments.

For short pipe segment length

$$\Delta\theta \simeq \frac{d^2y}{dx^2} l \tag{8}$$

The joint opening due to this joint rotation is a function of Δx_t. If $\Delta x_t > \Delta\theta\,\phi/2$ then Δx_r is simply $\Delta\theta$ times the pipe radius

$$\Delta x_r = \Delta\theta \cdot \phi/2 = \frac{\phi l}{2} \cdot \frac{d^2 y}{dx^2} \qquad \Delta x_t > \Delta\theta \cdot \phi/2 \qquad (9)$$

and there is a separation around the whole perimeter of the joint. However, if $\Delta x_t < \Delta\theta \cdot \phi/2$, then there is a contact between adjacent pipe segments for some of the joint perimeter and

$$\Delta x_r = \Delta\theta \cdot \phi = \phi l \cdot \frac{d^2 y}{dx^2} \qquad \Delta x_t < \Delta\theta \cdot \phi/2 \qquad (10)$$

Again using the sinusoidal variation of lateral soil displacement given by eqn. (5) Δx_r becomes

$$\Delta x_r = \begin{cases} \pi^2 \dfrac{\delta}{W} \cdot \dfrac{\phi}{W} \, l \, \cdot \cos\dfrac{2\pi x}{W} & \Delta x_t > \Delta\theta \cdot \phi/2 \\[2ex] 2\pi^2 \dfrac{\delta}{W} \cdot \dfrac{\phi}{W} \, l \cdot \cos\dfrac{2\pi x}{W} & \Delta x_t < \Delta\theta \cdot \phi/2 \end{cases} \qquad (11)$$

This function is a maximum at $x = 0$, $W/2$ and W

The total opening or joint separation at one side of a joint due to transverse PGD, Δx is simply the sum of axial plus rotation effects. Note however, that the axial and rotational components are largest at different points along the lateral spread zone (axial component largest at $W/4$ and $3W/4$ while rotations component largest at 0, $W/2$ and W).

It can be shown that Δx has a maximum value of

$$\Delta x = \begin{cases} \dfrac{\pi^2 \, l \, \delta^2}{2W^2} \left[1 + (\phi/\delta)^2 \right] & \phi/\delta \leq .268 \text{ or } \phi/\delta \geq 3.73 \\[3ex] \dfrac{\pi^2 \, l \, \delta^2}{W^2} \left[\dfrac{2\phi}{\delta} \right] & .268 \leq \phi/\delta \leq 3.73 \end{cases} \qquad (12)$$

For segmented pipe subject to transverse PGD, Figure 4 is a plot of the maximum joint opening from eqn. (12) as a function of the δ/W ratio and the ϕ/δ ratio. In a subsequent section of this paper, Figure 4 will be combined with information on leakage thresholds to evaluate failure.

SEGMENTED PIPELINES – LONGITUDINAL PGD

For segmented pipelines, longitudinal PGD induces axial stress (tension or compression) in the pipe segments and relative extension or contraction at the pipeline joints. If the pipe segments are rigid, as assumed herein, all of the longitudinal PGD is accomodated by extension or contraction of the joint. Herein we restrict ourselves to cases when longitudinal PGD induces axial extension at the joint. We further assume that α in Figure 1d is constant over the whole length L of the lateral spread zone. That is we consider a model with uniform tensile ground strain over a length L.

442

ElHmadi and O'Rourke (1989) have considered the response of segmented buried pipe to uniform tensile ground strain. Using realistic variations of joint stiffness, the resulting joint displacements for uniform ground strain varied from joint to joint. That is, a relatively flexible joint experienced larger joint displacements than adjacent stiffer joints. Table 1 presents the mean joint displacement, Δx in centimeters and coefficients of variation μ in percent as a function of ground strain α for various diameters of Cast Iron pipe with lead caulked joints (C.I.) and Ductile Iron pipe with rubber gasketed joints (D.I.). Note that the mean values for both C.I. and D.I. pipes are about equal

$$\Delta \bar{x} \simeq \alpha \cdot l \tag{13}$$

where l is the pipe segment length. Since D.I. joints are substantially more flexible than C.I. joints, the μ values for D.I. are quite small.

The largest joint displacement within the lateral spread zone is a function of the number of pipeline joints subject to longitudinal PGD, $n=L/l$, and the mean and coefficient of variation of the joint displacement distribution given in Table 1. Herein we take the largest joint displacement as that value with a 50% chance of not being exceeded after n independent samples.

$$\text{Prob} (x < a) = (0.50)^{1/n} \tag{14}$$

Assuming the joint displacements have a normal distribution, the largest joint displacement is plotted in Figure 5 as a function of ground strain α, for various lengths L of the lateral spread zone. In a subsequent section, Figure 5 will be combined with information on leakage thresholds to evaluate failure.

CONTINUOUS PIPELINE – TRANSVERSE PGD

Most of the research to date on pipe response to PGD is for a continuous pipe subject to transverse PGD. Simplified analytical models by O'Rourke (1989) provides a physical foundation for interpreting results. For sinusoidal transverse PGD as shown in Figure 1b affecting a given pipeline, the amount of PGD, δ, as well as the width, W, of the lateral spread zone are critical parameters. If W is small, the pipe displacement is substantially smaller than δ and the pipe acts more or less like a beam subject to soil structure interaction forces due to soil flow over and under the pipe. In this case the "stiff" pipe survives irrespective of δ if W is less than a critical value. However, if W is large, the pipe displacement is essentially identical to δ (compliant pipe). In this case the "flexible" pipe survives if δ/W is small enough so that the pipe can conform to the imposed soil deformation without failure. O'Rourke (1989) combined both of these considerations (i.e."stiff" and "flexible" pipe) into a failure diagram for mild steel pipe which is reproduced in Figure 6. For any combination of δ and W below the solid horizontal line, the "stiff" pipe is strong enough to resist the soil structure interaction forces. For any combination of δ and W above and to the left of the solid curved line, the pipe is flexible enough to conform to the transverse PGD.

The availability of new information on the geometry of lateral spreads allows one to detrmine the mode of pipe responce to realistic transverse PGD. As mentioned previously, the Japanese data on sinusoidal transverse PGD suggests that W $\geq$80 m and $1/1000 \leq \delta/W \leq 1/100$, while limited data from a couple of U.S. earthquakes suggests W $\geq$ 30 m and $1/700 \leq \delta/W \leq 1/25$. For the purposes of this paper we will define typical

transverse PGD as having $1/1000 \leq \delta/W \leq 1/50$ and $W \geq 20$ m. These limits are shown as dashed lines in Figure 6. Notice that the typical transverse PGD region coincides with the "flexible" pipe response region. That is for $W \geq 20$ m and $\delta/W \leq 1/50$, the maximum pipe displacement is approximately δ.

Assuming the pipe displacement matches the ground displacement pattern given by eqn. 5, O'Rourke (1989) showed that the maximum bending stress for the "flexible" pipe is

$$f_b = \pi^2 E \, \frac{\delta \, \phi}{W^2} \tag{15}$$

and hence the maximum bending strain ϵ_b becomes

$$\epsilon_b = \pi^2 \frac{\delta \, \phi}{W^2} \tag{16}$$

The approximate analytical result in eqn. 16 will be compared with finite element (FE) results by others. We will restrict the comparison to FE results for $W \geq 20$ m and $\delta/W \leq 1/50$. O'Rourke (1988) used the program UNIPIP to study the responce to a 610 mm (24 in) diameter pipe with 9.5 mm (3/8 in) wall thickness buried 1.2 m (4 ft) below ground. The maximum tensile strain for various width W of the lateral spread zone are presented in Table 2. Table 2 also shows FE results for 610 mm (24 in) pipe with 12.7 mm (1/2 in) wall thickness by Suzuki et. al. (1988) using the program Line–Flex, and results for 406 mm (16 in) and 610 mm (24 in) diameter pipe with 7.9 mm (5/16 in) and 9.5 mm (3/8 in) wall thicknesses respectively by Kobayashi et.al. (1989). For all cases presented in Table 2, there was a nearly linear increase in strain with increasing δ up to $\delta/W = 1/50$.

Figure 7 is a plot of the strain values in Table 2 plotted against the quantity $\delta\phi/W^2$. Some of the differences among the FE results are likely attributed to the assumed ground displacement patterns. For example O'Rourke (1988) used a soil displacement pattern proportional to the beta probability density function while Suzuki et.al. (1988) and Kobayashi et.al. (1989) use the cosine function to an integer power. However, the analytical relationship for bending strain in eqn. 16 yield values within about 10% of all of the FE results for "typical" transverse PGD geometries. Hence eqn. 16 can be used for design purposes, at least, for usual situations where $W \geq 20$ m and $\delta/W \leq 1/50$.

CONTINUOUS PIPELINE – LONGITUDINAL PGD

For continuous buried pipeline subject to longitudinal PGD axial movement and stress in the pipeline are due to friction–like forces at the soil/pipeline interface. Tests performed by Colton et. al. (1981) on a full–scale pipe indicate that the axial force/displacement relationship at the soil/pipeline interface is linear at small displacements. The soil resistant force reaches a "plateau" when slippage of the pipe with respect to the soil occurs. Of particular interest is the specific value of relative displacement at which slippage occurs. This relative axial displacement inferred from tests on soil/pile interaction performed by Holloway (1975), ranges between 0.01 and 0.04 inch (0.025 and 0.1 cm). Lower values correspond to denser soils with higher overburden pressure and vice versa.

As a first approximation, we assume that the relative displacement at the soil pipeline interface is larger than 0.04 in over a significant length of the pipe. Hence the pipeline is subject to a constant friction force f_m per unit length. For the case where the pipeline trench is backfilled with cohesionless soil, the friction force per unit length at the

soil/pipeline interface f_m is simply the coefficient of friction times the product of the pipe circumference and the average of the vertical and the horizontal pressure on the pipeline, that is:

$$f_m = \mu \cdot \gamma H \cdot \frac{(1+K_0)}{2} \cdot \pi\phi \qquad (17)$$

where μ is the coefficient of friction at or near the soil/pipeline interface, γ is the unit weight of the soil, H is the depth to the pipe centerline, K_0 is the coefficient of lateral earthpressure and ϕ is the outside diameter of the pipe.

Experimental studies have shown that the coefficient of friction between the soil and the pipeline, μ, depends mainly on the nature of the pipe surface, the angularity of the soil grains and the relative roughness of the pipe surface with respect to the soil grains. Elhmadi and O'Rourke (1989) have reviewed the experimental studies and suggest the following $\mu = 0.9 \tan\phi_s$ for Concrete pipes with smooth surface and for normal Steel, Cast Iron or Ductile Iron pipes where ϕ_s is the angle of shearing resistance of the soil.

The magnitude of K_0 for normally consolidated cohesionless soil typically range from 0.35 to 0.47. However, because of the backfilling and compaction of the soil around the pipeline, one expects K_0 to be somewhat larger. $K_0 = 1.0$ is recommended as a conservative estimate under most conditions of pipeline burial.

Figure 8 shows a model of a continuous pipe subject to longitudinal PGD. The assumed longitudinal ground movement u(x) is:

$$u(x) = \begin{bmatrix} 0 & x \leq 0 \\ \alpha x & 0 \leq x \leq L \\ \alpha L & x \geq L \end{bmatrix} \qquad (18)$$

where L is the length of the lateral spread zone. Figure 8 also shows the axial movement of the pipeline $u_p(x)$. Note that the relative displacement between pipe and surrounding soil is greatest at the margins of the lateral spread zone (i.e. x = 0 and L). By symetry the pipe and soil displacements match at the center of the zone (i.e. $u(L/2) = u_p(L/2) = \alpha L/2$)

As a first approximation, we assume that slip occures over a length $2L_e$ and that the relative displacement between the pipe and soil is very small beyond L_e. The pipe displacement at center of the lateral spread zone can be calculated by integration of pipe strain over the slip length L_e

$$\frac{\alpha L}{2} = \int_0^{L_e} \frac{f_m x}{AE} dx = \frac{f_m L_e^2}{2AE} \qquad (19)$$

where A = pipe cross-sectional area and E = pipe modulus of elasticity. Note that the maximum axial force in the pipe occurs at the center of the lateral spread zone and equals $f_m \cdot L_e$. Equations 17 and 19 combine to give the maximum axial strain in a continuous pipe due to longitudinal PGD.

$$\epsilon_a = \sqrt{\frac{\mu\gamma H(1+K_0)\alpha L}{tE}} \qquad (20)$$

FAILURE CRITERION – SEGMENTED PIPE

For the cases considered herein, the failure criterion is joint opening which exceeds a leakage threshold. The only published test data on leakage of segmented pipe is Prior (1935). Prior performed a series of laboratory tests on AWWA Class D cast iron water pipe having diameters from 6 to 60 in (15.2 to 152 cm). An analysis by Elhmadi and O'Rourke (1989) of Prior's results indicates that the relative joint displacement corresponding to significant leakage, Δx, is a function of the depth, d, of the joint. On average a lead caulked joint will leak significantly if it is pulled about halfway out. Herein we use 0.5d as the leakage threshold for Cast Iron pipe. This leads to the values listed in the first column in Table 3, which gives the relative joint displacement corresponding to significant leakage.

The authors are not aware of published leakage data for other pipe materials. However, manufactures literature contain the maximum recommended joint deflection angle for laying purposes. These maximum recommended angles vary somewhat from manufacture to manufacture. However, for Ductile Iron pipe with push on rubber gasket, or mechanical joints the average value is about 2.5° for a 61 cm (24 in) diameter pipe. For concrete pipe, prestressed cylinder pipe, embedded cylinder pipe, etc., the values are somewhat lower, about 1.4° for a 61 cm (24 in) diameter pipe and about 1.05° for a 122 cm (48 in) diameter pipe. Based upon joint geometry, we assume herein that the leakage threshold Δx for Ductile iron and concrete pipe is 1.5 times the joint opening corresponding to the manufacture's maximum recommended joint angle. These values appear in the second and third columns of Table 3. It should be mentioned that there are special joints such as the US Pipe USI Flex or the EBAA Iron FlexTend which allow joint rotations up to 15° for a wide range of pipe diameters.

Comparison of Longitudinal and Transverse Effects

Longitudinal PGD and transverse PGD effects on segmented pipe are compared in this section. A 61 cm (24 in) diameter cast iron pipe and the same diameter ductile iron pipe will be considered. From Table 3 the leakage thresholds are 5.28 cm and 3.58 cm respectively. In addition we use the data in Suzuki and Hagio (1990) to establish the geometry of an "average" PGD zone. For longitudinal PGD we have $\alpha = 0.007 = 1/143$ and L = 110 m while for sinusoidal transverse PGD we have $\delta = 0.75$ m, W = 250 m and $\delta/W = .003 = 1/333$.

From Figure 4 or eqn. (12) the maximum joint opening for transverse PGD is about 0.15 cm for $\phi/\delta = 1.24$ and $\delta/W = 0.003$. This is more than an order of magnitude lower than the leakage thresholds for 61 cm (24 in) diameter C.I. or D.I. pipe. However, for longitudinal PGD with $\alpha = 0.007$ and L = 110 m , figure 5 gives a maximum joint opening of about 4.2 cm for D.I. pipe and about 5.5 cm for C.I. pipe. These values for longitudinal PGD are about equal to the leakage thresholds in Table 3. Hence it appears from this analysis that longitudinal PGD is much more likely to cause leakage in segmented pipe than transverse, at least for the PGD geometry qualified by Suzuki and Hagio (1990). This analytical result is in agreement with empirical data developed by Suzuki (1988). He found that PGD damage to 250 mm (10 in) diameter cast iron gas distribution pipe during the 1964 Niigata earthquake was heaviest when the ground displacement vectors were almost parallel to the pipe axis (longitudinal PGD).

FAILURE CRITERION – CONTINUOUS PIPE

An appropriate failure criterion for continuous butt welded steel pipe is yeilding or local buckling (wrinkling) in the case of a thin walled pipe. The allowable pipe strain must be reduced if welded slip joints are used to construct the pipeline. As pointed out by Tawfik and O'Rourke (1984) yeilding at the weld of the slip joint and plastic flow in the curvilinear belled ends must also be considered for welded slip joints.

Comparison of Longitudinal and Transverse Effects

Longitudinal PGD and transverse PGD effects on continuous pipe are compared in this section. A 61 cm (24 in) diameter pipe with 12.7 mm (1/2 in) wall thickness is considered. As before the "average" longitudinal PGD zone has α =0.007 and L=110 m while the "average" sinusoidal transverse PGD zone has δ = 0.75 m, W = 250 m and δ/W = 0.003 = 1/333.

For the "average" transverse PGD zone defined above, equation 16 gives a maximum bending strain ϵ_b = 7.23 $\cdot$ 10^{-5}. However, for the "average" longitudinal PGD zone defined above, equation 20 give a maximum axial strain ϵ_a = 1.95 $\cdot$ 10^{-3} for μ = 0.9 tan 40° = 0.75, γ = 100 lbs/ft^3 and K_0 = 1.0, and 2.5ft of cover over the top of the 61 cm (24 in) diameter pipe.

Note that the strain due to longitudinal effects is more than an order of magnitude larger than that due to transverse effects. Hence, as was the case with segmented pipe, longitudinal PGD appears much more likely to cause damage to continuous pipe than transverse PGD, at least for the PGD geometry quantified by Suzuki and Hagio (1990).

SUMMARY AND CONCLUSIONS

The responce of buried pipe lines to PGD in which there is no abrupt relative displacement at the margins of the lateral spread zone was studied. Analytical relationships for the amount of joint opening in segmented pipe and the longitudinal strain in continuous pipe were developed. Separate relationships for longitudinal PGD (ground movement parallel to pipe axis) and transverse PGD (ground movement perpendicular to the pipe axis) were developed. The analytical relation for bending strain in continuous pipe subject to transverse PGD was found to be within 10% of finite element results by other, for expected PGD zone geometries.

For segmented pipe, leakage thresholds for joint opening were developed from laboratory tests by others and through manufactures literature on the maximum allowable angular deflection at a joint for pipeline laying purposes.

The following conclusions were reached:

* For a reasonable range of transverse PGD geometries, the lateral displacement of typical continuous pipe is essentially identical to that of the soil (compliant pipe)

* For both segmented and continuous pipe, leakage or damage is more likely for longitudinal PGD.

REFERENCES

Colton, J.D., Chang, P.H.P., Lindberg, H.E., and Abrahamson, G.R., (1981), "Measurement of Dynamic Soil–Pipe Axial Interaction for Full–Scale Buried Pipelines under Field Conditions," Project PYU–1434, SRI International , Menlo Park, California, November.

Elhmadi, K., O'Rourke, M., (1989) "Seismic Wave Propagation Effects on Straight Jointed Buried Pipeline,"Tech. Rept. NCEER–89–0022, Natl Center for Earthquake Engineering Research, Buffalo, N.Y.

Finn, L., (1988), "Permanent Deformations in Ground and Earth Structures During Earthquakes," Proc. Ninth World Conference on Earthquake Engineering, Tokyo–Kyoto, Japan, Vol. VIII, pp. VIII–201 to VIII–212.

Hamada, M., Yasuda, S., Isoyama, R., and Emoto, K., (1986), "Study of Liquefaction Induced Permanent Ground Displacements," Assoc. for the Development of Earthquake Prediction, Japan, pp. 87.

Holloway, D.M., (1975), "The Mechanics of Pile–Soil Interaction in Cohesionless Soil," Ph.D. Thessis, Duke University, Durham, North Carolina.

Kobayashi, T., Nakane, H., Suzuki, N., and Ishikawa, M., (1989), "Parametric Study on Flexibility of Buried Pipeline Subject to Large Ground Displacement," Proc. Second U.S.–Japan Workshop on Liquefaction, Large Ground Deformation and Their Effects on Lifelines, Buffalo, NY, September 1989, Tech. Rept. NCEER–89–0032, pp. 348–362.

O'Rourke, T. (1988), "Critical Aspects of Soil–Pipeline Interaction for Large Ground Deformation," Proc. First Japan–U.S. Workshop on Liquefaction, Large Ground Deformation and Their Effects on Lifeline Facilities, Tokyo, November 1988, pp. 118–126.

O'Rourke, M., (1989), "Approximate Analytical Procedures for Permanent Ground Deformation Effects on Buried Pipelines," Proc. Second U.S. – Japan Workshop on Liquefaction, Large Ground Deformation and Their Effects on Lifelines, Buffalo, NY Sept. 1989, NCEER–89–0032,pp. 336–347.

Prior, J., (1935), "Investigation of Bell and Spigot Joints in Cast Iron Water Pipes," Bulletin No. 87, The Engineering Experiment Station, Ohio State University Studies Engineering Series, Vol. IV, No. 1.

Suzuki, H., (1988), "Damage to Buried Pipes Caused by Large Ground Deformation," Proc. First Japan – U.S. Workshop on Liquefaction Large Ground Deformation and Their Effects on Lifeline Facilities," Tokyo, Japan, November, pp. 127–132.

Suzuki, N., Arata, O., Suzuki, I., (1988), "Parametric Study of Deformation Analysis of Welded Pipeline Subject to Liquefaction–Induced Permanent Ground Deformation," Proc. First Japan–U.S. Workshop on Liquefaction, Large Ground Deformation and Their Effects on Lifeline Facilities, Tokyo, Japan, November 1988, pp. 155–162.

Suzuki, N. and, Hagio, A., (1990), "Safety Assessment of Welded Pipelines Undergoing Large Ground Deformation," Proc. Pipeline Design and Installation Conf., ASCE, Las Vegas, NV, March, pp. 108–119.

Tawfik, M and, O'Rourke, T., (1984), "Welded Slip Joint Response to Earthquake Axial Loads," 1984 PVP Exhibition and Conference, San Antonio, TX, June, ASME, paper No. 84–PVP–68.

Youd, T. and, Perkins, D., (1987), "Maping of Liquefaction Severity Index," J. Geotechnical Engineering, ASCE, Vol. 113, No. 11, Nov., pp. 1374–1392.

Ground strain α	16"ϕ C.I. (40 cm)		30" ϕ C.I. (76 cm)		48" ϕ C.I. (122 cm)		16 to 48" ϕ D.I. (40 to 122 cm)	
	$\Delta\bar{x}$(cm)	μ(%)	$\Delta\bar{x}$(cm)	μ(%)	$\Delta\bar{x}$(cm)	μ(%)	$\Delta\bar{x}$(cm)	μ(%)
0.001 (1/1000)	.54	64	.56	54	.58	52	.59	2
0.002 (1/500)	1.14	56	1.16	49	1.17	43	1.19	2
0.005 (1/200)	2.92	39	2.95	24	2.97	14	3.00	1
0.007 (1/150)	4.12	26	4.16	19	4.16	16	4.19	1

Table 1   Joint Displacement Mean and Coefficient of Variation for Segmented Pipe Subject to Longitudinal PGD

ϕ (m)	δ (m)	W (m)	δ/w	ϵ	Reference
0.61	1.0	50	1/50	0.002	O'Rourke 1988
0.61	0.60	30	1/50	0.003	O'Rourke 1988
0.61	1.0	50	1/50	0.0029	Suzuki et al. 1988
0.61	0.6	30	1/50	0.0046	Suzuki et al. 1988
0.406	0.8	40	1/50	0.00208	Kobayashi et al. 1989
0.406	0.6	30	1/50	0.0033	Kobayashi et al. 1989
0.406	0.4	20	1/50	0.00516	Kobayashi et al. 1989
0.60	0.48	24	1/50	0.006	Kobayashi et al. 1989

Table 2   Maximum Strain in Continuous Pipe for Transverse PGD by Finite Element Method

Diameter ϕ	$\Delta\bar{x}$ (cm)		
	Cast Iron	Concrete	Ductile Iron
30.5 cm(12 in)	5.28	–	4.06
61.0 cm(24 in)	5.28	2.24	3.98
91.4 cm(36 in)	5.94	2.87	5.26
122 cm(48 in)	6.60	3.35	4.77
152 cm(160 in)	7.26	3.78	–

Table 3   Leakage thresholds $\Delta\bar{x}$ for Segmented Pipeline

(b) Section AA - Sinusoidal Transverse

(c) Section AA - Shear Mode Transverse

(d) Section BB - Longitudinal

(a)
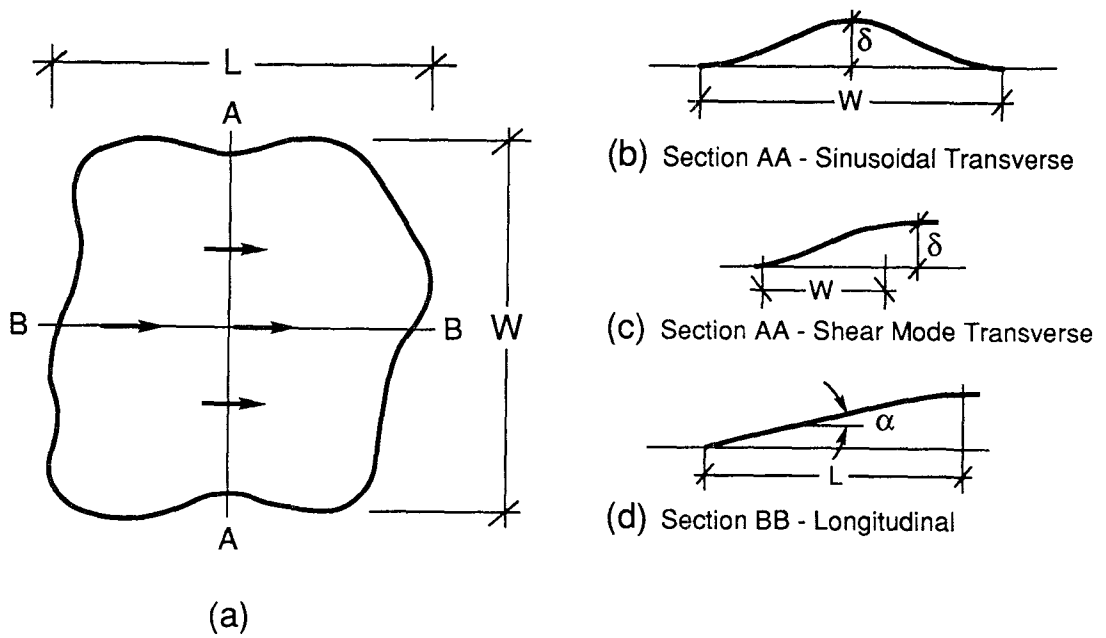
Figure 1.   Lateral Spread Geometry
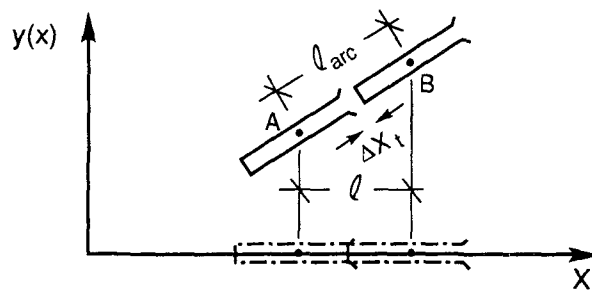
Figure 2.   Plan View of Transverse PGD showing Joint Extension
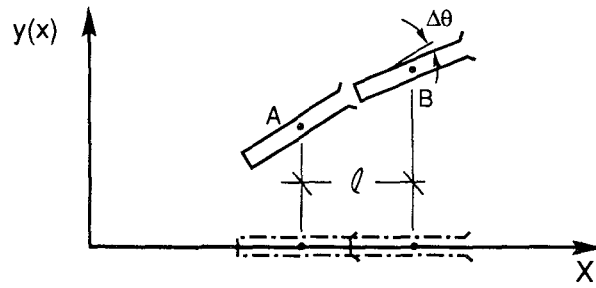
Figure 3. Plan View of Transverse PGD showing Joint Rotation
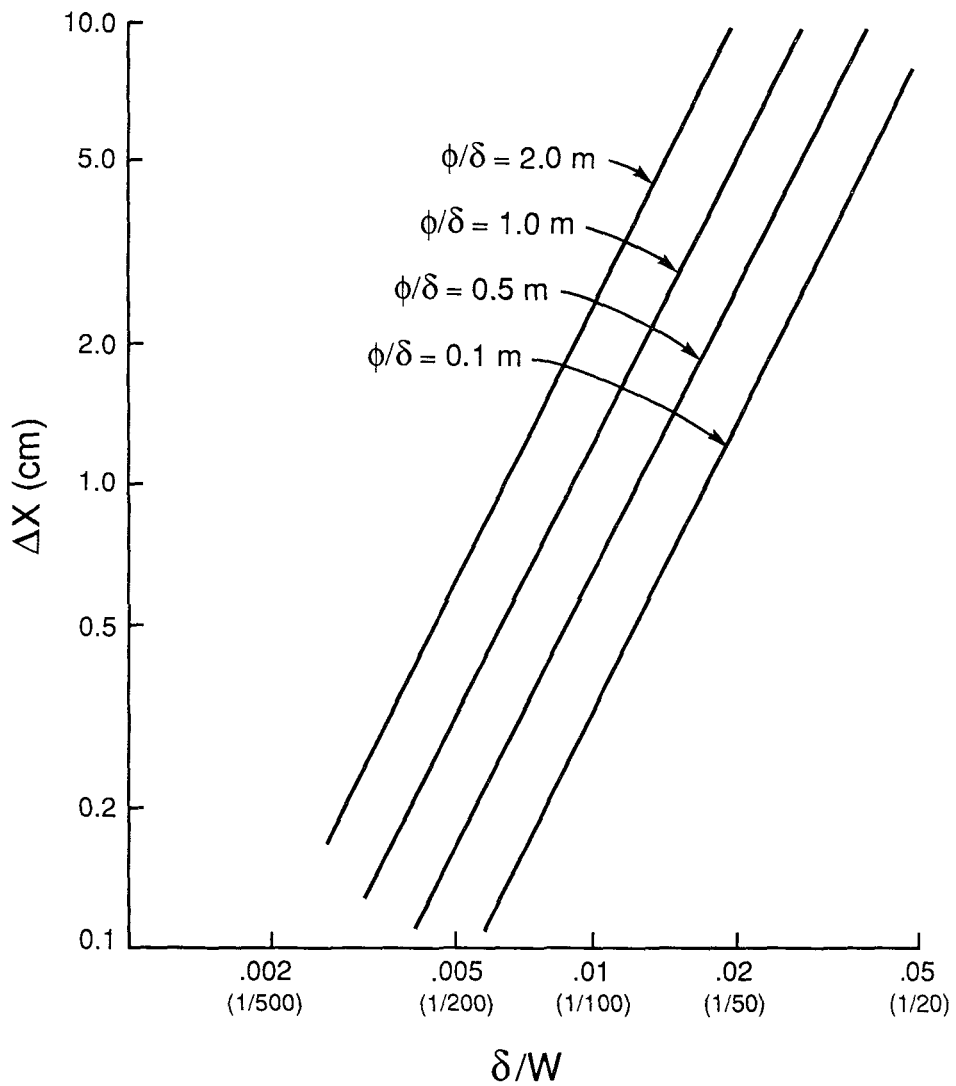
Figure 4. Maximum Joint Opening for Transverse PGD (ℓ=6 m)
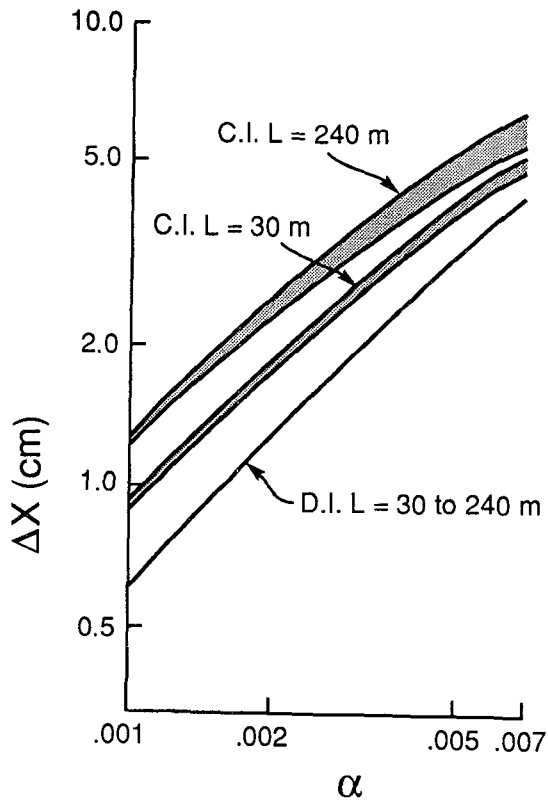
Figure 5. Largest Joint Opening for Longitudinal PGD
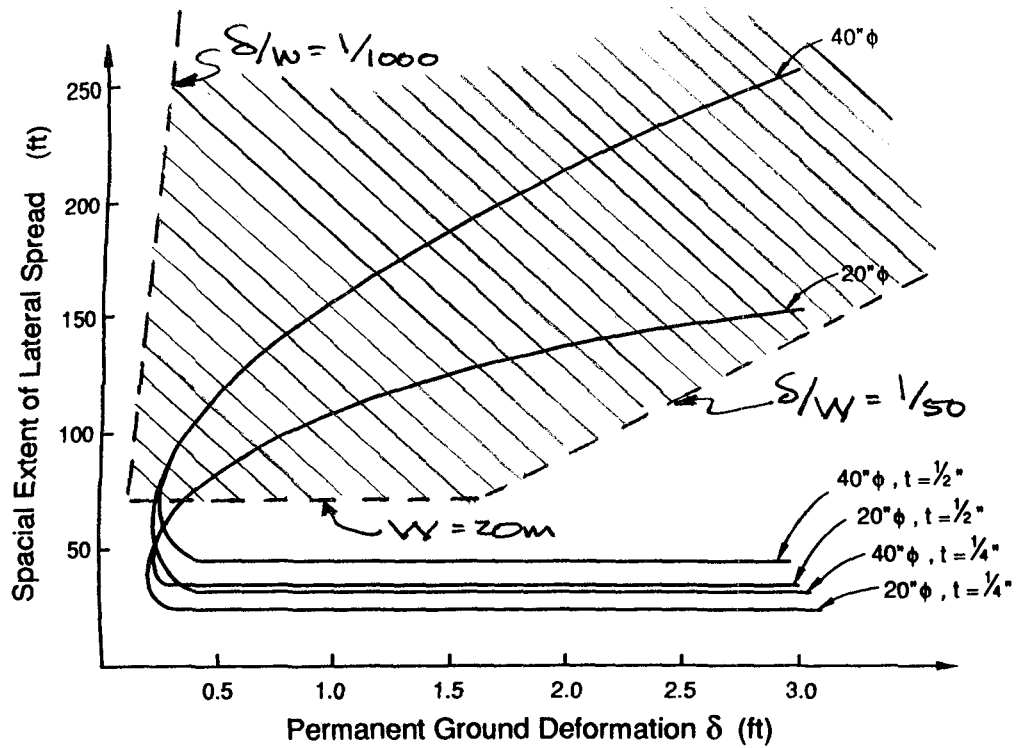
Figure 6. Failure Diagram for Mild Steel Pipe Subject to Transverse PGD (after O'Rourke 1989)

$$\epsilon = \frac{\uparrow^2 \delta\phi}{W^2}$$
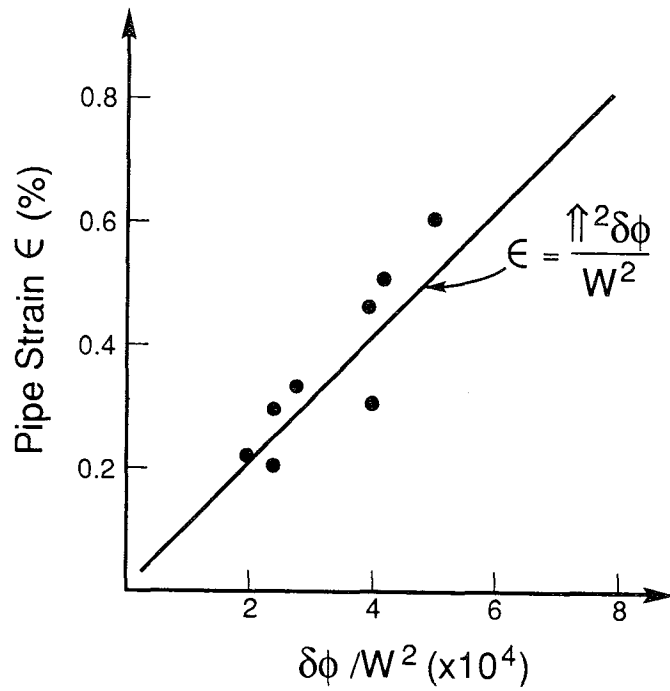
Figure 7.   Comparison of FE Results for Transverse PGD with Eqn. 1b
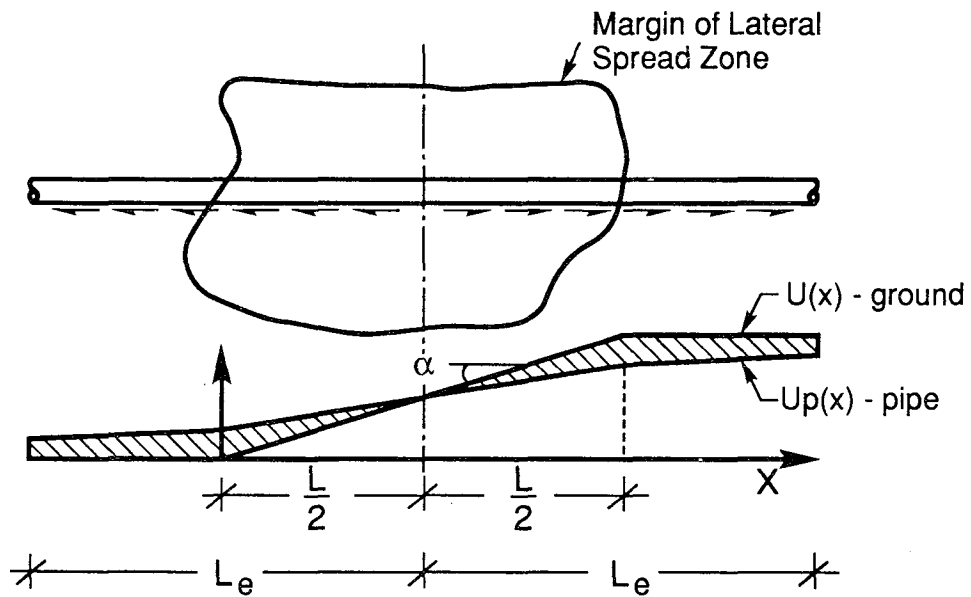
Figure 8.   Model of Continuous Pipe Subject to Longitudinal PGD

453

IDEALIZATION OF PERMANENT GROUND MOVEMENT AND
STRAIN ESTIMATION OF BURIED PIPES

Nobuhisa Suzuki
Senior Research Engineer
NKK Engineering Research Center

Naoyuki Masuda
Senior Engineer of Pipeline Engineering Div.
NKK Corporation

ABSTRACT

Idealization of spatial distribution of liquefaction-induced permanent ground displacements (PGD) is presented in this paper. Spatial extent of the PGD, which would be required for the design and the safety assessment of buried pipelines, are idealized on the basis of case history information of the 1964 Niigata earthquake and the 1983 Nihonkai Chubu earthquake. The patterns of the PGD are idealized into three basic models which are an axial deformation model, a lateral deformation model and a vertical deformation model. The spatial extent of the PGD defined by the three models is represented with two parameters, which are a length or a width of non-uniform ground movement and the maximum ground displacement.

Also presented is linear finite element solutions of networks consisted of small diameter pipes and fittings. The network is discretized into four basic models they are a straight pipe model, an elbow model, a tee junction model and a cross junction model. Gray cast iron pipes (GCIP) and asbestos cement pipes (ACP) are considered for distribution lines of the network. Response characteristics of these models to an uniaxial constant ground strain are compared in order to explain the failure rates of buried pipes due to past earthquakes, which ground strain can be generated by the PGD. Deformation of the models are analyzed by a finite element code.

INTRODUCTION

The liquefaction-induced large PGD, which is closely related to soil layer profiles of estimated liquefaction zone, is one of the significant parameters for the design and the safety assessment of the pipelines and the distribution networks buried in a liquifiable zone[1-6].

It is required to estimate the spatial extent of distribution of the PGD for the seismic design and deformation analysis of the buried pipelines. The estimation of the spatial extent of the PGD, however, is very difficult because we have not developed any effective analytical procedure. And the secondary reason is the fact that we have to deal with a great number of information over a very wide area where lifeline networks are extensively spreaded. Pipeline engineers therefore have required to develop some sort of methodology, a semi-empirical formula for example[4,5].

The first objective in this paper is therefore to perform idealization or modeling of the spatial extent of the PGD to be required for the safety assessment of the buried pipelines. This idealization has accomplished through investigating deformation patterns of the PGD occurred during the 1964 Niigata earthquake and the 1983 Nihonkai Chubu earthquake[1]. The deformation patterns of the ground are classified into three simple models which are an axial displacement model (ADM), a lateral displacement model (LDM) and a vertical displacement model (VDM).

On one hand, seismic damage due to past earthquakes to the buried pipes have been concentrated to old diameter pipes of distribution networks such as cast iron pipes (CIP) and asbestos cement pipes (ACP)[6,7]. From a point of view of material properties, the strength of the pipes are very low compare with the pipes made of modern materials so that the old pipes are most vulnerable to seismic excitation and the large PGD.

The second objective in this paper is to investigate the effects of the PGD on the old pipes and fittings in the distribution networks. In order to study this subject, the network will be discretized into four basic models such as a straight pipe model (STR), an elbow model (ELB), a tee junction model (TEE) and a cross junction model (CRS). Furthermore the basic elements are to be subjected to uniaxial PGD. Response characteristics of the basic models to an uniaxial ground strain are compared and the data give us a useful information.

LIQUEFACTION INDUCED PERMANENT GROUND DISPLACEMENT

Observed Permanent Ground Displacement

Figure 1 shows displacement vectors measured in a 1000*800 meter rectangular area of interest in Niigata City, which covers the centeral are of Niigata City where lifeline network systems for gas distribution and water supply had been constructed before 1964. The Niigata Railway Station is located in the south of the area[1].

Figure 2 also represents the PGD vectors occurred during the 1983 Nihonkai Chubu Earthquake in two rectangular areas of 800*1600 meters located in the northern and the southern parts of Noshiro City[1]. Every data is obtained by comparering aerial photographs taken before and after the quakes.

The displacement vectors shown in Figs.1 and 2 were measured at a number of specified points on the ground such as manholes, the lower end of electric poles and corners of buildings. While, we neglected the data measured at roof edges, fences and guard rails because they are not supposed to have behaved similarly to the PGD. The areas of interest illustrated in Figs.1 and 2 are discretized into 50*50 meter regular squares.

Interpolation of Observed Permanent Ground Displacement

As shown in Figs.1 and 2, the measured displacement vectors are distributed over the entire areas of interest. In order to estimate the spatial distribution of the PGD we have to evaluate the magnitude of the PGD at any point.

Figure 3 shows a schematic illustration of interpolation of the displacement vector at a point of intersection (A) using several adjacent displacement vectors. If we express the deformation of the circular region including the point of intersection as,

$$u = ax^2 + bxy + cy^2 + dx + ey + f \qquad (1)$$

$$v = gx^2 + hxy + iy^2 + jx + ky + l. \qquad (2)$$

The displacement at any point within the region can be calculated by knowing the coefficients from (a) through (1) by the Least Square Method. Where u and v respectively express the displacement vector in the horizontal and vertical direction.

Figures 4 and 5 show calculated results of the spatial distribution of the PGD and the deformed configuration of the rectangular area in Niigata City. Furthermore, Figs.6 and 7 are provided as supplementary data for the PGD vectors vectors separated along the grid lines and perpendicular to the grid lines. Also the same methodology was applied to the analysis of the spatial distribution of the PGD in the vertical direction and the results are illustrated in Fig.8.

The spatial distribution in the northern part and the southern part of Noshiro City were estimated in the same manner as Niigata City. Estimated horizontal displacement at ground surface in the areas are presented in Figs.9 and 10.

IDEALIZATION OF SPATIAL EXTENT OF PERMANENT GROUND DISPLACEMENT

It would be possible for us to estimate the ground displacement along the buried pipelines having arbitrary shape by the above-mentioned methodology. If we regard the grid lines as the straight continuous pipelines, we can express

the general spatial distribution by investigating the PGD along the grid lines presented in Figs.1 and 2.

Then the liquefaction-induced PGD can be idealized as Figs.11, 12 and 13 for the straight pipelines. Figure 11 shows the axial displacement models (ADM) of the PGD, which may result in the axial deformation of the buried pipelines. The ADM can be defined by the length of transition zone L and relative ground displacement D.

While the buried pipelines may subject to flexural deformation under the deformation models illustrated in Figs.12 and 13. These models correspond to the lateral deformation model (LDM) and the vertical deformation model (VDM ; ground settlement or rise) in which the displacement vectors are perpendicular to the pipe axis.

The models of these PGD can be expressed by parameters of the spatial extent of the PGD W or L and the maximum ground displacement D. The lateral spreading and the settlement expressed by a sinusoidal function are illustrated in Figs.12a and 13a. While, Figs. 12b and 13b represent the shear mode deformation having a transition zone.

Axial Displacement Model (ADM)

Figure 14 shows the relationship between L and D of the ADM. The length of transient zone and the maximum PGD are expressed by L and D. The solid lines and the dotted lines represent the results of the linear regression analysis and envelopes of the calculated data. The positive values of the relative displacement, D, correspond to the tensile deformation of the pipeline and the negative values the compressive deformation.

Furthermore, the open marks represent the data measured along the horizontal grid lines and the solid marks correspond to the data along the vertical grid lines. Round marks, triangular marks and rectangular marks respectively represent the measured data in Niigata City and the northern part and the southern part of Noshiro City.

Lateral Displacement Model (LDM)

Figures 15 and 16 show the W or L versus D relationships for the LDM defined as Figs.12a and 12b respectively. The proportional coefficient related to the sinusoidal pattern of the LDM, illustrated as Fig.12a, is approximately 60% less than the coefficient for the ADM shown in Fig.11. On the other hand, the coefficient for the shear pattern of the LDM, expressed as Fig.12b, is approximately the same value as that of the LDM.

Vertical Displacement Model (VDM)

Figures 17 and 18 represent a relationship between W and D of the VDM illustrated as Figs. 13a and 13b. It can be recognized that the magnitude of the horizontal ground movement exceed those of the vertical ground displacement from the fact that the proportional coefficient for the sinusoidal pattern of the VDM is the minimum among all the coefficients.

Summary of Idealized Displacement Models

Table 1 summarizes the results of the linear regression analysis of the idealized models of the PGD. The coefficients for the ADM are almost the same for both of the tensile and compressive patterns. The compressive pattern of the ADM has the largest values in the table. The sinusoidal pattern and the shear pattern in horizontal direction are two times as large as the deformation in vertical direction. On the contrary, the shear mode deformation in horizontal and vertical direction are also approximately double the sinusoidal displacement pattern.

The envelopes were defined by bi-linear curves and drawn considering the coefficient obtained from the regression analysis for the larger values of L and D. The simplified equations to represent the envelopes of the plotted measured data are listed in Table 2. We can obtain useful information from these functions for the design and the safety assessment of the buried pipelines.

RESPONSE CHARACTERISTICS OF NETWORK TO UNIAXIAL GROUND STRAIN

Material Properties of Gray Cast Iron Pipe (GCIP)

Gray cast iron had been produced as a pipe material in the first period of a long history of cast iron pipe (CIP)[8]. The gray cast iron, however, is very fragile and bittle to compare with modern matrials used for pipelines or pipings[8].

Production of GCIP had been ceased for long time, however, a number of GCIP has been in active service for gas distribution or water supply network especially in cities. It is estimated that tensile strength of the GCIP is as high as 1,200-2,400 kgf/cm^2 and the Young's modulus $0.6-1.0*10^6$ kgf/cm^2.

Material Properties of Asbestos Cement Pipe (ACP)

Asbestos cement pipe (ACP) have been mainly used in water supply network. It is reported in Japan that they have still been used for approximately 60 percent of the water supply network[9]. However most of the ACP is gradually taking over other modern pipes as they have spent 25 durable years. Failure rates of the ACP due to past earthquakes are known to be highest among any other pipes because of low strength of the material.

It is well known that the strength of ACP decrease as time passes. The bending strength S_b, tensile strength S_t and compressive strength S_c are represented as the following equations[9].

$$S_b=0.43D-1.93Y+133.7 \quad (kgf/cm^2) \tag{3}$$

$$S_t=0.62D-4.57Y+176.1 \quad (kgf/cm^2) \tag{4}$$

$$S_c=-9.75Y+617.2 \quad (kgf/cm^2) \tag{5}$$

Where, D; diameter of pipe (mm) and Y; passed time (year). Assuming an ACP with a diameter of 100 mm constructed 20 years ago, for example, S_b, S_t and S_c can be estimated respectively as 138, 147 and 422 kgf/cm^2.

Discretization of Network and Assumptions for Finite Element Analysis

When a distribution network is subjected to the ground deformations induced by wave propagation or the PGD, higher strains can be caused in or near pipe fittings such as elbows, tee junctions and cross junctions. In order to discuss strain concentration characteristics of the network with finite element analysis, four basic elements, a straight pipe (STR), an elbow (ELB), a tee junction (TEE) and a cross junction (CRS), should be defined to idealize the network successfully. The four elements are illustrated in Fig.19.

The four elements are assumed to be buried where an uniaxial constant ground strain is generated. This assumption may be justified by the fact that the maximum distance separating the two farthest nodes in the model is smaller than the length of non-uniform PGD[10]. The assumption is also acceptable if the maximum distance of the model is many times smaller than the seismic wave length[10].

Soil spring constants for a longitudinal and a lateral directions are assumed to be k_1=1.57 and k_t=0.47 kgf/cm^2 as described in the seismic design code for high pressure gas pipelines in Japan[11]. Elastic constants, inside diameters and wall thicknesses of the GCIP and the ACP are assumed as GCIP=8*10^5 kgf/cm2, 100 mm, 7.5 mm and ACP=10^5 kgf/cm^2, 100 mm, 10 mm.

The segmented pipes are idealized as continuous pipes in the finite element analysis and flexibility factors of the fittings are provided to be 1.0 because of the following two reasons. First of all the damage of the GCIP and the ACP due to past earthquakes have been observed at straight pipes adjacent to the joints and fittings. The second reason is that the flexibility of the joints are negligibly small and the fittings are comparatively stiffer than straight pipe. Behaviors of the joints and the fittings, therefore, will not be discussed in this paper.

Response Characteristics of the Model

Figures 20 and 21 respectively compare the strain distribution and bending moment diagrams of the four elements of GCIP with different encounter angles, which are defined by X-axis of the model and the axis of ground strain. The finite element solutions in this paper are obtained for the permanent ground strain of 1 percent.

As shown in Fig.20 the maximum strains induced in the every straight pipe reach to the ground strain along the axis of straight pipe as,

$$e_p = e_g(A_e) = e_g * \cos^2(A_e). \tag{6}$$

Where, e_p; pipe strain, $e_g(A_e)$; ground strain along the pipe axis, e_g; ground strain and A_e; encounter angle. The pipe strain induced in the STR model can be defined by equation (6).

Axial strains of straight pipes of the ELB model become smaller near the elbow. The strain distribution near the elbow, however, is disturbed due to an effect of bending moments induced in the elbow. The reason why the axial strains of the straight pipes decrease near the elbow is that the elbow cannot resist the axial deformation of the straight pipes.

The strain distribution of main pipes of the TEE model are similar to that of the STR model, and the strain distribution of a branch pipe is similar to the ELB model. The strain distribution near an intersection is disturbed due to bending moments. The bending moments generated in the TEE model is the maximum among the four models.

Strains induced in every pipe of the CRS model distribute as the STR model. The strains near the intersection are also disturbed due to bending moment. The bending moments, however, are very small compare with the ELB model and the TEE model.

Response Curves of Pipe Strain to Uniform Ground Strain

Strains of the GCIP and the ACP induced at the designated points of the model are represented in Figs.22 and 23. In these figures the vertical axis expresses the ratio of the pipe strain to the ground strain and the horizontal axis represents the encounter angle.

In the case of the STR model the strain of the pipe having infinite length can be analitically expressed as equation (6). In the case of the ELB model, the pipe strains generated at No.1 and No.2 sections are illustrated in the figure. Also No.3 section coincide the point where the bending moment become the maximum. The similar illustrations to the ELB model are used for the TEE model. In the case of the CRS model No.1 and No.2 sections are observed due to the symmetricity of the model.

The maximum pipe strain of the STR model is generated at the encounter angle Ae=0 degree when the axis of pipe and the axis of ground strain coincide. The pipe strain is decreasing as the encounter angle, Ae, increases. It becomes 0.5 when Ae=45 degs. and vanished Ae=90 degs. This is a common tendency for the GCIP and the ACP.

In the case of the GCIP of the ELB model, strains at No.1 section are predominant and we can find the maximum value at A_e=0 deg. On one hand, the strain distribution of the ACP of the ELB model is very similar to the GCIP except the values of A_e ranging from 30 degs. to 45 degs., where the strains at No.3 section are predominant.

It is very interesting in the case of the GCIP and the ACP of the TEE model that the maximum strain induced in the main pipes are almost independent upon the encounter angle and approximately the same value as the ground strain. The strains at No.3 section increases when Ae is less than 60 degs., and decreases when the A_e is greater than 60 degs. In the case of GCIP the strains caused in main pipes are always predominant and the maximum strain of No.3 section can remain only 20 percent of the strains at No.1 and No.2 sections. In the case of the ACP the ratio grow to 30 percent.

Variation of the strain in the CRS model is very similar to the STR model as observed at No.1 and No.2 sections. The CRS model is geometrically very similar to the TEE model geometrically, however, the strain distribution is quite different from the TEE model. The strain distribution should be expressed with two straight pipes perpendicular to each other. We can therefore observe the maximum strain of the CRS model on the straight pipe which axis is closer the axis of ground strain.

Expectation of the response curves are listed in Table 3. These data are obtained by dividing the integrated values of the response curves from Ae=0 deg. to 360 degs. by 2*3.14. As shown in the table the maximum expectation is observed at No.1 and No.2 sections of the TEE model, which means the main pipe of the model is the most vulnerable piping element and has the highest failure probability.

CONCLUSIONS

The spatial extent of the PGD observed in the 1000*800 meter rectangular area in Niigata City and the 800*1600 meter rectangular areas in Noshiro City were discussed on the basis of case history information of the 1964 Niigata earthquake and the 1983 Nihonkai Chubu earthquake.

The deformation patterns of the PGD were quantitatively investigated, which patterns include the axial deformation model, the lateral deformation model and the vertical deformation model. The spatial extent patterns of the models are successively represented with a length or a width of non-uniform ground movement and the maximum ground displacement.

In order to explain failure rates of gray cast iron pipe and asbestos cement pipe in a distribution network, behaviors of the network were discussed by discretizing the network into a straight pipe model, an elbow model, a tee junction model and a cross junction model. The models were subjected to uniaxial constant ground strain.

Analytical results obtained by a linear finite element method indicate that the tee junction model shows the highest strain concentration factor and become consequently the most vulnerable piping element.

Flexibility factors and strain concentration factors of the fittings were neglected in the analysis because the flexibility of the joints are negligibly small and the fittings are relatively stiffer than straight pipe. Their effect on deformation of network, however, cannot be ignored for the distribution network consisted of welded steel pipes.

ACKNOWLEDGEMENTS

contribution for the successful implementation of this research. The authors also would like to thank Mr.I.Kubo and Mrs.M.Nishigaki of the Japan Industrial Technology Co., Ltd. for their help in the preparation of this paper.

REFERENCES

1. Hamada,H., Yasuda,S., Isoyama.,R. and Emoto,K., "Study on Liquefaction Induced Permanent Ground Displacements," ADEP, 87p., 1986.

2. Kobayashi,T., " Recommended Practice for the Earthquake-Resistant Design of Gas Pipelines, with Liquefaction Considered," Proc. of First Japan-U.S. Workshop, 212-221, 1988.

3. O'Rouke,T.D., "Critical Aspects of Soil-Pipeline Interaction for Large Ground Deformation," Proc. of First Japan-U.S. Wokshop, 118-126, 1988.

4. Suzuki,N., Arata,O. and Suzuki,I., "Parametric Study on Deformation Analysis of Welded Pipeline Subject to Liquefaction-Induced Permanent Ground Displacement," Proc. of First Japan-U.S. Workshop, 155-162, 1988.

5. O'Rourke,M.J, "Approximate Analysis Procedures for Permanent Ground Deformation Effects on Buried Pipelines," Proc. of Second U.S.-Japan Workshop on Liquefaction, 1989.

6. O'Rourke,T.D., Stewart,H.E., Blackburn,F.T. and Dickerman,T.S., "Geotechnical Lifeline Aspects of the October 17, 1989 Loma Prieta Earthquake in San Francisco," Tech. Rep. NCEER-90-0001, 1990 January.

7. Suzuki,N. and Ohbo,N., "Damage to Buried Water Pipes due to Liquefaction -induced Permanent Ground Displacements during the 1964 Niigata Earthquake," The 8th Symposium on Seismic Engrg., 1990 December.

8. Edited by Japan Ductile Iron Pipe Assoc., A Brief note on Earthquake and Pipelines, JDPA-T-05, 81p.

9. Edited by the Ministry of Health and Welfare, A Guideline for Strength Estimation of Asbestos Cement Pipe, Technical Center for Water Pipelines, 1989.

10. O'Rourke,M.J. and Bouabid,J., "Seismic Wave Propagation Behavior of Elbows in Buried Segmented Pipelines," ASME-PVP-Vol.162, 243-248, 1989 July.

11. Japan Gas Association, Earthquake Resistant Design Code for Gas Pipeline, 1982.
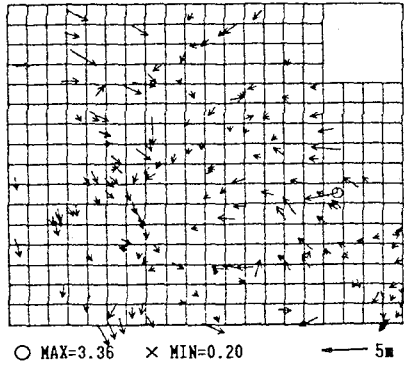
Figure 1. Measured Displacement in Niigata City

○ MAX=2.97   × MIN=0.01 ——5�

○ MAX=5.04   × MIN=0.01 ——5�

(a)Northern Part   (b)Southern Part
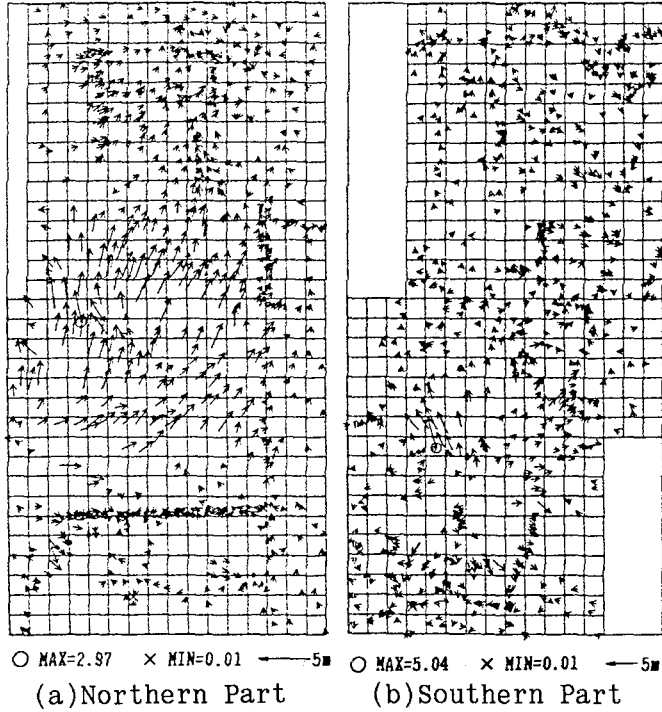
Figure 2. Measured Displacement in Noshiro City
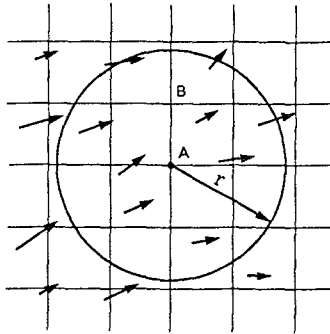
Figure 3. Interporation of Displacement Vector

○ MAX=2.82   × MIN=0.09 ——5ᴍ
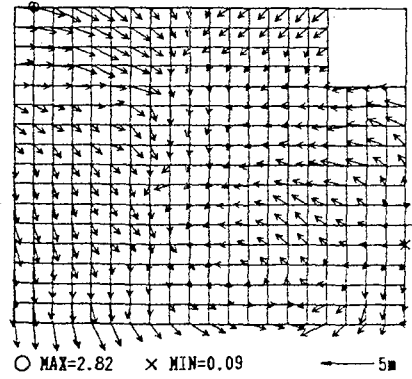
Figure 4. Estimated Displacement Vector in Niigata City

○ MAX=2.82   × MIN=0.09 ——5ᴍ
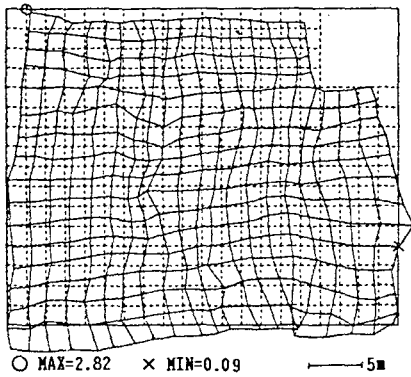
Figure 5. Deformation in Niigata City

○ MAX=2.73   × MIN=0.0 ——5ᴍ
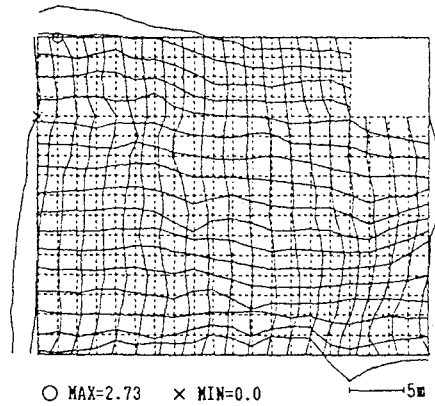
Figure 6. Axial Displacement

464

○ MAX=2.73   ✕ MIN=0.0   ⊢————5m
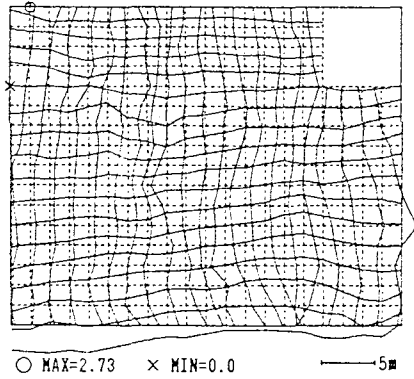
Figure 7. Lateral Displacement

+ MAX=0.67   ✕ MIN=-1.89   DEL=0.30
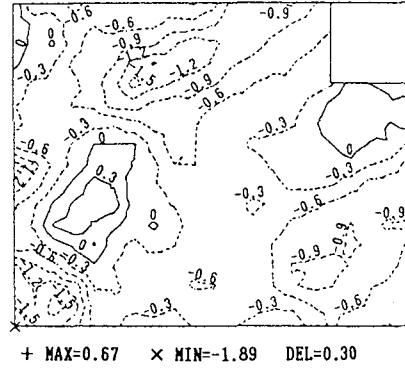
Figure 8. Vertical Displacement

○ MAX=2.61   ✕ MIN=0.01   ⊢————5m
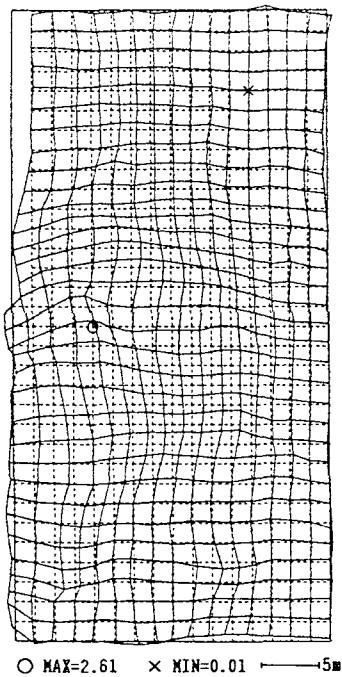
Figure 9. Deformation in Northern
Part of Noshiro City

○ MAX=3.12   ✕ MIN=0.02   ⊢————5m
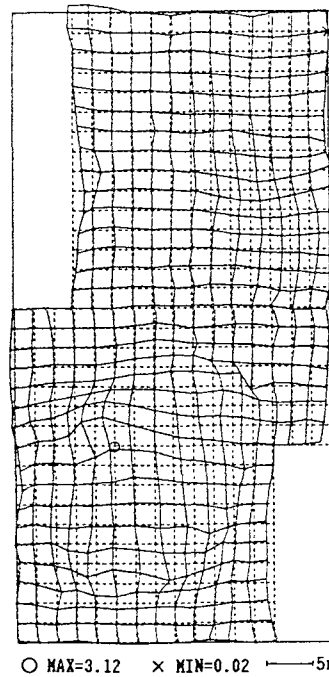
Figure 10. Deformation in Southern
Part of Noshiro City
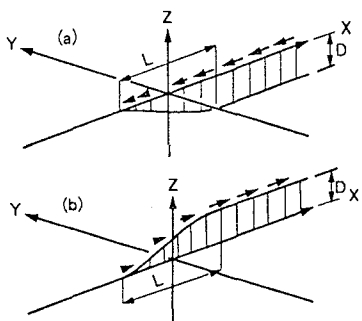
Figure 11. Axial
Displacement
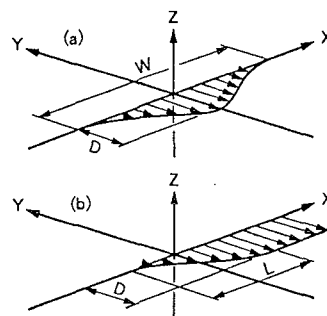
Figure 12. Lateral
Displacement
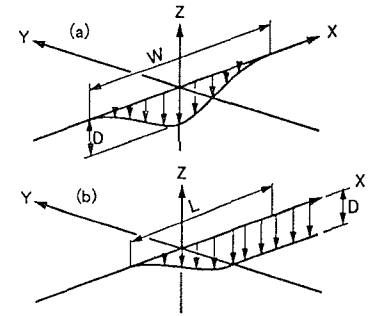
Figure 13. Vertical
Displacement

465
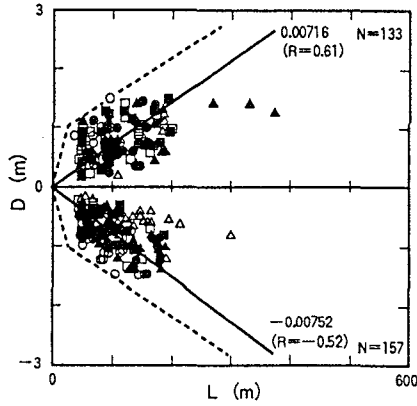
Figure 14. Axial Displacement
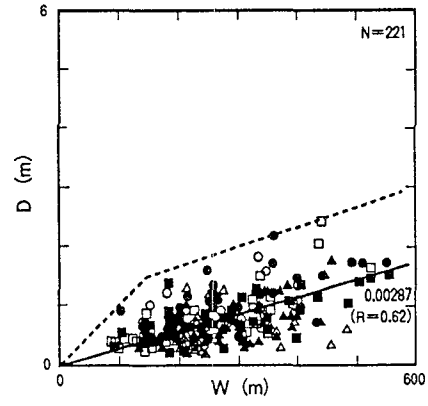
Figure 15. Lateral (Sinusoidal)
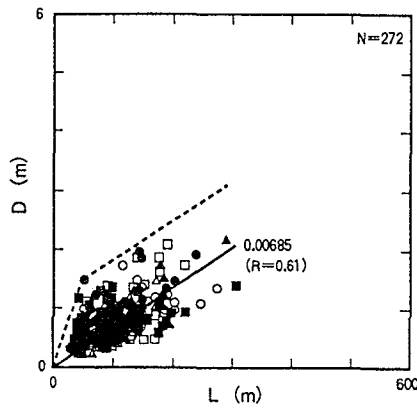
Figure 16. Lateral (Shear)
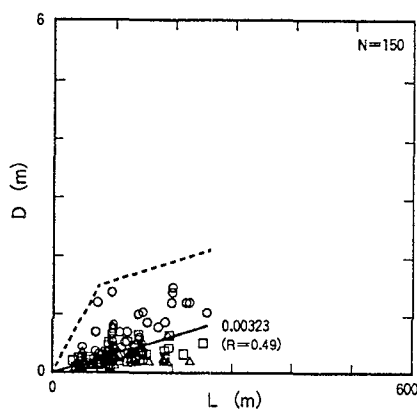
Figure 17. Vertical (Sinusoidal)
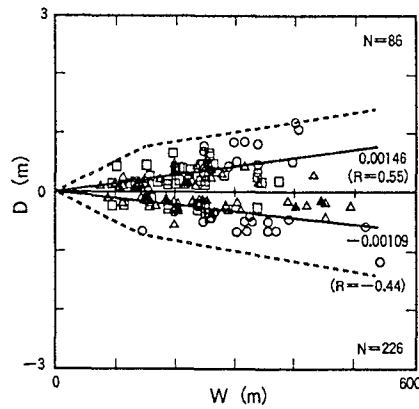
Figure 18. Vertical (Shear)

(1)STR Model   (2)ELB Model   (3)TEE Model   (4)CRS Model
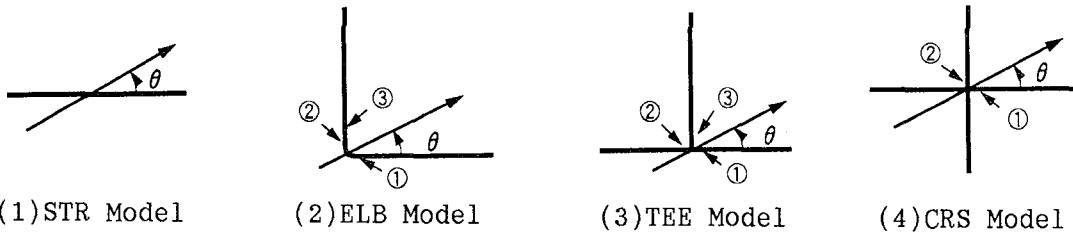
Figure 19. Basic Elements for Discretization of Network

θ = 0°

45°

90°

(1)STR Model (2)ELB Model (3)TEE Model (4)CRS Model
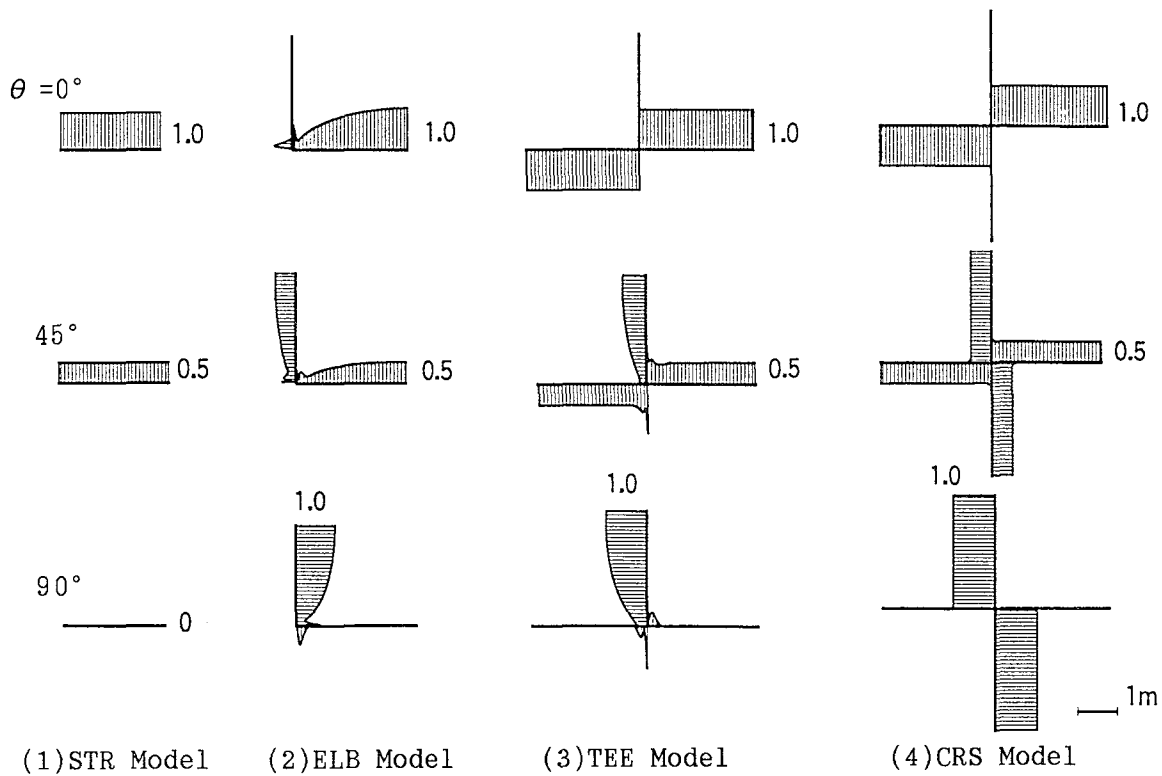
Figure 20. Strain Distribution of Basic Elements

θ = 0°

45°

90°

(1)STR Model (2)ELB Model (3)TEE Model (4)CRS Model
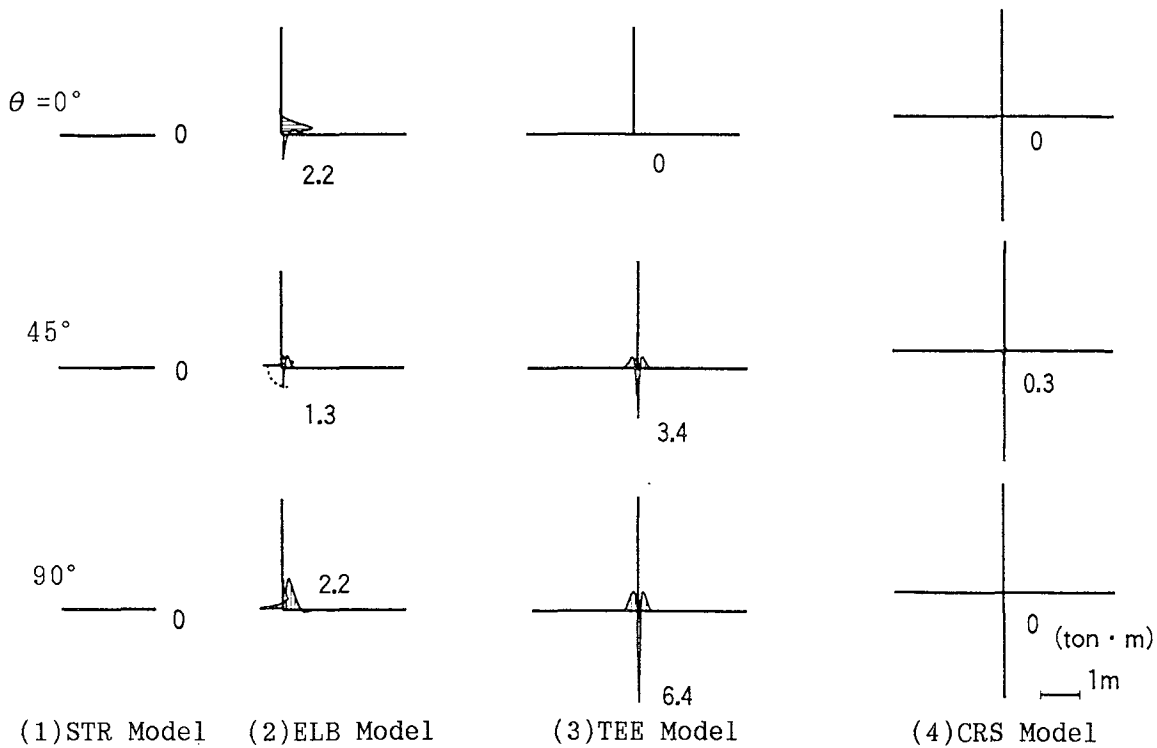
Figure 21. Bending Moment Diagram of Basic Elements

467
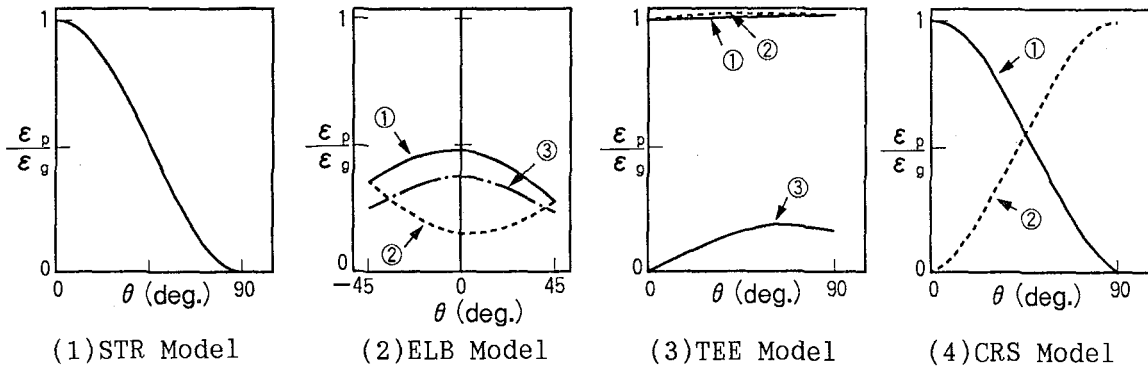
Figure 22. Ratio of Pipe (GCIP) Strain to Ground Strain of Basic Elements

(1)STR Model (2)ELB Model (3)TEE Model (4)CRS Model
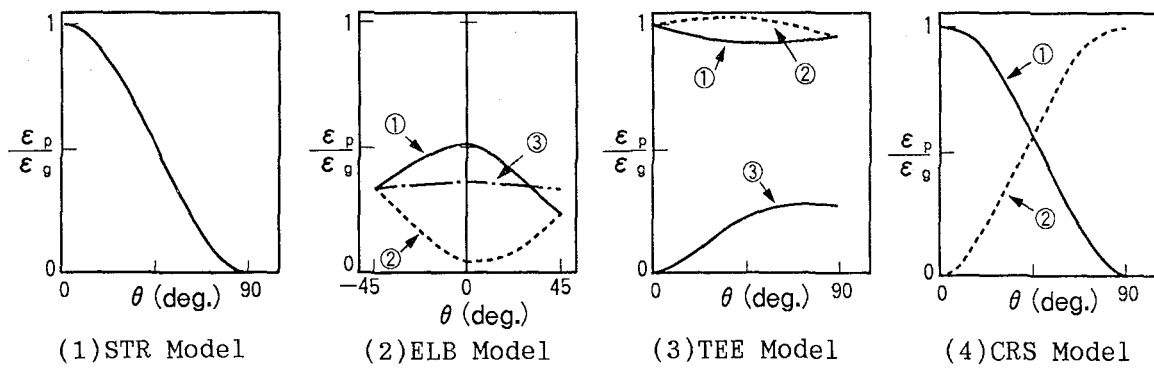
Figure 23. Ratio of Pipe (ACP) Strain to Ground Strain of Basic Elements

(1)STR Model (2)ELB Model (3)TEE Model (4)CRS Model

Table 1. Results of Regression Analysis

Deform. Pattern		A	R
Axial	Tension	0.00716	0.61
	Compression	-0.00752	-0.52
Lateral (Sinusoidal)		0.00287	0.62
Lateral (Shear)		0.00685	0.61
Vertical (Sinusoidal)	Up	0.00146	0.55
	Down	-0.00109	-0.44
Vertical (Shear)		0.00323	0.49

Table 2. Idealized Permanent Ground Displacement

Deform. Pattern	Range(L, W)	Max. Disp.
Axial Deform. (Tension & Compression)	L ≦ 25	1/25 × L
	25 < L	1/150 × L +5/6
Lateral Spreading (Sinusoidal)	W ≦ 150	1/100 × W
	150 < W	1/300 × W +1
Lateral Spreading (Shear)	L ≦ 50	3/100 × L
	50 < L	1/150 × L +7/6
Vertical Deform. (Sinusoidal)	W ≦ 100	1/150 × W
	100 < W	1/600 × W +1/2
Vertical Deform. (Shear)	L ≦ 75	1/50 × L
	75 < L	1/300 × L +5/4
Dimensions	m	m

Table 3. Mean Ratio of Pipe Strain to Ground Strain

Model	G C I P			A C P		
Straight	1.00			1.00		
Elbow	(1) 0.63	(2) 0.63	(3) 0.52	(1) 0.56	(2) 0.56	(3) 0.68
Tee	(1) 2.03	(2) 2.03	(3) 0.26	(1) 1.95	(2) 1.95	(3) 0.37
Cross	(1) 1.07	(2) 1.07		(1) 1.08	(2) 1.08	

PIPELINE BUCKLING CAUSED BY COMPRESSIVE GROUND FAILURE DURING EARTHQUAKES

W.D. Meyersohn[1] and T.D. O'Rourke[2]

ABSTRACT

Earthquake-induced ground failures can result in sudden and unstable deformations of buried pipelines. Buckling of steel pipelines may be manifested either as a beam buckling, when the pipe lifts out of the ground, or as a shell wrinkling, characterized by local crippling and distortion of the pipe wall.

The buckling mode is highly dependent on the pipeline cover depth. Deeply buried pipes tend to undergo shell wrinkling, as opposed to shallow pipes, which may have an opportunity for beam buckling. In this paper, it is shown that, for a certain wall thickness-to-diameter ratio (t/D), there is a critical cover depth which separates both buckling modes. The critical cover depth is influenced, primarily, by the soil density and the steel grade, and increases with increasing t/D.

Analytical studies indicate that, for pipelines composed of Grade B steel in loose sands, the critical cover depth ranges between 0.20 to 1.10 m for t/D ratios of 0.01 and 0.05, respectively. If the pipes are buried in dense sands, the critical cover depth decreases by about 50%, whereas if they are composed of X-60 grade steel, the cover depth increases by about 110%.

1, 2 - Graduate Research Assistant and Professor, respectively, Cornell University, Ithaca, NY.

INTRODUCTION

Buried pipelines may fail by buckling when permanent ground deformations induce significant compressive forces along the pipe axis. Buckling of pipelines occurs in two distinctive modes. The first resembles the buckling of a slender beam or long column in which the pipeline undergoes large transverse displacements. This mode is referred to as beam buckling. In this mode, the pipe breaks out of the ground, deforming in a characteristic bell-shaped pattern. The second mode of buckling involves local instability of the pipe wall. This mode is most often referred to as local buckling, although terms such as shell wrinkling and crippling are also used for the phenomenon. After the initiation of local wrinkling, all further distortion caused by ground deformation tends to concentrate at the wrinkle, thereby accelerating local strains and rapidly leading to failure. In contrast, beam buckling allows relative ground movement to be distributed over a larger portions of the pipe so that local strains do not accumulate as rapidly, permitting the pipeline to accommodate more differential ground displacement.

Whether a pipeline is prone to beam or local buckling is a matter of some practical significance. The ability to identify burial conditions which promote local buckling allows for a more realistic assessment of the risk of failure associated with compressive ground movement. Likewise, the identification of burial conditions which promote beam buckling can provide opportunities for reducing the potential for failure.

There have been two general approaches in the modeling of beam buckling of structures in contact with the ground. Buckling loads have been determined on the basis of small deflection theory (e.g., Marek and Daniels, 1971; Hobbs, 1981) to evaluate the compressive loads causing vertical lift-off of crane rails and submarine pipelines. Beam buckling also has been modeled by numerical techniques which account for large deflections and nonlinear behavior (e.g., Yun and Kyriakides, 1988; Ariman and Lee, 1989). The later approach provides for a comprehensive analysis of buckling and post buckling deformation. Such analyses are best suited for site specific and individual pipe conditions. In this paper, a simplified procedure is developed by following the former approach. This process has the advantage of working with closed form solutions which can be generalized and readily compared with criteria for local buckling. Predicted performance from this simplified procedure is then compared with the actual field performance of pipelines subjected to large compressive ground movements. A reasonable good agrement is shown between predicted and observed performance.

BEAM BUCKLING

During beam buckling, compressive forces acting on the pipe cause it to break from the ground in a bell shaped configuration. Beam buckling tends to occur in small diameter, shallow buried pipelines. This type of buckling has been observed as a result of earthquakes (McCaffrey and O'Rourke, 1983) and creep along faults (Koch, 1933).

Analytical solutions for beam buckling have been published by Marek and Daniels (1971) who studied the behavior of continuous crane rails due to temperature rise. Hobbs (1981) adapted the Marek and Daniels model to evaluate the buckling of submarine pipelines. Bruschi, Cimbali, and Orselli (1987) developed a finite element formulation for beam buckling of submarine pipelines. Their formulation allows for nonlinear pipe-soil interaction and geometric nonlinearities. Inelastic buckling has been also addressed by Kyriakides, Yun, and Yew (1983)

472

and later by Yun and Kyriakides (1988).

In this study, an analytical model for beam buckling is adapted from the work by Marek and Daniels (1971) and Hobbs (1981). The model is based on elastic beam theory and involves an infinitely long continuous buried pipeline, which under a far-field compressive load, P_0, causes vertical buckling over a length L_b. The load P_0 may arise, for example, from a temperature increase in the pipeline or symmetrical compressive ground displacement, such as the type that would occur at the center of a subsidence basin. Loading situations arising from asymmetric compression, such as at margins of slides and spreads, and at fault crossings can also be studied with a slight modification as discussed later.

The buckled portion of the pipe is subjected to an axial load P, and a uniformly distributed load w, as shown in Figure 1a. The load w represents the uplift capacity of the pipe, which includes the weight of the pipe, its contents, and the uplift resistance of the overlying soil. The load w is counteracted by vertical reactions on either side of the uplifted pipe, which are assumed to act as concentrated forces.

After buckling, points B, C, and D move to the new positions B', C', and D', respectively (Figure 1b). Points A and E do not move and represent the limits of the portion of the pipe directly affected by buckling. The inward movement of points B and D mobilizes the soil-pipeline frictional resistance, t_u, over a length L_f at both sides of the buckle. The frictional resistance counteracts the far-field compressive force, which results in a stress relief over the buckled portion of the pipe. The maximum longitudinal frictional force per unit of pipe length is obtained by the expression:

$$t_u = \frac{(1+K)}{2} \pi D H \gamma \tan \delta \tag{1}$$

in which γ is the unit weight of the surrounding soil, H is the depth to the centerline of the pipe, K is the coefficient of horizontal earth pressure, and δ is the frictional interface angle.

The resulting far-field buckling load P_0 is given by the expression:

$$P_0 = \frac{80.76 \, E_i I}{L_b^2} + \frac{w L_b \tan \delta}{2} - \frac{t_u L_b}{2} + B^{1/2} \tag{2}$$

where I is the pipe moment of inertia, A is the cross–sectional area of the pipe. B is a coefficient equal to:

$$B = 1.598 \times 10^{-5} \frac{w^2 A}{E_i I^2} t_u L_b^7 - 0.5 \, w \, t_u L_b^2 \tan \delta + 0.25 \left(t_u L_b \right)^2 \tag{3}$$

which reflects the effect of the soil reaction to pipe uplift, w, and friction, t_u, on the buckling load. The buckling stress, σ_b, is found by dividing the load Po by the pipe cross-sectional area.

a) Unbuckled Pipe

b) Buckled Pipe

c) Equilibrium of Buckled Portion   d) Equilibrium of Straight Portion
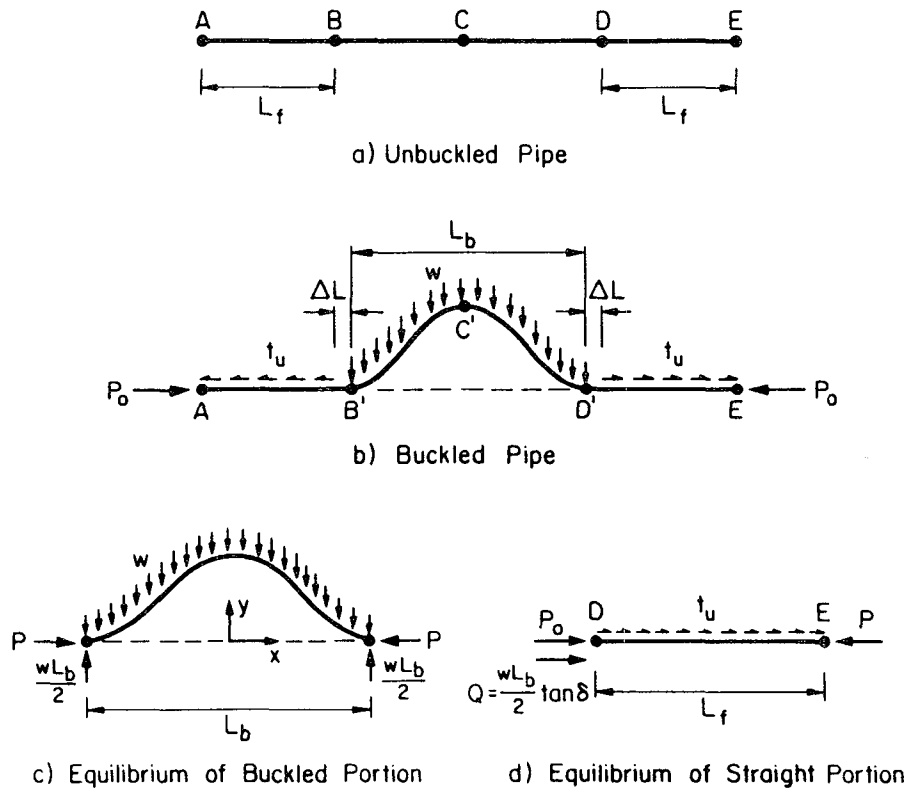
Figure 1   Equilibrium and Boundary Conditions Associated with Beam Buckling due to a Far-Field Load P_0.

Derivation of Equations 2 and 3 can be found in the Appendix at the end of this paper.

The soil reaction per unit length to pipe uplift, w, is determined by:

$$w = N_v \gamma H D \tag{4}$$

in which N_v is a dimensionless parameter which is evaluated on the basis of experimental evidence (Committee on Gas and Liquid Fuel Lifelines, 1984) as a function of soil friction angle,ϕ', and H/D.

Figure 2 shows the general trends, in solid lines, of the buckling load as a function of the buckling length, L_b, and the maximum buckling amplitude, y_0. The buckling load reaches a minimum value at point B for which the buckling length is L_{bm}. Apparently, for any load higher than that at point B, there are two possible buckling lengths, and correspondingly, two different buckle amplitudes.

The dashed lines in Figure 2 represent various paths of load versus displacement, expressed here as buckling length and maximum buckle amplitude, that would normally occur during a displacement-controlled test. The initial imperfections associated with each load path are shown

474
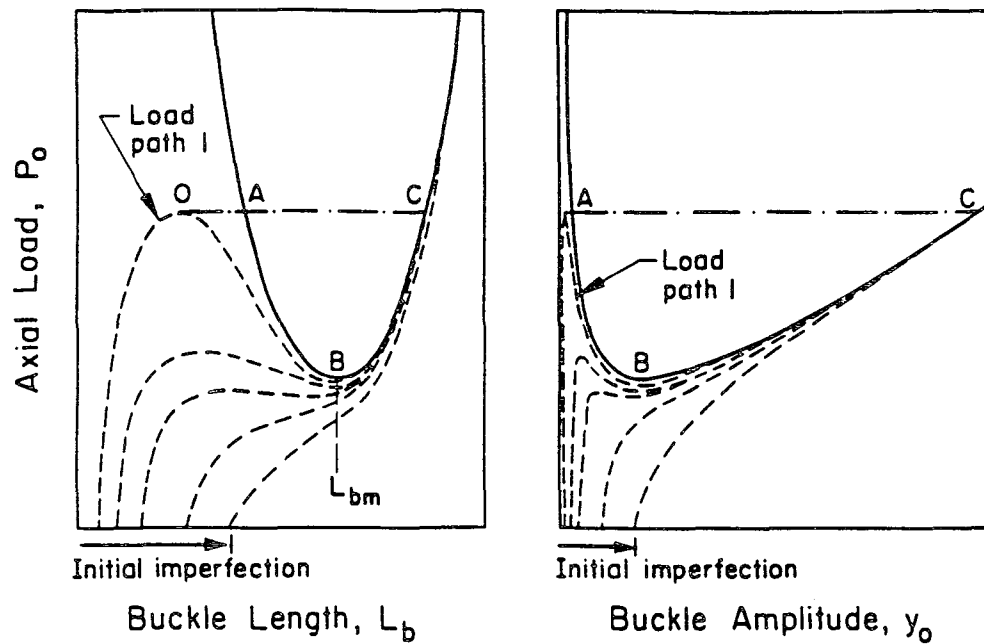
Figure 2   Vertical Buckling and Equilibrium Paths for Increasing Imperfection Levels (after Hobbs, 1981).

by different intersections with the horizontal axes. In load path 1, for example, the load would increase to point O. With increasing deformation there will be an appreciable reduction in the axial load. Once point O is reached, any small disturbance will cause the stress path to jump to point A. This situation is unstable and the pipe will tend to snap through to point C at a constant axial load. In contrast, no snap can occur below the load at point B, although additional loading above this point will generate increasingly larger deformation. The load at point B is the minimum axial load needed to induce beam buckling.

With large enough initial imperfections, no snap is observed since now the imperfections are gradually magnified. However, since the nature and magnitude of the initial imperfections are unknown or can not be perfectly controlled in the field during construction, results from sophisticated nonlinear analyses that account for initial imperfections may not represent a substantial improvement as compared to predictions made with simplified methods.

As mentioned above, if the force P_0 results from a temperature increase in the line, the pipe will be subjected to a state of uniformly distributed compressive load before buckling. The distribution of axial forces along the pipe, before and after buckling, that result from far-field loading is illustrated in Figure 3. Since buckling causes a portion of the pipe to displace inwards, the frictional forces that are mobilized at both sides of the buckle result in stress relief over the buckled portion.

In contrast to a uniform distribution of loading, Figures 4a and 4b show the distribution of axial compressive forces, before and after buckling respectively, that can be generated at a fault or at the margins of lateral spreads and landslides. The frictional forces, acting inwards, are generated by the longitudinal component of the ground motion and result in a triangular distribution of compressive force. The length of the stressed portion of pipe is directly related

a) Before Buckling   b) After Buckling
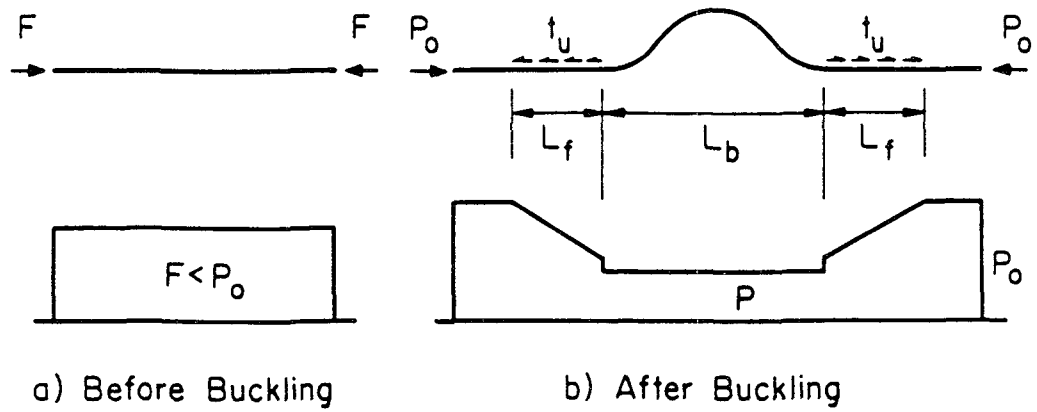
Figure 3   Axial Force Distribution Caused by a Constant Far-Field Compressive Force.

a) Before Buckling   b) After Buckling
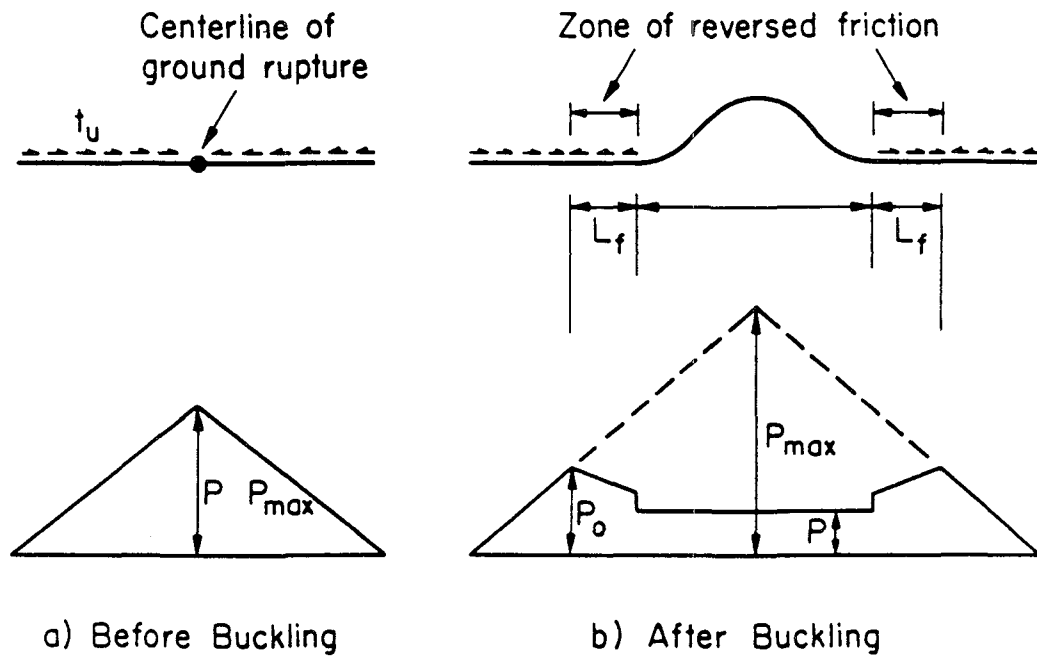
Figure 4   Axial Force Distribution Due Compressive-Induced Ground Deformations.

476

to the magnitude and extent of the ground displacements. Once P equals or exceeds a certain axial load, referred to as P_{max}, buckling occurs. Frictional forces are then relieved over the uplifted length of pipe. In addition, over a portion of the pipe on both sides of the buckle, the frictional forces change direction, allowing some relief of axial stress. The force P_0 represents, in this case, the maximum axial load after equilibrium is restored.

SHELL BUCKLING

Shell buckling occurs as a localized wrinkling of the pipe wall resulting from axial compression. This type of buckling is associated usually with large local deformations, fracturing of the pipe, and disruption of flow. Shell buckling is predominant in pipelines with large diameters and high diameter-to-thickness ratios.

Several investigators have addressed the problem of shell buckling, from theoretical and experimental bases (e.g., Wilson and Newmark, 1933; Donnell and Wan, 1950; Kyriakides, Yun, and Yew, 1983; Yun and Kyriakides, 1988). Their results have shown that the critical wrinkling stress is strongly influenced by the magnitude and form of initial imperfections of the pipe wall. As for beam buckling, the successful application of sophisticated analytical methods depends, to a great extent, on how accurate the wall imperfections are modelled. This represents a limitation since the magnitude of the imperfection is not always known. On the other hand, it has been found that soil stiffness does not have a significant effect on the shell buckling stress (Yun and Kyriakides, 1988) and, therefore, the effect of soil stiffness can be conservatively disregarded in normal calculations.

Schilling (1965) presented a method for determining the critical wrinkling stress, which accounts for both initial imperfections and nonlinearities of the pipe material. The wrinkling stress is given by the expression:

$$\sigma_{cr} = aCE_i\left(\frac{t}{R}\right)$$

(5)

in which E_i is the Young's modulus and 'a' is a plasticity reduction factor expressed as a function of the tangent and secant moduli. The coefficient C is a local imperfection parameter, which accounts for imperfections due to the fabrication process. The C parameter normally ranges from 0.55 to 0.40 for R/t values between 10 and 100.

CRITICAL COVER DEPTH

The beam buckling load is a direct function of the uplift soil resistance, which means that it is a function of the cover depth. The deeper the pipe, the higher the buckling load. If the pipe is buried at a sufficient depth, the external pressure exerted by the soil may be high enough that the pipe can not displace upward in response to compressive force, but instead, it will develop wall wrinkling.

It is useful to evaluate whether a pipe will buckle as a beam or as a shell. If the pipeline buckles as a beam, it generally can accommodate significantly more compressive ground movement

477

than if it were to buckle locally. Since the beam buckling mode is a function of burial depth, one can use the cover depth, H_o, as a geometric parameter for assessing the type of buckling that may occur. The goal is to determine the critical cover depth, H_{cr}, for which the lowest beam buckling stress (point B in Figure 2) equals the wrinkling stress.

Any pipe buried with less cover than the critical depth has the potential to buckle as a beam. If, however, the pipe is buried at a depth more than the critical depth, it will always tend to buckle as a shell. A soil cover less than or equal to the critical depth does not ensure that beam buckling will occur, it only establishes the opportunity for beam buckling. For burial less than the critical depth, beam buckling can be realized only when the pipeline is installed with an initially deflected shape that exceeds its critical imperfection value.

The analytical determination of the critical cover depth can be performed using the procedures for evaluating beam and shell buckling loads described above. Because the wrinkling stress is assumed to be independent of the cover depth of the pipe, H_o, one can calculate the wrinkling stress directly from the pipe geometry and material properties. Also, since the beam buckling stress depends on the magnitude of the cover depth, one can determine the beam buckling stress for several cover depths while maintaining all other variables constant. The cover depth for which both the minimum beam buckling and wrinkling stresses are equal is the critical cover depth.

There is, however, an important restriction on the suitability of the above approach. It can only be applied if the pipe buckles elastically (that is, the buckling stress must be equal to or less than the yield point of the pipe material). This restriction arises from the fact that the method for calculating beam buckling loads is based on linear elastic theory. It is important, therefore, to investigate the necessary conditions to achieve elastic buckling.

Since the determination of the critical depth involves the calculation of the wrinkling stress of the pipe, it suffices to consider conditions leading to elastic wrinkling. Equation 5 lends itself for this purpose because it accounts for material nonlinearities. Accordingly, wrinkling stresses were determined for pipes with diameter-to-thickness ratios ranging from 10 to 120, which are typical of most steel pipelines. Three steel grades were used: X-70, X-60, and Grade B with yield points equal to 520, 400, and 245 MPa, respectively. The stress-strain curves were modeled using the Ramberg-Osgood representation (Ramberg and Osgood, 1943).

Table 1 presents the calculated wrinkling stresses along with their values normalized with respect to the yield stress. The results indicate that for both X-grade steels, the normalized wrinkling stress is only marginally different than 1.0, especially for D/t larger than 50. This suggests that shell buckling is initiated when the compressive stress is near the yield point of the material. As the yield stress is reduced, the pipe tends to wrinkle inelastically. Table 1 shows that the Grade B steel pipe will wrinkle inelastically for the range of D/t shown.

In essence, the procedure in this work consists of calculating the cover depth such that P_{max} of Figure 4 equals the wrinkling load with P_o in the linear elastic range. As a simplification, it is assumed that local buckling will occur at stresses less than or equal to yield. This simplification is consistent with the limits summarized in Table 1, and results in slightly shallower critical depths than would otherwise be predicted.

478

Table 1   Calculated Wrinkling Stresses for Three X-Grade Steels:
                 X-70, X-60, and Grade B.

Diameter to Thickness Ratio (D/t)	X-70 Grade (σ_y = 520 MPa)		X-60 Grade (σ_y = 400 MPa)		Grade B (σ_y = 245 MPa)	
	σ_{cr} (MPa)	σ_{cr}/σ_y	σ_{cr} (MPa)	σ_{cr}/σ_y	σ_{cr} (MPa)	σ_{cr}/σ_y
10	563.7	1.090	506.8	1.267	319.3	1.277
20	550.6	1.066	479.2	1.198	306.2	1.225
50	530.5	1.027	439.3	1.098	287.9	1.150
75	521.0	1.008	422.1	1.055	279.6	1.118
100	513.2	0.993	409.2	1.023	273.6	1.094
120	508.1	0.983	399.5	1.000	269.0	1.076

The critical cover depth was determined from Equation 2 for pipes with diameters ranging from 100 mm to 600 mm and D/t ratios between 20 and 100. Two soil types were considered, loose and dense sand with unit weights of 16.0 and 20.0 kN/m^3 respectively. The internal friction angle of the soils were assumed as 31 and 44 degrees, respectively. The ratio between the soil friction angle and the pipe-soil interface angle, ϕ'/δ, was taken as 0.8.

The results are shown in Figure 5a and 5b which correspond to Grade B and X-60 grade steels, respectively. The critical cover depth H_{cr} is plotted against the wall thickness-to-diameter ratio, t/D, for the two types of soil backfills considered. Expressing the depth ratio as a function of t/D, instead of D/t, gives an essentially linear trend in the results. The shaded areas associated with each soil type comprise different families of curves for pipelines with constant diameter. The calculations were carried out by holding the diameter constant and varying the wall thickness. As expected, pipes buried in loose sand require deeper cover to initiate wrinkling than pipes buried in medium or dense sands.

The effect of the steel grade is apparent. Critical cover depths for the X-60 steel plot above those for Grade B steel pipes. This observation brings about an important conclusion. For a given backfill material, higher strength pipes have to be buried deeper than weaker pipes to attain wrinkling. Consider, for example, a pipeline buried in loose sand such that its combination of cover depth, H_o, and t/D plots between the bands corresponding to the X-60 and Grade B steels. Clearly, the pipe would tend to lift off the ground more easily if it is composed of X-60 steel, while it may wrinkle if it is made of Grade B steel. Thus, increased strength lowers the possibility of shell buckling in the pipe.
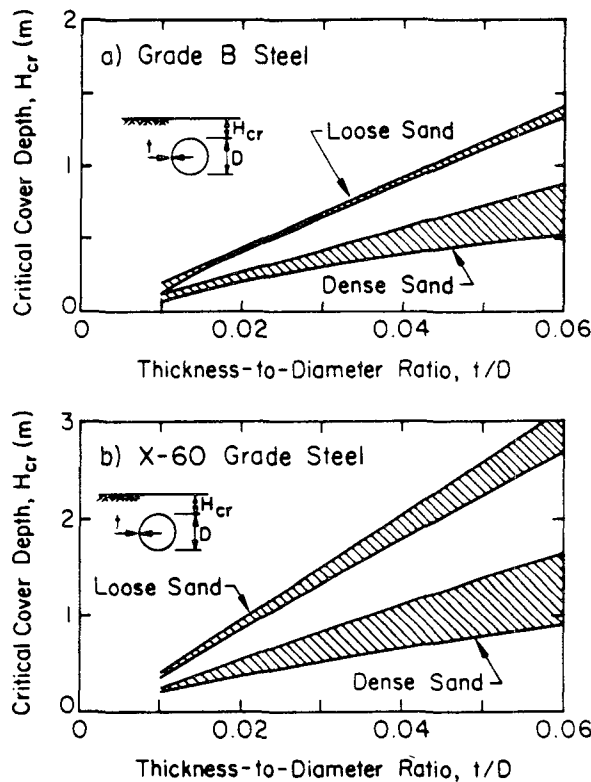
Figure 5   Analytical Results of Critical Cover Depth.

FIELD EVIDENCE

Pipeline performance data were collected for four different earthquakes: 1952 Kern County, 1971 San Fernando, 1979 Imperial Valley, and 1988 Tennant Creek earthquakes. In addition, observations were made of pipeline response to compressive ground movements caused by creep along the Buena Vista fault at the Taft Oil Field in California. In all these events, significant pipe deformations were caused by fault movements.

During the 1952 Kern County earthquakes, an 860-mm-diameter, 11-mm-wall thickness steel pipeline was affected by reverse slip on the White Wolf fault. Estimations by Stein and Thatcher (1981) indicate that the strike-slip movement near the point of crossing was 1.0 m and the reverse slip was 0.40 m. The fault trends 43 degrees to the northeast and dips 20 degrees.

The pipeline crossed the fault at approximately 100 degrees and was covered by about 0.75 m of medium to dense material (Lind, 1954). The pipe did not buckle, nor was it compressed sufficiently to cause shell wrinkling. However, removal of cover during operations to relieve locked stresses caused the pipe to lift as a beam a total of 720 mm over an exposed length of 170 m (Lind, 1954). Based on the fault geometry and pipeline orientation, the axial compressive deformation imposed on the pipe was approximately 560 mm. The compressive deformation at the onset of yielding is estimated as 370 mm. Accordingly, it is likely that irrecoverable deformations were sustained by the pipe, and shell wrinkling may have occurred had the deformation been more severe. Partial excavation of the pipe caused it to lift vertically

480

from the ground in a beam mode of buckling.

Movement along the Sylmar segment of the San Fernando fault was responsible for the rupture of many transmission and distribution pipelines during the 1971 San Fernando earthquake. Compressive wrinkling failure was observed in a 410-mm-diameter, 8-mm-wall thickness steel pipeline (McCaffrey and O'Rourke, 1983). The pipeline, constructed in the 1930's, was buried in a medium to dense sand at a depth of 1.40 m. During the earthquake, the mean operating pressure was around 1.4 MPa.

During the 1979 Imperial Valley earthquake, ground deformations caused by right-lateral strike slip along the Imperial fault affected natural gas pipelines located approximately 9.5 km north of the City of El Centro, California. Two high pressure pipelines, 219-mm and 273-mm-diameter, crossed the main trace of the fault at an angle of about 120 degrees. The pipes were covered by 0.90 m of loose sandy backfill. No evidence of shell wrinkling or beam buckling was observed, however, removal of cover during inspection after the earthquake caused both pipes to displace laterally (McNorgan, 1989). Assessments of cumulative fault displacement by Roth et al.(1991), suggest that the fault movement may have caused net axial shortening of 110 and 160 mm in the 219-mm and the 273-mm-diameter pipes, respectively. It is estimated that the pipelines could have sustained approximately 140 mm of elastic axial deformation. Since the elastic deformation compares closely with the imposed deformations, it is likely that both pipes were on the verge of plastic deformation as a result of the fault movement.

The 1988 Tennant Creek earthquake in the Australian Northern Territory was associated with surface faulting extending over a length 30 km. Surface ruptures along two reverse faults were observed, each trending south-east with up to 2.0 m of throw accompanied by minor left-lateral slippage (Bowman, 1988). A 360-mm-diameter, 6-mm-thickness pipe suffered severe wall distortion as a result of the compressive forces induced by the fault. The pipe was oriented at 40 degrees with respect to the fault trace. At the point of crossing, the measured vertical ground displacement was 600 mm (Sommerville, 1988). At the time of the earthquake the pipe was delivering gas at an internal pressure of 9.7 MPa. Despite the pronounced deformation, the pipe was not ruptured and service was maintained.

Creep of the Buena Vista reverse fault was monitored for several years, showing an average rate of movement of about 21 mm per year (Wilt, 1958). Maximum cumulative vertical and horizontal displacement of 360 mm was measured during the 1932 – 1959 period (Howard, 1968). Large ground movements caused by creep of the fault led to compression of oil field pipelines. Oil pipelines, ranging from 51 to 406-mm in diameter, lifted from the ground as a result of compressive forces. These pipes were buried at depths between 0.15 and 0.30 m in loose to medium soil. Shell wrinkling was also observed in a 510-mm-diameter, 5-mm-thickness water pipe placed between 0.75 and 0.91 m below the ground surface in dense soil.

A summary of the relevant data presented above is given in Table 2. This table lists the diameter, wall thickness, and cover depth for ten different pipelines, as well as their observed modes of failure and the conditions of cover at the moment of failure. A comparison between observed modes of buckling with theoretical predictions is shown in Figure 6. The figure has been divided into three graphs, each associated with different soil density and steel yield stress. The field data have been plotted on the graph that more closely coincide with the yield stress of the pipe and the soil density. Shell wrinkling and beam buckling failure are represented by

481

Table 2   Summary of Pipeline Characteristics, Soil Conditions, and Observed Modes of Deformation for Pipelines Affected by Surface Faulting.

Pipe No	Data[1] Source	Diameter D (mm)	Wall Thickness, t (mm)	Cover Depth (m)	Thickness to Diameter Ratio, t/D	Yield Stress (MPa)	Soil Density	Observed Deformation
1	a	51	4	0.25	0.078	250	Loose	Beam Buckling
2	a	102	6	0.25	0.059	250	Loose	Beam Buckling
3	a	152	7	0.25	0.046	250	Loose	Beam Buckling
4	a	406	13	0.25	0.032	250	Loose	Beam Buckling
5	a	508	5	0.85	0.010	250	Dense	Shell Wrinkling
6	b	406	8	1.40	0.020	172	Dense	Shell Wrinkling
7	c	365	6	0.90	0.016	400	Dense	Shell Wrinkling
8	d	860	11	0.75	0.013	330	Medium	2
9	c	219	7	0.90	0.032	240	Loose	3
10	e	273	5	0.90	0.018	280	Loose	3

1   Key to Data Source:

   a   Buena Vista Oil Field, from observations and measurements in conjunction with lifeline earthquake engineering research at Cornell University (e.g., McCaffrey and O'Rourke; 1983, O'Rourke, Grigoriu,and Khater, 1985)

   b   1971 San Fernando earthquake (McCaffrey and O'Rourke, 1983)

   c   1988 Tennant Creek earthquake (Sommerville, 1988)

   d   1952 Kern County earthquake (Lind, 1954)

   e   1979 Imperial Valley earthquake, (McNorgan, 1989)

2   No wrinkling observed, although vertical beam buckling was observed after the depth of cover was reduced during excavation of the pipe.

3   No wrinkling or beam buckling observed, although likely that strains induced by fault movement were near or above yielding.

Legend:

O   Beam buckling

⊕   Shell wrinkling

▣   No buckling observed until removal of cover
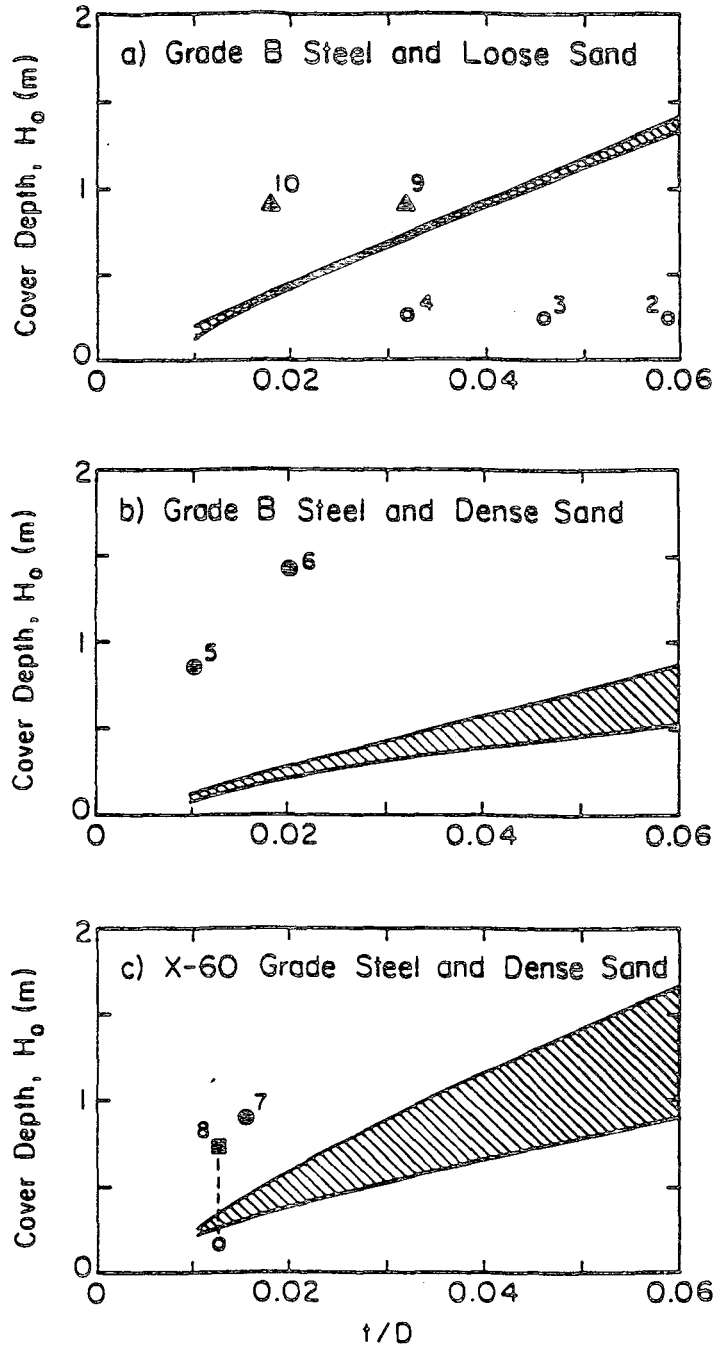
▲   No beam buckling although pipeline on verge of plastic deformation

Figure 6.   Comparison of Actual Buckling Modes with Theoretical Predictions.

483

filled and open circles, respectively. The numbers associated with each data point correspond to the pipe designation in Table 2. Data points for the 1952 Kern County earthquake are plotted as both a dark square and open circle, indicating that beam buckling was not observed at the actual pipe burial depth, but developed only after excavation of the pipe was undertaken. The data plot on the expected side of the limiting bands (that is, data points of pipelines that failed by shell wrinkling lie above the limiting band while pipelines that failed by beam buckling plot below.) Despite the relatively small number of sample points, there appears to be a reasonable correlation between the predicted and observed modes of buckling.

CONCLUDING REMARKS

Buckling of buried pipelines can take place as a beam, in which the pipe tends to lift out of the ground, or as a shell, in which the pipe wall undergoes local distortion and wrinkling. The type of buckling that a pipe can experience is highly dependent on the cover depth. It is found that there exists a critical cover depth that separates the two types of buckling associated with a given pipe. Pipelines buried at depths larger than the critical cover depth will undergo shell wrinkling if subjected to a compressive axial force exceeding a certain critical value. In contrast, pipelines buried at shallower depths have the opportunity to buckle as a beam. The critical cover depth increases with increasing wall thickness-to-diameter ratio. It also is affected by soil density and the yield point of the steel.

Cover depths of pipelines that buckled during several earthquakes have been compared with critical cover depths. There is a fairly good agreement between observed and predicted modes of pipeline buckling.

Analytical studies indicate that, for pipelines composed of Grade B steel in loose sands, the critical cover depth ranges from 0.20 to 1.10 m for t/D ratios of 0.01 and 0.05, respectively. If the pipes are buried in dense sands, the critical cover depth decreases by about 50%, whereas if they are composed of X-60 grade steel, the cover depth increases by about 110%. It appears that a relatively shallow cover is necessary to promote beam buckling. As a general rule, cover depths of 0.25 to 0.50 m are required to provide an opportunity for beam buckling of continuous steel pipelines in dense sandy backfill. Depths of approximately 0.50 to 1.0 m will apply for loose sandy backfill. At depths exceeding these values, it can be assumed that local buckling will occur.

ACKNOWLEDGEMENTS

REFERENCES

Ariman, T., and Lee, B.J., "On Beam Mode of Buckling of Buried Pipelines," Second U.S.–Japan Workshop on Liquefaction, Large Ground Deformation and Their Effects on Lifelines, Buffalo, NY, Sept., 1989, pp 401-412.

Bowman, R.J., "The January 22, 1988 Tennant Creek Earthquake: Three Ms 6.3-6.7 Earthquakes in the Proterozoic Shield," <u>Geological Society of Australia</u>, Specialty Group on Solid-Earth Geophysics, Newsletter No. 7, June, 1988, pp. 3-6.

Bruschi, R., Cimbali, W., and Orselli, B., "Euler Mode Buckling of Submarine Flowlines Under Operating Conditions," <u>Offshore and Arctic Pipelines – 1987</u>, ASME, New York, NY, 1987, pp. 51-61.

Committee on Gas and Liquid Fuel Lifelines, "Guidelines for the Seismic Design of Oil and Gas Pipeline Systems," ASCE, New York, NY, 1984.

Donnell, L.H., and Wan, C.C., "Effect of Imperfections on Buckling of Thin Cylinders and Columns Under Axial Compression," <u>Journal of Applied Mechanics</u>, Vol. 17, March, 1950, pp. 73-83.

Hobbs, R.E., "Pipeline Buckling Caused by Axial Loads," <u>Journal of Constructional Steel Research</u>, Vol. 1, No. 2, Jan., 1981, pp. 2-10.

Howard, J.H, "Recent Deformation at Buena Vista Hills, California," <u>American Journal of Science</u>, Vol. 266, Nov., 1968, pp. 737-757.

Koch, T.W., "Analysis and Effects of Current Movements on an Active Fault in Buena Vista Hills Oil Field, Kern County, California," <u>Bulletin of the Americal Association of Petroleum Geologists</u>, Vol. 17, No. 6, June, 1933, pp. 694-712.

Kyriakides, S., Yun, H.D., and Yew, C.H., "Buckling of Buried Pipelines Due to Large Ground Movements," <u>Earthquake Behavior and Safety of Oil and Gas Storage Facilities, Buried Pipelines and Equipment</u>, PVP, Vol. 77, ASME, New York, NY, Jume, 1983, pp. 140-150.

Lind, R.J., "Earthquake Effects on a Gas Pipeline," <u>Proceedings</u>, Pacific Coast Gas Association, San Francisco, CA, Vol. 54, 1954, pp. 103-105.

Marek, P.J., and Daniels, J.H., "Behavior of Continuous Crane Rails," <u>Journal of the Structural Divison</u>, ASCE, Vol. 97, ST4, April, 1971, pp. 1081-1095.

McCaffrey, M.A., and O'Rourke, T.D., "Buried Pipeline Response to Reverse Faulting During the 1971 San Fernando Earthquake," <u>Earthquake Behavior and Safety of Oil and Gas Storage Facilities, Buried Pipelines and Equipment</u>, PVP, Vol. 77, ASME, New York, NY, Jume, 1983, pp. 151-159.

McNorgan, J.D., "Relieving Seismic Stress Locked in Gas Pipelines," <u>Second U.S–Japan Workshop on Soil Liquefaction, Large Ground Deformation, and Their Effects on Lifeline Facilities</u>, Buffalo, NY, Sept. 1989, pp. 363-369.

Ramberg, W., and Osgood, W., "Description of Stress-Strain Curves by Three Parameters," <u>National Advisory Committee for Aeronautics</u>, Technical Note, No. 902, July, 1943, 28p.

Roth, B.L., O'Rourke, T.D., and Dobry, R. "Lifeline Performance During the 1979 Imperial Valley Earthquake," <u>Third Japan–U.S. Workshop on Soil Liquefaction, Large Ground Deformation, and Their Effects on Lifeline Facilities</u>, San Francisco, CA, Dec. 1991.

Schilling, C.G., "Buckling Strength of Circular Tubes," Journal of the Structural Division, ASCE, Vol. 91, ST5, Oct., 1965, pp. 325-348.

Sommerville, P., "Pipeline Survives Earthquakes Unruptured," Journal of the Institute of Engineers, No. NPB 1628, 1988, pp. 21-22.

Stein, R.S., and Thatcher, W., "Seismic and Aseismic Deformation Associated with the 1952 Kern County, California, Earthquake and Relationship to Quaternary History of the White Wolf Fault," Journal of Geophysical Research, Vol. 86, No. B6, June, 1981, pp. 4913-4928.

Wilson, W.M., and Newmark, N.M., "The Strength of Thin Cylindrical Shells as Columns," Bulletin No. 255, University of Illinois Engineering Experimental Station, Urbana, IL, Feb., 1933.

Wilt, J.W., "Measured Movement Along the Surface Trace of an Active Thrust Fault in Buena Vista Hills, Kern County, California," Bulletin of the Seismological Society of America, Vol. 48, No. 2, April, 1958, pp. 169-176.

Yun, H., and Kyriakides, S., "On the Beam and Shell Models of Buckling of Buried Pipelines," Engineering Mechanics Research Laboratory, Report No. 88/9, The University of Texas at Austin, Austin, TX, Sept., 1988.

APPENDIX

This appendix presents the derivation of Equations 2 and 3. The derivation follows that in Marek and Daniels (1971) with the main difference that here the uplift reaction, w, and the longitudinal frictional force, t_u, are treated independently.

The differential equation of the deflected shape of the buckled portion of the pipe is determined by considering the pipe as a beam subjected to a bending moment given by (see Figure 2c):

$$M_{(x)} = \frac{w}{2}\left(0.25L_b^2 - x^2\right) - Pv_{(x)} \tag{A1}$$

where $v_{(x)}$ is the deflected shape of the pipe. The resulting differential equation if found by replacing Equation A1 into $E_iIv''_{(x)} = M_{(x)}$, which gives:

$$v''_{(x)} + n^2\, v_{(x)} + \frac{m}{8}\left(4x^2 - L_b^2\right) \tag{A2}$$

in which $m = w/(E_iI)$ and $n^2 = P/(E_iI)$. In solving Equation A2, the required boundary conditions are zero displacement at both ends $(x = \pm L_b)$, zero slope at the mid-point $(x=0)$, and zero slope at both ends $(x = \pm L_b)$. This last condition results in the expression:

$$\tan\frac{nL_b}{2} = \frac{nL_b}{2} \tag{A3}$$

or

$$\frac{nL_b}{2} = 4.4934 \tag{A4}$$

from which the critical load P is found:

$$P = \frac{80.7629 \, E_i I}{L_b^2} \tag{A5}$$

The equation for the deflected shape of the pipe is given by:

$$v_{(x)} = \frac{m}{n^2} \left(-\frac{\cos nx}{\cos \frac{nL_b}{2}} - 0.5n^2x^2 + 0.125n^2L_b^2 + 1 \right) \tag{A6}$$

The next step consists of relating the far-field load P_o to the axial load in the buckled portion of the pipe, P. From Figure 2d, equilibrium in the axial direction yields:

$$P_o = P + t_u L_f + 0.5wL_b \tan\delta \tag{A7}$$

To determine the length L_f, it is necessary to set a compatibility condition on the kinematics of the problem. The final length of the buckled portion of the pipe, as determined from the reduction of axial load from P_o to P, must be equal to the final length of the pipe determined from the equation of the deflected shape ($v_{(x)}$). That is:

$$\overline{B'C'D'} = \int_{-\frac{L_b}{2}}^{\frac{L_b}{2}} \sqrt{1 + (v'_{(x)})^2} \, dx \cong L_b + \int_0^{\frac{L_b}{2}} (v'_{(x)})^2 dx \tag{A8}$$

and

$$\overline{B'C'D'} = \left(L_b + 2\Delta L\right) \left(1 + \frac{P_o - P}{AE_i}\right) \tag{A9}$$

where ΔL is the net movement of points B and D to points B' and D', respectively, and is given by:

$$\Delta L = \frac{t_u L_f^2}{2AE_i} \tag{A10}$$

Combining Equations A8, A9, and A10 results in:

$$P_o = \frac{80.76 \, E_i I}{L_b^2} + \frac{wL_b \tan\delta}{2} - \frac{t_u L_b}{2} + B^{1/2} \tag{A11}$$

which is Equation 2 in the text.

487

TENSION/BENDING BEHAVIOR OF BURIED PIPELINES UNDER LARGE GROUND DEFORMATIONS IN ACTIVE FAULTS

Teoman Ariman and Bor-Jen Lee*
College of Engineering and Applied Sciences
University of Tulsa, Tulsa, OK

ABSTRACT

This paper deals with the tensile failure of buried pipelines subject to abrupt fault movements. The pipe is modeled as a thin cylindrical shell which is essentially semi-infinite. The Sanders' nonlinear shell theory is used with the inclusion of soil effects, and a simply flow theory of plasticity is introduced via the concept of effective stress from an uniaxial tension test. A constant radius of curvature for the curved section of the pipe is assumed to predict both the tension and bending responses of the pipe to the fault movements. A modified Euler method based on a finite difference scheme is utilized to solve the problem. A number of parametric studies are carried out and discussed to identify some design parameters of buried pipelines.

---

* Previous address.

INTRODUCTION

Earthquake safety of utility systems and in particular buried pipelines have attracted a great deal of attention in recent years.[1-4] The two most important characteristics that distinguish buried pipeline systems from other types of structures and facilities are: 1) their overall size which cover large areas and subject to a variety of geotechnical hazards and 2) they form networks so that optimal performance requires a system-wide evaluation for which probability and reliability techniques need to be utilized.

Since a pipeline system generally is built up over a large territory so that its response to permanent earthquake ground movements will be greater than that of a facility occupying a small area. Many water, oil and natural gas transmission pipelines in California must cross active faults and liquefaction areas, whereas individual buildings can be sited away from these features. Permanent ground movements should be considered during the design of new pipelines and for risk assessment and retrofitting strategies in existing systems. Measures for mitigating the effects of earthquake displacements should begin with understanding the principal forms of permanent movement.

During an earthquake, permanent differential movements of ground can be caused by faulting, soil liquefaction, slope instability and local compaction of the ground.[5,6] Buried pipelines can be damaged either by permanent movements of this type and/or by seismic ground waves. For instance surface faults, landslides and local compaction of the ground in the 1971 San Fernando earthquake caused the rupture and/or buckling failures in water, gas, and sewage lines[5,6] with high concentration of pipeline damage along the Sylmar segment of the San Fernando fault.[7,8] Similarly, the 1972 Managua earthquake caused surficial displacement along four prominent strike-slip faults through the downtown area of the city and nearly all water mains crossing the faults ruptured. Although relatively old and/or corroded pipelines have been damaged by wave propagation[9], seismic ground shaking alone generally cannot be expected to cause any major rupture and/or buckling failure in properly designed, manufactured and laid out welded steel pipelines.[10-13] This outcome is in complete agreement with the investigation of Youd.[14] After examining the 1971 San Fernando earthquake in detail, he concluded that strong and ductile steel pipelines withstood ground shaking but were unable to resist the large permanent ground deformations generated by faulting and ground failure.

Furthermore, it is important to recognize that permanent differential movements may be caused by any earthquake and that the movements can assume a variety of patterns depending on local

soil conditions and the presence of faults. Therefore, the response of buried pipelines to permanent ground movement is an important part of the lifeline earthquake engineering and its investigation is in line with the recommendations of a number of committees and individual researchers.

TENSION/BENDING BEHAVIOR

Frequently, a specific type of ground failure in a fault zone will cause both tension and compression failures, depending on the orientation of the pipeline and location within the zone of movement (Fig. 1). A thin cylindrical shell model of the pipeline may be required to simulate the local structural behavior, depending on the form of the buckling and tensile failure modes. Thus, a shell model is chosen herein to analyze tension and bending behavior.
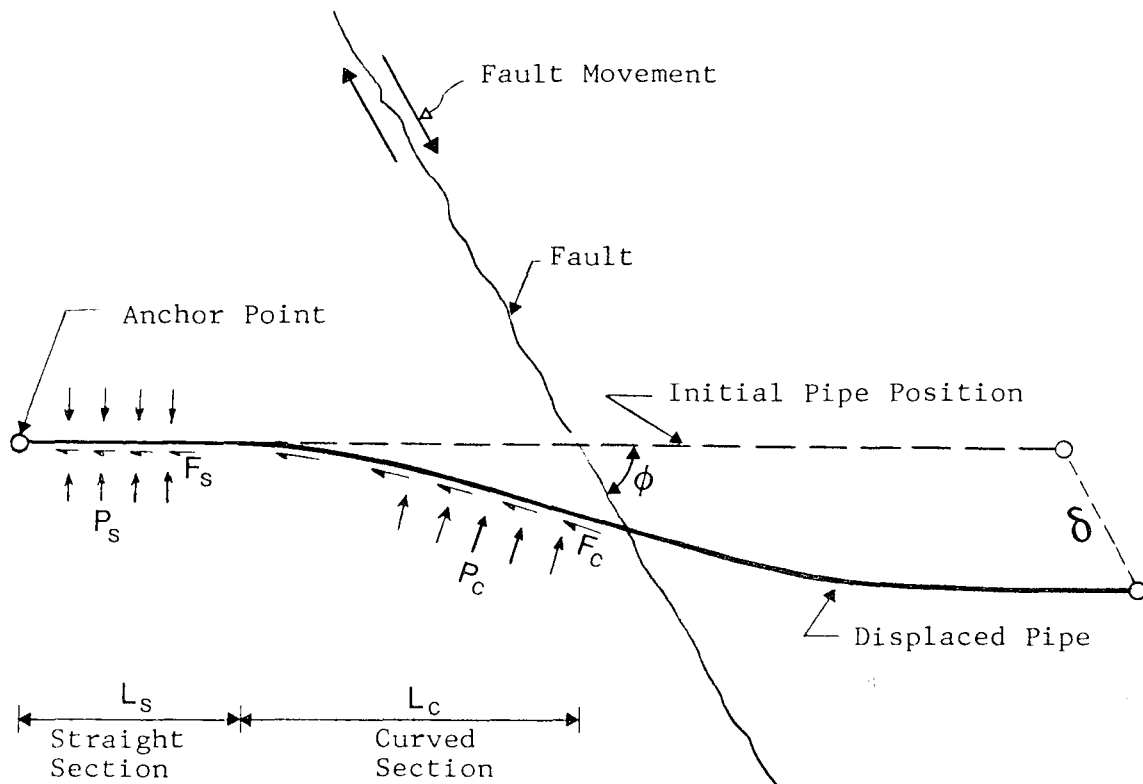
Fig. 1. Buried Pipe Deformation Due to Strike-Slip Fault Movement

Regarding tensile behavior due to large abrupt fault movements, a number of investigations have been conducted based on a beam model. Among these are three well-known procedures: Newmark-Hall procedure[15], Kennedy, et al. procedure[16] and finite element

approach[17]. Wang[18] also extended Kennedy, et al. procedure based on a beam on an elastic foundation for the straight portion of the pipe, and the curved portion is again assumed to have a constant radius of curvature. However, it should be noted that under large fault displacements, the pipe axial stress may exceed the yield stress for quite a long distance away from the fault. Thus, the conjunction point between the elastic and inelastic zones may extend even into the straight portion of the pipe.

In this paper, a shell model is used to investigate the tensile and bending behavior of pipelines subject to abrupt fault displacements. The pipe is assumed to be placed in a shallow trench, and readily conforms to the transverse components of fault motion. Thus, the tension in the pipe, introduced by the longitudinal component of fault motion plus an additional extension due to the geometric distortion resulting from the transverse component of fault motion, are investigated. The Sanders' nonlinear shell theory[19] is used by including soil effects, and a simple flow theory of plasticity[20] is introduced. Some typical results of the analysis for certain key variables, such as the crossing angle of pipeline/fault intersection, burial depth, pipe diameter, and soil effects are presented.

SELECTED RESULTS

A series of parametric studies are carried out to further understand the pipe tensile performance under the abrupt fault motion based on a cylindrical shell model. The X-60 grade pipes are considered to be 600 ft long, 42 in. in diameter, 0.562 in. in wall thickness, placed in loose to moderately dense sand with a depth cover of 3 ft with a fault crossing angle (ϕ) of 70 dynes.

Table 1. The Influence of ϕ on ε_b (%)

δ (ft) \ ϕ	30°	40°	50°	60°	70°	80°
5	0.580	0.583	0.636	1.015	1.138	1.216
10	0.549	0.550	0.555	0.566	0.586	1.132
15	0.536	0.537	0.542	0.549	0.562	0.841
20	0.529	0.529	0.533	0.540	0.551	0.579

Some of the characteristic results for bending strains are shown by Tables 1-4. The effects of fault crossing angle (ϕ) and fault displacements (δ) on bending strains are shown in Table 1. It is clear that the bending strains do not vary significantly for smaller angles, ϕ = 30°-40°, despite a large increase in fault displacements from 5 ft to 20 ft since the axial force reaches a

plateau. It is found that the axial force is not affected significantly by the bending curvature of 80 percent of the axial strain is more than the corresponding bending strain or the axial strain far exceeds the yield strain. On the other hand, the bending rigidity is strongly affected by the magnitude of the axial strain, i.e. under small axial strains the pipe would withstand larger bending strains for smaller fault displacements or larger crossing angles.

Table 2. The Influence of ϕ_s on ε_b (%)

δ (ft) \ ϕ	20°	25°	30°	35°	40°	45°
5	0.202	0.366	0.621	1.015	1.509	2.548
10	0.171	0.258	0.374	0.566	0.810	1.339
15	0.167	0.251	0.363	0.549	0.787	1.297
20	0.164	0.246	0.357	0.540	0.774	1.276

The effect of the soil angle of shearing resistance ϕ_s on the pipe bending strain is shown by Table 2 for a variation range of 20° to 45°. For large values of ϕ_s bending strains increase substantially and if the axial tension strain cannot compensate for the corresponding compressive bending strain, local buckling may occur even for small fault crossing angles and under small fault displacements. In other words, even if the fault crossing angle is below 80°, it would be possible that the pipe could be buckled by bending alone. Therefore, considering a small increase in axial strain and a substantial increase in bending strain, it is recommended to have ϕ_s as small as possible to accommodate transverse movement of the pipe in fault crossings.

Table 3. The Influence of H_c on ε_b (%)

δ (ft) \ H_c (ft)	1	2	3	4	5	6
5	0.484	0.744	1.015	1.256	1.626	1.933
10	0.291	0.423	0.566	0.691	0.886	1.057
15	0.283	0.412	0.549	0.672	0.863	1.026
20	0.278	0.405	0.540	0.661	0.847	1.007

The effect of the burial depth H_c (ft) of the pipe on the bending strains is shown in Table 3. An increase in H_c would provide larger longitudinal and lateral soil resistances on the straight as well as the curved sections of the pipe. An increase in lateral forces causes larger bending strains which are not

desirable. Therefore, as in the case of the axial buckling[21] again a shallow burial depth is recommended for pipes which are subjected to tension and bending in active fault crossings.

Table 4. The Influence of D on ε_b (%)

δ (ft) \	D (in.) 30	34	38	42	46	50
5	0.699	0.807	0.917	1.027	1.137	1.250
10	0.386	0.446	0.509	0.571	0.635	0.698
15	0.375	0.434	0.494	0.555	0.616	0.679
20	0.369	0.427	0.486	0.546	0.607	0.668

An increase in the pipe diameter for a constant thickness causes larger cross-sectional area and larger bending rigidity for the pipe. Thus frictional forces and lateral soil resistance would increase. As shown in Table 4 the stated factors result in considerable increases in bending strains. However, this situation is compensated by a substantial increase in the bending rigidity for larger diameter pipes.

REFERENCES

1.   Ariman, T., S. C. Liu, and R. E. Nickell (Eds.), Lifeline Earthquake Engineering-Buried Pipelines, Seismic Risk and Instrumentation, PVP-34, ASME, New York, 285 pgs., June 1979.

2.   Shibata, H., T. Katayama, and T. Ariman (Eds.), Recent Advances in Lifeline Earthquake Engineering in Japan, PVP-43, ASME, New York, 158 pgs., August 1980.

3.   Ariman, T. (Ed.), Earthquake Behavior and Safety of Oil and Gas Storage Facilities, Buried Pipelines and Equuipment, PVP-77, ASME, New York, 478 pgs., June 1983.

4.   The Current State of Knowledge of Lifeline Earthquake Engineering, ASCE, New York, 1977 and 1981.

5.   O'Rourke, T. D. and C. H. Truatmann, "Buried Pipeline Response to Permanent Earthquake Ground Movement," ASME Paper 80-C2/PVP-78, 1980.

6.   O'Rourke, T. D. and M. A. McCaffrey, "Buried Pipeline Response to Permanent Earthquake Ground Movements,"

Proceedings of the Eight World Conference on Earthquake Engineering, Vol. 8, 215-222, 1984.

7.   U. S. Geological Survey Staff, "Surface Faulting, The San Fernando, California, Earthquake February 9, 1971," U. S. Geological Survey, Professional Paper 733, 55-76, 1971.

8.   Youd, T. L., R. F. Yerkes, and M. M. Clark, "San Fernando Faulting Damage Its Effect on Land Use," Proc. Conf. Earthquake Engineering and Soil Dynamics, ASCE, Vol. 11, 1111-1125, 1978.

9.   Steinbrugge, K. V., W. K. Cloud, and H. N. Scott, "The Santa Rosa California Earthquake of October 1, 1969," U. S. Department of Commerce, Rockville, MD, 1970.

10. Muleski, G. E., T. Ariman, and C. P. Aumen, "A Shell Model of a Buried Pipe in a Seismic Environment," J. Pressure Vessel Technology, ASME, 101, 44-50, 1979.

11. Chen, C. C., T. Ariman, and L.H.N. Lee, "Elastic Buckling Analysis of Buried Pipelines Under Seismic Loads," ASME Paper 80-C2/PVP-76, 1980.

12. Lee, L.H.N., T. Ariman, and C. C. Chen, "On Buckling of Buried Pipelines by Seismic Excitation," ASME Paper 80-C2/PVP-75, 1980.

13. Ariman, T. and G. E. Muleski, "A Review of the Response of Buried Pipelines Under Seismic Excitations," Earthquake Engineering and Structural Dynamics, Vol. 9, 133-151, 1981.

14. Youd, T. L., "Ground Movements in the Norman Lake Vicinity During San Fernando, California, Earthquake of February 9, 1971," U. S. Dept. of Commerce, Vol. III, 197-206, 1973.

15. Newmark, N. M. and W. J. Hall, "Pipeline Design to Resist Large Fault Displacement," Proc. of the U. S. National Conference on Earthquake Engineering 1975, Earthquake Engineering Research Institute, Oakland, CA, June 1975.

16. Kennedy, R. P., A. W. Chow, and R. A. Williamson, "Fault Movement Effects on Buried Oil Pipeline," Transportation Engineering Journal of ASCE, Vol. 103, No. TE5, pgs. 617-633, Sept. 1977.

17. O'Rourke, T. D. and C. H. Trautmann, "Analytical Modeling of Buried Pipeline Response to Permanent Earthquake Displacements," Geotechnical Engineering Report 80-4, July 1980.

18. Wang, L.R.L. and Y. H. Yeh, "Seismic Analysis and Design of Buried Pipeline for Fault Movement," unpublished manuscript, 1984.

19. Sanders, J. L., Jr., "Nonlinear Theories for Thin Shells," Quarterly of Applied Mathematics, Vol. 21, pgs. 21-36, 1963.

20. Murphy, L. M. and L.H.N. Lee, "Inelastic Buckling of Axially Compressed Cylindrical Shells Subject to Edge Constraints," Int. J. Solid Structures, 7, 1153-1170, 1971.

21. Lee, B. J. and T. Ariman, "Buckling of Buried Pipelines Crossing an Active Fault," Seismic Performance of Pipelines and Storage Tanks, PVP-Vol. 98-4, Edited by A. C. Singhal and T. Ariman, ASME, 1985.

NONLINEAR ANALYSES OF PILES SUBJECTED TO LIQUEFACTION INDUCED LARGE GROUND DEFORMATION

F. Miura

Associate Professor of Computer Science & Systems Engineering
Yamaguchi University

T. D. O'Rourke

Professor of Civil Engineering
Cornell University

ABSTRACT

In this paper, a simple method to analyze the nonlinear pile response to liquefaction-induced large ground displacement is proposed. Nonlinear bending moment-curvature characteristics of the pile are modeled by rotational spring-slider elements which had tri-linear characteristics. The method is applied to simulate the performance of piles which were damaged during the 1964 Niigata earthquake. The results from the proposed method are compared with those from analytical procedures which utilize bi-linear moment-curvature relationships for the reinforced concrete piles. Analytical results are reported for reinforced concrete piles of 0.35, 0.45, and 0.60m diameter subjected to the same liquefaction-induced displacement pattern as inferred from the site of piles damaged during the Niigata earthquake.

Increased pile diameter is shown to have little influence on the development of a plastic hinge where the piles penetrate a dense bearing stratum at depth. However, increased pile diameter has a strong effect in reducing the likelihood of a second plastic hinge at the interface between the upper intact soil layer and underlying liquefiable deposit.

497

INTRODUCTION

To interpret the observed pile damage at N-building caused by the 1964 Niigata earthquake, we have performed numerical analyses to estimate the maximum bending moment induced in piles subjected to liquefaction-induced large ground displacements in light of possible ground deformation mechanisms[1]. We also performed parametric analyses to estimate the ground displacement at which the pile under consideration would yield, and conversely, to judge whether the pile would be damaged or not at a given ground displacement[2].

The numerical analyses in those studies were performed using a computer program "B-STRUCT". The computer code is based on the finite element method which takes into account the geometric nonlinearity and material nonlinearity of pile and soil. Spring-slider elements were employed to represent the nonlinear force-displacement relationship of soil, and rotational spring-slider elements were employed to represent the nonlinear bending moment-curvature relationship of piles. These nonlinear characteristics were modeled by bi-linear representation in the analyses. Although the representation could explain the general tendency of the process of pile damage, more accurate modeling was needed to simulate and understand the detailed damage process.

In this paper, we first propose a tri-linear model to represent the material nonlinearity of piles. Then the proposed method is applied to examine the pile response at N-building to the liquefaction-induced large ground displacement. The results are compared with those obtained from the analyses assuming bi-linear moment-curvature characteristics of the pile. In addition to the pile at N-building, two more piles with larger diameters are analyzed to assess the effect of diameter on pile response.

ANALYSIS METHOD

Bending Moment-Displacement Relation of a Pile

Figure 1 is a representative relation between applied bending moment and resulting curvature when a pile is subjected to a bending moment. The diagram is linear to the cracking moment Mc, after which a straight line of somewhat flatter slope is obtained. At the moment which initiates yielding, My, the curvature increases rapidly. Further application of moment causes extensive curvature, until eventual collapse is obtained when the curvature equals the ultimate capacity.

Mc is the bending moment at which a crack initiates in the pile. My is the yielding moment at which steel reinforcement in the pile starts to yield due to tension. Mu is the ultimate bending moment at which the compressive strain of the concrete reaches an ultimate strain, 0.003[3], and dc, dy, and du are displacements which correspond to Mc, My and Mu, respectively.

The curve is modeled as a tri-linear relationship shown line in Figure 1. To

specify the relationship, we need to obtain the cracking moment, the ultimate moment and corresponding curvatures. The bending moment-displacement curve is obtained directly by tests. A bending moment-curvature curve is also obtained theoretically, as is described in the following section.

The Strength Interaction Diagram

It is convenient to construct a "strength interaction diagram", or the bending moment – axial force diagram to determine the Mc, Mu and corresponding curvatures ψ_c and ψ_u. The diagram defines the relation between the axial force and bending moment for a given pile for the full range of eccentricities from zero to infinity. For any eccentricity, there is a unique pair of values of axial force N and bending moment M that will result in both crack initiation and ultimate capacity.

Figure 2 is an example of the distribution of strain in a cross section of a pile when the pile is subjected to axial force N and bending moment M. The curvature, which corresponds to the bending moment, can be calculated from the eccentricity and the maximum strain induced in the cross-section of the pile. The axial force N and the bending moment M are calculated from the following equations.

$$N = \int_{A1} E_c \varepsilon_x dA_1 + \int_{A2} \sigma_{cy} dA_2 + \sum_i^n A_s E_s \varepsilon_i' \qquad (1)$$

$$M = \int_{A1} E_c \varepsilon_x x dA_1 + \int_{A2} \sigma_{cy} x dA_2 + \sum_i^n A_s E_s \varepsilon_i' r_0 \cos\theta_i \qquad (2)$$

where
Ec : Young's modulus of the concrete
Es : Young's modulus of the reinforcement
ε_x : strain of the concrete at x
x : distance from the center of the cross-section
σ_{cy} : yielding stress of the concrete
A_1 : area of cross-section of the concrete which has not yielded
A_2 : area of cross-section of the concrete which has yielded
A_s : area of cross-section of a reinforcement
r_0 : distance of a reinforcement from the center of the cross-section of the pile.
θ_i : angle between the reinforcement i and the x-axis
n : number of reinforcements
ε_i' : strain in the reinforcement which is taken as follows

$$\varepsilon_i' = \begin{cases} \varepsilon_i & for \quad \varepsilon_i \leqq \varepsilon_y \\ \varepsilon_y & for \quad \varepsilon_i > \varepsilon_y \end{cases} \qquad (3)$$

where, ε_i is the strain in reinforcement i.

To change the eccentricity is equivalent to changing the length of 1 in the figure which is the distance from the neutral axis to the pile surface where

the ultimate compressive strain is induced.

The curvature ، is given by

$$\varkappa = \frac{0.003}{l}$$ (4)

For the state of cracking moment, the same procedure can be used. In this case, however, N and M are calculated under the situation that the maximum tensile strain is zero at the pile surface as shown in Figure 3. This neglect of tensile capacity of concrete is commonly done, and it involves a small error on the conservative side. The maximum strain $\varepsilon_{max.}$ is changed here instead of changing 1, which was done for the ultimate state. The axial force N, bending moment M and corresponding curvature are given as:

$$N = \int_{A1} E_c \varepsilon_x dA_1 + \sum_{i}^{n} A_s E_s \varepsilon_i$$ (5)

$$M = \int_{A1} E_c \varepsilon_x x dA_1 + \sum_{i}^{n} A_s E_s \varepsilon_i r_0 cos\theta_i$$ (6)

$$\varkappa = \frac{\varepsilon_{max.}}{2D}$$ (7)

Where, D is the radius of the pile and $\varepsilon_{max.}$ is the maximum strain.

Note that neither concrete nor reinforcement has yielded in this situation, therefore, the relationship between M and $\varkappa$ is linear.

The stress-strain curves of the concrete and the reinforcement employed in this study are shown in Figures 4(a) and (b), respectively. The M-N curves and M-$\varkappa$ curves are shown later (Figures 9 and 10).

Equivalent Spring Coefficient of the Rotational Spring-Slider Element

In this study, piles are modeled by beam elements with material properties that are linear elastic and rotational spring-slider elements which have non-linear properties. That is, the material non-linear behavior of the pile is represented by that of rotational spring-slider elements. In the previous section, the relation between the bending moment and curvature was determined. This relation must be converted to the relation between the bending moment and rotational angle of the rotational spring-slider element. The bending moment and the angle are related through the spring coefficient of the element. The next step is, therefore, to determine the equivalent spring coefficient, k_ω, of the rotational spring-slider element.

The spring coefficient is determined by:

$$M_u = k_\omega \theta$$ (8)

where θ is the rotational angle. The basic idea of determining the equivalent

coefficient is to adjust the displacement of the pile which is modeled by beam elements and tri-linear rotational spring-slider elements to the displacement which has homogeneous tri-linear characteristic throughout the beam.

Figures 5 (a)-(f) describe the basic idea. Figure (a) is the schematic drawing of the comparison of displacements when a pile of length, 2l, is subjected to bending moment M. The solid line is the displacement from the model of beam elements and a rotational spring-slider element and broken line is that from the homogeneous tri-linear model (actual deformation). Figures (b) and (c) show equivalent displacements to that shown in Figure (a). As shown in Figure (c), the total displacement d is the summation of displacements de and dp. The displacement, de, is due to the deformation of the beam element, and dp is caused by rotation of the rotational spring -slider element. The curvatures of deformations (i) and (ii) in Figure (c) are the same.

The displacements de and dp are explained in the moment-displacement curve in Figure (d). As we can not calculate the curve directly, we need to calculate these displacements from the corresponding moment-curvature curve shown in Figure (e). The curvature, ψ_e, is induced in a linear elastic pile, and ψ_p is the additional curvature due to the material non-linearity. Until the bending moment reaches the cracking moment Mc, no rotation should occur in the rotational spring-slider element. That is, the rotational spring-slider element contributes only to the displacement dp.

From Figure(c)

$$dp = \theta l \tag{9}$$

From Figure(d)

$$dp = du - de \tag{10}$$

From Eq.(8)

$$\theta = \frac{M_u}{k_\omega} \tag{11}$$

From Eqs. (9), (10) and (11), we get

$$k_\omega = \frac{l}{du - de} M_u \tag{12}$$

On the other hand, from the geometry of the curvature ψ and displacement d under the assumption that the displacement is expressed as the part of circle with the curvature ψ, as shown in Figure (6), the displacement and the curvature have the following relation.

$$d = \frac{1}{\psi} - \sqrt{\frac{1}{\psi^2} - l^2} \tag{13}$$

Therefore, for the ultimate,

$$du = \frac{1}{\psi_u} - \sqrt{\frac{1}{\psi_u{}^2} - l^2} \tag{14}$$

and for the cracking moment state,

$$de = \frac{1}{\psi_e} - \sqrt{\frac{1}{{\psi_e}^2} - l^2}$$ (15)

By substituting Eqs.(14) and (15) into Eq.(12), we can determine the equivalent spring coefficient, k_ω. The equation (12) is derived from a model in which only one beam element and one rotational spring-slider element are employed. When a pile with length, 1, is modeled by n beam elements and n rotational spring-slider elements, the equivalent k_ω is obtained as follows.

The displacement due to rotations of n rotational spring-slider elements, dp, is given by the following equation (Refer to Figure 5(f). In this figure, two rotational spring-slider elements are employed, i.e. n=2).

$$dp = \theta l + \frac{n-1}{n}\theta l + \frac{n-2}{n}\theta l + \cdots + \frac{1}{n}\theta l$$

$$= \frac{n+1}{2}\theta l$$ (16)

From this equation and Eqs. (10) and (11), the equivalent spring coefficient is given by:

$$k_\omega = \frac{n+1}{2} \frac{l}{du - de} M_u$$ (17)

MODEL OF THE PILE-SOIL INTERACTION SYSTEM

The interaction between the pile and adjacent soil was simulated by means of the finite element configuration shown in Figure 7. Beam elements with linear elastic and geometric nonlinear properties and rotational spring-slider elements with material nonlinearity were used to represent the pile, and the soil reaction was modeled by means of spring-slider elements.

Soil Properties

A relatively simple model for the horizontal force-displacement relationship between pile and soil was adopted in this study, based on the coefficient of horizontal subgrade reaction proposed by Terzaghi[4] and the lateral bearing capacity factors proposed by Hansen[5]. The bi-linear force-displacement relationship is used to model the pile-soil interaction as shown in Figure 8. The soil yielding force, Fy, at a nodal point of the finite element model was determined by the following equation.

$$F_y = \sigma_z' Nq DL$$ (18)

Where, σ_z' is the effective stress at the point, Nq is the dimensionless coefficient proposed by Hansen for pile foundation in sand, D is the pile radius, and L is the length of a beam element as shown in Figure 7. The yielding

displacement, dy, was determined by dividing the yield force by the soil spring stiffness, k_h.

The spring stiffness, k_h, is given by

$$k_h = n_h z L \tag{19}$$

in which n_h is the constant of horizontal subgrade reaction which is given by Terzaghi, and z is the depth from the surface to the section of the pile of interest. Values of n_h employed in this paper are listed in Table 1.

Pile Properties

The M-N curve and the M-ψ curve for the ultimate state of the damaged RC pile at N-building are shown in Figures 9(a) and (b). The pile with the diameter of 0.35m and the length of 11m was subjected to a 185KN vertical load due to the building's static load. From Figures 9(a) and (b) with the axial load of 185KN, we get 60.7 KN-m for Mu and 0.0425 for ψ_u. The M-N curve and ψ-N curve for the cracking initiation state are shown in Figures 10 (a) and (b). From these figures with the appropriate axial load, we obtain 9.48 KN-m for Mc and 0.000482 for ψ_c. From Eqs.(14)-(17) with l=11m and n=21, the equivalent spring coefficient of the rotational spring-slider element is 2720 KN-m/rad. The rotational angle of the rotational spring-slider element at the ultimate state, then, is given as ψ_u=Mu/k_ω =0.0223 (rad). Material constants of concrete and reinforcement listed in Table 2 were used to obtain these quantities.

To examine the effect of pile diameter on pile response, we analyzed two more piles with diameters of 0.45m and 0.60m. Constants for the piles are listed in Table 3 with those of 0.35m diameter pile. For these piles, one third of their bearing capacities were used as their axial loads N. The resultant Mu, Mc, ψ_u, ψ_c, and k_ω are summarized in Table 4.

ANALYTICAL RESULTS

Comparison of Bi-Linear and Tri-Linear Results

The ground displacements versus bending moments at the liquefiable-nonliquefiable soil layers are shown in Figures 11 and 12. Figure 11 is for the bilinear model, and 12 is for the tri-linear model. The symbol, L, in the figure designates the lower interface between the liquefiable layer and the basal nonliquefiable layer, and U the upper interface between the liquefiable layer and the surface nonliquefiable layer.

From Figure 11, a plastic hinge would develop initially at the lower interface, followed by development of a plastic hinge at the upper interface. Only these two plastic hinges developed in this analysis. The magnitudes of soil displacements when plastic hinges developed at the upper and lower interfaces are about 5.5 cm and 13.5 cm, respectively. On the other hand, the first plastic hinge

appears in Figure 11 when the displacement is about 52 cm and at the upper interface when it is about 73 cm. The magnitudes are very large compared with those of the bi-linear model. The displacements required to damage the pile with the tri-linear model, however, were still well below the maximum surface displacement of 1.1-1.2 m at the site.

Before the formation of these plastic hinges, cracks appeared at very small ground displacement, i.e., about 1.0 cm at the lower interface and about 2.5 cm at the upper interface. It should be noted that the curves have more inflection points than those at Mc and Mu, even though the relationship between bending moment and curvature was modeled by tri-linear representation. For example, there are inflection points on both L and U curves at the bending moments which are designated by arrows in the figures. These points were caused by the development of cracks at adjacent rotational spring-slider elements. The pile nonlinear behavior after cracks' appearance was not taken into account in bi-linear representation. This resulted in very small displacement which formed plastic hinges in the pile. The magnitude is about one tenth of that from tri-linear model at the lower interface.

Response of Piles with Larger Diameter

The bending moment – ground displacement curves for the piles with diameters of 0.45 m and 0.6 m are shown in Figures 13 and 14, respectively. The tri-linear model was used in these analyses. These two figures are similar to each other but different from Figure 12. The most significant difference is that a plastic hinge was formed only at the lower interface. For the piles with larger diameters, no plastic hinge appeared at the upper interface. The bending moments for the piles at the upper interface have "saturated" far below the ultimate bending moments. This is attributed to the material non-linearity of soil. Once the soil yielded, the interaction forces acting on the pile do not increase.

Although there is a significant difference in plastic formation at the upper interface, the magnitudes of ground displacements at which a plastic hinge developed at the lower interface are similar and are 0.52, 0.62, and 0.67 m for the piles with 0.35, 0.45 and 0.6 m diameter, respectively. The ground displacement at the plastic hinge formation of the 0.6 m diameter pile is larger only by 0.15 m than that of the pile with 0.35 m diameter, although the ultimate bending moment is more than seven times that of pile with 0.35 m diameter. Piles with larger diameter will have larger interaction forces from soil, therefore, increasing the pile diameter alone will not be sufficient to protect the pile from damage. The ultimate bending moments for all three piles were determined using the material constants listed in Tables 2 and 3. A potential solution for the problem of pile damage is to increase the yielding stresses of concrete and reinforcement through the use of prestressed concrete (PC) piles.

All of the piles analyzed in this study are reinforced concrete (RC) piles. The RC pile tends to be brittle compared with the PC pile which is commonly used these days. The PC pile has higher ultimate bending moment than that of RC pile for the same diameter. Furthermore, Pretensioned Spun High Strength

Concrete Piles (PHC piles) are also available. The yielding stress of the concrete of PHC piles is more than 7.8 KN/cm^2. In addition to PC and PHC piles, Steel Pipe & Concrete Composite Piles (SC piles) have been developed. The SC pile has very high resistance to bending. The investigation of the responses of these piles to lateral spreading should be conducted as a future work.

CONCLUSION

A tri-linear model to represent the material nonlinearity of a pile is proposed in this study. The model was applied to examine the response of a pile at N-building which had been damaged during the 1964 Niigata earthquake due to lateral spreading. The results were compared with those obtained from previous analyses based on a bi-linear model for moment-curvature response of the pile. The magnitude of ground displacement when a plastic hinge developed for the tri-linear model was about ten times of that for the bi-linear model. The displacement required to damage the pile was, however, still well below the maximum surface displacement of 1.1-1.2 m at the site. In addition to the N-building pile, two piles with larger diameter were analyzed. It was found that a plastic hinge would develop at almost the same magnitude of ground displacement as the N-building pile, although the ultimate bending moments of these two piles were several times larger than that of the N-building pile. This means that only increasing the pile diameter will not be sufficient to protect piles from damage. Therefore, we need to study piles which have high yielding strength and ductility such as PC, PHC and SC piles.

REFERENCES

1. H.E.Stewart, F.Miura and T.D.O'Rourke, Pile Damage to Large Ground Displacement, Proc. of 1st Japan-U.S. Workshop on Liquefaction, Large Ground Deformation and Their Effects on Lifeline Facilities, pp.173-182, Tokyo, Japan, Nov. 1988.

2. F.Miura, H.E.Stewart and T.D.O'Rourke, Lateral Spreading Effects on Pile Foundation, Proc. of 2nd U.S.-Japan Workshop on Liquefaction, Large Ground Deformation and Their Effects on Lifelines, pp.295-307, Buffalo, U.S.A., Sept. 1989.

3. A.H.Nilson and G.Winter, Design of Concrete Structures, 10th Ed., McGraw Hill, New York, pp.380, 1986.

4. K.Terzaghi, Evaluation of Coefficients of Subgrade Reaction, Geotechnique, Vol.5, No.4, pp.297-326, 1955.

5. J.B.Hansen, The Ultimate Resistance of Rigid Piles Against Transversal Forces, Bulletin 12, Danish, Geotechnical Institute, Copenhagen, pp.1-9, 1961.

Table 1 The constant of horizontal subgrade reaction.

Layer	$n_h\,(kN/m^3)$
Surface nonliquefiable layer	2420
Liquefiable layer	1380
Basal nonliquefiable layer	11000

Table 2 Young's modulus and yield stress of the pile.

	Young's modulus (kN/cm^2)	Yield stress (kN/cm^2)
Concrete	2840	3.43
Reinforcement	20580	23.5

Table 3 Constants of piles.

Diameter (m)	M_{cr} (kNm)	M_u (kNm)	ψ_s (m^{-1})	ψ_u (m^{-1})	k_ω (kNm/rad)
0.35	9.48	60.7	0.000482	0.0425	2720
0.45	31.9	248	0.000552	0.0256	19400
0.60	83.8	431	0.000487	0.0217	7400

Table 4 Moments, curvatures and spring constants for the tri-linear model.

Outer diameter (m)	Inner diameter (m)	Number of reinforcement	Diameter of the reinforcement (m)
0.35	0.18	8	0.013
0.45	0.30	22	0.016
0.60	0.42	22	0.016
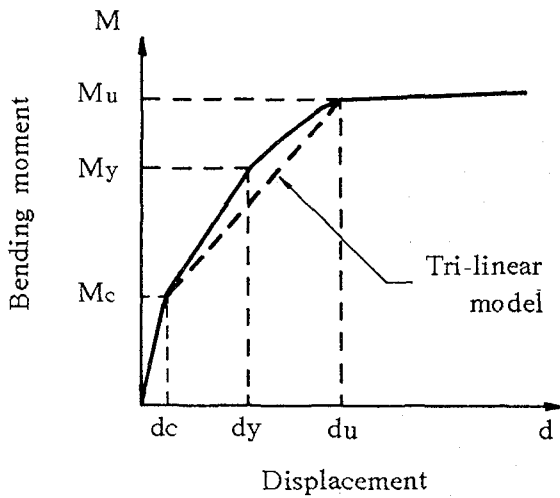
Figure 1 Bending moment-displacement relation.
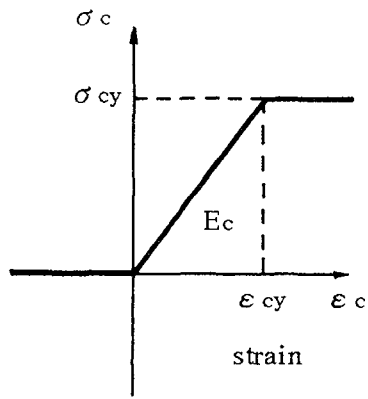
(a) Concrete
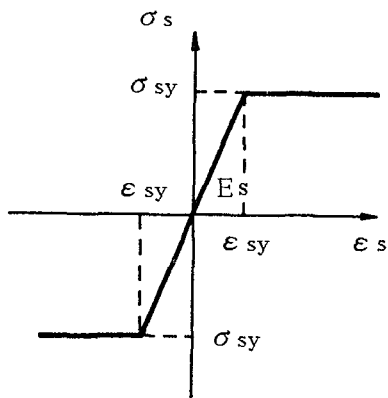
(b) Reinforcement

Figure 4 Stress-strain curve employed.
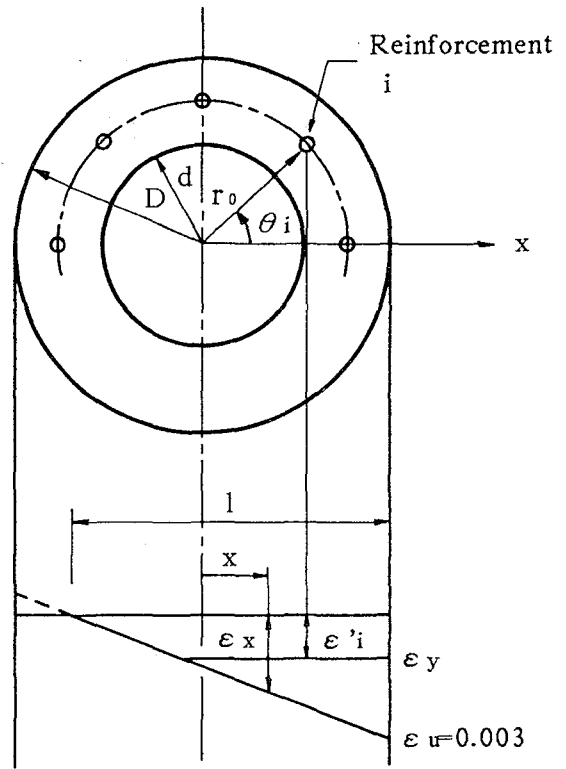
Figure 2 Constants which are used at the ultimate state.
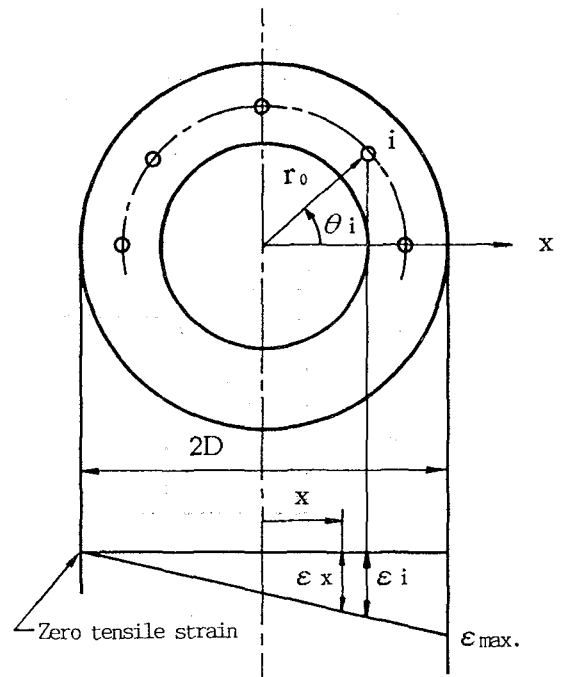
Figure 3 Constants which are used at cracking state.
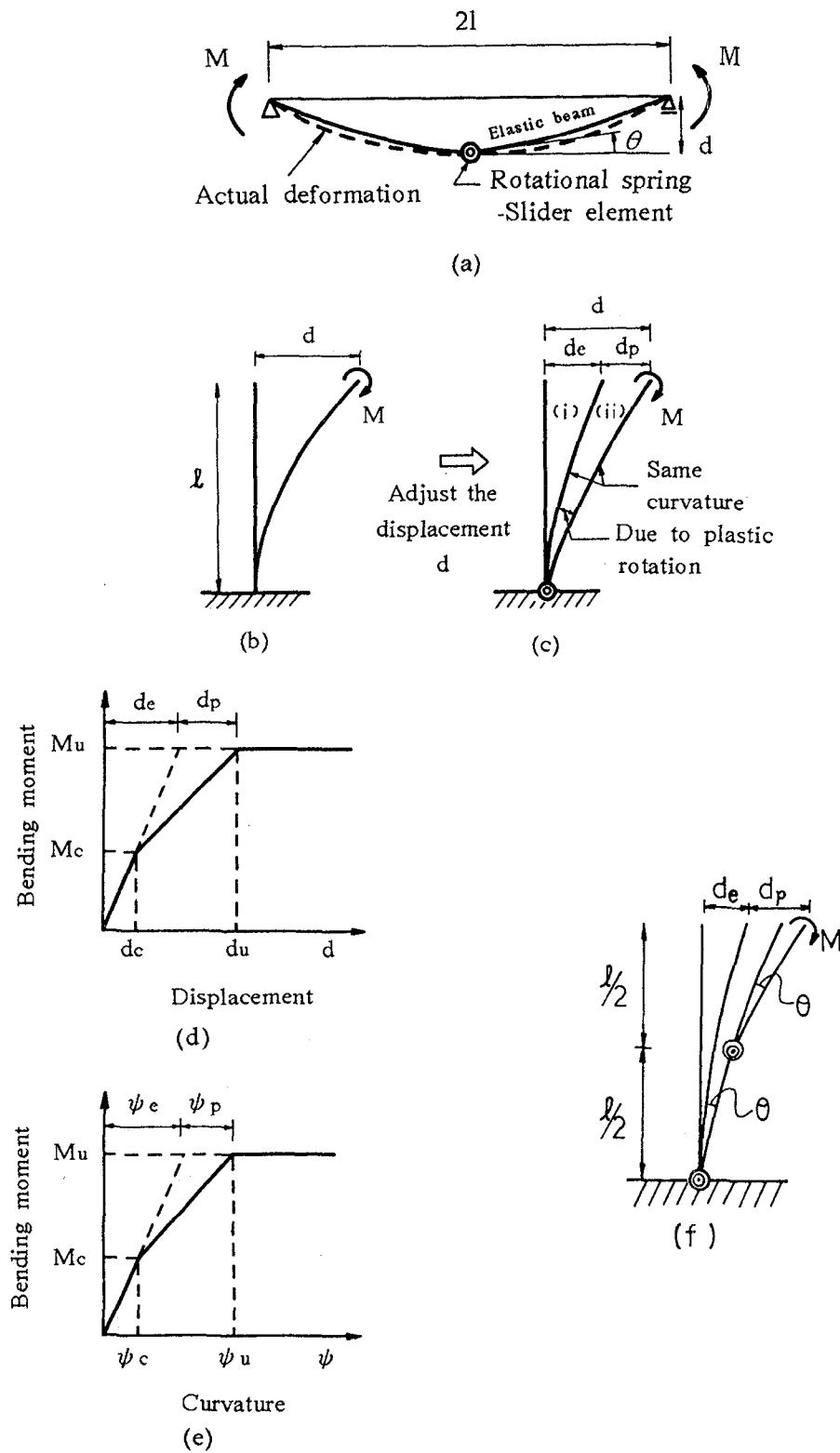
Figure 5 Schematic drawing to obtain the equivalent spring coefficient of the rotational spring—slider element.
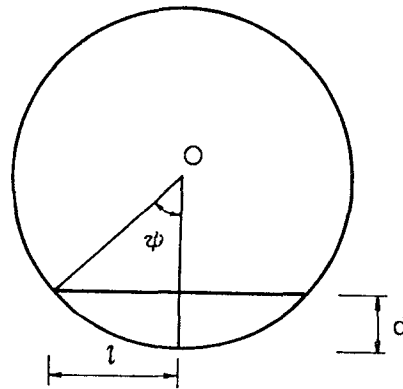
Figure 6 Relation of the curvature and displacement.
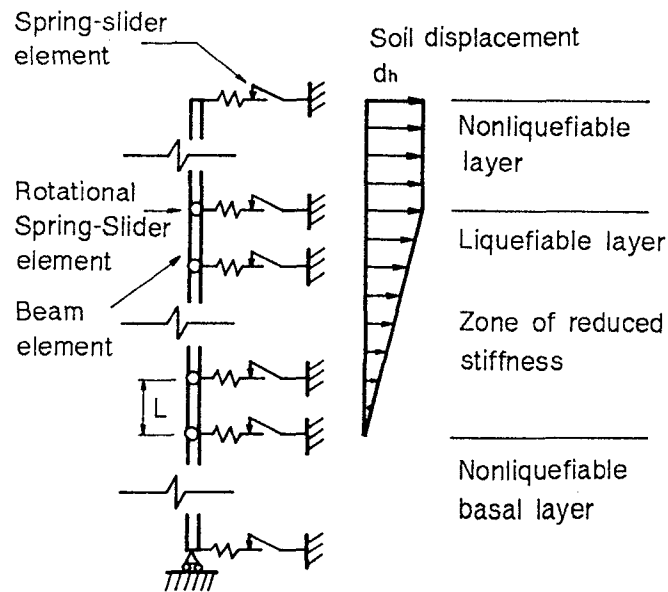
Figure 7 Profile of pile-soil interaction model.
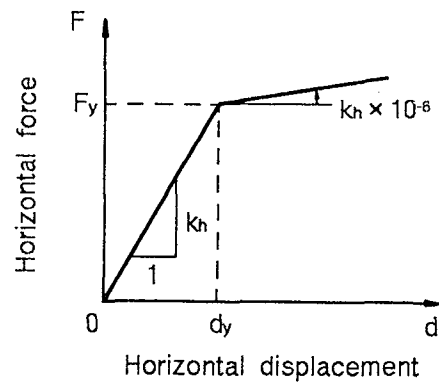
Figure 8 Force and displacement relation of soil.

509
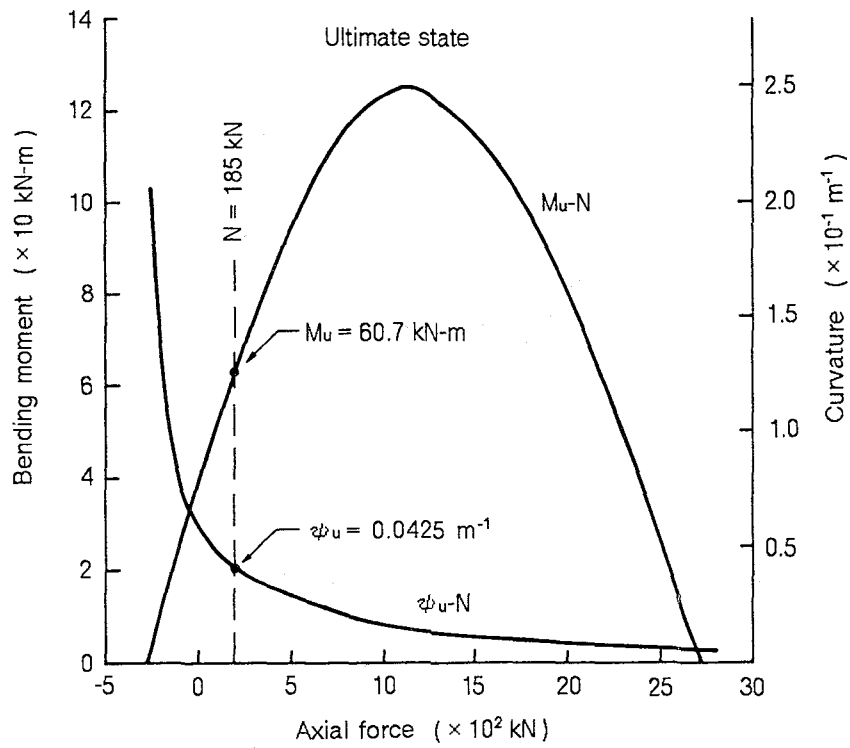
Figure 9   The M–N and ψ–N curves for the N–building
pile at the ultimate state.
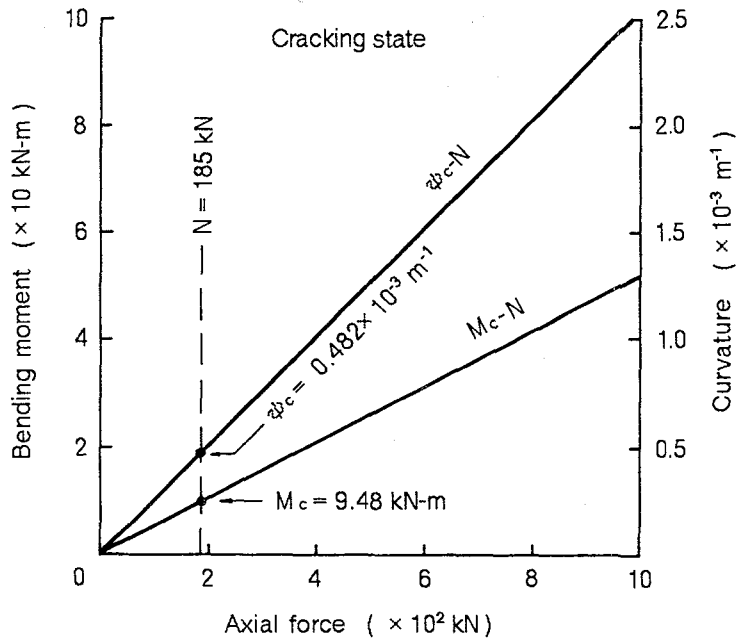
Figure 10   The M–N and ψ–N curves for the N–building
pile at the cracking state.
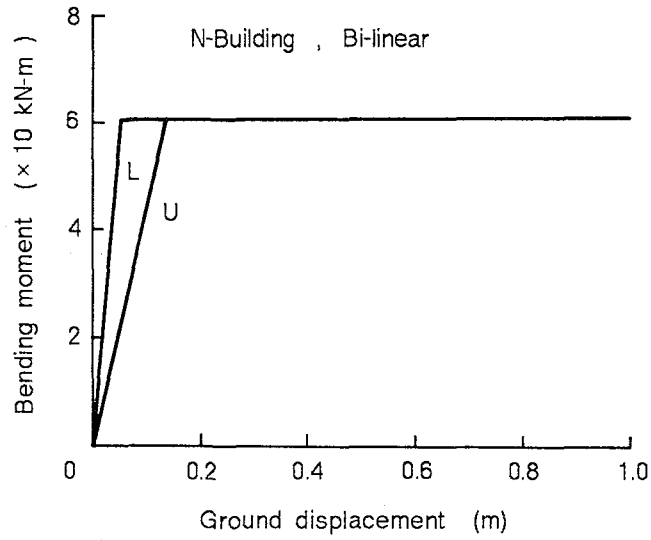
Figure 11   Bending moment–ground displacement curves
from the bi-linear model.
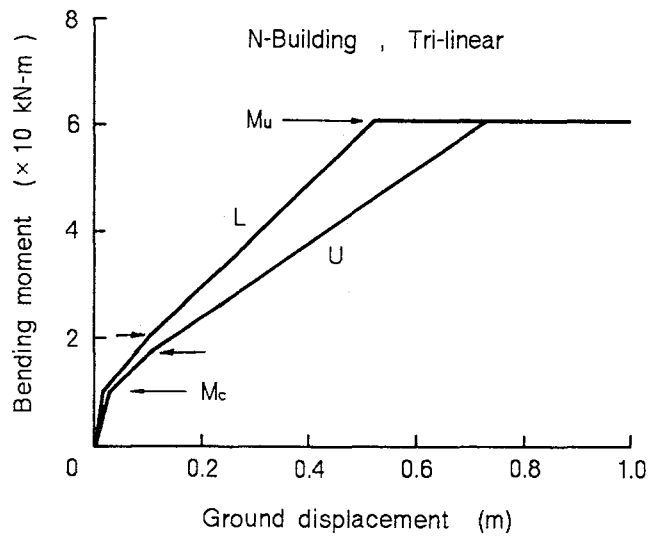
Figure 12   Bending moment–ground displacement curves
from the tri-linear model.
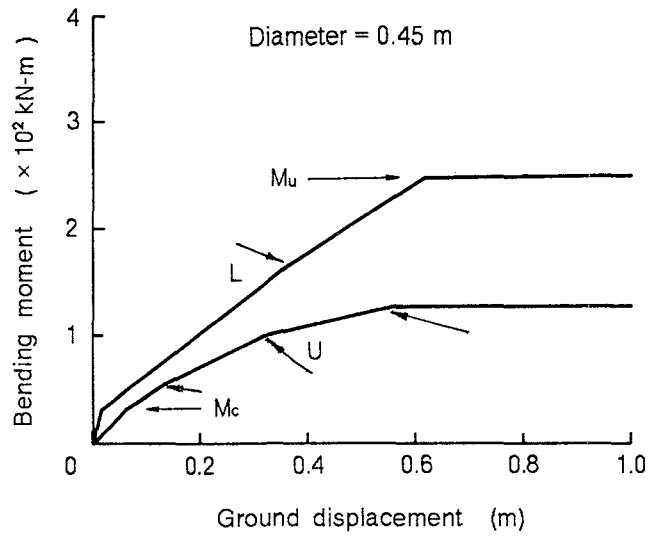
Figure 13 Bending moment-ground displacement curves
from the pile with 0.45m diameter.
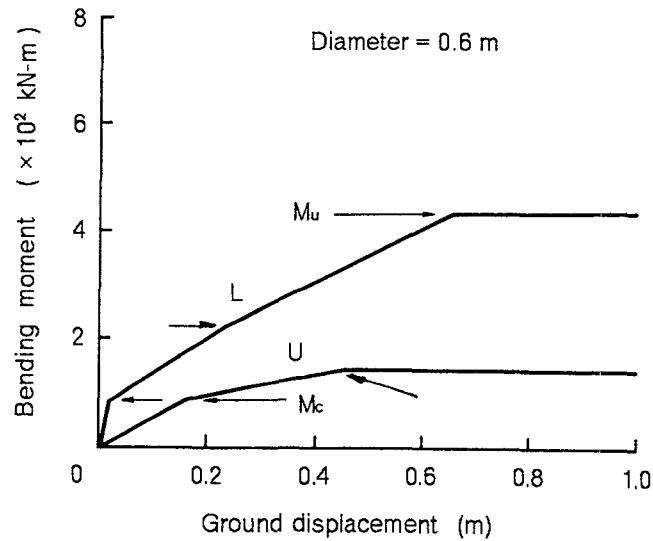
Figure 14 Bending moment-ground displacement curves
from the pile with 0.60m diameter.

SEISMIC RESPONSE OF SHAFT FOR UNDERGROUND TRANSMISSION LINE

Nobuhiro KAIZU

Engineering Research Center
The Tokyo Electric Power Co., Inc.

ABSTRACT

This report describes seismic response of a shaft for an underground transmission line constructed in the Metropolitan Tokyo. Based on earthquake observation records, it is clear that the seismic response behavior of the shaft is controlled by the deformation of the surrounding soil, and the proper correlation exists among the behavior of the shaft, the relative deformation of the soil in contact with the shaft, the dynamic earth pressure on the shaft wall and the reinforcing bar stress of the shaft during the earthquake. According to numerical study, it is confirmed that the observed response behavior of the shaft can be well simulated by two-dimensional dynamic finite element analysis using FLUSH.

INTRODUCTION

In the Tokyo Metropolitan area, subway tubes and other underground structures are crisscrossed, and it is difficult to construct underground power cable tunnels without interfering with such existing structures. Consequently there is no way but to construct power cable tunnels deeper in the ground, and the situation leads to construct the shafts reaching the depth deeper than 30 m.

The construction of deep shafts will be increasing in future, but seismic response behavior of these shafts is not clear so far, and observed records of shafts during earthquakes are limited in number. In order to develop rational and economical earthquake-resistant design, it is necessary to understand seismic response behavior of the shafts.

We have been observing the earthquake response of the shaft constructed in the northeast of the Metropolitan Tokyo since 1985 and obtained the response records more than one hundred times. Kaizu et al[1] and Katayama et al[2] have reported the seismic response of the shaft in the event of the Southern Ibaragi Prefecture earthquake on October 4, 1985.

This paper describes the seismic response of the shaft and the free-field soil based on the observed and simulated response motions in the event of the Tokyo Metropolitan Earthquake on May 18, 1988. The records marked the second largest peak re-bar stress among all the observed records since 1985.

OBSERVATION SITE AND SYSTEM

The observation site is located in the northeast of the Metropolitan Tokyo. Figure 1 shows the vertical section of the shaft, the soil profile and the location of instruments.

The surrounding soil layers consist of the alluvial silt, clay and sand (Vs=110-250 m/s) and the diluvial sand (Vs=360-480 m/s). The values of the S-wave velocity and the material constants of the soil have been obtained through in-situ PS-logging and dynamic laboratory tests of undisturbed soil samples.

The shaft is the reinforced concrete structure which has rectangular cross-section; 7.95 by 11.40 m. The shaft consists of the shaft wall and the temporal earth retaining wall for construction. The thickness of the shaft wall is 0.3-0.8 m and the depth is 31.2 m. The earth retaining wall contacts with the shaft wall. The thickness of this wall is 0.9 m and the depth is 44.4 m. There are the struts at 6 levels inside of the shaft. The power cable tunnel of diameter 3.7 m connects with the shaft at the depth about 28 m.

514

The accelerometers are installed in the free-field soil about 31 m away from the center of the shaft, and on the struts of the shaft. We supposed that the position of the above vertical array is not affected by the response of the shaft. These accelerometers of the array and the shaft are installed at almost common depths. The reinforcing-bar stress transducers and the earth pressure meters are also installed at the shaft.

As shown in Figure 1, the direction of X component of the accelerometers is arranged as the shorter axis of the shaft.

The records in the event of the Tokyo Metropolitan Earthquake on May 18, 1988, magnitude 6.0(JMA), epicentral distance 21 km and focal depth 96 km, marked the second largest peak re-bar stress among all the observed records until then. The acceleration records include higher frequency components than those by the earthquake on October 4, 1985 which the author already reported[1]. In this paper, the author reports the seismic response of the shaft and the free-field soil in the direction parallel to the shorter axis of the shaft (X component).

ACCELERATION RESPONSE OF SHAFT AND FREE-FIELD SOIL

Figure 2 shows the recorded acceleration time histories of the shaft and the vertical array at two levels; depths around GL-2 m and GL-25 m. These records are corrected by the band-pass filter with designated frequency band of 0.1-35.0 Hz. The maximum accelerations of the records on the surface of the free-field soil and at the top of the shaft are 36.8 Gal and 21.9 Gal respectively.

Figure 3 shows the Fourier spectra of these acceleration records. The upper part of Figure 3 shows the comparison of the records of the shaft and the free-field soil at GL-2 m. The predominant frequencies of the two records are in common and 1.0-1.7Hz, 3.3 Hz and 4.4 Hz, respectively. The Fourier spectral amplitudes of the free-field soil are strongly amplified at 1.6 Hz and 4.4 Hz. The peaks at 1.6 Hz and 4.4 Hz agree approximately with the first natural frequency of the alluvial layers shallower than GL-17 m (Vs=110 m/s) and the second natural frequency of the layers shallower than GL-27 m (Vs=110-250 m/s), respectively. The Fourier spectral amplitudes of the shaft in the frequency range higher than 1.3 Hz are half as much as the amplitudes of the free-field soil.

The lower part of Figure 3 shows the comparison of the records of the shaft and the free-field soil at GL-25 m near the boundary of the alluvial and diluvial layers. The Fourier spectral amplitudes are almost same in the frequency range lower than 4.0 Hz.

From the above observed behavior, we estimate that the dynamic response of the shaft reflects correctly the behavior of the surrounding soil within the alluvial layers, and the response of the shaft became the filtered one of its original frequency characteristics which the first natural frequency of the shaft shallower than GL-27 m is 4.5 Hz which will be shown.

ANALYTICAL MODEL OF FINITE ELEMENT ANALYSIS

In order to evaluate the applicability of two-dimensional dynamic finite element analysis to the structure-soil system, the author performed the numerical simulation by linear scheme using FLUSH and the observed records. In this chapter, the finite element model and the used input motion are explained.

Figure 4 shows the two-dimensional finite element model and the boundary conditions used. The shaft, the temporal earth retaining wall and the free-field soil are modeled by solid elements. The elements corresponding to the position of the instruments are divided into smaller elements as shown in Figure 4. The region of the analytical model is limited to the half size of the shaft and the free-field soil. The dimension of the finite element model is 35.0 m wide and 82.6 m deep. The right hand side boundary is attached with the energy transmitting boundary, and the bottom is attached with the viscous boundary, respectively.

According to the earthquake observation records, it is clear that the shear moduli of soil materials were not degraded during the earthquake, and hence the soil material constants can be used such values at very small strain level as shown in Figure 1. The shaft, which is actually a three-dimensional structure, was modeled by assuming plane strain condition. The shear moduli(Gs') for the shaft were estimated as follows.

$$Gs'=Gs(2t/ls) \qquad\qquad (1)$$

where Gs' = estimated shear modulus of shaft; Gs = original shear modulus of shaft; t = wall thickness of shaft; ls = length of shaft. The material damping constant of the shaft was assumed as 5 %.

The deconvolved outcrop motion at the depth of GL-82.6 m, which was used as the input motion at the bottom of the finite element model, was obtained through one-dimensional wave propagation analysis by the linear scheme using the soil material constants as shown in Figure 1. Figure 5 shows the time history and the Fourier spectrum of the input motion. The maximum acceleration is 21.1 Gal (2E), and the frequency components from 1.0 Hz to 7.0 Hz are predominant.

OBSERVED AND SIMULATED RESPONSE OF SHAFT

In this chapter, the dynamic response behavior of the shaft and the free-field soil are shown based on observed and simulated records.

Deformation of Shaft and Free-Field Soil

Figures 6(a) and 6(e) show the displacement time histories of the shaft and the free-field soil computed by frequency method using the acceleration records obtained at two levels; GL-8.6 m and GL-24.9 m. The displacement phases of the motions of the shaft well agree with those of the free-field soil. The amplitudes of the shaft are in average about 20 % smaller than those of the free-field soil at GL-8.6 m (Vs=110 m/s) and become almost equal to or greater than those of the free-field soil at GL-25m (Vs=250 m/s).

These results show that the shaft behavior depends on the deformation of the surrounding soil within the soft alluvial layers (Vs=110 m/s).

Relationship among Shaft and Soil Deformation, Earth Pressure and Re-bar Stress

Figures 6(b)-(d) and 6(f)-(h) show time histories of the relative displacements between the shaft and the free-field soil, the dynamic earth pressures on the shaft wall and the vertical re-bar stresses of the shaft at two levels; depths around GL-8.5 m and GL-26 m. The phases of time histories of the relative displacement, the earth pressure and the re-bar stress agree well with each other at GL-8.5 m belonging to the upper part of the free-field soil.

According to this result, we suppose that the three records have proper correlation with each other, and the dynamic earth pressure is produced by the relative displacement between the shaft and the free-field soil.

When we discuss the relationship among the shaft and soil deformation, the earth pressure and the re-bar stress, it is inevitable to understand quantitatively the stiffness of the shaft and the free-field soil. In order to evaluate the stiffness of the shaft, a numerical study by two-dimensional dynamic finite element analysis was performed. In the finite element model shown in Figure 4, the solid elements corresponding to the surrounding soil shallower than GL-27 m (Vs=110-250 m/s) was eliminated, i.e. the author assumed the analytical model which the shaft protrudes from the diluvial layers (Vs=360-480 m/s). The results of the dynamic response analysis with the model were examined in term of the spectral ratio of the motions between the top of the shaft and the point

of the shaft at the diluvial ground level GL-27 m. The first peak frequency (natural frequency) of the spectral ratio was 4.5 Hz, whereas that of the surrounding soil within the alluvial layers of the previous analysis was 1.4 Hz.

If we estimate the stiffness of the shaft and the soil from the natural frequencies obtained in the above, the shaft stiffness corresponding to 4.5 Hz can be said as much stronger than that of the soil which corresponds to 1.4 Hz.

Considering these points, the author studied the relationship among the deformation of the shaft and the surrounding soil, the dynamic earth pressure and the re-bar stress based on the vertical distribution of the amplitudes of these records at the time 4.68 sec when the re-bar stress shows the maximum value as shown in Figure 7.

In the upper part of the soil shallower than GL-17 m, the displacement of the soil is amplified very much, and the shaft deformation is constrained by the surrounding soil. However, since the shaft stiffness is stronger than that of the soil as mentioned above, the shaft displacement becomes smaller than that of the surrounding soil, and the difference in these displacements, i.e. the relative displacements, will be generated as shown in Figures 7(a) and (b) and Figures 6(a) and (b). On the other hand, in the lower part of the soil deeper than GL-17 m, the soil with stronger stiffness can resist against the shaft deformation transferred from the portion of the shaft within the soft alluvial layers. Because the shaft stiffness is stronger than that of the soil, the transferred shaft displacement is still larger than that of the soil, and the relative displacement is produced in the opposite direction in comparison with that of the upper part of the soil as shown in Figures 7(a) and (b) and Figures 6(e) and (f).

We obtained the good correlation of the dynamic earth pressure with the relative displacement. Similarly, the active direction of the dynamic earth pressure in the lower part of the soil was opposite to the upper part of the soil as shown in Figures 7(b) and (c) and Figures 6(b),(c),(f) and (g). But the active direction of the re-bar stresses did not change from the top of the shaft to the bottom because the shaft stiffness is strong enough to keep its deformation pattern same, as shown in Figure 7(d) and Figures 6(d) and (h).

Figure 8 shows the Fourier spectra of the observed records given in Figure 6, the relative displacements, the earth pressures and the re-bar stresses, at two levels; depths around GL-8.5 m and GL-26 m. The Fourier spectrum amplitudes of these records are predominant from 0.8 to 2.0 Hz in common regardless to the level. As mentioned above, there exists proper correlation among these three records.

Summarizing the above results, we may point out that the shaft behavior during the earthquake is controlled by the deformation of the surrounding soil within the soft alluvial layers, but that because the shaft stiffness is stronger than that of the soil, the relative displacement is produced between the shaft and the soil, and finally this relative displacement caused the earth pressure on the shaft wall and also the re-bar stress in the shaft.

As shown in Figures 6 and 7, the calculated time histories of the relative displacement well agree with the observed records, and therefore the re-bar stresses of the shaft and the dynamic earth pressures on the shaft wall might have been well reproduced by the two-dimensional dynamic finite element analysis using FLUSH.

CONCLUSIONS

The author discussed the seismic response behavior of the shaft and the surrounding free-field soil based on the observed records of the earthquake occurred on May 18, 1988, and the results of numerical studies assuming linear scheme using two-dimensional dynamic finite element analysis were presented.

Major results of this paper are as follows;

1. The seismic response behavior of the shaft is controlled by the deformation of the surrounding soil within the soft alluvial layers.

2. Because the shaft stiffness is stronger than that of the soil, the relative displacement is produced between the shaft and the soil, and this relative displacement caused the earth pressure on the shaft wall and also the re-bar stress in the shaft.

3. The observed re-bar stress of the shaft and the dynamic earth pressure on the shaft wall can be well simulated by the two-dimensional dynamic finite element analysis using FLUSH.

The above results were obtained by the records whose maximum ground accelerations were less than 100 Gal. Therefore, it seems necessary to study further the seismic response behavior during larger earthquake which may cause a non-linear behavior to the structure-soil system.

519

ACKNOWLEDGMENTS

REFERENCES

1. Kaizu, N., Harada, M., Annaka, T., Ohki, H.,"Observations and Numerical Analyses of Shaft for Underground Transmission Lines," Proc. of The American Society of Mechanical Engineers, PVP - Vol.162, pp.183-190, 1989.

2. Katayama, I., Ozeki, K., Kaizu, N., Harada, M., "Seismic Response of Shaft for Underground Transmission Line," Proc. of 8th JEES, pp.1305-1310, 1990.

3. Kaizu, N., Sugi, T., Kuwahara, H., Suzuki, H., "Observation and Numerical Analyses of Dynamic Earth-Pressure of In-Ground LNG Tanks," Proc. of 9WCEE, Vol.6, pp.685-690, 1988.

Figure 1 Vertical Section of Shaft, Soil Profile and Location of Instruments

GL m	SOIL PROFILE	N-VALUE	H m	ρ t/m³	Vp m/s	Vs m/s	G t/m²	h %
	SILT		4.70	1.82	1500	110	2250	4.1
−5	FINE SAND							
−10	SILT		12.30	1.71	1500	110	2110	3.4
−15								
−20	SILT		3.75	1.69	1660	250	10780	2.8
	CLAY							
	FINE SAND	58						
−25	SILT	125	6.25	1.69	1660	250	10780	2.1
	CLAY	115						
	MEDIUM SAND	88						
	GRAVEL							
−30	MEDIUM SAND	65	11.00	1.96	1770	480	46080	1.9
−35								
−40	FINE SAND	75	7.00	1.82	1770	360	24070	1.6
−45								

(UNIT: m)

30.68

GL−1.26
GL−2.00
GL−8.35
GL−8.61
GL−15.65
GL−15.90
GL−24.55
GL−24.90
GL−29.30
GL−44.81

GL−5.06
GL−8.46
GL−15.96
GL−22.56
GL−26.06
GL−30.06
GL−34.56
GL−42.06

0.9
7.95

● :ACCELEROMETER
■ :EARTH PRESSURE METER
‖ :REINFORCING BAR STRESS TRANSDUCER

Figure 3 Fourier Spectra of Observed Acceleration Records of Shaft and Free-Field Soil
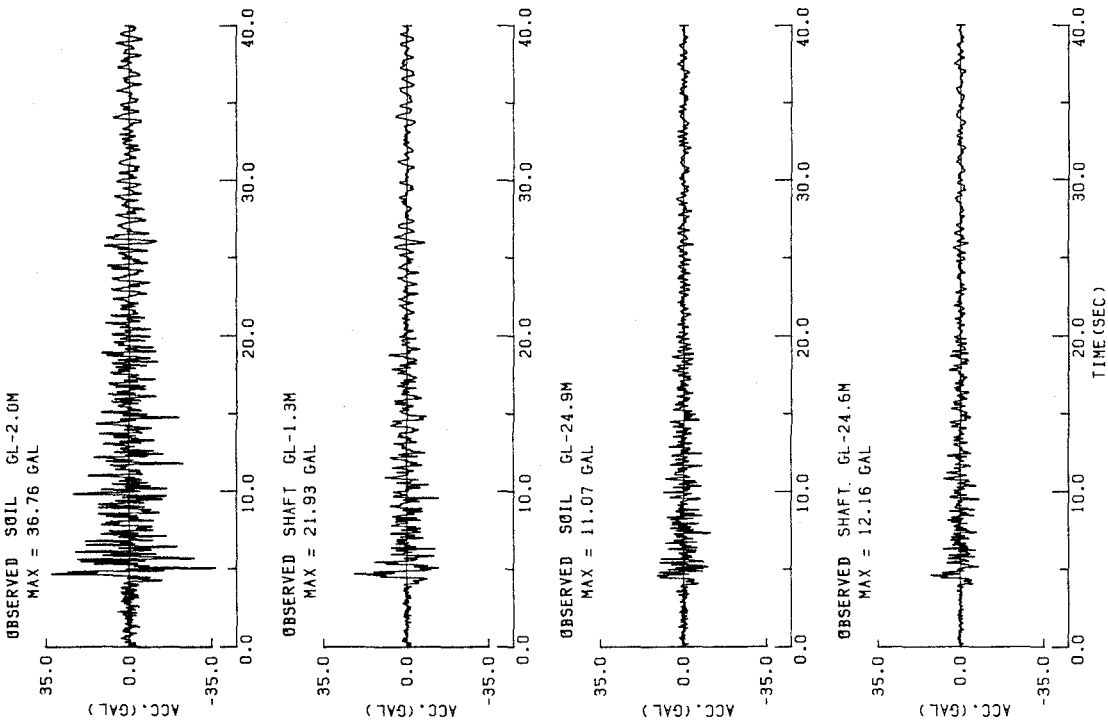
Figure 2 Observed Acceleration Records of Shaft and Free-Field Soil

522
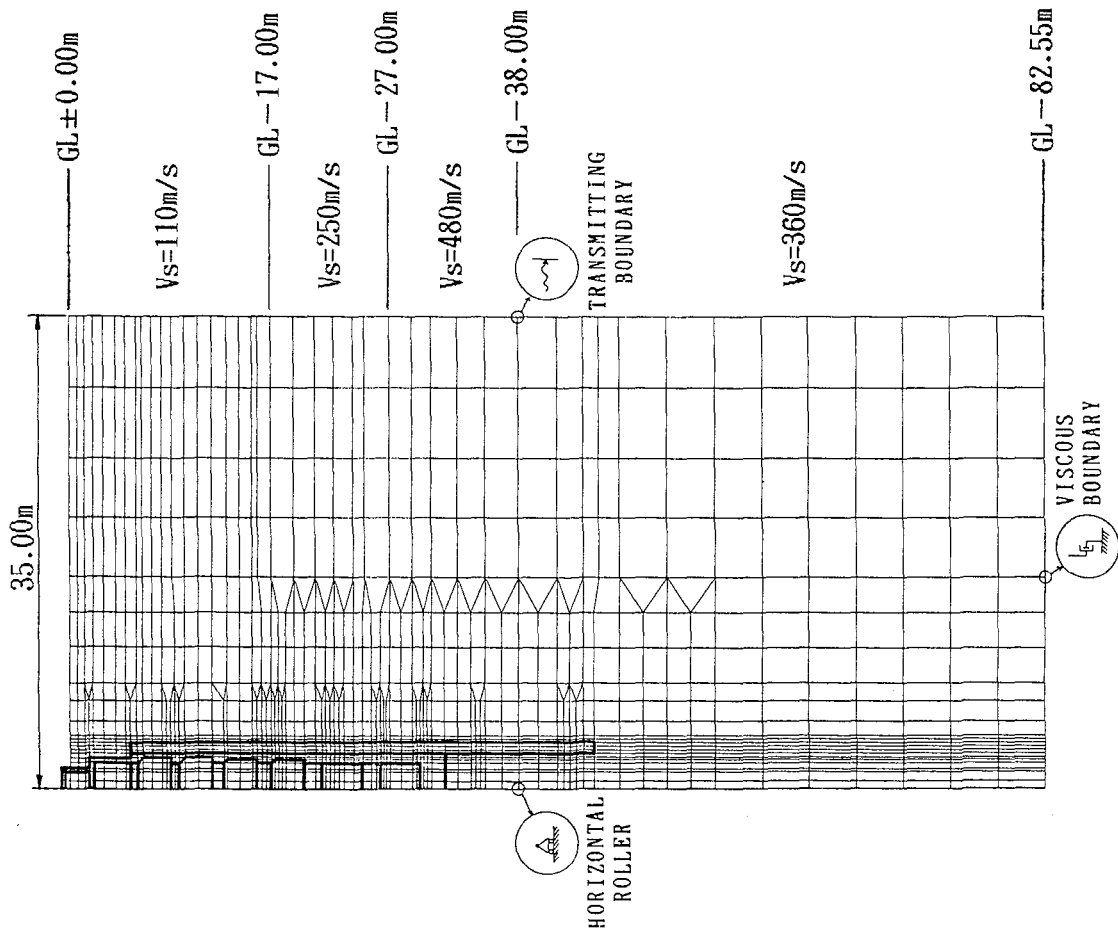
Figure 4 Two-Dimensional Finite Element Model
and Boundary Condition

GL±0.00m
Vs=110m/s
GL—17.00m
Vs=250m/s
GL—27.00m
Vs=480m/s
GL—38.00m
TRANSMITTING BOUNDARY
Vs=360m/s
GL—82.55m
35.00m
HORIZONTAL ROLLER
VISCOUS BOUNDARY
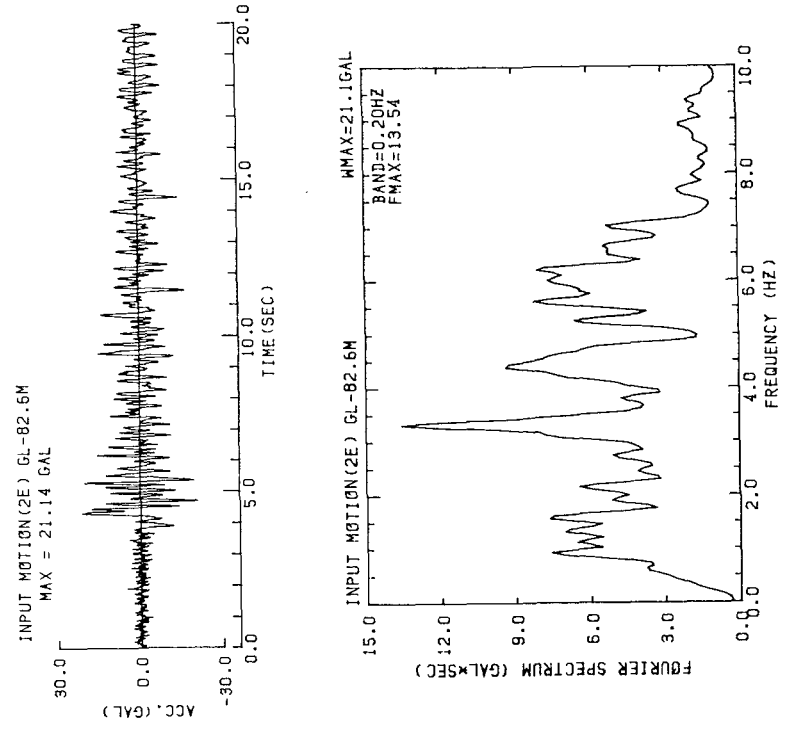
Figure 5 Input Motion at Bottom of Finite
Element Model

INPUT MOTION(2E) GL-82.6M
MAX = 21.14 GAL
ACC.(GAL)
TIME(SEC)
30.0
0.0
-30.0
0.0   5.0   10.0   15.0   20.0

WMAX=21.1GAL
BAND=0.20HZ
FMAX=13.54
INPUT MOTION(2E) GL-82.6M
FOURIER SPECTRUM (GAL*SEC)
FREQUENCY (HZ)
15.0
12.0
9.0
6.0
3.0
0.0
0.0   2.0   4.0   6.0   8.0   10.0
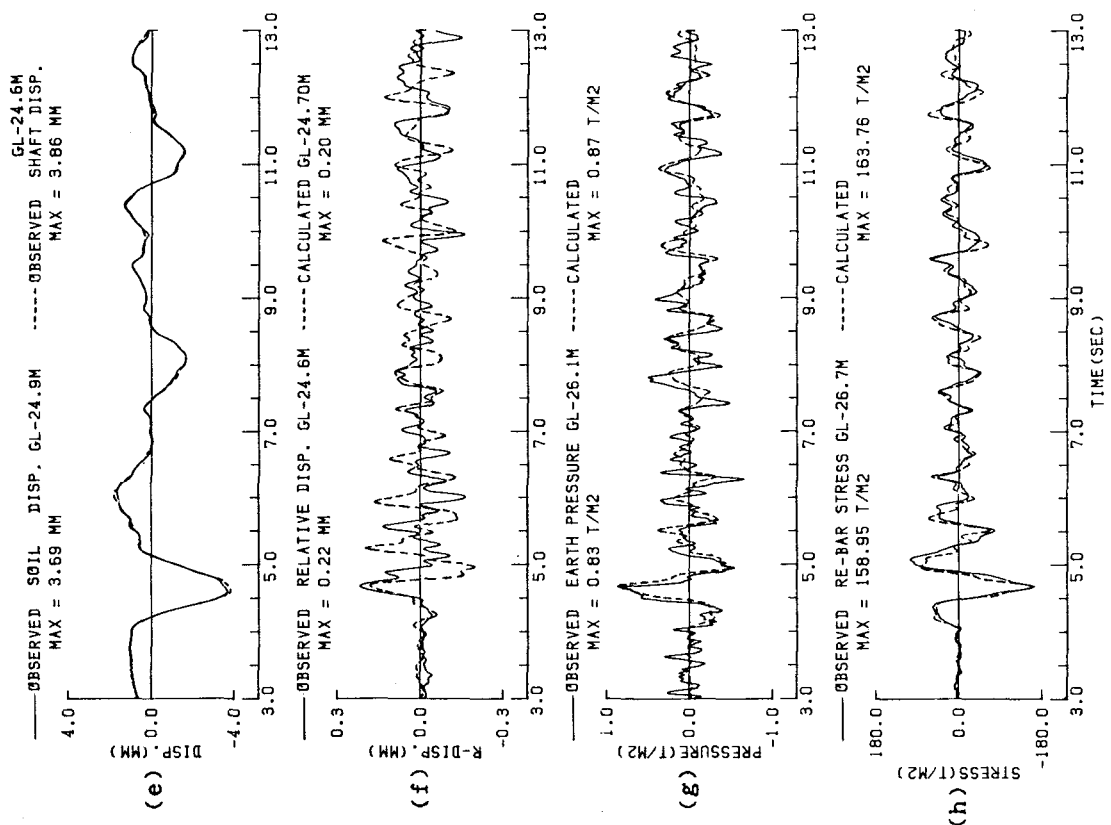
Figure 6 Time Histories of Shaft and Free-Field Soil Displacement,
Earth Pressure and Re-Bar Stress

524

Figure 8 Fourier Spectra of Relative Displacement, Earth Pressure and Re-Bar Stress
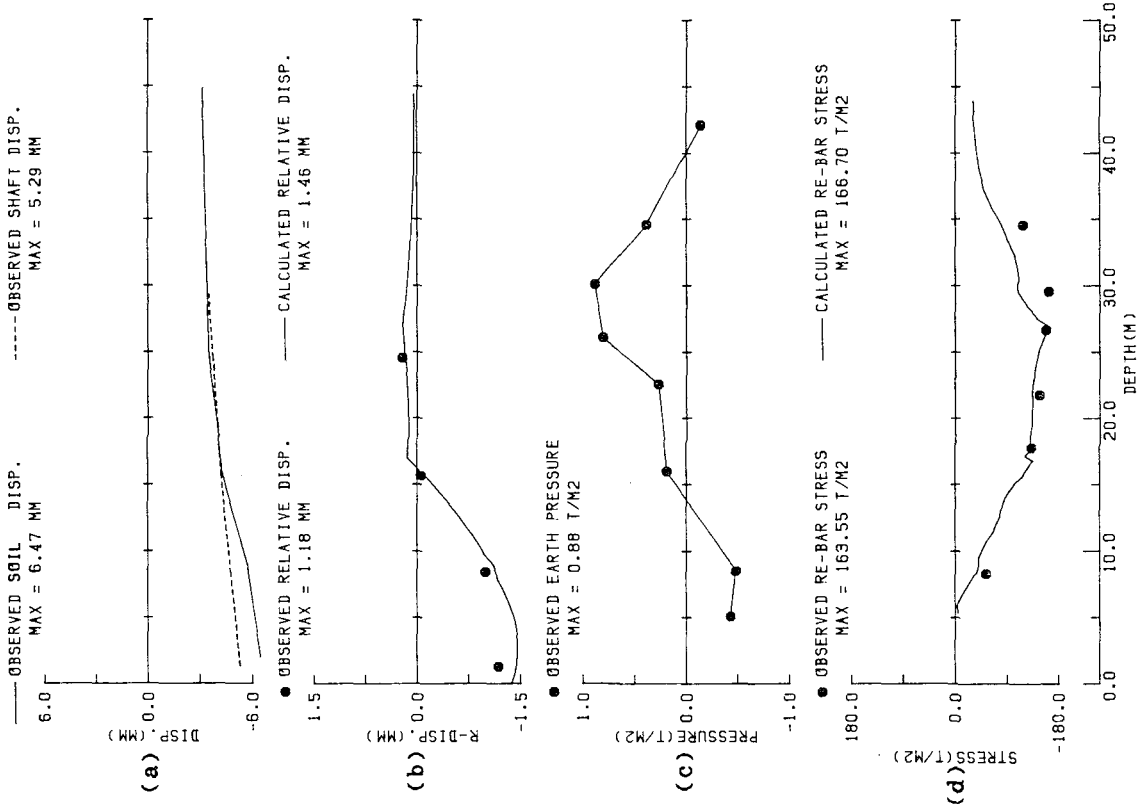
Figure 7 Relationship among Shaft and Free-Field Soil Displacement, Earth Pressure and Re-Bar Stress

525

V. EARTHQUAKE COUNTERMEASURES AND EMERGENCY RESPONSE

LOMA PRIETA EARTHQUAKE AND THE SAN FRANCISCO AWSS: ANALYSIS AND OBSERVED PERFORMANCE

C.R. Scawthorn[1], T.D. O'Rourke[2], M.M. Khater[3], and F. Blackburn[4]

ABSTRACT

The performance of the Water Supply Systems of San Francisco following the 1989 Loma Prieta earthquake is summarized with reference to the initiation and suppression of the fire in the Marina. Observed damage to water mains and hydrants of the Auxiliary Water Supply System (AWSS) is discussed, and used to establish the hydraulic conditions in the system immediately after the earthquake. The results of analyses with the special computer program, GISALE, are presented for the damage state of the system on the night of the earthquake. The analytical response of the system is compared with actual performance, and recommendations are made for improving AWSS reliability.

INTRODUCTION

The October 17, 1989 Loma Prieta earthquake (M_S 7.1) was the largest event to occur in northern California since 1906. This event demonstrated that earthquakes can still cause severe damage to modern urban areas - although only few building were actually destroyed, major lifelines and vital services were lost. The critical importance and seismic vulnerability of utility systems was strongly emphasized in the Loma Prieta earthquake. In order to understand this vulnerability this paper briefly describes the damage and performance of the San Francisco Auxiliary, Municipal and Portable Water Supply systems, during the Loma Prieta earthquake. A graphical interactive computer program GISALLE (Graphical Interactive Serviceability Analysis of LifeLines for Engineering) has been used to simulate the Performance of the Auxiliary Water Supply System (AWSS) of San Francisco during the Loma Prieta earthquake.

SYSTEMS DESCRIPTION

Auxiliary Water Supply System (AWSS): The AWSS is one of only a few high pressure system of its type in the U.S. It is separate and redundant from the municipal water supply system (MWSS) of San Francisco, and is owned and operated by the San Francisco Fire Department (SFFD). It was built in the decade following the 1906 San Francisco earthquake and fire, primarily in the north-east quadrant of the City (the urbanized portion of San Francisco in 1906 and still the Central Business District), and has been gradually extended into other parts of the City, although the original portion still constitutes the majority of the system.

The AWSS supplies water to dedicated street hydrants by a special pipe network with a total length of approximately 125 miles of buried pipe, with nominal diameters ranging from 10 - 31 inches. Nearly 100 miles of the system is cast iron, to which about 25 miles of ductile iron pipe have been added during the past several decades. The system, which is shown in Figure 1, is intended to augment the city's existing fire fighting capacity by providing a supplementary network that would work independently of, and in parallel with, the MWSS. It is separated into upper and lower pressure zones. Each zone operates nominally at a pressure of about 150 psi, which is approximately 2.5 times the pressure in the municipal system.

---

[1] Vice President, EQE, Inc., San Francisco, CA
[2] Professor, Cornell University, Ithaca, NY
[3] Senior Research Engineer, EQE, Inc. San Francisco, CA
[4] Fire Protection Consultant, San Francisco, CA 94127

The main source of water for the AWSS system under ordinary conditions is a 10 million gallon reservoir centrally located on Twin Peaks, the highest point within San Francisco (see Figure 2). Water from this source supplies two zones: the Upper Zone, and the Lower Zone where the pressure is controlled at Ashbury Tank (0.5 million gallon) and Jones St. Tank (0.75 million gallon) respectively.

The Twin peaks reservoir supply may not be adequate under emergency conditions. Two pump stations exist to supply water from San Francisco Bay (each has four diesel pumps)- Pump Station No. 1 is located at 2nd and Townsend Streets, while Pump Station No. 2 is located at Aquatic Park - each has 10,000 gpm at 300 psi capacity. Both pumps were originally steam powered but were converted to diesel power in the 1970's. The pipe network has five manifold connections along the City's waterfront, in order to permit the City fireboat *Phoenix* to act as an additional "pump station", drafting from San Francisco Bay and supplying the AWSS. The *Phoenix's* pump capacity is 9,600 gpm at 150 psi.

Lastly, in addition to the above components, San Francisco has 151 underground cisterns, again largely in the northeast quadrant of the City These cisterns are typically of concrete construction (a few are brick and predate the 1906 earthquake) 75,000 gallons capacity (about one hour supply for a typical fire department pumper) and are located at street intersections, accessible by a manhole. They are highly reliable and extremely low maintenance. The cisterns are completely independent of all piping and are filled by hose by fire department pumpers supplied from hydrant. In the event of water main failure, water may be drafted from these cisterns via the manhole. In 1986, due to a recognition that these cisterns are mostly only in the northeast quadrant of the City, a bond issue was passed for construction of an additional 95 cisterns, in outlying portions of the City.

Control of the AWSS is centered at Jones Street tank house, where gauges provide pressure readings at a limited number of locations in the network. A limited number of gate valves can be remotely operated from Jones Street tank house via land lines, the Lower Zone- pressure can be increased by opening valves at the tank house, and the Twin Peaks pressure Zone-can be "cut-in" by remotely operating valves located at Ashbury tank. However, many other gate valves in the system must be operated manually.

In 1906, San Francisco had sustained major ground failures (leading to water main breaks) in zones generally corresponding to filled-in land and thus fairly well defined. Because it was anticipated these ground failures could occur again, these zones (termed "infirm areas") were mapped and the pipe network was specially valved where it entered these infirm areas. Under ordinary conditions, all of the gate valves isolating the infirm areas are closed, except one, so that should water main breaks occur in these infirm areas, they can be quickly isolated. On the other hand, should major fire flows be required in these areas, closed gate valves can be quickly opened, increasing the water supply significantly.

Municipal Water Supply System(MWSS): The MWSS supplies potable water for domestic and commercial uses, as well as for fire fighting via hydrant and sprinkler systems. The MWSS provides water from 18 different reservoirs and a number of smaller storage tanks. The water is stored at different levels creating zones, or districts, where water is distributed within a certain range of pressure. There are 23 different pressure districts, of which the Sunset and University Mound Reservoir Systems are the largest. Figure 3 shows a plan view of the Sunset Reservoir and University Mound Systems. The pipelines in these systems range in diameter from 8 to 60 inches, and vary in composition from riveted and welded steel to cast iron.

Portable Water Supply System (PWSS): While the AWSS provides high assurance of firefighting water supply in the northeast quadrant of San Francisco, major fires can and do occur at large distances from the AWSS pipe network. In recognition of this, and to provide

528

greater flexibility in deployment and to further extend the "reach" of the AWSS, the San Francisco Fire Department has developed in recent years the Portable Water Supply System (PWSS). The basic components of the PWSS are:

o   Hose Tenders, trucks capable of carrying 5,000 ft. of large diameter (5 inch) hose, and a high pressure monitor for a master stream,

o   Hose Ramps, which allow vehicles to cross the hose when it is charged,

o   Gated Inlet Wye, allowing water supply into large diameter from standard fire hose,

o   Gleeson valve, a pressure reducing valve,

o   Portable Hydrants, that allow water to be distributed from large diameter hose

The large diameter (five inch) hose is carried on the hose tenders, together with portable hydrants, pressure reducing Gleeson valves and other fittings. Each hose tender carries almost one mile of hose, and is capable of laying this in about twenty minutes. Hose lengths are intermittently fitted with the portable hydrants, permitting water supply at many locations along the hose, which can be gridded and in effect provides an above ground water main, see Figure 4. At the time of the Loma Prieta earthquake, SFFD had four PWSS hose tenders, and has since requested acquisition of an additional eleven.

PERFORMANCE OF WATER SUPPLY SYSTEMS

The locations of pipeline repairs after the 1989 Loma Prieta earthquake are shown in Figure 5. Zones of potential soil liquefaction, based on maps by Youd and Hoose (1975) and Hovland and Darragh (1981) are also shown. Repairs to both the MWSS and AWSS are indicated by the appropriate symbols. The site of the Marina is shown, but because of the extensive MWSS damage at this location, repair plots are indicated. in Figure 6.

Figure 6 shows a plan view of the MWSS pipelines and repairs in the Marina relative to the current street system, 1899 shoreline (Sanborn Ferris Map Co., 1899) and 1857 shoreline (U.S. Coast Survey, 1857). Most repairs were concentrated in the area of hydraulic fill within the lagoon bounded by the 1899 seawall, or along the eastern margins of the seawall and 1857 shoreline.

There were about 123 repairs in the Marina, more than three times the number of repairs in the entire MWSS outside the Marina. Repairs were made at locations of sheared or disengaged service connections with mains, flexural round cracks in mains, and longitudinally split sections of main. In some cases, damage was concentrated at or near gate valves. These devices tend to anchor the pipelines, and therefore may contribute to locally pronounced deformation and stresses. The figure shows the locations of repairs to: a) services, b) mains, and c) sections of line at or near gate valves. The MWSS pipelines were composed predominantly of cast iron, with cement-caulked joints and nominal diameters of 4", 6", 8", and 12".

The most serious damage in the AWSS was the break of a 12" diameter cast iron main on 7th St. between Mission and Howard Sts. This location is on the boundary of Infirm Area No. 3 and, moreover, the AWSS pipe at this location crosses over a sewer line. Soil settlements in this area are thought to have occurred prior to and also as a result of the earthquake, causing the AWSS pipe to bear on the sewer line, and break. Water flow through this break, supplemented

by losses at broken hydrants, emptied the Jones St. Tank. Loss of this supply led to loss of water and pressure throughout the lower zone of the AWSS. This resulted in critical condition in the Marina, where damage in the MWSS had cut off alternative sources of pipeline water.

Other breaks in the AWSS system included: (a) a break in an 8 inch hydrant branch, on Sixth between Folsom and Howard Streets (where the hydrant branch crossed up and over a sewer line) and (b) five 8 inch elbow breaks, four within Infirm Area No. 3 including one on Bluxome Street where a portion of a building collapsed onto an AWSS hydrant.

Hydrants were the most vulnerable parts of the system, with damage being concentrated at elbows. Typical construction involves an 8 inch diameter cast iron elbow affixed to a concrete thrust pad beneath the street surface hydrant. Damage at hydrant elbows occurred as 45° fractures centered on the elbows.

MARINA FIRE AND PWSS

The Marina fire was the largest earthquake-related fire in the loma Prieta earthquake. Ignition occurred in a four-story wood-frame apartment building at northwest corner of Divisadero and Beach Sts. Major leakage resulted from the AWSS breaks such that Jones Street tank completely drained. Leakage continued so that first arriving engines at the Marina fire, found only residual water when they connected to AWSS hydrants. Due to uncertainty as to the number and location of AWSS breaks, valves connecting the Upper Zone to the Lower Zone were not opened, and Pump Stations 1 and 2, although available, were not placed in-service immediately but only at 8 PM, following identification and isolation of broken mains. As a result, pressure in the AWSS Lower Zone was lost for several hours following the earthquake. The pump stations were operated at half capacity so as to fill the AWSS mains slowly, out of concern for entrapped air which was exhausted out of the Lower Zone through Jones Street tank (air could be heard exhausting through the tank) This operation continued until 10 PM when full pressure was restored and Jones Street tank had been filled with salt water.

Water to fight the fire was drafted and relayed from the lagoon in front of the Palace of Fine Arts, approximately three blocks away. The fireboat, "*Phoenix*," and special hose tenders were dispatched to the site. Approximately one and a half hours after the main shock, water was being pumped from the fireboat and conveyed by means of 5 inch diameter hosing, which had been brought to the site by the PWSS hose tenders. Eventually, the supply of water to the fire was about 6,000 gpm at 180 psi, which continued for over 18 hours. The fire was brought under control within about three hours after the earthquake.

ANALYSIS OF AWSS

An extended computer simulation of the AWSS network was performed with the program GISALLE (Graphical Interactive Serviceability Analysis of LifeLine for Engineering). This program was developed to represent the AWSS as part of a special demonstration project to develop advanced techniques of computer graphics for lifeline systems and to prove the feasibility of applying these techniques to a real system (Khater, et al., 1989; Grigoriu, et al., 1989). GISALLE has been checked successfully against special fire flow tests run by the San Francisco Fire Department. GISALLE is developed to (i) perform seismic hazard analysis (ii) generate damage states for lifelines consistent with the seismic intensity at the site; (iii) perform connectivity analysis; and (iv) perform hydraulic analysis for simulated damage states of the system.

Figure 7 shows a plan view of the system that was simulated to reproduce the conditions on the night of the earthquake. Water in the lower zone was supplied by the Jones St. Tank. The

lower and upper zones were isolated from one another with closed gate valves. Pump Stations 1 and 2 were not included in the simulation to replicate the system conditions immediately following the earthquake.

Damage of the AWSS considered in the simulation was a broken 12" diameter main on 7th St., four broken hydrants, and two leaking joints. The approximate locations of these damaged components are illustrated in the figure.

Figure 8 pictures the water height in Jones Street Tank during the extended computer simulation (drop in water level in Jones Street Tank was considered in the analysis). Leaking joints were modeled as open hydrants during the simulation. This figure shows that the time required to empty the Jones St. Tank was about 32 minutes.

This estimated time to loss of tank agrees with observations during the earthquake. Scawthorn and Blackburn (1990) report that, when the first engine arrived at the Marina fire approximately 45 minutes after the earthquake, it could not draw water from the AWSS hydrants. This time for engine arrival exceeds that analyzed for loss of the Jones St. Tank. Moreover, it was estimated that loss of water from a height of 35 to 18 ft in the Jones St. Tank took approximately 15 minutes which is consistent with the analytical results.

CONCLUSIONS

The AWSS performance and computer simulations emphasize how rapidly water can be lost and how important automatic control of isolation gate valves can be. The simulations also underscore the importance of hydrant breaks.

The AWSS, would have survived the earthquake and provided adequate water supply for extinguishment of the Marina fire except that the North-South division of the AWSS, part of the original concept and design, was eliminated in 1964, resulting in South of Market Street breaks draining the section of the AWSS North of Market, including the Marina district.

Although the AWSS pipe network failed in the short term due to a small number of breaks, this system failure could have likely been precluded if the breaks could have been identified sooner, leading to placing the pump stations on-line more rapidly. The need for a rapid damage assessment/reconnaissance technology is emphasized.

The fireboat/PWSS back-up system fulfilled its mission, and the fire was suppressed. This was due in large part to the extremely fortuitous circumstance of the unusual lack of wind. Normal prevailing wind conditions would almost assuredly have resulted in loss of several city blocks, with losses in the hundreds of millions of dollars

ACKNOWLEDGMENTS

REFERENCES

Grigoriu, M.D., T.D. O'Rourke, and M. M. Khater, "Serviceability of the San Francisco Auxiliary Water Supply System," Proceedings, International Conference on Structural Safety and Reliability, San Francisco, CA, Aug. 1989.

Hovland, H.J. and R.D. Darragh, "Earthquake-Induced Ground Movements in the Mission Bay Area of San Francisco in 1906," Proceedings, 2nd Specialty Conference of the Technical Council on Lifeline Earthquake Engineering, Oakland, CA, Aug. 1981, pp. 293-309.

Kafka, A.L., E.A. Schlesinger-Miller, and N.L. Barstow, "The Earthquake Activity in the Greater New York City Area: Magnitudes, Seismicity, and Geologic Structures," Bulletin of the Seismological Society of America, Vol. 75, No. 5, Oct. 1985, pp. 1285-1300.

Khater, M.M., M.D. Grigoriu, and T.D. O'Rourke, "Serviceability Measures and Sensitivity Factors for Estimating Seismic Performance of Water Supply Systems," Proceedings, 9th World Conference on Earthquake Engineering,-Tokyo, Japan, Vol. VII, 1989, pp. 123-128.

Khater, M.M., and M.D. Grigoriu " Graphical Demonstration of Serviceability analysis," Proceedings, International Conference on Structural Safety and Reliability, San Francisco, CA, Aug. 1989, pp. 525-532.

O'Rourke, T.D., M.D. Grigoriu, and M.M. Khater, "Seismic Response of Buried Pipes," Pressure Vessel and Piping Technology - A Decade of Progress, C. Sundararajan, Ed., ASME, New York, NY, 1985, pp. 281-323.

O'Rourke, T.D. and B.L. Roth, "Performance of Pipeline Systems in the Marina," Open File Report 90-253, USGS, Menlo Park, CA, Effects of the Loma Prieta Earthquake on the Marina District, San Francisco, CA, Apr. 1990, pp. El-E8.

O'Rourke, T.D., H.E. Stewart, F.T. Blackburn, and T.S. Dickerman, "Geotechnical and Lifeline Aspects of the October 17, 1989 Loma Prieta Earthquake in San Francisco," Technical Report NCEER-90-001, National Center for Earthquake Engineering Research, Buffalo, NY, Jan. 1990.

O'Rourke, T.D., T.E. Gowdy, H.E. Stewart, and J.W. Pease, "Lifeline and Geotechnical Aspects of the 1989 Loma Prieta Earthquake," Proceedings, 2nd International Conference on Recent Advances in Geotechnical Earthquake Engineering and Soil Dynamics, St. Louis, MO, Vol. II, 1991.

Sanborn Ferris Map Company, "Insurance Maps, San Francisco, California," Vol. 4, New York, NY, 1899.

Scawthorn, C. and T.D. O'Rourke, "Effects of Ground Failure on Water Supply and Fire Following Earthquake: the 1906 San Francisco Earthquake," Technical Report NCEER-89-0032, National Center for Earthquake Engineering Research, Buffalo, NY, Dec. 1989, pp. 16-35.

REFERENCES (Cont.)

Scawthorn, C. and F.T. Blackburn, "Performance of the San Francisco Auxiliary and Portable Water Supply Systems in the 17 October, 1989 Loma Prieta Earthquake," Proceedings, 4th U.S. Conference on Earthquake Engineering, Palm Springs, CA, Vol. 1, 1990, pp. 171-180.

Trautmann, C.H., T.D. O'Rourke, M.D. Grigoriu, and M.M. Khater, "Systems Model for Water Supply Following Earthquakes," Lifeline Seismic Risk Analysis - Case Studies, R. Eguchi, Ed., ASCE, New York, NY, 1986, pp. 30-50.

U.S. Coast Survey, Topographic Map of "City of San Francisco and Its Vicinity, California," surveyed by A.F. Rodgers, 1857.

Youd, T.L. and S.N. Hoose, "Historic Ground Failures in Northern California Triggered by Earthquakes," Geologic Survey Professional Paper 993, U.S. Government Printing Office, Washington, D.C., 1978.
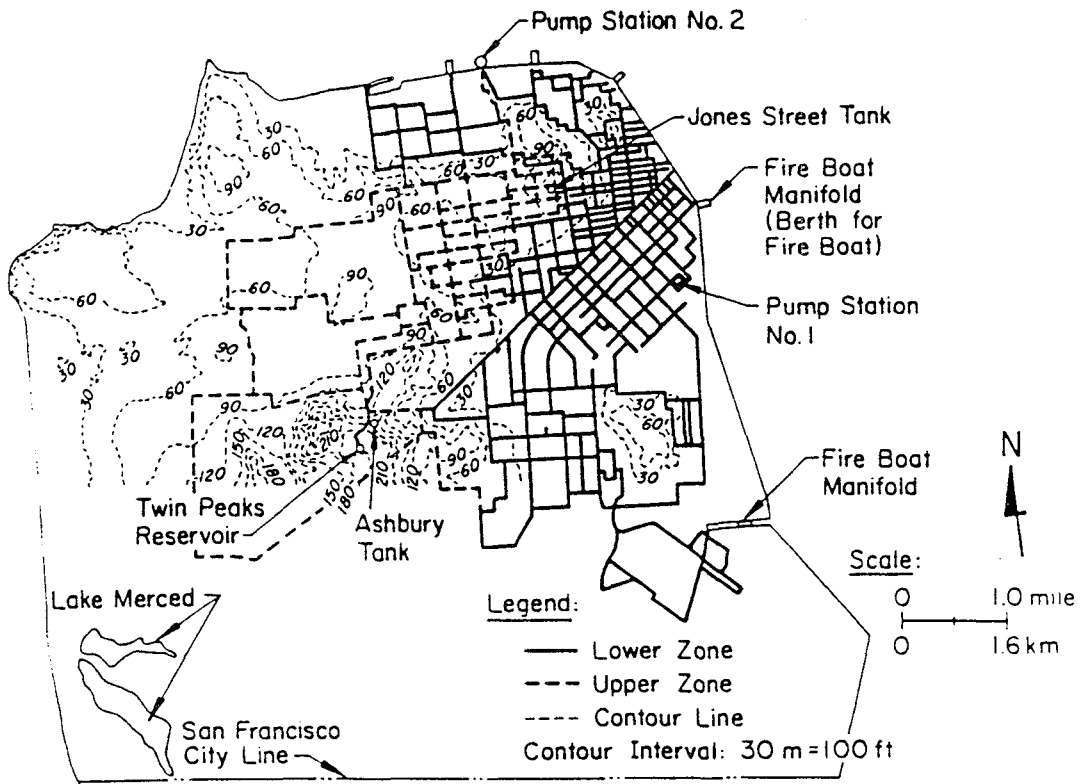
Figure 1: San Francisco AWSS
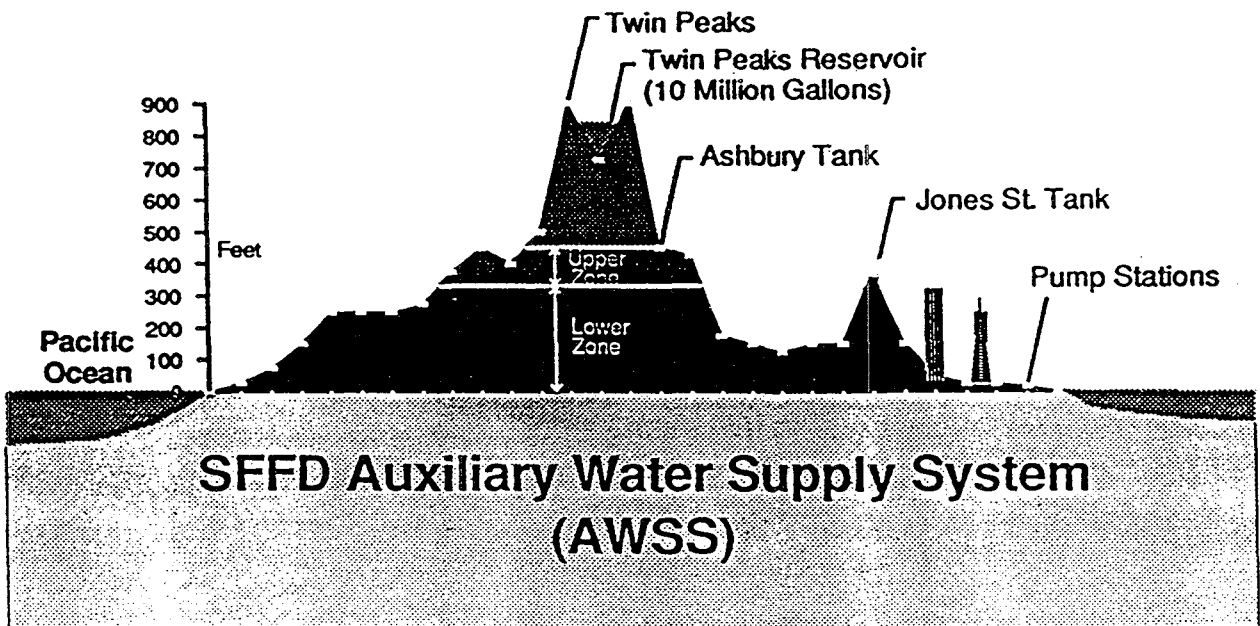
Figure 2: Schematic Cross-section San Francisco Auxiliary Water Supply System
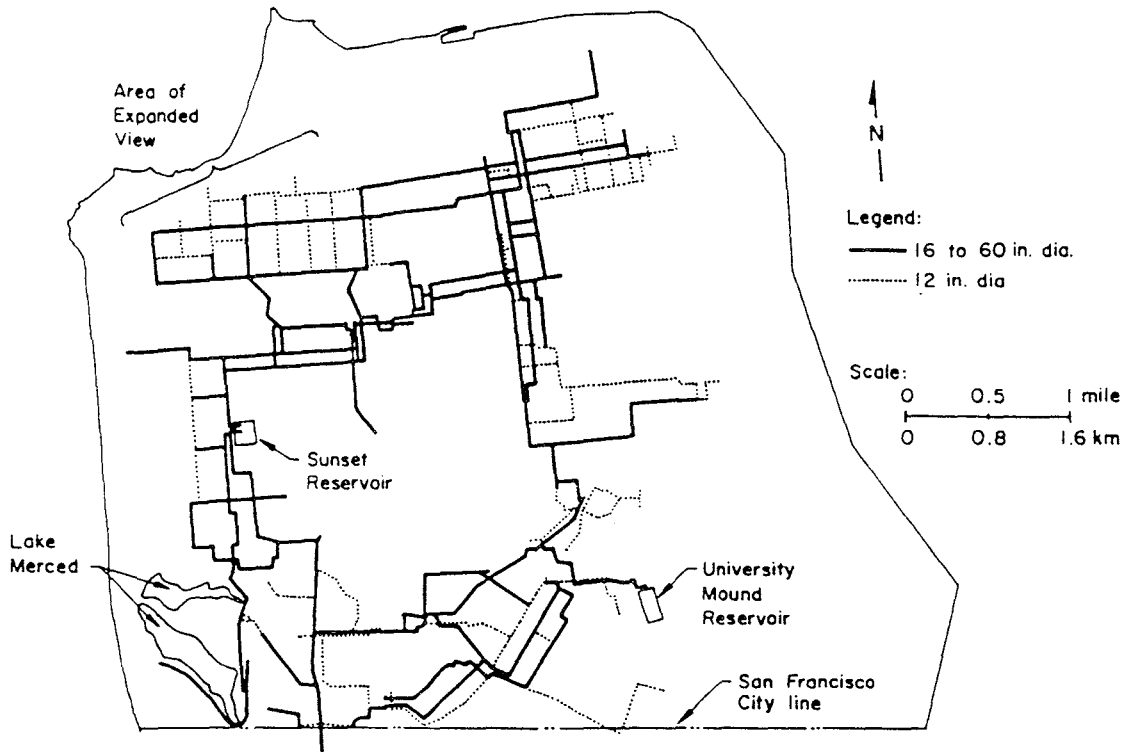
Figure 3a: Sunset Reservoir System of the MWSS

Figure 3b: University Mound Reservoir System of the MWSS

535
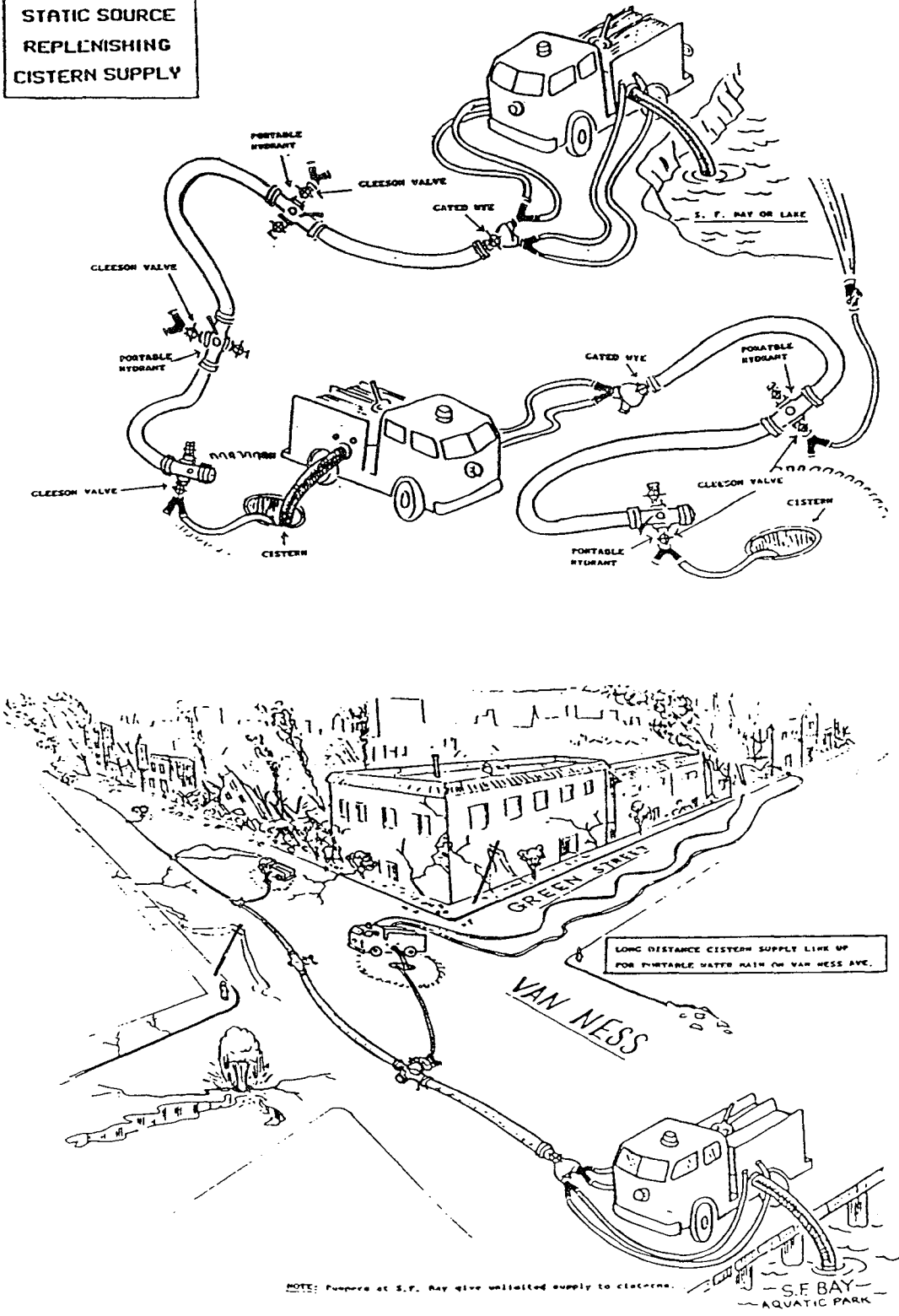
Figure 4: San Francisco Portable Water Supply System (schematic)
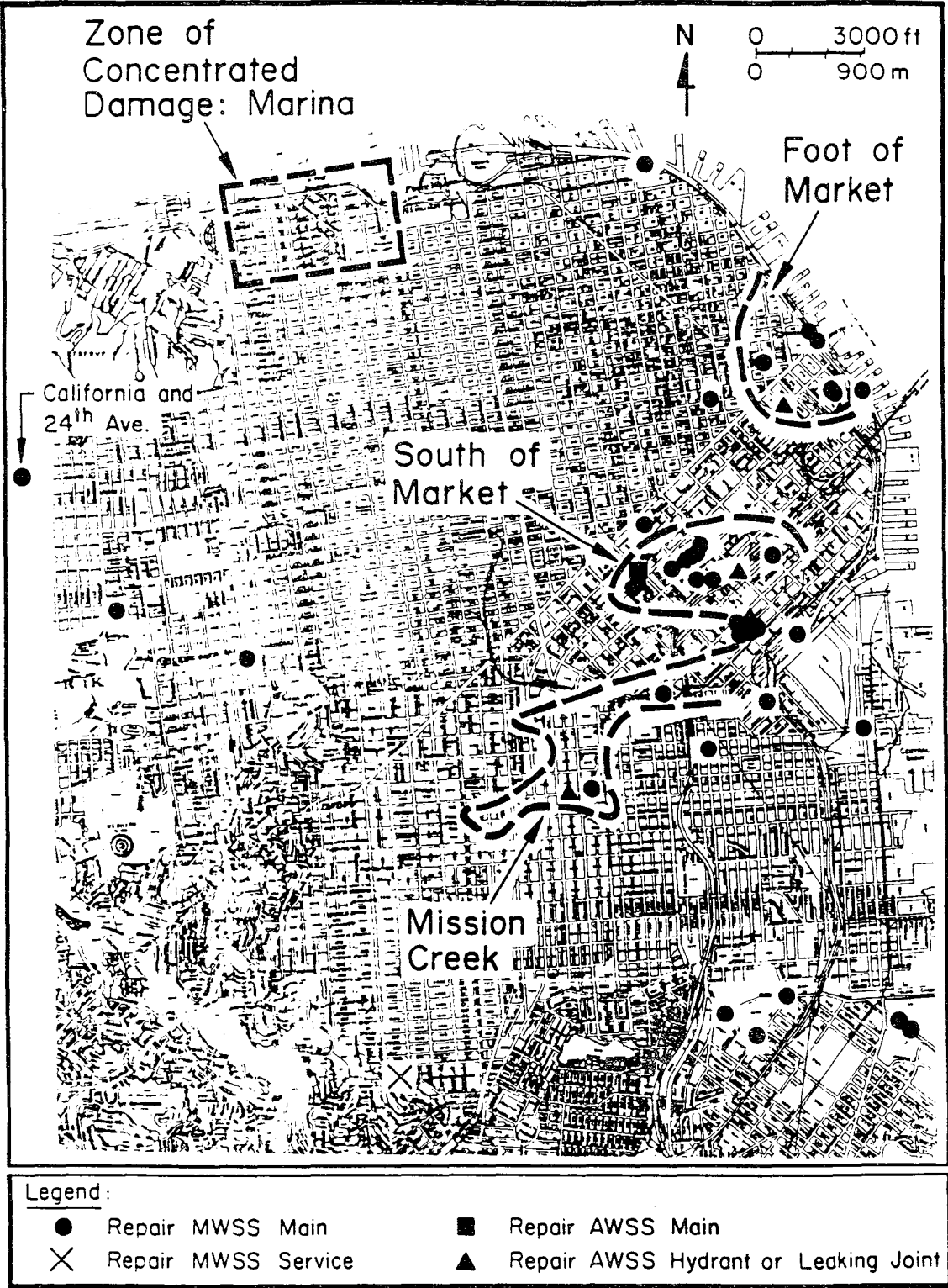
Figure 5:   Water Supply Pipeline Breaks and Zones of Soil Liquefaction Caused by 1989 Loma Prieta Earthquake (after O'Rourke, et al., 1991)
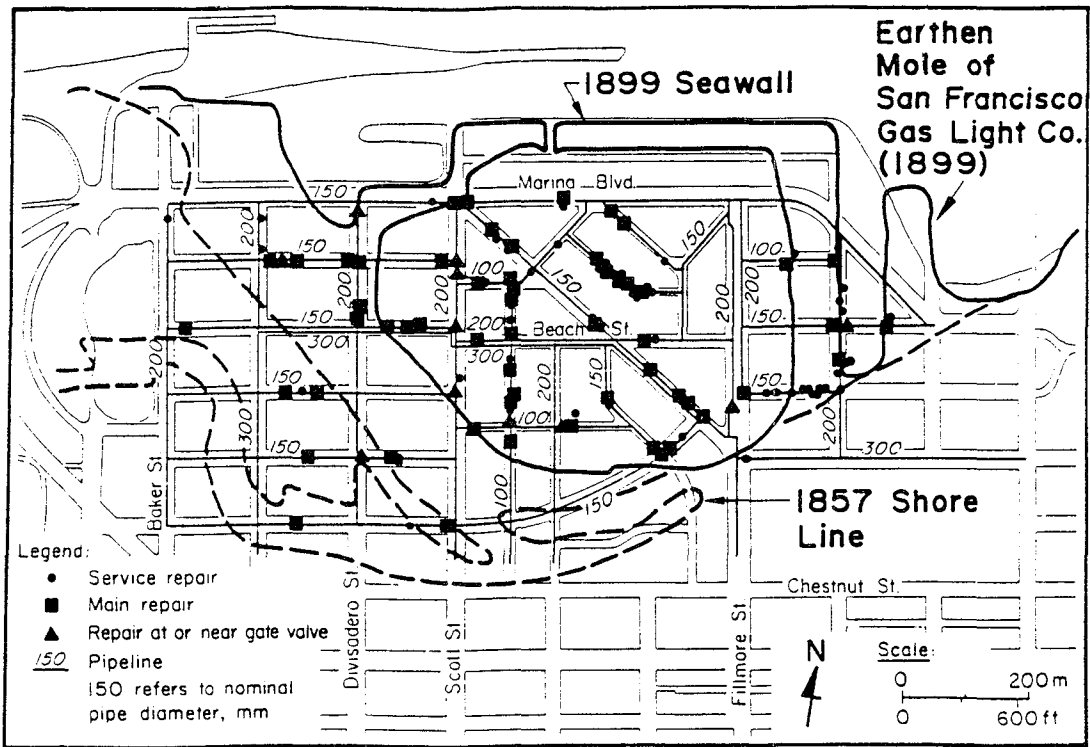
Figure 6: MWSS Repairs in the Marine (after O'Rourke and Roth, 1990)
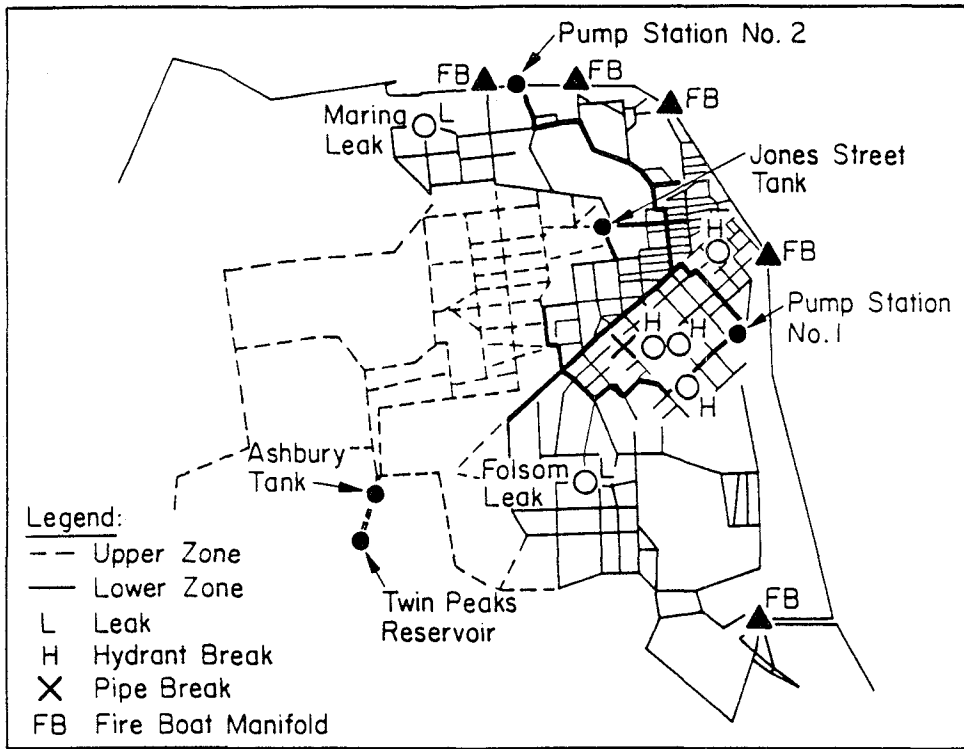
Figure 7: Conditions Used in Computer Simulation of AWSS Performance During the Loma Prieta Earthquake
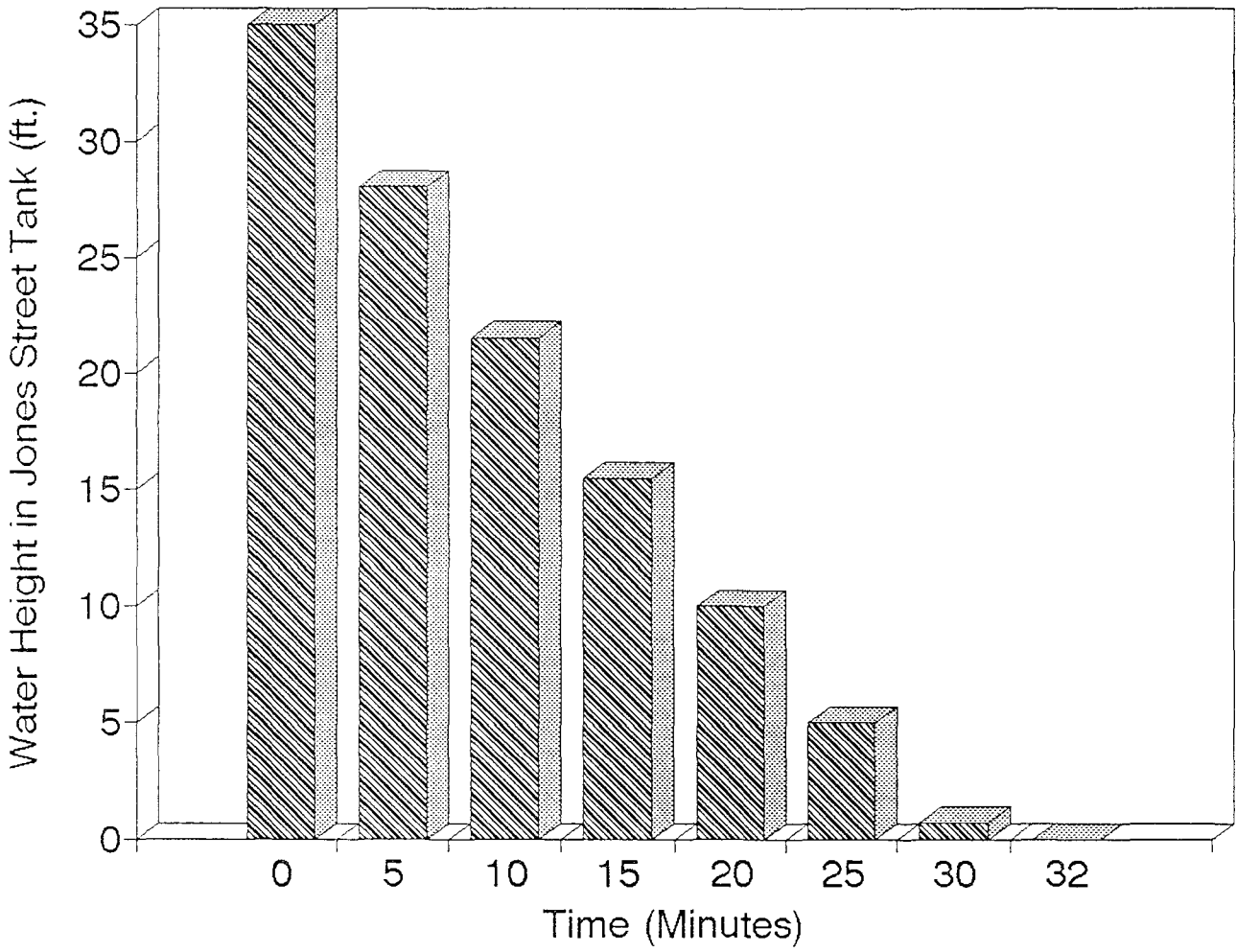
Figure 8: Results of AWSS Extended Simulation

EARLY POST-EARTHQUAKE DAMAGE
DETECTION FOR LIFELINE SYSTEMS
A METHODOLOGY APPLIED TO THE 1985 MICHOACAN EARTHQUAKE

R. T. Eguchi
Associate
Dames & Moore, 911 Wilshire Blvd., Suite 700
Los Angeles, California 90017 USA

J. D. Chrostowski
Vice President
Engineering Mechanics Associates, 3820 Del Amo Blvd., Suite 318
Torrance, California 90503 USA

C. W. Tillman
Project Engineer
Dames & Moore, 911 Wilshire Blvd., Suite 700
Los Angeles, California 90017 USA

A. Gustavo Ayala
Professor
Institute de Ingenieria, UNAM
Mexico, D.F. 04510 Mexico

ABSTRACT

The present paper discusses a methodology for early, post-earthquake damage detection for lifeline systems. It is based on integrating methods from two existing areas of technology: model verification and system vulnerability methods for lifelines. This methodology is demonstrated on the Federal District water system in Mexico City using data from the 1985 Mexico City (Michoacan) earthquake. The results presented in this paper represent findings from an ongoing research project being performed for the National Science Foundation.

INTRODUCTION

Lifeline systems are essential to the health, safety and survival of a community. They provide the supply and the means of conveyance for people, goods, information, energy, water and waste. During disasters, such as earthquakes, the survival of a city can very well depend on the survival of key lifeline systems. For example, the failure of the San Francisco city water supply system during the 1906 earthquake led to the near destruction of the city because of uncontrolled fires. Similar instances of catastrophe have occurred in Japan, e.g., 1923 Tokyo earthquake.

Those responsible for the operation and maintenance of lifeline systems recognize the significance of the problem. Comprehensive emergency response plans acknowledge the low damage thresholds of some systems, and attempt to mitigate the effects of earthquakes through rapid repairment. Essential in these plans, however, is the ability to quickly detect severely damaged portions of the system.

The benefits of an early, post-earthquake damage detection system for lifelines are considerable. Early detection would allow utility lifeline operators to quickly isolate severely damaged portions of their systems. This would insure that valuable lifeline supplies, such as water, are not unnecessarily lost. An early detection system would also allow utility operators to identify undamaged parts of their system. This ability is extremely important in insuring minimum safety coverage. Finally, an early damage detection system would allow utility lifeline operators to more effectively manage available resources, e.g., repair inventories and crews. High priority restoration areas could be identified and available crews quickly dispatched.

To date, however, no such system or methodology exists for early damage detection of lifelines following an earthquake. Because of this, lifeline operators commonly call for automatic shutdown of large portions of their system in the event of an earthquake. Although prudent from the standpoint of conserving available supplies, this procedure could lead to serious ramifications, and could even exacerbate the damage brought about by a major earthquake through the shutdown of critically needed water supplies for fire control and emergency medical aid. Furthermore, implementation of such an ad hoc procedure would in effect lead to slow and ineffective recovery of the system.

The need for an early damage detection system for lifelines was reinforced during the 1985 Mexico City earthquake. Initial response and recovery efforts involving the water network would have been significantly improved had such a system been available. Disaster response to lifeline systems serving major population centers, such as Mexico City, often involve the commitment of millions of dollars in resources. These commitments are often formulated by disaster response command staff under severe time constraints and political pressures to react quickly and effectively. Significant monetary contributions in the form of equipment, material and manpower were provided by the U.S. Office of Foreign Disaster Assistance (O.F.D.A) over a three-week period, much of which was procured in the early hours immediately following the Mexico City disaster.

Lack of proper assessment tools and methodology certainly hampered the effectiveness of the O.F.D.A. team. If analytical models for decision making could have been available, the following might have resulted:

1. A more accurate and timely assessment by field response teams regarding the magnitude and impact of the earthquake on the water system.

2. A more structured approach in the formulation of emergency plans by field personnel.

3. With these advantages, command level personnel who had the ultimate responsibility for committing resources would have been able to act with greater confidence. This would most likely have resulted in a faster commitment of resources.

The present paper discusses the results of a National Science Foundation research study to develop an early, post-earthquake damage detection methodology for underground lifeline systems.

TECHNICAL APPROACH

The use of parameter estimation techniques has been quite common in validating the response estimates of undamaged structural models (Hasselman, 1985). Recently, their application has been extended to predicting damage to buildings, offshore platforms and space-based structures (Coppolino et al., 1980). The application to large, underground systems such as water distribution networks, however, has been virtually nonexistent. Some of the reasons why parameter estimation techniques have not been applied to lifeline systems are (1) lifeline systems tend to be highly redundant, encompassing many parallel components; (2) there exists limited observations of actual lifeline performance during an earthquake; (3) there has been no previously defined measure of lifeline performance (or model parameters) which could easily be related to earthquake damage; (4) estimation of localized damage based on global information has always been a major problem with parameter estimation methods; and (5) estimation of lifeline performance after an earthquake requires processing of time sequenced data, a procedure which further complicates the estimation process.

The objectives of this research project are admittedly ambitious. However, we believe that even given the obstacles discussed above, the application of parameter estimation techniques can provide better, more reliable information on lifeline damage after an earthquake. Therefore, the primary objectives of this project are to: (1) identify what types of post-earthquake information are available to characterize system performance; (2) examine whether inclusion of this data in a systematic manner enhances our ability to locate and detect post-earthquake damage; (3) based on our review of (2), determine the parameters and level of information necessary for implementing a post-earthquake damage

detection methodology; and (4) identify the future requirements (i.e., data, models, and system tools) of a better post-earthquake, damage detection tool.

Overview

The technical approach for early, post-earthquake damage detection is illustrated in Figure 1. The approach has two major steps: (1) "A Heuristic Search" is performed to identify a likely damage scenario given initial earthquake data, and (2) "Parameter Estimation" techniques are used to adjust the parameters of a hydraulic model until estimated performance "matches" actual post-earthquake performance.

Given the actual occurrence of a damaging earthquake, Box 1 of Figure 1 shows that early earthquake information (e.g., magnitude, location, outages) is utilized in Box 2 to compute a set of potential system damage states (represented as hydraulic models). In Box 3, these scenarios are compared against early field performance data to determine which scenario might best match the actual system performance. This likely scenario forms the basis for the nominal hydraulic damage model shown in Box 4. A hydraulic analysis that is performed with this initial damage model is then used to produce a set of performance predictions (Box 5) measured in terms of flow rates and pressures.

As additional post-earthquake field data begins to arrive (Box 6), the differences between actual performance and model performance are used to update damage parameters of the nominal hydraulic model until actual performance data are "matched" in a statistical sense. As the parameter estimation process proceeds, a visual image of the damaged lifeline system is updated and displayed for operator review.
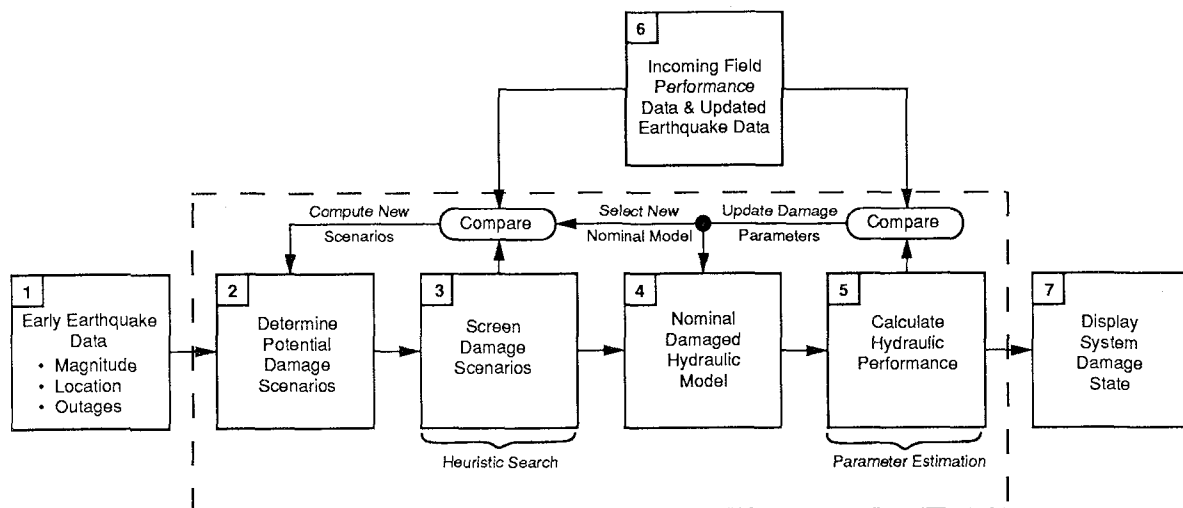
Figure 1. Flow Diagram for Early Post-Earthquake Damage Detection for Lifelines

544

MODEL DEVELOPMENT

Leak Modeling

The use of parameter estimation methods to identify the damage states of a lifeline system requires that parameters of the hydraulic model be defined which can be adjusted to simulate a wide range of damage states. Previous damage studies (Eguchi et al., 1983; Shinozuka and Kameda, 1989) have used the "pipe break" concept to determine the connectivity of the system and a corresponding hydraulic model to estimate hydraulic performance. Trautmann et al. (1983), in a more recent study, bypass the connectivity model and represent a break in the hydraulic model as piping vented to atmosphere.

To cover the full range of potential damage states, a pipe model must be developed which will allow various sizes of leaks to be characterized. In this study, the pipe break model used by Trautmann et al. (1983) is extended to allow for the simulation of pipe leakage ranging continuously from full flow (no break) to no flow (complete break).

ℓ = Pipe Length

C = Roughness Coefficient

D_0 = Original Pipe Diameter

a. Parallel Pipe Simulation of Single Pipe Segment

b. Leak Model - (Pipe With Diameter, D_1 , Connected Pipe With Diameter, D_2 , Vented to Atmosphere)
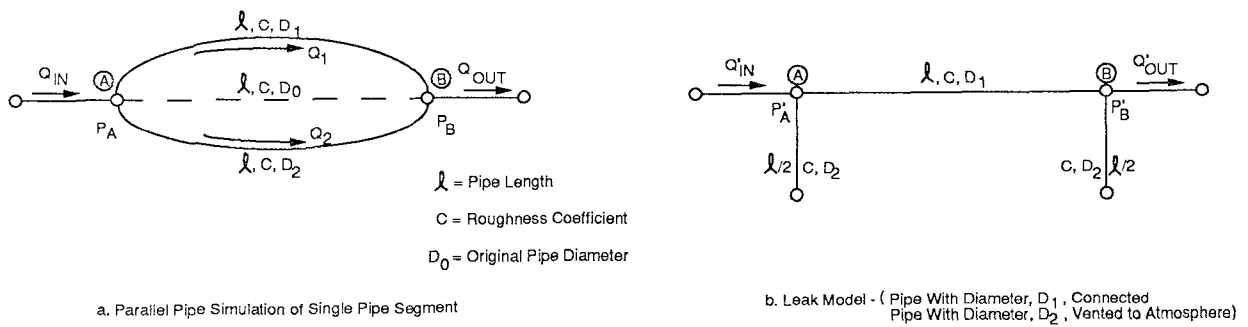
Figure 2. Pipe Leak Model

To accomplish this, it is assumed that two parallel unbroken pipes of differing diameter replace the original pipe between nodes that might be damaged (see Figure 2). In keeping with Trautmann et al. (1983), one of the pipes is split in half (the pipe with diameter, D_2 in Figure 2) and each end is vented to atmosphere as shown in Figure 2b. At one extreme, a full break is modeled by letting D_1 ----> 0 and D_2 -----> D_0 (the original pipe diameter). At the other extreme, full uninterrupted flow is modeled by letting D_1 -----> D_0 and D_2 ----> 0. Leakage states in between these two extremes are modeled by varying the ratio of D_1/D_2 until the desired flowrates and pressures of the damaged system (Q' and P' in Figure 2b) are obtained.

Automation of the Parameter Estimation Routine

Assessing the damage state of a lifeline system in real-time after an earthquake requires automation of the parameter updating scheme. To accomplish this, hydraulic modeling software must be integrated with parameter estimation algorithms to allow for the continuous revision of model parameters as field performance data is acquired and processed.

Figure 3 shows a top-level flow diagram of the procedure developed for this study. An undamaged, verified hydraulic model of the system is input as the reference model. The nominal damage state is then generated from an input file which specifies which pipes, or groups of pipes, have potential leaks and which system demands may change for the scenario selected from the screening process. In this study, the reference hydraulic model and the damage parameter input files are formatted to be consistent with the University of Kentucky (U.K.) Code (Wood, 1980).
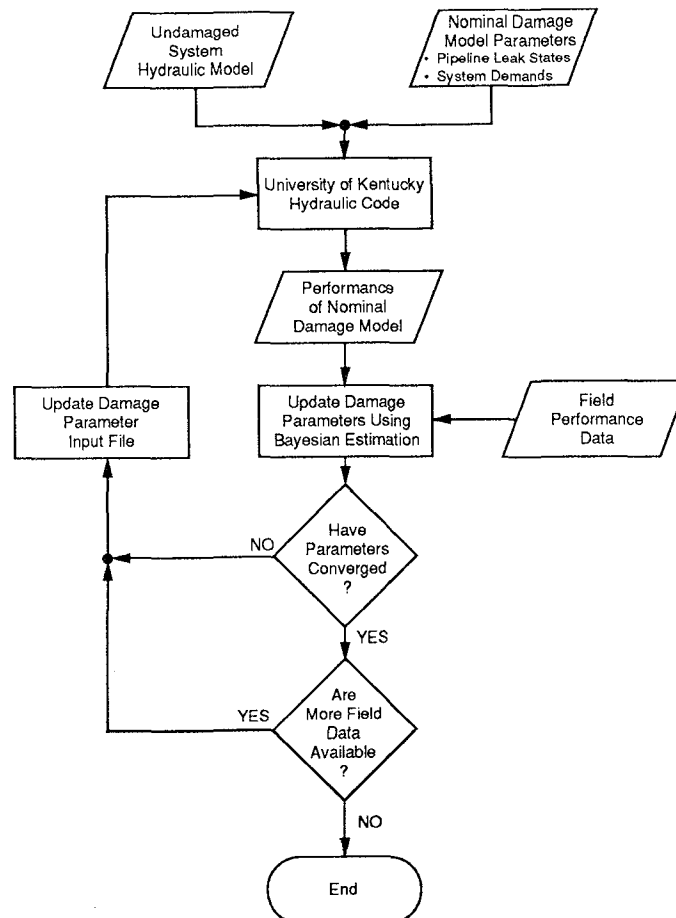
Figure 3. Flow Diagram of Parameter Estimation Scheme

546

As Figure 3 shows, the U.K. code is integrated within the parameter estimation scheme as a module, and is used to determine the performance of the nominal hydraulic model. Pipeline flowrates and nodal pressures are stripped from the U.K. output and used to define model performance. Model performance is then compared to incoming field data and the differences are used to drive a Bayesian estimator which updates the pipeline leak states and the system inflow/outflow demands.

Because system performance varies non-linearly with flowrate, the parameter estimation must be performed iteratively, i.e., the updated damage parameters are used to define a new nominal hydraulic model and another update cycle performed. This process continues until the parameters have converged, or until more field data become available and can be sequenced in for further estimation.

To demonstrate the feasibility of this portion of the damage estimation methodology, the parameter estimation process has been automated on a microcomputer. This includes integration of the U.K. hydraulic code with the parameter estimation algorithm, along with editing software which allows the nominal hydraulic model input files to be continuously updated. The integrated software (i.e., computer program WIZARD) has been tested using data from the 1985 Mexico City earthquake.

APPLICATION TO MEXICO CITY WATER SYSTEM

In order to assess whether the concept of an early, post-earthquake damage detection methodology is a feasible one, we have applied the procedures using actual damage and performance data from the 1985 Mexico City earthquake. We have coordinated our efforts with engineers at the General Directorate of Hydraulic Construction and Operation of the Federal District Government of Mexico to collect data on the earthquake performance of the primary distribution water network in the Federal District (there were two complete water networks which experienced earthquake damage, the Federal District, and the neighboring State of Mexico).

According to Ayala and O'Rourke (1988), major damage occurred to the aqueducts that were responsible for bringing water to the city. Approximately 60 pipeline breaks, mostly in prestressed concrete pipe with locked joints, occurred along the Federal District aqueduct system. In the primary Federal District network, 175 breaks or leaks were observed after the earthquake. The majority of the repairs to the system were made to the secondary distribution network, i.e., pipelines with diameters less than 18 inches. Over 5000 breaks or leaks were recorded here.

Furthermore, the types of damage and performance data available after the earthquake included (1) individual reports of water outage brought in by customers; (2) system performance maps showing pressure gradients as a function of time; (3) actual pressure readings from 31 pressure measuring stations; and (4) field observations of water leakage.

For purposes of demonstrating the methodology, the following steps were completed:

1. Ground motion areal maps were developed using available empirical models in order to replicate the actual ground motion patterns experienced during the 1985 event.

2. A hydraulic model of the Mexico City water system was constructed and verified with pre-earthquake hydraulic calculations provided by the Department del Distrito Federal (DDF) water engineers.

3. Initial estimates of pipe leakage were computed using the ground motion maps developed under (1) and empirical earthquake vulnerability models developed from pipeline damage data from other earthquakes.

4. Initial estimates of pipe leakage were updated using hydraulic performance data from Mexico City. Major zones of pipe leakage are based on estimates of reduced pressure within particular service areas or zones.

The following sections describe each of these steps.

Ground Motion Maps

The development of seismic hazard maps for Mexico City involved the examination of several candidate models to account for ground motion attenuation and local soil amplification. Our objective was to accurately simulate the conditions experienced during the 1985 earthquake, based on a level of knowledge about attenuation and soil characteristics that would be reasonably attainable before the occurrence of the event. In keeping with this objective, more detailed information about pockets of high shaking intensities due to geomorphic focusing, locally non-homogeneous soil characteristics, etc., were disregarded in compiling the ground motion maps.

To accurately model the ground motion in the Valley of Mexico, a literature search was conducted to review valid attenuation models for subduction zone events off the coast of Mexico. Attenuation functions for velocity, acceleration, and intensity were examined. Based on our evaluation, the velocity attenuation function developed by Singh et al. (1987) was found to be the most appropriate for predicting bedrock ground motion in the Mexico City region. In order to convert the hard rock velocity estimates to Modified Mercalli Intensities (MMI), Trifunac's (1976) equation for velocity was employed.

The region's soil characteristics were modeled using geotechnical information produced for the Valley of Mexico by Romo (1988) and Sanchez-Sesma et al. (1988). Figure 4 gives a generalized view of the soil conditions used in the current simulation. There are five basic soil types delineated by the different hill, transition and lake bed regions on the map. For the lake bed region, typical soils are Lacustrian - soft clay deposits with a very high water content. In some of the hill and transition zones, loose alluvial river deposits are present. In the hill zone west of the major metropolitan areas, old and highly cemented alluvial river deposits are present. These areas also tend to have a high gravel content. The

548

region's oldest volcanoes, to the southwest of the City University, tend to have Middle and Upper Tertiary soils, along with volcanic soil types. Finally, some of the hills (Cerro de la Estrella) in the region are associated with Pleistocene volcanic soils.

These regions were assigned separate amplification factors to reflect soil amplification during strong ground motion. Table 1 presents these amplification factors for the different soil types.

Table 1. Soil Amplification Factors for Mexico City

Soil Type	MMI Increment (I)
Lacustrian - highly saturated soft clay, lake bed regions	2.5
Alluvial deposits	0.5
Lacustrian - Transition Zone regions	1.0
Pleistocene volcanics, Middle & Upper Tertiary, and Pliocene volcanics - hill regions	0.0

Figure 5 shows the ground motion map developed for the Valley of Mexico assuming the parameters of the 1985 Michoacan event. This map shows that the lake bed regions of the valley have MMI levels of VII and higher. This region encompasses a major portion of the metropolitan area including Zocalo, the airport region, and northern portions of Ixtapalapa. Areas of less severe shaking include the transition zones between the lake bed area and the hill areas. The MMI levels here range from VI to VII. The suburban area of Ixtapalapa includes some transition regions on the map. Shaking intensities of MMI VI or less were experienced in the hill zone. Cerro de la Estrella and the City University (UNAM) are located in these lower intensity regions.

Hydraulic System Model

The hydraulic model developed for the Mexico City water system was restricted to the primary water distribution system (pipe diameters $\geq$ 20 inches). This model excludes the large aqueducts which supply partial system demands and the secondary network which delivers potable water to consumers. The southern aqueduct was also not included as the study is aimed at demonstrating damage detection in a complex network rather than for supply systems, e.g., aqueducts and tanks, whose post-earthquake conditions can easily be determined by air reconnaissance. A University of Kentucky hydraulic model of the Mexico City primary network was developed using the DDF computer model as a reference. The DDF model contained almost 300 pipe elements in addition to reservoir supply tanks and nodal demands (inflow/outflows); pumps, valves

Figure 5 - Modified Mercalli Intensity Contours in the Vicinity of Mexico City

Ground Shaking Intensity [MMI]

- 7 - 7.5
- 6.5 - 7
- 6 - 6.5
- 5.5 - 6
- 5 - 5.5
- <5

TEXCOCO LAKE

Zocalo

Airport

Ixtapalapa

Cerro de la Estrella

Figure 4 - Generalized Soil Types in the Valley of Mexico

Soil Types

- Lacustrian - Soft Clay
- Lacustrian - Transition Zone
- Tacubaya - Alluvial
- Tarango - Alluvial
- Pleistocene Volcanics
- Middle & Upper Tertiary & Pliocene Volcanics

Texcoco Lake

Airport

Ixtapalapa

Zocalo

Mexico City

Cerro de la Estrella

Xochimico Lake

City University

and regulators were not included. Piping loss coefficients originally modeled with the Manning formula by the DDF were converted to approximate Hazen-Williams coefficients. A comparison of UK and DDF steady-state hydraulic model analyses (for supply conditions around 5 a.m. in the morning) showed good comparison in both pressures and flowrates throughout the network.

Definition of Pressure Zones

The damage detection algorithm (Bayesian damage parameter estimator) used in this study correlates the initial damage state performance with post-earthquake pressure and flowrate readings to better identify areas and levels of damage.

The estimator modifies the damage parameters of the hydraulic model (pipe break state and nodal demands) assuming that the form of the model is an accurate representation of the system. As previously discussed, errors will be inherent in any hydraulic model of a complex water distribution system, and our Mexico City model, has some significant deficiencies. Furthermore, the post-earthquake performance data are limited to a few pressure readings.

To minimize the effects of modeling error, the Mexico City water system was separated into five pressure zones. The formation of these zones was an attempt to average out the inherent modeling errors associated with the estimation procedure and to work with limited performance data. The objective is to identify damage within areal zones so that (1) modeling errors which affect point pressure predictions will tend to average out over the zones, and (2) sufficient data are available to allow for damage estimation within each zone. The drawback of this modeling approach is that localized damage cannot be easily detected.

The pressure zones that have been defined for Mexico City tend to be independent in the sense that model changes in one zone will have a little impact on other zones. This zonation is in keeping with the physical design of water systems which are zoned to prevent problems in one subsystem affecting another. To determine this zonation, a perturbation study was conducted to estimate the pressure sensitivity of each measuring station. The assumption here was that a network node could be grouped with the measuring station to which it was most sensitive. This information was then used to define several sets of nodes, each set defining a unique pressure measuring zone.

It was found that changes in the pressure stations generally only affect nodes one or two pipe links away. It was also found that nodes above the grade line of the perturbed pressure station were not affected, even if they were adjacent to the pressure station. These source nodes were treated as being correlated with pressure measuring nodes directly downhill to them. Assigning these nodes to a different zone would be incorrect because damage at the uphill nodes would affect the perturbed station pressure. Therefore in assigning zone groupings, consideration was given to the node elevation and source node to sink node interdependence as well as the individual pressure ratios.
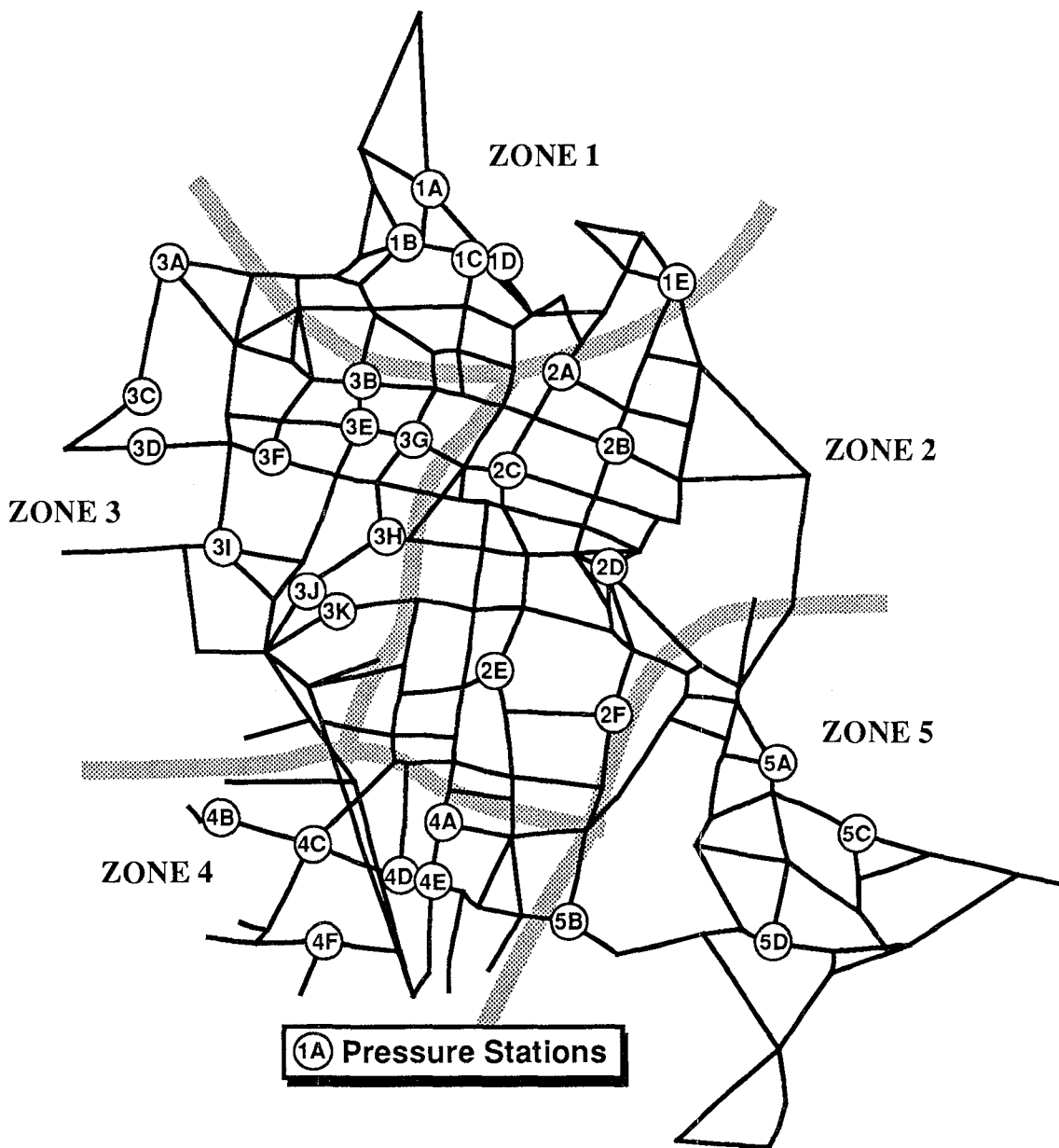
Figure 6 - DDF Network as Modeled with Pressure Zones

Figure 6 shows the final pressure zonation which minimizes the influence between zones.

Initial Damage State

The initial damage estimate for the DDF water system was obtained using specialized software designed to combine seismic hazard mapping, spatial configuration of the pipeline network, and pipe fragility models to estimate which pipes in the network would most likely be damaged. The software uses a gridded form of the hazard map (previously shown in Figure 5) to calculate which fraction of a particular pipe lies in a unique grid area. Each grid has an MMI associated with it and the pipe break algorithms are employed to find the number of breaks expected for the fraction of pipe contained within the grid. The damage algorithms are empirically-based pipe breakage models that consider different pipe constructions and earthquake intensities (Eguchi et al., 1989). Ayala and O'Rourke (1988) have documented that the primary system is constructed of mostly asbestos cement and concrete pipe with diameters ranging from 20 to 48 inches. Some older parts of the metropolitan area are serviced by clay and cast-iron pipes. The pipe break model used in the damage calculations assumed all pipes to be of concrete construction.

In Figure 7, the initial damage state (in terms of pipe break states) of the water system model is presented. Pipe damage has been divided into three groups, those with no leaks, small to moderate leaks, and those with large leaks. Figure 7, shows the individual pipe leak states superimposed on the hazard map for the Mexico Valley region. Large pipe leaks were confined to areas of MMI VII or higher. Small and moderate-sized leaks tended to be in areas of MMI VI to VII. No leaks were predicted in areas of MMI VI. The initial damage estimate predicted an average of 0.019 breaks per thousand feet of pipe. In all, at least 200 of the 279 pipes in the Mexico City primary water system were predicted to have some possibility of leakage from the 1985 earthquake.

If we compare that initial damage state to the actual damage that has been documented, it becomes apparent that our estimate is in need of refinement. In their actual damage assessment, Ayala and O'Rourke (1988) documented 175 repairs to the primary water distribution system. This translates into approximately 0.037 repairs per thousand feet of pipe. Thus, the initial damage state calculated underestimates the overall rate at which pipes are broken, but overestimates the number of pipes damaged.

The initial damage state also implies a different spatial distribution of damage than the actual damage patterns. Figure 8 shows the distribution of the actual repairs made to the DDF primary distribution system after the earthquake. Comparing Figure 8 to Figure 7, it is apparent that the initial damage state overestimates the amount of damage in most areas of the network except for the southeast portion of the system (Ixtapalapa) where comparisons are reasonable.

Figure 8 - Actual System Damage from 1985 Michoacan Earthquake

Ground Shaking Intensity [MMI]
7 - 7.5
6.5 - 7
6 - 6.5
5.5 - 6
5 - 5.5
<5

Damage State
Undamaged Pipe
Damaged Pipe

Figure 7 - Initial Network Damage Estimate

Ground Shaking Intensity [MMI]
7 - 7.5
6.5 - 7
6 - 6.5
5.5 - 6
5 - 5.5
<5

Damage State
No Breaks
Small or Medium Breaks
Large Breaks

554

The initial damage estimate is a preliminary attempt to identify those areas that are vulnerable to shaking-induced pipe failures. The estimate uses available technical knowledge about earthquake energy attenuation, soil attributes with regard to MMI amplification, and pipeline fragility models to make a first approximation of the severity and location of damage in the network.

Mexico City Network Damage Updates

This section summarizes the actual damage updates performed on the initial damage model of the Mexico City water system. The damage updates were performed on a zone by zone basis. As each zone's damage update was completed, the hydraulic model was updated with the piping parameter changes for that zone; then the next zone was updated, and so on. Because post-earthquake flowrate information was not available, estimating pipe diameter ratios for the pipe leak model and estimating nodal demands separately was not possible. This is because the damage estimator cannot distinguish between how much water should be vented to atmosphere through the added pipes and how much should be allocated to a nodal demand change. Because of this, only pipe ratio parameters were estimated for the Mexico City system and these were linked together within each zone; that is, the performance of all pipes within a particular pressure zone were uniformly varied.

With the network model modified to reflect the initial damage estimates and the post-earthquake pressure data used as a target for system performance, the Bayesian estimation procedure was first applied to Zone #1 (northern zone). Using the five Zone #1 post-earthquake pressure observations, the estimator modified all pipe parameters to an undamaged state making the predicted model pressures more closely match those observed. Figure 9 summarizes the results of the update process. The second row of bars in Figure 9 shows that the pressure measuring stations in Zone #1 are markedly improved and reflect more closely the actual pressure measurements (described here as a percentage of the pre-earthquake nominal pressures) displayed in the row labeled "Post EQ Data". For Zone #1 only one iteration through the estimation procedure was necessary to determine that the initial damage model was in error.

After completion of the damage update on Zone #1, the updated Zone #1 model parameters were substituted into the UK hydraulic program to define the starting damage state for the next damage zone update. For Zone #2 (eastern), the initial damage estimate was not modified because the initial damage performance state already closely reflected the reduced pressure state seen in the actual post-earthquake measurements. This is reflected in the barchart of Figure 9 where the first row clearly shows that the trends of the initial damage model follow the low pressure trends of the post-earthquake performance summarized in the last row.

The initial damage performance of Zone #3, however, shows much lower pressures than indicated by the post-earthquake data. A damage update was therefore performed to improve the hydraulic model's estimate. The damage model used as a starting point by
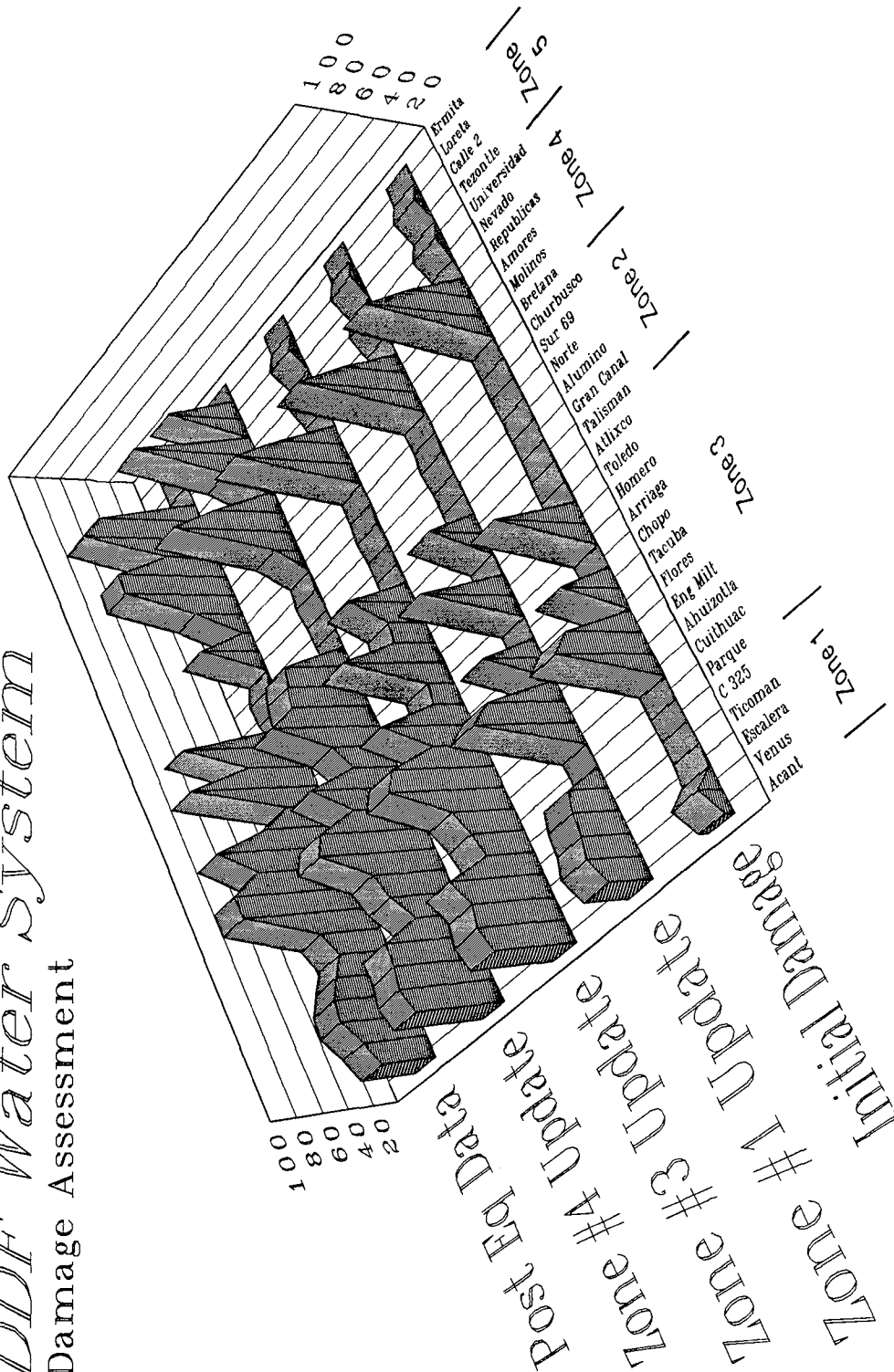
Figure 9 - Relative Pressure Estimates During the Sequential
Damage Estimation Procedure as a Percentage of Pre-earthquake Nominal Pressures

the estimator had undamaged pipes in place of the initially damaged pipes of Zone 1, but still had the damaged pipes in Zone 2 as initially estimated. Using the actual post-earthquake pressure measurements recorded in Zone 3, the estimator once again determined that all pipes in Zone 3 should be undamaged to increase the pressures and be in better agreement with post-earthquake observations. Examining Figure 9, we can see that the pressure distribution, after the Zone 3 update, as reflected in the third row of the barchart is even a better representation of the actual post-earthquake performance. Note also, that the damage update in Zone 3 does have an impact on the pressure in adjacent Zone 1, which has risen and is in even better agreement with the post-earthquake measurements. This interaction between pressure zones shows that they are not completely independent and that changes in one zone can still have some impact on adjacent zones.

Using a damage model which now consists of undamaged pipe elements in Zones 1 and 3, and the original damaged pipe estimates in Zone 2, an attempt was made to update Zone 4 (southern), where comparisons between the model and post-earthquake performance were generally erratic. It is worth noting that Zone 4 is the area where the undamaged hydraulic performance varied most from pre-earthquake measurements; this indicates that Zone 4 contains significant modeling error. Initial attempts at damage updates using all Zone 4 post-earthquake readings produced unstable results; the erratic and large difference between model predictions and actual observations made the model incapable of matching the measured data. It was determined that the difference between the model and post-earthquake pressures at the Republicas station was the cause of the instability. The Republicas pressure measurement was therefore removed from the Zone 4 observations. The damage update then became stable and the estimator determined that all pipe elements in Zone 4 should be undamaged to best match the post-earthquake measurements. The fourth row of Figure 9 reflects system performance after the Zone 4 update and the trends compare reasonably well with the post-earthquake data.

No damage update was performed in Zone 5 (southwestern) because, as with the situation in Zone 2, the initial damage in Zone 5 closely reflected the actual zero pressure distribution.

Figure 10 shows the DDF water system and the revised pipe break estimates after application of the damage update. As is shown in the diagram, only Zones 2 and 5 still have damaged pipes. Referring to the actual damage observations after the 1985 Michoacan earthquake (Figure 8), it is apparent that the damage estimator has been able to improve the initial damage prediction and better identify areas of outage.

CONCLUSIONS

The results of the Mexico City damage update can be summarized as follows:

Ground Shaking Intensity [MMI]

- 7 - 7.5
- 6.5 - 7
- 6 - 6.5
- 5.5 - 6
- 5 - 5.5
- <5

Damage State

- No Breaks
- Small or Medium Breaks
- Large Breaks

Figure 10 - Updated Network Damage Estimates
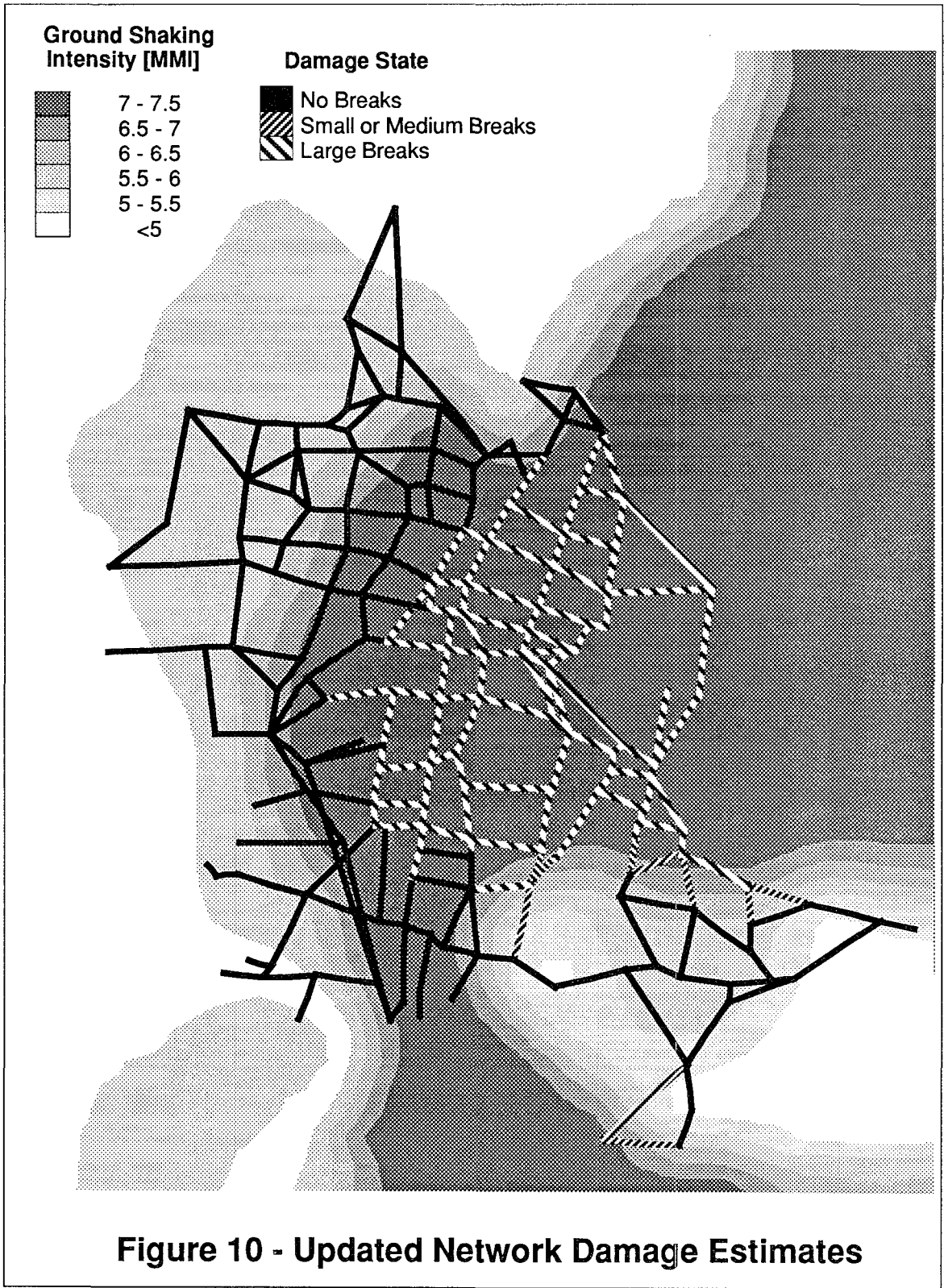
- The initial damage estimate which was based on earthquake magnitude and location only overestimates the extent of pipeline damage to the system.

- The sequential damage update by pressure zone indicates that a better representation of damage can be obtained by employing a Bayesian-type damage estimator.

- Errors in the Mexico City hydraulic model, and limited post-earthquake performance data forced damage updates to be made on a zonal basis (i.e., localized pipeline damage could not be detected)

ACKNOWLEDGEMENTS

REFERENCES

Ayala, A. Gustavo, and M.J. O'Rourke, "Effects of the 1985 Michoacan Earthquake on Water Systems and Other Buried Lifelines in Mexico." Technical Report NCEER 88, National Center for Earthquake Engineering Research, Buffalo, New York, 1988.

Coppolino, R.N. and Rubin, S., "Detectibility of Structural Failures in Offshore Platforms by Ambient Vibration Monitoring", Proceedings of the Offshore Technology Conference, Vol. 1, Paper OTC 3865, May 1980, pp. 101-110.

Eguchi, R.T., J.D. Chrostowski and G.M. Lee, "Early Post-Earthquake Damage Detection for Lifeline Systems," Proceedings of the 3rd U.S.-Japan Workshop on Earthquake Disaster Prevention for Lifeline Systems, Tsukuba, Japan, May 11-13, 1989.

Eguchi, R.T., Taylor, C.E., Legg, M.R., and J.H. Wiggins, "Earthquake Performance of Water Supply Systems," Earthquake Behavior and Safety of Oil and Gas Storage Facilities, Buried Pipelines and Equipment, PVP - Vol. 77, ASME, New York, 1983.

Hasselman, T.K. and Chrostowski, J.C., "Parameter Estimation for Large Space Structures," Proceedings of the ST Division/ASCE/Spring Convention, May 1985.

Lee, G.M. and S.M. Mejia, "The Effects of the 1985 Mexico City Earthquake on Underground Water and Sewer Pipelines, Lifeline Seismic Risk Analysis - Case Studies, R.T. Eguchi and C.B. Crouse, editors, ASCE, New York, 1986.

559

Romo, M.P., A. Jaime, and D. Resendiz, The Mexico Earthquake of September 19, 1985 - General Soil Conditions and Clay Properties in the Valley of Mexico, Earthquake Spectra, Vol. 4, No. 4, 1988.

Sanchez-Sesma, Francisco J., Sergio Chavez-Perez, Martha Suarez, Miguel A. Bravo, L. Edwardo Perez-Rocha, On the Seismic Response of the Valley of Mexico, Earthquake Spectra, Vol. 4, No. 4, 1988.

Shinozuka, M., and H. Kameda, "Reliability and Risk Assessment of Lifeline Systems," Proceedings of U.S.-Japan Workshop on Earthquake Disaster Prevention for Lifeline Systems, Tsukuba, Japan, May 11-13, 1989.

Singh, S.K., E. Mena, R. Castro, and C. Carmona, Empirical Prediction of Ground Motion in Mexico City from Coastal Earthquakes, Bulletin of the Seismological Society of America, Vol. 77, pp. 1862-1867, 1987.

Trautmann, C.H., O'Rourke, T.D., Grigoria, M., and M.M. Khater, "Systems Model for Water Supply Following Earthquakes," Lifeline Seismic Risk Analysis - Case Studies, R.T. Eguchi, and C.B. Crouse editors, ASCE, New York, 1986.

Trifunac, M.D., "A Note on the Range of Peak Amplitudes of Recorded Accelerations, Velocities and Displacements with Respect to the Modified Mercalli Intensity Scale," Earthquake Notes, Vol. 47, No. 1, 1976.

Wood, D.J., "Computer Analysis of Flow in Pipe Networks including Extended Period Simulations", Department of Civil Engineering, University of Kentucky, 1980.

ac:\risk\rte\detect.pap

EARTHQUAKE RESPONSE CONTROL FOR PILE FOUNDATIONS
USING VISCOUS DAMPING DEVICE

Takaharu Yamamoto   Seiji Uehara   Hiroshi Mikami
General Manager   Chief Research Engineer   Research Engineer

Laboratory of Research and Development
Sumitomo Construction Co., Ltd.
Tokyo Japan

ABSTRACT

In order to improve the earthquake resistance of structures, active research and development efforts have recently been conducted on structural control methods, some of the results of which have been introduced into practical applications.

The authors have proposed a new aseismic design method called "Sumitomo Earthquake Response Control with Viscous Damping for Foundations" (hereinafter referred to as "SEV"). This method employs highly viscous damping devices embedded into pile foundations to reduce the amplitude of input earthquake acceleration to structures supported by pile foundations on soft ground.

The present paper first provides an outline of SEV, then discusses the results of model tests for verification of the effects of this method. Finally, a preliminary analysis of SEV applied to a typical oil tank foundation constructed on soft ground is described.

INTRODUCTION

Recently, active efforts have been conducted to develop various earthquake response control systems for structures, in addition to approaches for improving the aseismic performance of structures themselves. Such response control systems include active control methods and passive control methods such as earthquake response control designs using viscous damping walls (V-D walls)[1-2] to reduce the earthquake response of structures, and base isolation methods such as lead-rubber bearings (LRB)[3-4] to reduce the amplitude of input earthquake acceleration at the foundation level.

However, a search of the literature reveals almost no studies dealing with response control of substructures, as compared to superstructures. Improved aseismic performance on soft ground is essential because construction works such as those involved in waterfront development projects on soft ground will tend to increase in number in the future. In view of this situation, the authors have been conducting R&D efforts on earthquake response control for pile foundations.

The present study proposes a method of applying the viscous damping mechanism of V-D walls to pile foundation structures, in order to reduce the amplitude of input earthquake acceleration to a superstructure. This method provides the combined effects of conventional response control functions; i.e., isolation and damping.

The present paper first provides an outline of this method which is still at the R&D stage for future implementation, and describes the results of model experiments for verification of the effects of the method in reducing seismic response. It then demonstrates that SEV has good potential as an aseismic design method for pile foundations on ground that is subject to liquefaction.

VISCOUS DAMPING DEVICE AND ITS MECHANISM

1. Components of SEV

    In order to reduce the amplitude of input earthquake acceleration to structures supported by piles, damping devices are attached to the piles and footing slab (see Fig. 1).

    The damping device has virtually the same basic construction as the damping walls conventionally used in building structures. The construction currently under consideration for such a device is described below.

    The SEV consists of the following components.

    (1) Inner steel plate: Supported by truss members (4) and connected so that the same displacement will be developed in the horizontal plane at the point of the pile where the truss members are installed.

(2) Outer steel plate: Embedded into the concrete footing, enclosing the viscous fluid (3) and inner steel plate (1).

(3) Viscous fluid: Filled in the outer steel plate (2).

(4) Truss member: Steel pipe connecting the inner steel plate (1) with the middle section of the pile.

Upon the occurrence of an earthquake, relative displacement takes place in the footing slab and underground pile, causing shear deformation of the viscous fluid filled in a minute gap between the inner and outer steel plates in the damping device. This results in viscous resistance, yielding a damping effect against earthquake waves. Therefore, it appears at present that the first point where the horizontal displacement of the pile=0 may be the optimal point of installation for the truss member to the pile.

Conventional damping systems used in building structures are arranged in walls between columns and beams on each floor, where inner steel plates are installed perpendicularly so that they intrinsically exhibit vectorial properties, with a pair of x and y directional systems comprising the entire system. In contrast, SEV is distinguished from conventional systems in that it has no vectorial property because the inner steel plates are arranged in a horizontal plane. Consequently, the necessary number of devices (pairs of devices) dictated by the design may be arranged and balanced in piles comprising a foundation so that no torsional moment of the foundation footing is developed in the horizontal plane.

2. Basic SEV Mechanism
The viscous resistant force of the damping device is given by:

$$Q_A = Q_D + Q_K \qquad (1)$$

where
Q_A: viscous resistant force
Q_D: viscous damping force
Q_K: restoring force

The resistant force of the viscous material includes not only the viscous resistant force but also the spring effect (viscoelastic behavior) and restoring force Q_K. Fig. 2 shows a typical relationship between load and displacement for V-D walls actually used in building structures[4].

The viscous fluid used in the present damping device exhibits the following damping characteristics:

1) The viscous resistant force is dependent upon the coefficient of viscosity (μ), or temperature (t).

563

2) The damping force bears a nonlinear relation to the velocity gradient (dv/dy).

3) The restoring force bears a nonlinear relation to the relative displacement (δ).

4) The mass of damping force or restoring force is dependent upon the vibration frequency.

The damping characteristics are empirically determined in the development of the V-D walls.

The viscous damping force Q_D is given by:

$$QD = \mu \cdot A \cdot f^\zeta \cdot (dv/dy)^\alpha \tag{2}$$

where it is assumed that the damping force Q_D is proportional to the coefficient of viscosity (μ: kgf·sec/cm^2) of the viscous material, to the effective shear area (A: cm^2), to the ζ-th power of the vibration frequency (f: Hz), and to the α-th power (Newtonian fluid: $\alpha = 1$) of the velocity gradient (dv/dy: sec^{-1}; see Fig. 3).

There are several types of viscous fluid. An empirical equation for polyisobuthylene used in the V-D wall is given below by way of example:

$$QD = 0.336\,e^{-0.0865t} \cdot A \cdot f^{-0.449} \cdot (dv/dy)^{0.650} \tag{3}$$

The restoring force Q_K is given by:

$$QK = \{C \cdot \mu \cdot A \cdot f^\eta/dy\} \cdot \delta^{1+\beta} \tag{4}$$

where it is assumed that the restoring force Q_K is proportional to the effective shear area (A); inversely proportional to the gap between the two steel plates (dy: cm); and proportional to the coefficient of viscosity (μ) of the viscous material, to the η-th power of vibration frequency (f), and to the $(1 + \beta)$-th power of relative displacement (δ; cm).

Similarly, an empirical formula for polyisobuthylene is given by:

$$QK = \{0.304\,e^{-0.0865t} \cdot A \cdot f^{0.844}/dy\} \cdot \delta^{1-0.647 \cdot f - 0.218} \tag{5}$$

As is clear from the above, the viscous resistant force of the damping device can be optimally set by adjusting the coefficient of viscosity (μ) of the viscous material, the shear area (A), and the gap (dy) between the two steel plates.

In the SEV method, the equivalent spring for the restoring force (Q_K) of the damping device is minimal as compared to that for the pile-ground system, so that it can be neglected in actuality.

INSTALLATION OF SEV FOUNDATION METHOD

Fig. 4 shows an example of installation of damping devices to an oil tank foundation. The necessary number of damping devices dictated by the design are installed in the center of an area surrounded by three or four adjacent piles. The damping devices should be balanced so as to avoid the development of torsional vibration of the entire foundation.

Consideration is currently being given to the method of on-site installation shown in Fig. 5. The foundation piles to which damping devices are attached are driven together with the truss members folded. After the piles are driven into the ground, the soil is cut away by water jets ejected from the numerous holes provided along the axis of the truss member to tilt and fix the truss member to a predetermined position (the pile and truss member are jointed by a pin). Subsequently, three or four adjacent truss members are connected together, onto which a factory-fabricated integrated damping device is installed.

A foundation footing concrete is placed and the damping device is embedded therein to form a structure integrated with the superstructure (see Fig. 1).

EXPERIMENTS AND RESULTS

Sine-wave shaking table tests were conducted using single degree-of-freedom system models in order to verify the effects of the SEV method. The four-pile model employed brass plates (20 mm wide, 3 mm thick) so that the vibration in one direction was prominent. Photo 1 show an outline of the experimental device.

Fig. 6 shows the viscosity of the viscous material vs. the maximum response ratio. It is clear that the response ratio of the model decreases with increasing viscosity, yielding a similar tendency to that of V-D walls[1)-2)].

Fig. 7 shows response curves derived with the viscous material having a coefficient of viscosity μ = 12,500 cp, and without the damping device. Both cases revealed virtually no difference in terms of natural vibration frequency in spite of the fact that the response ratio was reduced in the case of the damped model. This finding bears out the supposition that the restoring force Q_K of the damping device may in actuality be neglected without any problem.

Fig. 7 also shows the results derived from studies of a Voigt model using the basic properties of the viscous material employed in the experiment. These results demonstrate fairly close agreement with the empirical values, suggesting that the SEV design method based on the same model provides potential feasibility for practical implementation.

With regard to the nonlinearity of the viscous material, characteristic values determined by the primary natural period were used.

EXAMPLE DESIGN OF TANK FOUNDATION

Based upon the findings presented above, the results of simulation analysis for the SEV method applied to a 20,000-ton class oil tank on soft ground as shown in Fig. 4 are described. Fig. 8 and Table 1 show the model and various conditions used in the analysis.

Fig. 9 shows the input acceleration waves and the typical response acceleration waves at a tank foundation obtained by analysis. Fig. 10 shows the effective area of the damping device vs. response acceleration at the tank foundation. As shown in Fig. 6, it is obvious that an effect of reducing the response acceleration is produced by increasing the area of the device. It is also apparent that there is an upper limit on the effective area of the damping device.

Fig. 10 also shows the results observed when liquefaction occurred to a depth of 5 meters from the ground surface. In this case, a still greater effect of reducing the response acceleration is apparent, wherein it is evaluated that the ground coefficient in the liquefied layer is one-hundredth of that in non-liquefied layers.

CONCLUSION

The following findings have been obtained on the basis of the present fundamental study.

1) It has been found that the V-D wall method for response control of structures developed mainly for buildings (superstructures) and introduced for practical use provides a feasible option for application in pile foundations.

2) When damping devices are arranged in the horizontal plane of the foundation slab, a damping system having no vectorial property can be configured.

3) The feasibility of an SEV design method based on the Voigt model has been identified.

4) It has been verified that a sufficient damping effect is provided even when the surface ground is liquefied. This finding suggests that the present damping device configuration serves as an effective aseismic measure for pile foundations in ground that is subject to liquefaction.

FUTURE STUDIES

The present paper has described preliminary verification of the applicability of the SEV method to pile foundations. The authors are

566

currently conducting model tests on shaking tables including ground, and hope to present some of the results obtained at the U.S.-Japan Workshop.

Although in the present study a viscous fluid was used as the viscous damping material, the use of viscoelastic material such as high-damping rubber is currently under consideration in view of the factors of workability and reliability.

REFERENCES

1) M. Miyazaki et al.: "Earthquake Response Control Design of Building Using Viscous Damping Walls," 1st East Asian Conf. on Structural and Construction, Bangkok, Jan. 1986
2) F. Arima et al.: "A Study on Building with Large Damping Using Viscous Damping Walls," 9th World Conf. on Earthquake Engineering, Tokyo, Aug. 198
3) I. Shimoda, et al.: "Experimental Study on Isolated Building Using Lead Rubber Bearing Through Vibration Test," 9th World Conf. on Earthquake Engineering, Tokyo, Aug. 1988
4) M. Miyazaki et al.:" Design and Its Performance Verification of A Base-Isolated Building Using Lead Rubber Bearings in Japan," 9th World Conf. on Earthquake Engineering, Tokyo, Aug. 1988

Table 1. Analytical Conditions

GROUND	Young's modulus	E_1=300tf/m^2 (GL~GL-10m) E_2=600tf/m^2 (GL-10~GL-20m)
	Damping ratio	h = 0.05
	Unit weight	γ = 1.8 tf/m^3
TANK	Weight	w = 47.73 tf/pile
PILE (steel pipe pile)	Size	ϕ = 508 mm t = 12.7mm
	Young's modulus	E = 2.1×10^{7}tf/m^2
DAMPING DEVICE	Viscous fluid	μ = 97000 poise
	Gap	dy= 1.0 cm
INPUT ACCELERATION	Max. acc.= 102.2 gal Recorded at Kaihoku-bridge in 1978 (Fig. 9)	
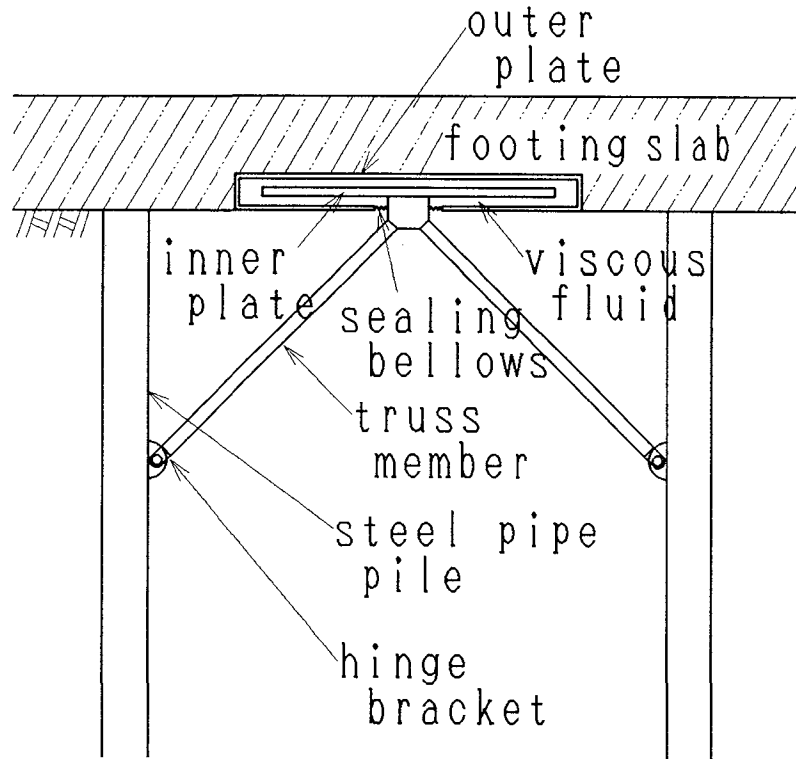
Fig. 1. SEV Configuration
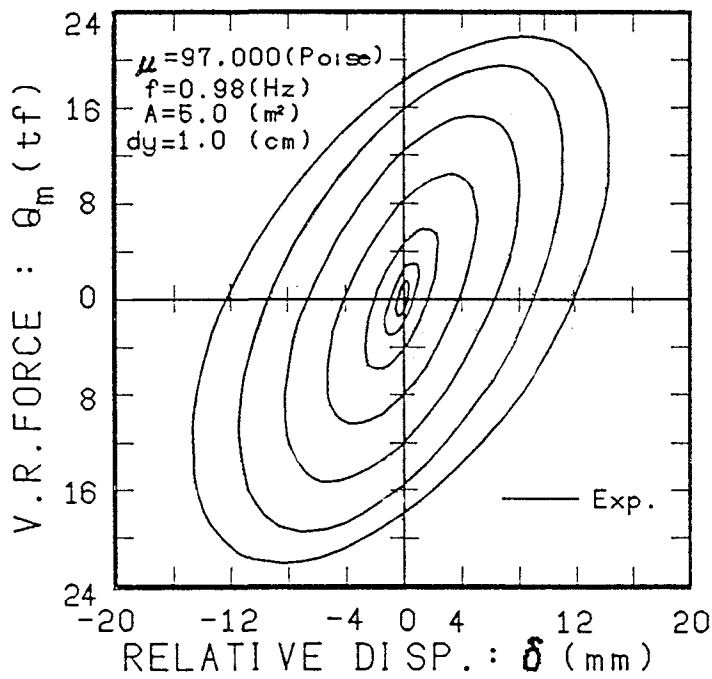
Fig. 2. Damping Capacity of Device

$$Q = \mu \cdot A \cdot (dv/dy)^{\alpha}$$

where
Q : viscous resistant shear force
μ : coefficient of viscosity
A : area
dv : relative velocity difference
dy : distance between 2 plates
α : exponent obtained from experiment
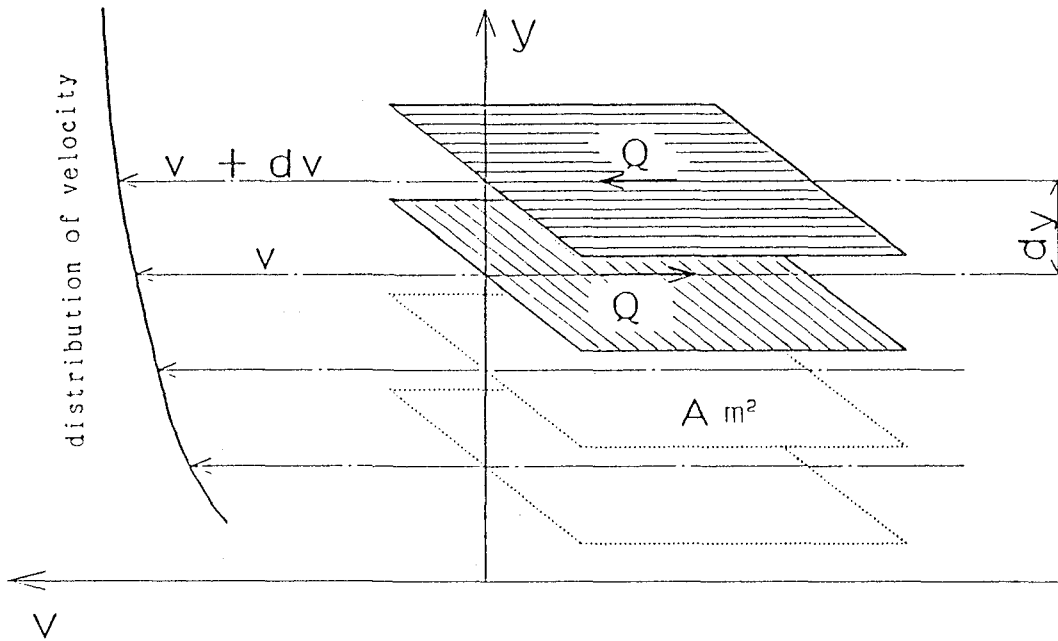
Fig. 3. Mechanism of Development of Viscous Resistant Force
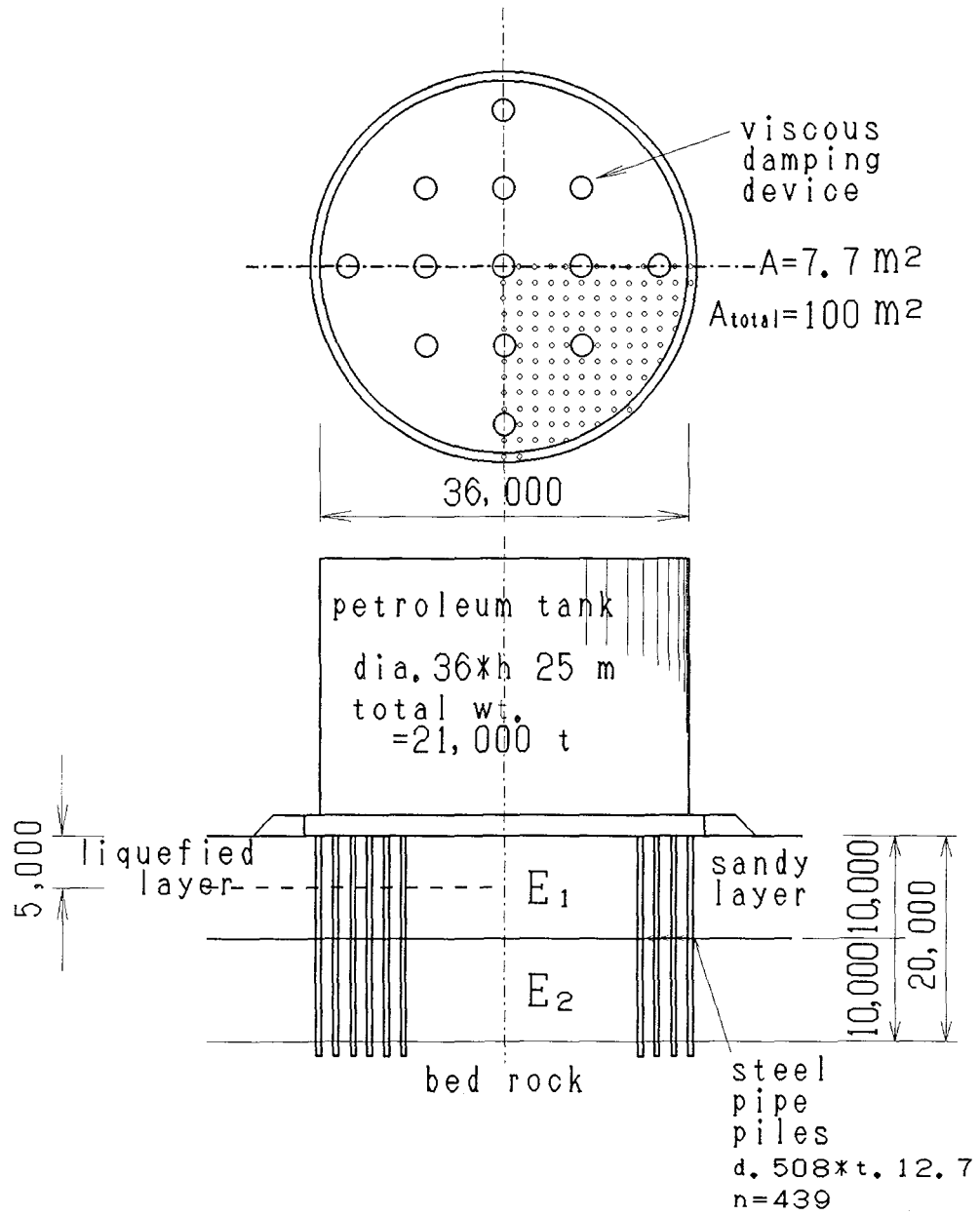
Fig. 4. Oil Tank Foundation
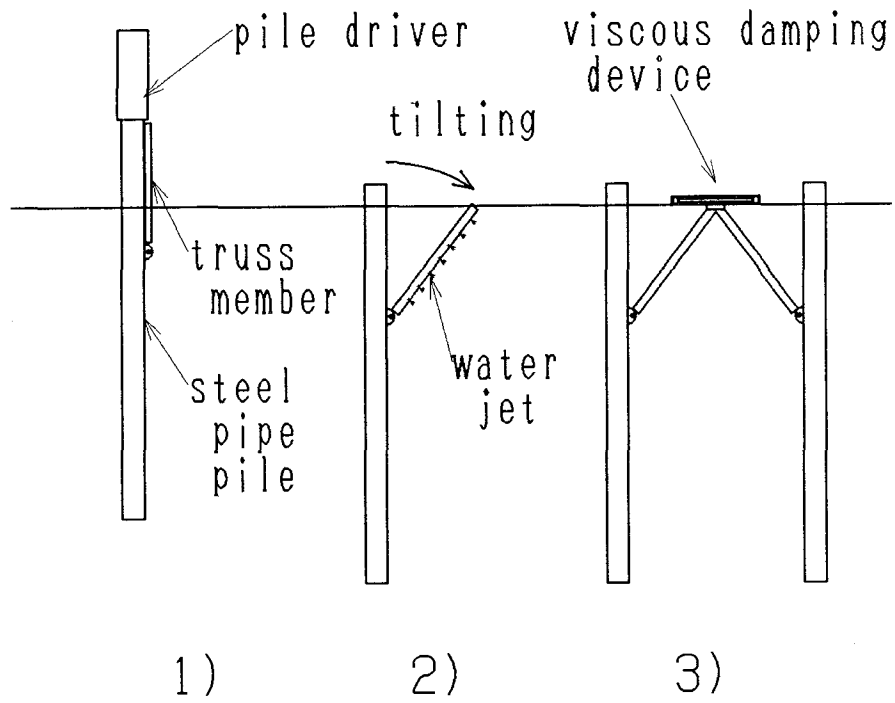
Fig. 5. Installation of Damping Device
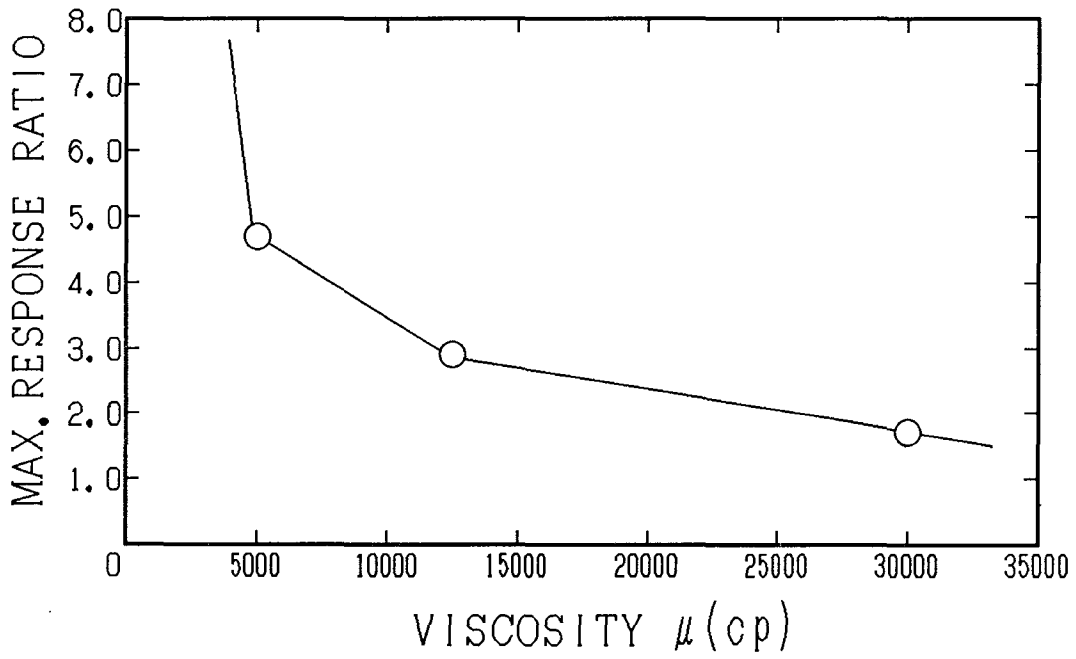
Fig. 6. Viscosity vs. Response Ratio
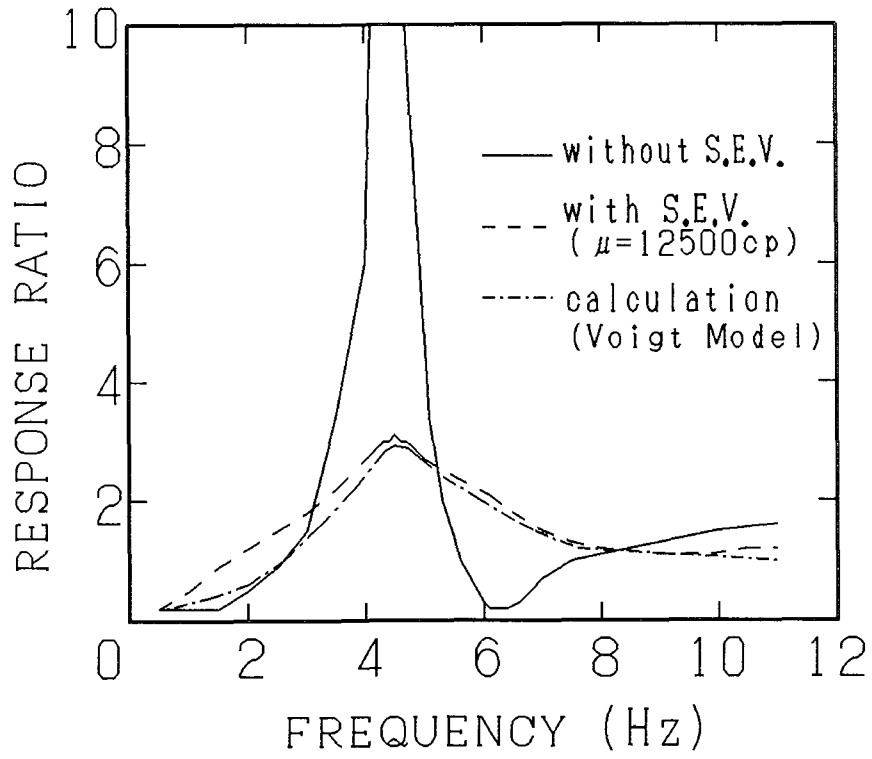
Fig. 7. Response Curves (μ = 12,500 cp)
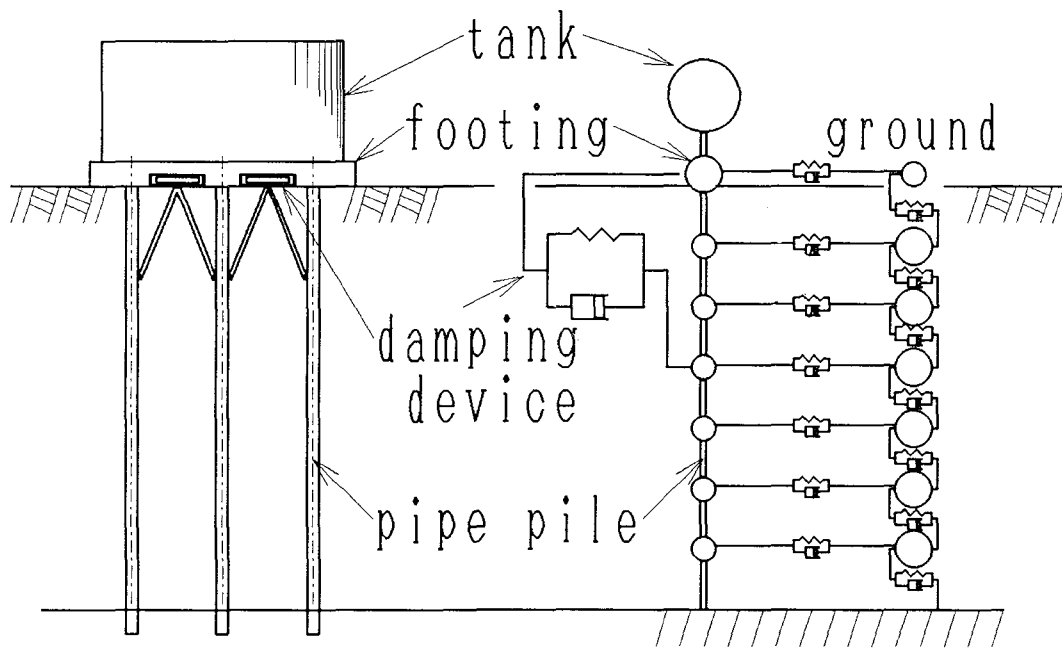
Fig. 8. Analytical Model
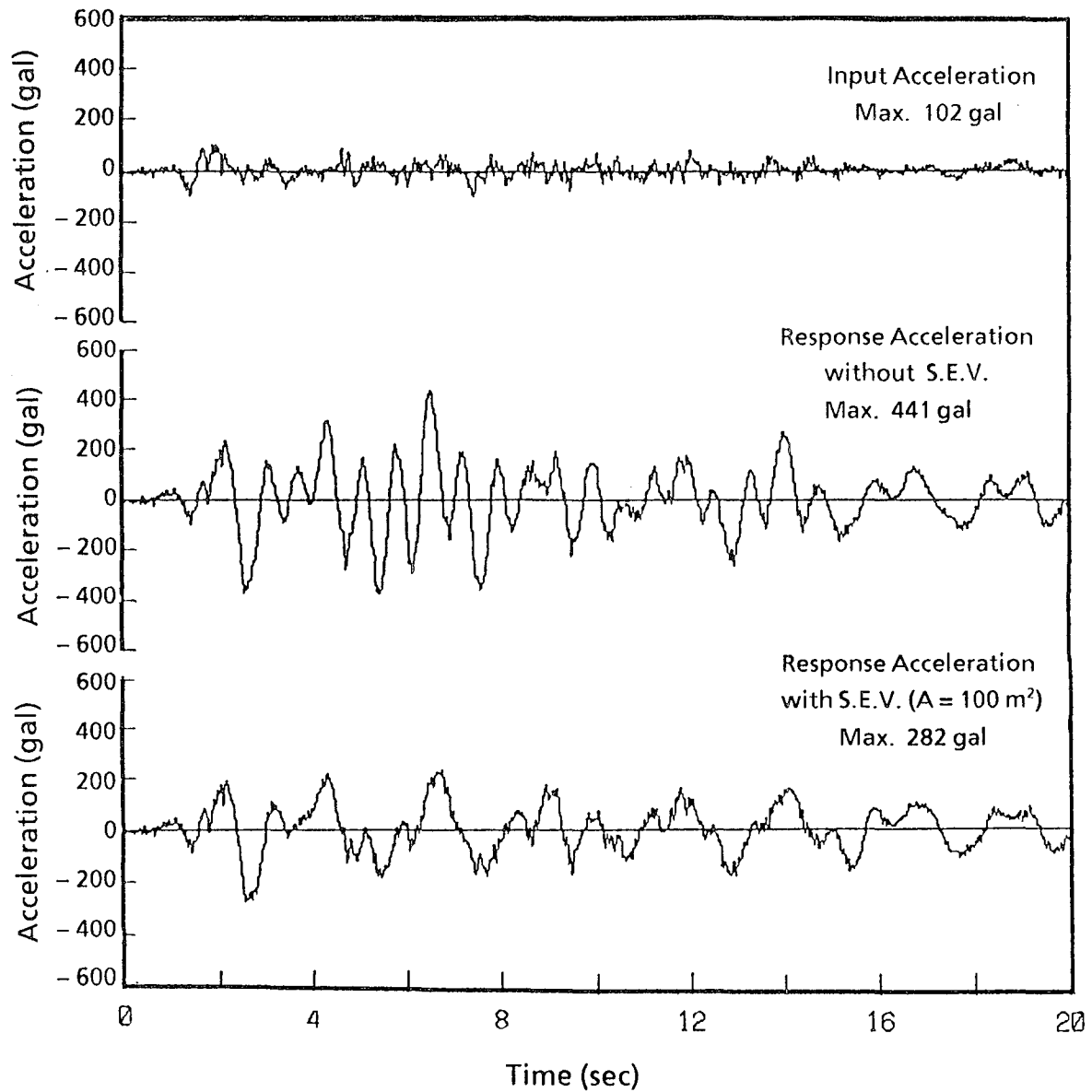
Fig. 9. Input and Response Acceleration Waves
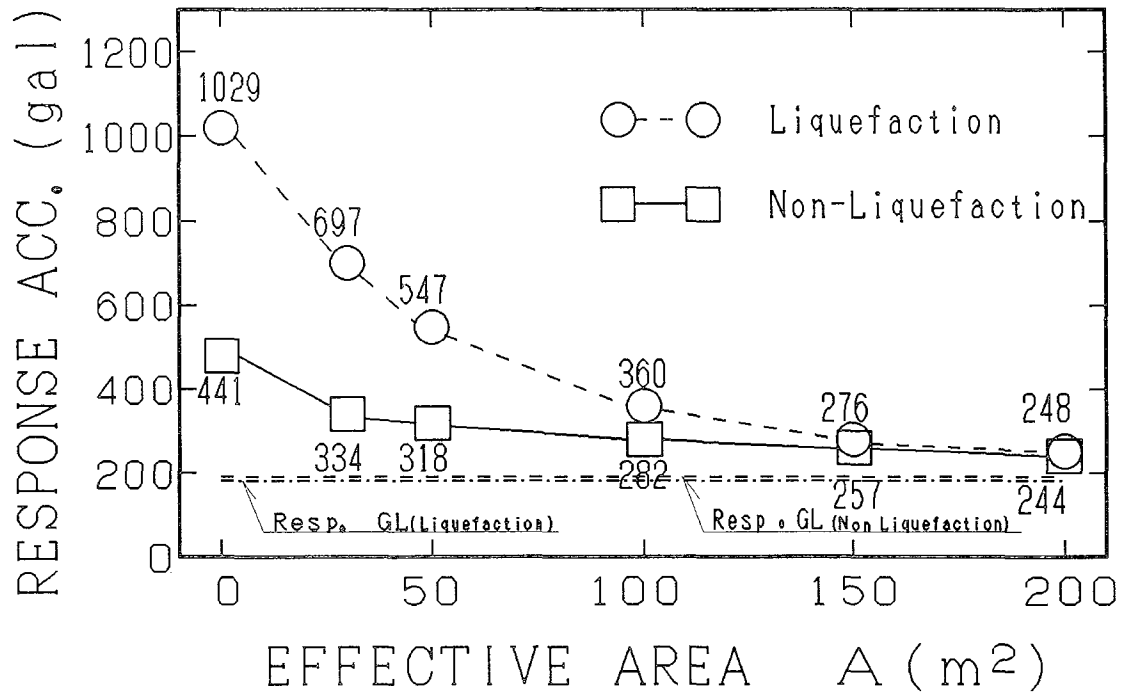
Fig. 10. Effective Area vs. Response Acceleration
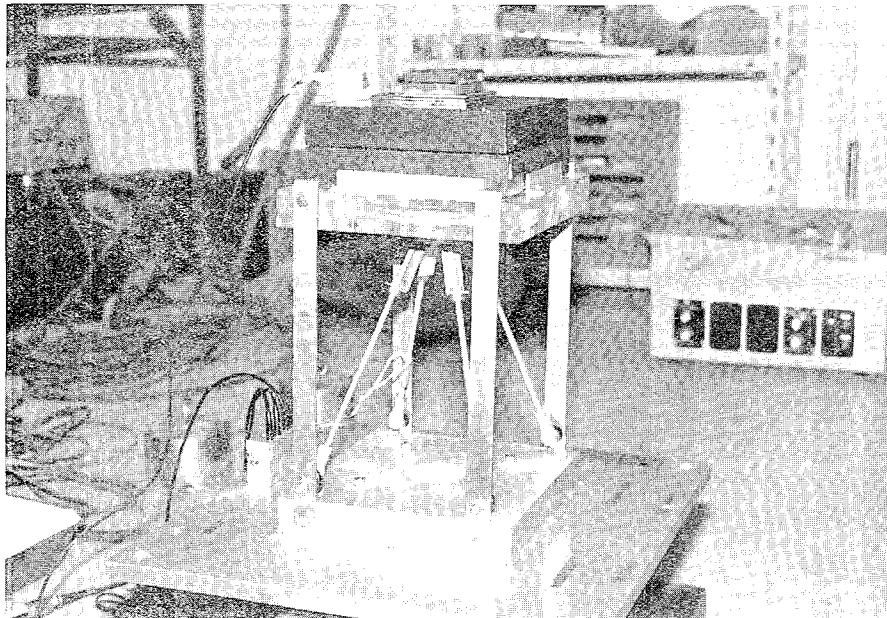
Photo 1. Experimental Device

STRATEGIES OF THE VENEZUELAN OIL INDUSTRY IN THE EVALUATION OF SEISMIC AND GEOTECHNICAL RISKS FOR LIFELINES. CASE STUDIES

E. GAJARDO (1), N. MODE (1), J. MURRIA (2), J. ABI SAAB (2)

(1) INTEVEP S.A., Los Teques, Venezuela

(2) MARAVEN S.A., Lagunillas, Edo. Zulia, Venezuela

ABSTRACT

The high to moderate seismic risk and the investment represented by lifeline infrastructure of the Venezuelan oil industry, led to establish a global and comprehensive research effort for hazard evaluation, consequences and the appropriate mitigation measures.

The hazard evaluation includes a complete study of past historical and instrumental seismicity, microearthquake surveys, seismic and strong motion networks, crustal model studies, attenuation laws, evaluation of active faults, paleoseismology, geotechnical caracterization, slope stability analysis, structural reliability, etc.

Three case studies are presented, all in Western Venezuela: the Coastal Protection System for the oil fields in the Lake Maracaibo Area; the new Products Pipeline and Distribution System for the Venezuelan Andean region (SUMANDES); and the Oil Refinery Complex in the Paraguaná Península.

INTRODUCTION

The major seismic hazards which significantly affect a lifeline system are: (1) differential fault movement and ground rupture, ground shaking, liquefaction, landslides and tsunamis; (2) tectonic uplift and subsidence, and (3) vibratory ground motion. The extent to which lifeline systems are able to perform under each of these major seismic hazards after an earthquake, greatly influences the toll in human life, property damage, and service restoration efforts. Therefore, the evaluation of an existing lifeline, as well as the design of a new one, includes a complete study of past historical and instrumental seismicity, microearthquake surveys, seismic and strong motion networks, crustal model studies, attenuation laws, evaluation of active faults, paleoseismology, geotechnical characterization, slope stability analysis, structural reliability, etc. Three case studies are presented, all in Western Venezuela: the Coastal Protection System for the oil fields in the Lake Maracaibo area; the new Products Pipeline and Distribution System for the Venezuelan Andean Region (SUMANDES); and the Oil Refinery Complex in the Paraguaná Península, (see Fig. 1).

BRIEF HISTORICAL SUMMARY

Case 1. The Coastal Protection System, Lake Maracaibo Area

Ground subsidence, associated with oil production in the East coast of Lake Maracaibo (Western Venezuela), was detected as early as 1929. Maximum cumulative subsidence as of April 1990 is 5.03 m. Murria and Abi Saab [1], state that typical subsidence rates range from 5 cm/yr along the coast to 20 cm/yr in inland areas subjected to intensive oil production. The geomorphology of the area (low, swampy lands) prompted the need to protect inhabitants and oil industry installations from lake waters. The construction of a coastal protection system was started in 1932 and is still in progress, as subsidence increases. The system consists of coastal and inner dykes as well as drainage networks, all conforming the "polders" of Tía Juana, Lagunillas and Bachaquero, consisting of:

- The coastal dyke to protect the subsided area from lake flooding.
- The inner diversion dykes to prevent run-off from the outer area getting into the subsided polder area.
- Drainage channels to convey the water to the pumping stations constructed along the coast.
- Pumping stations to dispose of the water over the dyke and into the Lake.

Fig. 2 shows the main features of the Lagunillas, Tía Juana and Bachaquero polders.

Case 2. Products Pipeline and Distribution System for the Venezuelan Andean Region (SUMANDES)

The SUMANDES project has been developed to satisfy consumer demands of oil products in the Venezuelan Andean region. This pipeline system will accrue economic benefits due to the reduction of traffic congestion, highway deterioration and accidents, as well as minimizing distribution costs and energy consumption.

The pipelines were planned for two construction stages, Fig. 1. Stage I was completed in early 1990. The second stage is still in the detail engineering phase.

Stage I is a 295 km, 12″ pipeline from Bajo Grande to El Vigia Distribution Plant, via the San Lorenzo Distribution Plant. This stage includes more than 100 km of submarine pipeline.

The second stage is a 150 km, 10″ buried pipeline from EL Vigia to the Murachi Distribution Plant. One of the main characteristics of this stage is the La Fría - Murachi section (60 km approximately) in which the geology and the topography lead to a wide variety of seismic hazards that could cause large ground deformations.

Case 3. The Paraguaná Refinery Complex.

One of the world's biggest oil refinery complexes is located in the Paraguaná Península and comprises the Amuay and Cardón refineries constructed about 40 years ago. Due to its strategic and economic importance, a seismic vulnerability study is under way. Both refineries include a dense network of pipelines and other types of lifeline facilities that need to be evaluated.

Recent tectonics and the seismicity of the area are not very well known and detailed studies are necessary to evaluate the seismic hazard and the behavior of the installations under seismic loading.

REGIONAL GEOLOGICAL FRAMEWORK

The complex tectonic environment of the study area has been described, but to understand the general geological framework, the work of James [2] has been followed for a good updated review of the genesis and state of stresses of the area. Northwest Venezuela is characterized by two major pull-apart basins, the Gulf of Venezuela and Lake Maracaibo. Dewey [3], based on the shallow seismicity pattern, supports a plate tectonic hypothesis where the present Western Venezuela is a result of continuing eastward motion of the Caribbean and South American plates as a single plate. The lack of shallow seismic activity associated with the intermediate-deep earthquake zone of northern Colombia suggests that the principal boundary between the plates has moved from a location West of the Sierra de Perija to its present position in the Cordillera de Merida, within the last 5 to 10 million years. This change in plate boundaries may have started the right-lateral strike-slip motion on the Bocono fault system.

Data related to the seismogenic potential of the existing faults in Western Venezuela was carried out. The active faults are shown in Fig. 3, the principal ones being: Boconó, Tuñame, Valera, Piñango, Piedemonte, Burro Negro, San Simón and Mene Grande. The main seismotectonic features are given in Table 1.

DATA BASE

A historical data base, including macroseismic information since 1530, was compiled for INTEVEP by Grases [4]. This information is available in a computerized data base and it was used to validate the seismicity parameters obtained from instrumentally recorded earthquakes.

Within the studied area, there have been more than 150 felt earthquakes during this century and Table 2 is an excerpt for the events of intensity MMI VII or more. In the last 50 years, the period during which the dykes have been continuously increasing in height, no significant earthquakes have occurred in the region, capable of generate local intensities greater than MMI VII in this area.

A compilation of instrumentally recorded events (1900 - 1988) was done for the whole Venezuelan region. The sources of data were international data files and seismic bulletins from local and Caribbean seismological stations.

The seismicity of the area of this study is shown in Fig. 4, where the earthquake magnitudes are represented with symbols of different sizes.

This data base is not homogeneous in time, due to the threshold in magnitude imposed by the detection capability of the worldwide seismic network. A completeness study was conducted to evaluate the time period during which the catalogue could be regarded as complete and reliable for each magnitude range. The procedure followed was the one suggested by Stepp [5].

SEISMIC SOURCE ZONES

The location and geometry of earthquake potential sources were defined using the surface trace of known faults and simple quadrangle geometry for diffuse random sources of greater depth.

The seismicity pattern for this area shows activity that goes from the surface to great depth. Therefore it was necessary to evaluate the focal depth distribution and locate the sources at three discrete depth ranges.

The shallow or crustal seismicity was modelled using the current seimological and tectonic knowledge for the region, assuming that most of the activity is associated with the active faults. The seismicity of intermediate depths (45 to 80 km) was modelled as a single rectangular diffuse seismic source with an assigned depth of 65 km. A further rectangular shaped seismic source was used to model the deep seismic activity, reaching an average depth of 160 km.

CHARACTERIZATION OF SEISMIC SOURCES

The characterization of earthquake sources was performed incorporating all available seismological and geological information. For each source, the following basic data is needed: type of source, maximum magnitude, recurrence relationship parameters,

annual rate of activity, characteristic or average depth of activity, and fault rupture-magnitude relationship.

Two types of seismic sources were defined. Linear segmented sources for the seismic activity assumed to be associated with the major identifiable faults. Random sources, modelled as uniform diffuse sources to account for undiscovered faults and historical seismicity that could not be associated with a particular tectonic feature.

The upper magnitudes for each fault were studied and are given in Table 1. For other faults, not fully evaluated, a best criterion was used taking into account the information available or judgement based on other known similar faults.

The Gutenberg-Richter frequency-magnitude relationship was established for the three defined depth ranges and for the whole studied area. Body wave magnitudes were selected, since most of the events were reported with mb. Those with Ms values (surface wave magnitude) were converted into mb magnitudes using standard worldwide conversion relationships.

The recurrence parameter values selected, for the seismic hazard evaluation, were those obtained through the least squares method applied to 0.5 magnitude intervals, which gave b = 0.98 for shallow seismicity. For intermediate and deep sources, b values of 1.29 and 0.85 were obtained.

The minimum magnitude of engineering interest was considered to be mb = 4.5 and the annual rate of activity of each source was evaluated accordingly. This rate was calculated following the procedure developed by Molnar [6].

The selection of a characteristic depth for linear shallow sources was performed using both the geological criteria, given by the tectonic studies, and the distribution of seismic activity with depth.

For intermediate depth diffuse sources an average depth of 60 km was selected. The deep seismic activity has a remarkable concentration around 160 km, therefore this depth was selected as characteristic for these sources.

A magnitude-length criterion is required as input for the modelling of the seismic activity of fault sources. No systematic studies have been carried out in Venezuela to correlate magnitude of earthquakes with rupture length of the causative fault. Therefore, after checking its behavior in the Venezuelan tectonic environment, a relationship developed by Utsu & Seki [7] was selected.

ATTENUATION RELATIONSHIP

The existing strong motion data for Western Venezuela is not sufficient to develop an empirical attenuation relationship. From the macroseismic information of instrumentally recorded events with known magnitude, it appears that the attenuation of intensities with distance is lower than applying other commonly used relationships.

An empirical approach for developing attenuation relationships was adopted, which utilizes selected modified Mercalli intensities obtained after the evaluation of effects

of well known earthquakes referred in the INTEVEP seismic data base. The MM intensity assignment was done after careful evaluation of all local effects of events with good epicentral and magnitude determination. To get more stable and robust intensity values for each event, a group of five experts was used and weighted values were given to each data point to account for the nonhomogeneous quality of the basic information.

After converting MM intensities values into acceleration, using a relation obtained by Murphy & O'Brien [8], using worldwide data, the following attenuation relation was obtained through this method:

$$Ln\ a = 4.32 + 0.56\ mb - 0.87\ Ln\ (R + 10) \qquad Sigma = 0.67 \qquad (1)$$

Where:

a:	Acceleration in gals
mb:	Body wave magnitude
R:	Hypocentral distance in km
Sigma:	Standard deviation

SEISMIC HAZARD ANALYSIS

Case 1. The Coastal Protection System, Lake Maracaibo.

Contribution of Individual Seismic Sources

In order of importance, taking a return period of 3000 years, the sources are: the Boconó fault, the intermediate rectangular seismic diffuse zone (Depth 65 kms), Valera, Oca-Ancon, Tuñame, Icotea, Piñango, the deepest rectangular seismic source (depth 160 km), Burro Negro, Mene Grande, Piedmont, Perijá, Pueblo Viejo, Cabimas and Tía Juana, (Fig. 3).

Expected Peak Ground Acceleration

The seismic hazard for the East coast of Lake Maracaibo was evaluated using a probabilistic Poisson distribution model, applying the ERA computer program developed by INTEVEP. The values of expected peak ground accelerations were evaluated for the three sites of interest: Tía Juana, Lagunillas and Bachaquero, Fig. 1. The acceptable risk assumed for the dykes can be consider similar to that for the design of a dam when populated areas are located downstream, which is normally taken between 1.0 to 5.0% of the excess probability for a service life of 100 years. This criterion is equivalent to taking a return period of 3000 years. In this case the expected peak ground acceleration is around 0,28 g. Fig. 5 shows the excess probability for 100 years of service life and the corresponding return period for different structures and other industrial facilities.

Case 2. Products Pipeline Distribution System for the Venezuela Andean Region (SUMANDES)

Contribution of Individual Seismic Sources

Fig. 6 indicates the percentage contribution of each seismic source. The Boconó fault is responsible for 80% of the total seismic hazard of the area, followed by the San Simón and Piedmont faults, with 11% and 7%, respectively.

Expected Peak Ground Accelerations

The seismic hazard was evaluated at different sites of interest: El Vigía (Sumandes), Mérida, Bajo Grande, Cabimas, San Lorenzo, and the mouth of Chama River. Fig. 7 shows the peak acceleration with the annual excess probability and the return period related to it. The maximum risk sites were found in Mérida and El Vígia, as was expected due to the vicinity of the Boconó fault.

A more rigorous assessment of earthquake risk were made in the El Vigia area due to the existence of a distribution plant. Design response spectra and synthetic accelerograms to be used for the seismic design of facilities were prepared.

The adoption of a excess probability of 10% in 50 years yields the design horizontal acceleration of 0.23 g for the El Vigía site. The design horizontal acceleration for the other sites of interest varies from 0.16 g to 0.18 g.

Seismic hazard evaluation for Stage II of the project

The complex tectonic setting of the section of the Stage II pipeline (El Vigía - Murachi) and the location of the final distribution plant require a detailed study of the active faults and geotecnical hazards particularly landslides and liquefaction. Field work, including geological trenching, now in progress, will give information about the geometry and seismic potential of the existing faults.

Detailed geotechnical and geophysical studies, already completed will give the information required to evaluate the geotechnical hazard.

Case 3. The Paraguaná Refinery Complex

An extensive seismicity study of the Paraguaná península and surrounding areas was initiated with a microseismicity survey using 60 portable and high gain digital seismological stations. The data acquisition was done for a three month period early in 1990. Processing and interpretation is now in progress.

Recent tectonics are also being evaluated through field work including a trenching in Oca fault, one of the most important in the area.

CONCLUSIONS AND RECOMMENDATIONS

Case 1. The Coastal Protection System, Lake Maracaibo

The coastal dykes are located in a moderate seismic risk environment, mainly due to the possibility of liquefaction of a fairly loose, saturated, silty sand layer in the foundation soils.

A peak ground acceleration of 0.28 g was estimated for a return period of 3000 years.

The results of this study led to the implementation of mitigation measures (downstream berms, and, in some cases, compaction piles) to reduce the failure potential and to increase the return period of the design earthquake to about 3000 years, typically used worldwide for design of earth dams in seismic areas.

Case 2. Products Pipeline Distribution System for the Venezuelan Andean Region (SUMANDES)

Preliminary seismic risk evaluation for the Phase I of the pipeline system for the Venezuelan Andean region has been made. Seismic risk analysis is planned for future works, including: analysis for reliability of the network system; analysis for seismic hazard losses; vulnerability analysis; and analysis for system performance.

It is of critical importance to continuously improve the seismogenetic parameters through field observations, seismic data recording and theoretical and mathematical modelling in order to reduce the currently existing uncertainties. The permanent automatic seismological and strong motion networks can supply, in the near future, very valuable information.

Case 3. The Paraguaná Refinery Complex

As it was mentioned in this paper, a seismic vulnerability study is under way. The final conclusions will be presented after results are analyzed and evaluated.

BIBLIOGRAPHY

1.- **Murria, and Abi Saab J.**, Engineering and Construction in Areas Subjected to Subsidence Due to Oil Production; 5th Int. (FIG) Symp. on Deformation Measurements and 5th Canadian Symp. on Mining Surveying and Rock Deformation Measurements, Fredericton, N. B., Canada, 1988, pp. 367-373.

2.- **James K.H.**, Venezuelan Hydrocarbon Habitat, Report EPC-10236, Maraven S.A., Caracas June 1986.

3.- **Dewey J.W.**, Seismicity and Tectonics of Western Venezuela, B.S.S.A., v62, n6, 1711-1751, December 1972.

4.- **Grases, J.**, Investigación sobre los Sismos Destructores que Han afectado El Centro y Occidente de Venezuela, INTEVEP S.A., Caracas, Septiembre 1980

5.- **Stepp J.C.**, Analysis of Completeness of the Earthquake Sample in the Puget Sound Area and Its Effect on Statistical Estimate of Earthquake Hazard. Proceedings of the International Conference on Microzonation for Safer Construction Research and Application, v. 2, pp. 897-906.

6.- **Molnar P.**, Earthquake Recurrence Intervals and Plate Tectonics, B.S.S.A., v. 69, n1, 115-133, August 1979.

7.- **Utsu, T. and A. Seki**, A Relation Between the Area of Aftershock Region and the Energy of Main Shock. Journal of the Seismological Soc. of Japan, v. 7, 233-240, 1954.

8.- **Murphy J.R., and L.J. O'Brien**, Analysis of Worlwide Strong Motion Data Sample to Develop an Improved Correlation between Peak Acceleration, Seismic Intensity and other Physical Parameters. U.S. Nuclear Regulatory Commission, January 1978.

TABLE 1. Seismogenetic characteristics of evaluated faults.

Fault	Length (kms)	Maximum Credible Ms	Return Period (years)	Fault Segment	Length (Kms)	Maximum Probable (Ms)	Return Period (years)	Slipping rate (mm/years)	Type of movement	Relation vert/horiz. components
Boconó	600	8	Improbable event	North of Mérida	400	7.8	> 350	9	Dextral	Horiz. very dominant
				South of Mérida (2 segments)	110 x 2	7.3	≥ 110	5.5-7.5	Dextral	Horiz. dominant vertical noticeable
Tuñame	50	6,8	> 100,000-200,000	NE Timotes	30	6.4	800-1600	0.5-1	Normal	Vertical very dominant Horiz. very small
				SW Timotes	20	6.5	> 100,000-200,000	?	Dextral(?) Normal	Horiz. dominant ?
Valera South of Valera	50-75	6,9-7	> 10,000-20,000	Páramo Miranda	25-50	6.4-6.9	> 10,000-20,000	< 0.1	Sinestral	Horizontal equivalent to vertical
				Valle Momboy	30	6.7	> 1600-5000	≤ 0.7	Normal	Normal
Valera North of Valera	100-125	7,2-7,3	> 15,000	Southern half	60	6.9	≥ 1500	1	Sinestral	Horizontal very dominant
				Northern half	60	6.9	> 15000 ?	Variable		
Piñango	25	6,4	≥ 1500	Piñango	25	6.4	≥ 1500	0,4-0,6	Dextral	Horizontal very dominant
Piedemonte	120	7,4	10,000-17,000	Piedemonte 1/2 North	60	7	7,000-12,000	0.15-0.25	Inverse	Vertical very dominant
Burro Negro	50		> 80,000-100,000	Burro Negro	30	6.6	80,000-100,000	≤ 0.01	Normal	Vertical very dominant
Mene Grande		7		Mene Grande	25	6.5	≥ 16,000-20,000	0.05	Vertical	Vertical very dominant

586

TABLE 2. Most destructive historical earthquakes on the region
since 1610.

No.	DATE	LOCATION	MMI	COORDINATES N - W	
1	1610-02-03	LA GRITA	IX	8.3	71.8
2	1775-12- ?	TRUJILLO	VII	9.3	70.4
3	1786- ?- ?	MERIDA	VII	8.5	71.2
4	1812-03-26	MERIDA	IX	8.5	71.3
5	1812-03-26	SAN FELIPE	IX	10.2	69.1
6	1849-02-26	LOBATERA	VIII	7.92	72.24
7	1870-06-26	EL TOCUYO	VII	9.80	69.85
8	1875-05-18	CUCUTA	IX	7.90	72.50
9	1886-09-29	TRUJILLO	VII	9.30	70.40
10	1888-11-17	GUANARE	VII	9.20	69.90
11	1894-04-28	MERIDA	IX	8.50	71.70
12	1894-11-04	CARACHE	VII	9.67	70.25
13	1910-03-22	MAPARARI	VII	10.87	69.45
14	1910-08-04	BOCONO (WCA)	VII	8.70	70.90
15	1912-06-21	GUANARE (WCA)	VII	9.20	70.10
16	1926-10-11	MERIDA (WCA)	VII	8.60	71.10
17	1929-03-16	RIO CLARO(WCA)	VII	9.90	69.39
18	1932-03-14	LA GRITA	VIII	8.29	71.88
19	1942-09-02	HUMOCARO ALTO	VII	9.61	69.99
20	1950-07-09	ARBOLEDAS	IX	7.79	72.59
21	1950-08-03	EL TOCUYO	IX	9.74	69.83
22	1956-11-16	LA PROVIDENCIA	IX	8.20	71.23
23	1959-06-30	ARICAGUA	VII	8.30	71.23
24	1965-07-19	LAS MESITAS	VII	9.20	70.28
25	1966-09-09	CHURUGUARA	VIII	10.87	69.38
26	1967-07-29	BETULIA	VIII	6.84	73.09
27	1970-06-14	LA MONTANA	VIII	10.90	69.08
28	1972-12-18	BUENOS AIRES	VIII	9.60	70.10
29	1975-03-05	GUANARE	VII	9.13	69.87
30	1975-04-05	SAN PABLO	VIII	10.08	69.65
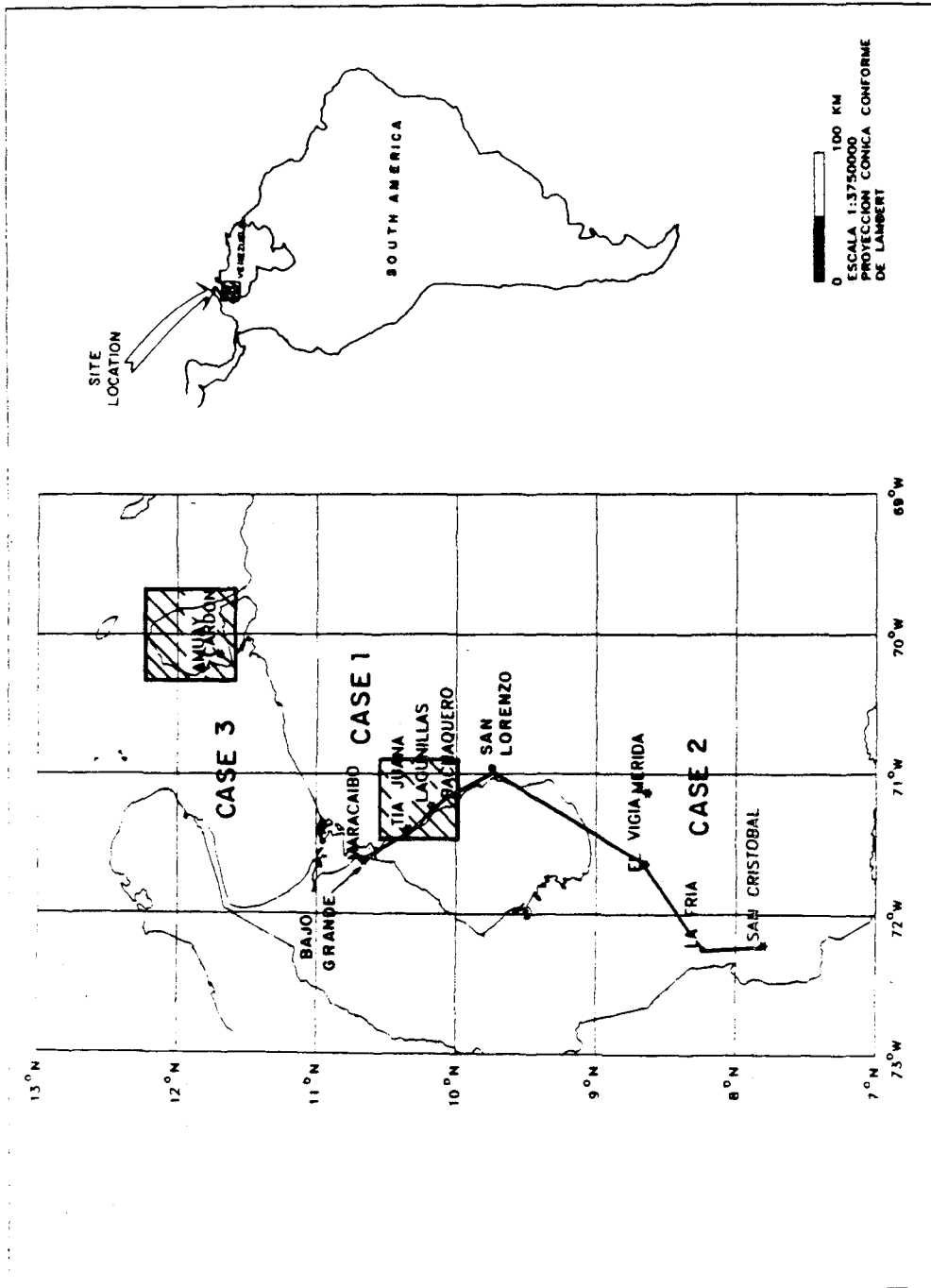
Fig. 1 Area of interest, (Western   Venezuela)

COASTAL DIKES: 47 km
INNER DIKES: 59 km
DRAINAGE CHANNELS: 490 km
PUMPING CAPACITY: 291000 m³/hr

MARACAIBO LAKE
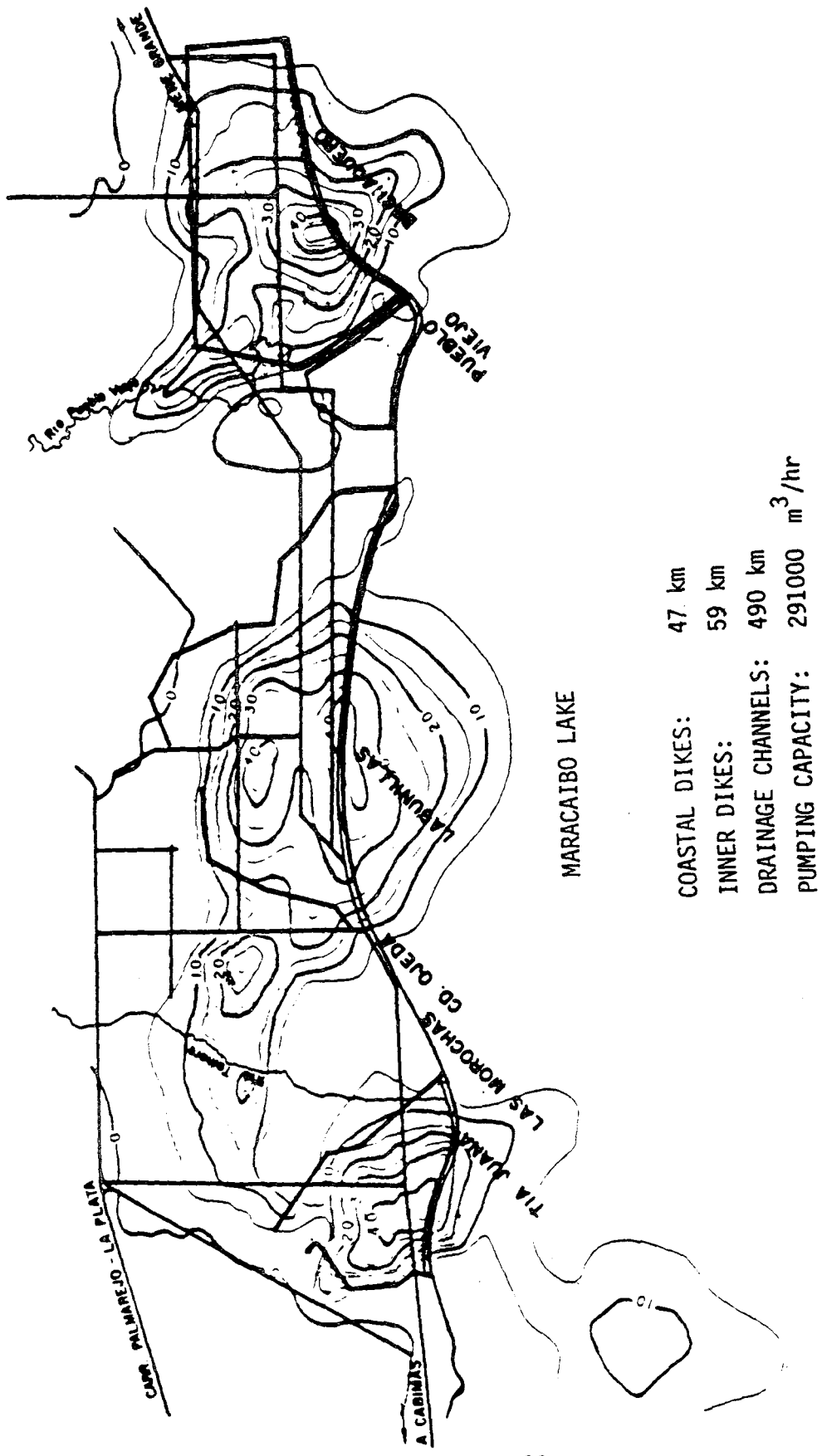
Fig. 2   Subsidence features of the Lagunillas, Tia Juana, and Bachaquero polders.

Fig. 3 Active faults in the region of interest.
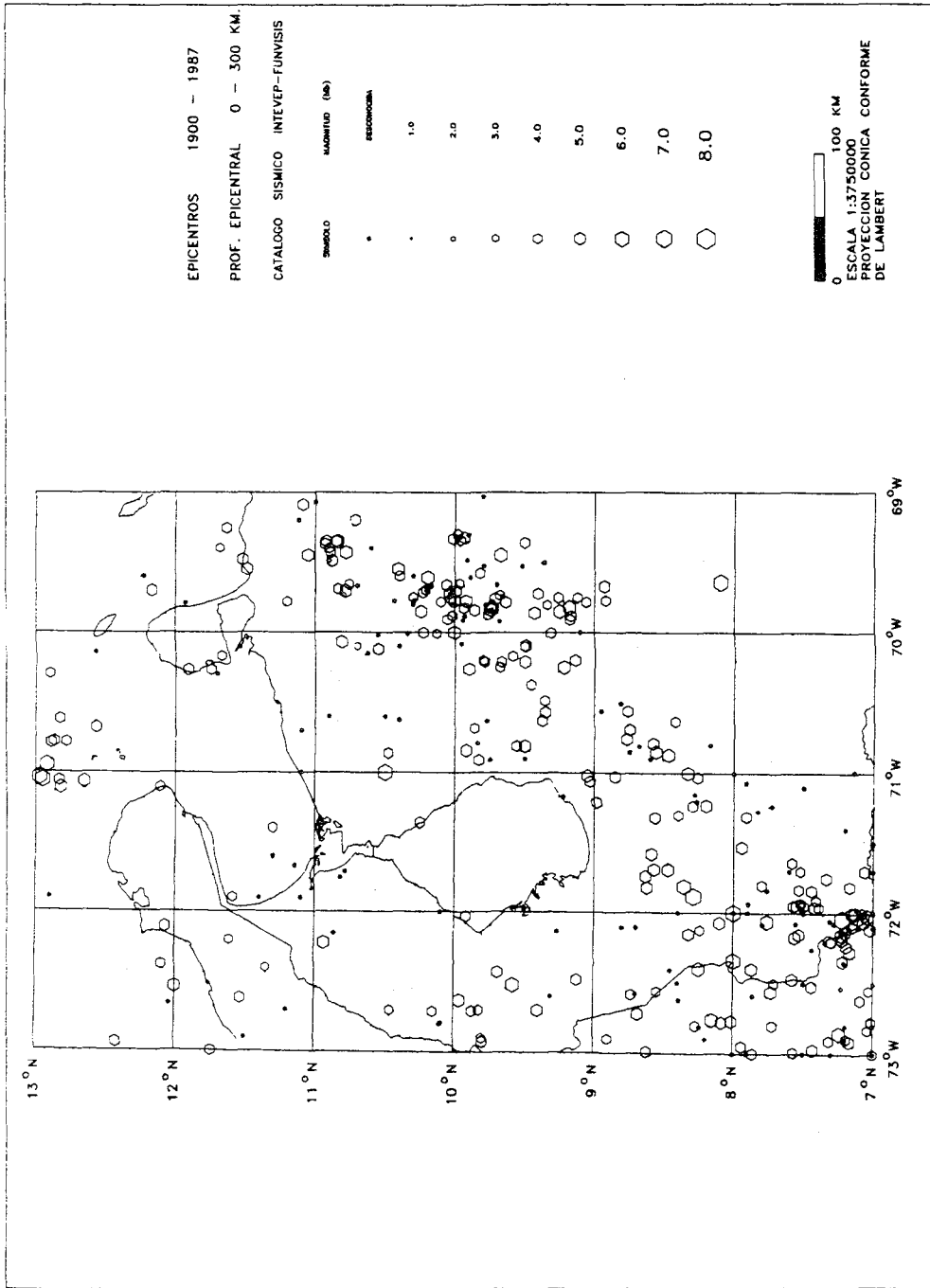
Fig. 4   Seismicity of the area. Earthquake magnitudes are
represented with symbols of different sizes.

591
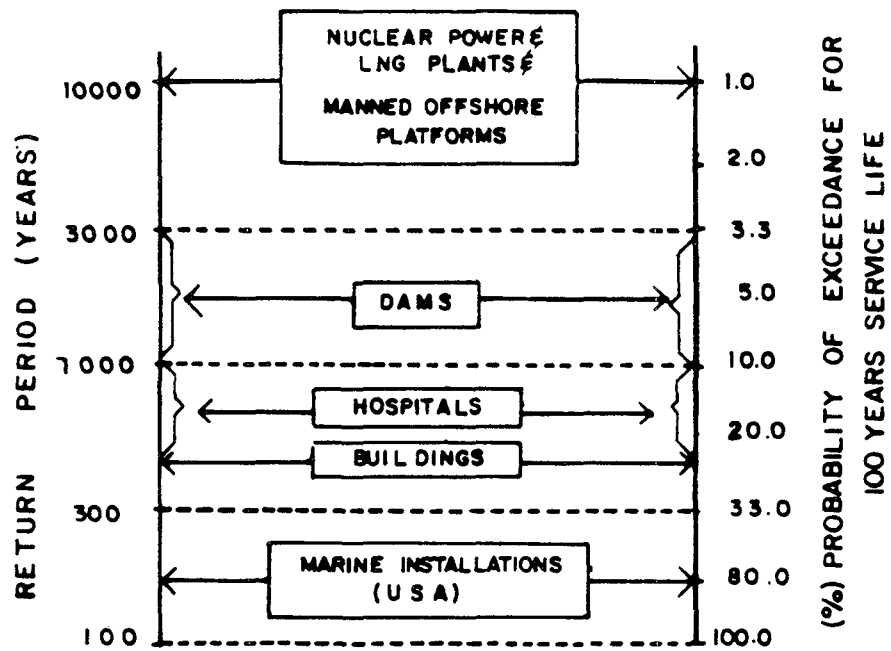
Fig. 5 Most common acceptable risk criteria for different
structures and industrial facilities.
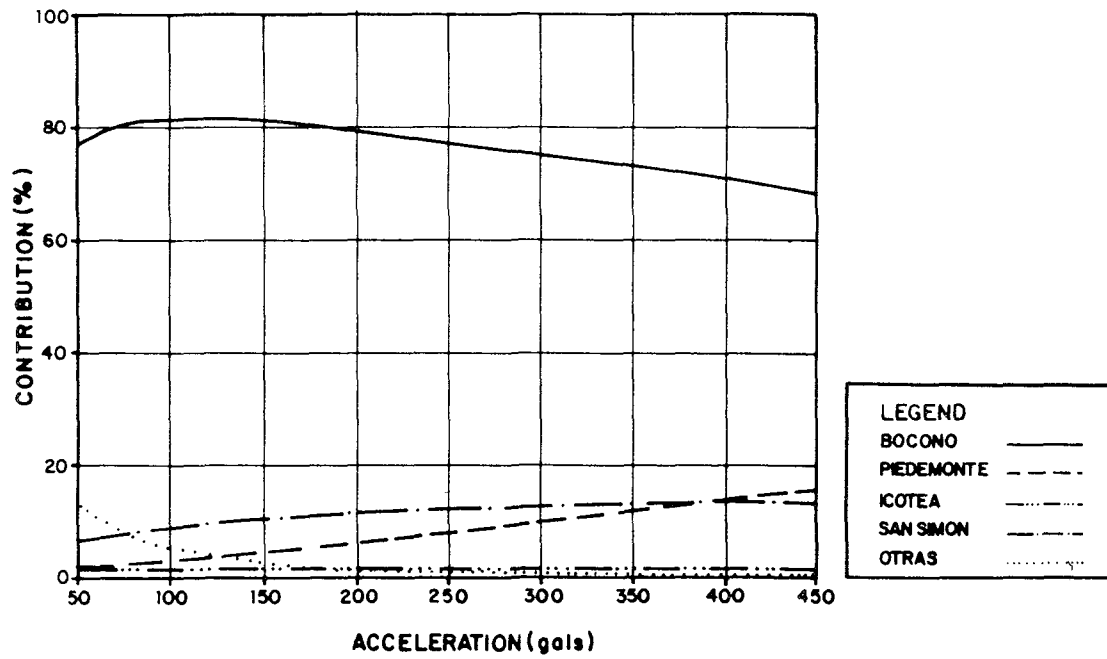
Fig. 6 Percentage contribution of each seismic source
El Vigía site (SUMANDES).
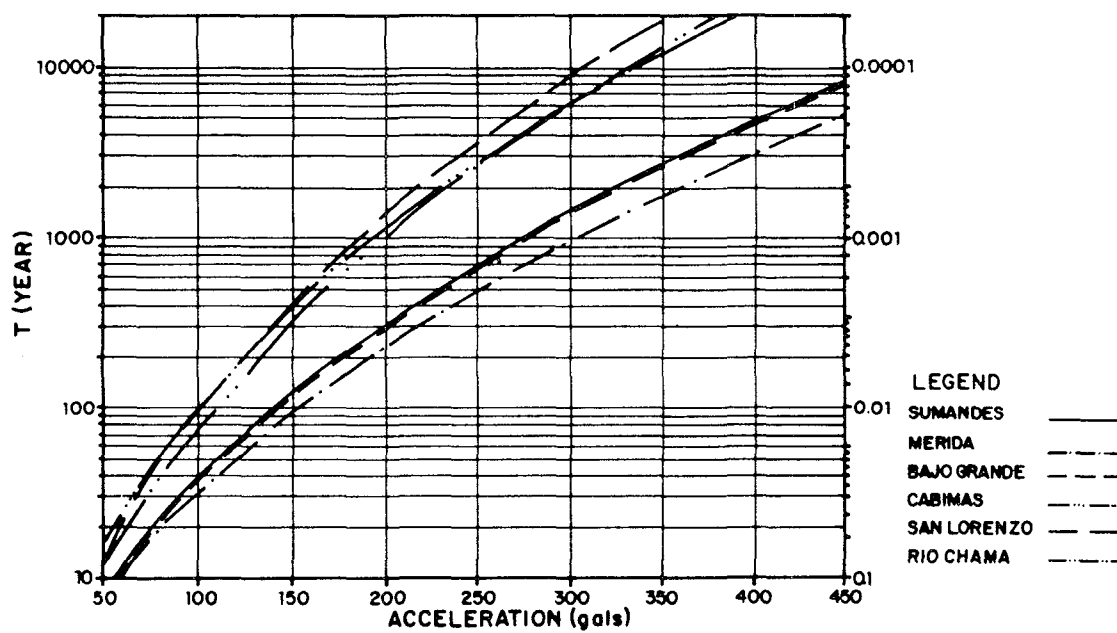
Fig. 7 Peak acceleration with the annual excess probability and return period.

ASEISMIC BASE ISOLATION DEVICE
USING HIGH-DAMPING LAMINATED FERRITE RUBBER

Hideyo SUZUKI

Engineering Research Center, Tokyo Electric Power Company

Nishi-tsutsujigaoka, Chofu, Tokyo 182

ABSTRACT

This paper is divided into two parts; at first I will describe comprehensive investigation of various kinds of base isolation systems, and next I will present a newly developed high-damping laminated ferrite rubber device.

In the first part, I will describe that optimum characteristics exist separately for three kinds of base isolation systems from a point of view of high reduction of response acceleration and moderate relative displacement due to base isolation systems.   Quantitative solutions of equations of movement and energy are presented in this paper for elasto-plastic, frictional and viscous type base isolati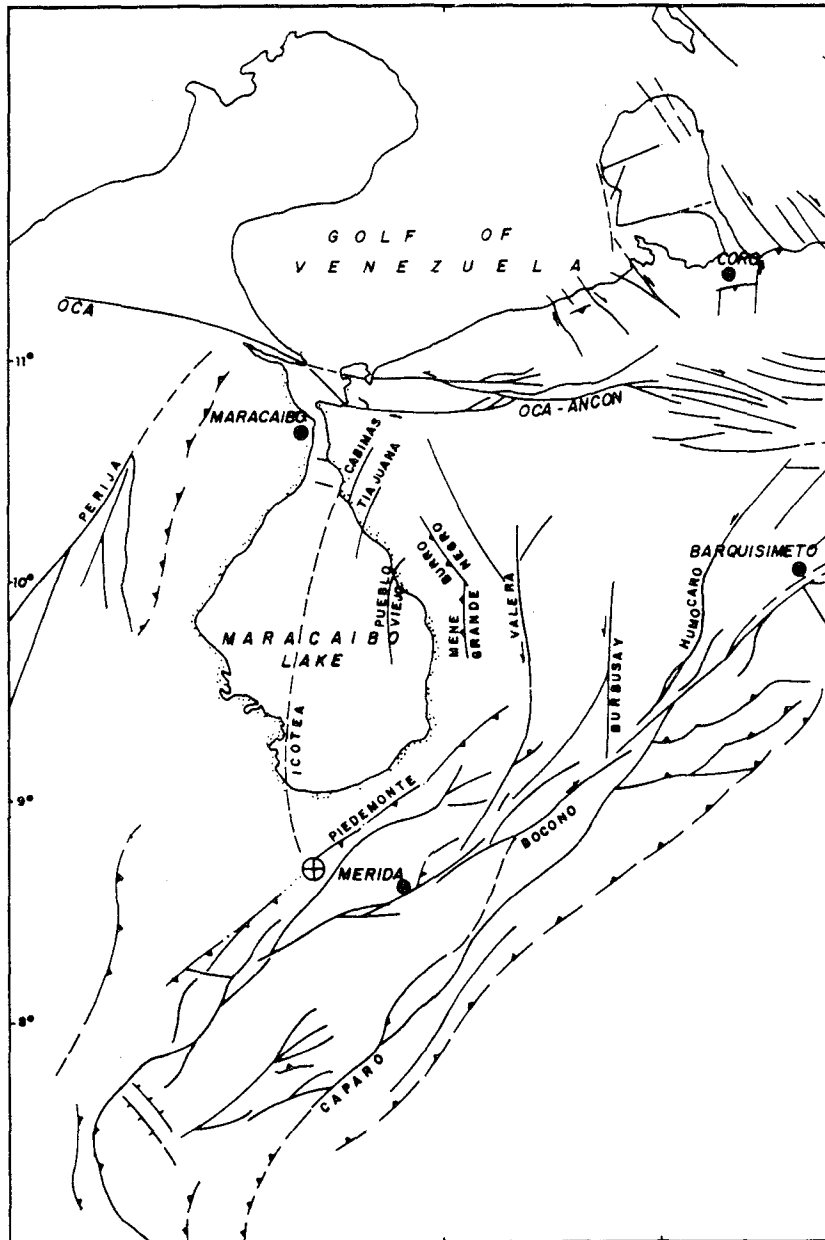on systems with various input wave patterns which can be expected to occur at major different types of ground conditions.   Comprehensive characteristics of general base isolation systems are shown and the presented data are available for designers in decision of base isolation method and for basic design.

In the second part, newly developed high-damping base isolation device using ferrite rubber is presented.   This new device successfully enables soft horizontal spring and high critical damping ratio over 10%, and sufficient stability in terms of temperature, vertical load, input wave frequency and so on, and durability can be expected in long term.

INTRODUCTION

Many structures both in Japan and United States, mainly buildings, have been already constructed adopting base isolating system so far. It seems that in those structures, all of possible methods for base isolation systems have appeared up to now; i.e., elasto-plastic, frictional and viscous types. When those designs were carried out, it seems that development of devices for base isolation systems and individual case studies were precisely done according to the desired specifications and the conditions of the grounds and seismicity of each construction site. On the other hand, we lack comprehensive study of isolation systems, concerning selection of methods for the system, expected input wave conditions, dynamic characteristics of upper structures and so on. Due to the lack of those knowledge, we can not examine whether the obtained designs of existing base-isolated structures are really optimal by using our past knowledge.

The author and his group have been studying optimum base isolation systems for electric power facilities aiming at establishment of rational countermeasures for earthquake proof. In the past authors' activity, frictional type base isolation devices has been selected for developing isolation devices for transformers in substation, because of its moderate relative displacement[Ref. 1 and 2]. And, fundamental examinations, including in-situ earthquake observation by means of actual transformer weighing about 200 tons, have been completed to make sure of its function.

This paper will describe basic consideration of base isolation systems at first, in which I will show the most desirable design parameters for each kind of of base isolation systems, i.e., elasto-plastic, frictional and viscous system, in order to obtain optimum base isolation function regarding response of dynamic systems[Ref. 3]. And next, I will present some characteristics of a newly developed high-damping laminated rubber i-solation device using ferrite-mixed rubber.

BASIC CONSIDERATION OF BASE ISOLATION SYSTEM

Basic consideration of aseismic base isolation system will be described in terms of fundamental characteristics of various kinds of base isolation systems, so as to recognize the optimum design parameters for any kinds of structures at any ground conditions. The results of the consideration might be helpful for the selection of method of base isolation devices and for the decision of specification for newly developing devices. This consideration was carried out using analytical method as follows.

Method of Analysis

Analytical model used in this study consists of one mass model with natural period of fist order of the upper structure of 0.25 second, and base isolation device installed under the upper structure, as shown in Figure 1. The base isolation devices paralleling combined systems with restoring spring and energy absorbing elements; the energy absorbing elements

are elasto-plastic, frictional and viscous systems. The restoring characteristics combined with energy absorbing elements are as shown in Figure 2. In this paper, balance of energy within the isolation systems is concerned so as to study how to maximize the consumed energy in the absorbers of the base isolation devices. Equations of motion and energy for each systems are as shown in Figure 2; and calculation for responses of the systems are carried out by linear acceleration method.
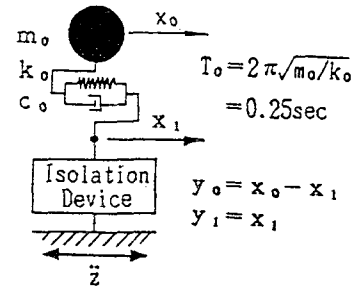

Figure 1 Analytical Model

Equation of Motion

a) Elasto-Plastic Systems

$$m_0\ddot{x}_0 + c_0(\dot{x}_0 - \dot{x}_1) + k_0(x_0 - x_1) = -m_0\ddot{z}$$
$$c_0(\dot{x}_0 - \dot{x}_1) + k_0(x_0 - x_1) = Q(x_1, t) \tag{1}$$

$Q(x_1, t)$: Restoring Force of Total Device

b) Frictional Systems

During "Fix"

$$m_0\ddot{x}_0 + c_0\dot{x}_0 + k_0(x_0 - x_1) = -m_0\ddot{z}$$
$$|c_0\dot{x}_0 + k_0(x_0 - x_1) - k_2x_1| \leqq Fr \tag{2}$$
$$x_1 = const. \quad , \quad \dot{x}_1 = 0$$

During "Slip"

$$m_0\ddot{x}_0 + c_0(\dot{x}_0 - \dot{x}_1) + k_0(x_0 - x_1) = -m_0\ddot{z}$$
$$c_0(\dot{x}_0 - \dot{x}_1) + k_0(x_0 - x_1) = k_2x_1 + Fr \cdot sgn(\dot{x}_1) \tag{3}$$
$$|c_0\dot{x}_0 + k_0(x_0 - x_1) - k_2x_1| > Fr$$

k_2, Fr: As defined in Fig.-2

c) Viscous Systems

$$m_0\ddot{x}_0 + c_0(\dot{x}_0 - \dot{x}_1) + k_0(x_0 - x_1) = -m_0\ddot{z}$$
$$c_0(\dot{x}_0 - \dot{x}_1) + k_0(x_0 - x_1) = C\dot{x}_1 + k_2x_1 \tag{4}$$

k_2, C: As defined in Fig.-2

Equation of Energy

$$\underbrace{\int_0^t m_0\ddot{x}_0\dot{x}_0 dt}_{E_1} + \underbrace{\sum\int_0^t c_i\dot{y}_i\dot{y}_i dt}_{E_2}$$

$$+ \underbrace{\sum\int_0^t k_i y_i\dot{y}_i dt}_{E_3} + \underbrace{\int_0^t Q(x_1, t)\dot{x}_1 dt}_{E_4} = \underbrace{-\int_0^t m_0\ddot{z}\dot{x}_0 dt}_{IE} \tag{5}$$

E_1: Energy of Motion
E_2: Absorbed Energy due to Upper Structure
E_3: Elastic Energy of Restoring Spring
E_4: Absorbed Energy due to Absorbing Element
IE: Input Energy

(a) Elasto-Plastic

$$q_y = Q_y/m_0 g$$
$$T_1 = 2\pi\sqrt{m_0/K_1}$$
$$T_2 = 2\pi\sqrt{m_0/K_2}$$

(b) Frictional

$$\mu = Fr/m_0 g$$
$$T_2 = 2\pi\sqrt{m_0/K_2}$$

(c) Viscous

$$h = C/2\sqrt{m_0 K_2}$$
$$T_2 = 2\pi\sqrt{m_0/K_2}$$
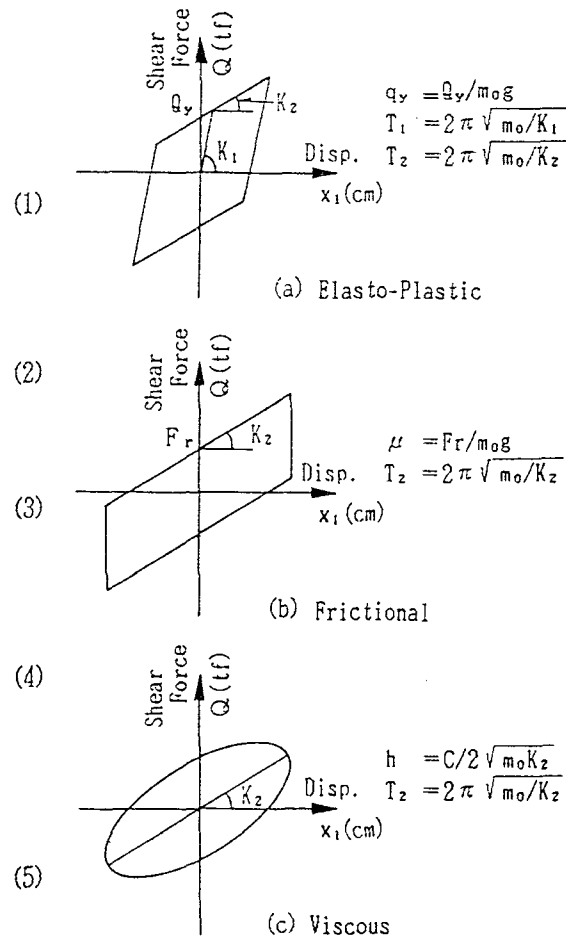
Q_y : Yielding Shear Force
q_y : Non-dimensional Shear Foece
K_1, K_2 : Restoring Stiffness
Fr : Frictional Force
μ : Coefficient of Friction
C : Coefficient of Damping (Isolation Device)
h : Equivalent Damping Factor

Figure 2 Characteristics of Three Kinds of Isolation Systems

597

Input acceleration waves used in this study are three kinds of waves for representative three kinds of ground, synthesized by spectrum fitting method.　When input waves were synthesized, real phase characteristics of three observed waves were used, referring standard spectra which appear in the Japanese conventional design code for road bridges as shown in Figure 3.　As the real observed waves, Kaihoku Bridge TR 1978, El Centro NS 1940 and Hosojima 1968 are selected for Group 1, 2/3 and 4, respectively.　The synthesized input waves are as shown in Figure 4.
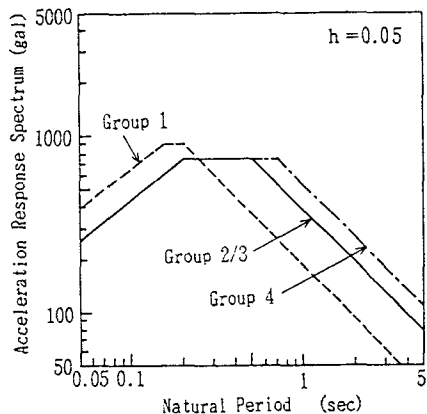
Figure 3　Acceleration Response
Spectrum
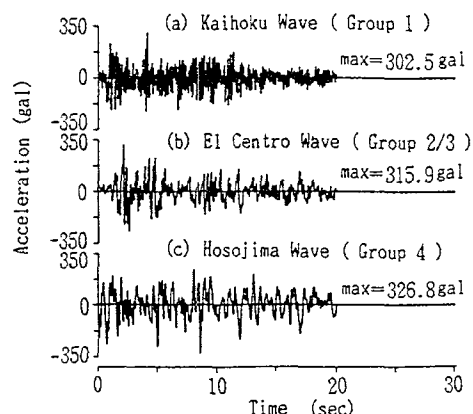
Figure 4　Synthesized Input
Waves Using Fig. 3

Results of Analyses

Results of analyses are as shown in Figure 5 through 7: in (a) through (b) series characteristics of each energy absorbing elements are selected as non-dimensional shear force q_y, coefficient of friction μ and modified damping ratio h, respectively; in (c) series Energy Absorption Ratio is defined as $[E_4]$ divided by [IE]; and in (d) series the characteristics is selected as T_2 defined in Figure 1.

a) Elasto-plastic Systems　Figure 5(a) and (b) show relations of q_y vs. maximum response acceleration and displacement in the case of T_1=1.0 second and T_2 = 2.0 seconds.　Maximum response acceleration curves show that minimum value appears at q_y is nearly 0.4 for every input wave.　Maximum relative displacement is almost constant in the region that q_y is larger than 0.04 for every input wave.

Figure 5(c) is relation of q_y vs. energy absorption ratio, showing that maximum values exist almost at the same position as minimum response acceleration as shown in Figure 5(a) in the region of q_y = 0.02 - 0.04.　Those results mentioned above suggest that optimum design using elasto-plastic method can be made if the parameter q_y is appropriately selected, and the appropriate q_y value is slightly larger, as the ground comes to softer. Figure 5(d) is relation of T_2 vs. response acceleration, maximum relative displacement and residual relative displacement, in which q_y is selected as almost optimum value of 0.04; and T_2 is as defined in Figure 1, using modified El Centro wave.　This figure shows that maximum relative dis-

placement has minimum value at T_2 is 2.0 seconds, and that response acceleration decreases simply as T_2 becomes larger.

As stated above, both response acceleration and relative displacement can be moderately designed in actuality, if T_2 is selected to be 2.0 seconds which is currently adopted in many base isolated buildings.

b) **Frictional Systems**   Figure 6(a) and (b) show relation of μ vs. maximum response acceleration and displacement in the case of T_2 = 2.0 seconds. Maximum response acceleration curves show that minimum value appears at μ is 0.04 through 0.08 for each input wave.   And, each minimum value is almost one quarter compared with non-isolated value which is the same ratio of elasto-plastic and viscous systems.   Maximum relative displacement can be decreased as μ comes to be larger, which means that relative displacement can be controlled as low as a desired value in frictional system if μ is selected adequately.

Figure 6(c) is relation between μ and energy absorption ratio, showing that maximum value exists almost at the same position as minimum response acceleration as shown Figure 6(b) in the region of μ = 0.04 through 0.08. Figure 6(d) is relation of T_2 vs. response acceleration and maximum relative displacement and residual relative displacement, in which μ is selected as almost optimal value of 0.06, using modified El Centro wave.   This figure shows that maximum relative displacement has maximum value at T_2 is 1.5 seconds, and that response acceleration decreases in simple manner as T_2 becomes larger.

As stated above, both response acceleration and relative displacement can be designed in an ideal way, if T_2 is selected to be 1.5 through 2.0 seconds and μ is selected to be 0.04 to 0.08.   But μ value of 0.08 to 0.12, which is able to obtain in real frictional devices easily, is considered to offer effective base isolation function.

c) **Viscous Systems**   Figure 7(a) and (b) show relation of h vs. maximum response acceleration and displacement in the case of T_2 = 2.0 seconds. Maximum response acceleration curves show that they are almost constant in the region that h is larger than 0.02, which means that response accelerations are not keenly effected by the parameter of h in that region. Maximum relative displacement is slightly decreasing in the region that h is larger than approximately 0.2.   Figure 7(c) shows that energy absorption ratio is simply increasing as h comes to larger within h is under 1.0 region.   Figure 7(d), which is drawn under the condition of h=0.2, shows that maximum relative displacement increases as h comes to be larger.   No residual displacement can be seen after shaking in viscous system as expected.

Considering both response acceleration and relative displacement, it is suggested that h = 0.1 through 0.2 and T_2= 1.5 through 2.0 seconds are preferable to keep effective function of base isolation.
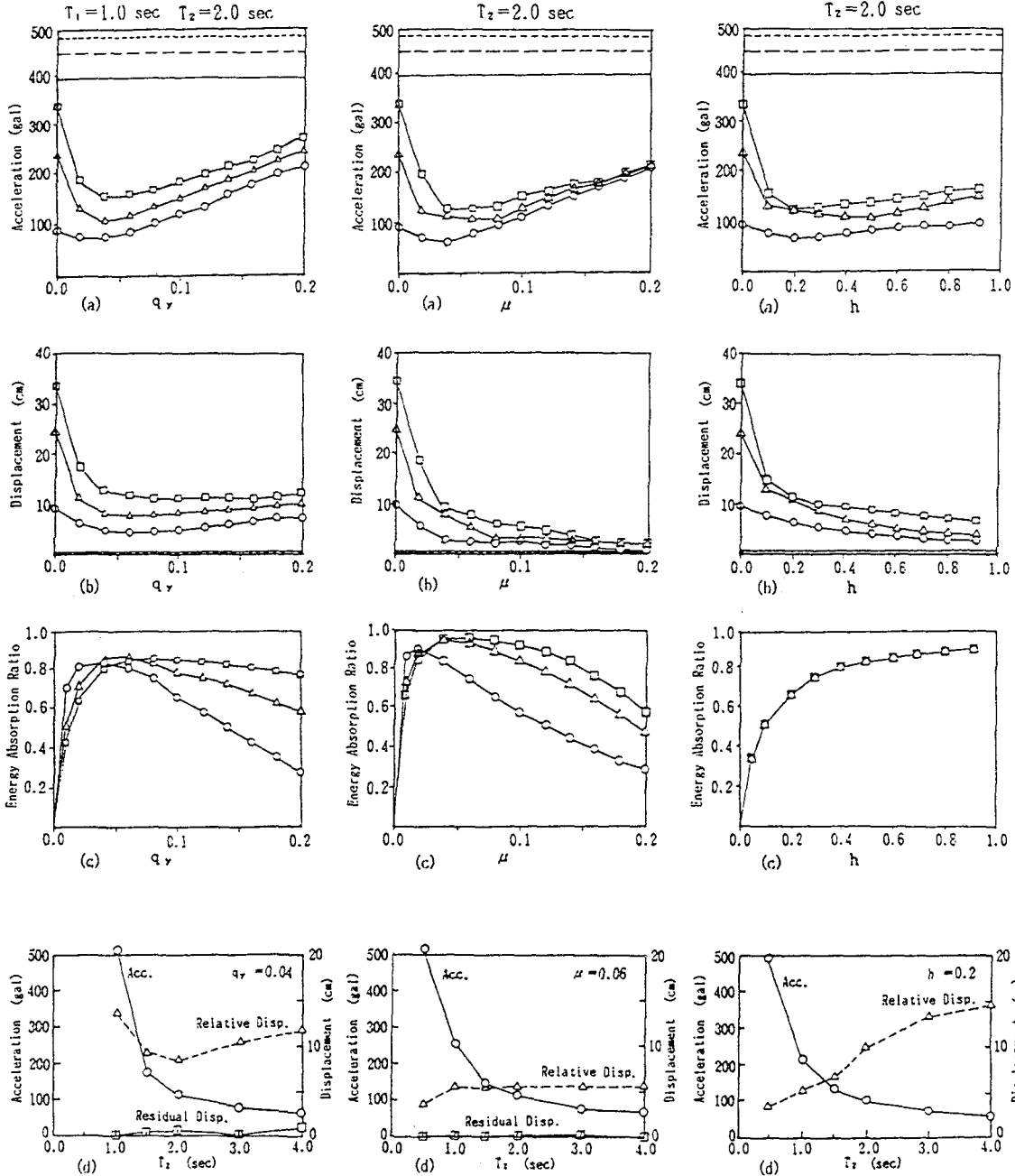
Figure 5 Result of Analysis (Elasto-plastic)

Figure 6 Result of Analysis (Frictional)

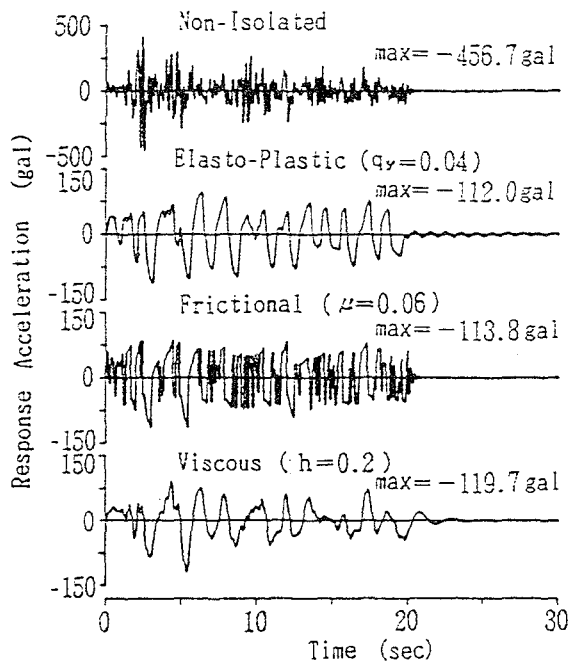Figure 7 Result of Analysis (Viscous)

600

Comparison of Response among Three Isolation Systems

Comparing study of response characteristics by three kinds of base isolation system have been carried out based upon the results by response analyses. In these analyses, common natural period of T_2 for each system was used, and parameters of energy absorbing devices were selected as thought to be optimal value in each method. The parameters adopted in the analyses were as follows: $T_1 = 1.0$ second, $T_2 = 2.0$ seconds and $q_y = 0.04$ for elasto-plastic system; $T_2 = 2.0$ seconds and $\mu=0.06$ for frictional method; and $T_2 = 2.0$ seconds and $h=0.2$ for viscous system, respectively. Analyzing model is as shown in Figure 1, and the input wave is synthesized El Centro which is the same as mentioned above.

Figure 8(a) shows response acceleration waves of the upper structures. It is notable that response acceleration waves of elasto-plastic and viscous systems contain almost no component of high frequency which appears in the input wave, and that, in the frictional system, strong acceleration part is restrained within a certain maximum value about 100 Gals and higher frequency component can be seen in the acceleration wave. As shown in Figure 8(b), in the frictional system "slip and fix" phenomenon appear alternatively, while in the elasto-plastic and viscous system displacement wave show continuous curves.

Relation between the maximum response value and the maximum input acceleration is shown in Figure 9(a) and (b). The results described in these figures can be understood if the hysteresis loops of displacement vs. resistant force for each damper are imagined in each point on the curves: i.e., in elasto-plastic system the loop has optimum area only when the input acceleration is moderate such as 100 to 300 Gals in which both K_1 and K_2 regions are used effectively; in the frictional system the loop has no area regions under input acceleration of about under 100 Gals and it works more effectively with stronger input acceleration; and in the viscous system the loop has sufficient enough area from weak to strong input acceleration.

Figure 10 is response spectrum of response acceleration waves as shown in Figure 8(a). Compared with non-isolated case, elasto-plastic and viscous systems show very low responses in the region of short period, though showing higher response in the long period region than non-isolated. In the frictional system, the response is higher than those of elasto-plastic and viscous, but it has no keen peak through the band shown in the spectrum.

Non-Isolated   max=−456.7gal

Elasto-Plastic (q_y=0.04)   max=−112.0gal

Frictional (μ=0.06)   max=−113.8gal

Viscous (h=0.2)   max=−119.7gal

(a) Response Acceleration

Non-Isolated   max=0.69 cm

Elasto-Plastic (q_y=0.04)   max=8.47 cm

Frictional (μ=0.06)   max=5.74 cm

Viscous (h=0.2)   max=10.00 cm
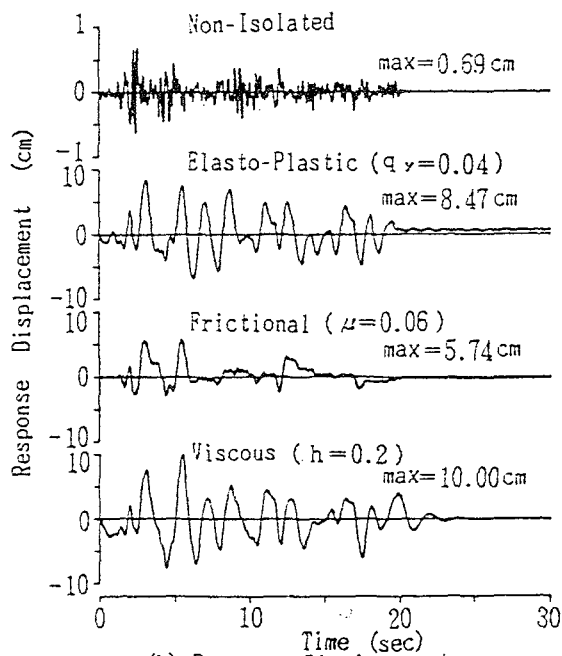
(b) Response Displacement

Figure 8 Response Waves

(a) Maximum Response Acceleration
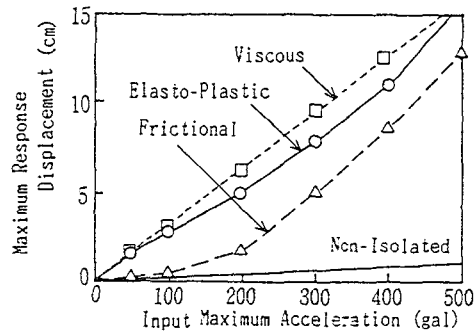
(b) Maximum Response Displacement

Figure 9 Relation between Input Maximum Acceleration vs. Maximum Response
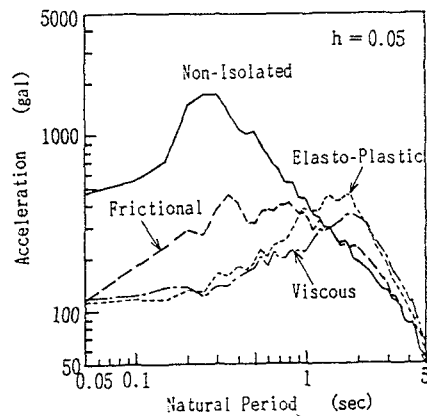
Figure 10 Acceleration Response Spectrum
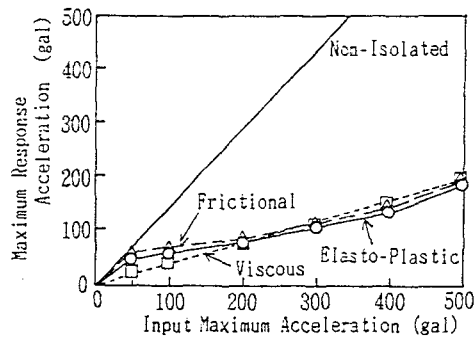
602

In this chapter I will present some features in developing procss of newly developed high-damping base isolation device using ferrite rubber. As mentioned above, base isolation system is essentially combination of a soft horizontal spring and a energy absorbing device. In the most of past actual base isolation systems, energy absorbing devices are installed besides isolators, whichis generally laminated rubber with low damping such as 3% or so. In order to complete simple constitution of base isolation system, many engineers have made efforts to develop a new material for high-damping rubber isolators. I and my group have paid attention to ferrite byproducts[Ref. 4], which is dumped from iron manufactures or electronic industries, for its fine characteristics of controlling vibration.
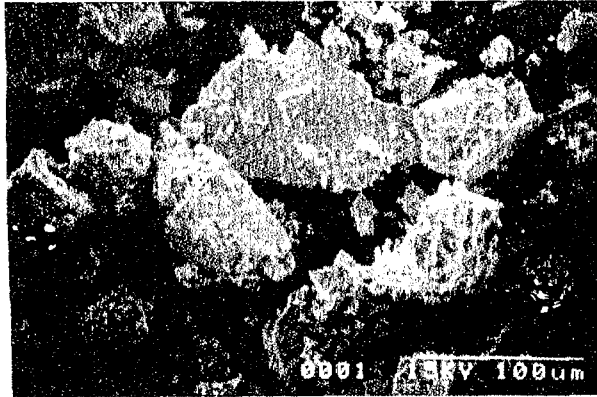
Photo 1 Electron Microscope Photo of Byproduct Ferrite

Before our developing activity, targeting damping ratio of the ferrite rubber was expected around 10%, according to our basic consideration of base isolation system as mentioned above. The system using high-damping ferrite rubber is categorized in the viscous method, and the damping ratio of about 10% is sufficient enough as actual base isolation system. The developing process and dynamic tests for those ferrite rubber were carried out as follows.

Material Test for Ferrite Rubber

Components of newly developed ferrite rubber are byproducted ferrite, natural rubber(NR) with synthetic rubber(NBR) and compounding ingredient such as vulcanizing agent, plastizer, antioxidant. A grain size accumulation curve of the ferrite used in this study is as shown in Figure 11, and electron microscope photo is as shown in Photo 1.

Mix proportion tests were carried out using Experimental Design Method, in which factors and levels are selected as shown in Table 1.
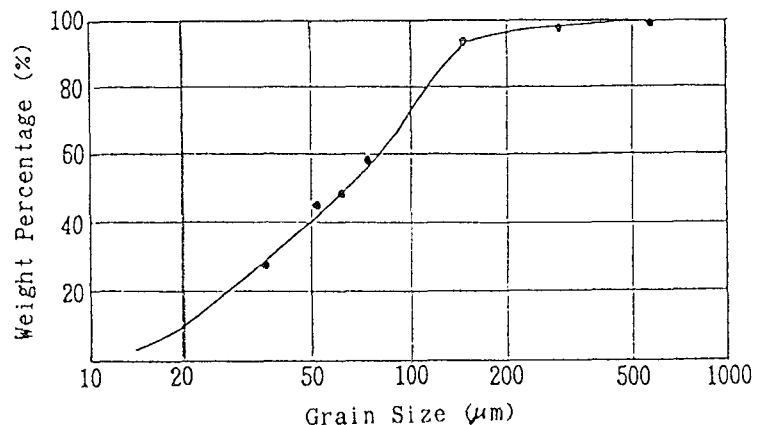
Figure 11   Grain Size Distribution of Ferrite

Table 1 Test Condition for Mix Proportion [Experimental Design Method]
Table 1 Test Condition for Mix Proportion [Experimental Design Method]
[Weight Percentage (%)]

	Level ⟶	1	2	3	4
F a c t o r	[A] Amount of Ferrite	100	200	300	400
	[B] Kind of Coating	Asph-1	Asph-2	Asph-3	--
	[C] Amount of Coating	0.0	1.0	2.0	3.0
	[D] Amount of Plastizer	32	48	--	--

In this test, strain amplitude level is restricted within 30% by means of Dynamic Mechanical Temperature Analyzer(DMTA). Major part of the testing equipment is as shown in Figure 12.

Results of the material tests are as shown in Figure 13 through 15.Figure 13 shows that amount of the ferrite by weight percent of 100 to 200 % gives the maximum damping ratio, and using this mix proportion, sufficient damping of about 10% can be success-fully obtained.
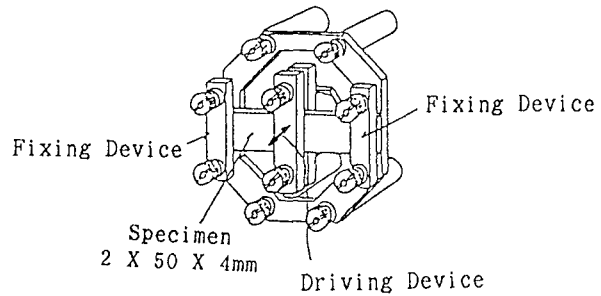
Figure 12 Major Part of DMTA

According to Figure 14, change of amount of the ferrite does not make effects on the strength of the ferrite rubber. And, Figure 15 suggests that dynamic characteristics are not keenly effected by the temperature difference, as far as it is used under usual circumstances.
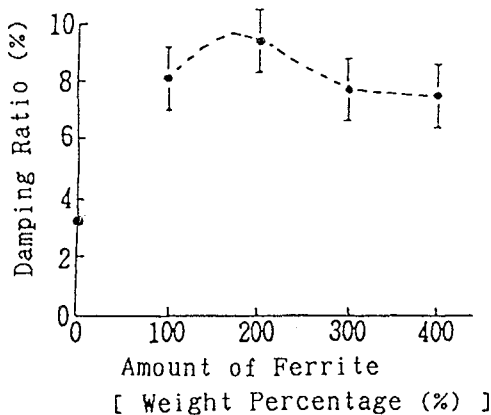
Figure 13 Relation between Damping Ratio vs. Ferrite Content
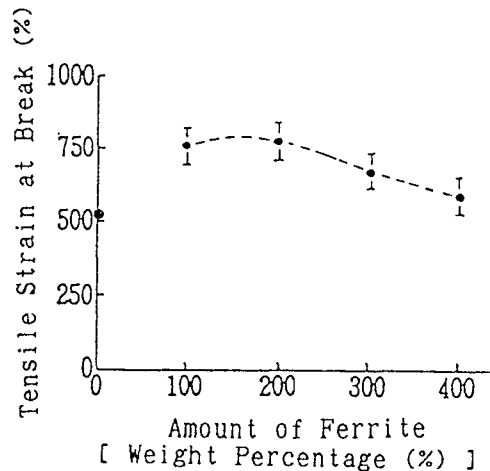
Figure 14 Relation between Strength vs. Ferrite Content
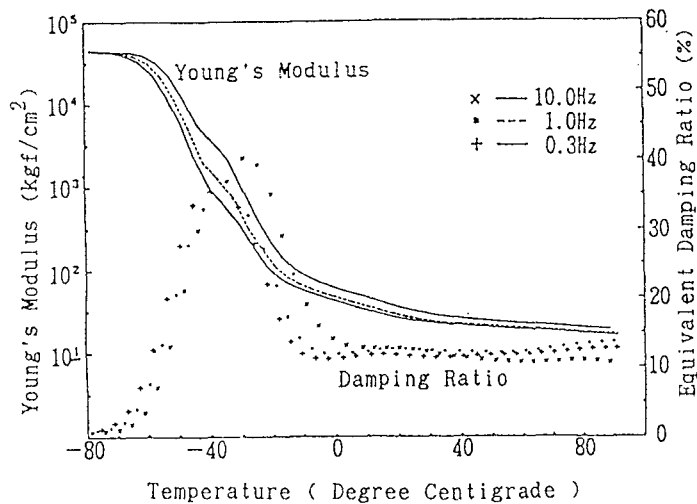
Figure 15 Dynamic Characteristics Effected by Temperature

Dynamic Characteristics of High-damping Ferrite Rubber Device

Generally speaking, laminated rubber is manufactured by vulcanization using thin crude rubber (natural or synthetic rubber) and steel disk plates. This manufactured rubber has a particular dynamic characteristics that shows very hard vertical spring constant, usually approximately 1000 times harder compared with horizontal spring constant.

We have tried to manufacture a laminated rubber with ferrite rubber as mentioned above. The drawing of the laminated ferrite rubber device for test is as shown in Figure 16. This device is designed to bear 30tf weight per a set, and the natural period of the total system is designed to be 2 seconds that gives about 0.3 tf/cm in horizontal spring constant. And the maximum horizontal displacement is 150mm that is equivalent to 125% shear strain of ferrite rubber. The test were carried out using a horizontal dynamic actuator with a vertical jack as shown Figure 17.
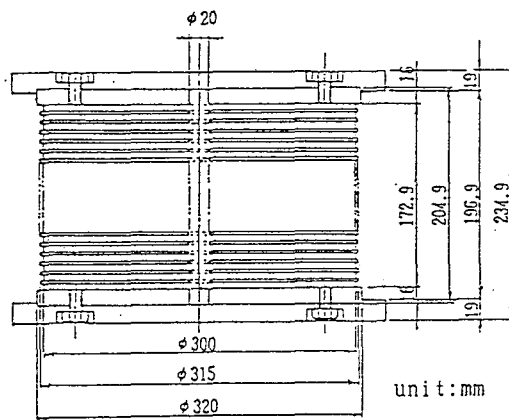
Figure 16 Outline of Laminated Ferrite Rubber Device for Test
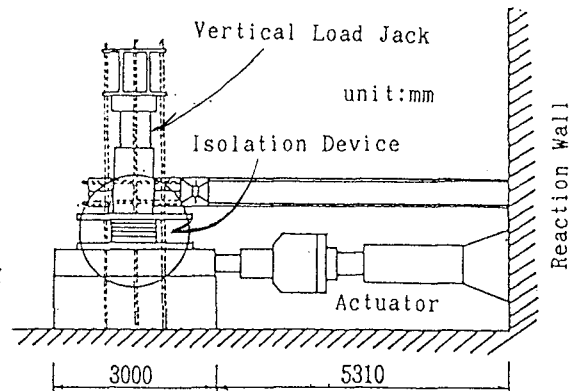
Figure 17 Testing Equipment for Dynamic Characteristics

605

Results of the dynamic tests are as shown in Figure 18 through 19. Figure 18 shows the comparison of hysteresis curve between ordinary natural rubber and ferrite rubber, in the case that vertical load is 30tf and that frequency is 0.5 Hz. While the laminated rubber device with ordinary natural rubber gives about 3% of equivalent damping ratio at the displacement of 150mm, the device with ferrite rubber gives 10.9% of damping.

Figure 19 shows the hysteresis curve of ferrite rubber in the case that horizontal displacement is 50mm, and that vertical load is 30tf. According to the change of the frequency, i.e., 0.25, 0.5 and 1.0 Hz, both spring constant and damping ratio make almost no change.

Testing equipment for creep shrinkage is as shown in Figure 20, and the result is as shown in Figure 21. This test was carried out for 30 days with 30tf compression force. Creep shrinkage after 60 years, estimated by extrapolation method, is 0.4mm for the ferrite rubber which is equivalent to 0.4% compressive strain of total thickness of the rubber.

(natural Rubber)   (Ferrite Rubber)
Figure 18 Hysteresis Curves of Laminated
Rubber Devices

Figure 19 Hysteresis Curve
of Ferrite Rubber
Effected by Frequency

Figure 20 Testing Equipment
for Creep Test

Figure 21 Result of Creep Test
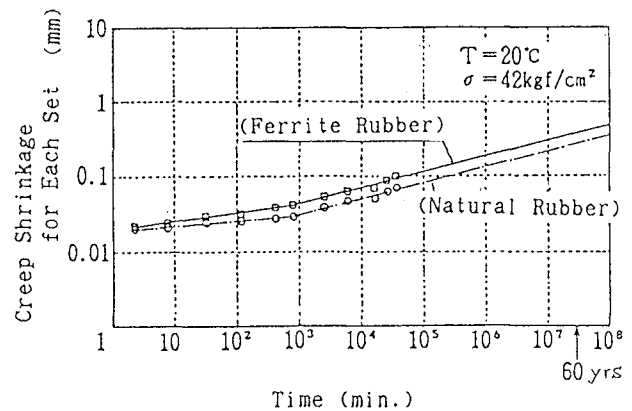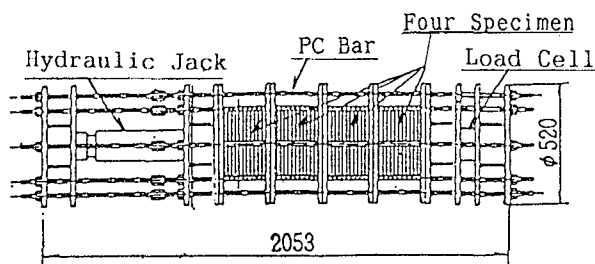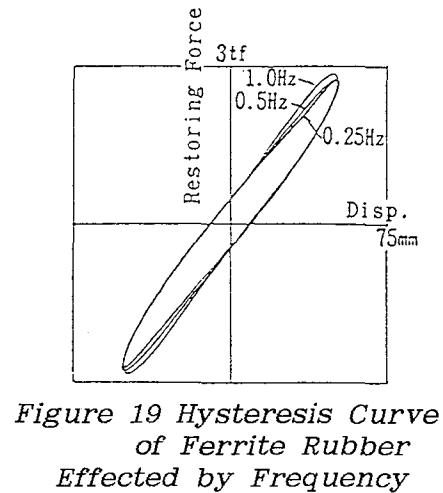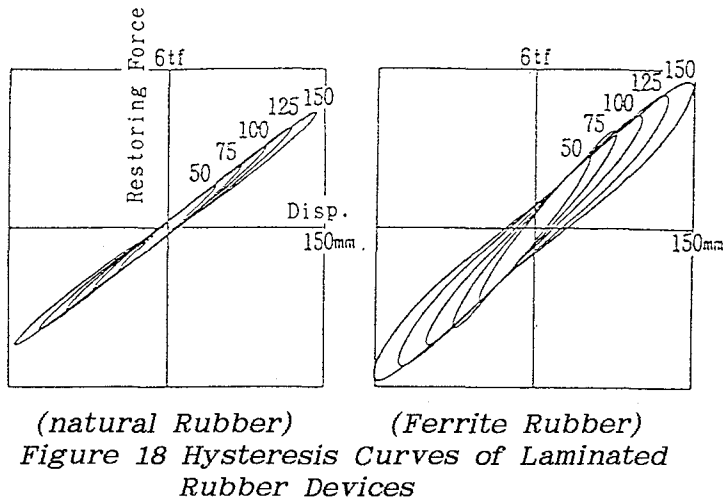
As the result of the test of both material and composed laminated rubber device tests, the followings are brought forth:

(a) Satisfactory damping ratio of over 10% can be obtained in ferrite rubber material when the weight percent ratio of ferrite to rubber is selected as 100 to 200 %. And this material shows moderate temperature dependence in dynamic characteristics within usual temperature.

(b) Using the ferrite rubber, laminated rubber device for isolation device can be successfully manufactured in terms of fundamental dynamic characteristics of frequency and vertical load; and durability.

CONCLUSION

Response characteristics of three kinds of base isolation systems have been studied from the point of view that they are compared impartially as far as possible. Those characteristics might be helpful for engineers in order to select the method of base isolation system and to decide some items of parameters of the devices for a certain requirement of facilities or structures at an installation site. More detailed consideration must be done when the final design is carried out, but those datum presented herein are available to comprehend the fundamental principal of general base isolation systems.

Based on updated base isolation technology, we have a need to develop a new type of high-damping laminated rubber isolator that has adequate specification according to the results of above mentioned comprehensive study, in order to make a base isolation device simple. One of the methods to attain the need, we have developed ferrite rubber material for laminated rubber.

Using those new knowledge and devices, adoption of base isolation technology for both industrial and private use is considered to be one of the reliable countermeasures for earthquake proof. In order to make spread the base isolation technology to many facilities and structures, much more available option of many kinds of devices and accumulation of actual effects at existing facilities are needed.

ACKNOWLEDGMENT

607

REFERENCES

1.   Horiguchi, J. et al.; "Development of an Aseismic Isolation Device for Electric Substation Equipment", Proc. 7th Japanese Symposium on Earthquake Engineering, Tokyo, 1986

2.   Suzuki, H. et al.; "Studies on Aseismic Isolation Device for Electric Power Substation Equipment", Developments in Geotechnical Engineering 43, 'Soil-Structure Interaction', Elsevier NY/Computer Mechanics Publications UK, 1987

3.   Suzuki, H. et al.;"Fundamental Studies on Optimum Design for Base Isolation System", 9th World Conference on Earthquake Engineering, Tokyo and Kyoto, 1988

4. Mayama, M;   "Vibration and Mechanical Properties of Ferrite-Epoxy Mixture", Proceedings of Japan Society of Engineers, No. 385,VI7, 1987

THE CONSTRUCTION METHOD PREVENTING A MANHOLE
FROM FLOATING DUE TO LIQUEFACTION

Koichi MURAKAMI, Masahiro NAKANO

Staff and Senior Manager of Tokyo Facility Construction Center
Nippon Telegraph and Telephone Corporation

ABSTRACT

When earthquakes have occurred occasionaly, some structures constructed
in the liquescent sandy ground floated up in the past. Researching after the
past damages of outside telecommunication facilities by earthquakes, the
manhole has floated upward, cant or sink in regions where the ground has
changed due to liquefaction. When the position of the manhole is shifted
greatly, the coupler section holding the manhole to the underground
conduit come loose and this may affect telecommunication services. For this
reason, Nippon Telegraph and Telephone Corporation (NTT) researched and
developed the construction method; covering the area around the manhole
with crushed grain to prevent excessive rises in pore pressure during
liquefaction, preventing the manhole from floating and canting. And the
method was used at the field of telecommunication facilities construction in
Haneda area near Tokyo Airport.

INTRODUCTION

The phenomenon of liquefaction of the soil was first assumed to be an important item during consideration of measures against earthquake disaster, after the occurrence of the Niigata earthquake in 1964. During this earthquake, sand and water spouted all over the Niigata city. The building in front of Niigata Station subsided for about one story while the 4-storys state-owned apartment blocks were uprooted.

Bridges collapsed and submerged septic tanks floated. These kinds of damages were also evident during other earthquakes like Tokachi-oki Earthquake in 1968, Miyagi-ken-oki earthquake in 1978 and Nihon-kai Chubu Earthquake in 1983. Liquefaction of the soil was occurred remarkably during the 1983 Quake where NTT's manholes floated and dipped. Examples of the damages are shown in photographs 1 and 2.

GENERAL OUTLINE ON THE METHOD OF CONSTRUCTION TO PREVENT MANHOLES FROM FLOATING AS A RESULT OF LIQUEFACTION

The method of construction (named as T-gravel Drain Construction Method) considered by NTT, is based on the principles of the gravel drain construction method whereby a layer of gravel is laid around the manhole during its construction so as to distribute the excess pore pressure occurring in the sand soil during an earthquake. In this method, the effective stress in the soil around the manhole can be prevented from dropping.

The conventional gravel drain construction method has the following advantage:

1) compared with other anti-liquefaction construction method, there are less vibrations and noise.

2) this method does not require heavy-duty construction machines.

3) construction works near existing structures are possible.

These advantages and its cost-effectiveness, environmentally non-destructive quality and its ease of construction has prompted NTT to select this method from many others.

CHARACTERISTICS OF THE T-GRAVEL DRAIN

Figure 1 shows a diagram of the T-gravel Drain Construction Method.
The characteristics of the T-gravel Drain Construction Method are as follows:
1) The manhole is made of cement-concrete.
2) A gravel layer of more than 50 cm thick is used to prevent the gravel type #5 (grain size: 20～30 mm) is used.
3) A filter material made of artificial fibers is used to prevent the gravel type #5 from clogging up the gaps by sand flowing into.
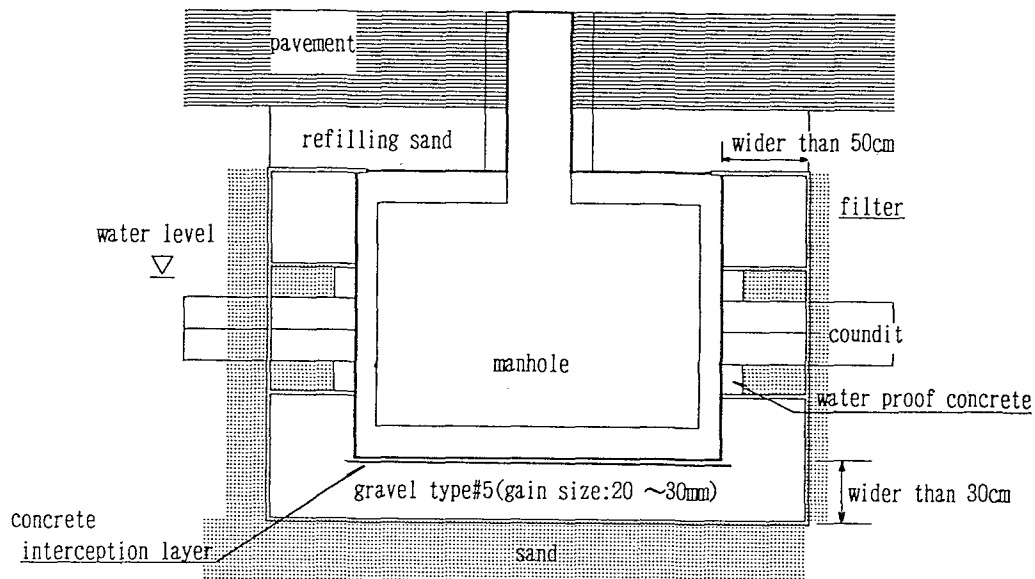
Fig.1. Diagram of T-gravel Drain Construction Method

GRAVEL SECTION

Vibrations were applied to a 1/5 scale model of NTT's #3 manhole (width 1.84m x length 2.84m x height 1.95m) surrounded by gravel to test the effectiveness of the gravel drain construction method in preventing the manhole from floating during liquefaction.

The manhole scale model was constructed inside the ground on the controllable shaking table.

It was found that the manhole floated an amount equivalent to 4/100 times that when no measured were taken, thus proving its effectiveness.

Experiments showed that the minimum effective width of the gravel should be 30 cm but a wider width of 50 cm would be more practical since this is the minimum gravel compacting width that can be done by machinery.

FILTER SELECTION

Since the gaps between the gravels of type #5 used in the gravel drain method are large, the sandy soil around the gaps will be able to easily flow through thus reducing the water drainage effectiveness and may even result in the settlement of the surrounding ground area. Therefore, it is essential that a filter is placed between the gravel and the surrounding ground.

The filter must also be selected for its function and strength after considerations given to its effects on the surrounding.

Nakajima et al. has found that liquefaction occurs most easily when the grain size is 0.2-2.0 mm. The standard filter should then have gaps of about 0.2 mm to effectively prevent clogging. Such filters made of polyethylene polymers were found to be superior in strength and was thus selected.

An outline of the functions of the polyethylene filter is listed in table 1. This filter is, due to the nature of the material, chemical-resistant and will not deteriorate through micro-organism activities.

Table 1. An outline of the function of polyethylene filter

Meshes	$0.2 \sim 0.3$ mm
Tensile strength	long way:95.3kg, wide way:107.2kg(3cm)
Coefficient of permeability	2.8×10^{-2}
Stretch ratio	long way:35.0%, wide way:27.0%(3cm)

CONSTRUCTION WORK FLOW

Figure 2 shows the construction steps in the T-gravel Drain Construction Method. The words in *italics* are those steps added to the standard manhole work for this construction method. The example is given for the construction executed in the Haneda area.

```
┌─────────────────┐                              ↓
│   Preparation   │                    ┌──────────────────────────┐
└────────┬────────┘                    │ Construction of sidewalls │
         ↓                             │ and upper plate reinforces │
┌─────────────────┐                    └────────────┬─────────────┘
│ Safety facilities│                                ↓
└────────┬────────┘                    ┌──────────────────────────┐
         ↓                             │ Construction of sidewall  │
┌─────────────────┐                    │   internal frames and     │
│  Leading frame  │                    │   upper plate frames      │
└────────┬────────┘                    └────────────┬─────────────┘
         ↓                                          ↓
┌─────────────────┐                    ┌──────────────────────────┐
│  Break pavings  │                    │ Molding and curing of sidewall│
└────────┬────────┘                    │  and upper plate concrete │
         ↓                             └────────────┬─────────────┘
┌─────────────────┐                                ↓
│   Excavation    │                    ┌──────────────────────────┐
│  Support beam   │                    │  Removal of internal and  │
│    Pavings      │                    │   external frame works    │
└────────┬────────┘──(ground)          └────────────┬─────────────┘
         ↓                                          ↓
```

Filter layering
Layering filter under
the lower plate
Layering sidewall filter

Foundation works
Placement of gravel
drain below lower plate

Layering of manhole
concrete interception layer

Construction of lower
plate frames

Construction of lower
plate reinforces

Molding and curing
of concrete

Construction of
sidewall frames

Construction of sidewalls
and upper plate reinforces

Construction of sidewall
internal frames and
upper plate frames

Molding and curing of sidewall
and upper plate concrete

Removal of internal and
external frame works

Construction of entry and exit
section, fixture of iron lid

Refilling,
Construction of gravel
drain in sidewall section
(up till below the
horizontal conduit)

Layering of sand and filter
around the conduit

Insertion of
horizontal conduit

Refilling, removal of support
beams and frameworks
Construction of gravel drain
in side wall section
(above conduit)

Attachment of accessories

Finishing touches to mortar

Completion of works

Fig.2. Construction procedures for manhole using
the T-gravel Drain Construction Method.

Conduit type manholes will be constructed in view of ① future expansion and ② as supportive structures for future road improvement works at the new airport at Haneda which is scheduled for operation in May, 1993.

The area around Haneda airport was reclaimed from the sea from 1945 ~ 1955. The foundation here is characterized by the fact that

1) the soil below the filled top soil is of a sandy nature

2) the water table is high at GL.-1.0 ~ 1.5 m

3) the filled sea areas have a very weak foundation.

It was proved that liquefaction occurs easily in those areas shown in figures 3.

The results of the simple liquefaction determining equation (Design Criterion Utility Tunnel: determination by FL value) by using the boring data obtained by this construction method at Haneda, are shown in Figure 4. As can be understood from these results, the finer the sand soil or silt, the easier liquefaction occurs since the water table is high. Further during the determination, the earthquake external force is assumed to be a surface acceleration of 200 gal.

Construction conditions of this method is shown in the photographs 3 ~ 19.
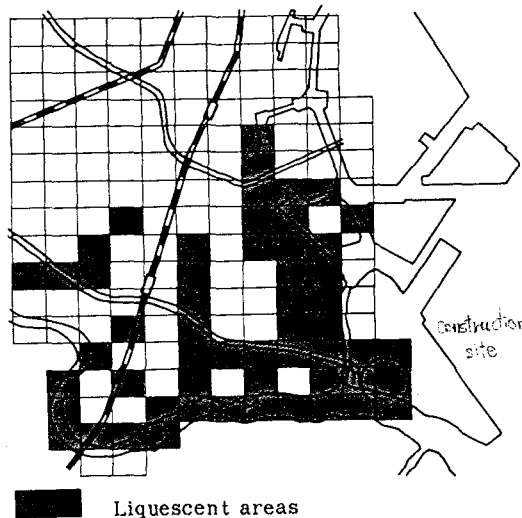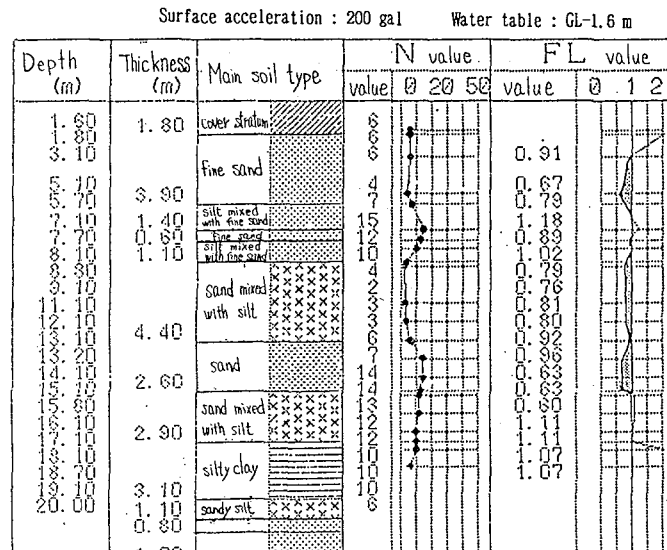

Liquescent areas

Fig.3. Ares that liquefaction occurrs easily.

Surface acceleration : 200 gal   Water table : GL-1.6 m

Thickness of liquefaction layer.....12.20 m   PL value.... 15

Fig.4. The result of liquefaction determining

AFTERWORD

NTT has successfully completed investigations into the effectiveness of anti-liquefaction construction methods in test constructive works at manholes in the vicinity of Haneda airport with the cooperation of road control organizations.

However, this method which encountered no problems at Haneda test area, may be hindered when considering applications to parts of Tokyo Metropolitan Area (ex. influences of underground facilities congestion and trafic condition). Besides research into ways to overcome this problem, the ease of construction and other problems must be grasped, understood and countermeasures developed as well.

ACKNOWLEDGE

Finally, we would like to express our deepest appreciation to all the research staff involved in "Researches in Measures against Changes in Foundation of Subterranean Structures" attached to the Association for the Development of Earthquake Prediction. Our sincere thanks also go to those technical staff attached to J COS Corporation involved in the Haneda work site.

REFERENCES

1) Nakazima et al.: *Grain Size Distribution of Gravel Drain*, Proceedings, 20th Symposium of JSSMFE.

2) Yagi, Suzuki, Hattori, Yoshikawa: *An Experimental Study on The Manhole Stabilizing Techniques against Liquefaction*, 1989 ASME Pressure Vessels and Piping Conference, July 1989.

3) Association for the Development of Earthquake Prediction: *Researches in Measures against Changes in Foundation of Subterranean Structures*, pp271 ~ 290
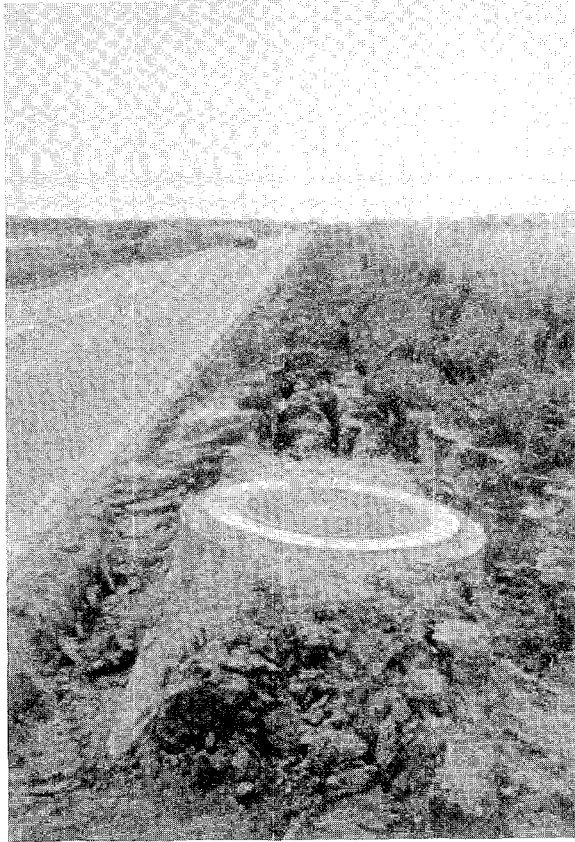
Photo 1
Manhole floating
(Nihon-kai Chubu
Earthquake)
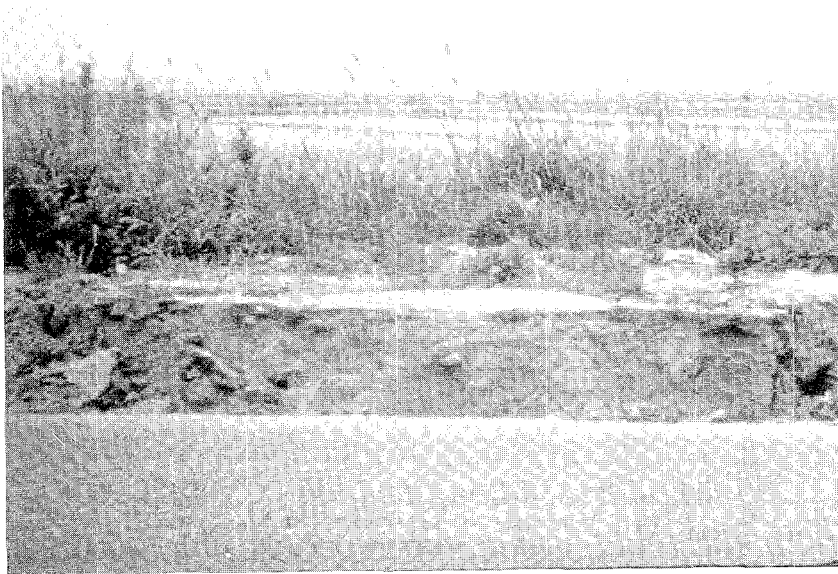
Photo 2
The same as photo 1
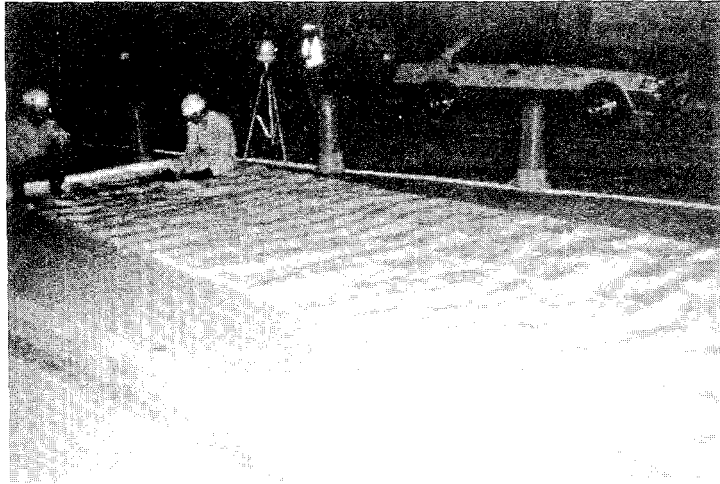
Photo 3
Preparation of filter

Photo 4
Glueing on filters
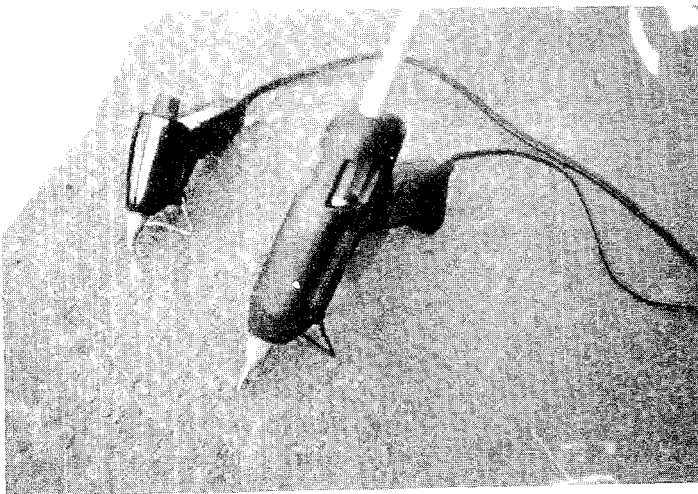
Photo 5
Device for glueing
on filters

617

Photo 6
Insertion of filter
into excavated hole
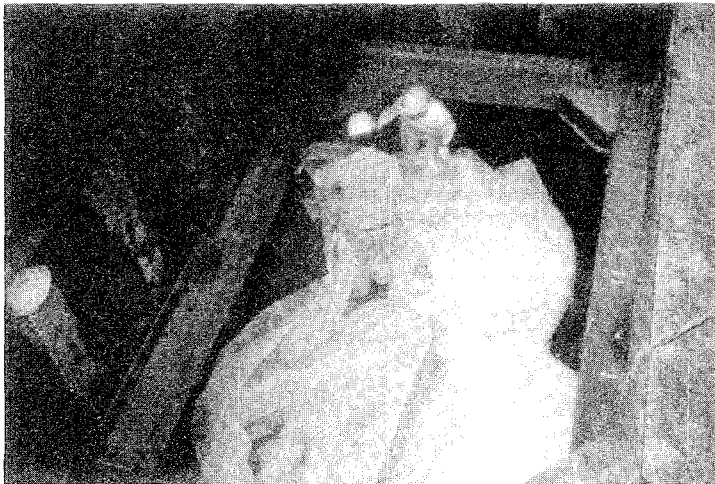
Photo 7
Placement of filter
at base of excavated
hole

Photo 8
Completion of filter
works
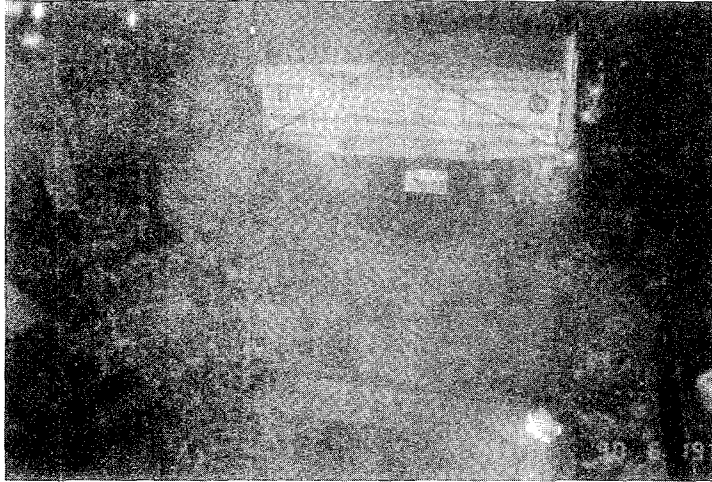
Photo 9
Insertion of gravel
type #5
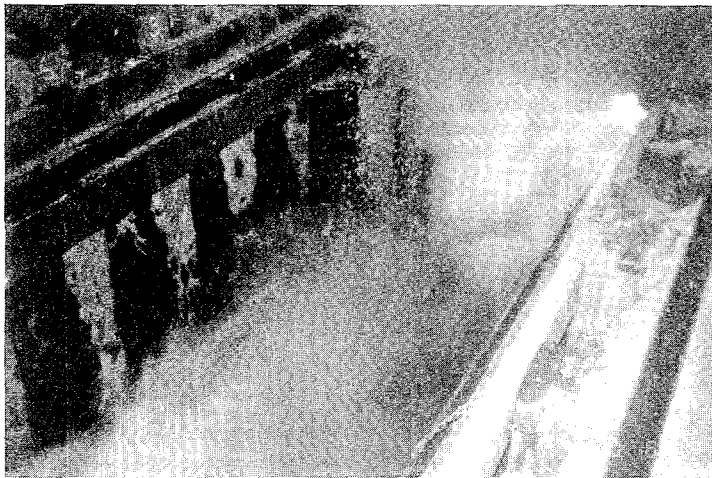
Photo 10
The same as photo 9
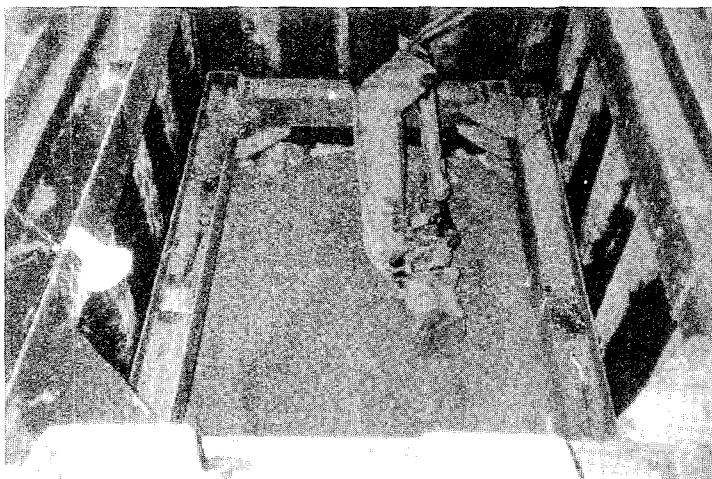
Photo 11
Levelling of layer
of gravel type #5

619

Photo 12
Compacting of gravel
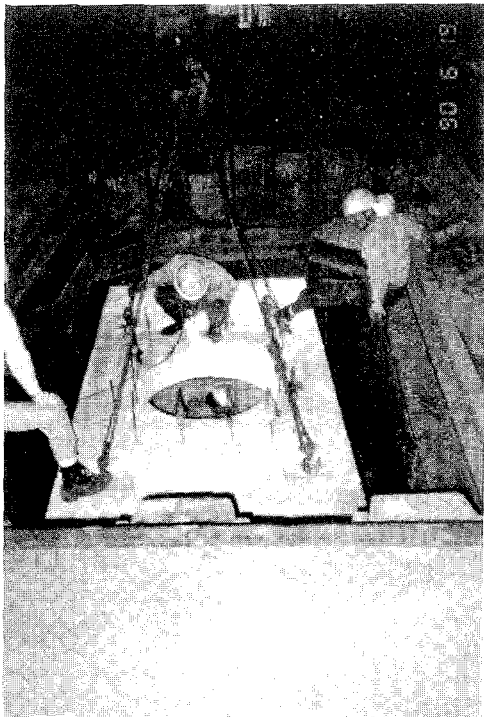
Photo 13
Lowering of precast
block manhole

Photo 14
Placement of filter
in sidewall section
of manhole

Photo 15
Refilling of manhole
with gravel type #5
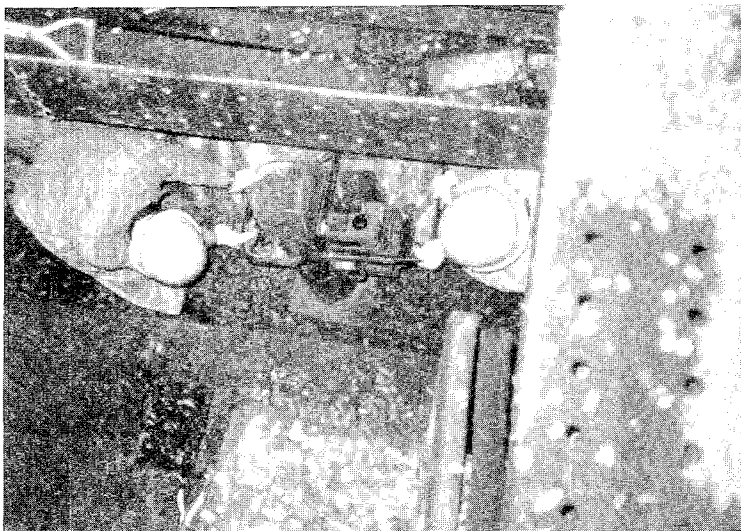
Photo 16
Compacting refilled
gravel

621
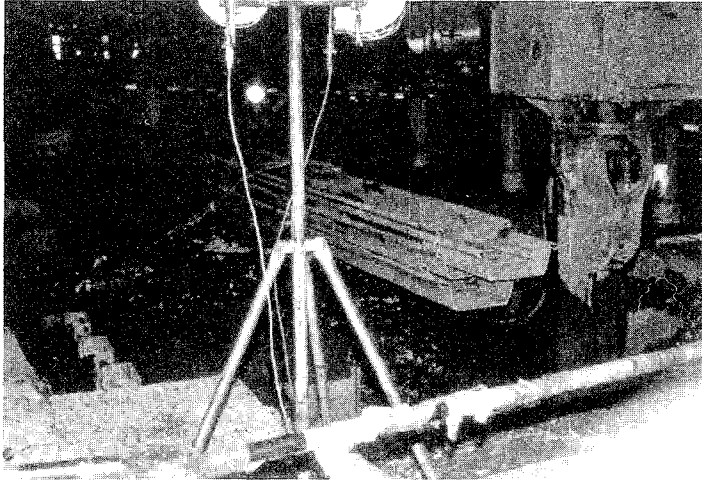
Photo 17
Refilling of sand
on manhole slab
Extraction of
temporary sheet pile
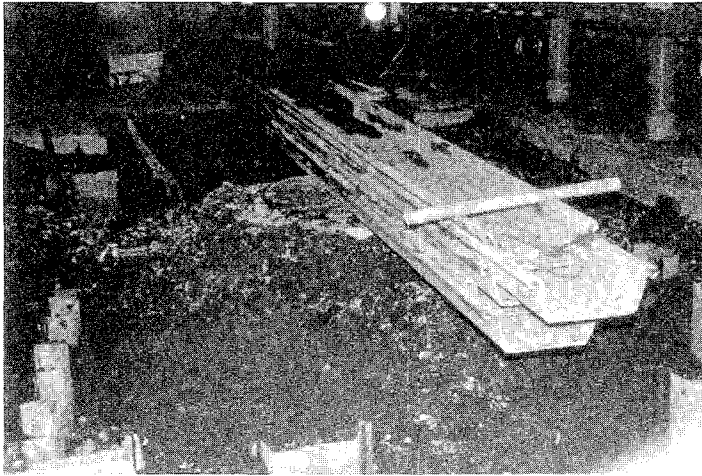
Photo 18
The same as photo 17
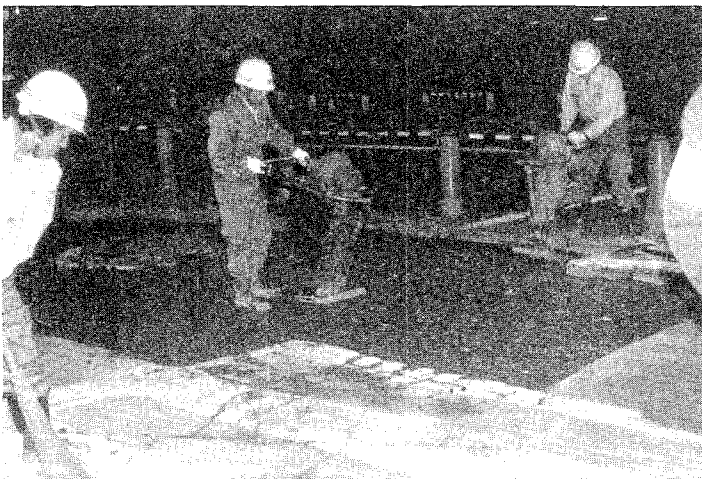
Photo 19
Compacting paved sections

A SEISMIC SIMULATION OF TELECOMMUNICATIONS NETWORK

Tomoaki NAKAYAMA

Staff Engineer
Civil Engineering Department,
Kanto Plant Engineering Center,
Nippon Telegraph and Telephone Corporation, NTT.

ABSTRACT

NTT has developed a Telecommunications Seismic Accident Prediction Program to evaluate the reliability of underground telecommunication networks using the Monte Carlo simulation method.

With this method, we simulated the 7.9 magnitude Great-Kanto-Earthquake of 1923 in the area of a local telecommunication office in Yokohama, a business district near Tokyo.

The results are summarized as follows:

(1) The ground surface acceleration was more than 250 gals over the entire area.

(2) More than 70% of the conduits were damaged.

(3) Less than 3% of the cables were affected.

(4) Cable damages were mainly caused by soil liquefaction and lateral movement.

Using information from Tel-SAPP, countermeasures should be implemented in a planned fashion to reinforce weak points in network systems.

INTRODUCTION

Seismic scientists have predicted that several big earthquakes will hit Japan within the next few decades. This has compelled governments and lifeline companies to investigate damage prevention measures and recovery plans. Since communications are especially important for coordinating, rescue and restoration activities, NTT is also making efforts to enhance the reliability of telecommunication facilities.

Accordingly, NTT has developed the Telecommunication Seismic Accident Prediction Program (Tel-SAPP) to evaluate the reliability of underground telecommunication networks. The network lines consist of cables and their protective conduits. Therefore, the relationship between cable and conduit damage must be estimated.

This paper describes the Tel-SAPP procedure, and discusses the results of seismic simulation at a local telecommunication office area in Yokohama.

OUTLINE OF TEL-SAPP

Tel-SAPP hardware is shown in Fig.1. The configuration of the system is shown in Fig.2.
Before testing the Tel-SAPP program for the first time, the reliability of each facility was experimentally calculated using a mainframe computer program with a beam-and-spring-model.

Experimental Facility Environment

Regarding the input of basic data about facility environments, the simulated earthquake is defined by it's magnitude and epicenter, based on the intensity of past seismic activity in the sample region. In addition, the simulated area is divided into a grid, and the land in each grid square is classified from type 1 to 4, shown in Table 1.[1] Furthermore liquefaction and soft ground areas are established according to soil survey data. The probability of liquefaction is estimated using the equations given in "Estimation of Degree of Soil Liquefaction during Earthquakes".[2]

Structural Data

Data on facilities are input for all manhole-to-manhole segments. This involves data about the structures of telecommunication conduits, including their type, span length and construction year, as shown in Fig.3-a. Cable structure data are also input, including their type, gauge and number of pairs, as shown in Fig.3-b.

Evaluation of Network Reliability

Using Tel-SAPP, telecommunications network reliability is evaluated in the following five ways as partly shown in Fig.5;
(1) The ground surface acceleration in each square of the area grid is calculated using an attenuation equation(Table 1)[3] with environmental data.
(2) Based on the acceleration rate, land displacement is also evaluated in each square using the formulas shown in Table 2.
(3) The probability of conduit line destruction between every two manholes is evaluated using Monte Carlo simulation, based on the precalculated reliability tables of each facility.
(4) The probability of cable trouble is evaluated using the same method at every point where conduit damage is detected. Fig.4 shows the evaluation points of conduit lines and cables.
(5) The reliability of every user route is evaluated by first evaluating the reliability of each facility.

Following this evaluation, a report on the calculated reliability for each user, route or manhole-span is output on a display or hard copy.

YOKOHAMA CASE STUDY RESULT

We evaluated the reliability of telecommunication networks in the area of a local branch office in Yokohama. (Fig.6) The test area is 2.2 km^2 and consists of about 50,000 users. The ground in the test area is made up of cohesive alluvium and local sand. (Fig.7)

Input Data

The simulated earthquake data equaled the 7.9 magnitude Great-Kanto-Earthquake of 1923. (Fig.6) The land in each square (250m x 250m) of the grid pattern was classified as shown in Fig.8. About 50% of the area was classified as type 4(i.e. softest ground). Liquefaction and soft ground areas are shown in Fig.9. The liquefaction area was 16% of the total area, and the maximum thickness of soft ground was more than 30m. Fig.10 shows input data of conduits and cables. About 90% of the conduits were metal and comparatively old. More than 85% of the cables were ST-type.

Output Data

Ground surface acceleration is shown in Fig.11. The acceleration of each square was between 270 and 370 gals. Fig.12 shows the land displacement of the area. In liquefaction areas, the maximum lateral movement was 2.8m, and the maximum settlement was 45cm. In soft ground areas, the maximum settlement was 20cm.

More than 70% of the conduits were damaged, but less than 3% of the cables (i.e.360m/12130m) were affected. These were all ST-

type, which account for about 90% of the cables in the area. The probability of having trouble for each cable was less than 30%. As a result, each user had a 97% probability of retaining the use of a telephone because each user has more than one cable route, as shown in FIg.13. The process of how conduit damage leads to cable trouble is shown in Fig.14.

Evaluation Result

Facilities evaluation

In liquefaction areas (see Fig.15-b), all V-type-conduits were damaged, as well as about 80% of the SA-type-conduits, and about half of the I-type-conduits.
In the soft ground areas (Fig.15-c), damage occurred in about 30% of V-type-conduits, about 85% of SA-type-conduits, and in about 90% of I-type-conduits.
In the other areas (i.e. regular ground areas, see in Fig.15-d), less than 7% of the conduits were damaged. Furthermore, damage increased in all types of conduits, except PS-types, according to the gal value of the area. This is because damage is caused by elastic deformation of the ground in regular ground areas.
Also, regarding PS-type-conduits, there were not available enough data on them in the test areas to evaluate.
No relationship was detected between damage of the conduit and the year of it's construction.

From these results, we have determined that,
(1) V-type-conduits are reasonably safe in soft ground areas because of their flexibility. However, they are easily damaged by ground displacements larger than their flexibility in liquefaction areas.
(2) I-type-conduits are safe in liquefaction areas because they have joints in every four meters.
(3) SA-type-conduits are nearly all vulnerable to damaged except in regular ground areas.

Area evaluation

Allowable levels of seismic damage for individual facilities making up the NTT network are described in Table 3. When ground surface acceleration corresponded with VI on the Japan Meteorological Agency Intensity(JMA) scale, the probability of service interruption was less than 3%. These results from the simulation indicate that the networks in the test area are stable enough to withstand a large earthquake and still remain operable.

EARTHQUAKE PREVENTION MEASURES FOR UNDERGROUND NETWORKS

NTT's earthquake prevention measures for underground telecommunication networks are shown in Fig.16. Beyond these

facilities, NTT has cable tunnels connected to main offices in large cities. Although this paper does not discuss cable tunnels in detail, a cable tunnel in Yokohama was confirmed in the case study to be stable enough to withstand a large earthquake. Telecommunications networks use redundant configurations as an anti-earthquake measures. NTT installs multiple or looped transmission routes and uses route doubling of important subscriber lines, as shown in Fig.13.

CONCLUSION

NTT network facilities exist in various states of readiness, in terms of their ability to withstand large earthquakes. It would be very costly to undertake a total restoration project in order to completely rebuild the network to make it earthquake proof. However, Tel-SAPP makes it possible to determine the weak points of a network, which enables more economical spot reinforcement measures to be taken in those areas where it is most needed. In this way, Tel-SAPP can be efficiently used to enhance the reliability of the entire telecommunications network, as confirmed in the case study. Thus, using information from Tel-SAPP, countermeasures should be implemented in a planned fashion to reinforce weak points in network systems.

ACKNOWLEDGMENTS

REFERENCES

1.   Specifications for Highway Bridges, Japan Road Association, 1970, p.14-p.16
2.   T.Iwasaki, H.Tatsuoka, K.Tokida, S.Yasuda, "Estimation of Degree of Soil Liquefaction during Earthquakes," JSSMFE, Ser.No.267, Vol.28, No.4, Apr.1980
3.   K.Kawashima, K.Aizawa and K.Takahashi, "Estimation of Peak Ground Acceleration, Velocity and Displacement Based on Multiple Regression Analysis of Strong Motion Record," Civil Engineering Journal, Public Works Research Center, Vol.26, No.2, Feb.1984

Table 1 Ground Type Classification [1&3]

Types of Ground	Natural Period of Surface Layer	Estimation Formulas of Ground Surface Acceleration
Type 1	$T_G < 0.2$ seconds	$\alpha smax = 1073.0 \times 10^{0.221M} \times (\Delta + 30)^{-1.251}$
Type 2	$0.2 \leqq T_G < 0.4$	$\alpha smax = 227.3 \times 10^{0.308M} \times (\Delta + 30)^{-1.201}$
Type 3	$0.4 \leqq T_G < 0.6$	
Type 4	0.6 seconds $\leqq T_G$	$\alpha smax = 403.1 \times 10^{0.262M} \times (\Delta + 30)^{-1.208}$

where $\alpha smax$: major surface acceleration
Δ : distance from the epicenter
M : magnitude

Table 2 Land Displacement Estimation Formulas

Areas	Land Movement	Estimation Formulas
Liquefaction	Permanent Lateral Movement	$DH = 0.75 \; H \cdot \theta$ where DH:Amount of Lateral Displacement H :Thickness of Liquefaction Layer θ :Incline of Grand Surface or Liquefaction Stratum
	Permanent Vertical Movement	$Dv = 0.15 \; H$ where Dv:Amount of Vertical Displacement H :Thickness of Liquefaction Layer
Soft Ground	Settlement	$D = 0.005 \; H$ where D :Amount of Settlement H :Thickness of Soft Ground Stratum

Table 3 NTT Criteria for Allowable Damage Level in Earthquakes

JMA Scale	Allowable Damage Level
V (80-250gals)	There should be no interruption in operation.
VI (250-400gals)	Interruption of service should be prevented even if the quality of communication deteriorated.
VII (400gals-)	A significant decline in the function of communication networks should be prevented.
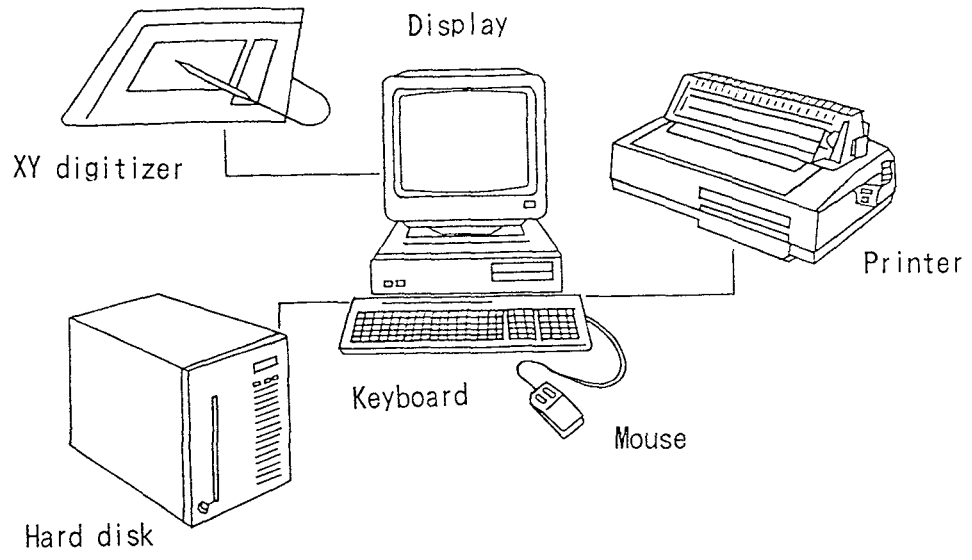
Fig. 1　Tel-SAPP Hardware
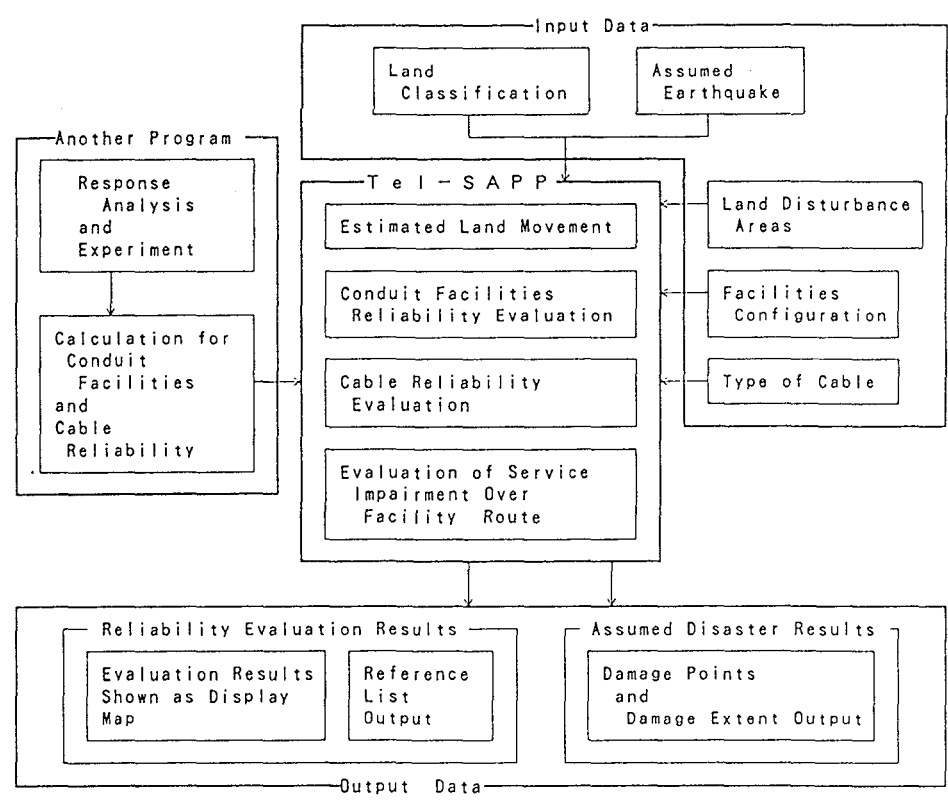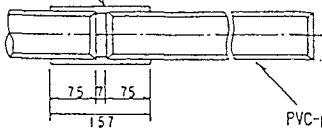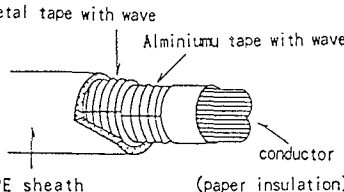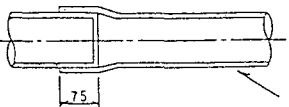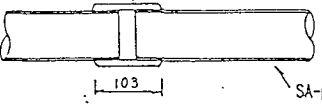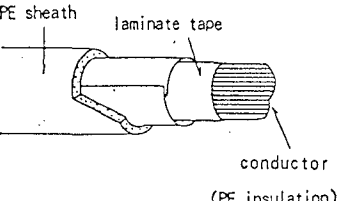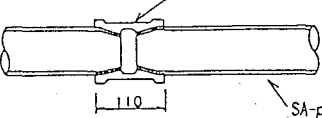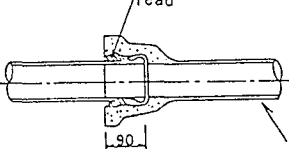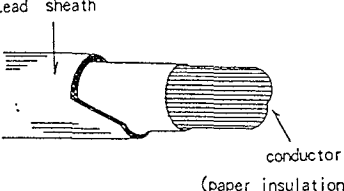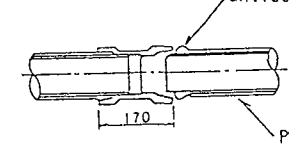
Fig. 2 Outline of Tel-SAPP

Conduit Types	Year of use	Structures of Pipe and Joint
V −type	1966 ~1976	Vinyl Pipe Socket / 75 7 75 / 157 / PVC-pipe
	1977 ~1984	75 / PVC-pipe
SA−type	1954 ~1962	Parallel Screw Joint / 103 / SA-pipe
	1963 ~1964	Taper Screw Joint / 110 / SA-pipe
I −type	1896 ~1963	lead / 90 / I-pipe
PS−type	1965 ~1984	antiseptics / 170 / PS-pipe

(a) Conduit

Cable Types	Structures
ST- Cable	Metal tape with wave / Alminiumu tape with wave / PE sheath / conductor / (paper insulation)
PEC- Cable	PE sheath / laminate tape / conductor / (PE insulation)
Pb- Cable	Lead sheath / conductor / (paper insulation)

(b) Cable

Fig. 3 Structures of Network Facilities

Side of MH / Joint / Along Conduit / Beside Unsettlement Object / Cables / Subway etc
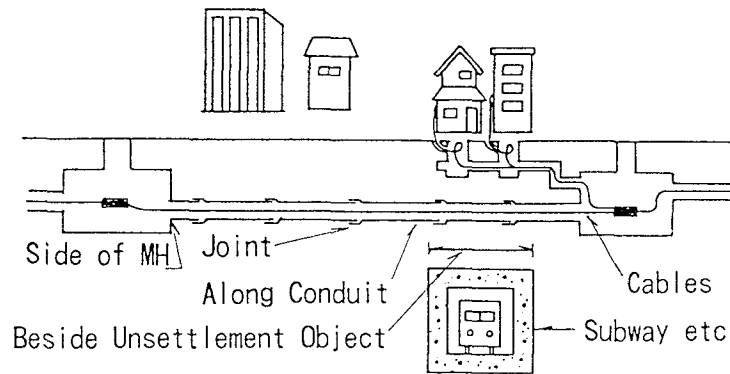
Fig. 4 Evaluation Point of Conduit and Cable

631
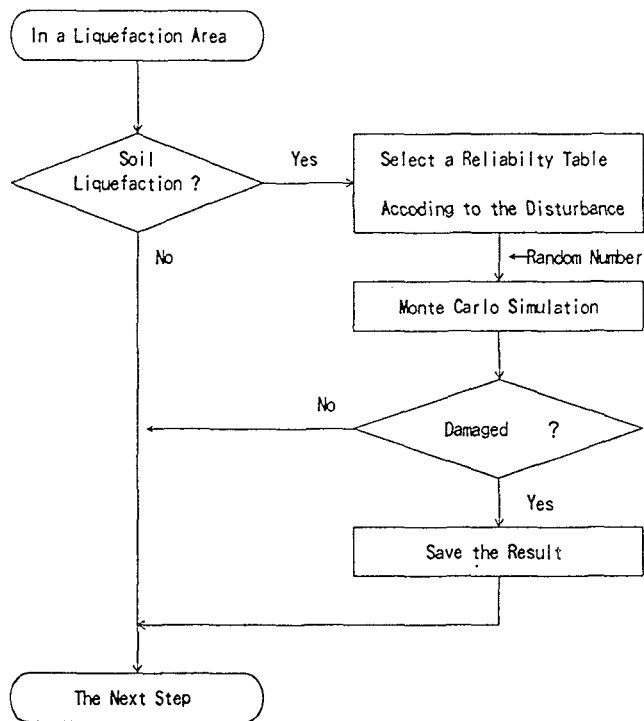
Fig. 5 Part of the Evaluation Procedure
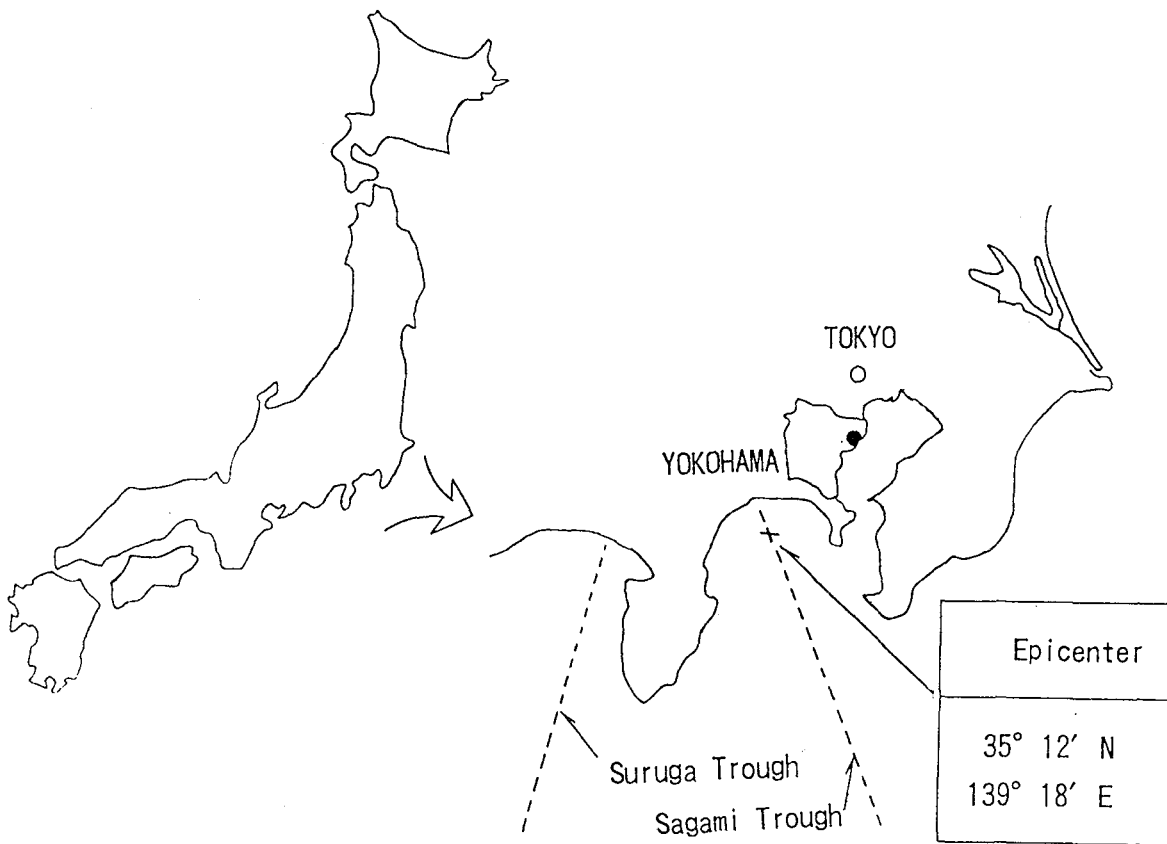
Fig. 6 Evaluated Area and Earthquake
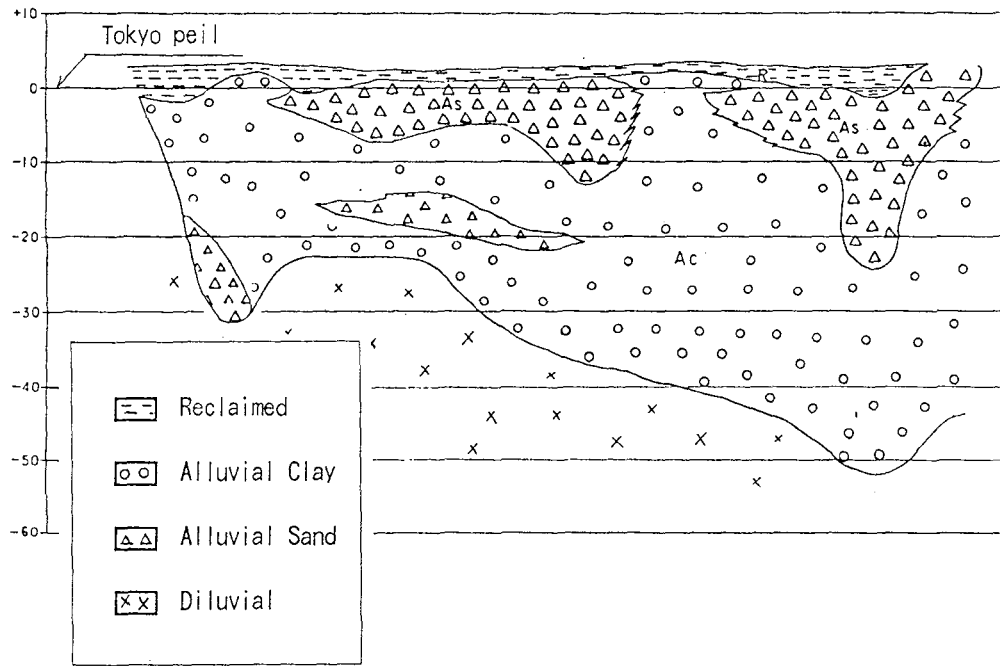
Fig. 7   Typical Soil Profile in the Area

Legend:
- Reclaimed
- Alluvial Clay
- Alluvial Sand
- Diluvial

Type 2   Type 3   Type 4

Fig. 8 Land Classification

Liquefaction Area where Settlement is Predicted

Liquefaction Area where Lateral Movement is Predicted
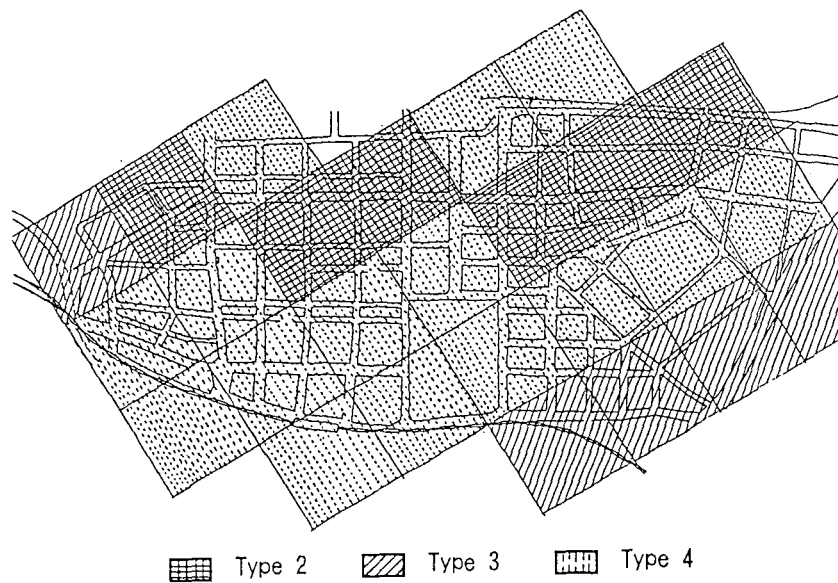
Numbers: Thickness of Soft Ground (m)
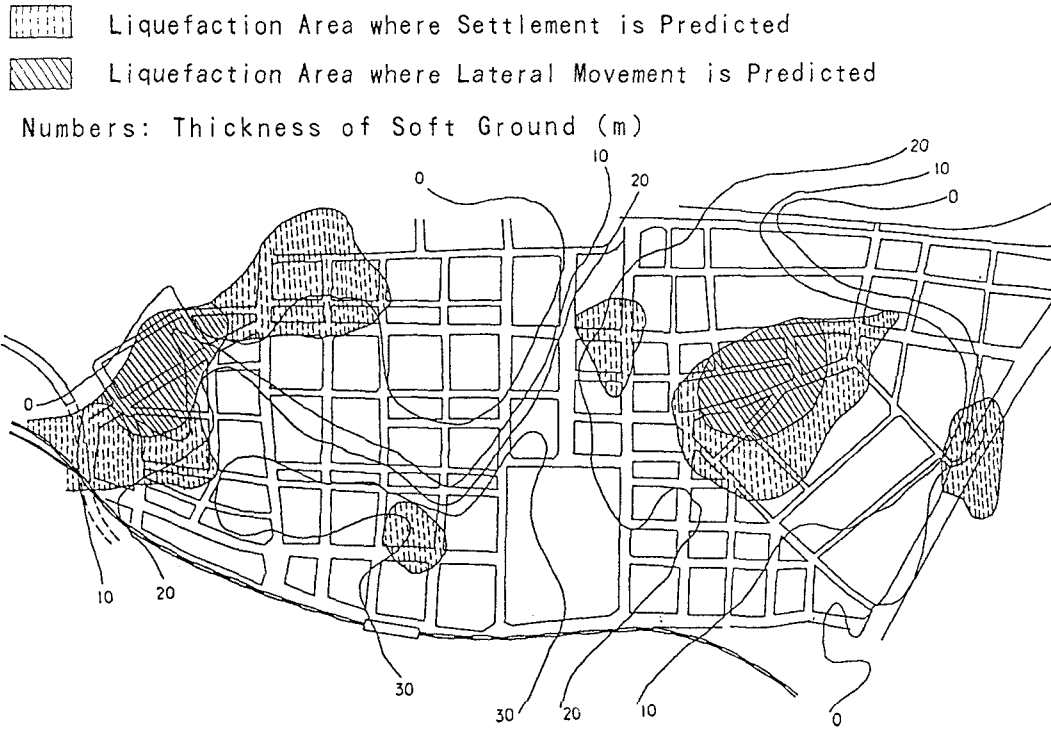
Fig. 9 Liquefaction Areas and Thickness of Soft Ground Layer
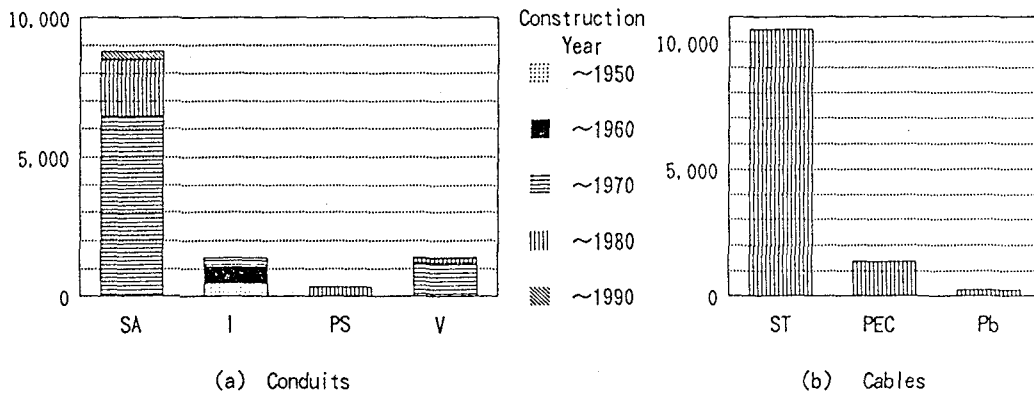
(a) Conduits

(b) Cables

Fig. 10 Input Data

634

Fig. 11   Ground Surface Acceleration

Legend:
- ☐ ~ 300 gals
- ▦ 300 ~

In Liquefaction Areas
  Amount of lateral Movement:Dh
    ▦ Dh ≧ 2.0 m
    ▦ Dh < 2.0 m
  Amount of Settlement:Dv
    ⊙⊙⊙ Dv ≧ 0.4 m
    △△△ 0.3 ≦ Dv < 0.4 m
    ⠿ Dv < 0.3 m
In Soft Ground Areas
  Amount of Settlement:Numbers

Fig. 12   Land displacement

635

A-route: Probability of cable damage is 29%.

User has more than 97% probability being able to use telephone.

×: Cable Damege Point

B-route: Probability of cable damage is 10%.
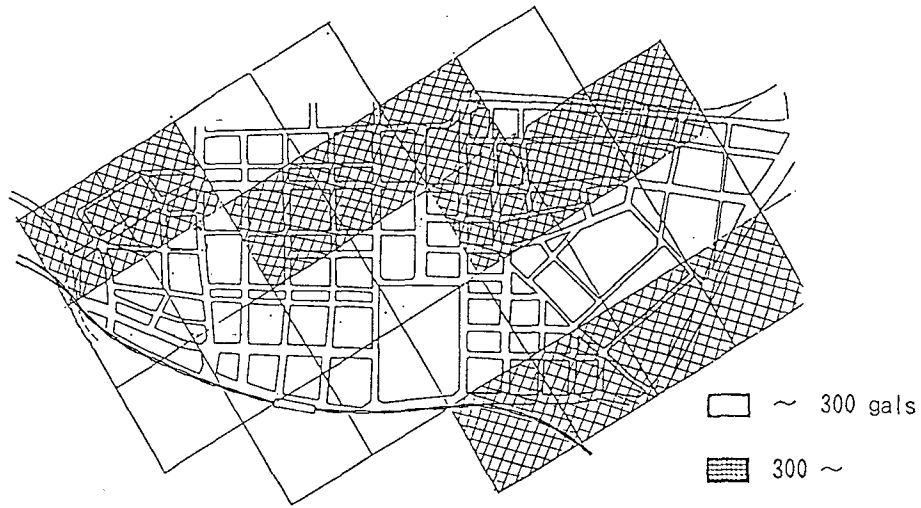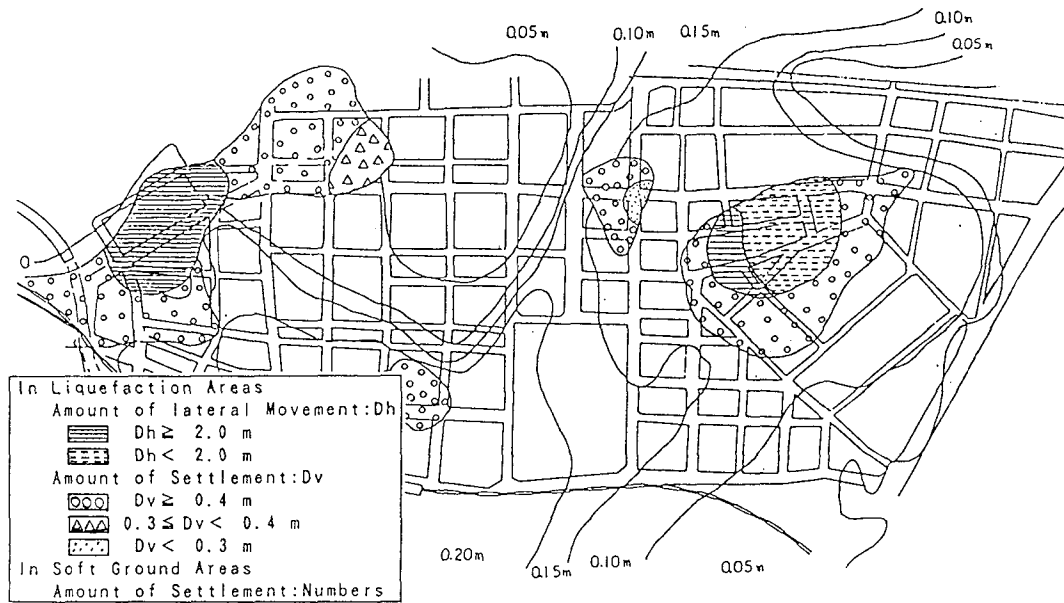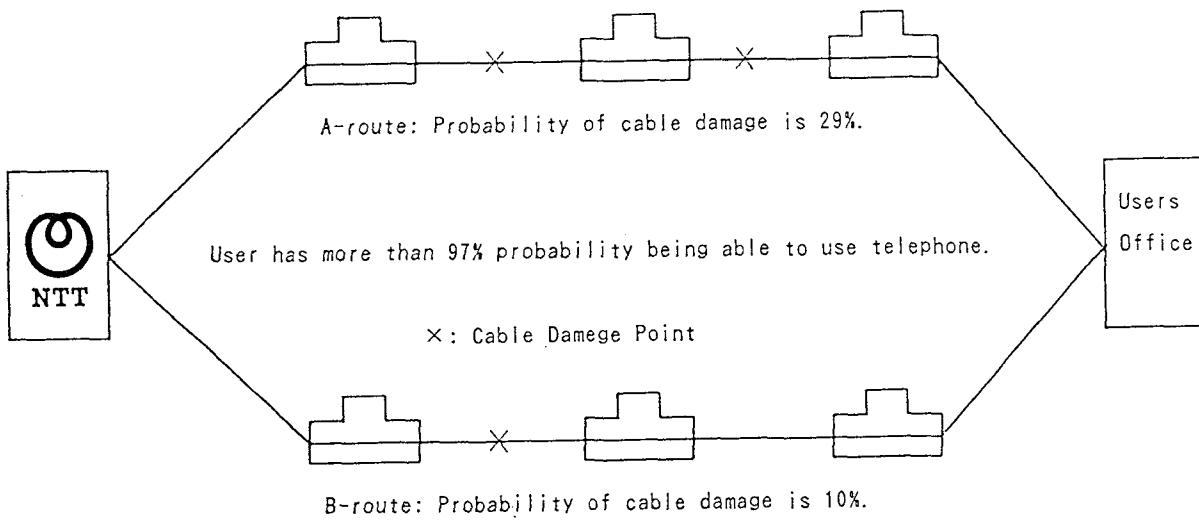
Fig. 13 Relationship between Route and User Reliability

Cable Condition	Conduit Movement
Safe	Pulled Off →
Almost Safe	Makes a Gap ↓
Damaged	Pushed Back ←

F i g . 1 4 C a b l e D a m a g e P r o c e s s

(a) In the Whole Area   (b) In the Liquefaction Area

(c) In the Soft Ground Area   (d) In the Regular Ground Area
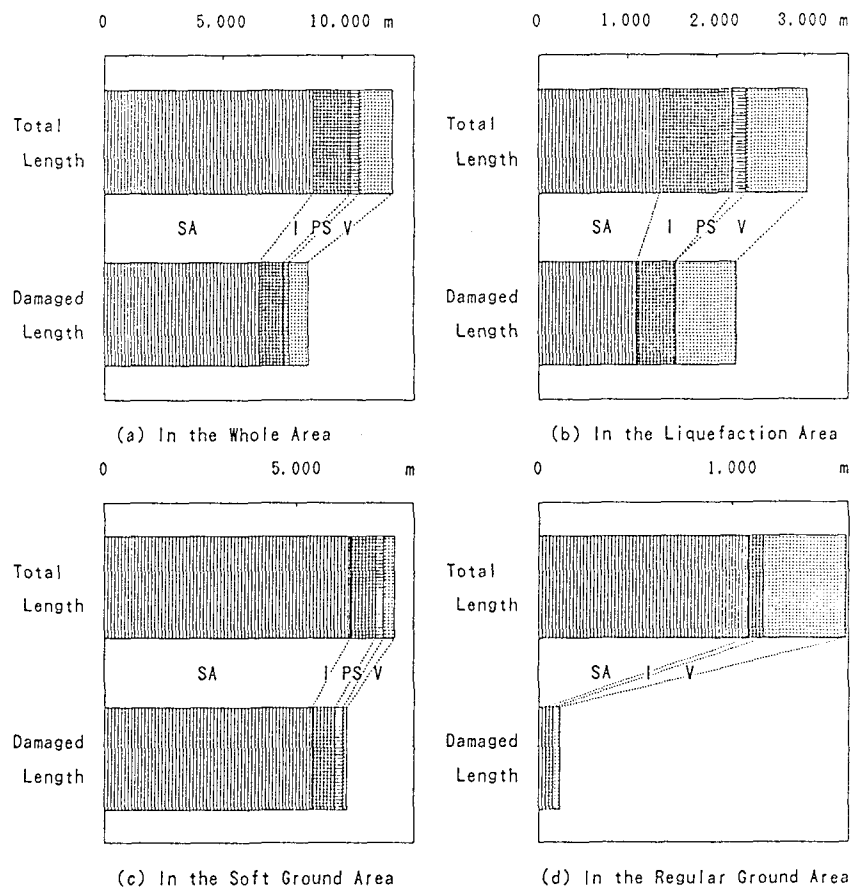
Fig. 15 Conduit Damages
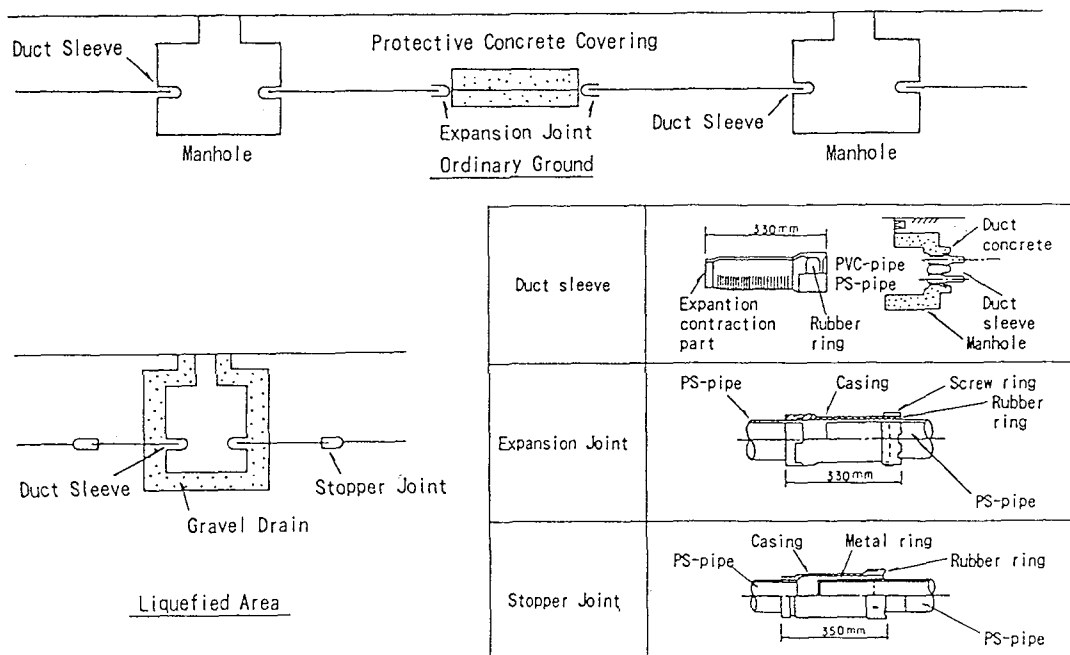
Fig. 16 Liquefaction Countermeasures of Underground Conduits

637

WORKING GROUP SESSIONS

SECOND US-JAPAN WORKSHOP ON LIQUEFACTION, LARGE GROUND DEFORMATIONS AND THEIR EFFECTS ON LIFELINES

REPORT FROM WORKING GROUP NO. 1:
EXPERIENCE DURING PAST EARTHQUAKES

Working Group Members:

From Japan	From the United States
Susumu Yasuda, Co-chairman	T. Leslie Youd, Co-chairman
Yoshimi Ogawa	Steven F. Bartlett
Kiwotaka Satoh	Mohamed Baziar
	Ted Gowdy
	Bruce Roth
	Mohamed Succarieh
	Henry Taylor
	Gerald Wieczorek

INTRODUCTION

During the workshop, Working Group 1 reviewed progress in compiling case histories of liquefaction and large ground displacement, assessed the development of empirical criteria for predicting ground displacement, and considered future research needs and opportunities on this topic. The purposes of compiling and evaluating cases histories from past events are (1) to utilize past experience to improve our understanding of ground failure processes and factors that control those processes, (2) to develop a set of case histories to assist the development of analytical models for predicting ground displacement, (3) to provide sufficient data for the development of empirical criteria for predicting ground displacement, and (4) to provide well-documented case histories to be used in the verification of the models and criteria developed.

To accomplish these objectives, a coordinated US-Japan program is in progress to compile case histories of liquefaction-induced ground displacements for several Japanese and US earthquakes, and the 1990 Philippines earthquake. The earthquakes being considered are listed in the following section. Data being complied include surface displacements, site topography, soil stratigraphy and properties, ground water levels, and where possible ground motion data.

CASE HISTORY COMPILATIONS

Reports were given by principal investigators were given of progress in completing case history compilation. A schedule was set to finalize the compilations by February 1991 and to publish a volume containing the case histories during the summer of 1991. The following synopses of progress were given by principal investigators:

1906 San Francisco, $M_w = 8.1$, and 1989 Loma Prieta, $M_w = 7.0$. The case history report for the 1906 earthquake was very nearly complete when the October 17, 1989 Loma Prieta earthquake struck the San Francisco Bay area. Progress on the 1906 case history compilation was interrupted while field investigations were conducted for the 1989 event. With the same areas being affected by both earthquakes, the opportunity was taken to enhance the 1906 report with some data from the 1989 event and with comparisons of liquefaction effects generated by both earthquakes in the City of San Francisco. The augmented report is on schedule to be completed by the February 1991 deadline.

1923 Kanto earthquake, $M = 7.9$. The case history report for this earthquake has been completed in Japanese. Translation is in progress and should be complete by the February deadline.

1948 Fukui earthquake, $M = 7.1$. The case history report for this earthquake has been completed in Japanese. Translation is in progress and should be complete by the February deadline.

1964 Alaska earthquake, $M_w = 9.2$. The report for the this earthquake has been submitted for review and editing by NCEER staff.

1964 Niigata earthquake, $M = 7.5$. The case history report for this earthquake has been completed in Japanese. Translation is in progress and should be complete by the February deadline.

1971 San Fernando earthquake, $M = 6.5$. The report for the this earthquake has been submitted for review and editing by NCEER staff.

1979-87 Imperial Valley earthquakes $M = 6.0\text{-}6.6$. A draft of this report has been completed by the lead author and is undergoing co-author review. A schedule has been set for completion to meet the February 1991 deadline.

1983 Nihonkai-Chubu earthquake, $M = 7.7$. The case history report for this earthquake has been completed in Japanese. Translation is in progress and should be complete by the February deadline.

1990 Philippines earthquake, $M = $. The Japanese team of investigators who investigated the 1990 Philippines earthquake are developing liquefaction case history information, primarily from Dagupan City and the coastal region of the Lingayen Gulf. A report is in preparation for publication in the case history volume.

EMPIRICAL CORRELATIONS FOR PREDICTING GROUND DISPLACEMENT

Both the Japanese and US sides are continuing an evaluation of case-history data for the purpose of developing empirical correlations for predicting ground displacement. Professor Hamada is leading the study for the Japanese side. He was not at the Wording Group discussion, so no report was received on his progress. Steve Bartlett and Professor Youd reported progress on their statistical analysis of data for the US side. Because of the large set of displacement measurements and numerous bore-holes drilled in Niigata, he Bartlett and Youd are analyzing that data set and have shown that nearness of a free face, ground slope, and

thickness and depth of the liquefied layer are all important parameters controlling ground displacement. Their study is still in progress and final results are not yet available.

PERSPECTIVES FROM WORKING GROUP 1

An immediate objective of the joint US-Japan effort is to complete the compilation and publish case histories for the earthquakes noted above. This publication should be available by mid 1991. After the case histories are completed, evaluations should be made of the completeness and degrees of uncertainty in the data set. Some known limitations and uncertainties are:

1. Only fragments of some important parameters are available, such as ground motion records. A notable exception is the Wildlife site where ground motions and pore-water pressures were recorded.

2. Some properties that are important to liquefaction evaluation have not been routinely measured and are not reported for all case histories. Examples are permeability and shear-wave velocity.

Gerald Wieczorek reported that the US Geological Survey has historically been very active in compiling and publishing case-history information including reports from the 1964 Alaska, 1971 San Fernando, and 1979-87 Imperial Valley earthquakes which are forming a basis for much of the US studies for the case history volume. USGS has conducted several investigations of liquefaction including subsurface drilling and soundings following the 1989 Loma Prieta earthquake. Additional subsurface investigations are planned for the coming year. Most of this information is not yet published. Dr Wieczorek suggested that investigators from USGS be invited to present their results at future workshops and that USGS should be encouraged to facilitate publication of compiled information that would compliment the studies being conducted by the joint Japan-US effort.

Work is in progress in both the Japan and the US to analyze the compiled data in order to develop improved empirical predictive correlations. Analyses are also being made to develop and verify analytical predictive techniques (see report from Group 2). As part of these studies, ground-failure mechanisms and factors controlling ground displacement are being investigated.

It is very probable that more information will be required to adequately develop empirical criteria and validate analytical techniques. To accomplish this need, it is likely that selected case history sites may be identified for further investigation including more detailed subsurface investigation to provide the required information.

The present work has concentrated on sites where significant ground displacements have occurred. Some additional case histories may be needed at liquefaction sites where displacement did not occur. This information is required to verify non-displacement conditions.

More and improved case histories from liquefaction and ground displacement occurrences are needed to validate analytical procedures and refine empirical correlations. To assure that this needed information is developed, the following suggestions might be considered.

1. More instrument sites are needed in liquefaction prone areas. Such sites might include devices for monitoring time histories of displacement as well as ground motions and pore pressures. At present, the Cholame Valley site near Parkfield, California, is the only instrumented site that is operational. The pore-pressure transducers at the Wildlife site in the Imperial Valley are inoperative. Thus only ground motion data would be recorded in the event of another of the frequent earthquakes that strike that part of California. Kokusho (1988) reports that 9 sites in Japan have been instrumented with both accelerometers and pore-pressure transducers. Most sites have 3 or more pore-pressure measuring devices.

2. Monitored sites without expensive electrical instrumentation might also be considered. Such sites could be equipped with surveyed points and inclinometer casings to provide three dimensional delineation of ground displacements.

3. Pre-earthquake aerial photography might be taken of pertinent localities of probable liquefaction. The photographs should be at large scale and with sufficient ground control to facilitate accurate measurement of ground displacements.

It is the general consensus of those attending the working group discussion that personal contacts and exchanges of provided during this and past Workshops have been very beneficial to research progress in understanding large ground deformations associated with liquefaction. The working group encourages the continuance of programs, such as the workshops, to facilitate continued exchange of information in the future.

Reference:

Kokusho, T., 1988, "Japanese Experiences on Test Site Studies," Workshop on National Test Sites for Earthquake Engineering and Geotechnical Engineering Research, University of New Hampshire, unpublished workshop report.

THIRD JAPAN-U.S. WORKSHOP ON EARTHQUAKE RESISTANT DESIGN OF LIFELINE FACILITIES AND
COUNTERMEASURES FOR SOIL LIQUEFACTION

REPORT FROM WORKING GROUP NO. 2:
MODELING LARGE GROUND DEFORMATION

<u>Working Group Members:</u>

<u>From Japan</u>	<u>From United States</u>		<u>Other International</u>
N. Yoshida[a]	R.	Dobry[a]	J. Murria (Venezuela)
M. Miyajima	A.	Elgamal	L. Finn (Canada)
N. Ohbo	J.H.	Prevost	
I. Towhata[a]	M.	Vucetic	
	B.	Kutter	
	G.	Castro	
	I.	Idriss	
	J.A.	Egan	
	Y.	Moriwaki	
	L.	Mejia	
	S.	Vahdani	
	H.E.	Stewart[a]	

a - Group Leaders

INTRODUCTION

During the workshop, Working Group 2 met to review current progress and to
define future directions and needs related to modeling of large ground deforma-
tions. The goal of this working group is to develop accepted site-specific
analytical techniques to predict the value and spatial pattern of ground deforma-
tions for a given earthquake shaking, in the absence of structures, i.e. the far
field. The key topical areas that will be addressed in the Guidelines were
identified and discussed.

The first important topical area relevant to the development of sound
analytical modeling must necessarily include a definition of the physical
mechanisms responsible for permanent ground deformations. The mechanisms are
mostly associated with gravity, although other contributing factors could be
present. Mechanistic effects that play important roles include, but may not be
limited to, gravity and seismic stresses per Newmark-type analyses, the effects
of delayed deformations, the roles of subsurface flow and the redistribution of
pore water pressures, shear strength reduction, creep, and progressive failure.
Another important topic relates to the distribution of shear strains within the
liquefied soil mass. The Guidelines will address the above mechanisms, with
emphasis on the physics of liquefaction-induced ground deformations.

A second topical area relevant to accurate analytical modeling relates to
specific site and earthquake parameters. These parameters must be measurable
or at least realistically determined. Four groupings of site parameters were
identified. The first group relates to earthquake shaking. The earthquake
shaking must be quantified as to the level, frequency content and duration.
The shape of the time record is an important factor as well, since unequal cyclic

intensities affect the ground response. The second grouping of site parameters revolve around the specifics of surface and subsurface topography and slope, the thickness and depth of liquefiable layers, and the presence of other layered features. Although these parameters can be quantified readily, the importance of subtle differences and features must be addressed. The third grouping of site and earthquake parameters relates to the other site properties not specifically addressed in the second grouping. These include the groundwater conditions, including both the location of the free surface and any subsurface flow conditions. Geologic features such as age, seismic history, cementation, stress history and initial stresses, and the effects of human activities are known to influence site response, but have not been fully quantified. The relative importance of all these factors needs to be understood so that site-specific differences in ground movement can be explained. The fourth grouping of site specific parameters consists of fundamental soil properties. In addition to simple descriptors such as grain size and unit weights, we must be able to account for the nonlinear cyclic stress-strain-strength properties, especially when dealing with large strains. Important properties necessary for accurate modeling also include hydraulic conductivity, compressibility, in-situ lateral stresses, and how these properties change during cyclic loading.

The third topical area identified during the Working Group session that will be included in the Guidelines is devoted to the general analytical methods that are available. Analytical methods for large ground deformation can be classified broadly into three groups: 1) two-phase effective stress, 2) total stress with reduced stiffness, and 3) displacement pattern or geometric methods. Within these broad categories there are several features that should be included in a comprehensive approach. These features relate to effects that can occur during the earthquake, such as sliding, and those that can occur following the motion. The Guidelines should include a description of what methods are available currently, the limitations imposed by small deformation theory versus more complete large deformation formulations, the benefits of one-, two-, and three-dimensional formulations, and the benefits and drawbacks of more complex approaches. The reliability of current methods must be addressed, focusing on how models have been used in the past and how well they agree with case history results.

The fourth topical area that will be included in the Guidelines deals with the role of physical modeling. Physical modeling, such as done using a centrifuge or shake table, is important to help calibrate analytical techniques and validate analytical approaches, augment case history studies, and to define and identify displacement mechanisms not covered by current analysis procedures. The Guidelines will serve to define what is an acceptable physical model. Scale effects will be discussed in light of the combination of model scales and gravitational accelerations suitable for centrifuges and shake tables.

The fifth topical area for inclusion in the Guidelines deals with the utility of laboratory- and field-test-based soil properties. The important soil properties necessary for accurate modeling will be identified. Critical issues from a property standpoint are: 1) what are the important properties, 2) how do we obtain reliable values, 3) how do we account for the level of stress intensity for physical modeling testing, e.g., low stress level for shake table versus high stress level for centrifuge, and 4) how reliable are the properties determined either by laboratory or field methods.

In addition to the specific topical areas discussed, the Guidelines will

644

include sections that summarize the analytical contributions made by both the Japanese and U.S. sides during the First, Second, and Third Workshops. These summaries will set the stage for where we are going based on what is available currently. The contributions supplied by Working Group 2 to the Guidelines will include recommendations for practicing engineers, recommendations for future research, and a consensual approach towards the development of rational analytical modeling techniques.

Third Japan–U.S. Workshop on Earthquake
Resistant Design of Lifeline Facilities and
Countermeasure for Soil Liquefaction

Report from Working Group No. 3
Earthquake Resistant Design

Working Group Members

From Japan	From United States	From Venezuela
I. Katayama[a]	M. O'Rourke[a]	J. Abi-Saab
N. Kaizu	T. Ariman	N. Mode
Y. Nojiri	A. Goldschmidt	
N. Suzuki	D. Honegger	
	H. Hwang	
	C.-H. Lee	
	C. Ng	
	A. Thompson	

a: group leaders

The Working Group concentrated on updating and revising a 33 page draft chapter on Seismic Resistant Design which was prepared after the Second U.S.–Japan Workshop. The draft chapter had four sections. The first three sections dealt with specific systems namely Buried Pipelines, Quay Walls and Pile Foundations, while the fourth section contained general information on the Probabilistic Approach which could be applied to any specific system. The working group decided to expand the draft chapter by including a section on Permanent Ground Deformation (PGD) affects on Tunnels, Vertical Shafts and Laterals, and short sections on Storage Tanks and Above Ground Piping.

Buried Pipelines

The working group decided to modify the Buried Pipeline section of the draft chapter in the following manner:

- shorten the material on continuous pipelines subject to abrupt PGD but include reference to the Finite Element approach.

- revise the material on beam buckling of continuous pipeline by including recent work by Meyersohn and O'Rourke.

- eliminate the material on coninuous buried pipelines subject to distributed longitudinal PGD.

- include USX test data on continuous pipe with welded slip joints.

- increase slightly the material on segmented pipe response to abrupt PGD.

- reduce by about 50% the material on continuous pipe subjected to distributed transverse PGD.

- expand the material on continuous pipe subject to distributed longitudinal PGD by including recent research results.

- expand the material on segmented pipe subject to distributed transverse and longitudinal PGD by including recent research results.

- expand the material on elbows, tees etc. by including recent research results.

Quay Walls and Pile Foundations

The working group leaders have asked G. Gazetas and H. Steward to review and revise the sections on Quay Walls and Pile Foundations, respectively, in the draft chapter.

Probabilistic Approach

The working group decided to expand this section of the draft chapter by including, among other items, data which Katayama presented at the 3rd Soil Dynamics and Earthquake Engineering conference in Mexico City.

Design Recommendations

The working group felt that the chapter on Seismic Resistant Design should also contain design recommendations for PGD. General recommendation proposed for segmented or continuous pipe were:

- ductile materials
- axial expansion/contraction and rotational capability for segmented pipe joints
- joint details for continuous pipe which avoid stress risers.

For continuous pipe subject to abrupt PGD (fault crossing), the proposed recommendations were

- place line in tension
- shallow burial, sloped sidewalls and/or loose compressible backpacking
- use materials or wraps with low coefficient of friction at soil–pipeline interface.
- for steel pipe, use steels with curvilinear stress–strain relationship.
- if pipeline is constrained by right–of–way consideration such that fault movement induces compression, increase wall thickness and cross fault as close to right angle as possible.

For PGD which induces net compression in a pipeline, the working group noted that beam buckling is preferable to wrinkling (local buckling). However beam buckling requires small diameters, and shallow burial which may be difficult to achieve.

THIRD JAPAN-U.S. WORKSHOP ON EARTHQUAKE RESISTANT DESIGN OF LIFELINE
FACILITIES AND COUNTERMEASURES FOR SOIL LIQUEFACTION

REPORT FROM WORKING GROUP NO. 4:
EARTHQUAKE COUNTERMEASURES AND EMERGENCY RESPONSE

Working Group Members:

From Japan	From United States	Other International
H. Hasegawa	F. Blackburn	G. Ayala (Mexico)
F. Miura[a]	T. Dickerman	E. Gajardo (Venezuela)
H. Suzuki	R. Eguchi	J. Murria (Venezuela)
	J. Isenberg	
	G. Martin[a]	
	L. Mualchin	
	J. O'Rourke	
	C. Scawthorn	

a - Group Leaders

INTRODUCTION

During the workshop, Working Group 4 met to review progress since the 2nd Workshop, and to define the scope and context of the final Technical Summary of the Group. At the 2nd Workshop, discussions focused on countermeasure methods. At that time, three categories of countermeasures were identified, namely:

1. Dispersion of critical lifeline facilities.

2. Facility design or retrofit to accommodate predicted liquefaction induced large deformations.

3. Site remediation through ground modification or stabilizing measures.

The summary report on these topics resulting from the 2nd Workshop primarily addressed the topic of site remediation, particularly in-situ ground improvement methods. The concept of dispersion of lifeline facilities as a countermeasure method is closely linked with the application of risk analyses and operational and emergency plans to accommodate a limited number of failures. This approach was discussed further during the group working sessions at this workshop. Facility design or retrofit to accommodate large deformations is closely related to Working Group 3 recommendations on approaches to earthquake resistant design. Consequently, this topic was not addressed in depth during Working Group 4 discussions.

The additional topic of Emergency Response was added to the scope of the Group's discussions for this workshop, and can be regarded as a form of "counter-measure". Problems discussed during the workshop in relation to emergency response covered a broad range of topics including the roles of microzonation and risk analyses in facilitating emergency planning, case histories resulting from the Loma Prieta earthquake, and the problem of locating damage in buried pipelines.

In summarizing discussions as a prelude to preparation of a final summary report covering the 1st, 2nd, and 3rd workshops, the following principal report sections were proposed:

1. General Introduction

2. Earthquake Countermeasures

3. Emergency Response

4. Conclusions, Recommendations and Research Needs

5. References

Comments related to the technical content of Sections 2 and 3 arising from group discussions and proposals for the content of our final report, are summarized below.

EARTHQUAKE COUNTERMEASURES

Group discussions were summarized under the following headings:

Site Remediation

The technical content of the Countermeasures section in our final report will encompass the existing summary report prepared after the 2nd workshop, which discusses site remediation and the various in-situ ground improvement methods presently available. The report provides guidelines to the selection of appropriate methods depending on site conditions, and references case histories based on both U.S. and Japanese experience.

Facility Improvement

Although facility improvement is closely related to design methods as covered by Working Group 3, specific comments will be made on structural retrofit techniques that have either been used or proposed to strengthen or prevent damage in the event of large ground deformations. For example, specific comments will be given on design countermeasures for pipelines crossing faults.

Case Histories

The Loma Prieta earthquake and recent Japanese earthquakes have provided specific case histories where countermeasures have been successfully used to prevent damage from large ground deformations. Of particular interest are cases where ground improvement has prevented ground deformation in a specific area, whereas unimproved adjacent areas have undergone liquefaction induced large displacements. Examples will be cited where this has occurred.

Role of Risk Studies

Risk studies were seen by the working group as playing an important role in supporting both the approach to and expediting countermeasures. In the first instance, they provide data to help set priorities for countermeasures. Secondly, they can provide economic evaluations (cost/benefit ratios) and related

incentives for action. Thirdly, they provide the means for optimization of a countermeasure approach based on dispersion of critical facilities. The final working group report will provide further commentary on all three aspects cited above. In addition, experiences from both the U.S. and Japanese perspective will be provided.

EMERGENCY RESPONSE

Group discussions were summarized under the following headings:

Case Histories

To illustrate the role of emergency planning and emergency response as a form of countermeasure (with respect to liquefaction induced ground failures), three specific case histories were suggested:

1. Experience in San Francisco as a result of the Loma Prieta earthquake, particularly that of the Water, Fire and Utility Departments.

2. Emergency planning in Japan in preparation for a potential magnitude 8 earthquake offshore of the Tokai region.

3. Contingency planning for the liquefaction prone Western Venezuela oil fields.

A commentary on emergency planning or response for the three cases cited above is planned for our final report.

Microzonation

Microzonation is seen as a basic tool for risk analyses and related emergency response planning. Whereas major advances have been made over the past 20 years, more work is needed to quantify liquefaction deformation hazards on the broader regional scale used for microzonation (versus site specific studies). More detailed zonation is required which in turn requires a better understanding of the relationship between liquefaction and deformation potential. The importance of such tools needs to be emphasized to administrators involved in either land use planning or emergency response. Comments on the value of microzonation in this regard, from both a U.S. and a Japanese perspective, are planned for our final report.

Role of Risk Studies

In the context of emergency planning and response, lifeline risk studies encompassing a range of modeling techniques such as those related to defining seismic hazard and component and system vulnerability, can play a major role ensuring survival of key systems. When linked with analytical models for decision making, such studies have the potential for providing the means for:

1. Optimizing the location of instrumentation systems

2. Prioritizing emergency response resources

3. Allowing rapid assessment of the effects of damage on system performance

4. Providing a more structured approach to overall planning

5. Communicating the significance of damage scenarios to city administrators

Our summary report will document current thinking and publications relevant to this approach.

Pipeline Instrumentation

Damage to pipelines in San Francisco, as a result of ground liquefaction and deformations occurring during the Loma Prieta earthquake, highlighted the problem of rapidly locating damaged and leaking buried pipelines. This led to group discussions on the need for active monitoring systems to overcome this problem. Further comment on this problem is planned in the final report.

RESEARCH NEEDS

A number of research needs were identified and discussed during Working Group meetings and will be summarized in the final report. A strong emphasis was placed on the need to focus research effort on specific problems of high priority, and to ensure studies lead to practical and cost effective solutions. Hopefully in this way, implementation of research conclusions can show early results and benefits, and hence generate support for continued work.

WORKSHOP PARTICIPANTS

PARTICIPANTS

U.S.

Teoman Ariman
College of Eng. & Applied Science

Clifford Astill
National Science Foundation

J.P. Bardet
University of Southern California

Steve Bartlett
Brigham Young University

Mohamed Baziar
Rensselaer Polytechnic Institute

Michael Bennett
U.S. Geological Survey

Frank T. Blackburn
San Francisco Fire Department

Gonzalo Castro
GEI Consultants

James A. Clark
Pacific Gas and Electric Co.

Thomas S. Dickerman
San Francisco Water Department

Ricardo Dobry
Rensselaer Polytechnic Institute

John A. Egan
Geomatrix Consultants

Ronald T. Eguchi
Dames & Moore

Ahmed Elgamal
Rensselaer Polytechnic Institute

George Gazetas
State Univ. of New York at Buffalo

Adlai Goldschmidt
CALTRANS

Ted Gowdy
Cornell University

Robert Hayden
Hayward Baker

Thomas Holzer
U.S. Geological Survey

Douglas G. Honegger
EQE Engineering

Kathy Howe
City of San Francisco

Howard H.M. Hwang
Memphis State University

I.M. Idriss
University of California at Davis

Jeremy Isenberg
Weidlinger Associates

Catherine Keane
Princeton University

Mahmoud Khater
EQE Engineering

Bruce L. Kutter
University of California at Davis

Chih-Hung Lee
Pacific Gas and Electric Company

James R. Lynch
San Francisco Fire Department

Geoffrey Martin
University of Southern California

Lelio H. Mejia
Woodward-Clyde Consultants

W.D. Meyersohn
Cornell University

James K. Mitchell
University of California

M. Miyajima
Cornell University

Yoshi Moriwaki
Woodward-Clyde Consultants

Frank Moss
City of San Francisco

Lalliana Mualchin
CALTRANS

Charles Ng
City of San Francisco

Andrew K. Nielsen
San Francisco Fire Department

John E. O'Rourke
Woodward-Clyde Consultants

Michael J. O'Rourke
Rensselaer Polytechnic Institute

Thomas D. O'Rourke
Cornell University

Jonathan Pease
Cornell University

Jean Prevost
Princeton University

J. David Rogers
Rogers/Pacific

Bruce Roth
GAI Consultants, Inc.

Charles Scawthorn
EQE Inc.

Raymond B. Seed
University of California at Berkeley

Masanobu Shinozuka
National Center for Earthquake
   Engineering Research

Harry E. Stewart
Cornell University

Mohamed Succarieh
Rensselaer Polytechnic Institute

Henry Taylor
Harding Lawson Associates

Alan Thompson
East Bay Municipal Utility District

Shahriar Vahdani
Harding Lawson Associates

Mladen Vucetic
University of California at Los Angeles

Gerald F. Wieczorek
U.S. Department of the Interior

T. Leslie Youd
Brigham Young University

Sherman Yu
San Francisco Clean Water Program

George Zorapapel
University of California at Los Angeles

Japanese

Masanobu Adachi
Tokyo Electric Power Serv. Co., Inc.

Masanori Hamada
Tokai University

Hisashi Hasegawa
Nippon Steel Corporation

Masaru Hoshiya
Musashi Institute of Technology

Nobuhiro Kaizu
The Tokyo Electric Power, Inc.

Ikuo Katayama
The Tokyo Electric Power
  Serv. Co., Inc.

Keizaburo Kubo
University of Tokyo

Naoyuki Masuda
NKK, Inc.

Fusanori Miura
Yamaguchi University

Koichi Murakami
NTT

Syunji Nagamachi
NTT

Tomoaki Nakayama
NTT

Yohichi Nojiri
Kajima Institute of Construction Tech.

Naoto Ohbo
Kajima Institute of Construction Tech.

Kiyotaka Satoh
Central Research Inst. of Electric
  Power Industry

Katsumi Shimizu
Shimizu Construction Co. Ltd.

Hideyo Suzuki
The Tokyo Electric Power Co., Inc.

Nobuhisa Suzuki
NKK

Yoshihiro Tanaka
Shinozuka Research Institute

Takashi Tazoh
Shimizu Construction Co., Ltd.

Ikuo Towhata
University of Tokyo

Seiji Uehara
Sumitomo Construction Co., Ltd.

Kazue Wakamatsu
Waseda University

Susumu Yasuda
Kyushu Institute of Technology

Nozomu Yoshida
Sato Kogyo Co., Ltd.

Other International

J. Abi Saab
MARAVEN, S.A.

Gustavo Ayala
Instituto de Ingenieria, UNAM

W.D. Liam Finn
University of British Columbia

Nicolino Mode
INTEVEP, S.A.

Juan Murria
MARAVEN, S.A.

Enrique Gajardo Wolff
INTEVEP, S.A.

NATIONAL CENTER FOR EARTHQUAKE ENGINEERING RESEARCH
LIST OF TECHNICAL REPORTS

The National Center for Earthquake Engineering Research (NCEER) publishes technical reports on a variety of subjects related to earthquake engineering written by authors funded through NCEER. These reports are available from both NCEER's Publications Department and the National Technical Information Service (NTIS). Requests for reports should be directed to the Publications Department, National Center for Earthquake Engineering Research, State University of New York at Buffalo, Red Jacket Quadrangle, Buffalo, New York 14261. Reports can also be requested through NTIS, 5285 Port Royal Road, Springfield, Virginia 22161. NTIS accession numbers are shown in parenthesis, if available.

NCEER-87-0001   "First-Year Program in Research, Education and Technology Transfer," 3/5/87, (PB88-134275/AS).

NCEER-87-0002   "Experimental Evaluation of Instantaneous Optimal Algorithms for Structural Control," by R.C. Lin, T.T. Soong and A.M. Reinhorn, 4/20/87, (PB88-134341/AS).

NCEER-87-0003   "Experimentation Using the Earthquake Simulation Facilities at University at Buffalo," by A.M. Reinhorn and R.L. Ketter, to be published.

NCEER-87-0004   "The System Characteristics and Performance of a Shaking Table," by J.S. Hwang, K.C. Chang and G.C. Lee, 6/1/87, (PB88-134259/AS). This report is available only through NTIS (see address given above).

NCEER-87-0005   "A Finite Element Formulation for Nonlinear Viscoplastic Material Using a Q Model," by O. Gyebi and G. Dasgupta, 11/2/87, (PB88-213764/AS).

NCEER-87-0006   "Symbolic Manipulation Program (SMP) - Algebraic Codes for Two and Three Dimensional Finite Element Formulations," by X. Lee and G. Dasgupta, 11/9/87, (PB88-219522/AS).

NCEER-87-0007   "Instantaneous Optimal Control Laws for Tall Buildings Under Seismic Excitations," by J.N. Yang, A. Akbarpour and P. Ghaemmaghami, 6/10/87, (PB88-134333/AS).

NCEER-87-0008   "IDARC: Inelastic Damage Analysis of Reinforced Concrete Frame - Shear-Wall Structures," by Y.J. Park, A.M. Reinhorn and S.K. Kunnath, 7/20/87, (PB88-134325/AS).

NCEER-87-0009   "Liquefaction Potential for New York State: A Preliminary Report on Sites in Manhattan and Buffalo," by M. Budhu, V. Vijayakumar, R.F. Giese and L. Baumgras, 8/31/87, (PB88-163704/AS). This report is available only through NTIS (see address given above).

NCEER-87-0010   "Vertical and Torsional Vibration of Foundations in Inhomogeneous Media," by A.S. Veletsos and K.W. Dotson, 6/1/87, (PB88-134291/AS).

NCEER-87-0011   "Seismic Probabilistic Risk Assessment and Seismic Margins Studies for Nuclear Power Plants," by Howard H.M. Hwang, 6/15/87, (PB88-134267/AS).

NCEER-87-0012   "Parametric Studies of Frequency Response of Secondary Systems Under Ground-Acceleration Excitations," by Y. Yong and Y.K. Lin, 6/10/87, (PB88-134309/AS).

NCEER-87-0013   "Frequency Response of Secondary Systems Under Seismic Excitation," by J.A. HoLung, J. Cai and Y.K. Lin, 7/31/87, (PB88-134317/AS).

NCEER-87-0014   "Modelling Earthquake Ground Motions in Seismically Active Regions Using Parametric Time Series Methods," by G.W. Ellis and A.S. Cakmak, 8/25/87, (PB88-134283/AS).

NCEER-87-0015   "Detection and Assessment of Seismic Structural Damage," by E. DiPasquale and A.S. Cakmak, 8/25/87, (PB88-163712/AS).

NCEER-87-0016   "Pipeline Experiment at Parkfield, California," by J. Isenberg and E. Richardson, 9/15/87, (PB88-163720/AS). This report is available only through NTIS (see address given above).

NCEER-87-0017   "Digital Simulation of Seismic Ground Motion," by M. Shinozuka, G. Deodatis and T. Harada, 8/31/87, (PB88-155197/AS). This report is available only through NTIS (see address given above).

NCEER-87-0018   "Practical Considerations for Structural Control: System Uncertainty, System Time Delay and Truncation of Small Control Forces," J.N. Yang and A. Akbarpour, 8/10/87, (PB88-163738/AS).

NCEER-87-0019   "Modal Analysis of Nonclassically Damped Structural Systems Using Canonical Transformation," by J.N. Yang, S. Sarkani and F.X. Long, 9/27/87, (PB88-187851/AS).

NCEER-87-0020   "A Nonstationary Solution in Random Vibration Theory," by J.R. Red-Horse and P.D. Spanos, 11/3/87, (PB88-163746/AS).

NCEER-87-0021   "Horizontal Impedances for Radially Inhomogeneous Viscoelastic Soil Layers," by A.S. Veletsos and K.W. Dotson, 10/15/87, (PB88-150859/AS).

NCEER-87-0022   "Seismic Damage Assessment of Reinforced Concrete Members," by Y.S. Chung, C. Meyer and M. Shinozuka, 10/9/87, (PB88-150867/AS). This report is available only through NTIS (see address given above).

NCEER-87-0023   "Active Structural Control in Civil Engineering," by T.T. Soong, 11/11/87, (PB88-187778/AS).

NCEER-87-0024   Vertical and Torsional Impedances for Radially Inhomogeneous Viscoelastic Soil Layers," by K.W. Dotson and A.S. Veletsos, 12/87, (PB88-187786/AS).

NCEER-87-0025   "Proceedings from the Symposium on Seismic Hazards, Ground Motions, Soil-Liquefaction and Engineering Practice in Eastern North America," October 20-22, 1987, edited by K.H. Jacob, 12/87, (PB88-188115/AS).

NCEER-87-0026   "Report on the Whittier-Narrows, California, Earthquake of October 1, 1987," by J. Pantelic and A. Reinhorn, 11/87, (PB88-187752/AS). This report is available only through NTIS (see address given above).

NCEER-87-0027   "Design of a Modular Program for Transient Nonlinear Analysis of Large 3-D Building Structures," by S. Srivastav and J.F. Abel, 12/30/87, (PB88-187950/AS).

NCEER-87-0028   "Second-Year Program in Research, Education and Technology Transfer," 3/8/88, (PB88-219480/AS).

NCEER-88-0001   "Workshop on Seismic Computer Analysis and Design of Buildings With Interactive Graphics," by W. McGuire, J.F. Abel and C.H. Conley, 1/18/88, (PB88-187760/AS).

NCEER-88-0002   "Optimal Control of Nonlinear Flexible Structures," by J.N. Yang, F.X. Long and D. Wong, 1/22/88, (PB88-213772/AS).

NCEER-88-0003   "Substructuring Techniques in the Time Domain for Primary-Secondary Structural Systems," by G.D. Manolis and G. Juhn, 2/10/88, (PB88-213780/AS).

NCEER-88-0004   "Iterative Seismic Analysis of Primary-Secondary Systems," by A. Singhal, L.D. Lutes and P.D. Spanos, 2/23/88, (PB88-213798/AS).

NCEER-88-0005   "Stochastic Finite Element Expansion for Random Media," by P.D. Spanos and R. Ghanem, 3/14/88, (PB88-213806/AS).

NCEER-88-0006   "Combining Structural Optimization and Structural Control," by F.Y. Cheng and C.P. Pantelides, 1/10/88, (PB88-213814/AS).

NCEER-88-0007   "Seismic Performance Assessment of Code-Designed Structures," by H.H-M. Hwang, J-W. Jaw and H-J. Shau, 3/20/88, (PB88-219423/AS).

NCEER-88-0008   "Reliability Analysis of Code-Designed Structures Under Natural Hazards," by H.H-M. Hwang, H. Ushiba and M. Shinozuka, 2/29/88, (PB88-229471/AS).

NCEER-88-0009   "Seismic Fragility Analysis of Shear Wall Structures," by J-W Jaw and H.H-M. Hwang, 4/30/88, (PB89-102867/AS).

NCEER-88-0010   "Base Isolation of a Multi-Story Building Under a Harmonic Ground Motion - A Comparison of Performances of Various Systems," by F-G Fan, G. Ahmadi and I.G. Tadjbakhsh, 5/18/88, (PB89-122238/AS).

NCEER-88-0011   "Seismic Floor Response Spectra for a Combined System by Green's Functions," by F.M. Lavelle, L.A. Bergman and P.D. Spanos, 5/1/88, (PB89-102875/AS).

NCEER-88-0012   "A New Solution Technique for Randomly Excited Hysteretic Structures," by G.Q. Cai and Y.K. Lin, 5/16/88, (PB89-102883/AS).

NCEER-88-0013   "A Study of Radiation Damping and Soil-Structure Interaction Effects in the Centrifuge," by K. Weissman, supervised by J.H. Prevost, 5/24/88, (PB89-144703/AS).

NCEER-88-0014   "Parameter Identification and Implementation of a Kinematic Plasticity Model for Frictional Soils," by J.H. Prevost and D.V. Griffiths, to be published.

NCEER-88-0015   "Two- and Three- Dimensional Dynamic Finite Element Analyses of the Long Valley Dam," by D.V. Griffiths and J.H. Prevost, 6/17/88, (PB89-144711/AS).

NCEER-88-0016   "Damage Assessment of Reinforced Concrete Structures in Eastern United States," by A.M. Reinhorn, M.J. Seidel, S.K. Kunnath and Y.J. Park, 6/15/88, (PB89-122220/AS).

NCEER-88-0017   "Dynamic Compliance of Vertically Loaded Strip Foundations in Multilayered Viscoelastic Soils," by S. Ahmad and A.S.M. Israil, 6/17/88, (PB89-102891/AS).

NCEER-88-0018   "An Experimental Study of Seismic Structural Response With Added Viscoelastic Dampers," by R.C. Lin, Z. Liang, T.T. Soong and R.H. Zhang, 6/30/88, (PB89-122212/AS).

NCEER-88-0019   "Experimental Investigation of Primary - Secondary System Interaction," by G.D. Manolis, G. Juhn and A.M. Reinhorn, 5/27/88, (PB89-122204/AS).

NCEER-88-0020   "A Response Spectrum Approach For Analysis of Nonclassically Damped Structures," by J.N. Yang, S. Sarkani and F.X. Long, 4/22/88, (PB89-102909/AS).

NCEER-88-0021   "Seismic Interaction of Structures and Soils: Stochastic Approach," by A.S. Veletsos and A.M. Prasad, 7/21/88, (PB89-122196/AS).

NCEER-88-0022   "Identification of the Serviceability Limit State and Detection of Seismic Structural Damage," by E. DiPasquale and A.S. Cakmak, 6/15/88, (PB89-122188/AS).

NCEER-88-0023   "Multi-Hazard Risk Analysis: Case of a Simple Offshore Structure," by B.K. Bhartia and E.H. Vanmarcke, 7/21/88, (PB89-145213/AS).

NCEER-88-0024   "Automated Seismic Design of Reinforced Concrete Buildings," by Y.S. Chung, C. Meyer and M. Shinozuka, 7/5/88, (PB89-122170/AS).

NCEER-88-0025   "Experimental Study of Active Control of MDOF Structures Under Seismic Excitations," by L.L. Chung, R.C. Lin, T.T. Soong and A.M. Reinhorn, 7/10/88, (PB89-122600/AS).

NCEER-88-0026   "Earthquake Simulation Tests of a Low-Rise Metal Structure," by J.S. Hwang, K.C. Chang, G.C. Lee and R.L. Ketter, 8/1/88, (PB89-102917/AS).

NCEER-88-0027   "Systems Study of Urban Response and Reconstruction Due to Catastrophic Earthquakes," by F. Kozin and H.K. Zhou, 9/22/88, (PB90-162348/AS).

NCEER-88-0028   "Seismic Fragility Analysis of Plane Frame Structures," by H.H-M. Hwang and Y.K. Low, 7/31/88, (PB89-131445/AS).

NCEER-88-0029   "Response Analysis of Stochastic Structures," by A. Kardara, C. Bucher and M. Shinozuka, 9/22/88, (PB89-174429/AS).

NCEER-88-0030   "Nonnormal Accelerations Due to Yielding in a Primary Structure," by D.C.K. Chen and L.D. Lutes, 9/19/88, (PB89-131437/AS).

NCEER-88-0031   "Design Approaches for Soil-Structure Interaction," by A.S. Veletsos, A.M. Prasad and Y. Tang, 12/30/88, (PB89-174437/AS).

NCEER-88-0032   "A Re-evaluation of Design Spectra for Seismic Damage Control," by C.J. Turkstra and A.G. Tallin, 11/7/88, (PB89-145221/AS).

NCEER-88-0033   "The Behavior and Design of Noncontact Lap Splices Subjected to Repeated Inelastic Tensile Loading," by V.E. Sagan, P. Gergely and R.N. White, 12/8/88, (PB89-163737/AS).

NCEER-88-0034   "Seismic Response of Pile Foundations," by S.M. Mamoon, P.K. Banerjee and S. Ahmad, 11/1/88, (PB89-145239/AS).

NCEER-88-0035   "Modeling of R/C Building Structures With Flexible Floor Diaphragms (IDARC2)," by A.M. Reinhorn, S.K. Kunnath and N. Panahshahi, 9/7/88, (PB89-207153/AS).

NCEER-88-0036   "Solution of the Dam-Reservoir Interaction Problem Using a Combination of FEM, BEM with Particular Integrals, Modal Analysis, and Substructuring," by C-S. Tsai, G.C. Lee and R.L. Ketter, 12/31/88, (PB89-207146/AS).

NCEER-88-0037   "Optimal Placement of Actuators for Structural Control," by F.Y. Cheng and C.P. Pantelides, 8/15/88, (PB89-162846/AS).

NCEER-88-0038   "Teflon Bearings in Aseismic Base Isolation: Experimental Studies and Mathematical Modeling," by A. Mokha, M.C. Constantinou and A.M. Reinhorn, 12/5/88, (PB89-218457/AS).

NCEER-88-0039   "Seismic Behavior of Flat Slab High-Rise Buildings in the New York City Area," by P. Weidlinger and M. Ettouney, 10/15/88, (PB90-145681/AS).

NCEER-88-0040   "Evaluation of the Earthquake Resistance of Existing Buildings in New York City," by P. Weidlinger and M. Ettouney, 10/15/88, to be published.

NCEER-88-0041   "Small-Scale Modeling Techniques for Reinforced Concrete Structures Subjected to Seismic Loads," by W. Kim, A. El-Attar and R.N. White, 11/22/88, (PB89-189625/AS).

NCEER-88-0042   "Modeling Strong Ground Motion from Multiple Event Earthquakes," by G.W. Ellis and A.S. Cakmak, 10/15/88, (PB89-174445/AS).

NCEER-88-0043   "Nonstationary Models of Seismic Ground Acceleration," by M. Grigoriu, S.E. Ruiz and E. Rosenblueth, 7/15/88, (PB89-189617/AS).

NCEER-88-0044   "SARCF User's Guide: Seismic Analysis of Reinforced Concrete Frames," by Y.S. Chung, C. Meyer and M. Shinozuka, 11/9/88, (PB89-174452/AS).

NCEER-88-0045   "First Expert Panel Meeting on Disaster Research and Planning," edited by J. Pantelic and J. Stoyle, 9/15/88, (PB89-174460/AS).

NCEER-88-0046   "Preliminary Studies of the Effect of Degrading Infill Walls on the Nonlinear Seismic Response of Steel Frames," by C.Z. Chrysostomou, P. Gergely and J.F. Abel, 12/19/88, (PB89-208383/AS).

NCEER-88-0047   "Reinforced Concrete Frame Component Testing Facility - Design, Construction, Instrumentation and Operation," by S.P. Pessiki, C. Conley, T. Bond, P. Gergely and R.N. White, 12/16/88, (PB89-174478/AS).

NCEER-89-0001   "Effects of Protective Cushion and Soil Compliancy on the Response of Equipment Within a Seismically Excited Building," by J.A. HoLung, 2/16/89, (PB89-207179/AS).

NCEER-89-0002   "Statistical Evaluation of Response Modification Factors for Reinforced Concrete Structures," by H.H-M. Hwang and J-W. Jaw, 2/17/89, (PB89-207187/AS).

NCEER-89-0003   "Hysteretic Columns Under Random Excitation," by G-Q. Cai and Y.K. Lin, 1/9/89, (PB89-196513/AS).

NCEER-89-0004   "Experimental Study of 'Elephant Foot Bulge' Instability of Thin-Walled Metal Tanks," by Z-H. Jia and R.L. Ketter, 2/22/89, (PB89-207195/AS).

NCEER-89-0005   "Experiment on Performance of Buried Pipelines Across San Andreas Fault," by J. Isenberg, E. Richardson and T.D. O'Rourke, 3/10/89, (PB89-218440/AS).

NCEER-89-0006   "A Knowledge-Based Approach to Structural Design of Earthquake-Resistant Buildings," by M. Subramani, P. Gergely, C.H. Conley, J.F. Abel and A.H. Zaghw, 1/15/89, (PB89-218465/AS).

NCEER-89-0007   "Liquefaction Hazards and Their Effects on Buried Pipelines," by T.D. O'Rourke and P.A. Lane, 2/1/89, (PB89-218481).

NCEER-89-0008   "Fundamentals of System Identification in Structural Dynamics," by H. Imai, C-B. Yun, O. Maruyama and M. Shinozuka, 1/26/89, (PB89-207211/AS).

NCEER-89-0009   "Effects of the 1985 Michoacan Earthquake on Water Systems and Other Buried Lifelines in Mexico," by A.G. Ayala and M.J. O'Rourke, 3/8/89, (PB89-207229/AS).

NCEER-89-R010   "NCEER Bibliography of Earthquake Education Materials," by K.E.K. Ross, Second Revision, 9/1/89, (PB90-125352/AS).

NCEER-89-0011   "Inelastic Three-Dimensional Response Analysis of Reinforced Concrete Building Structures (IDARC-3D), Part I - Modeling," by S.K. Kunnath and A.M. Reinhorn, 4/17/89, (PB90-114612/AS).

NCEER-89-0012   "Recommended Modifications to ATC-14," by C.D. Poland and J.O. Malley, 4/12/89, (PB90-108648/AS).

NCEER-89-0013   "Repair and Strengthening of Beam-to-Column Connections Subjected to Earthquake Loading," by M. Corazao and A.J. Durrani, 2/28/89, (PB90-109885/AS).

NCEER-89-0014   "Program EXKAL2 for Identification of Structural Dynamic Systems," by O. Maruyama, C-B. Yun, M. Hoshiya and M. Shinozuka, 5/19/89, (PB90-109877/AS).

NCEER-89-0015   "Response of Frames With Bolted Semi-Rigid Connections, Part I - Experimental Study and Analytical Predictions," by P.J. DiCorso, A.M. Reinhorn, J.R. Dickerson, J.B. Radziminski and W.L. Harper, 6/1/89, to be published.

NCEER-89-0016   "ARMA Monte Carlo Simulation in Probabilistic Structural Analysis," by P.D. Spanos and M.P. Mignolet, 7/10/89, (PB90-109893/AS).

NCEER-89-P017   "Preliminary Proceedings from the Conference on Disaster Preparedness - The Place of Earthquake Education in Our Schools," Edited by K.E.K. Ross, 6/23/89.

NCEER-89-0017   "Proceedings from the Conference on Disaster Preparedness - The Place of Earthquake Education in Our Schools," Edited by K.E.K. Ross, 12/31/89, (PB90-207895).

NCEER-89-0018   "Multidimensional Models of Hysteretic Material Behavior for Vibration Analysis of Shape Memory Energy Absorbing Devices, by E.J. Graesser and F.A. Cozzarelli, 6/7/89, (PB90-164146/AS).

NCEER-89-0019   "Nonlinear Dynamic Analysis of Three-Dimensional Base Isolated Structures (3D-BASIS)," by S. Nagarajaiah, A.M. Reinhorn and M.C. Constantinou, 8/3/89, (PB90-161936/AS).

NCEER-89-0020   "Structural Control Considering Time-Rate of Control Forces and Control Rate Constraints," by F.Y. Cheng and C.P. Pantelides, 8/3/89, (PB90-120445/AS).

NCEER-89-0021   "Subsurface Conditions of Memphis and Shelby County," by K.W. Ng, T-S. Chang and H-H.M. Hwang, 7/26/89, (PB90-120437/AS).

NCEER-89-0022   "Seismic Wave Propagation Effects on Straight Jointed Buried Pipelines," by K. Elhmadi and M.J. O'Rourke, 8/24/89, (PB90-162322/AS).

NCEER-89-0023   "Workshop on Serviceability Analysis of Water Delivery Systems," edited by M. Grigoriu, 3/6/89, (PB90-127424/AS).

NCEER-89-0024   "Shaking Table Study of a 1/5 Scale Steel Frame Composed of Tapered Members," by K.C. Chang, J.S. Hwang and G.C. Lee, 9/18/89, (PB90-160169/AS).

NCEER-89-0025   "DYNA1D: A Computer Program for Nonlinear Seismic Site Response Analysis - Technical Documentation," by Jean H. Prevost, 9/14/89, (PB90-161944/AS).

NCEER-89-0026   "1:4 Scale Model Studies of Active Tendon Systems and Active Mass Dampers for Aseismic Protection," by A.M. Reinhorn, T.T. Soong, R.C. Lin, Y.P. Yang, Y. Fukao, H. Abe and M. Nakai, 9/15/89, (PB90-173246/AS).

NCEER-89-0027   "Scattering of Waves by Inclusions in a Nonhomogeneous Elastic Half Space Solved by Boundary Element Methods," by P.K. Hadley, A. Askar and A.S. Cakmak, 6/15/89, (PB90-145699/AS).

NCEER-89-0028   "Statistical Evaluation of Deflection Amplification Factors for Reinforced Concrete Structures," by H.H.M. Hwang, J-W. Jaw and A.L. Ch'ng, 8/31/89, (PB90-164633/AS).

NCEER-89-0029   "Bedrock Accelerations in Memphis Area Due to Large New Madrid Earthquakes," by H.H.M. Hwang, C.H.S. Chen and G. Yu, 11/7/89, (PB90-162330/AS).

NCEER-89-0030   "Seismic Behavior and Response Sensitivity of Secondary Structural Systems," by Y.Q. Chen and T.T. Soong, 10/23/89, (PB90-164658/AS).

NCEER-89-0031   "Random Vibration and Reliability Analysis of Primary-Secondary Structural Systems," by Y. Ibrahim, M. Grigoriu and T.T. Soong, 11/10/89, (PB90-161951/AS).

NCEER-89-0032   "Proceedings from the Second U.S. - Japan Workshop on Liquefaction, Large Ground Deformation and Their Effects on Lifelines, September 26-29, 1989," Edited by T.D. O'Rourke and M. Hamada, 12/1/89, (PB90-209388/AS).

NCEER-89-0033   "Deterministic Model for Seismic Damage Evaluation of Reinforced Concrete Structures," by J.M. Bracci, A.M. Reinhorn, J.B. Mander and S.K. Kunnath, 9/27/89.

NCEER-89-0034   "On the Relation Between Local and Global Damage Indices," by E. DiPasquale and A.S. Cakmak, 8/15/89, (PB90-173865).

NCEER-89-0035   "Cyclic Undrained Behavior of Nonplastic and Low Plasticity Silts," by A.J. Walker and H.E. Stewart, 7/26/89, (PB90-183518/AS).

NCEER-89-0036   "Liquefaction Potential of Surficial Deposits in the City of Buffalo, New York," by M. Budhu, R. Giese and L. Baumgrass, 1/17/89, (PB90-208455/AS).

NCEER-89-0037   "A Determinstic Assessment of Effects of Ground Motion Incoherence," by A.S. Veletsos and Y. Tang, 7/15/89, (PB90-164294/AS).

NCEER-89-0038   "Workshop on Ground Motion Parameters for Seismic Hazard Mapping," July 17-18, 1989, edited by R.V. Whitman, 12/1/89, (PB90-173923/AS).

NCEER-89-0039   "Seismic Effects on Elevated Transit Lines of the New York City Transit Authority," by C.J. Costantino, C.A. Miller and E. Heymsfield, 12/26/89, (PB90-207887/AS).

NCEER-89-0040   "Centrifugal Modeling of Dynamic Soil-Structure Interaction," by K. Weissman, Supervised by J.H. Prevost, 5/10/89, (PB90-207879/AS).

NCEER-89-0041   "Linearized Identification of Buildings With Cores for Seismic Vulnerability Assessment," by I-K. Ho and A.E. Aktan, 11/1/89.

NCEER-90-0001   "Geotechnical and Lifeline Aspects of the October 17, 1989 Loma Prieta Earthquake in San Francisco," by T.D. O'Rourke, H.E. Stewart, F.T. Blackburn and T.S. Dickerman, 1/90, (PB90-208596/AS).

NCEER-90-0002   "Nonnormal Secondary Response Due to Yielding in a Primary Structure," by D.C.K. Chen and L.D. Lutes, 2/28/90.

NCEER-90-0003   "Earthquake Education Materials for Grades K-12," by K.E.K. Ross, 4/16/90.

NCEER-90-0004   "Catalog of Strong Motion Stations in Eastern North America," by R.W. Busby, 4/3/90.

NCEER-90-0005   "NCEER Strong-Motion Data Base: A User Manuel for the GeoBase Release (Version 1.0 for the Sun3)," by P. Friberg and K. Jacob, 3/31/90.

NCEER-90-0006   "Seismic Hazard Along a Crude Oil Pipeline in the Event of an 1811-1812 Type New Madrid Earthquake," by H.H.M. Hwang and C-H.S. Chen, 4/16/90.

NCEER-90-0007   "Site-Specific Response Spectra for Memphis Sheahan Pumping Station," by H.H.M. Hwang and C.S. Lee, 5/15/90.

NCEER-90-0008   "Pilot Study on Seismic Vulnerability of Crude Oil Transmission Systems," by T. Ariman, R. Dobry, M. Grigoriu, F. Kozin, M. O'Rourke, T. O'Rourke and M. Shinozuka, 5/25/90.

NCEER-90-0009   "A Program to Generate Site Dependent Time Histories: EQGEN," by G.W. Ellis, M. Srinivasan and A.S. Cakmak, 1/30/90.

NCEER-90-0010   "Active Isolation for Seismic Protection of Operating Rooms," by M.E. Talbott, Supervised by M. Shinozuka, 6/8/9.

NCEER-90-0011   "Program LINEARID for Identification of Linear Structural Dynamic Systems," by C-B. Yun and M. Shinozuka, 6/25/90.

NCEER-90-0012   "Two-Dimensional Two-Phase Elasto-Plastic Seismic Response of Earth Dams," by A.N. Yiagos, Supervised by J.H. Prevost, 6/20/90.

NCEER-90-0013   "Secondary Systems in Base-Isolated Structures: Experimental Investigation, Stochastic Response and Stochastic Sensitivity," by G.D. Manolis, G. Juhn, M.C. Constantinou and A.M. Reinhorn, 7/1/90.

NCEER-90-0014   "Seismic Behavior of Lightly-Reinforced Concrete Column and Beam-Column Joint Details," by S.P. Pessiki, C.H. Conley, P. Gergely and R.N. White, 8/22/90.

NCEER-90-0015   "Two Hybrid Control Systems for Building Structures Under Strong Earthquakes," by J.N. Yang and A. Danielians, 6/29/90.

NCEER-90-0016   "Instantaneous Optimal Control with Acceleration and Velocity Feedback," by J.N. Yang and Z. Li, 6/29/90.

NCEER-90-0017   "Reconnaissance Report on the Northern Iran Earthquake of June 21, 1990," by M. Mehrain, 10/4/90.

NCEER-90-0018   "Evaluation of Liquefaction Potential in Memphis and Shelby County," by T.S. Chang, P.S. Tang, C.S. Lee and H. Hwang, 8/10/90.

NCEER-90-0019   "Experimental and Analytical Study of a Combined Sliding Disc Bearing and Helical Steel Spring Isolation System," by M.C. Constantinou, A.S. Mokha and A.M. Reinhorn, 10/4/90.

NCEER-90-0020   "Experimental Study and Analytical Prediction of Earthquake Response of a Sliding Isolation System with a Spherical Surface," by A.S. Mokha, M.C. Constantinou and A.M. Reinhorn, 10/11/90.

NCEER-90-0021   "Dynamic Interaction Factors for Floating Pile Groups," by G. Gazetas, K. Fan, A. Kaynia and E. Kausel, 9/10/90.

NCEER-90-0022   "Evaluation of Seismic Damage Indices for Reinforced Concrete Structures," by S. Rodríguez-Gómez and A.S. Cakmak, 9/30/90.

NCEER-90-0023   "Study of Site Response at a Selected Memphis Site," by H. Desai, S. Ahmad, G. Gazetas and M.R. Oh, 10/11/90.

NCEER-90-0024   "A User's Guide to Strongmo: Version 1.0 of NCEER's Strong-Motion Data Access Tool for PCs and Terminals," by P.A. Friberg and C.A.T. Susch, 11/15/90.

NCEER-90-0025   "A Three-Dimensional Analytical Study of Spatial Variability of Seismic Ground Motions," by L-L. Hong and A.H.-S. Ang, 10/30/90.

NCEER-90-0026   "MUMOID User's Guide - A Program for the Identification of Modal Parameters," by S. Rodríguez-Gómez and E. DiPasquale, 9/30/90.

NCEER-90-0027   "SARCF-II User's Guide - Seismic Analysis of Reinforced Concrete Frames," by S. Rodríguez-Gómez, Y.S. Chung and C. Meyer, 9/30/90.

NCEER-90-0028   "Viscous Dampers: Testing, Modeling and Application in Vibration and Seismic Isolation," by N. Makris and M.C. Constantiou, 12/20/90.

NCEER-90-0029   "Soil Effects on Earthquake Ground Motions in the Memphis Area," by H. Hwang, C.S. Lee, K.W. Ng and T.S. Chang, 8/2/90.

NCEER-91-0001   "Proceedings from the Third Japan-U.S. Workshop on Earthquake Resistant Design of Lifeline Facilities and Countermeasures for Soil Liquefaction, December 17-19, 1990," edited by T.D. O'Rourke and M. Hamada, 2/1/91.